BNL--52517

ACTIVITY REPORT

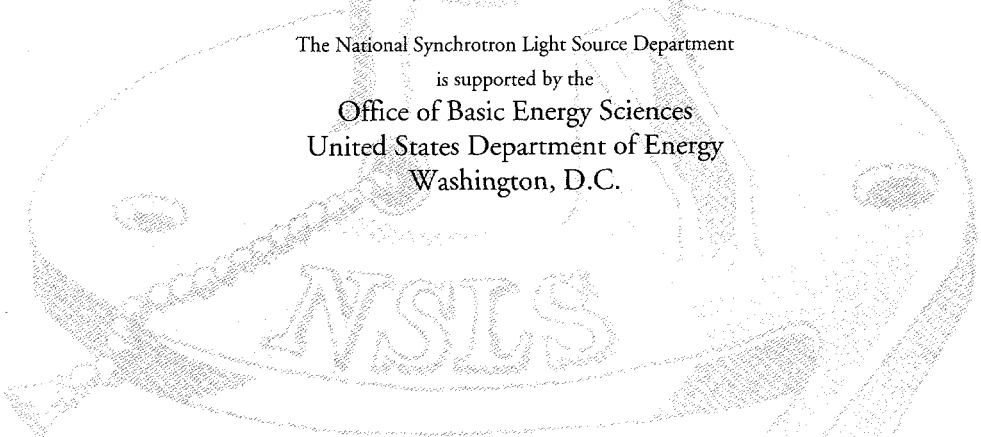
NATIONAL SYNCHROTRON LIGHT SOURCE

(For the period October 1, 1995 through September 30, 1996)

Managing Editor
E.Z. Rothman
Science Editor
J. B. Hastings
Production Assistants
L. Feierabend
L. Rogers
N. Wright

May 1997

The National Synchrotron Light Source Department
is supported by the
Office of Basic Energy Sciences
United States Department of Energy
Washington, D.C.



Brookhaven National Laboratory
Associated Universities, Inc.
Upton, New York 11973-5000

DISTRIBUTION OF THIS DOCUMENT IS UNLIMITED

MASTER

Under Contract No. DE-AC02-76CH00016 with the
United States Department of Energy

DISTRIBUTION OF THIS DOCUMENT IS UNLIMITED

BNL 52517
UC400
(General Energy Research)

Front cover: NEXAFS spectromicrograph of an annealed bilayer of polystyrene (PS) and poly(methyl methacrylate) (PMMA) polymer thin film, acquired with the Stony Brook X1A Scanning Transmission X-ray Microscope. The micrograph, acquired at a photon energy most specific to the C=O bond in the PMMA (288.4 eV), shows the PS to be thick ellipsoidal dispersions within a thin "shell" of PMMA and a thin PMMA layer between the PS dispersions, and elucidates the spinodal decomposition of this constrained system. Experiments and theoretical work on spinodal decomposition of thin films of binary polymer blends indicated large changes in phase behavior and dynamics relative to bulk behavior. Currently used techniques are able to sense growing domain sizes but are unable to sense local two and three dimensional variations within domains. The common assumption that phase separated domains rapidly reach their equilibrium composition and then agglomerate into ever larger domains is not likely to hold. Current and planned STXM measurements will allow us to address this important issue, particularly for polymer systems where heavy metal staining in a TEM is failing, and will provide a critical test for theories of polymer dynamics. Figure courtesy of A. Smith and H. Ade (NCSU) and their co-workers D. Slep (Highlord Chemical), S. Qu, M. Rafailovich, and J. Sokolov (SUNY @ Stony Brook).

DISCLAIMER

This report was prepared as an account of work sponsored by an agency of the United States Government. Neither the United States Government nor any agency thereof, nor any of their employees, nor any of their contractors, subcontractors, or their employees, makes any warranty, express or implied, or assumes any legal liability or responsibility for the accuracy, completeness, or usefulness of any information, apparatus, product, or process disclosed, or represents that its use would not infringe privately owned rights. Reference herein to any specific commercial product, process, or service by trade name, trademark, manufacturer, or otherwise, does not necessarily constitute or imply its endorsement, recommendation, or favoring by the United States Government or any agency, contractor, or subcontractor thereof. The views and opinions of authors expressed herein do not necessarily state or reflect those of the United States Government or any agency, contractor, or subcontractor thereof.

Printed in the United States of America
Available from
National Technical Information Service
U.S. Department of Commerce
5285 Port Royal Road
Springfield, VA 22161

DISCLAIMER

Portions of this document may be illegible in electronic image products. Images are produced from the best available original document.

Introduction

Introduction by the Chairman 2
Michael Hart
Environment, Safety and Health Update 5
William Thomlinson
User Administration Report 7
Eva Z. Rothman
Users' Executive Committee 10
Peter W. Stephens

Science Highlights

Applied Science 16

Biological Sciences 26

Chemical Sciences 32

Geological Sciences 36

Structure of Surfaces and Interfaces 38

Material Sciences 44

Nuclear Physics 57

Instrumentation and Techniques 63

Meetings & Workshops

The 1996 NSLS Annual Users' Meeting 70
Peter W. Stephens
In Situ Applications of X-ray Absorption Fine Structure Workshop 73
Simon R. Bare
Opportunities in Polymer Research using Synchrotron Radiation Workshop 74
Thomas P. Russell
Multiple Wavelength Anomalous Dispersion (MAD) in Protein Crystallography Workshop 78
Lisa J. Keefe and Stephan L. Ginell
Strategy and Methods for Area Detector Data Collection Workshop 79
Alex Darovsky
The Application of Synchrotron Radiation to the Study of Magnetic Materials Workshop 80
Boris Sinkovic
Hard X-ray Precision Fabrication Workshop 81
D. Peter Siddons and Erik Johnson

Operations

VUV Machine 86
Stephen Kramer
VUV Storage Ring Parameters 90
Beamline Technical Improvements 91
Roger Klaffky
X-Ray Ring 94
Roger Klaffky
X-Ray Storage Ring Parameters 97

Projects

The NSLS Source Development Laboratory 100
Erik D. Johnson
The Accelerator Test Facility (ATF) 102
Ilan Ben-Zvi
NSLS Facility Improvements 105
Frank Terrano and Mike Kelly
Insertion Device R&D at X13 106
Peter M. Stefan, Sam Krinsky, and Chi-Chang Kao

Organization

NSLS Advisory Committees 112
NSLS Staff 114
VUV Beamline Guide 117
X-Ray Beamline Guide 121

Research Anthology

Lighting the Way to the Future 132

Abstracts & Publications

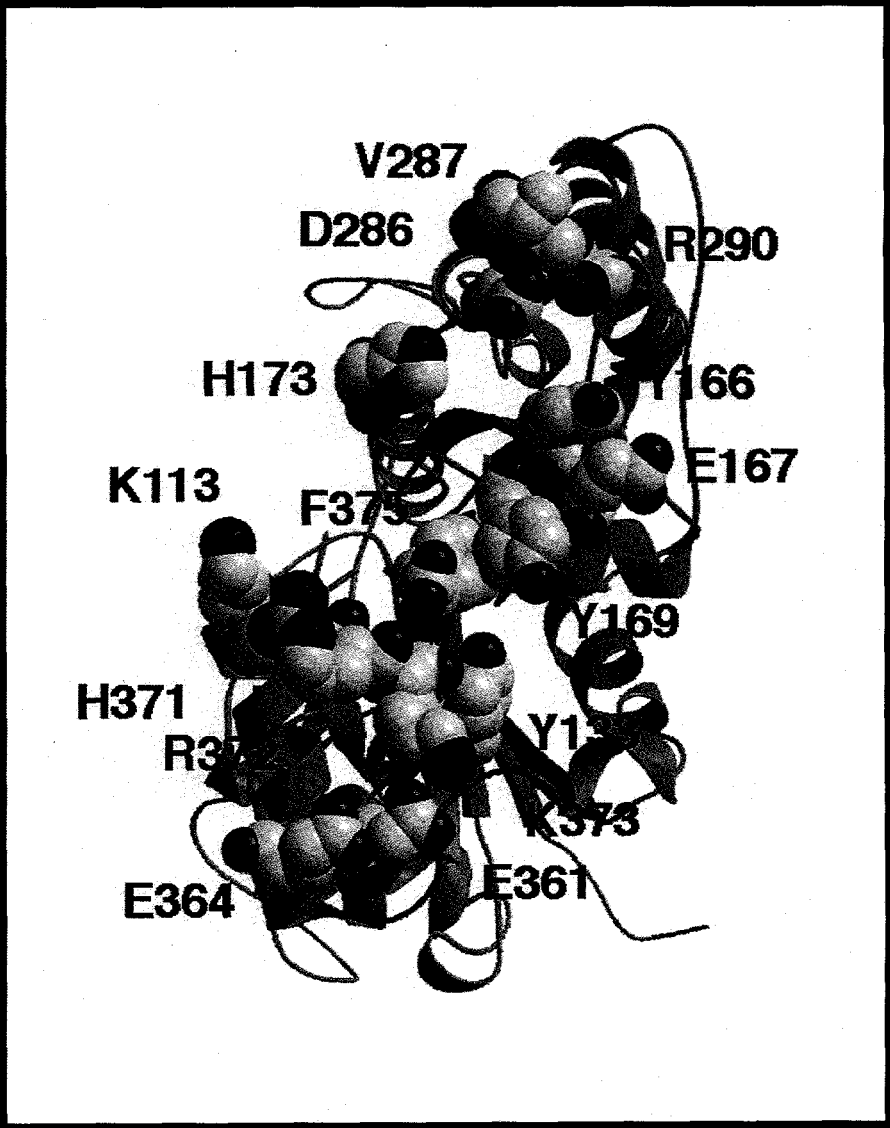
VUV Beamline Abstracts A-1
X-ray Beamline Abstracts B-1
NSLS User Publications C-1
NSLS Staff Publications D-1
BNL Formal and Informal Reports D-6



Beamline X12C: The profilin binding site of actin. On the right is a ribbon depiction of actin displaying the side chains which contact profilin in the profilin-actin complex. On the left, the same contact residues shown in standard atom colors with the outline of the profilin binding site shown in yellow. K.S. Thorn, . . . C.E. Schutt,"The Crystal Structure of a Major Allergin from Plants", *Structure* 5, 19-32 (1997).

ONE

INTRODUCTION



INTRODUCTION

Michael Hart
NSLS Chairman

The hard work done by the synchrotron radiation community, in collaboration with all those using large-scale central facilities during 1995, paid off in FY 1996 through the DOE's Presidential Scientific Facilities Initiative. In comparison with the other DOE synchrotron radiation facilities, the National Synchrotron Light Source benefited least in operating budgets because we were unable to increase our running time beyond 100%- nevertheless, the number of station hours was maintained. The major thrust at Brookhaven came from a 15% increase in budget which allowed the recruitment of seven staff in the beamlines support group and permitted a step increment in the funding of the extremely long list of upgrades; both to the sources and to the beamlines.

During the December 1995 shutdown, the VUV Ring quadrant around U10-U12 was totally reconstructed. New front ends, enabling apertures up to 90 mrad on U10 and U12, were installed. During the year new PRTs were in formation for the infrared beamlines, encouraged by the investment we were able to commit from the initiative funds and by awards from the Scientific Facilities Initiative. A new PRT, specifically for small and wide angle



NSLS Management Group:

(front, from left)
Jerome Hastings, Long-Range/R&D;
Michael Hart, Chairman;
Sam Krinsky, Deputy Chairman;
Marty Woodle, Mechanical Engineering;
Bill Thomlinson, Associate Chairman;

(back, from left)
John Keane, Electrical Systems;
Peter Siddons, Beamline Support/R&D;
Frank Terrano, Assistant to the Chairman;
Richard Heese, Operations;
Ilan Ben-Zvi, Accelerator Test Facility.

x-ray scattering from polymers, will start work on X27C in FY 1997 and existing PRTs on X26C and X9B working on macromolecular crystallography will be joined by new members.

Plans to replace aging radio frequency cavities by an improved design, originally a painfully slow six or eight year project, were brought forward so that the first pair of cavities (half of the project for the X-Ray Ring) will now be installed in FY 1997. Current upgrades to 350 mA initially and to 438 mA later in the X-Ray Ring were set aside due to lack of funds for the necessary thermally robust beryllium windows. The Scientific Facilities Initiative allowed us to purchase all 34 windows in FY 1996 so that the power upgrade will be achieved in FY 1997. Half of the windows were installed during the December 1996 shutdown and the remainder will be installed during the May 1997 shutdown.

The NSLS Phase III upgrade, proposed in March 1994 and validated by DOE in 1995 showed how $22.5M could be used to maximize both the scientific output of the facility and the return on DOE's investment. Sixteen beamlines, four on the VUV Ring and twelve on the X-Ray Ring, could be made state of the art; improvements in beam position monitoring would lead to improved beam stability and reliability; replacement radio frequency cavities would insure reliability; and new narrow gap insertion devices could be developed. In addition 9,400 square feet of sorely needed laboratory and office space could be created on the second floor of the NSLS.

In the *one year* Scientific Facilities Initiative parts of this plan were realized. The results are dramatic; for a tiny investment, we will have *for the first time* a facility-owned general user Marr image plate and a CCD area detector available to optimize bending magnet and insertion device beamlines. Five x-ray beamlines will benefit from new focusing mirrors—impacting on the research of almost 200 users. As mentioned above, the first two new RF cavities will be available in FY 1997. The instrumentation pool will be almost doubled in value and program influence with the addition of a detector and two displex refrigerators.

In addition to the increased facility funding, the Scientific Facilities Initiative provided peer reviewed grants to users for specific beamline upgrades. Twelve user groups secured funds by this mechanism as follows:

Eric S. Jensen for *Ultra High Resolution Angle-Resolved Photoemission Spectrometer*

Malcolm Capel and Robert Sweet for *CCD Detector for Macromolecular Crystallography*

John W. Sutherland for *Monochromators for Elliptically Polarized Wiggler Beamline*

John D. Axe for *Magnets for Neutron and X-Ray Scattering*

L. Doon Gibbs for *Mirror Upgrades for Beamlines X22B,C*

Russell J. Hemley for *High Pressure Infrared Beamline*

Peter Pershan for *Upgrade of Harvard/Brookhaven Liquid Surface X-ray Spectrometer*

Dale Sayers for *Upgrade of Beamline X11A*

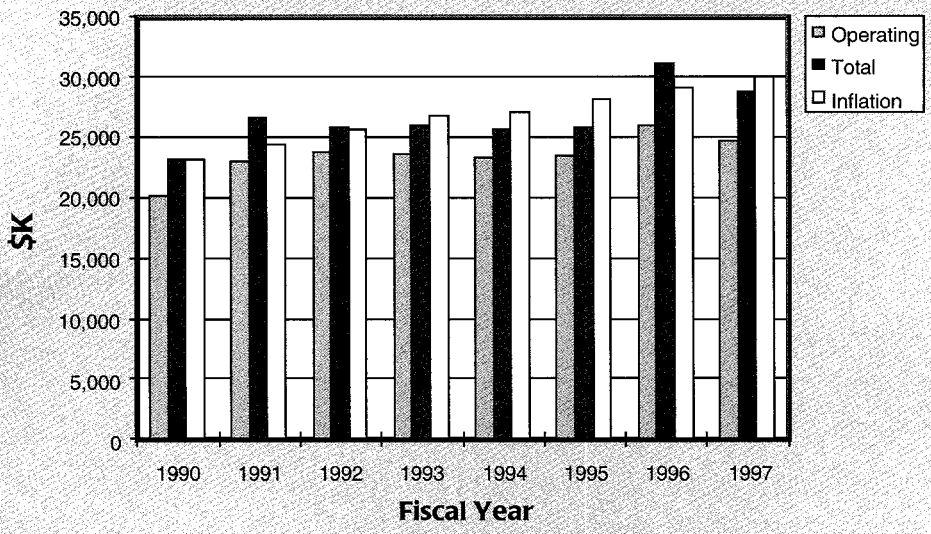
Theodore Madey for *Upgrade for Core-Level Photoemission Spectroscopy*

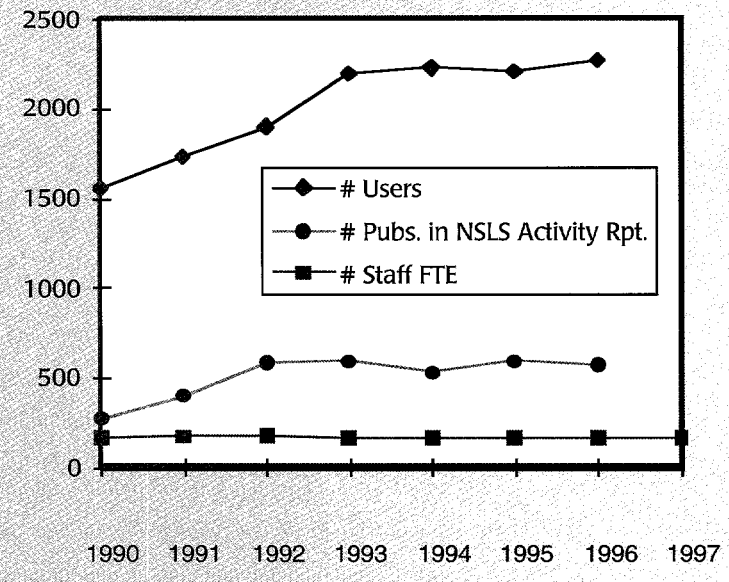
Janos Kirz for *Enhancement of the Scanning Transmission X-ray Microscope Facilities*

David Tanner for *Time-Resolved Far Infrared Spectrometer*

David Heskett for *Upgrade of Beamline X24A with Improved Electron Detector*

After such a glorious year it would be a shame to have to end on a down beat. Next year, however, the FY 1997 budgets once again seem to be below FY 1990 in real terms for NSLS (see figures).





(Above) NSLS Budgets over the past several years.
(Right) Chart showing number of users coming to the NSLS each year, number of publications listed in the Activity Report, and NSLS Staffing levels.

Apart from the individual years FY1991, FY1992 and FY1996 the NSLS budgets for Operations, Capital and Accelerator Repairs Improvements and Maintenance have not kept up with inflation. Level or slightly decreasing budgets lead essentially to constant levels of staffing. This has been so throughout the 1990s when user numbers and the scientific output of the facility have almost doubled.

Now, at the start of 1997, there is good news once again. The political climate is more encouraging for science and technology than it was in the recent past. The Energy Department in October 1996 announced a review, fundamental and far reaching in scope, of the provision by DOE of facilities for synchrotron radiation research in the U.S.A. As a third-generation facility serving research programs over by far the widest spectral range in the world (from 15mm to 3fm wave length), providing 75% of the station hours in the country in FY 1996 and having clear up-grade paths to the future, we anticipate making an exceptionally strong case for reinvestment.

ENVIRONMENT, SAFETY AND HEALTH UPDATE

William Thomlinson
Associate Chairman
NSLS

The ES&H efforts at the NSLS have continued to expand both in response to external pressures and to a more pro-active approach taken by the members of the ES&H group. The result was a year that saw significant progress in updating and expansion of our guiding safety documentation, full realization of the benefits of a well coordinated Tier I safety program, expanded training programs, rapid and thorough response to reportable incidents, active pursuit of increased radiation safety by the ALARA Committee, and expansion of the chemical safety and hazcom programs. Each of these efforts has had a direct impact on safety at the NSLS. Of course, they are all on-going activities which require constant attention. The occasional reportable incidents must always be met with improvements in our operations, education of users and staff in order to avoid recurrences of problems and better training programs. For example, we had an incident in which an unlabeled acid bottle exploded in a storage shed. Fortunately no one was hurt, but we treated the incident with the highest priority and significantly increased our efforts in labeling of chemicals and supplied information to the staff and users on proper handling and storage of acids. The Tier I inspections which look at OSHA and housekeeping types of safety issues are never ending. It seems that we are unable to change human nature. But now the program has efficient methods of following up with cognizant personnel to rectify problems. The shielding of the VUV Ring to decrease levels of radiation (neutron and gamma) to the experimental floor and surrounding offices is well underway. Monitoring of the effectiveness of the first sections will determine the future course of action for the VUV and booster shielding.

Perhaps the highlight of the year was the NSLS participation in a BNL motivated safety stand-down. This activity had several primary purposes: clean-up of the laboratory grounds and buildings, involvement of the entire laboratory staff in maintaining and improving safety, and a follow-up Tier II self-assessment (to be completed in FY 1997). The NSLS management and ES&H group took this effort very seriously. Even though we had had an NSLS staff meeting in which safety was featured, our NSLS safety stand-down consisted of a collective staff meeting followed by separate section meetings. At the stand-down meeting, the two most important issues were the results of a BNL safety questionnaire and a report on personnel radiation monitoring with the new TLD badges. The results of the questionnaire indicated that most NSLS staff members are informed about safety and feel that the NSLS does a very good job. However, it did show that problems exist in certain areas and has given guidance to some of our efforts. Doses measured with the new TLD badges show increased levels being reported above those reported with the old film badges. That was expected since there is a significantly lower threshold of response for the new badges. This data is being used now to improve the general understanding of our sources of radiation and to reinforce our efforts to make sure that all personnel handle the badges properly.

The separate meetings of the sections were intended to allow any staff member to openly discuss or question whatever safety related issues they had. The result was a comprehensive compilation of problems and concerns important to the staff. They ranged from concerns about snow removal, to the desire for more safety training in areas such as electrical safety, to radiation issues and to traffic safety on and off site. Since the meetings, the ES&H staff, with the aid of others, has reviewed each issue and is preparing to answer each question or correct the problem. The results will be distributed to the staff. Along with issues raised by BNL, we will take our lessons learned from the stand-down meetings into account when we prepare our Tier II self-assessment. For example, two of the most common issues raised were safety training of the staff and the need to improve the work habits of personnel. The feeling of many staff members was that safety could be greatly improved if more people had training appropriate to their actual work, not determined by job title, and if work practice safety could be coupled with Tier I inspections.

The major on-going efforts are thus to continue to decrease the small but measurable personnel doses from the VUV and booster operation, education of the staff in areas such as use of dose monitors and electrical safety, studying behavior in the work place to determine effectiveness of and new directions for training, preparation of responses to all of the questionnaire and stand down issues raised by the staff, improvement of quality of life issues by upgrading the working environment, and continued vigilance to maintain our high level of safety. The main thing that we were all reminded of this year is that the key to safety is the involvement of every staff member and user in the safety programs. Coupled with the professional guidance and efforts of the NSLS and BNL staff, the workplace can indeed be safe and productive.



User Administration Report

Eva Z. Rothman
User Administrator
NSLS

The User Administration Office not only deals first-hand with every user that comes through the NSLS' door, we also count them. Based on the numbers of users registering in our office, being trained, getting radiation badges, and attending the Annual Users' Meeting and Workshops, I am happy to say that the NSLS users' activities at the NSLS have been relatively steady and even increasing slightly. During FY 1996, in fact, there was a record number of 2261 new or returning users who came to the NSLS to perform research on a beamline! The statistics for the past four years are shown in the Table.

Fiscal Year	Users Coming to do Research	General User Proposals	User Meeting Attendance	Abstracts for Activity Rpt.	User Publications
1996	2261	446	368	476	567
1995	2206	428	322	480	641
1994	2228	435	(no mtg.-SRI)	414	562
1993	2193	420	328	506	666

Note that for publications and abstracts, the NSLS relies on the users to volunteer this information to the NSLS. Therefore the fluctuations in those columns are usually due to other factors besides actual facility usage e.g. how much time the NSLS invested that year in searching for and requesting the information, and how well the users responded that year. Unfortunately, these are both items which are scrutinized as indicators of a facility's productivity - the user community should be prepared for renewed efforts on the part of the NSLS to collect this important information. Some other interesting facts and analyses emerge from our yearly statistics:

- The NSLS still gets over half of its users from universities. Although there is some proprietary research being conducted where the institution is not required to publish or share the data, most of the research done at the NSLS is published in open literature where anyone who needs it can have access to it. Indeed, the data belongs to the people of the U.S. who fund the DOE facilities through tax dollars and the information is out there, available to be used in the next invention or new technology.
- Our users are young crowd - over 40% are 30 or under and another 33% are between 30 and 40 years old. It seems that a significant population of young scientists is being introduced to the capabilities and usefulness of synchrotrons, in many fields of science, at a point in their career where they have many years of research to look forward to.
- New York, California, New Jersey, and Pennsylvania, in that order, are the states with the most institutions sending users to the NSLS. Illinois and Maryland are tied for fourth place. This illustrates that the NSLS not only has a strong regional customer base here in the East, but despite the SSRL and the Advanced Light Source in Berkeley there are users with special needs in California who still come to the NSLS. The pattern is likely to hold true for the Advanced Photon Source in Illinois - a good fraction of those Illinois users will probably continue to use the NSLS, at least in addition to the new APS.

- The industrial institutions with the largest numbers of NSLS users are also local: Dow Chemical Company, Exxon, IBM, and Lucent Technologies.
- Users in the field of structural biology have increased each year from 267 in 1993 (12%) to 518 in 1996 - now 23%, or almost a quarter of all NSLS users. The recently completed structural biology addition to the experimental floor is providing much-welcomed lab and set-up space for this growing community.

The User Administration Office meets the varied information needs of the NSLS by collecting information from users, compiling statistics like those above, and producing publications and pamphlets. Our other equally important mission is to support the NSLS user community by administering the General User Program, organizing and running the Annual Users' Meeting (more on that in Section 3 of this Activity Report), and helping the users get to their experiments as quickly as possible with efficient registration and training procedures.

The General User Program has seen some major changes this year. Up until recently, all the proposal information was being data-entered and stored in a large WordPerfect file. This worked well for a number of years but had its limitations. The system constrained the type and complexity of reports and statistics we could extract, allowed only one person to data-enter the proposals at one time (which therefor dictated our processing schedules), and precluded future development of electronic methods of submitting and storing proposals. During FY 1996, a Proposal Database was designed and implemented by NSLS Administration programmer Liz Hicks, with the assistance of information systems consultant Peggy Sutherland (now with BNL's Business Information Systems division) and Eileen Pinkston (the General User Program Coordinator). The Proposal Database is actually part of the User Database in which everyone registers when they arrive, so that information such as user addresses can be shared instead of duplicated. The new database has enabled the User Administration Office to accommodate more complex requests for queries and reports; since more than one person can use the database at one time, it will allow us to shorten the proposal processing schedule and become more flexible in accepting different types of proposals in the future - again, without sacrificing turnaround time. Finally, the database opens the possibility for electronic submission us-



User Administration Group:
(front, left to right) Eileen Pinkston, Eva Rothman, and Nancye Wright
(back, left to right) Lydia Rogers and Linda Felerabend.

ing e-mail or the Web or some combination - this is because unlike the WordPerfect file, the database could link to or store the 1 to 3 page narratives attached to the proposal forms.

In May of 1996 Lydia Rogers joined the User Administration Office, beginning her stay here by helping to test the new Proposal Database. She and Eileen have already used the new Proposal Database for the May 31 and the September 30 submission deadlines. In addition, Lydia has taken a major role in the annual production of the Activity Report by taking charge of the abstract submissions.

New technology continues to positively impact the User Administration Office. Over the summer of 1996, the old Polaroid camera used for taking user ID badge photos was replaced by a digital camera attached to a PC. The software allows the User Administration Office to take the user's photo, choose the best image from a set of nine which the computer automatically generates with various contrast settings, and then electronically send it in the correct format to the Safeguards and Security Division where the BNL ID badges are physically made. In the past, the Polaroid snapshots the User Administration Office took had to be delivered to Security and re-photographed and digitized for the Security Divisions photo database. This Polaroid database stored the images in a proprietary format, which means they could not be decoded and used for anything else. Now, besides resulting in a much better image quality, the new non-proprietary format allows them to be used with Human Resources personnel files, or at the BNL main gate or HFBR where guards could verify visitor ID with the computer screen. The NSLS for its part will be enhancing the electronic NSLS user and staff directory in the lobby to display everyone's photos - if a user needs to locate someone for assistance, they will know exactly for whom to look!



NSLS

USERS' EXECUTIVE COMMITTEE

Peter W. Stephens
SUNY @ Stony Brook
UEC Chair

The Users' Executive Committee exists to facilitate communication, in all forms, between the community of users and the NSLS administration. Its membership is listed in the caption of the accompanying photograph. We conduct an annual user meeting and three public town meetings each year, followed by discussions with the NSLS and Brookhaven Laboratory staff and management to discuss relevant issues. I am grateful to all of the members of the UEC and the staff and directorate of the NSLS and BNL for the time, thoughtfulness, and candor which they have brought to this work. The annual user meeting drew 368 attendees, 80% of whom attended one or more of the six workshops. These covered a wide range of topics: the application of synchrotron radiation to magnetic materials, precision fabrication with hard x-rays, strategy and methods for area detector data collection, *in situ* applications of x-ray absorption fine structure, multiple wavelength anomalous dispersion, and opportunities in polymer research. The keynote speech was given by Malcolm Browne, Pulitzer Prize-winning Senior Science Writer of The New York Times, who spoke on "Lamplighters and Tool Makers." The users also heard from NSLS Chairman Michael Hart, from William Oosterhuis of the Department of Energy, and from seven scientists who covered a fraction of the spectrum of current research at the NSLS.

Two of the important discussions in which the UEC is currently participating are future operating conditions and the review of all of the Participating Research Teams. In the first case, some of the X-Ray Ring users wish to increase the electron energy from 2.584 to 2.8 GeV to provide a harder spectrum, particularly for certain gamma ray experiments using LEGS. Operation of the storage ring at the higher energy has been demonstrated, but it is necessary to weigh the impact on the programs of all of the users. Discussions are also open between the accelerator physicists and the users of the VUV Ring over the feasibility and desirability of operating in a "top-off" mode. The NSLS has embarked on the project of renegotiating its relationship with all of the PRTs, starting with a review of each PRT by the Science Advisory Committee, which reports to the NSLS chair. The user community at large is represented by the chair of the UEC as an ex-officio member of the SAC. I believe that there are very important issues here for the future of the facility, as we seek the means to assure access to the large and continuously evolving community of users. At the present time, there are some existing PRTs which are insufficiently funded and staffed to be able to operate full time, while there are others which have insufficient beam time to satisfy the needs of their members, as well as groups who are interested in forming new PRTs.

One change in the pattern of usage is reflected in the formation of a new Special Interest Group devoted to industrial users of the NSLS. Some aspects of the current access policy are inappropriate for industrial research, and this group is seeking to effect changes which will improve the utility of the NSLS to its membership.

With the continued growth of synchrotron radiation facilities in the world, we see the use of x-rays, infrared, and ultraviolet light from such sources becoming more of a commodity and less of an independent enterprise. This forces a hard-headed look at cost effectiveness, and the NSLS has an enviable record. No other Department of Energy supported synchrotron facility comes within a factor of two of our productivity (2268 registered users active during FY 1996/ $30.7M annual budget).

1996 has been another year of very strong scientific output at the NSLS. Even a casual glance at the abstracts and publication lists in this volume will show the reader that there is a tremendous variety of interesting work going on here. We have become used to the excellent operating conditions at the Light Source, and it is worthwhile to reflect on the efforts of the NSLS staff that have led to the continuous improvements in beam brightness, stability, and reliability over the years. At the same time, this is above all a user facility, and it is the scientific programs of the users which drive the health of the NSLS. I have every reason to look forward to having a vital facility here long into the future.



Users' Executive Committee and
Special Interest Group Representatives

(Front, from left to right)
Michael Dudley (SUNY@ Stony Brook), Eva Rothman (BNL-NSLS), Peter Stephens (SUNY@ Stony Brook), Ian Robinson (U. of Illinois), and Doon Gibbs (BNL-Physics).

(Back, from left to right, standing)
Richard Harlow (The DuPont Co.), Paul Zschack (ORNL), Carl Zimba (MIT), Thomas Russell (U. of Massachusetts), Mark Chance (Albert Einstein College of Medicine), Stephen Ginell (ANL), D. Peter Siddons (BNL-NSLS), David Johnson (BNL-Chemistry), Kim Mohanty (BNL-Physics), Ralf Wehlitz (U. of Tennessee), and Benjamin Ocko (BNL-Physics).

Absent from photo are Steven Whisnant (U. of South Carolina) and Yves Idzerda (Naval Research Lab).



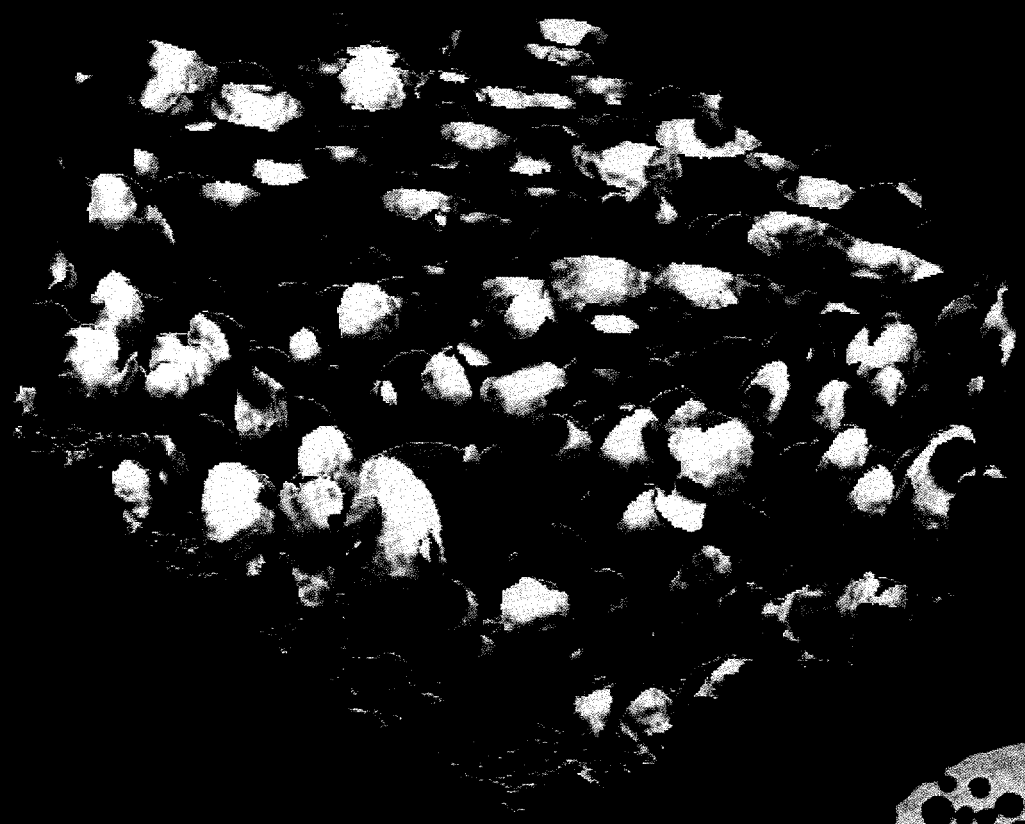
Beamline X27C: X-Ray Computed Microtomography (CMT) has been applied at X27C this year to the study of various types of porous materials. This technique allows the nondestructive 3-D imaging of sample through mapping and reconstructing the linear attenuation coefficients, μ, of the sample. Two examples of studies using X-Ray CMT are illustrated in the figures.

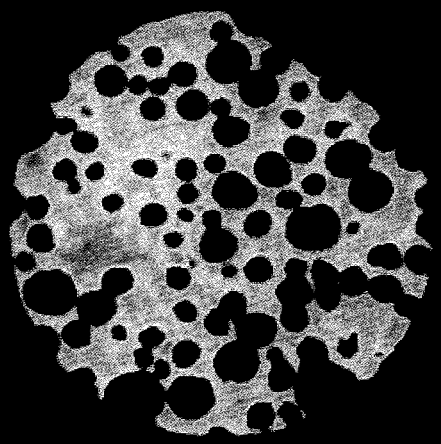
Microtomography is being used in forestry and forest products research to study tree diseases and fungal degradation of lignocellulose in wood. The above left image is a 3-D rendering of a volume of healthy pine wood with an approximate outer dimension of 1 mm x 1 mm x 0.2 mm. The solid green areas are middle lamella and cell walls of tracheids. Above right is a transverse 2-D section extracted from the volume. Air values are represented in black. (B. Illman, U.S. Dept. of Agriculture, Forest Products Laboratory)

The images on the opposite page were rendered using CMT at X27C by geologists who are interested in studying the behavior of volcanic activity by characterizing parameters of basalt, such as bubble size, morphology, and connectivity. The top image is a 3-D rendering of vesiculated African basalt. The volume shown was extracted from the middle of a cylindrical sample of 6mm diameter; its dimensions are 4mm x 4mm x 2mm. A full 2-D 6mm diameter slice from the sample is shown below it. (S.-R. Song, National Taiwan U.)

TWO

SCIENCE HIGHLIGHTS





SCIENCE HIGHLIGHTS

Preface

This year we have a new approach to presenting the science highlights in the NSLS Activity Report. The material is organized by research field rather than by technique, with the hope of making the document more accessible to the non-expert in synchrotron science. We would like to acknowledge the specific contributions to the text that follows. The liquid surfaces discussion was prepared by M. Deutsch (Bar-Ilan U.), P.S. Pershan (Harvard U.), and B. Ocko (BNL-Physics), the inelastic x-ray scattering by C.-C. Kao (NSLS), and the nuclear physics section by B. Preedom (U. of South Carolina). Important contributions to several sections have been made by L.E. Berman, G.L. Carr (NSLS), M. R. Chance (Albert Einstein College of Medicine), M. Dudley (SUNY @ Stony Brook), L. Furenlid, S. Hulbert, M.L. Shek-Stefan, D.P. Siddons, P. Stephens (NSLS), M. Vaughan, D. Weidner (SUNY @ Stony Brook), and G.P. Williams (NSLS). Without their efforts this document would not be possible.

J.B. Hastings

APPLIED SCIENCE

The research activities categorized as applied science include energy, technology, and the environmental sciences. The projects are perhaps more closely geared towards solving immediate problems than other kinds of fundamental research.

Environmental Science

The application of synchrotron techniques to the area of environmental science has been one of the key areas of development at the NSLS in the last year. Particular progress has been made in the study of waste metals in soils. EXAFS and XANES are among the core techniques applicable towards understanding the typically heterogeneous samples relevant to hazardous waste remediation. For example, M. Szulczewski, W.F. Bleam, and P.A. Helmke (U. of Wisconsin) examined the structure of metal ions in a number of soil environments using the facilities of beamlines X11A and X23B. In one series of experiments, XANES spectroscopy was used to identify the oxidation state of chromium (Cr(III) versus Cr(VI)) in contaminated soil samples (**Figure 1**). Due to the significant differences in the pre-edge features of various oxidation states of chromium, the presence of the notoriously toxic Cr(VI) can be identified (and accurately quantified) even when the more benign Cr(III) predominates. Other studies by this group have examined a range of first row transition elements in soil, concluding that the elements are bound to humic substances.

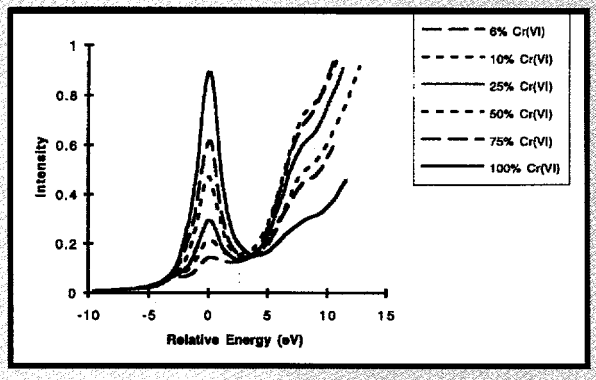


Figure 1: Cr K-edge spectra of the pre-edge region of standard physical mixtures with varying fractions of Cr(VI):Cr(III). (X23B)

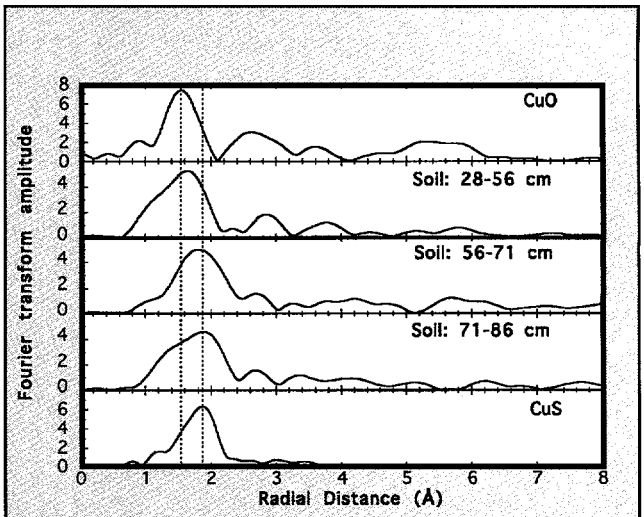


Figure 2: Radial structure functions for Cu(II) in soil samples from different depths and selected standards. Data are not corrected for phase shift. (X11A)

D.E. Sayers, D. Hesterberg, W. Zhou, W.P. Robarge, and G.M. Plummer (North Carolina State U.) have also carried out a number of environmental chemistry of soils studies on beamline X11A. In one investigation, the chemical forms of metals occurring at different depths in contaminated soil in a superfund site were examined, with the hypothesis that redox potential and oxygen availability would play a significant role in metal speciation. The hypothesis was to some degree confirmed, in that analysis of copper EXAFS data showed reduction in Cu-oxygen bonding and increases in copper-sulfur bonding with soil depth (**Figure 2**). Cu-S was determined to be the primary mineral species in the sub-surface samples.

Another example is the collaboration between K. Xia, F. Weesner, W.F. Bleam (U. of Wisconsin), P.R. Bloom, and U.L. Skyllberg (U. of Minnesota), who carried out sulfur K-edge XANES studies on beamline X19A to characterize the oxidation states of sulfur in both soil and aquatic environments. They identified six major sulfur containing functional groups in humic material and demonstrated the ability to distinguish sulfur oxidation states in aquatic, organic, and mineral soils.

Trace metals in the environment are important for their effects on biological systems, and so these element-specific techniques are particularly interesting when applied to organisms. The x-ray fluorescence microprobe was used to study a number of problems of environmental importance, including measurements of trace Pb in bone by C.S. Fullmer (Cornell U.) and K.W. Jones (Brookhaven National Laboratory). These studies, on chick tibia, investigated how lead affected bone growth by studying Ca and Pb distributions in normal and calcium deficient bones. Another study of metals in tissue was that undertaken by W.J. Berry, D.J. Borsay (U.S. Environmental Protection Agency) and K.W. Jones (BNL) of marine organisms living in sediments. In this case, the location of absorbed metals could be established for clam worms exposed to metals in controlled ways. Additionally, samples of dredged material from the NY/NJ harbor were studied by K.W. Jones (BNL) and S.-R. Song (BNL and Yale U.). By screening for contaminants as a function of sample particle size it was possible to check whether a simple physical separation method could be useful in decontaminating such materials. It was found that contaminants were present for all particle sizes at about the same concentration. A somewhat related experiment was performed by T.K. Tokunuga, S. Bajt (Lawrence Livermore National Laboratory) and G. Shea-McCarthy (U. of Chicago) on the oxidation state of selenium in sediments, decomposing plant residue and algae. These studies are of interest because the toxicity of selenium is highly related to its oxidation state.

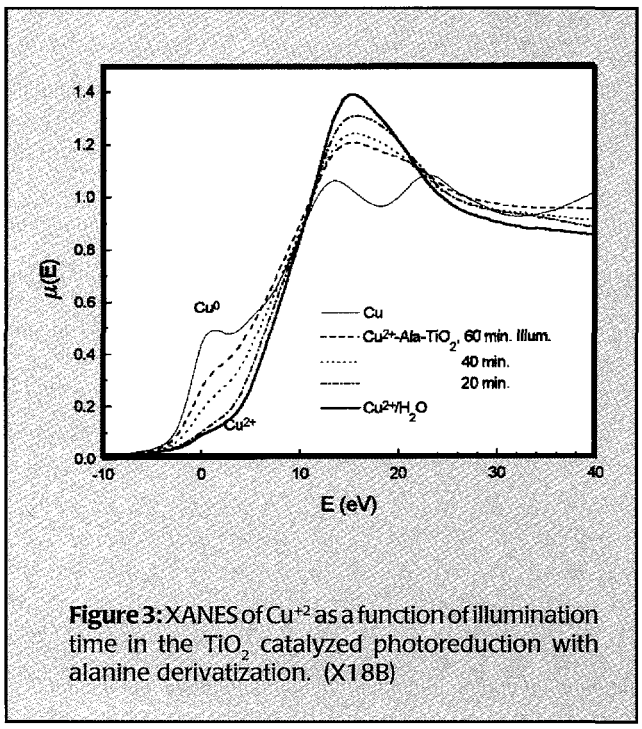


Figure 3: XANES of Cu^{+2} as a function of illumination time in the TiO_2 catalyzed photoreduction with alanine derivatization. (X18B)

Energy Conversion and Storage

Environmental systems are interesting not only from the life science point of view, but also as mechanisms for efficient energy and chemical conversions. There is perhaps no better example than photosynthesis, the natural harvesting and ultimate storage of solar energy. Researchers have been studying a variety of simpler systems, such as nanoclusters, for potential applications in photochemistry and electronics. For example, L.X. Chen, T. Rajh, D.M. Tiede, P.A. Montano, and M.C. Thurnauer (Argonne National Laboratory) studied titanium oxide clusters on beamline X18B. When photoirradiated, these semiconductor particles produce charge separation on their surfaces. They can thus act as electron donors or acceptors in oxidation/reduction reactions with molecules in their surrounding media, making them interesting for environmental remediation applications. The researchers studied the titanium k edge EXAFS on clusters of varying sizes and found systematic variations as the ratio of surface to bulk atoms changes. They studied the photoreduction of Cu^{+2} ions on the TiO_2 colloid surface with and without surface derivatization with alanine. They were able to confirm the production of Cu^0 and could see complexes between copper ion and alanine as seen in **Figure 3** along with their time dependence. Further studies were also carried out with mercury ions, which are environmentally relevant.

One of the important technological challenges is the development of inexpensive and efficient means of energy storage. The advent of more and more portable electronics, not to mention electric vehicles, is continuing to press the development of new battery technologies. The central obstacles in these developments are, of course, materials questions. T. Thurston, N.M. Jisrawi, S. Mukerjee, X.Q. Yang, J. McBreen (Brookhaven National Laboratory), M.L. Daroux, and X.K. King (Gould Electronics) have continued to exploit the high energy diffraction capabilities of beamline X27A for *in situ* structural characterization of working $Li_xMn_2O_4$ batteries. With measurements made through the external case, electrolyte, and binding materials, the experimenters were still able to collect diffraction patterns at reasonable count rates. The researchers found, among other results, evidence for coexisting phases over a range of voltages.

In work on X23A2 and X23B, P.E. Stallworth (U.S. Naval Academy), M.L. denBoer, S. Kostov, and S. Greenbaum (Hunter CUNY) also investigated the properties of lithium based battery cathodes. In systematic studies of $Li_xV_6O_{15}$ {x=0,0.5,1,1.5,2,3,4,5,6} carried out with NMR techniques to determine the environment of the intercalated lithium and XAS to determine the local

environment of the vanadium, the researchers found several structural regimes as a function of x. Using both the near edge quadrupolar peak intensity and the EXAFS as measures of the degree of symmetry of VO_6 octahedra, the team found a region of slight increase in the distortion from O_h with $0<x<1$, followed by a region of rapid increase in asymmetry for $1<x<3$, finally followed by a region of only small change. This is illustrated in **Figure 4(a)** which shows both the XANES and EXAFS results. The NMR evidence suggests that Li enters a single site at the lowest concentrations, but a variety of sites at the higher ones. The disorder extends beyond the first shell [**Figure 4(b)**], as evidenced by a decline in the outer shell amplitudes relative to the first shell.

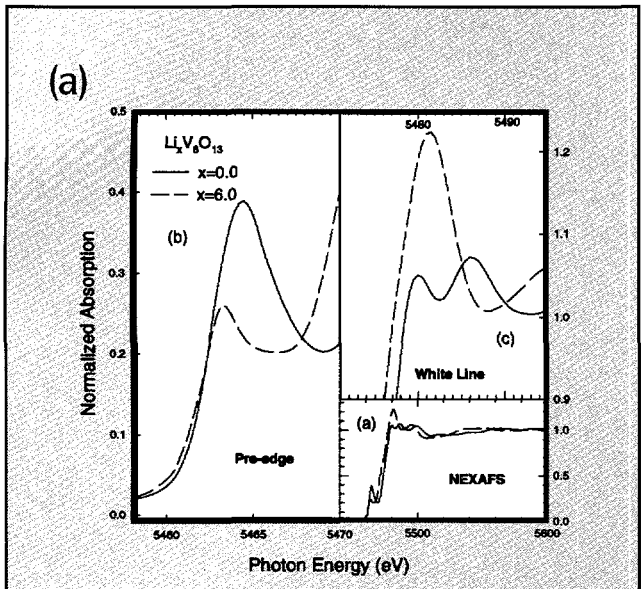
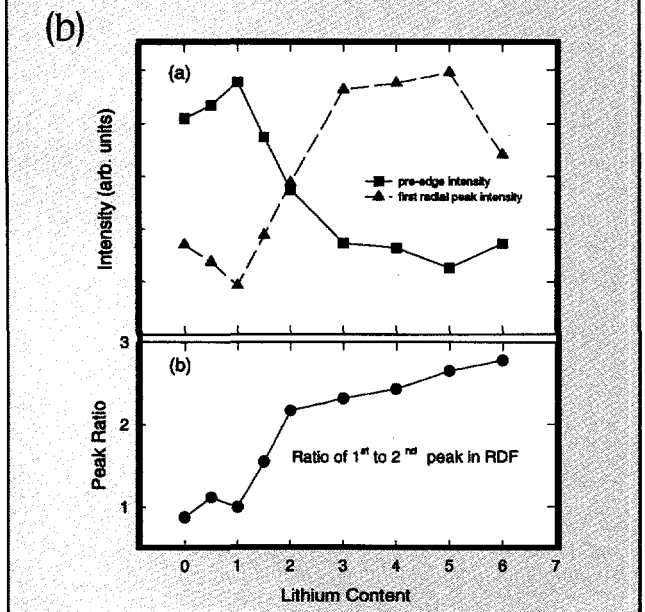


Figure 4: (a) Representative vanadium K-edge x-ray absorption spectra for a few compositions of $Li_xV_6O_{13}$ battery cathode materials. (X23A2, X23B)



(b) The vanadium 1s-3d pre-edge transition intensity for $Li_xV_6O_{13}$ as a function of x.

Superconductivity

Superconducting wires and tapes made with high-T_c cuprates are a prime example. Such wires are typically a composite mixture of $Bi_2Sr_2Ca_2Cu_3O_x$ (Bi-2223) with silver, processed to yield a high critical current at a particular operating temperature. Like many of the cuprates, the superconducting properties of Bi-2223 are robust only for transport along the Cu-O planes, making grain orientation a key factor in determining the critical current density. For example, T.R. Thurston, W. Wildgruber, N.M. Jisrawi, M. Suenaga, Y.L. Wang (Brookhaven National Laboratory), and P. Halder (IGC Corporation) continued to exploit the high energy powder diffraction capabilities of beamline X27A for *in situ* characterization of Ag-clad Bi-2223 high-temperature superconducting wires. In the experiment shown in **Figure 5**, the phase and texture development of Bi-2223 are monitored as it is generated from precursor materials (Bi 2212 + CuO) within its silver sheath. The reaction was driven in a series of temperature steps at 600° and 840°C. The researchers found that the formation of the Bi 2223 phase and the overall texturing were decoupled processes.

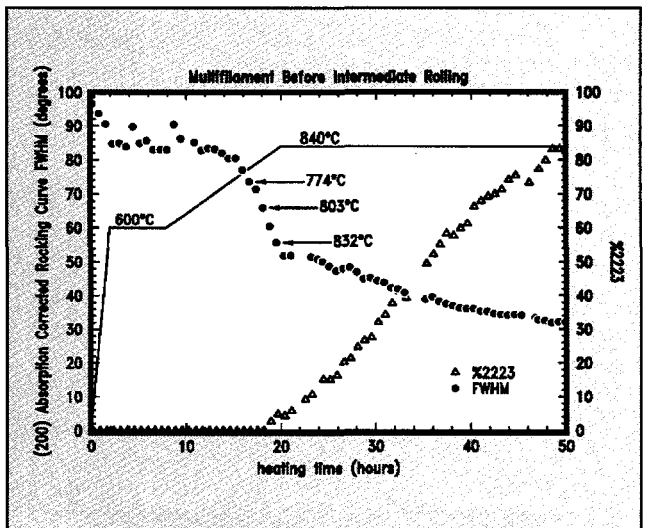


Figure 5: Time dependence of the phase and texture development in a multifilament wire. (X27A, X22A)

Electronic Materials

The rapid developments in the electronics and semiconductor industries provide ample motivation for materials studies. There are many important problems which require diffraction information from areas of a few square microns or less within a patterned sample, for example a semiconductor device and its interconnections. There have been several such microdiffraction experiments performed at the NSLS this year, with significant technical applications. E.D. Isaacs, K. Evans-Lutterodt, M.A. Marcus, A.A. MacDowell, W. Lenhart, L.J.P. Ketelsen, J. Vandenberg, W.T. Tsang, J.E. Johnson, J.A. Grenko, and S. Sputz (Bell Laboratories) have produced a 5 micron monochromatic spot, and used it for studies of patterned InP multi-quantum well (MQW) lasers. The variation in MQW period and strain as a function of position across the fabricated structure is clearly seen in the data of **Figure 6**. These measurements could only be made with x-rays since these structures are buried and thus inaccessible to electron diffraction measurements.

In a somewhat different approach, G.S. Cargill, P.-C. Wang (Columbia U.), I.C. Noyan, E.G. Liniger, C.-K. Hu, and K.Y. Lee (IBM Research) used a tapered capillary to obtain a 10 micron white x-ray beam and measured a diffraction pattern with an energy dispersive detector at X26C. They applied their setup, the first real-time strain measurements permitting such fine spatial resolution, to the study of electromigration and annealing in aluminum interconnect lines. Due to the stability and reproducibility of the detector in terms of peak shape and the use of an *in situ* tungsten standard, peak positions were easily measured to within 1% of the peak width. This was sufficient to directly deduce the strain induced from the electromigration in the aluminum interconnects under study.

H.Y. Lee (Synchrotron Radiation Research Center), C.H. Lee (Nat. Tsing Hua U., Taiwan), and K.S. Liang (Exxon) made *in situ* measurements of sputter-deposited thin films of $LaNiO_3$ on X22A. This material is an interesting substrate for integrated ferroelectric capacitors for microelectronic applications. They found that the material first deposits as an amorphous film, of about 100 Å thickness. Another application of x-ray analysis to very thin films was made by C. Kim, I.K. Robinson, J. Myoung, K.-H. Shim, and K. Kim (U. of Illinois) on X16C, where they studied the evolution of the in-plane and out-of-plane lattice parameters of GaN films in the range of 50-10,000 Å.

Metal silicides are potential candidates as contact materials in advanced semiconductor applications, but many fundamental issues of resistivity and stability

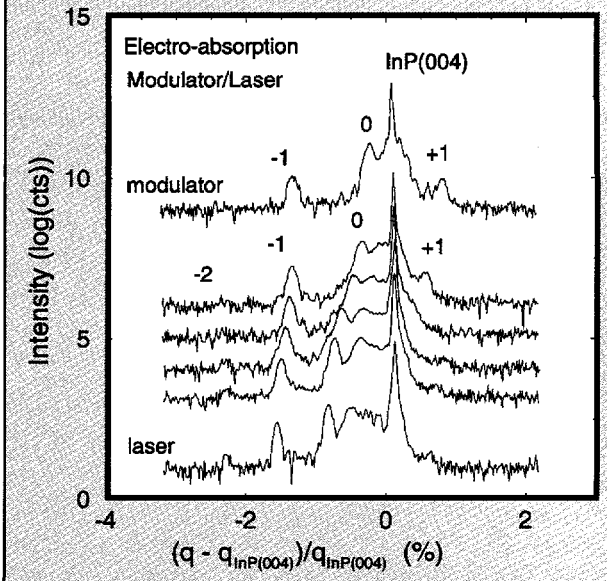


Figure 6: Radial Bragg scans along the InP(004) substrate direction taken at positions inside the laser structure (bottom line), through the transition region (middle four lines) and into the modulator region (upper line) taken with 5 μm spatial resolution. The variation in MQW period and strain as a function of position is observed as a variation in spacing between superlattice peaks (labeled by order) and the position of the other order peak, respectively. The data are offset for clarity. (X16C)

remain to be investigated. Z. Wang, P.T. Goeller, B.I. Boyanov, D.E. Sayers, and R.J. Nemanich (North Carolina State U.) designed, constructed and tested a UHV system for *in situ* studies of structures grown on semiconductor wafers via electron-beam evaporation. In first EXAFS measurements on beamline X11A (at the Co k edge) on cobalt and silicon codeposited and annealed in a 1:2 stoichiometric ratio on $Si_{0.8}Ge_{0.2}$ films, the researchers found evidence for the formation of stable cobalt silicide ($CoSi_2$). At annealing temperatures below 600° C, there was evidence as well for presence of a small amount of CoSi. The UHV chamber permits full characterization with a variety of techniques in addition to XAS. These include AES, XPS, UPS, RHEED, and ARXPS/UPS, and it is again appropriate to point out that well conceived XAS science backs up conclusions with corroboration by as many methods as possible.

InP is an important semiconductor material for long wavelength optoelectronic devices and high frequency electronic devices. The performance of these devices is controlled by the structural and chemical

uniformity of the epitaxial layers, which in turn, is strongly dependent on the structural perfection and compositional homogeneity of the substrates on which they are grown. It is, therefore, imperative to improve the crystalline quality and homogeneity of InP substrates. However, the relatively low yield stress of InP makes it susceptible to deformation by stresses generated during crystal growth, making it difficult to produce InP crystals with low dislocation density. In addition, temperature fluctuations imposed by turbulent convective flow give rise to uncontrolled variations in the local solidification rate and in diffusion layer thickness, leading to microscopic and macroscopic chemical inhomogeneity.

In work aimed at studying and improving the growth of InP and other semiconductor crystals, V. Prasad, H. Zhang, M. Dudley, H. Chung, and W. Si (SUNY @ Stony Brook), D.F. Bliss (Air force Rome Laboratories), and A. Maniatty (RPI) have been correlating defect microstructures and interface shapes observed using Synchrotron White Beam X-ray Topography (SWBXT) with the theoretical predictions of heat transfer and stress generation during the single step, high pressure Kyropoulos growth of doped InP boules. This enables a correlation between observed defect structures and both the growth parameters and modeling predictions. The results can provide feedback to the crystal grower to enable optimization of these growth parameters.

Figure 7(a) is a transmission x-ray topograph recorded from a S doped InP crystal. Numerous slip bands (S) nucleated from the cylindrical outer surface of the boule and propagating into the interior of the crystal were revealed. In the growth of indium phosphide, boric oxide is used as an encapsulant to prevent the decomposition of the melt. The encapsulant also reduces the radiative heat loss from the outer surface of the crystal since B_2O_3 acts as a heat shield. Detailed heat transfer modeling reveals that the maximum heat loss occurs at the point where the hot solid material emerges from the encapsulant giving rise to maximum temperature gradients in this region. X-ray topographs revealed that slip bands are most likely to be nucleated at this stage to relieve the large thermal stresses. The distribution of excess resolved shear stresses in the crystal at various stages in the growth process has been calculated using an anisotropic thermo-elastic finite element model for InP single crystals. The result is shown in **Figure** 7(b). It is worth noting that the maximum excess resolved shear stresses are generated on the outer surface of the crystal at the point where the crystal emerges from the encapsulant corresponding to the region with maximum temperature gradients. The calculated result is in good accord with the slip band distributions revealed by x-ray topography.

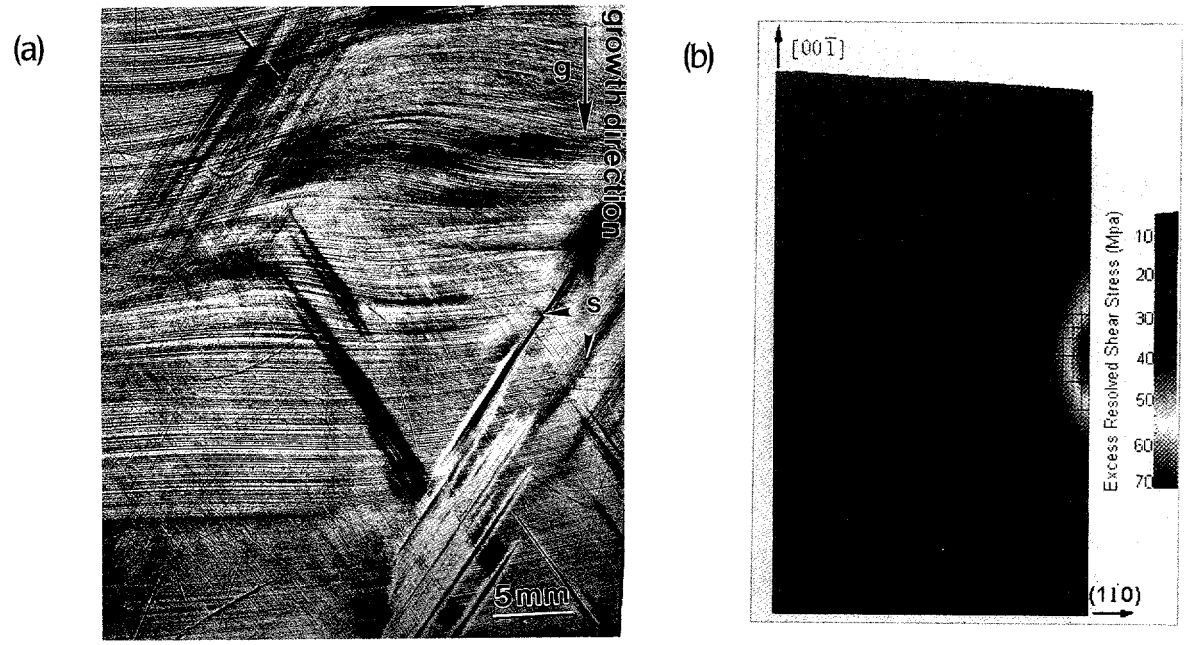


Figure 7: (a) Synchrotron White Beam X-ray Topograph (g=004, λ=0.45Å) recorded in transmission geometry from a longitudinal cut (110) S doped InP wafer showing the distribution of slip bands (S) and (b) the distribution of the total excess resolved shear stress on the (110) plane through the center of the crystal subject to an intermediate growth stage temperature field. (X11A)

Silicon Carbide (SiC), is a very promising semiconductor material for high temperature, high power, and high frequency electronic devices owing to its excellent thermal and electrical properties. One key issue for the fabrication of these devices is the availability of epitaxial layers with high crystalline quality, good dopant homogeneity, and good reproducibility. However, SiC has over 200 polytypes with different properties. Since these polytypes coexist over a wide range of temperatures, obtaining single crystals of large size, containing only one designated polytype is often difficult. In the case of 4H-SiC epitaxial growth on (0001) substrates, one of the big obstacles is the occurrence of triangular inclusions in the epilayer. One method of preventing the formation of triangular inclusions during epitaxial growth is to use substrates misoriented from (0001). The vicinal surfaces of such off-axis substrates provide high densities of surface steps. which facilitates epitaxial growth on such surfaces proceeding through a step-flow mechanism. However, in 4H-SiC epitaxy, the occurrence of triangular inclusions was still found to persist even when substrates misoriented by 3.5° from (0001) were used, although their numbers decreased drastically as the misorientation angle approached 8°.

C. Carter, J. Sumakeris, and H.S. Kong (Cree Research Inc.), and W. Si and M. Dudley (SUNY @ Stony Brook) carried out a detailed study of 4H-SiC epilayers grown on 4H-SiC substrates. Synchrotron White Beam X-ray Topography (SWBXT) and Nomarski Optical Microscopy (NOM) have been used to study the character of triangular inclusions in 4H-SiC epilayers (0001) 4H-SiC substrates with misorientations ranging from 3.5° to 8°. X-ray diffraction pattern analysis carried out on an epilayer grown on a 3.5° misoriented substrate reveal that there are two additional phases, 3C(I)-SiC and 3C(II)-SiC, present in the 4H-SiC epilayer associated with the triangular inclusion. The detailed correlation between the NOM micrograph and reflection topographs is shown in **Figure 8 (a) to (d)**. Evidently, all triangular inclusions belong to one or the other of the two 3C-SiC structural configurations. Most of the triangular inclusions are single crystal 3C-SiC, although they appear to be severely strained. There is only one triangular inclusion consisting of both 3C(I) and 3C(II)-SiC, which indicates the existence of a double position boundary (DPB) within the inclusion. This research shows unambiguously that the triangular defects observed in the 4H-SiC epilayers studied are 3C-SiC inclusions.

It is well known that in 4H-SiC single crystal substrates, there exist superscrew dislocations along the <0001> axis whose Burgers vector magnitudes are equal to a multiple of the c lattice constant (c = 10.05 Å). **Figure 9 (see next page)** shows (a) a NOM micrograph of an epilayer grown on such a substrate and (b) a back-reflection topograph. Triangular inclusions (TI), growth pits (P), and scratch (S) marks are observed on the micrograph. The directions from the apex of the triangle to the base are <-1 2 -1 0> directions, which correspond to the down-step directions (direction of lateral step growth). The length of altitude from base of the triangle to the peak is around 97 to 120 microns. The density of growth hillocks is 3 - 4 X 10^4 /cm^2, and the diameter is around 1 micron. Superscrew dislocations including micropipes (M) and elementary screw dislocations (ED) show circular white features on the topograph. By comparison, it is evident that there is no obvious correlation between superscrew dislocations and 3C-SiC triangular inclusions. Also there is no evidence showing that the growth hillocks are related to the superscrew

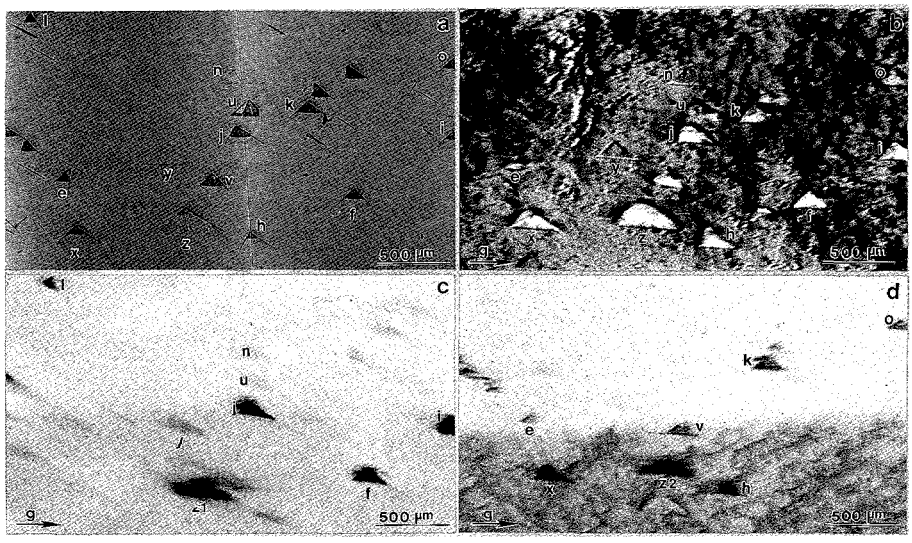


Figure 8: 4H-SiC epilayers on 4H-SiC substrates misoriented by 3.5° from (0001), (a). a NOM micrograph, (b). the reflection topograph from the same region, 4H-SiC, g = 1-1 0 6, λ = 0.78 Å, (c). the reflection topograph of 3C(I)-SiC, g = 202, λ = 0.91 Å, and (d). the reflection topograph of 3C(II)-SiC, g = 131, λ = 0.67 Å. (X11A)

dislocations since the density of growth hillocks is one order of magnitude higher than that of superscrew dislocations (~10^3/cm^2).

Magnetic Materials

Magnetic materials, particularly thin film structures, find immediate application in magnetic recording media for computer and entertainment applications. Several experiments of technical importance were carried out in the past year. Fe-Cr superlattices are of interest because of their giant magnetoresistance, but this effect depends strongly on the preparation conditions. W. Dmowski and T. Egami (U. of Pennsylvania) used beamline X7A to study the interfaces of sputtered films, and inferred that roughness at relatively short length scales increases the magnetoresistance.

T.R. Thurston, L.H. Lewis, U. Wildgruber, D.O. Welch (Brookhaven National Laboratory), and V. Panchanathan (Magnequench International) used X27A to characterize the texture distribution in thermomechanically deformed $Nd_2Fe_{14}B$ magnets. This type of work is still relatively new at synchrotron sources, and is representative of a wealth of potential applications which will increasingly appear at the NSLS. L.H. Lewis, C.H. Sellers (Idaho National Engineering Laboratory), and V. Panchanathan(Magnequench International) have also studied $Nd_2Fe_{14}B$ magnets, using X7A to determine the phases present in the multiphase samples which result from rapid solidification.

Q. Zhu (Brookhaven National Laboratory) used beamline X7A, to study the increase in the structural order parameter in the soft magnetic alloy Fe-Co-V with thermal aging, and was able to identify a minority phase comprising only 0.3% of the sample. The results call into question the widely-accepted belief that a fully ordered Fe-Co alloy exhibits the optimal magnetic properties.

Properties of Materials

X-ray scattering techniques are an old and established probe of structural properties of bulk matter. They can detect the presence of small amounts of a second phase in nominally single phase systems, residual strain, the existence of precipitates, etc. Thus these techniques remain fundamental to understanding details of technologically relevant problems in ceramics and alloys, for example.

The X3A2 beamline was used by Y. Gao, W. Hasz, and C.A. Johnson (GE Corporate Research and Development) for a spatially-resolved crystallographic study of yttria-stabilized zirconia, oriented toward the development of x-ray diffraction techniques to derive the temperature history of a ceramic sample. A. Sahiner, D. Wittmer, and M. Sweeney (S. Illinois U.) used the same beamline to study the effects of thermal shock on the residual stress of Si_3Ni_4 ceramic composites. They found that the compressive stress decreases as the temperature is increased above 1130°C, becoming a tension in the in-plane direction at 1400°C.

The tunability of synchrotron radiation has been used to advantage by D. Alexander (APS, Argonne) on X6B to study defects in steels used in reactor pressure vessels. For example, using anomalous small angle scattering it was possible to identify CuMn precipitates in a Fe-Cu-Mn alloy. Such precipitates are known to cause embrittlement in alloys.

Polymers and Polymer Composites

Polymer composites take many forms, depending on the application. Structural composites, such as Nextel fibers in ceramic matrices and carbon fibers in polyamide, are being investigated by R.J. Meilunas and A. Tobin (Northrop Grumman) at beamline U2B. Some of these

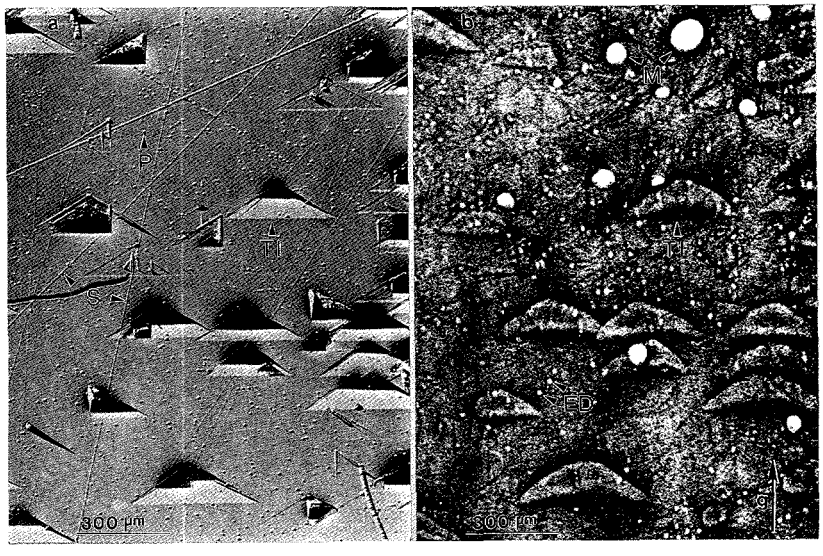


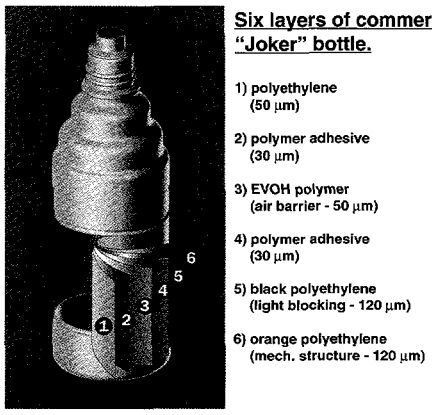
Figure 9: 4H-SiC epilayers on the 4H-SiC substrates misoriented by 3.5° from (0001), (a). a NOM micrograph, and (b) the back-reflection topograph recorded from the same region, g = 00024, λ = 0.83 Å. (X11A)

composites are intended for use in hostile environments (elevated temperatures, oxidative atmospheres, etc.) and the local chemistry (e.g. at the fiber - host matrix interface) controls many of the desired properties. By performing IR microspectroscopy on such localized regions, Meilunas and coworkers have identified fiber sizings (coatings) that inhibit thermo-oxidative degradation of the surrounding matrix.

Another type of polymer composite is in the form of laminates. The layers are frequently a few microns to several tens of microns in thickness, depending on the laminate's intended purpose e.g. photographic film emulsion or food container. In the latter case, the various layers provide the proper combination of structural integrity, sanitary surfaces, and barriers against penetration by light or gases. Much thinner layers are used in photographic emulsions. However, in both cases the interdiffusion of chemicals between the layers must be understood and controlled. Several studies of this nature have been conducted, including one study of a laminated polymer used for plastic containers. **Figure 10** shows such a laminate in cross section, and a linear spectroscopic absorption map. While the optical image of the microtomed section suggests a clear delineation of the layered materials, the infrared map provides evidence of chemical diffusion. This is especially apparent between layers 3 and 4 where the absorption features in the "fingerprint region" (below 1500 cm^{-1}) show an overall gradient from the interface to a depth of 10 mm or more into layer 4. Similar behavior is seen, though to a lesser extent, between layers 2 and 3.

In a collaboration between D.L. Wetzel (Kansas State U.) and R.O. Carter (Ford Science Research Center), degradation profiles from photochemical reactions, were measured into the surfaces of acrylic polymers with and without polyethylene or polypropylene protective surface coatings. Cross sections of the exposed acrylic were microtomed and measured in transmission. The unprotected acrylic materials showed damage that extended from the surface to a depth of about 20 microns. In particular, the absorption signatures for the acrylic were weak at the surface. Actual photochemical reaction products (OH, carbonyl) were detected several microns into the surface. Measurements of protected acrylic material showed no evidence of damage, even near the surface.

A considerable number of measurements were made at X1A by H. Ade, A.P. Smith, T. Coffey (North Carolina State U.), and collaborators both on mixtures of copolymers and polymers and on laminate structures, further demonstrating the capability of the technique as an analytical tool. The morphology and composition of a macrophase separated blend of poly[(styrene-r-isoprene)'-b-(styrene-r-isoprene)" random block copolymer (RBC) (20%) with homopolystyrene (PS) (80%) was investigated and micron sized ellipsoidal dispersions of the RBC were found within the matrix. Polycarbonate styrene-acrylonitrile copolymer blends grafted on to polybutadiene and titanium oxide were also studied. In another example, the spinodal decomposition of two polymers PS/PMMA constrained to a surface was imaged and showed segregation of the PS into spheroids within the PMMA matrix. Studies were also made of polymeric isomers, which could be distinguished spectroscopically due to the differences in the local chemical environment. Finally, to ensure that radiation damage was not a problem in these experiments, radiation damage experiments were carried out on PET up to 2.7 Mrad.



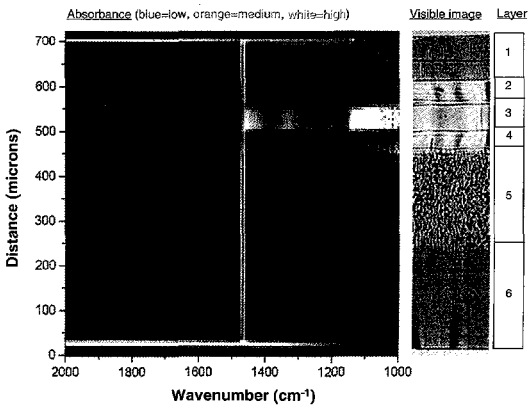


Figure 10: Laminated plastic material investigated by scanning IR microspectroscopy. (Top) A description of the plastic layers, their purpose and respective thicknesses. (Bottom) Linear scanned IR absorbance map across a 6 mm thick microtomed section. Also shown is a photographic image of the section, and labels for the various layers. (U2B)

Projection Lithography

A. MacDowell and O. Wood II (Lucent Technologies) continued phase-measuring, lateral shearing interferometry on a multilayer-coated extreme ultraviolet (EUV) imaging system using 13.5 nm radiation from the U13 undulator. This common-path interferometer addresses one of the major challenges confronting EUV lithography, namely the lack of wavefront measuring metrology at the multilayer coating's operational wavelength.

Experimentally a 0.08 NA subaperture of a 10:1 reduction Mo/Si multilayer-coated Schwarzschild camera is illuminated by 13.5 nm radiation emerging from a 4.5 micron pinhole. An open-stencil amplitude grating, with period chosen so that the lateral shear between diffracted orders is small enough that multiple-beam interference can occur in the region of overlap, is positioned in the camera's image plane. A phase-shifting technique, in which a CCD detector is used to record 13 interferograms produced by shifting the grating in the shear direction one twelfth of its period, is used to determine the difference in phase between the two interfering wavefronts. Phase difference data from the same wavefront recorded with shears in orthogonal directions are combined using a method involving least squares to produce a two-dimensional phase map of the camera's wavefront, as shown in **Figure 11**. The measured wavefront error over the camera's aperture after piston, tip, tilt and defocus have been removed is 0.098 waves RMS at a wavelength of 13.5 nm. While this value only slightly exceeds the Marechal condition (0.071 waves RMS), for "diffraction-limited" imaging, the wavefront errors in an imaging system for production EUV lithography will have to be considerably smaller. Since the sensitivity of this lateral-shearing interferometer was shown in earlier experiments to be better than 0.021 waves RMS at 13.5 nm wavelength, even in its current state of development it can be used to evaluate the image quality and improve the alignment of existing EUV imaging systems.

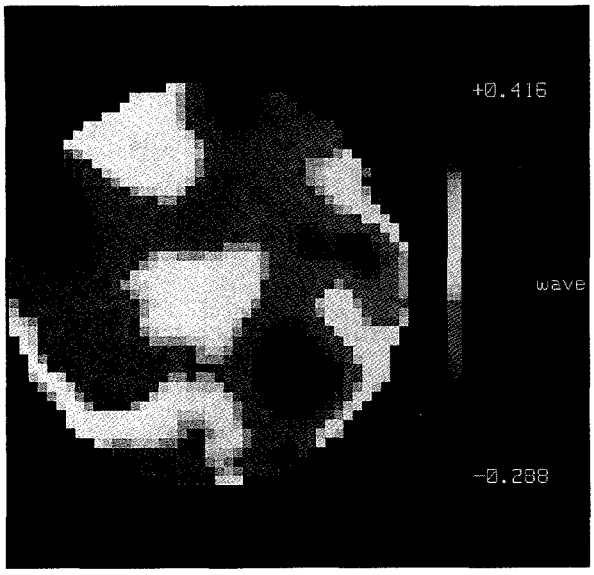


Figure 11: A two-dimensional phase map of the U13 camera's wavefront obtained by combining phase difference data from the same wavefront recorded with shears in orthogonal directions. the measured wavefront error over the camera's aperture after piston, tip, tilt, and defocus have been removed is 0.098 waves RMS at a wavelength of 13.5 nm. (U13)

Hard X-Ray Lithography

To extend lithographic techniques to structures thicker than 0.5 mm it has been shown to be beneficial to employ a hard x-ray source such as the NSLS X-Ray Ring. The NSLS has established a program in this area currently located at X27B which is centered on exposure technique development. They have succeeded in manufacturing precise fully figured 3-dimensional objects on a length scale of many millimeters. So far, the material of choice as a resist has been polymethyl-methacrylate (PMMA) since it is well know in other lithographic applications. In the present protocol, x-ray exposed areas are subsequently removed in a selective solvent system. To produce a pattern on the resist, an x-ray opaque mask is placed in front of a resist sample. The mask and sample are scanned together vertically through the x-ray beam. Often filtering is employed to tailor the high energy cutoff of the beam to the particular application, and parameters such as scan rate, total dose, and substrate temperature are controlled to manipulate the exposure. The patterning masks used to date have included shadow masks assembled from thick high Z materials (tool blocks and rods for example), and in collaboration with H. Guckel *et al.* (U. of Wisconsin), 50 micron thick patterned gold absorber on silicon wafers; objects which are themselves lithographically produced. **Figure 12 (see next page)** shows an example of the finish provided by hard x-ray lithographic exposure (the side walls) as compared with conventional diamond machining (the front face of the PMMA). It also exhibits faithful reproduction of the mask features (crisp corners and defects) and no observable runout from the front of the resist to the wafer surface.

To facilitate prototype hard x-ray exposures, the NSLS group developed a controlled aperture system which allows objects to be directly written. The aperture consists of two pairs of molybdenum rods mounted on actuators which compensate for beam induced heating. They can be moved under computer control to form rectangular apertures of arbitrary height and width anywhere within the 40 mm fan of beam available from X27B. By placing the sample on a rotary stage coupled to a vertical scan stage, objects of arbitrary shape and orientation can be patterned. **Figure 13** shows an SEM image of a series of long channels in 1 mm PMMA sheet produced with one axis of the writer. An array of 50 channels were machined that are 40 mm long, 125± 3 mm wide, placed 500 mm apart. In order to produce longer channels and multiple wafer exposure, a long-throw scanner was built for X27B. It has a stroke of over 600 mm, and can scan at rates over 250 mm/s. This high speed has proven useful for exposure parameter studies, in particular fixing not only the total dose, but the dose rate received in an exposure. The whole system has been automated with a Labview based control system. The scanner has proven sufficiently reliable and robust that it is being duplicated for the new X14B exposure station.

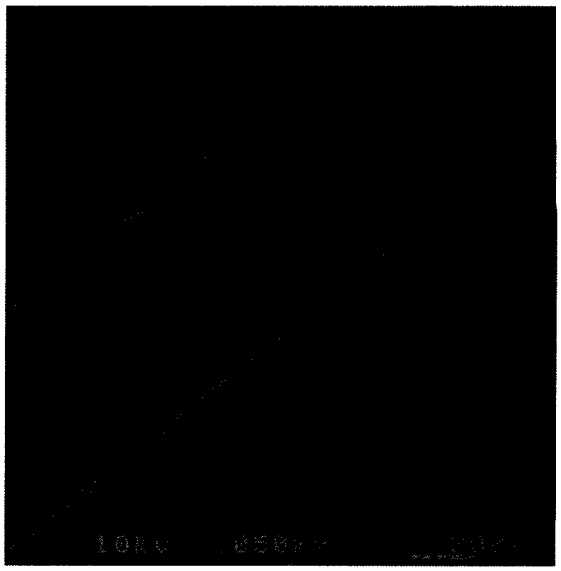


Figure 13: 125 micron wide tracks in 1 mm thick PMMA sheet. Pitch is 500 microns. (X27B)

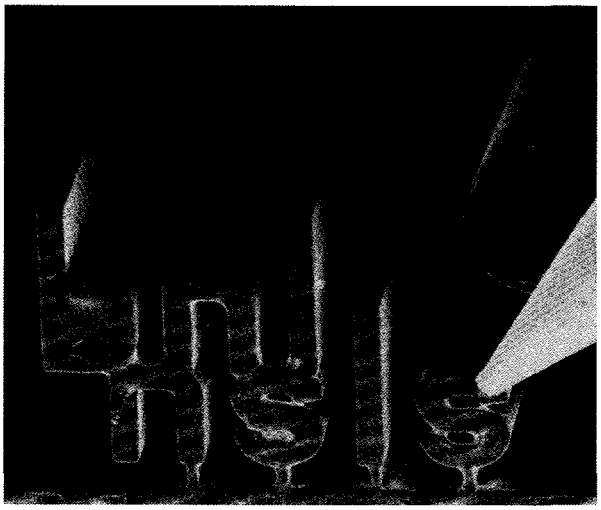


Figure 12: Lettering in 1 mm thick PMMA sheet. At right is the point of a tailor's pin. Note the smooth side walls as compared of the conventionally diamond machined surface of the acrylic sheet. (X27B)

This beamline is being built to provide more user access to beam time for prototype production runs. The X14B beamline also provides a roughly 100 mm wide exposure field which should improve throughput over X27B which only has a 40 mm fan of radiation. Expansion of this capability will be important, as some users have already started moving to the next step of device fabrication. For example, J. Song *et al.* (Argonne National Laboratory), used the X26C beamline to pattern resist which was ultimately fabricated into mm-Wave Accelerating Cavities. They electroplated 99.9% oxygen free copper into cavities prepared in PMMA resist by hard x-ray lithography. The assembly was then diamond-lapped to provide a uniform thickness cavity. They have successfully made a 30 cell prototype of a rectangular 108-GHz structure using this technique.

Conclusion

Synchrotron x-rays are ideal tools for applied science. Their penetrating abilities permit *in situ* experiments; their wavelengths are well matched to structures at the atomic scale; and the large number of available photons enable high precision measurements.

Biological Sciences

Biological sciences at the NSLS utilize a wide range of techniques and have one of the largest user groups with a single unifying theme at the NSLS, comprising nearly 30% of all registered users at the facility. The experiments have as their goal the identification of details of molecular chemistry and structure that explain the functions of biomolecules and cells. Macromolecular crystallography is used to provide detailed structural information, for example, about protein-DNA binding or protein-drug interactions. In cases where biomolecules cannot be crystallized, small-angle scattering can be used to follow structure changes. When detailed structure changes of protein active site metals are important to the function, EXAFS spectroscopy is commonly used to provide structure information. Microscopy techniques, like infrared and soft x-ray imaging, extend the range of biological investigations from the examination of chemical and structural information on biomolecules to the study of integrated biological systems, like cells.

Macromolecular Crystallography

A good example of a protein structure determination that relied on complementary features of two different beam lines, was that of the SecA translocation ATPase, by J. Hunt and J. Deisenhofer (Howard Hughes Medical Institute and the U. of Texas Southwestern Medical Center), and D. Oliver (Wesleyan U.). This work was carried out on beam lines X12B and X4A. SecA is a homologue of the family of membrane transport proteins known as ATP binding-cassette, or ABC, transporters, which couple the hydrolysis of ATP to the active transport of ligands across membranes. These proteins are of strong medical and pharmacological interest, and include, for example, the cystic fibrosis transmembrane conductance regulator (CFTR) and the P-glycoproteins which mediate the multidrug resistance phenotype observed in many tumor cells.

It is quite difficult to undertake high-resolution structural studies of integral membrane proteins, but insight into their basic structural organization can be gained by studying structural and functional homologues such as SecA, a soluble enzyme which functions in translocating secretory proteins through the bacterial periplasmic membrane. It is believed to function as a molecular ratchet in the protein translocation reaction, pulling segments of the secretory protein through the membrane in conjunction with ATP-driven membrane insertion cycles.

The high-resolution structure (to 2.9 Å) of the membrane-retracted state of SecA was determined from crystallography data collected on X12B. Data were collected on a native crystal and from various derivatives, for which the high beam line intensity and wavelength tunability (to effect measurements of anomalous differences in the diffraction patterns) allowed for rapid screening. A selenomethionyl derivative data set was measured on X4A, taking advantage of the strong anomalous scattering at the Se K absorption edge and the excellent energy resolution of that beamline. While the selenomethionyl derivative crystals didn't grow large enough to allow for their direct use in multiwavelength anomalous diffraction (MAD) phasing, this data set was still useful for pinpointing the methionine locations. The overall preliminary structural refinement points to the need to collect further data from SecA and its complexes with various physiological ligands at even higher resolution, yet a working model for rearrangements of its ATP-binding domains in the course of the transport cycle has already been formulated on the basis of the data collected.

A macromolecular crystallography program was begun on beam line X9B in 1996 by Albert Einstein College of Medicine. A group from this institution led by S. Almo, Z.-Y. Zhang, and D. Lawrence has spearheaded an effort to design potential therapeutic agents for and understand the structures of protein tyrosine phosphatases, whose roles in oncogenesis and signal transduction are of great significance. The structure of PTP1B (human protein tyrosine phosphatase 1B), complexed with several synthetic non-peptide substrates, has been solved to a resolution of 1.9 Å. Data were collected using Fuji imaging plates, which were read out via an off-line scanner. These results have given insight into phosphotyrosine binding sites, information that is crucial to the design of a new class of tight-binding inhibitors specific to the phosphatase. This is becoming of importance as the role of PTB1B in oncogenesis and non-insulin diabetes mellitus becomes clear.

The arrest of DNA replication in response to the detection of DNA damage is a fundamental mechanism by which the cell minimizes the potential transmission of lethal mutations. A primary mediator of this response is the protein p21WAF1/CIP1, an inhibitor of the cyclin dependent protein kinases that also binds to and blocks the action of DNA polymerase enzymes directly. An elevation of nuclear levels of the tumor suppressor protein p53 occurs upon detection of DNA damage. This thereby stimulates transcription of p21WAF1/CIP1 as part of a

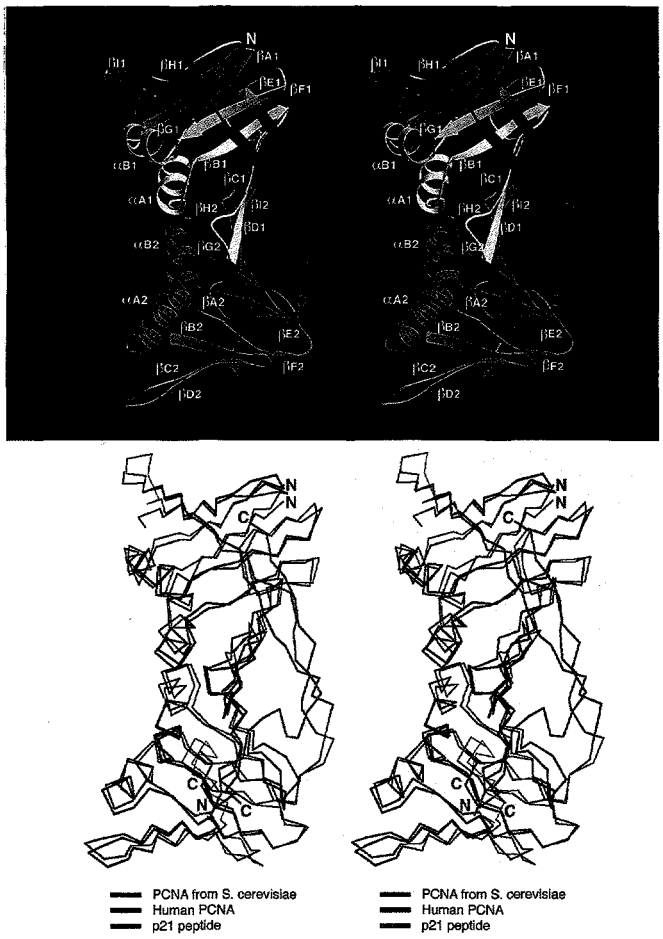


Figure 14: Ribbon diagram of the PCNA monomer with bound p21 peptide. (a) Stereo diagram of the three-dimensional structure of one monomer of the PCNA-p21 peptide complex, looking directly onto the face of the ring. The peptide (colored red) runs alongside the interdomain connecting loop (green). The N-terminal domain of PCNA is drawn in yellow and the C-terminal domain in plum, with five residues at the terminus shaded blue.
(b) Superimposition of the C^{α} trace of PCNA from *S. Cerevisiae* (red) onto that of human PCNA (black) with bound p21 peptide (green). The orientation is similar to that in (a). (X25)

p53 signalling pathway, via which the cessation of DNA replication is coupled to the stalling of cellular mitosis.

Using crystallography data measured at the wiggler beam line X25, a group led by J. Kuriyan (Howard Hughes Medical Institute and Rockefeller U.) determined the structure of the complex of the C-terminal region of p21WAF1/CIP1 with the human DNA polymerase delta processivity factor PCNA (proliferating cell nuclear antigen), to a resolution of 2.6 Å (work to be published in *Cell* by J. Gulbis, Z. Kelman, E. Gibbs, J. Hurwitz, M. O'Donnell, and J. Kuriyan). PCNA is a circular protein that encircles DNA and allows the polymerase to ride on it without dissociation during DNA replication, by forming a sliding clamp that tethers the polymerase to DNA during strand synthesis. The ability of p21WAF1/CIP1 to inhibit the action of PCNA may be due to its masking of PCNA elements that are required for the binding of components of the polymerase assembly. The derived structure (**Figure** 14) provides a view of a disabled PCNA molecule, which maintains a closed ring structure but is unable to support DNA replication. It also maps regions of the PCNA surface that might be important for polymerase attachment, and these are potential targets for the design of molecular analogs that would mimic the action of p21WAF1/CIP1.

Low Angle Scattering

Small angle scattering was used by K. Poole and K. Holmes (Max Planck Institute) and collaborators, on beam line X9B, to gain insight into structural differences between different muscle fiber complexes. Specifically, the motor protein myosin was isolated from both chicken skeletal and smooth muscles, and then introduced and bound to actin filaments in rabbit psoas muscle fibers. Small angle diffraction patterns were first measured from the two types of actomyosin complexes, and found to be different. Subsequent binding of the nucleotide ADP to each of these complexes resulted in little change to the diffraction pattern of the actomyosin complex derived from skeletal muscle myosin, but substantial change to the pattern of the complex derived from smooth muscle myosin (**Figure 15, see next page**), which became similar to the pattern associated with skeletal muscle myosin. These findings imply that at least some part of the power stroke associated with the motor function of these two kinds of muscle arises from different configurational changes of the actomyosin complex. While the data are still being analyzed, this already represents a novel finding and will be an intense subject of future study.

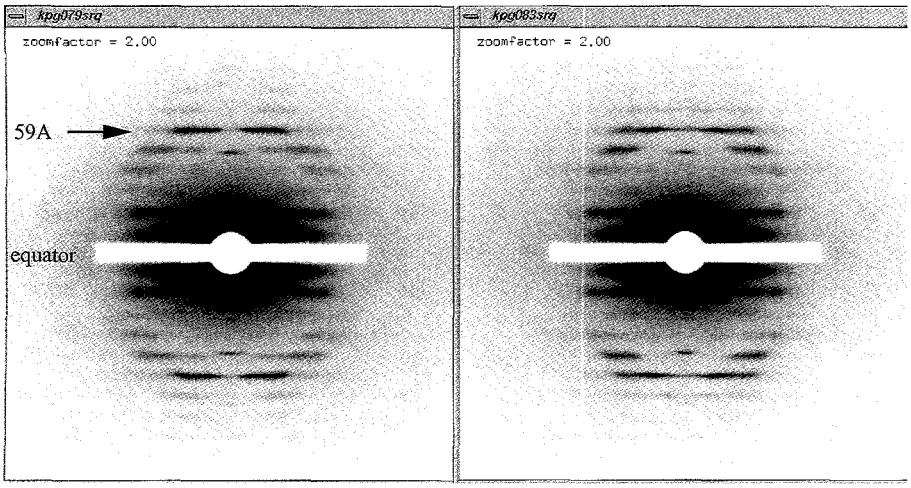


Figure 15: The effect of ADP on smooth-S1 decorated skeletal muscle action on low angle diffraction pattern. (X9B)

Crystal Growth for Macromolecular Crystallography

The growth of crystals that diffract well is the major rate limiting step in the collection and analysis of structural data from crystallography. The growth of such crystals, despite the improvements provided by mass screening procedures, is still an art. Thus it is important to try and quantify the results of a given growth procedure. One technique, used widely in materials science, is x-ray topography. Topography provides information specifically about crystalline perfection.

An experiment performed by V. Stojanoff (European Synchrotron Radiation Facility) and D.P. Siddons (National Synchrotron Light Source), E. Snell (National Aeroeronautical and Space Agency), and T. Boggon and J. Helliwell (U. of Manchester), on beamline X26C, addressed the study of crystalline perfection of various proteins grown in space (zero gravity conditions) and on earth (earth gravity conditions). Triple-axis diffractometry and x-ray topography were employed to characterize the samples. Using Si(111) monochromator and analyzer crystal reflections, the resolution in reciprocal space was sufficient to reveal fine structure in some of the Bragg peaks that would not have been resolvable using conventional double-axis diffractometry; employing triple-axis resolution, Bragg peaks were observed to be split in some instances. Fine structure in these peaks could be isolated and were further studied with x-ray topography, to provide insight into the spatial nature of crystallite domains responsible for the fine structure. From these studies, no definitive differences in the quality of the two classes of protein crystals (grown in zero gravity vs. in earth gravity) were revealed. These topography studies demonstrate a detailed method of examining crystal quality and may lead to a better evaluation of methods of crystal growth.

Micro-Spectroscopy Techniques

Synchrotron Radiation is well suited to spectroscopy on the μm scale due to the superior collimation and brightness compared to conventional sources. These advantages are illustrated in several biological applications, using infrared and x-ray radiation to interrogate a number of spectral transitions of interest. Thus, specific chemical information is derived associated with specific cellular structures.

Though the infrared absorption features of various organic molecules are well-known, very little work exists that relates specific infrared signatures with particular ultra-structural features in cells and tissues. Much of this is due to the small size scale frequently encountered. Several groups have begun investigations into biological tissues, and a few of the results from beamline U2B are described below.

One application of infrared microspectroscopy is for the identification and classification of various diseases in tissue samples. In a collaboration between the NRC (Canada), U. Manitoba, Kansas State U., and the U. Kansas Medical Center, Lin-P'ing Choo and coworkers studied microtomed sections from Alzheimer's diseased brain tissue. By following the shift of the amide I band from 1651 cm^{-1} to 1631 cm^{-1} (associated with b-amyloid), a map of diseased locations in a tissue region was obtained.

Developing non-destructive techniques is particularly important since alternative methods, such as chemical staining, can destroy the biochemical integrity of the tissue. In related work by the same collaboration, D.L. Wetzel (Kansas State U.) examined brain tissues exhibiting multiple sclerosis, and identified spectroscopic features directly associated with diseased regions.

Measurements on single living cells were conducted for the first time by N. Jamine, P. Dumas, and coworkers from DIEP-CEA, the Institute Curie and LURE (all in France) as well as the NSLS. A technique was developed whereby live cells (mouse hybridoma B) are dispersed onto BaF_2 substrates. The cells, which are about 20 μm across, remain alive for several hours. Also there is no evidence that the incident synchrotron infrared (~10 mW, or 100mW/mm^2) causes damage. Various cells were spectroscopically mapped using an effective aperture size of 3 μm. In this situation, diffraction limits the spatial resolution to a size scale ~10 μm. The IR spectra for the cells (**Figure 16**) show absorption features that can be attributed to particular chemical species. For example the absorption at 2920 cm^{-1} is due to the C-H stretch of aliphatic methylene groups associated mostly with lipids and proteins. As these lipids and proteins are found to be non-uniformly distributed within the cell, the chemical maps of the cell shown in **Figure 15**, and the relationship between the lipid distribution and cell division (mitosis) is one area of intense interest.

The soft x-ray microscope on beamline X1A is capable of imaging with chemical sensitivity by appropriately combining frames collected at photon energies which correspond to maxima and minima in absorption spectra. J. Boese, A. Osanna, C. Jacobsen, J. Kirz, E. Tall (SUNY @ Stony Brook) and X. Zhang (Harvard U.) are exploring the possibilities of protein specific imaging, ie mapping the concentrations of selected proteins in biological systems. As first steps, they have collected carbon K-edge near edge spectra of pairs of amino acids and compared them to the spectra of the corresponding dipeptide (the two amino acids bound via a peptide bond). As shown in **Figure 17** **(see next page)**, the researchers found in the case of glycine and tyrosine that the spectrum of the dipeptide is very close to a simple sum of the individual spectra. The formation of the bond had only a small effect, a ~0.3 eV shift in the C 1*s*-π* peak at 289 eV. If this result holds true for arbitrary combinations of amino acids, the absorption spectra of simple proteins can be predicted. (However, the inverse problem is made more difficult: given a spectrum, there is no information regarding the amino acid order or whether there are multiple molecules.)

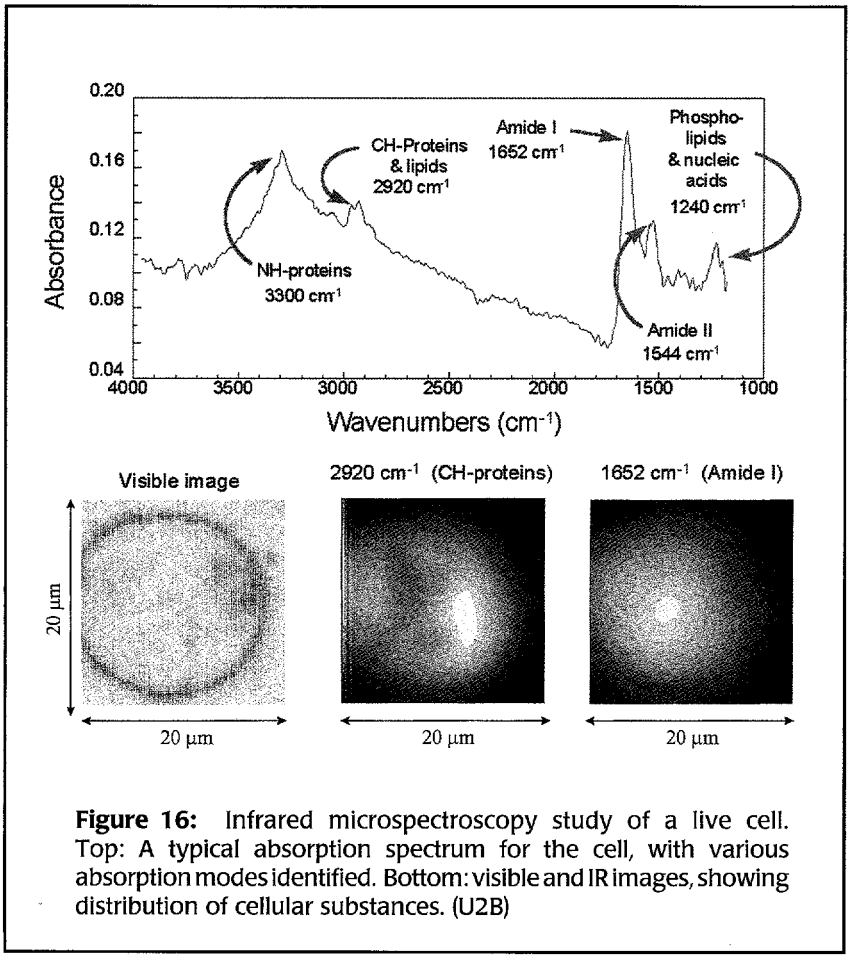


Figure 16: Infrared microspectroscopy study of a live cell. Top: A typical absorption spectrum for the cell, with various absorption modes identified. Bottom: visible and IR images, showing distribution of cellular substances. (U2B)

X-Ray Absorption Spectroscopy

Zinc is ubiquitous in biological systems, appearing in countless metalloenzymes. It is found, for example, in the active sites of many proteases, metalloproteins which cut other proteins in half at sites with specific amino acid sequences. One of the most interesting fundamental biological questions currently being addressed with micro-x-ray absorption spectroscopy concerns the egg. As an essentially closed system it must be preloaded with the full complement of metals required for complete development. In work on beamline X19A, K. Pearlso, C. van Huis, R. Denver, and J. Penner-Hahn (U. of Michigan) have been studying the structural evolution of

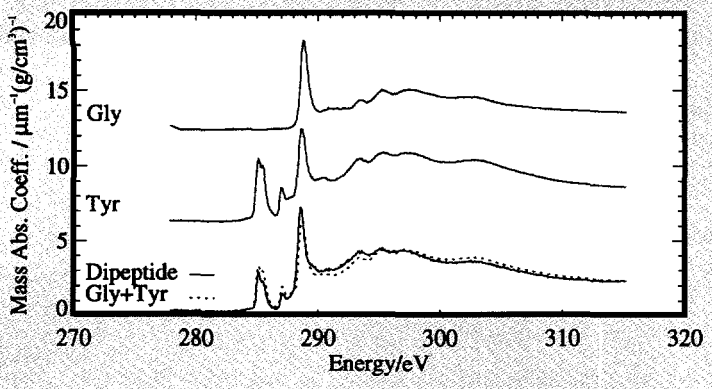


Figure 17: The x-ray absorption spectra of glycine, tyrosine, and a Gly-Tyr dipeptide (solid lines) are shown together with a weighted sum of the two monomer spectra (dashed line). (X1A)

the 1 mM zinc found in zebrafish and African clawed toad (*Xenopus*) eggs as a function of time after fertilization. Due to the mm dimensions and high zinc concentration of these eggs, they offer a strong zinc signal on beamline X19A. Transcription factors, called zinc fingers, play important roles in early development. The spectra in **Figure 18** show the large changes in zinc structure that occur during development from single cell to late blastula phase. This suggests substantial synthesis of new classes of zinc proteins during these developmental phases.

Figure 18 shows Zn k-edge XANES difference spectra relative to an unfertilized (nondeveloping) egg at various stages in the embryo development. Changes are clearly evident even in the first few cell divisions. The researchers note that the changes indicate the formation of multiple zinc sites in a complex process. Planned extensions to this work include two and three dimensional imaging of metal concentrations.

The use of EXAFS and XANES to examine the metal center structure in metalloproteins has been one of the most popular applications of synchrotron technology in biology since the initial phases of synchrotron development. The ability to derive metal-ligand bond length information on dilute and chemically poised samples of metalloproteins is extremely valuable in understanding mechanisms of protein function. Biological molecules are, of course, often large and difficult to study with conventional spectroscopies. The element specificity of XAS techniques make them useful for ignoring the background of thousands of amino acid residues to focus on the local structure around metals or other heavy elements. They complement 2d NMR studies and protein crystallography by determining oxidation states and precise bond lengths, metal properties that are essential for fully understanding active site structure function.

For example, in recent work on X9B, H. Anni (Thomas Jefferson Medical College), J. Vanderkooi (U. of Pennsylvania), M.R. Chance, and E. Scheuring (Albert Einstein College of Medicine) studied the structure of zinc II substituted cyctochrome c. NMR studies had proposed a six coordinate zinc site with five nitrogens and one sulfur as ligating atoms. This structure is highly unusual, there are no previously known six coordinate zinc sites in biological molecules in solution. However, XAS studies followed by refinement against theoretical models indeed confirmed the Zn site as six coordinate, with bond lengths resolved as Zn-N (porphyrin core) = 2.05 Å, Zn-N (histidine) = 2.10-2.20 Å, and Zn-S = 2.34 Å. In denatured protein, the zinc was found to have lost the sulfur coordination. The researchers conclude that the unique zinc environment must be imposed by the protein structure.

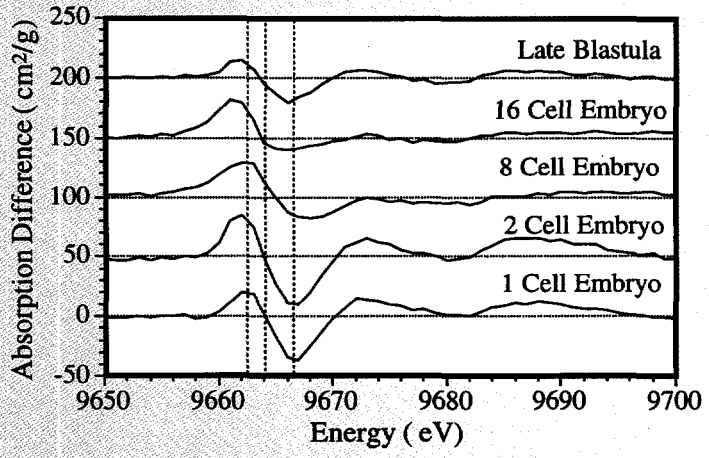


Figure 18: Time-dependent Zn XANES spectra of *Xenopus* eggs following fertilization. Spectra shown are difference spectra relative to an unfertilized control sample. Vertical dashed lines at 9662.5 eV, 9664.1 eV, and 9666.6 eV mark the critical points for the 1 cell difference spectrum, illustrating the change in spectra with time. (X19A)

The study of metalloenzyme chemistry by L. Que and co-workers (U. of Minnesota) on beamline X9B has been particularly focused on non-heme iron proteins and the activation of molecular oxygen to carry out oxygen insertion chemistry. For methane monooxygenase, EXAFS analysis has shown two Fe-Fe distances of about 3 Å and 3.4 Å which may reflect two populations of the enzyme with varying diiron (III) core structures.

L. Powers and co-workers (U. of Utah), using beamline X9B, have continued their examination of heme iron containing enzymes, called peroxidases, which, unlike the diiron proteins, use hydrogen peroxide to oxidize iron to the unusual Fe(IV) valence. These hi-valent iron species and associated protein radicals then are used to oxidize various substrates depending on the peroxidase. Site directed mutagenesis studies that varied the basicity of the iron coordinating ligands were correlated with specific iron-nitrogen bond length changes. As the basicity of the histidine axial ligand was increased by changing the hydrogen bonding to the remote nitrogen, the distance from iron to the directly coordinated nitrogen of the histidine axial ligand decreased by 0.15 Å. This definitively demonstrated that changes in hydrogen bonding 3-4 Å from the metal site can control structure and functionality of the iron site through coupling of the iron to the histidine pi electronic system.

M. Chance and co-workers (Albert Einstein College of Medicine) also carried out studies of heme metalloproteins on beamline X9B, in this case the oxygen transport protein myoglobin was examined. Synchrotron crystallography experiments by I. Schlichting (Max Planck Institute), J. Berendzen (Los Alamos National Laboratory) and co-workers carried out on beamline X12C had identified a "docking" site for the ligand, essentially identifying a way station for the ligand on its way to its binding site coordinated to the heme iron. These results had been challenged by other crystallography groups. EXAFS experiments were carried out by the Chance group examining the same intermediate. In addition, a new global mapping procedure, where crystallographic coordinates are refined to EXAFS data using the *ab initio* EXAFS code FEFF, (discussed also below) was used to show that the Berendzen structure is essentially correct.

The global mapping procedure was also used to examine metalloprotein structure in cobalamin enzymes by Chance and co-workers (Albert Einstein College of Medicine) in collaboration with scientists from U. of Michigan and U. of Nebraska, using beamline X9B. Cobalamin co-factors are cobalt containing prosthetic groups containing cobalt-carbon bonds, and are the only known organometallic species in the biological realm. Some similarities exist with the hemeproteins, in that an axial histidine ligand coordinates the metal perpendicular to the planar organic cofactor. The enzymes carry out unusual carbon-carbon bond re-arrangements and methylation reactions critical for cell metabolism. Mutant forms of the enzyme, methionine synthase, were examined, where the axial histidine is replaced with various amino acids. The changes in electronic structure at the cobalt ion, and the role of the histidine ligand in controlling enzyme activity were better understood as a result. The global mapping technique is illustrated in **Figure 19**, where particular minima based on the FEFF simulations can be directly compared to each other in an evenhanded manner.

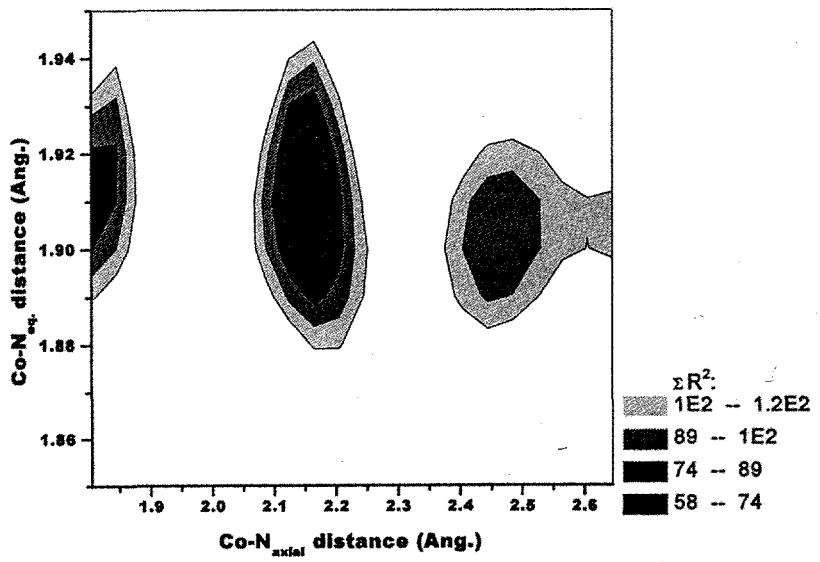


Figure 19: A contour plot of the goodness-of-fit versus FEFF 6.01 simulation geometry for the Adenosylcobalamin cofactor reconstituted into methylmalonyl CoA-mutase. (X9B)

CHEMICAL SCIENCES

Chemical Crystallography

Time Resolved Experiments

The moving image-plate system at X7B has proved extremely productive, with a wide variety of reactions and phase transitions studied. This system has been developed to the point where it routinely provides large quantities of high-quality data, too much to be listed here. For details the reader is encouraged to browse the relevant abstracts. Whereas those experiments relate to the conversion between various crystal structures, there are other important structural problems which are interesting when addressed in the time domain. Many small angle scattering experiments on polymers made use of time-resolved data sets.

One other example, with much faster time resolution, is an experiment on the electrodeposition of Cu on Pt(111), performed on X20A by A. Finnefrock *et al.* (Cornell U.). In that work, the Cu is electrodeposited on the Pt surface within 0.02 second after a step in the applied potential, but the overlayer structure requires from 2 to 5 seconds to develop long-range order. More detailed studies of this phenomena should lead to interesting information about the mass-transfer of ions near the electrode surface and other aspects of the deposition process.

Single Crystals

The brightness of synchrotron radiation can be very favorably combined with the use of image plate detectors for structural studies with relatively small single crystal samples. Mentioned here are a few characteristic examples. A. M. Andersen *et al.* (Odense U.), used 25 x 25 x 50 μm^3 crystals at beamline X7B to solve the structure of $Zr(HPO_4)_2$. At the same station, T. Jensen *et al.* (Odense U.), solved the structure of $\alpha LiZnAsO_4$ from a crystal of 17 x 17 x 60 μm^3 and of $\delta ILiZnPO_4$ from a crystal of 39 x 16 x 18 μm^3.

The image plate technique has application to crystallographic problems with normal-sized crystals as well. P. Coppens *et al.* (SUNY @ Buffalo), have been working on techniques to extract the best-quality intensities from image plates, and extending the limits of electron density analysis. For example, using a $Cr(NH3)_6Cr(CN)_6$ crystal of 80 x 30 x 30 micron^3 and an x-ray wavelength of 0.394 Å, they have collected and analyzed data out to 0.25 Å resolution. B. Iversen *et al.* (U. of California @ Santa Barbara), have extracted the electron density (rather than only the atomic positions) of the actinide $Th(S_2P(CH_3)_2)_4$ from data taken at X3A1. They avoided the problem of dominance of the heavy Th atom by collecting reflections for which the Th ion core did not contribute. By this means they could determine the charge density, rather than merely atom positions quite readily. Other image plate based studies on X3A by A. Darovsky (SUNY @ Buffalo) include anomalous scattering measurements of mixed valence Mn compounds, resolving the Mn^{2+}-Mn^{3+} thermal equilibrium vs. temperature, and separation of Mn^{3+} and Mn^{4+} sites in two different mixed valence compounds. Both the above studies benefitted from a new technique for extracting unbiased integrated intensities from the image plate data (called the seed-skewness method, R. Bolotovsky and P. Coppens (SUNY @ Buffalo). It relies on the statistical properties of noise to

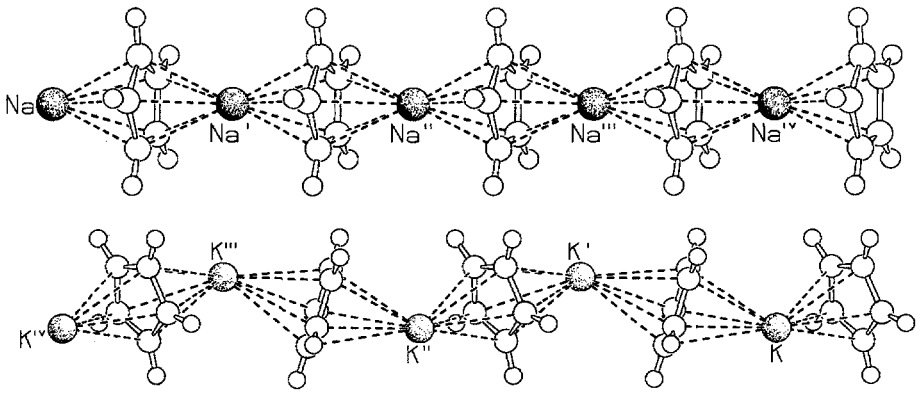


Figure 20: Polymeric chain of cyclopentadienylsodium (top) and cyclopentadienylpotassium (bottom). (X3B1)

isolate the data region corresponding to a diffraction spot (i.e. a region which is not noise).

J. Parise *et al.* (SUNY @ Stony Brook), have used image plate techniques on beamline X3A1 to solve the structures of several new open framework compounds, e.g., GeS_2 and $[(C_6H_{13}N_2)_2(H_3O)(H_2O)][AgGe_4S_{10}]$ with quite small samples, on the order of 30 microns.

Powder Studies

For many materials, single crystals are simply not available, and one must resort to powder diffraction data for whatever structural information is to be gleaned. Some of the (conceptually) simplest organic salts, like alkali cyclopentadianides AC_5H_5 (A=Li, Na, K, Rb) are sufficiently unstable that single crystals cannot be prepared, but they are of particular interest because theoretical calculations are unable to reproduce the observed structures of related, but more complicated molecules, e.g., $M(C_5H_5)_2$ (M=Be, Mg, Ca). R. Dinnebier (U. Bayreuth) and collaborators have solved a number of these compounds, purely from powder diffraction data at beamline X3A1. In one noteworthy example, they solved the structures of two polymorphs of RbC_5H_5 present in one sample from a single powder pattern. They found that the chains buckled to a different degree as a function of cation size (**Figure 20**).

Electron Spectroscopy

Valence Electron Excitations

The gas phase research on Beamline U11 has addressed the thermochemistry and spectroscopy of bromine oxides and chlorine oxides with photoionization mass spectrometry. These oxides are not well understood because they have low thermal stability and are difficult to obtain in a pure state. Br_2O has been prepared via the reaction of bromine vapor on solid mercuric oxide. **Figure 21(a)** shows the first direct determination of the photoionization efficiency (PIE) spectrum of Br_2O. The experimental ionization threshold is in good agreement with the only published value of 10.23 eV from an *ab initio* calculation. The heat of formation of Br_2O can be determined using the appearance energy (AE) of BrO^+ shown in **Figure 21(b)**, together with the previously determined ionization energy of BrO and tabulated heats of formation of BrO and Br. The 0 K value of 124.1 ± 3.5 kJ mol^{-1} thus determined has been selected and cited in the latest NIST-JANAF Thermochemical Tables for the Bromine Oxides. Discharge flow photoionization mass spectrometry has also been used to obtain the PIE spectrum of Cl_2O, ClO radical, the AE of ClO^+, and a value for the heat of formation of Cl_2O.

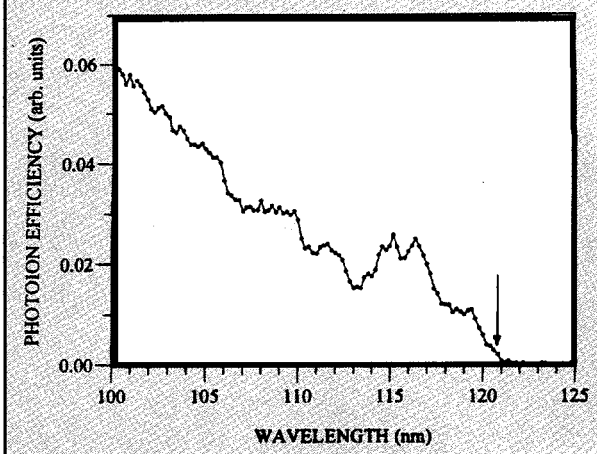
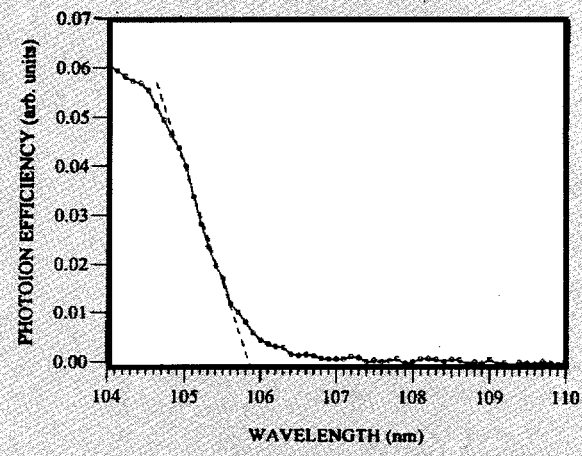


Figure 21: (a) Photoionization efficiency spectrum of Br_2O at a nominal resolution of 0.13 nm. The arrow indicates the onset of ionization at a wavelength of 120.8 nm, yielding an ionization energy 10.26 ± 0.01 eV. (U11)



(b) Photoionization threshold region for the appearance of BrO^+ via the dissociative ionization of Br_2O, at a nominal resolution of 0.13 nm. The linear extrapolation of the spectrum to the baseline yields an onset at 105.84 nm corresponding to an appearance energy of 11.71 ± 0.01 eV.

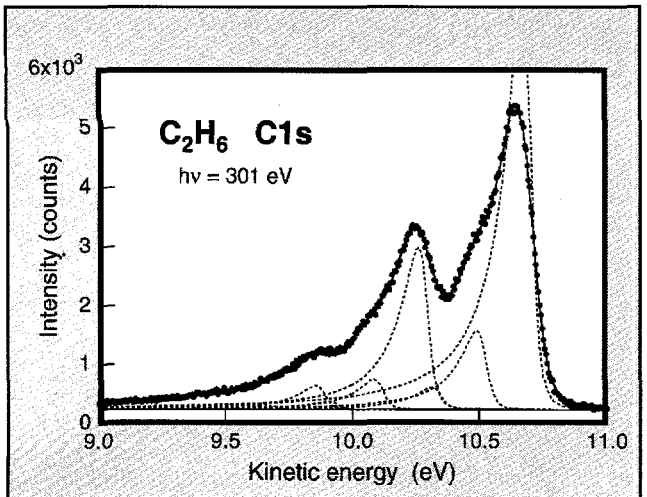


Figure 22: The C 1s photoelectron spectrum of C_2H_2 at a photon energy of 301 eV. The dashed lines represent the individual vibrational states; the fuill line through the data points represents their sum and convolution with the instrumental profile. The spectrum is dominated by the totally symmetric C-H and C-C vibrational modes, which increase to 407 ± 5 meV and 176 ± 5 meV, respectively, upon C 1*s* photoionization. (X1B)

Core Electron Excitations

The interest in atomic-site-selective core-electron excitation at Beamline U15 has been extended to 5-Oxohexanenitrile isolated in D_2 matrices. *In situ* infrared spectroscopy is used to monitor the C-O and the C-N stretches at excitation energies corresponding to the C, N and O resonances and continuum. One of the most interesting results from preliminary experiments is that excitation at resonances, resulting in autoionization producing a single valence hole, favors the photodissociation of carbonyl groups while nitrile group photodissociation is favored by continuum excitation resulting in Auger decay producing a doubly charged molecular ion.

As a continuation of the high-resolution studies of dynamic effects in core excitation on Beamline X1B, the complex vibrational structure in the C 1*s* photoelectron spectrum of ethane has been studied as the prototype for the alkanes. **Figure 22** shows a least-squares-fit of the vibrational structure. The vibrational energies of the C-H stretch and the C-C stretch are found to increase significantly upon ionization. The bond lengths are also found to be reduced by 0.036 Å for C-H and 0.043 Å for C-C. These and other results on alkenes contribute to the discussion on the correlation between shape resonances and bond lengths. Furthermore, the recent grating upgrade has enabled the vibrational fine structure in the O 1*s* photoelectron spectrum in CO_2 to be measured for the first time. It is observed that the antisymmetric C-O stretch mode (307 ± 3 meV) is dominant, as predicted for the lowering of symmetry and core orbital-vibronic coupling upon O 1*s* core ionization.

On Beamline X24A, polarization-dependent resonant x-ray emission has been studied with excitation at the sulfur K absorption threshold in carbonyl sulfide. **Figure 23** shows the sulfur K-valence emission for different polarizations, at excitation energies for 1*s* transitions to the lowest unoccupied molecular orbitals, Rydberg states and the continuum. The emission line shape and its differences with respect to the post-threshold emission spectrum are explained by *ab initio* calculations of the intermediate and final state energies. Variations with polarization are explained by a dipole model of absorption and emission.

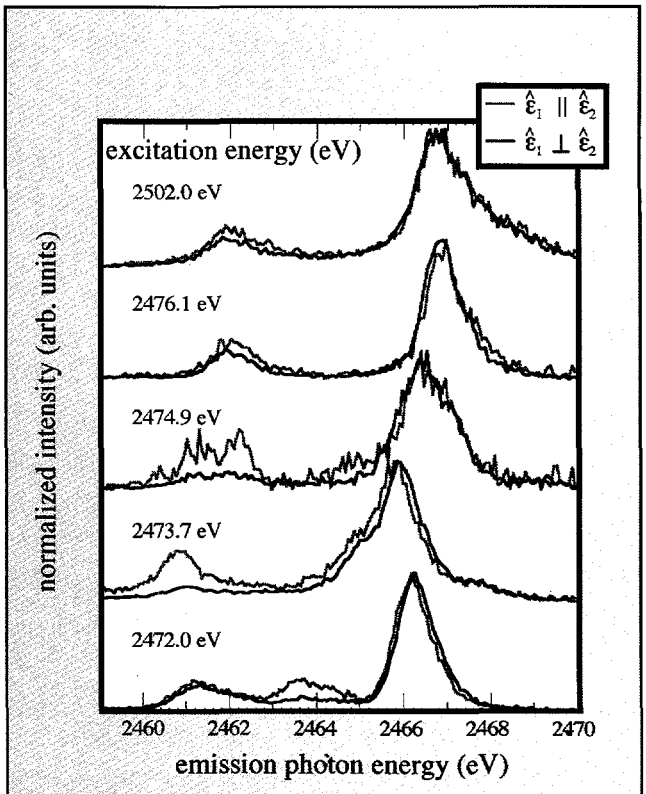


Figure 23: Sulfur K-valence emission in carbonyl sulfide for excitation energies at and above the K absorption threshold. Separate spectra are shown for polarization vectors oriented parallel to or perpendicular to the excitation polarization vector. (X24A)

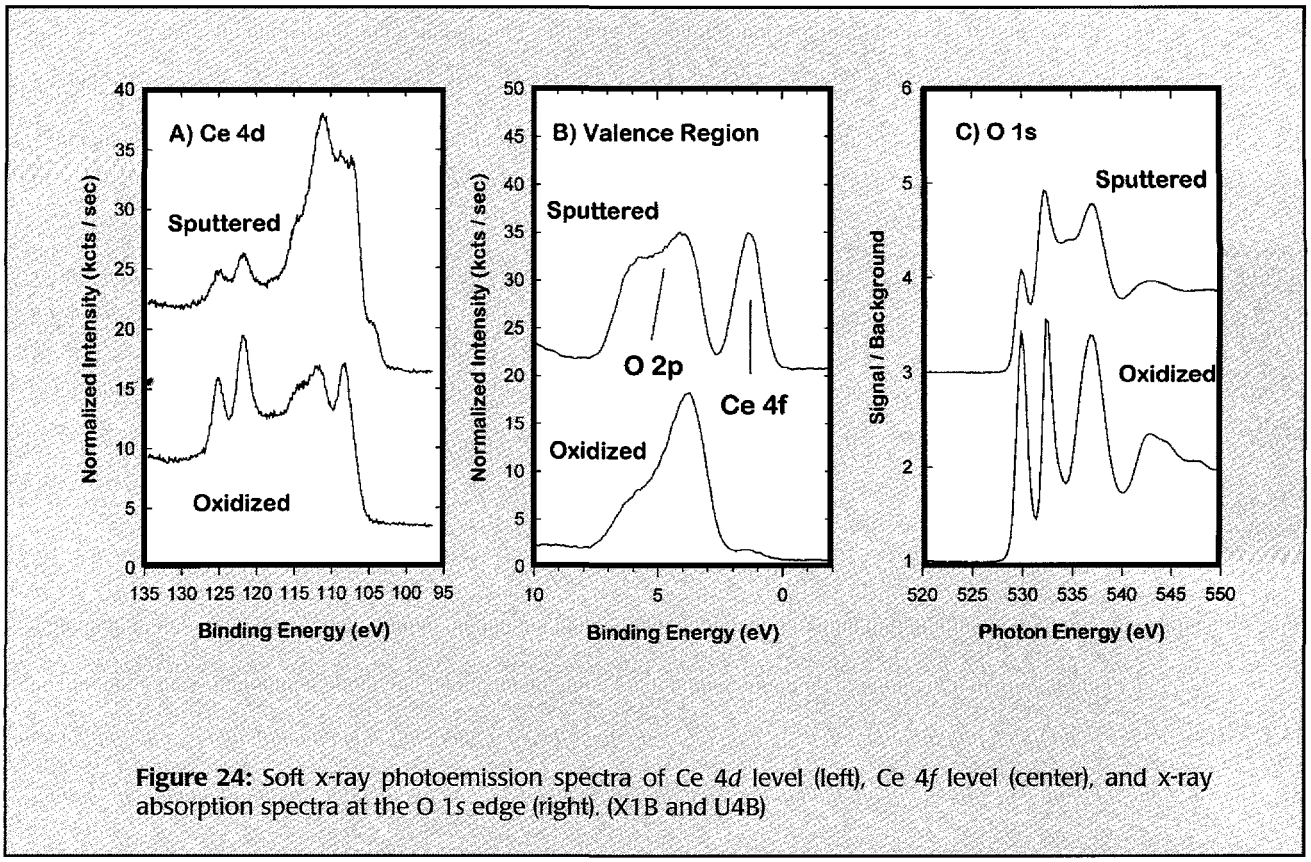


Figure 24: Soft x-ray photoemission spectra of Ce 4*d* level (left), Ce 4*f* level (center), and x-ray absorption spectra at the O 1*s* edge (right). (X1B and U4B)

Photoemission and Photoabsorption from Rare Earth Oxides

The surface chemistry group at Oak Ridge National Laboratory (D. Mullins, D. Huntley and S. Overbury) has begun a series of investigations to study the properties of metals supported on metal oxides. In the initial investigations, the ORNL group has used single crystal films of CeO_2 produced by laser ablation that are ~ 5000 Å thick. CeO_2 is used to enhance the performance of environmental control catalysts such as automotive catalytic converters. The films are highly oriented as indicated by x-ray diffraction, transmission electron microscopy and low energy ion scattering. Submonolayer amounts of Rh were deposited on the oxide films in vacuum and then the samples were exposed to NO. The reactivity was then studied as a function of Ce oxidation state, Rh coverage and temperature.

Sputtering the oxide with Ar^+ ions reduces the Ce from Ce^{4+} to Ce^{3+} and enhances the reactivity of the Rh/CeO_2 sample. Several highly sensitive indicators of the Ce oxidation state were measured using soft x-ray photoemission (SXPS) and x-ray absorption (XAS). SXPS from the Ce 4*d* and Ce 4*f* levels and XAS at the O 1*s* edge are shown in **Figure 24(a) to (c)**, respectively. These spectra were recorded at beamlines X1B and U4B. The Ce 4*d* spectra are very complex and are characterized by peaks resulting from $4f^0$, $4f^1$ and $4f^2$ final states. The high binding energy peaks near 122 eV are indicative of Ce^{4+}, while peaks at lower binding energy, and in particular the shoulder at 104 eV, are characteristic of Ce^{3+}. The emission from the Ce 4*f* level is much easier to interpret. The Ce 4*f* level lies in the oxide band gap. It is unoccupied in Ce^{4+} and therefore shows very little intensity from a fully oxidized surface. The Ce 4*f* level is occupied in Ce^{3+} and emission from this level is evident from the sputtered surface. Finally, in the O 1*s* XAS spectra, hybridization between the O 2*p* and Ce 4*f* orbitals permits excitation of an O 1*s* electron into the Ce 4*f*. The peak at 530 eV results from excitation into the $4f^0$ initial state of Ce^{4+}. The resonance energy shifts to ca. 532 eV for excitation into the $4f^1$ initial state of Ce^{3+} so that the decrease in intensity at 530 eV on the sputtered surface indicates the reduction of Ce^{4+} to Ce^{3+}.

When NO is deposited on Rh on a fully oxidized CeO_2 surface at room temperature, most of the NO remains intact as indicated by N 1*s* SXPS and XAS. As the sample is heated, most of the NO desorbs while some dissociates into atomic N and O. On a sputtered CeO_2 surface, however, most of the NO dissociates at room temperature.

GEOLOGICAL SCIENCES

Rheology

Dynamic processes within the Earth are limited by the strength of the minerals at elevated pressure and temperature. Deviatoric stresses cause earthquakes and mantle flow. Deviatoric stresses in the high pressure systems can now be monitored and quantified. Their time dependence reveals the relaxation mechanism. Pressure and temperature dependencies can relate to depth variations in the Earth. Current x-ray resolution of deviatoric stress is about a kilobar, far more than exists in most of the Earth's mantle, but comparable to seismic regions. Thus, even now we can approach geologically relevant *P*, *T*, and stress conditions. Within this framework, rheological studies for several materials are reported in this volume. Earthquakes persist into the Earth's transition zone. The time dependence of strength for the relevant minerals of this region are reported by J.-I. Ando *et al.*, Y. Wu *et al.*, and J. Chen *et al.* (SUNY @ Stony Brook) Included in these studies are the silica rich garnet, majorite, and the high pressure phase of olivine, wadsleyite. Indeed, the role of water weakening is also reported. Olivine is a classic material in which a small (ppm) amount of water drastically reduces the strength. The high pressure forms of olivine (wadsleyite and ringwoodite) can structurally bound a considerable amount of water (up to 3 wt %). The results of J. Chen *et al.* and T. Inoue *et al.* (SUNY @ Stony Brook) suggest that these high pressure phases are not appreciably weakened by the presence of large amounts of water, even though olivine, at these high pressures, is still strongly affected by trace amounts of water. These studies have significant implications concerning the seismic potential of different chemistries within the upper mantle and transition zone. All of these studies were carried out on X17B1.

Equation of State

High temperature equations of state are important in extrapolating phase boundaries to higher pressures and temperatures than where they are defined. Significant work in this area has also been carried out on X17B1. This motivated K. Bose *et al.* (Princeton U.), to obtain the equation of state of antigorite, a hydrous rich low pressure phase. The stability field of hydrous minerals help define the mass balance of hydrogen into the Earth's deep interior.

Equations of state of stishovite (J. Liu *et al.*, SUNY @ Stony Brook) and Ca(Ti/Si) perovskite (Y. Sinelnikov, *et al.* SUNY @ Stony Brook), provide important information concerning the temperature dependence of the bulk modulus and are relevant to matching the depth behavior in the Earth of the bulk modulus. The equation of state and phase equilibria of Fe-Si alloys studied by J. Zhang (SUNY @ Stony Brook) and F. Guyot (U. of Paris) address possible alloying in the Earth's core.

Phase Equilibria

T. Shen *et al.* (Los Alamos National Laboratory), with the double hot plate high pressure high temperature system continue the exploration of the iron phase diagram. In the study reported here, they find no evidence of the illusive phase transition in the epsilon phase as previously reported by suggesting that this phase may be created on quench. Surely, this debate has not ended.

With the expansion of the experimental environmental envelope has come a remarkable expansion in types of studies that can be done in conjunction with x-ray synchrotron radiation. The most significant breakthrough for Earth related studies is the inclusion of acoustic velocity measurements at high pressure and temperature and simultaneously with x-ray diffraction. This development is discussed in the instrumentation section and has already been used on X17B1 to collect acoustic data on polycrystalline specimens of majorite, a silica rich garnet (G. Gwanmesia *et al.*, Del. State U.) and the high pressure form of olivine, wadsleyite (B. Li *et al.*, SUNY @ Stony Brook). These two phases are stable at the high pressures and temperatures of the Earth's transition zone and are expected to constitute the bulk of this region of the Earth's interior. With these new data, we will be able to examine various chemical models of this region of the Earth.

P. Conrad *et al.* (Carnegie Inst. of Washington), use the focusing capability of the X17 system to explore a natural high pressure device, that is a natural diamond with inclusions as specimens. Presumably, the inclusions were emplaced while the entire system was at high pressure. Residual stresses will still exist within the inclusion owing to the extremely large bulk modulus of diamond. Removal of the inclusion risks back transformation of the minerals to low pressure phases. Thus, the structural determination with synchrotron x-rays provides a nondestructive probe.

Microprobe and Microspectroscopy

There were a number of experiments carried out on geological samples at X26C, including those by I. Steele (U. of Chicago) on Au in sulfides, and Ni, Zn, Ga, Y and Zr in garnet. J. Rakovan and R. Reeder (SUNY @ Stony Brook) studied the spatial resolution of trace elements such as Y, Sr, Mn, La, Ce and Pr in apatite samples the interest being in the relationship between the details of the structure of the host material and the amount and distribution of the impurity. Other types of impurity, namely fluid inclusions were studied by R. Mayanovic (Southwest Missouri State U.), A. Anderson (St. Francis Xavier U., Canada) and S. Bajt (LLNL). Here ppm concentrations of Zn, Pb and Fe were found in individual inclusions and in particular ZnCl dominated and was studied at elevated temperatures where its persistence was attributed to a high concentration of chloride in the inclusions. Trace elements were also studied in samples of interplanetary dust particles (G. Flynn, SUNY @ Plattsburgh), S. Sutton (U. of Chicago) and S. Bajt (Lawrence Livermore National Laboratory) of two main types and compared to the distribution in meteorites.

G. Cody (Carnegie Institute of Washington), H. Ade (North Carolina State U.), and S. Wirick (SUNY @ Stony Brook) at X1A used carbon XANES analysis to examine organic rich sedimentary rocks. The $1s$-π^* transition of carbon revealed specific chemical signatures for particular layers and phases.

STRUCTURE OF SURFACES AND INTERFACES

Liquid Surface Studies

Liquid interfaces are relevant to many disciplines, including biology, physics, and chemistry, yet relatively little is known about the structure of these interfaces. For example, the physical interactions that stabilize the liquid/vapor interface and give rise to surface tension can also give rise to interfacial structure which is very different from that found in the underlying bulk. Scattering experiments that make use of the high brilliance of x-ray synchrotron sources are one of the few experimental methods - compared to those available at solid interfaces - which are capable of investigating the microscopic structure of liquid interfaces. Over the last decade a wide variety of liquid surfaces and interfaces have been studied at NSLS including liquid crystals, simple dielectric liquids, liquid metals, molten chain molecules and organic monolayers on both water and liquid metal subphases. Many of these studies were scientific "firsts", and revealed new phenomena and novel features for the corresponding surfaces. Some of the more important scientific results obtained at the NSLS are the quantitative confirmation of long-standing theoretical predictions of the capillary contribution to the surface roughness in water, ethanol, alkanes, and liquid metals, the roughness and surface correlations of a surfactant monolayer at an oil-water interface in equilibrium with a microemulsion, the microscopic structural relaxation of condensed Langmuir monolayer phases of fatty acids and esters, the nature of the layering transition at the surface of isotropic phase of a liquid crystal, the adsorption at, and structure of polymers at liquid surfaces, surface crystallization at temperatures above the bulk melting point in normal alkanes and alcohols. In addition, measurements resulted in the first unambiguous proof of the long standing theoretical predictions of surface induced atomic layering along the surface normal of liquid Hg, Ga and In. The surface induced layering in Ga-In and Ga-Bi alloys and the in-plane structure of the solute-rich surface layers of dilute Bi-Ga and Sn-Ga alloys, and the oxide formation on liquid Ga, were also studied recently, and provided important insights into fundamental issues of surface segregation and surface oxidation, respectively.

This broad spectrum of liquid surface studies at NSLS helped to provide an essential basis for obtaining a microscopic understanding of liquid interfaces in general. In this short overview, we will concentrate only on the more recent findings at NSLS concerning liquid surfaces. Earlier results are well documented in the literature.

Experimental

Spectrometers for studying liquid surfaces are fundamentally different from standard four-circle diffractometers. The free liquid surface is always horizontal, and thus the horizontal beam originating at the ring has to be deflected downward to impinge on the surface at a given angle. This is usually accomplished by tilting a crystal in the Bragg geometry downward as shown in **Figure 25**. Specialized instruments employing this method have been employed at X19C, X20, X22B, and X25. This

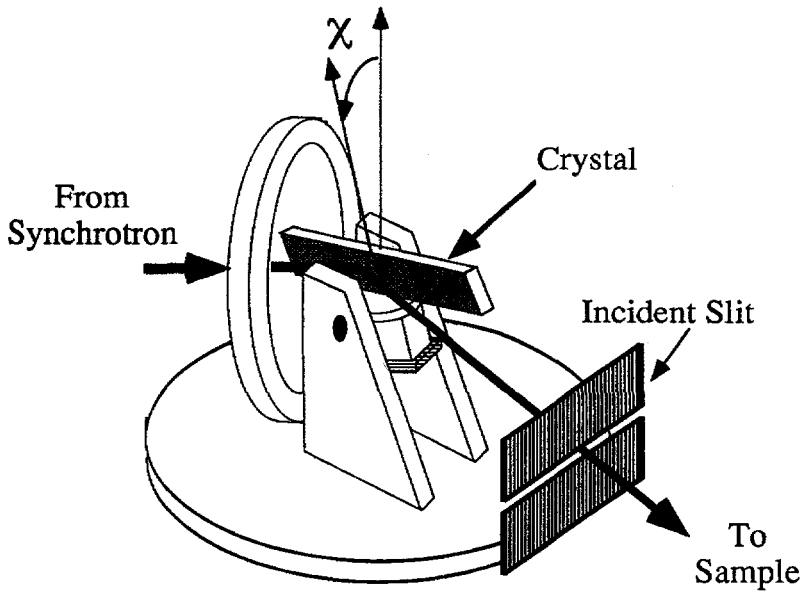


Figure 25: Steering monochromator for deflecting synchrotron beam downward.

requires precise control of the vertical positions of the sample, beam defining slits and detector. General purpose liquid spectrometers employing this method are capable of studying the structure within the plane of the surface (by grazing incidence x-ray diffraction, GIXD) as well as along the surface normal direction (by x-ray reflectivity, XR). While downward deflection of the beam can also be done using an x-ray mirror, and was implemented in some liquid metal experiments on X10A, this geometry is suitable for GIXD only and can not accommodate reflectivity measurements.

Environmental chambers for liquid surface measurements depend on the nature of the surfaces studied, and range from sophisticated UHV chambers (for studies of highly reactive liquid metal surfaces, for example) equipped with residual gas analyzers and ion beam sputtering guns for cleaning the sample's surface, through Langmuir troughs (for studying monolayers of amphiphiles and polymers on water) equipped with moveable barriers for *in situ* monolayer compression and Wilhelmy plate balances of surface tension monitoring, to small and simple temperature controlled sealed cells (e.g. for studying surface crystallization of alkanes). A detailed description of these cells is beyond the scope of this brief review, and can be found in the literature. Selected examples follow:

Liquid Metals

An important prediction, central to the theoretical understanding of the structure of liquid metals is that of atomic layering at the surface. According to this prediction, atoms near the surface will be ordered in layers parallel to the surface, and the layering amplitude should decay with depth below the surface with a characteristic length of several atomic diameters. Although over two decades old this prediction was hitherto untested experimentally in spite of substantial efforts by several groups worldwide. In a series of experiments by a group from Bar-Ilan, Harvard and the Brookhaven Physics Department (BHB) at X22B and X25 this effect has been confirmed for both liquid mercury and gallium. The surface layering gives rise to a broad quasi-Bragg peak in the x-ray reflectivity spectrum at a momentum transfer $q_z \approx 2.2\text{-}2.5$ Å^{-1} corresponding to the layer spacing $d=2\pi/q_z \approx 2.5\text{-}2.8$ Å, which is close to the value for the atomic diameter of the metal. The layering is an intrinsic, and highly persistent, property of liquid metals, as indicated by the nearly identical layering observed for bare and self-assembled thiol monolayer covered mercury surface. The studies of the Hg and Ga surface have been extended to cover a wide temperature range, and also to various alloys. In addition, the effects that varying oxygen exposure has on the surface of liquid Ga have also been studied at room and elevated temperatures. The formidable challenge to all of measurements on liquid metals is the need to measure over a large dynamic range in both qz and reflected intensity while maintaining an oxide-free surface for samples almost all of which are highly reactive.

In the case of binary liquid metal alloys, surface segregation of one of the components often reduces the interfacial energy, e.g. the surface tension, and even for very dilute alloys, the surface may have a very different composition than that of the underlying bulk alloy. Studies by Ning Lei, and colleagues at X19C have investigated the structure of gallium alloys with bismuth and tin. In the case of the bismuth alloy, grazing angle diffraction studies indicate that the bismuth segregates into a nearly complete monolayer atop the bulk alloy where the bismuth monolayer has the structure of a supercooled liquid. The surface tension of the alloy is obtained by interpretation of measurements of the diffuse scattering around the specular axis in terms of thermally excited capillary waves. From reflectivity measurements of the gallium-tin alloy, it is found that the tin concentration at the surface is in excess of the bulk concentration and that it decreases with increasing temperature, in accord with the Gibbs isotherm. X-ray reflectivity measurements of the gallium-indium alloy at X25 by the BHB group leads to a surface layer with a much higher electron density than the underlying liquid. Model fits assign this to single indium layer, with subsequent layers at the bulk eutectic composition. Ga oxidation studies by the same group show that on exposure to ~180 Langmuirs of oxygen, a thin layer of gallium oxide forms at the liquid Ga surface. As shown in **Figure 26 (see next page)** this leads to modulations in the reflectivity profiles which are well described by a uniform 5 Å thick oxide layer. The reflectivity does not change for exposures up to 1600 Langmuir, nor for elevated temperatures up to 300°C, indicating that the oxide layer is solid. The oxide layer is, however, most probably amorphous, since first GIXD measurements failed to show any dpeaks. Finally, the previous x-ray reflectivity measurements on Hg by the BHB group have been extended at X22B down to temperatures just above the melting point, -38.9°C. Here it is found that the peak in the reflectivity (associated with surface layering) increases dramatically in intensity with decreasing temperature with no corresponding change in the peak width. The latter result demonstrates that the intrinsic local decay of the stratified density profile is independent of temperature, consistent with similar results obtained for the Ga surface.

Langmuir Monolayers

Studies of organic molecules adsorbed on the surface of water, Langmuir monolayers, continue to be one of the more active areas of investigation. Ever since 1917, when Langmuir first developed what subsequently became know as the Langmuir film balance, surfactant or Langmuir monolayers (LM) have been extensively studied using a variety of techniques. It is only recently that the availability of synchrotron radiation sources has allowed grazing incidence diffraction to be used to learn the microscopic, molecular structure of these films. Part of the reason for the broad current interest in LM is that they are one of the few realizable systems in which a film exhibiting two dimensional (2D) statistical physics can be tuned in a manageable way by varying the molecular structure. As a result, the phase diagrams of LM are enriched in comparison with those of simpler monatomic systems. In addition, many of the properties of LM can be related to those of biological membranes and to thin organic films that are used for lubrication and other purposes Although initial investigations were carried out on simple soap like molecules which contain a hydrophobic tail and a hydrophilic headgroup, increasingly more complex molecular architectures were investigated over the last few years and recent studies addressed such systems as fullerene derivatives, gold colloids, discotic and nematic liquid crystalline materials and water-soluble pigments at lipid interfaces.

One unfortunate aspect associated with application of the GIXD technique to probe the structure of 2D phases of LM is the fact that the scattering cross section for most of the surfactants that have been studied is not sufficient to observe the structure factor of phases with the short positional correlation lengths that are typical of liquid phases. One exception to this is the study by a group from Harvard and Ames Laboratory, at X22B, in which they measured the structure factor of an amorphous phase of a LM of a fullerene-propylamine adduct (C_{60}-PA), consisting of a C_{60} molecule and twelve propylamine ($NH_2(CH_2)_2CH_3$) chains attached to it. This molecule is sufficiently large that the structure factor of the LM could readily be separated from the diffuse background scattering from the ambient He gas above the monolayer and the bulk liquid water below. **Figure 27** illustrates GID scans (with background subtracted) for LM of C_{60}-PA at different surface densities. When the effect of the calculated molecular form factor is included the peak position at ~0.42 Å^{-1} corresponds to the average nearest neighbor distance of ~13.2 Å which is close to the diameter of the molecule and corresponds to a molecular area of ~151 Å^2/mol. This is very close to the specific area at which the surface pressure increases (inset to **Figure 27**). Although this LM was an amorphous solid, the hope is that if LM systems can be developed in which the fullerenes phase will be fluid it would be possible to study 2D melting/solidification. A second system in which GIXD studies of a disordered phase reveal the broad peak associated with a system having only short range order is gold colloid monolayers, studied by Clarke and collaborators at X22B. In addition to GIXD studies x-ray reflectivity measurements indicate a monolayer to bilayer transition with increasing 2D density.

Studies of LM systems with smaller molecules, for which the in-plane order was only observed for phases with relatively long range order include the discotic liquid

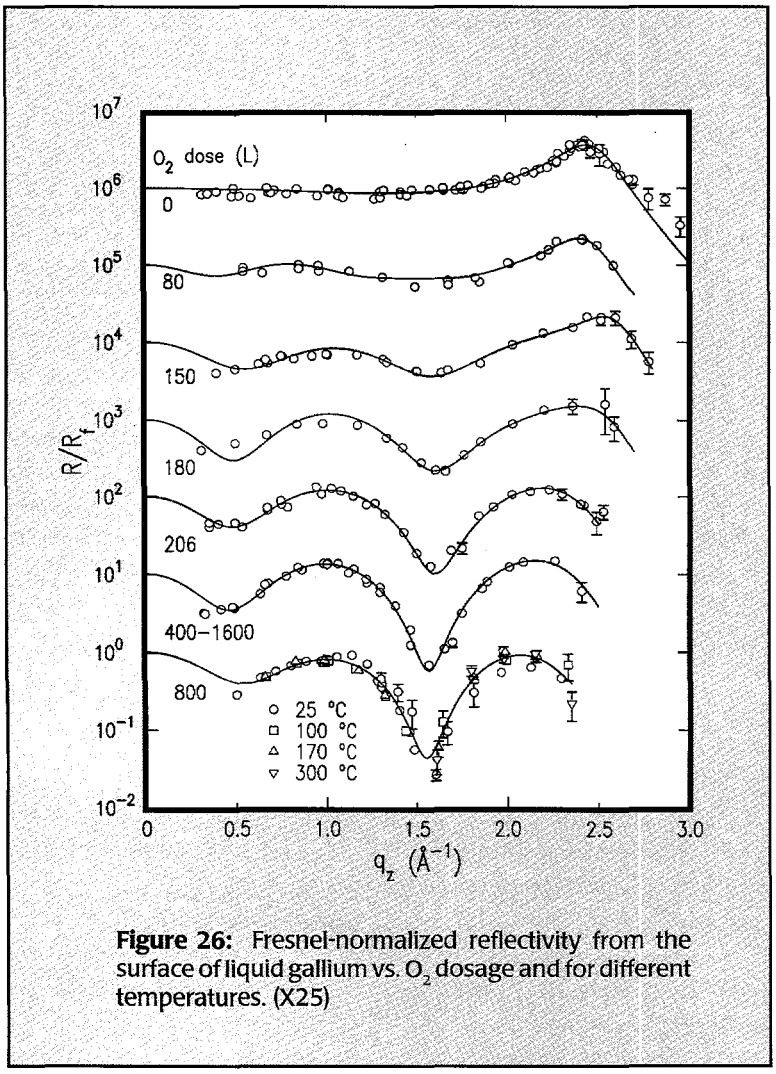


Figure 26: Fresnel-normalized reflectivity from the surface of liquid gallium vs. O_2 dosage and for different temperatures. (X25)

crystalline monolayers studied by a group from U. Penn at X22B. They studied LM of two different molecules, of which only one showed a single GIXD peak. A group from Northwestern, working on X14A, carried out similar studies on a LM of an azobenzene containing molecule. Although Brewster angle microscope studies carried out prior to the synchrotron measurement indicated the existence of a phase transition from a low density fluid phase to a higher density solid phase, the GIXD measurements indicated that both phases have the same degree of positional order, implying correlation lengths from 100 Å to 300 Å in each phase.

The Ames Laboratory/BNL collaboration also carried out a GIXD and reflectivity study at X22B to determine the structure of charged water soluble pigments that are adsorbed by charged lipid monolayers at the air-water interface. The combination of pressure/area isotherms and x-ray measurements shows that when the LM is spread on micro-molar solutions of the pigments the LM order is substantially different from that of the LM spread on pure water.

Finally the BHB group studied the formation of thiol mono- and multilayers on liquid mercury. This novel system is intermediate between Langmuir films on water and self-assembled organic layers on crystalline solids. It forms on a disordered liquid surface like the former, while its structure is dominated by the strong substrate-headgroup interaction like the latter. The monolayers formed were found to be well-defined and densely packed, with molecules aligned normal to the surface. Surprisingly, however, no long range in-plane order was observed for any of the chain lengths studied. The multilayers were found to have a complex bi-layer structure with Hg atoms intercalated in the center, and are well-ordered in-plane, with a highly oblique unit cell resembling that of bulk mercury thiolate.

Surface Freezing

A group of researchers from Brookhaven, Exxon, Argonne and Bar-Ilan found in measurements carried out at NSLS a few years ago that normal-alkanes and alcohol exhibit surface freezing, i.e. a spontaneous formation of a solid layer at the surface of the melt at temperatures of a few degrees above the bulk melting temperature. This is a very rare phenomenon, since almost all other materials show the opposite surface melting effect following a general Statistical Mechanics principle. X-ray measurements at X22B showed the surface-frozen layer to be a single monolayer in alkanes and single bilayer in alcohols. Their crystalline structure was fully characterized as a function of both chain length and temperature, resulting in a rich phase diagram including rotator and non-rotator phases of surface-normal and tilted molecules. More recent studies showed the same effect in alkane-alkane and alcohol-alcohol mixtures, which also exhibit a novel quasi-2D phase diagram for the surface layer, depending on the chain length difference of the components.

In related studies by the same group during this year, O. Gang (Bar-Ilan U.) and coworkers have shown that it is possible to tune the temperature range of existence as well as the surface layer structure of alcohols by judiciously chosen molecules added to the bulk at a few percent concentration level. Water molecules added to long chain alcohols were found to intercalate in between the two

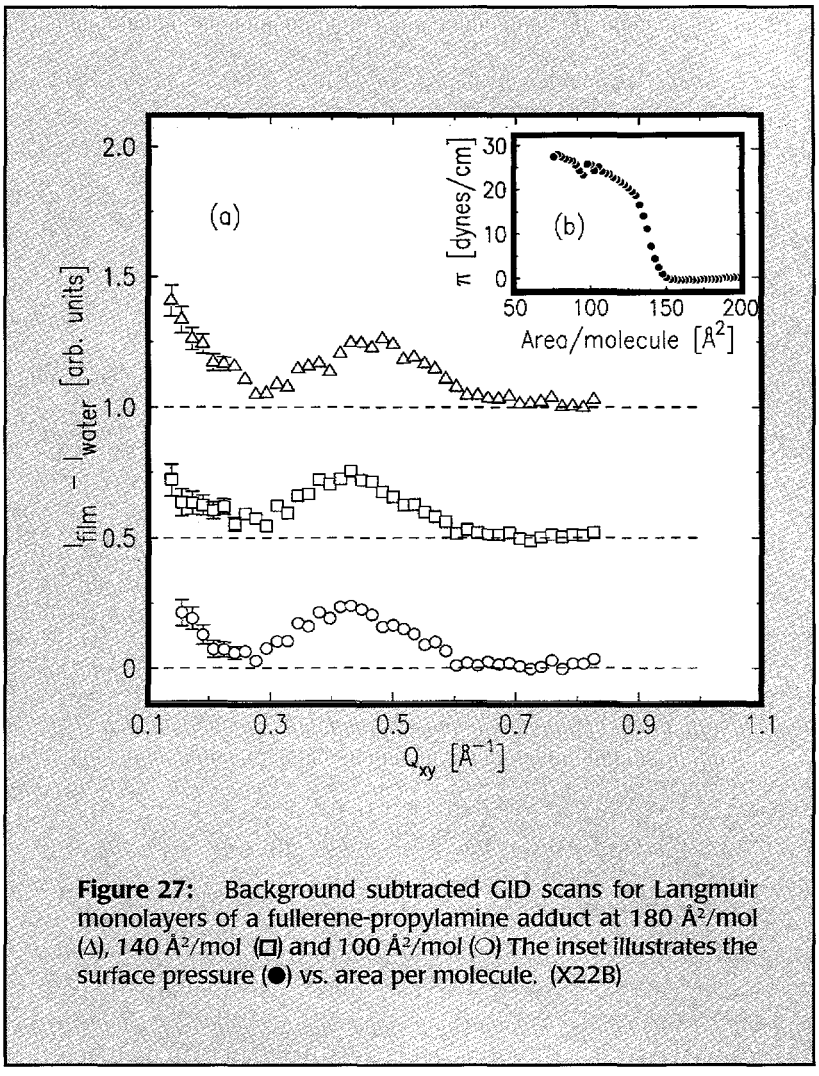


Figure 27: Background subtracted GID scans for Langmuir monolayers of a fullerene-propylamine adduct at 180 Å²/mol (Δ), 140 Å²/mol (□) and 100 Å²/mol (○) The inset illustrates the surface pressure (●) vs. area per molecule. (X22B)

layers comprising the surface bilayer causing it to swell by ~2 Å. In addition, the bilayer formation and bulk freezing temperatures are shifted up, and an increase of 1-2 °C is obtained in the range of existence of the bilayer. For longer chain alcohols, where tilted phases are observed, the intercalating water also reduces the molecular tilt by a few degrees, as compared to the dry pure alcohol. Another additive, a short a,w-diol, was found to induce a transition from a bilayer to a monolayer in the surface layer, which could be affected either through a concentration or a temperature variation Reflectivities of the surface-frozen layer in the mono- and bilayer phases of the diol-laced C_{20} alcohol are shown in **Figure 28**, where their characteristically different shapes can be clearly observed. The monolayer phase seems to be stabilized by the adsorption of an excess concentration of diol molecules at its lower surface, probably attracted by the layer of OH groups facing the melt. This demonstrate that "engineering" the structure of the surface phase by bulk additives is a viable, and exciting, possibility.

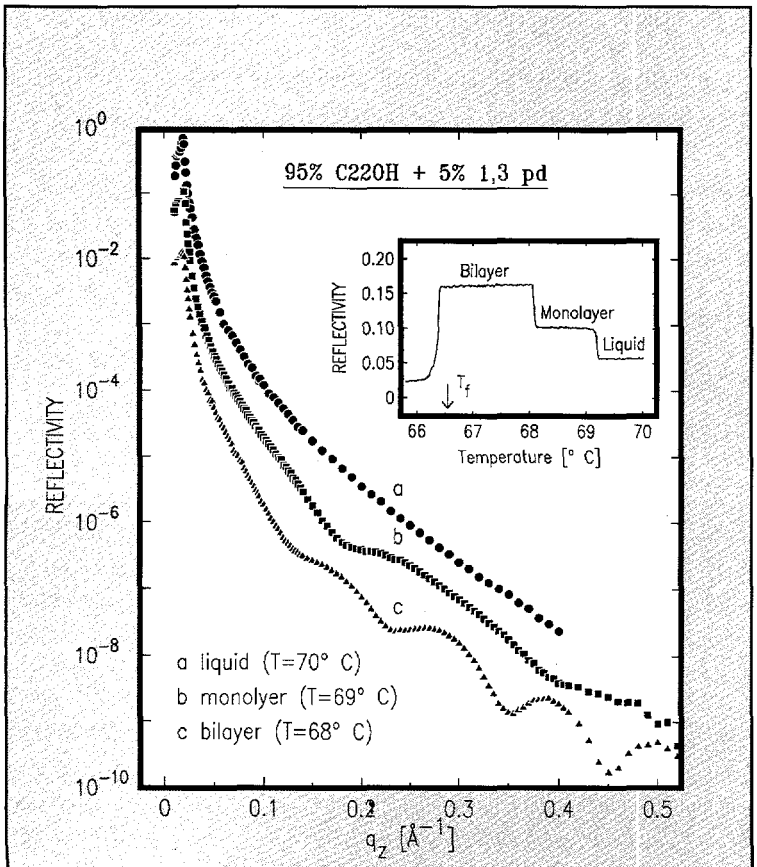


Figure 28: X-ray reflectivity curves of the surface of a melt of a n-docosanol (95%) + 1,3-propanediol (5%). Three characteristic curves are observed: one for the liquid surface phase (a), and two for the surface-frozen phases: the monolayer (b) and bilayer covered surfaces. The monolayer phase is not observed in pure alcohols of any chain lengths. The inset shows the reflectivity at a fixed q_z=0.3 Å^{-1}. The surface phase transitions are clearly observed as jumps in the reflectivity. (X22B)

Liquid-Liquid Interfaces

In addition to the liquid vapor interface, x-ray reflectivity studies have also been extended to the liquid-liquid interface. Following on the earlier work by McLain *et al.* (MIT), on the structure of the oil/water interface in equilibrium with a middle-phase microemulsion, M. Schlossman *et al.* (U. of Illinois @ Chicago), carried out a series of XR and GIXD studies on the oil/micremulsion interface of several ternary microemulsions containing a straight chain oil, water, and a surfactant from the homologous series C_iE_j (n-alkyl plyglycol ether $CH_3(CH_2)_{i-1}(OCH_2\ CH_2)_jOH$). The main interest here is in the interplay between the non-monotonic interfacial profiles of the two liquids and the large amplitudes of the thermally-induced capillary waves, expected from the ultra-low, ~0.1 mN/m, interfacial tension. The challenge for these measurements arises from the large absorption losses of the x-rays, which must traverse a long path inside the oil phase, as well as the very low reflectivity due to the high surface roughness. Schlossman's measurements used 15 keV x-rays and a sample cell ~ 35mm wide. Preliminary analysis indicates that the roughness of the surface of the mixture containing $C_{10}E_4$ (s >200 Å) is considerably greater than that of mixtures containing either C_4E_1 (s = 57 Å) or C_6E_2 (s = 45 Å). All of these values are much larger than the corresponding molecular sizes, and indicate strongly fluctuating interfaces, as expected. Preliminary analysis of the measured diffuse scattering spectra yields a higher surface roughness than the reflectivity results, indicating the need for a more sophisticated approach then the step-function distorted wave Born approximation.

The application of synchrotron radiation to the structure of liquid surfaces is currently providing atomic level information that is not otherwise available. For LM as an example, GIXD measurements have revealed rich phase diagrams involving multiple two dimensional solid-solid phase transitions that correspond well with three-dimensional solid-solid phase transitions. Similarly XR measurements have confirmed the decades old predictions of the

layered structure of liquid metal surfaces and revealed new features that will continue to be the subject of future research for some years. Other technically challenging systems, like the liquid/liquid interface, will also continue to draw much attention, and will no doubt benefit from the high-energy mode of operation currently being explored at the NSLS as well as the higher brilliance and intensity available at present insertion-device sources at the NSLS.

Solid Surfaces

X-ray diffraction continues to be an important experimental probe for the determination of the atomic structure of single-crystal surfaces, and the problems which are tackled by this technique grow successively more difficult. For example, the bulk crystal structure of gallium consists of dimers tilted slightly away from the (001) direction, and so it is interesting to know whether the surface simply truncates the bulk structure, or if there is a more complicated rearrangement. Preliminary results by D. Walko *et al.* (U. of Illinois), on X16A indicate that the surface is different from the bilayer self-wetted structure proposed theoretically. There has also been work on X22C to study whether Ir(001) becomes incommensurate, roughens, or disorders at high temperature, motivated by the behavior of Au and Pt. G. Watson *et al.* (U. of Maryland), found that it remains commensurate, and roughens above 2000 K. Under very different conditions, J. Wang and R. Adzic (Brookhaven National Laboratory) studied the (111) surface of Au in contact with a solid electrolyte. The experimental conditions guaranteed that the observed lifting of the reconstruction with electric potential was caused by the surface charge rather than by anion adsorption.

The addition of a monolayer film on a single crystal surface opens a rich variety of possibilities, and in-vacuum x-ray measurements are well-suited to their study. P. Bennett *et al.* (Arizona State U.), made use of the high resolution intrinsic to x-ray scattering techniques to show that the monolayer Au on Si(001) 5x1 structure is actually incommensurate, in contrast to earlier LEED and STM results. A different technique, x-ray standing wave analysis, has been used to study the initial stages of adsorption of In on GaAs(001) and of Te on Si(001), (T.-L. Lee, *et al.,* Northwestern U. and P. Lyman, *et al.* LBNL), on X15A. It is also possible to prepare well-defined adsorbed phases from solution, and x-ray diffraction is particularly useful in penetrating the liquid overlayer to obtain atomic-scale information. L. Cheng *et al.* (Northwestern U.), used the x-ray standing wave technique to study the adsorption of selenite (SeO_3^{2-}) ions on calcite. J. Wang *et al.* (Brookhaven National Laboratory), used beamline X22A to discover that mono- and bi-layers of electrochemically-deposited Ag form an incommensurate phase on Pt(111) which is compressed relative to bulk Ag. This is quite unexpected, because the reduced coordination at the surface usually leads to expanded surface layers. On the same beamline, B. Ocko *et al.* (Brookhaven National Laboratory), studied the ordering of Br on Ag(001), and observed Ising model critical behavior.

There were two interesting experiments on the formation of thin oxide surfaces in aqueous environments. A. Davenport *et al.* (Brookhaven National Laboratory), have studied thin oxide films on Fe(001) and (110) on beamline X20A. They find an epitaxial relationship between oxide and substrate. According to their results, the film is not one of the bulk forms of iron oxide, but rather is similar to the spinel Fe_3O_4, with a large fraction of oxygen vacancies and some displacement of the oxygen ions. In related work, Y. Chu and I. Robinson (U. of Illinois) have used X16C to study the oxidation of Cu(111) in perchloric acid. They find epitaxial cubic Cu_2O grows in two different orientations, in which one alignment grows to only a few monolayers, while the other can become significantly thicker.

MATERIALS SCIENCES

Magnetism

X-Ray Scattering

In recent years, synchrotron radiation has become an important technique for the study of magnetic properties of thin films and surfaces. Recent examples include magnetic diffraction measurements by M. Conover *et al.* (U. of Illinois @ Urbana-Champagne), on X22C studying the influence of monolayer superlattice doping of rare earth metal films: Dy in Ho and Y in Er. They found that the imposed superlattice produced significant changes in the magnetic lock-in structure relative to bulk samples. On the same beamline, Helgesen studied the magnetic and structural properties of Er films grown epitaxially on Lu and Y, producing, respectively, compressed and expanded lattices relative to bulk Er. The depth profile of the magnetization was measured directly in a study of the magnetic disorder at the surface of a crystal of UO_2 by G. Watson *et al.* (U. of Maryland), on beamlines X22C and X25. Using X22C, A. Hiess *et al.* (EITU), found that thin films of the heavy fermion superconductor UPd_2Al_3 do not develop long range magnetic order, in contrast to bulk samples, and attributed that fact to the restricted dimensionality.

X-ray techniques continue to prove their importance in the determination of magnetic structures. Several recent experiments at beamline X22C include a determination of the magnetization of different lattice sites in (magnetically incommensurate) Nd by G. Watson *et al.* (U. of Maryland), the use of resonant exchange scattering to find the magnetic moment directions in $SmNi_2B_2C$ and $NdNi_2B_2C$ (C. Detlefs, *et al.* Iowa State U.), and the magnetic structure of $TbNi_2Ge_2$ by A.H.M. Islam *et al.* (Iowa State U.).

Spin- and Angle-Resolved Photoemission

FY 1996 was a very active year for the spin-resolved undulator beamline U5UA. Just prior to this replacement, the Magnetic Thin Films group from ANL (D. Li, J. Pearson and, S. Bader) joined the NSLS R&D group (E. Vescovo) and the BNL Physics Department's Surface Physics group (D.J. Huang, and P.D. Johnson) to perform a very challenging experiment. The goal was to elucidate the electronic states responsible for the magnetic coupling in the Cr/Fe giant magnetoresistance (GMR) materials.

Over the past few years, spin-resolved photoemission, notably the work done at U5UA, has been successful in identifying the electronic states which drive the magnetic coupling in the noble-metal based GMR materials. In this "simple" case, the long-range magnetic coupling is transmitted through the *noble-metal* spacer material via the formation of discrete, *sp*-derived, quantum-well-states (QWS). The spin of these states is determined by the spin-polarized boundary conditions at the adjacent ferromagnetic layers. The QW-like thickness dependence of these states accounts for the oscillatory behavior observed in the magnetic coupling as a function of the separation between consecutive magnetic layers.

The experiment on the atomically flat Cr/Fe(100)

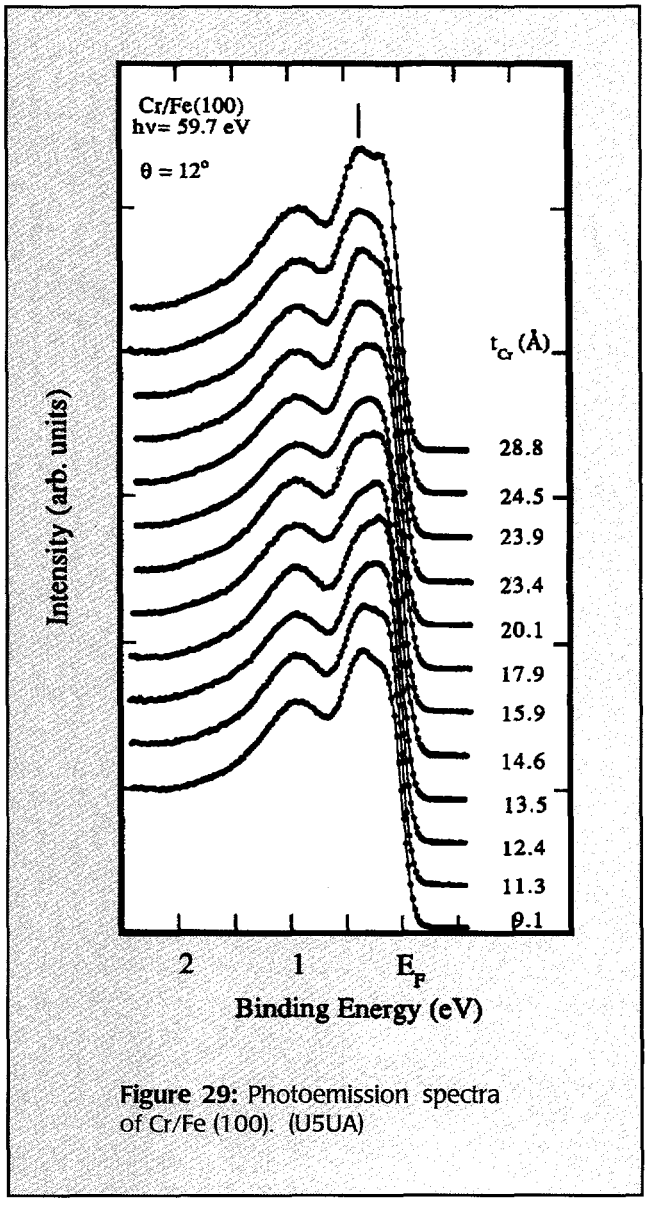


Figure 29: Photoemission spectra of Cr/Fe (100). (U5UA)

whisker was designed to attack the considerably more complex situation in which the spacer layer material is not a noble-metal: Cr has 3*d* states at the Fermi level (E_F). The QW model is hard pressed to predict the correct magnetic coupling in this case. An essential ingredient of this picture is the highly delocalized nature of the electronic states which characterize the Fermi surface of a noble metal. In the Cr case, an analysis of the bulk Cr Fermi surface suggests different pieces of the Brillouin zone as most likely to be active. Then, using angle-resolved photoemission, a careful investigation of the evolution of the photoemission spectra vs. the thickness of the Cr layer deposited on the Fe(001) whisker was conducted at these various "hot" **k**-points. The main result is the unambiguous identification of a 17± 2 Å oscillation period in the intensity at E_F of the energy distribution curves collected at 12° off-normal with 59.7 eV photon energy (**Figure 29**). This observed periodicity is in full agreement with the long-period magnetic oscillations (18 Å) found in Cr/Fe(001) multilayers. Furthermore, the "hot" **k**-points are in the vicinity of the d-derived "lens" feature of the Cr Fermi surface. The observation of QW-like behavior there suggests the "lens" region as the **k**-space origin of the long period oscillation in Fe/Cr multilayers.

Near the end of FY 1996, significant new results were obtained by a collaboration between the NYU spin-resolved group (B. Sinkovic, W. Zhu) and the NSLS R&D group (E. Vescovo) on an important magnetic materials problem of both fundamental and applied interest: half-metallic systems. The novelty of this entirely new class of magnetic materials, which was predicted theoretically a few years ago, lies in the fact that their spin-dependent electronic structure is metallic in one spin and semiconducting ~ 0.5 eV band gap in the other. Experimental evidence has so far been limited, possibly as a consequence of the considerable difficulties involved in preparing high quality surfaces of these intermetallic samples. Spin-integrated photoemission measurements from bulk single crystals have been made, which could not address the question of half-metallic character owing to lack of spin sensitivity. Recently, J.S. Moodera and coworkers from MIT have been able to prepare high quality magnetic thin films grown on various substrates, which are ideally suited for investigation by spin-resolved photoemission.

Spin-resolved measurements at the U5UA beamline were performed on a set of thin NiMnSb films (~600 Å thick) grown *ex situ* on glass and Si(001). Although *in situ* magneto-optical Kerr effect measurements indicate high magnetic remanence for these films, the measured spin-polarization of the photoemitted electrons has been found to be quite modest. In particular, the polarization of the electrons close to the Fermi level is found to be only ~20%, in contrast to the prediction of half-metallic behavior (100% polarization at E_F). Encouragingly, however, the spin-resolved photoemission measurements (**Figure 30**) show NiMnSb spin-resolved density of states features in good agreement with recent linear muffin tin orbital calculations. Considering the very high surface sensitivity of the photoemission measurements, these results strongly suggest that the origin of the discrepancy lies in a lowered remanent magnetization of the surface region. The next step will be to search for surface preparation methods which increase the surface remanence. Success would have great technological implications for the magnetics industry, for which the possibility of using materials with large single-spin electric carriers is often seen as a necessary prerequisite to engineer a variety of new magnetic devices.

Structural Studies of Novel Materials

The NSLS has a long history of being able to provide important characterization of new materials as they are produced, and the current year is no exception.

One newly synthesized material for which synchrotron x-ray diffraction has been important is periodic arrays of Au nanocrystals of 50-500 atoms, passivated by

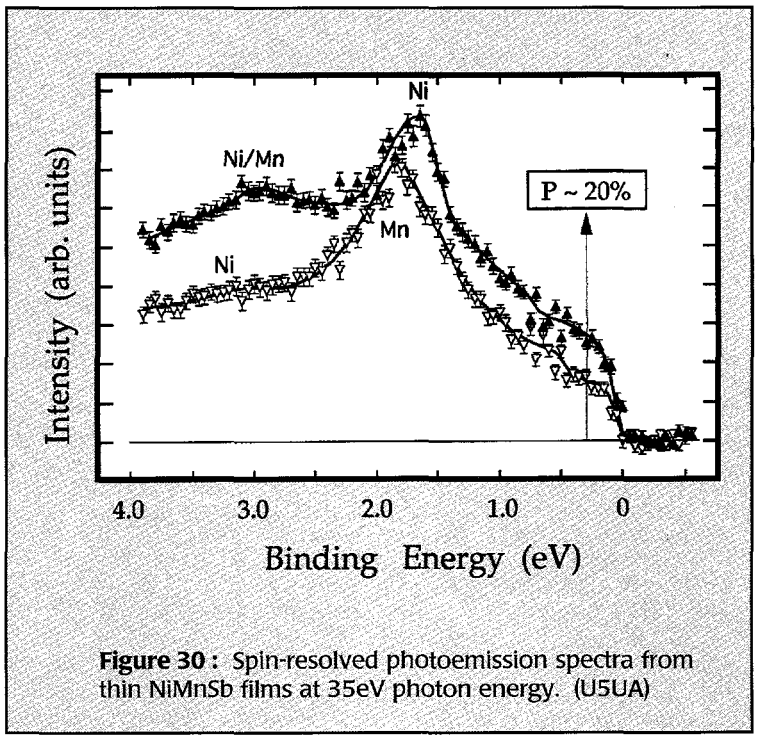


Figure 30 : Spin-resolved photoemission spectra from thin NiMnSb films at 35eV photon energy. (U5UA)

self-assembled monolayers of alkylthiolate molecules. R. Whetten *et al.* (Georgia Institute of Technology and SUNY @ Stony Brook) have developed techniques to separate fractions containing controlled shapes and sizes of the Au nanocrystals, and these materials show a very interesting diffraction pattern (**Figure 31**).

Another colloidal crystal system, studied by G. Beaucage *et al.* (U. of Cincinnati) on X23A3 this year, has a much larger length scale: silica in a polymer matrix with lattice parameters in the range of several μm permit an interesting opportunity to compare x-ray measurements with optical and scanning electron microscopy. This experiment makes use of the Ultra-SAXS Bonse-Hart apparatus at this beamline.

A completely different technique was applied by T. Gog *et al.* (Argonne National Laboratory) on the wiggler beamline X25 to study 50 Å GaP clusters imbedded in a Si matrix. In this work, they extended their variable energy x-ray holography technique to dilute samples, in which the lattice match between the clusters and the matrix would have made conventional x-ray diffraction analysis quite difficult.

Fullerene materials continue to generate interest, and there are several important new results from powder diffraction measurements. G. Bendele and co-workers (SUNY @ Stony Brook, X3B1) have shown that the quenched dimer phase of RbC_{60} has a different interfullerene bonding pattern than the polymeric chains found in stable RbC_{60}; a single bond between one C atom on each buckyball instead of a [2+2] cycloaddition. If one is sufficiently patient, Na_2RbC_{60} spontaneously transforms from its high-temperature cubic phase to an orthorhombic structure; previously it was thought that this transformation required the application of pressure. Incidentally, this work also showed that the orthorhombic polymer phase is not a superconductor, in contrast to what had been previously thought by some authors. M. Stetzer *et al.* (U. of Pennsylvania), have continued their investigations on beamline X7A of fullerenes with handles, viz. $C_{61}H_2$ and $C_{63}H_6$, finding two thermal phase transitions of the former and a likely unit cell for the latter.

Sliding charge-density waves exist in certain substances, and J. Brock and his colleagues at Cornell U. have made measurements using X25 to elucidate both their structure and dynamics. They have been able to provide strong evidence against recent theoretical models, which predict that the equal time phase-phase correlation function should be algebraic at large distances. Similarly, their time-resolved measurements of the decay from sliding to pinned states contradict the theoretical conclusions.

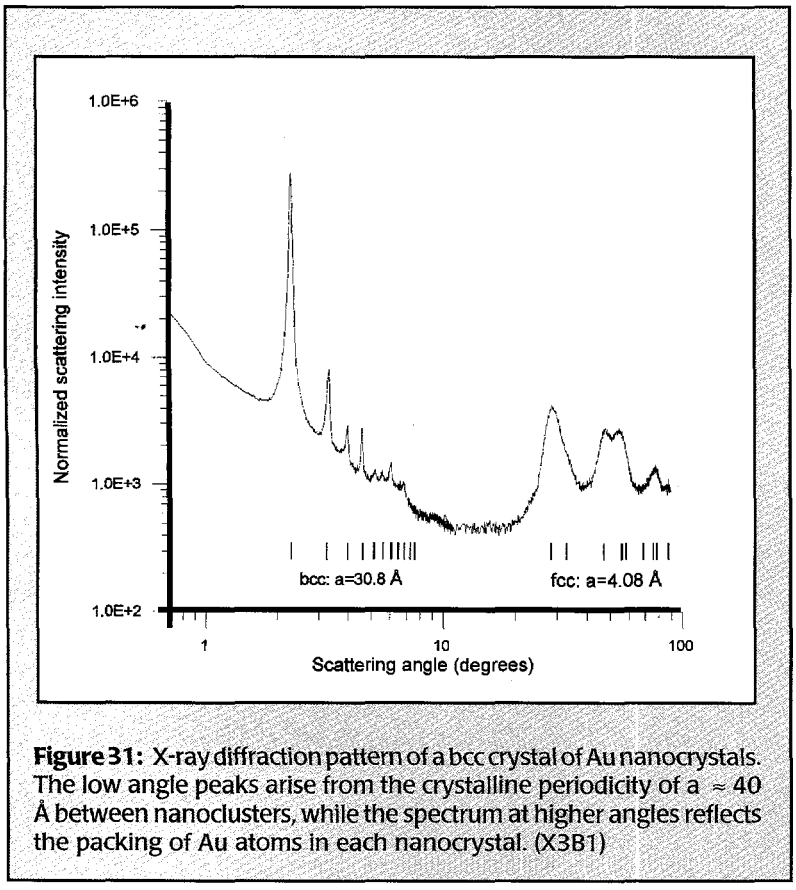


Figure 31: X-ray diffraction pattern of a bcc crystal of Au nanocrystals. The low angle peaks arise from the crystalline periodicity of a ≈ 40 Å between nanoclusters, while the spectrum at higher angles reflects the packing of Au atoms in each nanocrystal. (X3B1)

Highly Correlated Systems

Far Infrared Ellipsometry

The technique of far infrared ellipsometry is being developed by a group from the Max Planck Institute (Stuttgart, FRG) at beamline U4IR. Ellipsometry is a method for directly extracting a material's optical constants, such as the frequency dependent conductivity and dielectric function, from reflectance measurements (as a function of polarization angle for non-normal incidence). The high-brightness synchrotron infrared source makes the technique practical, as sample sizes are often very small (less than 1 mm by 1 mm) and the angle of incidence must be restricted to achieve accurate results. R. Henn (Max Planck Institute) and coworkers are using this technique to investigate the c-axis infrared response of $La_{2-x}Sr_xCu_4$ for various values of x. They observe that the conductivity along this direction changes character as the Sr fraction passes through x=0.15 (which yields the optimal T_c), consistent with dc transport measurements.

X-Ray Scattering

The recent discovery of colossal magnetoresistance behavior in the perovskite-derived manganite system $La_{1-x}Ca_xMnO_3$ has stimulated much interest in the structural properties of these materials. A high resolution powder diffraction study by P.G. Radaelli *et al.* (Institut Laue Langevin), at X7A in the temperature range 20-300 K has revealed the presence of weak satellite peaks below the antiferromagnetic transition at ~180 K associated with a transverse modulation (0.5- ,0,0), corresponding to an approximate doubling of the orthorhombic a axis. The satellite intensities are consistent with charge-ordering of Mn^{3+} and Mn^{4+} ions and orbital ordering of the Jahn-Teller-distorted $Mn^{3+}O_6$ octahedra, resulting in a monoclinic structure in which the $Mn^{4+}O_6$ octahedra and one-half of the La atoms are shifted by ~0.1 and 0.05 Å respectively as indicated in **Figure 32.** Since then, D. Cox *et al.* (Brookhaven National Laboratory), have studied the pyrochlore $Tl_2Mn_2O_7$, and found that it does not have any lattice anomaly at the metal-insulator transition.

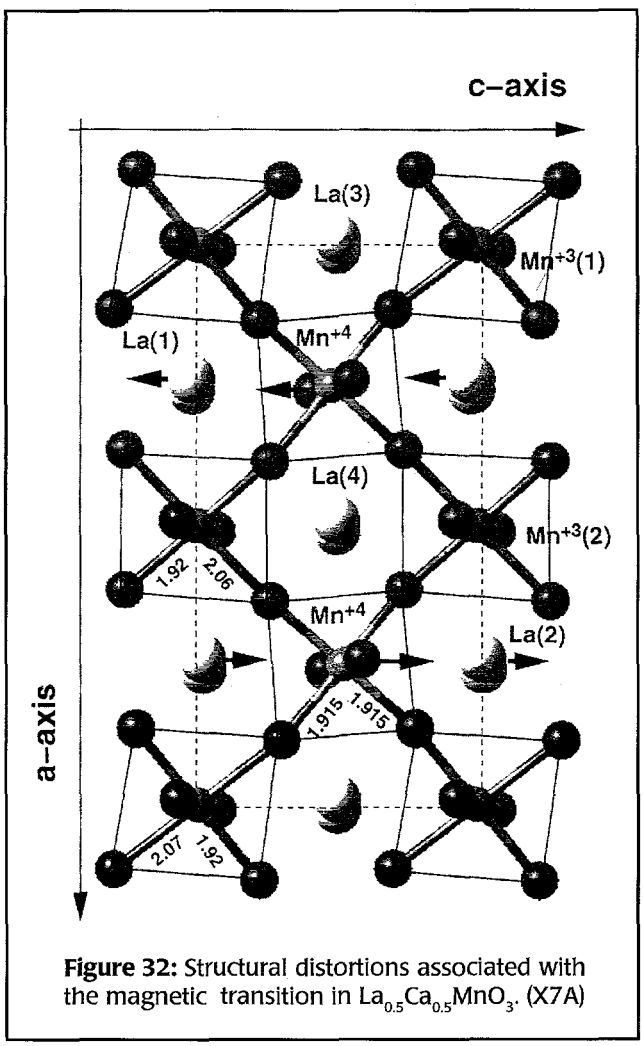


Figure 32: Structural distortions associated with the magnetic transition in $La_{0.5}Ca_{0.5}MnO_3$. (X7A)

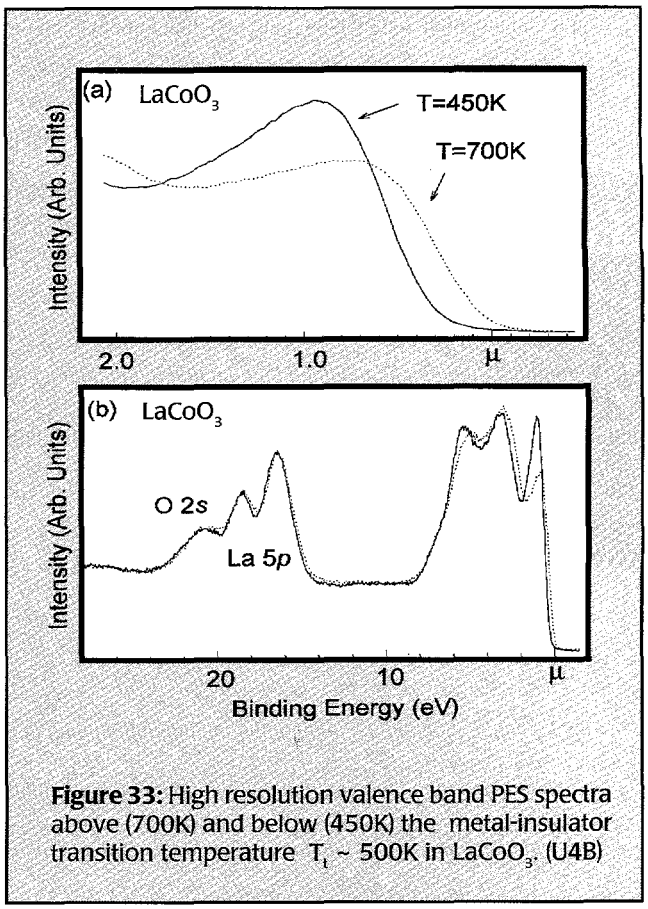


Figure 33: High resolution valence band PES spectra above (700K) and below (450K) the metal-insulator transition temperature T_t ~ 500K in $LaCoO_3$. (U4B)

X-rays are not merely a passive probe in some experiments on GMR materials. V. Kiryukhin *et al.* (Princeton U.), noted an x-ray photoinduced transition from insulating to metallic phases in $Pr_{0.7}Ca_{0.3}MnO_3$ on beamline X22B.

High-Resolution Photoemission

J.-H. Park (NSLS), S-W. Cheong (Bell Labs.) and C.T. Chen (SRRC) have investigated the high temperature metal-insulator transition of $LaCoO_3$ utilizing a high resolution valence band photoemission spectroscopy (PES) at beamline U4B. $LaCoO_3$, which exhibits a diamagnetic to paramagnetic transition around 90 K upon heating, undergoes a gradual insulator to metal transition around 500 K upon heating. **Figure 33** shows the high resolution valence band PES spectra above (700 K) and below (450 K) the transition temperature T_t ~ 500 K. Upon heating through T_t, the insulating band gap disappears [**Figure 33(a)**], demonstrating the occurrence of the insulator to metal transition. Furthermore, considerable differences in spectral lineshape are observed in entire valence band [**Figure 33(b)**] at the two temperatures. These differences indicate that the metal-insulator transition is accompanied by a symmetry change, which results in an additional spin state change.

X-Ray Spectroscopy

The impact of EXAFS and XANES in the field of superconductors was evidenced by several abstracts from beamline U4B and X11A, using soft and hard x-ray spectroscopy respectively. Oxygen K-edge NEXAFS was used to understand how oxygen orbital structure correlates with the superconductivity of the material. For example, several groups examined superconductors of the type: $(Y_zRE_{1-z})Ba_2Cu_3O_y$. Generally, rare earth substitution has little effect on the superconducting properties, with the notable exception of Pr. Oxygen 1*s* NEXAFS of superconductors with increasing concentrations of Pr were examined and showed specific changes in oxygen orbital structure consistent with the presence of Fehrenbacher-Rice states.

In another investigation on beamline X11A, D. Haskel and E. Stern (U, of Washington) investigated the structural consequences of Sr^{+2} substitution for La^{+3} in $La_{2-x}Sr_xCuO_4$. Sr^{+2} in the range of 0.075 to 0.25 leads to high T_c superconductivity by inducing hole carriers in the Cu-O planes. By examining the Sr-K edge EXAFS of oriented powders, it was shown that the Sr-O bonding structure is quite different from that of La-O bonding. In particular, the apical oxygen atoms are split into 2 sites separated by 0.3 Å (**Figure 34**). This implies a fluctuating number of holes at the Cu sites near the Sr atoms. The hole-lattice interaction could be involved in the pairing mechanism, leading to high T_c.

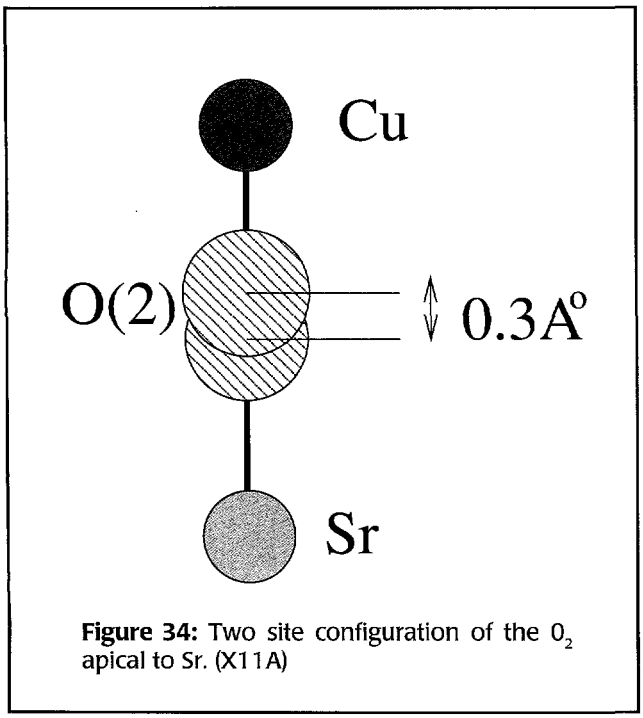


Figure 34: Two site configuration of the 0_2 apical to Sr. (X11A)

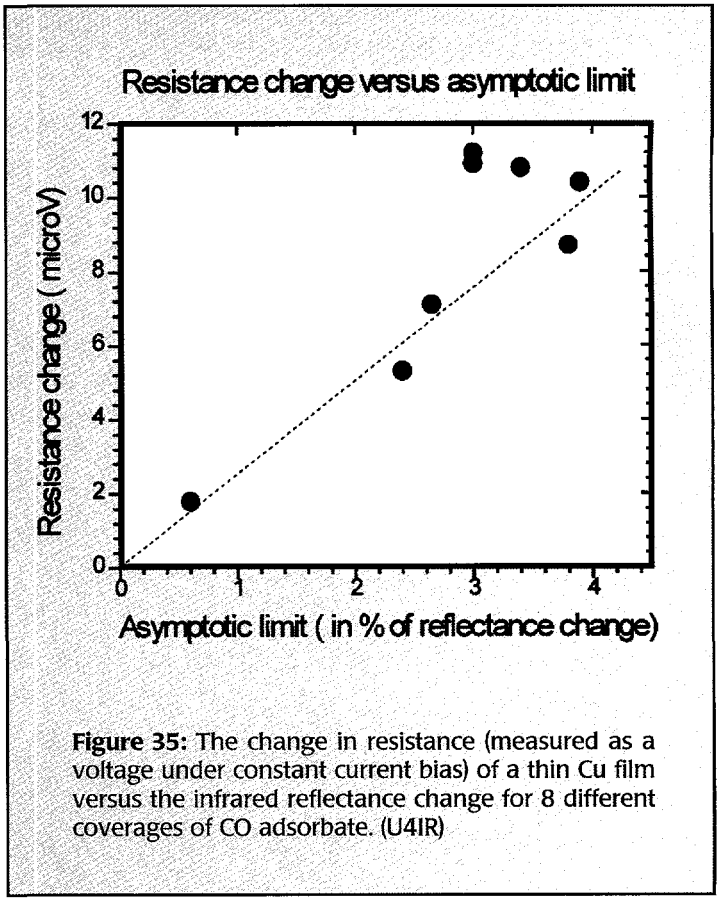


Figure 35: The change in resistance (measured as a voltage under constant current bias) of a thin Cu film versus the infrared reflectance change for 8 different coverages of CO adsorbate. (U4IR)

Surface Dynamics

The primary program at beamline U4IR continues to be studies of molecular adsorbates on metal surfaces by grazing incidence reflectance spectroscopy. Of particular interest is the broadband reflectance change of the metallic substrate as a function of the particular adsorbate and its coverage. Research groups from Duesseldorf, LURE, Tufts, the ALS and the NSLS are studying various aspects of this behavior. The theoretical model of B.N.J. Persson explains the reflectance change as due to enhanced scattering of the metal's electrons from the adsorbate. This scattering affects the surface resistance, and the theory predicts a linear relationship between the electrical surface resistance and the reflectance change. In work by M. Hein, P. Dumas, and collaborators (Duesseldorf, LURE and the NSLS), both the reflectivity change and resistivity were measured for thin Cu(111) films as a function of coverage for CO, oxygen, and ethylene adsorbates as shown in **Figure 35**. In accord with theory, the reflectance change for CO and ethylene was found to be linear with the resistivity change. However, the behavior for oxygen showed some departures from the model predictions.

Another adsorbate-on-metal system, namely C_{60} on various noble metals [Ag(111), Au(110), Cu(111)], was

investigated by P. Rudolf (LISE-Namur, Belgium) and coworkers from LURE (France), Lucent Technologies, and the NSLS. C_{60} readily accepts charge from alkali metals (such as potassium) to form a conducting "fulleride", which is accompanied by distinct changes in several of the C_{60} molecule's IR vibrational modes. In this study of C_{60} deposited on Ag, Au, and Cu, only one absorption mode is observed (**Figure 36**), assigned to the Raman active Ag(2) mode. The mode has become IR active due to symmetry breaking upon adsorption. The appearance of such a mode suggests a strong interaction between the metal and the C_{60} molecule. However, none of the fulleride modes were apparent, indicating that if charge transfer (from the metal to the C_{60} molecule) occurs, it is quite different from that associated with alkali metal doping. Pre-dosing the noble metal surface with K leads to even more interesting behaviors when C_{60} is deposited. For C_{60} on 1ML of K, the Ag(2) mode absorption appears as an anti-resonance. This is similar to what is found for CO on Cu, indicating that conduction electrons in the metal substrate must experience strong scattering from the adsorbate. Apparently some charge transfer occurs from the K onto the C_{60}, leading to a larger scattering cross section for conduction electrons near the substrate surface. A fulleride does form when C_{60} is deposited onto thicker layers of K, as witnessed by the appearance of an absorption mode at 1356 cm^{-1}. The anti-absorption mode at 1450 cm^{-1} persists.

High Pressure Research

The group from the Carnegie Institution of Washington (R. Hemley, A. Goncharov, R. Lu, H.K. Mao *et al.*) continued their investigations of dense hydrogen at beamline U2B, while expanding their program to include other compounds and minerals at extremely high pressures. Results of IR spectroscopy on hydrogen to pressures above 200 GPa have contributed to our understanding of the phase diagram for the solid. A transition from the low pressure, high temperature phase (I) to an intermediate phase (II) occurs for pressures above ~100 GPa and T<100 K. A third phase (III) is observed for pressures above 150 GPa. In phases II and III, the absorption associated with coupled vibrational modes in the molecular solid (vibrons) shifts in frequency and strength as a function of pressure and temperature (**Figure 37, on next page**). The oscillator strength (expressed as an effective charge) and frequency shift were found to share a common temperature dependence in both phase II and phase III. This allowed the Carnegie group to relate both quantities to an order parameter that characterizes the particular phase. This information, combined with results from Raman studies, have led to a picture where phase II consists of molecules with ordered angular momentum, and in phase III the molecules themselves are physically ordered. Thus, the high pressure phases of solid hydrogen can display quantum mechanical or classical ordering.

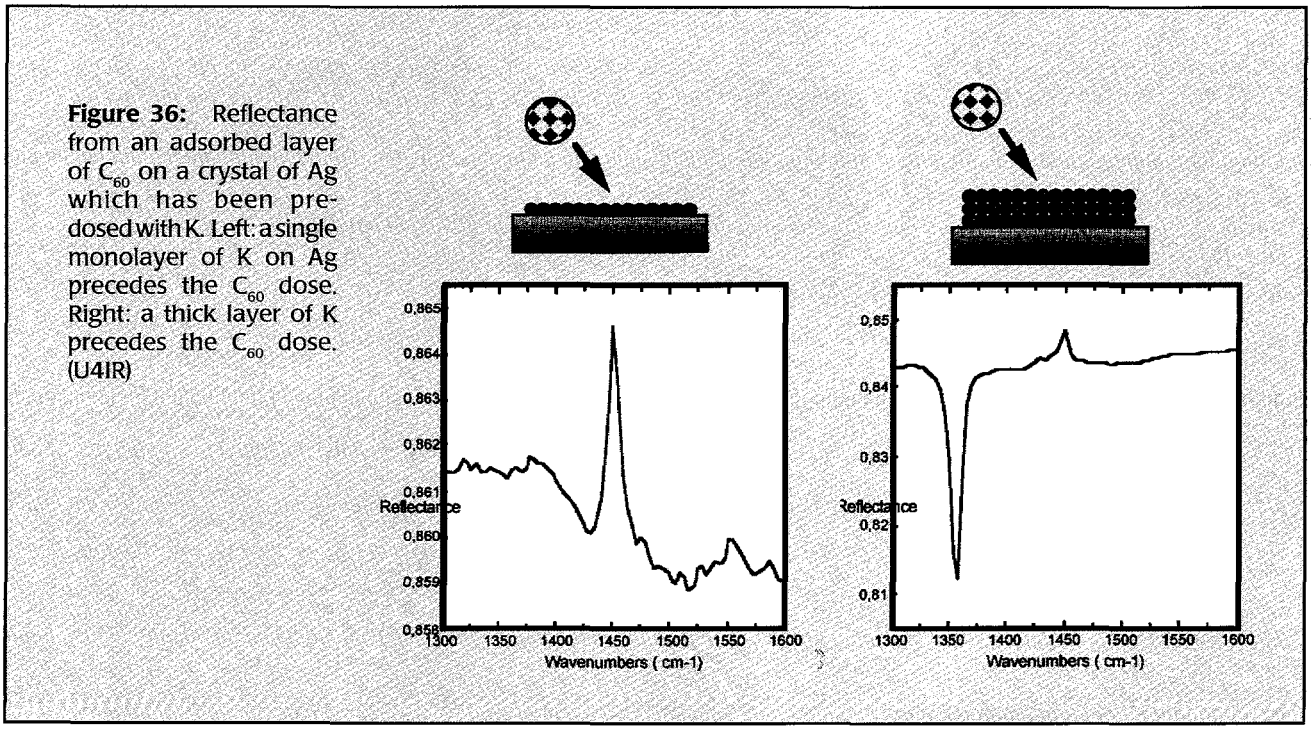


Figure 36: Reflectance from an adsorbed layer of C_{60} on a crystal of Ag which has been pre-dosed with K. Left: a single monolayer of K on Ag precedes the C_{60} dose. Right: a thick layer of K precedes the C_{60} dose. (U4IR)

The Carnegie group have also investigated mixtures of hydrogen with other simple gases (e.g. CH_4, Ar) to high pressures. Similar to the situation for pure H, the molecular solids show IR absorption features associated with vibrational and rotational modes, but there has been no evidence of metallic behavior to the highest pressures achieved so far.

Equation of State

While P-V-T measurements have become routine in synchrotron studies over the past few years, they still provide new insights into material properties and a probe to bonding characteristics. Peiris and Heinz demonstrate the effects of vacancies in ScS on the bulk modulus. They find that the vacancies actually increase the bulk modulus, a result which they explain in terms of the changing bonding characteristics of the material. Zhang and Reeder demonstrate that the bulk modulus-volume systematics for calcite-structure carbonates is sensitive to the cation, with alkaline earth cations defining a different relationship than transition metals, suggesting differences in bonding characteristics.

Phase Equilibria

X-ray diffraction patterns serve as fingerprints for the phases that exist in the high pressure system. S. Qadri *et al.* (Naval Research Laboratory), document the effect of particle size on phase transitions of PbS and E. Skelton *et al.* (Naval Research Laboratory), examine transition rates in Pd as affected by electrochemical absorption of deuterium both on X17C. J. Hriljac *et al.* (U. of Birmingham), explore, on X7A, the phase stability fields of mercury-based superconductors.

J. Chen *et al.* (SUNY @ Stony Brook), explore the pressure induced amorphization of zironium tungstate, the interesting material with a negative thermal expansion, Q. Chen *et al.* (U. of Western Ontario) combined x-ray diffraction with electrical conductivity to study silver sulfate and various tellurium salts. These studies utilized various high pressure systems and share in common the goal to use pressure as a thermodynamic variable to map out the stability fields of a variety of novel materials. Both of these studies were carried out on X17B1.

Electronic Structure

Inelastic X-Ray Scattering

Inelastic X-Ray Scattering Spectroscopy (IXSS) is becoming a routine experimental technique in the study of electronic excitations in atomic, molecular, and condensed matter systems. It provides information complementary to photoelectron spectroscopy, optical spectroscopy, electron energy loss spectroscopy, and x-ray absorption spectroscopy. It also allows greater flexibilty in the selection of sample environment and experimental conditions.

The IXSS measurements carried out at NSLS can be divided into two categories: non-resonant Raman scattering and resonant Raman scattering. In the case of non-resonant Raman scattering, the energy of the incident x-ray is far away from that of any absorption edge of the sample. The double differential cross section is then

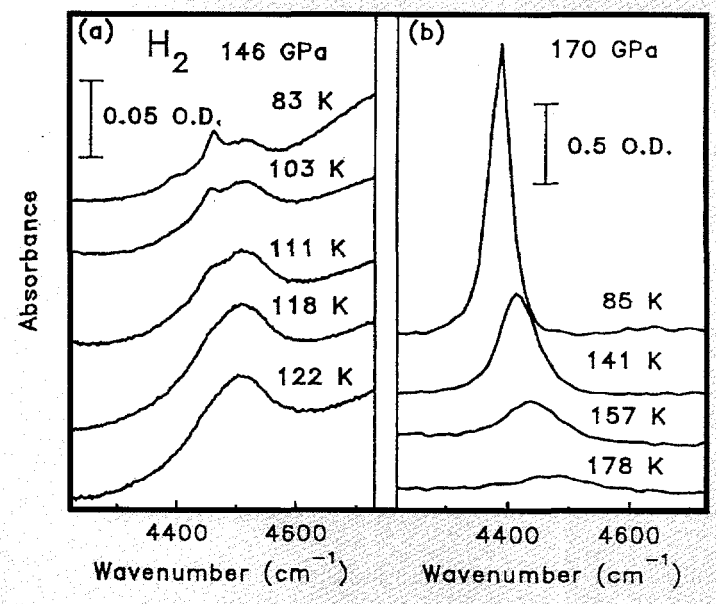


Figure 37: Absorbance measurements of H_2 at high pressures and low temperatures, showing the change in the vibron mode's frequency and strength. Left: Intermediate (angular momentum ordered) phase, Right: High pressure (classically ordered) phase. (U2B)

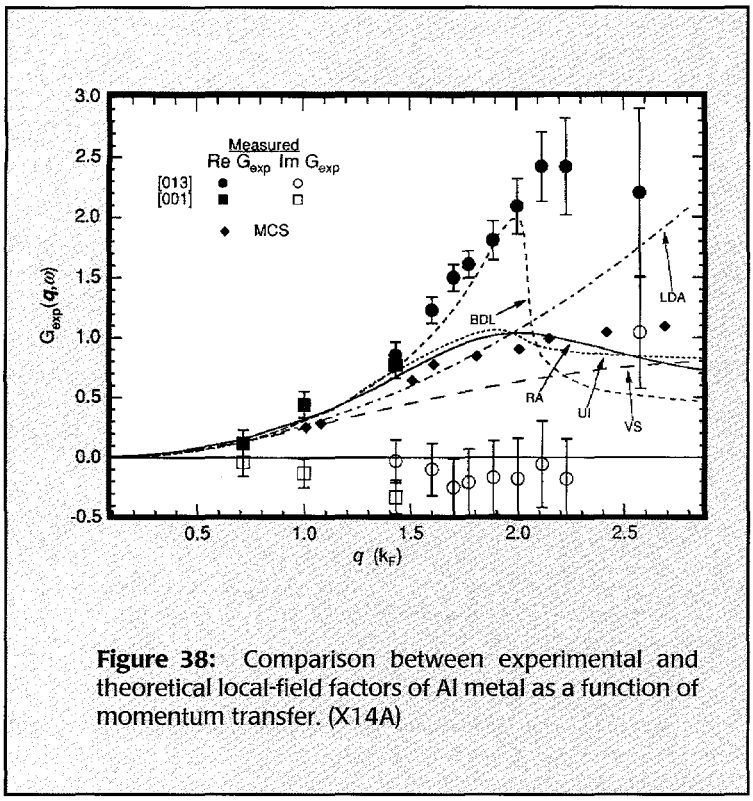


Figure 38: Comparison between experimental and theoretical local-field factors of Al metal as a function of momentum transfer. (X14A)

related directly to the dielectric response function of the system under investigation. Although electron energy loss spectroscopy (EELS) also provides the same information, it suffers from multiple scattering problem at medium to high momentum transfers. As a result, few reliable experimental results are available in these momentum transfer regimes. Another problem with EELS is that samples have to be very thin and vacuum compatible.

To take special advantage of IXSS, several groups have measured the dynamical structure factor, S(q,w), of simple metals near q = $2k_F$, where q is the momentum transfer and k_F is the Fermi momentum. The measured lineshape shows large discrepancies from the prediction of the simplest many-body theory, often referring to as the Random Phase Approximation (RPA). B. Larson (ORNL) *et al.* measured the dynamical structure factor of Al from 0.7 to 2.57 k_F, and compared them with first principle dynamical electronic response calculations to extract the local-field factors as a function of momentum transfer (**Figure 38**). They found that for q = $2k_F$ and larger the experimentally determined local-field factors are nearly twice as large as the calculated values; and suggested that even in simple metals dynamical electron correlations are quite strong. In a closely related experiment, J. Hill *et al.* (Brookhaven National Laboratory), following on from their earlier work on liquid Li and Na, measured the dynamical structure factors of solid and liquid Al near q = $2k_F$ to disentangle the effects of long-range order from intrinsic many-body electron-electron correlation effects. They found that the overall lineshape is very similar between the liquid and the solid; while the fine structure in the linehape for the solid phase is significantly reduced in the liquid (**Figure 39**). These findings suggest that the overall lineshape of the response is due to electron correlations, and that the fine structure in the solid phase is not related to many-body effects. A similar study was also extended to single crystal Na by P. Chow *et al.* (University of Houston). These and future experimental studies in combination with more first principle calculations will certainly contribute to our understanding of the many-body exchange-correlation effects in simple metals.

In the case of resonant Raman scattering, the energy of the incident x-ray is tuned near that of an absorption edge of the sample. By exploiting the resonant condition in the $\vec{A} \cdot \vec{P}$ terms of the electron-photon interaction Hamiltonian, the inelastic scattering cross section can be greatly enhanced. The wider tuneability of the new X21 monochromator was designed so that the K edges of the late 3*d* metals and the L edges of all of the rare earth elements can be easily

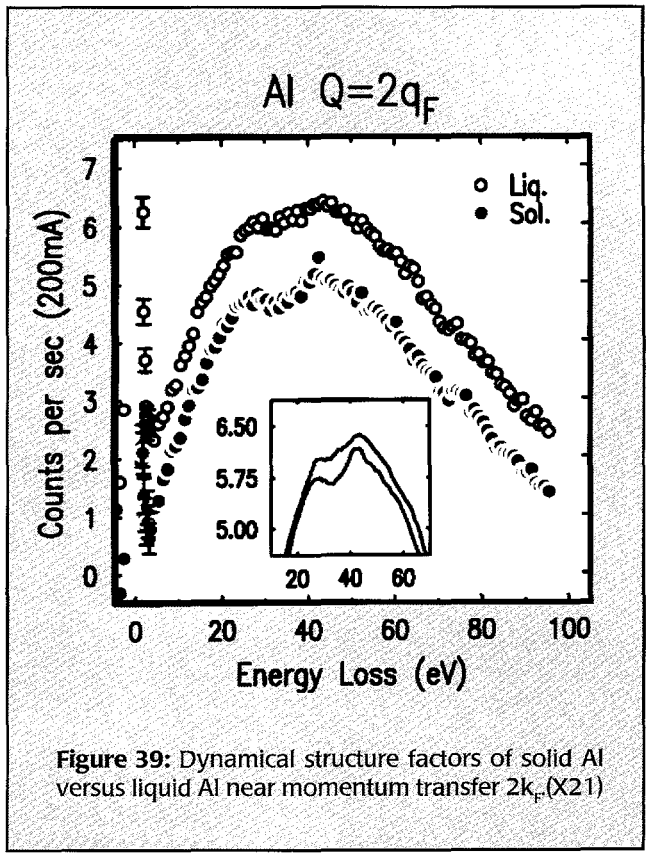


Figure 39: Dynamical structure factors of solid Al versus liquid Al near momentum transfer $2k_F$.(X21)

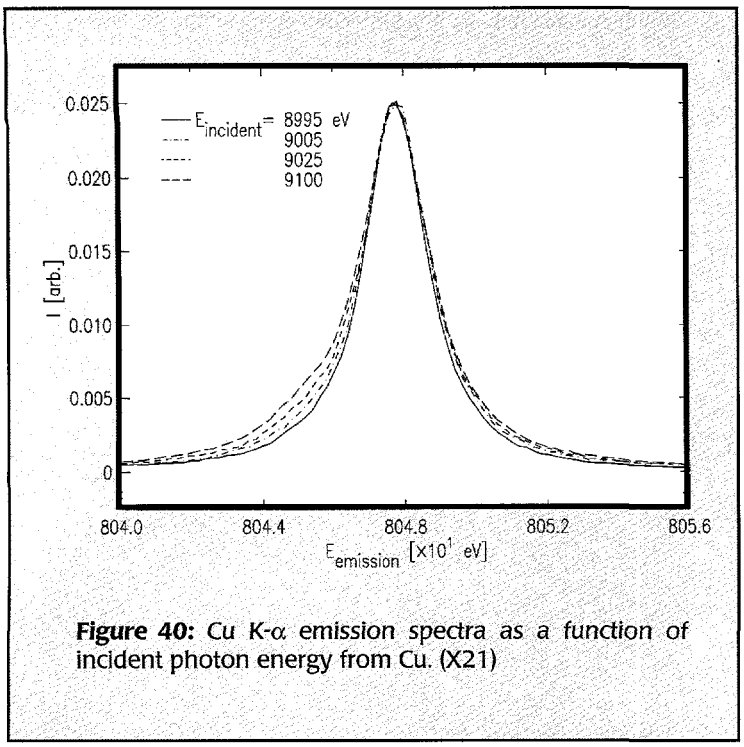


Figure 40: Cu K-α emission spectra as a function of incident photon energy from Cu. (X21)

covered to facilitate this class of experiment. Resonant Raman experiments conducted near the K edges of Mn, Fe, Ni, and Cu were reported this year.

Continuing their study of many electron excitations near the K edge threshold of $3d$ metals, M. Deutsch *et al.* (Bar-Ilan U.) studied the near-threshold behavior of the Cu K-$\alpha_{1,2}$ emission lines. Three regimes were identified: (1) For incident energies below 8981 eV, the energies of K-$\alpha_{1,2}$ emission lines show linear dispersion with incident photon energy, and the intensities of the emission lines show rapid decrease with decreasing incident photon energy. Both are characteristic behavior of resonant Raman scattering below an absorption threshold. (2) For incident energies between 8981 eV and 8995 eV, the lineshape is purely Lorentzian indicating that the $3d$ spectator transitions are still energetically forbidden within this energy range. (3) For incident energies above 9000 eV, $3d$ spectator transitions become energetically allowed. As shown in **Figure 40**, the contributions from the spectator transitions are most pronounced on the low-energy side of the K-α_1 emission line. Lineshape analysis is used to extract the evolution of the strength of the $3d$ spectator transitions with incident photon energy, which is important in the understanding of electron-electron correlation in these systems.

A common feature in the K edge x-ray absorption spectra of $3d$ transition metal compounds is a weak pre-edge peak below the absorption threshold. It is typically assigned to $1s \rightarrow 3d$ transition. The strength of the transition depends on the symmetry of the local environment around the transition metal. With 0.2 eV incident energy resolution, the splitting of the pre-edge feature due to the crystal-field can be resolved in some cases. In resonant Raman scattering experiments, one can then selectively excite the $1s$ electron to one of the crystal-field split states, and monitor the decay of the core hole through either $2p \rightarrow 1s$ emission channel or $3p \rightarrow 1s$ emission channel. The final state of the resonant Raman process then becomes either $2p^5 3d^{n+1}$ or $3p^5 3d^{n+1}$, the same final state configurations reached by either $L_{2,3}$ edge or $M_{2,3}$ edge soft-x-ray absorption processes. As a result, the rich $L_{2,3}$ edge many-electron multiplet structure can be obtained at the K edge x-ray energies, a combination that is very important in cases where samples are not vacuum compatible. An example was given by W. Caliebe *et al.* (U. of Kiel), in a high resolution resonant Raman scattering study of Fe_2O_3, -hematite at the Fe K edge. **Figure 41** shows the two Raman spectra taken at incident x-ray energy tuned to the two crystal-field split states. Notice that it is the final state energies that are plotted. Also shown in the figure is the Fe $L_{2,3}$ edge absorption spectrum. Clearly, the energies of the two

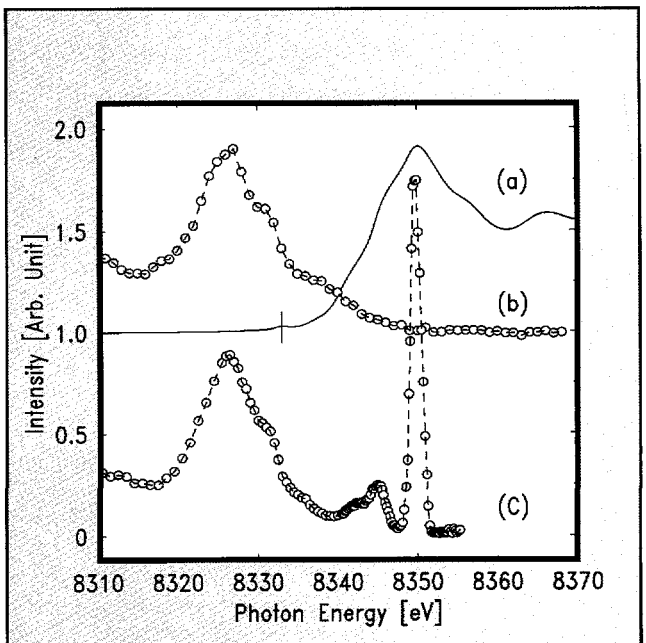


Figure 41: (a) Fe $L_{2,3}$ absorption spectrum of Fe_2O_3; (b) Resonant Raman spectrum from Fe_2O_3 obtained with incident photon energy tuned to 7113.4 eV (t2g symmetry); (c) Resonant Raman spectrum from Fe_2O_3 obtained with incident photon energy tuned to 7114.8 eV (e.g. symmetry). (X21)

main features in the soft-x-ray absorption spectrum agree very well with the main peak in the two Raman spectra.

Large resonant enhancement of valence electron excitations was also observed. C.-C. Kao *et al.* (Brookhaven National Laboratory) reported a high resolution resonant Raman scattering study of NiO, a prototypical Mott-Hubbard system. As the incident photon energy is tuned through the Ni K edge, a new loss feature, which is not observed for incident energies far from the absorption edge, is observed. **Figure 42** shows the Ni K absorption spectrum of NiO (**a**), the valence band emission spectrum of NiO (**b**), and the Raman spectrum taken with the incident energy tuned to the peak of the white line in the absorption spectrum (**c**). The new loss feature can be roughly fit with two peaks centered around 5 eV and 8 eV. These observations were interpreted by using a configuration interaction cluster model, and the new loss feature is identified as the charge transfer excitation in NiO. Subsequently, resonant enhancement of charge transfer excitations near the K edge of Cu have been observed by Hill *et al.* in Nd_2CuO_4, and by Isaacs *et al.* in $Sr_2CuO_2Cl_2$.

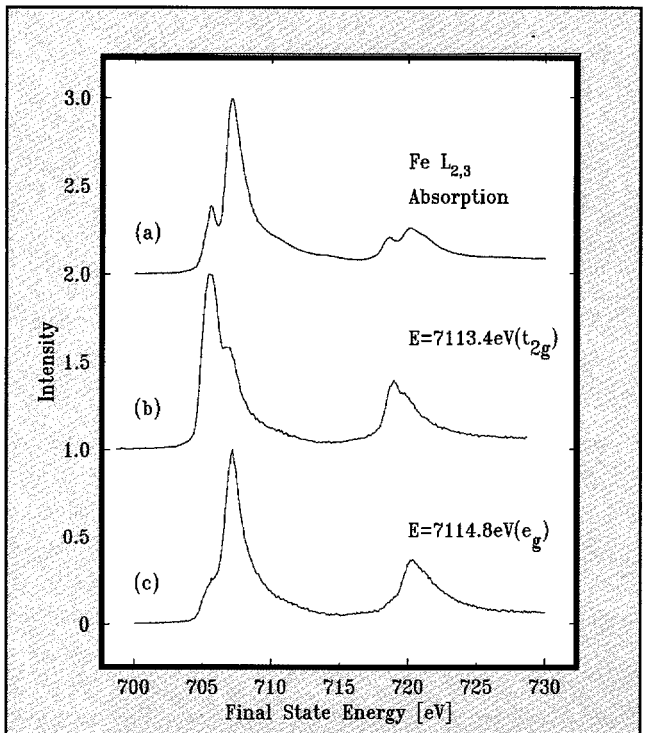


Figure 42: (a) Ni K absorption spectrum of NiO; (b) Normal valence band x-ray emission spectrum of NiO; (c) Resonant inelastic x-ray scattering spectrum of NiO obtained with the incident photon energy tuned to the main peak of the absorption spectrum (a). (X21)

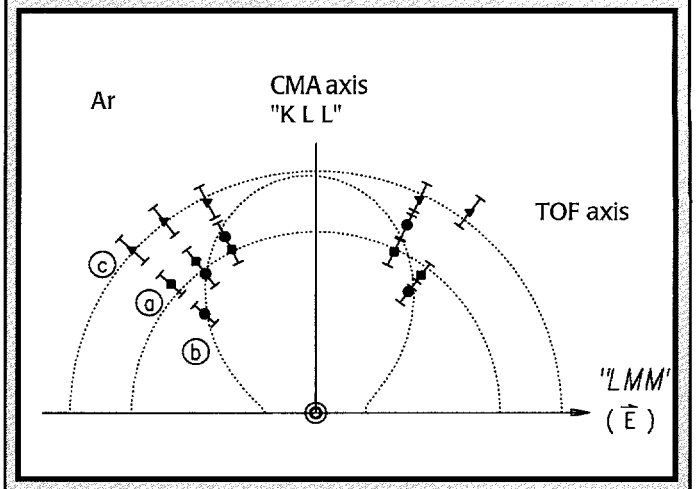


Figure 43: Auger-Auger electron coincidence measurement from Ar gas excited at the 1s→4p resonance (3203.5eV). Polar plotshowing the angular correlation between three slices (a, b, and c) of the LMM Auger group and the $KL_{2,3}L_{2,3}$ Auger electrons. (X24A)

In summary, the examples highlighted above are a good demonstration of the versatility of IXSS as a probe of electronic excitations in a wide range of systems.

Core Excitation

An Auger-Auger electron coincidence experimentat beamline X24A has been able to detect a large non-isotropic angular correlation between different components of the well-known Auger electron cascade following the 1s → 4p resonant excitation of Ar gas. One electron detector, a time-of-flight (TOF) spectrometer, was set to collect large portions of the LMM Auger envelope while the other, a cylindrical mirror analyzer (CMA) equipped with multichannel detection in order to determine the polar and azimuthal angles, was set to collect the precursor $KL_{2,3}L_{2,3}$ Auger electrons. The TOF spectrometer was oriented along the electric field vector of the monochromatized synchrotron radiation and the CMA was aligned perpendicular to both the TOF axis and the photon beam direction. Operation of the TOF spectrometer requires single-bunch operation of the X-Ray Ring in order to avoid overlapping signals from adjacent electron bunches.

By dividing the LMM Auger envelope into three slices, a large non-isotropic angular correlation was observed for one of these slices (Figure 43), whereas the others were isotropic. The large anisotropy observed is believed to be an alignment effect rather than a dynamical post-collision interaction effect.

Angle-Resolved Photoemission

The first results of a program and experimental chamber dedicated to high resolution (in angle and electron energy) angle-resolved photoemission were obtained at the end of FY 1996 by E. Jensen, T. Balasubramanian (Brandeis U.), X. Wu and S. Hulbert (NSLS) at beamline U12B. This first experiment was a study of the electronic structure of the (0001) surface of beryllium (Be) near the Fermi level (E_F). The electronic density of states (DOS) at the Fermi level of the Be(0001) surface is about four times larger than in the bulk. Many properties such as the electron-phonon interaction, the resistivity, and the specific heat depend strongly on the DOS at E_F. In particular, the electron-phonon coupling parameter λ is directly proportional to the DOS at E_F.

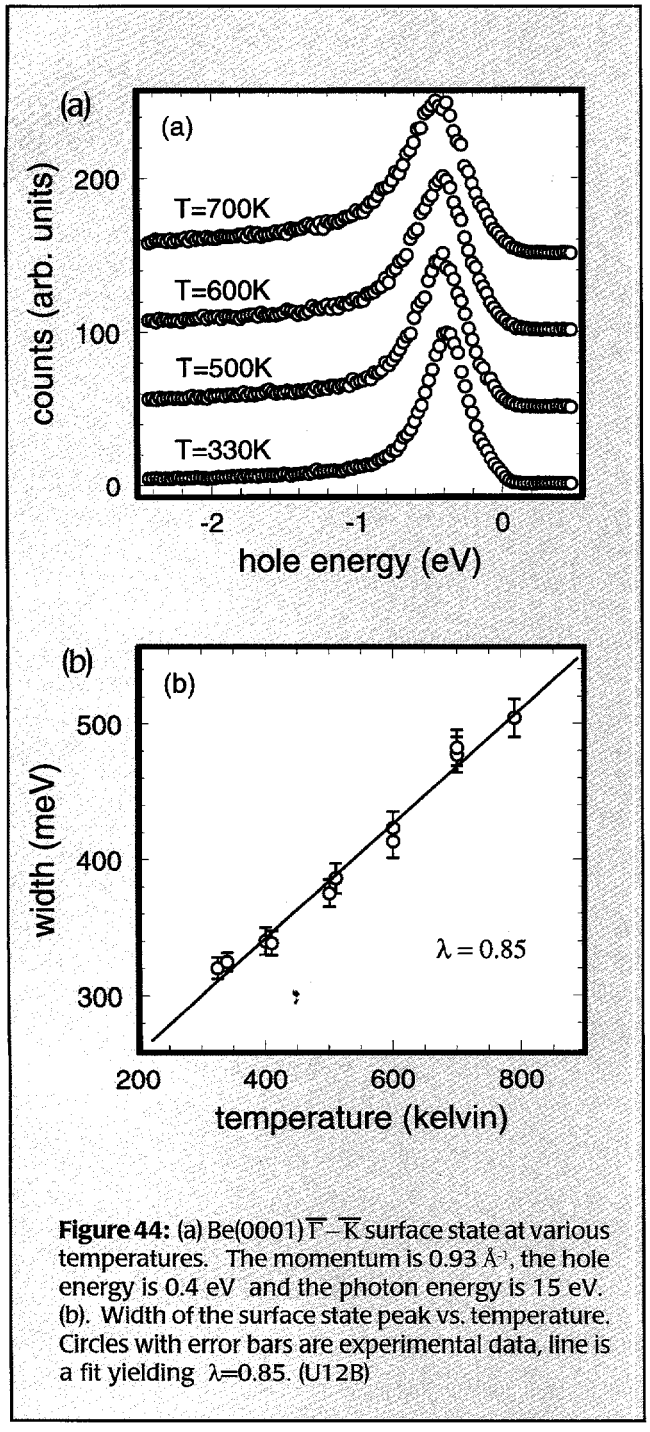


Figure 44: (a) Be(0001) $\overline{\Gamma}-\overline{K}$ surface state at various temperatures. The momentum is 0.93 Å^{-1}, the hole energy is 0.4 eV and the photon energy is 15 eV. (b). Width of the surface state peak vs. temperature. Circles with error bars are experimental data, line is a fit yielding λ=0.85. (U12B)

For bulk Be, λ is 0.24. Thus one would expect the surface λ to be about unity. λ was measured at the Be(0001) surface using angle resolved photoemission. The full width at half maximum (fwhm) of the surface state (SS) is interpeted as the inverse hole life time. All of the temperature dependence of the lifetime at high temperature comes from the phonon contribution, which is given by $2\pi\lambda kT$. Thus by measuring the SS fwhm vs. temperature one can determine λ. The $\overline{\Gamma}-\overline{K}$ SS, one of three on the Be(0001) surface, was chosen for measurement. This state has a binding energy of 2.8 eV at $\overline{\Gamma}$ and disperses parabolically, crossing E_F at $k_{||}$ =0.95 Å^{-1}. **Figure 44(a)** shows photoemission from this SS at $k_{||}$ =0.93 Å^{-1} (0.4 eV hole energy) for several temperatures. The fwhm of the SS is plotted vs. temperature in **Figure 44(b)**. Fitting these data to a straight line yields λ=0.85 ± 0.1.

Using λ=0.85 in the standard formula relating λ to a superconducting transition temperature T_c, one finds that T_c rises to about 50 K (from 0.026 K in the bulk). This should be observable in ultra-thin films, and may have observable consequences for the surface of a thick crystal at low temperatures.

The success of this experiment was determined in large part by the ability to prepare an extremely clean Be(0001) surface, an exercise which required more than one calendar year of effort. During FY 1997, an effort will be made to determine the electron-electron and electron-impurity contributions to the Be(0001) SS lifetime. Also, a new high-resolution angle-resolved photoemission analyzer and experimental endstation, funded by the DOE Scientific Facilities Initiative, are being fabricated.

Significant progress has been made recently by S. Dhesi, C. Stagarescu, and K. Smith (Boston U.) in the study of the electronic structure of wide band gap nitride semiconductors. Such semiconductors (for example, GaN) are an important class electronic materials primarily due to potential use in optoelectronic devices operating in the blue to ultraviolet spectral range. Using angle-resolved photoemission on beamline U4A, the band dispersion of the valence states along all the high symmetry directions in the bulk Brillouin zone has been measured for wurtzite GaN thin films. The n-type wurtzite GaN(001) thin films were grown using electron cyclotron resonance assisted molecular beam epitaxy on sapphire substrates at Clean GaN(0001) surfaces were prepared by repeated cycles of N_2^+ sputtering and

annealing in UHV. Following this procedure Auger electron spectroscopy shows minimal contamination, and low energy electron diffraction displays a sharp hexagonal pattern with no evidence of a surface reconstruction.

Figure 45 shows a series of normal emission spectra taken from atomically clean GaN(0001) surface of a wurtzite film. The spectra in **Figure 49** reflect the dispersion of the states along the ΓAΓ direction of the bulk Brillouin zone. By measuring spectra in the off-normal geometry, the dispersion of states along directions in the bulk Brillouin zone parallel to the surface were also measured. The results of these experiments reveal very good agreement with local density approximation calculations for the bulk band structure. One notable result of the angle resolved photoemission measurements is the observation of a non-dispersive surface state about the $\bar{K}$ point in the surface Brillouin zone. This state exists in a projected bulk band gap, and is sensitive to oxygen adsorption.

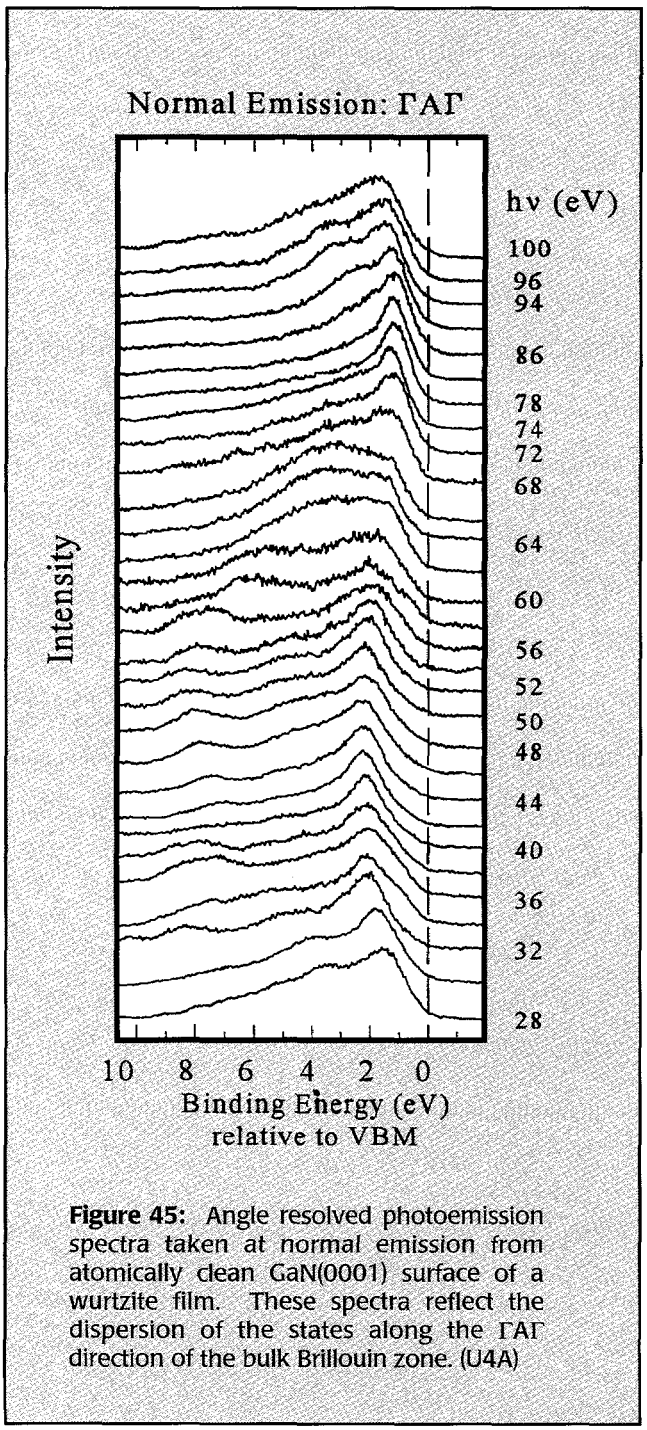


Figure 45: Angle resolved photoemission spectra taken at normal emission from atomically clean GaN(0001) surface of a wurtzite film. These spectra reflect the dispersion of the states along the ΓAΓ direction of the bulk Brillouin zone. (U4A)

Auger Photoelectron Coincidence Spectroscopy (APECS)

The Auger Photoelectron Coincidence Spectroscopy endstation continues to utilize its unique capabilities to study interesting surface science phenomena. During FY 1996, two APECS experiments were performed at beamline U14A.

In one of these, the $N_{2,3}VV$ Auger spectra from the Ru(0001) surface taken in time coincidence with Ru $4p_{3/2}$ or $4p_{1/2}$ core photoelectrons are compared. As would be expected for highly correlated late transition metals such as Ru, the measured APECS Auger spectra are not well represented by the self-convolution of the Ru(0001) valence band density of states. On the other hand, an attempt to model the Auger spectra by multiplets of a d^6 configuration, appropriate if the 4p core hole is fully screened prior to Auger decay, has met with some success: the differences between the two experimental spectra can be explained by a stronger coupling of the high kinetic energy ^5D multiplet term to the $4p_{3/2}$ level than the $4p_{1/2}$ level. Calculation of the appropriate matrix elements is underway. This experiment is the result of a collaboration between R. Bartynski and R. Gotter (Rutgers U.), X. Wu and S. Hulbert (NSLS), and H. Nozoye (Japan National Institute of Materials and Chemical Research).

The second APECS experiment of FY 1996, also performed at U14A, has put the finishing touches on a set of APECS measurements of the lineshape of the Ti *3p* core level spectrum from stoichiometric ("nearly perfect") and defective TiO_2(110) surfaces, measured in time coincidence with $M_{2,3}VV$ Auger electrons. The selection of only those Ti *3p* core holes which decay by $M_{2,3}VV$ Auger emission provides a new spectroscopic view of this surface. **Figure 46 (a),(b), and (c)** **(see next page)** show coincidence Ti *3p* core level spectra from the stoichiometric, 900 K vacuum annealed, and ion bombarded (~10^{14} Ar^+ ions/cm^2 at 500eV) surfaces, respectively. **Figure 46 (d), (e), and (f)** show non-coincidence (ordinary, or "singles") spectra from the same three surfaces. The excess emission in the 68-70eV kinetic energy range in **Figure 50(a)** is attributed to Ti^{3+} and Ti^{2+} ions in sites

adjacent to surface oxygen vacancies. The density of these residual surface defects (either point defects or step edges) is rather low (~1% of a monolayer) on the stoichiometric surface, but the associated sub-oxide emission accounts for ~20% of the total surface Ti 3*p* emission [**Figure 46(a)**]. The enhanced sensitivity in the coincidence spectrum is attributed to the extra charge density at the reduced Ti sites as compared to Ti^{4+} sites, which strongly affects the $M_{2,3}VV$ Auger decay rate. The assignment of this excess emission as defect- related is supported by the spectra in **Figure 46(b) and (e)**. 900 K annealing induces only a small (~4%) defect-related shoulder in the singles spectrum [**Figure 46(b)**] while in the coincidence spectrum [**Figure 46(e)**] over 50% of the Ti 3*p* emission is associated with reduced Ti oxidation states. Ion bombardment produces a greater fraction of defect-related emission in the singles spectrum [**Figure 46(f)**] than does 900 K annealing [**Figure 46(e)**], but results in a very similar coincidence spectrum. This shows that this ion dose produces a concentration of surface defects similar to what 900 K annealing produces, and that a substantial fraction of the defect-related emission in the singles spectra arises from subsurface damage.

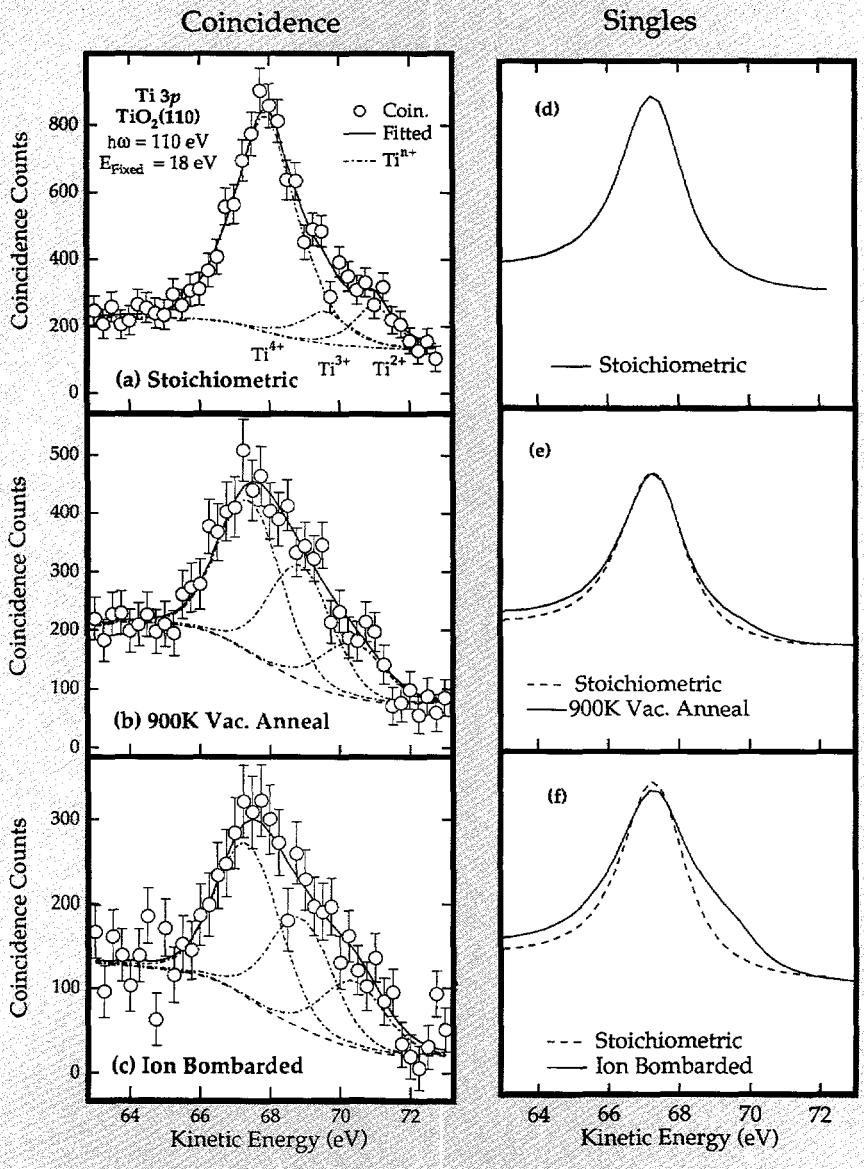


Figure 46: A series of Ti 3p core level photoemission spectra from TiO_2(110) taken at 110eV photon energy, both with (a-c) and without (d-f) the requirement of time coincidence with $M_{2,3}VV$ Auger electron emission. Surface treatments: (a),(d): nearly-perfect stoichiometric surface; (b),(e): after 900K vacuum anneal; (c),(f): after ion bombardment. (U14A)

NUCLEAR PHYSICS

LEGS Facility Overview

The Laser Electron Gamma Source facility (LEGS) provides intense, polarized, monochromatic γ-ray beams by Compton backscattering laser light from relativistic electrons circulating in the X-Ray Ring of the National Synchrotron Light Source at Brookhaven National Laboratory. Such a beam has a high degree of polarization (~90%) with very low background and the energies of the photons are well determined by measuring the loss of energy of the struck electrons. Photon Energies up to 330 MeV can be obtained with the present laser shining on 2.58 GeV electrons. With a new frequency-quadrupled laser that is now under development and the possibility of 2.8 GeV electrons, photon energies up to 470 MeV can be obtained.

LEGS has its high degree of polarization because the interaction of the laser photons with relativistic electrons preserves the polarization of the photons. By orienting the linear or circular polarization of the laser to give the desired polarization for the γ-rays, measurements can isolate specific contributions to nuclear reaction amplitudes. If the linear polarization (direction of the electric field vector) is in the plane of the reaction, the cross section is sensitive to electric multipole moments. This cross section is denoted as $\sigma_{||}$. If the linear polarization is perpendicular to the reaction plane, the cross section is sensitive to magnetic multipole moments. This cross section is symbolized by $\sigma_{\perp}$. The data is usually presented in terms of $\sigma_{||}/\sigma_{\perp}$, or $\sigma_{||} - \sigma_{\perp}$, or as the asymmetry $\Sigma = \frac{\sigma_{||} - \sigma_{\perp}}{\sigma_{||} + \sigma_{\perp}}$. Comparing these cross sections permits the separation of effects due to static charge distributions from those due to spin and current distributions. Thus this polarization degree of freedom is extremely important in the understanding of nucleon and nuclear structure.

Since 1990, experiments have concentrated on single polarization observables (polarized beams on unpolarized targets) in nuclear reactions involving the Δ resonance. The Δ resonance is the first excited state of the nucleon with an energy of 294 MeV above the mass of the proton and a width of 120 MeV. It decays with a 99.4% branch to pion-nucleon (πN) final states and a 0.6% branch to γN. By studying photon induced nuclear reactions in the energy region of this excitation, it is possible to measure fundamental quantities such as the deformation of the Δ, to test models describing the internal structure of the nucleon and the Δ and the transition between them, and to study the effects of Δs produced inside of nuclei. Highlights of the last two years are given below. An updated status of LEGS, including recent publications, is available on the World Wide Web via http://WWW.LEGS.BNL.GOV/~LEGS/ .

In 1997 a new phase of operations will begin, focusing on double-polarization measurements with circularly polarized photon beams and longitudinally polarized nucleon targets. This work requires the development of (i) a new frozen-spin hydrogen-deuteride target that provides high polarizations for both nuclear species, and (ii) a new large acceptance detector array for measuring total reaction cross sections in both neutral and charged-particle channels. Progress on these instrumentation developments is an ongoing effort of the LEGS Spin Collaboration (LSC) and is discussed in the last section.

The E2 $N \rightarrow \Delta$ Transition from $p(\vec{\gamma},\pi)$ and Compton Scattering

In constituent quark models, a tensor interaction mixing quark spins with their relative motion is needed to reproduce the observed baryon spectrum. This necessarily results in a D-wave component in the nucleon wave function which breaks spherical symmetry and leads to a static deformation for the Δ. The Δ is photo-excited mainly by M1 radiation. However, the D-state component results in a small E2 transition strength. The magnitude and sign of the E2/M1 mixing ratio are quite sensitive to the internal structure of the proton. Isolating the $N \rightarrow \Delta$ transition requires a decomposition of the multipoles into resonant and background (non-resonant) components. This decomposition requires a model, and model dependences enter the analysis of π-production and Compton scattering in different ways. These two final states have different E2 sensitivities and both have been studied at LEGS.

The $p(\vec{\gamma},\pi^0)$ and $p(\vec{\gamma},\gamma)$ reactions were separated by detecting photons in a high resolution NaI(Tl) spectrometer in coincidence with the recoil protons whose trajectories were tracked through wire (drift) chambers and whose energies were measured both by energy deposition and by time of flight in an array of plastic scintillators. This arrangement is shown in **Figure 47**. The full data set consisted of 3 sets of runs with different NaI and scintillator-bar orientations chosen to provide overlap angles. The π^0/Compton separation for the full data set centered at 90° in the center of momentum (c.m.) is shown in

Figure 48 where the γ-ray energy is plotted against the recoil proton energy. Here the γ and proton recoil energies for Compton scattering, as calculated from the tagged beam energy and the proton recoil angles measured in the drift chambers, have been subtracted from the measured energies. Compton scattering is clearly resolved here, and in *all* other runs.

In p(γ,π), the observable most sensitive to an E2 component is the cross section, $\sigma_{||}$, for π° production by linearly polarized photons whose electric vector is oriented parallel to the reaction plane. The corresponding cross section for the perpendicular orientation, $\sigma_{\perp}$, is completely insensitive to E2 excitation at all but extreme angles. Thus, the ratio $\sigma_{||}/\sigma_{\perp}$ maximizes E2 sensitivity, while dividing out systematic uncertainties. The first new measurements of this ratio over a limited angular range suggested E2 transition strengths significantly larger than expected from previous multipole analyses. In our 1994 LEGS Progress Report, and at the SPIN'94 Conference, we presented the results of new measurements of this π° polarization ratio taken over a large angular range. These were compared to the model

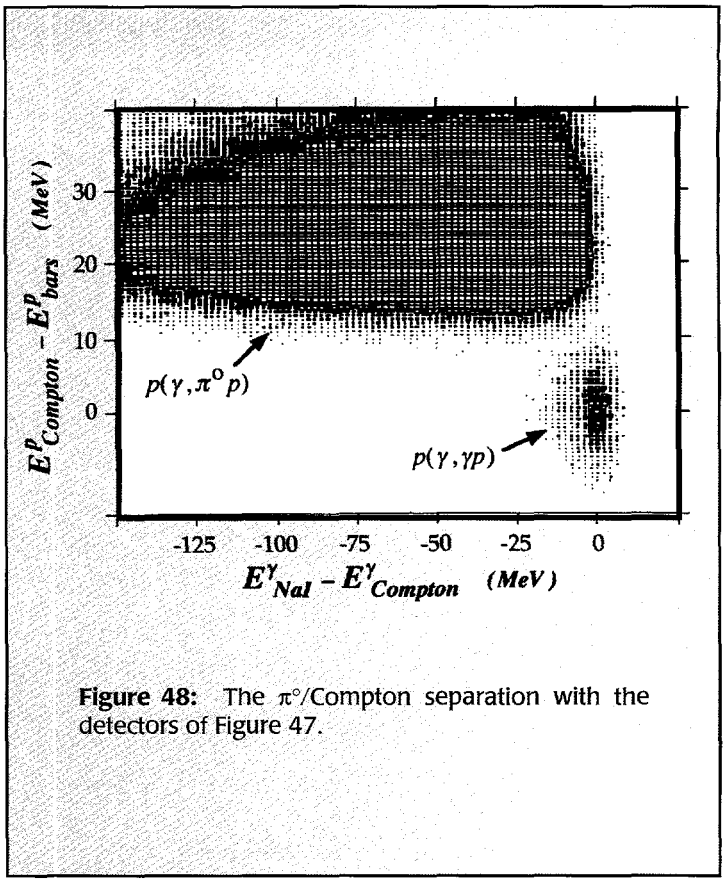


Figure 48: The π°/Compton separation with the detectors of Figure 47.

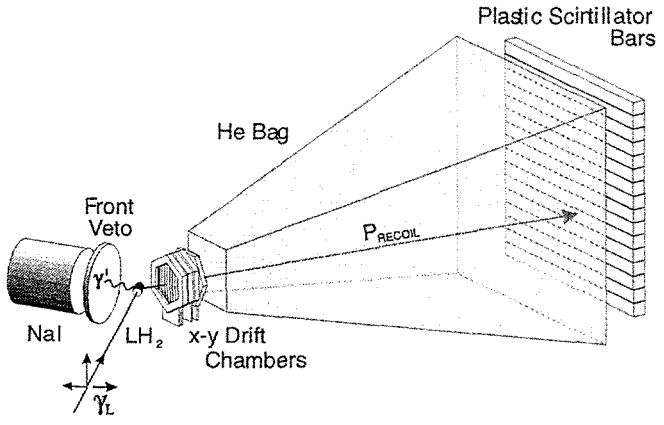


Figure 47: The detector arrangement used to separate the (γ,π) and (γ,γ) reactions (see text).

predictions of Davidson, Mukhopadhyay and Wittman (DMW). This model contains five free parameters, the electric and magnetic coupling constants at the $\gamma N\Delta$ vertex (G_E and G_M), and three constants parameterizing the off-shell behavior. In addition to the polarization ratios, cross sections are needed to fix these 5 parameters. Since absolute cross sections from our experiments were not available at the time, our polarization data was combined with previously published unpolarized results from other laboratories. The results of fitting this composite data set to the DMW parameters gave a value for G_E/G_M (the $N\rightarrow\Delta$ part of the E2/M1 mixing ratio) of - **2.7±0.1%**. (The error of ± 0.1% reflected only the variations in the methods of unitarizing the pion amplitudes.)

The analyses of the LEGS experiments are now complete. We present here a selection of cross section and polarization data for both Compton scattering and π°-production and examine the consistency of previous E2/M1 determinations in the light of the full data set. The 90° excitation functions for the

two reactions are shown below in **Figures 49 and 50.**

There had been a long standing discrepancy between earlier Compton measurements and dispersion calculations that used π-production as input. The LEGS measurement was designed to remove all of the uncertainties associated with separating Compton scattering from the π° channel by a large overdetermination of kinematic parameters. Both reactions are completely specified by two kinematic observables. In this experiment, six quantities were measured: the beam energy, the scattered γ-ray energy, the polar and azimuthal angles of the recoil proton, and the proton's time of flight to the detector and the energy it deposited in the detector. This large degree of over-determination has two important consequences. First, it guarantees an accurate separation of the two competing channels (**Figure 48**). Secondly, it enables all detector efficiencies to be evaluated directly from the data itself, without resorting to simulations and thus avoiding their associated uncertainties. The data shown as solid points in **Figure 49** reflect all statistical and *polarization-dependent* systematic errors. Additional systematic scale errors are less than 2%. Near the peak of the Δ, our results are substantially higher than the earlier measurements (open squares). Other recently published measurements from Mainz (crosses) and from Saskatoon (SAL) (circles) are in excellent agreement. Data from earlier experiments at Cornell (1961), Tokyo (1964), Illinois (1967), and Bonn (1976) at energies higher or lower than the Δ peak are either consistent or slightly lower than these new measurements. Why the earlier results are so dramatically lower near the resonance energy is not known.

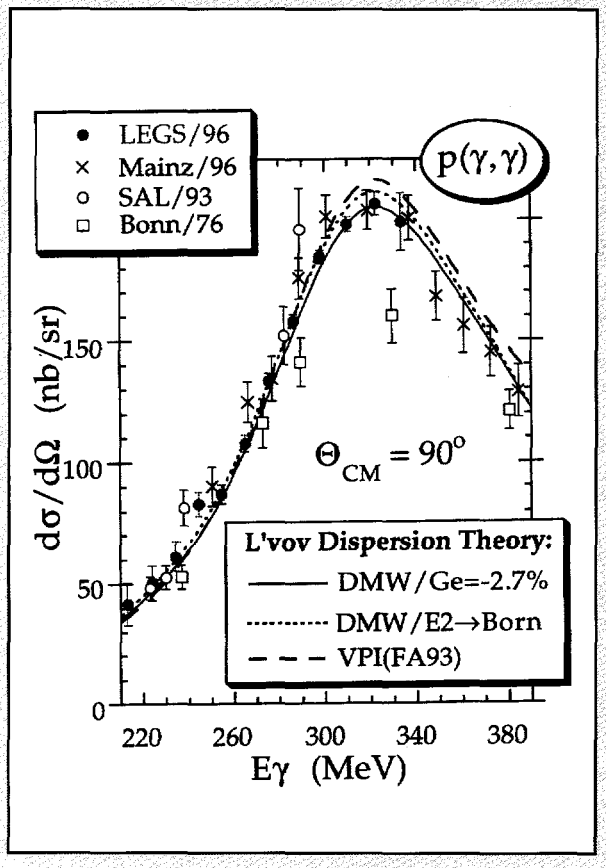


Figure 49: LEGS Compton scattering cross sections at 90° (solid points.), compared with recent data from Mainz and SAL, and earlier data from Bonn. In addition to the indicated errors, the systematic scale uncertainties are ~2% (LEGS), 5% (Mainz), 3.9% (SAL), and 4.4% (Bonn).

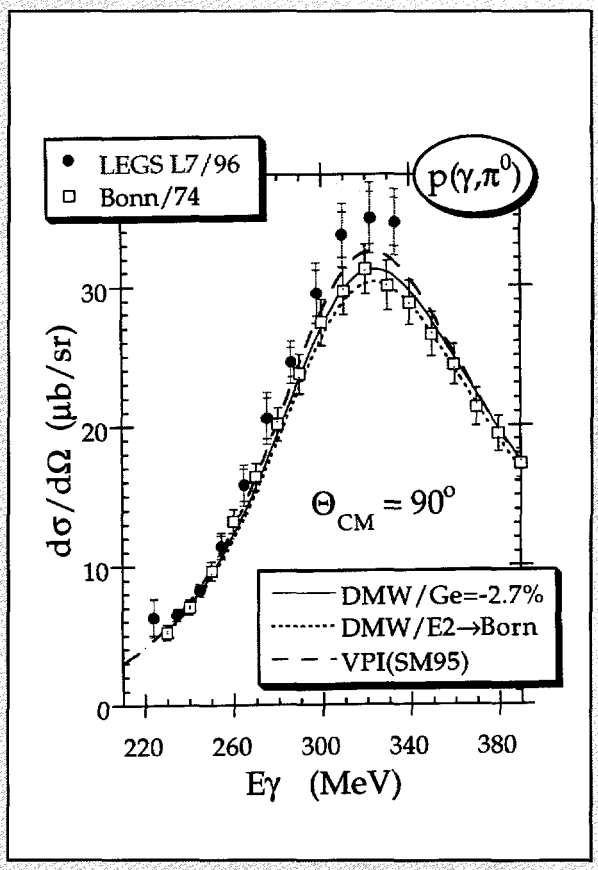


Figure 50: The LEGS π° cross sections at 90° (solid points) compared with earlier data from Bonn. Two error bars are shown for each point, the smaller reflects the measurement error (statistical, and other sampled uncertainties) and the larger includes systematic scale errors added linearly (see text).

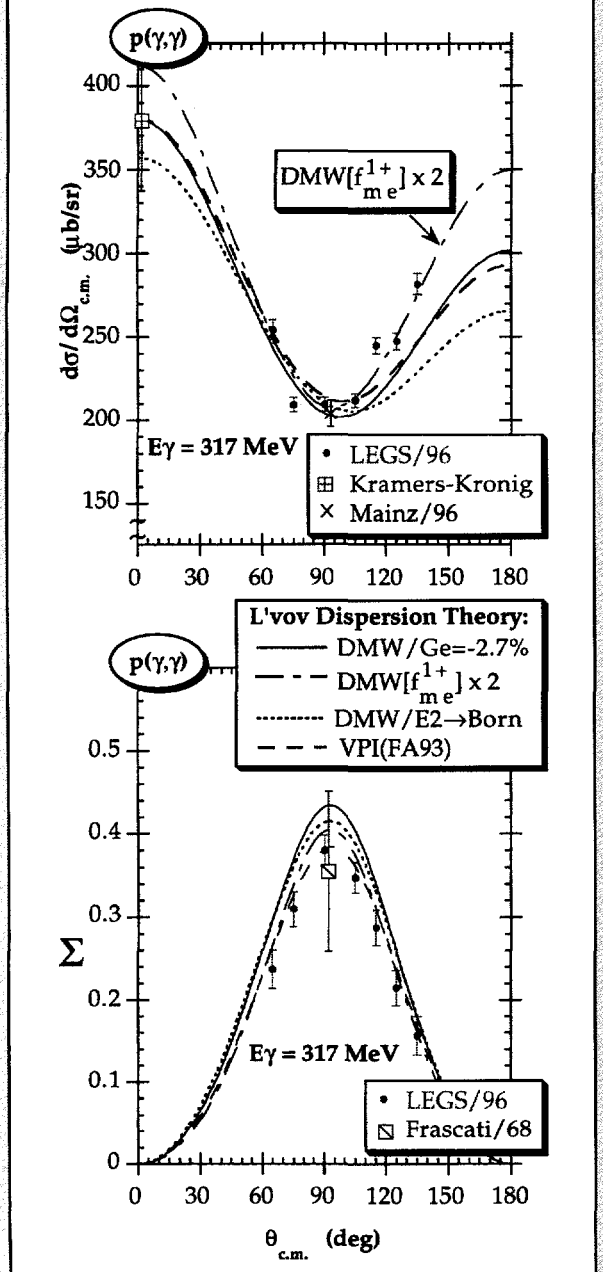


Figure 51: Angular distributions for the unpolarized cross section and linear polarization asymmetry in $p(\gamma,\gamma)$ from LEGS (solid circles).

Angular distributions of the cross sections and linear polarization observables for Compton scattering and π°-production for energies near the Δ peak are shown as the solid points in **Figures 51 and 52.** The recent Mainz 90° Compton cross section is plotted in the top panel of **Figure 51.** For the Compton asymmetry, the only previously published datum (from Frascati) is also shown. For π° production, the results of applying the most restrictive cuts to the LEGS data ("*Compton-like*" kinematics), are shown with statistical errors as the crosses at 90° and 120° in the top panel of **Figure 56.** Also plotted are the older Bonn and Lund cross sections and a Khar'kov asymmetry measurement.

Three sets of curves for $p(\gamma,\pi^\circ)$ are plotted in **Figures 50 and 52.** The solid curves are calculations in which the parameters of the DMW model were optimized to reproduce a combination of the LEGS π° polarization ratio results, together with the Bonn unpolarized cross sections. This was the exercise carried out with the first new results that yielded the value of -2.7 % for G_E/G_M. The result of turning off the E2 part of the $N\rightarrow\Delta$ transition in this calculation (i.e setting $G_E=0$) is shown as the dotted curve. (Setting the entire E2 amplitude, including Born contributions, to zero produces dramatic effects but is not terribly informative.) For comparison, the predictions of current VPI multipole analyses are shown as the dashed curves. Although the DMW and VPI predictions are both quite close to the π° polarization data, the cross section predictions indicate a need for some readjustment of parameters.

Compton scattering provides an additional constraint on this problem. The imaginary parts of the Compton amplitudes can be calculated from (γ,π) multipoles using s- and u-channel unitarity (s,t, and u are the standard Lorentz-invariant Mandelstam variables) and dispersion integrals can be written for their real parts. The solid, dotted, and dashed curves in **Figures 49 and 51** have been calculated by L'vov in this way using as input the pion multipoles corresponding to the three calculations in **Figures 50 and 52.** In particular, the predictions of the solid and dashed curves started with the DMW model (adjusted to give G_E=-2.7% of G_M) and with recent VPI multipole analyses of π-production, while the dotted curves were obtained by setting the $E2^{j=3/2}$ Compton multipoles to their s- and u-channel Born and t-channel pole values.

The Compton cross sections at back angles are quite sensitive to E2/M1 interference and these *are not reproduced* by either the solid or dashed curves. The prediction corresponding to the solid curve also gives the poorest description of the polarization asymmetry. The leading E2 interference term, f^{1+}_{me} corresponding to E2

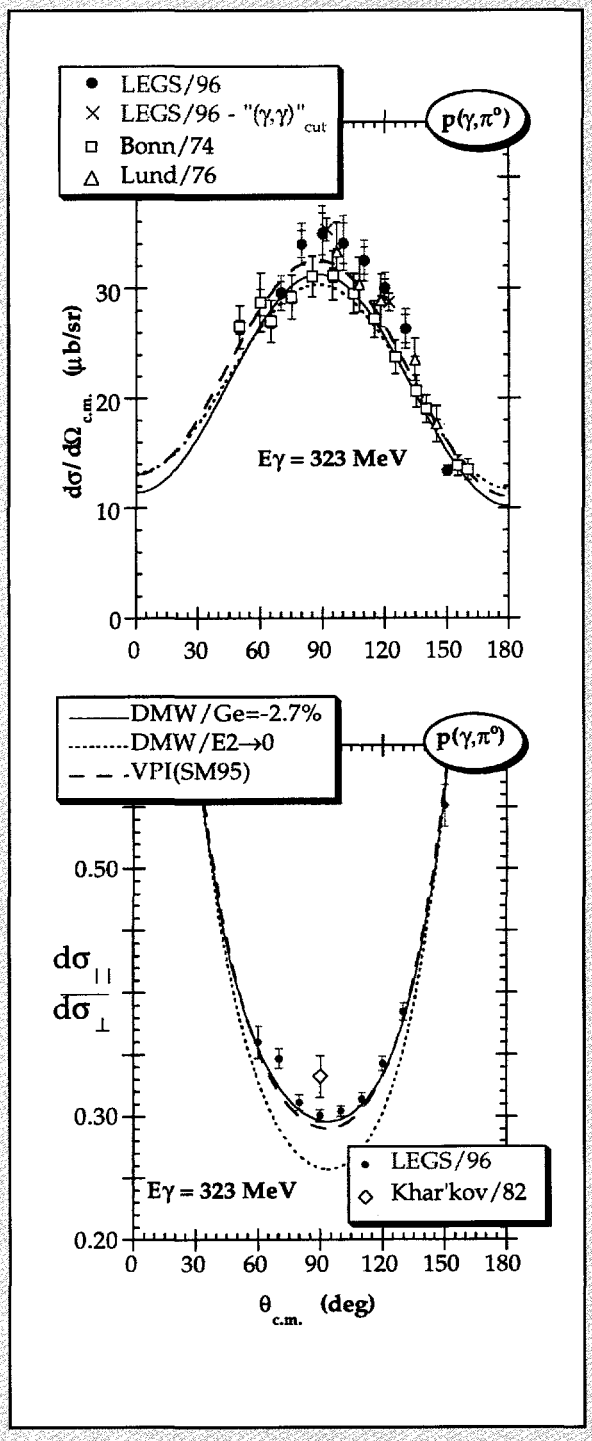


Figure 52: Angular distributions for the unpolarized cross section (top) and polarization ratio (bottom) in p(γ,π^o) from LEGS (solid circles).

photoexcitation followed by M1 decay, is dominated by the $N \rightarrow \Delta$ transition. Doubling this amplitude results in the long-dashed/short-dashed curves in **Figure 51** which seem to describe most of the cross section data although the asymmetry calculation remains a little high.

The new Compton results clearly show the deficiencies in our earlier estimate of G_E/G_M= -2.7% which was driven solely by the pion polarization data. A complete determination of the E2 component in N→Δ requires a simultaneous fit to both Compton scattering and π-production. This is presently underway.

Deuteron PhotoDisintegration and Coupled NΔ/NN Interactions

Although the Δ resonance dominates nuclear reactions from pion threshold to about 1 GeV, its interaction with the nucleon is still poorly known. Understanding nuclear reactions in this energy region necessarily requires a consistent treatment of the NΔ and NN interactions. The NN force can be studied directly using nucleon-nucleon reactions but the NΔ interaction must be inferred from processes with the two nucleon deuteron such as $\pi D \rightarrow \pi NN$ and $\pi D \rightarrow NN$ for which the Δ plays a prominent role in the intermediate state. Because of the strong coupling of the Δ to πN, realistic models must satisfy three-body unitarity, connecting reactions starting from NN, πD, or γD entrance channels leading to NN, πD, or πNN final states. While elastic scattering and breakup reactions for the deuteron are reasonably well understood because the interaction with a single nucleon dominates, pion and photon absorption channels have proven to be problematic. Since the effects of the NΔ interaction are the largest near the energy of the Δ resonance and since both the cross section and the polarization observables have been shown to be strongly affected by the NΔ interaction, the LEGS collaboration measured cross sections and asymmetries in the same experiment for the first time in order to remove ambiguities in existing data.

Five independent measurements of the $D(\vec{\gamma},p)n$ reaction have been carried out at LEGS with three different detector systems, different photon end-point energies from different laser wavelengths, different polarizations and two different liquid deuterium targets. These measurements overlap in various kinematic regions between 113 and 325 MeV, and the agreement in the regions of overlap is excellent. By taking weighted averages of overlapping measurements, a "net" data base has been constructed and is available from the LEGS WWW page.

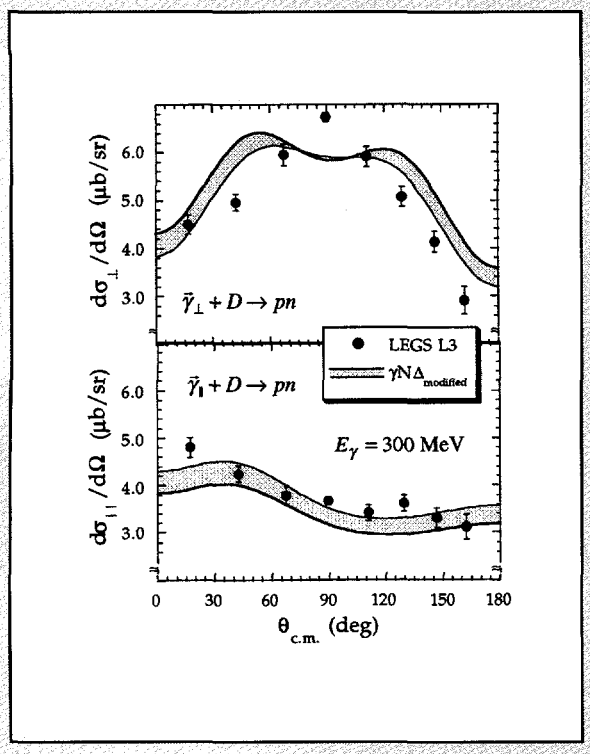


Figure 53: Angular distributions at 300 ± 5 MeV.

Selections of these data at 300 MeV are compared to recent coupled-channel calculations in **Figure 53** (note the suppressed zero). The calculations are in agreement with cross sections measured with linear polarization parallel to the reaction plane but fail to account for the data taken with perpendicular kinematics. The shaded band reflects uncertainties in the pion meson exchange currents used in the calculations.

At present, there is no clear explanation for the success of the coupled-channel calculations in one polarization kinematics and their failure for the orthogonal state. Spin observables provide a considerably more sensitive test of the angular momentum modeling than do cross sections. Although the model parameters of the calculations presented here were fitted to NN phase shifts, all assumed static NN potentials, with retardation effects included only in the NΔ and NN-NΔ-transition potentials. The additional use of retarded potentials in the NN interaction could significantly alter the angular momentum mixing.

INSTRUMENTATION AND TECHNIQUES

The development of new techniques and instrumentation goes hand in hand with the continuing scientific advances at any state of the art facility. The NSLS is no exception. Because of its unique infrastructure these developments are advanced on many fronts by the entire community. As in past years significant innovations are being made over the entire photon energy spectrum covered by the NSLS facility.

Developments in UV and Soft X-Ray Instrumentation

A new area of focus for UV photoemission studies is in the realm of very high energy and momentum resolution. These techniques have been applied to questions of interest in the field of high T_c superconductors over the past several years. As part of the push in that direction at NSLS, a new high energy resolution angle-resolving photoemission instrument based on the use of a Scienta hemispherical analyzer has recently been commissioned in the BNL Physics Department. This spectrometer, with the capability of multiplexing in both energy and angle, has an energy resolution of better than 5 meV and an angular resolution of better than 0.2 degrees, resulting in an order of magnitude improvement of the momentum resolution. It is intended to couple this instrument to the new undulator beamline U13UB, which features high throughput collection/focusing optics and a high resolution (> 10^4 resolving power) normal incidence monochromator operating in the 5 to 30 eV photon energy range.

Imaging science using soft x-rays is now well established. The instrumentation, however, continues to develop as experimenters push ever harder toward the physical resolution limit of $\lambda/2$. The X1A scanning x-ray microscopes all use Fresnel zone plates as their focusing elements. In collaboration with D. Tennant (Lucent Technologies Bell Laboratories), S. Spector *et al.* (SUNY @ Stony Brook), have fabricated zone plates by etching Ge or, more recently, plating Ni. Outer zone widths of 30 nm are in use, and 20 nm zones have been fabricated in tests; diameters of 80 and 160 microns are in use.

The Stony Brook team has not only made advances in the x-ray optics but have also commissioned a scanning transmission x-ray microscope, cryo-STXM, which is designed (by J. Maser, *et al.* SUNY @ Stony Brook,) to image frozen hydrated specimens of a few microns in thickness at temperatures below -165°C. At this temperature, the effects of radiation damage to biological samples should be reduced by several orders of magnitude compared to room temperature hydrated specimens. This should enable images to be taken at higher resolution and even multiple images to be obtained from the same sample, a feature which is crucial for elemental and chemical mapping and for tomography. In contrast to most x-ray microscopes in use, the cryo-STXM has been designed to operate at a vacuum of 10^{-7} Torr. This limits thermal drifts to around 1 nm per second while also helping to reduce contamination of the sample. Samples are prepared on EM grids which in turn are mounted on a TEM style liquid nitrogen cooled holder. The sample temperature can be controlled by a heater. The holder itself can tilt by ± 80° to allow tomography to be done. Sample introduction is done through a JEOL TEM airlock, and takes only a few minutes without breaking vacuum. Images are obtained by scanning the sample in a raster pattern, the x-ray light being focused at a fixed point using a Fresnel zone plate. Coarse scans with a resolution of 1 micrometer are performed by out-of-vacuum stepping motors with a range of 9 mm by 25 mm. A piezo driven in-vacuum flexure stage provides finer steps of 20 nm and a field of 70 by 70 μm^2. Refocusing during spectral scans is done using an in-vacuum DC motor. Samples can be previewed using an optical microscope with infinity-corrected visible light lenses in vacuum but with the head outside vacuum. The data acquisition system has multiple digital and analog channels so that several parameters can be recorded. The cryo-STXM is now permanently mounted on a separate vibration isolation system at the beamline.

Scanning transmission x-ray microscopy provides a two dimensional image of the sample under study. Holographic techniques hold out the promise of providing information about the third dimension. Previous experiments in x-ray holography have yielded high quality images of dried specimens at ~40 nm resolution. These experiments have employed the photoresist PMMA for recording the image, a specialized scanning force microscope with a linear scanning stage for hologram readout, and computer reconstruction. In 1996, the experimental apparatus was completely rebuilt (by S. Lindaas (LBNL), and collaborators from Stony Brook) to allow holograms to be recorded of frozen hydrated specimens using a cryo holder similar to that which is used in cryo-STXM. First holograms of frozen hydrated malarial erythrocytes were

recorded, and reconstructions have been obtained at a resolution similar to that of room temperature samples. Moreover, iterative twin image elimination algorithms have been developed for higher quality image reconstruction. Plans for 1997 include efforts towards holographic tomography.

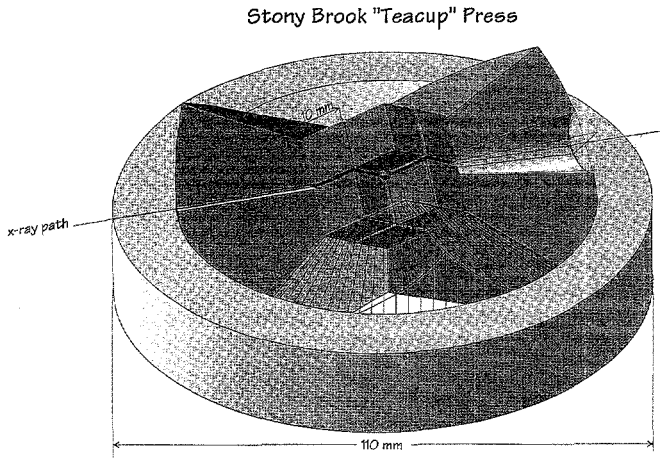
X-Ray Methods and Instrumentation

High Pressure Research

The high pressure tools that are used in conjunction with the NSLS source have undergone major advances as reported in this volume. The variables: magnitude, uniformity, and isotropy of pressure, magnitude and uniformity of temperature, and sample volume all compete in defining the envelope available to the researcher. The diamond anvil cell sets the high pressure limit at the price of sample volume, and pressure and temperature uniformity. The "double hot plate" system used by T.-D. Shen *et al.* (Los Alamos National Laboratory), in their study of iron defines new boundaries in this experimental space. Two multi-mode laser beams are focused on opposite faces of the sample through the opposed diamond anvils. By heating both surfaces of the sample to the same temperature, the normally large temperature gradients within the sample are virtually eliminated. Using Kirkpatrick-Baez mirrors, the x-ray beam is focused to a diameter of about 10 μm, providing sufficient intensity for diffraction spectra to be collected in a few minutes. This spot size is much smaller than the laser spot size, thus, providing x-ray data for a sample at uniform pressures and temperatures.

"Large volume" high pressure systems define the portion of the experimental envelope with sample volumes three orders of magnitude greater than diamond anvil cells with a sacrifice in maximum pressure and a gain in pressure and temperature homogeneity as well as sample volume for x-ray studies. The new anvil geometry reported by M. Vaughan *et al.* (SUNY @ Stony Brook), the Tea-Cup cell [**Figure 54(a) and (b)**], is beginning to compete with diamond anvil cell pressures having broken 21 GPa with tungsten carbide anvils while maintaining large sample volumes. Future plans include using sintered diamonds as anvils with the hope of further increasing pressure with little loss of other parameters; cost.

The conventional large volume system used at X17 is a DIA style multi-anvil apparatus. This workhorse at NSLS and the Photon Factory (where it is known as MAX-80 and MAX-90) can routinely produce 10 GPa with WC anvils with a 4 mm truncation. Wang *et al.* (U. of Chicago) report slight modifications to the anvil geometry that have provided a 30% increase in pressure, fewer failures, and more productive experimental runs, all



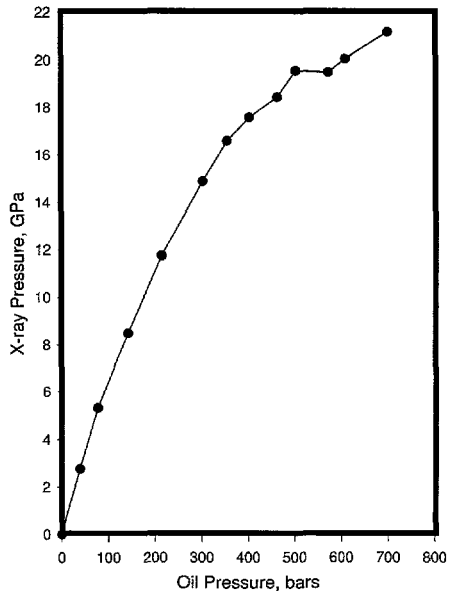


Figure 54: (a) Stony Brook "Teacup" Press, a two-stage device using eight-cubic anvils to generate high pressure, with x-ray access. (X17B1)

(b) Pressure performance of Teacup apparatus.

with no cost in sample size or environment.

With the expansion of the experimental environmental envelope has come a remarkable growth in the types of studies that can be done in conjunction with x-ray synchrotron radiation. The most significant breakthrough for Earth-related studies is the inclusion of acoustic velocity measurements at high pressure and temperature and simultaneously with x-ray diffraction. As reported by R. Liebermann *et al.* (SUNY @ Stony Brook), acoustic interferometry is used to measure acoustic velocities of samples to fractions of a per cent accuracy (see **Figure 55** for diagram of cell assembly). X-rays are essential to provide *in situ* determinations of the pressure using a NaCl pressure marker, with thermocouples measuring temperature. These experiments are all performed in the tapered anvil DIA apparatus, reproducing conditions of the transition zone of the Earth. Such measurements at simultaneously high pressure and temperature are extremely important in interpreting seismic velocities as a function of depth in the Earth. Despite their inherent importance, such measurements have been limited to a few samples, most notably, MgO, collected a quarter century ago. The MgO data reported here by G. Chen *et al.* (SUNY @ Stony Brook), using the new technology, cover a pressure range one order of magnitude larger than the older data with temperatures of twice the previous study.

H.-K. Mao *et al.* (Carnegie Institute of Washington), have developed a technique to estimate elastic anisotropy and strength at room temperature and megabar pressure in a diamond anvil cell. Experimentally, the cell geometry must be altered so that the x-rays enter and exit through the gasket and not the diamonds. Energy dispersive spectra are collected at varying diffraction directions, ranging from nearly parallel to the diamond axis to perpendicular to it. With assumptions as to the orientation and homogeneity of the deviatoric stress field, they can recover information about the elastic anisotropy and material strength. Their new results for iron have exciting implications about the elastic anisotropy and evolution of the Earth's inner core.

Macromolecular Crystallography

Multilayer monochromators can provide x-ray intensities from NSLS x-ray bending magnet beam lines that surpass currently available intensities from NSLS x-ray wiggler beam lines which use silicon monochromators. Using beam line X25, collaborators S. Burley and J. Kuriyan (Howard Hughes Medical Institute and Rockefeller U.), and L. Berman, M. Capel, and R. Sweet (Brookhaven National Laboratory), employed broad bandwidth multilayers (with a relative wavelength spread of 1.5%) as monochromating elements instead of

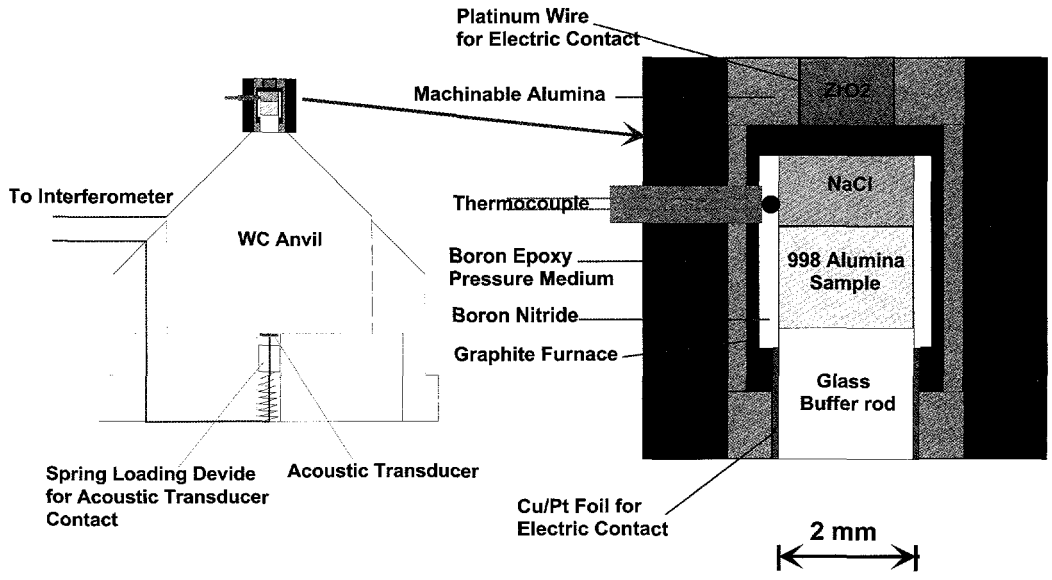


Figure 55: Diagram of anvil insert and cell assembly for ultrasonic experiments in X17BI.

conventional narrow bandwidth silicon, in trial macromolecular crystallography experiments. The multilayers provide an additional two orders of magnitude of flux in the incident x-ray beam. Diffraction data were measured from two test specimens: single crystals of hen egg-white lysozyme and of TAFIA, a heterodimer of two eukaryotic transcription factors (**Figure 56**). These are being analyzed to determine how well the Bragg spots can be resolved and indexed, and their structure factors extracted, in the presence of the peculiar, highly anisotropic resolution function associated with the multilayer-monochromated x-ray beam. These tests at X25 were performed under single-bunch operation conditions, for which the x-ray intensity approximates that available on bending magnet stations under normal 25-bunch operation conditions. Nonetheless, exposure times were surprisingly short, ranging from one to five seconds for a 1° oscillation, and pushed the technical limits of the data collection apparatus' shutter cycle and phi axis rotation. Certain classes of crystallography problems should be solvable using such an x-ray beam. The major restriction is that the ratio of the smallest Bragg spacing resolution attainable to the longest crystallographic axis repeat is limited by the relative bandwidth of the x-ray beam from the multilayer monochromator. Within this limitation, the dramatic intensity enhancement derived (compared with the use of a silicon monochromator) should make possible high-resolution studies of weakly diffracting crystals on NSLS x-ray bending magnet beam lines, that are now impossible to execute there.

Advances have been made in crystallographic data collection. J. Skinner and R. Sweet (Brookhaven National Laboratory) have been developing, on beamline X12C, beamline-control software that incorporates intelligence and experience into a user-friendly graphical interface to the experimental apparatus. They operate a "hybrid" instrument that combines a commercial kappa-axis goniometer and interchangeable x-ray area imaging detectors. The software provides the user with a simple graphical user interface (GUI) to control both the diffraction equipment and the beamline (e.g. wavelength changes and alignment). Important features of the software are that it allows "one-button" operation of many functions that are actually quite complex, and provides automatic documentation of the experiment by writing log files to describe the operations that are performed, and others that contain data about them.

For example, the software facilitates the measurement of diffraction data for MAD phasing of macromolecular structures. Following a simple table set

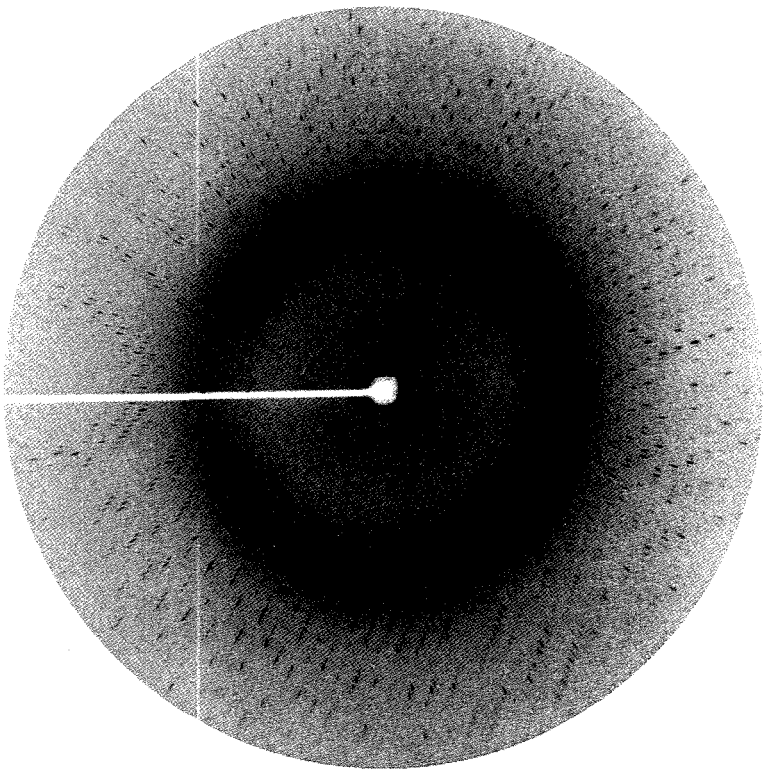


Figure 56: Single diffraction pattern of crystal of hen egg-white lysozyme collected with a multilayer monochromator. (X25)

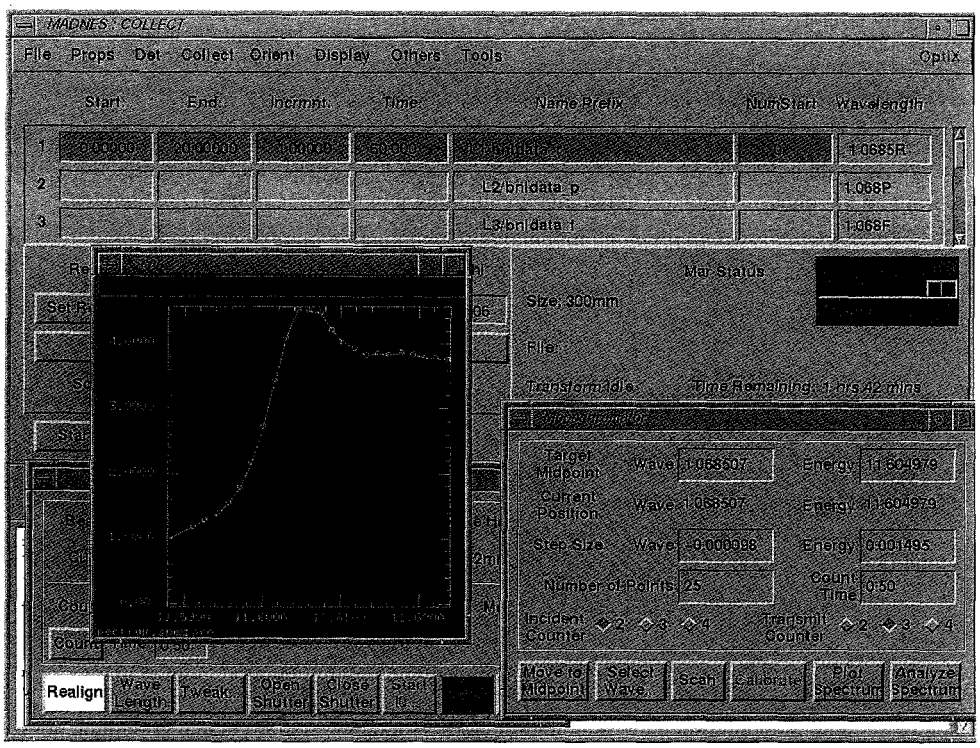


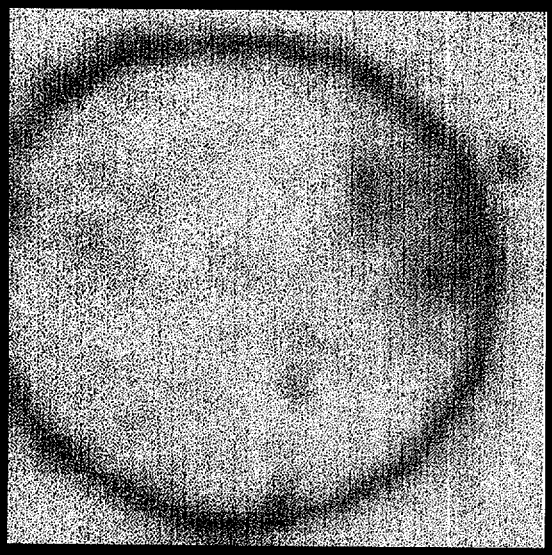
Figure 57: Beamline control software with a sample of an EXAFS scan. (X12C)

up by the operator to describe the experiment, the software will measure the x-ray absorption spectrum of the heavy atom incorporated in the crystal, analyze that spectrum to locate a particular feature at which data should be collected (e.g. the inflection point of the absorption edge), and then collect diffraction data at that wavelength (**Figure** 57). Numerous "ordinary" MAD structures have been solved with the system. Recently, a 1000-residue protein structure with over a dozen heavy (Se) atoms was solved. A small protein structure also was solved during single-bunch running, just 54 hours after the users commenced data collection and while they were still at the beam line collecting data on other problems.

Diffraction Physics

A recurrent issue in x-ray diffraction is the phase problem. Although it is not generally an obstacle in conventional crystallography, there are still areas where the answer is not overdetermined and interference phenomena can be helpful in retrieving the phase Information. An interesting attempt to provide phase information in a 2-D diffraction experiment was made by Y. Yacoby *et al.* (Hebrew U.). They were able to use an adsorbed gold layer to reflect the diffracted wave back into the sample in a surface-diffraction geometry, and to show that additional interferences resulted. These interferences may prove helpful in assigning reflection phases and hence determining structures.

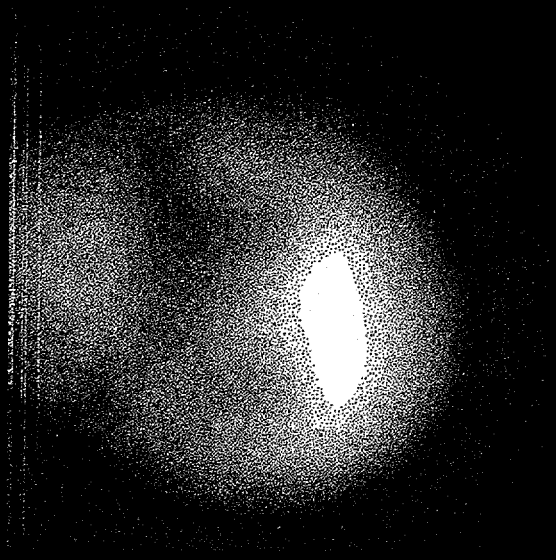
Techniques for focusing and guiding x-ray continue to be pursued throughout the x-ray scientific community. C. Liu and J. Golovchenko (X15A, Harvard U.) have successfully observed the propagation of surface-trapped x-ray waves along the surface of a curved silicon mirror. The wave undergoes successive total external reflections on the surface, and its evanescent tail is simultaneously diffracted by the substrate lattice. The phenomenon may have important applications for x-ray optical elements such as lenses and waveguides.

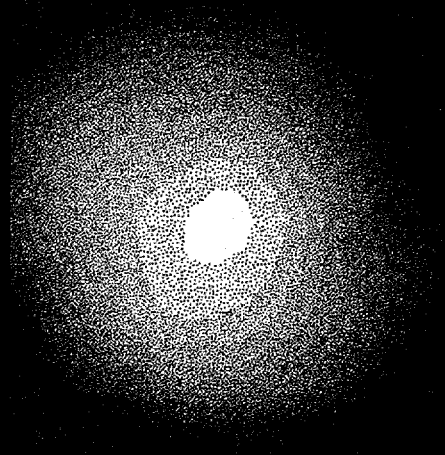


Beamline U2B: Visible and infra-red images of a living cell. Infrared microspectrometers provide chemical specificity and the average power at the sample is too weak to damage living cells. An IR synchrotron source overcomes the limitation of low brightness sources, so that areas less than 25 microns can be imaged. Here the visible image is shown along with two chemical profiles, with each image representing an area 20 μm by 20 μm. Of particular interest is the stretching mode of aliphatic methylene groups (-CH_2), associated mostly with lipids and proteins (opposite page, at left). This mode shows a lateral separation not apparent in the visible image. N. Jamin (DIEP-CEA, France), J.L. Teillaud (Inst. Curie, France), P. Dumas (LURE and LASIR, CNRS, France), G.L. Carr and G.P. Williams (NSLS).

THREE

MEETINGS & WORKSHOPS

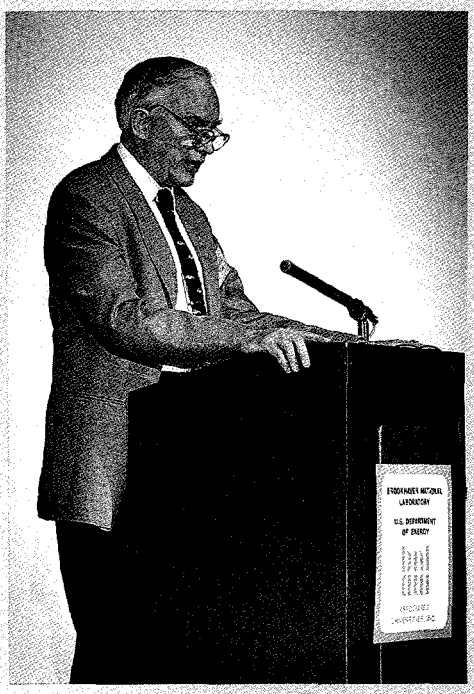




THE 1996 NSLS ANNUAL USERS' MEETING

Peter W. Stephens
SUNY @ Stony Brook
NSLS Users' Executive Committee Chairman

The NSLS users held their 1996 Users' Meeting on May 21st, 1996 at Brookhaven National Laboratory, where they had an opportunity to celebrate another year of scientific and technical achievement, to welcome Michael Hart as the new NSLS Chairman, to hear the latest news about Department of Energy support for its scientific facilities, and to visit once again with old friends.



Keynote Speaker Malcolm Browne, Senior Science Writer of the New York Times.

Three workshops on various scientific and technical subjects met on May 20, and three more on the 22nd. The workshops have continued to grow as an important part of the annual get-together; of the 368 people who registered for any part of the meeting, 80% attended a workshop.

The user community saw the vision for the future held by the new NSLS Chairman, Michael Hart. Reminding his audience that the NSLS operates with the high-brightness Chasman-Green lattice, he noted that the opening of third-generation synchrotron radiation sources in Europe (ESRF and Elettra) has not reduced the demand nor the productivity of second generation facilities, such as the NSLS. Since many experiments are limited by such factors as flux, detector capability, and source stability, they will not necessarily be improved by the newer accelerators, and the NSLS can expect to play an important scientific role in the foreseeable future. Many of these points are discussed in the recently released white paper, "NSLS Into The 21st Century."

Hart also told the users that he has reactivated the NSLS Science Advisory Committee, and has instructed it to initiate the process of tenure review for each beamline. He pointed out that the mission of many of the PRTs has changed substantially since they were created, and that the PRT system does not necessarily provide the best-supported access for all users. The NSLS is working to broaden the access available to the user community for such popular measurement techniques as EXAFS, powder diffraction, and reflectivity.

William Oosterhuis of the Department of Energy described the Scientific Facilities Initiative within the Office of Basic Energy Sciences. In the present fiscal year, $57 million was made available to the DOE programs at twelve facilities. This gave the NSLS a $5 million increase in funding, its first real increase in five years. Consequently, the NSLS has increased its beamline support staff by 20%, and made significant upgrades to the injection system, water supply, computer controls, and the accelerators themselves. Oosterhuis congratulated the user community in communicating the importance of the SFI to Congress. He indicated that the SFI is in the President's FY1997 budget (although 2% less than this year) so that we can expect to continue activities started this year.



(From Left to right) Uli Hillebrecht (University of Dusseldorf), Franz Himpsel (U. Wisconsin, Madison), Steve Hulbert and Xilin Wu (NSLS, Brookhaven National Laboratory).

The keynote speaker was Malcolm Browne, Pulitzer Prize-winning Senior Science Writer of The New York Times. His talk, entitled "Lamplighters and Tool Makers," described two complementary modes of scientific progress: the abrupt discovery and the methodical advancement of new knowledge. He drew a number of interesting conclusions about the role of science and technology in society.

The talks about scientific topics began with Stephen Harrison of Harvard University and the Howard Hughes Medical Institute. He spoke about the role of protein crystallography in understanding how genes are switched on and off in the cell. He described his group's work on the transcription factor NF-*B, specifically on the complex of one protein dimer with a strand of DNA. This work, performed at beamlines X4A and X25, used the multiple wavelength anomalous diffraction (MAD) technique for solving the structure. It is also highlighted in a report entitled "Structural Biology Research at the NSLS" (BNL Informal Report 62916, May 1996).

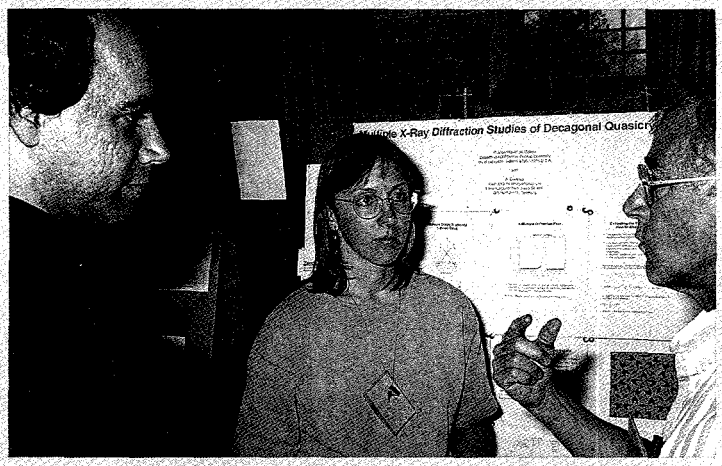
Peter Siddons of the NSLS spoke about precision machining of plastic (PMMA photoresist) using hard x-rays. The NSLS group concentrates on making three-dimensional parts, in contrast with the rest of the world's micromachining efforts, which are mostly on thin, planar structures. Among other points, he described the serendipitous discovery of a technique for making re-entrant cavities, illustrated with a tiny hexagonal wine glass. The ultimate goal is to develop these techniques to the point where they could be economically feasible on a production-line basis rather than a technical curiosity.

The next talk moved to a different part of the electromagnetic spectrum — the use of infrared radiation to elucidate high-temperature superconductivity. Dmitrii Basov of the Brookhaven Physics Department spoke about three regimes that are observed in layered cuprates as a function of oxygen concentration: insulating, "conventional" superconductivity with a gap (range of frequencies with zero conductivity), and a pseudo-gap state in which the infrared conductivity is suppressed but nonzero. In these materials, the pseudo-gap occurs at rather high temperature, and grows deeper as the temperature is lowered, with no abrupt change at the superconducting transition.

Gary Prinz of the Naval Research Laboratory spoke about magnetoelectronic devices, in particular about the role of synchrotron radiation in their development. Rapid progress in this field is leading to significant applications in sensors, memories, and logic elements. These can only be pursued with the detailed understanding of the magnetism of electronic states, especially at surfaces and interfaces, which comes from elegant ultraviolet spin-resolved photoemission and magnetic circular dichroism experiments.



Peter Stephens (SUNY @ Stony Brook), and D. Peter Siddons (Brookhaven National Laboratory, NSLS).



At the Poster Session: (From left to right) Steven Ehrlich (Purdue University), Rachel Eisenhower (University of Illinois @ Urbana-Champagne), and Bill Thomlinson (NSLS Associate Chairman for Environment, Safety and Health/User Programs).

John Fulton of the Pacific Northwest Laboratories discussed recent work on ion solvation in supercritical water. This has been suggested as an attractive method for cleaning and disposing of hazardous materials, and it is important to have a detailed understanding of the fundamental differences between usual solution chemistry and solutions in supercritical water. *In situ* EXAFS experiments are able to reveal such information as the fact that Sr^{2+} is coordinated by half the number of water molecules in supercritical water than at standard temperature and pressure. These experiments also have significant relevance to catalysis and to geochemistry.

Polymer diffraction patterns usually have relatively few, broad peaks, whereas one normally associates synchrotron-based powder diffraction with a high resolution technique. Nevertheless, DuPont scientist Kenn Gardner described several significant advantages to the use of synchrotron radiation for his work in polymer crystallography. Particularly important is the fact that the lineshape is accurately known, whereas laboratory measurements need good standards (which do not exist), e.g., to distinguish paracrystalline disorder from finite-size broadening for low angle peaks.

Erik Johnson of the NSLS concluded the series of scientific talks with the tantalizing question, "Could you Use a Couple of Orders of Magnitude?" He proposes to deliver that improvement in the intensity of pulsed ultraviolet and infrared light at the Source Development Laboratory. This is a broadly-based project of research and development on an ultraviolet free electron laser amplifier and on the use of very short electron bunches for FEL and coherent synchrotron radiation experiments.

Two other important features of the Users' Meeting were the scientific poster session, with a reception at the Brookhaven Center, and the equipment show in the Berkner Hall lobby. Both were popular opportunities to sniff out some of the latest work at the facility, and to see the exciting new tools and ideas for synchrotron radiation research.

By way of administrative business, the NSLS Users' Association elected three new general members to the Users' Executive Committee: Joel Brock of Cornell University, Ian Robinson of the University of Illinois, and Thomas Russell of the University of Massachusetts. It also approved a charter revision so that future Special Interest Group elections will be held by electronic mail, and approved a new SPIG for industrial users. In executive session, the UEC chose Brock to be its Chairman-elect.



At the Equipment Show/Vendor Exhibit: (From left to right) Andrew J. Howard (Illinois Institute of Technology), Chris Nielson and Ronald C. Hamlin (Area Detector Systems, Inc.).

In Situ Applications of X-ray Absorption Fine Structure

Simon R. Bare
(Dow Chemical Company)

The ability of x-rays to penetrate matter was emphasized in this year's XAFS workshop on studying materials under *in situ* conditions. Eight speakers addressed the 60 attendees with topics ranging from catalysis to electrochemistry to biology. Jim McBreen (BNL) led off the workshop with a presentation on using XAFS to probe the electronic and geometric structure of fuel cell catalysts under applied voltages. He was able to draw a correlation between the Pt-Pt bond length and Pt d-band vacancies with reaction rates for several Pt-M alloy catalysts. Mark Antonio (ANL) described a novel bulk electrolysis cell for probing the structure of species in solution during electrolysis. The focus of the talk was on the Eu^{2+}/Eu^{3+} couple. He showed, and explained why, the addition of a single f-electron to Eu dramatically changed the Eu L3-edge XANES. Simon Bare (Dow Chemical) followed the oxidation state of vanadium in a supported vanadium phosphate catalyst during the oxidation of butane using dispersive XANES with on-line product analysis. He showed a direct correlation between the presence of V^{5+} and the formation of maleic anhydride. The ability to study surfaces under corrosive conditions using XAFS was illustrated by Inho Song (Case Western Reserve). He described a total electron yield detector designed to perform *in situ* studies of the atmospheric degradation of materials. The state of sulfur in gaseous SO_2 in dry and humid environments was determined, together with that on the surface of Cu films during exposure to the corrosive gas. Following lunch, during which several posters were presented, Di-Jia Liu (AlliedSignal) nicely demonstrated the need for true *in situ* experiments to study the form of Cu in a ZSM-5 de-NO_x catalyst. He showed that there is an excellent correlation between the presence of Cu(I) and the rate of selective catalytic reduction over this type of catalyst. A fascinating presentation on the use of micro-XANES to follow the uptake and metabolism of metals (Cr and Se) in aquatic plants was given by Doug Hunter (Savannah River Ecology Lab.). His data indicated that there is localized uptake and reduction of both elements. For example there is localized reduction of Se in the leaf of the fern from Se^{6+} to Se^{2-}. John Fulton (PNL) described both a high temperature (500 C), high pressure (1 kbar) reaction chamber for studying ion solvation in supercritical water, and a quartz capillary reactor for investigating metal species in supercritical CO_2 using EXAFS. He showed that there is a difference in solvation of Sr^{2+} and Rb^{+} ions in supercritical water compared to ambient water solutions: there is a reduction in the average coordination and a concomitant reduction in metal-oxygen bond length. The formal program ended with a presentation by graduate student Mike Nasher (U. of Illinois) on the use of *in situ* EXAFS to monitor the preparation of Re-Ir clusters on alumina prepared from novel bimetallic carbonyl complexes.

WORKSHOP

Opportunities in Polymer Research Using Synchrotron Radiation

Thomas P. Russell
(IBM Almaden Research Center*)

The use of synchrotron radiation for the investigation of polymers began in the early 1980's with exclusive use of small angle scattering methods to elucidate the morphological characteristics of bulk polymers. Despite the fact that the results from these studies were impressive, in quantity and quality, the growth in the application of synchrotron radiation for studying polymers was slow. Recently, however, there has been a tremendous growth in polymer related research. Not only has the number of experiments that are performed on polymers grown in that time, but the diversity of scientists performing research on polymers has grown. Initially, only those scientists whose major research interests were in polymers performed work in this field. Now, however, scientists with more traditional physics and chemistry backgrounds must be included. This growth can be attributed to several factors. First, there is the nature of the polymer chain. Typically, polymer chains pervade volumes on the tens of nanometers size scale. Thus, features characteristic of phase transitions are easily observable. Second, due to the entangled nature of the polymer chains, relaxation processes are longer. Thus, polymers are ideal candidates for the investigation of kinetic phenomena. Third, some of the potentials for using the variable wavelengths in the hard and soft x-ray region of the spectrum for the study of polymers have been realized. Thus, entire new avenues of research have been uncovered. Finally, the realization that the surfaces of polymers are quite smooth (an rms roughness of 0.6 nm) has permitted the exploitation of the numerous surface characterization techniques that have been developed at synchrotron sources. Both the increase in the number of scientists investigating polymers and the number of techniques available to pursue polymer research have had significant impact on basic and applied research topics. A Workshop on Opportunities in Polymer Research Using Synchrotron Radiation was held during the 1996 NSLS Users' Meeting. It was designed to highlight some of the recent pioneering studies on polymers and to demonstrate areas of potential use of these versatile light sources in polymers.

Professor Benjamin Chu from the State University of New York in Stony Brook spoke on small angle x-ray scattering studies on polyelectrolyte gel/surfactant complexes. The low contrast between the scatterers, the low concentrations and the large size of the chains mandate the use of a very high resolution small angle spectrometer with high flux. These conditions can only be realized at a synchrotron source. The results from the experiments described by Chu have provided significant insight into the fundamental behavior of polyelectrolyte gels, the influence of the pH of the swelling solvent and the testing of different theoretical concepts.

One of the important developments that has occurred with synchrotron sources is the ability to perform several different measurements simultaneously, as for example small angle scattering and wide angle diffraction. Obtaining multiple results on a single sample has tremendous advantages in the case of polymers. Due to entanglements, it is often difficult to get two different polymer samples into precisely the same state and, consequently, errors are introduced when multiple samples are used. Simultaneously using multiple techniques eliminates this error. Dr. Benjamin Hsiao of DuPont discussed a series of studies where both small and wide angle x-ray diffraction were used to investigate the crystallization and melting of some semi-rigid polymers, namely poly(ether-ether-ketone), PEEK. Typical data obtained from such studies are shown in **Figures 1a and 1b** where the time resolved small angle x-ray scattering and the wide angle diffraction data for a PEEK sample are shown after the sample has been cooled from the melt to 290°C. In **Figure 1a** the small angle scattering data show a growth in a peak which is due to the crystallization of the PEEK molecules into a lamellar type of morphology. Simultaneously the diffraction data in **Figure 1b** show the development of the crystal structure in the lamellar morphology. Large anisotropic changes in the unit cell parameters occurred in these materials during secondary crystallization processes. By correlating the small and wide angle

[* Now with the University of Massachusetts]

scattering data a model for the crystallization process in PEEK was developed. Information of this nature is crucial in deriving structure property relationships which directly impact the processing and end use of polymers.

Another area where synchrotron radiation has played an important role is in the characterization of single fibers or small bundles of fibers. Using standard laboratory equipment the available flux is simply too small obtain acceptable signal to noise ratios. Professor David T. Grubb of Cornell University described experiments on high modulus polyethylene fibers, single fibers of Kevlar (about 12 microns in diameter) and bundles of spider dragline silk fibers (~ 4 μm in diameter) where the fibers are placed under a load and stretched. Within seconds, full two dimensional fiber patterns could be obtained which permitted the investigation of dynamic processes and real-time crystal orientation. His lecture focused on deformation mechanisms that were dominated by elastic processes. Dr. N. Sanjeeva Murthy of AlliedSignal Inc. then described experiments on the fibrillar and lamellar structures in nylon-6 fibers. Again, with the ability to obtain full two dimensional patterns in seconds allowed the investigation of structural changes to the fibers during drawing and post thermal treatments. However, as pointed out by Murthy, since massive amounts of data are collected, much information has been ignored. He then described some of the efforts he has been making in the utilization of the full pattern.

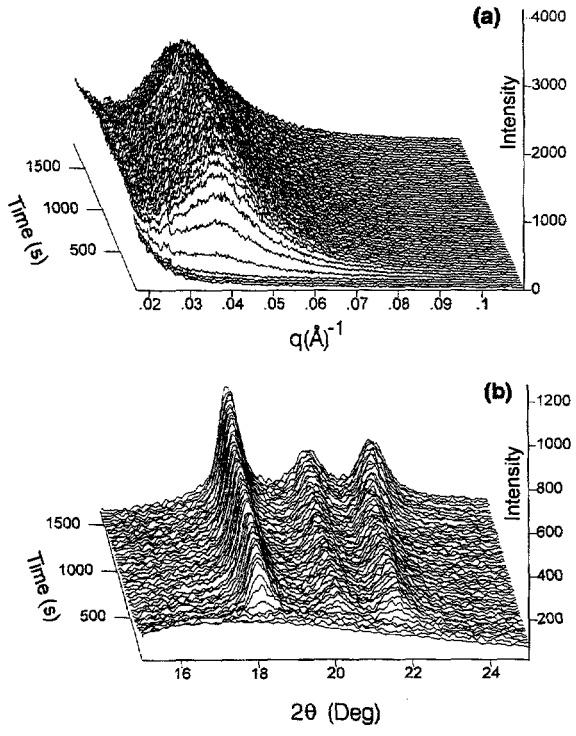


Figure 1a: Time resolved small angle x-ray scattering of a PEEK sample undergoing crystallization.

Figure 1b: Time resolved x-ray diffraction for a PEEK sample undergoing crystallization. These data were collected simultaneously with the small angle data in Figure 1a.

The afternoon lectures in the workshop focused on the surface and interfacial behavior of polymers. Professor Miriam Rafailovich of the State University of New York discussed specular reflectivity and off-specular scattering studies on Langmuir films of ionic block copolymers at the air/water interface. Block copolymers, which are essentially two different polymers covalently bound together at one end, can be made such that one block is hydrophobic and the other is hydrophilic. On a water surface the difference in the functionalities of the two blocks cause the formation unique and unusual two dimensional structures. The lateral surface pressure dictates the concentration and, consequently, the morphology. These surface structures and the transition from one structure to another can be followed by use of off-specular scattering where a component of the diffraction vector is in the surface plane. However, the off-specular scattering is orders of magnitude less than the specular reflectivity and, consequently, requires the use of a synchrotron source to obtain good statistics. Rafailovich then demonstrated another area where off-specular scattering was being brought to use. This related to the conformality of the polymer films on a rough or periodic surface. **On the following page, Figure 2 shows** the rocking curve of a substrate that has a 1μm grating on the surface. This spectacular profile was obtained by rocking the sample by an angle λ about the specular condition at Q_z= 0.2 $Å^{-1}$ (where the diffraction vector is oriented normal to

the surface plane of the sample). The multiple peak results from the periodic structure, i.e. the grating, on the surface of the sample. Coating this surface with a polymer film and then observing the time dependent changes in the off-specular scattering have yielded considerable insight into the motions of polymers on surfaces and the ability of polymers to planarize the free surface.

Following this, Dr. Thomas P. Russell of the IBM Almaden Research Center described a series of studies using Grazing Incidence X-ray Scattering (GIXS) to probe the structure of polymers near a surface. In the particular case of an aromatic polyimide, GIXS showed that, in the vicinity of a surface, order in the polymer was enhanced. Polishing or buffing of the polymer surface, a process used in the production of flat panel displays, was shown, by GIXS, to produce a strong orientation of the polymer chains in the vicinity of the surface in the buffing direction. This surface orientation is directly correlated with the orientation of liquid crystals in displays. Prefacing the next two lectures, Russell also described the use of Near Edge X-ray Absorption Fine Structure (NEXAFS), where the polarization of the incident x-ray beam was used to probe the orientation of the polymer chains at the surface. For example, shown in **Figure 3** are the NEXAFS results for an aromatic polyimide that has been buffed. By measuring the Auger and total electron yield as the energy of the polarized x-rays is changed where the electric field vector of the radiation is either parallel or perpendicular to the orientation direction, information concerning the surface (first 10 Å from the surface) and the near surface (about 0.70 Å from the surface) orientation of polymer chains is found. These results, combined with the GIXS results, have led to a detailed understanding of the buffing process and the manner in which information can be transferred across a boundary.

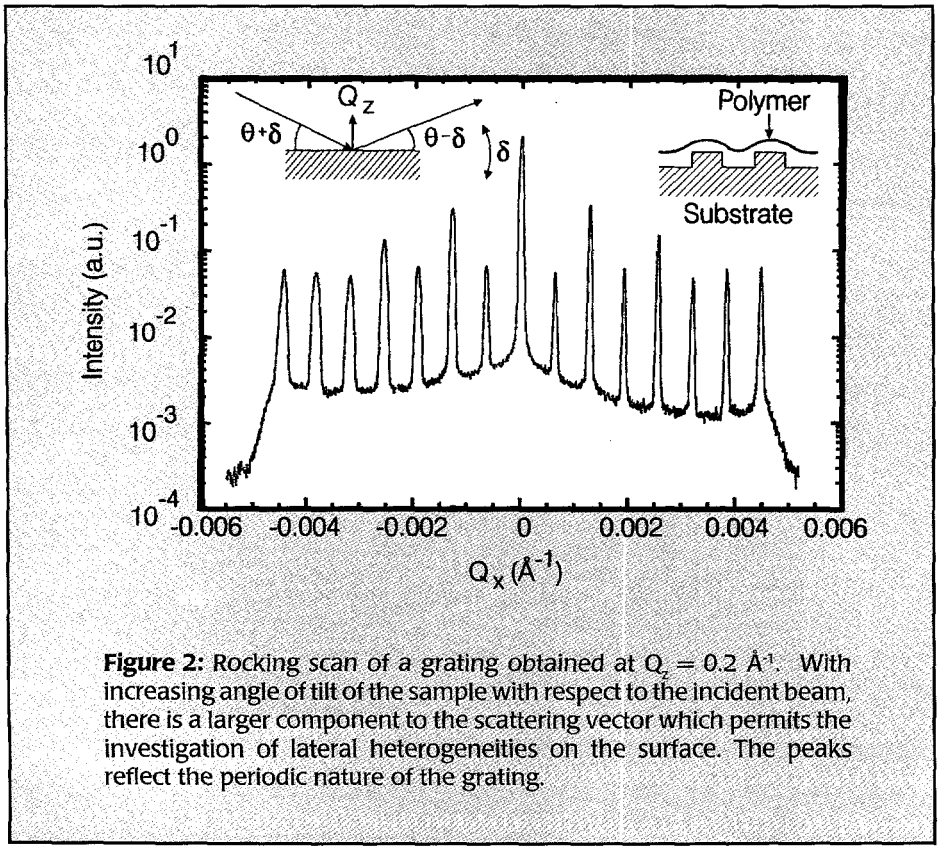


Figure 2: Rocking scan of a grating obtained at $Q_z = 0.2$ Å^{-1}. With increasing angle of tilt of the sample with respect to the incident beam, there is a larger component to the scattering vector which permits the investigation of lateral heterogeneities on the surface. The peaks reflect the periodic nature of the grating.

Much emphasis has been placed lately on the behavior of thin films of multicomponent polymer systems. Numerous techniques are available for depth profiling concentration in such systems, however, there is a paucity of techniques for investigating lateral heterogeneities. Professor Harald Ade of North Carolina State University described advances that he and his collaborators have made in the use of x-ray microscopy to this end. The advantage of x-ray microscopy over the more traditional techniques, like light microscopy and atomic force microscopy methods, is that different chemical components can be seen with a lateral resolution of 0.1 micron. In addition, since the x-rays are polarized, lateral variations in the orientation of

the same or different components can be seen. Ade described investigations on liquid crystalline polymers, ternary polymer mixtures and polyethyleneterephthalate where x-ray microscopy has provided key insight into the morphology and orientation. X-ray microscopy is relatively new but, as explained, the number of microscopes available for study is growing at a rapid rate. In the study of the surface and interfacial behavior of polymers it is increasingly more important to distinguish the behavior of the polymers immediately at the surface or interface without having to extract such information from a techniques that averages over the first 5-7 nm. In the case of polymers, at a distance of only several monomer diameters from the surface, about 1-2 nm, the bulk characteristics of the polymer chain are found. Dr. Benjamin Dekoven of the Dow research laboratories described studies using near edge x-ray absorption spectroscopy on materials ranging from self-assembled monolayers to perfluorinated polymers where chemical information was obtained on the first nanometer from the surface. Such information is crucial for developing a quantitative understanding of the surface wetting characteristics of polymers and the transfer of information, be this chemical or structural, across an interface.

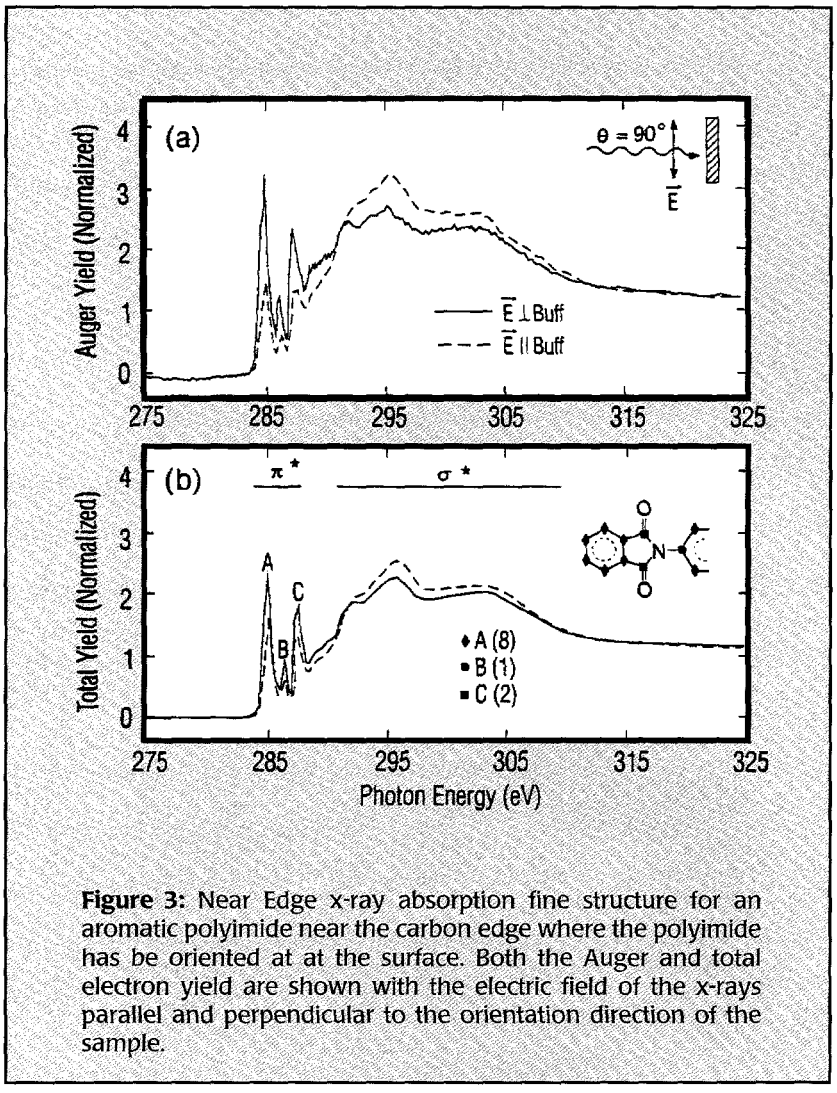


Figure 3: Near Edge x-ray absorption fine structure for an aromatic polyimide near the carbon edge where the polyimide has be oriented at at the surface. Both the Auger and total electron yield are shown with the electric field of the x-rays parallel and perpendicular to the orientation direction of the sample.

Each of the lectures focused on specific research problems. However, there were several underlying messages that became quite clear as the workshop progressed. First, synchrotron radiation sources offer a tremendous battery of techniques for the characterization of polymers. The results presented beautifully demonstrated several examples where quantitative information was obtained. Second, the number of experiments performed at synchrotron sources with polymers as the central research theme has increased tremendously over the past few years. Finally, there is still much that these sources offer for performing polymer related research, a resource that will lead to pioneering developments in the field.

WORKSHOPS

Multiple Wavelength Anomalous Dispersion (MAD) in Protein Crystallography

Lisa J. Keefe and Stephan L. Ginell
(Argonne National Laboratory)

Multiple wavelength anomalous dispersion (MAD) has developed into a powerful crystallographic phasing technique for solving macromolecular structures. Synchrotron radiation is essential in order to implement MAD phasing, and with the increasing accessibility of synchrotron beamlines, the technique is gaining widespread use. The focus of this workshop was to present and discuss the theoretical approaches to MAD phasing, the preparation of selenomethionyl-substituted protein for MAD phasing, the strategies of MAD data collection, processing and scaling, and examples of the application of MAD phasing in solving crystal structures.

Axel Brunger (Yale University) presented a comparison of algebraic and probabilistic methods applied to a MAD data set of a fragment of the carbohydrate binding domain of mannose binding protein A. Tom Terwilliger (Los Alamos National Laboratory) discussed a Bayesian approach to MAD phasing, as implemented in his program HEAVY (v 4.5). In a comparison of Bayesian MAD phasing with other methods, namely treatment of MAD data as approximate relationships of dispersive and anomalous differences among wavelengths and treatment of MAD data as multiple isomorphous replacement, Bayesian MAD phasing gives more accurate phasing, especially for incomplete data sets. Alan Friedman (Purdue University) discussed data reduction and scaling for MAD, the inherent problems with MAD data and solutions to those problems, and MAD phase determination. With MAD data, the signal is inherently less than the noise and data collation can be problematic. To overcome these two obstacles, local scaling with flexible automatic data collation can be performed and robust phase determination can be used.

Robert Sweet (BNL-Biology) presented a talk for Venki Ramakrishnan (University of Utah School of Medicine) on the use of standard MIR data reduction, scaling, and phasing programs to analyze MAD data. Dan Leahy (Johns Hopkins School of Medicine) discussed his experiences with the use of selenomethionyl-substituted protein to solve structures by MAD. He reviewed strategies for substituting selenomethionine for methionine in proteins, methods for growing bacteria in media containing selenomethionine and expression of selenomethionine-substituted protein, tips on purification and crystallization of selenomethionine- substituted protein, assays for selenomethionine in purified proteins, and valuable advice on how to prepare for and perform a MAD experiment at a synchrotron. Robert Sweet (BNL-Biology) discussed issues in data collection for MAD phasing, with much emphasis on the integrated and user-friendly beamline-control software used at his beamline at NSLS.

Chi-Hon Lee (Rockefeller U.) presented the crystal structure of HIV-1 Nef complexed with a src-family SH3 domain. Yee Liu (Columbia U.) discussed a MAD experiment at the M4 edge of uranium. This is a very difficult and unique experiment due to the low energy (3728 eV) of the M4 edge of uranium. The advantage of using this heavy atom is that the MAD signal is very strong and thus phasing can be accomplished for very large molecules or complexes.

The workshop ended with a lively question and discussion session which focussed on the details of solving structures using MAD phasing. These included the likelihood of solving a structure using MAD phasing. This is correlated with the signal to noise ratio, and methods for calculating this ratio were reviewed. Also discussed was the determination of the anomalous and dispersive components, f'' and f', respectively, of the structure factor and the refinement of these components, with and without anisotropy. MAD phasing is rapidly becoming the technique of choice for the determination of crystal structures and the increasing availability of synchrotron radiation beamlines and development of cryocrystallographic techniques for performing MAD experiments is enabling many otherwise very difficult crystal structures to be solved.

WORKSHOPS

Strategy and Methods for Area Detector Data Collection

Alex Darovsky
(Brookhaven National Lab., NSLS)

The rapid progress in the technology of area detectors (AD) increases their advantages for many scientific applications utilizing x-ray diffraction techniques. Being primarily oriented to macromolecular studies, AD data collection techniques and subsequent reduction and interpretation of the data need to be readjusted for the new applications, particularly for small molecule crystallography, powder diffraction, and synchrotron crystallography.

This one day workshop was intended as a forum for the discussion and evaluation of methods, procedures, and algorithms for AD data collection and processing. The morning session was dedicated to in-depth analysis of methods for 2D data processing; the afternoon session being focused on practical aspects of 2D data collection strategy. Following opening remarks by NSLS Chairman Michael Hart, Robert Bolotovsky (SUNY @ Buffalo) gave a detailed description of a new method for intensity integration of 2D diffraction peaks. He emphasized the advantage of using the "seed-skewness" method for integration of weak peaks or some abstinent peaks with irregular shapes.

Joseph Reibenspies (Texas A&M U.) discussed the topological property of 2D arrays of data with implication to peak/anomaly classification of diffraction pattern - another example of generalization of data reduction procedures for the AD technique. Finally, analysis of a severely delocalized diffraction pattern in terms of its crystalline and amorphous components was demonstrated by Peter Moran (SIEMENS). He applied a Fourier filtering technique for estimation of crystallinity of partially oriented polycrystalline samples.

The afternoon session, chaired by Richard Harlow, began with a detailed analysis of geometrical conditions inherent to the oscillation method presented by Robert Sweet (BNL-Biology). The impact of the presentation was greatly enhanced by remarkable drawings by co-author, Zbyszek Dauter (EMBLO,Germany). An advocate of image plate technology, Wladek Minor (U. of Virginia) gave an extensive overview of recent developments in area detector systems and auxiliary x-ray equipment which enhanced the capability of in-lab diffractometers making them competitive with the existing synchrotron sources. His talk also focused on the practical aspects of data reduction, particularly, on the analysis of possible pitfalls and adequate criteria for data quality. The first two speakers referring predominantly to macromolecular crystallography were complemented by aggressive enthusiasts from the small moiety community. Patrik Carroll (U.of Pennsylvania) demonstrated a superb performance of the R-AXIS image plate system for accurate structure analysis. A vast array of interesting molecular structures illustrating his presentation exemplified the effective and professional approach in utilizing the commercial hard- and software systems. A competitive, also an expensive so far, utilization of a CCD detector for single crystal data collection and processing was introduced by James Phillips (SIEMENS). While offering a versatile set of sophisticated hardware, he stressed the importance of optimization of experimental technique in order to obtain the best quality data. A detailed description of optimized strategy and tools implemented in SMART SYSTEM was given and evaluated.

Finally, Fabienne Adolphe (ESRF,France) reviewed the experience accumulated at the BL2 beamline (ESRF) with area detectors. The variety of approaches which were reported indicates that synchrotron sources, being multi-user facilities with diversified areas of research, provide a fertile field for further applications and development of area detector techniques as was manifested by the superb attendance at the workshop. Comprehensive Workshop Notes (partially supported by DuPont de Nemours Co. and SIEMENS) made a valuable addition to the educational objective of the workshop.

The Application of Synchrotron Radiation to the Study of Magnetic Materials

Boris Sinkovic
(New York University)

The workshop brought together a diverse group of researchers involved in the application of a variety of synchrotron radiation (UV and x-ray) based techniques (scattering, spectroscopy and microscopy) to study of magnetic phenomena in magnetic thin films and multilayers, interfaces, surfaces, and low dimensional magnets. Gary Prinz's (NRL) talk during the NSLS Users' Meeting, a day before the workshop, describing applications of variety of novel magnetic structures for storage, sensors and logic technologies, was an excellent introduction to the workshop. The workshop's opening remarks by Denis McWhan's (BNL) reiterating the increased interest and activity in studies of magnetism in recent years, which were also reflected in larger then anticipated workshop participation, resulted in a need to move the workshop from Berkner Hall to the NSLS Seminar Room.

The first talk was given by Bernhard Keimer (Princeton U.) who discussed x-ray diffraction experiments on compounds undergoing structural transitions induced by high magnetic fields. These studies led to the discovery of a novel "soliton lattice" phase in the quantum spin-chain compound $CuGeO_3$, which provide an important test for theories of low-dimensional quantum magnetism. Gavin Watson (BNL - Physics) reported on recent progress in applying resonant x-ray scattering techniques to study the temperature-dependent magnetic order near the surface of an antiferromagnet. The studies show that within ~50 Å of the (001) surface of UO_2, the magnetic scattering intensity decreases continuously as the bulk N'eel temperature is approached from below, which is in contrast to the bulk transition. Rogerio Paniago (U. of Houston) talked about x-ray diffuse scattering study of interfacial roughness in metallic multilayers using a novel 2-dimensional Image Plate detector. The technique allows the measurement of the conformal roughness in the initial stages of growth of a lattice matched Fe/Au buffer and the height-height correlation function. The interfacial cutoff length was shown to be dependent on the lattice mismatch, indicating it to be an important parameter for the growth of high quality metallic multilayers. Stuart Parkin (IBM Almaden) talk gave several examples how his work in thin film magnetism has benefited by the application of synchrotron radiation techniques, in particular EXAFS and MCD. Yves Idzerda (NRL) talked about recent development in the absorption and reflection of circularly polarized soft x-rays demonstrating the ability to obtain element-specific magnetic information for heteromagnetic thin films, including a means to determine the magnetic structure, to measure the film thickness with very high accuracy, to identify sequence of multilayer switching with applied field, and possibly to determine the magnetic roughness of an interface.

In the afternoon session Elio Vescovo (BNL- NSLS) showed, through various examples, how a combination of spin- and angle-resolved valence-band photoemission spectra and *ab initio* slab calculations can yield a very detailed description of the electronic structure of magnetic surfaces, interfaces and thin films. Such studies reveal the precise relation between the electronic structure and the magnetic properties. Jeahoon Park (BNL-NSLS) talked about electronic aspects of the ferromagnetic transition in materials exhibiting colossal magnetoresistance (CMR). The high-resolution photoemission data found the insulator-metal transition near the Curie temperature and suggesting that strong small-polaron effects are responsible for the enigmatic insulating behavior above T_C. Neville Smith (LBNL) discussed opportunities for magnetic materials research at that high brightness synchrotrons, like ALS, with special emphasize on the microscopic studies. Ulrich Hillebrecht (U. of Duesseldorf) talked about element specific magnetic imaging with Photoelectron Microscopy using a commercial, Staib PEEM-150 microscope. Finally, Andrew Kent (NYU) summarized his research on the fabrication and study of nanometer scale ferromagnetic structures prepared using a scanning tunneling microscope. The work demonstrates that geometrical similar iron nanostructures are magnetically distinct, indicative of important contributions to the magnetic anisotropy other than the shape.

WORKSHOPS

Hard X-ray Precision Fabrication

D. Peter Siddons and Erik Johnson
(Brookhaven National Lab., NSLS)

This workshop was intended to be a true workshop rather than a mini-conference. It was our intention to bring together people who are active in fabricating lithography-based structures in order to stimulate discussion around the topic area, and to seek advice on how to proceed in our development of the X14B beamline as a manufacturing research end-station for hard x-ray fabrication. There were approximately 15 attendees. Judging from the level of enthusiasm among the attendees it would seem we met with reasonable success in these objectives. There were five key areas of concern regarding this program which were addressed at the meeting:

- Support Capabilities
- Exposure Station Properties
- Interoperability with Other Facilities
- Qualification of Customer Vendors and Tools
- Beamline Access and Allocation

The resulting discussion of each of these areas is described briefly below.

Support Capabilities:

It was felt by many at the workshop that some supporting laboratory space be available which would provide a clean area to assemble fixtures and package samples for shipment. At present we believe this can be met by cooperative use of the existing cleanroom in the basement of instrumentation, and by allocation of some of the X13 Lab space for setup. A measurement metrology capability is also regarded as desirable, and in this respect, our measurement microscope system (Nikon microscope plus the Quadracheck QC-4000 measurement package) was deemed to be adequate to the present state of process development.

A sample development capability was also requested. Currently two developer systems are in use, GG and MIBK. Although some attendees favored the GG system, our research here indicates that for high aspect ratio material processing the MIBK/EtOH system seems to perform as well or better than the GG system. We would only consider the GG system if one of the users was sufficiently motivated to organize and fund its implementation.

Exposure Station Properties:

In our presentation we described the properties of our planned scanner. There was general agreement that a high linear velocity device was desirable. Our prototype hydraulic stage will be capable of scan rates up to 25cm/s with position and speed servo-feedback. One key feature which was strongly advocated was interoperability of fixturing with other facilities. Since at present, no other facility is performing hard x-ray exposures it is largely up to us to establish a standard configuration in consultation with potential future facilities. Most notable among these in the USA is CAMD, who are adding a wiggler to their machine for this type of work. The scanner enclosure should have a controlled environment which includes class 100 particle counts, less than 50% relative humidity, electrostatic reduction, and temperature stability the order of $_1$C. Ideally the scanner should be capable of exposing a 15cm by 15cm mask without step and repeat motions. The space constraints at X14B are such that we can only expose a field about 12 cm wide. This was viewed as a satisfactory step in the right direction from our present 4cm field at X27B.

Interoperability with Other Facilities:

This issue extends beyond fixturing and facilities. To make this a viable production technology, it was strongly felt that in the long run a μprint shop-capability should be created. In essence the idea is that customers would take their work to a broker (like MCNC) who

would then distribute the masks, fixtures, and materials to whatever exposure station was suitable and available. This implies some dovetailing of scheduling of maintenance and possibly redundancy within facilities. In this way if a scanner goes down another is available as backup. At the NSLS, beamline X27B might, for example, serve as backup for X14B. In the case of facility maintenance, ALS, CAMD and NSLS might coordinate shutdown activities.

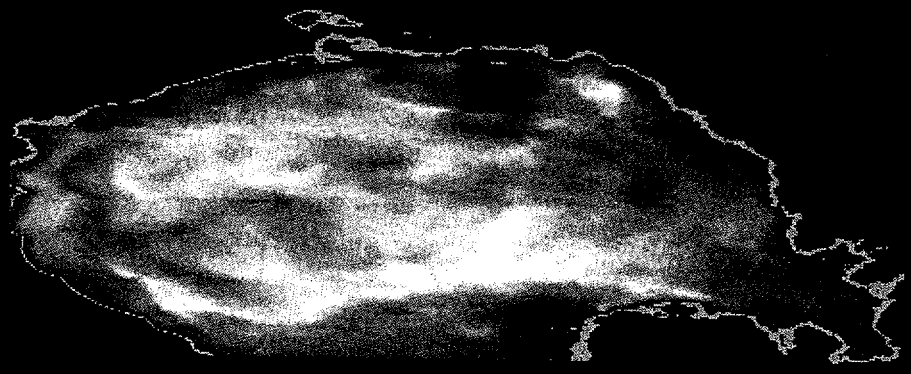
Although it seems early these days to be too concerned about this issue, there was a general awareness of its longer term impact on the viability of hard x-ray machining as a manufacturing technology. It was pointed out that this problem is not as acute as it is for the specialized analytical work of the type ALS and SSRL are undertaking for wafer analysis. In their case full time availability is essential to recover from manufacturing line problems. In our case, a brief unavailability is part of the normally expected contingency in any sound production plan. Still it is an issue worth noting.

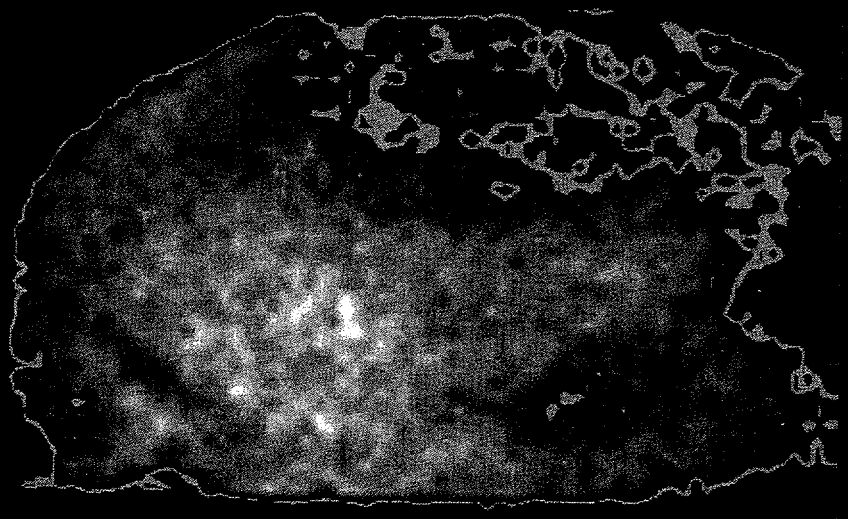
Qualification of Customer Vendors and Tools:

If the technology proves both successful and popular, a concern was raised about liability, or at least culpability, for production runs that don't work out. If a customer provides a mask or fixture that won't work, or sub-specification material that cannot be properly processed, establishing responsibility for a failed production run could prove both difficult and contentious. This should not be a problem with our first users, who will essentially be collaborators. If the print shop model takes hold we will need to establish standards for acceptable material and qualified vendors of masks, fixtures, etc.

Beamline Access and Allocation:

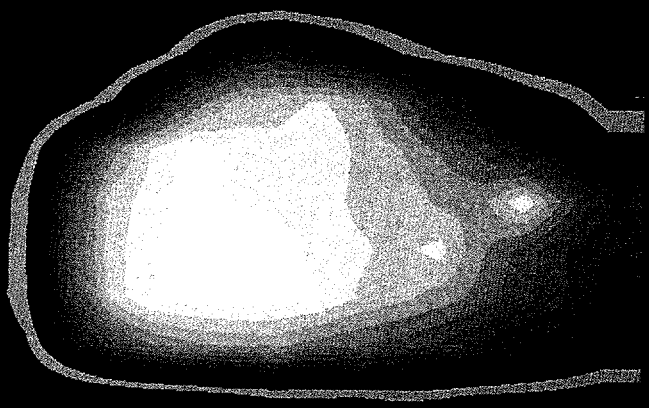
Several questions arose which, again, are somewhat in the future regarding access to the station currently under construction at NSLS. The attendees of the meeting predicted that within a year of establishing the production research line, it will be oversubscribed by as much as a factor of 10! While NSLS would be pleased with such a success, the administrative issues must be established well in advance of such a demand. NSLS is seeking advice on these issues from the DOE.

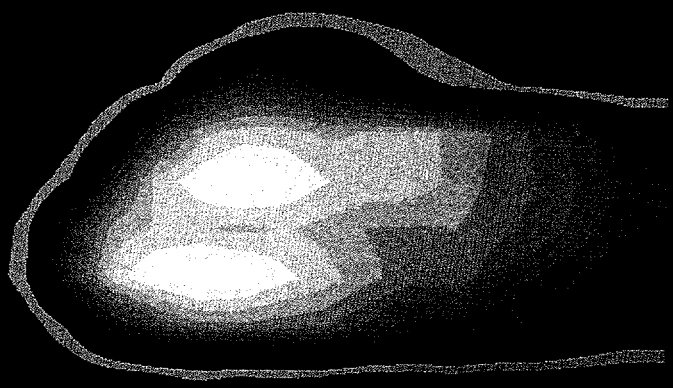




Beamline X26A: False color contour plots of zinc fluorescence in a *Xenopus laevis oocyte* and fertilized embryos during various stages of development. The unfertilized oocyte (above left) and eight-cell embryo (above right) were measured using white beam to monitor the location of zinc in the embryo as development progresses. The sixteen-cell embryo measurements (opposite page) were made using a monochromatic beam to observe different zinc environments present at the same stage of development. In all plots, the white areas represent the most intense zinc fluorescence and the blue areas represent the least intense. K. Peariso, D.L. Tierney, C. VanHuis, R.J. Denver, and J.E. Penner-Hahn (U. of Michigan)

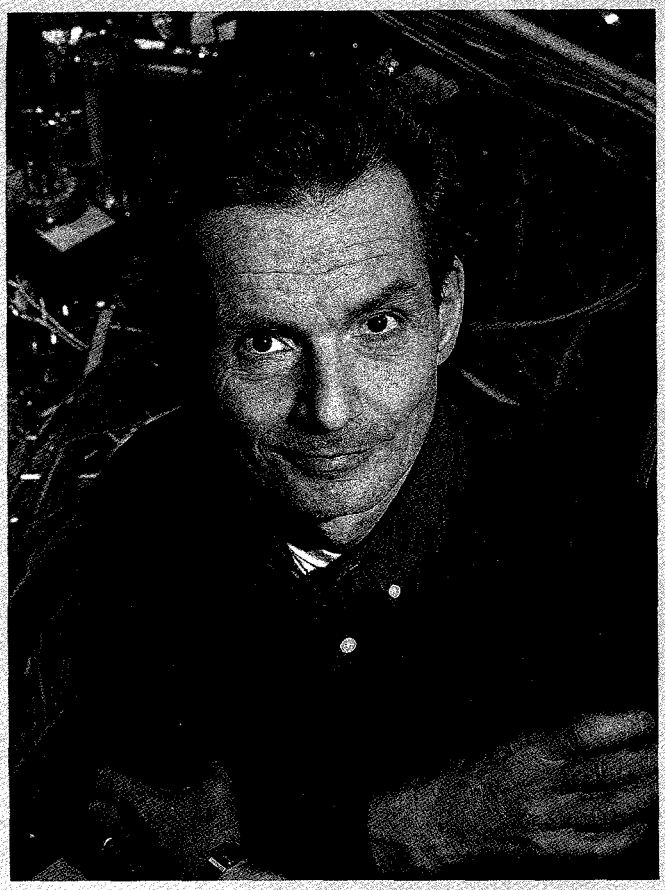
FOUR
OPERATIONS





VUV MACHINE

Stephen Kramer
VUV Ring Manager



Stephen Kramer, VUV Ring Manager

Figure 1 shows the breakdown of the VUV Ring operating statistics for the Fiscal Year 1996. The monthly breakdown of the most significant operational statistics for the year, are shown in **Figures 2 through 6.** After the problems with the booster power supplies in FY1995 were overcome, the operating reliability of the VUV Ring improved such that the unscheduled downtime decreased by almost a factor of two to 1.6%, the lowest level achieved to date. Despite this unscheduled loss of user beam time, the actual beam time delivered to the users was 1% greater than originally planned,as the result of a reduction in maintenance, commissioning, injection and studies time from that originally scheduled. The planned operating schedule for the year was one of the lowest in recent years of 62%, this was due to the extended winter shutdown (November 1995 through January 1996). This reduced schedule provided the necessary break for upgrading of the VUV beam ports and the user's beamlines. The VUV Ring returned from this shutdown ahead of schedule and with no change in operational properties of the beam, despite a somewhat longer vacuum conditioning period than originally planned. The entire year of operation was at the higher energy of 808 MeV which was commissioned in FY 1995. Consequently the integrated current delivered to the user's while not being as great as previous years, due to the reduction in the number of hours of operation, actually represents more than a 30% increase in total energy radiated by the beam during the year compared to previous years.

The winter shutdown of the VUV Ring was required to replace two of the ring eight dipole vacuum chambers of the with new chambers having larger aperture beam ports for the two new infrared beamline U10IR and U12IR. These beamlines will more than double the IR research potential of the VUV Ring and help alleviate the long list of users waiting for access to the present IR beamlines. The U12IR beam port is a new beam port similar in design to the world leader beamline at U4IR. This port increases the VUV ring beam ports from 17 to 18, a 12% increase over the originally planned 16 beam ports. This beam port extracts beam with a 45 degrees mirror at the exit from the dipole vacuum chamber, allowing a solid angle of 90(H) X 90(V) mradians to be extracted for the diffraction limited IR beamline. The U10IR beam port replaces the previous small solid angle beam port U10, which provided beam to

U10A and U10B beamlines. The new beam port provides the largest vertical aperture possible in the standard dipole chamber, yielding a solid angle of 100(H)X 48(V) mradians. These two beamlines will use the floor space previously occupied by the U10 beamlines and therefore will not require an elevated platform, with the intrinsic vibration issue faced by the U4IR platform.

The process of replacing these two dipole vacuum chambers required taking two of the spare chambers, machining and welding the new beam ports onto them while maintaining the exacting dimension for the other two unchanged beamlines (U9, U11 and U12) that share the same chambers. Once the new chambers were leak checked and ready for installation, the magnets and shielding had to be disassembled and the old chambers cut-out of the ring. The new chambers were then welded to the ring in situ and then leak checked. The magnets and shielding were re-installed and the alignment checked and adjusted to better than 100 microns. After baking and re-installing the old beamlines, beam was injected and conditioning of the new vacuum chambers began. The old vertical betatron tune of the ring proved to be more sensitive to the poorer vacuum in the ring. By shifting the tune above the quarter integer resonance, good injection and greater freedom from ion problems was obtained. With the higher injection rate available from the booster, conditioning was faster than previous conditioning periods and the distributed ion pumps showed their ion currents leveling off after about 50 Amp-hours, as expected. However, the new ion gauges and the lifetime both showed that it took at least 150 Amp-hours for the vacuum desorption and lifetime to approach within 10% of the old values. The booster performance allowed this to be accomplished more than 3 days ahead of schedule. Prior to that integrated current level U10, U9 and U13U beamlines were able to take beam and verify that the photon beam was off from its pre-shutdown vertical position by less than 50 microns. This upgrade process will be repeated again during the winter 96/97 shutdown, when U2IR is planned to get a new larger aperture beam port, similar to the U10IR port. Although only one dipole chamber will be replaced at that time, the new chamber will go in just ahead of a ceramic vacuum chamber that just started to leak in September 1996. Replacement of the ceramic chamber was added to the task of replacing the dipole chamber without requiring a great deal of additional effort.

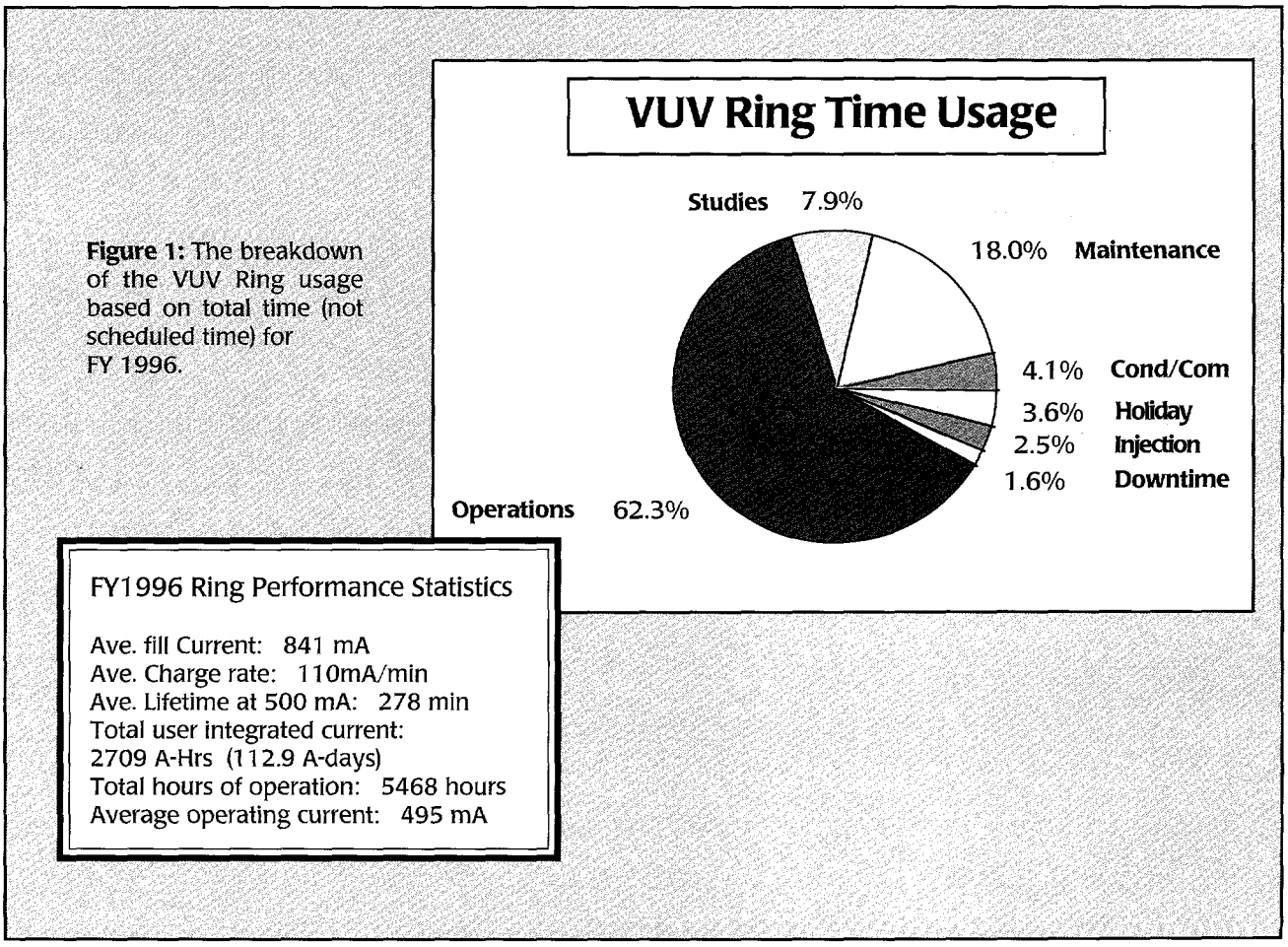


Figure 1: The breakdown of the VUV Ring usage based on total time (not scheduled time) for FY 1996.

VUV Ring Performance

FY 1996

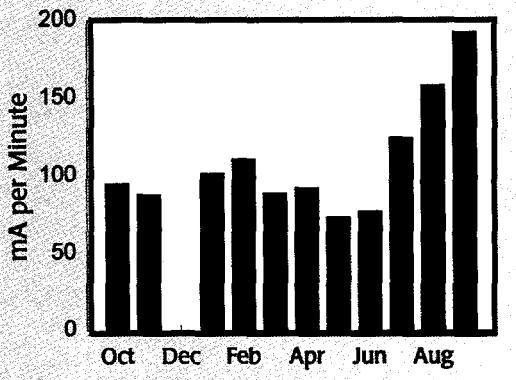


Figure 2: The VUV Ring injection charge rate average over all fills in each month.

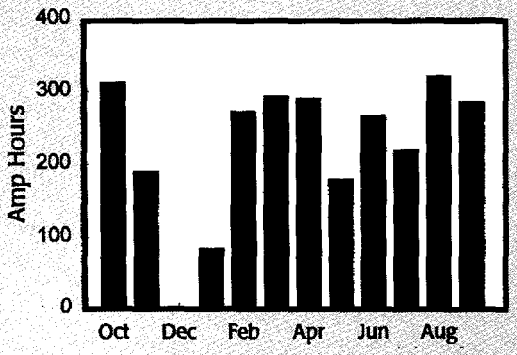


Figure 3: The total integrated current for the VUV Ring accumulated each month.

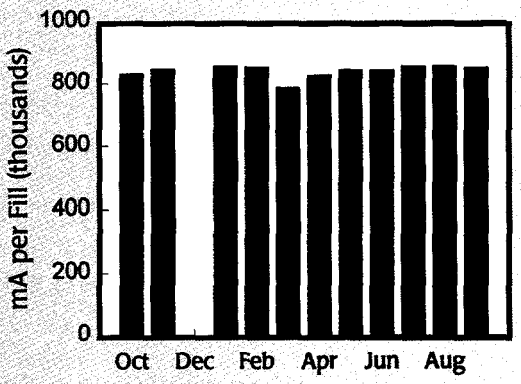


Figure 4: The injection current averaged over all fills in a month for the VUV Ring.

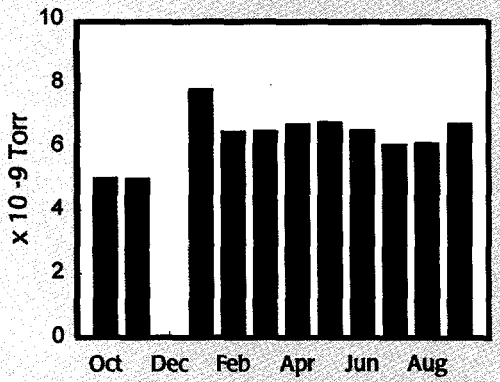


Figure 5: The VUV ring vacuum pressure at 500 mA beam Current averaged over each month.

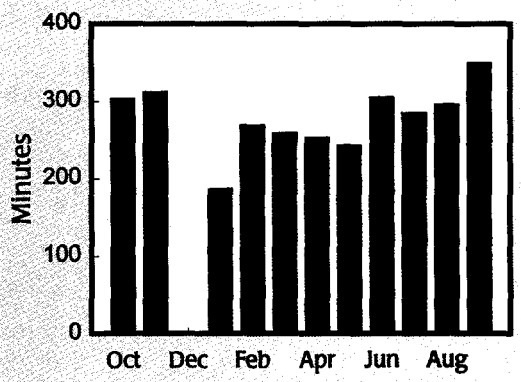


Figure 6: The VUV Ring exponential beam lifetime at 500 mA beam current (seven bunch operation only) average over each month.

Another improvement in the VUV Ring this year was the installation of a new coupling loop in the first harmonic RF cavity. This loop allowed the RF amplifier to be optimized in its coupling to the RF cavity at the higher currents. This increases the RF power efficiency of the system and will allow future improvements in reducing the affects of higher order modes in the cavity. After some initial tuning difficulties were overcome, this system was working as expected, although additional studies will be required to more fully utilize this new capability.

Additional improvements were made in the booster system, which had an increase in its repetition rate from 0.8 Hz to 1.0 Hz for operations and was tested up to 1.2 Hz for studies. The average injection rate into the VUV Ring has shown almost a factor of two increase during this year (**Figure 2**), with injection time to fill the VUV Ring taking only about 3 minutes instead of 5 to 6 minutes. The faster injection rate will allow the operators to gradually work on improving the injection efficiency, since changes in the rate will appear more instantaneous as parameters are tuned, allowing a smoother search for the parameters which yield greater efficiency of injection. Along these same lines new diagnostics to measure the beam motion and current loss after injection were installed and testing started in FY 1996. These improved diagnostics already have allowed greater understanding of the beam motion and loss during injection. Improved radiation monitoring and shielding have been planned during this past year for installation in FY 1997. When these improvements have been successful in reducing the radiation on the VUV floor and the second floor offices, then additional studies on the testing of the Top-Off method of injection will continue, with a goal of demonstrating the improved orbit stability possible with that method.

VUV Storage Ring Parameters as of November 1996

Normal Operating Energy	0.808 GeV
Peak Operating Current (multibunch ops.)	0.85 amp (0.9×10^{12} e$^-$)
Circumference	51.0 meters
Number of Beam Ports on Dipoles	8
Number of Insertion Devices	2
Maximum Length of Insertion Devices	~ 2.25 meters
$\lambda_c(E_c)$	19.9 Å (622 eV)
B(ρ)	1.41 Tesla (1.91 meters)
Electron Orbital Period	170.2 nanoseconds
Damping Times	$\tau_x = \tau_y = 13$ msec; $\tau_\varepsilon = 7$ msec
Lifetime @ 200 mA with 52 MHz	360 min
(with 211 MHz Bunch Lengthening)	(590 min)
Lattice Structure (Chasman-Green)	Separated Function, Quad, Doublets
Number of Superperiods	4
Magnet Complement	8 Bending (1.5 meters each) 24 Quadrupole (0.3 meters each) 12 Sextupole (0.2 meters each)
Nominal Tunes (ν_x, ν_y)	3.14, 1.26
Momentum Compaction	0.0235
RF Frequency	52.886 MHz
Radiated Power	20.4 kW/amp of Beam
RF Peak Voltage with 52 MHz (with 211 MHz)	80 kV (20 kV)
Design RF Power with 52 MHz (with 211 MHz)	50 kW (10 kW)
Synchrotron Tune (ν_s)	0.0018
Natural Energy Spread (σ_e/E)	5.0×10^{-4} , $I_b < 20$ mA
Bunch Length (2σ)	9.7 cm ($I_b < 20$ mA)
($2I_{rms}$ with 211 MHz Bunch Lengthening)	(36 cm)
Number of RF Buckets	9
Typical Bunch Mode	7
Horizontal Damped Emittance (ε_x)	1.62×10^{-7} meter-radian
Vertical Damped Emittance (ε_y)	$\geq 3.5 \times 10^{-10}$ meter-radian (2.8×10^{-9} in normal ops.) *
Power per Horizontal milliradian (1A)	3.2 Watts

Arc Source Parameters

Betatron Function (β_x,β_y)	1.18 to 2.25 m, 10.26 to 14.21 m
Dispersion Function (η_x, $\eta_{x'}$)	0.500 to 0.062 m, 0.743 to 0.093 m
$\alpha_{x,y} = -\beta'_{x,y}/2$	-0.046 to 1.087, 3.18 to -0.96
$\gamma_{x,y} = (1 + \alpha_{x,y})/\beta_{x,y}$	0.738 to 0.970 m^{-1}, 1.083 to 0.135 m^{-1}
Source Size (σ_x, σ_y)	536 to 568 μm, >60 to >70 μm (170-200 μm in normal ops.) *
Source Divergence ($\sigma_{x'}$,$\sigma_{y'}$)	686 to 373 μrad, 19.5 to 6.9 μrad (55-20 μrad in normal ops.) *

Insertion Device Parameters

Betatron Function (β_x, β_y)	11.1 m, 5.84 m
Source Size (σ_x, σ_y)	1240 μm, >45 μm (130 μm in normal ops.) *
Source Divergence ($\sigma_{x'}$, $\sigma_{y'}$)	112 μrad, >7.7 μrad (22 μrad in normal ops.) *

* ε_y is adjustable

BEAMLINE TECHNICAL IMPROVEMENTS

Roger Klaffky
Beamline Technical Liaison

VUV BEAMLINES

There were a number of technical beamline improvements on the VUV Ring during FY 1996. Beamline U3A was in a re-commissioning phase during FY 1996 after extensive changes during FY 1995. New interlocks were installed and the monochromator was interfaced to the beamline control computer. In the next few years there will be a major upgrade of the U4A beamline from a toroidal grating monochromator to a spherical grating monochromator (SGM) design. An upgrade of the angle-resolved photoemission (ARP) chamber has begun with the installation of a cluster of metal evaporators and a thin film thickness monitor. A sample transfer and load lock system will be installed in the future. A new data acquisition computer for the ARP system has been acquired and Labview based software is being upgraded. At U4B a new high photon energy resolution SGM-based beamline was installed with most of its components coming from the U13UA beamline. A magnetic circular dichroism end station was constructed, installed and commissioned.

Construction of the new U5UA SGM-based beamline took place and commissioning of this line was underway. A resolving power of about 10,000 was demonstrated at 30 eV photon energy. After commissioning is completed, the U5UA spin-resolved valence band photoemission program will resume with a 50 % General User allocation.

There was extensive progress at the new U7A soft x-ray photoemission and absorption spectroscopy beamline. The SGM monochromator entrance slit was rebuilt; and installation of the downstream refocusing mirror and the surface chemistry end station with its lifting platform and kinematic mounting plate took place. The upstream refocusing mirror chamber and end station holder were delivered. The initial commissioning and debugging of the surface chemistry station began with preliminary unfocused beam experiments being performed.

The U9B fluorescence detection system development was completed with the addition of a polarizer to the emission optics and the modification of detection electronics to determine photon polarization as well as wavelength and time of arrival.

At the U13UB extreme ultraviolet lithography (EUVL) beamline, the Offner 1:1 Ring Field camera was assembled and commissioned. It was used to image programmed mask defects down to 75 nm. The 10X Schwarzschild EUV camera installation was also underway in FY 1996.

Two modified ring vacuum chambers were installed during the Spring 1996 shutdown. The chambers incorporate a large 100 horizontal by 50 vertical milliradian port for IR microscopes at U10, and a 90 milliradian by 90 milliradian port at U12. Construction and commissioning of IR beamlines at these ports will be underway in FY 1997.

X-RAY BEAMLINES

At X1A new high resolution zone plates were tested and put into operation. Commissioning of a cryogenic scanning transmission microscope and holography instrument began. This equipment is designed to study radiation sensitive biological specimens near liquid nitrogen temperature where the morphology is "frozen in". At the end of FY 1996, the beamline was shutdown for a major upgrade to achieve higher spectral resolution and independent wavelength control.

The X1B monochromator performance was enhanced after the installation of a new holographically recorded laminar grating in May. Above 500 eV the photon flux increased by a factor of 5 to 10. As a result, high resolution measurements are now possible using first order of the grating over the first harmonic range of the X1 undulator (200 to 800 eV).

The X2B microtomography data acquisition speed and spatial dynamic range were increased with the upgrade of the detector from a 512x512 200 kHz CCD to a 1024x1024 800 kHz CCD.

At X5 equipment development continued in preparation for double-polarization measurements with circularly polarized gamma-rays and longitudinally-polarized nucleon targets. This equipment included: (i) a new

frozen-spin hydrogen-deuteride target that provides high polarization for both nuclear species, (ii) a new large acceptance detector array for measuring total reaction cross sections in both neutral and charged-particle channels, and (iii) circularly-polarized gamma-rays extending up to 400 MeV (with 2.584 GeV electrons) and 470 MeV (with 2.80 GeV electrons) using a new ring-laser system.

The X9A beamline resumed operation as a white beamline. Design work was underway to upgrade X9A with the installation of a sagittal focusing monochromator and mirror for MAD crystallography. A new computer system running the NSLS-DAC software was installed on X9B for x-ray absorption spectroscopy. An X9B upgrade planned for 1997 is the installation and testing of larger crystals that can accept over 200 mm of beam (12 horizontal mrad) to increase the flux up to 3 fold.

The X10A hutch was extended to allow higher resolution and a 2D detector was implemented. A major upgrade of the X11A computer system was achieved with the installation of two Macintosh 7500 computers, one for data acquisition using the NSLS-DAC software, and the other for data analysis.

At X12B a robotic fluid sample changer was implemented which allows for the automatic injection of small (100 microliter) liquid samples into a fixed observation cell and for subsequent recovery. An in-vacuum attenuator/shutter mechanism was installed. The flight paths and theta-arm detector mount points were in the process of being rebuilt to accommodate a Mar scan head. Finally, portable visualization and data reduction software for 2D diffraction images was developed.

The X13B beamline was modified to allow experiments to be conducted inside a hutch. A new spherical grating monochromator for X13A was designed and ordered for circular dichroism measurements using the elliptically-polarized wiggler (EPW). The EPW began 100 Hz operation during Summer 1996.

White beam was brought into the X16C hutch and a pair of Kirkpatrick-Baez mirrors were used to produce a 4 micron by 25 micron white or monochromatic focal spot size.

At X19A a solid state multi element detector, developed in collaboration with the BNL Instrumentation Division, was put into operation. The detector has 250 -350 eV resolution and is used for spectroscopy and scattering applications. Also, plans we made to replace the X19A zerodur mirror which was discovered to be damaged by synchrotron radiation.

At the X19C beamline, new motor control electronics were installed. There were a number of changes and upgrades in the x-ray topography hardware. A high precision scanning stage was installed, enabling imaging of six inch diameter wafers. A high resolution digital camera was purchased to enhance image processing capability. Projects that were in progress included the addition of an analyzer crystal axis to the goniometer detector arm. The analyzer will allow analysis of the diffracted beam harmonic content. Also, the attachment of a CCD camera to the goniometer was underway. There were also upgrades in the surface scattering spectrometer. A very high precision, short travel sample stage was installed and the long travel stage was upgraded with an optical encoder. New motorized Huber slits were installed and motorized fixed small gap slits were designed and tested.

The X21 phase II beamline was commissioned during FY 1996. The monochromator is tunable from 5 keV to 10 keV with 0.2 eV energy resolution. On the X22A beamline a vertically-focusing mirror was added which simplifies many experiments by eliminating harmonic contamination. The X22B computer was upgraded. A gear reducer was added to the spectrometer table allowing vertical motion without the loss of steps. Also, a new elevator was added to the spectrometer, enhancing mercury and Langmuir trough measurements. The X23B collimating mirror was replaced providing an improved energy resolution of less than 2.6 eV at 6 keV. The monochromator bearings were replaced and the crystal re-etched, and an additional degree of freedom was provided for crystal alignment.

The X24A beamline was upgraded with the installation of a new first mirror, increasing the flux by a factor of two. At X27A a new control system using Labview with a graphical user interface was under development. A hydraulic powered vertical scan stage was installed to give better control of the exposure rate for micromachining experiments.

Just prior to the December 1995 shutdown, a test was performed which entailed firing the X24 front end fast valve with a 10 mm thick molybdenum blade when there was 408 mA of stored beam current. The exposure time was 1.93 seconds, to simulate the heating that would occur at 500 mA beam current for a 1 second exposure, which is the time it takes for the front end mask to close after a fast valve is fired. The blade successfully withstood the exposure to the x-ray beam, indicating that it will not be necessary to dump the X-Ray Ring when a fast valve fires after the stainless steel blades are replaced with molybdenum blades. During FY 1996 molybdenum blades were installed on the X9, X19 and X24 front ends. More blade replacements will occur during future shutdowns. There has been a major effort to design and build new fast valve sensor boxes and interface boxes. The new sensor boxes have been tested and calibrated. They have CMOS electronics to provide improved noise rejection

and they have troubleshooting indicators. The new interface boxes have a capacity of 3 sensors per beamline and provide for individual lock-out of each sensor. The system will be interfaced to the NSLS computer system for display on the present X-Ray Beam Line Status Channel.



X-RAY RING

Roger Klaffky
X-Ray Ring Manager

The X-Ray Ring usage for FY 1996 is broken down by categories in **Figure 1**. There was a 7% increase in operations largely resulting from a 25% decrease in downtime and a 9% decrease in the time allocated to maintenance, studies, and conditioning. There were a total of 1081 Ampere-hours of operations. The monthly integrated Amp-hrs are shown in **Figure 2**.

The X-Ray Ring active interlock system certification for all insertion device straight sections was completed in Fall 1995 when the calibration and linearity of the last straight section system (X13) was verified up to 350 mA during 25 bunch operation. The active interlock pre-fill test was modified to test the 6 different active interlock chains simultaneously so that only one injection is required for the test. This reduced the testing time from 15 minutes to 2 or 3 minutes. The number of pre-fill test failures was reduced by accounting for the non-linear response of the orbit to the trim strengths.

To enable operation of the orbit measuring pick-up electrodes (PUEs) from 7 mA (for active interlock pre-fill tests) to 434 mA, the AGC dynamic range was extended from 35 dB to 55 dB for all the PUEs. In addition, band pass filters were installed before every PUE switch to prevent saturation of the PUE receivers in single bunch operation. The resolution of the PUEs was increased from 14 to 16 bits, improving the orbit position resolution from 2 microns to 0.5 microns.

During the December 1995 shutdown, a change in the RF2 damping antennae configuration successfully removed the horizontal and vertical beam size changes that had occurred at specific XRF2 tuner positions (i.e. higher order modes) during a fill. Changes in several load resistors on the XRF3 anntennae resulted in a several-fold decrease in the beam size changes occurring at the resonance position.

After studies demonstrated that the effects on the horizontal and vertical orbit of running the Elliptically Polarized Wiggler (EPW) at 100 Hz were compensated, 100 Hz operation commenced in Summer 1996. At 100 Hz, there is a significant improvement in the signal-to-

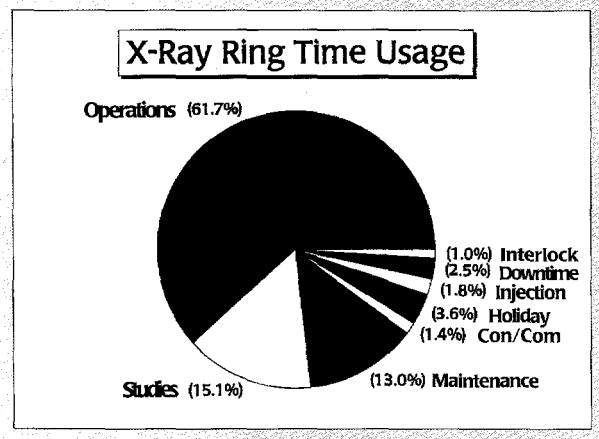


Figure 1: The Breakdown of the X-Ray Ring usage based on total time (not scheduled time) for FY 1996.

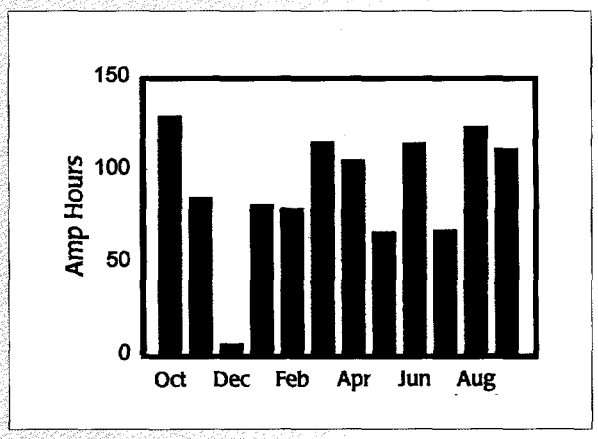


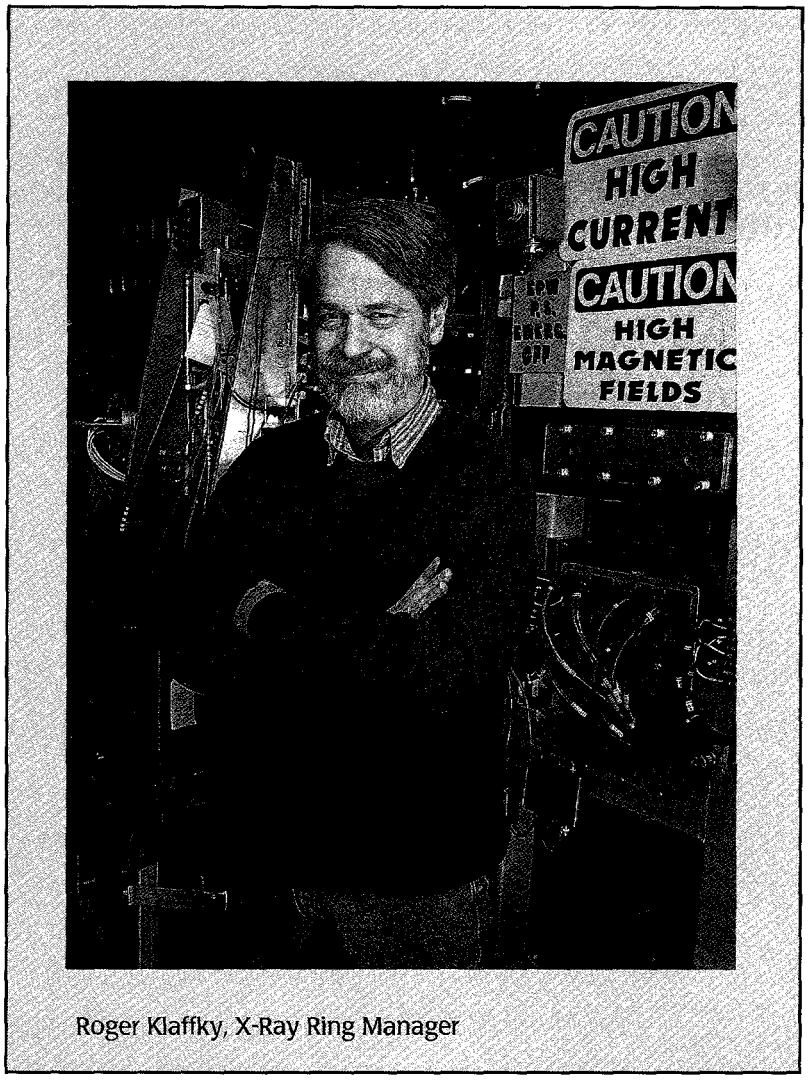
Figure 2: The total integrated current for the X-Ray Ring accumulated each month for FY 1996.

noise ratio for magnetic circular dichroism experiments. Studies on a lattice with a factor of 2 reduction in horizontal emittance continued to progress during FY 1996. During the midnight studies shifts there were several successful trial runs of the digital orbit feedback system in either the horizontal or vertical planes, and also in both planes simultaneously. This sytem is close to an operational state in the vertical plane. In the horizontal plane, studies have shown that even though the digital feedback system does a better job of keeping the orbit fixed at the PUEs, the horizontal ring chamber motion over each 12 hour fill may cause the orbit to show greater horizontal motion with the digital feedback system. This is not a problem in the vertical plane since the chambers show little motion vertically. Sensor stands were fabricated for installation during the December 1996 shutdown. The chamber motion will be mapped out around the ring as a function of ring current. This information will be used to remove the horizontal orbit changes caused by the PUEs moving with the chamber.

There were also studies to demonstrate the feasibility of running the X-Ray Ring at 2.8 GeV and to determine the impact of 2.8 GeV on experimental beamlines. In Spring 1996 a ramp from 744 MeV injection energy to 2.8 GeV was established and skew quadrupoles were adjusted to maintain the small vertical beam size present during 2.584 GeV operation. In August it was demonstrated that 250 mA of beam could be reliably ramped to 2.8 GeV, as had been previously predicted from RF power considerations. In the future, studies will be conducted to determine if the dual hybrid RF power amplifier installation on RF System 2 in December will increase the 250 mA operational limit. The maximum allowable current at 2.8 GeV is 320 mA, as determined by ring vacuum chamber heating limits. Careful beamline measurements were performed on the X19A beamline at 100 mA beam current at both 2.584 GeV and 2.80 GeV. The ratio of the third harmonic to fundamental was determined from rocking curves of the X19A second Si(111) monochromator crystal. The factor by which this ratio increases at 2.8 GeV was in good agreement with calculated flux ratios at the two energies. A 2.8 GeV Users Executive Subcommittee will conduct a survey of users in the future as to the desirability of 2.8 GeV operation.

Beam "drop-out" studies indicated the possibility of producing substantial levels of high energy gamma ray bremsstrahlung radiation in the straight sections during single and five bunch operation. In these few bunch operational modes, the high peak currents heat the injection septum and other straight section ring components causing elevated gas pressures and increased bremsstrahlung radiation. The gamma rays can scatter off beamline optical components producing detectable radiation levels near these components. Radiation monitors were installed on the straight section beamlines to alert users to the presence of radiation.

In addition, levels from these monitors are displayed in the Control Room and are logged on the NSLS computer history program. Operators have been instructed to close shutters if the beam lifetime is reduced to a few hours.



Roger Klaffky, X-Ray Ring Manager

In preparation for the December 1996 shutdown, water lines have been installed that will bring BNL Central Chilled Water Facility (CCWF) water to the NSLS experimental water system in Mechanical Equipment Room A. The control valve/controller installation for this system in underway with completion expected before December. This system will significantly improve temperature regulation with the present NSLS system providing redundancy in case the CCWF goes down for maintenance. Since tuning of the new control system requires operational beamlines, there will be variations in the experimental water temperature when operations first resume in January 1997.

Since the present Biology cold rooms are cooled by the CCWF water, there is a problem on maintaining biological samples if there is a CCWF failure since there is no automatic backup cooling. Over the past year, there have been several instances where samples were lost when the CCWF went down. To address this problem, procedures were established so that Operations Coordinators can valve off the CCWF water when it is down and open valves to provide domestic water for cooling of the cold room compressors. In the future this changeover will be automated.

A major effort during the December shutdown will be the installation of new beryllium windows to enable 350 mA operation in January 1997. The design of the windows was completed and orders placed for delivery in November 1996.

Brazing and welding of the windows will be done by Brush Wellman Electrofusion with the pieces being fabricated by BNL Central Shops. The NSLS will pay for these windows and for any adaptor flanges required to fit the windows to the X-Ray beamlines. A second wave of windows will be installed in 1997 to permit operation up to 438 mA.

All parts were ordered for the dual hybrid RF power amplifier slated for installation on RF System 2 in the December 1996 shutdown. Two 120 kW amplifiers will be combined in this system to enable 438 mA operation and to prevent a beam dump if one of the other three RF systems drops out.

There has been an ongoing effort to replace existing stainless steel frontend fast valve blades with molybdenum blades which can be fired without dumping the X-Ray Ring. There has been a parallel effort to redesign the fast valve electronics. New circuitry will be installed during the December shutdown at beamlines where fast valves are presently operational. Additional fast valves will be hooked up in the future.

Finally, in February 1996 a new X-Ray Ring fill policy was established with scheduled fills at 0700 and 1900 hours.

X-Ray Storage Ring Parameters as of November 1996

Normal Operating Energy	2.584 GeV
Maximum Operating Current	0.30 amp (10^{12} e$^-$)
Lifetime	~20 hours
Circumference	170.1 meters
Number of Beam Ports on Dipoles	30
Number of Insertion Devices	5
Maximum Length of Insertion Devices	< 4.50 meters
$\lambda_c(E_c)$ at 1.25 T (B)	2.23 Å (5.6 keV)
$\lambda_c(E_c)$ at 5.0 T (W)	0.56 Å (22.2 keV)
B(ρ)	1.25 Tesla (6.875 meters)
Electron Orbital Period	567.2 nanoseconds
Damping Times (2.584 GeV)	$\tau_x = \tau_y = 6$ msec; $\tau_\varepsilon = 3$ msec
Touschek (2.584 GeV, 0.25A)	≥27 hrs ($v_{RF} = 700$ kV)
Lattice Structure (Chasman-Green)	Separated Function, Quad Triplets
Number of Superperiods	8
Magnet Complement	16 Bending (2.7 meters each) 40 Quadrupole (0.45 meters each) 16 Quadrupole (0.80 meters each)
32 Sextupole	(0.20 meters each)
Nominal Tunes (ν_x, ν_y)	9.15, 6.20
Momentum Compaction	0.0056
R.F. Frequency	52.88 MHz
Radiated Power for Bending Magnets	144 kW/0.25 amp of Beam
R.F. Peak Voltage	1000 kV
Design R.F. Power	400 kW
ν_s (Synchrotron tune)	0.002
Natural Energy Spread (σ_e/E)	8.6×10^{-4}
Natural Bunch Length (2σ)	10.5 cm
Number of RF Buckets	30
Typical Bunch Mode	25
Horizontal Damped Emittance (ε_x)	1.0×10^{-7} meter-radian
Vertical Damped Emittance (ε_y)	1×10^{-10} meter-radian
Power per Horizontal milliradian (0.25A)	23 watts

Arc Source Parameters

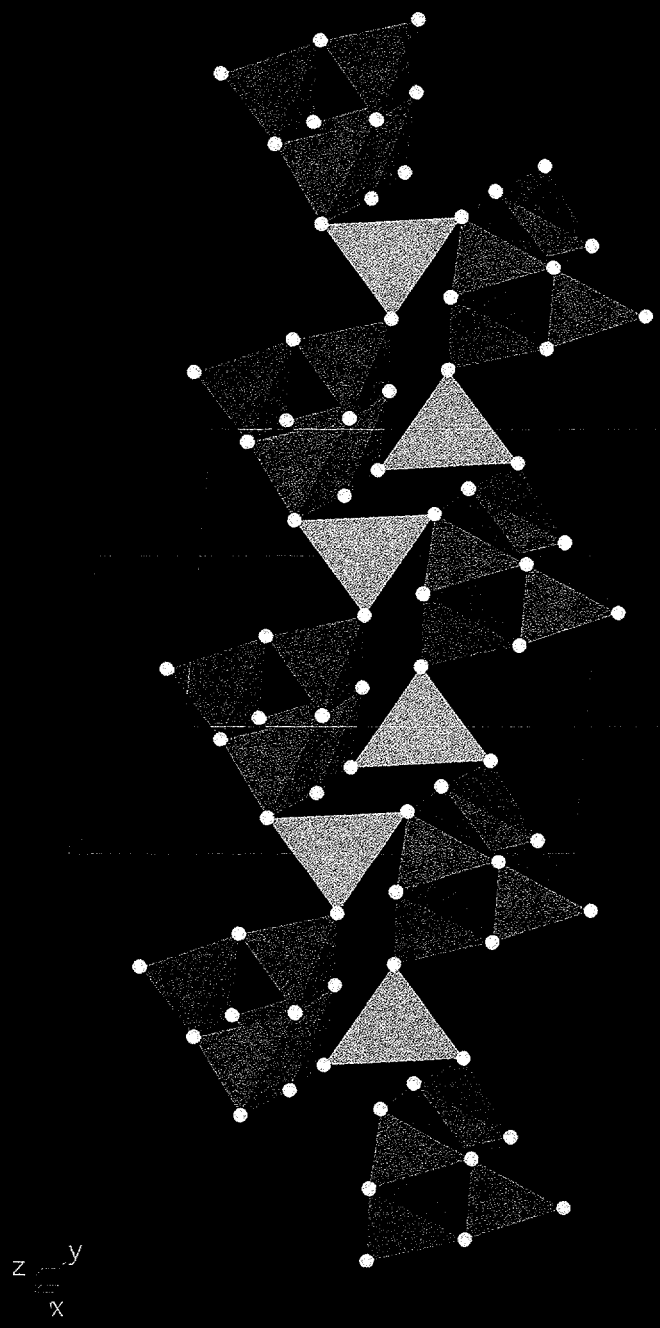
Betatron function (β_x,β_y)	1.0 to 3.8 m, 7.9 to 26.5 m
Dispersion function (η_x,$\eta_{x'}$)	0.47 to -0.11, -0.39 to 0.22
$\alpha_{x,y} = -\beta'_{x,y}/2$	-0.49 to 1.62, -3.4 to 4.5
$\gamma_{x,y} = (1 + \alpha_{x,y}^2)/\beta_{x,y}$	0.952 to 0.962 m^{-1}, 0.81 to 0.52 m^{-1}
Source size (σ_x,σ_y)	371 to 565 μm, 27 to 49 μm
Source divergence ($\sigma_{x'}$,$\sigma_{y'}$)	439 to 324 μrad, 8 to 7 μrad

Insertion Device Parameters

Betatron function (β_x,β_y)	1.60 m, 0.35 m
Source divergence ($\sigma_{x'}$,$\sigma_{y'}$)	260 μrad, 35 μrad

Beamline X3B1: Polyhedral representation of the structure of a novel framework comprised of $[Ge_4S_{10}]^{4-}$ adamantine-clusters (red) linked by trigonal AgS_3-units (blue). The material was synthesized hydrothermally and its structure determined utilizing data collected on a 36 pL single crystal using an x-ray synchrotron/imaging plate combination at the X3A1 beamline. Each cluster consists of 4-corner linked germanium-centered sulfide tetrahedra.
J.B. Parise and K. Tan, "Synthesis and structural characterization using synchrotron radiation of $[(C_6H_{13}N_2)_2(H_3O)(H_2O)][AgGe_4S_{10}]$ (Dabco-AgGS-SB2): knitting sulfide metal clusters to form frameworks, *J.Chem. Soc.*, Chem. Comm., 1687 (1996).

FIVE
PROJECTS



THE NSLS SOURCE DEVELOPMENT LABORATORY: A WORK IN PROGRESS

Erik D. Johnson
SDL Project Manager

The objective of the Source Development Laboratory (SDL) is to facilitate the coordinated development of sources and experiments to produce and utilize coherent sub-picosecond synchrotron radiation. It is part of the fabric of accelerator technology development at Brookhaven, and of amplifier based free electron laser (FEL) development internationally. The NSLS provides much of the intellectual drive for this community, as well as support for the SDL experiments. Fundamental theoretical and experimental contributions have been made to the field by NSLS physicists. Without this groundwork, stretching back over more than a decade, the SDL program, and indeed those of other laboratories, would not exist as we now know them. Of particular note are the development of high current - high brightness electron beam technologies at the Accelerator Test Facility, and the theoretical framework for high gain FELs and subharmonically seeded single-pass FELs. These are the BNL "home-grown" cornerstones of the ultra-violet FEL experiments to be undertaken at the SDL.

For the NSLS, the SDL represents a new opportunity for its user community. The ultra-violet FEL (UV-FEL) will operate to wavelengths below 100 nm, and will produce radiation with substantially shorter pulses than are available from the VUV Ring (as brief as *5 fs*!) with peak power ranging from hundreds of Megawatts to as high as 100 Gigawatts for the shortest pulses. The bandwidth of the FEL can to some extent be controlled within the constraints of the Fourier transform limited nature of the source (trading pulse length for bandwidth). In terms of peak power, this source will open territory completely uncharted by existing tunable sources. From the standpoint of average power however, the picture is not nearly as exciting. The repetition rate available from the SDL linac will be at most 10 Hz, so for many experiments, the SDL will be a site for "proof-of-principle" studies. None the less, it will provide a new tool for the study of nonlinear and ultrafast phenomena. Furthermore, once the principles have been demonstrated, the selection of a different linac or linac technology could increase the repetition rate to kiloHertz or higher. One might then reasonably ask why not incorporate these capabilities from the outset? The answer lies in the costs, the budgets, and the obligations of the NSLS. No one reading this annual report will be amazed by the statement that budgets have been

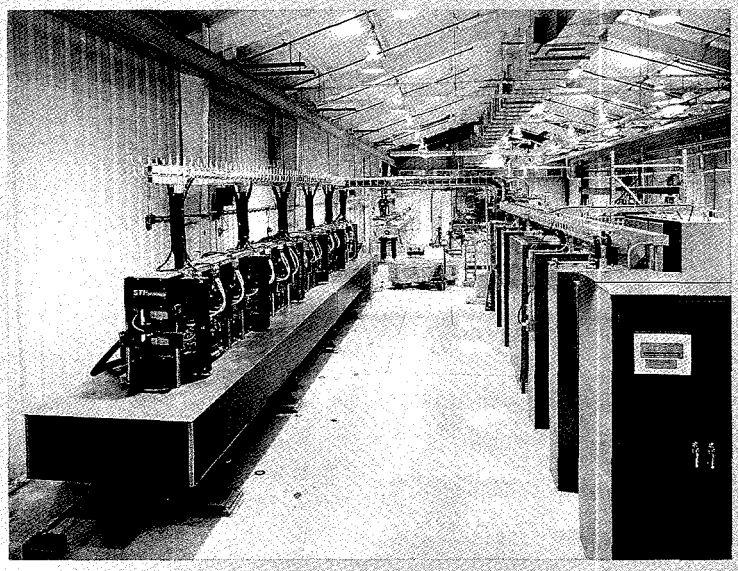


Figure 1: Photograph of the SDL assembly in progress, November 1996.

extremely tight in recent years, which makes long range planning and investment especially difficult. Nor would the statement that NSLS takes its obligations to its user community very seriously meet with any surprise. The NSLS management and staff continue their commitment to attain the highest possible reliability and availability of the storage rings, while pushing their performance to the greatest extent possible. However, they also recognize their responsibility to explore new source technologies, and have embarked on a program of source development which to the greatest extent possible utilizes existing hardware.

These factors account for the 10 Hz repetition rate limit for the facility, since that was the design point for the 230 MeV linac built as an injector for the SXLS project. So while significant modifications to the linac are required to make it a suitable driver for an amplifier FEL, it provides a huge head start on the SDL accelerator. Similarly, the main undulator for the FEL experiment is recovered from an Army program for a high average power FEL, which is another major element of the facility. The electrical work for control of the 10 meter long NISUS undulator was completed this year in collaboration with STI Optronics, although the required vacuum modifications are being deferred until the completion of the linac installation. An NSLS/ATF designed photocathode gun is being built for the SDL in collaboration with SLAC and UCLA, and a magnetic pulse compressor will be installed to achieve the high brightness-high peak current electron beam required for short wavelength FEL amplifier operation. New diagnostics and controls are also in the process of being implemented on the linac. Building 729 even required some expansion to house the SDL accelerator, which was completed last year. Further modifications to the building, including the chilled water system and the installation of an overhead crane, were completed this year. Early in 1997 the machine water system and a class 1000 cleanroom to house the laser will be installed, completing the "infrastructure" modifications required for the SDL. The focus of activity in the coming year will be the installation and commissioning of the linac. Experiments in non-linear emittance correction and pulse compression are planned, as well as studies to examine various aspects of emittance degradation, which could have a significant impact on the range of FEL operations which are possible. Assembly of the machine to undertake actual FEL experiments will follow as soon as possible. The actual time table for the SDL is very sensitive to the available resources. The same can be said of many other "fourth generation" source projects hence, where reasonably possible, some aspects of the project are being pursued in collaboration with institutions who have programs with technological requirements similar to those of the SDL. In addition, the BNL management continues to support the effort through significant LDRD contributions, although the availability of NSLS staff and other department resources plays a major role in setting the pace of the project. So, while maintaining its high standard for supporting the operation and utilization of the existing storage rings remains the first priority for the department, the NSLS remains committed to moving forward with the SDL, making it very much, a work in progress . .

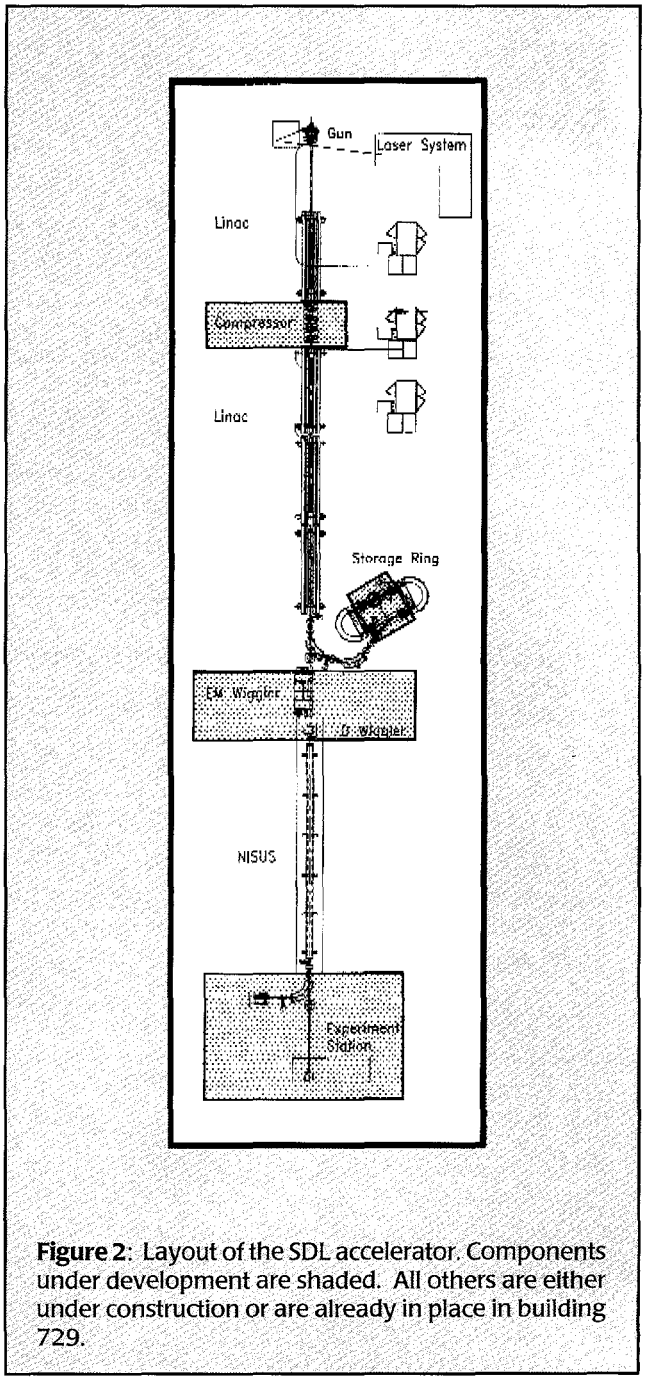


Figure 2: Layout of the SDL accelerator. Components under development are shaded. All others are either under construction or are already in place in building 729.

THE ACCELERATOR TEST FACILITY

Ilan Ben-Zvi
ATF Head

THE ATF - A USERS' FACILITY WITHIN A USERS' FACILITY

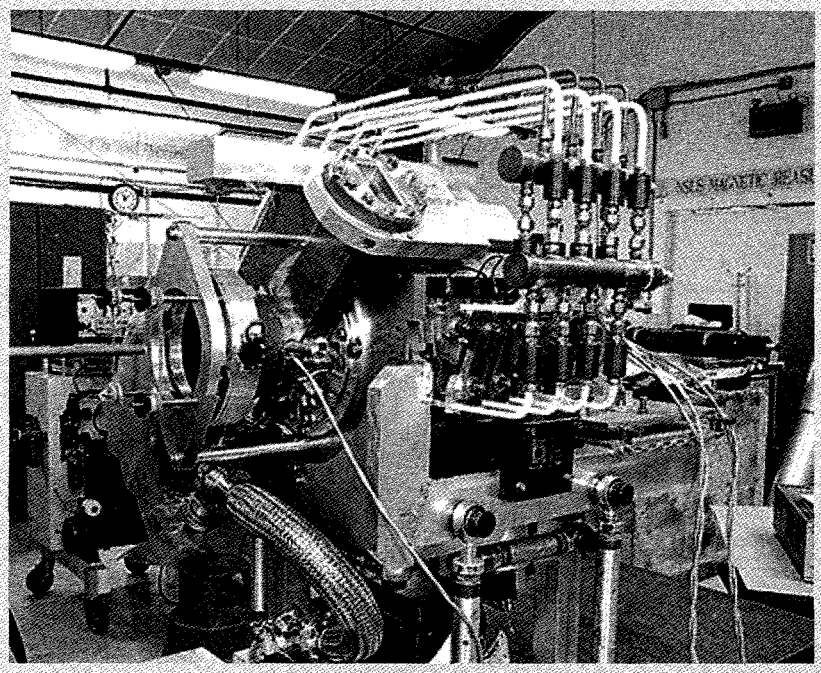
The Accelerator Test Facility (ATF) is a User's Facility for accelerator and beam physicists, operated by the NSLS and the BNL Center for Accelerator Physics. There is no other proposal-driven, peer-reviewed facility like the ATF that is dedicated for long range R&D in accelerator and beam physics. In addition to its singular role the ATF has also a unique combination of a high-brightness electron beam, synchronized, high power lasers and a well equipped, 3 beamline experiment hall. The high brightness electron beam of the ATF, produced by a laser-photocathode RF gun, make it an ideal site for R&D on Free-Electron Lasers (FEL). The ATF receives funding from the DOE and the laboratory directorate as well as important support from the NSLS. The NSLS has an active program in R&D in the production of short-wavelength coherent radiation through its involvement in the ATF. Taking advantage of the expertise and hardware that accumulated at the ATF, the NSLS is pursuing a program that touches the most fundamental issues of short wavelength FEL R&D today, such as the development of electron sources, single pass FEL experiments and more.

TOWARDS A BRIGHTER SOURCE

Electron beams with a high density of electrons in 6-D phase space are the keystone for future high performance machines such as X-ray Free-Electron Lasers and linear colliders, as well as the generation of intense sub-picosecond x-ray pulses through the process of Compton back-scattering of laser pulses off the electron beam. The length of both accelerator and wiggler of any short-wavelength FEL will decrease sharply with improved beam brightness. In a remarkable case of parallel evolution, this work is also important to High Energy Physics for the construction of future linear colliders. Thus the ATF is enjoying considerable support from the DOE Office of High Energy Physics. R&D at the ATF on the generation of high brightness beams placed the NSLS in an international leadership position. The electron gun of the ATF generates its high current, low emittance beam by irradiating a high-quantum-efficiency metal-cathode in the presence of very high intensity RF electric fields. A new magnesium photocathode has demonstrated an order-of-magnitude increase in quantum efficiency with a (so far) unlimited lifetime. The ATF is leading two new collaborations for the development of RF guns, one with SLAC and UCLA, and the other with Japanese collaborators. The ATF's gun is now recognized internationally as "The BNL Gun" and versions of it are in use in many places around the world as well as in BNL's Center for Radiation Chemistry Research and soon at the Source Development Laboratory.

THE USERS OF THE ATF

Among the fourteen currently approved experiments on the ATF, there is a number of experiments dedicated for research into novel radiation generating processes, from the IR to x-rays. Among these are some FEL experiments and an experiment in the generation of Smith-Purcell radiation and Compton back-scattering. A few of them are centered about ATF beamline #3, where a microundulator oscillator experiment is nearing operation and others are conducted on beamline #2, like the High Gain Harmonic Generation FEL, or beamline #1, like the Smith-Purcell experiment and the Compton back-scattering experiment. A superconducting 68 period micro-undulator (with a period of 0.88 cm and 0.5 Tesla peak field at a gap of 0.44 cm) has been developed at the NSLS. Prototypes of this undulator (up to 23 periods long) were built and performed extremely well in superconducting tests. The field errors of the undulator were very low as constructed, making this perhaps the first undulator that will require no trimming after manufacture. The FEL experiment makes use of the short period of the undulator and the low emittance beam generated by the RF photocathode gun to operate at 500 nm with a 50 MeV electron beam. Since the ATF electron beam energy is currently at about 70 MeV, lasing at below 250 nm should be possible. The technology developed for this



The latest ATF RF gun, developed in collaboration with SSRL and UCLA.

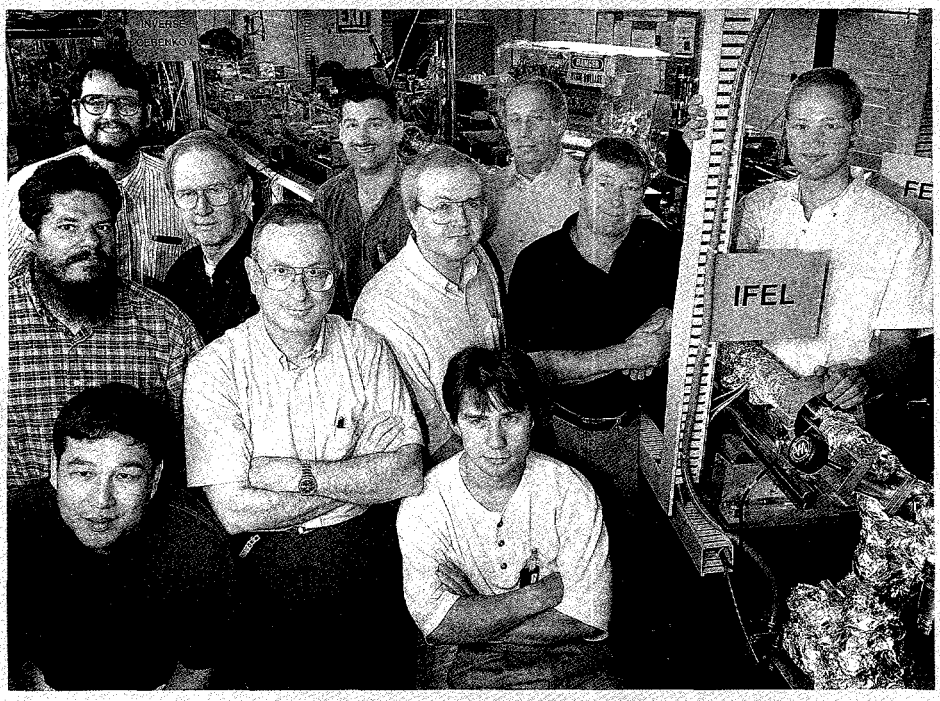
undulator will be used to develop a 4 to 5 mm period, small gap undulator prototype for the National Synchrotron Light Source X-Ray Ring.

An MIT group is carrying out a test of a pulsed microundulator. This undulator, which is currently installed on the beamline, has parameters that are very similar to those of the superferric undulator. Spontaneous emission has already been observed from this device and preparations are under way to get lasing in the near future. A third user group is from Columbia University. They will be using the oscillator experiment for studies of spiking and optical guiding in FELs.

The high-gain harmonic-generation experiment will be located on beamline #2. This experiment is carried out by a NSLS group headed by Li-Hua Yu. In the first stage of this experiment, done in collaboration with the Advanced Photon Source, a two meter long undulator (a prototype of Undulator-A built by Cornell) will be installed to study single pass FEL gain, start-up from spontaneous emission and saturation. The next step of this experiment will be done in collaboration with Northrop - Grumman, which is providing many components of the undulator for the experiment. This undulator is a derivative of the superconducting micro-undulator of the visible FEL oscillator. It uses the same principle of a continuous yoke but has parabolic pole faces for two-axis focusing and four distinct regions: a prebunching undulator, a dispersive section, an exponential growth section and a tapered section. This experiment emulates the FEL physics of the NSLS approach to VUV FELs. This approach is based on single pass, seeded FEL amplifiers driven by Ti:sapphire lasers. The final stage of harmonic generation is being done in the FEL. The principle of high-gain harmonic-generation will be tested and characterized in these experiments, as well as the superconducting undulator, the undulator diagnostics, error and alignment studies and tapering control. Another experiment at beamline #2 has recently broken the world record for Inverse FEL acceleration of electrons. This experiment, headed by Arie van Steenbergen, used the high-power CO_2 laser of the ATF and a special variable period wiggler to impart 2% acceleration to a 40 MeV beam, using about 0.5 GW of the CO_2 laser. This experiment, which is like an FEL amplifier operated in reverse, is motivated by the interest to develop a compact, high-gradient electron accelerator.

ACCELERATOR R&D AND GRADUATE EDUCATION AT THE ATF

Two significant experiments have been recently reported by the ATF staff. The first is a measurement of the slice-emittance of an electron bunch from the ATF electron gun. This newly developed technique makes it possible to study in detail the longitudinal dependence of the transverse beam-matrix of short slices with 1 picosecond resolution. The slice-emittance measurement enabled us to examine the evolution of the beam while it goes through the important emittance-compensation process. Emittance compensation is a linear correlation-removal process that has led to the improvements in photocathode RF gun beam brightness and to the recent enhanced interest in x-ray FELs. The slice-emittance measurement should allow us to do non-linear emittance corrections that promise even better x-ray FELs. The second development is the observation of micro-bunching of the ATF'S beam. Under certain conditions it is possible to obtain



NSLS Staff Assigned to the Accelerator Test Facility (ATF):
(Top, from left to right) John Skarita (Mechanical Section), Marc Montemagno (Electronics), and Igor Pogorelsky (Lasers).
(Middle, from left to right) Bob Harrington (Mechanical and Optical Systems), Joe Sheehan (Electrical Section), Robert Malone (Computer and Control), Bill Cahill (Technical Supervisor and Users' Coordinator), and Marcus Babzien (Lasers).
(Bottom, left to right) Xijie Wang (Accelerator, gun, diagnostics), Ilan Ben-Zvi (Head of ATF) , and Vitaly Yakimenko (Accelerator, gun, diagnostics).

sub-picosecond long bunches with a high charge and good emittance. This happens when the photocathode laser is adjusted to a small phase, leading to bunch compression in the drift space between the gun and the linac. One picosecond bunch length have been measured (using a variation of the slice emittance set-up). Much shorter bunches are predicted theoretically, but await a further refinement of Eric Blum's coherent radiation detector. Eric has already observed coherent radiation from the ATF's beam. An installation of a spectrometer will allow sub-picosecond bunch length measurement. The motivation for this R&D is that sub-picosecond bunch length, high brightness electron beams can generate high-intensity, sub-picosecond radiation from the far-IR to x-rays.

As a result of the bunch compression, the bunch length of the ATF can be changed easily from about 10 picoseconds to under one. If this bunch is collided with an energetic pulse from the ATF'S synchronized CO_2 laser, a pulse with the same short length of x-rays is produced. Compton back-scattering of lasers by electrons is a unique x-ray source. Preliminary estimates indicate that it should be possible to generate elliptically polarized $2x10^8$ photon pulses of 8 keV x-rays using the ATF'S future 1 TW CO_2 laser and its 70 MeV linac. A contract for the construction of parts for the ATF'S compact picosecond Terawatt laser has been signed last year.

In a significant contribution to the education of future generation of accelerator physicists, eight graduate students have finished their thesis at the ATF and six others (from Columbia, MIT, Stanford, Stony Brook UCLA and the University of New Mexico) are currently doing thesis research at this facility. More information on the ATF can be found on the World Wide Web, with a hyperlink from either the National Synchrotron Light Source or BNL Home Pages.

PROJECTS

NSLS Facility Improvements

Frank Terrano
Mike Kelly

Although there was no major construction at the NSLS during FY 1996, a number of facility related projects were accomplished and initiated.

BUILDING #725 RAMP TO INNER X-RAY RING AREA

The driveway which provides access to the inner courtyard of the x-ray ring was resurfaced and regraded. This was done to prevent puddles from occurring and eroding the concrete over the X-Ray Ring and x-ray power supply areas.

BUILDING #725 TURNAROUND

The circular drive at the main entranceway to building #725 was becoming unsightly due to cracks and puddles resulting from uneven grading. When combined with freezing temperatures, the puddles presented a safety hazard as well. The area was resurfaced and graded thus eliminating the puddles and improving the overall appearance.

COOLING TOWER REPLACEMENT

A jointly funded NSLS/BNL Plant Engineering Division project has been implemented for the replacement of the sixteen year old Baltimore Cooling Tower on the roof of building #725. This is one of two cooling towers which are part of the NSLS "in house" chilled water system. This system provides coverage during shutdowns of BNL's central chilled water facility which is becoming our primary source of machine and comfort cooling. The tower was purchased during late summer/ early fall, with installation completed in December 1996.

EXPERIMENTAL WATER UPGRADE

The connection of the experimental water system is the final phase of the NSLS hookup to BNL's central chilled water facility. This project gives the NSLS the added reliability and operating flexibility of being able to cool the experimental water system from both the central chilled water system and the NSLS "in house" chilled water system. Installation will be completed during the December 1996 shutdown.

BUILDING #729 TWO TON BRIDGE CRANE

This Project installed an overhead crane to cover approximately ninety percent of the floor area in building #729, which houses the Source Development Laboratory.

IMPROVEMENTS TO THE EXPERIMENTAL FLOOR AREAS

Recognizing the concerns expressed in the responses to a DOE survey of NSLS users taken in the Spring of 1996, we have taken steps to remedy three commonly repeated themes; seating, sound levels and lighting.

During the summer months, over two hundred new multi-adjustable swivel arm chairs were purchased and distributed throughout the X-Ray and VUV experimental floor areas. These chairs have replaced the worn out "old gray chairs", adding much to the comfort and appearance of the facility.

Sound surveys had been performed around the X-Ray and VUV Ring areas in 1994 both before and after sound insulating panels were installed in the VUV area. Recently in the summer of 1996 sound surveys were again conducted and experts are being consulted in a continuing effort to minimize noise levels. Results of these surveys can be found on a poster in the main lobby of building #725. Comments or suggestions are invited.

A 400 Watt mercury vapor lamp fixture was installed over the main entrance area to the VUV Ring on a trial basis. This fixture has replaced the original 250 Watt high pressure sodium lamp which is the type currently used throughout the experimental areas. The mercury vapor lamp is brighter and sheds a whiter "daylight" type of lighting than the yellow and dimmer sodium lamp. The feedback from the users in the area has been generally favorable and we are currently in the process of obtaining estimates for the replacement of all the lighting fixtures on the X-Ray and VUV experimental floor.

PROJECTS

INSERTION DEVICE R&D AT X13

Peter M. Stefan
Sam Krinsky
Chi-Chang Kao

On the NSLS X-Ray Storage Ring, the X13 straight section and beamline have been used for insertion-device-related R&D since 1990. The development work at X13 has succeeded in significantly advancing the state-of-the-art in important aspects of insertion device design, and the light sources produced have the promise of delivering significant new capabilities for the NSLS user community. Three important projects will be described below: the Prototype Small-Gap Undulator (PSGU), the in-vacuum undulator (IVUN), and the Time Varying Elliptically Polarized Wiggler (EPW). The PSGU and the EPW are presently installed for use at X13. IVUN is under construction, and in Spring of 1997 it will be installed at X13, replacing the PSGU.

SMALL-GAP UNDULATORS

The PSGU [1,2] combines a short-period (16 mm) undulator magnet and a variable-aperture vacuum chamber to produce high-brightness undulator light with a higher photon energy in the fundamental than would otherwise be possible in the X-Ray Ring. The PSGU was built in a collaboration between the NSLS and Rockwell International Rocketdyne Division. Rocketdyne built the permanent magnet arrays. The light produced by the PSGU is concentrated in the fundamental and in a few higher harmonics, as illustrated in **Figure 1** for a magnet gap of 7.5 mm. The brightness is between 100 and 1000 times that of the X-Ray Ring bend magnet sources, while the flux in the fundamental is about equal to that from 8 milliradians of the bend magnet.

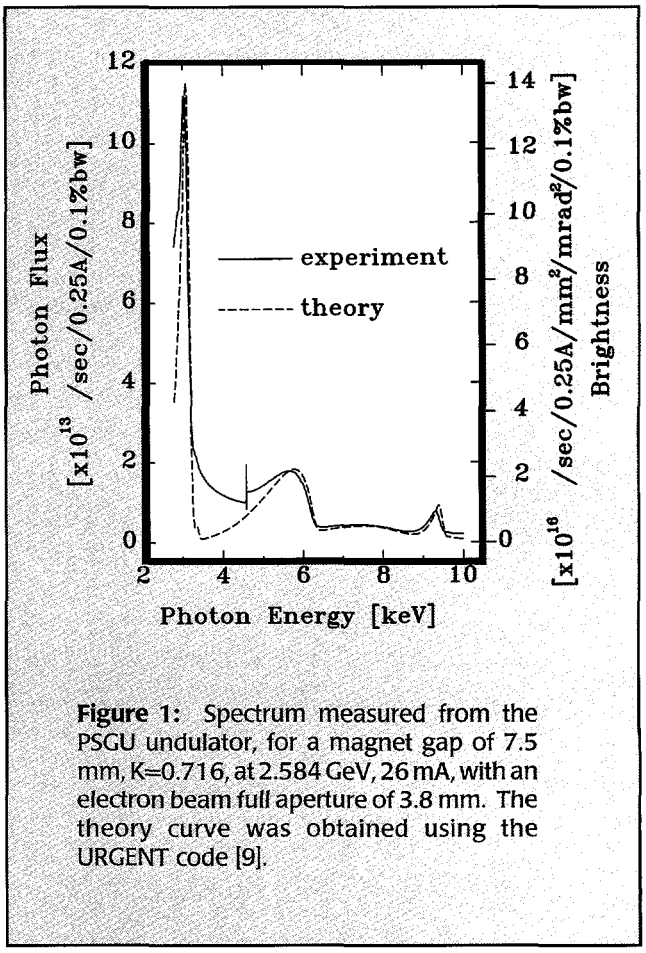


Figure 1: Spectrum measured from the PSGU undulator, for a magnet gap of 7.5 mm, K=0.716, at 2.584 GeV, 26 mA, with an electron beam full aperture of 3.8 mm. The theory curve was obtained using the URGENT code [9].

Photons from the PSGU have been used to develop a coherent x-ray beam for X-ray Photon Correlation Spectroscopy (XPCS). A coherent beam of 3×10^9 photons/sec at 3 keV (4.1Å) was produced through a 10 μm pinhole.

The long straight sections of the NSLS X-Ray Ring (such as the X13 straight) are particularly well-suited for small-gap insertion devices. The stored electron beam focuses to a minimum dimension both in the vertical and in the horizontal at the center of the long straight. The same strong focussing occurs for an imaginary tube surrounding the electron beam, which represents a "stay-clear" aperture. As long as the vacuum chamber stays outside the stay-clear region, the beam lifetime is unaffected. Therefore, the PSGU is installed in the center of the straight section, and is quite short. The minimum-aperture-region of its variable vacuum chamber is 390 mm long, and the undulator magnet arrays are 320 mm long. In the regions closest to the electron beam, the PSGU vacuum chamber is thinned to 1 mm. The magnet

arrays are in air, located just outside the thinned vacuum chamber. The magnet gap is always at least 3 mm greater than the vertical aperture of the vacuum chamber for the electron beam.

One of the most important studies conducted with the PSGU determined the vertical dimension of the stay-clear tube mentioned above, and measured the reduction in the electron beam lifetime as the variable vacuum chamber cut into this tube. The results are illustrated in **Figure 2**. The lifetime was essentially unaffected to a full aperture of 4 mm, but then started to decrease. In a practical sense, an aperture of about 3 mm is operationally acceptable, since the overall lifetime reduction is small.

In order to take full advantage of the ability to run with a 3 mm aperture, we are pursuing an in-vacuum undulator project (IVUN). This is a logical extension of the PSGU, with the variable vacuum chamber eliminated, and the undulator magnet arrays placed directly in the storage ring vacuum. For IVUN, the magnet gap and the corresponding electron beam aperture are very nearly the same dimension. A comparison between the parameters of the PSGU and IVUN is presented in **Table 1**.

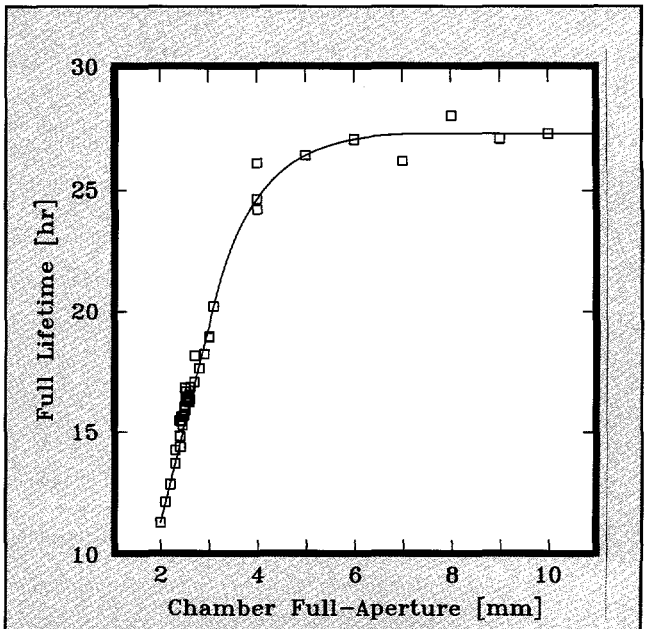


Figure 2: Stored beam lifetime as a function of the electron beam aperture presented by the PSGU vacuum chamber, at 220 mA. The line drawn is a guide for the eye.

Table 1: PSGU/IVUN Comparison

	PSGU	IVUN
Period λ_u	16mm	11 mm
Nominal Magnet Gap	6.0 mm	3.3 mm
Corresponding Maximum Beam Aperture	3.0 mm	3.0 mm
Peak On-Axis Field	0.623 T	0.678 T
$h\upsilon_{1\,out}$, $(\lambda_{1\,out})$	2.77 keV, (4.48 Å)	4.64 keV, (2.67 Å)

The IVUN design goal is for a photon output at 4.6 keV (2.7Å) in the fundamental, with high flux at the second and third harmonics, at a magnet gap of 3.3 mm. Experiments spanning the whole spectrum of synchrotron-light applications, from spectroscopy and diffraction to microscopy and scattering, can benefit from this high-brightness, high-flux source. In addition the electron beam characteristics of the X-Ray Ring allow IVUN to produce good second-harmonic intensity on-axis, at just over 8 keV, with a half-intensity bandwidth of over 2 keV. IVUN is being built in a collaboration between the NSLS and the Japanese SPring-8 Project. Our collaborators at SPring-8 worked on the first successful in-vacuum undulator and are fabricating the 11 mm-period magnet arrays for IVUN. When installed in the X13 straight section, IVUN will replace the PSGU,which is now situated at the center of the straight. Studies are planned to begin in the Summer of 1997.

TIME VARYING ELLIPTICALLY POLARIZED WIGGLER

The Time Varying Elliptically Polarized Wiggler (EPW) [3] is a very different kind of insertion device, compared with the PSGU or IVUN. As the name implies, it produces elliptically-polarized light on axis, with the sense of rotation of the field vectors, i.e. the helicity, alternating at up to 100 Hz. The EPW was built in a collaboration between the NSLS, the APS at Argonne National Lab, and the Budker Institute of Nuclear Physics at Novosibirsk. Usable fluxes of photons are available from 100 eV to 10 keV, with the measured degree of circular polarization exceeding 50%. Such a source is extremely useful for circular dichroism studies of both magnetic materials and materials with natural optical activity. The stable alternation of the helicity, at frequencies up to 100 Hz, is an extremely powerful aspect of the source. This allows gating or lock-in techniques to separate the responses of the sample to opposite helicities. When a lock-in amplifier is used, any steady-state or background signals are summarily removed from the start, since the lock-in only detects the signals which follow the EPW reference signal. Adjustment of the lock-in phase selects the sample response to the individual helicities. This holds the promise of being a very sensitive probe for circular dichroism.

The concepts [4] behind the EPW are also quite interesting, and may be explained as follows: First consider the synchrotron light emitted by a bend magnet source in a storage ring. In the NSLS X-Ray Ring, as viewed from above, the electron beam enters a bend magnet and makes a gentle turn to the right. The light emitted into the horizontal plane (which contains the electron beam path) is linearly polarized, with the electric field vector contained in this same plane. Light directed above or below the plane is elliptically polarized, with opposite helicity above and below. In a normal wiggler, the electron beam makes a bend to the right, then one to the left, etc. The polarization of the output light from the wiggler is linear everywhere, that is, in the plane of the wiggles and above and below. This is due to a cancellation of the elliptical nature of the *right* turns by the *left* turns. In the EPW, a special electromagnet adds vertical deflection to the electron trajectory, as illustrated in **Figure 3.** The right and left turns are twisted out of the horizontal plane, but with all the right turns twisted *up* and the left turns twisted *down.* The photons illustrated in the figure were initially directed parallel to the z direction, before the twists were applied. As a result, the light which is now directed parallel to the z direction comes from *below* the plane of the right turns and *above* the plane from the left turns. Thus, it is elliptically polarized, with the two types of turns re-enforcing each other. When the current flow in the electromagnet is reversed, the opposite helicity is produced on axis.

The EPW was installed in December 1994, commissioned during Spring 1995 at an operating frequency of 2 Hz, and became operational subsequently [5]. Utilizing trim coils at the wiggler ends and the high-precision

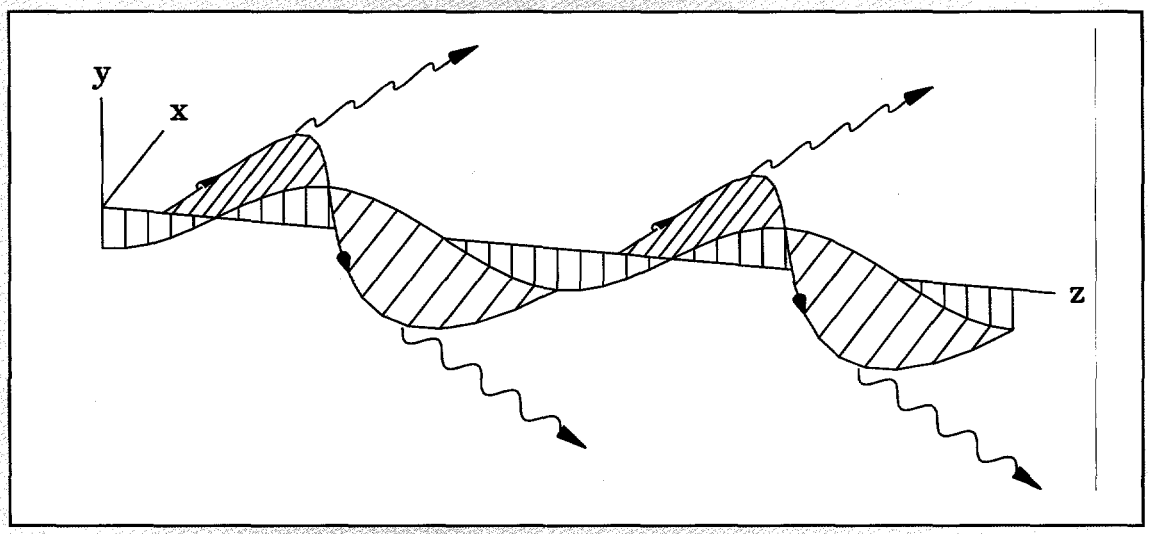


Figure 3: The electron trajectory in the EPW. A special electromagnet adds the vertical deflection to the electron trajectory. The right and left turns are twisted out of the horizontal plane; all the right turns are twisted *up* and the left turns twisted *down.* The photons illustrated in the figure were initially directed parallel to the z direction, before the twists were applied.

orbit measurement system of the NSLS X-Ray Ring, the residual orbit motion was reduced to a level below 0.5 μm [6]. No adverse effects on other experiments have been observed. The degree of circular polarization of the radiation from the wiggler was characterized by making Magnetic Circular Dichroism (MCD) measurements using the X13A soft-x-ray beamline [7]. For vertical deflection parameters, K_x, of 1.2 and 1.6, the MCD effects at the Fe $L_{2,3}$ edges indicated a degree of circular polarization of 60% and 75%, respectively, in good agreement with calculated values. Experimental programs based on the device, including MCD, Natural Circular Dichroism, and Resonant Magnetic Scattering, have also started. As an example, very small MCD effects near the Cr $L_{2,3}$ edges were observed in a series of Co-Cr alloys (a promising candidate for a high-density perpendicular magnetic recording medium) by a collaboration of the Naval Research Laboratory, AT&T, and the NSLS [8]. From these results, the Cr in the alloys was found to be polarized, and the induced Cr moment aligned anti-ferromagnetically with respect to that of the neighboring Co. These results also showed that MCD effects much smaller than 1% can be easily detected with the EPW, as illustrated in **Figure 4**. To fully utilize the EPW, a new soft x-ray spherical grating beamline and a double-crystal x-ray monochromator are being constructed, and will be operational in fiscal year 1997. Studies are now underway utilizing the EPW switching at 100 Hz.

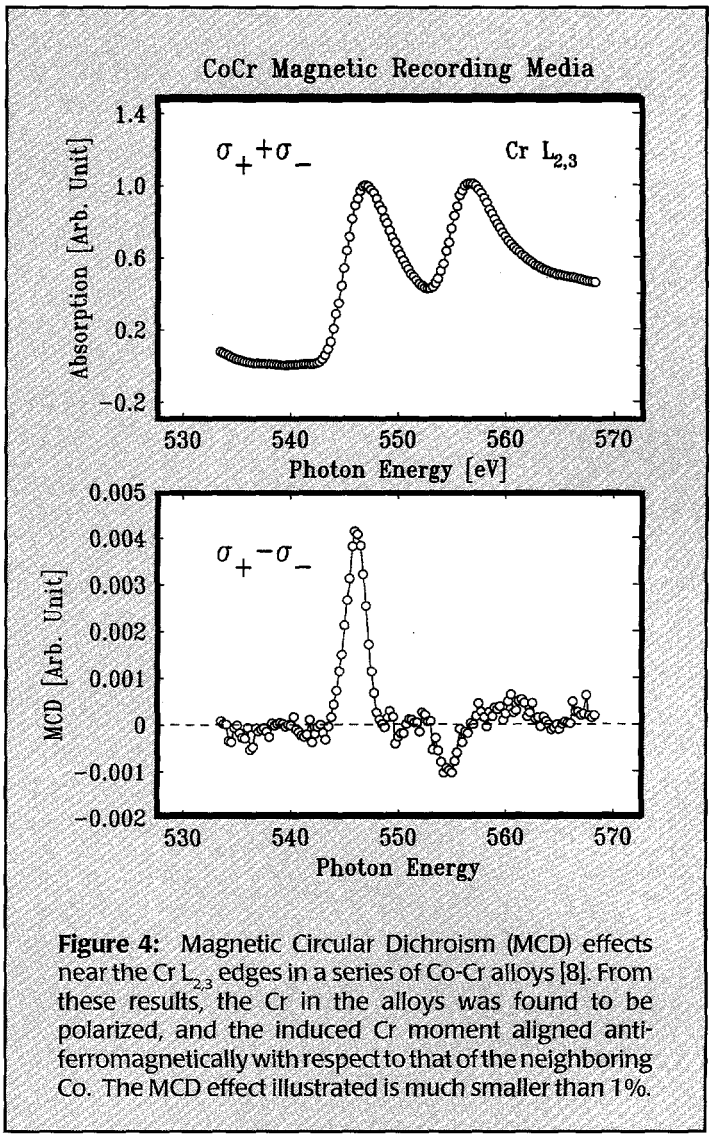


Figure 4: Magnetic Circular Dichroism (MCD) effects near the Cr $L_{2,3}$ edges in a series of Co-Cr alloys [8]. From these results, the Cr in the alloys was found to be polarized, and the induced Cr moment aligned anti-ferromagnetically with respect to that of the neighboring Co. The MCD effect illustrated is much smaller than 1%.

References:

[1] P.M. Stefan, L. Solomon, S. Krinsky and G Rakowsky, Proc. 1991 Part. Accel. Conf., San Francisco, CA, p. 2542, (1991).

[2] P.M. Stefan, S. Krinsky, G. Rakowsky and L. Solomon, Proc. 1995 Part. Accel. Conf., Dallas, TX, p. 2435, (1995).

[3] A. Friedman, S. Krinsky and E. Blum, "Polarized Wiggler for NSLS X-Ray Ring: Design Consideration", Informal Report, BNL 47317, (1992); E.Gluskin, *et al.*, Proc. 1995 Part. Accel. Conf., Dallas, TX, (1995).

[4] S. Yamamoto and H. Kitamura, *Japan J.of Appl. Phys.*, **26**, p.L1613, (1987).

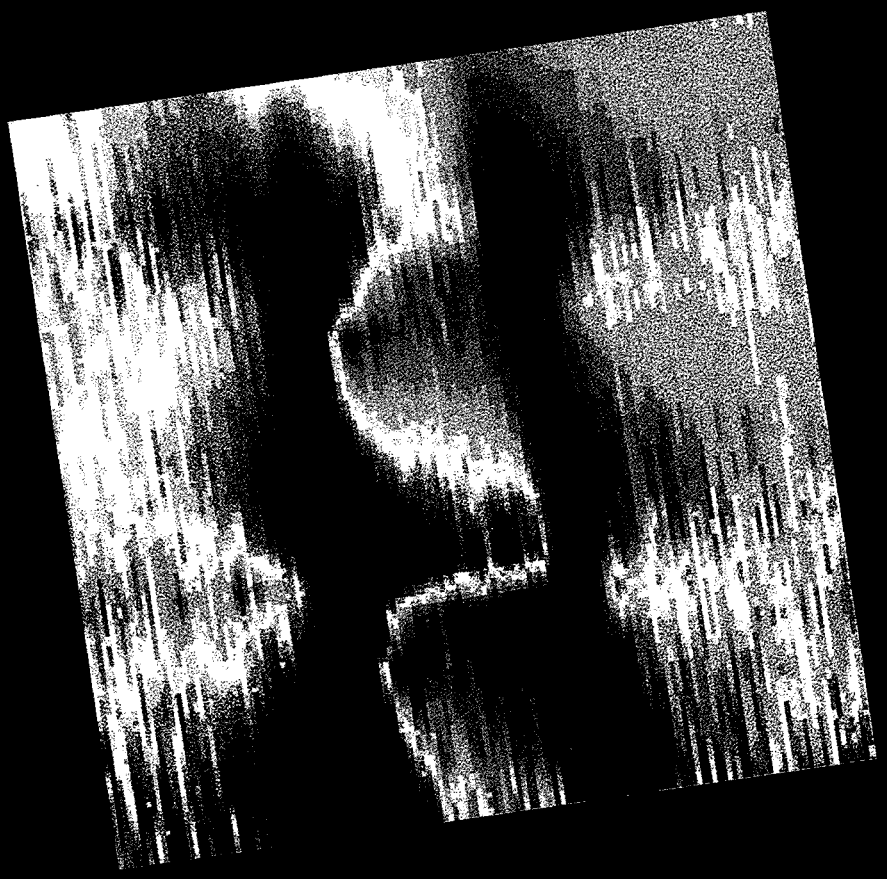
[5] S. Krinsky, and C.-C. Kao, Synchrotron Radiation News, **8**, 38, (1995).

[6] O. Singh, S. Krinsky, P.M. Ivanov and E.A. Medvedko, Proc. 6th Int. Synch. Rad. Instrum. Conf., Argonne, IL, October 1995.

[7] K.J. Randall, Z. Xu, E. Gluskin, I. McNulty, R. Dejus, S. Krinsky, O. Singh, C.-C. Kao, E.D. Johnson, C.T. Chen, and G. Meigs, *J. Electron Spectroscopy and Related Phenomena*, **80**, 433, (1996).

[8] K.M. Kemner, V.G. Harris, V. Chakarian, Y.U. Idzerda, W.T. Elam, C.-C. Kao, Y.C. Feng, D.E. Laughlin, and J.C. Woicik, *J. Appl. Phys.* **79**, 5345, (1996), Proceedings of the 40th Annual Conference on Magnetism and Magnetic Material Nov. 6-9, 1995 Philadelphia.

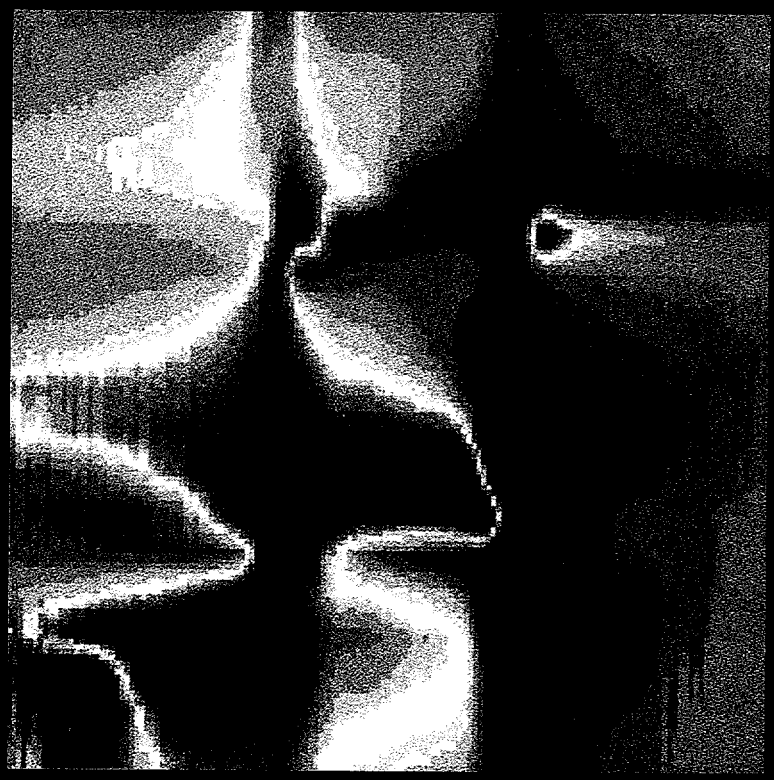
[9] R.P. Walker and B. Diviacco, *Rev. Sci. Instrum.* **63/1**, 392, (1992).



Beamline U4B: Energy and angular dependence of the asymmetry between the specular reflectivity of left- and right-circularly polarized soft x-rays from a 37 C bcc Co film near the $L_{2,3}$ resonance energies. Experiment (above) and theory (at right) are shown for comparison. The data was acquired at the NSLS U4B Magnetic Circular Dichroism (MCD) beamline. Y.U. Idzerda (Naval Research Laboratory).

SIX

ORGANIZATION



ORGANIZATION

NSLS Advisory Committees

1996-1997
Users' Executive Committee

The Users' Executive Committee (UEC) provides for organized discussions among the user community, NSLS administration, and laboratory directorate. It aims to communicate current and future needs, concerns, trends within the user community to NSLS staff and management, and to disseminate to the users information about NSLS and BNL plans. Members were:

Chairperson: Peter Stephens, SUNY-Stony Brook
Vice-Chairperson: Joel D. Brock, Cornell U.
Past -Chairperson: Paul Zschack, ORNL
Secretary: Ben Ocko, BNL-Physics
Doon Gibbs, BNL-Physics
Kim Mohanty, BNL-Physics
Ian Robinson, U. of Illinois
Thomas Russell, IBM
D. Peter Siddons, NSLS
Ex-Officio: Eva Rothman, NSLS

Special Interest Group Representatives

Special interest groups in areas of common concern communicate with NSLS management through the UEC. Group representatives were:

Biological Scattering, Crystallography	Stephan Ginell, ANL
Energy Dispersive Diffraction	No SPIG elected as of this date
Imaging	Carl Zimba, MIT
Industrial Users	Richard Harlow, Dupont
Nuclear Physics	Steven C. Whisnant, U. of S. Carolina
Students and Post Docs	David Johnson, BNL-Chemistry
Time Resolved Spectroscopy	Ralf Wehlitz, U. of Tennessee
Topography	Michael Dudley, SUNY-Stony Brook
UV Photoemission, Surface Science	Yves Idzerda, Naval Research Laboratory
XAFS	Mark Chance, Albert Einstein Coll. of Med.
X-Ray Scattering , Crystallography	Ben Ocko, BNL-Physics

Science Advisory Committee

The Science Advisory Committee (SAC) evaluates the science programs at the NSLS and makes recommendations to the Chairman. The SAC met in March of 1996 and its members were:

B. Batterman, CHESS, Cornell U.
Stephen Harrison, HHMI, Harvard U.
Franz Himpsel, U. of Wisconsin, Madison
Jochen Schneider, HASYLAB, DESY
Albert J. Sievers, Cornell U.
Paul Sigler, HHMI, Yale U.
Sunil Sinha, APS, Argonne National Laboratory

General User Proposal Study Panels

The Proposal Study Panels met in November 1995, March 1996, and July 1996 to review and rate General User research proposals for the FY 1996 cycles. PSP members are drawn from the scientific community and usually serve a two year term. Members during FY 1996 were:

UV Panel

David Hanson	SUNY
Boris Sinkovic	NYU
David Tanner	U. of Florida

X-Ray Spectroscopy Panel

Chuck Bouldin	NIST
Steven Heald	APS
Linda Powers	Utah State U.
William Orme-Johnson	MIT
Dale Sayers	U. of NC

X-Ray Imaging/Other Panel

Alastair MacDowell	AT&T
Steve Sutton	U. of Chicago

X-Ray Scattering Panel

Jerome Cohen	NWU
Simon Moss	U. of Houston
Thomas Russell	IBM
Sunil Sinha	ANL
Ian Robinson	U. of Illinois
Cullie Sparks	ORNL

X-Ray Biology

Howard Einspahr	Bristol-Myers Squibb
Thomas Terwilliger	LANL

General User Oversight Committee

The General User Oversight Committe (GUOC) met in November 1995, March 1996, and July 1996 to allocate time on beamlines to each General User proposal for the FY 1996 cycles. GUOC members are drawn from the scientific community and usually serve a two year term. Members during FY 1996 were:

UV Members

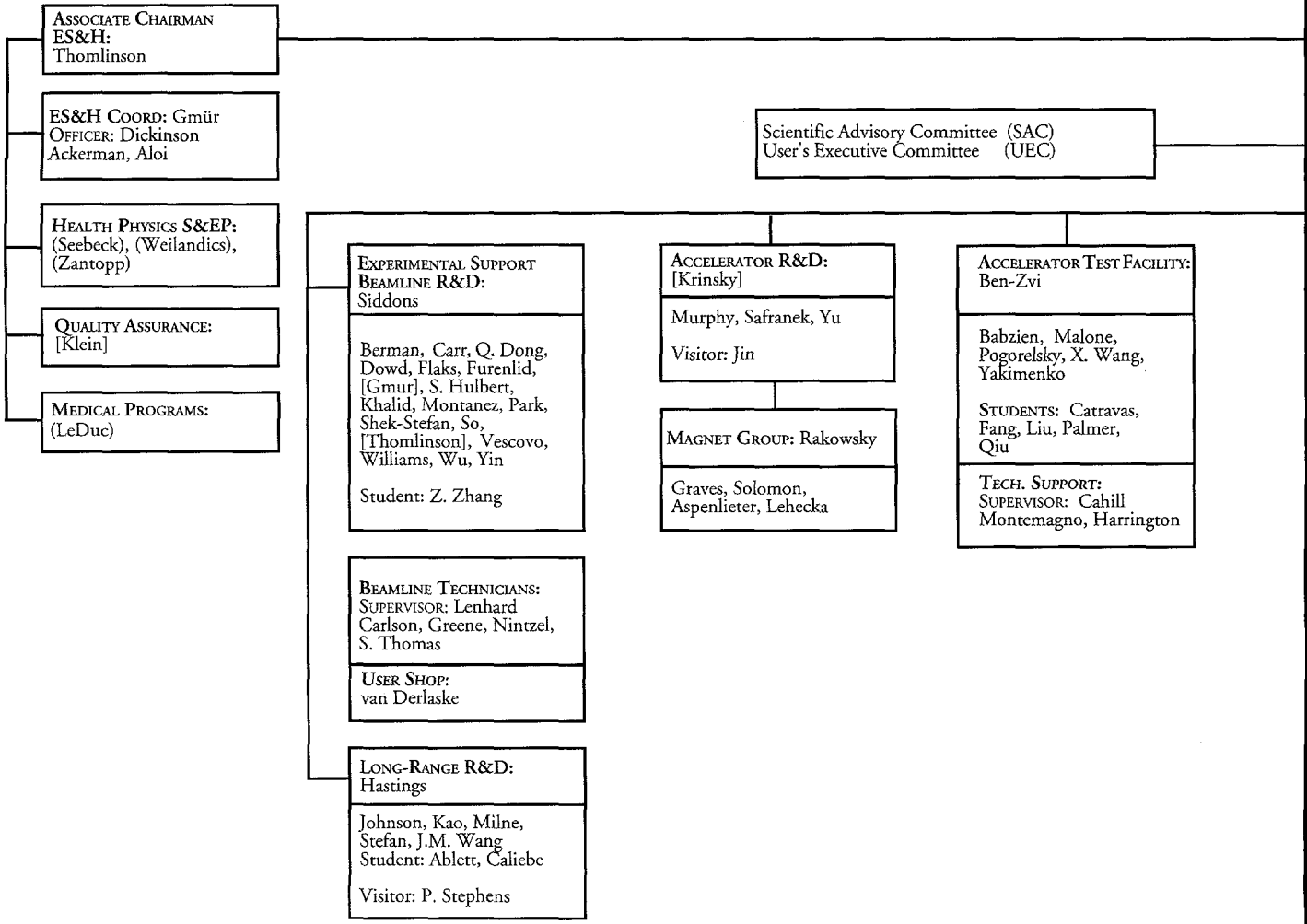
Harold Ade	NCSU
David Heskett	U. of R.I.
Jan Hrbek	BNL-Chemistry

X-Ray Members

Malcolm Capel	BNL-Biology
Mark Chance	Albert Einstein
Alex Darovsky	SUNY-Stony Brook
Lars Furenlid	BNL-NSLS
James McBreen	BNL-DAS
Gavin Watson	BNL-Physics

ORGANIZATION

NSLS STAFF



* Temporary

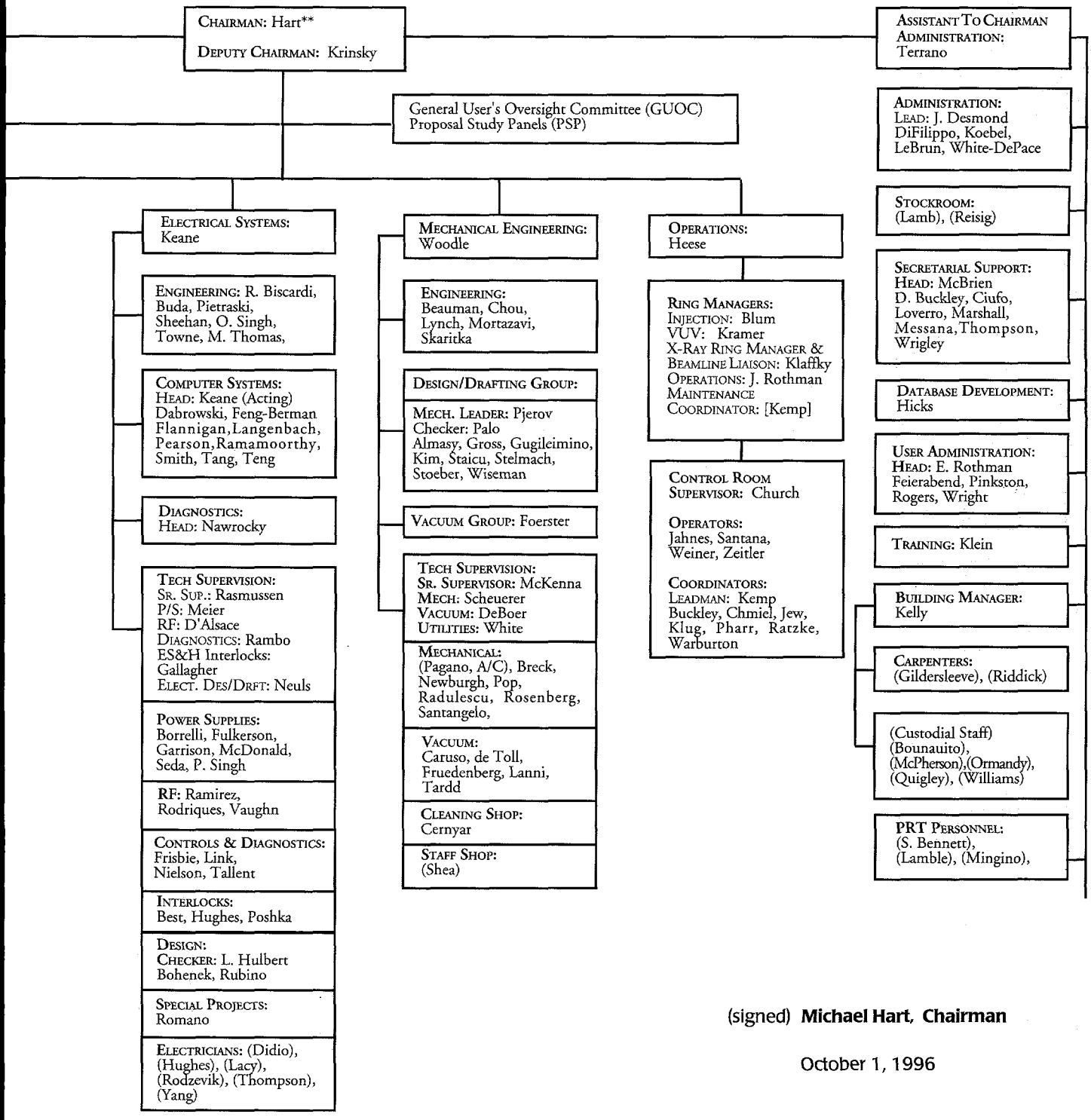
** Reports to Denis McWhan, Assoc. Dir. for Basic Energy Sciences

[ ] NSLS personnel with multiple functions

( ) PRT personnel or member of non-NSLS division

ORGANIZATION

NSLS STAFF



(signed) **Michael Hart, Chairman**

October 1, 1996

NSLS Beamline Guide

October 1996

This table lists the abbreviations appearing in the Beamline Guides.

ARUPS	=	Angle-Resolved Ultraviolet Photoemission Spectroscopy
CD	=	Circular Diachroism
C-T	=	Czerney-Turner
ERG	=	Extended Range Grasshopper
EXAFS	=	Extended X-ray Absorption Fine Structure
IR	=	Infared
LEGS	=	Laser Electron Gamma Source
MCD	=	Magnetic CD
MI	=	Michelson Interferometer
NEXAFS	=	Near Edge X-ray Absorption Fine Structure
NIM	=	Normal Incidence Monochromator
PGM	=	Plane Grating Monochromator
SEXAFS	=	Surface EXAFS
SGM	=	Spherical Grating Monochromator
S-N	=	Seya-Namioka
SXES	=	Soft X-ray Emission Spectroscopy
TGM	=	Toroidal Grating Monochromator
TOK	=	Transverse Optical Krystron
UPS	=	Ultraviolet Photemission Spectroscopy
WB	=	White Beam
WDI	=	Wavefront Dividing Interferometer
XPS	=	X-ray Photoemission Spectroscopy
XAS	=	X-ray Absorption Spectroscopy

VUV Beamline Guide

Beam line	Research Program	Mono.	Affiliation	Local Contact	Spokesperson
U1A	SEXAFS, ARUPS, XPS	ERG	Exxon	B DeVries 516-344-5206 516-344-5206	J Chen 908-730-2738
U1B	(Conceptual)	TGM	Exxon	B DeVries 516-344-5206 516-344-5206	J Chen 908-730-2738
U2A	(Unassigned)				
U2B	High pressure, pump-probe, high Tc abs., IR microscopy	MI	SUNY@SB BNL-NSLS Northrop Grumman Carnegie Inst. Wash	G Williams 516-344-7529	G Carr 516-344-5502 516-344-2237
U3A	Time-resolved and DC radiometry; reflectometry for optical constants	DC/DG	Los Alamos Natl Lab Smiths Astro Obs Bechtel Nevada	A Burek 516-344-5503	R Blake 516-344-5521 505-466-0566
U3B	(Conceptual)				
U3C	Photoelectron spect.; exp. system and detector calibrations	ERG	Bechtel Nevada Sandia Natl Lab Los Alamos Natl Lab	W Towell 516-344-7245	R Bartlett 516-344-5708 505-667-5923
U4A	ARUPS of solids,surfaces; hi res. core level photo-emission; total yield absorption	TGM	No Carolina St U BNL - NSLS Boston U	S Dhesi 516-344-5504	K Smith 617-353-6117
U4B	Soft x-ray photoemission spectroscopy; NEXAFS; SXMCD	SGM	Naval Res Lab BNL-NSLS	V Chakarian 516-344-7718 J Freeland 516-344-7718	Y Idzerda 516-344-7718 202-767-4481 J Park 516-344-7290 516-344-4744

Beam line	Research Program	Mono.	Affiliation	Local Contact	Spokesperson
U4IR	Vibr. spectr of molecules on surfaces; abs of hi Tc superconductors; hi res gas abs.; fast detectors	MI,WDI	BNL-NSLS Lucent Tech Fairleigh Dickinson U Exxon	D Van Campen 516-344-7419 516-344-2738	G Williams 516-344-7529
U5	Diagnostics		BNL-NSLS	R Nawrocky 516-344-4449	R Nawrocky 516-344-4449
U5UA	Spin polarized angle-resolved ultraviolet photoemission	TGM	BNL-NSLS U of Nebraska U of Texas New York U ANL	E Vescovo 516-344-7399 S Hulbert 516-344-7570	E Vescovo 516-344-7399
U6	Lithography	WB	IBM	J Silverman 914-945-2099	J Silverman 914-945-2099
U7A	Photoemission; SEXAFS; Fluorescence yield spectroscopy	TGM	BNL-Chemisry BNL-Physics Rutgers U Dow Chemical NIST U of Michigan Texas A&M	D Fischer 516-344-5177	Q Dong 516-344-5507 516-344-5505
U7B	Photoemission; SEXAFS	PGM	BNL-Physics SUNY@SB	Q Dong 516-344-5507 516-344-5505	M Strongin 516-344-3763
U8A	ARUPS NEXAFS	TGM	IBM	R McFeely 914-945-2068	R McFeely 914-945-2068
U8B	ARUPS NEXAFS	TGM	IBM	K Zhang	J Yarmoff 909-787-5336 909-787-3537
U8C	Zone plate monochr evaluation; reflectivity measurements of thin films and multilayers	ZONE PL.	IBM	R McFeely 914-945-2068	R McFeely 914-945-2068
U8D	(Conceptual) Scanning soft x-ray microscopy		IBM	R McFeely 914-945-2068	R McFeely 914-945-2068

Beam line	Research Program	Mono.	Affiliation	Local Contact	Spokesperson
U9A	(Planned) Lithography				M Strongin 516-344-3763
U9B	CD; MCD; time-resolved fluorescence (lifetimes)	C-T	BNL-NSLS BNL-Biology	J Sutherland 516-344-3406 516-344-3279	J Sutherland 516-344-3406 516-344-3279
U10A	(Unassigned)				
U10B	PSD - general vacuum R&D	WB	BNL-NSLS		
U11	Gas phase photo-ionization and Spectroscopy	NIM	BNL-NSLS BNL-Biology Brandeis U BNL-DAS	S Kuo 516-344-7003 516-344-4001	S Hulbert 516-344-7570 B Klemm 516-344-4022 516-344-4001
U12	High resolution core level Spectroscopy ARUPS	TGM	U of Pennsylvania Oak Ridge Natl Lab	P Lyman 516-344-5615 516-344-7395	E Plummer 423-974-3055 D Zehner 516-344-5512 615-574-6291
U12A	High resolution core level spectroscopy (construction)	TGM	Oak Ridge Natl Lab U of Tennessee	P Lyman 516-344-5615 516-344-7395	E Plummer 423-974-3055 D Zehner 516-344-5512 615-574-6291

Beam line	Research Program	Mono.	Affiliation	Local Contact	Spokesperson
U12B	Angle-resolved photoemission	TGM	Oak Ridge Natl Lab U of Tennessee	P Lyman 516-344-5615 516-344-7395	D Zehner 516-344-5512 615-574-6291 E Plummer 423-974-3055
U13UA	High res. VUV/soft x-ray abs and electron spectroscopy (incl. spin-pol photoem.)	SGM	BNL-NSLS	S Hulbert 516-344-7570	S Hulbert 516-344-7570
U13UB	Optical metrology for extreme ultraviolet projection lithography	WB	Sandia Natl Lab BNL-Instrum	A MacDowell 516-344-5334	A.MacDowell 516-344-5334
U14A	Solid state photoemissions studies	PGM	BNL-NSLS	M Shek 516-344-5930 S Hulbert 516-344-7570	M Shek 516-344-5930 S Hulbert 516-344-7570
U14B	Detector Research and Development	WB	BNL-NSLS	J Hastings 516-344-3930	J Hastings 516-344-3930
U15	Soft x-ray spectroscopy (solids and gases)	TGM	BNL-NSLS SUNY@SB SUNY@Buff	A Wen 516-632-7918 Y Soo 516-344-2702 716-645-2576	D Hanson 516-632-7917 Y Kao 716-645-2576
U16A	(Unassigned)				
U16B	ARUPS; XPS; SEXAFS; stimulated desorption; NEXAFS	ERG	Cornell U Sandia Natl Lab		R Merrill 607-255-9857

X-Ray Beamline Guide

Beam line	Research Program	Energy (keV)	Affiliation	Local Contact	Spokesperson
X1A	Soft x-ray imaging	10-80 Å	BNL-NSLS SUNY@SB LBNL No Carolina St U ANL	S Wirick 516-344-4723 516-632-8095	J Kirz 516-344-4723 516-632-8106
X1B	Soft x-ray spectroscopy	10-50 Å	BNL-NSLS BNL-Physics FA - Juelich Fritz-Haber-Inst	P Johnson 516-344-3705 F Loeb 516-344-2092	P Johnson 516-344-3705
X2A	Surface scattering		Exxon ORNL U of Tennessee	V Jahns 516-344-2823 516-344-5057 S Bennett 516-344-4719	K Liang 908-730-3032 A Baddord 423-574-5241
X2B	X-ray microtomography	6.5-30, WB	Exxon	J Dunsmuir 908-730-2548	J Dunsmuir 908-730-2548
X3A1	Short wavelength crystallography, diffraction and scattering	14, 19, 31	SUNY@SB SUNY@Buff	A Darovsky 516-344-3770	P Coppens 716-645-6800 ext. 2217
X3A2	Diffractometry; x-ray spectroscopy; scattering; crystallography; small angle scattering	3-31	SUNY@SB SUNY@Buff	A Darovsky 516-344-3770	P Coppens 716-645-6800 ext. 2217
X3B1	X-ray spectroscopy; powder diffraction	4.6-40	SUNY@SB SUNY@Buff	P Stephens 516-344-3176 516-344-5634 516-632-8156	P Coppens 716-645-6800 ext. 2217
X3B2	Surface science	4-20	SUNY@SB SUNY@Buff	P Stephens 516-344-3176 516-344-5634 516-632-8156	P Coppens 716-645-6800 ext. 2217

Beam line	Research Program	Energy (keV)	Affiliation	Local Contact	Spokesperson
X4A	Multiwavelength anomalous diffraction analysis of crystalline biological macromolecules	4-30	Howard Hughes Med In	C Ogata 516-344-7435 516-344-5466	W Hendrickson 516-344-4938 212-305-3456
X4B	(Conceptual)				
X4C	Diffraction measurements from biological macromolecules	7-20	Howard Hughes Med In	C Ogata 516-344-7435 516-344-5466	W Hendrickson 516-344-4938 212-305-3456
X5A	Laser Electron Gamma Source (LEGS); medium energy nuclear physics	80-400 MeV	BNL-Physics	C Thorn 516-344-7798 O Kistner 516-344-3991	A Sandorfi 516-344-7951 B Preedom 803-777-6559
X5B	Diagnostic				
X6A	Time and space resolved dispersive x-ray spectroscopy	4-20	ANL	P Lee 516-344-2210 516-344-3955	P Montano 708-252-6239
X6B	X-ray scattering	2.4-21.0	ANL U of Illinois Northwestern U BP	P Lee 516-344-2210 516-344-3955	P Montano 708-252-6239
X7A	Structural char. through powder diffraction	5-45, WB	BNL-NSLS BNL-Physics Carnegie Inst of Was E I DuPont Mobil UOP Air Products Corp SUNY@SB U of Cal @ Santa Barbara U of Pennsylvania NIST Chevron	D Cox 516-344-3818 Q Zhu 516-344-3818	D Cox 516-344-3818 Q Zhu 516-344-3818
X7B	Crystallography; wide angle scattering	5-21	BNL-Chemistry Swedish Nat Res Coun	J Hanson 516-344-4381 516-344-4378	T Koetzle 516-344-4384 J Larese
X8A	Photoionization cross-sections; photoelectron spectr; mirror reflect.; detector calib.; spectr.	0.26-5.9	Los Alamos Natl Lab Smiths Astro Obs	M Sagurton 516-344-5708	R Blake 516-344-5521 505-466-0566

Beam line	Research Program	Energy (keV)	Affiliation	Local Contact	Spokesperson
X8C	Diffraction from biological macromolecules and detector calibrations	5-20	Los Alamos Natl Lab Sandia Natl Lab LLNL ANL	M Sagurton 516-344-5708	G Idzorek 516-344-7245 505-667-8848
X9A	XAS	3.4-18.6	Albert Einstein	M Sullivan 516-344-3800 L Miller 516-344-2091 516-344-3800	M Chance 516-344-3800 718-430-2894
X9B	Time resolved x-ray spectroscopy; scattering; diffraction; XAS	3.2-18.8	Albert Einstein	M Sullivan 516-344-3800 L Miller 516-344-2091 516-344-3800	M Chance 516-344-3800 718-430-2894
X10A	Diffraction; small angle scattering; crystallography; scattering	6-15.2	Exxon	S Bennett 516-344-4719	E Sirota 908-730-3407 K Liang 908-730-3032
X10B	Scattering; crystallography	8, 12	Exxon	S Bennett 516-344-4719	E Sirota 908-730-3407 K Liang 908-730-3032
X10C	EXAFS	3.5-24.7	Exxon	M Sansone 516-344-5759 908-730-0100 B DeVries 516-344-5206	P Stevens 516-344-4828 908-730-2584
X11A	EXAFS	4.5-35	No Carolina St U U of Connecticut BNL-NSLS Naval Res Lab Mobil E I DuPont Hoechst Celanese Naval Surf Warf Center Notre Dame U U of Washington Ill Inst of Tech Georgia Inst of Tech Rice U	G Lamble 516-344-7734	G Lamble 516-344-7734 D Sayers 516-344-7731 919-515-4453

Beam line	Research Program	Energy (keV)	Affiliation	Local Contact	Spokesperson
X11B	EXAFS	1.7-8	No Carolina St U U of Connecticut BNL-NSLS Mobil E I DuPont Naval Res Lab Hoechst Celanese Naval Surf Warf Center Notre Dame U U of Washington Ill Inst of Tech Georgia Inst of Tech Rice U	G Lamble 516-344-7734	G Lamble 516-344-7734 D Sayers 516-344-7731 919-515-4453
X12A	Instrument development		BNL-NSLS	B Dowd 516-344-2738	DP Siddons 516-344-2738 516-344-5627
X12B	Time-resolved and static x-ray diffr. of macromol. systems in both wide and small angle regimes	6-15	BNL-NSLS BNL-Biology	M Capel 516-344-5712	T Langdon 516-344-5712 M Capel 516-344-5712
X12C	Protein crystallography	7.8-13.6	BNL-Biology	R Sweet 516-344-3401	R Sweet 516-344-3401
X13	R&D optics development; soft x-ray utilization		BNL-NSLS	E Johnson 516-344-4603 J Hastings 516-344-3930	E Johnson 516-344-4603
X14A	Scattering; crystallography; spectroscopy	3.5-40	Oak Ridge Natl Lab U of Illinois	R Eisenhower 516-344-5614	G Ice 423-574-2744
X14B	(Conceptual) X-ray microprobe; x-ray micro-focussing; micro-diffraction	WHITE	Oak Ridge Natl Lab	E Johnson 516-344-4603 J Milne 516-344-5910	E Johnson 516-344-4603 P Siddons 516-344-5627 516-344-2738
X15A	X-ray standing waves	3-20, WB	ANL Northwestern U Harvard U	P Lyman 516-344-5615 516-344-7395	M Bedzyk 516-344-7395 708-252-7763

Beam line	Research Program	Energy (keV)	Affiliation	Local Contact	Spokesperson
X15B	SEXAFS EXAFS NEXAFS	1.5-15	Lucent	P Northrup 516-344-5334 A MacDowell 516-344-5334	P Citrin 908-582-5275
X16A	Surface diffraction	4-12	Lucent U of Illinois	W Lehnert 516-344-5715 A MacDowell 516-344-5334	K Evans-Lutterodt 516-344-2125 908-582-2154 I Robinson 516-344-7024 217-244-2949
X16B	Diffraction	7.85	Lucent	L Flaks 516-344-2738	P Siddons 516-344-5627 K Evans-Lutterodt 516-344-2125 908-582-2154
X16C	Novel spectroscopy; diffraction	3-16	Lucent U of Illinois	W Lehnert 516-344-5715 A MacDowell 516-344-5334	W Brown 908-582-3941 M Marcus 908-582-2749
X17A	(Conceptual)				
X17B1	Chemical crystallography; hi P physics; tomography; x-ray scattering; x-ray fluorescence microprobe	10-100, WB	BNL-NSLS	J Hastings 516-344-3930 P Siddons 516-344-5627 516-344-2738	J Hastings 516-344-3930 P Siddons 516-344-5627 516-344-2738
X17B2	Medical research: Angiography; computed tomography; radiotherapy	33.02,33.3	BNL-NSLS Stanford U Illinois Inst Tech SUNY@SB LBNL BNL-Medical	N Gmür 516-344-2490	W Thomlinson 516-344-3937
X17C	Hi P research; energy dispersive diffraction from microscopic sample volumes	10-100, WB	Naval Res Lab Carnegie Inst of Was LLNL U of Chicago	J Hu 516-344-5343 202-686-2410	H Mao 202-686-2410 ext. 2467 E Skelton 202-767-3014
X18A	Diffuse and surface scattering	4-20	Purdue U Northwestern U U of Illinois U of Missouri Penn State U	S Ehrlich 516-344-7862 J Schwanof 516-344-5618 516-344-5635	G Liedl 317-494-4100 S Ehrlich 516-344-7862

Beam line	Research Program	Energy (keV)	Affiliation	Local Contact	Spokesperson
X18B	EXAFS; optics char.; reflectivity measurements	4-26	BNL-NSLS AlliedSignal UOP Chevron	S Khalid 516-344-7496	DP Siddons 516-344-2738 516-344-5627 L Furenlid 516-344-5699
X19A	X-ray Absorption Spect.; EXAFS and XANES	2.1-25.6	BNL-NSLS UCA@Davis U of Kentucky U of Michigan BNL-DAS	F Lu 516-344-2338	L Furenlid 516-344-5699
X19C	Topography; liquid surface scattering	4-25, WB	BNL-NSLS SUNY@SB Johns Hopkins U Army Research Lab U of Illinois U of Chicago	M Dudley 516-632-8500	M Dudley 516-632-8500
X20A	Scattering (hi Q-res)	5.6-12	MIT IBM	J Jordan-Sweet 516-344-5192 914-945-3322	R Birgeneau 617-253-4937 J Jordan-Sweet 516-344-5192 914-945-3322
X20B	Scattering at fixed energy	17.36	IBM MIT	J Jordan-Sweet 516-344-5192 914-945-3322 R Birgeneau 617-253-4937	J Jordan-Sweet 516-344-5192 914-945-3322
X20C	Scattering (hi and low Q res)	4-11	IBM MIT	J Jordan-Sweet 516-344-5192 914-945-3322 R Birgeneau 617-253-4937	J Jordan-Sweet 516-344-5192 914-945-3322
X21	High energy resolution inelastic scattering	> 4	BNL-NSLS	C Kao 516-344-4494	C Kao 516-344-4494
X22A	In-plane diffr. & refl. studies of surfaces under electro-chem. cond., and thin films and multilayer	10 Nom.	BNL-Physics BNL-DAS	B Ocko 516-344-4299 B Ocko	D Gibbs 516-344-4608
X22B	High resolution x-ray diffraction	5-10	BNL-Physics Harvard U ANL	B Ocko 516-344-4299	D Gibbs 516-344-4608

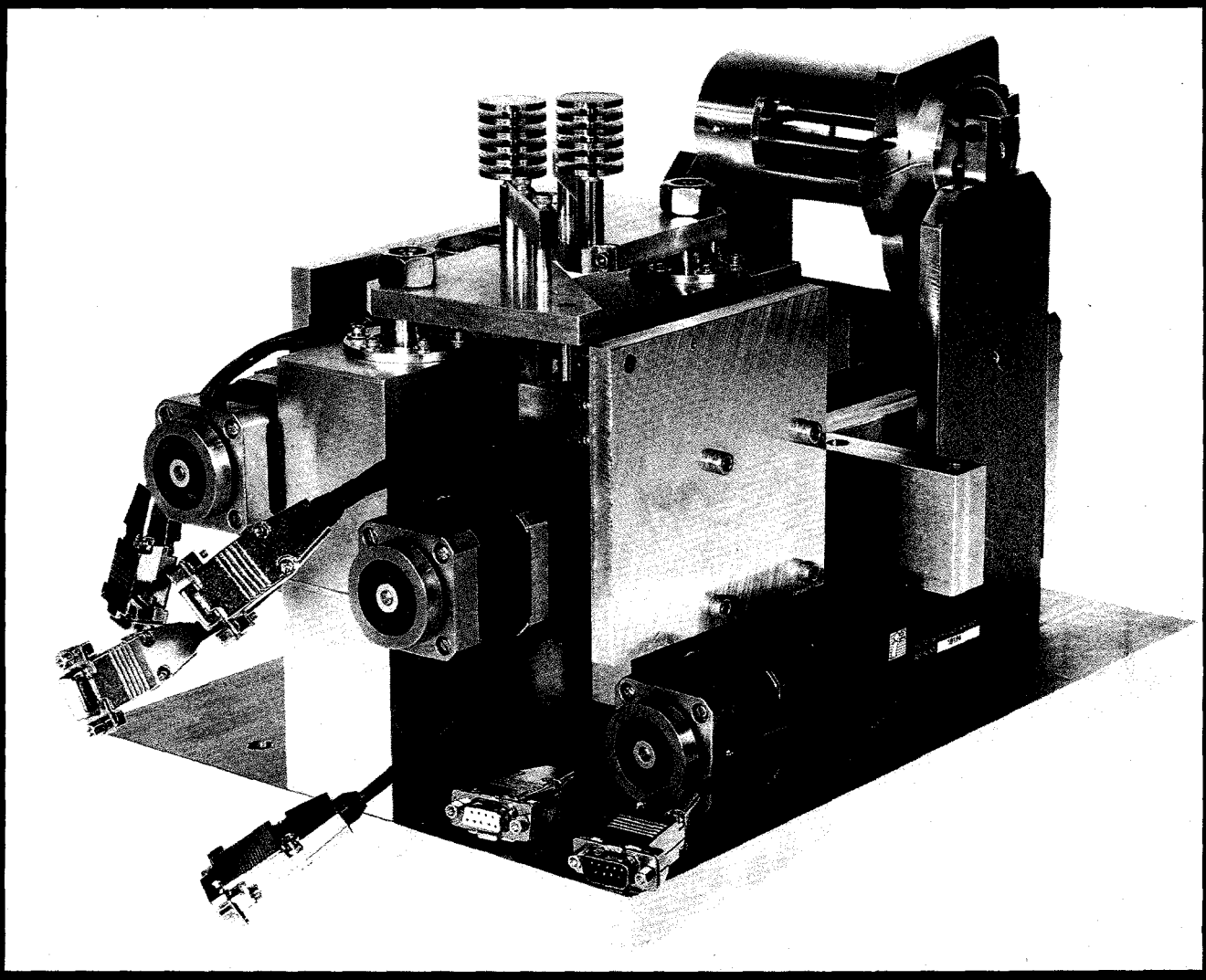
Beam line	Research Program	Energy (keV)	Affiliation	Local Contact	Spokesperson
X22C	Diffraction studies of magnetic and structural phase transformations; surface scattering	3-12	BNL-Physics ANL	J Hill 516-344-3736 516-344-4730	D Gibbs 516-344-4608
X23A2	EXAFS	5.4-30	NIST	J Woicik 516-344-5823 516-344-5236 S Chu 516-344-3923 301-975-5975	J Woicik 516-344-5236 516-344-5823
X23A3	Topography; small-angle scattering	5-30, WB	NIST	D Fischer 516-344-5177 S Chu 516-344-3923 516-346-9285	G Long 301-975-5975
X23B	EXAFS; scattering; crystallography	3-11	Naval Res Lab	J Kirkland 516-344-2258	T Elam 202-767-3015
X24A	Atomic, molecular, and optical physics with x-rays	1.8-5.0	NIST ANL	B Karlin 516-344-7863 516-344-5624	T Jach 301-975-2362
X24C	Photoemission and reflectance spectroscopy	2-1500 eV	Naval Res Lab	J Rife 202-767-4654 J Kirkland 516-344-2258	J Rife 202-767-4654 J Kirkland 516-344-2258
X25	High Q-resolution elastic scattering	> 3	BNL-NSLS	L Berman 516-344-5333 Z Yin 516-344-5525 516-344-5625	L Berman 516-344-5333
X26A	Dev. and application of analytical techniques (e.g. microprobe)	4-20, WB	BNL-DAS U of Chicago U of Georgia BNL-Biology Cold Spring Harb Lab	G Shea-McCarthy 516-344-2229	S Sutton 312-702-9930
X26C	Dev. and applic. of x-ray microscopy techniques; Laue diffraction protein crystallography	4-30, WB	BNL-DAS U of Chicago BNL-Biology U of Georgia Cold Spring Harb Lab	G Shea-McCarthy 516-344-2229	S Sutton 312-702-9930
X27A	Instrument development		BNL-NSLS	B Dowd 516-344-2738	DP Siddons 516-344-2738 516-344-5627

Beam line	Research Program	Energy (keV)	Affiliation	Local Contact	Spokesperson
X27B	Instrument development		BNL-NSLS	E Johnson 516-344-4603	E Johnson 516-344-4603
X27C	Instrument development		BNL-NSLS	B Dowd 516-344-2738	DP Siddons 516-344-2738 516-344-5627
X28A	Instrument development; Photon-based diagnostics and detector development		BNL-NSLS	P Stefan 516-344-2117	P Stefan 516-344-2117
X28B	Photon-based diagnostics and detector development		BNL-NSLS	P Stefan 516-344-2117	P Stefan 516-344-2117
X28C	Photon-based diagnostics and detector development		BNL-NSLS	P Stefan 516-344-2117	P Stefan 516-344-2117
X29A	(Unassigned)				
X29B	(Unassigned)				
X30	Diagnostic				

Beamline X27B: Photograph of the new "mask writer" developed by E. Johnson and C. Milne of the NSLS for use on beamline X27B. Through the use of variable apertures, the mask writer allows the creation of DXRL (Deep X-Ray Lithography) masks in one step instead of the usual three steps, saving not only time but also a large investment in capital equipment.

SEVEN

RESEARCH ANTHOLOGY



LIGHTING THE WAY TO THE FUTURE:

An Anthology of Improvements, Developments, and Research by NSLS Staff and Collaborators

Following the commissioning phase of a scientific facility, it is essential to invent, adapt and improve new technologies so that the specification and performance of the facility is upgraded over it's lifetime. It is equally important that staff keep their expertise and research interests at the cutting edge and contribute, based on their unique experience, to the present and next generation of experiments at existing facilities and to the specification and R & D on which the next generation of facilities will be based.

A synchrotron radiation facility such as the National Synchrotron Light Source (NSLS) at Brookhaven National Laboratory supports a very wide range of science which is dependent on the breadth of the electromagnetic spectrum which is generated. Scientists from many disciplines use radiation from the far infra-red (λ = 12 mm, Energy = 0.1 meV) through to extreme gamma rays (λ = 4 fm, Energy = 300 MeV). All aspects of the facility need continual improvement, development and research including the source itself, the optics of beamlines, experimental concepts and the performance of detectors. This collection of papers shows the scope of past work by NSLS staff and their collaborators, serves as a reminder of their achievements and as an indicator of the range, quality and quantity of work which is required to maintain a scientific user facility at the cutting edge.

Michael Hart
Chairman, NSLS

* * * * * * * * * * * * * * * * *

SEMINAL PAPERS ON STORAGE RING CONCEPTS

Coherent Synchrotron Radiation in the SXLS Phase I Electron Storage Ring

J. B. Murphy, S. Krinsky, and R.L.Gluckstern, "Longitudinal Wakefield for Synchrotron Radiation," Proc. 1995 Part. Accel. Conf., Dallas, TX (1995).

*J. B. Murphy and S. Krinsky, "Millimeter Wave Coherent Synchrotron Radiation in the SXLS Phase I Electron Storage Ring," Nucl. Instrum. Meth. A **346**, 571 (1994).*

It is suggested that employing a superconducting RF cavity in the low energy SXLS Phase I storage ring would facilitate the generation of coherent synchrotron radiation in the far infrared. This might provide a path to extend the infrared program now rapidly growing on the VUV Ring. Also, operation of such a storage ring with electron bunch length (0.3mm) an order of magnitude shorter than presently achieved, will explore a new regime of accelerator physics, where the beam impedance due to synchrotron radiation is the dominant ring impedance.

SXLS Phase I Storage Ring

J. B. Murphy, R. Biscardi, J. Bittner, L.N. Blumberg, E. Bozoki, E. Desmond, H. Halama, R. Heese, H. Hsieh, J. Keane, S. Kramer, R. Nawrocky, T. Romano, J. Rothman, J. Schuchman, M. Thomas, J.M. Wang, "Commissioning of the Phase I Superconducting X-ray Lithography Source (SXLS) at BNL," Proc. 1991 IEEE Part. Accel. Conf., San Francisco, CA (1991) p. 1107.

R. Heese and T. Romano, "The Ultra-Fast Injection Kicker for SXLS," Proc. 1991 IEEE PAC, San Francisco, CA (1991), p. 993.

As part of the superconducting x-ray lithography source project funded by DARPA, a 200 MEV electron storage ring was built and commissioned to carry out studies of injection into compact storage rings. Currents as high as 1.3 Amp were stored. The novel injection scheme utilized a single fast kicker magnet.

Global Orbit Feedback: 1989 R&D 100 Award.

*L.H. Yu, E. Bozoki, J. Galayda, S. Krinsky, G. Vignola, "Real Time Harmonic Closed Orbit Correction," Nucl. Instrum. Meth. A **284**, 268 (1989).*

The first real time feedback systems to stabilize the entire orbit in a storage ring were developed at the NSLS. These systems have improved the orbit stability at the NSLS by an order of magnitude. We are now developing new digital global orbit feedback systems as an improvement over the existing analog systems. A digital design will allow more flexibility in the orbit correction algorithm and will provide for the use of an increased number of position monitors and correction dipoles.

Vignola Lattice

G. Vignola, "The Use of Gradient Magnets in Low Emittance Electron Storage Rings", Proc. Synch. Rad. Instrum. Conf., Stanford, CA (1985).

Gaetano Vignola developed a triple bend achromatic lattice utilizing gradients in the bending magnets. This design was adopted at Lawrence Berkeley National Laboratory for the Advanced Light Source storage ring.

Chasman-Green Lattice

*R. Chasman, G. K. Green and E. M. Rowe, "Preliminary Design of a Dedicated Synchrotron Radiation Facility," IEEE Trans. Nucl. Sci. **NS-22**, 1765 (1975).*

Proposal for NSLS (1977) BNL 50595, Vol. I and II.

This lattice was the first designed to optimize brightness of the synchrotron radiation sources and to provide many dispersion free straight sections for insertion devices. The design of the third generation hard x-ray sources (ESRF, APS, and SPring-8) are all based on the design of Chasman and Green.

SEMINAL PAPERS ON SCIENCE WITH SYNCHROTRON RADIATION

X-ray Holography

S. Lindaas, M. Howells, C. Jacobsen, A. Kalinovsky, "X-ray In-line Holography Sub-50 nm Resolution Imaging Using Photoresists and Atomic Force Microscope Examination," Jour. of the Optical Soc. of America, 1996, in press.

S. Lindaas, M. Howells, C. Jacobsen, and A. Kalinovsky, "X-ray Holographic Microscopy via Photoresist Recording and Atomic-force Microscope Readout," J. Opt. Soc. Am. A ***13****, 1788 (1996).*

C. Jacobson, M. Howells, J. Kirz, S. Rothman, "X-ray Holographic Microscopy Using Photoresists," Jour. Of the Optical Soc. Of America A ***7****, 1847-1861 (1990).*

M. Howells and J. Kirz developed the first successful soft x-ray holographic apparatus at NSLS, initially on beamline U15 and subsequently using the X1 undulator beamline.

High Energy Resolution Resonant Raman Scattering

M.H. Krisch, C.-C. Kao, F. Sette, W.A. Caliebe, K. Hämäläinen, J.B. Hastings, "Evidence for Quadrupolar Contribution to the Absorption Cross Section at the L_{III} Edge of Gadolinium in Gadolinium Gallium Garnet," Phys. Rev. Lett. B ***74****, 4931 (1995).*

X-ray resonant Raman scattering with total energy resolution of 1 eV is achieved. Since x-ray absorption near edge structure is the intermediate state in the resonant Raman process, analyzing the energies of the scattered photons with high resolution can be used to resolve overlapping features in the absorption spectra if the final states of these features can be separated energetically.

Speckle and Intensity Fluctuation Spectroscopy Using Coherent X-rays

S.B. Dierker, R. Pindak, R.M. Fleming, I.K. Robinson, and L.E. Berman, "X-ray Photon Correlation Spectroscopy Study of Brownian Motion of Gold Colloids in Glycerol," Phys. Rev. Letts. ***75****, 449 (1995).*

M. Sutton, S.G.J. Mochrie, T. Greytak, S.E. Nagler, L.E. Berman, G.A. Held, and G.B. Stephenson, "Observation of Speckle by Diffraction with Coherent X-rays," Nature ***352****, 608 (1991).*

Analysis of the scattering of coherent x-ray beams from disordered materials can provide a wealth of information on their static and dynamic structures, which cannot be had via other methods. In a pioneering experiment on beamline X25, the diffuse scatter, of a suitably-prepared coherent x-ray beam, from a disordered copper-gold alloy crystal was observed, and studied over time as the crystal was driven thermally into an ordered state, revealing the evolution of its ordered crystalline domains. In a later experiment on X25, using a coherent x-ray beam of far higher intensity, the diffusion coefficient associated with the Brownian motion of gold colloid particles dispersed in a glycerol medium was measured through analysis of the temporal correlations among the scattered x-ray photons. The use of x-rays in these experiments, as compared with conventional visible light, has opened the possibility to study very short length scale dynamics, down to atomic length scales, in bulk materials (whether or not in equilibrium) that are opaque to other probes.

Soft X-ray Microscopy and Spectromicroscopy: 1991 R&D 100 Award

J. Kirz, C. Jacobsen, M. Howells, "Soft X-ray Microscopes and their Biological Applications," Quarterly Reviews of Biophysics ***28****, 33 (1995).*

The scanning x-ray microscope was developed by Kirz (SUNY@SB) and Rahrback (NSLS). It provided improved performance and ease of alignment over the imaging x-ray microscopes popular in Europe. The adaptation of the scanning x-ray microscope to provide a microspectroscopic capability was done by Johnson (NSLS) and Ade (NCSU) in collaboration with Kirz. This unique capability enables a wide variety of important materials questions to be attacked, since even the same chemical species show different spectral features in the near-edge region. Thus, for example the different polymers in a polymer mixture can be mapped out using variations in the carbon K-edge structure.

*H. Ade, J. Kirz, S. Hulbert, E. Johnson, E. Anderson and D. Kern, "Scanning Photoelectron Microscope with a Zone Plate Generated Microprobe," Nucl. Inst. & Meth. A **291**, 126 (1990).*

X-ray photoelectron spectroscopy (XPS) is a widely used, technologically important analytical technique for the study of surface chemistry and electronic structure. Standard XPS instruments are devoid of spatial resolution, and commercial (lab based) microscopes have resolution typically no better that 25-100 μm. This instrument takes advantage of the coherence available from an undulator based source to form a microbeam using Fresnel zone-plate optics. The sample is scanned through the beam, and the resulting photoelectron signal correlated with position. With this instrument, we achieved resolution better than 0.3 μm over an energy range of 400 to 700 eV. We also performed some of the first high spatial resolution spectro-microscopy with our first instrument. An improved instrument has subsequently been built at the NSLS, and similar instruments are now found at ALS, ELETTRA, and under construction at SRRC.

Medical Applications of Synchrotron Radiation at the NSLS

W. Thomlinson, "Synchrotron Radiation in the Biosciences," eds. B. Chance, et al, Oxford University Press, New York, 674-680 (1994).

The NSLS is the world leader in breadth of medical research projects and new innovative research programs due to the existence of SMERF and our technical developments of the programs.

Soft X-ray Magneto-Optical Kerr Effect

*C.-C. Kao, C.T. Chen, E.D. Johnson, J.B. Hastings, H.J. Lin, G.H. Ho, G. Meigs, J.-M. Brot, S.L. Hulbert, Y.U. Idzerda, C. Vettier, "Dichroic Interference Effects in Circularly Polarized Soft-X-Ray Resonant Magnetic Scattering," Phys. Rev. B **50**, 9599 (1994).*

*C.-C. Kao, J.B. Hastings, E.D. Johnson, D.P. Siddons, G.C. Smith, G.A. Prinz, "Magnetic Resonant Exchange Scattering at the Fe L_{II} and L_{III} Edges," Phys. Rev. Lett. **65**, 373 (1990).*

Dramatic enhancement of the magneto-optical Kerr effect was observed near the L_{II}, L_{III} edges of 3d transition elements and the M_{IV}, M_V edges of rare earth elements using both linearly and circularly polarized soft-x-rays. The element-specific nature of the probe and the enhanced magnetic sensitivity make it an important tool in the study of magnetic thin films and multilayers.

Spin-Polarized Photoemission

*P.D. Johnson, N.B. Brookes, S.L. Hulbert, R. Klaffky, A. Clarke, B. Sinkovic, N.V. Smith, R. Celotta, M.H. Kelly, D.T. Pierce, M.R. Scheinfein, B.J. Waclawski, and M.R. Howells, "Spin-Polarized Photoemission Spectroscopy of Magnetic Surfaces Using Undulator Radiation," Rev. Sci. Instrum. **63**, 1902 (1992).*

Spin-polarized photoemission, in which the spin of electrons photoemitted from the surface of a well-characterized, usually magnetic, solid is measured in addition to their energy and angle, can be further subdivided into core-level or valence-band types. Core-level spin-polarized photoemission is practiced at NSLS by two groups (P. Johnson, BNL Physics and B. Sinkovic, NYU) at various soft x-ray beamlines, but valence-band spin-polarized photoemission is all performed at the purpose-built U5UA beamline. This undulator-based beamline is a unique national resource, providing high flux and high photon energy resolution and a dedicated spin-polarized photoemission end station based on the NIST compact low-energy spin polarimeter. Both the core-level and valence-band programs have produced a wealth of significant results in the area of surface magnetism, including especially the discovery and measurement of surface and interface states in thin film magnetic systems which are at the heart of the magnetic recording industry. For example, one class of experiment at beamline U5UA has examined the development of interfacial magnetism when a noble metal is deposited on a ferromagnetic substrate and the subsequent evolution of interfacial states into spin-polarized quantum well states as the overlayer films become thicker. These studies have provided the first indication that spin polarization effects are present in the non-magnetic layer of the associated magnetic multilayers. Indeed, it is these spin-polarized quantum well states that are thought to mediate the oscillatory exchange coupling in technologically important magnetic multilayers.

Nuclear Forward Scattering

J.B. Hastings, D.P. Siddons, U. van Bürck, R. Hollatz, and U. Bergmann, "Mössbauer Spectroscopy using Synchrotron Radiation," Phys. Rev. Lett. ***66****, 770 (1991).*

For nearly twenty years prior to this work the idea of using synchrotron radiation for Mössbauer spectroscopy had been proposed. This work was the first demonstration of the technique that is now used worldwide to do Mössbauer spectroscopy in the time domain, namely measure the time evolution of the delayed nuclear forward scattering.

The use of high-order Bragg reflections to generate extremely high-resolution beams for various x-ray physics experiments was brought to practical utility at NSLS. The optical layouts and principles embodied in these instruments have been widely emulated. At the time of our NFS experiments (see above) the device used for those measurements was the highest resolving power x-ray monochromator in the world.

Infrared Beamline IR4

G. P. Williams, "The Initial Scientific Program at the NSLS Infrared Beamline," Nucl. Instrum. Meth. A ***291, 8*** *(1990).*

The development of the infrared beamline U4IR and its scientific program was a unique contribution from the NSLS. The beamline and accelerator scientists worked together to eliminate sources of noise, and the global orbit feedback system played an important role in the success of the infrared program. At the present time many laboratories around the world are planning the development of infrared beamlines based on the success at the NSLS including LURE, France; Daresbury, England; MAX Lab, Sweden; SRRC, Taiwan; ALS, Berkeley; ALADDIN, Wisconsin.

Tunable Linear X-ray Polarimeter

D. P. Siddons, M. Hart, Y. Amemiya, and J. B. Hastings "X-ray Optical Activity and the Faraday Effect in Cobalt and its Compounds," Phys. Rev. Lett. ***64****, 1967 (1990).*

M. Hart, D.P. Siddons, Y. Amemiya, and V. Stojanoff, "Tunable X-ray Polarimeters for Synchrotron Radiation Sources," Rev. Sci. Instrum. ***62****, 2540 (1991).*

This instrument was the first to demonstrate the x-ray Faraday effect in a magnetic metal and x-ray optical activity in a chiral compound. This instrument was also the first x-ray polarimeter with a spectroscopic capability, and was thus able to observe resonance phenomena analogous to those seen in absorption, but with higher sensitivity.

STORAGE RING ENHANCEMENT

Fourth Harmonic Bunch Lengthening Cavity on VUV Ring

R. Biscardi, S.L. Kramer, G. Ramirez, "Bunch Length Control in the NSLS VUV Ring," Nucl. Instrum. Meth. A ***366****, 26 (1995).*

The lifetime of the electron beam in the VUV Ring is limited by intrabunch Coulomb scattering, and hence is inversely proportional to the bunch density. For high brightness one wants to keep the transverse dimensions of the bunch small, but for most experiments increasing the bunch length is acceptable. The lifetime of the beam in the VUV Ring has been doubled by use of a second RF cavity operating at 211 MHZ, which is the fourth harmonic of the fundamental RF cavity. Stable operation of this system required the development of a novel approach to the control of the phase of the RF waveform.

Small Gap Undulator

P. Stefan, S. Krinsky, G. Rakowsky, and L. Solomon, "Small-Gap Undulator Experiment on the NSLS X-Ray Ring," Proc. 1995 Part. Accel. Conf., Dallas, TX (1995).

Utilizing the small value of the vertical betafunction at the center of the X-Ray Ring insertions, an undulator with a 16cm period has been successfully operated with a vertical electron aperture of only 3 mm with only slight reduction in the beam lifetime. This provides strong support for the belief that small gap undulators will play an important role in the future at synchrotron radiation facilities. Presently, a small gap device is being built in collaboration with SPring-8 in Japan, with the permanent magnet material in the ring vacuum, so that the magnet gap will only be a few hundred microns larger than the beam aperture. This device will be tested in the X-Ray Ring.

Time-varying Elliptically Polarized Wiggler

E. Gluskin, D. Frachon, P.M. Ivanov, J. Maines, E.A. Medvedko, E. Trakhtenberg, L.R. Turner, I. Vasserman, G.I. Erg, Yu.A. Evtushenko, N.G. Gavrilov, G.N. Kulipanov, A.S. Medvedko, S.P. Petrov, V.M. Popik, N.A. Vinokurov, A. Friedman, S. Krinsky, G. Rakowsky, and O. Singh, "The Elliptical Multiple Wiggler Project," Proc. 1995 Part. Accel. Conf., Dallas,TX (1995).

A. Friedman, S. Krinsky and E. Blum, "Polarized Wiggler for the NSLS X-Ray Ring" (1992) BNL-47317.

In collaboration with Argonne and the BINP, Novosibirsk, Russia, an elliptically polarized wiggler has been constructed and operated in the X-Ray Ring with the horizontal wiggler field generated by an electromagnet operated AC to produce radiation with a time-varying circular polarized component. The AC elliptically polarized wiggler makes it possible to detect the very weak signatures of circular dichroism and other effects associated with right versus left handedness of some physical systems. The key technical challenge, which was successfully met, was to oscillate the horizontal wiggler field without moving the electron beam and disturbing any of the experimenters using other beamlines around the X-Ray Ring. At 2 Hz, a residual orbit motion of less than 0.5 micron has been observed, and the device has run several months in regular X-Ray operations without complaint from other users. We are now working to achieve 100 Hz operation of the wiggler.

Beam Based Storage Ring Lattice Modeling

J. Safranek, "Experimental Determination of Linear Optics Including Quadrupole Rotations," Proc. 1995 Part. Accel. Conf, Dallas,TX (1995).

This approach uses the very precise orbit measurements now available, to calibrate the mathematical model of the storage ring. In the X-Ray this method has been used to reduce the horizontal and vertical emittances. It has been employed at the ALS at Berkeley to eliminate a beta-beat caused by variation in the strength of the defocusing quadrupoles. There are plans to use this program at MAXLAB, SPEAR, ALLADIN and APS.

THEORETICAL WORK ON PHOTON SOURCES

Theory of Short Wavelength FEL Amplifiers

Proposal for the DUV Free Electron Laser (1994) BNL 49713.

L.H. Yu, S. Krinsky, R. L. Gluckstern and J.B.J. van Zeijts, "The Effect of Wiggler Errors on FEL Gain," Phys. Rev. A ***45****, 1163 (1992).*

L.H. Yu, "Generation of Intense UV Radiation by Subharmonically Seeded Single Pass FEL," Phys. Rev. A ***44****, 5178 (1991).*

I. Ben-Zvi, L.F. Di Mauro, S. Krinsky, M.G. White, and L.H. Yu, "Proposed UV-FEL User Facility at BNL," Nucl. Instrum. Meth. A ***304,*** *181 (1991).*

L. H. Yu, S. Krinsky and R.L Gluckstern, "Calculation of Universal Scaling Function for FEL Gain," Phys. Rev. Lett. ***64****, 3011 (1990).*

S. Krinsky, "Introduction to the Theory of Free Electron Lasers," AIP Conf. Proc. ***153****, 1015 (1987).*

J.M. Wang and L.H. Yu, "A Transient Analysis of a Bunched Beam Free Electron Laser," Nucl. Instrum. Meth. A ***250****, 484 (1986).*

S. Krinsky and L.H. Yu, "Output Power in Guided Modes for Single Pass Free Electron Laser Starting from Shot Noise," Phys. Rev. ***35****, 3406 (1985).*

R. Bonifacio, C. Pelligrini, and L.M. Narducci, "Collective Instabilities and High-gain Regime in a Free Electron Laser," Opt. Commun. ***50,*** *373 (1984).*

There has been a continuing effort to develop the theory underlying short wavelength free electron laser amplifiers. Above is given a selection of the key publications resulting from the work at the NSLS. Subjects covered include: description of the high gain exponential growth regime, self amplified spontaneous radiation, effect of electron beam quality on gain, gain reduction due to wiggler errors, subharmonically seeded FELs, proposal for a user facility utilizing subharmonically seeded FELs. A large scale experiment to study short wavelength FEL amplifiers is under construction at the TESLA facility at DESY, Germany. At Brookhaven we are working to carry out experiments on FEL amplifiers at the Accelerator Test Facility and the Source Development Laboratory.

Theory of Undulator Radiation

S. Krinsky, "Undulators as Sources of Synchrotron Radiation," IEEE Trans. Nucl. Sci. ***NS-30****, 3083 (1983).*

M.R. Howells, J. Kirz, and S. Krinsky, "A Beamline for Experiments with Coherent Soft X-rays," (1982) BNL-32519.

An analysis of undulator radiation was carried out which showed that low-beta insertions were suitable locations for these devices. This led to the development of the soft x-ray undulator in the X1 straight section of the X-Ray Ring. The relatively large horizontal angular spread does not degrade the brightness, but does allow splitting the undulator beam to illuminate three separate experiments.

X-RAY OPTICS

X-ray Schlieren Imaging

D. Chapman, W. Thomlinson, and Z. Zhong (to be published).

A new x-ray technique applied to mammographic imaging. Separation of the absorption image and index of refraction image should provide additional information to the mammographers about various tumors.

Collimating Mirrors for X-ray Beamlines

J.B. Hastings, "NSLS EXAFS Beamline Design," BNL Informal Report BNL-30617.

In general at typical x-ray synchrotron sources the vertical opening angle of the bending magnet radiation is greater than the intrinsic width of typical perfect crystal rocking curves. In order to maintain high throughput and improve the energy resolution of standard two-crystal instruments the use of an x-ray collimating mirror was proposed followed by the monochromator and then a condensing optic to provide a small focus at the sample position. This idea was executed at X19 and has proven very successful, reducing the bandwidth of the monochromator by almost a factor of three with very little loss in intensity.

High Resolution Bent-Crystal Analyzers

K. Hämäläinen, M. Krisch, F. Sette, C.-C. Kao, W. Caliebe, J.B. Hastings, "High Resolution X-ray Spectrometer Based on a Cylindrically Bent Crystal in Nondispersive Geometry," Rev. Sci. Instrum. ***66****, 1525 (1995).*

V. Stojanoff, K. Hämäläinen, D.P. Siddons, J.B. Hastings, L.E. Berman, S. Cramer, G. Smith, "A High-resolution X-ray Fluorescence Spectrometer for Near Edge Absorption Studies," Rev. Sci. Instrum. ***63****, 1125 (1992).*

Spherically and cylindrically bent crystal analyzers with large solid angle acceptance were developed for inelastic x-ray scattering experiments. These analyzers can also be used in high resolution fluorescence analysis and fluorescence yield x-ray absorption spectroscopy. Multi-element analyzer array is being developed at the moment.

High Resolution Inelastic X-ray Scattering

C.-C. Kao, W.A. Caliebe, K. Hämäläinen, M. Krisch, J.B. Hastings, "The Studies at the Inelastic Scattering Beamline at the NSLS," National Conference on Synchrotron Radiation Instrumentation 1995, Argonne National Laboratory, October 17-20 1995. Rev. Sci. Instrum. (to be published).

The inelastic x-ray scattering program is focused on the study of elementary electronic excitations in condensed matters. In comparison with other inelastic scattering probes, such as light scattering and neutron scattering, inelastic x-ray scattering is unique in providing frequency- and wavevector-dependent dielectric responses of materials.

Optimized Beamline for Low Energy (2-8 keV) Spectroscopy Techniques

L.R. Furenlid, P.E. Stefan, and J.B. Hastings, 5th International Conference on Synchrotron Radiation Instrumentation, Stony Brook, NY, 1994 (unpublished).

Beamline X19A has been developed through a series of R&D projects to optimize the transport, monochromatization, and detection of x-rays in the 2-8 keV domain. Key components include a full collimating mirror/focussing mirror arrangement for optimum resolution and intensity; an 8 = μm Be foil thin window and associated fast shutter system; a horizontal feedback system to keep beam position constant on the sample; triple bounce monochromator crystals for superior rejection of harmonics via detuning; a high performance, high stability UHV monochromator with external drive componentry; a modular, kwik flange based sample holder and cryostat system for rapid setup of air excluded beam paths, and low energy ion-chamber detectors.

A Single Crystal Bent Laue Monochromator for Coronary Angiography

P. Suortti, W. Thomlinson, D. Chapman, N. Gmur, D.P. Siddons and C. Schulze, Nucleur Instrument Methods, A ***336****, 304 (1993).*

The development of the bent Laue crystal monochromator increased the available flux for angiography by a factor of 6. This allowed greater flexibility in the human imaging program at the NSLS. The concept has been used at most major synchrotron medical research centers and for many programs, especially on bending magnet beamlinesi, where an increase in flux and bandwidth is useful.

High Power Diamond Crystal X-ray Monochromator

L.E. Berman, J.B. Hastings, D.P. Siddons, M. Koike, V. Stojanoff and M. Hart, "Diamond Crystal X-ray Optics for High-power-density Synchrotron Radiation Beams," Nuclear Instruments and Methods in Physics Research A ***329,*** *555 (1993).*

L.E. Berman and M. Hart, "Preserving the High Finesse of X-ray Undulator Beams from Perfect Water-jet-cooled Diamond Monochromators," Nuclear Instruments and Methods in Physics Research A ***334,*** *617 (1993).*

Radiated x-ray power densities at present and future synchrotron radiation sources are unprecedented, and cannot be tolerated by conventional silicon and germanium crystal monochromators designed to diffract x-rays efficiently and simultaneously preserve the ray optics of the primary beam, when used at room temperature. Single crystal diamond is an attractive alternative to silicon and germanium as a room temperature x-ray monochromator, because of its substantially superior mechanical and thermal properties, foremost among them being an exceptionally high thermal conductivity. Experiments performed at X25 have proven the efficacy of diamond as a high-power-density x-ray monochromator material, with its implementation as such carried out in a relatively simple and inexpensive manner. This bodes well for the highest power beam lines being commissioned at the newer sources such as the APS, where plans to use diamond monochromators are being pursued.

Adaptive Silicon Crystal X-ray Monochromators

L.E. Berman and J.B. Hastings, "An adaptive Crystal Bender for High Power Synchrotron Radiation Beams," Proc. SPIE ***1739****, 489 (1993).*

L.E. Berman, M. Hart, and S. Sharma, "Adaptive Crystal Optics for Undulator Beamlines," Nucl. Instr. and Meth. A ***321****, 617 (1992).*

L.E. Berman and M. Hart, "Adaptive Crystal Optics for High Power Synchrotron Sources," Nucl. Inst. and Meth. A ***302,*** *558 (1991).*

A foremost challenge to proper operation of an x-ray monochromator in a high power x-ray beam, lies in eliminating the crystal Bragg plane strains arising from thermal distortion, which reduce the diffraction efficiency and spoil the beam brightness. A major research program at beam line X25 has been undertaken to study this, with implicit benefits for existing high power beam lines such as X25, as well as for future ones such as those under construction at the APS. A solution, which has been adopted for the X25 beam line monochromator, involves adaptive mechanical compensation of the thermal strain field. This is centered on the use of a bendable triangular silicon wafer that is
thermally coupled to a cooled heat sink via a liquid metal interface. Tests and use have demonstrated that this device faithfully delivers the intrinsic x-ray beam brightness at X25.

X-ray Optical Delay Line.

S. Joksch, W. Graeff, J.B. Hastings, and D.P. Siddons, "Performance of an X-ray Optical Delay Line with Synchrotron Radiation," Rev. Sci. Instrum. ***63****, 1114 (1992).*

An optical delay line for x-rays was demonstrated which can deliver a monochromatic beam with a variable delay following illumination of the sample with the broad band SR spectrum. This is a technique that should find usefulness in a wide variety of pump probe experiments where statistical significance can be acquired through cyclic excitation.

High Energy, High Q-resolution X-ray Scattering

J.B. Hastings and D.P. Siddons, "The Use of High Energy Synchrotron Radiation for X-ray Scattering," Proc. of 2nd European Conf. on Progress in X-ray Synchrotron Radiation Research, A. Balerna, E. Bernieri, and S. Mobilio, Eds., Vol. 25, p. 159, SIF, Bologna (1990).

The use of high energy x-rays for a broad range of x-ray scattering experiments is summarized. This work describes research started in collaboration with Dr. Jochen Schneider from HASYLAB. Both our group and a team at HASYLAB have continued to pursue this effort and it has expanded to include beamlines at ESRF and SPring-8.

Mosaic Crystal Two-crystal Monochromator

D. Hohlwein, D.P. Siddons, and J.B. Hastings, "A Graphite Double Crystal Monochromator for X-ray Synchrotron Radiation," J. Appl. Cryst. ***21****, 911 (1988).*

A two crystal monochromator utilizing mosaic graphite crystals was constructed. It provides a significant increase in bandwidth and intensity when compared with typical perfect crystal instruments. Furthermore, in the two crystal arrangement, the mosaic spread only contributes to an increase in the divergence in the non-Bragg direction. This idea will be useful in a variety of quasi-monochromatic x-ray techniques including diffuse scattering and various film techniques applied to structure solution.

Fluorescence Detection for Low-Z X-ray Spectroscopy

J. Stöhr, E.B. Kollin, D.A. Fischer, J.B. Hastings, F. Zaera, and F. Sette, "Surface Extended X-ray Absorption Fine Structure of Low Z Adsorbates Studied with Fluorescence Detection," Phys. Rev. Lett. ***55,*** *1468 (1985).*

This work demonstrated the efficacy of using fluorescence detection for low z x-ray spectroscopy. Prior to this work electron detection was thought to be the only viable measure of the variation in absorption for low z-materials. Application of fluorescence detection has opened the field of x-ray spectroscopy to low z elements in non UHV environments.

High-Resolution Synchrotron Powder Diffraction

J.B. Hastings, W. Thomlinson, and D.E. Cox, "Synchrotron X-ray Powder Diffraction," J. Appl. Cryst. ***17****, 85 (1984).*

The use of crystal analyzers for monochromatic SR powder diffraction is presented in detail including all the advantages of their use. Also, the detailed analysis of measured peak shapes is presented. This contribution has lead to the worldwide use of crystal analyzers for high resolution SR powder diffraction.

Kirkpatrick-Baez Multilayer Optics for an X-ray Microprobe

M.R. Howells and J.B. Hastings, "Design Considerations for an X-ray Microprobe," NIM ***208****, 379 (1983).*

Design considerations for an x-ray microprobe were presented and the conclusion drawn that the most effective instrument would be a Kirkpatrick-Baez mirror pair where the reflecting optics were coated with multilayers. This choice provides the best compromise of large demagnification and quasi-monochromaticity. The idea has been executed by several groups including people from LBNL.

Sagittally Focusing Crystal Monochromators

C. Sparks, B. Borie, J.B. Hastings. "X-ray Monochromator Geometry for Focusing Synchrotron Radiation above 10 KeV," NIM ***172,*** *237 (1980).*

The concept of using crystals to do sagittal focusing was presented. The optimal position of the monochromator was discussed giving the 3:1 position as that of choice. Detailed calculations of collection efficiency were presented. This paper is the basis for all sagittal focusing systems presently in use at synchrotron sources.

ULTRA VIOLET OPTICS

Economical Upgrade Path for Outdated Toroidal Grating Monochromators.

N. V. Smith, S. L. Hulbert, P. D. Johnson, and J. L. Erskine, "Spherical-grating Monochromator System with Circular-polarization Capability for the U5U Undulator at Brookhaven," Nucl. Instrum. & Methods A ***347,*** *119 (1994).*

It has been shown that out-of-date soft x-ray toroidal grating monochromators (TGMs) can be efficiently, and therefore cheaply, upgraded to state-of-the-art spherical grating monochromators (SGMs) by replacing only the reflecting and diffracting optical elements. In most cases, the collecting and focusing functions in these beamlines are provided by a single mirror, usually of toroidal figure. An appropriate replacement toroid, near unity magnification, can provide the same throughput as the "standard" Kirkpatrick-Baez mirror pair. The new resulting beamline, dubbed TSGM for toroidal-mirror SGM, provides photon energy resolution and flux equal to the "standard" SGM configuration, and can fit in substantially less floor space since it has no horizontal deflections.

UHV Compatible Two-Crystal Monochromator.

P. Cowan, J.B. Hastings, T. Jach, and J. Kirkland, "A UHV Compatible Two-Crystal Monochromator for Synchrotron Radiation," NIM ***208,*** *349 (1983).*

J. Golovchenko and co-workers had developed a mechanical coupling to provide a constant offset wide angular range two crystal x-ray monochromator. This mechanical design was adapted to a UHV environment. Several innovations were made, including a UHV-compatible long-stroke piezo translator. These instruments are used in several locations on the x-ray floor and remain the most functional of all designs to date for this application. It is of particular importance for x-ray energies below 4 KeV.

INFRA RED OPTICS

Research on the First Infrared Beamlines

F.M. Hoffmann, B.N.J. Persson, W. Walter, D.A. King, C.J. Hirschmugl, and G.P. Williams, "Anti-absorption Resonances in the Infrared Reflectance Spectroscopy of Alkali-Cu(111) Adsorbate Systems," Phys. Rev. Lett. ***72,*** *1256 (1994).*

R.J. Hemley, Z.G. Soos, M. Hanfland, and H.-K. Mao, "Charge Transfer States in Dense Hydrogen," Nature ***369,*** *384 (1994).*

C. Meade, J.A. Reffner, and E. Ito, "Synchrotron Infrared Absorbency Measurements of Hydrogen in $MgSiO_3$ Perovskite," Science ***264,*** *1558 (1994).*

G.L. Carr, M. Quijada, D.B. Tanner, C.J. Hirschmugl, G.P. Williams, S. Etemad, B. Dutta, F. DeRosa, and T. Venkatesan, "Fast Bolometric Response by High T_c Detectors Measured with Subnanosecond Synchrotron Radiation," Appl. Phys. Lett. ***57,*** *2725 (1990).*

L. Forro, G.L. Carr, G.P. Williams, D. Mandrus, L. Mihaly, "Far Infrared Transmission Study of Single Crystal $Bi_2Sr_2Ca_2Cu_2O_x$," Phys. Rev. Lett. ***65,*** *1941 (1990).*

The U4IR beamline was the first infrared beamline developed on the NSLS VUV Ring. The scientific program was directed toward far infrared spectroscopy of adsorbates on metal surfaces; a model system for exploring the surface physics and chemistry that control catalysis as well as other phenomena. This program determined the importance of interactions between adsorbed atoms and conduction electrons. Other scientific investigations include the first (and only) far infrared spectra of free-standing high-T_c cuprate crystals, and demonstrations of time-resolved measurements (such as pump-probe spectroscopy) that utilize the synchrotron's pulse structure.

The U2B beamline enables high brightness spectroscopy in the mid-infrared. It is used for microspectroscopy studies of materials at extremely high pressures (i.e. geo-physical sciences) and for micro-analysis of materials such as semiconductors, polymers, ceramic composites, biological cells, and even forensics. As a result of a CRADA between the NSLS and the Northop-Grumman Corporation, the NSLS was able to initiate construction on two new infrared beamlines (U12IR and U10), optimized for microspectroscopy and very far infrared spectroscopy.

Lamellar-grating IR Interferometer

K.D. Moeller, T. Sears, H.T. Liu, C.J. Hirschmugl, and G.P. Williams, "A High Resolution Interferometer for use with Synchrotron Radiation," Nucl. Instr. Meth. Phys. Res. A ***319,*** *250 (1992).*

K.D. Moeller, D.P. Siddons, C.J. Hirschmugl, D. Scardino, P. Petrone, D. Carlson, and G.P. Williams, "Two Mirror Wavefront Dividing Interferometer for Infrared Synchrotron Radiation," Appl. Optics ***30,*** *4297 (1991).*

The lamellar grating interferometer is a spectrometer optimized for performance in the very far infrared (wavelengths beyond 100 microns); the region where the NSLS VUV Ring outperforms the standard far IR spectrometer source (the high pressure mercury arc lamp) in both brightness and flux. This is an important spectral range for investigating metals, semiconductors and superconductors, including the "bad metals" which are the central theme of the new joint research initiative between the physics department and the NSLS. The high degree of transverse coherence to the NSLS source enabled a highly efficient, wide-spectral range, wave-front dividing interferometer to be built and demonstrated. The high degree of transverse coherence inherent in synchrotron IR radiation permitted a very simple interferometer design capable of operation over a very large wavelength range. The coherence properties meant that the wavefront could be divided into only two parts (rather than the 20-100 parts used in conventional LGI's). These parts could, therefore, be made of high quality quite easily, thus the coherence could be maintained up to quite short wavelengths (a few microns). The long wavelength limit is diffraction driven at about 5 mm. Key to the advantages of this instrument is its lack of a beamsplitter; essential if such a wide spectral range is to be probed.

CONSTRUCTION AND OPERATION OF THE BNL ACCELERATOR TEST FACILITY: A USER FACILITY FOR THE PHYSICS OF BEAMS

The BNL Accelerator Test Facility (ATF) is this country's only proposal-driven, peer-reviewed user's-facility for accelerator and beam physics, including studies in the generation of high-brightness electron-beams, Free-Electron Laser experiments and many others. Milestone experiments at the ATF include:

Inverse FEL Acceleration of Electrons

A. van Steenbergen, J. Gallardo, J. Sandweiss, J.-M. Fang, "Observation of Energy Gain at the BNL Inverse Free-Electron Laser," Phys. Rev. Lett. (to be published).

Generation of Femtosecond Pulses of High-brightness Electrons

X.J. Wang, X. Qiu and I. Ben-Zvi, "Experimental Observation of High-Brightness Micro-Bunching in a Photocathode RF Gun," Phys. Rev. Lett. (submitted).

Electron beam bunches with an extremely high brightness have been produced by the BNL gun at the ATF, from a nanoCoulomb at 10 picosecond FWHM with rms normalized emittance of 4 mm mrad to 40 picoCoulomb at 0.4 picosecond FW and 0.5 mm mrad.

Slice Emittance Measurement

X. Qiu, K. Batchelor, I. Ben-Zvi and X.J. Wang, "Demonstration of Emittance Compensation Through the Measurement of the Slice Emittance of a 10 Picosecond Electron Bunch," Phys. Rev. Lett. ***76****, 3723 (1996).*

This electron beam diagnostic technique makes it possible to study the phase space of the electron beam in 6-D phase space with picosecond resolution. It is an essential element for further improvement of electron beam brightness.

Inverse Cherenkov Acceleration of Electrons

W.D. Kimura, G.H. Kim, R.D. Romea, L.C. Steinhauer, I.V. Pogorelsky, K.P. Kusche, R.C. Fernow, X.J. Wang and Y. Liu, "Inverse Cerenkov Acceleration of Electrons by 3.7 MeV using 580 MW of the ATF's CO_2 Laser," Phys. Rev. Lett. ***74****, 546 (1995).*

High-upshift, Forward Angle Smith-Purcell Radiation Measurement

K.J. Woods, J.E. Walsh, R.E. Stoner, H.G. Kirk, R.C. Fernow, "Forward Directed Smith-Purcell Radiation from Relativistic Electrons," Phys. Rev. Lett. ***74****, 3808 (1995).*

Development of the High Gain Harmonic Generation FEL

High-Gain Harmonic-Generation (HGHG) FEL has been developed at BNL's NSLS as a method to achieve UV and x-ray coherent and tunable radiation with a high peak-power, narrow bandwidth, high-stability and single pass amplifier approach.

Chirped-pulse Amplification with HGHG FEL

L.-H. Yu, E. Johnson, D. Li and D. Umstadter, "Femptosecond Free-electron Laser by Chirped Pulse Amplification," Phys. Rev. E ***49****, No. 5, 4480 (1994).*

Development of a Multiple-function Superconducting-undulator

G. Ingold, I. Ben-Zvi, S. Krinsky, D. Lynch, J. Sheehan, L. Solomon, M. Woodle, L. Yu, X. Zhang, W. Sampson, K. Robins, I. Lehrman, R. Heuer, J. Sheehan, D. Weissenburger, "A Superconducting Short Period Undulator for a Harmonic Generation FEL Experiment," Proceedings 1993 Particle Accelerator Conference, Washington DC, May 17-20, (1993).

'Fresh-Bunch' Technique

I. Ben-Zvi, K.M. Yang and L.H. Yu, "The 'Fresh-Bunch' Technique in FELs," Nuclear Instruments & Methods in Physics Research A ***318****, 726 (1992).*

A Proof-of Principle experiment in High Gain Harmonic Generation

I. Ben-Zvi, A. Friedman, C.M. Hung, G. Ingold, S. Krinsky, L.H. Yu, I. Lehrman and D. Weissenburger, "Design of a Harmonic Generation FEL Experiment at BNL," Nuclear Instruments & Methods in Physics Research A ***318****, 208 (1992)*

ACHIEVEMENTS IN TECHNOLOGY AND ENGINEERING

NSLS-DAC: A Flexible Beamline Control Program

L.R. Furenlid, A. Mayer, and J. Kirkland, "NSLS-DAC: A Flexible Beamline Control Program," Journal de Physique (submitted).

Synchrotron beamline control software was developed in the last year and implemented on the experimental floor on XAS beamlines U7, X11A, X18B, X19A, and X23B. It is currently being implemented on beamline X9B, and in the near future on X23A2. This software presents the novice as well as experienced researchers with an intuitive, graphical-user-interface environment for a full complement of experimental techniques. Though the software is geared for spectroscopy, a full macro capability and the inclusion of calls to user supplied external routines accommodate general purpose data collection. The establishment of this software as a standard on the XAS beamlines on the experimental floor is already resulting in a significant reduction in the resources spent on user training and enhancing experiment quality.

Very High Aspect Ratio and 3-dimensional Micromachining Using Hard X-rays

E.D. Johnson, J.C. Milne, D.P. Siddons, H. Guckel, and J.L. Klein, "Precision Machining with Hard X-rays: Experiments at the NSLS," Synchrotron Radiation News ***9****, no. 4, 10 (1996).*

D.P. Siddons, E.D. Johnson and H. Guckel, "Precision Machining Using Hard X-rays," Synchrotron Radiation News ***7****, 16, (1994).*

At the NSLS, we initiated a program to explore the features of lithography utilizing hard x-rays with the aim of developing methods for the very precise manufacture of macroscopic, three-dimensional structures. We have demonstrated lithographic processing of resist materials to the scale of several centimeters while maintaining precision at the level of microns. This technology allows complex 3-dimensional objects to be machined with sub-micron precision. A production beamline is being constructed based on this work, and on the substantial interest from companies who want to use hard x-ray lithography for manufacturing products.

Multielement Solid State Detector

A. Pullia, L. Furenlid, H.W. Kraner, G. Bertuccio, P.J. Pietraski, and D.P. Siddons, "Multielement Solid State Detector," Rev. Sci. Instrum. (in press).

A multielement detector has been developed for x-ray absorption spectroscopy and diffraction applications at the NSLS. The front end, developed in collaboration with the Instrumentation Division, comprises a silicon wafer based pixel detector and an array of charge sensitive preamplifiers. Powerful NIM-bin based modules based on field programmable gate arrays and modular circuit inserts handle all subsequent signal processing under complete computer control. A significant scientific and engineering effort has lead to outstanding resolution performance. The instrument has been proven in prototype form and is now in a manufacturing stage.

Development of RF Guns, Photocathode Materials and Diagnostic Techniques

X.J. Wang and I. Ben-Zvi, High-Brightness Electron Beam Diagnostics at the ATF, Proc. Beam Instrumentation Workshop, Argonne National Lab., May 6-8, 1996. BNL 63151.

*X.J. Wang, T. Srinivasan-Rao, K. Batchelor, I. Ben-Zvi and J. Fischer, "Measurements on Photoelectrons from a Magnesium Cathode in a Microwave Electron Gun," Nuclear Instruments and Methods in Physics Research A **356**, 159 (1995).*

MacXAFS: An EXAFS Analysis Package for the Macintosh

*C. Bouldin, W.T. Elam, and L.R. Furenlid, "MacXAFS: An EXAFS Analysis Package for the Macintosh," Physica B **208&209**, 190 (1995).*

An analysis package for x-ray absorption spectroscopy was developed to permit real-time analysis during data acquisition, as well as full, documented work for publication. A front-end application which presents a unified interface ties together well tested numerical algorithms for data normalization, background subtraction, Fourier analysis, non-linear least squares fitting, and ab-initio modeling. The package has a world-wide user base numbering in the hundreds.

Testing of APS Vacuum Chambers

C.L. Foerster, C. Lanni, J.R. Noonan and R.A. Rosenberg, "Photon Stimulated Desorption Measurement of an Extruded Aluminum Beam Chamber for the Advanced Photon Source," 42nd National Symposium of Amer. Vac. Soc., Oct. 1995.

PSD measurement on X28A beamline of an extruded aluminum APS storage ring chamber. The data was used by ANL to evaluate chamber construction and preparation.

High Stability, High Power Nd:YAG Laser for Photocathode Illumination

M. Babzien, I. Ben-Zvi, J. Fischer, A.S. Fisher, K. Kusche, I.V. Pogorelsky, T. Srinivasan-Rao, "A High Power Picosecond Nd:YAG/CO_2 Laser System for Electron Guns, Laser Acceleration and FEL," Proc. of Lasers '94 Conference, Quebec, Canada, Dec. 12-16, 1994. BNL 61399. Feb. 1995.

High Power, Picosecond Pulse CO_2 Laser

I. Pogorelsky, W.D. Kimura, C.H. Fisher, F. Kannari, N.A. Kurnit, "Approach to Compact Terawatt CO_2 Laser System for Particle Acceleration." Presented at the 6th Workshop on Advanced Accelerator Concepts, Lake Geneva, Wisconsin, June 12-18, 1994. BNL 60826.

Non-linear, Non-instantaneous Adaptive Feed-forward Control System for Linac Energy
*R. Zhang, I. Ben-Zvi and J. Xie, "A Self-Adaptive Feed-forward RF Control System for Linacs," Nuclear Instruments and Methods in Physics Research A **324**, 421 (1993).*

Copper Chamber Desorption Measurements
*C.L. Foerster, H. Halama, G. Korn, M. Calderon and W. Barletta, "Desorption Measurements of Copper and Copper Alloys For PEP II," Vacuum, **44**(5-7), 489 (1993).*
PSD measurements of copper and its alloys for PEP II. Neutral gas, photo electron and scattered photon data taken on beamline U10B. PEP II prototype copper chamber was tested on X28A beamline. Work supported by LLNL and SLAC.

Compact UHV Valve with Field Replaceable Windows
*E.D. Johnson, J. Freeman, F. Powell, "Compact UHV Valve with Field Replaceable Windows," Rev. Sci. Instrum. **63**,1282 (1992).*
There are many applications in synchrotron radiation research where window valves can be usefully employed. Examples include gas cells for monochromator calibration, filters for high-order light rejection, and as vacuum isolation elements between machine and experimental vacua. We took advantage of a new valve seal geometry developed by VAT corporation to make a simple removable window insert in a gate valve sealing plate. The window design was similarly based on a standard geometry available from Luxel Corporation. Working together, we developed what has become a very popular commercial product for both companies, and a high quality, modest cost device for use at many synchrotrons. At present, there are several hundred of these valves in service.

Bittner-Biscardi Receiver for Beam Position Monitor
R. Biscardi and J.W. Bittner, "Switched Detector for Beam Position Monitor," IEEE Proc. 1989 Part. Accel. Conf., Chicago, IL,Vol. III, p. 1516 (1989).
This high precision receiver forms the basis for orbit measurement and control at the NSLS. Duke University FEL Laboratory, ALS at Berkeley, and APS at Argonne plan to use receivers based on this design for all of or a subset of their orbit measurements.

High-Power Ultra-High Vacuum (UHV) Photon Beam Position Monitor
*E.D. Johnson and T. Oversluizen, "Compact High Flux Photon Beam Position Monitor," Rev. Sci. Instrum. **60**, 1947 (1989).*
In synchrotron radiation sources, from the standpoint of the users, *photon beam stability* is vital for the realization of state of the art research. This is particularly true for undulator beamlines where due to the brightness of the source, small shifts in beam position can result in unacceptable intensity and energy fluctuations. Reliable measurement of the photon beam position is necessary to apply stabilization techniques. Prior to this research, no such device existed. The monitor utilizes electrically isolated blades introduced into the edge of the beam. Schemes such as this had been tried before, without success. In our case, a geometry was developed which stabilized the positions of the blades, provided electrical isolation with significant cooling, and embodied an efficient collection geometry for the photoelectrons generated from the blades. This device achieved sub-micron resolution, and has been the acknowledged model for similar instruments placed in *all* of the third generation machines, world wide.

UHV Synchrotron Radiation Pumped Absorber

C.L. Foerster, T.S. Chou H. Halama, and C. Lanni, "Measurements of a Prototype Synchrotron Radiation Pumped Absorber For Future Light Sources," AIP Conf. Proc. ***171****, 334 (1988).*

Measurements were made at NSLS U10B beamline as joint effort of NSLS and LBNL. The concept was used for the ALS at LBNL.

In Situ Reactive Cleaning of X-ray Optics by Glow Discharge

E.D. Johnson and R.F. Garrett, "In Situ Reactive Cleaning of X-ray Optics by Glow Discharge," Nucl. Instrum. & Meth. A ***266,*** *381 (1988).*

E.D. Johnson, S.L. Hulbert, R.F. Garrett, G.P. Williams, and M.L. Knotek, "In Situ Reactive Glow Discharge Cleaning of X-ray Optical Surfaces," Rev. Sci. Instrum. ***58****, 1042 (1987).*

In soft x-ray monochromators, particularly at synchrotron radiation facilities, carbon contamination can severely limit the throughput and resolution of the instrument, even for wavelengths far away from the carbon K edge. We developed a method of in-situ cleaning using RF glow discharges which is capable of complete removal of carbon contamination. The various reactors developed at the NSLS are quite simple, and have been retrofitted to a variety of instruments. The results achieved are far superior, and require significantly less time to obtain than with conventional cleaning methods. This technology, our reactor design, and process method have been adopted at essentially every soft x-ray synchrotron facility in the world.

Demountable UHV Beryllium Window

T. Oversluizen and P.M. Stefan, "Replaceable Be and Al Windows for X-ray Beamlines," Nucl. Instrum. & Meth. A ***266,*** *375 (1988).*

Beryllium windows are essential for a wide range of x-ray apparatus. The standard technology for UHV compatible windows was to vacuum-braze the beryllium wafer into a copper or stainless steel assembly. This process is expensive and inflexible. T. Oversluizen devised a scheme which used soft metal compression seals to capture the beryllium in a stainless steel flange assembly. Thus, the window could be easily replaced if damaged, or remounted into a different assembly if the experiment needs changed. Such a flange assembly is inexpensive to produce, and the beryllium material can be standard sizes, allowing ready production of custom window assemblies.

A Program for Synchrotron Radiation Dose Calculations

D. Chapman, N. Gmür, N. Lazarz and W. Thomlinson,"PHOTON: A Program for Synchrotron Radiation Dose Calculations," Nucl. Instrum. and Meth. A ***266,*** *191 (1988).*

A user friendly program to calculate dose from scattered and direct photon beams through arbitrary absorbers and storage ring. It has been copied (and much improved) by other labs as well as by our staff.

Measurement of Photon Stimulated Desorption of NSLS Beam Chamber

H.J. Halama, C. Foerster, and T. Kobari, "Vacuum Performance of the UV and X-Ray Rings at the NSLS," J. Vac. Sci. Technol., A ***5*** *(4), 2342 (1987).*

Measurements of PSD in a NSLS aluminum vacuum chamber. The data was used to design new higher power beam chambers by the NSLS, BNL and other laboratories worldwide.

Fast Valve Protection System

C. Foerster and R. Larson, "Evaluation of NSLS Beamline Fast Valve Protection System," J. Vac. Sci. Technol., A 5 (4), 2401 (1987).

This valve was designed and built by BNL (T. Oversluizen). Response time, shockwave effects and vacuum sealing were tested to establish beamline protection needs and vacuum sensor locations. The NSLS design was used by Vacuum Generators Ltd. for their fast valve product line.

High Flux Photon Beam Monitor

P. Mortazavi, M.H. Woodle, H. Rarback, D. Shu, and M. Howells, paper SRI Mtg Stanford, CA (1985).

The device first used heatpipes to transport absorbed heat from detector blades to heat exchanger. Eliminated waterflow vibrations at detector and risk of water to UHV leak.

Fast Vacuum Valve for Vacuum Safety

T. Oversluizen, "Fast Valve for the National Synchrotron Light Source," Nucl. Instrum. & Meth. ***195,*** *399 (1982).*

The need for all-vacuum beamlines with minimal vacuum protection from thick windows prompted this design, which extends the time for the shock-wave produced by a vacuum accident at the end-station to propagate to the storage ring chamber, thus allowing a fast-acting shutter to close in time to protect the ring vacuum.

Development of In-vacuum Sliding Electrical Contacts

Work done by P. Mortazavi for 52 MHZ RF Cavity Tuners, (1982).

The reliability of sliding electrical contacts in vacuum had been a significant problem. A custom spring finger design was developed which has reliably operated for years in the NSLS RF cavity tuners.

Development of Helicoflex Seal for NSLS 52 MHZ RF Cavities

Work done by P. Mortazavi resulted in a reliable UHV vacuum seal for the RF Cavity cover which allowed frequency tuning of the cavity by virtue of seal deflection while maintaining vacuum tightness.

Optical Metrology: 1993 R&D 100 Award

The collaboration between P.Z. Takacs and E. Church produced what has become the standard description of figure and finish in the optics industry. Previously the standards were extremely qualitative, using ill-defined terms such as "scratch" and "dig." Application of high-resolution optical interferometry and Fourier analysis of the results has led to international standards bodies adopting their descriptions of surface figure and finish. The industry standard instrument for measuring surface figure in large optics (the Long-trace Profilometer) was developed in the BNL Instrumentation Department by P. Takacs and funded by the NSLS.

HIGH BRIGHTNESS ELECTRON BEAMS

Development of High Brightness Electron Beams

X.J. Wang, T. Srinivasan, K. Batchelor, M. Babzien, I. Ben-Zvi, R. Malone, I. Pogorelsky, X. Qiu, J. Skaritka and J. Sheehan, "Experimental Characterization of High-Brightness Electron Photoinjector," Nuclear Instruments and Methods in Physics Research A ***375,*** *82 (1996).*

Electron beams with a high density of electrons in 6-D phase space are the keystone for future high performance machines such as X-ray Free-Electron Lasers and linear colliders. The BNL S-band photocathode RF gun has been adopted for use by many laboratories and industries, notably: BNL ATF, SDL and CRCR, CERN, Japanese Laboratory for High-Energy Physics, Northrop-Grumman Corporation, Rocketdyne Corporation, Stanford Linear Accelerator Center, University of California at Los Angeles. The robust metal photocathode for RF guns has been developed at BNL. BNL-developed guns have achieved a record peak-surface-electric-field (150 MV/m).

BNL RF Photocathode Electron Gun

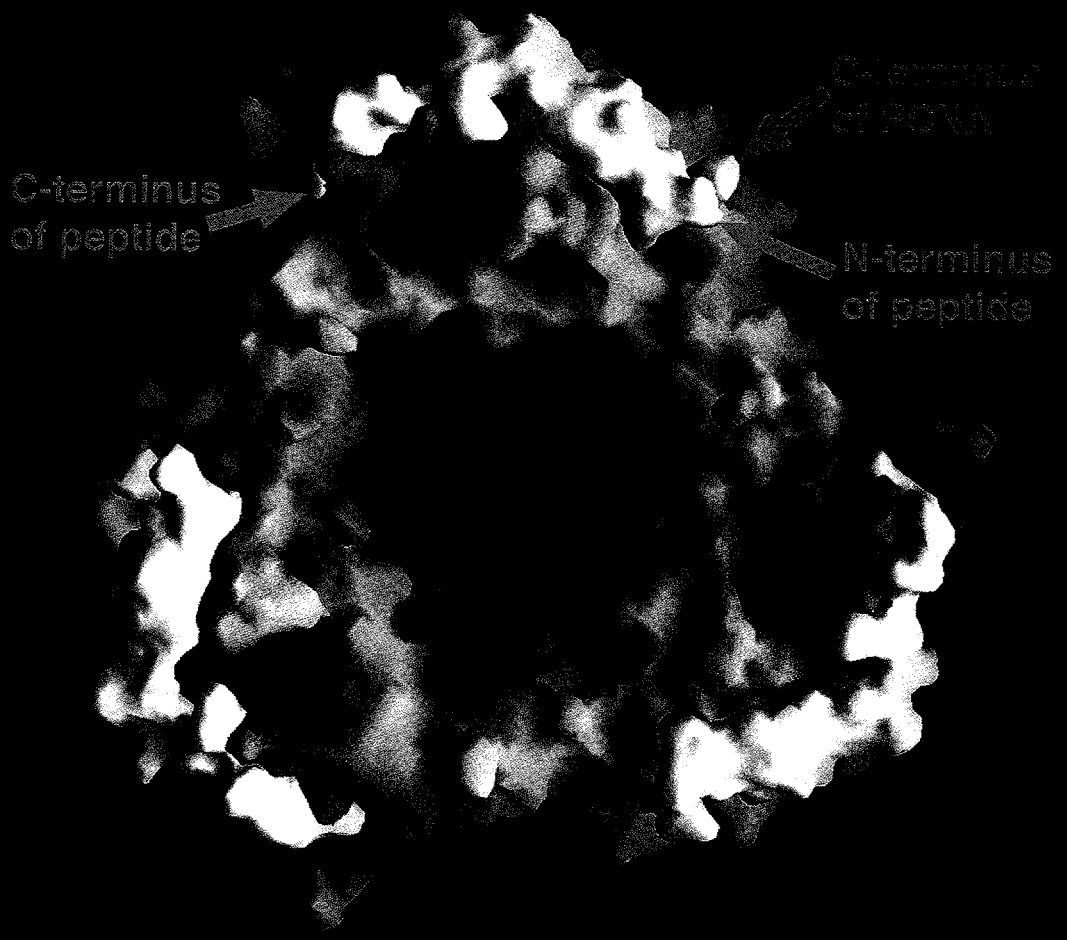
K. Batchelor, H. Kirk, J. Sheehan, M. Woodle, and K. McDonald, "Development of a High Brightness Electron Gun for the Accelerator Test Facility," European Particle Accelerator Conference (1988).

Describes the design and testing of the first generation of the BNL design RF Photocathode Electron Gun. Derivative designs used at CERN, SLAC, UCLA , KEK and elsewhere.

Beamline X25: Solvent-accessible surface of the PCNA trimer. The figure shows the molecular surface of the complex, with PCNA colored according to electrostatic potential and the peptide shown in white. In the calculation of electrostatic potential, dielectric constants of 2.0 for the protein interior and 80 for solvent at an ionic strength equivalent to 100 mM KCl were used. Side chains of lysine and arginine residues were given a net positive charge and aspartate and glutamate negative, with other residues considered neutral. Regions of intense positive charge appear blue, and electronegative regions of the surface are red.
J.M. Gulbis, Z. Kelman, J. Hurwitz, M. O'Donnel, and J. Kuriyan, *Cell* 87, 297-306 (1996).

EIGHT

APPENDICES



From the Managing Editor

This year's Activity Report abstracts were once again entered by the authors via the Electronic Submission System (ESS). The ESS takes information entered through the Forms function on the World Wide Web and stores it in a database optimized for document handling. Composition routines then perform the integration of text and figures and output our choice of PostScript or PDF file (for the author to view and also to go to the printer), SGML file (Standardized Generalized Markup Language) for electronic publishing, and HTML (Hyper Text Markup Language) for dissemination on the World Wide Web. Furthermore, the ESS allows full storage and retrieval of the abstracts, sorted by beamline and author.

The ESS was much more user-friendly this year, due to the addition of the PDF file format that the authors could view using Adobe Acrobat Reader and some modifications to the Web form and program. Judging by the decrease in questions and problems from authors, the system seems to be moving out of its development phase and into a real production mode. About 480 abstracts were received for this 1996 edition, consistent with the previous few years. In addtion, there were another 100 abstracts which authors had begun but did not finish in time for the production deadline - these are being "rolled over" into the 1997 Activity report and the authors will have opportunity to finish them up as soon as the ESS opens once again. Next year, just as in this past year, authors may elect to submit on diskette or via e-mail but for a deadline earlier than for the ESS submissions. Please watch the NSLS Newsletter and/or the NSLS Home Page for details.

We thank everyone who used the ESS to report the results of their work at the NSLS. I would especially like to thank Lydia Rogers and Linda Feierabend of the User Administration Office, who kept almost 600 abstracts well organized, worked with lots of new software, and assisted all the authors who called with questions.

You can access the completed abstracts as well as the ESS on the World Wide Web on the NSLS Home Page at **http://www.nsls.bnl.gov** All instructions are provided in both viewable and downloadable formats.

ABSTRACTS

VUV Beamlines

Beamline U1A

Self-assembled Monolayers of Oligo(p-phenylene)s on Gold Investigated with NEXAFS A-07
D. Fischer, G. Hähner, N.D. Spencer, S. Brunner, W.R. Caseri, and U.W. Suter (ETH Zurich)

Beamline U2B

Implementation of an Extrinsic Germanium Photoconductive Detector on the U2B Irμs Infrared Microspectrometer A-07
G.L. Carr (NSLS)

Infrared Microspectrometer and Beamline Optical Analysis A-08
G.L. Carr (NSLS)

Infrared Microspectroscopy Functional Group Mapping of Normal and Diseased Brain Tissue. ... A-08
L-P. Choo, M. Jackson, H.H. Mantsch (NRC, Canada), W.C. Halliday (U. Manitoba), D.L. Wetzel (Kansas State U.) and S.M. Levine (U. Kansas).

Chemical Profile of a Polymer Composite: The Case of a Commercial Orange Bottle. A-09
G.Fuchs, J.J.Barieux, C.Wilhem (ELF-Atochem, France), P.Dumas (LURE and LASIR-CNRS, France), G.L.Carr and G.P.Williams (NSLS)

Fourier Transform Microspectroscopy of Defect Structures in Si Diamond-Like Coatings A-09
G.P. Halada (SUNY Stony Brook), C.G. Fountzoulas (USARL), G. Williams and L. Carr (NSLS)

Fourier Transform Infrared Microspectroscopy of Acetone Wash Induced Pitting in Al2024-T3 .. A-10
G.P. Halada, S.V. Kagwade (SUNY Stony Brook), L. Carr and G. Williams (NSLS)

Classical and Quantum Mechanical Ordering in Dense Hydrogen: Evidence from Synchrotron Infrared Spectroscopy A-10
R. J. Hemley, I. I. Mazin, A. F. Goncharov, M. Li, H. K. Mao (Carnegie Inst. of Washington /CHiPR)

Evidence for Intracellular Structure From IR Microspectroscopy. A-11
N.Jamin (DIEP-CEA, France), J.L.Teillaud (Inst. Curie, France), P.Dumas (LURE and LASIR,CNRS, France), G.L.Carr and G.P.Williams (NSLS)

Drug Distribution in Hair Determined by Infrared Microspectroscopy A-11
K.S. Kalasinsky (Armed Forces Inst. Path.), D.G. Cameron (DHC Analysis), and D.L. Wetzel (Kansas St. U.)

Synchrotron Micro-Infrared Spectroscopy of Hydrous $(Mg,Fe)_2SiO_4$ Phases A-12
R. Lu, R. J. Hemley, H. K. Mao (Carnegie Inst. of Washington / CHiPR), J. H. Chen, T. Inoue, and H. Kagi (SUNY Stony Brook, CHiPR)

High-Pressure Synchrotron Infrared Spectroscopy of Hydrogen in Garnets A-12
R. Lu, R. J. Hemley, H. K. Mao (Carnegie Inst. of Washington / SUNY Stony Brook, CHiPR), G. R. Rossman (Caltech)

Synchrotron Based IR Microspectroscopy of Thermal Degradation Mechanisms in Polymer Composite Systems A-13
R.J. Meilunas and T. Donnellan (Northrop Grumman Corp)

Application of Infrared Synchrotron Radiation to Microanalysis of Advanced Ceramic Composite Systems A-13
R. J. Meilunas and A. Tobin (Northrop Grumman Corp.)

Polymer Depth Profiling with Synchrotron Infrared Microspectroscopy A-14
D.L. Wetzel (Kansas State U.) and R.O. Carter III (Ford Science Res. Ctr.)

Localized Heterogeneity of Biological Tissues and Textile Surfaces Revealed with Synchrotron IR Microspectroscopy A-14
D.L. Wetzel, L. Cho, J. Sweat, (Kansas St. U.), S.M. LeVine (U. Kan. Med. Ctr.), and J.A. Reffner (Spectra-Tech, Inc.)

Diffraction-Limited Infrared Microspectroscopy of Polymer Laminates A-15
Carl G. Zimba (MIT)

Beamline U4A

The Electronic Structure of GaN Measured Using ARP A-15
S.S. Dhesi, C.B. Stagarescu, L.-C. Duda and K.E. Smith, R. Singh and T. Moustakas, (Boston University)

Angle Resolved Photoemission of of V_2O_3 and VO_2 Near the Metal-Insulator Transition A-16
E. Goering, M. Schramme, O. Mller, H. Paulin, M. Klemm, S. Horn (U. Augsburg), M. L. denBoer (CUNY Hunter)

Photoemission Studies of Ordered and Disordered Cu-Au Alloys A-16
Wei Liu, R.G. Jordan and S.L.Qiu (Florida Atlantic U.)

Electronic Structure of the Organic Superconductor κ-(BEDT-TTF)Cu[N(CN)$_2$]Br A-17
C.B. Stagarescu, S.S. Dhesi, and K.E. Smith (Boston U.), R. Haddon (Bell Labs), J. S. Brooks, (Florida State U.)

Beamline U4B

C 1*s* NEXAFS of La@C_{82} A-17
J. F. Armbruster, N. Nücker, S. Schuppler, D. Fuchs (Forschungszentrum Karlsruhe, FRG), R. H. Michel, M. M. Kappes (U. of Karlsruhe, FRG)

Magnetic Circular Dichroism Studies of FeV Alloys A-18
V. Chakarian and Y. U. Idzerda (NRL), C.T. Chen (Bell Labs)

Linearly Polarised Soft X-ray Resonant Magnetic Scattering from Fe_xMn_{1-x}/Ir (001) Superlattices A-18
A. Déchelette-Barbara, J.M. Tonnerre, F. Bartolomé, D. Raoux (CNRS, France), H.M. Fischer (CNRS, Univ. Nancy I, France), V. Chakarian (NRL), and C.C. Kao (NSLS)

O 1*s* NEXAFS of $Pr_xY_{1-x}Ba_2Cu_3O_y$ Single Crystals A-19
M. Merz, N. Nücker, E. Pellegrin, S. Schuppler (Forschungszentrum Karlsruhe, FRG), M. Kielwein, M. Knupfer, M. S. Golden, J. Fink (IFW Dresden, FRG), C. T. Chen (SRRC, Taiwan), V. Chakarian, Y. U. Idzerda (NRL), and A. Erb (U Geneve, Switzerland)

High Temperature Metal-Insulator Transition of $LaCoO_3$ A-19
J.-H. Park (NSLS), S-W. Cheong (Bell Labs.), and C. T. Chen (SRRC)

Polarization Dependence X-ray Absorption Studies of V_2O_3 ..... A-20
J.-H. Park (NSLS), L. H. Tjeng (U. of Groningen), J. W. Allen (U. of Michigan), C. T. Chen (SRRC), and P. Metcalf (Purdue U.)

Soft X-ray Magnetic Circular Dichroism Study of $La_{1-x}Sr_xMnO_3$ A-20
E. Pellegrin, L. H. Tjeng, F. M. F. de Groot, R. Hesper, G. A. Sawatzky (RUG), J. D. O'Mahony, C. F. J. Flipse (TUE), Y. Moritomo, Y. Tokura (JRCAT), C. T. Chen (SRRC)

Nature of the Unoccupied Electronic States in Sr_2RuO_4 ..... A-21
M. Schmidt, N. Nücker, T. R. Cummins, D. H. Lu, S. Schuppler (Forschungszentrum Karlsruhe, FRG), F. Lichtenberg (Varta Batterie AG, FRG)

Beamline U4IR

Pump-probe, Far-infrared Study of Pair Breaking and Recombination in Superconducting b .. A-21
G.L. Carr and G.P. Williams (NSLS), D.B. Tanner (U. Florida)

Low-Frequency Modes in Polypeptides and Proteins A-22
M.R.Chance, A. Xie, B. Sclavi, Q. He, L.M. Miller, M. Sullivan (AECOM)

Doping Dependence of the IR Response of $La_{2-x}Sr_xCuO_4$ A-22
R. Henn, A. Wittlin, M. Cardona (Max-Planck Institut) and S. Uchida (U. of Tokyo)

Carbon Dioxide Activation and Alkali Compound Formation A-23
F.M. Hoffmann (SCI-MED) D.G. Van Campen, G.P. Williams (NSLS), J. Paul (Royal Inst. of Tech., Sweden)

Simultaneous Infrared Spectroscopy and DC Resistivity Measurements on Adsorbate-covered Epitaxial Copper Films A-23
A. Otto, M. Hein (U. Duesseldorf, Germany), P. Dumas (LURE, U. Paris-Sud, France), G.P. Williams (NSLS)

Infrared Study of Fullerenes and Fullerides on Ag(111), Au(110) and Cu(111) A-24
P.Rudolf (LISE-Namur, Belgique), P.Dumas (LURE and LASIR-CNRS, France), Y.J.Chabal (Lucent Technologies), D.Van Campen and G.P.Williams (NSLS)

Beamline U5UA

Branch Crossings of Quantum Well States in Cu Films Deposited on Ni(001) A-24
D.-J. Huang and P. D. Johnson (BNL - Physics)

The k-Space Origin of the Long Period Oscillation in Fe/Cr Multilayers: A Photoemission Study of Epitaxial Cr Grown on an Fe(100) Whisker A-25
J. Pearson, S. D. Bader (ANL), E. Vescovo, D.-J. Huang, P. D. Johnson (BNL), B. Heinrich (SFU)

The U5UA SGM-beamline: First Tests on the Performances A-25
E. Vescovo, Q.-Y. Dong, G. Nintzel, D. Carlson, and S. Hulbert (NSLS)

Spin-polarized Electronic Structure of Fe(100): A New Surface-related State A-26
E. Vescovo (NSLS), D.-J. Huang, P.D. Johnson (BNL- Physics)

Beamline U7B

Photoemission Study of Ni-Al Alloys A-26
H. Niu, S.L. Qiu and R.G. Jordan (Florida Atlantic U.)

Beamline U13UB

Extreme Ultraviolet Lithography - Commissioning of an Offner 1:1 Imaging Camera A-27
A.MacDowell, O.Wood II (Lucent Technologies), K.Fuji (NEC)

Beamline U14A

Auger Decay of a Core Level Satellite Feature Observed by Auger Photoelectron Coincidence Spectroscopy A-27
R. Gotter (Laboratorio TASC-INFM, Italy) , R.A. Bartynski (Rutgers U.), Xu. Wu, S.L. Hulbert (NSLS), and H. Nozoye (Natl. Inst. of Materials and Chemical Research, Japan)

Core Hole Decay Mechanisms in Ru Studied by Auger-photoelectron Coincidence Spectroscopy A-28
R. Gotter, R.A. Bartynski (Rutgers U.), X. Wu, S.L. Hulbert (NSLS), and H. Nozoye (Nat. Inst. of Materials and Chemical Research)

Defects on the TiO_2(110) Surface Observed by Auger-photoelectron Coincidence Spectroscopy A-28
W.K. Siu, R.A. Bartynski, (Rutgers U.) A. Namgia, A.H. Weiss, (U. of Texas Arlington), X. Wu, and S.L. Hulbert (NSLS)

Beamline U15

Atomic-Site-Selective Core-Electron Excitation of 5-Oxohexanenitrile Isolated in D2 Matrices A-29
S. Sambasivan, A. T. Wen and D. M. Hanson (SUNY Stony Brook)

Self-assembled Monolayers of Oligo(p-phenylene)s on Gold Investigated with NEXAFS	U1A

D. Fischer, G. Hähner, N.D. Spencer, S. Brunner, W.R. Caseri, and U.W. Suter (ETH Zurich)

Adsorbing organic molecules by self-assembly on inorganic surfaces is an effective way of modifying surface properties. The behavior of ultrathin polymer layers on metals is particularly interesting for optimizing those properties, which play an important role in adhesion, sensor technology, tribology and corrosion.

We have investigated the adsorption of substituted oligo(p-phenylene)s of various lengths (i.e. different number of phenyl moieties) from solution onto gold substrates. The behavior of these model systems is between that of flexible and rod-like molecules, and they have been especially synthesized in order to establish self-assembled monolayers. NEXAFS was used to study the chain orientation and electronic structure of the adsorbed molecules.

Fig.1 shows NEXAFS spectra taken at the C1s edge for different angles of incidence, Θ, for A5C6 (see Figure below), adsorbed from a 1mM solution in toluene for 4h. As for all investigated oligomers the thickness of the adsorbed layer is in the 5-10Å range. On the basis of the spectra it can be concluded that no coordination occurs upon adsorption. The angular dependence of the transition into (unoccupied) π^* orbitals can be used to determine the average tilt angle of the phenyl moieties. However, due to the small number of adsorbed molecules the error limits are large. The determined average tilt angle amounts to 43- 45° relative to the surface with error limits of 6-9°. We interpret the measurements as showing that the influence of the substrate on the adsorbates is rather weak, regarding both electronic structure and orientation, although a slight deviation from a random orientation (corresponding to an average tilt angle of 55°) due to the interaction with the surface is supported by our data.

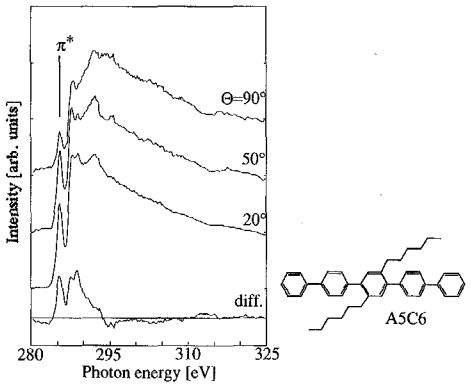


Figure 1.

Implementation of an Extrinsic Germanium Photoconductive Detector on the U2B Irμs Infrared Microspectrometer	U2B

G.L. Carr (NSLS)

The standard detector for mid-infrared spectrometers (including microspectrometers) is the intrinsic ternary alloy $Hg_{1-x}Cd_xTe$ (MCT), operated in a photoconductive (PC) mode. Such detectors offer the best signal-to-noise commercially available for the wavelength range from <4μm to about 15μm. However, in many instances these detectors have a non-linear (with intensity) photoresponse, and some applications require performance to beyond 25μm. Photovoltaic (PV) MCT is more linear, but the long wavelength response limit is less than for PC MCT. An alternative detector for mid-infrared spectroscopy is extrinsic germanium, doped with Cu or Zn. The noise level is typically a factor of two higher than for MCT, but response extends to 30μm and linearity is very good. To accomodate such a detector, a beam exit port, optics, and provision for external signal input were added to the Irμs instrument, and comparison tests were conducted. The figures below illustrate the relative performance of the two types of detectors. Figure 1 illustrates the noise, which is higher for the Ge:Cu detector. Note that the Ge:Cu detector provides data down to 400 cm^{-1} (25μm), which is limited by the spectrometer's KBr beamsplitter rather than the detector. Figure 2 shows the measured transmission of a 10±1% neutral density filter. The Ge:Cu detector provides an accurate measure, whereas the MCT detector has an error of ~40%!

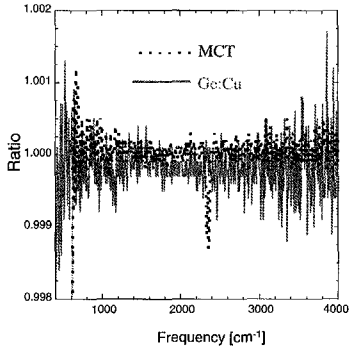


Figure 1. Signal-to-noise comparison (100% lines) for the MCT and Ge:Cu detectors. Signal for MCT detector ends abruptly at 650 cm^{-1} (16μm).

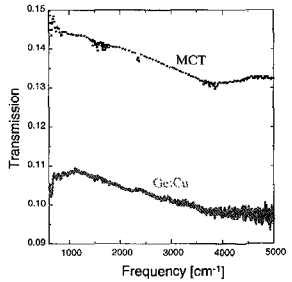


Figure 2. Linearity comparison for the MCT and Ge:Cu detectors, showing the measured of a neutral density filter (10±1%).

Infrared Microspectrometer and Beamline Optical Analysis | U2B

G.L. Carr (NSLS)

The present mid-infrared beamline at U2B has a 10x10mr port and spherical mirror optics. In addition, the optical train inside the Irμs infrared microspectrometer endstation includes a spherical pre-focusing optic. This optical configuration leads a $\sim$30 μm spotsize at the sample location, determined by both ray-tracing and actual measurements (Fig. 1, top). The ray tracing also reveals that this spotsize is determined by aberrations rather than diffraction (Fig.1 bottom). Despite this limitation, the signal throughput is 1 to 2 orders of magnitude greater than that obtained with a conventional source. A new infrared port with improved optics is being constructed at beamline U10. Calculations based on the improved beamline design, and replacing one optic inside the Irμs with an off-axis paraboloid, are shown in Figure 2. The optics are now diffraction limited, and the combination of increased flux (>5x) and reduced spotsize should result in a 40-fold increase in brightness at the sample. Installation of the Irμs at U10B is expected to occur early in 1997.

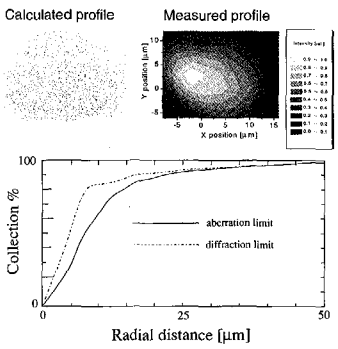


Figure 1. Optical performance f present configuration at U2B. Calc lated and measured image (top) an calculated encircled energy distributio (bottom).

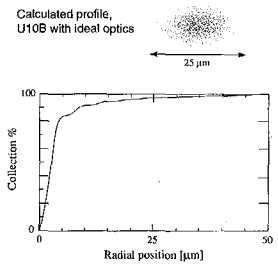


Figure 2. Optical performance for improved configuration at U10B. Calculated image profile (top) and calculated encircled energy distribution (bottom).

Infrared Microspectroscopy Functional Group Mapping of Normal and Diseased Brain Tissue. | U2B

L-P. Choo, M. Jackson, H.H. Mantsch (NRC, Canada), W.C. Halliday (U. Manitoba), D.L. Wetzel (Kansas State U.) and S.M. Levine (U. Kansas).

Multiple frozen sections of human brain tissue, representing Alzheimer's and multiple sclerosis (MS) diseased cases, were prepared for examination by microtoming and thaw-mounting on BaF_2 optical windows. Lesion sites typical of both diseases, and also normal tissue, were selected to allow contrast in functional group mapping. Synchrotron infrared microspectroscopy provided detailed mappings of IR absorptions associated with disease-specific functional groups. For each diseased brain, the IR functional group features were found coincident with the lesion sites.

Figure 1 shows a 3-D stacked contour map of MS brain tissue, in which contrast is obtained from the peak area of the C-H bending vibration at 1469cm^{-1}. The unaffected white matter (center) with the normal amount of lipid is high. The affected area where the white matter is destroyed has reduced 1469cm^{-1} absorption (gray matter is shown for comparison). Alzheimer's diseased (AD) brain tissues were also mapped. Spectra in figure 2 show the highly localized β-amyloid among a series of spectra from 12μm by 12μm apertures collected at 13μm intervals across the tissue mapped. This represents the first *in situ* mapping of β-amyloid in human brain tissues. Frequency shifts of the amide I band from 1651cm^{-1} to 1631cm^{-1} were used to construct the amide I band position image shown in figure 3. After mapping, histological staining of the same tissue confirmed the plaque location.

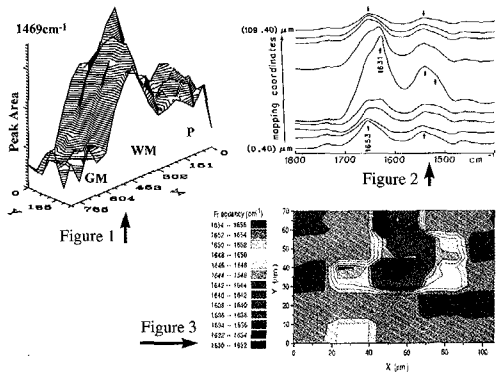


Figure 1. MS brain 1469cm^{-1} peak area map, contrasting gray matter (GM), normal white matter (WM), and plaque (P). Figure 2: AD brain amide I spectra at 13μm intervals showing 1631cm^{-1} maximum at plaque location. Figure 3: AD brain map showing β-amyloid frequency shift.

Chemical Profile of a Polymer Composite: The Case of a Commercial Orange Bottle.	U2B

G.Fuchs, J.J.Barieux, C.Wilhem (ELF-Atochem, France), P.Dumas (LURE and LASIR-CNRS, France), G.L.Carr and G.P.Williams (NSLS)

Numerous plastic components are now used in everyday life. One such example is an orange juice bottle that is produced as a multi-component, layered polymer. As depicted on Fig. 1, this bottle, commercialized in France as "JOKER bottle", is composed of six layers. Each layer has a characteristic infrared spectrum. Therefore, profile analysis of the frequency and intensity changes through the plastic layers allows one to study the different interfaces, and the inter-diffusion of species.

Such a study was carried out at beamline U2B. A microtome preparation of the bottle wall was linearly mapped, with an aperture of 6x6 μm^2, and steps of 6 μmm. A typical mapping is represented on Fig. 2, in the 1000-2000 cm^{-1} frequency region. A visible image of the cross-section is shown to the right.

From the spectra, two dimensional profiles of each vibrational band, characteristic of a particular chemical function, can be obtained, e.g., such as that associated with the OH stretching mode of the alcohol functional group. For the case investigated, there is evidence that material from adhesive layers 2 and 4 has diffused into the adjacent material. Control of such diffusion is important for maintaining the structural integrity of the plastic. This demonstrates the utility of synchrotron IR microspectroscopy interface and interphase analysis of polymer laminate, as the useful information is contained mainly within a few microns of the layer interfaces.

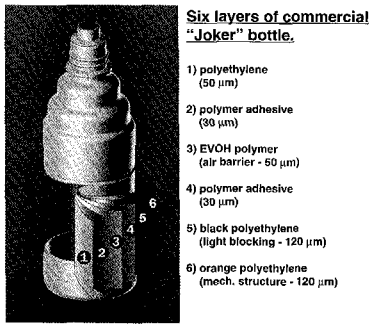


Figure 1. Schematic view of laminated plastic ("Joker") bottle material, showing 6 layers.

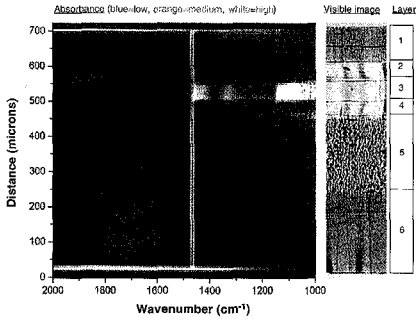


Figure 2. Linear absorption map across the plastic layers (left), visible image of microtomed section, showing the 6 layers (right).

Fourier Transform Microspectroscopy of Defect Structures in Si Diamond-Like Coatings	U2IR

G.P. Halada (SUNY Stony Brook), C.G. Fountzoulas (USARL), G. Williams and L. Carr (NSLS)

FTIR microspectroscopy at U2IR was used in a preliminary (and ongoing) study of the surface of a Si-diamondlike carbon coating deposited on Si using an ion beam assisted deposition process. This process uses Ar^+ ions and tetraphenyl-tetramethyl-trisiloxane (type 704 Dow-Corning silicone oil) as a precursor material, resulting in an average film stoichiometry of $C_{59}Si_7O_5H_{26}Ar_3$. In particular, we analyzed areas showing apparent defect structures (pinholes and optically dark or speckled surface features as seen in Figure 1) to look for correlations with mid-infrared absorbtion data. Figure 2 shows the FTIR line scan (collected along the line - from top to bottom - shown on Figure 1). This data was acquired with a 6x6 micron aperature in 5 micron steps. Background infrared absorbtion data from a non-coated area of the Si substrate was subtracted from each feature to limit the effects of water vapor and carbon dioxide on the observed data. The broad absorbtion peak centered at about 2600 wavenumbers has appeared in earlier FTIR spectra of Si-DLC films and appears to be associated with C-H (and perhaps some Si-H) bond stretching in the film. The small feature at about 1250 wavenumbers has been postulated to be evidence of $Si-CH_3$ bonding in the coating. Si-H bond stretching also results in the absorbtion of frequencies around 800-850 wavenumbers. It is of interest to note that the Si-H and $Si-CH_3$ features strengthen slightly for darkened regions of the film in which there is a shift of the primary broad peak to higher wavenumbers. Additional analyses will be performed to further explain these features and results. As noted in the line scan data, the broad feature falls off completely in the region of the scan associated with the hole in the coating and seems to build in intensity as the coating thickens at the edge of the hole. As noted, the peak shifts slightly to higher wavenumbers as the analysis beam crosses an area which shows a dense region of dark inclusions (which appear in a lower density scattered across the film). This change may relate to a higher force constant in this region, indicating a different H coordination chemistry. In further work, we will attempt to find correlations between such shifts in infrared absorbtion features and changes in both surface chemistry and mechanical properties (such as hardness).

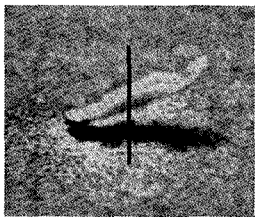


Figure 1. Optical micrograph of hole (light) and defect-enriched area (dark) in diamond-like coating on Si. Line indicates location of line scan (from top to bottom)

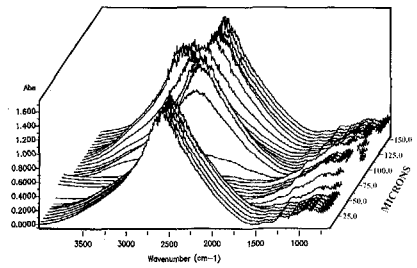


Figure 2. 150 micron FTIR line scan of defects in diamond-like coating on Si.

Fourier Transform Infrared Microspectroscopy of Acetone Wash Induced Pitting in Al2024-T3 — U2IR

G.P. Halada, S.V. Kagwade (SUNY Stony Brook), L. Carr and G. Williams (NSLS)

The process of pitting in aluminum alloy Al2024-T3 in aqueous NaCl has been a subject of numerous investigations due to the alloy's importance to aircraft structural engineering. Multiple cleaning and surface preparation processes using organic solvents such as acetone and isopropanol are commomly used in industry. Ongoing electrochemical and X-ray Photoelectron Spectroscopy (XPS) studies of corrosion characteristics of Al2024-T3 following various surface preparation methods have indicated that an acetone wash prior to introduction to an aqueous NaCl environment leads to changes in the alloy surface. Acetone was shown to enhance the formation of pits in the presence of aqueous NaCl, and XPS indicated the formation of various corrosion products, including acetates, oxides and chlorides, on the sample surface. In order to further our understanding of the spatial association of these chemical species with visible pits in the alloy surface, a study was undertaken using Fourier Transform Infrared microspectroscopy. Figure 1 shows an optical micrograph of a typical pit in an alloy surface washed in acetone and then exposed to an aqueous NaCl environment. An FTIR line scan was performed n a 150 micron long path across this region, from left to right, as shown. This data is presented in Figure 2, in which the origin of the line is to the left. Mid-infrared spectra were taken using a 6x6 micron square aperature, moved in 5 micron steps. Background from an adjacent clean alloy surface was subtracted from each spectra to limit the effects of water vapor and carbon dioxide on the observed data. The data shows that the broad hydroxide/bound water peak centered at about 3300 wavenumbers shifts slightly to higher frequency as we approach the edge of the pit (at about the dark ring about the pit shown in Figure 1), probably indicating a higher force constant related to increased metal coordination. Strong absorbtion features due to COO-bonding (about 1550) and CH_3 bonding (about 1425) (both features of acetate or acetyl-acetone) are also clearly evident in the region surrounding the pit. Within the pit, however, these features decrease dramatically, and are partly replaced by absorbtion features both in the 500-1000 and 1700-2800 wavenumber region, possibly indicating mixed oxides or metal oxy-chlorides. Ongoing work involving both standards and complementary spectroscopies is being pursued to further clarify these results.



Figure 1. Optical micrograph showing a pit on the surface of the alloy. Line on figure indicates location of 150 micron scan (from left to right)

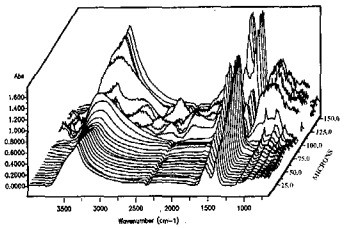


Figure 2. FTIR line profile across the pit area

Classical and Quantum Mechanical Ordering in Dense Hydrogen: Evidence from Synchrotron Infrared Spectroscopy — U2B

R. J. Hemley, I. I. Mazin, A. F. Goncharov, M. Li, H. K. Mao (Carnegie Inst. of Washington /CHiPR)

High-pressure synchrotron infrared spectroscopy has been instrumental in detailing the rich evolution of the physical properties of solid hydrogen with increasing density. Recent work, in particular, has allowed us to identify two fundamentally different kinds of pressure-induced orientational ordering transitions at megabar pressures.

As in previous work, synchrotron infrared absorption spectra were measured on hydrogen samples contained in modified megabar diamond-anvil cells using the high-pressure facility at U2B. Measurements were carried out as a function of temperature to 200 GPa through phase I (the low-pressure, high-temperature phase), phase II (the low-temperature broken symmetry phase), and phase III (the higher pressure phase stable above 150 GPa). The intensity of the vibron was carefully measured and characterized in terms of effective charges. In phase III, for example, the effective charge of the strong vibron is $q^*=0.032e$ at 167 GPa and 85 K; it increases with pressure and reaches $0.037e$ at 230 GPa. In contrast, in phase II q^* is slightly less than $0.004e$ at 140 GPa and the same temperature, and in phase I, there is a broad, weak disorder-induced band instead of a sharp vibron.

Further understanding can be obtained from analysis of the temperature dependence of the effective charges. The data indicate that the infrared activity, which is proportional to $(q^*)^2$, is linearly related to $\Delta\nu^2$, or $\Delta\nu \propto q^*$, over the entire range of temperatures and pressures studied. In formal terms, $\Delta\nu \propto q^*$ can be interpreted as both quantities being linear functions of a scalar order parameter, $\Delta\nu \propto \eta$, and $q^* \propto \eta$. Taken together with previous Raman data, we conclude that phase III is qualitatively different from the lower-pressure broken-symmetry phase II. Both are orientationally ordered, but the ordering objects in phase II are angular momenta of rotating molecules (quantum ordering), and in phase III it is the molecules themselves (classical ordering).

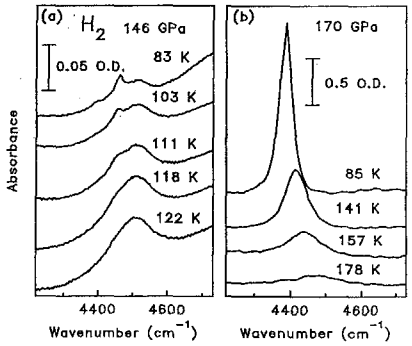


Figure 1. Temp. dependence of infrared vibron spectra. (a) I-II transition. (b) I-III transition.

Evidence for Intracellular Structure From IR Microspectroscopy. | U2B

N.Jamin (DIEP-CEA, France), J.L.Teillaud (Inst. Curie, France), P.Dumas (LURE and LASIR,CNRS, France), G.L.Carr and G.P.Williams (NSLS)

Probing the chemical composition of a living cell is very challenging due to the small dimensions (<40μm). Infrared microspectrometers provide chemical specificity, and the average power (at the sample) is too weak to damage living cells. But the low brightness of its IR (globar) source restricts its utility to areas ~25μm or greater. The IR synchrotron source overcomes this limitation, and we present a study demonstrating the successful imaging of a live cell (Mouse hybridoma B) using the microspectroscopy system at beamline U2B.

The cells were dispersed on BaF_2 using a cytospin technique, and their live character confirmed before and after IR analysis. Infrared spectra were recorded using a 3x3μm^2 aperture, and a typical spectrum is shown in the top panel. Absorption features associated with various cellular chemicals are labelled. Chemical profiling of a cell was achieved by collecting spectra at 3μm intervals in a raster-like fashion (~1 min. per spectrum). Two chemical profiles, along with a visible image of the cell, are shown in the lower panels of the figure. Of particular interest is the stretching mode of aliphatic methylene groups (-CH_2), associated mostly with lipids and proteins, which shows a lateral separation not apparent in the visible image. This demonstrates the great potential of IR synchrotron microspectromscopy for investigating the intracellular chemical composition of live cells.

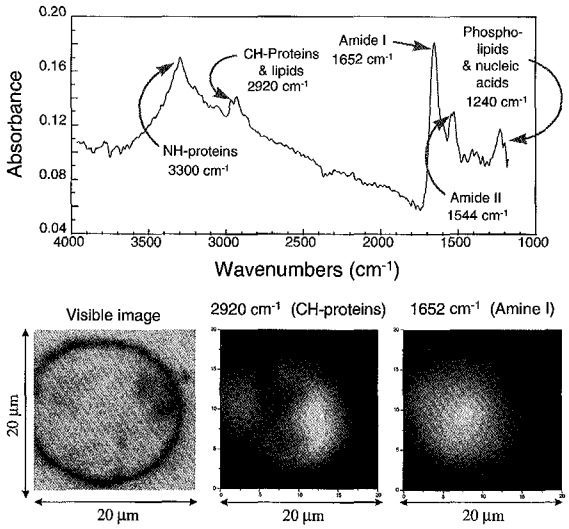


Figure 1.

Drug Distribution in Hair Determined by Infrared Microspectroscopy | U2B

K.S. Kalasinsky (Armed Forces Inst. Path.), D.G. Cameron (DHC Analysis), and D.L. Wetzel (Kansas St. U.)

Localization of drug metabolites within human hair is important in determining the pharmacokinetics of drug incorporation in hair. This information is critical to validate drug testing data from hair. Microspectroscopic probing of small areas (<10μm in diameter) within longitudinally microtomed hair sections provides a profile of the drug deposition along a growth line and thus indicates localization as a function of time. Probing across individual hairs may reveal the hydrophobic/hydrophilic characteristics of the substance. Hydrophobic drugs tend to bind to the central core of the hair medulla, while hydrophilic drugs tend to be spread throughout the cortex of the hair, and generally appear in lower concentrations per dose. High spatial resolution distribution profiles of hair regions are necessary for these determinations. This information is not readily available through conventional infrared microspectroscopy.

Initial work at the NSLS infrared microspectrometer has shown the feasibility of resolving the drug incorporation issue. Sample handling has been determined and initial work with spiked or doped hairs has shown the presence of drugs in the protein profile. Previous data by conventional infrared microscopy has not been sensitive enough to show evidence of the drug in the hair without extensive data manipulation. The figure below shows NSLS IR microscope protein spectra of spiked hairs superimposed on a reference hair spectrum. The indicated band in the spiked hairs at 1735 cm^{-1}, which is not present in the reference spectrum, is the carbonyl band of 6-monoacetyl morphine (the primary metabolite of heroin). Unfortunately, contamination from a sample preparation procedure led to an absorption which obscured distribution profiles. Corrective preparation techniques have been devised and subsequent data collections at the NSLS are expected to reveal the distribution profiles. We also anticipate obtaining high spatial resolution information, which is required for determining drug transport and binding in hair, using the synchrotron infrared microspectrometer system.

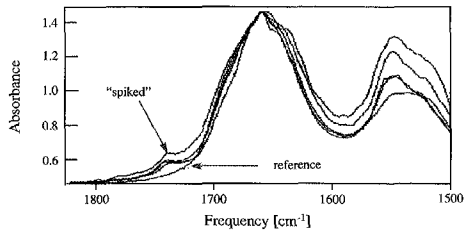


Figure 1. Spectra from micro-sections of reference (drug-free) and spiked hair, showing the shoulder at 1735 cm^{-1} associated with heroine metabolite.

Synchrotron Micro-Infrared Spectroscopy of Hydrous $(Mg,Fe)_2SiO_4$ Phases — U2B

R. Lu, R. J. Hemley, H. K. Mao (Carnegie Inst. of Washington / CHiPR), J. H. Chen, T. Inoue, and H. Kagi (SUNY Stony Brook, CHiPR)

Infrared spectroscopy provides detailed information on bonding characteristics of crystals, liquids and glasses and it is a useful probe of structural symmetry. It is also widely applied to studying structural, thermochemical, and electronic properties of materials.

We have used synchrotron micro-infrared spectroscopy to characterize the effects of hydrogen on the phase relations and physical properties of olivine polymorphs α-, β-, and γ-$(Mg,Fe)_2SiO_4$. Samples of either San Carlos olivine or forsterite mixed with H_2O were subjected to high temperatures and pressures and quenched to ambient conditions. We use the high spatial resolution of the Nicolet microscope as a structural probe for phase identification and characterization of the pressure- and temperature-quenched material. Grains and structurally zoned areas as small as ~10 microns were probed and identified in situ by reflectance measurements of the polished samples while inside capsules. Absorbance spectra were also measured from crystals freed from the capsule. Both sets of measurements are used to determined hydroxyl concentrations.

The presence of structurally bound OH in the Fe-containing olivine system expands the stability field of the β-phase into both α- and γ-phases. This effect is not observed in the Mg-end member systems. The advantages of the synchrotron micro-IR approach for phase identification include the high-spatial resolution (down to diffraction limits of the infrared beam) and the non-destructive nature (due to the weak IR beam) in comparison to XRD and laser-Raman. Both of these advantages are particularly important for such studies because many mantle minerals are both fine grained and metastable at ambient condition.

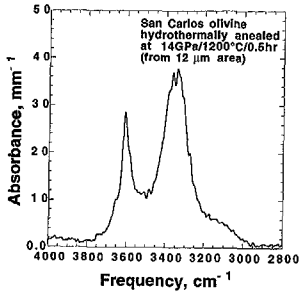


Figure 1. High-frequency infrared spectrum of San Carlos olivine hydrothermally annealed at 14 GPa and 1200 C for 0.5 hr. The spectrum was measured under ambient conditions.

High-Pressure Synchrotron Infrared Spectroscopy of Hydrogen in Garnets — U2B

R. Lu, R. J. Hemley, H. K. Mao (Carnegie Inst. of Washington / SUNY Stony Brook, CHiPR), G. R. Rossman (Caltech)

Hydrogarnet substitution (Si$\leftarrow\rightarrow$4H) is known to be responsible for incorporation of hydrogen in garnets from the Earth's mantle. It is also known, however, that the infrared spectra of garnets have complex OH bands that suggest alternative mechanisms for hydrogen substitution. Study of these mechanisms is important for understanding the uptake of hydrogen in mantle minerals in general. We selected two garnets, grossular ($Ca_3Al_2Si_3O_{12}$) and spessartine ($Mn_3Al_2Si_3O_{12}$), as models for studying hydroxyl substitution. These garnets show respresentative multiple OH bands that are expected to originate from both hydrogarnet substitution as well as previously undocumented alternative structural sites. We studied these hydroxyl bands at high pressures with a diamond anvil cell by synchrotron infrared spectroscopy at beam line U2B. We used custom designed instrumentation based on a Nicolet FTIR spectrometer and microscope consisting of two Cassergrain objectives optically interfaced with a symmetrical diamond anvil cell. Frequencies of the OH bands in grossular garnet range from 3534 to 3688 cm^{-1} which corresponds to O-H...O bonds from 2.93 to 3.27 Å . These bands exhibit both positive and negative frequency shifts with pressure ranging widely from -7.7 to 3.0 cm^{-1}/GPa. Such large frequency shifts reflect significant changes in O-H...O bond lengths. By contrast, the OH bands in spessartine (ranging from 3582 to 3649 cm^{-1}) all have positive pressure shifts, and range from 0.23 to 2.91 cm^{-1}/GPa indicating very weak hydrogen bonding. Moreover, the frequency shifts for both garnets show a well defined linear dependence on OH frequency, with the slopes $(d\nu/dP)/\nu$ of 0.05 (grossular) and 0.04 (spessartine). These values are systematically higher than those for hydrous β-$(Mg,Fe)_2SiO_4$ and serpentine, for which similar high-pressure spectroscopic data are available. Systematics and structural implications of these results are under investigation.

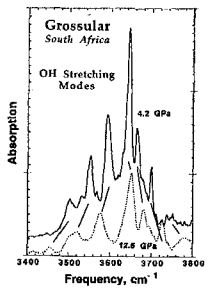


Figure 1. High-pressure infrared spectrum of grossular (South Africa)

Synchrotron Based IR Microspectroscopy of Thermal Degradation Mechanisms in Polymer Composite Systems	U2B

R.J. Meilunas and T. Donnellan (Northrop Grumman Corp)

The enhanced sensitivity of an infrared microscope integrated with a synchrotron light source was used to characterize the time dependent thermal degradation in several polymer matrix composite systems. For graphite fiber/ polyimide composites, the increased spatial resolution provided by the microscope allows IR characterization of the inter-fiber polymer matrix component of the samples without the spectral distortion effects contributed by the broad band absorbance of the graphite fibers. This advantage allows for unambiguous determination of local variations in chemical structure in the composite materials such as in the surface and interior regions of samples exposed to thermo-oxidative environments as well as identifying preferential attack between interply and intraply regions.

In this study the FTIR microscope was used to chemically quantify the effectiveness of different fiber sizing pretreatments on composite thermo-oxidative durability. A series of unidirectional, graphite fiber (Amoco T650-75) / PMR-II-50 polymide composite samples were prepared with different reactive coupling based fiber sizing pretreatments. The samples were heat treated at 370C for up to 700 hrs in air. Polished cross-sections were prepared of samples aged at specific time intervals and IR microreflectance measurements taken from select matrix rich regions at the surface, center and interply areas of the specimens. The IR spectral features associated with the time dependent, diffusion limited, thermo-oxidative degradation of the matrix phase were analyzed through the thickness of the composite. Specific fiber sizings formulations were identified which significantly reduced the degree of matrix degradation in the subsurface regions of the composite specimens. Synchrotron IR microspectroscopy is demonstrated as a powerful technique for determining local variations in chemical structure in polymer composite materials and for identifying degradation mechanisms in these materials and the kinetics of these mechanisms under specific exposure conditions.

Application of Infrared Synchrotron Radiation to Microanalysis of Advanced Ceramic Composite Systems	U2B

R. J. Meilunas and A. Tobin (Northrop Grumman Corp.)

The utility of characterizing ceramic matrix composites using the enhanced sensitivity provided by an infrared microscope integrated with a synchrotron light source, was investigated. In this study the influence of pyrolysis process parameters on the oxidation stability of a Nextel fiber /silicon carboxide glass ceramic matrix composite system was evaluated. A series of 2D Nextel 312 fiber/ Blackglas 493 ceramic matrix composite samples were prepared by several pyrolysis processing conditions. The samples were then oxidized at 600C from 100 to 1000 hours in air. Polished cross-sections were prepared of samples exposed at specific time intervals and IR microreflectance measurements taken from select fiber rich and matrix rich regions at the surface and the interior of the specimens. The increased spatial resolution provided by the microscope enabled identification of an oxidation induced, interfiber silica phase, whose IR spectral signature would have otherwise been overlapped with the Nextel fibers' silicate spectral band at larger, conventional sampling (aperture) areas. During the initial thermo-oxidative exposure, the inter-fiber Blackglas regions throughout the composite were found to convert to a silica phase through oxidation via pipe diffusion of oxygen along the fiber matrix interface. By this oxidation mechanism, the carbon stabilized glass matrix eventually is converted to a thin shell of silica surrounding all fiber rich regions of the composite. Though little variation was found in the IR spectra of the matrix phase as a function of pyrolysis conditions, differences were found in the suboxide structure formed during oxidation depending on the pyrolysis treatment. The significance of these observations on the mechanical performance and long term stability of the Blackglas composites were assessed.

Polymer Depth Profiling with Synchrotron Infrared Microspectroscopy — U2B

D.L. Wetzel (Kansas State U.) and R.O. Carter III (Ford Science Res. Ctr.)

Various polymer specimens, previously subjected to surface treatment, have been the objects of surface preferenced IR probing at the laboratories of both investigators. ATR infrared microspectroscopy has been used to compare chemical changes at the treated surface with the virgin (back) surface of the same specimen. Photoacoustic infrared spectra of treated surfaces were also recorded prior to the NSLS work. The surface IR techniques show dramatic changes in the surface chemistry but attempts to establish the depth of the effect proved unsatisfactory. Acrylic polypropylene and polyethylene samples were involved. At beamline U2B of the NSLS, 6μm thick microtomed cross-sections of polymer laminates were prepared and mounted between BaF_2 windows in a microcompression cell. With a high signal, low noise, narrowly apertured beam of the microspectrometer, infrared transmission spectra were collected in a linear mapping pattern from a 6μm wide 24μm long target in a progression of 3μm steps. Even at the high spatial resolution required good quality spectra resulted. Transmission spectra showed reduction in the relative intensities of major polymer absorption bands near the surface exposed to photochemical attack. At intermediate depth additionally the degregation reaction products were in evidence as OH and a new broad band in the fingerprint region. Figure 1 shows the beam pattern projected onto the polymer section. Figure 2 shows spectra of the changed material compared to the unexposed acrylic film. Acrylic film subjected to different photon fluxes and exposures times were interrogated and a control was run by mapping corresponding material that was completely protected from photochemical attack. Surface treated polypropylene and polyethylene specimen mapping was attempted but no penetration into a 3μm or 6μm depth was evident.



Figure 1. Photomicrograph of mapped region.

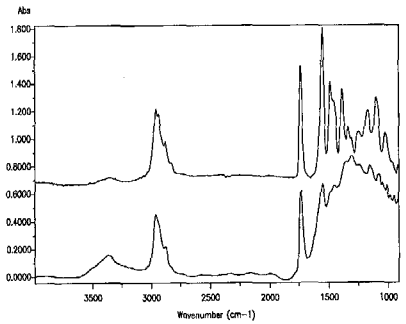


Figure 2. IR microspectroscopy map of region.

Localized Heterogeneity of Biological Tissues and Textile Surfaces Revealed with Synchrotron IR Microspectroscopy — U2B

D.L. Wetzel, L. Cho, J. Sweat, (Kansas St. U.), S.M. LeVine (U. Kan. Med. Ctr.), and J.A. Reffner (Spectra-Tech, Inc.)

Infrared microspectroscopic mapping of biological tissue is routinely done at the KSU Microbeam Molecular Spectroscopy Laboratory using an "IRμs" with conventional globar (thermal) source. The chemical microstructure has been studied *in situ* for plant (wheat kernel slices, etc.) and mammalian (normal and diseased brain) tissues. Additionally, single fibers are analyzed in both ATR and transmission modes. Smaller spot sizes are achieved with the same model microspectrometer coupled to beamline U2B of the NSLS, producing better spatial resolution and greater detail. It has been possible to identify localized heterogeneity using smaller aperture and step sizes (6μm or 12μm) that achieve 100% representation of the sampled area. A high S/N even at small apertures eliminates excessive scan times and makes high definition mapping practical. Tissue samples from mammalian brains and several grains that appear visually homogenous have been interrogated by this technique, revealling wavelength specific (chemically defined) heterogeneity. Figure 1, a 3-D stacked contour plot of a section of corn (Figure 2 shows a visible image), provides an example of the detail achieved. Mapping the amide I (protein) band clearly resolves the five aluerone cells of the corn, surrounded on one side by pericarp and by endosperm on the other. Other wavelengths can be used to reveal the different chemical species present in each morphological part.

Adapting the ATR microscope objective to the IRμs installed at U2B beamline has resulted in the ability to interrogate a 10μm spot on the surface of a single textile fiber to reveal variation in the surface treatment, e.g. permanent press, on a cotton fiber. Previously, 42μm was the practical limit with a conventional source. Figure 3 shows variation in spectra obtained using 10μm spots taken 15μm apart.

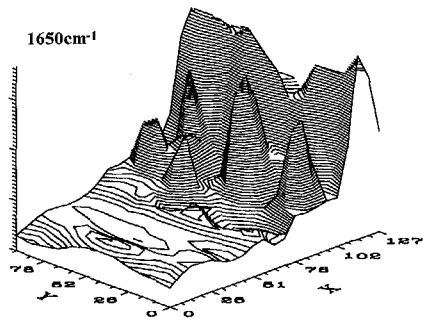
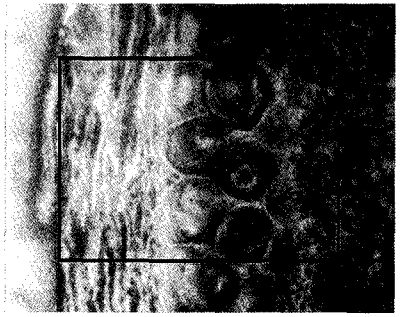


Figure 1. Corn 1650 cm^{-1} peak area map (pericarp, aleurone cells, endosperm) Figure 2. (right) Photomicrograph of corn section showing and endosperm (right). Figure 3. (right) cotton fiber.



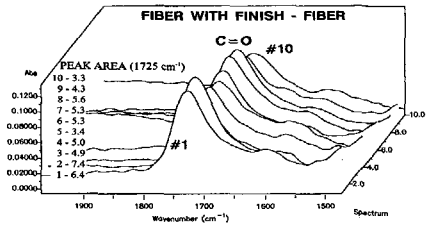


Figure 2. (top), Figure 3. (bottom).

Diffraction-Limited Infrared Microspectroscopy of Polymer Laminates | U2B

Carl G. Zimba (MIT)

By combining the chemical specificity afforded by infrared spectroscopy with the spatial resolution of optical microscopy, infrared microspectroscopy (IMS) has become a mainstay analytical tool in both academia and industry. While applications abound in a wide variety of fields including chemistry, physics, biology, polymer science, material science, forensic science, and art conservation, IMS has been limited in spatial resolution to sampling areas above ten microns in diameter. Replacing the traditional thermal emission source of a conventional infrared microscope with the infrared emission from the VUV ring at the NSLS, substantial improvements in both spatial resolution and signal-to-noise ratio of IMS measurements have been achieved, as illustrated in the figure below. (A false color image of this data was shown in the 1994 NSLS Activity Report on pages 118-9.) The sample used to obtain this data was a cross-section of a ten-layer polymer laminate, composed of alternating layers of a acrylic acid/ethyl acetate/methylmethacrylate copolymer and either poly(N-vinylpyrrolidone) or poly(vinyl alcohol), sandwiched between thick layers of polycarbonate and ethyl cellulose. The approximate thicknesses of the individual layers in the interior of this laminate range from 2.5 to 4.5 microns. The IMS data was acquired using a 3 micron wide slit sampling aperture oriented parallel to the laminate layers while the sample was rastered in 1 micron steps across the individual layers. Each of the layers can be easily discerned in this map of absorption intensity in the CH and OH stretching region. Presently, the lower limit of spatial resolution appears to be governed by diffraction effects and to be wavelength-dependent. In addition to this optical approach to improve the spatial resolution, various mathematical treatments, including chemometrics and correlation analysis, are being pursued.

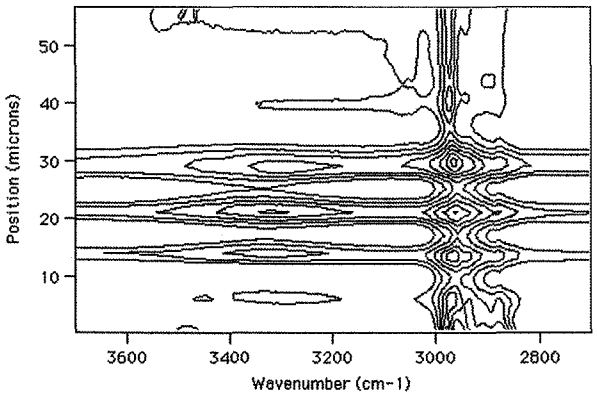


Figure 1.

The Electronic Structure of GaN Measured Using ARP * | U4A

S.S. Dhesi, C.B. Stagarescu, L.-C. Duda and K.E. Smith, R. Singh and T. Moustakas, (Boston University)

Refractory III-V nitrides such as GaN are an important class of wide band gap semiconductors, with possible use in optoelectronic, high power and high temperature devices. Advances in growth techniques have enabled the production of high quality single crystal GaN films on a variety of substrates. We have studied the electronic structure of thin film wurtzite (hexagonal) GaN using angle resolved photoemission spectroscopy. Our samples were grown by electron cyclotron resonance assisted molecular beam epitaxy at Boston University, and cleaned in the spectrometer chamber by Ga evaporation followed by repeated cycles of nitrogen sputtering and annealing in UHV. Samples showed sharp hexagonal LEED patterns, with no carbon and minimal oxygen contamination visible in Auger spectra following this procedure. The films were auto-doped n-type. Figure 1 shows initial results of our measurents of the GaN bulk and surface electronic structure. Clear band dispersion was visible in the ARP spectra, and this could be converted into the experimentally determined band structure of Fig. 1 by assuming a free electron final state. The solid lines in Fig. 1 are the results of an LDA calculation of the band structure by Rubbio *et al* (Phys. Rev. B **48** 11810 (1993)). The agreement with the calculation is excellent over a wide area of the Brillouin zone. Note, however, that a state was observed at the top of the valence band that has no counterpart in the calculated bulk structure. We tentatively identify this as a surface state, and have shown that it is sensitive to the absorption of O_2.

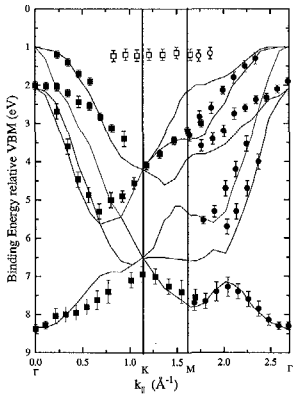


Figure 1. Measured and calculated band structure of GaN.

* Work supported in part by the National Science Foundation under DMR-9504948.

Angle Resolved Photoemission of of V_2O_3 and VO_2 Near the Metal-Insulator Transition — U4A

E. Goering, M. Schramme, O. Mller, H. Paulin, M. Klemm, S. Horn (U. Augsburg), M. L. denBoer (CUNY Hunter)

Vanadium oxides have been studied for several decades because of their unusual properties, including temperature-induced metal-insulator transition (MIT) and electronic correlations in VO_2 and V_2O_3. However, good quality surfaces are hard to prepare, limiting angle-resolved photoemission. We have been able to measure angular resolved photoemission on single crystals grown by chemical transport, which have specular surfaces and can be characterized by LEED after *in situ* heating in oxygen. Spectra were taken above and below the MIT for both materials. Fig. 2 shows angle resolved photoemission spectra of V_2O_3. Fig. 1 shows spectra of the VO_2 (110) (rutile) surface in both the metallic and insulating monoclinic phases. The MIT is clearly reflected in these spectra. For quantitative analysis spectra were fitted; the region near E_F required a Fermi cutoff and two Gaussians, with linewidths 1.2eV and 1.0eV,i.e., considerably larger than the instrumental resolution.

The observed dispersion is much less than band structure calculations suggest [1], implying the electrons are less mobile than predicted. Two possible causes are: (a) Electron-electron correlations, which are expected in these materials. In fact, the two peak structure of the valence band in angle integrated measurements has been interpreted in terms of a lower Hubbard band (incoherent peak) and a coherent peak at E_F. However, as band structure calculations predict the existence of two partially filled bands near of E_F another explanation is possible. (b) Strong electron-lattice interactions, possibly related to the well-known structural instability of VO_2 and V_2O_3. This suggestion, while speculative, is perhaps supported by the observed peak widths, which are fit best not be Lorentzians (implying lifetime effects), but by Gaussians, implying broadening due to a superposition of lines, as would arise from coupling of electronic and lattice degrees of freedom. Such effects are observed, for example, for molecules chemisorbed on surfaces.

[1] E. Goering, M. Schramme, O. Mller, H. Paulin, M. Klemm, M. L. denBoer, and S. Horn, Physica B (in press).

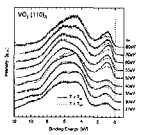


Figure 1. Normal emission photoemission of VO_2 (110) rutile, above (solid) and below (dotted) the MIT (upper part). Photon energies are indicated on the right.

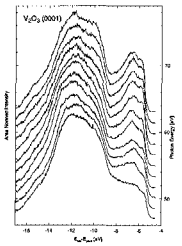


Figure 2. Normal emission photoemission of V_2O_3. Photon energies are indicated on the right.

Photoemission Studies of Ordered and Disordered Cu-Au Alloys * — U4A

Wei Liu, R.G. Jordan and S.L.Qiu (Florida Atlantic U.)

Our interest in the electronic structure in CuAu and Cu3Au alloys is based on the fact that the CuAu alloy undergoes two transformations with increasing temperature: from CuAuI (L10-structure) to CuAuII (a one-dimensional long- period superlattice) at about 380 C and from CuAuII to disordered fcc at about 410 C. Cu3Au undergoes a transformation at about 390 C from the L12 structure to disordered fcc. Our objective is to gain some fundamental understanding of the driving force for these transformations. The order-disorder transformation depends on the competition between interatomic forces that, in turn, are intimately related to the underlying electronic structure. We have carried out a series of photoemission measurements from polycrystalline samples of CuAu and Cu3Au at different temperatures. Figure 1 shows the valence band spectra of CuAu in the ordered and disordered phases. There are considerable changes in the electronic structure in the region spanned by the Au-related d states. Figure 2 shows the shift of the Au 4f core level in CuAu alloy due to the phase difference. Similar changes in the valence band and core level spectra were also observed for Cu3Au alloy. It should be pointed out that using AES we found no significant difference in surface composition between the ordered and disordered phases. Thus, the changes we observe in the photoemission spectra are due to modifications in the electronic structure. More detailed data analysis is under way.

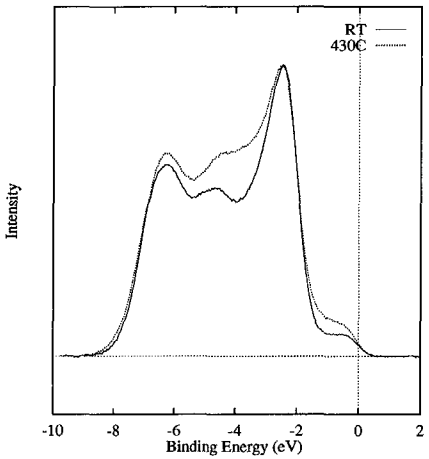


Figure 1. Valence band spectra of CuAu alloy in ordered and disordered phases

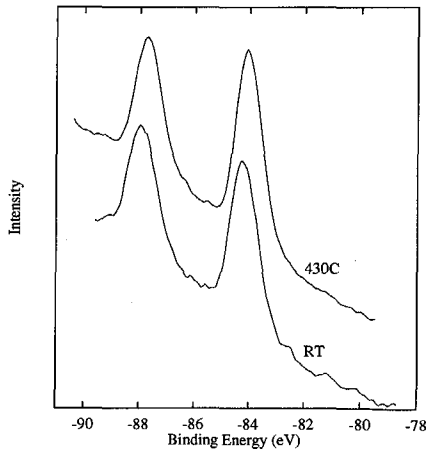


Figure 2. Au 4f core level spectra of CuAu alloy in ordered and disordered phases

* Supported by NSF Grant DMR-9500654.

Electronic Structure of the Organic Superconductor -(BEDT-TTF)Cu[N(CN)$_2$]Br *	U4A

C.B. Stagarescu, S.S. Dhesi, and K.E. Smith (Boston U.), R. Haddon (Bell Labs), J. S. Brooks, (Florida State U.)

The organic solid κ - (BEDT-TTF)Cu[N(CN)$_2$]Br (where, BEDT-TTF = bis(ethylenenedithiolo)tetrathiafulvalene is a quasi-two dimensional (2D) conductor, with layers of BEDT-TTF stacks separated from each other by insulating anion sheets. This material, commonly referred to as ET, is metallic at room temperature and becomes superconducting at approximately 10 K. Despite extensive studies of the transport properties of this material, numerous aspects of the electronic structure of ET are unknown. We have begun a study of ET using angle resolved photoemission (ARP) spectroscopy and soft x-ray emission spectroscopy. Since ET is a layered material with a large unit cell, ARP will measure primarily the electronic structure of the outer layer. We have studied a series of crystals cleaved in UHV, and examined the electronic structure of the cleaved surfaces, ion bombarded surfaces, surfaces exposed to O_2, and Cs- dosed surfaces. Figure 1 shows a series of normal emission spectra taken as a function of the angle of incidence of the light from a cleaved ET crystal. Virtually no emission is visible close to E_F in any of the spectra. This is likely to result from the poor quality of the cleaves, which are visibly rough. However, ARP can still provide information on the orbital charatcter of the valence band. As the angle if incidence is increased, the intensity of the feature at 3 eV below E_F increased dramatically. This is consistent with a C 2p character for this part of the valence band. These experiments are continuing, with emphasis on measuring the intrinsic electronic structure close to E_F.

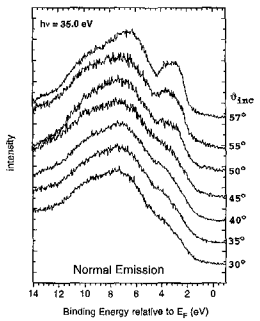


Figure 1. ET normal emission as a function of photon angle of incidence.

* Work supported in part by NSF CAREER award DMR 95-01174.

C 1s NEXAFS of La@C$_{82}$	U4B

J. F. Armbruster, N. Nücker, S. Schuppler, D. Fuchs (Forschungszentrum Karlsruhe, FRG), R. H. Michel, M. M. Kappes (U. of Karlsruhe, FRG)

Endohedral metallofullerenes like La@C$_{82}$ should be rather stable in air. To study possible effects of air exposure, we determined the unoccupied electronic structure of air- and oxygen-exposed La@C$_{82}$ by C 1s NEXAFS, taken both in transmission and in total electron yield (TEY) mode, and compared the results to annealed ($\approx$ oxygen-free) films and to the parent compound C$_{82}$.

The figure depicts C 1s NEXAFS for air and oxygen exposures and heat treatments. C$_{82}$, after heating to 400°C, is shown at the top (a) for comparison. The fully air-exposed La@C$_{82}$ spectrum (b) exhibits two features next to the main π^* peak: a shoulder S at lower and a peak A at higher energies. After heating to 300°C (c), S is reduced but still substantial, while A has vanished. S is further reduced by heating to 600 and 710°C (d), (f). These two traces are virtually identical, suggesting that air has been completely removed from the films. The films were exposed to O_2 at 5×10^{-5} mbar before taking traces (e) (no heating) and (g) (heating to 170°C during exposure). In the latter case part of the intensity at S is restored, as seen from the dotted line denoting trace (f). Concurrent with this effect is a broadening and a slight shift of the π^* feature, cf. (b). The surface-sensitive TEY data exhibits a behavior similar to the bulk; however, in (g') peak A reappears, indicating that the surface region already saturates with oxygen.

The NEXAFS for air- and oxygen-loaded La@C$_{82}$ resembles closely the annealed C$_{82}$. This suggests the simple view that the 3 electrons donated by La to the C$_{82}$ cage are in part removed by oxygen, thus in effect restoring the electronic structure of the empty cage. Caution is necessary, of course, since there is some mixing of La with cage orbitals, and since it is not clear yet if S could be caused by a Jahn-Teller-like effect from lattice expansion. Also, for C$_{82}$ the annealing temperature has to remain low and, thus, still some air may be left in those films. Still, we conclude that part of the intensity at S is due to such a "p type oxygen doping".

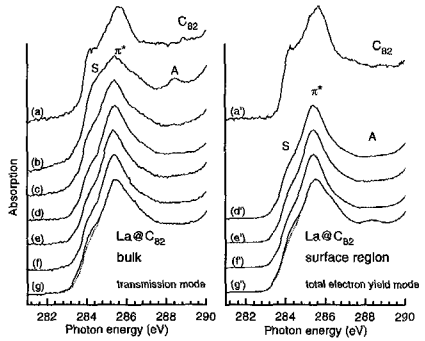


Figure 1.

Magnetic Circular Dichroism Studies of FeV Alloys — U4B

V. Chakarian and Y. U. Idzerda (NRL), C.T. Chen (Bell Labs)

There are only a few elements in the periodic table that are ferromagnetic at room temperature, somewhat limiting the range of applications of magnetic materials. One way to extend the range of applications is to ´engineer˜ new magnetic materials formed of alloys and multilayers of these normally ferromagnetic materials. Among these alloys and multilayers, Fe-V system has been receiving a renewed attention. Studies have focussed on induced V moments as well as inverse magnetoresistance in artificially engineered Fe-V multilayers and alloys. The FeV alloys have some interesting properties in their own right. Based on numerous early neutron scattering experiments the alloy system is ferromagnetic at room temperature for V concentrations of up to 70 atThe induced V moments are as large as 1.2 5B for in the dilute V limit and decrease rapidly to zero near 15 atthroughout the entire ferromagnetic phase, the V moments are anti-aligned to Fe moments which in turn decrease monotonically with increasing V concentration and finally reach zero near 70 atthis system does not display bulk antiferromagnetism. In this study, the magnetic characteristics of disordered FeV alloys have been studied via magnetic circular dichroism (MCD). The use of MCD allows the determination of Fe and V moments (the extraction of absolute V moments are somewhat more difficult but trends can be established). The measurements have been conducted in transmission on thin films grown in situ, minimizing surface effects and allowing for direct comparison of the measured moments to bulk moments determined via earlier neutron scattering experiments. The figures below show representative Fe and V absorption spectra as well as the corresponding MCD spectra. The V MCD spectrum, somewhat more complex than that of Fe due to different multiplet structure of V, clearly shows that V atoms possess a net moment anti-aligned to Fe moments as indicated by the positive MCD signal in the V L3 region. Surprisingly, though, for all the alloys studied, the orbital moment is near zero but positive, i.e., aligned with the Fe moments. A more detailed description of the experiment and the results for the entire ferromagnetic phase will be presented in an upcoming publication.

VC is supported by the Office of Naval Research.

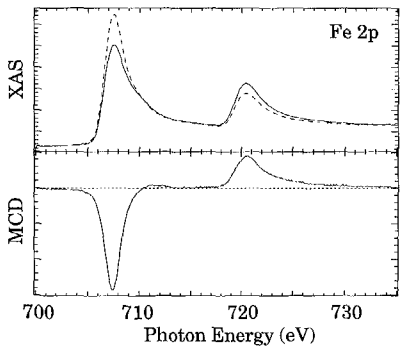


Figure 1. Representative Fe L-edge XAS and MCD spectra from a FeV alloy.

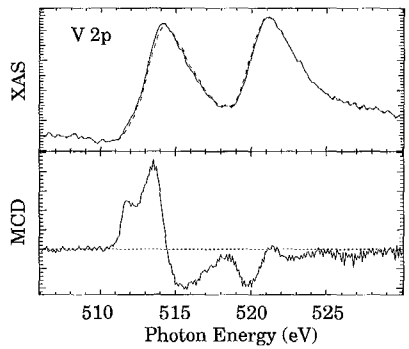


Figure 2. V L-edge XAS and MCD spectra for the FeV alloy of Fig. 1.

Linearly Polarised Soft X-ray Resonant Magnetic Scattering from Fe_xMn_{1-x}/Ir (001) Superlattices * — U4B

A. Déchelette-Barbara, J.M. Tonnerre, F. Bartolomé, D. Raoux (CNRS, France), H.M. Fischer (CNRS, Univ. Nancy I, France), V. Chakarian (NRL), and C.C. Kao (NSLS)

Soft x-ray resonant magnetic scattering (SXRMS) has been used in order to study the magnetic transition which occurs in Fe_xMn_{1-x}/Ir(001) superlattices (SL's) for x=0.8. SQUID magnetometry and Mossbauer spectroscopy suggest a transition from an antiferromagnetic state to a ferromagnetic one for increasing x values. This result is remarkable since the bulk alloys are antiferromagnetic in the whole range of the alloy composition. Two samples, having an Fe concentration here and there of the transition (x=0.7 and x=0.9), have been studied. The first sample, $[(Fe_{0.7}Mn_{0.3})_{27\mathring{A}}/(Ir)_{18\mathring{A}}]_{20}$, is labelled SL/0.7 and the second one $[(Fe_{0.9}Mn_{0.1})_{27\mathring{A}}/(Ir)_{18\mathring{A}}]_{20}$ is noted SL/0.9. SRXMS allows to discriminate the properties of Fe from those of Mn by working at their respective L-edges. Figure 1 and 2 shows the energy dependence of the reflectivity measured using p-polarised soft x-rays in the transverse Kerr geometry as well as the derived asymmetry ratios. The incident angle was set to 15 degrees. While the whole shape of Ra is about the same for both samples and show a resonant effect near the Fe L_3 and L_2 edges, there is a strong decrease in the amplitude of the effect forSL/07. For SL/0.9 alloy the maximum of the amplitude reaches 45% of magnetic effect where as for the sample where as for SL/0.7, the effect is of 3-4% only. The Fe magnetic moment appears to be much more affected by the change of the stoechiometry which is much more than that expected from SQUID measurements (average magnetic moment: 1.75 for SL/0.9 and 0.35 for SL/0.7). To discuss further our experimental results, we need to fit the reflectivity curves and the asymmetry ratios. At the $L_{2,3}$ edges of Mn and no magnetic effects have been observed within our statistic which suggests that Mn atoms do not carry a net magnetic moment or a very small one.

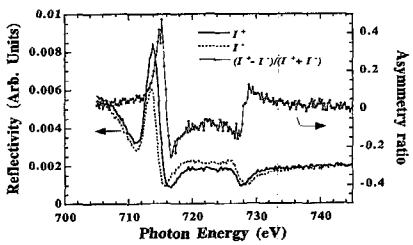


Figure 1. Asymmetry ratio obtained on SL/09 at fixed angle, θ=15, at the Fe L-edges.

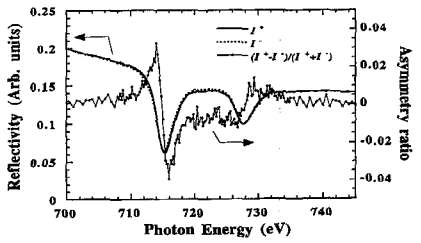


Figure 2. Asymmetry ratio obtained on SL/07 at fixed angle, θ=15, at the Fe L-edges.

* Work was supported by NSF Grant No. NSF-222-44-94.

O 1s NEXAFS of $Pr_xY_{1-x}Ba_2Cu_3O_y$ Single Crystals | U4B

M. Merz, N. Nücker, E. Pellegrin, S. Schuppler (Forschungszentrum Karlsruhe, FRG), M. Kielwein, M. Knupfer, M. S. Golden, J. Fink (IFW Dresden, FRG), C. T. Chen (SRRC, Taiwan), V. Chakarian, Y. U. Idzerda (NRL), and A. Erb (U Geneve, Switzerland)

Substituting Y in orthorhombic (Y,RE)$Ba_2Cu_3O_y$ by a rare-earth element RE has in general little effect on the superconducting properties. For RE = Pr, however, superconductivity is completely suppressed. To understand this effect we studied the unoccupied electronic structure of $Pr_xY_{1-x}Ba_2Cu_3O_y$ using polarization-dependent O 1s NEXAFS of detwinned single crystals. In this way, it was possible to identify hole states in the CuO_2 planes and the CuO_3 chains and to give estimates of the relative contributions of the O $2p_x$, $2p_y$, and $2p_z$ orbitals to these states.

Fig. 1 shows the O 1s NEXAFS for $Pr_xY_{1-x}Ba_2Cu_3O_{6.9}$ for x = 0.0, 0.4, and 0.8. The polarization was set parallel to the crystal axis **a**. With increasing Pr concentration, the first peak above threshold decreases, while the second one increases substantially. In accordance with previous work, these peaks are attributed to the Zhang-Rice (ZR) state and to the upper Hubbard band (UHB). Among other things, Fig. 1 illustrates for the PrYBCO system the well-established transfer of spectral weight between the ZR state and the UHB, related to the Cu character of both features.

In Fig. 2, the O 1s NEXAFS for $Pr_{0.8}Y_{0.2}Ba_2Cu_3O_y$ is compared for y = 6.9 and 6.1. The UHB has the same intensity for both spectra. Thus, the additional states observed for y = 6.9 at the ZR state energy (cf. Fig. 1) cannot have any Cu character (as the ZR state does) but must be of different origin. This points to states resulting from Pr 4f – O $2p_\pi$ hybridization, the Fehrenbacher-Rice (FR) states. Expanding upon and quantifying this observation [1], we were able to test the current theoretical explanations for the Pr-induced suppression of superconductivity. While we can rule out models involving hole filling or charge transfer between the planes and the chains, a detailed evaluation [1] of our data is indeed consistent with approaches based on FR hybridization.

[1] M. Merz et al., to be published

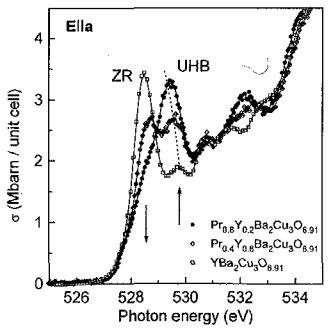


Figure 1.

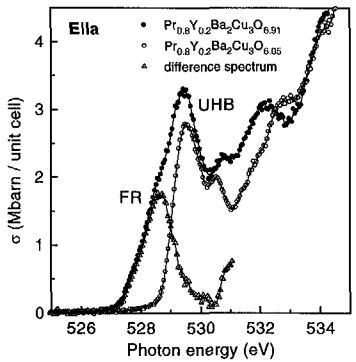


Figure 2.

High Temperature Metal-Insulator Transition of $LaCoO_3$ | U4B

J.-H. Park (NSLS), S-W. Cheong (Bell Labs.), and C. T. Chen (SRRC)

$LaCoO_3$ displays interesting electrical and magnetic anomalies in wide temperature range of 0K to 700K. $LaCoO_3$, which undergoes a gradual insulator to metal transition in the neighborhood of 500K, has been reported to exhibits a magnetic (diamagnetic to paramagnetic) transition around 90K upon heating. in the insulating phase. In order to understand this peculiar physical behavior, various groups have been proposed different interpretations based on partial experimental results. However, the nature of the transitions, both the low and high temperature transitions, are far away from the universal understanding. We have investigated the high temperature transition utilizing a high resolution photoemission spectroscopy. Fig. 1(a) shows the photoemission spectra of the valence band including shallow core levels (O 2s and La 5p) below (450K) and above (700K) the high temperature transition temperature. The spectra were taken at 110eV photon with 70meV experimental resolution. The binding energy was determined relative to the chemical potential of a clean Pt in electrical and thermal contact with the sample. As can be seen in Fig. 1(a), considerable spectral changes have been observed in whole valence band at the two different temperatures without any significant changes in the shallow core levels. This large spectral change in the entire valence band shows that the high temperature transition is accompanied with a symmetry change, indicating a spin state change (probably the intermediate spin state to the high spin state). Furthermore, the insulator to metal transition has also been observed in the near-m spectra, which were taken at the same experimental conditions, as shown in Fig. 1(b). At 450K, the spectrum starts well below the chemical potential, indicating the insulating state, and the band gap (a half of the band gap if the chemical potential lie at middle of the band gap) was estimated to be 250 meV 50 meV. At 700K, spectrum displays a finite spectral weight at the chemical potential even though the clear metallic Fermi edge feature is not observed due to the broad Fermi thermal function ($4k_BT$ 240 meV).

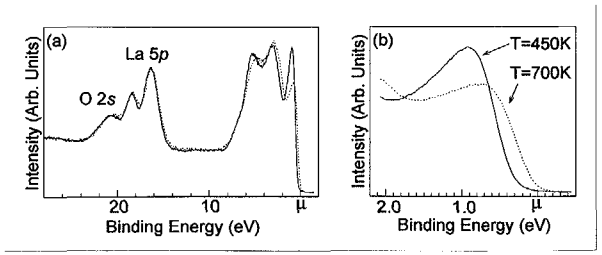


Figure 1. High resolution valence band PES spectra above and below T_t~500K. (a) Broad range. (b) near μ.

Polarization Dependence X-ray Absorption Studies of V_2O_3 | U4B

J.-H. Park (NSLS), L. H. Tjeng (U. of Groningen), J. W. Allen (U. of Michigan), C. T. Chen (SRRC), and P. Metcalf (Purdue U.)

V_2O_3 system, which exhibits a paramagnetic metal to antiferromagnetic insulator transition upon cooling though the transition temperature T_N 155K, has been considered as one of the prototype Mott systems. More than 500 papers related to this system have been published since the discovery of the transition in 1953, but the full understanding of the transition is very far away. The vanadium site in V_2O_3 has the trigonal point symmetry, in which the atomic five-fold $3d$ orbital splits into a singlet a_{1g}, a doublet e_g^{π},and a doublet e_g^{σ}. The d^2 configuration state of V^{3+} becomes either $(a_{1g})^1(e_g^{\pi})^1$ or $(e_g^{\pi})2$. Although the configuration state is widely accepted to provide a critical clue for understanding the transition, it is not established yet. Different studies have suggested different configuration states, and various models based on the different configuration states have been proposed to be applied for the metal-insulator transition. In order to clarify the occupation states in both the metallic and insulating phases, we have performed polarization dependence x-ray absorption measurements at V $L_{2,3}$ and O K edges on well annealed stoichiometric V_2O_3 single crystals. The polarization dependence studies were performed in two different circumstances: the angle θ between the electric field $\vec{E}$ vector of the incoming photon and the structural hexagonal c axis, in which the a_{1g} orbital lies, was set to be 15° (solid) and 75° (dotted). All the spectra in the figures consist of V L_3 edge , V L_2 edge, and O K edge absorption features in the 512eV-519eV, 519eV-528eV, and 529eV-555eV photon energy regions, respectively. In the measurements, we found considerable polarization dependence, especially in the starting feature, which is deeply related to the corresponding core level to a_{1g} transition, of the each absorption edge, indicated by arrows in the figure. The 15° spectra give more intensity at all three starting features both above and below T_N, and further the polarization dependence turns out to be much stronger below T_N. These results show that the occupation configurations are the mainly $(e_g^{\pi})^2$ state in both above and below T_N but the mixing with the $(a_{1g})^1(e_g^{\pi})^1$ state strongly increases in the metallic phase.

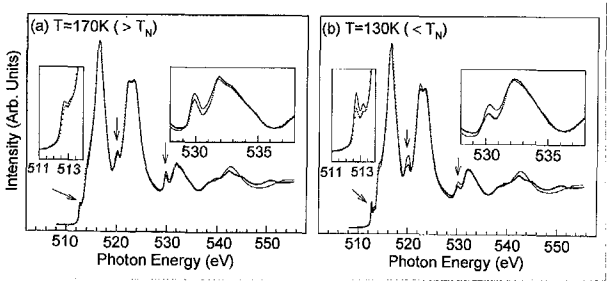


Figure 1.

Soft X-ray Magnetic Circular Dichroism Study of $La_{1-x}Sr_xMnO_3$ | U4B

E. Pellegrin, L. H. Tjeng, F. M. F. de Groot, R. Hesper, G. A. Sawatzky (RUG), J. D. O'Mahony, C. F. J. Flipse (TUE), Y. Moritomo, Y. Tokura (JRCAT), C. T. Chen (SRRC)

Soft x-ray magnetic circular dichroism (SXMCD) measurements have been performed on the O K- and Mn L-absorption edges of $La_{1-x}Sr_xMnO_3$ single crystals in their ferromagnetic regime (see Fig. 1 and 2). This has been done using a recently developed experimental technique for magnetizing the samples offering the possibility to get high-accuracy SXMCD effect measurements on bulk specimen.

The very strong doping-induced O K-edge prepeak intensity as shown in Fig. 1 is proof of an enhanced O2p hole component of the doped holes. The orbital magnetic moment of this O2p component determined with the SXMCD difference spectra in Fig. 1 suggests a large spin moment on the O sites ferromagnetically coupled to the Mn moments. The shape of the Mn L SXMCD difference spectrum in Fig. 2 shows fine structures which are consistent with crystal field multiplet calculations assuming a local lattice distortion of the MnO_6 octahedra even in the low-temperature metallic phase.

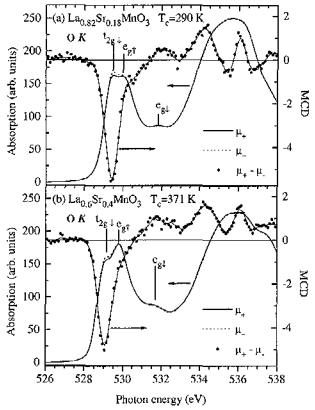


Figure 1. O K soft x-ray magnetic circular
dichroism spectra (a) $La_{0.82}Sr_{0.18}MnO_3$ and (b) $La_{0.6}Sr_{0.4}MnO_3$; solid (dotted) lines: spectra taken with the spin of the incident photons parallel (antiparallel) to the spin of the Mn3d majority electrons. Solid circles: SXMCD difference spectra resulting from the above data. The thin solid lines guides to the eye.

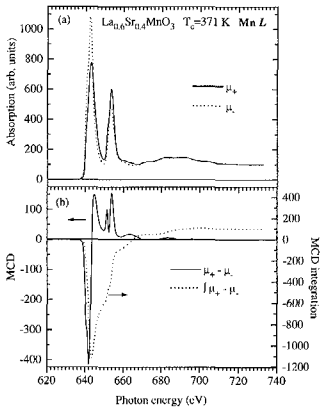


Figure 2. (a) Mn L SXMCD spectra of $La_{0.6}Sr_{0.4}MnO_3$; solid (dotted) lines: spectra taken with the spin of the incident photons parallel (antiparallel) to the spin of the Mn3d majority electrons. (b) Solid line: SXMCD difference spectrum resulting from the above data after correction for the finite degree of circular polarization of 88%; dotted line: integrated difference spectrum.

Nature of the Unoccupied Electronic States in Sr_2RuO_4 — U4B

M. Schmidt, N. Nücker, T. R. Cummins, D. H. Lu, S. Schuppler (Forschungszentrum Karlsruhe, FRG), F. Lichtenberg (Varta Batterie AG, FRG)

Sr_2RuO_4 is the first noncuprate layered perovskite superconductor. At U4B, we determined the unoccupied electronic structure using O 1*s* NEXAFS in fluorescence yield mode. The figure shows NEXAFS spectra for three orientations of the RuO_2 planes towards the polarization vector, with the 90° spectrum having been deduced from the 0° and 75° spectra. At the angle $\theta = 0°$ (90°), only unoccupied O $2p_{x,y}$ (O $2p_z$) orbitals can be excited.

Comparing the near-threshold features for $\theta = 0°$ and 90° one notes that feature *A*, at $h\nu = 528.5$ eV, is pronounced for 0° and weak for 90°, and that its spectral weight is small relative to the other features. Of course, for $\theta = 0°$ only half of the in-plane orbitals ($p_{x,y}$) are detected. This means that for feature *B*, e. g., the spectral weight perpendicular to the plane is just twice as large as the in-plane weight – not 4 times, as the figure seems to suggest. This ratio is reversed for peak *D*. Peak *C* is less pronounced and appears more "isotropic".

In Sr_2RuO_4, the main contribution near E_F comes from O $2p$ states hybridized with Ru $4d$ states of t_{2g} and e_g symmetry that are split by about 4 eV. This and the spectral weight and angular dependence observed for peaks *A* – *D* leads to the following assignments: *A* and *B* result from the hybrids with t_{2g} symmetry, *C* and *D* from those with e_g symmetry. Presuming that for O(1) E_F corresponds to 529 eV (broken line in the figure), peak *A* is related to the apical oxygen, O(2), whose binding energy is expected to be 1.5 eV smaller than for O(1) [1]. For *B*, the large contribution of holes perpendicular to the planes is due to O(1) $2p_\pi$ orbitals hybridized with Ru $4d_{xz,yz}$, which are found in photoemission [2] to cross E_F. Similarly, the in-plane contribution of *B* is caused by O(1) $2p_\pi$ – Ru $4d_{xy}$ orbitals, which also cross E_F. Peak *C* may be explained by Ru $4d_\gamma$ states hybridized with O $2p_\sigma$ states, since it has an in-plane and an out-of-plane contribution. Spectral weight at higher photon energies is more difficult to assign [3].

[1] D. J. Singh, Phys. Rev. B 52, 1358 (1995).
[2] D. H. Lu et al., Phys. Rev. Lett. 76, 4845 (1996).
[3] M. Schmidt et al., Phys. Rev. B 53, 14761 (1996).

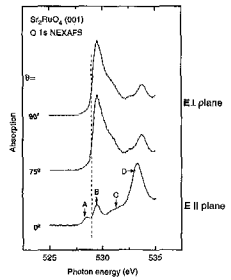


Figure 1.

Pump-probe, Far-infrared Study of Pair Breaking and Recombination in Superconducting b — U4IR

G.L. Carr and G.P. Williams (NSLS), D.B. Tanner (U. Florida)

We have begun an investigation of the pair breaking and (quasi-particle) recombination processes in low-T_c superconductors using far-infrared pulses from the VUV ring. The recombination of quasi-particles into Cooper pairs depends on the electron-phonon coupling constant, and the relaxation of phonons with energy greater than 2Δ (the pair breaking energy). The q-p relaxation time is expected to be on the order of a nanosecond at liquid helium temperatures. Far infrared measurements are sensitive to superconductivity details, such as the condensate strength, magnitude of the energy gap, and perhaps variations in the occupation of electronic states.

In our first study, we examined a thin niobium film. Fig. 1 shows the ratio of its transmission in the superconducting and normal states, along with the expected behavior, as calculated using BCS theory. The time-resolved study used pulses from an $Al_{1-x}Ga_xAs$ diode laser for the pump and far IR pulses from the VUV ring as the probe. Pulse duration for both sources was 2.2ns (FWHM, limited by the laser diode). The diode delivered approximately 2nJ into an area of 0.2 cm^2, sufficient to break approximately 1 pair in 1000. The complete transition from superconducting to normal state resulted in a $\sim 100\mu$V signal change on the far IR detector; from this we estimate a ~100nV photo-induced pair breaking signal. Fig. 2 shows the pair breaking signal, measured in a derivative mode. The signal magnitude is in agreement with our estimate, and the signal rise and fall times are consistent with a lifetime ~1ns.

Spectral analysis was impractical due to poor spectrometer efficiency below 25 cm^{-1}, and low laser power. Both problems will be surmounted when the time-resolved laser system and far IR beamline at U12IR become operational in 1997.

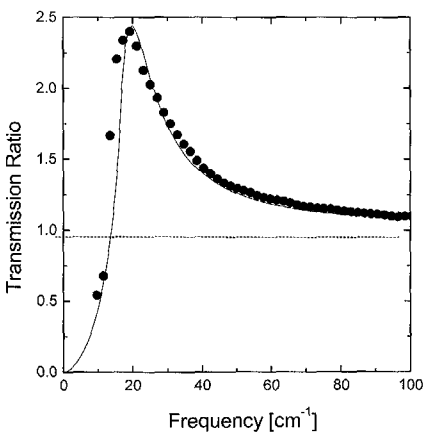


Figure 1. Superconducting to normal state transmission ratio for the Nb film.

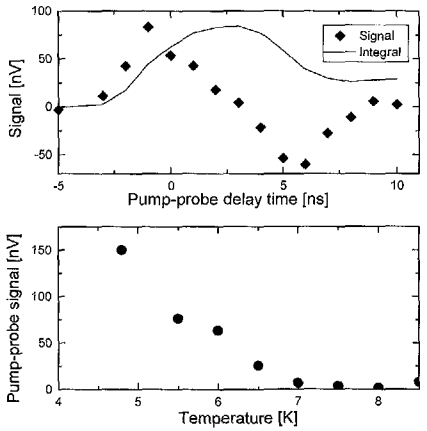


Figure 2. Pump-probe correlation signal (top) and temperature dependence (bottom).

Low-Frequency Modes in Polypeptides and Proteins | U4IR

M.R.Chance, A. Xie, B. Sclavi, Q. He, L.M. Miller, M. Sullivan (AECOM)

Anharmonic motions leading to atomic rearrangements are essential for proteins to function. We report here the first far-infrared absorption studies on anharmonities of low frequency modes in protein model compounds, namely homopolymers of L-phenylalanine, L-Alanine, L-Leucine, and L-Tryptophan.

The bright synchrotron light source was utilized in collecting high signal-to-noise data, so that it is possible to perform quantitative data analysis. The far-infrared absorption spectra of each model compound were collected at two temperatures (100 K and 295 K) in the region of 20-450 cm-1.The results show that (1) each of the homopolymers exhibit a small number of absorption bands in the region of 50 to 150 cm-1, and the peak positions of these bands are well resolved; (2) the peak frequencies of far-infrared bands are temperature dependent, and decrease as temperature is increased from 100 K to 295 K; (3) the band-widths of these low frequency modes, obtained from Gaussian fits are narrower at 100K as compared to those at 295 K. These results strongly infer that the low frequency modes in protein model compounds are highly anharmonic. The results are consistent with various computational studies, as well as indirect experimental studies.

This method can be further extended to study anharmonicities of functionally important low frequency models in proteins, including hydrogen bonding interactions, metal-ligand interactions, and collective modes in proteins.

Doping Dependence of the IR Response of $La_{2-x}Sr_xCuO_4$ | U4IR

R. Henn, A. Wittlin, M. Cardona (Max-Planck Institut) and S. Uchida (U. of Tokyo)

We have measured the c-axis complex dielectric function of $La_{2-x}Sr_xCuO_4$ by far infrared ellipsometry for different dopant concentrations x. Four phonons, which dominate the observed response, can be well decribed by Lorentzian profiles. Two of these modes are weak and appear as a consequence of the small orthorhombicity of these materials. The variation of the TO-frequency, the phonon lifetime (FWHM) and the oscillator strength of the two strongest (tertragonal) modes with the Sr content is given in the left figure. The TO-frequencies of both modes behave differently: the softening of the 500 cm^{-1} mode can be related to an increase of the lattice parameter c, while the decrease of the a-axis lattice constant with doping results in a hardening of the 240 cm^{-1} mode.

Especially for the higher doped samples there is an electronic background present in our normal state data, which in a preliminary analysis is accounted for by a Drude-term contributing to the dielectric function. DC-resistivities extracted from the Drude-parameters obtained for the spectra taken at different temperatures are displayed in the figure on the right hand side and agree well with data in the literature. Our Drude-resistivities are conform with an almost temperature independent c-axis conductivity of the optimally doped sample with $x = 0.15$, while the overdoped sample with $x = 0.2$ exhibits an almost linear temperature dependence of the c-axis resistance. The variation of the temperature dependence with doping reflects reflects a change in the dominating scattering process of charge carriers. The well known linear temperature dependence of the resostivity within the CuO_2-planes might indicate the same scattering process dominating the transport parallel and perpendicular to the CuO_2-planes for the overdoped samples, whereas for the optimally doped sample different scattering mechanisms have to be considered for the transport along these directions.

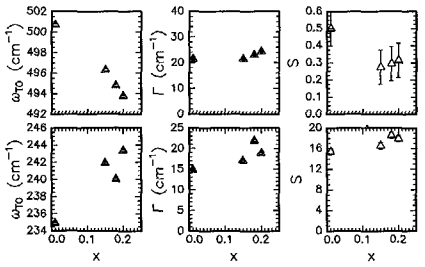


Figure 1.

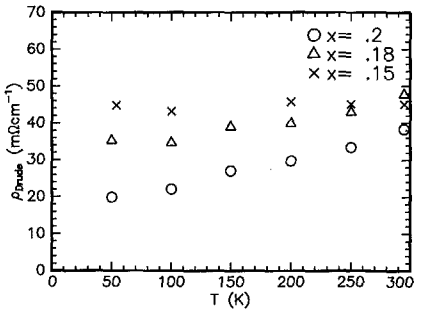


Figure 2.

Carbon Dioxide Activation and Alkali Compound Formation	U4IR

F.M. Hoffmann (SCI-MED) D.G. Van Campen, G.P. Williams (NSLS), J. Paul (Royal Inst. of Tech., Sweden)

The activation of carbon monoxide on metal surfaces is an important elementary step in many catalytic reactions, such as the alcohol synthesis reaction, or the water=gas shift reaction. Alkali promoters are frequently used to activate CO_2 in catalytic reactions and consequently the interaction of carbon dioxide with alkali metals has received much attention in surface science studies. The focus of the present work is on the vibrational chracterization of reaction intermediates, particularly of the oxalate in co-evaporated systems of CO_2 and K. The use of synchrotron radiation allows the K-O vibrations in the far-IR to be studied, as well as all the other modes up to 2500 cm^{-1}. The experiments were conducted by evaporating the K in a CO_2 atmosphere. The pressure of the CO_2 and the evaporation rate of the K could be controlled, thus controlling the stoichiometry, and providing selectivity for certain intermediates.

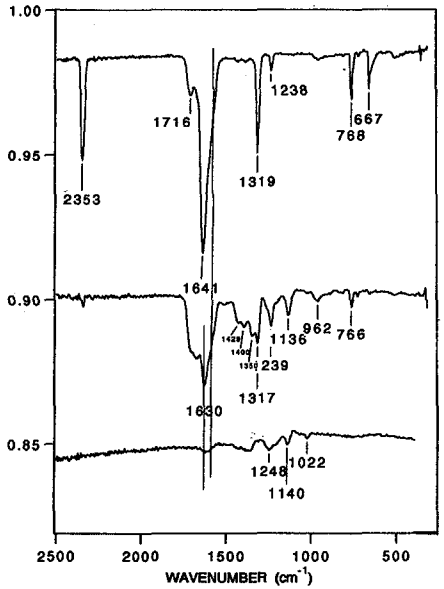


Figure 1. Reflectance changes induced by co-dosing with CO_2 and K with differentratios. Top spectrum, CO_2 rich, middle spectrum K:O=1.25, lower spectrum, CO_2 poor.

Simultaneous Infrared Spectroscopy and DC Resistivity Measurements on Adsorbate-covered Epitaxial Copper Films	U4IR

A. Otto, M. Hein (U. Duesseldorf, Germany), P. Dumas (LURE, U. Paris-Sud, France), G.P. Williams (NSLS)

Previous far-IR reflectance studies at metallic surfaces, using synchrotron radiation, revealed two main intriguing features:

- Dipole forbidden modes of the adsorbates are observed as anti-absorption infrared bands, with Fano-type lineshapes.
- Broadband reflectance changes are simultaneously observed, with a continuous decrease in reflectivity reaching an asymptotic value at around 1500 cm^{-1}.

To account for these observations, B.N.J.Persson proposed a model based on resistivity theory. Accordingly, scattering of the conduction electrons by the adsorbed molecules results in the observed broadband IR absorption. This should be proportional to the change of the DC resistivity of a thin copper film by exposure to the same admolecules. The objective of the present study is to test quantitatively the theoretical predictions of the relationship between the IR broadband reflectance change and the DC resistivity, and to quantify the influence of the ratio of film thickness and skin depth on the strength and lineshape of the frustated motion of the admolecule. The experiments, performed in a first step, on CO adsorbed on a Cu(111) thin film grown on a TiO_2 substrate, have revealed two important observations:

1- A linear relationship between the DC resistivity change and the broadband reflectance change in the asymptotic limit(Fig.1).

2- A non linear relationship between IR integrated intensity of the CO stretching mode and the DC resistivity change (Fig.2) Theoretical calculations are underway to quantitatively account for these experimental results.

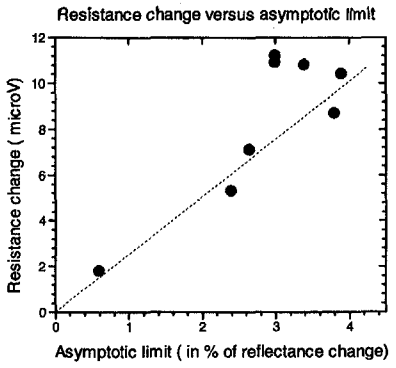


Figure 1. Resistance change versus asymptotic limit for increasing dose of CO on a Cu(111) film.

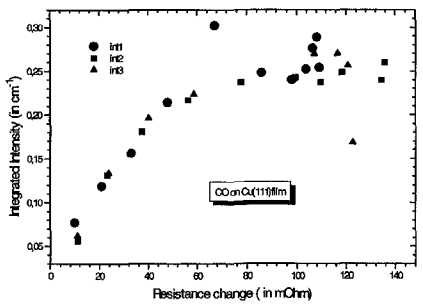


Figure 2. Integrated intensity of the CO stretch band of CO/Cu(111) versus resistance change at various exposures.

Infrared Study of Fullerenes and Fullerides on Ag(111), Au(110) and Cu(111) — U4IR

P.Rudolf (LISE-Namur, Belgique), P.Dumas (LURE and LASIR-CNRS, France), Y.J.Chabal (Lucent Technologies), D.Van Campen and G.P.Williams (NSLS)

Synchrotron infrared reflection-absorption (IRAS) studies of C_{60} deposited on clean and alkali-covered Ag(111), Au(110) and Cu(111), have been performed. On bare substrates, the frequencies and intensities of the only observable dipole active mode are as shown in Fig.1. The remarkable observation is that the frequency shift, as well as the integrated intensity of the dipole active mode, does not follow what one could expect if charge transfer between the substrate and the C_{60} admolecule is the dominant mechanism. These results suggest that complex electron-phonon coupling occurs at these interfaces. Such a coupling is also thought to play an important role when C_{60} is deposited on 1ML K/Ag(111). This is illustrated in Fig. 2. When C_{60} is adsorbed on 1ML of K pre-deposited on Ag(111), an antiabsorption band is clearly seen, at the frequency position of the initial Ag(2) mode. However, for thicker alkali layers, two bands are observed: one, showing up as an absorption band at 1356 cm^{-1}. This is the fulleride mode, of the "bulk" phase. However, the observation of the antiabsorption mode shows that the entire alkali layer is involved with the process.

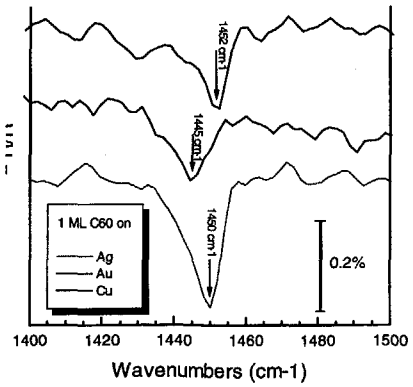


Figure 1.

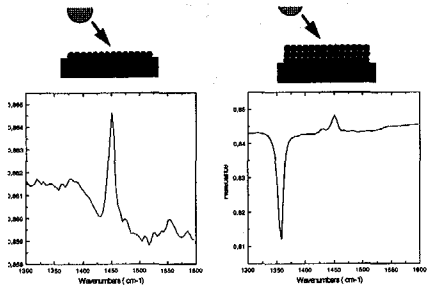


Figure 2.

Branch Crossings of Quantum Well States in Cu Films Deposited on Ni(001) * — U5UA

D.-J. Huang and P. D. Johnson (BNL - Physics)

The existence of minority spin quantum well states in copper films deposited on a Co(001) substrate is well established.[1,2] These states are thought to mediate the oscillatory exchange coupling in the associated magnetic multilayers with the anti-ferromagnetic configuration favored whenever the quantum well states cross the Fermi level.[3,4]

Theoretical studies of this sytem predict a branch crossing whenever the binding energy of the quantum well states corresponds to a well defined d-resonance in the Co substrate. The branch crossing reflects the additional phase shift introduced at the interface by the scattering from a localized level. Whilst this phenomenon has never been observed in copper films deposited on Co, we show in this study that it is observable in copper films deposited on a Ni(.001) substrate.

Copper films were deposited on a thin Ni film previously deposited on a Cu(001) substrate. As a function of thickness the binding energies observed for the quantum well states in the copper films were identical to those observed in the earlier studies using a Co substrate.[1,2] However as shown in the figure, at a thickness of 3-4 monolayers of copper a branch crossing to the second branch starts to occur. We attribute this crossing to resonant scattering from the quantized Ni d levels in the substrate. Such a scattering will introduce a rapid oscillation in the wavefuction of the quantum well state.

References. 1. K. Garrison, Y. Chang, and P.D. Johnson, Phys. Rev. Lett. 71, 2801 (1993). 2. C. Carbone, E. Vescovo, O. Rader, W. Gudat, and W. Eberhardt, Phys. Rev. Lett. 71, 2805 (1993). 3. D.M. Edwards, J. Mathon, R.B. Muniz and M.S. Phan, Phys. Rev. Lett. 67, 493 (1991). 4. J.E. Ortega, F.J. Himpsel, G.J. Mankey, and R.F. Willis, Phys. Rev. B 47, 1540 (1993).

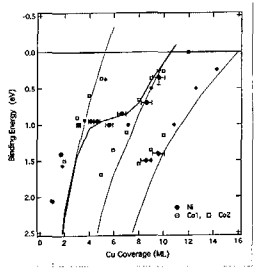


Figure 1. The binding energies of quantum well states at the center of the surface Brillouin zone in Cu films deposited on Ni(001) (filled circles) and Co(001) (open symbols) as a function of Cu overlayer thickness. The data with open circles is taken from ref. 1 and that with open squares from ref. 4.

* This work was supported by the DOE under Contract No. DE-AC02-76CH00016.

The k-space Origin of the Long Period Oscillation in Fe/Cr Multilayers: A Photoemission Study of Epitaxial Cr Grown on an Fe(100) Whisker *	U5UA

J. Pearson, S. D. Bader (ANL), E. Vescovo, D.-J. Huang, P. D. Johnson (BNL), B. Heinrich (SFU)

Fe/Cr multilayers are the prototype giant magnetoresistance (GMR) material. The microscopic origin of its 1.8 nm long-period oscillatory magnetic coupling is still being debated by theorists, while its short-period (of 2 monolayers) is universally ascribed to the nesting of the Cr Fermi surface in the <100> direction. We have carried out angle-resolved photoemission experiments at the NSLS U5 undulator beamline to investigate the k-space origin of the long-period coupling. Exceptionally well-ordered and smooth Cr layers (0.8 - 5 nm) were deposited onto an atomically flat Fe(100) whisker at 300°C for epitaxial growth. We searched different candidate regions of k-space at off-normal geometry for thickness dependent Cr quantum-well (QW) states, and monitored their resultant photoemission intensity oscillations at the Fermi level (E_F). In the vicinity of the d-derived lens feature of the Fermi surface, the intensity at EF oscillates with a period of 1.7±0.2 nm as a function of Cr thickness. This indicates the d-derived QW states pass through E_F periodically. This period coincides with that for the magnetic coupling in Fe/Cr multilayers, which suggests the extremal spanning vector across the lens as the origin of the long period oscillation. The work demonstrates that angle-resolved photoemission provides a novel methodology to distinguish the k-space origin of different oscillation periodicities in the interlayer magnetic coupling.

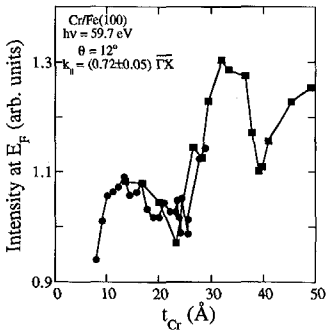


Figure 1. The intensities at E_F vs. film thickness at $k_{||} = 0.72$ in units of the surface Brillouin zone, ΓX (around the "lens"), which yield a periodicity of 17±2 Å. Independent thickness sequences are indicated with different symbols.

* Work at ANL is supported by DOE BES-MS under W-31-109-ENG-38 and ONR N-00014-94-F-0085; work at BNL by DOE under DE-AC02-76CH00016.

The U5UA SGM-beamline: First Tests on the Performances	U5UA

E. Vescovo, Q.-Y. Dong, G. Nintzel, D. Carlson, and S. Hulbert (NSLS)

During this year a new beamline has been installed at the end of the U5-undulator on the UV floor. It replaces an old toroidal single-grating monochromator serving the spin-polarized photoemission experiments. The new design is based on the use of 4 spherical gratings. The conceptual design is described in detail in ref.1. The main goals to be reached with this new SGM-beamline with respect to the old one are: 1) a superior photon energy resolution; 2) a flatter coverage of the available photon energies (10 - 160 eV); 3) a higher photon density at the sample. All the three have been reached. The energy resolution of the beamline has been tested at 30 eV photon energy using the Ar autoionization resonance lines. Typical results are shown in fig.1 where the excited np lines can be seen up to n=19. Fig.2 shows a blow up of peak corresponding to n=16: a full width half maximum of 3.5 meV is derived, giving a resolving power close to 10,000. Using typical entrance and exit slits settings which provide enough photon-flux to perform spin-resolved experiments, the photon energy resolution at 30 eV is still below 10 meV. The use of 4 different gratings greatly enhances the performances of the beamline at the high photon energies side. As an example, measurements of spin-polarized Fe 3p core-level spectra up to hv = 160 eV are now possible. Finally visual inspection of the fluorescent light emitted by a P-covered plate positioned in place of the sample, clearly shows sub-mm spot-size dimensions.

[1] N.V. Smith et al., Nucl. Instr. Meth. A 347 , 119(1994)

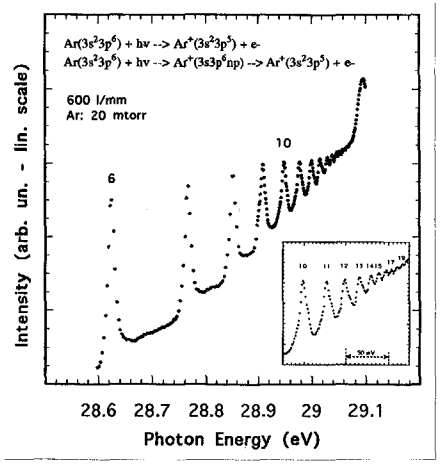


Figure 1. The data are not normalized to the incoming photon flux and the increasing background reflects the intensity of the first harmonic of the undulator.

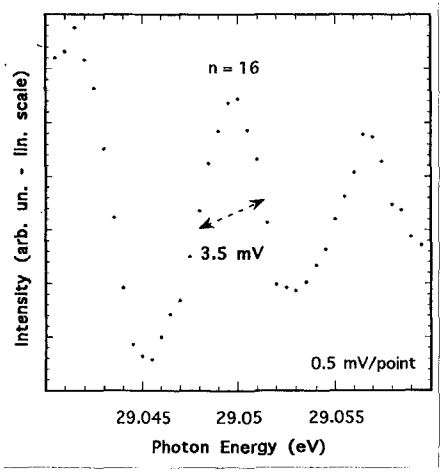


Figure 2. Short scan around the Ar autoinization line corresponding to n = 16.

Spin-polarized Electronic Structure of Fe(100): A New Surface-related State | U5UA

E. Vescovo (NSLS), D.-J. Huang, P.D. Johnson (BNL- Physics)

Magnetic surfaces and thin films display a magnetic behavior which can be quite different from that of the corresponding bulk materials. This is generally understood in terms of modification of the electronic structure as a result of the lowered symmetry and coordination number at the surface. In this connection, in recent years, a considerable experimental and theoretical effort has been devoted to the study of surface electronic structure of simple ferromagnets. Here we report on a spin- and angle-resolved photoemission study of 10 Ml Fe/W(110). Fe grows epitaxially on W(110). To probe the surface sensitivity of the spectral features, we exposed the clean surface to a few Langmuir (L) of oxygen. Oxygen adsorbs in a sequence of structurally ordered structures on this surface. Although the Fe(110) surface has been already studied quite extensively by various groups [e.g. 1, 2], at beamline U5 we have carried out spin- and angle-resolved photoemission on this system using p-polarized light, thereby sampling a different portion of the electronic structure. Our main result is the observation of a sharp surface related feature right at the Fermi level. In Fig. 1 the normal-emission spectrum of the clean Fe(110) surface is compared to that after 2 L oxygen exposure. Clearly the peak at the Fermi level is considerably reduced by the oxygen adsorption. The spin-resolved spectrum presented in Fig.2 reveals that this peak is of minority character.

[1] A.M. Turner et al., Phys. Rev. B29, 2986 (1983) [2] E. Vescovo et al., Phys. Rev. B48, 285 (1993)

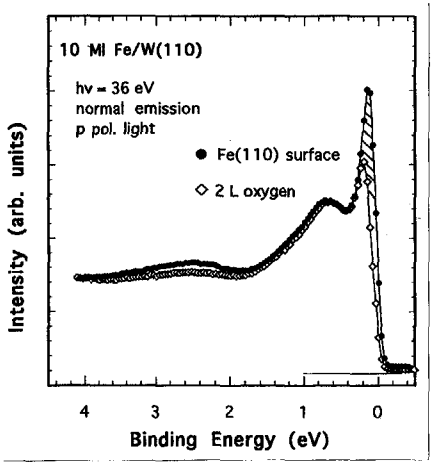


Figure 1. Normal emission spectra of clean (close circle) and 2 L oxygen covered (open diamond).

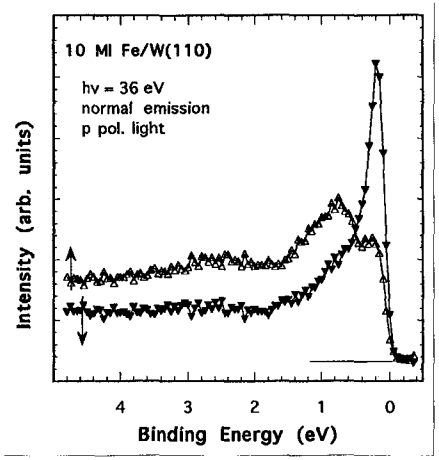


Figure 2. Spin-resolved spectrum of the clean Fe(110) surface.

Photoemission Study of Ni-Al Alloys * | U7B

H. Niu, S.L. Qiu and R.G. Jordan (Florida Atlantic U.)

There is a wide phase field in the near-equiatomic region of the Ni-Al binary phase diagram. β'-NiAl has the CsCl structure and in order to preserve the overal lattice coherence the Ni-rich alloys within this phase field contain anti-site defects, i.e., some of the atoms on the Al sites are replaced by Ni atoms. On the other hand, the Al-rich alloys contain constitutional vacancies (since one can imagine that the 'large' Al atoms will not 'fit' on the Ni-sites). We are carrying out photoemission measurements of a number of near equi-atomic Ni-Al alloys containing anti-sites defects and constitutional vacancies. Since the local environments of the Ni- and Al- sites in such alloys are expected to be rather different our aim is to investigate the effects of such 'imperfections' on the Ni and Al core level shifts on alloying and differences in the lineshapes of the core level photoemissin spectra. A large body of spectra were collected over the summer using the facilities on the U7B. Figure 1 and 2 show the Al 2s and Ni 3s core level spectra respectively and the data are currently being analyzed.

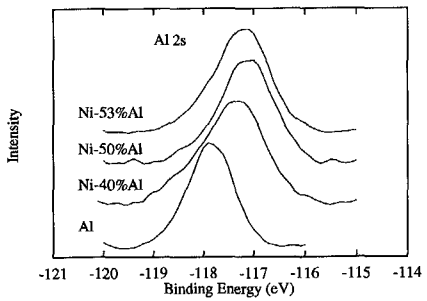


Figure 1. Al 2s core level spectra.

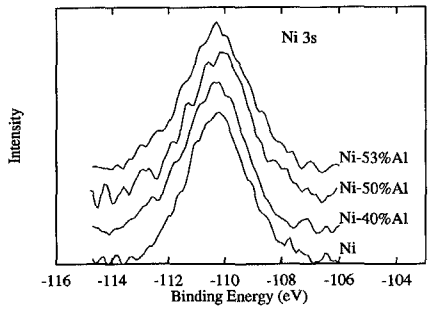


Figure 2. Ni 3s core level spectra.

* This work is supported by NSF Grant DMR-9500654.

Extreme Ultraviolet Lithography - Commissioning of an Offner 1:1 Imaging Camera	U13UB

A.MacDowell, O.Wood II (Lucent Technologies), K.Fuji (NEC)

The Extreme Ultraviolet Lithography (EUVL) program is aimed at developing the basic technology required for the printing of semiconductors features of dimensions aprox. 100nm and below. The EUVL technique consists of diffraction limited imaging of 13nm light by means of Multilayer coated imaging optics.

This year saw the commissioning of the rebuilt 1X Offner Ring Field (EUVL) camera. This machine consists of a 3 mirror projection imaging camera with a Numerical Aperture (NA) of 0.0835. The mirrors are multilayer coated with 40 layer pairs of Mo/Si optimized to reflect at a wavelength of 13.4nm. This camera can image a patterned multilayer reflection mask onto a resist coated wafer. Masks and wafers are mounted on stages with the relevant 6 degrees of freedom. In many ways the machine represents the closest to what an EUVL stepper would look like if built with 1993-95 technology. By building such a machine one is forced to confront many of the problems that present day technology must surmount before this lithographic technology can become viable. The estimated timeframe for EUVL technology to come on line as a viable commercial tool is at around 2005.

The imaging performance of this machine was characterized. The nominal resolution of the camera by the Raleigh criteria (lambda/2NA) was 80nm. The camera was found to be capable of imaging 75nm lines and spaces, however the contrast was found to be poor. The fact that 75nm lines and spaces were printed at all indicates that the mirrors had good figure - this was confirmed by visible light interferometry which measured the mirror figure shape and was found to have an error of about 0.8nm rms over the used part of the optics. This is viewed as a quite good figure for this wavelength range, but a real stepper would require a factor of 4 improvement to maintain consistent imagery across the imaging field. The low image contrast that was observed is consistent with significant amounts of small angle scattering from the mirror surfaces. This is considered a problem with the mirror surface in the mid-spatial frequency range (ca. 1mm - 1micron). This spatial frequency region is still under investigation - its effect on imaging is at present poorly understood in a quantitative manner.

The commissioning of this machine highlighted the lack of understanding of how to specify mirrors. This is a common problem for x-ray mirrors. It is becoming apparent to the general optics community that optics require to be specified over the complete spatial bandwidth for them to perform their required function. Work to develop the understanding of what the full spatial bandwidth specification should be for future EUVL mirrors is underway.

Auger Decay of a Core Level Satellite Feature Observed by Auger Photoelectron Coincidence Spectroscopy	U14A

R. Gotter (Laboratorio TASC-INFM, Italy) , R.A. Bartynski (Rutgers U.), Xu. Wu, S.L. Hulbert (NSLS), and H. Nozoye (Natl. Inst. of Materials and Chemical Research, Japan)

We have measured Auger electrons emitted from the Ru(0001) surface in the energy region of the $N_{23}N_{45}N_{45}$ Auger transition in coincidence with photoelectrons emitted in the satellite feature shifted 10 eV below the 4p core level. We find that the coincidence spectrum has a high energy threshold that exceeds the threshold of standard Auger measurements an amount corresponding to the energy shift of the satellite feature. As seen in the figure below, the high energy cut-off for Auger emission from direct decay of the $4p_{3/2}$ core hole is 38 eV, while the threshold observed in this spectrum, taken in coincidence with the satellite feature, is approximately 48 eV. This indicates that the excitation state associated by the satellite is long lived and participates in the Auger decay.

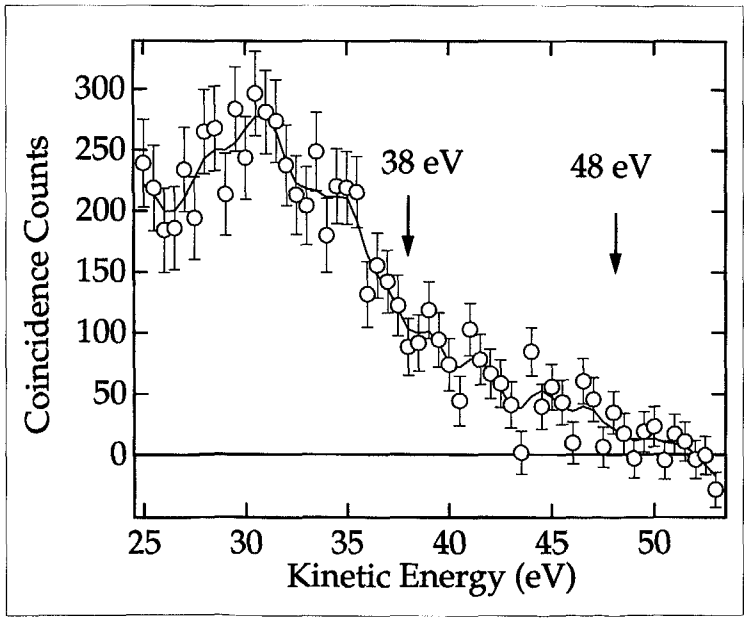


Figure 1.

Core Hole Decay Mechanisms in Ru Studied by Auger-photoelectron Coincidence Spectroscopy — U14A

R. Gotter, R.A. Bartynski (Rutgers U.), X. Wu, S.L. Hulbert (NSLS), and H. Nozoye (Nat. Inst. of Materials and Chemical Research)

The 4p core levels of the late 4d transition metals are particularly interesting as they are unusually broad, with the 1/2 spin-orbit component typically having a larger width than the 3/2 component. To explore the photoexcitation and decay mechanisms in these metals, the $N_{23}VV$ Auger spectrum of Ru(0001) has been measured in coincidence with $4p_{3/2}$ and $4p_{1/2}$ photoelectrons. These coincidence spectra are shown as the circles with error bars in Figs. (a) and (b) below. The solid curves in each figure is an attempt to model each spectrum with the self convolution of the valence band density of states, as would be expected in the independent electron approximation. The threshold region of the Auger spectrum in coincidence with Ru $4p_{3/2}$ photoelectrons is consistent with the solid curve, but the lines width is of the experimental data is larger and the line shape exhibits structure indicative of significant electron-electron interaction. In contrast, the spectral weight of Auger electrons detected in coincidence with $4p_{1/2}$ photoelectrons is shifted away from threshold to lower kinetic energy. The dashed curved in the figure is an attempt to model the spectra the multiplets of the d^6 configuration, appropriate if the core hole is fully screened prior to the Auger decay. The differences between the two experimental spectra could be explained if the high kinetic energy ^5D multiplet term, couples more strongly to the $4p_{3/2}$ than the $4p_{1/2}$ level. Calculations of these matrix elements are currently underway.

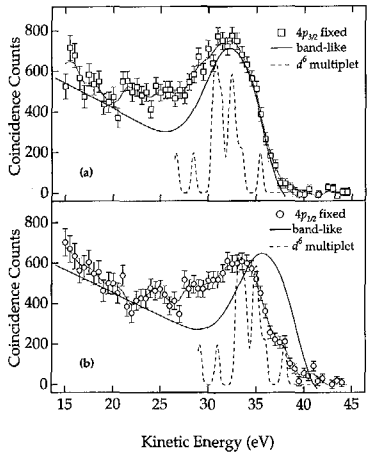


Figure 1.

Defects on the TiO_2(110) Surface Observed by Auger-photoelectron Coincidence Spectroscopy — U14A

W.K. Siu, R.A. Bartynski, (Rutgers U.) A. Namgia, A.H. Weiss, (U. of Texas Arlington), X. Wu, and S.L. Hulbert (NSLS)

We have measured the lineshape of the Ti 3p core level in coincidence with Ti $M_{23}VV$ Auger electrons from the stoichiometric and defective TiO_2(110) surfaces. Figs. 1(a), (b), and (c) are coincidence core level spectra from the stoichiometric, 900K vacuum annealed, and ion bombarded surfaces, respectively. The latter surface was subjected to $\sim 10^{14}$ Ar^+ ions/cm^2 at 500 eV. Figs. 1(d), (e), and (f) show noncoincidence (singles) spectra from the same surfaces. The excess emission in the kinetic energy range of 68 - 70 eV in Fig. 1(a) is attributed to Ti^{3+} and Ti^{2+} ions associated with Ti sites adjacent to surface O-vacancies. This emission accounts for ~20% of the total Ti 3p emission on the stoichiometric surface, and arrises from residual surface defects (either point defects or step edges) at the ~1% monolayer level; a concentration that does not produce a significant contribution to the single spectrum. The enhanced sensitivity in the coincidence spectrum is attributed to the extra charge density at the reduced Ti-sites as compared with Ti^{4+} sites. The assignment of this excess emission as defect induced is supported by the spectra in Figs. 1(b) and 1(e), where 900K annealing induces only a small (~4%) defect-related shoulder in the singles spectrum, while in the coincidence spectrum, over 50% of the Ti 3p emission is associated with reduced Ti oxidation states. In Figs. 1(d) and 1(f), we see that, compared to the 900K annealed surface, ion bombardment produces a greater fraction of defect-related emission in the singles spectrum, but results in a very similar coincidence spectrum. This indicates that, for this ion dose, a similar concentration of surface defects are formed, and a substantial fraction of the defect-related emission in the single spectrum can be associated with subsurface damage.

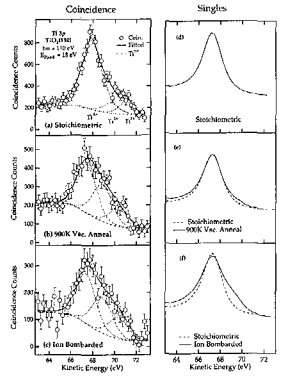


Figure 1.

Atomic-Site-Selective Core-Electron Excitation of 5-Oxohexanenitrile Isolated in D2 Matrices	U15

S. Sambasivan, A. T. Wen and D. M. Hanson (SUNY Stony Brook)

Preliminary data of $CH_3CO(CH_2)_3CN$ isolated in D_2 condensed on a 4.5 K KBr cryo-substrate, illustrates the atomic-site-selectivity in core-electron excitation. The chemical changes following soft x-ray irradiation in the matrices are monitored by *in-situ* Infrared spectroscopy. Figure 1 exhibit the intensity changes (before and after the irradiation) at the carbonyl (C-O) and nitrile (C-N) stretching frequencies. A negative peak here indicates a decrease in concentration of the parent molecule, while a positive peak signifies an increase due to new photoproduct formation caused by x-ray irradiation. The new peaks appearing at 2138 cm-1, in Fig.1 is been assigned to the carbon monoxide and a new CN compound respectively. The data indicate that, the IR intensity loss of the carbonyl stretching mode is approximately 5 to 10 times larger than that of the nitrile. Excitation were performed at C continuum (380 eV), 404 eV (N resonance), 425 eV (N-shape resonance), 500 eV (N-continuum), 535 eV (O- resonance), and 560 eV (O-continuum), showed the largest loss occurs at 380 eV, when the C 1s electron is completely ionized. In addition, from Fig. 2, an enchancement enhancement in decrease in carbonyl stretches occurs at 404 eV and 535 eV, which are excitation of 1s electrons of N and O to a (quasi) bound state (pre-edge) resonance. On comparison of number of reactions per absorbed photon, we observed that the quantum yields were at least 20% higher at O and N resonance as opposed to continuum excitations. Such differences observed between bound state and ionization continuum excitation may be associated with the degree of ionization during the core-hole decay process. While the carbonyl groups in the reactant prefer the excitation at resonances for photodissociation, and nitrile group photodissociation favors continuum photon energies. Although the exact mechanism leading to these results is still unclear at this point, the photodecomposition rates indicate site-selectivity in fragmentation following core-electron excitation.

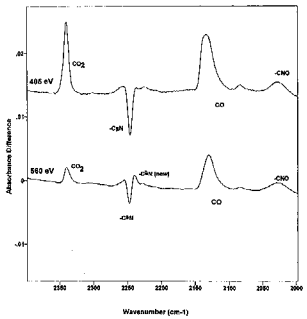


Figure 1. Difference IR Spectra of 5-Oxohexanenitrile/D2 Irradiation at 560 and 405 eV.

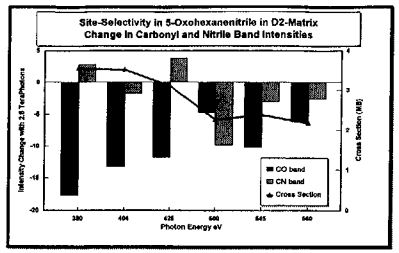


Figure 2 : Intensity change in the 5-Oxohexanenitrile C=O and C=N stretch with 2.8 Tera photon dosage at various energies.

Figure 2. Intensity Change in the 5-Oxohexanenitrile C=O and CN Stretch with 2.8 Tera Photon Dosage at Various Energies.

ABSTRACTS

X-Ray Beamlines

Beamline X1A

Determination of Urea/Urethane Ratios in Complex Polyurethanes using X-ray Microscopy .. B-27
H. Ade, A. P. Smith (NCSU), E. G. Rightor (Dow Chemical), and
A. P. Hitchcock (McMaster U.)

Critical Radiation Dose of Poly(ethylene terephthalate) (PET) B-27
H. Ade, A. P. Smith (NCSU), S.G. Urquhart, A. P. Hitchcock (McMaster U.), and
E. G. Rightor (Dow Chemical)

X-ray Absorption Near Edge Structure of Amino Acids and Peptides B-28
J. Boese, A .Osanna, C. Jacobsen, J. Kirz, E. Tall (SUNY Stony Brook), and
X. Zhang (Harvard U.)

The Application of Soft X-ray Microscopy to the *in-situ* Chemical Analysis of Ancient Spores in Organic-Rich Sedimentary Rocks B-28
G. D. Cody (Carnegie Institution of Washington), H. Ade (NCSU), and
S. Wirick (SUNY Stony Brook)

Carbon Measurements on Interplanetary Dust Particles B-29
G. J. Flynn (SUNY Plattsburgh), S. Bajt, H. Chapman (LLNL), and
Lindsay P. Keller (VA Associates)

First Holographic Images of Fast-frozen Hydrated Biological Specimens B-29
S. Lindaas, M. Howells, D. Pinkas, C. Magowan, K. Downing (LBNL) and
C. Jacobsen (SUNY Stony Brook)

Commissioning of the Cryo Scanning Transmission X-ray Microscope B-30
J. Maser, C. Jacobsen, J. Kirz, A. Osanna, S. Spector, S. Wang, and
J. Warnking (SUNY Stony Brook)

Luminescent Molecular Probes for X-ray Microscopy B-30
M.M. Moronne (LBNL)

Morphological Characterization of Polycarbonate/Acrylonitrile-Butadiene-Styrene Polymer Blends B-31
A. P. Smith, H. Ade, R. Fornes, R. Gilbert (NCSU) and C. Sloop (IBM)

Investigation of the Spinodal Decomposition of Constrained Thin Polymer Films with X-ray Microscopy B-31
A. P. Smith, H. Ade (NCSU), D. Slep (Highlord Chemical), S. Qu, M. Rafailovich, and
J. Sokolov (SUNY Stony Brook)

NEXAFS Spectroscopy of Polymeric Isomers of Poly(ethylene terephthalate) (PET) B-32
A. P. Smith, H. Ade (NCSU), S. G. Urquhart, A. P. Hitchcock (McMaster U.) and
E. G. Rightor (Dow Chemical).

Characterization of the X1-STXM Spectroscopy Acquisition Mode Utilizing Carbon Dioxide B-32
A. P. Smith, T. Coffey, and H. Ade (NCSU)

NEXAFS Microspectroscopy of Macrophase-Separated Random Block Copolymer/ Homopolymer Blends B-33
A. P. Smith, J. H. Laurer, H. Ade, R. Spontak (NCSU), A. Ashraf, and
S. Smith (Procter and Gamble Co.)

Considerations for A Soft X-ray Spectromicroscopy Beamline B-33
B. Winn, X. Hao, C. Jacobsen, J. Kirz, J. Miao, B. Sullivan, S. Wirick (SUNY Stony Brook), H. Ade (NCSU), C. Buckley (King's College), M. Howells (ALS), S. Hulbert (NSLS), I. McNulty (APS), T. Oversluizen (Creative Instrumentation)

X1-SPEM-II Application to Tribological Surfaces B-34
H. Zhang, G. R. Zhuang, H. Ade (NCSU), C.-H. Ko, B. Winn, J. Kirz (SUNY Stony Brook), S. Cameron, D. Leta (Exxon), S. Hulbert, and E. Johnson (NSLS)

Characterization of Polymer Interfaces Using X-ray Microscopy B-34
C. G. Zimba (MIT), A. P. Smith and H. Ade (NCSU)

STXM of Polymer Laminates: NEXAFS Microspectroscopy B-35
C. G. Zimba (MIT), A. P. Smith and H. Ade (NCSU)

Beamline X1B

The Vibrationally Resolved O 1s Photoelectron Spectrum of CO_2 ..... B-35
A. Kivimäki, B. Kempgens, H.M. Köppe, K. Maier, M.N. Piancastelli, M. Neeb, and A.M. Bradshaw (FHI)

Vibrational and Shake-up Excitations in C 1s Ionisation of Ethane B-36
H. M. Köppe, K. Maier, B. Kempgens, A. Kivimäki, M. Neeb, and A. M. Bradshaw (Fritz-Haber-Institut der Max-Planck-Gesellschaft, Germany)

Improvement in Monochromator Performance on X1B B-36
M. Neeb, A. Kivimäki, K. Maier, H.M. Köppe, B. Kempgens, and A.M. Bradshaw (FHI), F. Loeb and P.D. Johnson (BNL - Physics)

Surface Studies of Model Supported Catalysts: Rh/CeO_2 (100) B-37
S.H. Overbury, D.R. Huntley, D.R. Mullins, K.S. Ailey and P.V. Radulovic (ORNL)

Beamline X3A1

Analysis of the Bias Due to Finite Size of the Peak Mask in Imaging Plate Integration Methods B-37
R. Bolotovsky and P. Coppens (SUNY Buffalo)

Electron Density Analysis at Synchrotron Sources B-38
P. Coppens, R. Bolotovsky and A. Darovsky (SUNY Buffalo)

Resonance Scattering Studies of Mixed-Valence Complexes B-38
A. Darovsky, V. Kezerashvili, P. Coppens (SUNY Buffalo), T. Weyhermuller, H. Hummel and K. Wieghardt (Max-Planck-Institut fur Strahlenchemie)

Temperature-dependence of the Electron Transfer in a $Mn_{II}Mn_{III}(\mu\text{-OH})$ Mixed-valence Complex B-39
A. Darovsky, V. Kezerashvili, P. Coppens (SUNY Buffalo), T. Weyhermuller, H. Hummel and K. Wieghardt (Max-Planck-Institut, Germany)

Studies of CdS/CdTe Heterostructures Using X-ray Scattering and XAFS Techniques B-39
S. W. Huang, Y. L. Soo, Y. H. Kao (SUNY Buffalo) and A. Compaan (U. of Toledo)

Investigations of Microstructures in ZnSe-based II-VI Semiconductor Thin Films Grown by MBE and MOCVD B-40
S. W. Huang, Y. L. Soo, Y. H. Kao, H. Luo, and T. J. Mountziaris (SUNY Buffalo)

Grazing Angle Scattering and XAFS Studies of (Si,Ge)/Si Heterostructures B-40
S. W. Huang, Y. L. Soo, Y. H. Kao (SUNY Buffalo) and K. L. Wang (UCLA)

The Electron Density of $Th(S_2P(CH_3)_2)_4$ B-41
B. B. Iversen, F. K. Larsen (U. of Aarhus), P. A. Reynolds (Australian National U.), A. Pinkerton (U. of Toledo), and A. Darovsky (SUNY Buffalo)

The Structure of Type 1 GeS_2 ..... B-41
J. B. Parise, K. Tan, C. Cahill and Y. Ko (SUNY Stony Brook)

Synthesis and Structural Characterization Using Synchrotron Radiation of$(C_6H_{13}N_2)_2(H_3O)(H_2O)][AgGe_4S_{10}]$ B-42
J. B. Parise, K. Tan (SUNY Stony Brook), and A. Darovsky (SUNY Buffalo)

The 154 K Phase Transition of Tetramethylammonium Tetrafluoroborate B-42
Thomas Schultz (Risoe National Laboratory) and Finn Krebs Larsen (Aarhus U.)

X-ray Induced Photoluminescence in Doped Nanocrystals B-43
Y. L. Soo, S. W. Huang, Y. H. Kao (SUNY Buffalo) and
R. N. Bhargava (Nanocrystals Technology)

XAFS Studies of Tb-Doping in Y_2O_3 ..... B-43
Y. L. Soo, S. W. Huang, Y. H. Kao (SUNY Buffalo) and
R. N. Bhargava (Nanocrystals Technology)

Beamline X3A2

Resonance Scattering Studies of Mixed-Valence Complexes B-44
A. Darovsky, V. Kezerashvili, P. Coppens (SUNY Buffalo), T. Weyhermuller, H. Hummel and
K.Wieghardt (Max-Planck-Institut fur Strahlenchemie)

Crystallographic Study of Thermal Barrier Coating by X-ray Microdiffraction B-44
Y. Gao, W. Hasz and C. A. Johnson (GE Corporate Research and Development)

On-Line SAXS Study of Nylon 66 Fiber Deformation B-45
B. Hsiao, A. Kennedy, R. Leach (DuPont), B. Chu, and P. Harney (SUNY Stony Brook)

On-Line WAXD Study of Nylon 66 Fiber Deformation B-45
B. Hsiao, A. Kennedy, R. Leach (DuPont), B. Chu, and P. Harney (SUNY Stony Brook)

Time-Resolved Synchrotron SAXS Study of the Miscible Blends of Semicrystalline Poly(vinylidenefluoride) and Semicrystalline Poly(1,4-Butylene Adipate) B-46
L.-Z. Liu, B. Chu,(SUNY Stony Brook), R. St. J. Manley (McGill U.)

Synchrotron SAXS Study of Crystallization and Microphase Separation in Compatible Mixtures of Tetrahydrofuran-Methyl Methacrylate Diblock Copolymer and Polytetrahydrofuran B-46
L.-Z. Liu, F. Yeh and B. Chu (SUNY Stony Brook)

The Effects of Thermal Shocking on the Residual Stress in Si_3N_4 Ceramic Composites B-47
A. Sahiner, D. Wittmer, and M. Sweeney (Southern Illinois U. at Carbondale)

Simultaneous SAXS/WAXD Morphological Studies of Nylon 66 Fibers B-47
J. R. Sharrow, J. M. Schultz (U. of Delaware), B. S. Hsiao, and H. Chang (DuPont)

SAXS Study of Gel-like Structures of Block Copolymers in DNA Separation Buffers B-48
C. Wu, T. Liu, and B. Chu (SUNY Stony Brook)

Nano-Structure of Gel-Surfactant Complexes B-48
F. Yeh, E.L. Sokolov, and B. Chu (SUNY Stony Brook)

Formation and Struction of Micelles and Supramolecules of Pluronic P103 in Water/O-xylene Mixture B-49
S. Zhou, J. Su and B. Chu (SUNY Stony Brook)

Beamline X3B1

Single C-C bond in $(C_{60})_2^{2-}$ B-49
G.M. Bendele (SUNY Stony Brook), P.W. Stephens (SUNY Stony Brook and NSLS), G. Oszlányi, G. Bortel, G. Faigel, L. Gránásy (SZFKI, Budapest), and L. Forró (EPF, Lausanne)

Na_2RbC_{60} is orthorhombic at low temperature B-50
G.M. Bendele (SUNY Stony Brook), P.W. Stephens (NSLS and SUNYSB), K. Prassides, K. Vavekis, K. Kordatos (U. Sussex, UK), and K. Tanigaki (NEC Tsukuba)

Powder Diffraction Structure of Indenyllithium B-50
R.E. Dinnebier (Univ. of Bayreuth, Germany), P. W. Stephens (SUNY Stony Brook), U. Behrens (U. of Hamburg, Germany) and F. Olbrich (U. of Magdeburg, Germany)

Powder Diffraction Structure of MC_5H_5 (M= Li, Na, K) B-51
R.E. Dinnebier (U of Bayreuth, Germany), P. W. Stephens (SUNY Stony Brook), U. Behrens (U. of Hamburg, Germany) and F. Olbrich (U. of Magdeburg, Germany)

Powder Diffraction Structure of Phenyllithium (C_6H_5Li) B-51
R.E. Dinnebier (U. of Bayreuth, Germany), P. W. Stephens (SUNY Stony Brook), U. Behrens (U. of Hamburg, Germany) and F. Olbrich (U. of Magdeburg, Germany)

Ab initio Structure Determination of Two Polymorphs of RbC_5H_5 in a Single Powder Pattern ... B-52
R.E. Dinnebier, S. van Smaalen (U. of Bayreuth, Germany), F. Olbrich (U. of Magdeburg, Germany) and P. W. Stephens (SUNY Stony Brook)

Structural Investigation of a Tetragonal Garnet: $Ca_3Mn_2Ge_3O_{12}$ B-52
S. Heinemann (Bayerisches Geoinstitut, U. of Bayreuth, Germany) and R.E. Dinnebier (Lehrstuhl für Kristallographie, U. of Bayreuth, Germany)

Alkali Occupancies and Fullerene Orientation in K_4C_{60} and Rb_4C_{60} B-53
C.A. Kuntscher, G.M. Bendele (SUNY Stony Brook), and P.W. Stephens (SUNY Stony Brook and NSLS)

Atomic Structure of Gold Nanoclusters B-53
P.W. Stephens (NSLS and SUNY Stony Brook), C.L. Cleveland, U. Landman, M. Shafigullin, R.L. Whetten (GA Tech)

High-resolution Study of the Ferroelectric $BaTiO_3$. B-54
P. Stephens (NSLS and SUNY Stony Brook), D. Balzar (NIST and Inst. Ruder Boskovic), and H. Ledbetter (NIST)

Crystals of Passivated Gold Nanocrystals B-54
P. W. Stephens (NSLS and SUNY Stony Brook), M. Shafigullin, M.M. Alvarez, S.A. Harfenist, J.T. Khoury, T.G. Schaaff, I. Vezman, Z.L. Wang, A. Wilkinson, and R.L. Whetten (GA Tech)

Powder Diffraction Structures of $Ca_8[Al_{12}O_{24}](MoO_4)_2$ (CAM) B-55
S. van Smaalen, R.E. Dinnebier (U. of Bayreuth, Germany), H. Katzke and W. Depmeier (U. of Kiel, Germany)

Beamline X4A

The Crystal Structure Determination of the SecA Translocation ATPase B-55
J.F. Hunt and J. Deisenhofer (HHMI, UT Southwestern)

Structure Determination of the Entire Extracellular Portion of Human CD4 ..... B-56
H. Wu, P.D. Kwong and W.A. Hendrickson (Columbia U.)

Beamline X6A

Determination of Transient Molecular Structure for Photoinduced Reaction Intermediates Using Time-Resolved Energy Dispersive XAS B-56
L. Chen, P. Lee, S. Weber, G. Jennings, J. Norris and P. Montano (ANL /U. of Chicago)

Contribution of Magnetic-EXAFS to the MCXD Signal at the Gd L_{III} Edge. B-57
K. J. Gofron, C. W. Kimball (NIU), P. L. Lee, and P.A. Montano (ANL)

K Absorption Edge Magnetic Circular X-Ray Dichroism of Fe-Ni alloys. B-57
K. J. Gofrona, C. W. Kimballa (NIU), P. L. Lee, G. Jennings and P. A. Montano (ANL)

Beamline X6B

Anomalous Small-angle X-ray Scattering Characterization of Reactor Pressure Vessel Steels .. B-58
D. Alexander, (ANL) and P. Jemian, (UNI-CAT, Advanced Photon Source)

Study of Strain and Crystal Structure of Epitaxial Grown La-Ca-Mn-O Thin Films B-58
M. C. Shih (NCHU, Taiwan), M.Y. Chen(NTU, Taiwan), T.S. Tsai (NCHU, Taiwan)

Beamline X7A

Bonding and Local Structure of Semiconductor Alloys, $In_{1-x}Ga_xAs$ B-59
S. J. L. Billinge and F. Mohiuddin-Jacobs (Michigan State U.)

Anomalous X-Ray Scattering Studies of Supermolecules and Aggregates in Organic Solution B-59
L. Chen, Q. Zhu, W. Svec, D. Price, M. Wasielewski (ANL)

The Nature of Structural Defects in C15 $NbCr_2$ and $Nb(Cr,V)_2$ Studied by Synchrotron X-Ray Powder Diffraction B-60
F. Chu (LANL), Q. Zhu (BNL), D. J. Thoma, and T. E. Mitchell (LANL)

High Resolution Powder Diffraction at 0.5 Å B-60
D. E. Cox (BNL)

Structural Studies of Giant Magnetoresistive $Tl_2Mn_2O_7$ B-61
D.E. Cox (BNL), P.G. Radaelli (ILL, Grenoble), M Marezio (MASPEC-CNR Parma), and S.-W. Cheong (Lucent Technologies)

Interfacial Roughness of Fe-CR GMR Superlattices B-61
W. Dmowski and T. Egami (U. of Pennsylvania)

Ultra-thin CeO_2 Overlayer on YSZ Studied by X-ray Surface Scattering B-62
W. Dmowski and T. Egami (U. Pennsylvania)

High Pressure Diffraction Studies of Mercury-Based Superconductors B-62
J. A. Hriljac, I. Gameson, A. Asab and P. P. Edwards (U. of Birmingham, UK)

Structural Studies of Bismuth Tin Oxides B-63
B.J. Kennedy (The U. of Sydney)

Phase Characterization in Rapidly-Solidified Magnetic Materials B-63
L.H. Lewis (BNL - DAS), C.H. Sellers (INEL) and V. Panchanathan (Magnequench International)

Investigation of Structural Changes in High-Temperature Treated Zeolite CaA B-64
H. Meyer zu Altenschildesche, Y. Huang, G.T. Kokotailo, C.A. Fyfe (UBC, Vancouver), and D. Cox (BNL)

Structural Study of the Layered Aluminophosphate Material NH_4-Taranakite B-64
H. Meyer zu Altenschildesche, G.T. Kokotailo, C.A. Fyfe (UBC, Vancouver), W. Schwieger (Universität Halle), and D. Cox (BNL - Physics)

High Pressure Synthesis and Structural Refinement of the New Double Perovskite Ca_2TiSiO_6 ... B-65
J. B. Parise (SUNY Stony Brook) and K. Leinenweber (ASU)

Structural Characterization of A Novel Open Framework $[(C_8H_{20}N][AgGe_2S_5]$ (TEA-AgGS-SB1) B-65
J.B. Parise (SUNY Stony Brook) and K. Leinenweber (ASU Tempe)

Synthesis and Structure of a Novel Aurate: $CdAu_2O_4$. B-66
J.-H. Park and J.B. Parise (SUNY Stony Brook)

Powder Diffraction Study of the Orientational Order of the Ammonium - Tetrahedra in NH_4Cl and ND_4Cl B-66
W. Press, B. Asmussen, H. Krull, O. Seeck (U. of Kiel, Germany), D. Cox, Q. Zhu (BNL)

Polymorphism of the Crystalline Low-Temperature Phases of t-Butyl Chloride B-67
R. Rudman, (Adelphi U.)

Structure and Thermal Behavior of Fullerene Derivatives B-67
M. R. Stetzer, P. A. Heiney, A. R. McGhie, J. E. Fischer, R. M. Strongin, B. M. Brandt, A. B. Smith III (U. of Pennsylvania), P. W. Stephens, R. E. Dinnebier, G. Bendele (SUNY Stony Brook), and Q. Zhu (BNL - Physics)

Phase Transitions and Thermal Expansion in Oxides at Low and High Temperatures B-68
P.M. Woodward, J.S.O. Evans, A.W. Sleight (Oregon State U.)

CO_3 Location in Carbonate Apatite B-68
R. A. Young (Georgia Institute of Technology)

The Crystal Structure of Beta-Eucryptite from 20 to 873 K: A High-Resolution Powder Synchrotron X-ray Diffraction Study B-69
H. Xu, P. J. Heaney, and D. M. Yates (Princeton U.)

An Increase of Structural Order Parameter in Fe-Co-V Soft Magnetic Alloy after Thermal Aging B-69
Q. Zhu (BNL-Physics)

An Increase of Structural Order Parameter in Fe-Co-V Soft Magnetic Alloy after Thermal Aging B-70
Q. Zhu (BNL-Physics), L. Li, M. S. Masteller and G. J. Del Corso (Carpenter Technology Corp.)

Beamline X7B

Control of Macromolecule Distribution Within Synthetic and Biogenic Single Calcite Crystals B-70
J. Aizenberg (Weizmann Institute), J.C. Hanson, T.F. Koetzle (BNL - Chemistry), S. Weiner and L. Addadi (Weizmann Institute)

High Temperature Phase Transformations of Tetraalkylammonium Tetrafluoroborates. B-71
J. Bager , F. Krebs Larsen (U. of Aarhus), T.M. Schultz (Risø, Denmark), P. Norby and J.C. Hanson (BNL - Chemistry).

Characterization of Catalysts by Temperature-Programmed Powder X-ray Diffraction B-71
M.M. Burcham, K.K. (Lehigh U.), and J.C.Hanson (BNL- Chemistry)

In Situ Studies of Hydrothermal Syntheses; Crystallization of Mg- and Zn-substituted Aluminophosphates B-72
A.N. Christensen (U. Aarhus), P. Norby and J.C. Hanson (BNL-Chemistry)

A Variable Temperature X-Ray Diffraction Study of HCFC-124a Reactions on Cation Exchanged Faujasites B-72
M.F.Ciraolo, F.I.Poshni, P. Norby, C.P.Grey (SUNY Stony Brook), J.C.Hanson (BNL - Chemistry), and D.R.Corbin (Dupont)

Structure and Phase Transitions in The Negative Thermal Expansion Material Zirconium Vanadate B-73
J.S.O. Evans, A.W. Sleight (Oregon St. U.) and J. C. Hanson (BNL - Chemistry)

The Structure of *d*-$Co(en)_3.Al_3P_4O_{16}.3H_2O$ B-73
M. J. Gray, A. P. Wilkinson (Georgia Tech) and J.C. Hanson (BNL - Chemistry)

Structural Characterization of Hydrofluorocarbon-134 Adsorbed on Zeolite NaY using X-ray Powder Diffraction: Observation of Cation Migration and Strong Sorbate-Cation Interactions ... B-74
C.P.Grey and F.I.Poshni (SUNY Stony Brook), A.F.Gualtieri (U. Modena), P.Norby and J.C.Hanson (BNL- Chemistry), and D.R.Corbin (DuPont)

Real Time Combined Fe K-edge XANES and XRPD *in-situ* Study of Hydrothermal Synthesis of Zeolites from Natural Clay Minerals. B-74
Alex F. Gualtieri (U. of Modena, Italy), P. Norby and J.C. Hanson (BNL - Chemistry)

Kinetic Study of the Synthesis of Zeolite Li-A(BW) from Natural Kaolinites B-75
A.F. Gualtieri, (U.of Modena, Italy), P. Norby and J. Hanson (BNL - Chemistry), and G.Artioli (U. of Milan, Italy)

Computer Movies of Time-resolved Dehydration of Natural Zeolites B-75
J. C. Hanson, J. Araujo (BNL), Kenny Stahl (DTU), G. Artioli (U. Milan)

Pyridine Adsorbed on Na-Faujasite: Low Temperature Single Crystal Studies B-76
J. C. Hanson (BNL- Chemistry), I. Mutikainen (U. of Helsinki), J. Pluth (U. of Chicago)

Studies of Excited-State Lifetimes of Hydrocarbons B-76
R.A.Holroyd and J.M. Preses (BNL-Chemistry)

Investigation of Disorder Using Micro Single Crystal Diffraction Data B-77
T.R. Jensen (U. of Odense, Denmark), P. Norby and J.C. Hanson (BNL - Chemistry)

Kinetic Study of Phase Transition of Microporous Lithium Zinc Phosphates B-77
T. R. Jensen (U. of Odense, Denmark), P. Norby and J.C. Hanson (BNL - Chemistry)

Powder Diffraction Study of Co Substitution in Microporous Lithium Zinc Phosphate B-78
T.R. Jensen (U. of Odense, Denmark), P. Norby and J.C. Hanson (BNL - Chemistry)

Structural Investigation of α-$LiZnAsO_4$, Using a Micro Crystal B-78
T.R. Jensen (U. Odense, Denmark), P. Norby, J. C. Hanson (BNL - Chemistry)

The Crystal Structure of a New Zinc Arsenate, $Zn_9(AsO_4)_6 \cdot 4H_2O$. B-79
T. R. Jensen (U. of Odense, Denmark) P. Norby and J. C. Hanson (BNL - Chemistry)

X-Ray Scattering Study of Simple Molecules Adsorbed on BN: Evidence for a Commensurate Phase of Kr B-79
D.E. Johnson, J. Hanson, and J.Z. Larese (BNL)

In-situ Diffraction Study of Ion Exchange: Exchange of Analcime to Ammonium Analcime. B-80
A.M. Krogh Andersen, E. Krogh Andersen and I.G. Krogh Andersen (U. Odense, Denmark), P. Norby and J.C. Hanson (BNL- Chemistry)

In-situ Powder Diffraction Studies of Intercalation Processes: Intercalation of Alkane Diamines in α-$Zr(HPO_4)_2 \cdot H_2O$ and γ-$Ti(PO_4)(H_2PO_4) \cdot 2H_2O$. B-80
A.M. Krogh Andersen, E. Krogh Andersen and I.G. Krogh Andersen (U. Odense, Denmark), P. Norby and J.C. Hanson (BNL - Chemistry).

In-situ Studies of Thermal Transformations in α-layered phosphates. B-81
A.M. Krogh Andersen (U. Odense, Denmark), P. Norby and J.C. Hanson (BNL - Chemistry)

The Crystal Structure of Tetragonal $Zr(HPO_4)_2$ by Synchrotron X-ray Single Crystal Diffraction and Neutron Powder Diffraction Data. B-81
A.M. Krogh Andersen (U. Odense), P. Norby, T. Vogt and J.C. Hanson (BNL - Chemistry)

Crystal Structure of Dimethylamine Grown *In-situ* from Liquid B-82
R. K. McMullan, W. Klooster, P. Norby and J. C. Hanson (BNL-Chemistry)

Real-Time X-Ray Powder Diffraction Studies of Li/Na Ion Exchange in Sodalite B-82
P. Norby, J. Hanson (BNL - Chemistry), C. L. Cahill and J. B. Parise (SUNY Stony Brook)

Hydrothermal Conversion of Zeolites Studied Using *in-situ* Powder Diffraction. B-83
P. Norby and J.C. Hanson (BNL - Chemistry)

Dehydration of Zeolite Li-A(BW); A Time Resolved Structural Study. B-83
P. Norby, J.C. Hanson (BNL), A. Kremenović, V. Dondur and R. Dimitrijević (U. Belgrade)

Adsorption of Hydrofluorocarbons on Zeolites; An *in-situ* Powder Diffraction Study. B-84
P. Norby, F.I. Poshni, M.F. Ciraolo, C.P. Grey, (SUNY Stony Brook) and J.C. Hanson (BNL - Chemistry).

An *In-situ* X-ray Powder Diffraction Study of the Dehydration of Zeolite CsY B-84
F.I.Poshni, M.F.Ciraolo, C.P.Grey (SUNY Stony Brook), A.F.Gualtieri (U. of Modena), P.Norby and J.C.Hanson (BNL - Chemistry)

In Situ Thermal Transformations of Nickel/Cobalt Molybdates B-85
J. Rodriguez, J. Hanson, S.Chaturvedi (BNL- Chemistry)

In-situ Powder Diffraction Study of Ca-ion Exchange of Zeolite MAP B-85
J. A. Stuart (Unilever, UK), P. Norby and J.C. Hanson (BNL - Chemistry)

In-situ Crystallization of Mechanically Treated Zeolites. B-86
B. Subotić, C. Kosanović (R. Bošković Inst., Zagreb), P. Norby and J.C. Hanson (BNL - Chemistry)

Are the Chains in Solid HCN Parallel or Anti-parallel? B-86
G. Svensson (Chalmers U. of Technology, Göteborg, Germany), J. C. Hanson (BNL-Chemistry)

In-situ Time Resolved Powder Diffraction Studies of the Hydrothermal Synthesis of Antimony Sulfides Templated by Dimethylammonium B-87
K. Tan, J. B. Parise, Y. Ko,(SUNY StonyBrook) P. Norby, and J. C. Hanson (BNL)

Competition Between Kinetic and Thermodynamic Control of Phase Transitions in Silica/Surfactant Mesophase Composites B-87
S. H. Tolbert and G. D.Stucky (U. of California/Santa Barbara), P. Norby and J.C. Hanson (BNL - Chemistry)

Beamline X8A

Iridium Optical Constants from X-ray Transmission Measurements, 2-12 keV B-88
R. L. Blake (LANL), J. J. Fitch, D. E. Graessle, B. Harris, J. Juda (SAO), E. M. Gullikson (LBL), and M. L. Shattenburg (MIT)

Modeling the Diffraction Efficiencies of the AXAF High Energy K. A., Transmission Gratings Above 2 keV B-88
K.A. Flanagan, T.T Fang, C. Baluta, J.E. Davis, D. Dewey, T.H. Markert (MIT); D.E. Graessle, J. Drake, J. E. Fitch, J.Z. Juda, J. Woo (SAO); J. Bauer (U. of Hawaii)

Reflectivity Measurements of Multilayer Optics for Use on the Advanced Photon Source Soft X-Ray Beamlines B-89
K.J. Randall, J.Z. Xu (ANL), D. Graessle and J.J. Fitch (Harvard-Smithsonian Center for Astrophysics), S. DiFonzo, B.R. Mueller, W. Jark (Sincrotrone Trieste)

Beamline X8C

Iridium Optical Constants from X-ray Transmission Measurements, 2-12 keV B-89
R. L. Blake (LANL), J. J. Fitch, D. E. Graessle, B. Harris, J. Juda (SAO), E. M. Gullikson (LBL), and M. L. Shattenburg (MIT)

Crystal Structure of the Metallo-beta-lactamase from *B. fragilis*, and Preliminary Crystallographic Data for Enzyme-I and a Deletion Mutant of the Class A Beta-lactamase from *S. Aureus* B-90
N. Concha, U. Pieper, S. Banerjee, and O. Herzberg (U. of Maryland)

Beamline X9A, X9B

Fimbrin and the Cytoskeleton B-90
S. Almo, S. Goldsmith, M. Sullivan (AECOM)

Synchrotron Crystallography Structural Analysis of Profillin B-91
S. Almo, M. Sullivan, J. Eads, N. Mahoney (AECOM)

EXAFS Studies of the Zinc Derivative of Cytochrome-C: An Unusual Coordination State B-91
H. Anni (Thom. Jeff. Med. Coll.), J. Vanderkooi (U. of Penn.), M.R.Chance, E. Scheuring (AECOM)

Resonance X-ray Diffraction Studies of Membrane Protein Monolayers B-92
J. K. Blasie, L. Prokop, E. Nordgren, J. Stzalka, L. Kneller, A. Edwards, R. Fischetti (Univ. of Penn.)

Heterotropic Effects on the Active Site Structure of Hemocyanin B-92
L. Bubacco, R. Magliozzo, M. Wirt, J. Peisach (AECOM), L. Powers (Utah St.U.)

Kinetics and Mechanism of Lipid Phase Transitions B-93
M. Caffrey (Ohio SU)

Protein Footprinting: Structures of Molten Globule States and Mass Spectrometic Analysis B-93
M.R.Chance, M.D. Brenowitz (AECOM)

Time-Resolved Synchrotron X-ray Footprinting B-94
M.R.Chance, M.D. Brenowitz, B. Sclavi, M. Sullivan (AECOM)

Beamline X-9A : A Resource Devoted to Time-Resolved X-ray Footprinting B-94
M.R. Chance, M.D. Brenowitz, M. Sullivan (AECOM)

AUTOFIT 1.0 : A New Software for XAS Global Mapping B-95
M.R.Chance, W. Huang, E.Scheuring (AECOM)

Global Mapping of EXAFS Data : Structure of the Photoproduct of Mb*CO B-95
M.R. Chance, E. Scheuring, W. Huang (AECOM)

Time-Resolved X-ray Spectroscopy on Microsecond Timescales B-96
M.R.Chance, E. Scheuring, A. Xie (AECOM)

X-ray Reflectivity of Mechanically and Optically Rubbed Polyimides B-96
S. S. Ghosh, P. A. Heiney, M. R. Stetzer, O. Y. Mindyuk (UPenn) and S. T. Sun (Alliant Techsystems)

XAS Studies of the Structure and Function of Ni in Chromatium Vinosum Hydrogenase B-97
Z. Gu, C.B. Allan, S.B. Choudhury, M.J. Maroney (U. of Massachusetts)

Structure and Kinetics: A Molecular Basis for Ligand Affinity In Hemeproteins B-97
C. Lee, E. Scheuring, M.R. Chance, J. Peisach (AECOM)

Biological Metal Clusters B-98
M. Maroney, S. Choudhury, C. Allan, Z. Ge (U. of Massachusetts)

A Low Angle Diffraction Study of the Effects of Nucleotide Binding on the Structure of the Actomyosin Complex B-98
K. Poole, P. Ellison, M. Lorenz, K. Holmes, (Max Planck Inst.), G. Evans, G. Rosenbaum, (ANL), P. Boesecke (ESRF), C. Cremo (Wash. St. U)

The *E. Coli* Primase Zinc Structure is Sensitive to the Binding of ATP and High Magnesium B-99
L. Powers, M. Griep (Utah State U.)

Active Site Targeting of Protein Tyrosine Phosphatase 1B by Synchrotron Crystallography B-99
Y. A. Puius, Y. Zhao, M. Sullivan, D. Lawrence, Z.-Y. Zhang, S. C. Almo (Albert Einstein College of Medicine)

EXAFS Studies of Nonheme Iron Enzymes B-100
L. Que, L. Shu, X. Wang, S. Mandal, K. Chen (U. of Minnesota)

XAFS Analysis of a Transition State Inhibitor of Chloroplast CF-1 ATPase B-100
I. Sagi, C. Carmelli (Weizmann Inst.)

Fe-S Centers in Energy Transducing Enzymes B-101
I. Sagi, Z. Mingtao, C. Carmelli (Weizmann Inst.)

Solution Iron-Edge XAS of Native Soybean Lipoxygenase-1 ..... B-101
R. Scarrow, N. Taufen, R. Ghiladi (Haverford Coll.)

Global Mapping of XAS Data from Cobalamin Enzymes B-102
E. Scheuring, M. Chance (AECOM), R. Banerjee (U. of Nebraska.), R. Matthews (U. of Michigan)

The Relationship Between Structure and Conductivity in Polymer Electrolytes B-102
L. Sharpe, L. Lyons (Grinnell Coll.)

Active Site Structure in Cytochrome c Peroxidase and Myoglobin Mutants B-103
R. Sinclair, S. Hallam, M. Chen, L. Powers (Utah St. U.), B. Chance (U. of Penn.)

Time-Resolved RNA Footprinting: Structure-Function of Splicing Intermediates of the Tetrahymena Ribozyme B-103
S. Woodson (Univ. of Md.), M. Brenowitz, B. Sclavi, M. Sullivan, M. Chance (AECOM)

X-Ray Absorption and Resonance Raman Spectroscopy of Human Myeloperoxidase B-104
K. Yue, K. Taylor, J. Kinkade, R. Sinclair, L. Powers (Utah SU)

Beamline X10A

X-Ray Characterization of Magnetic Epitaxial Multilayer Thin Films B-104
C-H. Lee (National Tsing Hua Univ), M.Y.Chern, C.Y.Huang (National Taiwan Univ), M.T.Tang (SRRC,Taiwan) and K.S.Liang (Exxon)

Small-angle X-ray Scattering Studies of the Growth of Particles in Cethyltrimethylammoniumbromide Micellar Solution Added with Tetraethoxysilane B-105
T.-L. Lin, W.-J. Liu (Nat. Tsinghua U.), H. H. Shao, K. S. Liang (Exxon)

Chirality, Structure and Free Energy of DNA Liquid Crystals B-105
H.H. Strey, R. Podgornik, D.C. Rau and V.A. Parsegian (NIH/DCRT/LSB), J. Wang (XFD/ANL), and E. Sirota (Exxon)

Beamline X10B

Unexpected Structure and Properties of ω-unsaturated Thiols Self-assembled Monolayers on Au(111) B-106
T.Y.B. Leung, P. Fenter, F. Schreiber, P. Eisenberger and G. Scoles (Princeton U.)

Structure of Rigid Biphenyl Monolayers by Vapor and Solution Phase Growth B-106
F. Schreiber, T. Y. B. Leung, P. Fenter, and G. Scoles (Princeton U.)

Study of the Structure and Growth of Co-assembled Surfactant/Silica Films B-107
L. Zhou, P. Fenter, I. Aksay and P. Eisenberger (Princeton U.)

Beamline X11A

Local Structure of V_2O_3 During the Metal-Insulator Transition B-107
A.Frenkel. E.A.Stern (U. of Washington) and F.A.Chudnovsky (Phys.-Tech. Inst., St. Petersburg, Russia)

XAFS Study of Cation Valence State and Site Distribution in Natural Schorlomite and Melanite Garnet B-108
A.F. Gualtieri, S. Quartieri (U. of Modena, Italy), K. Pandya (NCSU) and G.M. Lamble (BNL - NSLS)

Sr-induced Local Distortions in $La_{2-x}Sr_xCuO_4$ B-108
D.Haskel and E.A.Stern (U. of Washington)

X-Ray Absorption Spectroscopy Analysis of Lead and Zinc Speciation in a Contaminated Groundwater Aquifer B-109
D. Hesterberg, D. E. Sayers, W. Zhou, G. M. Plummer, and W. P. Robarge (NCSU)

XAFS Characterization of Copper in Model Aqueous Systems of Humic Acid and Illite B-109
D. Hesterberg, D. E. Sayers, W. Zhou, W. P. Robarge, and G. M. Plummer (NCSU)

Application of X-ray Absorption Spectroscopy for Studying Pyromorphite Formation in Lead Contaminated Soil B-110
D. Hesterberg, W. Zhou, P. Zhang, D. E. Sayers, J. A. Ryan, and W. P. Robarge (NCSU and US-EPA)

Characterization of Heavy Metal Incorporation in Calcite by XAFS Spectroscopy B-110
R.J. Reeder, P. Northrup (SUNY Stony Brook) and G.M. Lamble (BNL- NSLS)

XAFS Characterization of Heavy-Metal Contamination in the Unsaturated and Saturated Zones of a Soil Profile B-111
D. E. Sayers, D. Hesterberg, W. Zhou, W. P. Robarge, and G. M. Plummer (NCSU)

The Kinetics of Nickel Sorption on Pyrophyllite as Monitored by X-ray Absorption Fine Structure (XAFS) Spectroscopy B-111
A. M. Scheidegger, D. L. Sparks (U. of Delaware), and G. M. Lamble (NSLS)

In Situ XAS Studies Of Metal-Semiconductor Interactions B-112
Z. Wang, P.T. Goeller, B.I. Boyanov, D.E. Sayers, and R.J. Nemanich (NCSU)

Evidence for Pb-phospate Cluster Formation at the Oxide-water Interface B-112
F.J. Weesner and W.F. Bleam (U. of Wisconsin-Madison)

Studies of the Nature of Binding Sites of First Row Transition Elements Bound to Aquatic and Soil Humic Substances Using X-ray Absorption Spectroscopy B-113
K.Xia, W. Bleam, and P.A. Helmke (U. of Wisconsin-Madison)

Studies of the Nature of Cu^{2+} and Pb^{2+} Binding Sites in Soil Humic Substances Using X-ray Absorption Spectroscopy B-113
K. Xia, W. Bleam, and P. A. Helmke (U. of Wisconsin-Madison)

X-Ray Absorption and Electron Paramagnetic Resonance Studies of Cu^{2+} Sorbed to Silica: Surface-Induced Precipitation at Low Surface Coverages B-114
K. Xia, W.F. Bleam (U. of Wisconsin-Madison), A.Mehadi, and R.W. Taylor (Alabama A&M U.)

Beamline X12B

Structure of Zn-fingers 1-6 of Transcription Factor IIIA (TFIIIA) Bound to a 31 bp DNA Site B-114
R.S. Brown, R.T. Nolte, S.C. Harrison, (HHMI/Children's Hospital Lab. of Molecular Medicine)

Large Strain Deformation Studies of Oriented Triblock Copolymers with a Cylindrical Morphology B-115
C. Honeker, E. L. Thomas (MIT), M.C. Capel (BNL - Biology)

The Crystal Structure Determination of the SecA Translocation ATPase B-115
J.F. Hunt and J. Deisenhofer (HHMI, UT Southwestern)

Structural Studies of the Yeast Bleomycin Hydrolase, Gal6 ..... B-116
L. Joshua-Tor, J. Rosenbaum (Cold Spring Harbor Lab), W. Zheng, H. Whelan and S. A. Johnston (UT-Southwestern)

Structure and Relaxation of Polyimides Using Small Angle X-ray Scattering B-116
S. X. Lu , P. Cebe (Tufts U.), and Malcolm Capel (BNL - Biology)

Structure of Horse Liver Alcohol Dehydrogenase at 1.25 A Resolution B-117
S. Ramaswamy, H. Eklund (Swedish U. of Agricultural Sciences) and B.V. Plapp (U. of Iowa)

Crystalization and Preliminary X-ray Analysis of Aα Subunit of Protein Phosphatase 2A B-117
M. Skidmore, M. Sawaya (UCSD), S. Parkin, B. Rupp (LLNL), H. Hope (UCD), and G.Walter (UCSD)

A Bent-Laue Crystal Monochromator for Monochromatic Radiography with an Area Beam B-118
Z. Zhong(NSLS), D. Chapman(CSRRI), W. Thomlinson, F. Arfelli, N. Gmür and R. Menk (NSLS)

The Structure of Calicivirus B-118
L. Zhou and M. Luo (U. of Alabama at Birmingham)

Beamline X12C

X-ray Crystal Structures of the S229A Mutant and Wild Type MurB in the Presence of the Substrate Enolpyruvyl-UDP-N-Acetylglucosamine at 1.8 Resolution B-119
T. Benson, C. Walsh and J. Hogle (Harvard Medical School)

Crystal Structure of the FASCICULIN2-MOUSE *Acetylcholinesterase* Complex B-119
Y. Bourne (TSRI), R.B.G. Ravelli (Lab. Crystall.& Structual Chem.), M. L. Raves, J. L. Sussman (Weizmann Inst.), P. Taylor and P. Marchot (UCSD)

Structure of the Hydroxylase Component of Methane Monooxygenase from Methylosinus trichosporium OB3b at 2 A Resolution B-120
N. Elango, R. Radhakrishnan, W.A. Froland, C.A. Earhart, J.D. Lipscomb and D.H. Ohlendorf (U of Minnesota)

Structural Studies of Nucleosomes. B-120
J. M. Harp, D. E. Timm (UTK), and G. J. Bunick (ORNL)

The Structure of the Complex of Concanavalin A with Methyl Alpha-D-Arabinofuranoside B-121
A.J. Kalb (Gilboa), F. Frolow, A.G. Evdokimov and R. Ventura (Weizmann Institute)

Crystal Structures of Two Thermostable Bacterial Alcohol Dehydrogenases B-121
Y. Korkhin, F. Frolow, A.J. Kalb (Gilboa) (Weizmann Institute of Science)

Structure of Lyme Disease Antigen OspA Complexed with a Fab B-122
H. Li and C.L. Lawson (BNL - Biology)

Crystal Structure of Δ^9 Stearoyl-acyl Carrier Protein Desaturase from Castor Seed and its Relationship to other Diiron Proteins. B-122
Y. Lindqvist, W Huang, G. Schneider (Karolinska Institute) and J. Shanklin (BNL- Biology)

Structure of Photolyzed Myoglobin B-123
G.N. Phillips, Jr. (Rice U.), J. Berendzen, (LANL), I. Schlichting, (Max Planck-Hedelberg), and R.M. Sweet (BNL - Biology)

Structure of a Plant Profilin at 1.6 by MAD at X12C B-123
R. Shigeta, K. Thorn (Princeton U.), H. Christensen (Nat U. Singapore), U. Lindberg (Stockholm U.), N.-H. Chua (Rockefeller U.), C. Schutt, (Princeton U.)

Crystallographic Studies of hnRNP A1 ..... B-124
R-M. Xu (Cold Spring Harbor Lab.)

Structural Basis for Dimerization of Hepatitis Delta Antigen B-124
H. Zuccola and J. Hogle (Harvard Medical School)

Beamline X13

Characterization of the Elliptical Polarized Wiggler at the Iron K-edge B-125
W. A. Caliebe, C.-C. Kao, P. Stefan, E. Johnson, D. P. Siddons, and J. B. Hastings (NSLS)

Generation of Coherent Soft X-rays with the Prototype Small Gap Undulator. B-125
E. Dufresne, S.B. Dierker (U. Michigan) L.E. Berman and Z. Yin (NSLS)

A Simple X-Ray Focusing Mirror Using Float Glass B-126
Z. Yin, L. Berman (NSLS), S. Dierker, E. Dufresne (U. Michigan) and D.P.Siddons (NSLS)

Beamline X14A

Ordered Phases of a Langmuir Monolayer of an Azobenzene-containing Molecule. B-126
M.K. Durbin, A. Malik, A.G. Richter, C.J. Yu, V. Bhashyam(Northwestern Univ.), R. Eisenhower(ORNL), and P. Dutta(Northwestern Univ.)

Inelastic X-Ray Scattering Measurement of the Many-Body Local-Field Factor in Aluminum ... B-127
B. C. Larson, J. Z. Tischler (ORNL), E. D. Isaacs (Lucent Technologies), P. Zschack (U. of IL.), A. Fleszar (U. Würzburg), and A. G. Eguiluz (U. of TN & ORNL)

Resonant Raman Scattering Excited by GeK_α Radiation Internal and External to the Ge Atom B-127
C.J. Sparks, T. Gog, G.E. Ice (ORNL), R.A. Eisenhower (U. of Illinois)

Beamline X15A

Adsorption and Structure of Selenite on the Calcite ($10\bar{1}4$) Surface B-128
L. Cheng, P.F. Lyman (Northwestern U.), N.C. Sturchio (ANL) and M.J. Bedzyk (Northwestern U. and ANL)

Spatial Resolution of the Variable-Period X-Ray Standing Wave Method B-128
R. Itri, R. Zhang and M. Caffrey (Ohio State U.)

Structural Study of 0.2 ML In/GaAs(001) 4x2 Surface B-129
T.-L. Lee (Northwestern U.), J. Zegenhagen (Max-Planck-Institut, Germany), P.F. Lyman (Northwestern U.) and M.J. Bedzyk (ANL & Northwestern U.)

Atomic Resolution X-Ray Standing Wave Characterization of Self-Assembled Chromophoric Superlattices B-129
W. Lin, T. -L. Lee, P. F. Lyman, J. Lee, T. J. Marks (Northwestern U.), M. J. Bedzyk (ANL & Northwestern U.)

Dynamical Diffraction of Trapped X-rays on a Curved Crystal Surface B-130
C. Liu (Harvard U.) and J. A. Golovchenko (Harvard U. & Rowland Inst. for Science)

Local Adsorption Geometry of Te/Si(001) Studied by XSW B-130
Paul F. Lyman (Northwestern U.), Michael J. Bedzyk (Northwestern U. and ANL), and Pedro A. Montano (U. of Illinois - Chicago & ANL)

Surface Relaxation by X-ray Standing Wave and Surface-extendedXx-ray Absorption Fine Structure B-131
J. Woicik (NIST)

Beamline X15B

Extremely Dilute Impurities in Silica Optical Waveguides B-131
L. Niu, R. M. Atkins, M. A. Marcus, D. C. Jacobson, P. F. Glodis, and P. H. Citrin (Bell Labs)

Optically Active Er Centers in Si B-132
L. Niu, D. C. Jacobson, D. J. Eaglesham, and P. H. Citrin (Bell Labs)

Pb-induced Instability in ZBLAN Glass B-132
L. Niu, A. R. Kortan, N. Kopylov, and P. H. Citrin (Bell Labs)

Ti Silicides in Submicron Dimensions B-133
L. Niu, R. Tung, M. A. Marcus, and P. H. Citrin (Bell Labs)

Distorted, Inequivalently Charged C_{60} Anions in $Yb_{2.75}C_{60}$ B-133
S. Schuppler (Bell Labs), E. Ozdas (Hacettepe U.), K. B. Lyons, A. R. Kortan, and P. H. Citrin (Bell Labs)

Beamline X16A

Structure of the Incommensurate Au/Si(100)-5x1 Surface B-134
P. Bennett (ASU), D. Walko and I. K. Robinson (U.of Illinois)

Oxygen-Induced Facetting of Cu(115) B-134
I. K. Robinson and D. A. Walko (U. of Illinois), H. L. Meyerheim and M. Albrecht (Inst. f. Kristallographie, U. Muenchen)

Surface Structure of α-Ga(001) B-135
D. A. Walko, I. K. Robinson (U. of Illinois), Ch. Grütter, and J. H. Bilgram (ETH Zürich)

Beamline X16C

Oxide Growth on Cu(111) in Acidic Solution B-135
Y. S. Chu and I. K. Robinson (U. of Illinois)

Chemical Ordering in Lead Magnesium Niobate B-136
D. M. Fanning and I. K. Robinson (U. of Illinois, UC)

Strain of GaN Thin Films on Sapphire (0001) B-136
C. Kim, I. K. Robinson, J. Myoung, K.-H. Shim, and K. Kim (U. of Illinois, Urbana-Champaign)

Beamline X17B1

Measurement of the Fission Branch for the 103 keV State in ^{235}U B-137
N. N. Ajitanand (SUNY Stony Brook), D. P. Siddons, and J. B. Hastings (NSLS)

In situ Measurement of the Rheology of Silicate Garnets at High Pressure B-137
J.Ando, J.Chen, D.J.Weidner Y.Wu (CHiPR, SUNY Stony Brook), and Y.Wang (CARS, APS)

In situ Equation of State Measurements of Antigorite B-138
K. Bose, A. Navrotsky (CHiPR, Princeton U.), P. J. Schields, J. Chen and D. J. Weidner (CHiPR, SUNY Stony Brook)

Elasticity of Single Crystal MgO from Simultaneous X-ray and Ultrasonic Measurements to 9 GPa and 1500 K in a Multi-Anvil Apparatus B-138
G. Chen, Y. Sinelnikov, J. Cooke, D. J. Weidner and R. C. Liebermann (CHiPR SUNY Stony Brook)

Rheology of Dry and Hydrous Phases of the α and β Forms of $(Mg,Fe)_2SiO_4$ B-139
J. Chen, T. Inoue, Y. Wu, D. J. Weidner and M. T. Vaughan (CHiPR, SUNY Stony Brook)

Pressure Induced Amorphization in Zirconium Tungstate ZrW_2O_8 ..... B-139
J. Chen, J. B. Parise, R. Li (CHiPR, SUNY Stony Brook) and A. W. Sleight (OSU)

Structural Studies of Ag_2SO_4 and TlX (X = Cl, Br, I) by *In-Situ* ED-XRD to 6GPa and 550°C B-140
Q. Chen and R. A. Secco, (U. West. Ont.), E.A. Secco, (St. Francis Xavier U.), J. Chen, M.T. Vaughan, G. Chen, J.Z. Zhang, and D.J. Weidner (CHiPR, SUNY Stony Brook)

Microbeam Irradiation of Duck Embryo Brains: Relevance to Microbeam Radiation Therapy [MRT] of Brain Tumors in Infants B-140
F.A. Dilmanian, X.Y. Wu, X. Huang, M. Kershaw, B. Ren, D.N. Slatkin, K. Trandem (Medical, BNL), R. Menk, W.C. Thomlinson, and Z. Zhong (NSLS)

Elasticity of Polycrystalline $MgSiO_3$-Majorite from Simultaneous X-ray and Ultrasonic Measurements to 9 GPa and 1000 K in a Multi-Anvil Apparatus B-141
G. D. Gwanmesia (DSU), G. Chen, Y. Sinelnikov, J. Cooke, L. Flesch, M. T. Vaughan and R. C. Liebermann (CHiPR, SUNY Stony Brook)

Rheological Study of Hydrous γ-Phase Using *in situ* X-ray Diffraction B-141
T. Inoue, J. H. Chen, Y. Wu, D. J. Weidner and M. T. Vaughan (CHiPR, SUNY Stony Brook)

Elasticity of Polycrystalline Beta-Mg_2SiO_4 From Simultaneous X-ray and Ultrasonic Measurements to 7 GPa and 900 K in a Multi-Anvil Apparatus B-142
B. Li, J. Liu, L. Flesch (CHiPR, SUNY Stony Brook), G. D. Gwanmesia (DSU), J. Chen and R. C. Liebermann (CHiPR, SUNY Stony Brook)

Simultaneous X-Ray and Acoustic Measurements of Equations of State of Solids at High Pressures and Temperatures in Multi-Anvil Apparatus B-142
R. C. Liebermann, G. Chen, B. Li, G. D. Gwanmesia, J. Cooke, L. Flesch, J. Liu, Y. Sinelnikov, M. T. Vaughan, J. Chen, J. Zhang, Y. Wang and D. J. Weidner (SUNY Stony Brook)

Thermal Equation of State of Stishovite B-143
J. Liu, J. Zhang, D. J. Weidner, L. Flesch, G. Chen, B. Li and R. C. Liebermann (SUNY Stony Brook)

Elasticity of $Ca(Ti,Si)O_3$ Perovskite. B-144
Y. D. Sinelnikov, J. Zhang, and R. C. Liebermann (CHiPR, SUNY Stony Brook)

Rheology of Cubic Boron Nitride at High Temperatures and Pressures B-144
J. S. Sweeney, J. Chen, D. J. Weidner, M. T. Vaughan (CHiPR, SUNY Stony Brook)

Phase Relations and Equations of State for High-Pressure Phases of Ferrosilite and Enstatite .. B-145
M. T. Vaughan, D. H. Lindsley, and Y. Silnelnikov (CHiPR, SUNY Stony Brook)

T-CUP: A New High-Pressure Apparatus for X-Ray Studies - Continued B-145
M. T. Vaughan, D. J. Weidner, and J. Chen (SUNY Stony Brook)

A New Anvil Geometry for SAM-85 for High P, T X-ray Studies B-146
Y. B. Wang, D. J. Weidner, M. T. Vaughan (CHiPR, SUNY Stony Brook), and I. C. Getting (CHiPR, U. Colorado)

Rheology Study of $Py_{60}Mj_{40}$ Garnet at High Pressure and High Temperature B-147
Y. Wu, D.J. Weidner, J. Chen, G. Gwanmesia, and M. Vaughan (CHiPR, SUNY Stony Brook)

Equation of State of Calcite-Structure Carbonates B-147
J. Zhang and R. J. Reeder (CHiPR, SUNY Stony Brook)

Effect of Silicon Incorporation in Iron: Equation of State and Phase Transition B-148
J. Zhang (CHiPR, SUNY Stony Brook) and F. Guyot (U. of Paris)

Beamline X17B2

Bronchial Imaging Using Xenon K-Edge Dichromography B-143
R. H. O'Neil, J. Giacomini, E. Rubenstein, A. Van Kessel, H. Gordon (Stanford), W. Thomlinson, N. Gmur, Z. Zhong (NSLS) and D. Chapman (IIT)

Contrast Imaging and Image Quantification With the Monochromatic CT - MECT B-146
X.Y. Wu, F.A. Dilmanian, X. Huang, E.C. Parsons, B. Ren (BNL - Medical), W.C Thomlinson, Z. Zhong (NSLS), L.D. Chapman (I.I.T.), T.M. Button, and M.J. Petersen (SUNY Stony Brook)

Beamline X17C

Rheology, Strength, and Elasticity Anisotropy of Iron at High Pressures B-148
H. Mao, J. Shu, R. J. Hemley (Carnegie Institute), and A. K. Singh (Nat. Aeronautical Lab., India)

Compression of Seven ScS Compositions with Sc Lattice Vacancies B-149
S. Peiris and D. Heinz (U. of Chicago)

Pressure Induced Structural Transitions in Nanometer Size Particles of PbS B-149
S. B. Qadri, E. F. Skelton, Y. Yang, B. R. Ratna (NRL), and J. Z. Hu (CIW)

High P-T Phase Diagram and Equation of State of Iron B-150
G. Shen, J. Hu, R. J. Hemley, H. Mao (Carnegie Institute), and T. S. Duffy (GSECARS)

In Situ Measurement of the Structural Transition Rate in Pd Associated with the Electrochemical Absorption of Deuterium B-150
E. F. Skelton, P. L. Hagans, S. B. Qadri, D. D. Dominguez (NRL), and J. Z. Hu (CIW)

Beamline X18A

Structure and Phase Transitions of Krypton in Porous Vycor B-151
D. W. Brown, P. E. Sokol (Penn. State U.), and S. N. Ehrlich (Purdue U.)

Multiple X-ray Diffraction Studies of Decagonal Quasicrystals. B-151
R. Eisenhower, R. Colella (Purdue U.), B. Grushko (Jülich)

Spot Shapes of Bragg Reflections in Decagonal Quasicrystals B-152
R. Eisenhower (U. of Illinois), Steve Ehrlich (Purdue U.), Benjamin Grushko (Forschungszentrum Juelich, Germany)

Anomalous X-ray Scattering Studies of a Lead Magnoniobate Single Crystal B-152
V. Gosula, H. Chen (U. of Illinois), S. Teslic and T. Egami (U. of Pennsylvannia)

High Temperature Studies of X-ray Scattering in a Lead Magnoniobate Single Crystal B-153
V. Gosula, H. Chen (U. of Illinois), S. Teslic and T. Egami(U. of Pennsylvannia)

Time and Depth Dependence Study of the Azimuthal Orientation in Confined Hybrid Smectic C* Films B-153
L. J. Martínez-Miranda, Y. F. Hu, T. K. Misra and M. W. Haung (U. of Maryland)

Time Dependence Study of In-Plane Layers in Confined Hybrid Smectic C* Films B-154
L. J. Martínez-Miranda, Y. F. Hu, T. K. Misra and M. W. Huang (U. of Maryland)

Anisotropic X-ray Diffuse Scattering Features in $La_{0.6}Pb_{0.4}MnO_3$ B-154
R. McQueeney (U. of Pennsylvania)

Anomalous Diffraction Studies of CMR Materials B-155
S. M. Mini (Northern Illinois U. & ANL), J. Mitchell, D. Hinks (ANL) and S. N. Ehrlich (Purdue U.)

The Defect Structure Studies of $La_{2-x}Ca_xCuO_{4-y}$ Superconductors B-155
X. Shi, J. B. Cohen, and T. O. Mason (Northwestern U.)

Atomic Structure of PMN Studied by Resonant X-ray Diffraction B-156
S. Teslic, T. Egami (U. of Penn.), V. Gosula and H. Chen (U. of Ill)

Structural Study of Giant Magnetoresistance Effect in La-Ca-Mn-O Epitaxial Films B-156
T. S. Tsai (NCHU, Taiwan), M.Y. Chen(NTU, Taiwan), M.C. Shih (NCHU, Taiwan)

Epitaxial Structures of Butane and Hexane Monolayers Adsorbed on a Ag(111) Surface B-157
Z. Wu (U. of Missouri-Columbia), S. N. Ehrlich (Purdue U.), B. Matthies, K. W. Herwig, and H. Taub (U. of Missouri-Columbia)

Structure and Growth of *n*-Alkane Films Adsorbed on the Ag(111) Surface B-157
Z. Wu, J. Wang (U. of Missouri-Columbia), S. N. Ehrlich (Purdue U.), B. Matthies, K.W. Herwig, and H. Taub (U. of Missouri-Columbia)

Structural Studies of Self-Assembled Alkynyl Thin Film Materials B-158
C.-M. Yam, A. K. Kakkar (McGill U.), A. Richter and P. Dutta (Northwestern U.)

The Structure of Diffuse Scattering in the Reciprocal Space of Al-Pd-Mn Quasicrystal. B-158
Y. Zhang, R. Colella (Purdue U.), S. Ehrlich (NSLS), S. Kycia, A. Goldman, (Iowa StateU.)

Beamline X18B

Photocatalytic Reduction of Heavy Metal Ions on Derivatized Titanium Dioxide Nano-Particle Surface Studied by EXAFS B-159
L. X. Chen, T. Rajh, D. M. Tiede, P. A. Montano and M. C. Thurnauer (ANL)

Structure of Supported Alkali and Alkaline Earth Modified Catalysts by X-ray Absorption Spectroscopy B-159
E.J. Doskocil, S. V. Bordawekar, and R. J. Davis (U. of Virginia)

Stabilization of Pd^{2+} Ions on H-ZSM-5 and Other Acidic Supports During the Selective Reduction of NO by CH_4 ..... B-160
D. E. Resasco, S. Stagg, W. Alvarez, and A. Ali (U. of Oklahoma)

Observation of Local Structural and Electronic Changes Accompanying Photodoping of $YBa_2Cu_3O_{6+x}$ B-160
T. A. Tyson, J. F. Federici, D. Chew, W. Savin (NJIT), L. Furenlid (NSLS), and W.Wilber (ARL)

Beamline X19A

Characterization of Phenyl Cuprate Solutions Using XANES B-161
H. Huang, J. Penner-Hahn (U. Michigan)

Zn Speciation in Developing *Xenopus* Embryos as Detected by XANES B-161
K. Peariso, C. van Huis, R. Denver, and J. Penner-Hahn (U. Michigan)

Structural Characterization of Ga-Substituted Ferredoxins B-162
J. Penner-Hahn, K. Peariso (U. Michigan) E. Vo, H. Liu and J. Germanas (U. Houston)

XANES Studies of Oxidation States of S in Humic Substances From Different Environmental Settings B-162
K. Xia, F. Weesner, and W. F. Bleam (U. of Wisconsin-Madison), P. R. Bloom, and U. L. Skyllberg (U. of Minnesota)

Structure of Ti in TiO_2-SiO_2 Catalysts B-163
J. Zhao, J. Rockwell, F. E. Huggins, F. Lu, and G. P. Huffman (U. of Kentucky)

Beamline X19C

Sychrotron White Beam X-ray Topography Investigation of Influence of Annealing on CdZnTe Substrate B-163
Y. Chen, M. Dudley (SUNY Stony Brook), D. R. Rhiger (Hughes Santa Barbara Research Center)

Characterization of Processing Induced Defects in Silicon Device Using Synchrotron White Beam X-ray Topography B-164
Y. Chen, W. Huang, W. Chen, M. Dudley (SUNY Stony Brook)

Characterization of Structural Defects in Microgravity Grown CdZnTe Single Crystals Using Synchrotron White Beam X-ray Topography II B-164
H. Chung, B. Raghothamachar, M. Dudley, and D. J. Larson, Jr. (SUNY Stony Brook)

Investigations of Dislocation Distributions in Microgravity Grown CdZnTe Single Crystals Using Synchrotron White Beam X-ray Topography B-165
H. Chung, B. Raghothamachar, M. Dudley, and D. J. Larson, Jr. (SUNY Stony Brook)

Studies of Defect Structures in Microgravity Grown CdZnTe Single Crystals Using Synchrotron White Beam X-ray Topography I B-165
H. Chung, B. Raghothamachar, M. Dudley and D. J. Larson, Jr. (SUNY Stony Brook)

Studies of the Influence of Cooling Rate to Defect Microstructure Development in Microgravity Grown CdZnTe Single Crystals B-166
H. Chung, B. Raghothamachar, M. Dudley and D. J. Larson, Jr. (SUNY Stony Brook)

Investigation of the Distribution and Configuration of Dislocations in Sulphur Doped InP Single Crystals I B-166
H. Chung, W. Si, and M. Dudley (SUNY Stony Brook), D. F. Bliss (Rome, AFB), A. Maniatty (RPI)

Investigation of the Distribution and Configuration of Dislocations in Sulphur Doped InP Single Crystals II B-167
H. Chung, W. Si, and M. Dudley (SUNY Stony Brook), D. F. Bliss (Rome Laboratory, AFB), and A. Maniatty (RPI)

Investigation of the Distribution and Configuration of Dislocations in Sulphur Doped InP Single Crystals III B-167
H. Chung, W. Si, and M. Dudley (SUNY Stony Brook), D. F. Bliss (Rome Laboratory, AFB), and A. Maniatty (RPI)

Modeling the Distribution of Dislocations Observed in MLEK Grown Fe Doped InP Single Crystals B-168
H. Chung, W. Si, and M. Dudley (SUNY Stony Brook), D. F. Bliss (Rome Laboratory, AFB), and A. Maniatty (RPI)

Observation of Growth Striations in MLEK Grown InP Single Crystals Using Synchrotron White Beam X-ray Topography B-168
H. Chung, W. Si, and M. Dudley (SUNY Stony Brook), D. F. Bliss (Rome, AFB), and A. Maniatty (RPI)

Observation of Growth Striations in MLEK grown InP Single Crystals Using Synchrotron White Beam X-ray Topography II B-169
H. Chung, W. Si, and M. Dudley (SUNY Stony Brook), D. F. Bliss (Rome Lab., AFB), A. Maniatty (RPI)

Studies of Dislocation Distributions in MLEK Grown Fe Doped InP Single Crystals Using Synchrotron White Beam X-ray Topography B-169
H. Chung, W. Si, and M. Dudley (SUNY Stony Brook), D. F. Bliss (Rome Laboratory, AFB), and A. Maniatty (RPI)

Characterization of Defect Structures in 3C-SiC Single Crystals using Synchrotron White Beam X-ray Topography B-170
W. Huang, M. Dudley (SUNY Stony Brook), and C. Fazi (Army Research Lab.)

Characterization of Slip Dislocations in 6H-SiC Single Crystals Using Synchrotron White Beam Topography B-170
W. Huang, M. Dudley (SUNY Stony Brook), C. Fazi (ARL), and D. Willkinson (Novecon Technologies)

Experimental Proof of the Energy Dispersion in Contrast Theory on Micropipe Image Formation B-171
W. Huang, M. Dudley (SUNY Stony Brook), S. Wang (ATMI), and C. Fazi (Army Research Lab.)

Synchrotron White Beam Topography Studies of Residual Stress in SiC Single Crystal Wafers with Epitaxial Thin Films B-171
W. Huang, Q. Wang, M. Dudley, F. P. Chiang (SUNY Stony Brook), J. Parsons (Oregon Graduate Institute), and C. Fazi (ARL)

In-plane Structure of the Liquid-Vapor Interfaces of Dilute Bismuth: Gallium Alloys B-172
N. Lei, Z. Huang, and S. A. Rice (U. of Chicago)

Structure of the Liquid-Vapor Interface of Tin: Gallium Alloy B-172
N. Lei, Z. Huang, and S. A. Rice (U. of Chicago)

Studies On the Formation Mechanism of Small Angle Tilt Boundaries in Ga Doped Ge Single Crystals by X-ray Topography B-173
B. Raghothamachar, H. Chung, M. Dudley (SUNY Stony Brook), and D C. Gillies (NASA)

Visibility of Growth Interfaces and Striations As a Function of Diffraction Geometry in Ga Doped Ge Single Crystals B-173
B. Raghothamachar, H. Chung, M. Dudley (SUNY Stony Brook), and D C. Gillies (NASA)

Characterization of Structural Defects in Vapor Grown CdTe Single Crystals by Synchrotron White Beam X-ray Topography B-174
B. Raghothamachar, H. Chung, M. Dudley (SUNY Stony Brook), D.C. Gillies, and W. Palosz (NASA)

Comparison of Defect Structures in Microgravity (μg) and Terrestrially (1g) Grown CdZnTe Single Crystals by Synchrotron White Beam X-ray Topography B-174
B.Raghothamachar, H. Chung, M. Dudley, and D. Larson Jr. (SUNY Stony Brook)

Investigations On the Effects of the Asymmetrical Gravity Vector on the Defect Distributions in Microgravity Grown CdZnTe Single Crystals B-175
B. Raghothamachar, H. Chung, M. Dudley, and D. J. Larson Jr. (SUNY Stony Brook)

Studies On the Surface of a Microgravity Grown CdZnTe Boule by Synchrotron White Beam X-ray Topography B-175
B. Raghothamachar, H. Chung, M. Dudley, and D. J. Larson Jr. (SUNY Stony Brook)

Synchrotron White Beam X-ray Topographic Characterization of Growth Defects in Bridgman-Stockbarger Grown CdZnTe Single Crystals B-176
B. Raghothamachar, H. Chung, M. Dudley, and D. J. Larson Jr. (SUNY Stony Brook)

Morphology of Basal Plane Dislocations in 4H-SiC Single Crystal Wafers B-176
W. Si and M. Dudley (SUNY Stony Brook), R. Glass, V. Tsvetkov, and C. Carter, Jr. (Cree Research, Inc)

Study of 6H-SiC Polytype Inclusions in 4H-SiC Single Crystals B-177
W. Si and M. Dudley (SUNY Stony Brook), R. Glass, V. Tsvetkov, and C. Carter, Jr. (Cree Research, Inc)

Investigations of 4H-SiC Epilayers on (11$\bar{2}$0) 4H-SiC Single Crystal Substrates B-177
W. Si and M. Dudley (SUNY Stony Brook), H. S. Kong, J. Sumakeris, and C. Carter, Jr. (Cree Research, Inc.)

Investigations of Triangular Inclusions in 4H-SiC Epilayers on 4H-SiC Single Crystal Substrates: (I) Identification of Phases B-178
W. Si and M. Dudley (SUNY Stony Brook), H. S. Kong, J. Sumakeris, and C. Carter, Jr. (Cree Research, Inc.)

Investigations of Triangular Inclusions in 4H-SiC Epilayers on 4H-SiC Single Crystal Substrates: (II) Effects of Superscrew Dislocations in substrates B-178
W. Si and M. Dudley (SUNY Stony Brook), H. S. Kong, J. Sumakeris, and C. Carter, Jr. (Cree Research, Inc.)

Investigations of Triangular Inclusions in 4H-SiC Epilayers on 4H-SiC Single Crystal Substrates: (III) Effects of Off-axis Angles of Substrates B-179
W. Si and M. Dudley (SUNY Stony Brook), H. S. Kong, J. Sumakeris, and C. Carter, Jr.(Cree Research, Inc.)

Studies of Growth Striations and Impurity Distribution of LEC Grown GaInSb Single Crystal B-179
J. Su, M. Dudley (SUNY Stony Brook), D. Fletcher, and W. Bonner (Johnson Matthey Electronics)

Synchrotron White Beam X-ray Topographic Studies of LEC GaInSb Seed Transition Region .. B-180
J. Su, M. Dudley (SUNY Stony Brook), D. Fletcher, and W. Bonner (Johnson Matthey Electronics)

A Comparison of Synchrotron White Beam and Lang X-Ray Topography of 6H-SiC Single Crystal Wafers B-180
W. M. Vetter and M. Dudley (SUNY Stony Brook)

Synchrotron White Beam X-Ray Topography of a Single Superscrew Dislocation in 6H-SiC Through All{100} Faces B-181
W. M. Vetter and M. Dudley (SUNY Stony Brook)

Surface Scattering from Ternary Mixtures of Oil, Water, and Surfactant B-181
S.M. Williams, Z. Zhang, D.M. Mitrinovic, M.L. Schlossman (U. of IL- Chicago), and Z. Huang (BNL)

Studies of Influence of Defects on the Performance of 4H-SiC Devices Using Synchrotron White Beam X-ray Topography: I. Defect Configuration B-182
C. Yang and M. Dudley (SUNY Stony Brook), H. M. Hogood and S. Seshadri (Northrop Grumman Science and Tech. Center)

Studies of Influence of Defects on the Performance of 4H-SiC Devices Using Synchrotron White Beam X-ray Topography: II - Influence of Defects B-182
C. Yang and M. Dudley (SUNY Stony Brook), H. M. Hobgood and S. Seshadri (Northrop Grumman Science Tech. Center)

Characterization of Defects in 4H-SiC Single Crystals by Synchrotron White Beam X-ray Topography B-183
C. Yang, W. Si and M. Dudley(SUNY Stony Brook), H. M. Hobgood and S. Seshadri (Northrop Grumman)

Beamline X20A

X-ray Scattering Studies of the Passive Film on Fe(001) and Fe(110) B-183
A. J. Davenport (U. Manchester), L. J. Oblonsky, M. P. Ryan (BNL), M. F. Toney (IBM), and C. Vitus (BNL)

Time-Resolved Measurements of Overlayer Ordering in Electrodeposition B-184
A.C. Finnefrock, L.J. Buller, H.D. Abruña, and J.D. Brock (Cornell U.)

Using X-ray Scattering to Examine Supra-molecular Organization and Surface-melting at Molecular Interfaces. B-184
S.E. Girdwood, A.R. Kennedy, J.N. Sherwood (U. Strathclyde) and K.J. Roberts (Heriot-Watt U.)

Structure and Kinetics of the Sliding Q_1 CDW in $NbSe_3$ B-185
K.L. Ringland, S.G. Lemay, R.E. Thorne, and J.D. Brock (Cornell U.)

Beamline X20B

Nanosuspensions in Helium B-185
V.Kiryukhin, B.Keimer (Princeton U.), E.Gordon, and V.Khmelenko (IEPCP, Russia)

Morphological Investigation of Nylon 66 Fibers Using Radial Distribution Function Analysis ... B-186
J. R. Sharrow, J. M. Schultz (U. of Delaware), B. S. Hsiao, and H. Chang (DuPont)

Beamline X20C

Effects of Rubbing Polyimide Films B-186
J.M. Sands, S.K. Kumar (Penn State U.), T.P. Russell, and M.F. Toney (IBM)

Beamline X21

Resonant Raman Scattering at the Fe K-edge in Fe_2O_3 ..... B-187
W. A. Caliebe, C.-C. Kao, and J. B. Hastings (NSLS)

High Energy Resolution Beamline B-187
W. A. Caliebe, C,-C. Kao, D. P. Siddons, and J. B. Hastings (NSLS)

Inelastic Xray Scattering from Single Crystal Sodium B-188
P.C.Chow and S.C. Moss (U. Houston), C.C. Kao and J.P. Hill (BNL)

High Resolution Kα Emission Studies of Iron(III) Porphyrins B-188
K. A. Daly (U. of Michigan), W. Caliebe, C.-C. Kao (NSLS) and James E. Penner-Hahn (U. of Michigan)

Near-Threshold Behaviour of the Cu K$\alpha_{1,2}$ Emission Spectrum B-189
M. Deutsch, O. Gang, M. Fritsch (Bar-Ilan U., Israel) and C.C. Kao (BNL)

Resonant and Non-resonant Inelastic X-ray Scattering Studies of Electronic Excitations B-189
J.P. Hill, C.-C. Kao and W.A.C. Caliebe (BNL)

Inelastic X-ray Scattering Spectroscopy in $Sr_2CuO_2Cl_2$ B-190
E.D. Isaacs, P. Platzman (Bell Labs), C. Burns (Western Michigan U.), P. Abbamonte, M. Klein (U. of Illinois), and L. Miller (Ames Lab)

X-Ray Resonant Raman Scattering in NiO: Resonant Enhancement of the Charge Transfer Excitations B-190
C.-C. Kao, W. A. Caliebe, J. B. Hastings (NSLS), and J.-M. Gillet (U. Marne, France)

Spin-Polarized Mn K-Edge Measurements of Doped $LaMnO_3$ B-191
T. A. Tyson (NJIT), C.-C. Kao, W. Caliebe (NSLS), and J. J. Neumeier (FAU)

Beamline X22A

Real-Time X-ray Scattering Study of Sputter-deposited $LaNiO_3$ Thin Films on Si Substrates B-191
H. Y. Lee (SRRC, Taiwan), C. H. Lee (National Tsing Hua U., Taiwan) and K. S. Liang (Exxon)

Structure Analysis of the Cu Metallization of AlN Using the Polyol Method B-192
L. J. Martínez-Miranda (U. of Maryland), G. M. Chow, L. K. Kurihara, D. Ma and P. E. Schoen (NRL)

In situ Structural Characterization of Lithium-ion Battery Electrode Materials B-192
T.R. Thurston, N.M. Jisrawi, S. Mukerjee, X.Q. Yang, J. McBreen (BNL - DAS), M.L. Daroux, and X.K. Xing (Gould Electronics)

In Situ Measurements of Texture and Phase Development in Bi-2223 Silver Cladded Superconducting Wires B-193
T.R. Thurston, U. Wildgruber, N.M. Jisrawi, M. Suenaga, Y.L. Wang (BNL), and P. Haldar (IGC Corporation)

Anomalous Lattice Expansion of an Underpotentially Deposited Ag Bilayer on Pt(111) B-193
J.X. Wang, R.R. Adzic, and B.M. Ocko (BNL - Physics)

Beamline X22B

Effect of Metallic Caplayers on the Magnetic Structure of Thin Cr(001) Films B-194
P. Bödeker and H. Zabel (Inst. für Experimentalphysik/Festkörperphysik, Ruhr-U. at Bochum, Germany)

X ray Reflectivity Study of Gold Colloid Monolayers B-194
C.J. Clarke, R.B. Lennox (McGill U), B.M. Ocko, D. Nguyen (BNL - Physics), M.H. Rafailovich, J. Sokolov and Z. Li (SUNY Stony Brook)

Temperature Dependent Surface Structure of Liquid Mercury B-195
E. DiMasi, O. M. Magnussen, B. M. Ocko (BNL - Physics), M. Deutsch (Bar-Ilan U., Israel), H. Tostmann, O. G. Shpyrko, M. J. Regan, and P. S. Pershan (Harvard)

X-ray Reflectivity of Silane Multilayers B-195
E. DiMasi, B.M. Ocko (BNL - Physics), W. Ke, R. Maoz, and J. Sagiv (Weizmann Institute of Science, Israel)

X-Ray Scattering Study of C_{60}-propylamine Adduct Monolayers at the Gas-Water Interface B-196
M. Fukuto, K. Penanen, R.K. Heilmann, P.S. Pershan (Harvard U.), and D. Vaknin (Ames Lab & Iowa State)

Structure Control of Surface Freezing in Alcohol Melts by Additives B-196
O. Gang(Bar-Ilan U., Israel), X.Z. Wu(ANL), B. Ocko(BNL), E. Sirota(EXXON), M. Deutsch(Bar-Ilan U.)

X-ray Scattering From Discotic Liquid Crystalline Compounds at the Air-water Interface. B-197
D. Gidalevitz, O. Mindyuk, J. Strzalka (U.Penn.), B. Ocko (BNL - Physics) and P. A.Heiney (U.Penn.)

An X-ray Photoinduced Insulator-to-Metal Transition in a Colossal-Magnetoresistance Manganite B-197
V. Kiryukhin, D. Casa, B. Keimer (Princeton U.), J.P. Hill, A. Vigliante (BNL), Y. Tomioka, and Y. Tokura (JRCAT, Japan)

Time Dependence Study of In-Plane Layers in Confined Hybrid Smectic C* Films B-198
L. J. Martínez-Miranda, Y. F. Hu, T. K. Misra and M. W. Huang (U. of Maryland)

Time and Depth Dependence Study of the Azimuthal Orientation in Confined Hybrid Smectic C* Films B-198
L. J. Martínez-Miranda, Y. F. Hu, T. K. Misra and M. W. Haung (U. of Maryland)

The 2D Ising Model: Br Electrodeposited on Ag(100) B-199
B.M. Ocko and J.X. Wang (BNL - Physics), T. Wandlowski (Ulm)

Two-Dimensional Monomolecular Pigment Assemblies at The Air-Water Interface B-199
D. Vaknin, B.W. Gregory, J. D. Gray, T.M. Cotton, W. S. Sturve (Ames Lab) and B.M. Ocko (BNL - Physics)

Surface Reconstruction at Metal-solid Polymer Electrolyte Interfaces B-200
J.X. Wang and R.R. Adzic (BNL - Physics)

Beamline X22C

Resonant Magnetic X-ray Scattering in Er Films with Monolayer Y Superlattice Doping B-200
M. J. Conover, C. P. Flynn (U. of Illinois), A. Vigliante, and D. Gibbs (BNL - Physics)

Resonant Magnetic X-ray Scattering in Ho Films with Monolayer Dy Superlattice Doping B-201
M. J. Conover, C. P. Flynn (U. of Illinois), A. Vigliante, and D. Gibbs (BNL - Physics)

Determination of Magnetic Moment Directions Using X-ray Resonant Exchange Scattering B-201
C. Detlefs, A. H. M. Z. Islam, A. I. Goldman, C. Stassis, P. C. Canfield (Ames Lab & ISU), J. P. Hill, and D. Gibbs (BNL - Physics)

Magnetic and Structural Properties of Erbium Films B-202
G. Helgesen (IFE, Norway), Y. Tanaka (RIKEN, Japan), J.P. Hill, P. Wochner, D. Gibbs (BNL-Physics), C.P. Flynn and M.B. Salamon (U. of Illinois)

Resonant X-ray Scattering From a Thin Film of UPd_2Al_3 ..... B-202
A. Hiess (EITU, CEA-Grenoble), S. Langridge (EITU, ESRF), M. Huth (U. Mainz, Germany), D. Gibbs (BNL - Physics), and G. H. Lander (EITU)

K-Edge Resonant Magnetic Scattering from a Transition Metal Oxide: NiO B-203
J.P. Hill (BNL - Physics), C.-C. Kao (NSLS) and D.F. McMorrow (Riso)

Charge Ordering in the Layered Perovskite $La_{0.5}Sr_{1.5}MnO_4$ B-203
J.P. Hill and B.J. Sternlieb (BNL - Physics)

Studies of Zero Field Magnetic Structures of $TbNi_2Ge_2$ B-204
A. H. M. Z. Islam, C. Detlefs, A. I. Goldman, P. C. Canfield (Ames Lab), J. P. Hill, and D. Gibbs (BNL - Physics)

Verifying Magnetic Structures Using X-Rays - Neodymium A Test Case. B-204
D. Watson, W.J. Nuttall, E.M. Forgan, D.Fort (U. Birmingham, UK), and S.C. Perry (Keele U., UK)

Ir(100) Surface Structure Determination by X-ray Scattering B-205
G.Watson (UMBC), D.Gibbs (BNL - Physics), V.Jahns and D.Zehner (ORNL)

Characterization of the Magnetic Disorder at the (001) Surface of UO_2 ..... B-205
G.M. Watson, D. Gibbs (BNL - Physics), L.E. Berman (NSLS), G.H. Lander, H. Matzke (EITU), W. Ellis (LANL), and B.D. Gaulin (McMaster U.)

Beamline X23A2

Cr-K-edge X-ray-Absorption Study of Cr Dopants in Mg_2SiO_4 and Ca_2GeO_4 Sol-gel Glasses B-206
K. E. Miyano (Brooklyn College), J. C. Woicik (NIST), Ding Huang (Brooklyn College), P. Sujatha Devi, and H. D. Gafney (Queens College)

X-ray Absorption Studies of Battery Materials B-206
P. E. Stallworth (USNA); M. L. denBoer, S. Kostov, S. Greenbaum (CUNY, Hunter), and C. Lampe-Onnerud (Quantum Energy Technologies)

XANES and EXAFS Characterization of Copper Halides in Nylon 6,6 ..... B-207
J. N. Weber, H. D. Rosenfeld (DuPont) and M. A. Walters (NYU)

A Look Inside the Unit Cell of Strained GeSi B-207
J.C. Woicik, C.E. Bouldin (NIST), K.E. Miyano, (Brooklyn College), and C.A. King (Lucent Technologies)

Beamline X23A3

Surface Defects and Fracture of Sapphire Single Crystals B-208
D. Black, H. Burdette (NIST) and D. Harris (NAWC)

Polishing Effects in Single-crystal Sapphire B-208
D. Black, H. Burdette (NIST) and F. Schmid (Crystal Systems)

X-ray Diffraction Imaging of Electrically Fixed Holograms in Strontium Barium Niobate (SBN) B-209
G. Fogarty, B. Steiner (NIST), T. Chang, and J. Hong (Rockwell International)

In situ X-ray Diffraction Imaging of Electrically Fixed Photorefractive Holograms in Barium Titanate B-209
G. Fogarty, B. Steiner (NIST), M. H. Garrett, J. Martin, and R. Uhrin (Deltronic Crystal Ind.)

In situ Measurements of Dislocation Structure Evolution in Al Single Crystals Deformed in Tension B-210
L. E. Levine (WSU), G. G. Long, D. R. Black and Robb Thomson (NIST)

Crack Correlation in Tensilely Strained Multifilamentary High-Tc Superconductor Composite Tapes B-210
R. D. Spal (NIST), G. N. Riley and C. J. Christopherson (American Superconductor Corp.)
Residual Disorder in Low Pressure, Low Thermal Gradient LEC Gallium Arsenide Observed in High Resolution Diffraction Imaging B-211
B. Steiner, L.E. Levine (NIST), M. Brown, and D. Larson (Grumman)

Beamline X23B

X-ray Absorption Studies of Battery Materials B-211
P. E. Stallworth (USNA); M. L. denBoer, S. Kostov, S. Greenbaum (CUNY, Hunter), and C. Lampe-Onnerud (Quantum Energy Technologies)
Measure of Hexavalent Chromium in Contaminates Soils B-212
M. Szulczewski, W.F. Bleam, and P. A. Helmke (U. Wisconsin-Madison)
XANES and EXAFS Characterization of Copper Halides in Nylon 6,6 ..... B-212
J. N. Weber, H. D. Rosenfeld (DuPont) and M. A. Walters (NYU)

Beamline X24A

X-ray Standing Wave Investigation of S/Ni(100) B-213
D. Heskett, J. Warner, and G. Sabatino (U. Rhode Island), D. Mullins (ORNL) and L.E. Berman (NSLS)
X-Ray Standing Wave Studies of Self-Assembled Monolayer Growth B-213
F. Schreiber, P. Fenter, G. Scoles, P. Eisenberger (Princeton U.), L. Berman (NSLS), M. Bedzyk (Northwestern U. & ANL)
Angular Correlation Between Subsequently Emitted Auger Electrons B-214
R. Wehlitz, L. Pibida, J. C. Levin, and I. A. Sellin (U. of Tenn.)

Beamline X24C

Band Structure of Nonlinear Crystal LiB_3O_5 in VUV Region Obtained From Reflection Spectra B-214
T.-J. Chen (Southern Illinois U.), W.R.Hunter (Sachs Freeman Assoc.), J. C. Rife (Naval Research Center), and R. Tao (Southern Illinois U)
Characterization of Multilayer Coated Gratings and Mirrors B-215
J. F. Seely, M. P. Kowalski, J. C. Rife, W. R. Hunter, and R. G. Cruddace (NRL)

Beamline X25

Structure of the Quaternary NF-ATp/Fos/Jun/DNA Complex B-215
L. Chen, S.C. Harrison (HHMI), A. Rao, P. Hogan, (Harvard Medical School)
The Near-Threshold Evolution of the $CuK\alpha_{3,4}$ Satellites B-216
M. Fritsch (Bar-Ilan U., Israel), K. Hämäläinen (Helsinki U., Finland), C. C. Kao (NSLS), O. Gang, M. Deutsch (Bar-Ilan U.)
Structural Investigation of GaP Clusters in a Si Matrix, using Multiple Energy X-ray Holography (MEXH) B-216
T. Gog (ORNL), R.-H. Menk (NSLS), R. Eisenhower,(U of Illinois) G. Le Duc, L. Berman, Z. Yin (NSLS)
K-Edge Resonant Magnetic Scattering from a Transition Metal Oxide: NiO B-217
J.P. Hill (BNL - Physics), C.-C. Kao (NSLS) and D.F. McMorrow (Riso)
High-Resolution XAS Investigations of MnO_2 Spinel-Based Li^+ Intercalation Battery Systems . B-217
C.R. Horne, E.J. Cairns (LBNL/UC, Berkeley), M.M. Grush and S.P. Cramer (LBNL/UC, Davis)
Crystallographic Studies of Cell Signaling and DNA Replication B-218
J. Kuriyan (Rockefeller U. & HHMI)
Multiple Energy Speckle in Reflectivity From Si(111) Wafers B-218
J. L. Libbert, J. A. Pitney and I. K. Robinson (U. of Ilinois, Urbana-Champaign)

X-ray Studies of Liquid Metal Surfaces: Oxidation and Alloy Surfaces B-219
M.J. Regan, H. Tostmann, P.S. Pershan (Harvard U.), O.M. Magnussen, E. DiMasi, B.M. Ocko (BNL), M. Deutsch (Bar-Ilan U., Israel)

Structure and Kinetics of the Sliding Q_1 CDW in $NbSe_3$ B-219
K.L. Ringland, S.G. Lemay, R.E. Thorne, and J.D. Brock (Cornell U.)

Characterization of the Magnetic Disorder at the (001) Surface of UO_2 ..... B-220
G.M. Watson, D. Gibbs (BNL - Physics), L.E. Berman (NSLS), G.H. Lander, H. Matzke (EITU), W. Ellis (LANL), and B.D. Gaulin (McMaster U.)

Structure Determination of the Entire Extracellular Portion of Human CD4 ..... B-220
H. Wu, P.D. Kwong and W.A. Hendrickson (Columbia U.)

Two Beam Diffraction Interference Method for 2D Crystallography B-221
Y. Yacoby (Hebrew U.), H. Baltes, R. Pindak, L. Pfeiffer (Lucent Technologies), R. Clarke (U. of Michigan), and L. Berman (NSLS)

The Structure of Calicivirus B-221
L. Zhou and M. Luo (U. of Alabama at Birmingham)

Beamline X26A

Tissue Localization of Metals Bioaccumulated in Marine Organisms Living in Sediments B-222
W. J. Berry, D. J. Borsay (US Env. Prot. Agency), and K. W. Jones (BNL - DAS)

Lead in Tadpole Brain B-222
H. T. Cline (Cold Spring Harbor Laboratory), S. Witte (U. of Iowa), and Keith Jones (BNL - DAS)

Distribution of Catalysts in Polyolefin Polymerization Particles B-223
W. C. Conner, Jr. (U. of Massachusetts) and K. W. Jones (BNL - DAS)

Chemical Compositions of "Cluster" Interplanetary Dust Particles B-223
G. J. Flynn (SUNY Plattsburgh), S.R. Sutton (The U. of Chicago), and S. Bajt (LLNL)

Spatial Distribution of Lead in Chick Tibia B-224
C. S. Fullmer (Cornell U.) and K. W. Jones (BNL - DAS)

Migration and Reduction of Cr(VI) in the Presence of Fe(II) B-224
D.B. Hunter, E.J. Gall, P.R. Nuessle and P.M. Bertsch (U. of Georgia)

Behavior of Dissolved Molybdenum During Localized Corrosion of Austenitic Stainless Steel ... B-225
H.S. Isaacs and S.-M. Huang (BNL - DAS)

Composition of Dredged Material From The NY/NJ Harbor B-225
K. W. Jones (BNL - DAS) and S.-R. Song (BNL and Yale U.)

Synchrotron Radiation in the Study of the Annual Growth Ring of Trees B-226
R. R. Martin, T. K. Sham (U. of Western Ontario), and K. W. Jones (BNL - DAS)

Structure Studies of Transition Metal Complexes in Fluid Inclusions at Elevated Temperatures . B-226
R. A. Mayanovic (Southwest Missouri State U.), A. J. Anderson (St. Francis Xavier U.-Canada), and S. Bajt (LLNL)

Stroke and Calcium Concentrations in the Brain B-227
G. Newman, S. Trowbridge (SUNY Stony Brook), and K. W. Jones (BNL -DAS)

Study of Chemical State of Toxic Metals During the Life Cycle of Fly Ash Using X-Ray Absorption Near-Edge Structure B-227
J. Osán, B. Török, S. Török (KFKI Atomic Energy Research Institute, Hungary), and K. W. Jones (BNL - DAS)

X-ray Fluoresence Imaging of Zinc in *Xenopus* Embryos B-228
K. Peariso, D.L. Tierney, C. VanHuis, R. J. Denver, and J. E. Penner-Hahn (U. of Michigan)

XANES Mapping of Zinc in *Xenopus* Embryos B-228
K. Peariso, D. L. Tierney, C. VanHuis, R. J. Denver and J. E. Penner-Hahn (U. of Michigan)

Spatially Resolved Trace Element Heterogeneities in Apatite Measured via Synchrotron X-ray Fluorescence Microanalysis B-229
John Rakovan and Richard J. Reeder, (SUNY Stony Brook)

Selective Uptake of Co and Zn in Surface Sites on Calcite During Growth B-229
R.J. Reeder (SUNY Stony Brook)

Elemental Microanalysis and Elemental Mapping on Biological Tissues B-230
R. Rizzo (U. of Trieste, Italy)

Manganese Oxidation: A Characteristic of Susceptibility in the *Pyricularia* - Rice Disease (Rice Blast) System B-230
D. G. Schulze, D.M. Huber, A.K.M. Shahjahan, M. Levy(Purdue U.), S. Bajt (U. of Chicago), and B. Illman (USDA Forest Products Lab.)

Analysis of Trace Elements: Au in Sulfides and Ni, Zn, Ga, Y and Zr in Garnet B-231
I.M. Steele (U. of Chicago)

Selenium XANES of Contaminated Soils, Plant Residue, and Algae B-231
T.K. Tokunaga (LBNL), S.R. Sutton (U. of Chicago), S. Bajt (LLNL), P. Nuessle (U. of Georgia), and G. Shea-McCarthy (U. of Chicago)

Beamline X26C

Real-Time Electromigration Strain Measurement on Individual Al Interconnect Lines by White Beam Microdiffraction B-232
G. S. Cargill III and P.-C. Wang, (Columbia University), and I. C. Noyan, E. G. Liniger, C.-K. Hu and K. Y. Lee (IBM Research)

X-ray Diffraction Data Collection for Microcrystals B-232
J. Pluth, L. Clark , S. Sutton (U. of Chicago), M. Helliwell (U. of Manchester), G. Harlow (Am. Museum of Nat. Hist.), and G. Shea-McCarthy (U. of Chicago).

Fabrication of a mm-Wave Accelerating Cavity, Using Deep X-ray Lithography B-233
J.J. Song, Y.W. Kang, R.L. Kustom, B. Lai, D.C. Mancini, A. Nassiri (ANL), and V. White (U. Wisconsin)

Characterization of Defects in Protein Crystals by Diffractometry and Topography B-233
V. Stojanoff (ESRF), D. P. Siddons (NSLS), E. Snell (NASA), T. Boggon and J. R. Helliwell (U. Manchester, UK.).

In situ Structural Characterization of Lithium-ion Battery Electrode Materials B-234
T.R. Thurston, N.M. Jisrawi, S. Mukerjee, X.Q. Yang, J. McBreen (BNL - DAS), M.L. Daroux, and X.K. Xing (Gould Electronics)

Beamline X27A

An Investigation into the Spatial Texture Distribution in Thermomechanically Deformed $Nd_2Fe_{14}B$-based Permanent Magnets B-234
T.R. Thurston, L.H. Lewis, U. Wildgruber, D.O. Welch (BNL- DAS), and V. Panchanathan (Magnequench International)

In Situ Measurements of Texture and Phase Development in Bi-2223 Silver Cladded Superconducting Wires B-235
T.R. Thurston, U. Wildgruber, N.M. Jisrawi, M. Suenaga, Y.L. Wang (BNL), and P. Haldar (IGC Corporation)

Beamline X27C

Determination of Topology and Transport in Porous Media Using Synchrotron Computed Microtomography B-235
P.M. Adler, J.-F. Thovert (IPGP, France), K.W. Jones, A.M. Peskin, D.P. Siddons, B. Andrews, and B. Dowd (BNL)

Region of Interest Tomography Correction for Subvolumes of Large Core Samples B-236
B. Andrews, B.A. Dowd, D.P. Siddons, and J. Yung (NSLS)

X-Ray Microtomography Applications to the Characterization of Oil Reservoir Seal and Source Lithologies B-236
W. Bell , R.D. Hazlett (Mobil Corp.), B. Andrews, B.A. Dowd, K.W. Jones, A. Peskin, and D.P. Siddons (BNL)

X-ray Refraction Imaging (XRI) Applied to Mammography B-237
D. Chapman (Illinois Inst. of Tech.), W.Thomlinson, N. Gmür, A. Zhong, R. Menk (NSLS), R.E. Johnson, D. Washburn,E. Pisano (U. of North Carolina), F. Arfelli (Sincrotrone Trieste), and D.Sayers (NCSU)

Applications of Synchrotron Microtomography in Experimental Petrology: Absorption Tomography of Pore Features in Synthetic Rock Samples B-237
T. Cohen, E. B. Watson (Rensselaer Polytech Inst.), B. Dowd, D. P. Siddons, B. Andrews and K. W. Jones (BNL)

X-Ray Microtomography of Reservoir Sandstone for the Characterization of Porosity and Permeability B-238
M.E. Coles, R.D. Hazlett, E.L. Muegge (Mobil Corp.), B. Andrews, B.A. Dowd, K.W. Jones, A. Peskin, D.P. Siddons (BNL), M. Schlackman (GTE), W.E. Soll (LANL), and P. Spanne (ESRF)

X-Ray Microtomography of Fungal Deterioration of Wood B-238
B.L. Illman (U. Wisconsin and Forest Products Lab.), B.A. Dowd and D.P. Siddons (NSLS)

MECT's Bent Laue-Laue Monochromator: Design and Test Results B-239
B. Ren, F.A. Dilmanian, X.Y. Wu, (BNL- Medical), L.D. Chapman, I. Ivanov (CSRRI, IIT) and Z. Zhong (NSLS)

X-Ray Microtomography of Basalts B-239
D. Sahagian (U.N.H.), B.A. Dowd, K.W. Jones, D.P. Siddons, S. Song (BNL)

Microstructures of Antarctic Meteorites in the Millimeter Size Range B-240
S.R. Sutton (The U. of Chicago), B.A. Dowd, K.W. Jones, D.P. Siddons, B. Andrews, A. Peskin (BNL)

Determination of Urea/Urethane Ratios in Complex Polyurethanes using X-ray Microscopy	X1A

H. Ade, A. P. Smith (NCSU), E. G. Rightor (Dow Chemical), and A. P. Hitchcock (McMaster U.)

Polyurethanes (PUR) are complex polymeric materials with polyether, polyurea, and polyurethane funcitonalities present in sometimes unknown quantities. The differentiation of polyurea and polyurethane functionalities is challenging, particularly when high spatial resolution is required to analyze precipitates in PUR foames. NEXAFS microscopy is a potentially powerful tool for the analysis of these materials. To verify this potential we have examined three model polyurethane compounds where the urea/urethane composition can be predicted from synthesis. NEXAFS spectra of these three compounds are shown in Fig. 1 with the samples having a urea/urethane compositions of a) #258 = 22/6%, b) #259 = 11/11%, and c) #260 = 6/22%, with a polyether fraction of 72 % in each case. The main area of interest in these spectra is the broad peak at 288-290 eV, which corresponds to the π^*(C=O) excitations of urea and urethane functionalies[1]. After background subtraction and intensity normalization, the spectra are simulated with fractional sums of NEXAFS spectra from model urea, urethane, and polyether compounds[2]. The polyether fraction is assumed to be equal to the stoichiometric prediction. The results of this analysis are presented in Fig.2 for the three model compounds. The determined fractions of urea and urethane components are plotted against the predicted stoichiometry from the synthesis. At present, x-ray microscopy should allow compositional analysis with better than 10 percent precision.

[1] S. G. Urquhart *et. al. J. Polym. Sci. B, Polym. Phys.* **33**, 1603 (1995)
[2] H. Ade *et. al. J. Electron. Spectrosc. Relat. Phenom.* (submitted)

*Work supported by NSF Young Investigator Award DMR-9458060) and Dow Chemical.

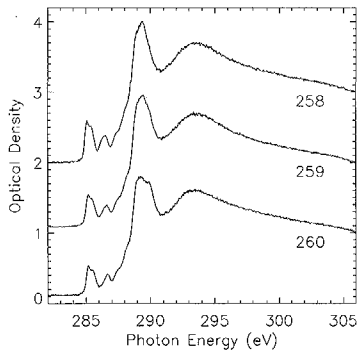


Figure 1. NEXAFS spectra of three model polyurethane samples. See text for description.

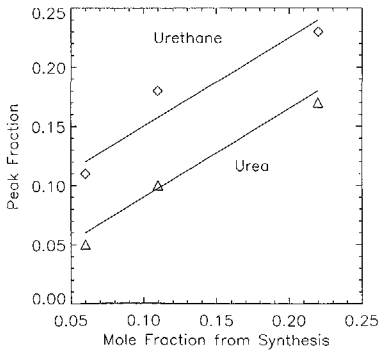


Figure 2. Comparison of the quantitative determination of the urea/urethane ratio with the expected composition.

Critical Radiation Dose of Poly(ethylene terephthalate) (PET) *	X1A

H. Ade, A. P. Smith (NCSU), S.G. Urquhart, A. P. Hitchcock (McMaster U.), and E. G. Rightor (Dow Chemical)

Near Edge X-ray Absorption Fine Structure (NEXAFS) spectroscopy is based on the excitation of an inner shell electron into unoccupied molecular orbitals[1]. These core excitations provide a sensitive probe of the local electronic structure of the excited atom in the presence of the core hole but can also damage the sample and alter the chemical composition. This is also, if not more so, the case for Electron Energy Loss Spectroscopy in an electron microscope (TEM-EELS). In order to understand the relative damage associated with TEM-EELS and NEXAFS microscopy we have studied X-ray damage of the common polymer poly(ethylene terephalate) (PET) at 302 eV, as exhibited by changes in the PET NEXAFS spectrum. Fig. 1 shows four absorption spectra acquired from PET which had been exposed to 302 eV x-rays for dosages of a) no exposure, b) 1.00 x 10^5 Mrad, c) 1.84 x 10^5 Mrad, and d) 2.68 x 10^5 Mrad. The spectral features at 285 eV and 288 eV decrease in intensity with increasing exposure while a transition at 286.5 eV increases in intensity. We have fitted gaussian functions for the spectral intensity changes with dose and estimated the average critical dose from three spectral features to be 1.386 $\pm$ 0.69 x 10^5 Mrad. By comparision to damage in TEM-EELS, a rule of thumb was devised that says that under the present typical data acquisition conditions utilized, NEXAFS microscopy can analyze areas 500 times smaller than TEM-EELS given the same radiation damage[2] .

[1] J. Stöhr. *NEXAFS Spectroscopy*, Springer-Verlag (Berlin), 1992.
[2] E. G. Rightor *et. al. J. Phys. Chem.* (in press)

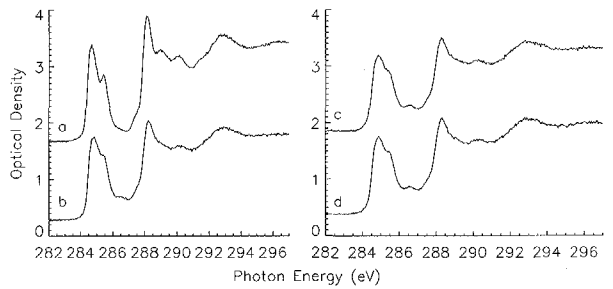


Figure 1. NEXAFS spectra acquired from PET after exposure to 302 eV x-rays for dosages of a) no dose, b) 1.00 x 10^5 Mrad, c) 1.84 x 10^5 Mrad, and d) 2.68 x 10^5 Mrad. The intensity of the excitations at 285 and 288 eV decreases with increasing exposure while an excitation at 286.5 becomes more pronounced.

* Work supported by NSF Young Investigator Award (DMR-9458060) and Dow Chemical.

X-ray Absorption Near Edge Structure of Amino Acids and Peptides | X1A

J. Boese, A .Osanna, C. Jacobsen, J. Kirz, E. Tall (SUNY Stony Brook), and X. Zhang (Harvard U.)

Combination of the spatial resolution of soft x-ray microscopes with x-ray absorption near-edge structure (XANES) analysis provides a new means for chemical state mapping [1]. Comparison of near edge absorption resonances with reference spectra makes it possible to map the concentrations of different double bonds. We tried to explore the applicability of this method to protein specific imaging. All proteins in living systems consist of only 20 different amino acids, linked together via the peptide bond. We wanted to find out if a protein spectrum can be predicted from amino acid spectra. This depends on how much spectra are affected by the peptide bond.

Preliminary work by X.Zhang and S.Williams [2] showed that a nitrogen edge XANES spectrum of the dipeptide consisting of arginine and aspartic acid was just the sum of the spectra of the two monomers. We have measured carbon edge XANES spectra of amino acids for the first time. Spectra of six amino acid monomers, four dipetides and one tripeptide were compared. Because of their heat sensitivity, amino acids cannot be evaporated but have to be analyzed in solid form. In order to obtain quantitative absorption measurements using transmission spectroscopy, the illuminated spot of the sample has to be of uniform thickness. Therefore a special sample preparation technique was used, and the spectra were obtained using the small spot size of the Stony Brook scanning transmission x-ray microscope at beamline X1A.

The spectra of the dipeptides and tripeptides investigated can indeed be explained as the sum of the spectra of the monomers involved. A typical result is presented in Figure 1. The spectra of glycine (Gly), tyrosine (Tyr), and the Gly-Tyr dipeptide (solid lines) are shown together with a weighted sum of the two monomer spectra (dashed line). The peptide bond has only a very small effect on spectra analyzed. It causes a very small shift ($\approx$0.3 eV) of the π^* resonance near 289 eV towards lower energies. If this result holds in general, it would allow the prediction of spectra of simple proteins, which could be used in protein specific imaging with x-ray microscopes.

[1] X.Zhang, R.Balhorn, J.Mazrimas, J.Kirz *J.Struct.Biol.*,116:335-344,1996
[2] X.Zhang Ph.D. Thesis, SUNY at Stony Brook, May 1995

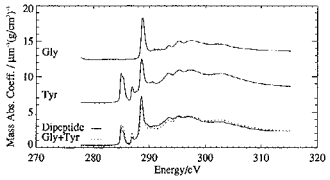


Figure 1.

The Application of Soft X-ray Microscopy to the *in-situ* Chemical Analysis of Ancient Spores in Organic-Rich Sedimentary Rocks | X1A

G. D. Cody (Carnegie Institution of Washington), H. Ade (NCSU), S. Wirick (SUNY Stony Brook)

Soft X-ray Imaging and C-NEXAFS has been used for the in-situ analysis of spores in a rank variable suite of organic rich sedimentary rocks. The acquisition of chemically based images (contrast based on the intensity of the 1s-pi * transition of unsaturated carbon), reveals a homogeneous chemical structure in the spore exine (cell wall). C-NEXAFS microanalysis indicates the path of chemical-structural evolution of the sporopollenin bio/geopolymer with increasing thermal maturity. The most significant change in the C-NEXAFS spectrum is an increase in the con-centration of unsaturated carbon, presumably aromatic, with maturity. Increases in the concentraion of unsaturated carbon are paralleled by losses of aliphatic and hydroxlyated aliphatic carbon components. Carboxyl groups are present in low and variable concentrations. Absorption due to carboxyl groups persists in the most mature specimen in this series. The results of this study reveal that the reactions that drive sporopollenin chemical structural evolution during thermal maturation are consistent with sequential dehydration, Diels-Alder cyclo-addition, and de-hydrogenation reactions that ultimately lead to a progressively aromatized bio/geopolymer. This chemical-structural evolution pathway is different than what has been determined for other organic constituents in these rocks.

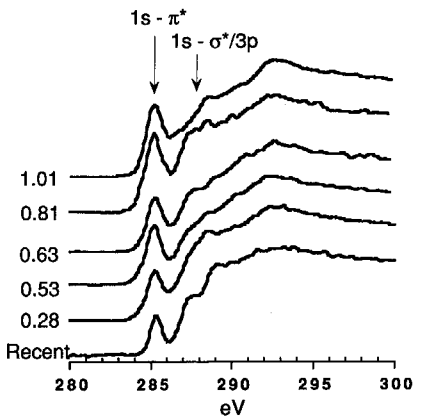


Figure 1. A Soft X-ray Image of a microspore in ancient sediments($\sim$ 90 MA). Contrast is based on absorption intensity at 285.5 eV, which corresponds to the 1s-pi* transition of aromatic carbon.

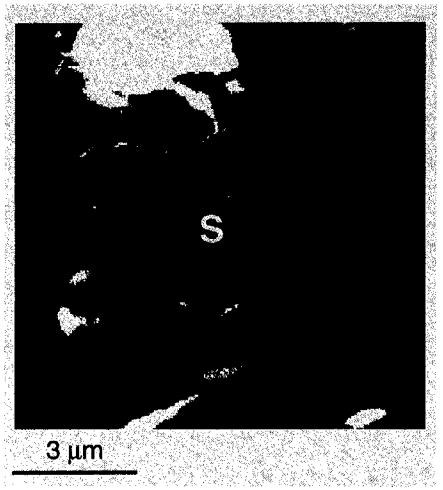


Figure 2. A Stack plot of the C-NEXAFS spectra for micro-spore samples in a suite of samples ranging in thermal maturity. Thermal maturity is gauged by the magnitude of the reflectance (%R) of a co-existing organic phase in each sedimentary rock.

Carbon Measurements on Interplanetary Dust Particles | X1A

G. J. Flynn (SUNY Plattsburgh), S. Bajt, H. Chapman (LLNL), and Lindsay P. Keller (VA Associates)

Interplanetary dust particles (IDPs), typically ~10 microns in size, have been recovered from the Earth's stratosphere by NASA aircraft. These IDPs are samples of the dust emitted by comets as well as debris produced by the fragmentation and erosion of asteroids. On average, the IDPs contain ~12 wt% carbon, about three times the carbon content of the most carbon-rich meteorites. These IDPs are believed to have been an important source of pre-biotic organic matter on the early Earth and possibly Mars.

Transmission electron microscope examination of ultramicrotome thin sections of IDPs has identified graphite, poorly-graphitized carbon, and carbonate in IDPs, while two-step laser mass spectroscopy has identified polycyclic aromatic hydrocarbons (PAHs) in some IDPs. However, the relative abundances and spatial distributions of individual carbon-bearing phases have not been established.

Thin sections fron three IDPs were examined using the Scanning Transmission X-ray Microscope (STXM) on beamline X1A of the National Synchrotron Light Source. The carbon abundances were determined, confirming the high concentrations reported by other techniques, the carbon distributiions were mapped, and X-Ray Absorption Near Edge Spectroscopy (XANES) measurements were made to determine the carbon bonding states present in selected carbon-rich regions. Carbon-XANES measurements at carbon-rich spots on two IDPs showed two peaks, at 285.6 and 288 eV, consistent with graphite or poorly-grahitized carbon.

The third IDP was selected for analysis because prior Electron Energy Loss (EELS) measurements showed an usually broad pi* peak which did not match that of any carbon bearing phase identified in IDP's. The higher energy resolution at X1A allowed us to resolve the broard pi* peak into two peaks, with energies of 284.8 and 286.3 eV. A peak at 288.5 eV was also seen in this particle by both C-XANES and EELS. The peak at 286.3 eV was not seen in any of the phases previously identified in IDPs: graphite, poorly graphitized carbon, carbonate, silicone oil (in which NASA collects IDPs), or the two PAHS (pyrene and dibenzoperylene). The three peak energies are a good match to C_{60}, fullerenes, though pure, well-crystallized C_{60}, shows peaks at 284.5 eV, 286.0 eV, and 288.4 eV, while the IDP sample shows peaks at 284.8 eV, 286.3 eV, and 288.4 eV. The IDP spectrum, descibed in detail by Bajt et al. [1], is consistent, within errors, with the pure C_{60} standard if the 286.0 and 286.4 eV peaks of C_{60} overlap to form the IDP peak at 286.3 eV due to inadequate spectrial resolution or sample degradation.

Further experiments are in progress to conclusively identify this carbon-bearing phase, obtain reference spectra of kerogens extracted from meteorites, and map and identify the carbon bearing phases in other IDPs.

[1] Bajt, S. et al. Lunar & Planetary Science XXVII, 57-58 (1996)

First Holographic Images of Fast-frozen Hydrated Biological Specimens | X1A

S. Lindaas, M. Howells, D. Pinkas, C. Magowan, K. Downing (LBNL) and C. Jacobsen (SUNY Stony Brook)

X-ray holography allows direct imaging of samples without the use of lenses. Our present technique employs photoresist (PMMA) to record the x-ray interference pattern, an atomic force microscope to examine and digitize the hologram, and a computer for numerical reconstruction. With this methodology, we have obtained sub 45 nm resolution images of room temperature biological specimens [1]. However, to minimize radiation artifacts, even in single exposures of unfixed specimens, it is necessary to "preserve" the specimen in a frozen state. To protect the specimen's morphology against ice-crystal damage, it must be fast frozen to liquid nitrogen temperature. Taking advantage of techniques developed in the electron microscopy community we have developed a cryo-holography station at beamline X1A which is capable of obtaining holograms of specimens prepared by fast freezing and held at cryogenic temperatures. We have recently obtained the first holograms of fast-frozen hydrated biological specimens measured at cryo temperatures [2]. Fig. 1 is a hologram of fast-frozen hydrated malaria infected red blook cells measured at cryo temperatures. Fig. 2 is the reconstructed image with a twin-image suppression algorithm implemented. This is an intermediate result and shows that the twin-image artifact is now the principle limitation to applications of holography. Our cryo-apparatus is already being upgraded to perform tomography experiments which we hope to report on soon. References: 1. S. Lindaas, et.al., "X-ray holographic microscopy by means of photoresist recording and atomic-force microscope readout" *J. Opt. Soc. Am.*A **13**, pp. 1788-1800 (1996), 2. S Lindaas, et.al, "X-ray Holography of Fast-Frozen Hydrated Biological Samples", to be published in *X-ray Microscopy and Spectromicroscopy proceedings of* **XRM96** Springer-Verlag (Ed) J. Thieme *et al.*. This research supported in part by DOE A. Hollaender Fellow. (SL) Pres. Fac. Fellow. Awd. RCD 92-53618 (CJ), and Comp. Sci. Grad. Fellow. (BC).

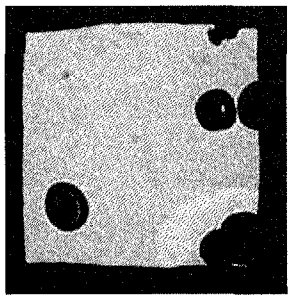


Figure 1. X-ray Gabor hologram (λ=2.4 nm) of fast-frozen malarial infected red blood cell. Readout using AFM (2048^2) pixels each $(22\,\mathrm{nm})^2$.

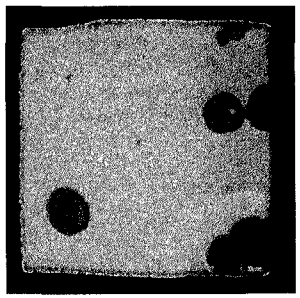


Figure 2. Reconstructed image (z = 425 μm with twin-image suppression implemented. Our work is concentrating on improving this algorithm.

Commissioning of the Cryo Scanning Transmission X-ray Microscope | X1A

J. Maser, C. Jacobsen, J. Kirz, A. Osanna, S. Spector, S. Wang, J. Warnking (SUNY Stony Brook)

X–ray Microscopy of biological specimens is severely restricted by radiation damage to the objects. To cope with this problem, we have developed a cryo–Scanning Transmission X–ray Microscope [1]. This system is designed to image hydrated objects of a thickness of several micrometers at temperatures of around 130 K. At these temperatures, structural changes to the sample due to radiation damage should be considerably reduced, enabling us to achieve higher spatial resolution and to take multiple images of one sample area for applications such as and chemical state mapping and tomograpy. Use of fast cooling methods will also allow us to freeze dynamical processes with a time constant of few milliseconds.

The images shown below were obtained during our first commissioning run. All images are taken at a wavelength of $\lambda = 2.4$ nm using a zone plate with an outermost zone width of 60 nm and a diameter of 160μm. For large photon flux, we used an exit slit of 200μm width.

[1] J. Maser, H. Chapman, C. Jacobsen, A. Kalinovsky, J. Kirz, A. Osanna, S. Spector, S. Wang, B. Winn, S. Wirick, X. Zhang. SPIE 2516, pp. 78 - 89, (1995).

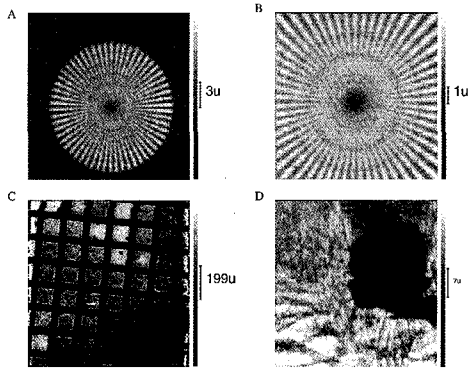


Figure 1. A: Image of Ge test pattern, demonstrating good orthogonality of piezo–driven fine scanning stage. B: Center of test pattern: lines and spaces of around 110 nm can be resolved, which corresponds well to size of x-ray probe at 200μ m exit slit. C, D: Images of plunge–frozen monkey kidney cells at T = 160 K. C: Image of a 2 mm $\times$ 2 mm area of sample, taken with the stepping–motor driven coarse scanning stage. D: Image of a 35 μm $\times$ 35 μm area of sample, ta

Luminescent Molecular Probes for X-ray Microscopy | X1A

M.M. Moronne (LBNL)

Synchrotron based scanning x-ray microscopes are capable of Rayleigh resolutions approaching 50 nm, with improvements expected to reach 20 nm in the near future. To take advantage of this high resolution for biological studies, specific labels for subcellular targets are needed. Using the scanning x-ray microscope at beamline X1A of the National Synchrotron Light Source, modified for luminescence detection (SLXM), we have shown that lanthanide based fluors are sufficiently bright and radiation stable to be the basis of a family of x-ray excitable probes. Initial experiments using lanthanide-polychelate conjugates of avidin and a secondary antibody to label actin stress fibers, validated this approach; however, non-specific cell labeling by these original compounds seriously compromised image quality. Subsequent studies established that there were two main causes of non-specific labeling: a) insufficient acylation of polychelate amino groups and b) high molecular weight aggregates created by unwanted crosslinking of polychelate chains.

We have addressed these problems in the last year by improved acylation techniques and by developing a biotinylated lanthanide-polychelate (bioLPC) that is virtually free of non-specific labeling artifacts. Biotinylating the polychelate greatly simplifies probes synthesis by eliminating the need for conjugation of the polychelate to large macromolecules such as antibodies that invariably generates a high percentage of cross linked aggregates. The biotinylated probe takes advantage of the tetravalency of avidin/streptavidin. For example, to label actin stress fibers, cells are treated with phalloidin-biotin (a specific probe for filamentous actin), followed by avidin, which has four biotin binding site. At this stage, only one avidin site is likely to be occupied by phalloidin-biotin leaving three available for binding to bioLPC. In this way, as many as 240 lanthanide atoms can be attached to a single molecular target, greatly increasing the brightness of the probe under x-ray excitation.

The efficacy of this strategy was confirmed using a rhodamine tracer on the polychelate probe and confocal microscopy. We demonstrated that bioLPC is capable of labeling with a specificity fully equivalent to conventional avidin-biotin probes for actin microfilaments, microtubules, and FISH DNA probes. In April of this year, we achieved the best x-ray excited luminescent images to date using bioLPC to label in vitro preparations of microtubule assemblies and actin filaments in 3T3 mouse fibroblasts. We believe that this data establishes the effectiveness of lanthanide polychelate probes for scanning x-ray microscopy, and fully expect to achieve a five fold improvement in resolution over visible light microscopic methods.

Morphological Characterization of Polycarbonate/Acrylonitrile-Butadiene-Styrene Polymer Blends *	X1A

A. P. Smith, H. Ade, R. Fornes, R. Gilbert (NCSU) and C. Sloop (IBM)

We employ the compositional sensitivity of Scanning Transmission X-ray Microscopy (STXM) to study the morphology of complex polymeric blends composed of polycarbonate (PC), styrene-acrylonitrile copolymer (SAN), SAN grafted on polybutadiene in latex form (SAN-g-PB), and titanium oxide (PC/ABS blends). These blends are utilized in computer housings and enclosures and we are interested in understanding the development of morphology and mechanical properties with repeated recycling of these materials. Some of the first steps in this study are the imaging of thin sections (100 nm) of the un-recyled material with the STXM. Figs. 1a and 1b are micrographs that let us determine the morphology, and in particular highlight the nitrile (SAN) distribution. The SAN is shown to mainly accumulate at the interface between the dispersed SAN-g-PB and the continuous PC matrix. There is also evidence of free SAN within the PC matrix. In addition, in images acquired below the carbon edge not shown here, the titanium oxide can be located and is shown to be associated with the SAN/SAN-g-PB aggregates.

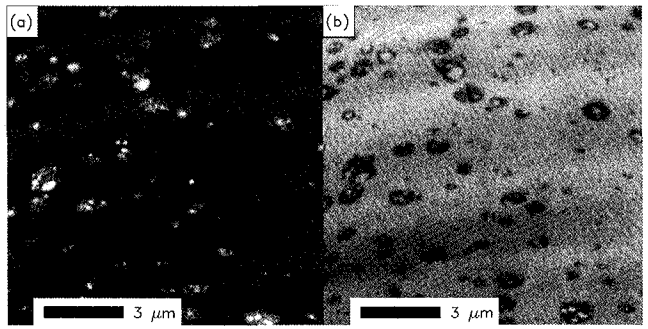


Figure 1. (A) NEXAFS image of polycarbonate/ABS blend acquired at 285.45 eV. PC is dark, SAN an intermediate gray and PB is bright. (B) Same sample area acquired at 286.55 eV. The brightest features are PB, while the darker areas are regions with high nitrile concentrations (SAN), that typically enclose the PB particles.

* Work supported by NSF Young Investigator Award (DMR-9458060).

Investigation of the Spinodal Decomposition of Constrained Thin Polymer Films with X-ray Microscopy	X1A

A. P. Smith, H. Ade (NCSU), D. Slep (Highlord Chemical), S. Qu, M. Rafailovich, and J. Sokolov (SUNY Stony Brook)

We have begun a study of the spinodal decomposition of two polymers (bi-layers or blends) constrained to a surface with the X1-STXM. Previous work with Atomic Force Microscopy (AFM) has shown segregation of one polymer into spheroids within the other upon annealing but was unable to chemically differentiate the species[1]. By utilizing NEXAFS spectromicroscopy, we are able to identify the polymers and their location within the system. The first system observed was a bi-layer of immiscible polymers, polystyrene (PS) and poly(methyl methacrylate) PMMA and an example of the morphology observed is shown in Fig. 1. This micrograph, acquired at an energy specific to the PMMA (288.4 eV), shows that the PS segregates into elipsoid like regions (dark) with the PMMA forming a shell around them and a thin layer between the PS dispersions. Due to the unsaturated bonding present in the PS, differentiation of phases within this system is simple with NEXAFS microscopy. The second system observed, a blend of PS and poly(brominated-styrene) (PBrS), was a more difficult test of the chemical differentiation via NEXAFS microscopy since the chemical structure of the materials is identical except a Br atom substituted on the phenyl ring of the PBrS. Fig. 2 shows a micrograph of this blend acquired at 286.2 eV (an energy specific to the C-Br bond) and shows that the PBrS segregates (dark regions) within the PS matrix (grey). Further studies of this material will allow a determination of the dynamics of the decomposition reaction with increasing annealing time.

1. S. Qu *et. al.* (in preparation)

Work supported by NSF Young Investigator Award (DMR-9458060).

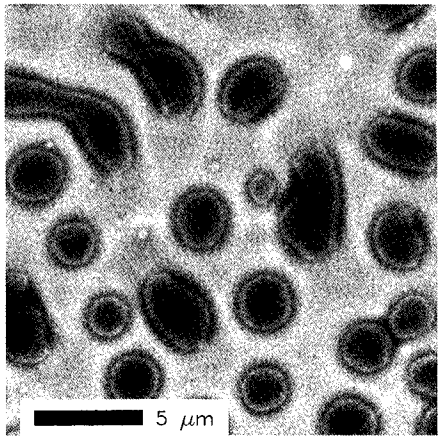


Figure 1. X-ray micrograph of PS/PMMA blend showing segregation of the PS within the PMMA.

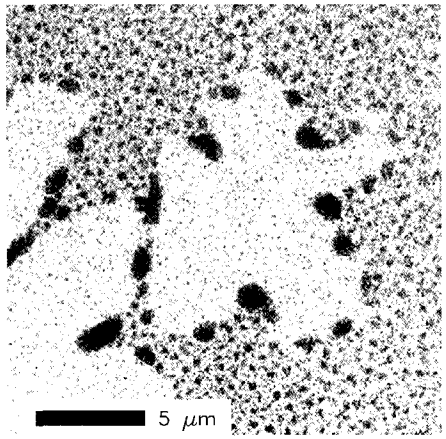


Figure 2. X-ray micrograph of PS/PBrS blend showing PBrS dispersions within the PS matrix. The lightest area is an open area.

NEXAFS Spectroscopy of Polymeric Isomers of Poly(ethylene terephthalate) (PET)	X1A

A. P. Smith, H. Ade (NCSU), S. G. Urquhart, A. P. Hitchcock (McMaster U.) and E. G. Rightor (Dow Chemical).

Due to the dependence of Near Edge X-ray Absorption Fine Structure (NEXAFS) spectroscopy on the local chemical environment of the excited atom[1], differences in these absorption spectra might also be expected for different isomers of the same material. In order to investigate this phenomenon, we have acquired carbon K-edge absorption spectra of poly(diallyl phthalate) (1,2 PDP), poly(diallyl isophthalate) (1,3 PDP), and poly(ethylene terephthalate) (1,4 PET), where the phthalate segment of these polymers are isomers with different patterns of substitution (ortho, meta, para) of the methyl carboxylate groups on the phenyl ring. Fig. 1 displays the chemical structure of these materials and Fig. 2 shows the x-ray absorption spectra of a) 1,4 PET, b) 1,3 PDP and c) 1,2 PDP and demonstrates that while the spectra are similar in overall shape, there are differences. The most obvious difference between the spectra is the split in the π^* peak at 285 eV present in the 1,4 PET and absent in the other oligimers. This peak intensity splitting has been shown to be due to the conjugation between the carbonyl groupsand the aromatic group[2] which is absent in the oligimers due to differences in electronic structure (1,3 PDP) and non-planar geometry (1,2 PDP)[3]. In addition, the absolute energy of the peaks at 285 and 288 eV shift upwards by .3 eV between the 1,4 PET and the 1,2 PDP spectra. These spectra demonstrate that NEXAFS spectroscopy can be quite sensitive to isomer substitution in conjugated moieties.

[1] J. Stöhr. *NEXAFS Spectroscopy*, Springer-Verlag (Berlin), 1992.
[2] E. G. Rightor *et al. J. Phys. Chem.* (in press)
[3] S. G. Urquhart *et. al. J. Phys. Chem.* (submitted)

Work supported by NSF Young Investigator Award (DMR-9458060) and Dow Chemical.

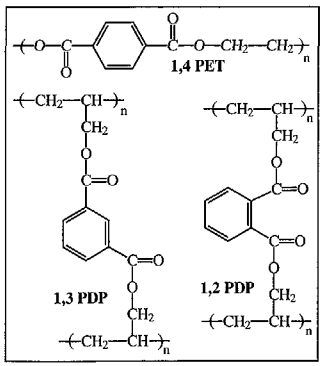


Figure 1. Chemical formulas of 1,4 PET, 1,3 PDP, and 1,2 PDP.

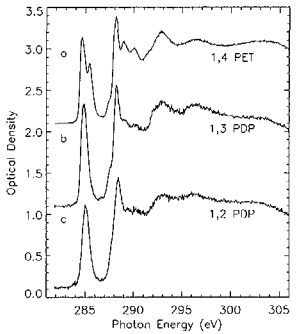


Figure 2. NEXAFS spectra of 1,4 PET, 1,3 PDP, and 1,2 PDP demonstrating changes due to chemical isomerism.

Characterization of the X1-STXM Spectroscopy Acquisition Mode Utilizing Carbon Dioxide	X1A

A. P. Smith, T. Coffey, and H. Ade (NCSU)

We have developed a procedure for the performance characterization of the X1-STXM utilizing carbon K-edge Near Edge X-ray Absorption Fine Structure (NEXAFS) spectra of carbon dioxide (CO_2). This procedure is necessitated by the need to acquire NEXAFS spectra of complex polymeric molecules with many excitations for which an accurate understanding of STXM performance, particularly between different data runs, is absolutely vital. CO_2 was chosen due to its non-toxicity at low concentrations and the existance of a high energy resolution NEXAFS spectrum in the literature[1]. The relatively simple spectrum of CO_2 allows for easy identification of microscope problems as shown in Fig. 1. Two different CO_2 spectra acquired during periods of microscope problems are shown. Fig. 1a exhibits "absorption" saturation of the πast peak (290.74 eV) as well as an anomolous dip at 285 eV which is consistent with saturation of the photon counter. Fig. 1b also exhibits absorption saturation of the πast peak but has an anomalous peak at 285 eV during another kind of STXM problem.

Several of the CO_2 NEXAFS spectral features are utilized to determine the absolute energy scale and to check for monochromator non-linearity. The sharp Rydberg excitations are used for energy resolution determination by fitting gaussians to the acquired spectra. In addition, the saturation of the π^* peak allows for a quantitative estimate of the higher order spectral contamination by acquiring CO_2 spectra with and without a pinhole to block the contamination. One particular adventageous feature of our procedure is that CO_2 can be added to the He purge while the sample is in place to calibrate spectra of any sample directly *in-situ* (see Fig. 2).

[1] Y. Ma *et. al. Phys. Rev. A*, 44: 1848 (1991)

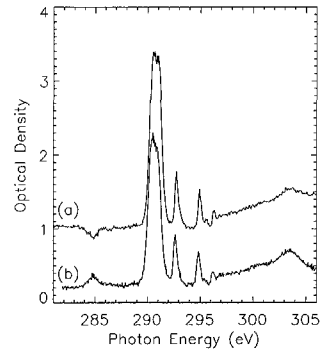


Figure 1. NEXAFS spectra of CO_2 exhibiting a) absorption saturation of the $\pi*$ peak at a very low OD and a dip near 285 eV; b) anomalous peak at 285.0 eV and saturation. Note offset of (a) by 1.

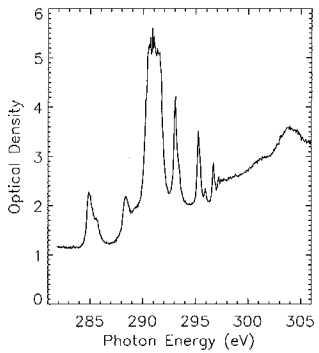


Figure 2. *In-situ* NEXAFS absorption spectrum of PET and CO_2. The apparent offset is due to the high concentration of CO_2. Note saturation of $\pi*$ at much larger OD than in Fig. 1.

NEXAFS Microspectroscopy of Macrophase-Separated Random Block Copolymer/Homopolymer Blends	X1A

A. P. Smith, J. H. Laurer, H. Ade, R. Spontak (NCSU), A. Ashraf, and S. Smith (Procter and Gamble Co.)

We have utilized NEXAFS microspectroscopy to study the morphology and composition of a macrophase separated blend of poly[(styrene-*r*-isoprene)'-*b*- (styrene-*r*-isoprene)"] random block copolymer (RBC) and homopolystyrene (PS) with a mass ratio of 20/80 RBC/PS[1]. X-ray micrographs of the unstained sample appear identical to TEM micrographs of stained samples and show micron sized ellipsoidal dispersions of the RBC within the PS matrix[2]. However, the composition can not be assessed in this way. We have thus acquired micro-NEXAFS spectra of several dispersions in order to examine their composition.

Fig. 1 shows NEXAFS reference spectra of the pure PS (a) as well as the pure RBC (b). Due to the presence of PS in the RBC and the comparable fraction of carbon-carbon double bonds in polystyrene and polyisoprene, the overall spectral shape of the RBC is similar to the PS spectrum. However, differences in the spectra are observed, especially in the 287-289 eV energy range. Fig. 2 shows NEXAFS spectra acquired from within two different RBC dispersions. The spectrum in Fig. 2a closely resembles the pure RBC spectrum, indicating that this dispersion is very similar in composition to the pure RBC with little or no PS present. However the spectrum in Fig. 2b more closely resembles the PS spectrum indicating the presence of PS within the RBC dispersion. These spectra demonstrate that the RBC dispersions possess a non-uniform composition and may contain pure PS. This information is unavailable at the required spatial resolution using any other characterization method.

[1] A. P. Smith *et al. Macromolecules* (submitted).
[2] J. H. Laurer *et. al. Langmuir* (submitted).

Work supported by NSF Young Investigator Award (DMR-9458060).

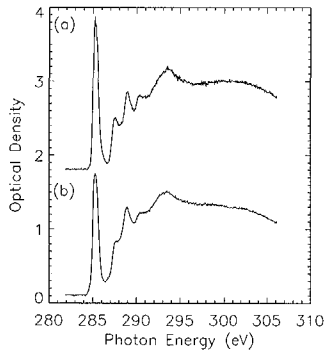


Figure 1. NEXAFS reference spectra of (a) pure homopolystyrene and (b) pure RBC.

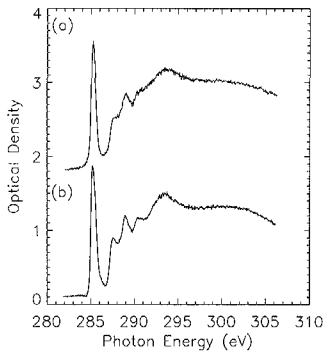


Figure 2. NEXAFS spectra of RBC dispersions showing that dispersion (b) contains PS, while (a) is "pure" RBC.

Considerations for A Soft X-ray Spectromicroscopy Beamline *	X1A

B. Winn, X. Hao, C. Jacobsen, J. Kirz, J. Miao, B. Sullivan, S. Wirick (SUNY Stony Brook), H. Ade (NCSU), C. Buckley (King's College), M. Howells (ALS), S. Hulbert (NSLS), I. McNulty (APS), T. Oversluizen (Creative Instrumentation)

The X1A soft x-ray undulator at the NSLS is the source for our experimental programs in spectromicroscopy. We require both spatial and temporal coherence. Due to the relatively large horizontal divergence of the electron beam in the low */beta* strait section of the x-ray storage ring, it has been possible to split the beam using a scraping mirror into two branches: X1A used by our program and X1B used for high resolution spectroscopy. We are now rebuilding the X1A beamline to provide improved resolving power and essentially linear trade-off between photon rate at the zone plate and resolving power for the soft x-ray spectromicroscopy experiments. This new beamline will exploit both additional floorspace due to the NSLS building expansion and increases in the brightness of the x-ray ring. Our beam will be further split into two separate beamlines, both of which will use toroidal mirrors to focus the source on the monochromator entrance slits horizontally and to focus on the monochromator exit slits vertically. This separation comes at no loss of coherent flux and permits low thermal loading on the optics, since we need little more than the coherent fraction of the beam at the Fresnel zone plate for microfocusing. Because of the small angular acceptance for spatially coherent illumination of the zone plates and the use of an approximately satisfied Rowland condition, our monochromators have sufficient resolving power with fixed exit arms. Experiments can then be placed near the exit slits, with spatial coherence established by the exit slit size. Resolving power will be controlled by adjusting the entrance slit alone with no change of spatial coherence. The zone plates will be overfilled to be less sensitive to beam vibration and drift.

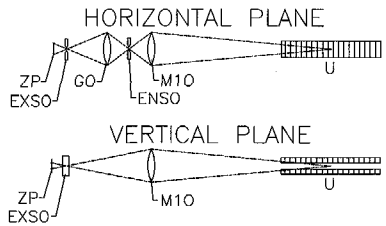


Figure 1. Focussing diagram in both the horizontal and vertical planes (not to scale) for both branches. Labels refer to undulator U, toroidal mirror M1O, entrance slit ENSO, grating GO, exit slit EXSO, and zone plate ZP

* X1A beamline supported in part by the DOE-BES, DOE-DMR and DOE-OHER, and by the APS. We thank our colleagues at Stony Brook, J. Dickerson, R. Hazel, A. Kalinovski, J. Maser, A. Osanna, I. Pogorelsky, S. Spector, S. Wang, and H. Zhang, at the LLBL, H. Chapman, and at the NSLS, E. Johnson and P. Takacs, for their input. We thank W. Mckinney for providing effic

X1-SPEM-II Application to Tribological Surfaces | X1A

H. Zhang, G. R. Zhuang, H. Ade (NCSU), C.-H. Ko, B. Winn, J. Kirz (SUNY Stony Brook), S. Cameron, D. Leta (Exxon), S. Hulbert, and E. Johnson (NSLS)

We presently investigate tribological surfaces in order to determine the distribution and the chemical state of various elements in a wear-scar. These applications are starting to produce the first scientific results after the upgrade of the scanning photoemission microscope (X1-SPEM-II) to a MCD hemispherical sector analyzer.

Three areas inside the wear-scar on the sample have been investigated. In one of the areas, a set of images (Fig.1) was acquired (75x75 pixels, 3x2.5 microns steps, 600 ms dwell time and 187eV pass energy) by centering the MCD at the peaks of S 2p, P 2p, Zn 3d, Mo 3d, Fe 3p, C 1s. A set of spectra (Fig.2) was acquired within the image area by moving the sample along the wear scar.

Due to the nature of the lubricant additives, it is expected that Mo and S, and Zn and P are highly correlated in these materials. The pattern of Mo looks similar to that of S 2p, but that of Zn also looks more like that of S rather than that of P. The pattern of C 1s is very similar to that of a secondary yield image not shown here and to that of Mo 3d. Overall, there is not a particularly strong correlation between any two elements in these images or in the spectra, contrary to what was expected. We also observe that Mo and Fe exhibit significantly different spectral lineshapes in spectra from this tribological surface. these differences reflect different oxidation states and chemical compounds.

Elemental maps of the wear-scars were produced and different although yet unidentified chemical states for Fe and Mo have been observed with point XPS spectra. While it is too early to draw definitive conclusions about the precise species and composition, we have observed chemical differences from areas that are well within the spatial resolution of the X1-SPEM-II. Higher resolution spectra of the specific elements of interest should be able to yield conclusive answers as to what the precise chemical nature of the local reaction layer is.

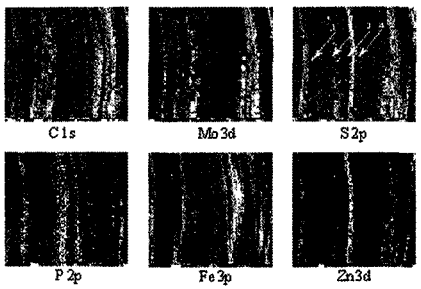


Figure 1. Elemental maps of area 1 after subtracting the background in the outer channels of the 16 channel MCD that do not correspond to the elemental peak. (All images: 75x75 pixels, 3x2.5 micron steps, 600 ms dwell time).

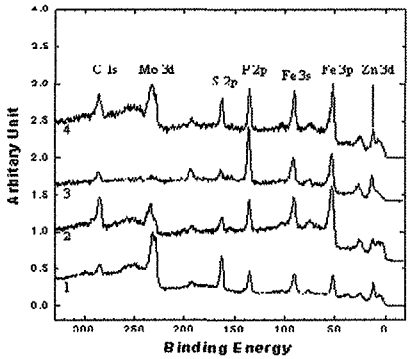


Figure 2. Spectra from nominal locations as indicated in Fig. 1. Both, Mo and Fe, exhibit different line shapes in these spectra reflecting different chemical species.

Characterization of Polymer Interfaces Using X-ray Microscopy | X1A

C. G. Zimba (MIT), A. P. Smith and H. Ade (NCSU)

One of the issues of interest in the study of polymer laminates is the interpenetration of adjacent layers. To characterize this phenomenon, analytical techniques which can discern the different chemical components of the laminate must be used. While transmission electron microscopy (TEM) is typically used to characterize this class of samples, the images often do not have sufficient chemical contrast to completely resolve the issue at hand. An additional technique which has superior chemical sensitivity, albeit at lower spatial resolution, is scanning transmission x-ray microscopy (STXM). Shown in the two figures at the left below are the images of a polymer laminate with four layers obtained using energies of 286.7 and 281.8 eV. Each image is of a 10 x 10 micron sample area. The area in the upper right third of the image is that of air while the lower left half is that of the mylar base. Coated on the mylar base are three thin layers of polyurethane, poly(styrene acrylonitrile) [SAN], and carbon black [CB] in poly(vinyl alcohol) with approximate thicknesses of 0.3, 1.0, and 0.8 microns, respectively. Of interest in this study was the extent of migration of the SAN into the porous CB layer. TEM images indicated that the boundary between the two layers might be diffuse. By acquiring spectra at finely spaced intervals across the interface, we were able to demonstrate that the penetration of the SAN into the CB layer was less than 200 nm. As indicated in the plot below, the the absorption feature near 287 eV, which arises from the SAN, is clearly present in spectra of a sample area within the SAN layer (+600 nm) and absent in an area within the CB layer (-300 nm). The level of SAN absorption remains nearly constant as the interface is approached and then decreases quickly as the interface is crossed.

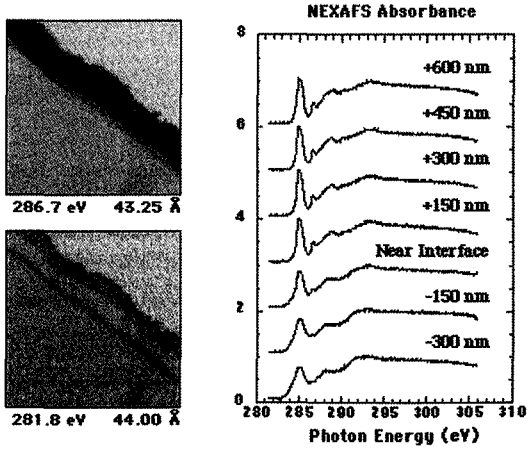


Figure 1.

STXM of Polymer Laminates: NEXAFS Microspectroscopy | X1A

C. G. Zimba (MIT), A. P. Smith and H. Ade (NCSU)

During the past year, we have characterized several polymer laminates using scanning transmission x-ray microscopy (STXM). In an imaging mode, the STXM can be used to acquire several images at different energies which exhibit different levels of "chemical contrast" due to the vaiation in NEXAFS absorption by the various chemical components. In a spectroscopic mode it is also possible to obtain high quality NEXAFS spectra which are characteristic of the majority components in each layer of the polymer laminate. Shown in the left figure below is the image of a polymer laminate with ten layers obtained using an energy of 288.3 eV. The scale bar at the lower right of image indicates the size of the image. At this imaging energy, each layer can be clearly discerned along the y-direction of the image. Along the x-direction, folds in the ultrathin cross-sectioned sample can also be observed, indicating the internal stresses inherent in this multilayer coating. The small white area in the right side of the image is a tear in the cross-sectioned film. As indicated in the right figure below, NEXAFS spectra of each layer can be readily obtained. The spectra are plotted starting with that of the top layer in the image and ending with the bottom layer in the image. While the top spectrum is clearly that of polycarbonate, it is clear from the spectra that the third, fifth, and seventh layers are quite chemically similar as are the fourth, sixth, and eighth layers also. This is consistent with the composition of the coating where the third, fifth, and seventh layers were a mixture of Carboset polymers and the fourth, sixth, and eighth layers were coatings of Elvacite loaded with different aromatic dyes. It is clear from these studies that the imaging and spectral capabilities of STXM can yield considerable information about multilayer polymer laminates. While not demonstrated in this abstract, we have also been able to discern variations in the concentration of major components in some model coatings.

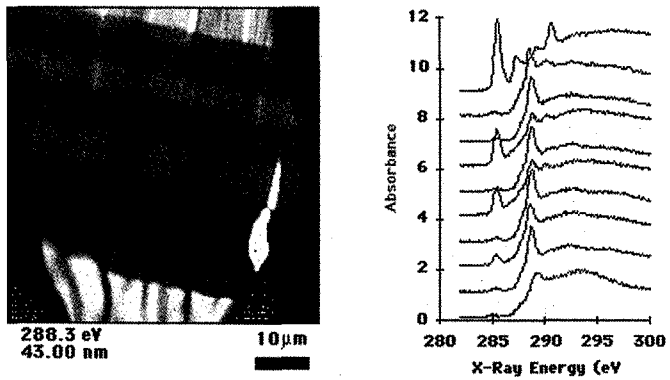


Figure 1.

The Vibrationally Resolved O 1s Photoelectron Spectrum of CO_2 | X1B

A. Kivimäki, B. Kempgens, H.M. Köppe, K. Maier, M.N. Piancastelli, M. Neeb, and A.M. Bradshaw (FHI)

Due to a recent change of grating on X1B it has been possible to measure the vibrational fine structure on an O 1s photoelectron line for the first time. For CO_2 we have shown that the antisymmetric C-O stretch (307 ±3 meVdominates totally the vibrational fine structure on the O 1s main line, in contrast to the totally symmetric vibrational mode observed on the C 1s line (161 ±7 meV. The antisymmetric mode is dipole-forbidden within the Born-Oppenheimer approximation, thus indicating that core orbital vibronic coupling plays a role. This was predicted almost 20 years ago by Domcke and Cederbaum [Chem. Phys. **25** , 189 (1977)]. Vibronic coupling in core ionization of equivalent atoms in a molecule also provides a mechanism for dynamic core hole localization.

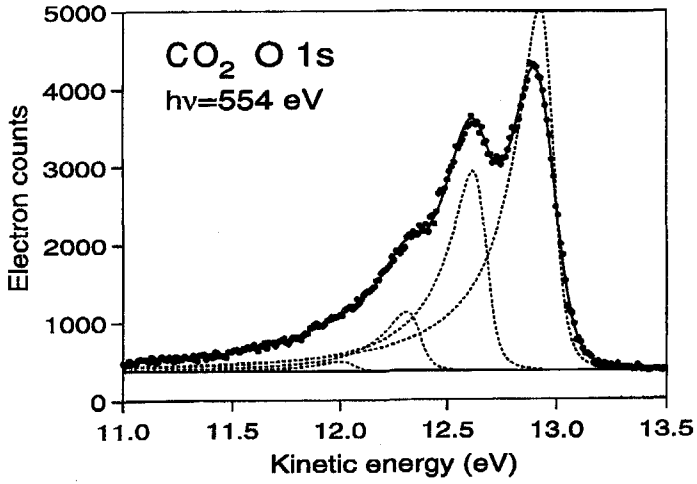


Figure 1. The vibrational fine structure on the O 1s line of CO_2. The points are the experimental data. The dashed lines show the individual vibrational components resulting from a lease square fit, including post-collision interaction.

Vibrational and Shake-up Excitations in C 1s Ionisation of Ethane | X1B

H. M. Köppe, K. Maier, B. Kempgens, A. Kivimäki, M. Neeb, and A. M. Bradshaw (Fritz-Haber-Institut der Max-Planck-Gesellschaft, Germany)

In continuation of our high-resolution studies of dynamic effects in core excitation we have investigated ethane as the prototype for the alkane series. The comparison with our recent work on methane is also interesting. Moreover, in combination with experiments performed on acetylene and ethylene the results lead to a new understanding of the role of shape resonances and multiply excited states and revive the discussion concerning the correlation between the energy of the shape resonance and bond length.

Maximum entropy deconvolution, the Poisson approximation for sudden limit conditions and coupled least-squares-fits were combined in the analysis to access the complex vibrational structure. The C 1s photoelectron spectrum is dominated by two totally symmetric vibrational modes, namely, the C-H stretch ν_1 and the C-C stretch ν_3. Upon ionisation the vibrational energies of ν_1 and ν_3 significantly increase to 407±5 meV and 176±5 meV, respectively. This is reflected in a reduction of the bond lengths by 0.036±0.002 Å(C-H) and 0.043±0.002 Å(C-C). The lifetime broadening is determined to be 98±10 meV, in good agreement with theory. A possible mixing with certain asymmetric modes of very similar vibrational energy such as ν_5 cannot at present be excluded. The errors given here are therefore restricted to the analysis itself. Fig. 1 shows the results of a least-squares-fit with the dashed lines representing the individual vibrational states; after summation and convolution with the instrument profiles they give the full line through the data points.

The shake-up structure of C_2H_6 resembles closely that of CH_4. The lowest lying satellite band (labelled '1') gains much intensity towards threshold which is thought to be due to conjugate shake-up processes.

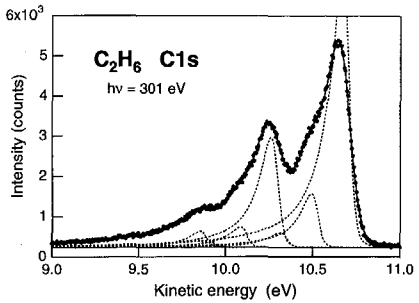


Figure 1. The C 1s photoelectron spectrum of C_2H_6 at $h\nu = 301$ eV.

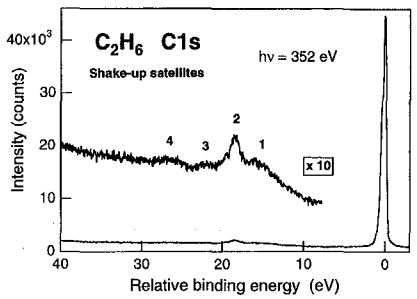


Figure 2. The C 1s shake-up satellites. Peak 1 is conjugate enhanced.

Improvement in Monochromator Performance on X1B | X1B

M. Neeb, A. Kivimäki, K. Maier, H.M. Köppe, B. Kempgens, and A.M. Bradshaw (FHI), F. Loeb and P.D. Johnson (BNL - Physics)

The mechanically ruled, blazed grating (fused silica blank, 800 l/mm, Au coating; Hyperfine Inc., Boulder, USA) on the spherical grating monochromator at X1B was replaced in May 1996 by a holographically recorded, laminar grating (silicon blank, 800 l/mm, Au coating; Zeiss, Oberkochen, Germany). The Figure shows the photocurrent I_0 as measured on a gold-coated copper plate behind the exit slit immediately before (dotted line, gap = 39.5 mm) and after (full (gap = 39.5 mm) and dashed-dotted (gap = 56.5 mm) line, respectively) the change of grating. The normalized intensity [nA/mA$_{ring}$*s] is displayed on the ordinate while the grating has been scanned from 280 to 980 eV photon energy. The transmission of the monochromator is now distinctly higher at energies above 450 eV. Note that the entrance slit during the tests with the new grating was approximately a factor of six narrower than for the previous measurements. For the same slit width the photon flux at the C 1s edge (300 eV) is approximately the same as before; at photon energies higher than 550 eV (O 1s) the flux is a factor of 5-10 greater. The maximum in the photon intensity distribution has been shifted by the new grating from 400 to above 600 eV. High resolution photoabsorption and photoelectron measurements up to 800 eV will now be possible with the first order of the grating, allowing a more effective use of the full energy range of the first harmonic of the X1-undulator (200-800 eV). In particular, the energy range above 500 eV will be interesting for many experiments since most of other high resolution spectroscopy beam lines at other facilities are presently used only below 500 eV.

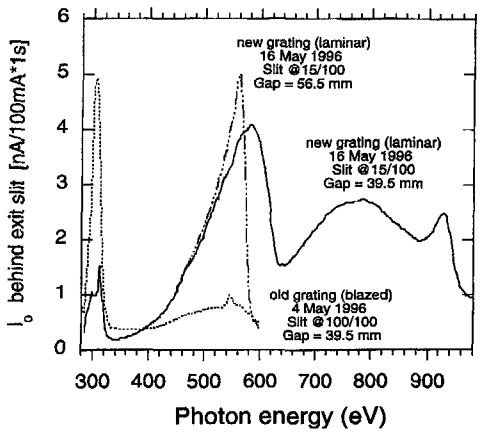


Figure 1. Photon flux vs. photon energy measured at X1B behind the exit slit.

Surface Studies of Model Supported Catalysts: Rh/CeO_2 (100) * — X1B

S.H. Overbury, D.R. Huntley, D.R. Mullins, K.S. Ailey and P.V. Radulovic (ORNL)

It is now well established that interactions between noble metal and reducible oxide supports can synergistically alter the activity for oxidation and reduction reactions, important for emission control catalysis. We have looked for such interaction in Rh supported on ceria. CeO_2 films were grown epitaxially by laser ablation onto $SrTiO_3(100)$ substrates. X-ray diffraction and TEM indicate the films are single crystalline with (100) orientation. The surfaces of these films, before and after deposition of Rh, and following exposure of NO were studied by soft x-ray photoemission and x-ray absorption spectroscopy. Photoemission from the Ce 4d levels exhibited complex features which differed between a partially reduced surface, induced by sputtering and a fully oxidized surface. The complex structure of the Ce 4d spectrum has been attributed to different final state occupancies in the Ce 4f level. Differences between the sputtered and the oxidized surfaces were also seen in the O 1s absorption spectra.

N 1s photoemission and photoabsorption clearly distinguished between adsorbed atomic N and molecular NO. NO does not adsorb on the Rh free, fully oxidized surface, although small amounts adsorb upon a sputter reduced surface. The photoemission and photoabsorption sugest that NO adsorption on the sputtered surface leads to nitride formation. The amount of NO adsorbed on the Rh loaded surfaces correlated with Rh 3d intensity. The thermally induced conversion from molecular to atomic N was measured as a function of Rh coverage to determine substrate affects on Rh surface chemistry. Rh deposited on a sputtered surface was much more active for NO decomposition. Following NO exposure at room temperature, most of the NO decomposes to atomic N and O on Rh / Sputtered CeO_2, whereas considerable molecular NO is observed on Rh / Oxidized CeO_2.

* Research sponsored by the Division of Chemical Sciences, Office of Basic Energy Sciences, U.S. DOE at Oak Ridge National Laboratory, managed by Lockheed Martin Energy Research Corp. under Contract No. DE-AC05-96OR22464.

Analysis of the Bias Due to Finite Size of the Peak Mask in Imaging Plate Integration Methods — X3A1

R. Bolotovsky and P. Coppens (SUNY Buffalo)

The "seed-skewness" method for integration of peaks on imaging plates provides an optimal integration mask for every peak, without any *a priori* information about the peak shape or profile, or about the background level in the integration box. The method is based on the fact that the skewness of the pixel intensity distribution in the integration box increases relative to the insignificant skewness of the noise distribution when a diffraction peak is superimposed on the noise in the integration box. The seed-skewness method identifies a contiguous area of pixels in the integration box responsible for the skewness increase, and defines this area as the peak mask.

In further work we have derived theoretical estimates of the bias in the integrated intensities due to finite size of the peak mask, and compared the results with experimental values based on synchrotron intensity measurements over a single oscillation range with different experimental parameters such as exposure time, and scanner sensitivity. A positive bias is found in the very weak reflections, not only with the seed-skewness method, but also with standard-box integration results. Appropriate corrections are being devised to allow the data are to be used to their fullest extent in high-accuracy applications.

Electron Density Analysis at Synchrotron Sources | X3A1

P. Coppens, R. Bolotovsky and A. Darovsky (SUNY Buffalo)

In the past two years we have been able to collect full synchrotron-data sets with an accuracy adequate for charge-density analysis. A data set at $\lambda = 0.656$ Å was collected on sodium nitroprusside, while full data sets at both 0.654 Å and 0.394 Å were collected on chromiumhexamine hexacyanochromium. The 0.394 Å data set on the chromiumhexamine gives unprecedented resolution. It is collected at 50K on a crystal of 80 x 30 x 30 μ, and contains 7026 observed reflections, of which 4250 are in the range of $1.25 < \sin\theta / \lambda < 2.00$ Å^{-1}. Refinement of subsets of the data with different $\sin\theta / \lambda$ ranges pass the test of internal consistency, indicating that systematic errors have been minimized in the integration procedure. Further, more detailed, checks are being undertaken.

range of sinθ/λ, Å^{-1}	R	χ^2	# of refl.	scale factor	β_{11} of Cr(1) Å$^2 \times 10^{-6}$	β_{11} of Cr(2) Å$^2 \times 10^{-6}$
0.2–1.97	3.5	1.6	7026	9.142(9)	1297(5)	1202(5)
1.0–1.97	3.7	1.4	5279	9.20(2)	1310(7)	1227(7)
1.25–1.97	3.9	1.3	4250	9.08(3)	1280(12)	1207(11)

Figure 1. Spherical atom refinements of the 0.394 Å data on chromiumhexamine hexacyanochromium, indicating absence of θ-dependent bias in the data set.

Resonance Scattering Studies of Mixed-Valence Complexes | X3A2, X3A1

A. Darovsky, V. Kezerashvili, P. Coppens (SUNY Buffalo), T. Weyhermuller, H. Hummel and K. Wieghardt (Max-Planck-Institut fur Strahlenchemie)

Oxygen-bridged mixed-valence manganese complexes are model compounds for the manganese-containing photosystem II, which catalyzes the water oxidation reaction and thereby produces dioxygen used by animals and aerobic bacteria during respiration.

Following our earlier study of μ-dioxo-(Mn(2,2'-bipyridyl)$_2$)$_2$ $(BF_4)_3.3H_2O$,[1] a second study was performed on the triclinic crystals of the complex Mn(IV)L(μ-O)$_2$(μ-MeCO$_2$) Mn(III)(MeCO$_2$)$_2$, L = 1.4.7-trimethyl-1,4,7-triazacyclononane.

Imaging plate data were collected at 15 different energies straddling the absorption edge. Results are shown in Figure 3. The shift of Mn(IV) relative to Mn(III) is again evident, though its magnitude appears less than observed for the dipyridyl-coordinated Mn-mixed-valence complex. This is unexpected, as the asymmetry of the Mn-O bonds (1.882 and 1.864 Å vs. 1.788 and 1.767 Å) is larger here than for the first compound discussed above. With the higher resolution achieved, the pre-edge feature of the absorption curve is evident in the f' curve of Mn(IV), but not in that of Mn(III). This clearly indicates that the spectroscopic transition to the unoccupied state occurs at Mn(IV) rather than at Mn(III). 1 Y. Gao, A. Frost-Jensen, M.R. Pressprich, P. Coppens, A. Marquez and M. Dupuis, *J. Am. Chem. Soc.* 114, 9214, 9214 (1992). A. Frost-Jensen, Z. Su, N. K. Hansen and F. K. Larsen, *Inorg. Chem.* 34, 4244 (1995).

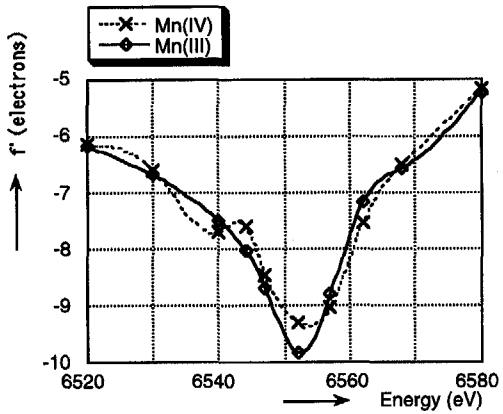


Figure 1. f' of the two manganese atoms in Mn (IV)(μ-O)$_2$(μ-MeCO$_2$)Mn (III)($MeCO_2$)$_2$L, where L = 1.4.7 trimethyl-1,4,7-triazacyclononane, as determined from refinement of data at different wavelengths.

Temperature-dependence of the Electron Transfer in a $Mn_{II}Mn_{III}(\mu$-OH) Mixed-valence Complex	X3A1

A. Darovsky, V. Kezerashvili, P. Coppens (SUNY Buffalo), T. Weyhermuller, H. Hummel and K. Wieghardt (Max-Planck-Institut, Germany)

At room-temperature the Mn(II)Mn(III) mixed valence complex [ttacnMn(II) (μ-O)(μ-pivalonato)$_2$Mn(III)ttacn](ClO$_4$)$_2$ (ttacn = 1.4.7 trimethyl-1,4,7-triazacyclononane), shows only small differences in the bridging Mn-O bond lengths, while a resonance scattering experiment gives little difference between the two Mn-atom scattering factor curves. However, a 20K structure determination shows a much larger asymmetry in the molecular geometry. Thus, at ambient temperature the valence electrons are partially 'detrapped' due to the smallness of the energy difference between the Mn(II)-Mn(III) and Mn(III)-Mn(II) configurations, while at low temperature the metal centers are distinct. From analysis of bond lengths observed at 20K, 62K and 293K, an estimate of the energy difference between the II-III and III-II configurations of 100cm^{-1}, or $\approx$1200 Jmol^{-1} is obtained. This is to our knowledge the first observation of a temperature-dependent equilibrium in mixed valence complexes.

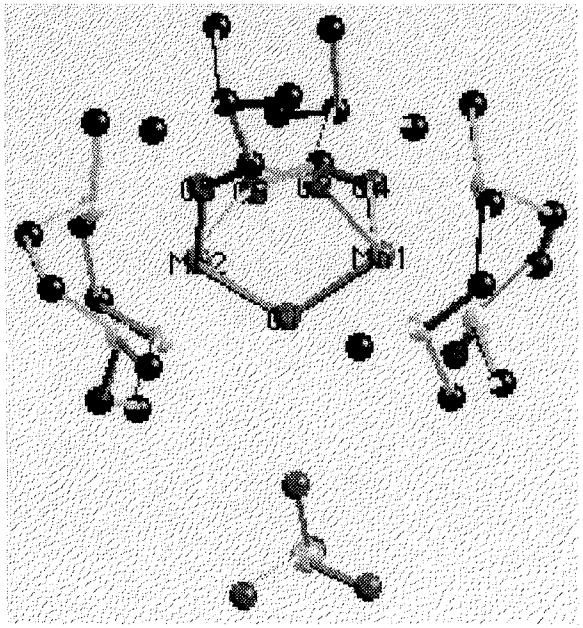


Figure 1.

Studies of CdS/CdTe Heterostructures Using X-ray Scattering and XAFS Techniques *	X3A1

S. W. Huang, Y. L. Soo, Y. H. Kao (SUNY Buffalo) and A. Compaan (U. of Toledo)

Heterostructures of CdS/CdTe form an important class of materials for the development of useful thin film photovoltaic (PV) devices. It is believed that the efficiency of many PV layer materials can be seriously affected by the interfacial microstructures. Thus far there has been no previous study of the interfacial structures in these heterojunctions. The x-ray scattering and XAFS techniques offer a convenient tool for nondestructive characterization of the interfacial roughness, correlation lengths of structural fluctuations, degree of intermixing of elements, and local structures around the constituent atomic species. Heterosturctures of various configurations have been prepared by sputtering under different annealing conditions.

* Research supported by DOE under Grant DE-FG02-87ER45283, and by NREL.

Investigations of Microstructures in ZnSe-based II-VI Semiconductor Thin Films Grown by MBE and MOCVD *	X3A1

S. W. Huang, Y. L. Soo, Y. H. Kao, H. Luo, and T. J. Mountziaris (SUNY Buffalo)

Various techniques of grazing incidence x-ray scattering, XAFS, and diffraction have been employed for nondestructive characterization of microstructures on buried interfaces in semiconductor heterojunctions and superlattices of ZnSe, ZnSSe, ZnFeSe, and ZnSeTe grown on GaAs substrates by MBE and MOCVD. The semiconductor films were prepared under different processing conditions and various compositions. The results are useful for a comparison of the two major epitaxial growth methods for this important class of semiconductors. This is particularly significant for fundamental studies as well as development of new blue lasers, detectors, modulators, light emitting diodes, and photovoltaic devices. Interfacial roughness, layer thickness, correlation lengths, and lattice strain in the films were obtained. This information allows a quantitative correlation of the overall film quality with various microstructural parameters.

* Research supported by DOE under Grant No. DE-FG02-87ER45283.

Grazing Angle Scattering and XAFS Studies of (Si,Ge)/Si Heterostructures *	X3A1

S. W. Huang, Y. L. Soo, Y. H. Kao (SUNY Buffalo) and K. L. Wang (UCLA)

The (Si,Ge)/Si heterostructures form a convenient system for physical studies of band structure engineering. The possibility of varying the Ge content affords a suitable degree of freedom to control the lattice mismatch and strain in layered semiconductor structures. We have been studying various Si1-xGex thin films grown on Si by molecular beam epitaxy under different growth conditions. This material also offers an ideal system for the study of fundamental physics concerning epitaxial growth of lattice-mismatched semiconductor layers as well as the interfacial morphology. Interfacial roughness parameters and lattice strain of Si1-xGex films with varying thickness epitaxially grown on Si(100) are determined using the techniques of grazing-incidence x-ray scattering (GIXS) and diffraction. We have discovered that the roughness of both the buried interface and sample surface follows a power-law scaling behavior as a function of film thickness for films below the critical thickness, and it undergoes a large change above the critical thickness. More recently, we have also performed XAFS measurements of the same set of films. These results show new interesting correlations between the interfacial roughness, lattice strain, and the local structures. Work is in progress to compare the interface morphology determined from our x-ray observations and the physical parameters obtained by other methods.

* Research supported by DOE under Grant No. DE-FG02-87ER45283.

The Electron Density of $Th(S_2P(CH_3)_2)_4$	X3A1

B. B. Iversen, F. K. Larsen (U. of Aarhus), P. A. Reynolds, (Australian National U.), A. Pinkerton (U. of Toledo), and A. Darovsky (SUNY Buffalo)

While it is possible to get structural information on actinide compounds from x-ray diffraction [1], the prospect of obtaining detailed electron density in- formation seems limited. This is primarily due to the dominance of the actinide core scattering relative to scattering from the bonding electrons. However in the present compound Th is at the origin of the unit cell in spacegroup P42212. Thus the Th core contributes only to the h+k+l=even reflections. The h+k+l=odd reflections can therefore be used to model the asphericity of the electron den- sities due to chemical bonding. To limit systematic errors it is imperative to use short wavelength radiation. We have collected a very large number of accurate Bragg diffraction data at 28 K using imaging plates and a DISPLEX cooler fitted with an antiscattering device. The internal consistency of the data is excellent, R(int)=0.033 for 36192 reflections averaged to 11206 unique ((sint/l)max = 1.76Å). Structural refinements show that it is possible to refine hydrogen positions and thermal parameters even in the presence of Th. Initial modelling of the electron densi- ties using the valence orbital formalism reveals that the Th atom is less ionic than expected. Comparisons with high quality theoretical calculations are in progress. The data also allow an experimental determination of the anomalous scattering contribution (f' and f") for Th. [1] A. Pinkerton, A. E. Storey, J. M. Zellweger, J. C. S. Dalton, 1475-1480 (1981)

The Structure of Type 1 GeS_2	X-3A1

J. B. Parise, K. Tan, C. Cahill and Y. Ko (SUNY Stony Brook)

Open frameworks consisting of corner linked polyhedral elements are capable of occluding organic molecules and so are of interest for their potential as selective agents for molecular sieving, catalysis, ion exchange and ion conduction. The most common of these frameworks are the aluminosilicates. However, the range of materials capable of forming open frameworks has increased greatly over the past decade since synthetic routes to knit isolated tetrahedral Sn- and Ge-sulfide clusters into frameworks have been found. This was accomplished using two procedures: self-condensation of the clusters in the presence of organic amines and condensation from solution using transition metal ions along with the organic amines. There is evidence that both the organic amines and the transition metal act as structure directing agents. However, no three dimensional network based only on the connection of GeS_2 tetrahedral units has been described. Type 1 is now shown to be such a framework based on x-ray structure determination from 30 micron single crytsals.s

By taking a slurry of amorphous GeS_2, $MnCl_2$, quinucilidine, and water, heating to 423 K for 3 days, single crytsals suitable for data collection using the imaging plate system at X-3 were obtained. The structure determined using this data consists of corner linked adamantine units, $[GeS_4S_{10}]$, corner-linkd to form an open framework akin to zinc blende (ZnS) or diamond (Figure 1).

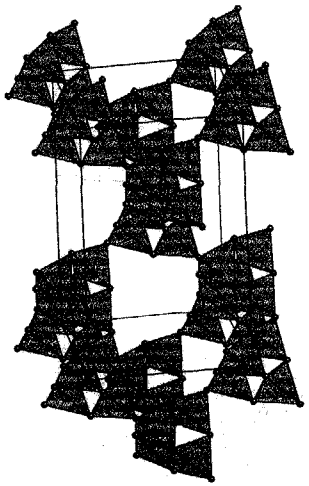


Figure 1. Structure of QUI-MnGeS-1 showing the connection of Ge_4S_{10} adamantine units. Molecules found in the channels of the structure are omitted for clarity.

Synthesis and Structural Characterization Using Synchrotron Radiation of$(C_6H_{13}N_2)_2(H_3O)(H_2O)][AgGe_4S_{10}]$	X3A1

J. B. Parise, K. Tan (SUNY Stony Brook), and A. Darovsky (SUNY Buffalo)

The open framework germanium sulfide system provides an opportunity to synthesize some compounds with certain designed structural features. A novel compound,$[(C_6H_{13}N_2)_2(H_3O)(H_2O)]$ $[AgGe_4S_{10}]$ was obtained using hydrothermal technique. In this structure, the silver was coordinated to three $Ge_4S_{10}{}^{4-}$ clusters in a trigonal plane fashion, realizing an expected structural type in this system. The single crystals of the compound were small and synchrotron radiation/imaging plate system made it possible to collect a set of high quality X-ray diffraction data for structural determination and refinement. A sample crystal, 30×30×40 μm in size was used for data collection at X3A1 beamline of NSLS in BNL with a 20×25 mm high resolution imaging plate as a detector . The wavelength was 0.394 Åand the maximum measured diffraction vector was 0.797. In total 13477 reflections including were collected in 36 imaging plates exposed in about 5 hours. These were merged to produce a data set containing 4104 unique structure factors. The structure was solved using direct methods. The primary building units of the compound consist of tetrahedral $[GeS_4]^{4-}$ and trigonal planar $[AgS_3]^{5-}$ clusters. The $[GeS_4]^{4-}$ units form $[Ge_4S_{10}]^{4-}$ adamantine-like clusters as secondary building units. The structure contains double chains, consisting of $[Ge_4S_{10}]^{4-}$ clusters connected by three coordinated silver (Figure below). These chains are infinite in [100] and occlude two partially protonated Dabco $[C_6H_{13}N_2{}^+]$ molecules, one hydroxynium $[H_3O^+]$ and one water $[H_2O]$, giving a charge balanced chemical formula of $[(C_6H_{13}N_2)_2(H_3O)(H_2O)][AgGe_4S_{10}]$.

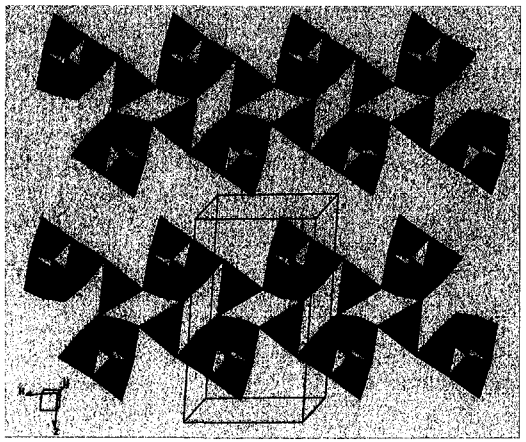


Figure 1.

The 154 K Phase Transition of Tetramethylammonium Tetrafluoroborate	X3A1

Thomas Schultz (Risoe National Laboratory) and Finn Krebs Larsen (Aarhus U.)

Tetramethylammonium Tetrafluoroborate (TMT) is an organic salt used as a supporting electrolyte in the field of electrochemistry. TMT has 2 phase transitions at 154 K and at 601 K, the nature of which is not yet entirely understood. At 298 K, TMT has a tetragonal unit cell (see Fig. 1) containing 16-fold disordered BF_4^- ions and ordered $(CH_3)_4N^+$ ions. Lowering the temperature to 160 K diminishes the disordering of the BF_4^- ions to 8-fold, freezing out a lowest energy configuration of these ions. At around 160K diffuse diffraction peaks appear at half order h- and k-values, the intensity of these grow rapidly upon further cooling. At around 155 K the half order diffraction peaks, start to split into 2 or 4 components. This splitting is explained by a model containing 4 orthorhombic twins, with unit cells twice as big as the tetragonal room temperature unit cell. In the period 22 August - 31 August, 1996, we performed single crystal measurements at the 4-circle instrument at beamline X3A1. Using Imaging Plates, we collected TMT data sets at 298 K, 240 K, 155 K, 145 K and 15 K. In addition careful measurements of the diffuse half order Bragg peaks and of the unit cell volume as a function of temperature (see Fig. 2) were carried out which will enable us to calculate the order parameter of the 154 K phase transition.

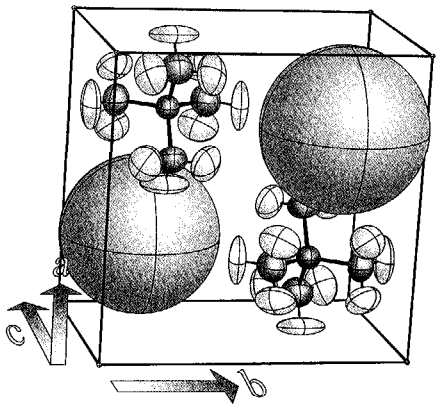


Figure 1. The tetragonal unit cell of TMT at 298K, showing the ordered tetramethylammoniumions and the disordered tetrafluoroborate ions (indicated using large blue balls).

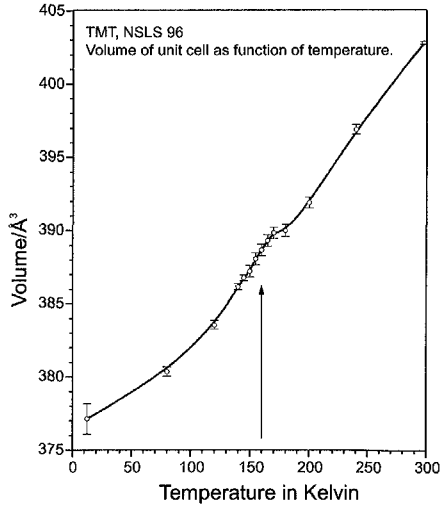


Figure 2. The variation of the TMT unit cell volume as a function of temperature, clearly showing the continous phase transition at around 154 K.

X-ray Induced Photoluminescence in Doped Nanocrystals * | X3A1

Y. L. Soo, S. W. Huang, Y. H. Kao (SUNY Buffalo) and R. N. Bhargava (Nanocrystals Technology)

Semiconductor nanocrystals chemically doped with transition metal or rare earth elements can exhibit novel optical properties which are not found in the bulk material. Both the quantum efficiency of photoluminescence (PL) and transition probablity are enhanced due to the effects of strong localization of electrons in the small particles. We are continuing a collaborative research program with Dr. R.N. Bhargava who first discovered this effect. This new class of material is of great interest for studying fundamental physics in systems of reduced dimensions. We have recently discovered that the PL output is sensitive to the energy of x-rays applied to excite the nanocrystals. The PL output exhibits EXAFS spectra which can be compared in detail with those measured by the conventional method of x-ray fluorescence. Thus, we have demonstrated a new site-selective technique for the detection of EXAFS. In view of its enhanced quantum efficiency and fast response, these nanocrystals are strong candidates for a new type of high-efficiency x-ray detector for a variety of technical applications.

* Research supported by DOE under Grant No. DE-FG02-87ER45283.

XAFS Studies of Tb-Doping in Y_2O_3 * | X3A1

Y. L. Soo, S. W. Huang, Y. H. Kao (SUNY Buffalo) and R. N. Bhargava (Nanocrystals Technology)

X-ray absorption fine structure (XAFS) measurements have been made in Tb-doped nanocrystals of Y_2O_3 with different size distributions. The interatomic distances between the impurity and neighboring atoms, coordination number, local disorder, and effective valency determined for the nanocrystals are compared with those in bulk Y_2O_3:Tb. Significant local structural changes have been observed. These local structures are closely related to the observed novel optical properties. Interesting features were found by a comparison of the photoluminescence spectra induced by x-rays with those excited by ultraviolet radiation.

* *Research supported by DOE under Grant DE-FG02-87ER45283.

Resonance Scattering Studies of Mixed-Valence Complexes

X3A2, X3A1

A. Darovsky, V. Kezerashvili, P. Coppens (SUNY Buffalo), T. Weyhermuller, H. Hummel and K. Wieghardt (Max-Planck-Institut fur Strahlenchemie)

Oxygen-bridged mixed-valence manganese complexes are model compounds for the manganese-containing photosystem II, which catalyzes the water oxidation reaction and thereby produces dioxygen used by animals and aerobic bacteria during respiration.

Following our earlier study of μ-dioxo-(Mn(2,2'-bipyridyl)$_2$)$_2$ (BF_4)$_3$.3H_2O,[1] a second study was performed on the triclinic crystals of the complex Mn(IV)L(μ-O)$_2$(μ-$MeCO_2$) Mn(III)($MeCO_2$)$_2$, L = 1.4.7-trimethyl-1,4,7-triazacyclononane.

Imaging plate data were collected at 15 different energies straddling the absorption edge. Results are shown in Figure 3. The shift of Mn(IV) relative to Mn(III) is again evident, though its magnitude appears less than observed for the dipyridyl-coordinated Mn-mixed-valence complex. This is unexpected, as the asymmetry of the Mn-O bonds (1.882 and 1.864 Å vs. 1.788 and 1.767 Å) is larger here than for the first compound discussed above. With the higher resolution achieved, the pre-edge feature of the absorption curve is evident in the f' curve of Mn(IV), but not in that of Mn(III). This clearly indicates that the spectroscopic transition to the unoccupied state occurs at Mn(IV) rather than at Mn(III). 1 Y. Gao, A. Frost-Jensen, M.R. Pressprich, P. Coppens, A. Marquez and M. Dupuis, *J. Am. Chem. Soc.* 114, 9214, 9214 (1992). A. Frost-Jensen, Z. Su, N. K. Hansen and F. K. Larsen, *Inorg. Chem.* 34, 4244 (1995).

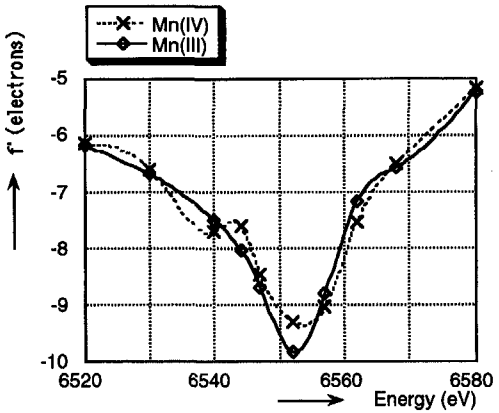


Figure 1. f' of the two manganese atoms in Mn (IV)(μ-O)$_2$(μ-$MeCO_2$)Mn (III)($MeCO_2$)$_2$L, where L = 1.4.7 trimethyl-1,4,7-triazacyclononane, as determined from refinement of data at different wavelengths.

Crystallographic Study of Thermal Barrier Coating by X-ray Microdiffraction

X3A2

Y. Gao, W. Hasz and C. A. Johnson (GE Corporate Research and Development)

Yttria stabilized zirconia (YSZ) is a commonly used thermal barrier coating (TBC) material for turbines. While the desirable phase for application is tetragonal ZrO2, both cubic and monoclinic phases have been found as a result of high temperature aging or chemical contamination. The yttria content and phase composition are critical to the mechanical and physical functioning of the coating.

We have developed a method at the beamline X3A2 to study polycrystalline YSZ coating by X-ray transmission microdiffraction using a wavelength below the Zr K-edge. The setup includes a high magnification CCD camera by which the X-ray beam position can be visualized from a TV monitor. The diffraction data was collected using a vacuum-mounted imaging plate system, and later converted into one-dimensional data for further analysis. Typical one-dimensional diffraction patterns (figure 1) show that this technique is capable of observing both cubic and monoclinic phases alone with the major tetragonal ZrO2 phase. It has been known that the yttria content in tetragonal phase can be derived from its c/a ratio [1,2]. Moreover, the phase composition varies with firing temperature and aging time [3]. Therefore, crystallographic data could be used to derive the yttria content, which is of importance to tetragonal phase stability, and temperature history of a sample.

[1] H. Toraya, J. Am. Ceram. Soc., 72(4), 1989, 662-664. [2] H. G. Scott, J. Materials Sci., 19, 1975, 1527-1535. [3] R. A. Miller, J. L. Smialek, R. G. Garlick, Adv. in Ceram. 3, 241-251

The SUNY X3 beamline at NSLS is supported by the Division of Basic Energy Sciences of the U.S. Department of Energy (DE-FG02-86ER45231).

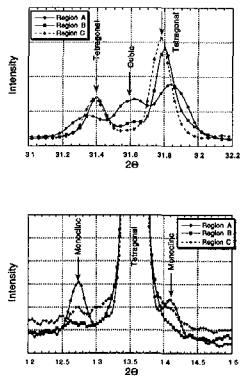


Figure 1. Phase composition variation. Top: cubic phase; Bottom: monoclinic phase.

On-Line SAXS Study of Nylon 66 Fiber Deformation *	X3A2

B. Hsiao, A. Kennedy, R. Leach (DuPont), B. Chu, and P. Harney (SUNY Stony Brook)

On-line SAXS characterization of crystal morphology development during continuous drawing of a nylon 66 fiber at different temperatures were carried out at the X3A2 beamline. For the extraction of morphological information, we have adopted two unique procedures to analyze the 2D SAXS image. These procedures include the use of correlation function analysis to determine the lamellar crystal and amorphous thicknesses (l_c and l_a), and invariant Q from the sliced meridional intensity(along the fiber direction), and Porod analysis to determine the crystal fibril width l_f from the integrated equatorial intensity profile (perpendicular to the fiber direction). Results of the analysis from two different temperatures (160°C and 218°C) are shown in Figures 1,2, and 3.

It is seen that both L and l_c increase with temperature. Since the cell parameter c, determined previously by WAXD, *decreases* with increasing temperature, the notion of thermal expansion is inconsistent with this finding. In contrast, the hypothesis of melting the small crystals does explain well the increases in L and l_c (larger residual crystals) as well as the decrease in Q (at low draw ratios) by temperature. By comparing results from the two temperatures (near and above the Brill transition temperature), we conclude that drawing also induces melting of small crystals. However, this strain effect is less than the temperature effect. This is the reason why all morphological changes observed below the Brill temperature (at 160°C) is far more enhanced than those at 218°C where few small crystals are present.

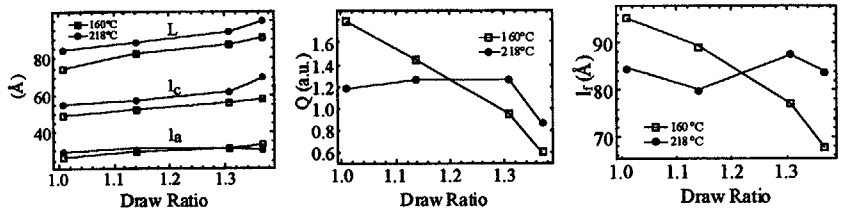


Figure 1. Morphological variables extracted from the SAX data.

* This work is partially supported by a NSF-GOALI Grant(DMR-9629825).

On-Line WAXD Study of Nylon 66 Fiber Deformation *	X3A2

B. Hsiao, A. Kennedy, R. Leach (DuPont), B. Chu, and P. Harney (SUNY Stony Brook)

On-line studies of crystal structure development during continuous drawing of a nylon 66 fiber at different temperatures were carried out using wide-angle X-ray diffraction (WAXD) techniques at the X3A2 beamline. A 3-pinhole collimator was used to reduce the beam dimension to 0.3 x 0.3 mm^2. WAXD images were recorded by image plates. The schematic diagram of our experimental setup is shown in Figure 1 below. The Brill transition was observed at about 160°C under all drawing conditions. However, form the analysis of the unit cell parameters, we confirm that the triclinic cell structure persists above the Brill transition temperature. With increasing temperature, the parameter a (dominated by hydrogen bonding) remains almost unchanged while b increases and c decreases (both show a step-change near the Brill transition. These results are shown in Figures 2 below. The constant value of a agrees with the argument that the hydrogen bonding is relatively immobile at high temperatures prior to melting. We thus suggest that the Brill transition is due to a premelting process of small crystals. As a result, the larger residual crystals undergo an enhanced anisotropic thermal expansion leading to the merging of two strong equatorial reflections. This hypothesis is consistent with the crystal density data which increases with temperature.

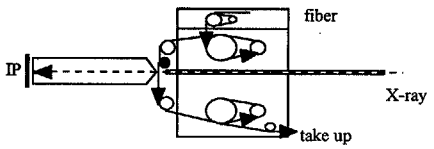


Figure 1. On-line draw machine diagram.

* This work is partially supported by a NSF-GOALI Grant DMR-9629825

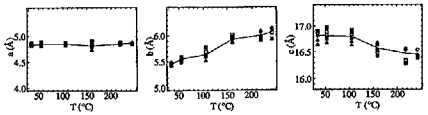


Figure 2. Unit cell parameters of nylon 66 as a function of temperature.

Time-Resolved Synchrotron SAXS Study of the Miscible Blends of Semicrystalline Poly(vinylidenefluoride) and Semicrystalline Poly(1,4-Butylene Adipate)	X3A2

Li-Zhi Liu, Benjamin Chu*,(SUNY Stony Brook), R. St. John Manley (McGill U.)

Poly(vinylidenefluoride) (PVF_2) and poly(1,4-butylene adipate) (PBA) are thermodynamically miscible in the melt. Since both components of the blend are crystallizable, the mixtures exhibit a complicated phase behavior. The melting points of PVF_2 and PBA are 175 and 60°C, respectively. The PVF_2/PBA blend could form a single miscible amorphous phase above the melting point of PVF_2, a two-phase morphology at a temperature between the melting points of PVF_2 and PBA, and a three-phase morphology below the melting point of PBA. In the present work, the crystallization dynamics of PVF_2 homopolymer and its blend with 60% PBA was studied. The sample was quenched from a single phase region (190°C) to a two-phase region (130°C) first, as shown in Figure 1, and then further quenched to a three-phase region (4°C), as shown in Figure 2. The PVF_2 homopolymer sample showed a decrease in long period with time when quenched to 130°C, while the blend showed a little increase in long period with time. The peak intensity of both PVF_2 homopolymer and the blend showed an appreciable increase in the first 25 seconds and reached a constant value at the same time (Figure 1), indicating that the crystallization rate of the two samples were same. When further quenched to 4°C, the blend showed a decrease in long period, as shown in Figure 2, and no PBA scattering peak was developed, indicating that, in this process, the crystalline structure of PBA was not very regular.

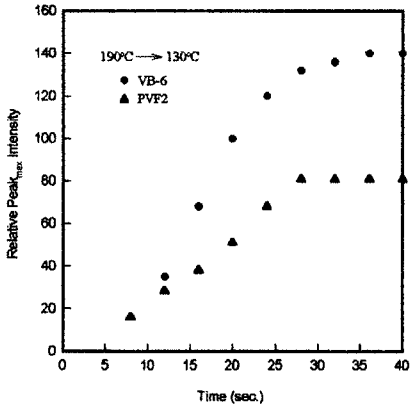


Figure 1. The time-dependent SAXS peak intensity of PVF_2 homopolymer and the blend with 60% PBA when quenched from 190°C to 130°C.

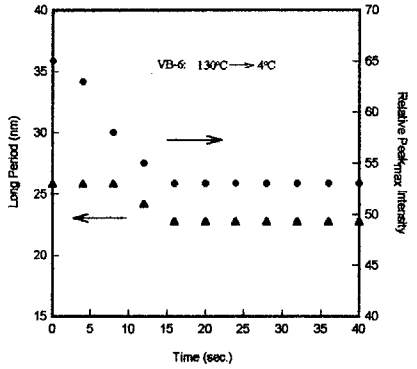


Figure 2. The time-dependent SAXS peak intensity and the long period of PVF_2 of the blend when further quenched to 4°C.

Synchrotron SAXS Study of Crystallization and Microphase Separation in Compatible Mixtures of Tetrahydrofuran-Methyl Methacrylate Diblock Copolymer and Polytetrahydrofuran	X3A2

L.-Z. Liu, F. Yeh and B. Chu (SUNY Stony Brook)

The crystallization and microphase separation of compatible mixtures of tetrahydrofuran methyl methacrylate diblock copolymers (PTHF b PMMA) with a tetrahydrofuran homopolymer (PTHF) were studied by means of synchrotron small angle X-ray scattering (SAXS). The crystallization of PTHF microphases in the blend showed almost no effect on the original phase separated structures in the amorphous state of the blend before crystallization including, for example, the PMMA interdomain distance, as shown in Figure 1. After crystallization, the blends with an alternating lamellar structure showed an appreciable intensity increase in the higher-order scattering peaks, suggesting that the lamellar packing had become more regular. The separation distance between two PMMA cylinders (or spheres) had a great effect on the crystalline structure of the PTHF matrix microphase. When the separation distance between two PMMA cylinders was about two times larger than the long period of the neat PTHF homopolymer, a nearly ordered micro-crystal packing could be formed in the PTHF matrix microphase. In the blends with 30 wt% or less copolymer and with larger separation distances, the micro-crystals could have a very ordered packing, exhibiting sharp X-ray peaks similar to that of the PTHF homopolymer (Figure 2.). The PTHF matrix microphase also showed an increase in the long period with increasing copolymer weight fraction, as also shown in Figure 2. The relationship between the long period and the crystallization temperature was different for blends with different amounts of copolymer.

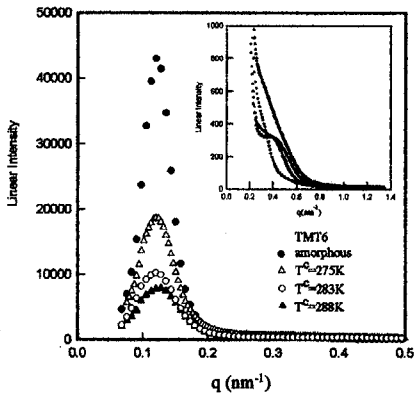


Figure 1. SAXS profiles of blend TMT6 with 60% homopolymer in the amorphous state and crystallized at different temperatures

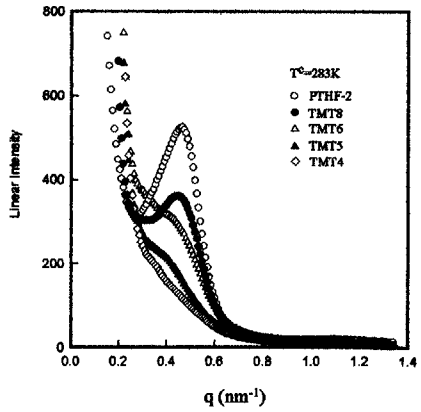


Figure 2. Crystalline scattering profiles of neat homopolymer and blends with 40% to 80% homopolymer; crystallization temperature at 283K.

The Effects of Thermal Shocking on the Residual Stress in Si_3N_4 Ceramic Composites *	X3A2

A. Sahiner, D. Wittmer, and M. Sweeney (Southern Illinois U. at Carbondale)

Residual stresses play an important role in the electrical, thermal, and mechanical properties in materials. The strain caused by this stress can be thought of as stored energy that is localized around some feature of the materials microstructure. The residual stress may originate from the mismatch between the crystal lattices caused by: a mismatch in coefficient of thermal expansion between the material phases during high temperature processing; preferred orientation of highly anisotropic phases; presence of metastable crystalline phases; density gradients across thin sections; and mechanical or thermal damage. Angle and energy dispersive x-ray diffraction experiments on Si_3N_4 ceramic composites are conducted in order to analyze the variations of the residual stress, as the preparation and the thermal treatment parameters are changed. Along with the elasticity theory, the shifts of the diffraction peak positions when the sample is tilted at various angles with respect to the incoming beam, are used to determine the stress in the sample. A detailed comparison of the residual stresses between the as-machined and the thermally shocked samples are made and the effects of thermal shocking temperature in terms of strength of the materials are discussed. In Fig. 1a, the 2θ-$\sin^2\psi$ plots for the data obtained on the beamline X3A2 of NSLS are shown for Si_3N_4 samples. From the slopes of the linear fits and the θ_0 measurement from the powdered Si_3N_4, the stress in the directions parallel and perpendicular to the surface were determined according to the elasticity theory. In these calculations, values of 304 GPa and 0.27 were used for the Youngs modulus and the Poissons ratio. The stresses (σ_{11} and σ_{33}) are calculated for the (441), (531), and (303) peaks and the average of these calculations are plotted with respect to thermal shocking temperature in Fig. 1b. Both of the stress values (in and out-of-plane) are compressive except T=1400°C. The compression increases as the thermal shocking temperature rises from 900 to 1100°C. After reaching to the maximum at 1130°C (according to quadratic polynomial fit) the compression decreases in both directions and even turns into a tension at 1400°C in the parallel to the surface direction.

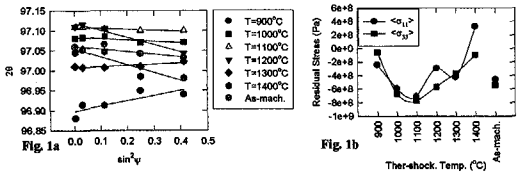


Figure 1.

* This work has been supported by Illinois Board of Higher Education.

Simultaneous SAXS/WAXD Morphological Studies of Nylon 66 Fibers	X3A2

J. R. Sharrow, J. M. Schultz (U. of Delaware), B. S. Hsiao, and H. Chang (DuPont)

Two-dimensional simultaneous small-angle X-ray scattering (SAXS) and wide-angle X-ray diffraction (WAXD) were used to investigate the morphology of nylon 66 fibers. The beam, was reduced to 0.3 x 0.3 mm^2 using a 3-pinhole collimator. Equatorial scans were taken from the WAXD images in order to obtain transverse crystal fibril widths. Deconvolution of the sliced WAXD patterns was accomplished by fitting the scans with four Gaussian curves. The four Gaussian curves represent the crystal (100) peak, the crystal (010), (110) doublet, the amorphous region, and the mesophase. While the amorphous phase is azimuthally independent, the mesophase is a broadly azimuthally dependent phase consisting of oriented amorphous material. A sample curve fit is displayed as Figure 1. The Scherrer equation was used to calculate the crystal fibril width from the crystal curve fits. For a fiber not subject to heatsetting, the average crystal fibril width was determined to be 60Å, while fibers subject to wet heatsetting displayed an increase in the transverse fibril dimension to 65Å. These number are in good agreement with radial distribution function analysis yielding correlation lengths in the transverse direction. A slice of the SAXS meridional intensity profile, corrected by a Lorentz factor, was examined using the correlation function $\gamma(r)$ in order to calculate the crystal thickness along the fiber. The correlation function is given as:

$$\gamma(r) = \int_0^\infty (I(q) - I_b) q^2 exp(\sigma^2 q^2) cos(qr) dq$$

where refers to the sliced profile, $q = 4\pi\sin(\Theta)/\lambda$, I_b designates the liquid scattering profile and σ is associated with the width of the interface. If the fiber structure conforms to a two-phase model, the first maximum of the correlation function yields the long period, crystal plus amorphous thicknesses. Figure 2 exhibits that fibers undergoing a wet heatset are characterized by a larger long period, 80Å, than fibers that have not been exposed to heatsetting, 70Å.

This work is supported by NSF-GOALI Grant (DMR-9629825).

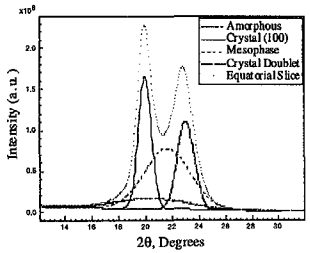


Figure 1. WAXS Gaussian Curve Fitting Method

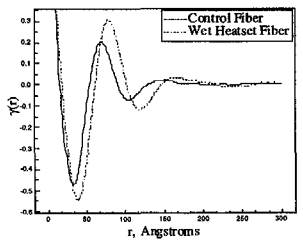


Figure 2. SAXS Correlation Functions Plot

SAXS Study of Gel-like Structures of Block Copolymers in DNA Separation Buffers	X3A2

C. Wu, T. Liu, and B. Chu* (SUNY Stony Brook)

Block copolymer AmBnAm in a selective solvent and at an appropriate concentration and temperature can form a gel-like phase with regular structures. The gel-like phase was presumably formed by close-packing micelles with condensed hydrophobic cores and entangled hydrophilic shells. The structural studies of EnPmEn and BnEmBn type block copolymers [with P, E, and B representing, respectively, poly(oxypropylene), poly(oxyethylene), and poly(oxybutylene)] in DNA separation buffers such as 1X TBE (89 mM Tris, 89 mM borate, 2 mM EDTA) and sequencing buffer (1X TBE, 3.5M urea and 30% formamide) were performed by using the SAXS technique.

According to the capillary electrophoresis results, both EPE- and BEB-type block copolymers show good DNA separation abilities. The following is the brief summary.

1. EPE-type copolymer: a. Micellar gel phase shows f.c.c. crystal structure. b. Higher copolymer concentration decreases intermicellar distance. c. Solvent does not effect f.c.c. micellar structure. d. Heating history of EPE gel preparation will effect ordering of crystalline domains.

2. BEB-type copolymer: a. Micelles are assembled differently when compared with EPE-type copolymer. b. Hydrogen-bond destroyers, such as urea and formamide in the sequencing buffer, tend to decrease the average inter-domain distance of the gel-like structure.

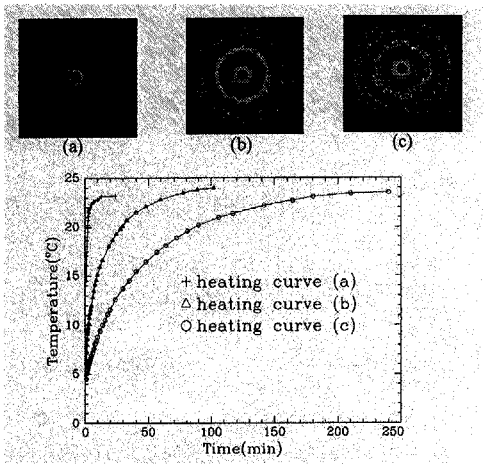


Figure 1. SAXS images of 25% EPE in sequencing buffer at different heating rates and the corresponding heating curves.

Nano-Structure of Gel-Surfactant Complexes *	X3A2

F. Yeh, E.L. Sokolov, and B. Chu* (SUNY Stony Brook)

Polyelectrolyte gels interacting with oppositely charged surfactants can produce discrete volumn transition in aqueous solutions when the surfactant concentration is lower than its critical micelle concentration. A well-defined structure could be formed in the gel-surfactant complex. Two types of ordered nanoscale supramolecular structures have been observed in the complexes of cationic poly(diallyldimethylammonium chloride) (PDADMACl) gels interacting with anionic sodium alkyl sulfates.[1] Our previous SAXS studies showed that the nanostructure formed by the PDADMACl-sodium decyl sulfate (SDCS) complex could be melted at higher temperatures. This process leads to the formation of more extensive spatial regions of crystallinity. Fig. 1 shows a series of SAXS images of the PDADMACl-SDCS complex obtained during recrystallization. The images were taken at room temperature, at 70°C, and at room temperature again after the sample was cooled down. It is evident that the type of nanostructure formed in the complex at 70°C is different - the sample has melted. Larger areas of crystallinity were formed after the sample was cooled from above the melting temperature (70°C) down to the room temperature.

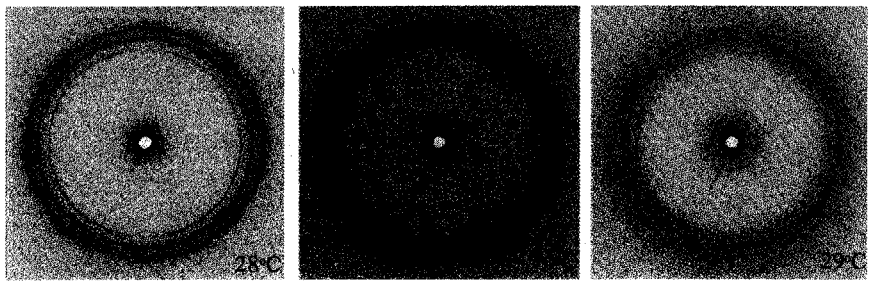


Figure 1. SAXS images of PDADMA-SDCS complex at different stages of heating-cooling process: 28°C (left), 70°C (center), and 29°C (right).

* 1. Sokolov, Eugene L.; Yeh, Fengji; Khokhlov, Alexei R.; Chu, Benjamin; submitted.

Formation and Struction of Micelles and Supramolecules of Pluronic P103 in Water/O-xylene Mixture — X3A2

Shuiqin Zhou, Jie Su and Benjamin Chu (SUNY Stony Brook)

Both laser light scattering (LLS) and small-angle X-ray scattering (SAXS) were used to study the water-induced formation and structure of micelles and supramolecules of Pluronic P103 [(EO)17(PO)60(EO)17] in o-xylene. The size and structure of micelles have been studied as a function of solubilized water content Z (the molar ratio of water to EO units) in micelles. In the dilute solution region (C $<$ 0.28 g/mL), the aggregation number, N; the core radius, Rc; and the hard-sphere volume fraction, f, of micelles increase with increasing Z. However, the hydrodynamic radius, Rh, decreases with increasing Z. The change of micellar structure from low Z to high Z leads to a decrease of the corona thickness, Rs, of micelles until a constant value is obtained. At low Z values (Z $<$ 0.9), micelles have a thick corona with Rs 17 nm because part of the poorly solvated PEO blocks are present in the corona. At high Z values (Z $>$ 1.8), the PEO blocks in the corona enter into the micellar core and the long solvated PPO blocks form loops in the corona resulting in a constant corona thickness of 9 nm. In the concentrated solution region (C $>$ 0.28 g/mL), and at lower Z values, bridging between micelles was formed due to the presence of PEO blocks in the corona. At high Z values, the packing of micelles form a stiff polymer network at a critical hard-sphere volume fraction f of 0.49. The higher the Z value, the lower the critical gelation polymer concentration. Both face-center cubic and hexagonal supramolecular structures were observed in the concentrated solution region.

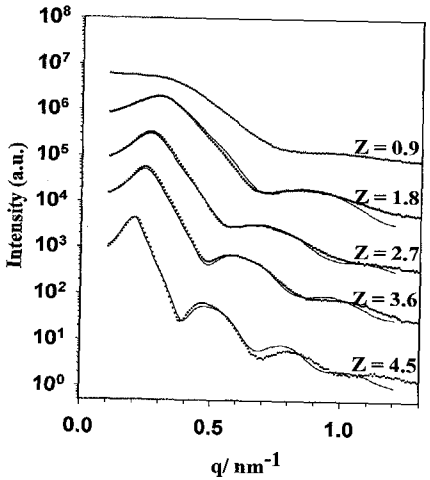


Figure 1. Intensity profiles of SAXS of P103/water/o-xylene micelle solution with c = 0.164 g/mL at different Z values.

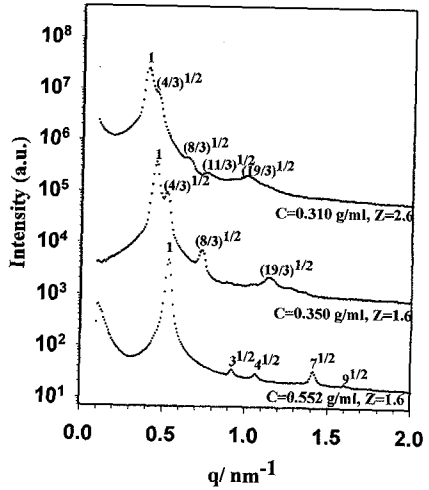


Figure 2. Intensity profiles of SAXS of P103/water/o-xylene micellar gel at the indicated concentration and Z values.

Single C-C bond in $(C_{60})_2^{2-}$ * — X3B1

G.M. Bendele (SUNY Stony Brook), P.W. Stephens (SUNY Stony Brook and NSLS), G. Oszlányi, G. Bortel, G. Faigel, L. Gránásy (SZFKI, Budapest), and L. Forró (EPF, Lausanne)

We have investigated the structure of the metastable dimer phases of AC_{60} (A=K,Rb) via x-ray powder diffraction. In both materials, the dimer molecule forms through a single C-C interfullerene bond.

The dimer phase of AC_{60} is obtained by quenching from high temperature to T=77K and subsequently cycling the temperature between 220K and 273K. X-ray powder diffraction spectra were then obtained at T=220K with λ=1.15Å. Given the abundance of possibilities for the bonding mechanism, the location and orientation in the monoclinic unit cell of the dimer molecule, we have performed on the order of 10^6 Rietveld refinements, mapping the orientations of the buckyballs in several possible space groups [1]. Among all cases considered, the single-bonded dimer in the *trans* configuration gives the best fit. The final results of the refinements are (for K): Lattice parameters a=17.153(5)Å, b=9.793(5)Å, c=19.224(5)Å, β=124.1°. Space group $P2_1/a$ (cell choice 3 of No. 14), C_{60} center at (0.007,0,0.246), K at (0,0.5,0.013) and (0,0.5,0.513). The Eulerian angles by which the buckyball is rotated in this position are θ=90°, ϕ=12°, ψ=281°. This is identical to the solution for Rb except for the rotation angle of the molecule around its bonding axis.

We have established that in these metastable phases of AC_{60} covalently bonded $(C_{60})_2^{2-}$ dimer anions form through a single C-C interfullerene bond. This type of bond is different from the four-membered rings of AC_{60} and C_{60} polymers. Details of the analysis are given in [1].

[1] G. Oszlányi *et al.*, Phys. Rev. B **54**, 11849 (1996)

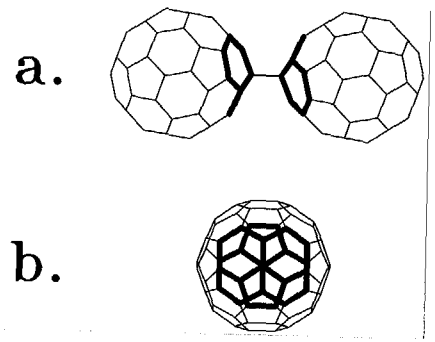


Figure 1. Single-bonded *trans* $(C_{60})_2^{2-}$ dimer **a.** side view **b.** view along dimer axis

* Work at the SUNY X3 beamline is supported by the Division of Basic Energy Sciences, U.S. Dept. of Energy (DE-FG0286-ER45231). Research at SUNY is supported by the NSF under grant DMR95-01325

Na_2RbC_{60} is orthorhombic at low temperature * | X3B1

G.M. Bendele (SUNY Stony Brook), P.W. Stephens (NSLS and SUNYSB), K. Prassides, K. Vavekis, K. Kordatos (U. Sussex, UK), and K. Tanigaki (NEC Tsukuba)

We have studied Na_2RbC_{60}, an alkali fulleride until now believed to be cubic at all temperatures (with a fcc→primitive cubic transition at around 300 K), at several temperatures using synchrotron x-ray powder diffraction measurements.

At elevated temperatures the structure is indeed fcc (space group $Fm\bar{3}m$, a=14.141Å at 370K), and at room temperature the known primitive cubic phase (space group $Pa\bar{3}$) coexists. However, lowering the temperature to below 230K results in the appearance of peaks not consistent with the cubic structure, indicating a phase of lower symmetry. Indeed, the sample transforms slowly into an orthorhombic phase with lattice parameters of a=9.3819Å, b=9.943Å, and c=14.559Å (space group Immm) at T=180K. The cubic→orthorhombic phase transition is extremely slow (fig. 1) and a small amout of the cubic phase remains quenched in even when the sample is cooled at a rate of only 1K/hr. between 230K and 180K.

The most interesting feature of the orthorhombic phase is its strongly reduced distance between C_{60}^{3-} anions (9.38Å) along the a direction. This strongly suggests covalent interfullerene bonding; however, the observed interfullerene separation is larger than in the known polymerised phases (9.11Å) and almost identical to the singly-bonded dimer phases in AC_{60}.

Further work on this system is in progress.

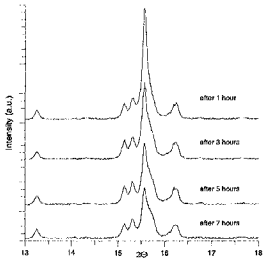


Figure 1. Powder spectra at T=220K as a function of evolved time. The strongest peak indexes to the cubic phase, all others to the orthorhombic phase.

* Work at the SUNY X3 beamline is supported by the Division of Basic Energy Sciences, U.S. Dept. of Energy (DE-FG0286-ER45231). Research at SUNY is supported by the NSF under grant DMR95-01325

Powder Diffraction Structure of Indenyllithium * | X3B1

R.E. Dinnebier (Univ. of Bayreuth, Germany), P. W. Stephens (SUNY Stony Brook), U. Behrens (U. of Hamburg, Germany) and F. Olbrich (U. of Magdeburg, Germany)

The crystal structure of the organometallic compound indenyllithium (LiC_9H_7) has been solved ab initio. The compound crystallizes in the orthorhombic space group Pnma (No. 62) with a = 20.5000(1) Å, b = 3.9645(1) Å, c = 8.3087(1) Å, V = 675.27(1) Å^3 and d = 1.201 g cm^{-3}. Data collection was carried out at room temperature using a wavelength of 1.14894 Å from double Si(111) monochromator and Ge (111) analyzer. The 2Θ range used for the Rietveld refinement was $5.0 < 2\Theta < 59.9°$. All positions of the carbon and lithium atoms were found by direct methods. The indenyl ring was refined as a rigid body and the hydrogen atoms were calculated in idealized positions. The actual Rietveld plot yields to R-wp=7.7%, R-p=5.2% and R-F^2=8.5%. Figure 1 shows the structure of LiC_9H_7. The LiC_9H_7 units are connected to polymeric chains along the crystallographic b axis. Herein the Li atoms are hapto5 coordinated by two indenyl rings. The indenyl rings are always bonded by the five member ring to the Li atoms. Because of the crystallographic mirror plane through the Li atoms and the indenyl ring, the indenyl rings are placed absolute coplanar and staggered.

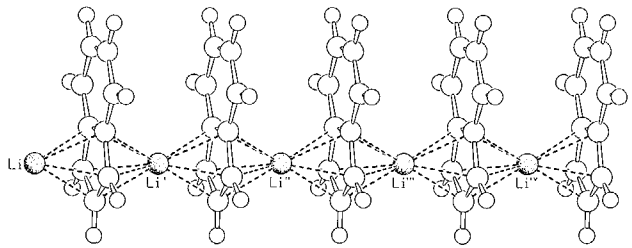


Figure 1. Polymeric chain of indenyllithium along b axes.

* Work at the SUNY X3 beamline is supported by the Division of Basic Energy Sciences, U.S. Dept. of Energy (DE-FG0286-ER45231).

Powder Diffraction Structure of MC_5H_5 (M= Li, Na, K) *	X3B1

R.E. Dinnebier (U of Bayreuth, Germany), P. W. Stephens (SUNY Stony Brook), U. Behrens (U. of Hamburg, Germany) and F. Olbrich (U. of Magdeburg, Germany)

The crystal structures of the basic organometallic compounds cyclopentadienyllithium (LiC_5H_5, **1**), -sodium (NaC_5H_5, **2**) and -potassium (KC_5H_5, **3**) have been solved *initio*. The following crystallographic data have been found: **1**: orthorhombic Pnam, a = 10.2626(3) Å, b = 11.1286(3) Å, c = 3.9366(1) Å; **2**: orthorhombic Pnam, a = 10.1339(9) Å, b = 11.0064(10) Å, c = 4.7128(2) Å; **3**: tetragonal P-42_1c, a = 9.9742(4) Å, b = 10.5035(3) Å. Data collection was carried out at room temperature using a wavelength of 1.14937(1) Åfrom double Si(111) monochromator and Ge (111) analyzer. The 2Θ ranges considered for the Rietveld refinements were: **1**: $10.0 < 2\Theta < 53.0°$; **2**: $6.0 < 2\Theta < 60.0°$; **3**: $7.0 < 2\Theta < 60.0°$;

The positions of the carbon and metal atoms were found by direct methods and simulation techniques. The C_5H_5 rings were treated as rigid bodies and the hydrogen atoms were calculated in idealized positions. The actual Rietveld plots yielded to **1**: F2 = 7.3%; **2**: F2 = 8.9%; **3**: F2 = 8.4%. All three compounds crystallize as polymeric chains along c-axis. The organic anion (C_5H_5-) is penta hapto bonded to the metal cations forming multidecker chain structures. In **1** and **2** the chains are linear, in **3** the K cations form a bent zigzag chain with an angle of 138°.

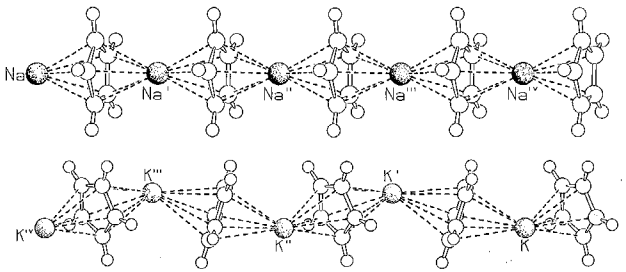


Figure 1. Polymeric chain of cyclopentadienylsodium (top) and cyclopentadienylpotassium (bottom).

* Work at the SUNY X3 Beamline is supported by the Division of Basic Energy Sciences, U.S. Dept. of Energy (DE-FG0286-ER45231).

Powder Diffraction Structure of Phenyllithium (C_6H_5Li) *	X3B1

R.E. Dinnebier (U. of Bayreuth, Germany), P. W. Stephens (SUNY Stony Brook), U. Behrens (U. of Hamburg, Germany) and F. Olbrich (U. of Magdeburg, Germany)

The crystal structure of the organometallic compound phenyllithium (C_6H_5Li) has been solved *ab initio* by high resolution powder diffraction. Crystallographic data are: space group $P2_1/n$, a = 11.527(1) Å, b = 4.554(1) Å, c = 10.406(1) Å, V = 498.08(2) $Å^3$, Z = 4, dcalc.= 1.134 g cm^{-3}. The data were collected at 293 K with a wavelength of 1.14966 Å using a double Si(111) monochromator and Ge(111) analyzer in a 2Θ range of $5.0 < 2\Theta < 49.03°$ for 16 seconds per step. The structure was solved by direct methods and difference-Fourier-analysis and subsequently refined by the Rietveld technique leading to final R-values of R-wp = 5.3%, R-p = 3.5% and R-F2 = 10.4%. Basefree phenyllithium crystallizes as a polymeric infinite ladder structure (Fig. 1), which continues in the crystallographic b direction. The absolute unit of this ladder is a planar Li_2C_2 four member ring with an crystallographic inversion center in the ring. Interactions to the next Li_1C_2 rings leads to the polymeric structure. Each phenylanion is bonded to three different Li atoms. We can discribe this type of bonding as a 2 electron three center bonding (2e3c). Beside this, the p-electrons of the phenylring interacts with one of these three Li atoms. That way the coordination number of the Li atoms is four and therefore completed.

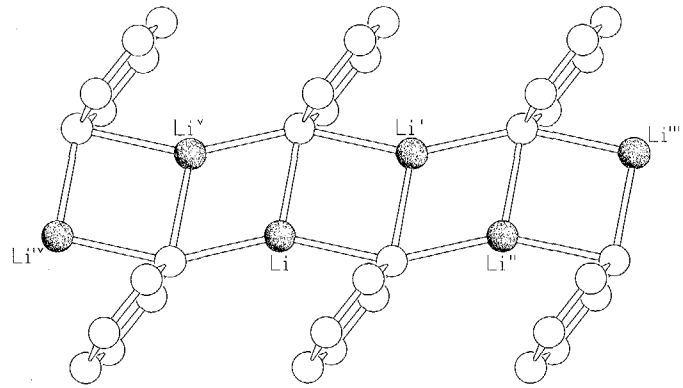


Figure 1. Infinite ladder of phenyllithium.

* Work at the SUNY X3 Beamline is supported by the Division of Basic Energy Sciences, U.S. Dept. of Energy (DE-FG0286-ER45231).

Ab initio Structure Determination of Two Polymorphs of RbC_5H_5 in a Single Powder Pattern *	X3B1

R.E. Dinnebier, S. van Smaalen (U. of Bayreuth, Germany), F. Olbrich (U. of Magdeburg, Germany) and P. W. Stephens (SUNY Stony Brook)

The structures of two polymorphic phases of solid RbC_5H_5 (RbCp) (Fig. 1, 2) have been solved *ab initio* by high resolution powder x-ray diffraction measured in a single powder pattern. The compound, crystallizes in space group Pbcm (phase II), Z=8, with unit cell parameters a= 9.3396(1) , b= 10.9666(1) , c= 10.5490(1) and in space group Pnma, Z=4 (phase I), with unit cell parameters a= 10.7990(2) Å, b= 8.6923(2) Å, c= 5.7061(2) Å. Data collection was carried out at room temperature using 1.15 Å from double Si(111) monochromator and Ge (111) analyzer. The two phases could be separated by their different FWHM distribution. Both structures could be solved by means of direct mthods. For the Rietveld refinements, the Cp-rings rings were treated as rigid bodies and the hydrogen atoms were calculated in idealized positions. The actual Rietveld plot yields to R-F = 4.3% (phase I) and R-F= 4.5% (phase II). Both phases show polymeric zigzag chains, so called bent-polydecker sandwich structures, with an average Rb-Cp_z (Cp-ring-centroid) distance of 2.97 Å. Phase (I) contains a single chain along the a-axis whereas phase (II) contains two similar but crystallographically independent chains perpendicular to each other along the b-axis and along the c-axis. The chains are bent with Cp_z-Rb- Cp_z angles ranging from 123.5° to 136.5°.

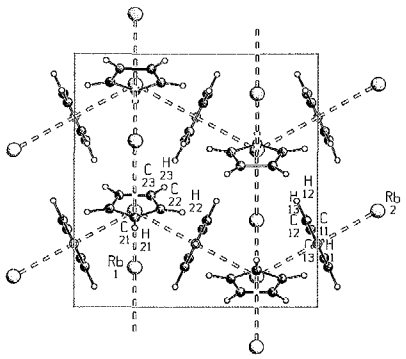


Figure 1. Unit cell drawing of RbCp (phase II).

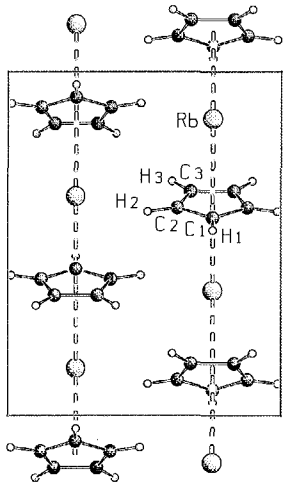


Figure 2. Unit cell drawing of RbCp (phase I).

* Work at the SUNY X3 Beamline is supported by the Division of Basic Energy Sciences, U.S. Dept. of Energy (DE-FG0286-ER45231).

Structural Investigation of a Tetragonal Garnet: $Ca_3Mn_2Ge_3O_{12}$ *	X3B1

S. Heinemann (Bayerisches Geoinstitut, U. of Bayreuth, Germany) and R.E. Dinnebier (Lehrstuhl für Kristallographie, U. of Bayreuth, Germany)

Cubic $Ca_3Mn_2Ge_3O_{12}$ (CMG) has a garnet structure and undergoes a phase transition to tetragonal symmetry below 520K [1]. Tetragonal (CMG) shows photo induced linear birefringence below 175K [1] and could possibly be used as a rewritable media for 3D holographic storage. The physical mechanism of this property is still unknown. Because of heavy twinning the structure of tetragonal CMG could not be determined by single crystal diffraction and has therefore been solved by high resolution powder diffraction. The lattice constants at room temperature are a=12.30801(3) Å and c=12.32325(4) Å in space group $I4_1/a$.

X-ray powder diffraction pattern were recorded at different temperatures using a wavelength of 1.14945 Å from double Si(111) monochromator and Ge(111) analyzer. The minimum FWHM was 0.02°2Θ. The actual Rietveld refinement with 797 reflections from 5°2Θ to 85°2Θ converged to R-Bragg = 5.6%. The structure can be desribed as a distorted garnet structure (Fig. 1) with MnO_6 octahedra distorted into two different species which build an ordered pattern.

It can be shown that the phase transtion is improper ferroelastic and its driving force is a cooperative Jahn-Teller effect of the octahedral coordinated Mn^{3+}. This information will certainly help to investigate the mechanism of the photorefractive effect.

[1] Bedarev, V.A. and Gnatchenko, S.L. (1993): Low Temp. Phys. 20, 100
[2] Kazei, P. et al. (1983): Sov. Phys. JETP 56, 854

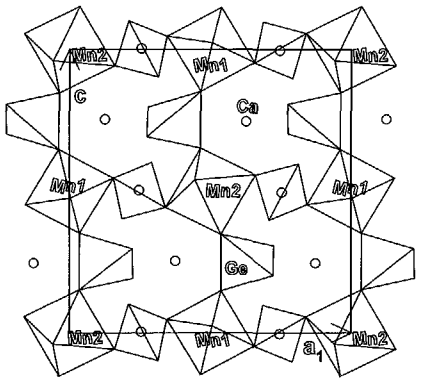


Figure 1. Part of the tetragonal garnet structure.

* Work at the SUNY X3 beamline is supported by the Division of Basic Energy Sciences, U.S. Dept. of Energy (DE-FG0286-ER45231).

Alkali Occupancies and Fullerene Orientation in K_4C_{60} and Rb_4C_{60} *	X3B1

C.A. Kuntscher, G.M. Bendele (SUNY Stony Brook), and P.W. Stephens (SUNY Stony Brook and NSLS)

The phase mixtures of alkali fulleride samples K_xC_{60} and Rb_xC_{60} with stoichiometries close to $x = 4$ were examined by x-ray powder diffraction measurements at room temperature.

All diffraction patterns exhibit the coexistence of either fcc or bcc minority phase. We have shown by Rietveld refinements that A_4C_{60} is a line phase which is stable only for exact stoichiometry $x = 4$, with no vacancies in the alkali metal sites. The C_{60} molecules are disordered between two possible orientations within the bct lattice, where the three orthogonal two-fold rotation axes are aligned with the unit cell edges in space group I4/mmm.

Figure 1 shows the part of the $Rb_{4.01}C_{60}$ diffraction pattern which indicates the coexistence of the bcc minority phase Rb_6C_{60}. The maximum number of counts for this pattern is 16660. The corresponding pattern of a sample $Rb_{3.99}C_{60}$ exhibits only diffraction peaks of the phases Rb_3C_{60} and Rb_4C_{60}.

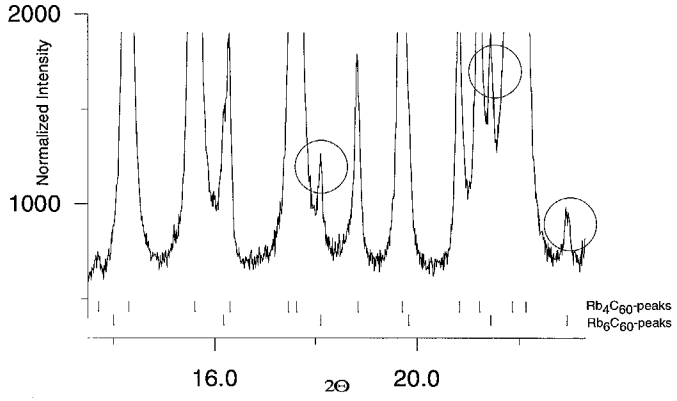


Figure 1.

* Work at the SUNY X3 beamline is supported by the Division of Basic Energy Sciences U.S. DOE (DE-FG02-86ER45231). Research at SUNY is supported by U.S. NSF (DMR95-01325).

Atomic Structure of Gold Nanoclusters *	X3B1

P.W. Stephens (NSLS and SUNY Stony Brook), C.L. Cleveland, U. Landman, M. Shafigullin, R.L. Whetten (GA Tech)

We use x-ray diffraction to study the structure of gold nanocrystals in the size range of 50-500 atoms.

The samples are purified fractions of materials prepared and separated by methods described in Ref. 1. These techniques produce annealed clusters, passivated and encapsulated by self-assembled monolayers of alkylthiolates. The figure shows the x-ray diffraction profiles of two samples, determined by mass spectroscopy to consist of 140±10 and 220±20 Au atoms, respectively. Calculated diffraction profiles of several theoretically-favored Au_N structures are shown for comparison. Dh denotes the Marks decahedron (roughly a pentagonal prism with notches in its edges), Ih the Mackay icosahedron, TO+ the truncated octahedron, and t-TO+ the truncated octahedron containing one stacking fault. Note the clarity with which the x-ray measurements can distinguish the various candidate structures.

In contrast to previous work done by other groups, it is not required to assume any polydispersity or polymorphism to account for these diffraction profiles.

1. R.L. Whetten *et al., Adv. Mater.* **8**, 428 (1996).

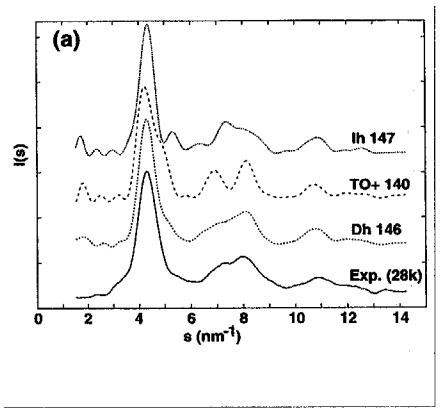


Figure 1.

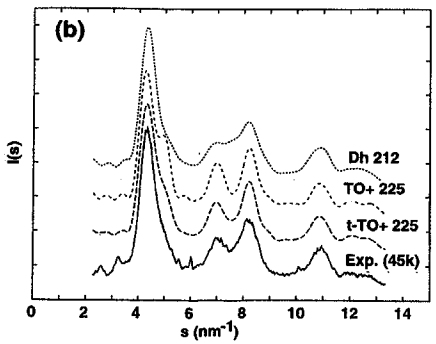


Figure 2.

* Supported by GA Tech Research Foundation, Packard Foundation, ONR, USDOE, and AFOSR.

High-resolution Study of the Ferroelectric $BaTiO_3$. | X3B1

P. Stephens (NSLS and SUNY Stony Brook), D. Balzar (NIST and Inst. Ruder Boskovic), and H. Ledbetter (NIST)

Among ferroelectric materials, $BaTiO_3$ is particularly interesting for its simple crystalline structure, good ferroelectric properties at ambient temperature, as well as chemical and mechanical stability, which facilitiates easy fabrication of ceramic samples. Both unpoled and poled $BaTiO_3$ pellets were studied by laboratory (Cu K_α) and synchrotron x-ray sources. We used a shorter wavelength (0.62 $\AA$) with a triple-axis configuration to probe deeper below the surface, with superior resolution to the laboratory measurements.

Lineshape analysis showed that the crystalline structure, particularly lattice parameters, remain unchanged upon poling. A $\sin^2\psi$ analysis of peak shift (not shown) indicates that no measureable change of elastic strain occurs upon poling. This indicates that poling may have induced excessive strain which was relieved by microcracking, or that a majority of domains reverse the orientation.

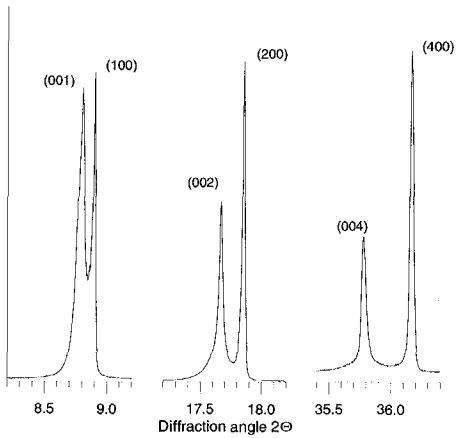


Figure 1.

Crystals of Passivated Gold Nanocrystals * | X3B1

P. W. Stephens (NSLS and SUNY Stony Brook), M. Shafigullin, M.M. Alvarez, S.A. Harfenist, J.T. Khoury, T.G. Schaaff, I. Vezman, Z.L. Wang, A. Wilkinson, and R.L. Whetten (GA Tech)

We are studying 3D arrays of Au nanocrystals of 50-500 atoms, passivated by self-assembled monolayers of alkylthiolate molecules.[1] The metal cores have diameter $2R$ from 1.65 to 3.1 nm (based on mass spectroscopy) and the alkyl chains are 0.73 to 1.7 nm long. It is possible to seperate obtain fractions containing only nanocrystals of distinct shape and size by repeated crystallization from solution. Separated fractions can then be crystallized into 3D arrays, which can be studied by means of x-ray diffraction. We generally observe several orders of diffraction with d-spacings from 3.5 to ~1.0 nm. The intensity distribution is that expected of a primitive (fcc, bcc, or bct) lattice of compact scatterers (the high-Z cores) surrounded by regions of low scattering power. Fig. 1 shows that the packing density (expressed as the Au volume fraction) is a smooth function of L/R, even as one passes from fcc to bcc structure. The atomic structure of the Au cores is described in an accompanying abstract.

[1] R.L. Whetten *et al., Advanced Materials* **8**, 428 (1996).

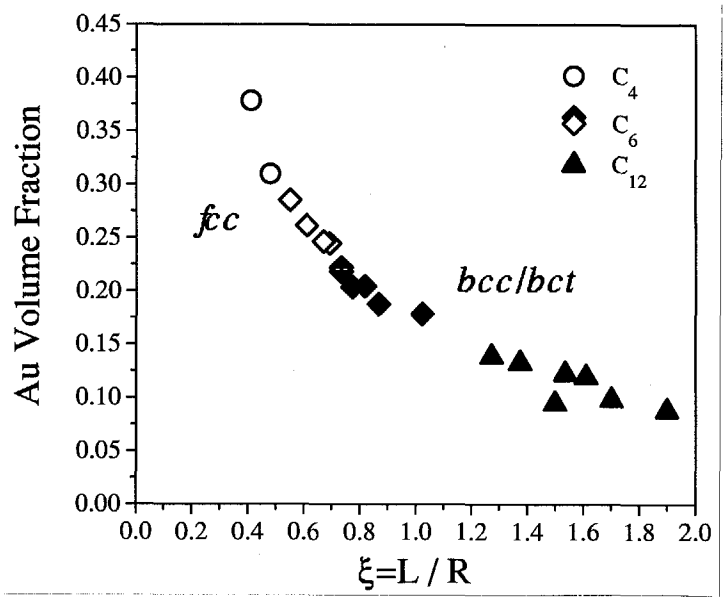


Figure 1.

* Supported by GA Tech Research Foundation, ONR, Packard Foundation and DOE

Powder Diffraction Structures of $Ca_8[Al_{12}O_{24}](MoO_4)_2$ (CAM) *	X3B1

S. van Smaalen, R.E. Dinnebier (U. of Bayreuth, Germany), H. Katzke and W. Depmeier (U. of Kiel, Germany)

Powder diffraction at various temperatures between room temperature and 650K have revealed two first-order and one second order phase transition. The crystal structures of all four phases have been determined by Rietveld refinement. On decreasing temperature , the phases are cubic, I-43m, a = 9.29377(4) Å; tetragonal (T2) P-4c2, a = 13.14536(6) Å and c = 9.29224(8) Å; tetragonal (T1) P-4c2, a = 13.12263(5) Å and c = 9.32081(5) Å; and orthorhombic Aba2, a = 26.14683(8) Å, b = 13.07061(4) Å and c = 9.31413(2) Å. The T2 phase is a superstructure of the cubic phase, while the T1 phase has an additional distortion whereby c is longer and $a\sqrt{2}$ is shorter than the cubic lattice constant. The phase transitions are found to be related to orientational ordering as well as positional ordering of the WO_4^{2-} anions within the cages of the sodalite framework structure.

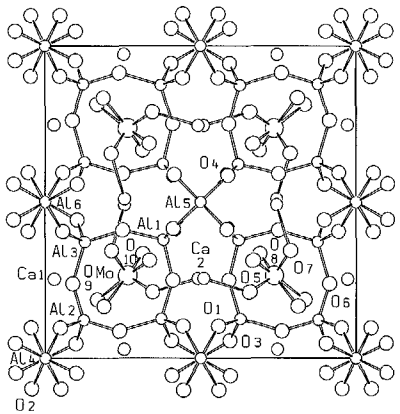


Figure 1. Unit cell of T1 phase (MoO_4 tetrahedra are disordered).

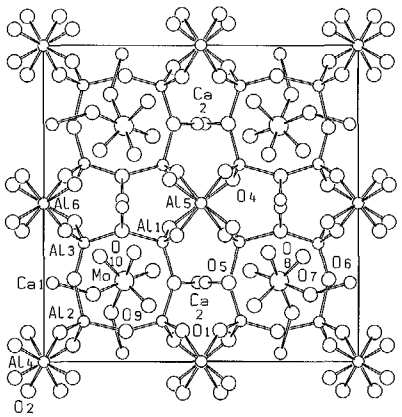


Figure 2. Unit cell of T2 phase (MoO_4 tetrahedra are disordered).

* Work at the SUNY X3 Beamline is supported by the Division of Basic energy Sciences, U.S. Dept. of Energy (DE-FG0286-ER45231).

The Crystal Structure Determination of the SecA Translocation ATPase	X12B, X4A

J.F. Hunt and J. Deisenhofer (HHMI, UT Southwestern)

SecA is the engine which drives the ATP-powered translocation of secretory proteins through the bacterial periplasmic membrane. Although SecA exists in a fully water-soluble form, it undergoes cycles of membrane insertion and retraction in the course of its ATPase cycle. SecA is believed to function as a molecular ratchet in the protein translocation reaction, pulling segments of the secretory protein through the membrane concomitant with the ATP-driven membrane insertion cycles. SecA also auto-regulates its own translation by binding to a specific RNA sequence overlapping the initiator codon in its messenger RNA. The SecA protein possesses two tandem ATP-binding domains with approximately 30 percent identity to the ATP-binding cassettes of the ABC transporter superfamily of transmembrane transport proteins. Based on its domain organization, its sequence homology, and its activity, it has been proposed that SecA may have structural and mechanistic similarities to the ABC transporters.

The crystal structure determination of the soluble, membrane-retracted state of SecA is now almost completed. Data collected on beamlines X12B and X4A at NSLS were instrumental in this process. Because our crystals only diffract to 3.5 angstroms using a rotating anode source, our high resolution data (currently to 2.9 angstroms) was collected on beamline X12B. This beamline was also used for rapid derivative screening. Candidate crystals soaked in either Pt, Au, or Hg compounds were mounted and measured with the energy of the beam tuned to optimize anomalous data from the element in question. 2 X 4 degrees of data were collected very quickly in inverse beam geometry, and the anomalous chi-square at low resolution was used used as the criterion to determine whether collection of a complete data set was merited. The breakthrough derivative for the project was identified in this manner. Data collected on beamline X4A from a selenomethionyl derivative of SecA allowed the position of 33 methionines in the protein to be observed in an anomalous difference fourier using MIR phases (the 3.8 angstrom diffraction from this crystal was too weak to be useful for MAD phasing).

The refinement of the structure is currently in progress. A working model for the domain rearrangements in the course of the SecA ATPase / transport cycle has been formulated, and, on this basis, further experiments are being designed to try to elucidate the structural mechanism by which the hydrolysis of ATP is coupled to transmembrane transport of nascent polypeptide chains.

Structure Determination of the Entire Extracellular Portion of Human CD4	X25, X4A

H. Wu, P.D. Kwong and W.A. Hendrickson (Columbia U.)

Diffraction data from two different selenomethionyl CD4 crystals were collected at the selenium K-shell edge at beamlines X4A and X25 of NSLS. CD4 crystals were extremely weak which mandate high flux synchrotron radiation. Both data sets were recorded with Fuji imaging plates at 100K. These two data sets belong to space groups P41(2)22 and P2, respectively and were used to obtain molecular replacement solutions. Selenium anomalous difference Fouriers were used to confirm the correctness of the structures.

Determination of Transient Molecular Structure for Photoinduced Reaction Intermediates using Time-Resolved Energy Dispersive XAS	X6A

L. Chen, P. Lee, S. Weber, G. Jennings, J. Norris and P. Montano (ANL and the U. of Chicago)

We have obtained preliminary data for time-resolved XAS measurements of triplet excited states of ZnTPP and ZnOEP (zinc tetraphenylporphyrin and zinc octaethylporphyrin) in organic solutions using energy dispersive XAS beamline at X6A. A Nd-YAG laser pumped OPO laser system (Spectra Physics), provides a continuously tunable nanosecond laser pulses from 420 to 2000 nm at 10 Hz with pulse energies around 50mJ at 500 nm, is installed at the beamline. This laser is used to illuminate the molecules in order to create excited states or photoreaction intermediates. The laser pulses are synchronized with the diode array detector readout, treating the x-ray pulses as a continuous source. Currently the time-resolution of the measurements is limited to the 5-ms readout time of the detector. A special sample cell has been designed for the experiment where the X-ray path is much longer than the laser light path. This design is to compensate the discrepancy between the cross sections of the X-ray and laser light. Our preliminary results showed that the spectral difference between the triplet state and the ground state is comparable to the fluctuation of the dark current of the detector. Further improvement of the technique is in progress, where the detector current will be reduced and the better transmission for the laser light will be achieved. We are also looking into other molecular systems, such as electron donor-acceptor complexes, where the metal ions change oxidation states and ligation during a photoinduced chemical reaction.

Contribution of Magnetic-EXAFS to the MCXD Signal at the Gd L_{III} Edge.	X6A

K. J. Gofron, C. W. Kimball (NIU), P. L. Lee, and P.A. Montano (ANL)

We measured, using an energy-dispersive spectrometer, the temperature dependence of the magnetic circular x-ray dichroism (MCXD) effect at the Gd L_{III} edge from 88 K up to 335 K. In the ferromagnetic state, the MCXD spectrum consists of a main positive peak with pre-edge and post-edge features, including a positive peak at -7 eV observed for the first time. With the exception of the main peak all features vanish slightly above the transition temperature. In the paramagnetic region, the MCXD consists only of the main positive peak with a post-edge background slowly decaying away from it over the range of 90 eV. We find evidence that many of the observed near-edge features originate from magnetic EXAFS.

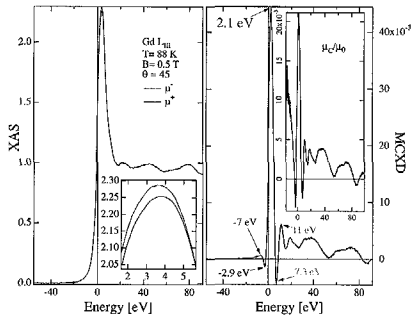


Figure 1.

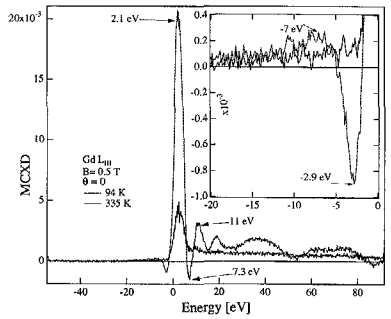


Figure 2.

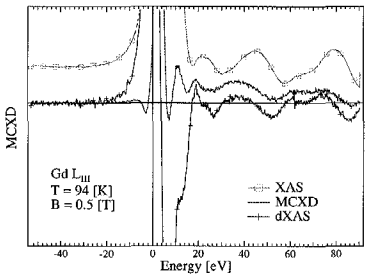


Figure 3.

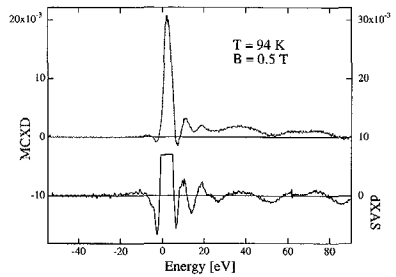


Figure 4.

K Absorption Edge Magnetic Circular X-Ray Dichroism of Fe-Ni alloys.	X6A

K. J. Gofrona, C. W. Kimballa (NIU), P. L. Lee, G. Jennings and P. A. Montano (ANL)

We report Magnetic Circular X-ray Dichroism (MCXD) measurements in Fe-Ni alloys. We used an energy dispersive beamline in our measurements. A polychromator spectrum contains self reference both in intensity and energy since all energies are measured at the same time and remain stable during an energy scan since no movement of the x-ray optics is necessary. We measured the K absorption edges of Fe and Ni (s-p electronic states) in the d ferromagnetic alloys of Fe-Ni. We observe that the signal at the invar composition is of comparable strength as other compositions in contrast to previous studies. We used cold rolled (disordered) foils instead of powders. The measurements reveal changes of the MCXD signal with composition and crystal structure.

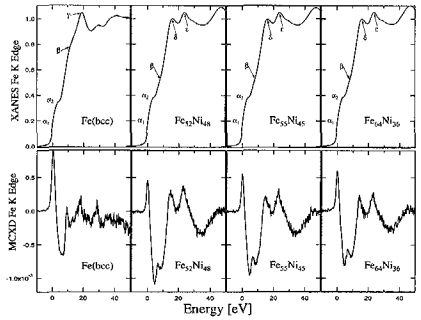


Figure 1. XANES (top) and MCXD (bottom) spectra at the Fe K-edge.

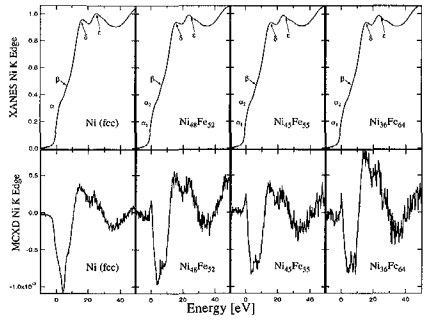


Figure 2. XANES (top) and MCXD (bottom) spectra at the Ni K-edge.

Anomalous Small-angle X-ray Scattering Characterization of Reactor Pressure Vessel Steels	X6B

D. Alexander, (ANL) and P. Jemian, (UNI-CAT, Advanced Photon Source)

Degradation pheonomena such as radiaiton embrittlement of the pressure vessel has important implications on the safe operation of nuclear power plants. Much of the difficulty in understanding this embrittlement on a fundamental, mechanistic level resides in the difficulty associated with characterizing the very small (¡50), finely-dispersed hardening centers (defect and solute clusters) which are believed formed during irradiation in steels. The synchrotron-based technique of anomalous small angle x-ray scattering (ASAXS) offers the unique ability to characterize scattering centers associated with a specific element among a diverse collection of scatterers typically present in a complex steel. Using ASAXS, volume-averaged sizes and number densities of solute clusters such as Cu-rich precipitates can be measured and the effects of irradiation upon such a microstructural component can be assessed.

Our initial efforts have focused on demonstrating the efficacy of the ASAXS technique for pressure vessel steels by first characterizing Cu-Mn precipitates in a thermally-annealed (450C, 24 hours) Fe-0.9 Cu-1.0 Mn model alloy. An analyzing crystal was used to diffract the small-angle scattering from the sample into a position sensitive detector for analysis. The use of an analyzing crystal suppresses matrix fluorescence when the scattering experiments are performed at X-ray energies above the Fe absorption edge. Scattering has been performed at three energies within a few hundred eV of the Mn edge. Analysis of this data is presently underway. Measurements at energies near the Cu edge (above the Fe absorption edge) were also attempted. The results were hampered by limited statistics owing to X-ray attenuation in the primarily iron sample thinner samples are obviously required for Cu measurements.

Study of Strain and Crystal Structure of Epitaxial Grown La-Ca-Mn-O Thin Films	X6B

M. C. Shih (NCHU, Taiwan), M.Y. Chen(NTU, Taiwan), T.S. Tsai (NCHU, Taiwan)

It has been demonstrated that the magnetoresistance (MR) of La-Ca-Mn-O expitaxial films exhibits a strong dependence on the films' thickness. Upon the speculation on possible strain induced giant MR response, it is hypothesized that the change of the lattice strain may be related to the change in film thickness. Therefore, our experiment plans to obtain the structural information of the expitaxial thin films in various film thickness. Six prepared samples of 30A, 70A, 300A, 700A, 1000A, and 3300A thick were examined. Figure 1 shows the surface x-ray diffraction results from the six samples in (200) direction. The sharp spikes (these twin peaks are from the twin domain in substrates) in the figures are verified as diffraction peaks from the substrate due to that they will disappear as either increasing the film's thickness or decreasing the x-ray grazing incident angle. No significant shift in the main in-plane diffraction peak of the samples is observed from 30 A through 3300 A film as suggested in Figure 1. A fourth peak from the film around 2.40 A^{-1} was found as film's thickness increased to few hundreds A and its intensity grows as film getting thicker. When the sample's thickness reaches 3300A , more diffraction peaks were found (see Figure 1f). It is clear that the number of diffraction peaks increases as the deposited films grown thicker. However, one interesting result is that all those peaks observed from every sample in this experiment do show the same four fold symmetry.

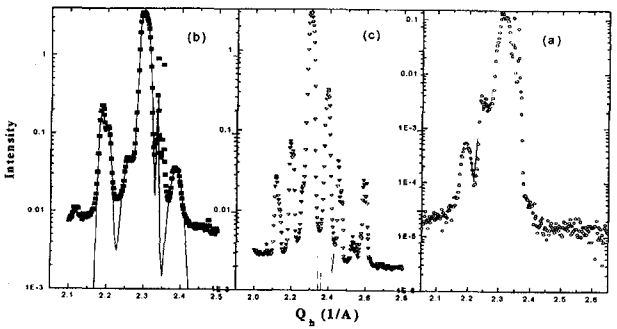


Figure 1.

Bonding and Local Structure of Semiconductor Alloys, $In_{1-x}Ga_xAs$	X7A

S. J. L. Billinge and F. Mohiuddin-Jacobs (Michigan State U.)

To better understand the properties of semiconductor alloys, such as $In_{1-x}Ga_xAs$, it is imporatnt to study local structure, because it is significantly different from the implied average crystal structure. For example, although the average bond length of $In_{1-x}Ga_xAs$ follows Vegards law over the entire concentration range of x, it is known that the nearest neighbor bonding structure exhibits a bimodal distribution of shorter (Ga-As) and longer (In-As) bonds. We are using Pair Distribution Function (PDF) analysis of x-ray powder diffraction data, measured over a wide range of momentum transfer, $Q = 4\pi sin\theta/\lambda$, to study the *local* structure of $In_{1-x}Ga_xAs$ directly. By taking a Fourier transform of the measured total structure function, $S(Q)$, we obtain the real-space atomic pair correlation function, $G(r)$, which contains the information about the local structure directly. This approach utilizes both Bragg peaks, which determine the average crystal structure, *and* the diffuse scattering, which is responsible for resolving detailed local structure. The experiments were performed in reflection mode at $18K$ to reduce the effect of the thermal diffuse scattering. Fig.1 shows the structure function, $Q[S(Q)-1]$, for $In_{.50}Ga_{.50}As$. The circles in Fig.2a show our preliminary data of the PDF obtained for this sample. The solid line is a least square profile fit to the data, assuming an average bond length. The difference curve between the experimental PDF and the model is shown in Fig.2b. We see that the virtual crystal approximation does not describe the experimental data well. In order to resolve the bimodal nearest-neighbor bond distribution directly in the PDF, we need to perform measurements to higher values of Q. Our results will be compared with theoretical predictions for the local structure in collaboration with Prof. Thorpe at Michigan State University.

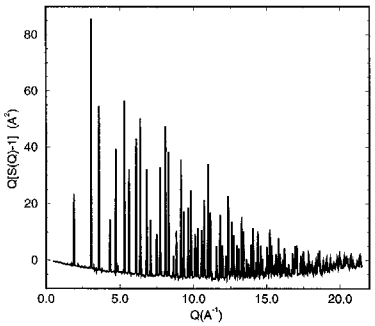


Figure 1.

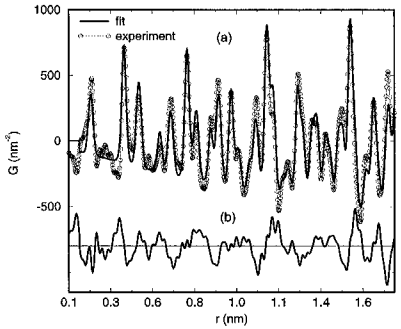


Figure 2.

Anomalous X-Ray Scattering Studies of Supermolecules and Aggregates in Organic Solution	X7A

L. Chen, Q. Zhu, W. Svec, D. Price, M. Wasielewski (ANL)

Anomalous X-ray scattering (AXS) study has been conducted on a covalently linked modified chlorophyll dimer, and its corresponding monomer with zinc as the central metal ions. The molecule under AXS studies is a chlorophyll dimer cyclophane, where two covalent linkages connect two macrocycles side-by-side. The ester linkages will make the two chlorophyll rings to fold into a "clam shell" like conformation. Our AXS experiment intends to probe the metal-metal distance in this "clam shell" like molecule in solid and in solution. Based on a preliminary molecular mechanical calculation, the metal-to-metal distance in bis-Zn-chlorophyllide cyclophane is 4.9 , a distance is beyond the probing range for EXAFS in disordered system. The coordination number of the metal ions is also an important structural factor in predicting the function of the molecule. We have found temperature dependence of the coordination state in these cyclophanes by EXAFS experiment, where the ligands bind to the metal at temperature below 200K, but not at room temperature. The coordination of the ligands requires the "clam shell" to open up, thus this is related also to metal-to-metal distance in the molecules. The covalently linked chlorophylls function as either electron donor or acceptor. The electron transport processes in these supermolecules are normally triggered by light. Thus, these supermolecules have potential applications as molecular devices. Structural parameters of these supermolecules are very important information in predicting their electron transfer properties. We have obtained AXS data for powder and solution of the dimer as well as the corresponding monomer. Significant differences in the spectral features have been observed between the dimer and monomer. However, in order to obtain Zn-Zn distance in this molecule, a correct method of background subtraction and data normalization is very crucial. We are in a process of completing the analysis of the AXS data.

The Nature of Structural Defects in C15 $NbCr_2$ and $Nb(Cr,V)_2$ Studied by Synchrotron X-Ray Powder Diffraction	X7A

F. Chu (LANL), Q. Zhu (BNL), D. J. Thoma, and T. E. Mitchell (LANL)

$NbCr_2$-based C15 Laves phases are promising high temperature structural materials. Physical metallurgy and mechanical behaviors of the Laves phases are subjects of extensive investigations. In this work, the structural and defect characteristics of C15 $NbCr_2$ and its vanadium alloys have been studied using high-resolution synchrotron x-ray powder diffraction at X7A beamline of NSLS. Contrary to common belief, Rietveld refinement indicated that extra Nb atoms occupy Cr site in a Nb-rich binary system and a formation of vacancies on Nb site in a Cr-rich phase, and it also revealed that V atoms occupy Cr sites in the ternary alloys. These results are inconsistent with the atomic size rule for the formation and stabilization of Laves phases. The alloying behavior and the defect structures/mechanisms in both binary and ternary $NbCr_2$-based Laves phases are better understood in terms of the electronic structure of C15 $NbCr_2$, calculated using the linear muffin tin orbital (LMTO) method. The total and l-D projected density of electronic states show that the valence electrons of C15 $NbCr_2$ fill the Fermi level in such a way that some anti-bonding d-states are occupied, the system is therefore energetically unfavorable. This allows Nb or V atoms to substitute Cr, which lowers the Fermi level and de-occupies the anti-bonding d-states, resulting in a more stable compounds. Our results suggest that the electronic structure of certain Laves phases, e.g. C15 $NbCr_2$, could determine its alloying behavior, although the atomic size rule plays a dominant role in most of the Laves alloys.

High Resolution Powder Diffraction at 0.5 Å *	X7A

D. E. Cox (BNL)

A series of experiments has been carried out during the past year to test the feasibility of routine data collection at a wavelength of 0.5 Å, in spite of the much lower photon flux compared to those in the working range of 0.7-1.8 Å~typically used at the beam-line. Although the counting rates are unacceptably low if crystal-analyzer geometry is used, high-quality data can be obtained in a few hours with the use of a multiwire linear position-sensitive detector filled with a mixture of 90% Kr/10% CO_2 operating in the escape-peak mode [1]. For well-crystallized samples loaded in narrow-diameter capillaries ($\approx$ 0.2-0.3 mm), peak widths from 0.03-0.05° are obtained over a wide angular range.

Under these conditions, systematic errors associated with preferred orientation, absorption and extinction are greatly reduced, resulting in more reliable and accurate structure refinements. Measurements can be made on highly absorbing materials containing heavy atoms such as Hg, Tl, Pb and Bi, which are constituents of many interesting electronic materials. One recent example is the giant magnetoresistive compound $Tl_2Mn_2O_7$, which is described in an accompanying abstract [2].

[1.] G. C. Smith. Synchrotron Radiation News 4, No. 3, 34 (1991). [2.] D. E. Cox, P. G. Radaelli, M. Marezio and S-W. Cheong, NSLS Annual Report (1996).

* Work supported by the Div. of Materials Sciences, US Dept. of Energy under contract DE-AC02-76CH00016.

Structural Studies of Giant Magnetoresistive $Tl_2Mn_2O_7$ * | X7A

D.E. Cox (BNL), P.G. Radaelli (ILL, Grenoble), M Marezio (MASPEC-CNR Parma), and S.-W. Cheong (Lucent Technologies)

Recently giant magnetoresistive (GMR) behavior has been reported in the pyrochlore-type compound $Tl_2Mn_2O_7$ [1,2], in which there is a simultaneous insulator-metal and paramagnetic-ferromagnetic transition at ≈140 K reminiscent of the GMR manganite perovkite systems. A powder diffraction study of $Tl_2Mn_2O_7$ was carried out over the temperature range 20-300 K. An extended data set was collected at 300 K from a sample sealed in a 0.4 mm diameter capillary. Because of the high absorption of Tl, a wavelength of 0.5003 Å was chosen so as to minimize systematic errors in the intensities, and a linear multiwire proportional detector filled with Kr at ≈4 bar and functioning in the escape-peak mode was used to ensure good counting statistics. The sample was transferred to a cryostat, and scans performed over selected angular regions between 20-300 K in order to determine the lattice parameters and check for possible anomalies or symmetry changes at the paramagnetic-ferromagnetic transition analogous to those previously observed for the (La,Ca)MnO_3 system [3]. For these measurements a Ge (220) crystal-analyzer was used to improve the resolution, and a wavelength of 0.9999 Å (slightly below the Tl L_{III} edge) was chosen so that acceptable counting statistics were obtained.

At 300 K the $Tl_2Mn_2O_7$ pattern could be indexed on the basis of a face-centered cubic unit cell (a = 9.8948 Å). Rietveld refinement gave results which were in good agreement with those recently reported by Subramanian and co-authors [4], i.e. Tl: U_{11} = 0.0053(1) Å^2, U_{12} = -0.0017(2) Å^2; Mn: U = 0.0016(2) Å^2; O(1): U = 0.002(2) Å^2; O(2): x = 0.3266(9), U = 0.003(2) Å^2. However, attempts to determine the stoichiometry of the compound by refinement of the oxygen occupancy factors yielded inconclusive results; overall values of 6.6(1) or 7.4(1) were obtained depending on whether scattering factors for O^{2-} or neutral O were used. Thus we cannot rule out the possibility of a few percent of vacancies on the O(2) sites.

In contrast to the behavior found for the (La,Ca)MnO_3 system , the lattice parameter measurements showed no evidence of any anomalies or discontinuities at the insulator-metal transition at 120 K, nor any peak broadening suggestive of a lowering of the lattice symmetry.

[1.] Y. Shimakawa, Y. Kubo and T. Manako. Nature **379**, 53 (1996). [2.] S-W. Cheong, H. Y. Hwang, B. Batlogg and L. W. Rupp, Jr. Solid State Commun. **98**, 163 (1996). [3.] P. G. Radaelli, D. E. Cox, M. Marezio, S-W. Cheong, P. E. Schiffer and A. P. Ramirez. Phys. Rev. Lett. **75**, 4488 (1995). [4.] M. A. Subramanian, B. H. Toby, A. P. Ramirez, W. J. Marshall, A. W. Sleight and G. H. Kwei. Science **273**, 81 (1996).

* Work supported by the Div. of Materials Sciences, US Dept. of Energy under contract DE-AC02-76CH00016.

Interfacial Roughness of Fe-CR GMR Superlattices | X7A

W. Dmowski and T. Egami (U. of Pennsylvania)

Fe-Cr superlattices exhibit giant magneto-resistance (GMR) effect which depends strongly on the preparation conditions. The x-ray reflectivity measurements show that with an increasing Ar pressure, the superlattice Bragg peaks become broad, their intensity decreased and the higher order finite size peaks strongly attenuated. Sputtering at an increased Ar pressure could cause atomic intermixing at the interface, change roughness at length scale comparable to electron mean free path and longer, affecting the magnetization process. To determine the more precise nature of the interface roughness in Fe-Cr multilayers we have studied both specular and off-specular x-ray scattering from several Fe-Cr multilayers produced by sputtering under different Ar pressures. We have measured [Fe(30Å)/Cr(12Å)]$_{10}$ superlattices which had been sputter-deposited in 4,5,6,7,8,9,10,11 and 12 mTorr of Ar. We used a position sensitive detector placed in the horizontal position to collect simultaneously the specular scattering intensity along O_z (z-component of the scattering vector Q being perpendicular to the film) as well as the off-specular intensity along Q_y which is in the plane of the sample and perpendicular to the incoming beam. To analyze interface roughness in these three samples we obtained a 2 dimensional Fourier transformation (2DFT) of the intensity distribution in the Q_z-Q_y plane, I(r), and the height-height fluctuation function g(r). Significant difference is observed between specular and integrated intensities indicating large contribution of off-specular intensity to the total signal. We found that the interface roughness for the 4 mTorr sample is almost conformal (correlated roughness) while for the other roughness is uncorrelated from layer to layer. We observed changes at three different length scales at the interface with an increasing Ar pressure. At long separations interface is rougher at a higher Ar pressure. Interface roughness at this length scale is very likely to affect magnetization process. From our data it is clear that short range roughness becomes smaller with a higher Ar pressure. At the same time there is more intermixing at the interface. This suggests that the changes at the interface at short lengths are responsible for the observed increase in the MR effect

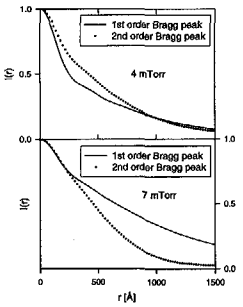


Figure 1. Height-height fluctuation function g(r) for 4 and 7 mTorr samples at the second order Bragg reflection.

Ultra-thin CeO_2 Overlayer on YSZ Studied by X-ray Surface Scattering | X7A

W. Dmowski and T. Egami (U. Pennsylvania)

Ceria is an essential component as a catalyst support in three-way automotive catalytic converter due to its capability of storing oxygen under oxidizing and releasing oxygen under reducing conditions. It is not well understood why this particular mixture of oxides can achieve the role as a oxygen buffer and why its lifetime is limited. In order to address this issue and to understand the structural interplay at the ceria/zirconia interface, we studied the atomic structure of ultra-thin ceria layers deposited on single crystals of (001) oriented Y-stabilized zirconia (YSZ), in situ, during annealing in air using the synchrotron x-ray surface diffraction technique. We applied, for the first time, the energy dispersive mode of x-ray diffraction in the surface scattering experiment [1]. Our experimental geometry was typical for the surface scattering study, with the scattering vector nearly in the plane of the sample. The samples were placed on a heater and were annealed in air during the x-ray scattering measurement to observe structural changes with temperature. Our study shows that a CeO_2 epitaxial overlayer can easily be formed on a Y stabilized cubic zirconia by simple oxidation of Ce metal layer deposited on the surface. The lattice constant mismatch most likely induces formation of contiguous ceria islands. This microstructure of ceria may be important for catalytic function of ceria/zirconia interface. In-situ studies of a deposited cerium metal layer show the following evolution with temperature:

- Crystallization of ceria starts at 420°C.
- At 520°C crystallization is completed and interface is modified.
- At 620°C preferential growth of some ceria grains occurs.
- At 720°C cerium diffuses into the bulk.

[1.] W. Dmowski, T. Egami, R. Gorte and J. Vohs, Physica B, 221 (1996) 420.

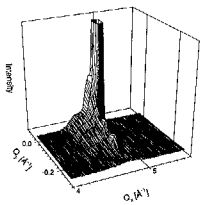


Figure 1. Ce/YSZ at 520°C. Diffraction shows a part of a (400) zirconia rod. The ridge at $Q_x = 4.6\text{Å}^{-1}$ represents scattering from the ceria film.

High Pressure Diffraction Studies of Mercury-Based Superconductors | X7A

J. A. Hriljac, I. Gameson, A. Asab and P. P. Edwards (U. of Birmingham, UK)

Continuing interest in High Temperature Superconductors is fueled, in part, by the discovery of new families of materials with even higher values of T_c. One of the most recent examples [1] is the homologous family of Hg based systems of formula $HgBa_2Ca_{n-1}Cu_nO_{2n+2+d}$, and denoted as Hg-1201, Hg-1212 and Hg-1223 for n = 1, 2 and 3, respectively. The latter material, Hg-1223, has a T_c of 135 K which is the highest yet reported at ambient pressure.

A common feature of nearly all High T_c superconductors is that T_c's increase under pressure, typically by 1-2 K/GPa. The mercury systems are no exception, with reported values of dT_c/dP of 1.75, 1 and 1.7-1.8 K/GPa for n = 1,2 and 3, respectively [2,3]. The structural changes as a function of pressure, however, have not been thoroughly investigated. In the work of Hunter *et al.*[4], the crystal structures of the Hg-1201 and Hg-1212 systems were only investigated to 0.6 GPa, while the Hg-1223 system was studied to 9.2 GPa. In all cases only ambient temperature data was reported. In order to further elucidate the structural changes of the Hg systems under pressure, we have started a programme of high resolution X-ray powder diffraction studies of these systems at beamline X7A at both ambient and low temperatures.

In the first set of experiments, only the Hg-1201 system (Fig 1) was investigated. Samples were loaded in diamond anvil cells with a mixture of methanol/ethanol as a pressure-transmitting medium. In addition, several small ruby chips were included for pressure calibration. Data sets were collected at ambient temperature to pressures of 6.74 GPa, and also from room temperature to 15 K at pressures of 2.9 and 6.2 GPa. The data analysis has so far consisted of measuring accurate lattice parameters for the ambient temperature data, Fig. 2. From this data we have determined the compressibilites along the *a*-axis, $3.37\text{x}10^{-3}$ GPa^{-1}, *c*-axis, $5.69\text{x}10^{-3}$ GPa^{-1}, and bulk modulus, 82.7 GPa. The compressibilities compare well with the earlier work of Hunter et al., whereas the bulk modulus is greater than their value (69.9) and much closer to that found for the other systems. Further analysis of all of the data is in progress. **References** [1] S. N. Putilin *et al.*, *Nature* **362**, 226 (1993). [2] A. Klehe *et al.*, *Physica C* **213**, 266 (1992). [3] C. W. Chu, Physics and Chemistry of Molecular and Oxide Superconductors (1993). [4] B. A. Hunter *et al.*, *Physica C* **221**, 1 (1994).

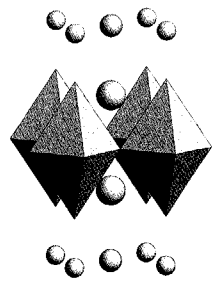


Figure 1. Hg-1201 System Structure

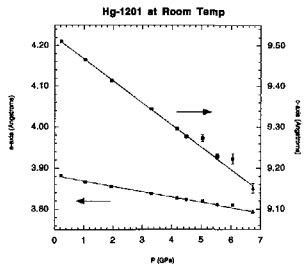


Figure 2. Lattice Constants as a Function of Pressure.

Structural Studies of Bismuth Tin Oxides | X7A

B.J. Kennedy (The U. of Sydney)

As part of a wider study of the structural and electronic properties of pyrochlore type metal oxides we have investigated the structure of the high temperature cubic form of $Bi_2Sn_2O_7$. Diffraction data were collected at room temperature and at 650 C using synchrotron x-ray diffraction at the X7A beamline at the NSLS and high resolution neutron diffraction at the HRPD at ANSTOs HIFAR reactor. The synchrotron data were collected using a flat-plate geometry at 0.78Åwith a Si(111) channel-cut monochromator and a Ge(200) analyser. The reflections were indexed on a supercell with a = 21.4582Å. Initial attempts to refine the synchrotron data alone demonstrated the Bi atoms were significantly displaced, presumably as a consequence of the presence of the Bi 6s lone pair electrons. However, these refinements were relatively unstable with respect to the positional and thermal parameters of the lighter O atoms. Consequently the structure was refined using the Rietveld method in the cubic space group F-43c in a combined x-ray/neutron refinement using the local Rietveld program LHPM. This refinement, whilst still in not complete reveals distortions in both the BiO_8 and SnO_6 polyhedra. Efforts to solve the room temperature structure are in progress.

Phase Characterization in Rapidly-Solidified Magnetic Materials * | X7A

L.H. Lewis (BNL - DAS), C.H. Sellers (INEL) and V. Panchanathan (Magnequench International)

Rapid solidification has been used as a synthesis route for the production of advanced permanent magnet materials based on the intermetallic composition $RE_2Fe_{14}B$ (2-14-1), where R is a rare-earth element such as Nd, Dy or Pr. The quench rate of the melt, in the range 10^4-10^6 K/sec depending on solidification method, produces in the solid a nanoscale, multi-phase, non-equilibrium microstructure that is difficult to characterize by conventional laboratory x-ray diffraction methods. An advantage of utilizing synchrotron radiation to probe these materials is that the excitation of iron fluorescense by $Cu_{K\alpha}$ radiation is avoided, and thus characteristics such as degree of crystallinity and minor phase content may be more clearly observed.

Synchrotron powder x-ray diffraction has been performed using radiation wavelengths in the range $0.9\mathring{A} \leq \lambda \leq 1.2\mathring{A}$ to examine the degree of crystallinity, lattice parameters, and minor phases present in a selection of rapidly-solidified $RE_2Fe_{14}B$-based materials. Research highlights are presented below:

1). It has been verified that the addition of the specific elements Ti and C to the compound $Nd_2Fe_{14}B$ prior to rapid solidification by inert gas atomization increases the glass-forming range of the 2-14-1 melt such that a large fraction of the as-quenched product possesses an amorphous or nanocrystalline structure. Since an increased proportion of the TiC-modified 2-14-1 powders exist in an overquenched (i.e., amorphous) state, relative to the unmodified powders, their magnetic properties may be more successfully optimized by brief annealing treatments.

2). Unlike the compound $Nd_2Fe_{14}B$, the isostructural compound $Pr_2Fe_{14}B$ holds promise as a permanent magnet material for low-temperature applications due to its lack of spin reorientation, during which the easy axis of magnetization gradually changes crystallographic direction in the vicinity of a specific temperature. In order to investigate the low-temperature magnetic properties, solid solutions of $(Nd_{1-x}Pr_x)_2Fe_{14}B$ were synthesized and their stoichimetry was verified by measurements of the lattice parameters.

3). The next generation of permanent magnets may be a magnetic nanocomposite comprised of a hard-magnet phase intimately combined with a soft-magnetic phase of high saturation magnetization, known as an "exchange-spring" magnet. X-ray diffraction was used to examine the nature of the phases that comprise a series of nanocomposite magnets consisting of the 2-14-1 compound and α-Fe. Preliminary results illustrate that each broad peaks constituting the α-Fe Bragg reflections actually contains two peaks, indicating that the phase may possess a shell of material of atomically-expanded material that contains Nd or B. Such an intermediate phase is expected to have important consequences with regards to the interphase exchange coupling and magnetic reversal.

* Research performed under the auspices of the USDOE, Division of Materials Sciences, Office of BES under Contract DE-AC02-76CH00016.

Investigation of Structural Changes in High-Temperature Treated Zeolite CaA	X7A

H. Meyer zu Altenschildesche, Y. Huang, G.T. Kokotailo, C.A. Fyfe (UBC, Vancouver), and D. Cox (BNL)

Knowledge of the thermochemical properties of zeolites is important for a variety of industrial applications. For example, most catalytic processes involving zeolites require elevated temperatures and the thermal stability of the catalysts is one of the major factors determining the efficiency of the processes. Another interesting application is the use as precursors for the manufacturing of dense aluminosilicate ceramics, since zeolites provide a homogeneous mixture of the oxides on an atomic scale. Thus diffusion processes are greatly simplified and the synthesis of a particular ceramic can often be achieved at significantly reduced temperatures.

We have investigated fully Ca^{2+}-exchanged zeolite A as part of a larger program to determine the framework stability as a function of cation content. When zeolite CaA is heated in air, a series of structural changes occur at temperatures of approx. 200°C, 810°C, and 850°C, respectively. As can be concluded from additional TGA- and DTA-analyses, most of the zeolitic water is lost between 100 and 200°C. At temperatures above 850°C zeolite CaA finally becomes x-ray amorphous. When zeolite CaA is heated to 810-850°C for 24-48h, its properties change drastically. The most striking feature is the complete loss of microporous adsorption capacity. Moreover, the intensities in the x-ray diffraction pattern are strongly affected with the relative intensity of the hkl=200 reflection in particular being drastically increased with respect to all others.

A Rietveld analysis of synchrotron diffraction data together with scanning electron micrographs revealed that the high-temperature treated material retains the zeolite A structure but becomes amorphous at these temperatures in a very slow process (days-weeks). The transformation to an amorphous phase starts on the outer surface of the individual crystallites and proceeds slowly inward. Moreover, angle-dependent broadening of Bragg reflections indicates that a significant amount of strain is introduced by heating the sample to temperatures above 800°C.

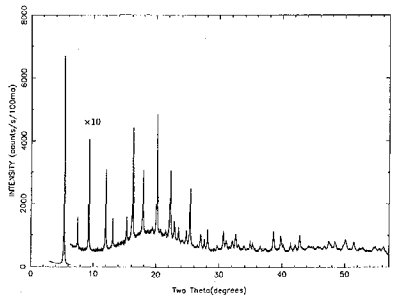


Figure 1. Powder diffraction pattern of CaA treated for 48 hours at 825°C.

Structural Study of the Layered Aluminophosphate Material NH_4-Taranakite	X7A

H. Meyer zu Altenschildesche, G.T. Kokotailo, C.A. Fyfe (UBC, Vancouver), W. Schwieger (Universität Halle), and D. Cox (BNL - Physics)

Taranakite [1] is a mineral with idealized chemical composition $H_6M_3Al_5(PO_4)_8 \cdot 18\ H_2O$ (M = K, NH_4) which can be synthesized under similar conditions as framework $AlPO_4$s. Though the structure of Taranakite is unknown, there is strong evidence that it is not a framework aluminophosphate but a layered material. The interlayer recognition, i.e. the ordering, of the NH_4^+-form is very high giving sharp reflections up to high angles (Figure 1). Moreover, crystallization occurs easily even at ambient temperatures and it has previously been suggested that Taranakite might form on contact of phosphate fertilizers with Al-rich clays [2]. On heating, the material first looses part of the interlayer water forming its lower hydrate Francoanellite. At temperatures between 100°C and 500°C gradually all the water, ammonia, and hydoxyl groups are lost and the material becomes x-ray amorphous. However, dense phases are formed only at temperatures well above 500°C. These properties make Taranakite an interesting candidate for pillaring and as a catalyst support.

The high-resolution x-ray powder pattern was successfully indexed with $a = 8.729$Å, $b = 95.039$Å, and space group $R3c$ or $R\bar{3}c$. The diffraction intensities were extracted using the LeBail method. The application of direct methods together with results from elemental analyses and solid state NMR experiments led to a partial determination of the layer structure. Rietveld refinement together with difference Fourier methods will be used to complete the structure determination.

[1] S. Fiore and R. Laviano, *Am. Miner.*, 1991, **76**, 1722-1727.
[2] W.F. Bleam, Ph.E. Pfeffer, and J.S. Frye, *Chem. Minerals*, 1989, **16**, 809-816.

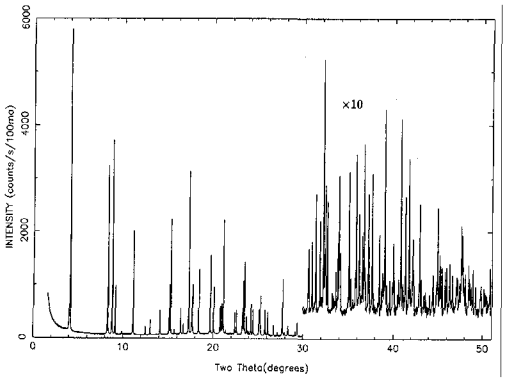


Figure 1. Powder diffraction pattern of synthetic NH_4-Taranakite showing the extremely high ordering of this layered aluminophosphate material.

High Pressure Synthesis and Structural Refinement of the New Double Perovskite Ca_2TiSiO_6	X7A

J. B. Parise (SUNY Stony Brook) and K. Leinenweber (ASU)

Double perovskites form a large family of materials whose structures are made up of a framework of corner-linked octahedra similar to that of ABO_3 perovskites, but with the B cations ordered onto two distinct octahedral sites. This leads to the stoichiometry $A_2B'B''O_6$ with the B' and B" cations forming a face-centered array like that of Na and Cl in rocksalt. The ordering of the B cations leads ideally to a reduction in symmetry from *Pm3m* with cell parameter a (ABO_3 perovskite), to an *Fm3m* cell with cell parameter 2a ($A_2B'B''O_6$ perovskite). A further reduction in symmetry to $P2_1/c$, due to rotations of octahedra in the framework, is also common. The structure of the *Fm3m* double perovskite is specified by 2 parameters, the unit cell parameter *a* and an oxygen position parameter which sets the sizes of the two different octahedra.

The double perovskite Ca_2TiSiO_6, which can be recovered to ambient by quenching from high pressure-high temperature conditions (Leinenweber et al., in prep), is midway along the join between $CaTiO_3$ and $CaSiO_3$. This material is the first of the ordered double perovskites compounds to be found with silicon as one of the octahedral cations.

Data, collected in high resolution mode using a Si(111)/Ge(220) channel-cut monochromator/crystal analyzer combination (λ=1.15032(2)Å)) confirmed the earlier observation of a powder diffraction pattern dominated by reflections indexed on the basis of a primitive cubic unit cell with a ~3.7Å. There was no obvious splitting of these peaks to indicate a symmetry lower than isometric. The weaker superlattice reflections consistent with the doubled F-centered cubic cell were also clearly present. The peak widths of the ordering reflections were consistent with those of the primitive reflections, indicating that both sets of peaks can be assigned to a single phase. Rietveld refinement of a starting model with Ca, Ti, Si and O ordered into positions 8*c*, 4*b*, 4*a* and 24*e* of *Fm3m* lead to convergence with the following results: oxygen at 0.2372(4),0,0; Ca-O (2.6217(1)Å), Ti-O (1.947(3)Å) and Si-O (1.758(3)Å)

Structural Characterization of A Novel Open Framework $[(C_8H_{20}N][AgGe_2S_5]$ (TEA-AgGS-SB1)	X7A

J.B. Parise (SUNY Stony Brook) and K. Leinenweber (ASU Tempe)

Open frameworks consisting of corner linked polyhedral elements are capable of occluding organic molecules and so are of interest for their potential as selective agents for molecular sieving, catalysis, ion exchange and ion conduction. The most common of these frameworks are the aluminosilicates. However, the range of materials capable of forming open frameworks has increased greatly over the past decade. For example, following their description by Krebs, synthetic routes to knit isolated tetrahedral Sn- and Ge-sulfide clusters into frameworks have been found. This was accomplished using two procedures: self-condensation of the clusters in the presence of organic amines and condensation from solution using transition metal ions along with the organic amines. There is evidence that both the organic amines and the transition metal act as structure directing agents. Hydrothermal titration, the injection of reagents to thermally activated precursor species, can lead to novel metastable materials. One such material is the title compound (**1**). The structure of **1** (Fig. 1) was determined[15] from data collected using a position sensitive detector at beamline X7A of the National Synchrotron Light Source (NSLS). A pattern suitable for Rietveld refinement was obtained by combining in 0.01° steps data from the central 2° of the detector, which was stepped at 0.25° intervals from 5 to 35° in 2θ. The starting model for Rietveld analysis, including the position of the $[TEA]^+$ ion, was taken from the single crystal structure analysis of TEA-CuGS-SB1. The Ag compound is isostructural with this material with $[Ge_4S_{10}]^{4-}$ clusters linked to form a three dimensional framework (Fig. 1). The position of the organic template, which was refined using soft constraints, is similar in the structures of both Cu and AgGS-SB1.

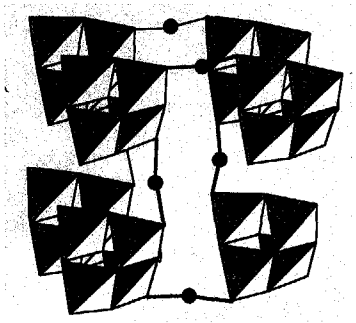


Figure 1. Tetrahedral clusters of $[Ge_4S_{10}]^{4-}$ anions joined by two-coordinated Ag^+ ions (solid circles) in the structure of **1**. For the sake of clarity the $[TEA]^+$ ions occupying the cavities within the structure are omitted.

Synthesis and Structure of a Novel Aurate: $CdAu_2O_4$. — X7A

J.-H. Park and J.B. Parise (SUNY Stony Brook)

Because of its high electron affinity the stability of gold oxide is expected to be low. Indeed Au_2O_3 decomposes to metallic gold below 250°C, well below the temperature required to activate most solid state reactions. However the application of pressure can stabilize the oxide to temperatures where reaction can occur. This strategy has been used to produce a new aurate, $CdAu_2O_4$ by solid-state reaction of $Cd(OH)_2$ and Au_2O_3 in a welded gold capsule at 12GPa and 1000°C using a uniaxial split-sphere high-pressure apparatus (USSA 2000) at Stony Brook. Preliminary diffraction patterns indicated this material is isostructural with $CaAu_2O_4$. Because of the small quantity of material available from high pressure experiments above 10Gpa, Synchrotron X-ray powder diffraction data were collected from a sample sealed in a 0.17 mm diameter glass capillary using the position sensitive detector (PSD) and a wavelength of 0.642803(1) Å at X7A. Two theta diffraction angles from 6° to 65 ° were scanned through step intervals of 0.25° with a counting time of 30 sec. per step. The central 2 degree portion of the linear PSD at each of the 0.25 degree steps were combined to produce a pattern with 0.01 degree resolution. The sample capillary was rotated in order to obtain better powder averaging. The correction to the Debye-Waller factor (ΔB=0.69 Å^2) was estimated. All peaks could be indexed on the basis of a tetragonal cell ($I4_1/a$, a = 5.90644(1), c = 10.03859 (3) Å and Z = 4). The structure of $CdAu_2O_4$ and consists of corner-linked AuO_4 square planes and distorted CdO_8 dodecahedra. The smaller ionic radius and greater electronegativity of Cd compared with Ca causes a distortion from ideal AuO_4 square planes.

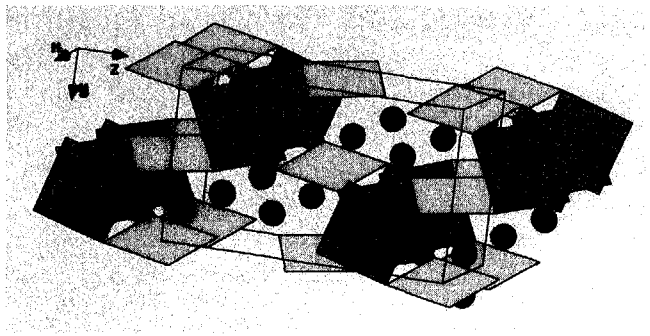


Figure 1. Projection of the structure of $CdAu_2O_4$ along [100]. The Cd ions are represented by the planes and circles.

Powder Diffraction Study of the Orientational Order of the Ammonium - Tetrahedra in NH_4Cl and ND_4Cl — X7A

W. Press, B. Asmussen, H. Krull, O. Seeck (U. of Kiel, Germany), D. Cox, Q. Zhu (BNL)

Ammoniumchloride crystals undergo an Ising–like order–disorder phase transition which displays a pronounced isotope effect. NH_4Cl shows a first order transition at T_c = 242.0K, whereas in ND_4Cl the transition is nearly second order and at T_c = 248.8K. In both cases the symmetry group for the high temperature phase is Pm3m (tetrahedra are disordered with two possible orientations) and for the low temperature phase $P\bar{4}3m$ (tetrahedras are 'ferro'–ordered). For reflections hkl with all indices different a calculation of the x-ray structure factor in both phases predicts a change of intensity in the range of 2%. As the unit cell does not change no superlattice reflections appear.

For both materials powder diffraction measurements have been performed at several temperatures above and below T_c. We used a wavelength of λ = 0.7007Å and got about 45 powder reflections in a range of wavevector transfer q up to 12Å^{-1}. A LeBail–fitting procedure has been used to extract the intensities of the measured reflections. The structure factor depends on the Cl^-–form factor (International Tables) and the NH_4^+/ND_4^+–form factor. The latter one has been calculated by a linear combination of atomic orbitals which allows to fit d_X, the distance N↔H/N↔D, and the electron localisation near the nitrogen atom.

As a result we get the Debye–Waller displacement of the Cl^-–ion as well as that of the ammonium tetrahedron. All fits show a distance d_X of about 1.05Å and a slightly increased electron density near the nitrogen atom. It is not possible to extract reliable information about the orientation of the ammonium tetrahedras up to now: the calculation seems to be too insensitive to this parameter. The best fit with an ND_4Cl data set is shown in figure 1. There an R–factor of 0.033 was reached. The analysis is still in progress.

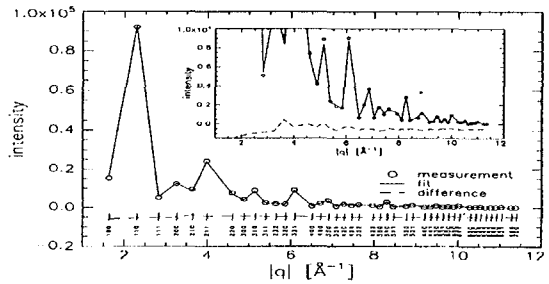


Figure 1. The structure refinement with the ND_4Cl data set at T=255 K. The inset shows a zoom of the main picture, scaled by a factor of 10.

Polymorphism of the Crystalline Low-Temperature Phases of t-Butyl Chloride * | X7A

R. Rudman, (Adelphi U.)

t-Butyl chloride (tBC) has a pseudo-spherical molecular envelope and forms an orientationally-disordered plastic crystalline phase (I) as it is cooled below its freezing point. It then forms a partially ordered phase (II) prior to forming the ordered phase (III). Previous attempts to determine the crystal structure of Phase III, were only partially successful. Recently, the study of tBC took on new relevancy for two reasons: Bartell and co-workers described a theoretically derived unit cell and crystal structure for Phase III and Ohtani and Hasabe, using DTA, reported a new phase, supposedly stable over a small 1.8K range (217.7 to 219.5K), between the known Phase I and II.

In this study the tetragonal Phase II (110) reflection and the fcc Phase I (111) reflection occur within 0.1° 2θ of each other near the I-II transition temperature, at the wavelength used. Powder data were collected approximately every 0.3K between 215K and 220K, as well as at selected temperatures up to 235K. The Phase II-(110) reflection intensities decreased as the temperature increased and the Phase I-(111) reflection appeared at 217K, from which point it increased in intensity as the Phase II-(110) intensity continued to decrease. This significant, easily discernible pretransition activity, as tetragonal Phase II transformed to fcc Phase I, reveals that the phase transition is not a concerted sudden change in crystal structure but a gradual growth of Phase I accompanied by a loss of Phase II. It is possible to have both phases exist simultaneously, at least during the timeframe of this investigation. Since these observations also account for the anomalous peaks in the DTA thermogram, it is concluded that no new crystalline phase is formed between 217.7K and 219.5K. These results agree with Ubbelohde's description of a heterophase pretransition effect wherein two crystalline phases coexist over a small temperature region.

Unfortunately, the several sets of powder data we collected at 15K, for the monoclinic Phase III of tBC, showed the presence of severe large crystallite formation so that it was not possible to refine the crystal structure using Rietveld analysis. Further work using a cryostat in which the sample is rapidly cooled is in progress.

* The assistance of David Cox and Qing Zhu (BNL - Physics) is greatly appreciated.

Structure and Thermal Behavior of Fullerene Derivatives * | X7A

M. R. Stetzer, P. A. Heiney, A. R. McGhie, J. E. Fischer, R. M. Strongin, B. M. Brandt, A. B. Smith III (U. of Pennsylvania), P. W. Stephens, R. E. Dinnebier, G. Bendele (SUNY Stony Brook), and Q. Zhu (BNL - Physics)

We have performed x-ray powder diffraction (XRPD) measurements using a position sensitive detector (PSD) in order to study the solid-state structures and thermal behavior of $C_{61}H_2$ cyclopropane and $C_{63}H_6$ cyclopropane. At room temperature, the $C_{61}H_2$ cyclopropane molecules are orientationally disordered in a face-centered cubic lattice as is observed in the 6,5-annulene isomer. Unlike the annulene isomer of $C_{61}H_2$, the low-temperature orientationally ordered phase of the cyclopropane isomer appears to be face-centered orthorhombic with lattice parameters of 13.97 Å, 14.00 Å, and 14.25 Å, although there may be a slight monoclinic distortion of this orthorhombic cell. In addition, as differential scanning calorimetry (DSC) studies have revealed the presence of two ordering transitions centered around 213 K and separated by ~10 K, we have carefully measured the XRPD as a function of temperature in the vicinity of these transitions in an attempt to identify the intermediate phase.

XRPD studies of $C_{63}H_6$ cyclopropane, a "larger" cyclopropane in which the two hydrogens of $C_{61}H_2$ have been replaced by methyl groups, indicate that this material is orientationally ordered at all temperatures that fall within the stability regime of the molecule itself. Patterns were collected at temperatures ranging from 20 K to 413 K, and the decomposition of the $C_{63}H_6$ molecules manifested itself in a sudden intensity decrease which was first observed in the 413 K pattern and remained even when the sample was cooled back down to room temperature. Preliminary attempts at indexing our room temperature data suggest that the ordered structure possesses tetragonal symmetry with a = 16.19 Å and c = 11.39 Å, although this indexing scheme leaves three weak peaks of anomalous widths unindexed.

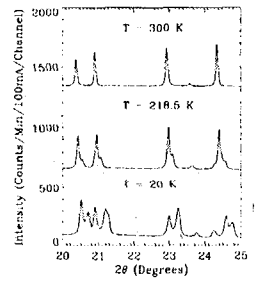


Figure 1. A selected portion of the x-ray powder diffraction patterns for the three phases of $C_{61}H_2$ cyclopropane. The patterns are offset for clarity.

* This work supported in part by NSF Grant DMR-MRL-92-20668; acknowledgment is made to Donors of Petroleum Research Fund, administered by American Chemical Society, for partial support of this research.

Phase Transitions and Thermal Expansion in Oxides at Low and High Temperatures — X7A

P.M. Woodward, J.S.O. Evans, A.W. Sleight (Oregon State U.)

The recent descovery of negative thermal expansion in ZrW_2O_8 from 0.3K to 1050K has sparked great interest in compounds which show negative or zero thermal expansion. Compounds in the family $A_2(WO_4)_3$ have framework structures which suggest they may also display negative thermal expansion. Dilatometer studies of $Al_2(WO_4)_3$ and $Al_{1.6}In_{0.4}(WO_4)_3$ indicate that these compounds show negative and essentially zero volume thermal expansion respectively. However, because these compounds are orthorhombic rather than cubic, no detailed information about the anisotropy of the thermal expansion behavior can be obtained from dilatometer data. Furthermore, even for volume thermal expansion, preferred orientation effects can result in misleading and inaccurate results. Therefore, the unit cell constants for these two materials were determined as a function of temperature from 300 to 800K. $Al_2(WO_4)_3$ was found to have a small positive coefficient of thermal expansion, $\alpha_l = 2.3x10^{-6}$ K^{-1}. The expansion was almost entirely along the b axis. The other two cell dimensions, a and c, showed practically no change over the same temperature interval. $Al_{1.6}In_{0.4}(WO_4)_3$ showed the same trends with slightly increased expansion in all three directions. Its coefficient of thermal expansion was $5.4x10^{-6}$ K^{-1}.

Tungsten trioxide has at least five stable phases between absolute zero and its melting point. The low temperature phase, ϵ-WO_3 is reported to exist below approximately 220K. At this temperature WO_3 is reported to transform from the low temperature monoclinic form to the triclinic δ-WO_3 form. High resolution neutron diffraction data was collected at the HRNPD at BNL which has been used to refine the structure of WO_3 at low temperatures (<150K). One unusual feature of the data was the presence of δ-WO_3 below the phase transition, even at 15K. High resolution synchrotron data was collected at 20K and 50K to validate the results of the neutron diffraction data, and to obtain more accurate tungsten positional parameters. Unfortunately, texture effects made the data unreliable for structural refinements. However, the synchrotron data did confirm the monoclinic symmetry (a=0.5278 nm, b=0.5156 nm, c=0.7664 nm, β=91.762°, space group=Pc) and the presence of δ-WO_3 (or a very similar phase). MgO has long been a primary choice as a substrate for the growth of cuprate based high temperature superconducting thin films, due to its low cost and availability as large single crystals. However, the lattice mismatch with YBCO is large and furthermore, the MgO surface degrades upon exposure to water vapor. For these reasons there is much interest in finding alternative substrate crystals which have a better lattice match to YBCO and preferably cubic symmetry from operating temperature (77K) to growth temperature (900K). The need for cubic symmetry and the absence of phase transitions over this temperature range are necessary to prevent formation of grain and twin boundaries, which are deleterious to the superconducting device performance. $La_{1-x}Sr_xAlO_{3-y}$ crystals have been reported as cubic, and provide a good lattice match with YBCO. A powdered sample of this compound, with x=0.25, has been measured at room temperature and 15K. No evidence of line splitting, indicative of a lower symmetry stucture, was observed at either temperature. These findings suggest that this material may be an effective alternative to MgO as a substrate for high temperature superconducting thin films.

CO3 Location in Carbonate Apatite — X7A

R. A. Young (Georgia Institute of Technology)

With Prof. J. C. Elliott of London (UK), we are working on carbonate apatite. The long standing question is just how the CO3 is oriented when it substitutes for OH in hydroxyapatite, as it does to some extent in human tooth enamel and bone. In tooth enamel and most synthetic hydroxyapatite preparations, the CO3 is disordered among several possible sites. This has made a clear definition of its orientation and location impossible. However, some specimens have been prepared (with special methods) in which the CO3 is so well organized as to make the crystal symmetry monoclinic rather than the usual hexagonal (due to orientational disorder of the CO3). Since single crystals are not available, Rietveld structure refinement with x-ray and neutron powder diffraction data must be used. We have not been able to determine the CO3 orientation convincingly with, even, our first synchrotron (Daresbury) x-ray data on a specimen of a few mg. Neither has it been possible with a set of HRNPD (High Resolution Neutron Powder Diffractometer at BNL) data on a larger specimen which has a minor phase impurity. (It is very difficult to make a phase-pure specimen of sufficient size.) It was our intention to do a combined refinement with the X-ray and the neutron data, along with rigid body constraints, using the GSAS program.

With the GSAS Rietveld refinement program, we found that the differences between the two specimens, though small, are enough to vitiate this attempt to do combined refinement with the x-ray and neutron data sets on hand. Thanks to Dr. D. E. Cox, we then acquired a new set of synchrotron x-ray powder diffraction data (X-7A) on the same material on which we have the HRNPD data. We are working on the analyses and taking every opportunity to work physically together as well as by e-mail and FAX. Our progress is very slow. It is a difficult problem, even with the excellent data and analysis tools we have. There are 80 atoms in the unit cell besides the CO3 and no guarantee that the CO3 is in only one of the possible types of positions. The unit cell is, roughly, 10 by 20 by 7 A in space group P 1 b, so there are a great many reflections and almost none clearly resolved. It is a challenging problem. However, we are still optimistic that useful new information will result from our efforts.

The Crystal Structure of Beta-Eucryptite from 20 to 873 K: A High-Resolution Powder Synchrotron X-ray Diffraction Study	X7A

H. Xu, P. J. Heaney, and D. M. Yates (Princeton U.)

Beta-eucryptite ($LiAlSiO_4$), a stuffed derivative of the β-quartz structure, is of considerable interest because of its superionic conductivity and near-zero thermal expansion [1]. A number of crystal structure analyses of β-eucryptite [2-4] have demonstrated that its translational periodicity is doubled along **c** and **a** relative to the β-quartz structure. Further, high- temperature neutron [5-6] and X-ray [4,7] diffraction experiments reveal an order-disorder transition involving Li ions at about 740 K that is accompanied by a transient incommensurate phase.

We have examined structural variations in β-eucryptite by high- resolution powder synchrotron X-ray diffraction with the crystal-analyzer method from 20 to 873 K. Rietveld analysis shows that with increasing temperature the unit-cell parameter *a* increases while *c* decreases (Fig. 1A). The unit-cell volume decreases up to 523 K and increases thereafter (Fig. 1B). While the variation in unit-cell parameters above room temperature can be explained by the repulsion between Li and Si/Al in the **a-b** plane with a concomitant decrease in *c*, the low-temperature behavior is possibly due to distortions of $[SiO_4]$ and $[AlO_4]$ tetrahedra. Moreover, difference-Fourier electron-density maps reveal the localization of Li ions below room temperature and progressive positional disordering with increasing temperature above 298 K. At about 740 K, some Li electron-density maxima are distinctly split, raising the possibility that the incommensurate phase results from dynamical disorder of Li cations at this temperature.

[1] Palmer, D.C. (1994) in Heaney, Prewitt and Gibbs (ed.), Reviews in Mineralogy, 29, MSA, DC, 83-122. [2] Buerger, M.J. (1954) Am. Min., 39, 600-614. [3] Tscherry, V., Schultz, H., Laves, F. (1972) Z. Krist., 135, 161-198. [4] Pillars, W.W., Peacor D.R. (1973) Am. Min., 58, 681-690. [5] Guth, H., Heger, G. (1979) in Vashista, Mundy and Shenoy (ed.), Fast Ion Transport in Solids, Elsevier North Holland, New York, 499-502. [6] Press, W., Renker, B., Schultz, H., Bohm, H. (1980) Phy. Rev. B 21, 1250-1257. [7] Tscherry, V., Laves, F. (1970) Naturwissenschaften, 57, 194.

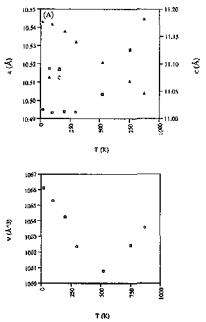


Figure 1. The dependence of (A) unit-cell parameters and (B) volume of β-eucryptite on temperature.

An Increase of Structural Order Parameter in Fe-Co-V Soft Magnetic Alloy after Thermal Aging	X7A

Q. Zhu (BNL-Physics)

Alloys of $Fe_{49}Co_{49}V_2$ (Hiperco^{TM} Alloy 50) both annealed and thermally aged, were studied using anomalous synchrotron x-ray at X7a beamline of NSLS and neutron powder diffraction. Rietveld and diffraction profile analysis indicated both an *increase* of the structural order parameter and a small lattice *expansion* ($\sim$ 0.0004 Å) after aging at 450 °C for 200 hours [1]. In addition, a cubic minority phase (<0.3%) was identified in the "annealed" sample, which increased noticeably (0.3% $\rightarrow$ 0.8%) as a result of aging. Primitive reflections exhibit shorter crystal coherence length than that of the fundamental peaks, indicating the presence of antiphase domain boundaries in the alloys. The subtle changes in structural order are attributed to vanadium and iron *interdiffusion* at elevated aging temperatures. These results directly correlate with the observed changes in the magnetization behavior and challenge the notion that a "fully" ordered Fe-Co alloy demonstrates optimum soft magnetic properties.

[1] Q. Zhu et. al. Appl. Phys. Lett. (in press).

An Increase of Structural Order Parameter in Fe-Co-V Soft Magnetic Alloy after Thermal Aging	X7A

Q. Zhu (BNL- Physics), L. Li, M. S. Masteller and G. J. Del Corso (Carpenter Technology Corp.)

Alloys of $Fe_{49}Co_{49}V_2$ (Hiperco^{TM} Alloy 50), both annealed and thermally aged, were studied using anomalous synchrotron x-ray and neutron powder diffraction. Rietveld and diffraction profile analysis indicated both an *increase* of the structural order parameter and a small lattice *expansion* ($\sim$ 0.0004 Å) after aging at 450 °C for 200 hours. In addition, a cubic minority phase (<0.3%) was identified in the "annealed" sample, which increased noticeably (0.3% $\rightarrow$ 0.8%) as a result of aging. The presence of antiphase domain boundaries in the alloys was also revealed. These results directly correlate with the observed changes in the magnetization behavior and challenge the notion that a lq lq fully" ordered Fe-Co alloy demonstrates optimum soft magnetic properties.

Control of Macromolecule Distribution Within Synthetic and Biogenic Single Calcite Crystals *	X7B

J. Aizenberg (Weizmann Institute), J.C. Hanson, T.F. Koetzle (BNL - Chemistry), S. Weiner and L. Addadi (Weizmann Institute)

The ability of organisms to exercise control over crystal growth is wonderfully exemplified by skeleton formation in echinoderms. A sea urchin spine is a unique composite of a single crystal of calcite and glycoproteins intercalated inside the crystal during its growth. Here we performed a detailed morphological and high-resolution synchrotron X-ray diffraction study of the textures of synthetic and biogenic calcite crystals. We show that the intracrystalline macromolecules from sea urchin spines, when allowed to interact with growing calcite crystals in vitro, selectively reduce the coherence lengths and degrees of alignment of the perfect domains in specific crystallographic directions. These directions also correspond to the newly-developed stable faces. In contrast, the defect distribution of young sea urchin spines composed entirely of spongy stereomic structure, is much more isotropic. In mature spines containing secondarily in-filled wedges of calcite, the degree of anisotropy is intermediate between the synthetic crystals and the young spines. The macromolecules extracted from young and mature spines are, however, very similar. These observations demonstrate the inherent capability of occluded matrix macromolecules to finely differentiate between crystal planes by stereochemical recognition processes. They also show that in biologically-produced calcite crystals this process can be overridden to produce a more isotropic material, due to sophisticated biological (cellular) control over the microenvironment of crystal growth. (Submitted to J. Am. Chem. Soc., August 1996)

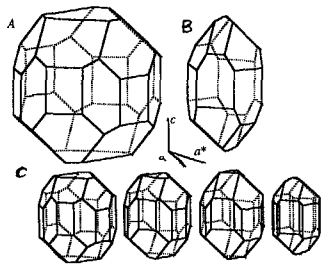


Figure 1. Average shapes of perfect domains of synthetic and biogenic calcite crystals. Coherence lengths, estimated from the diffraction peak widths, are used to define the distance between different crystallographic directions. the presence of intracrystalline proteins from reduced in the a* direction relative to c, indicating a specific protein crystal interaction. C- Sea urchin spi

* Contract DE-AC02-76CH00016 with US DOE, Div of Chem. Sci.,Office of BES and Binational Sci. Foundation.

High Temperature Phase Transformations of Tetraalkylammonium Tetrafluoroborates. *	X7B

J. Bager , F. Krebs Larsen (U. of Aarhus), T.M. Schultz (Risø, Denmark), P. Norby and J.C. Hanson (BNL - Chemistry).

Tetraalkylammonium tetrafluoroborates, R_4NBF_4, R = CH_3, C_2H_5, n-C_3H_7 and n-C_4H_9 show interesting thermal transformation behaviour with both low-temperature and high temperature phase transformations(1,2). The crystal structures are known only for the methyl and ethyl compounds (room temperature refs. 3,4, low temperature ref 2). Static and dynamic order/disorder arrangements can be expected for both anions and cations in the structures. In order to characterize the high temperature phase transformations a powder diffraction study has been initiated. All compounds undergo one or more phase transitions between room temperature and the melting point. An intermediate high temperature phase, appearing only upon cooling, was observed for tetrabutylammonium tetrafluoroborate. Analysis of the powder diffraction data is in progress.

1. G. Zabinska, P. Ferloni, M. Sanesi Thermochimica Acta, 122 (1987) 87-94.
2. Thomas M. Schultz, Dissertation, Aarhus University 1996.
3. G. Giuseppetti, F. Mazzi, C. Tadini, P. Ferloni, S. Torre Zeitschrift Kristallogr., 202 (1992) 81-88.
4. G. Giuseppetti, C. Tadini, P. Ferloni, G. Zabinska, S. Torre Zeitschrift Kristallogr., 209 (1992) 509-511.

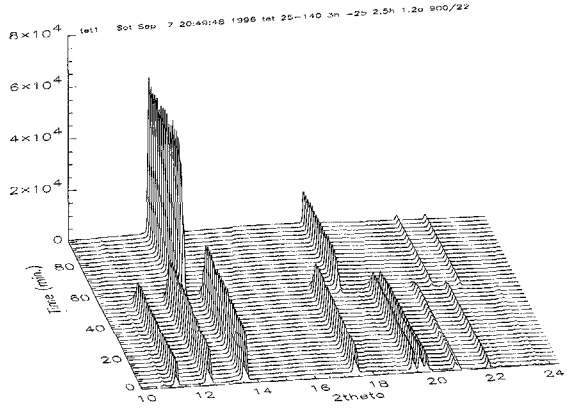


Figure 1. The figure shows the high temperature phase transformation of tetraethylammonium tetrafluoroborate. The room temperature structure is monoclinic. The high temperature phase can be indexed as cubic.

* This work was supported by US DOE (DE-AC02-76CH00016, Div. Chem. Sci., BES) and by the Danish Natural Science Research Council.

Characterization of Catalysts by Temperature-Programmed Powder X-ray Diffraction	X7B

M.M. Burcham, K.K. (Lehigh U.), and J.C.Hanson (BNL- Chemistry)

Recently, WO_3/ZrO_2 has emerged as a useful solid acid catalyst in applications including alkane isomerization and ether synthesis. Tungsten oxide, as well as other dopants such as sulfate and yttria, is known to stabilize the tetragonal phase of the zirconia support. The catalyst, which is amorphous as prepared, is subjected to heat treatment during which the desired tetragonal phase is formed. If the heat treament is too severe, the monoclinic phase of zirconia forms, and the catalytic activity is reduced. Calcination was performed *in situ* in the X-ray diffractometer and the results illustrated the development of these phases in a WO_3/ZrO_2 catalyst. This information can be used to help develop a better calcination procedure for these catalysts.

Another catalyst of interest is the ternary copper/zinc oxide/chromia methanol synthesis catalyst. The precursor of the final catalyst is a hydrotalcite-like hydroxycarbonate layered solid. Heat treatment of these copper-based catalysts yields the final catalytically active mixture of copper, zinc, and chromium oxides. Severe heat treatments of these catalysts lead to the formation of copper and zinc spinel-like structures and reduced catalytic activity. X-ray diffraction measurements of the *in situ* calcination of this catalyst can also be used to refine the pre-treatment conditions for the methanol synthesis catalyst.

In each case, catalyst precursors were placed in 0.5 mm quartz capillaries which were mounted in the diffractometer. Temperature was increased by a resistance heater also mounted in the diffractometer. XRD patterns were measured every ten minutes as the samples were heated from ambient temperature to 850°C.

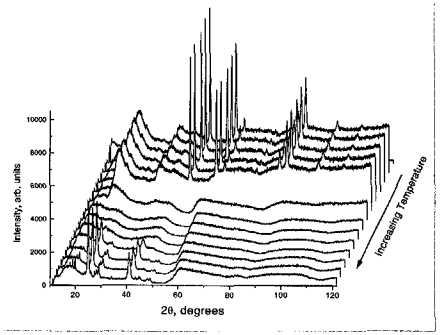


Figure 1. XRD patterns of WO_3/ZrO_2 taken as temperature was increased from ambient to 850°C.

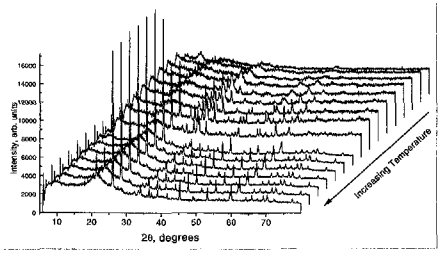


Figure 2. XRD patterns of $Cu/ZnO/Cr_2O_3$ taken as temperature was increased from ambient to 850°C

In Situ Studies of Hydrothermal Syntheses; Crystallization of Mg- and Zn-substituted Aluminophosphates *	X7B

A.N. Christensen (U. Aarhus), P. Norby and J.C. Hanson (BNL-Chemistry)

Open framework aluminophosphates are of interest as catalysts, especially when metal cations are substituted into the framework. Substituting divalent ions for trivalent aluminum creates a charged framework. This also means that charge compensating cations must be introduced into the cavities. This introduces some parameters, which can be varied in order to tune the catalytic properties.

The present experiment was performed in order to compare crystallization behaviour of zink and magnesium substituted aluminophosphates. Four different pastes were prepared as starting materials. The template used was di-n-propylamine = Pr_2NH. Zink and Magnesium were introduced as the acetates.

The compositions were:

A and B: 1.0 Pr_2NH 0.4 ZnO 0.8 Al_2O_3 P_2O_5 40 H_2O

C: 1.0 Pr_2NH 0.4 MgO 0.8 Al_2O_3 P_2O_5 40 H_2O

D: 1.0 Pr_2NH 1.0 Al_2O_3 P_2O_5 40 H_2O

Crystallization of the gels were followed in-situ using temperature ramps and isothermal runs at temperatures between 25 and 200°C.

Paste A gave an unidentified precursor phase, while the final product was MAPO-39. Paste B, with the same composition, gave the same end-product, but occurrence of MAPO-46 was observed in the early stage of crystallization. While substituting Mg for Zn (paste C) did not effect the final product (MAPO-39), occurence of MAPO-5 as an intermediate phase was observed. At higher temperatures MAPO-11 seems to be the stable phase. The pure aluminophosphate paste (D) resulted in formation of ALPO-54, ALPO-31 and ALPO-11.

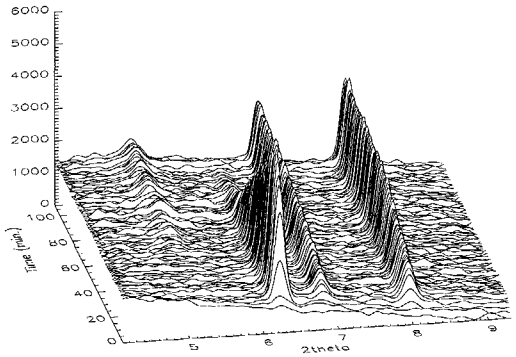


Figure 1. 3-Dimensional plot. The intermediate phase is MAPO-5.

* This work was supported by US DOE (DE-AC02-76CH00016, Div. Chem. Sci., BES) and by the Danish Natural Science Research Council.

A Variable Temperature X-Ray Diffraction Study of HCFC-124a Reactions on Cation Exchanged Faujasites *	X7B

M.F.Ciraolo, F.I.Poshni, P. Norby, C.P.Grey (SUNY Stony Brook), J.C.Hanson (BNL - Chemistry), and D.R.Corbin (Dupont)

A study of the adsorption of Hydrochlorofluorocarbon (HCFC)-124a (CF_2ClCF_2H) on zeolite ZnX is described. HCFCs are used as temporary CFC alternatives, since they are destroyed in the troposphere and only small amounts reach the ozone in the stratosphere. HCFC-124a is, for example, used as a replacement for CFC-114(CF_2ClCF_2Cl) in refrigerant and air-conditioning applications. Basic and acidic molecular sieves have been suggested as materials for separating and trapping mixtures of CFCs, HFCs and HCFCs to remove impurities formed during the HFC and HCFC syntheses.

In addition, our recent ^{19}F NMR studies have shown that HCFC-124a undergoes dehydrochlorination and dehydrofluorination reactions over ZnX at moderate temperatures. We have,therefore, been investigating a series of HFCs and HCFCs in order to determine some of the interactions that are responsible for the adsorption and catalytic properties of ZnX. Samples were prepared by first dehydrating the zeolites for 24 hours under vacuum at 400°C. Gas adsorption was carried out using a calibrated vacuum system. Samples were loaded in 0.5mm glass capillaries under dry nitrogen and sealed. Data was collected with an image plate at 3.5 sec/step with 900 steps. Figure 1 shows a ramp of HCFC adsorbed ZnX from 90 to 300°C. The first changes occur below 150°C and are most likely a consequence of cation migrations. No evidence of reaction is seen at this temperature from the NMR studies. A loss of intensity occurs at higher temperatures which can be attributed to desorption of the HCFC. In contrast, bare ZnX shows no changes throughout the temperature ramp. These results demonstrate the need to determine the structure of these materials in the presence of different adsorbates and binding sites.

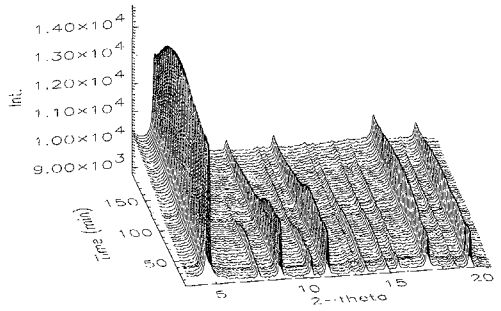


Figure 1. A ramp of HCFC-124a adsorbed ZnX from 90 to 300°C.

* Acknowledgement is made to the donors of the Petroleum Research Fund, administrered by the Am. Chem. Society for partial support of this research and NSF for an interagency transfer of support to the USDOE, BES (DE-FG02-96ER14681.

Structure and Phase Transitions in The Negative Thermal Expansion Material Zirconium Vanadate	X7B

J.S.O. Evans, A.W. Sleight (Oregon St. U.) and J. C. Hanson (BNL - Chemistry)

Compounds in the $ZrV_{2-x}P_xO_7$ series show the unusual property of negative thermal expansion. Since these materials are cubic, this contraction with increasing temperature is isotropic in nature. At high temperature ZrV_2O_7 has a simple cubic unit cell (a=8.8Å), but undergoes two phase transitions on cooling (102°C and 72°C) and at room temperature has a unit cell with a 3x3x3 superstructure. Despite a number of studies (Powder X-ray/neutron diffraction, solid state NMR), the precise structure of the room temperature and intermediate phase remained unclear.

To investigate the phase changes occurring we have collected full single crystal data sets of ZrV_2O_7 at 3 temperatures, 25°C, 90°C and 102°C, and also limited data sets every 5°C from 25°C to 102°C, using a Fuji imaging plate system on beam line X7B. At 25°C a total of 77,000 reflections were recorded and merged (R=6%) to yield 6972 reflections with $I \gg 3\sigma$. Of these 6647 are superlattice reflections. The structure has been refined to an R_F of 3.6%, and consists of highly regular corner sharing ZrO_6 octahedra and VO_4 tetrahedra. Valence calculations show that each of the 6 Zr octahedral sites and 4 V tetrahedral sites have identical coordination environments, and there is no need to invoke chemically implausible bond distances or disordered oxygen models to describe the structure.

As the structure is warmed to 72°C it undergoes a phase transition which retains the 3x3x3 superstructure, though in which the intensity of the superlattice reflections are markedly decreased. Peak positions of the superlattice reflections are observed to shift relative to those of the sublattice suggesting that this superlattice phase is incommensurate in nature. The intensity distribution of the superlattice reflections suggest that the modulations of the incommensurate phase are closely related to the polyhedral tilts observed at room temperature. Further work on this incommensurate phase is in progress.

At 102°C the intensity of the remaining superlattice reflections is observed to fall drastically (and essentially to zero), and the structure can be successfully refined on the basis of a simple 8.8 Åsubcell. Bond distances and angles over the entire temperature range studied suggest the phase transitions in ZrV_2O_7 can be understood in terms of coupled 3 dimensional rotations of essentially rigid, undistorted polyhedra. Simple modelling on these assumptions is in progress, and it is hoped that this will help explain the origin of the incommensurate phase.

The Structure of *d*-$Co(en)_3.Al_3P_4O_{16}.3H_2O$ *	X7B

M. J. Gray, A. P. Wilkinson (Georgia Tech) and J.C. Hanson (BNL - Chemistry)

There is increasing regulatory pressure to sell chiral pharmaceuticals in optically pure form. However, the preparation of such products requires the use of either enantioselective separations or synthesis technology. In principle, the use of chiral zeolitic materials is a potentially attractive approach to both enantioselective separations and heterogeneous catalysis, but a chiral zeolitic material has never been prepared in optically pure form.

We have been exploring the use of chiral metal complexes as templates for the synthesis of chiral inorganic frameworks. Many of the new materials that we have made are only available as small single crystals or powders. Single crystal diffraction/imaging plate detection were used to obtain a diffraction data set for a sample of *d*-$Co(en)_3.Al_3P_4O_{16}.3H_2O$. ($C222_1$, a = 8.502, b = 14.620, c = 20.89 Å, Z = 4, crystal size 20 x 20 x 80 μ m). This layered aluminophosphate was prepared using *d*-$Co(en)_3^{3+}$ as a template cation. It contains chiral $Al_3P_4O_{16}^{3-}$ macroanions with the metal complexes and water sandwiched between the layers (see Figure 1). We believe that it is the first example of a bulk inorganic material to be made with good optical purity by a template synthesis approach.

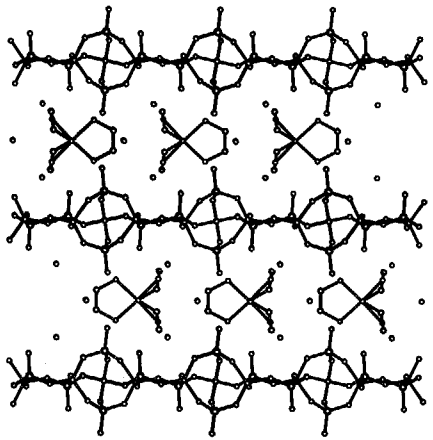


Figure 1. A view down the a-axis of *d*-$Co(en)_3.Al_3P_4O_{16}.3H_2O$.

* We are grateful to the Donors of the Petroleum Research Fund, administered by the American Chemical Society, and the Georgia Institute of Technology Molecular Design Institute, supported under ONR contract N00014-95-1-1116, and contract DE-AC02-76CH00016 with the US DOE, Div of Chem. Sciences, Office of Basic Energy Sciences for fundng this work

Structural Characterization of Hydrofluorocarbon-134 Adsorbed on Zeolite NaY using X-ray Powder Diffraction: Observation of Cation Migration and Strong Sorbate-Cation Interactions *	X7B

C.P.Grey and F.I.Poshni (SUNY Stony Brook), A.F.Gualtieri (U. Modena), P.Norby and J.C.Hanson (BNL- Chemistry), and D.R.Corbin (DuPont)

Basic zeolites have been found to be effective for separating various hydrofluorocarbon (HFC) and hydrochlorofluorocarbon (HCFC) mixtures. This represents one approach for removing unwanted side products generated during the synthesis of the HFCs and for trapping halocarbon pollutants present in industrial wastes. We have been studying the adsorption of HFC-134a and HFC-134 on Y zeolites, with X-ray powder diffraction and ^{23}Na MAS NMR, to investigate the interactions of the HFCs with the extra-framework and framework sites, and to determine how the HFC molecules are bound to the zeolite framework.[1]

A contraction of the volume of the unit cell (u.c.) is observed on gas adsorption in NaY and the interaction of HFC-134 with the extra-framework sodium cations is so strong that extra-framework sodium cations in the sodalite cages (site I') migrate into the supercages. These sodium cations are found on positions close to the site III' positions of zeolite NaX, in the structural refinements of data collected at 100K. Both ends of the HFC molecules are bound to sodium cations, the HFC molecule bridging the site II and III' cations in the supercages.

Changes in the cation positions occur as the 32HFC-134/NaY sample is warmed from 100K to room temperature. At 160K, a significant fraction of the site III' sodium cations move to the site II position, which becomes fully occupied. The cation migration is associated with an increase in the disorder of the HFC location. The system becomes increasingly disordered as the temperature is raised further: At approximately 205K, the remaining site III' cations move off the mirror plane and onto a general position.

1. C.P.Grey, F.I.Poshni, A.F.Gualtieri, P.Norby, J.C.Hanson, D.R.Corbin, submitted (1996).

* Support from the NSF (DMR-9458017 and CHE-9405436, and through an interagency transfer of support to the US DOE (DE-AC 02-76CH00016)) and DuPont is gratefully acknowledged

Real Time Combined Fe K-edge XANES and XRPD *in-situ* Study of Hydrothermal Synthesis of Zeolites from Natural Clay Minerals. *	X7B

Alex F. Gualtieri (U. of Modena, Italy), P. Norby and J.C. Hanson (BNL - Chemistry)

Variations in the chemical composition of zeolites is a well known phenomenon. A common feature of natural zeolites is the presence of Fe and other cations such as Sr, Li, Be, Cs and Pb mainly as subordinate or occasional elements. The question whether iron is present in the tetrahedral framework, or in extra-framework sites, or as micro-impurities of iron oxides and/or hydroxides is still under debate. There is, however, a general agreement, albeit not supported by clear experimental data, that iron is not substituting for Al and/or Si in tetrahedral sites.

Spectroscopic studies (optical absorption, Mossbauer, EPR) showed that Fe^{2+} detected in red heulandite crystals from Val di Fassa (Italy) is actually mainly present as hematite and marcasite inclusions, and that Fe^{3+} is located as extraframework cations [1]. XRD, SEM (EDAX), XPS, XAFS data carried out on a clinoptilolite and mordenite-bearing samples from Cuba revealed that Fe is not located in the tetrahedral framework but resides in an octahedral environment as extraframework cations in clinoptilolite [2]. The presence of iron in tetrahedral environment was, however, detected in synthetic samples such as Fe-silicalite and synthetic Fe-silicate analogues of mordenite [3]. Most natural zeolites are white or pale colored and show negligible content of Fe; in many occurrences, Fe-rich smectites are formed before or after the formation of zeolites and captures iron.

We are interested in observing the role and behaviour of structural iron in hydroxides associated with clay minerals used as precursor for zeolite synthesis. The precursors were thermally activated and are structurally similar to those of natural glassy precursors of zeolites. We have chosen for the experiments thermally activated precursors of a disordered kaolinite and a smectite containing 1.2 and 3.4% of Fe_2O_3, respectively. The samples were heated at 600°C before the synthesis experiments.

In-situ hydrothermal syntheses were carried out at the X7B beamline. A 120° curved INEL Position Sensitive Detector was used to collect time resolved powder diffraction patterns. The starting mixture was loaded in a 0.7 quartz glass capillary and kept under a pressure of 10 atm. A hot air blower was used to keep the temperature at 100°C. Powder patterns and XANES spectra (6950-7200 eV) were collected during hydrothermal synthesis of zeolite A from the activated clay precursors. XANES spectra were collected in fluorescence mode by using an scintillation detector positioned close to the capillary. Albeit the data analysis is still in progress, preliminary data show that Fe is in octahedral coordination in the pseudoamorphous Fe-hydroxides at the beginning of the reaction and it does not change its environment during or after the formation of the zeolite phase. This supports the hypothesis that in conditions reproducing the natural environments Fe does not enter the framework structure of zeolites.

References: [1] Bonnin D., Calas G. (1978) Bull. Mineral. 101(395-398). [2] Marco J.F., Gracia M., Gancedo J.R., Gonzales-Carreno T., Arcoya A., Seoane X.L. (1995) Hyperfine Interact. 95(53-70). [3] Chandwarkar A.J., Date S.K., Bill E., Trautwain A. (1992) Zeolites, 12(180-182).

* This work was supported by US DOE (DE-AC02-76CH00016, Div. Chem. Sci., BES.)

Kinetic Study of the Synthesis of Zeolite Li-A(BW) from Natural Kaolinites *	X7B

A.F. Gualtieri, (U.of Modena, Italy), P. Norby and J. Hanson (BNL - Chemistry), and G. Artioli (U. of Milan, Italy)

Following the study of the kinetics of synthesis of zeolite A and hydroxysodalite from natural kaolinites with different degree of stacking disorder and thermal history [1,2], we investigated the kinetics of formation of zeolite Li-A(BW) from a natural ordered kaolinite (international standard Kga-1) and a disordered kaolinite (international standard Kga-2). Kaolinites were both thermally activated at 600°C. Hydrothermal synthesis of zeolite Li-A(BW) using the activated kaolinites and a 2M LiOH solution were performed in the temperature range 65-130°C. The synthesis experiments were carried out at the X7B beamline, which is equipped with equipment for real time *in situ* studies. Hydrothermal syntheses were performed in 0.7 mm quartz glass capillaries using an applied pressure of 10atm. inside the capillary. The capillaries were heated by a hot air stream, and time resolved data were collected using a Translating Imaging Plate Camera.

Isothermal experiments were performed at 65,80,100,115 and 130°C. The raw integrated intensities of several Bragg peaks were converted into phase fractions and used to plot alfa-time curves. The population balance method and Avrami model were used for analysis of the kinetic curves[3]. The kinetic behaviour was studied in the light of the structural differences of the activated precursors (metakaolinite) as advanced in [4].

[1]Gualtieri A.F., Norby P., Hanson J., Artioli G. (1996) in preparation for Phys. Chem. Min. [2]Gualtieri A.F., Norby P., Hanson J., Artioli G. (1996) in preparation for Microporous Materials. [3]Thompson R.W., Dyer A. (1985) Zeolites, 5:202-210. [4]Gualtieri A.F. (1995) Phd thesis., Univ. Of Modena Italy.

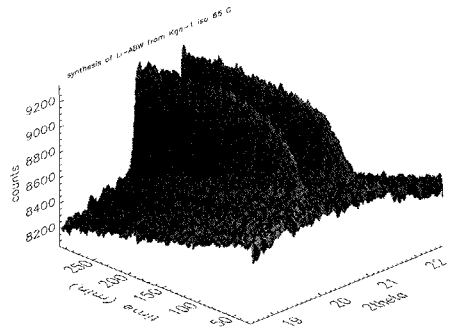


Figure 1. 3D plot showing in-situ synthesis (65°C) of zeolite Li-A(BW) from kaolinite Kga-1 activated at 600°C.

* This research was supported under Contract DOE DE-AC02-76CH00016 Division of Chemical Sciences, BES.

Computer Movies of Time-resolved Dehydration of Natural Zeolites *	X7B

J. C. Hanson, J. Araujo (BNL), Kenny Stahl (DTU), G. Artioli (U. Milan)

We have demonstrated that the structural changes occuring during dehydration of natural zeolites can be determined by measuring the time-resolved powder patterns at series of temperatures and refineing this data by Reitveld Powder refinement.[1]

The changes can be made clear by movies made up from a series of picutres derived from the experimentally determined and refined coordinates. The program CERIUS2 was used to generate the frames. The movies can be viewed on www site http://www.chemistry.bnl.gov/x7b/x7bhome.html

The Laumontite movie illustrates the step-wise dehydration of the Calcium ion bound which is bound to the framework oxygen atoms and the water molecules. The framework variations during this dehydration are also illustrated[2].

The stilbite movie also shows large framework rearrangements which ultimately result in the breaking of one framework bond and the forming of a different framework bond[3].

[1] K. Stahl and J. C. Hanson, J. Appl. Cryst. (1994) 27, 543-550
[2] K. Stahl, G. Artioli and J. C. Hanson, Phys. Chem. Miner.(1996) 23, 328-336
[3] C. Cruciani, G. Artioli, A. Gualtieri, K. Stahl and J. C. Hanson, Amer. Minerologist.(submitted)

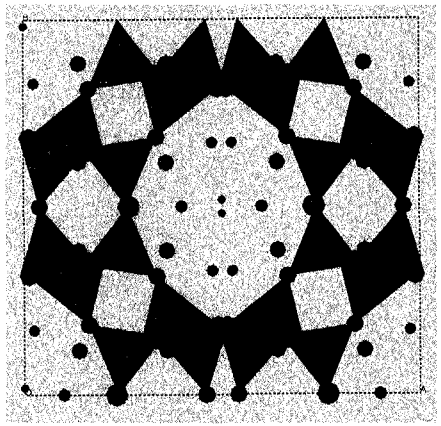


Figure 1. Laumonite cavity.

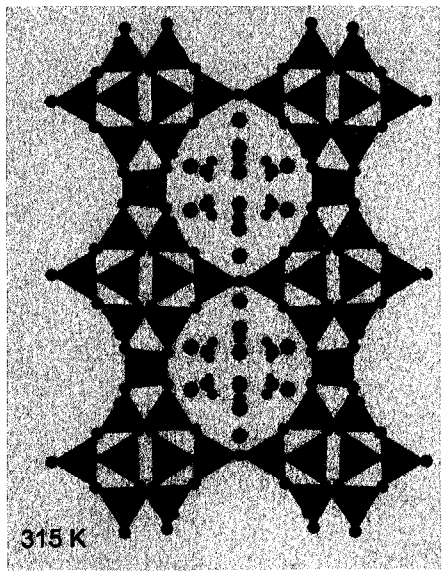


Figure 2. Stilbite cavity.

* Contract AC02-76CH00016 with US DOE Div. of Chem. Sci., Office of Basic Energy Sciences and the Swedish Natural Science Council

Pyridine Adsorbed on Na-Faujasite: Low Temperature Single Crystal Studies *	X7B

J. C. Hanson (BNL- Chemistry), I. Mutikainen (U. of Helsinki), J. Pluth (U. of Chicago)

Studies of the binding of adsorbants to zeolite solids can provide information about the selectivity of these materials in adsorption and catalysis. We have carried out single crystal studies of the binding of pyridine to Faujasite at five temperatures using both sintilation counter and image plate data collection techniques. The lowest temperature data was collected in a cryostat at temperature 20K. A Oxford cryocooler was used to collect data at 105K, 140K, 190K and 240K. The cryostat data was collected using a sintilation detector. There were 1667 reflections measured. They were merged with Blessing's SORTAV program to give a symmetry R factor of .05. The image plate data were scanned offline on a Fuji Bas2000. The data were indexed, integreted and merged with the HKL package of Z. Otwinowski and W. Minor. There were 8204 reflections in the 105K data set which gave a symmetry R factor of .07.

The binding sites were found from difference Fourier maps. The structures were refined with Shelxtl. The R factors were .138 and .097 for the 20K and 105K data.

The prydine binds in the super cage above the Na II in a manner similiar to the binding of benzene in NaY[1].

[1] A. N. Fitch, H.Jobic and A.Renouprez (1986) J. Phys. Chem. 90, 1311-1318

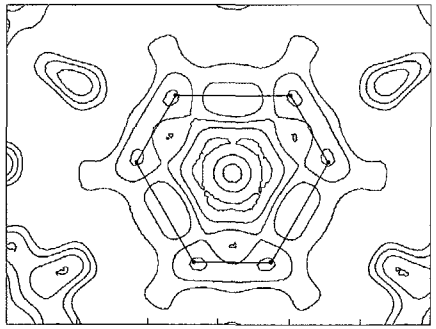


Figure 1. Difference Fourier map through pyridine. Cryostat / scintilation counter data at 20K.

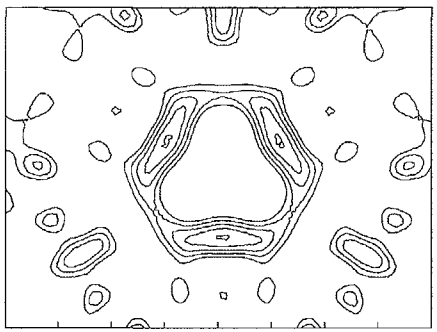


Figure 2. Difference Fourier map through pyridine. Cryocooler / image plate data at 105K.

* Supported by contract DE-AC02-76CH00016 with the US DOE by its Div of Chemical Sciences, Office of Basic Eneregy Sciences.

Studies of Excited-State Lifetimes of Hydrocarbons *	X7B

R.A.Holroyd and J.M. Preses (BNL-Chemistry)

Saturated hydrocarbons, when irradiated with UV or x-rays, mostly decompose. However, bound, excited molecules are produced that can fluoresce (F 10-3), leading to determination of excited-state lifetimes. examination of these lifetimes as functions of excitation energy can provide information about energy flow and release during reactions.1 During our studies of UV-fluorescence from cis- and trans-decalin excited by x-rays on beamline X7B, we realized that the relative fluorescence quantum yields of these molecules could be made absolute by comparison with the known fluorescence quantum yield of liquid benzene, measured under identical experimental conditions. Liquid benzene is well-known to exhibit a single excited-state fluorescence lifetime of 27 ns (λ = 295 nm) when excited by UV in the 250-270 nm region.2 Since, in the liquid phase, fluorescence is observed only from the lowest (S1) excited state, essentially independent of the excitation process, the same behavior is expected when the excitation process is due to recombination of ions in radiation tracks produced by electrons generated by x-ray absorption. When this experiment was performed at X7B, two lifetimes were observed, a short lifetime of 1 ns and another of 10 ns, with approximately equal amplitudes. Explanation of this surprising result demands elimination of the possibility that the observation is an experimental artifact. Therefore, measurement of the fluorescence lifetime of the benzene sample with UV excitation using beamline U9B seemed in order. Fluorescence from three samples was observed: one, the same aliquot used on X7B, another, an assuredly purified sample, and, a third, a sample exposed in the cuvette used on X7B, with a Mylar window, glued to the cuvette with epoxy cement. Samples freshly bubbled with N2 exhibited the literature value of the fluorescence lifetime. Shorter lifetimes were observed from the same samples as atmospheric oxygen dissolved and formed charge-transfer complexes. It seems clear that further study of the x-ray-excited UV fluorescence behavior of liquid benzene needs to be pursued.

References 1. R.A. Holroyd, J.M. Preses and J.C. Hanson, Radiat. Res., 135 312 (1993). 2. W.P. Helman, J. Chem. Phys., 51 354 (1969).

* This research was carried out at Brookhaven National Laboratory under Contract No. DE-AC02-76CH00016 with the U.S. Department of Energy and supported by the Division of Chemical Sciences, Office of Basic Energy Sciences

Investigation of Disorder Using Micro Single Crystal Diffraction Data *	X7B

T.R. Jensen (U. of Odense, Denmark), P. Norby and J.C. Hanson (BNL - Chemistry)

A methode for preparing micro single crystals of δ_I-$LiZnPO_4$ suitable for structure determination has been developed using an aqueous solution of H_3PO_4, $Zn(NO_3)_2$ and LiOH, at 70°C. The cristobalite type structure of δ_I-$LiZnPO_4$ has been solved [1] and disorder on the lithium and zinc positions were found [2]. Difference Fourier maps has proven valuable for characterization of these kinds of materials [3]. Due to the smallness of the crystals (39 x 16 x 18 μm^3) it was decided to use the synchrotron X-ray radiation and an imaging plate (IP) system for the data collection at chemistry beamline X7B.

The absorption edge of zinc in δ_I-$LiZnPO_4$ was initialy found from a fluorecens spectrum. Two data sets were collected as ϕ-scans, at different wavelength. Below the zinc edge, λ = 0.9540 Å, 2θ = -40°, using steps of 8° in ϕ. A total of 1431 refl. (695 independent refl.) were measured form 23 IP. At the zinc edge, λ = 1.2830 Å, data were collected, at 2θ = -40°, using steps of 8° in ϕ. The orthorhombic unit cell was refined from two independent IP, giving a = 10.019(2) Å, b = 4.966(1) Å, and c = 6.675(1) Å.

[1] W.T.A. Harrison, T.E. Gier, J.M. Nicol and G.D. Stucky, *J. Solid State Chem.* **114** (1995) 249. [2] T.R. Jensen, P. Norby, P.C. Stein and A.M.T. Bell, *J. Solid State Chem.* **117** (1995) 39. [3] M. Helliwell, J.R. Helliwell, A. Cassetta, J.C. Hanson, T.E. Ericsson, A. Krick, V. Kaucic and C. Frampton *Acta Cryst.* **B52** (1996) 479-486.

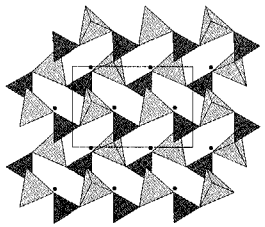


Figure 1. The crystal structure of δ_I-$LiZnPO_4$. ZnO_4 is shown as light shaded tetrahedra, PO_4 as dark and Li as spheres.

* This work was supported by contract DE-AC02-76CH00016 with the US DOE, Div. Chem. Sci. , BES, and by the Danish Natural Science and Technical Research Councils.

Kinetic Study of Phase Transition of Microporous Lithium Zinc Phosphates	X7B

T. R. Jensen (U. of Odense, Denmark), P. Norby and J.C. Hanson (BNL - Chemistry)

In situ powder diffraction has proven a valuable technique for kinetic studies of solid state or hydrothermal chemical reactions and phase transitions. $LiZnPO_4 \cdot H_2O$ is a microporous material (zeolite ABW type structure) which transforms to δ_I-$LiZnPO_4$ by heating hydrothermally *or* dry to T > 130°C [1,2]. It is of interest to study phase transitions following different mechanisms.

The starting material was a suspension of $LiZnPO_4 \cdot H_2O$ and $LiNO_3$ in water to resemble the synthesis conditions. The samples were placed in 0.7 mm quartz capillaries and mounted in a special developed goniometer head allowing a pressure of N_2 gas (up to 45 atm) to be applied. Several isothermal experiments were performed heating the samples up within one minute to a fixed temperature (160°C < T < 210°C). The diffraction data were recorded using a position sensitive detector (INEL CPS 120) covering 120° in 2θ and sampling time of 30s, 60s or 120s, and λ = 1.3080 Å. Figure 1 illustrates a typical data set.

Semi-automatic integration of selected Bragg reflections using a Gaussian peak shape allows extraction of data for kinetic studies. Figure 2 shows the formation of δ_I-$LiZnPO_4$ using the (201) and (011) reflections.

[1] T.R. Jensen, P. Norby, P.C. Stein and A.M.T. Bell, *J. Solid State Chem.* **117** (1995) 39. [2] W.T.A. Harrison, T.E. Gier, J.M. Nicol and G.D. Stucky, *J. Solid State Chem.* **114** (1995) 249. This work was supported by contract DE-AC02-76CH00016 with the US DOE, Div. Chem. Sci., BES, and by the Danish Natural Science and Technical Research Councils.

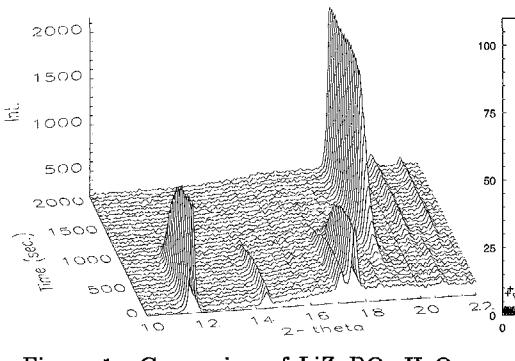


Figure 1. Conversion of $LiZnPO_4 \cdot H_2O$ to δ_I-$LiZnPO_4$ at 200°.

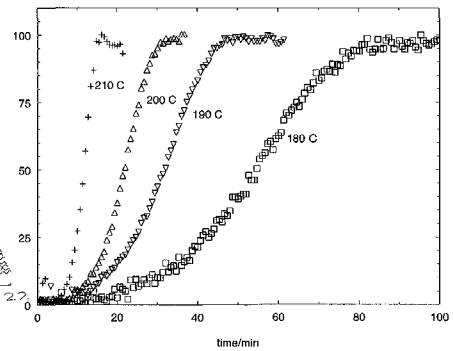


Figure 2. Formation of δ_I-$LiZnPO_4$.

Powder Diffraction Study of Co Substitution in Microporous Lithium Zinc Phosphate *	X7B

T.R. Jensen (U. of Odense, Denmark), P. Norby and J.C. Hanson (BNL - Chemistry)

Substitution of transition metal ions in microporous materials (e.g. ALPOs and related materials) are subject to intense interest due to potential catalytic activity. We have prepared a Co substituted zeolite type ABW material, $Li(Zn/Co)PO_4 \cdot H_2O$, and a cristobalite type material, δ_I-$Li(Zn/Co)PO_4$, from a gel with a modified composition (to [1,2]) using Zn/Co ratios of 1/x, $0.05 < x < 0.5$, pH 5-7. $Li(Zn/Co)PO_4 \cdot H_2O$ was initialy forming but on heating (to $T > 130°C$) it recrystalizes to δ_I-$Li(Zn/Co)PO_4$ with a higher Co content. The Co K edge of δ_I-$Li(Zn/Co)PO_4$ was measured to 7.762 keV using a fluorescence spectrum. Powder diffraction data were collected at different wavelengths above, on and below the Co K edge to determine the Co content and Co positions of the phases by Rietveld refinement, using 0.3 mm glass capillaries as sample holder.

An understanding of the reaction mechanism can be gained in a study of the time dependence of, $\alpha(t)$, the degree of reaction. The phase transition of $Li(Zn/Co)PO_4 \cdot H_2O$ to δ_I-$Li(Zn/Co)PO_4$ is of interest due to the increased Co content of the more dense δ_I-phase. Data were collected at isothermal (set) temperatures of 180, 190, 200, 210, 220°C, using a wavelength above (42 eV) the Co K edge, $\lambda = 1.6111$ Å.

The phase transition has also been studied with a combination of X-ray fluorescence and powder diffraction, placing the gel in 0.7 mm quartz capillaries, heating rate of 1°C/min. Fluorescence spectre (7.72 to 7.87 keV) were measured in 75 steps, with counting time of 5 s/step. After each spectrum powder diffraction data were collected, at $\lambda = 1.6111$ Å, (counting time 300s/diag).

[1] W.T.A. Harrison, T.E. Gier, J.M. Nicol and G.D. Stucky, *J. Solid State Chem.* **114** (1995) 249. [2] T.R. Jensen, P. Norby, P.C. Stein and A.M.T. Bell, *J. Solid State Chem.* **117** (1995) 39.

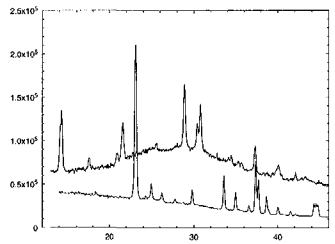


Figure 1. Powder diffraction patterns of $Li(Zn/Co)PO_4 \cdot H_2O$ (upper) and δ_I-$Li(Zn/Co)PO_4$.

* This work was supported by contract DE-AC02-76CH00016 with the US DOE Div. Chem Sci., BES, and by the Danish Natural Science and Technical Research Councils.

Structural Investigation of α-$LiZnAsO_4$, Using a Micro Crystal *	X7B

T.R. Jensen (U. Odense, Denmark), P. Norby, J. C. Hanson (BNL - Chemistry)

Single crystals of α-$LiZnAsO_4$ suitable for structure determination were prepared from an aqueous solution of H_3AsO_4, $Zn(NO_3)_2$ and LiOH, under hydrothermal conditions at 240°C. Due to the smallness of the crystals (17 x 17 x 60 μm^3) it was decided to use the synchrotron X-ray radiation beamline X7B and an imaging plate (IP) system for the data collection. A thin (4 μm) glass fiber was used for mounting the crystal on the Huber diffractometer.

The data were collected at 2θ = -40° and at 0° as a ϕ-scan, using steps of 6° and 14°. The 39 IP (2304 reflections) were scaled together to give 917 independent reflections. The wavelength of the synchrotron X-ray radiation was, $\lambda = 0.9540$Å. The hexagonal unit cell was refined from two independent IP, giving $a_h = 13.923(2)$ Å, and $c_h = 9.395(2)$ Å. This is in agreement with results of Durif [1].

On refining the structure in s.g. $R\bar{3}$ the As/Zn distances to oxygen were intermediate to the expected values from known related compounds. Removing the centrosymmetry revealed that one As/Zn position in the s.g. $R\bar{3}$ splits up in one As- and one Zn-position (i.e. an ortho arsenate with distinct AsO_4 tetrahedra). The crystal structure of α-$LiZnAsO_4$ is isomorph to e.g. a new phase of $LiZnPO_4$ prepared recently [2]. This phenacite like structure shows the characteristic nets of 6-rings surrounded by six 4-rings stacked in the direction of the *c*-axis.

[1] A. Durif, Bull. Soc. Franc. Miner. Crist. **84** (1961) 322. [2] X. Bu, T.E. Gier and G.D. Stucky, Acta Cryst **C52** (1996) 1601.

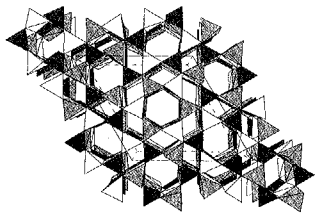


Figure 1. The crystal structure of α-$LiZnAsO_4$ viewed along the *c*-axis.

* This work was supported by contract DE-AC02-76CH00016, US DOE, Div. Chem. Sci., BES, and by the Danish Natural Science and Technical Research Councils.

The Crystal Structure of a New Zinc Arsenate, $Zn_9(AsO_4)_6 \cdot 4H_2O$. * | X7B

T. R. Jensen (U. of Odense, Denmark) P. Norby and J. C. Hanson (BNL - Chemistry)

Micro single crystal diffraction using synchrotron X-ray radiation and an imaging plate (IP) as dector is developing to an important technique for structural investigation of new materials.

A hydrothermal synthesis were performed using H_3AsO_4, $Zn(NO_3)_2$ and LiOH at 240°C. Optical microscopy of the batch revealed crystals with three distinct morphologies. "Hexagonal rods" were identified to be α-$LiZnAsO_4$. "Plate-like" (< 40w/w%) crystals and "octahedron-like" (< 1w/w%) were mounted on the Huber diffractometer at beamline X7B and were indexed from two independent IP, each. The "octahedron-like" crystals were found to be the well known Adamite phase, $Zn_2(AsO_4)OH$. The "Plate-like" crystals appeared to be a new triclinic phase with the unit cell dimensions: $a = 6.68$ Å, $b = 9.69$ Å, $c = 10.04$ Å, $\alpha = 72.21°$, $\beta = 77.53°$ and $\gamma = 75.85°$. Data were collected with the IP at, 2θ = -40° and 0°, using ϕ-scans of 6° and 14°, respectively ($\lambda = 0.9540$ Å). The 44 IP were scaled together giving 1819 independent reflections. The dimensions of the selected crystal was 83 x 66 x 12 μm^3.

The structure was solved and refined in the s.g. $P\bar{1}$. It is built from distinct AsO_4-tetrahedra and 4, 5- and 6-coordinated Zn atoms linked together to form a 3-dimensional network with channels running in the direction of the a-axis. The water molecules are placed in the channels.

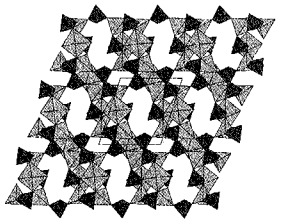


Figure 1. The crystal structure of a new Zinc Arsenate, $Zn_9(AsO_4)_6 \cdot 4H_2O$, viewed along the a-axis.

* This work was supported by contract DE-AC02-76CH00016 with the US DOE Div. Chem. Sci., BES, and by the Danish Natural Science and Technical Research Councils.

X-Ray Scattering Study of Simple Molecules Adsorbed on BN: Evidence for a Commensurate Phase of Kr | X7B

D.E. Johnson, J. Hanson, and J.Z. Larese (BNL)

We have initiated a series of experiments to investigate the layering behavior of small molecules (rare gases, light hydrocarbons, etc.) on highly-uniform BN powders. BN has a hexagonal crystal structure and lattice constants only a few percent larger than graphite. Therefore a comparison between the behavior of films adsorbed on graphite and BN should provide insight into the delicate balances between the adsorbate-adsorbate and adsorbate-adsorbent interactions which are responsible for the wide variety of phases and transitions observed for these systems. These measurements are aided by our use of image plate technology which allows rapid collection ($\leq$1 min/exposure) of the data over a large Q-range ($\approx$600 cm2 active area, 100 um resolution).

Our first experiment was to observe the scattering from submonolayer films of Kr, due to its large cross section. It is well-known that Kr adsorbed on graphite exhibits a commensurate phase at low coverages which gives way to a compressed, incommensurate phase at higher coverages. It has been suggested that the slightly larger spacing of the BN substrate and its smoother corrugation would not permit a commensurate phase to form. However, our results clearly show the formation of a commensurate solid phase. As in the graphite case, this commensurate phase has a spacing consistent with the $\sqrt{3}$x$\sqrt{3}$ R 30 structure, and can be driven to the incommensurate phase by increasing the Kr density. The change in peak position of the Kr (1,0) peak by either lowering the temperature or increasing the amount adsorbed is shown below (ML = monolayer) and is consistent with going from the $\sqrt{3}$x$\sqrt{3}$ R 30 structure to a close-packed structure. The diffraction profiles shown are the difference between exposures taken with BN and BN with adsorbed Kr. The peaks exhibit the characteristic saw-tooth or Warren profile and are clearly evident despite nearly coinciding with the BN (002) peak which is $\approx$200 times more intense. These experiments are currently continuing and application to more complicated adsorbates such as C_2H_4 is expected.

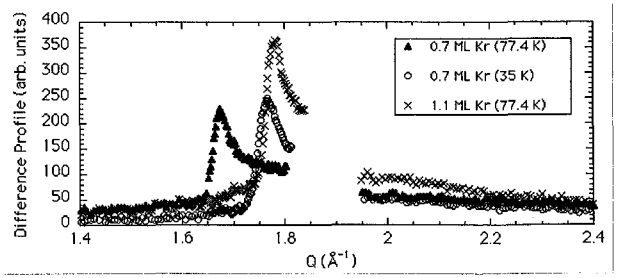


Figure 1.

In-situ Diffraction Study of Ion Exchange: Exchange of Analcime to Ammonium Analcime.	X7B

A.M. Krogh Andersen, E. Krogh Andersen and I.G. Krogh Andersen (U. Odense, Denmark), P. Norby and J.C. Hanson (BNL- Chemistry)

We have made preliminary experiments where we studied the kinetics of ammonium ion exchange of analcime. The natural zeolite analcime (sodiumform, with the standard formula $Na_{16}[Al_{16}Si_{32}O_{96}]\cdot 16H_2O$) was exchanged to the ammonium form from molten NH_4NO_3 at three temperatures (175, 180, and 200°C). An INEL CPS90 detector was used. The wavelength was 1.0987 A. During the exchange diagrams were taken with 5.17 minutes interval. When analcime in sodium form is changed to the ammonium form the crystal system is changed from orthorhombic to tetragonal.

The rate of the ion exchange was estimated by determination of the time dependence of the integrated intensity of the 400 reflection of ammonium analcime and the intensity of the 332 reflection of sodium analcime. Figure 1 shows how the intensity of the two reflections varies with time. The curves were calculated from the following simple first order equations: For production of ammonium analcime: Intensity = -b(exp(-k(t-t_0)))+c . For consumption of sodium analcime: Intensity = b(exp(-k'(t-t_0))+c, where b, c, and k are parameters determined from the graph and t_0 time of the start of the exchange.

Arrhenius plots for the ammonium exchange were drawn. They are shown in Figure 2. We take the liniarity of these plots as indication that we are only dealing with one rate determining process.

This work was supported by US DOE (DE-AC02-76CH00016, Div. Chem. Sci., BES) and by the Danish Natural Science Research Council.

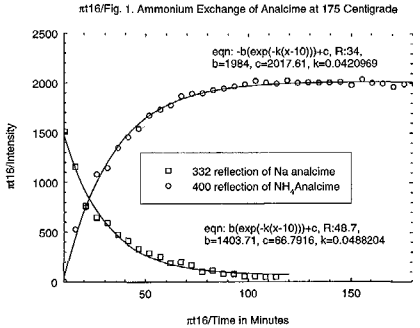


Figure 1. Ammonium exchange of analcime at 175°C.

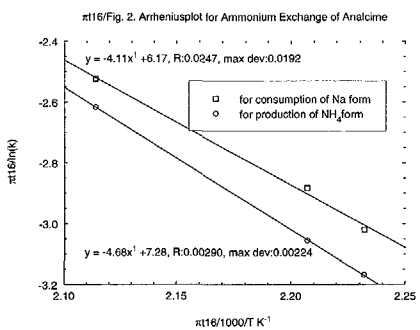


Figure 2. Arrheniusplot for ammonium exchange of analcime.

In-situ Powder Diffraction Studies of Intercalation Processes: Intercalation of Alkane Diamines in α-$Zr(HPO_4)_2\cdot H_2O$ and γ-$Ti(PO_4)(H_2PO_4)\cdot 2H_2O$. *	X7B

A.M. Krogh Andersen, E. Krogh Andersen and I.G. Krogh Andersen (U. Odense, Denmark), P. Norby and J.C. Hanson (BNL - Chemistry).

We have investigated whether time resolved powder diffraction can be used to study kinetics of intercalation of alkane diamines into layered phosphates (*e.g.* α-$Zr(HPO_4)_2\cdot H_2O$ (α-ZrP) and γ-$Ti(H_2PO_4)(PO_4)\cdot 2H_2O$ (γ-TiP)). The amine intercalation processes of these layered materials proceed discontinuously. This means that as soon as the intercalation starts the materials become multiphased. We report briefly some of the results from the experiment with α-ZrP. The experiment was made on X7B at room temperature. The detector was an INEL CPS90 detector. The sample was in a quartz capillary. A small amount of a concentrated solution of hexane diamine was introduced into the capillary, and the intercalation process was started by pressing this solution into contact with the α-ZrP. The graph below shows how the intensities of the 002 reflections of the α-ZrP and the intercalate change with time.

The diffraction profiles were recorded at 20 seconds interval. When the part recorded in Figure 1 was ended we continued the experiment at 40 oC and later at 60 oC. At these temperatures the reflection at 12.5 A disappear and new reflections appear as a sign of an increase of intercalated amine. The curves in Figure 1 were calculated from the following rate equations: for production of intercalate with d=12.5 A: Intensity$_{(200i)}$ = -b(exp(-k_i(t-t_0)))+c for consumption of α-ZrP with d=7.54 A : Intensity$_{(200\alpha)}$ = b(exp(-k_α(t-t_0))+c, where b, c, and k are parameters determined from the graph and t_0 time of the start of the intercalation.

The experiments show that kinetic data for intercalation processes can be obtained by time resolved diffraction.

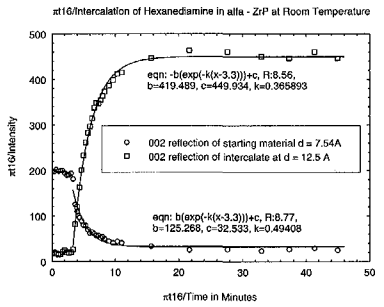


Figure 1. Intercalation of hexanediamine in α-ZrP at room temperature.

* This work was supported by US DOE (DE-AC02-76CH00016, Div. Chem. Sci., BES) and by the Danish Natural Science Research Council.

In-situ Studies of Thermal Transformations in α-layered phosphates. *	X7B

A.M. Krogh Andersen (U. Odense, Denmark), P. Norby and J.C. Hanson (BNL - Chemistry)

Layered phosphates of the α-type has the general formula $M(IV)(HPO_4)_2 \cdot H_2O$, M(IV) being *e.g.* zirconium, titanium, tin or lead. We have used temperature resolved powder diffraction to study the thermal transformations of α-ZrP ($Zr(HPO_4)_2 \cdot H_2O$), α-TiP ($Ti(HPO_4)_2 \cdot H_2O$) and α-SnP ($Sn(HPO_4)_2 \cdot H_2O$).

The three compounds are isostructural(1), but do not undergo the same thermal transformations. Common to the compounds is the formation of a layered pyrophosphate phase with P-O-P links between the layers, which then transforms into cubic pyrophosphate $M(IV)P_2O_7$ (2).

The experiments were carried out at X7B, using a position sensitive detector (INEL CPS90). The wavelength was 1.0987 Å. The samples were placed in 0.5 mm capillaries and heated to 1000°C at a rate of 7.6°C/min. The counting time per diagram was 30 seconds.

Figure 1 shows a 3-dimensional plot of the thermal transformations of α-TiP when heating to 800°C. Formation of an anhydrous phase ($Ti(HPO_4)_2$) is followed by condensation of the HPO_4^--groups whereby the layered pyrophosphate phase is formed and finally the cubic pyrophosphate phase. Figure 2 shows the transformation from the layered pyrophosphate phase to the cubic pyrophosphate phase. Relative crystallinity is estimated from integrated intensities of diffraction lines from the two phases.

1. S. Bruque *et al.*, *Inorg. Chem.* **34** (1995) 893
2. U. Costantino and A. La Ginestra, *Thermochimica Acta* **58** (1982) 179

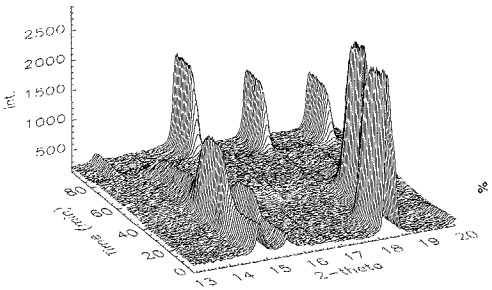


Figure 1. 3-dimensional plot of the thermal transformations of α-TiP

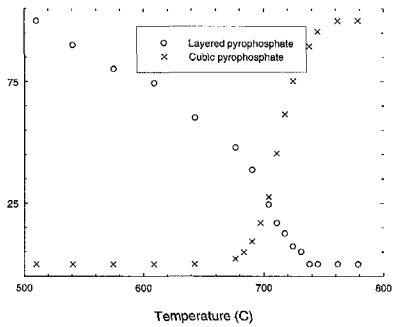


Figure 2. Transformation in α-TiP from layered pyrophosphate to cubic pyrophosphate

* This work was supported by US DOE (DE-AC02-76CH00016, Div. Chem. Sci., BES) and by the Danish Natural Science Research Council

The Crystal Structure of Tetragonal $Zr(HPO_4)_2$ by Synchrotron X-ray Single Crystal Diffraction and Neutron Powder Diffraction Data. *	X7B

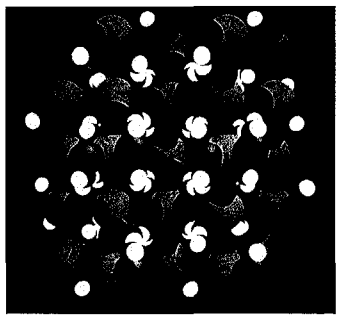
A.M. Krogh Andersen (U. Odense), P. Norby, T. Vogt and J.C. Hanson (BNL - Chemistry)

Layered zirconium and titanium hydrogen phosphates have been studied extensively because of their intercalation, catalytic, ion exchange and ion conductivity properties. Especially the intercalation chemistry of α-zirconium hydrogen phosphate, α-ZrP, $Zr(HPO_4)_2 \cdot H_2O$ has attracted significant attention (1). Systematic studies of the hydrothermal syntheses and thermal transformations of zirconium and titanium phosphates (2) revealed the existence of a new phase in the zirconium system, having a very narrow window of formation. The composition of the new phase is $Zr(HPO_4)_2$ which is similar to the composition for dehydrated α-ZrP. The material was found to be tetragonal with a unit cell: $a = 11.2593$, $c = 10.7691$ Å, spacegroup $I4_1cd$.

By carefully optimizing the hydrothermal syntheses conditions it was possible to grow very small single crystals of the tetragonal material. The crystals were too small for conventional single crystal diffraction. Data were collected on a 25 $\times$ 25 $\times$ 50 μm crystal using imaging plate technique. The crystal structure was solved using direct methods. Neutron powder diffraction data were collected at the high resolution powder diffractometer at the HFBR. The atomic positions from the single crystal refinement was used as starting parameters for the neutron powder diffraction refinement. After some initial cycles of refinement, a difference Fourier map was calculated, and the hydrogen positions were easily found as holes in the map.

The O-H groups form a hydrogen bonded spiral along the 4_1 axes, with each hydrogen phosphate group both donating and accepting hydrogen bonds. Figure 1 shows a space-filling representation of the structure, where the hydrogen bonding spirals are clearly visible.

(1.) A. Clearfield and G.D. Smith, *Inorganic Chemistry* 8 (1969) 431.
(2) A.M. Krogh Andersen, Dissertation, Odense University 1993.



* This work was supported by US DOE, DE-AC02-76CH00016, Div. Chem. Sci., BES, and by the Danish Natural Science Research Council.

Crystal Structure of Dimethylamine Grown *In-situ* from Liquid * | X7B

R. K. McMullan, W. Klooster, P. Norby and J. C. Hanson (BNL-Chemistry)

As part of a project to study thermal motion of small molecules by neutron diffraction and inelastic scattering we have grown crystal of dimethylamine(DMA) from liquid in a capillary. The crystal was grown by slowly translating a capillary containing liquid DMA into a cold stream at 105 K. The capillary translation was accomplished by fixing the z translation knob while moving the phi axis motor.

The data were collected using image plates and an offline Fuji Bas2000 image plate scanner. Two hemispheres of data were collected, with one set being measured with an attenuator to prevent saturation of the IP. The data was reduced with the HKL package of Z. Otwinowski and W. Minor. There were 1191 reflections measured on 22 plates which were scaled to give an merging R(I) of 6.7% in a monoclinic space group $P2_1/c$ with unit cell of a=6.075, b=15.645, c=7.528, β=111.24.

The structure was determined by direct methods. The hydrogen positions were all found in difference maps and the structure was refined to a R1(F)= 5.3%, wR2(I)=14.5%. The CH distances were restrained to 1.0.

The dominant feature of the structure is H-bonded chains as shown in Fig 1.

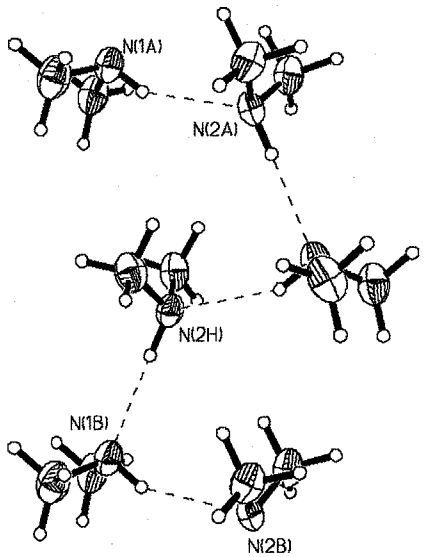


Figure 1. Packing diagram showing H-bond chains. The thermal ellipsoids on the non-hyrdorgen atom are drawn at the 50% probability level.

* This work was supported under contract DE-AC02-76CH00016 with the US DOE and supported by the Div. of Chemical Sciences, Office of Basic Energy Sciences.

Real-Time X-Ray Powder Diffraction Studies of Li/Na Ion Exchange in Sodalite | X7B

P. Norby, J. Hanson (BNL - Chemistry), C. L. Cahill and J. B. Parise (SUNY Stony Brook)

Hydrothermal and solid state ion exchange of lithium for sodium in natural sodalite has been studied utilizing the real time x-ray powder diffraction/imaging plate system at Beamline X7B. Slurries and dry mixtures of $LiNO_3$ or LiCl and sodalite were prepared in a 3:1 Li:Na molar ratio and heated to 650°C via a variety of pathways. Many experiments were necessary to determine the optimum reaction conditions to study this system. Such was found to be a ramp heating to 650°C over three hours with LiCl as the lithium source. Preliminary results indicate that the unit cell edge length of sodalite decreses from 8.878 to 8.482Å. This contraction is expected, as the smaller lithium ions (ionic radius=1.23Å) replace the larger sodium ions (ionic radius=1.54Å). Rietveld refinement of the data at various times during the experiment is in progress. This analysis should provide information regarding the mechanism by which the exchange proceeds.

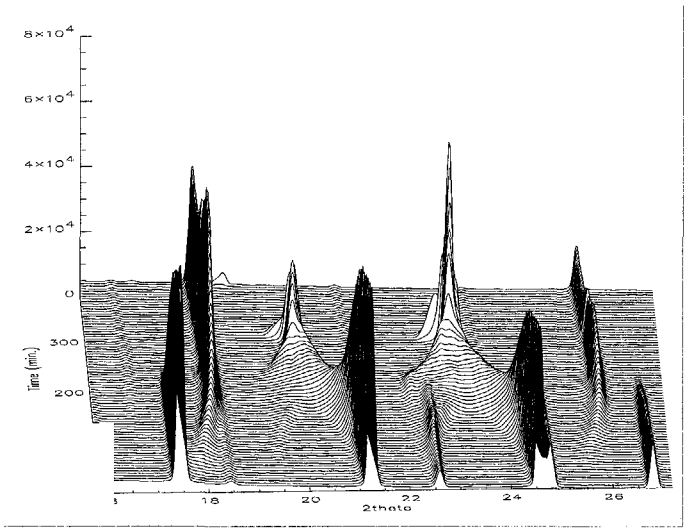


Figure 1. The sodalite, $Na_4Al_3Si_3O_{12}Cl$ framework is defined by AlO_4 and SiO_4 tetrahedra. Oxygen atoms are small hollow circles; Al and Si are small, black circles. Large black circles are the Na cations that are replaced by Li. Chlorine is not shown.

Hydrothermal Conversion of Zeolites Studied Using *in-situ* Powder Diffraction. *	X7B

P. Norby and J.C. Hanson (BNL - Chemistry)

Hydrothermal conversion of zeolites is an alternative route for preparation of new zeolitic and aluminosilicate materials, and for preparation of pure and well crystalline samples. In order to understand the crystallization mechanism it is crucial to know how the hydrothermal conversion process proceeds; whether it is a reaction taking place in the solid phase, via formation of an intermediate amorphoius phase, or via a solution mediated process.

Using *in-situ* powder diffraction combined with ex-situ Scanning Electron Microscopy (SEM) we have followed the hydrothermal conversion of zeolite Na-LTA into zeolite Li-A(BW) using $LiCl_{(aq)}$ at temperatures between 200 and 260°C.

The hydrothermal conversion process was followed using a Translating Imaging Plate (TIP) camera, developed especially for time- temperature- and wavelength dependent powder diffraction studies(1,2 and references therein). Hydrothermal reactions were performed in 0.7mm quartz glass capillaries.

Partially converted samples were prepared in-situ on the diffractometer, and by using the integrated intensities of diffraction peaks it was possible to estimate the conversion ratio. SEM images were obtained for two partially converted sample (40 and 60% conversion). The fit of crystallization curves and the SEM images made it possible to conclude that the hydrothermal crystallization proceeds via a solution mediated dissolution/crystallization process. No signs of autonucleation mechanisms were observed.

(1) P. Norby, *Mater. Sci. Forum*, **228-231** (1996) 147-152. (2) P. Norby, *J. Appl. Cryst.*, (1996) in press.

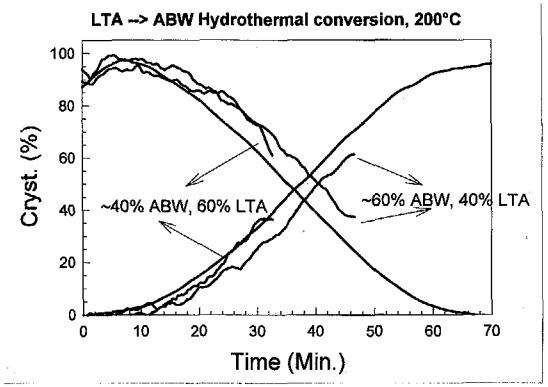


Figure 1. *In-situ* preparation of partially converted samples

* This work was supported by Contract DE-AC02-76CH00016, US DOE, Div. Chem. Sci., BES, and by the Danish Natural Science Research Council.

Dehydration of Zeolite Li-A(BW); A Time Resolved Structural Study.	X7B

P. Norby, J.C. Hanson (BNL), A. Kremenović, V. Dondur and R. Dimitrijević (U. Belgrade)

In zeolite Li-A(BW), $LiAlSiO_4 \cdot H_2O$, the lithium cations in the 8-ring channels are tetrahedrally coordinated to three framework oxygens and a water molecule(1). Upon dehydration the 8-ring channels are elongated and narrowed, and the lithium cation coordinates across the channel, obtaining a tetrahedral coordination to only framework oxygen atoms(2). Thus, although the ABW topolygy of the zeolite framework is retained upon dehydration, rehydration is hindered because of the favourable Li-coordination in the anhydrous material. In most zeolites, which retain their framework topology upon dehydration, rehydration occur at ambient conditions. However, rehydration of the fully dehydrated Li-ABW is not possible even by submerging it in water. Only at hydrothermal conditions will it rehydrate to zeolite Li-A(BW).

In order to follow the dehydration process we performed an in-situ powder diffraction study where zeolite Li-A(BW) was heated from RT to 800°C while collecting powder diffraction data using a Translating Imaging Plate (TIP) Camera(3). Using Rietveld refinement the crystal structure of zeolite Li-A(BW) was refined through the dehydration process, yielding information about framework distortions, water population cation positions etc.

Figure 1 shows a 3-dimensional plot of the powder diffraction profiles obtained through dehydration and the thermal transformation into γ-eucryptite. Figure 2 shows the population of the water molecules, determined from Rietveld refinement, as a function of temperature.

1. P. Norby, I.G. Krogh Andersen, and A. Nørlund Christensen *Acta Chem. Scand.*, **A40** (1986) 500. 2. P. Norby *Zeolites* **10** (1990) 193. 3. P. Norby, A. Darovsky, J.C Hanson, and I. Meshkovsky 1996 (In preparation).

Supported by US DOE, Div. Chem. Sci., BES (DE-AC02-76CH00016)

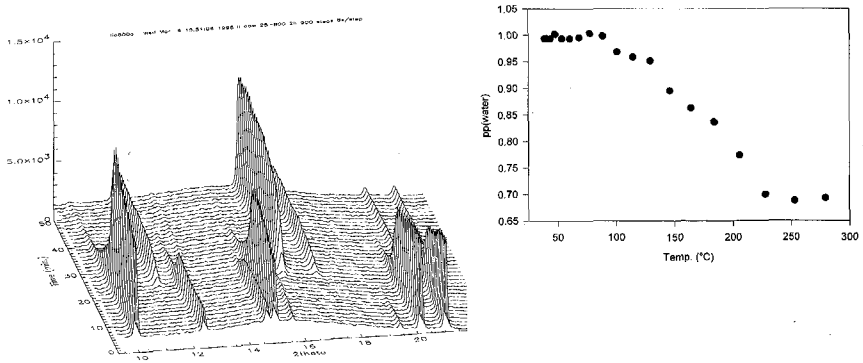


Figure 1.

Figure 2.

Adsorption of Hydrofluorocarbons on Zeolites; An *in-situ* Powder Diffraction Study. *	X7B

P. Norby, F.I. Poshni, M.F. Ciraolo, C.P. Grey, (SUNY Stony Brook) and J.C. Hanson (BNL - Chemistry).

Zeolites are extensively used for gas separation and adsorption, where both structural properties and extra framework cations play important roles. To understand the differences in adsorption properties towards different Hydrofluorocarbon (HFC) isomers we have initiated *in-situ* time resolved powder diffraction studies to determine binding sites, kinetics and mechanism of adsorption/desorption. By combining the *in-situ* studies with MAS nmr and structural studies of pre-loaded samples(1) we hope to gain insight in the adsorption process.

In-situ adsorption/desorption experiments were performed using faujasite type zeolites loaded in 0.7mm quartz glass capillaries. The *in-situ* setup is described elsewhere(2). The equipment at X7B was modified to allow switching between vacuum and a known pressure of HFC during the experiment. The zeolite was first dehydrated *in-situ* under vacuum, and then cooled to the adsorption temperature (-10 - 100°C). Adsorption was followed by time resolved powder diffraction using the Translating Imaging Plate (TIP) camera(2). The HFC was afterwards desorbed at ~300°C under vacuum (again following the process using the TIP-camera). The adsorption/desorption cycle was performed using different HFC gases, and varying the HFC partial pressure, the adsorption temperature, and the zeolite.

The adsorption is very fast, and it was necessary to use time resolutions down to 5 seconds. Even with 5s time resolution it was possible to follow the kinetics of adsorption using the strongest zeolite diffraction peaks.

1. C.P. Grey, F.I. Poshni, A.F. Gualtieri, P. Norby, J.C. Hanson and D.R. Corbin, (1996) Submitted. 2. P. Norby, Materials Science Forum, 228-231 (1996) 147-152.

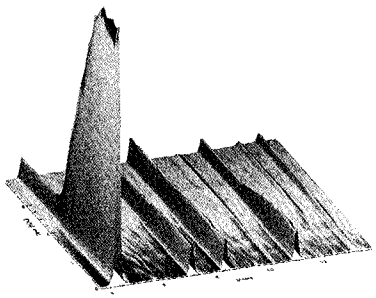


Figure 1. 3-D plot of powder diffraction profiles during adsorption of HFC-134 on zeolite Na-Y at room temperature. The dominating effect upon adsorption is a dramatic decrease of the intensity of the 111 reflection.

* Supported by US DOE (DE-AC02-76CH00016, Div. Chem. Sci., BES) and NSF

An *In-situ* X-ray Powder Diffraction Study of the Dehydration of Zeolite CsY	X7B

F.I.Poshni, M.F.Ciraolo, C.P.Grey (SUNY Stony Brook), A.F.Gualtieri (U. of Modena) P.Norby and J.C.Hanson (BNL - Chemistry)

Zeolites with basic porperties have been found to be effective, for example, as catalysts and for gas separations. A study of the structural properties and the location of the extra-framework cations is important in understanding their role in these processes.

Differences can be observed by comparing the diffraction patterns of CsY dehydrated at two different temperatures: 500°C and 300°C (Figure 1). Preliminary Rietveld refinements show changes in the location of the extra-framework cations. For example, at a dehydration temperature of 300°C, almost all of the cesium cations are located in the SII position in the supercages. By 500°C, a significant fraction of the cesium cations are now located in the SI' positions in the sodalite cages and a decrease in the SII population is observed. In contrast, the sodium cations migrate from SI' to SI and SII positions.

Subtle changes in the zeolite structure were followed by in-situ dehydration under vacuum. The sample was loosely packed in a 0.7mm quartz capillary and was ramped to a final temperature of 500°C over a period of 8 hours. Figure 2 shows the diffraction patterns during dehydration process obtained with the Translating Image Plate (TIP) set-up.

Support from the NSF (DMR 9458017) and for an interagency transfer of support to the US DOE, BES (DE-FG02-76ER14681) is gratefully acknowledged.

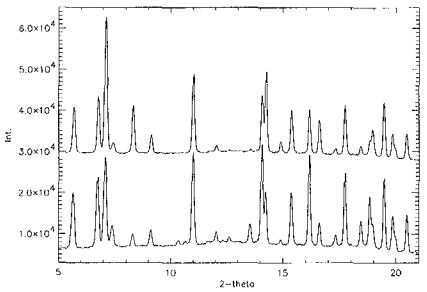


Figure 1. X-ray Powder Diffraction Patterns of CsY dehydrated at 500°C (top) 300°C (bottom).

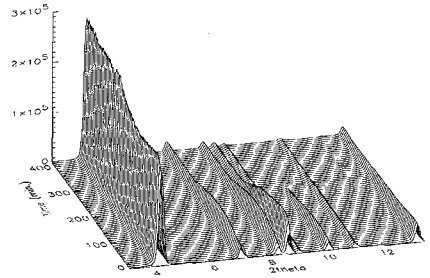


Figure 2. In-situ dehydration of Zeolite CsY

In Situ Thermal Transformations of Nickel/Cobalt Molybdates *	X7B

J. Rodriguez, J. Hanson, S.Chaturvedi (BNL- Chemistry)

Nickel molybdate is a mixed oxide which can be potentially present in supported precursors of Ni-Mo hydro treatment catalysts. It is used as a catalyst for the oxidative dehydrogenation of propane and also serves as a precursor for Hydrodesulfurization (HDS) catalysts. Under atmospheric pressure, it has two stable phases; the α and the β phase. The β phase has a higher HDS activity than the α phase. It is therefore essential to understand the phase transformations of $NiMoO_4$ in order to correlate them to the catalytic activity.

X-ray diffraction (XRD) patterns taken at X7B of $XMoO_4$ (X=Co/Mo) as a function of temperature have given us insights into the various phase transformations that occur. The hydrated $NiMoO_4$ looses water by about 300 °C to form purely the β phase. On heating to 500 °C, the α phase starts to transform into the β phase and the transformation is complete by 700 °C. This β phase, on cooling to room temperature yields a mixture of the α and β phases. $CoMoO_4.(H_2O)_n$ dehydrates at a much lower temperature at about 100-200 °C to form the corresponding β phase. This β phase does not revert back to the α phase on being cooled to room temperature. The XRD patterns allow us to monitor the nature and the temperature of these transformations and also give us information about the kinetic parameters of these transformations.

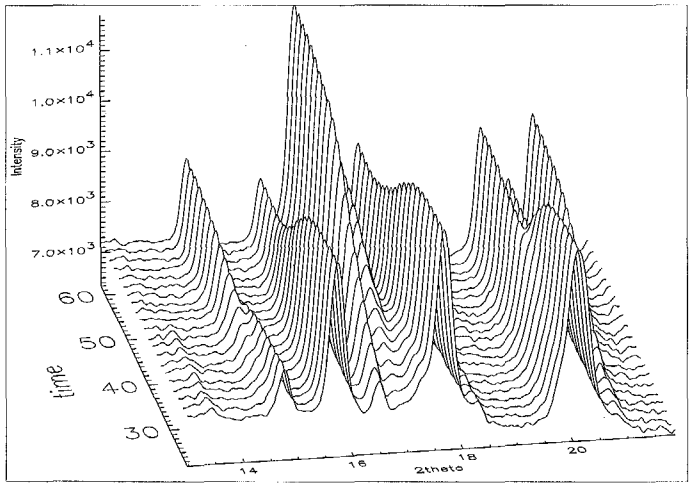


Figure 1. Time-resolved powder diffraction patern obtained during heating from the α to the β phase.

* Supported by contract DE-AC02-76CH00016 with the US DOE by its Div. of Chemical Sciences, Office of Basic Energy Sciences.

In-situ Powder Diffraction Study of Ca-ion Exchange of Zeolite MAP *	X7B

J. A. Stuart (Unilever, UK), P. Norby and J.C. Hanson (BNL - Chemistry)

A series of *in-situ* experiments were performed in order to test the feasibility of observing real-time ion-exchange at a crystallographic level and to observe transient phases during Ca-ion exchange. This is of industrial relevance, as a primary application of zeolites is as ion-exchangers in washing powders, where the timescale of interest is in seconds or minutes.

The sample examined was zeolite MAP (Maximum Aluminum P-zeolite), produced commercially as Doucil A24 by Crosfield, a Unilever company. This zeolite exhibits an unusual degree of structural flexibility, and its ion exchange isotherm suggests the presence of a significant two-phase region(1). Being a very rapid ion exchanger, both time resolution and angular resolution is of the essence.

Figure 1 shows the experimental setup for *in-situ* powder diffraction studies of ion exchange from aqueous solutions. The sample was contained in a glass capillary, and a flow of solution was obtained by a nitrogen pressure. To minimise the development of a reaction front and to improve the flow, the zeolite column was as short as practicable.

Experiments were performed under three conditions: A) *In-situ* ion exchange using a commercial rapid exchange material. B) *In-situ* ion exchange using a lab-prepared slow exchanging material. C) Diffraction paterns of lab-prepared equilibrated samples.

The *in-situ* studies showed that it iwas possible to follow the ion exchange process, although refinements of the experimental setup is necessary. The existence of a two-phase region is supported, but deviations from the model were observed.

1) Adams et al., Proceedings 11'th Int. Zeolite Conf., Seoul 1996 (in press).

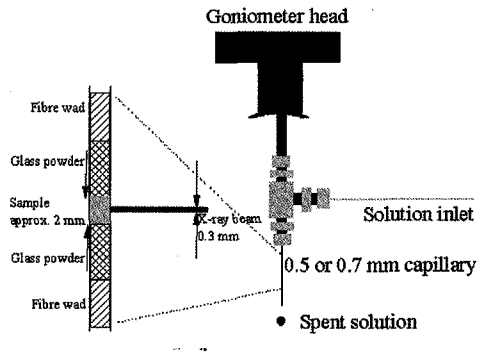


Figure 1.

* Supported by US DOE (DE-AC 02-76CH00016, Chem. Sci. Div., BES)

In-situ Crystallization of Mechanically Treated Zeolites. * | X7B

B. Subotić, C. Kosanović (R. Bošković Inst., Zagreb), P. Norby and J.C. Hanson (BNL - Chemistry)

One route of preparing high temperature aluminosilicate ceramics is by thermal transformation of zeolites. There are many advantages of this method, e.g. well defined starting material, homogeneous composition and low transformation temperatures.

Recently it was shown that mechanochemical treatment of zeolites by ball milling produced amorphous materials having different thermal transformation properties that the parent zeolite(1,2). The transformation temperatures are lowered, and the phase composition of the high temperature ceramics formed are different than those obtained from the untreated zeolite.

Time resolved high temperature powder diffraction experiments were performed using the Translating Image Plate (TIP) camera at X7B(3,4). The thermal transformation of mechanically treated zeolite K/Na-LTA into kalsite/kaliophphilite was followed and compared to thermal transformations of the parent zeolite. Clear differences both in transformation temperature and formation rates were observed. Figure 1 shows a 3-dimensional representation of the transformation of "amorphous zeolite K/Na-LTA" by heating to 950°C.

1. C. Kosanović, J. Bronić, A. Čižmek, B. Subotić, I. Šmit, M. Stubičar and A. Tonejc *Zeolites* **15** (1995) 247. 2. C. Kosanović, B. Subotić, I. Šmit, A. Čižmek, M. Stubičar and A. Tonejc *J. Mater. Sci.* (1996) In press. 3. P. Norby, *Mat. Sci. Forum*, **228-231** (1996) 147. 4. P. Norby, A. Darovsky, J.C Hanson, and I. Meshkovsky (In preparation).

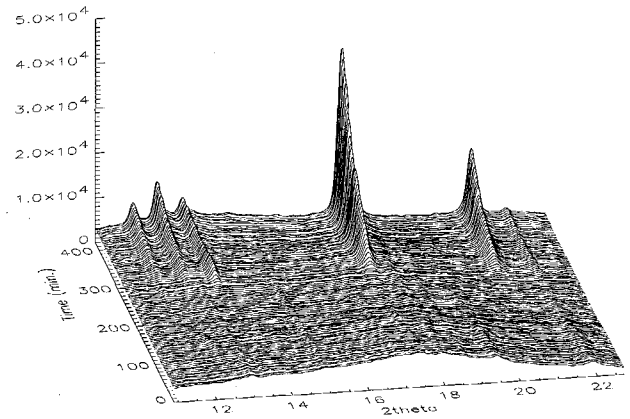


Figure 1.

* This work was supported by US DOE (DE-AC02-76CH00016, Div. Chem. Sci., BES)

Are the Chains in Solid HCN Parallel or Anti-parallel? * | X7B

G. Svensson (Chalmers U. of Technology, Göteborg, Germany), J. C. Hanson (BNL-Chemistry)

Two crystal structures of solid HCN are known. The phase transition between the low temperature form, space group Imm2, and the high temperature form, space group I4mm or P4/nmm, occurs at about 170 K. The main question is: are the HCN-chains parallel (Fig 1) or anti-parallel?. In principle, the problem can be reduced to a choice between two Bravais lattices, P (anti-parallel) or I (parallel). An old single crystal structure determination [1] suggested parallel chains while theoretical calculations have indicated anti-parallel chains [2] and parallel chains [3].

Neutron diffraction data, below and above Tc, from powders of HCN and DCN have been collected at Studsvik Neutron Research Laboratory in Sweden. At NSLS, at beamline X7B, synchrotron powder data were collected on HCN. These data show that HCN crystallize with an I-centered orthorhombic unit cell and a crystal structure with parallel HCN-chains, as shown in Fig. 1. In order to study the phase transformation data were also continuously collected, using a moving image plate, while the temperature was decreased from 170 to 125 K, Fig. 2. The transition was found to be completely reversible.

[1] Dulmage, W.J. & Lipscomb, W.N., Acta Cryst. 4, 330, 1951. [2] Cummins, P.L., Bacskay, G.P., Hush, N.S. & Jnsson, B., Chem. Phys. Lett. 145 399, 1988. [3] Panas, I., Chem. Phys. Lett. 201 255.

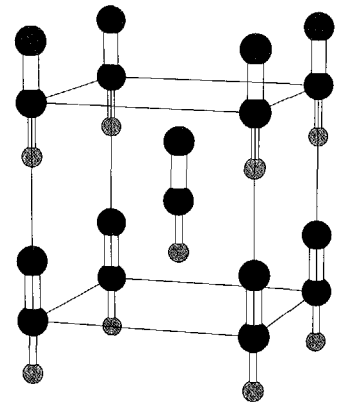


Figure 1. The unit cell of HCN.

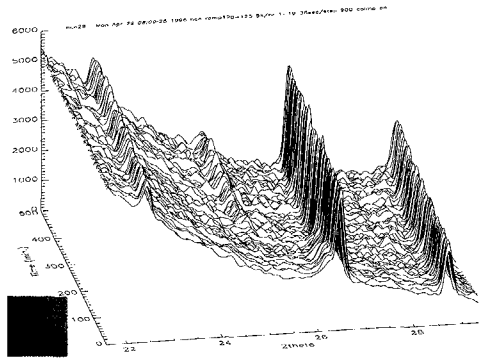


Figure 2. A continuous X-ray diffraction spectra for HCN where the 170 to 125 K.

* Contract AC02-76CH000016 with US DOE by its Div of Chem. Sciences, Office of Basic Energy Sciences and the Swedish Natural Science Council.

In-situ Time Resolved Powder Diffraction Studies of the Hydrothermal Synthesis of Antimony Sulfides Templated by Dimethylammonium	X7B

K. Tan, J. B. Parise, Y. Ko,(SUNY StonyBrook) P. Norby, and J. C. Hanson (BNL)

Under autogenous hydrothermal conditions, crystallization of antimony sulfide in the presence of organic templates produce a mixture of phases, which depend on temperature and heating conditions. Preliminary *in-situ* experiments on the DMA-SbS (DMA, dimethylammonium) system provide some insights into the chemistry of the digestion of crystalline starting materials and the structural transformation involved in the synthesis. Antimony and sulfur were mixed and ground into fine powders and then packed into a quartz capillary of 0.7 mm. Dimethylamine solution was injected into the capillary and the powder mixture was wetted gradually. The capillary was fitted into the head of a specially designed goniometer, which was mounted on a Huber diffractometer. A pressure of 300 psi was introduced into the capillary and an air heater was programmed to control the temperature.

Upon heating the Sb and S first react to produce antimony polysulfides, which condensed quickly to form the S-rich precursor phase with an open structure DMA-SbS-SB8 at 100 oC. When the temperature is increased to 200 oC, the first open structures gradually transform to a new phase (DMA-SbS-SB8). The transformation was slow suggesting a solid-state reorganization to form the highly-ordered crystalline phase, DMA-SbS-SB8.

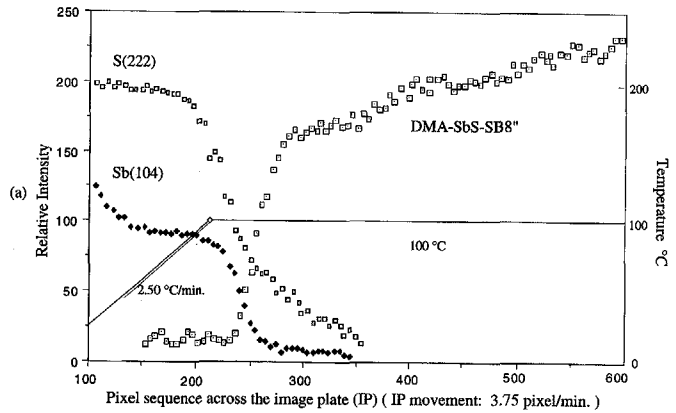


Figure 1. The phase transformation and phase formation during the hydrothermal synthesis of DMA-SbS

Competition Between Kinetic and Thermodynamic Control of Phase Transitions in Silica/Surfactant Mesophase Composites	X7B

S. H. Tolbert and G. D.Stucky (U. of California/Santa Barbara), P. Norby and J.C. Hanson (BNL - Chemistry)

Ordered inorganic/surfactant mesophase composites represent a major advance in the synthesis of materials with nanoscale periodicity. The materials are formed by the self assembly of combined inorganic/organic species and represent a unique non-equilibrium solid phase. A key feature of these materials is that they can be calcined to remove the surfactant and produce an ordered mesoporous solid.

In an effort to understand the kinetics and thermodynamics that control structure in these materials, we have followed phase transformations in these composites under hydrothermal conditions using real time X-ray diffraction. Transformations in polymerized silica/surfactant composites between hexagonal (P6m), lamellar, and micellar hexagonal (P63/mmc) phases were observed. In all cases, the structural transformations appeared to be driven by packing constraints of the organic component of the composite, suggesting that this organic phase packing plays a dominant role in determining the observed structures of these materials. Similar packing constraints have be used to understand equilibrium structural changes in pure surfactant/water systems. In this case, however, all transformations are intrinsically non-equilibrium, exemplified by the observation that the transitions are not reversible. Thus, while organic packing may control the observed structures of these materials, the cross-linked inorganic component plays a large role in determining transformation energetics.

Because of the detailed chemical control available during the synthesis of these materials, it is possible to observe both hexagonal (P6m) to lamellar and lamellar to hexagonal transitions under similar conditions. This offers a unique opportunity to follow both forward and reverse reactions of a transformation that occurs far from equilibrium. Hexagonal to lamellar transformation are discontinuous (1st order) and proceed through a modulated lamellar phase. Lamellar to hexagonal transitions also proceed through a modulated lamellar phase, but in this case the reaction appears to be continuous (likely 2nd order). This result, along with further analysis of kinetic data obtained on these systems should proved insight into the energetic that control the structures observed in these materials.

Iridium Optical Constants from X-ray Transmission Measurements, 2-12 keV	X8A, X8C

R. L. Blake (LANL), J. J. Fitch, D. E. Graessle, B. Harris, J. Juda (SAO), E. M. Gullikson (LBL), and M. L. Shattenburg (MIT)

Precise transmission measurements of free standing Ir foils and of Ir coatings on thin polyimide films have been made from 2 to 12 keV. These measurements were conducted to provide Ir optical constants in support of NASA's Advanced Astrophysics Facility (AXAF). Transmission measurements were made at small energy increments, matching those used for reflectivity measurements, across the Ir M- and L-edge regions to study detailed edge structures. From these data the imaginary part (absorption coefficient) of the complex optical constant was derived at each energy increment. Real parts were computed from the imaginary parts via the Kramers-Kronig dispersion integrals. Most of the measurements had an accuracy within one percent for transmissions. Derived absorption coefficients are less accurate in the 6-12 keV range because the foil thicknesses were not optimum, and in the 2-7 keV range because of foil thickness uncertainty and possible nonuniformity. Absorption coefficients were compared to the semi-empirical compilations commonly called the Henke Tables, with agreement as good as the estimated accuracy of those tables. Transmission derived absorption coefficients were also compared with reflectivity derived values, with agreement to plus or minus ten percent over 2-12 keV and within a two percent range over the high absorption region of the M-edges. At 10 keV transmission, reflection, and Henke Table results agreed within a two percent range. No other measured Ir absorption coefficients have been found in the literature. Our work will continue on additional foils and mirrors until systematic errors have been reduced to the one percent level.

Modeling the Diffraction Efficiencies of the AXAF High Energy Transmission Gratings Above 2 keV	K. A., X8A

K.A. Flanagan, T.T Fang, C. Baluta, J.E. Davis, D. Dewey, T.H. Markert (MIT); D.E. Graessle, J. Drake, J. E. Fitch, J.Z. Juda, J. Woo (SAO); J. Bauer (U. of Hawaii)

The High Energy Transmission Grating Spectrometer (HETGS) is a high-spectral resolution instrument which includes 336 individual transmission grating elements. It is designed to fly aboard the Advanced X-ray Astrophysics Facility (AXAF), a NASA X-ray observatory scheduled for launch in 1998. The gratings of the HETGS are of two types. High energy gratings (HEGs) have a 2000 Angstrom period and an average bar height of 0.52 microns, with a line/period ratio of 0.6. Medium energy gratings (MEGs) have a 4000 Angstrom period and an average bar height of 0.37 microns, with a line/period ratio of 0.52. The calibration approach relies on synchrotron radiation (SR) tests of a few gratings to establish the validity and accuracy of the physical model we use. The model uses scalar diffraction theory, and considers the period, height, width, shape and tilt of the grating bar, as well as absorption by the polyimide support structure and the plaring base materials. The goal of the modeling is to obtain efficiencies accurate to the 1% level, except near absorption edges where the requirement is at the level of 5% to 10%. Gratings that have been tested at the SR facilities are then used as transfer standards in laboratory X-ray tests of each individual grating element, to minimize systematic errors and allow normalization against a known efficiency. We present here the results of a series of new SR tests performed at NSLS in October, 1995. These (and other) results are detailed in Flanagan, et al, SPIE Proceedings vol. 2808, 1996. One MEG grating (MA2047) and one HEG grating (HA2021) were tested. Both of these gratings were from AXAF flight lots. The focus was on a dense sampling of zeroth and first order diffraction efficiencies over most of the NSLS energy range of beamline X8A. The data and results of our model fitting for grating HA2021 is presented in Figures 1 and 2, where the first and zeroth diffraction orders were fit simulatneously. Analogous results apply to the NSLS data for grating MA1047. Note that, for much of the energy region, the residuals are generally within the calibration goal. Future work will include modeling with data from higher orders (obtained at NSLS in March, 1996) and data from PTB at energies below 2 keV. We plan to explicitly take into account edge structure as we pursue modeling in this energy region.

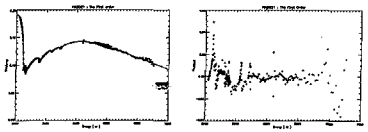


Figure 1. Best fit model and residuals for the first order NSLS data of grating HA2021 when both the first and the zeroth diffraction orders are fit simultaneously. Wing corrections have been included. Residuals scale: -4% to +6%.

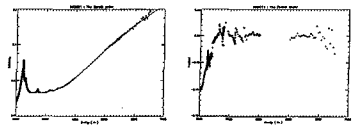


Figure 2. Best fit model and residuals for the zeroth order NSLS data of grating HA2021 when both the first and the zeroth diffraction orders are fit simultaneously. Wing corrections have been included. Residuals scale: -15% to +5%.

Reflectivity Measurements of Multilayer Optics for Use on the Advanced Photon Source Soft X-Ray Beamlines *	X8A

K.J. Randall, J.Z. Xu (ANL), D. Graessle and J.J. Fitch (Harvard-Smithsonian Center for Astrophysics), S. DiFonzo, B.R. Mueller, W. Jark (Sincrotrone Trieste)

The Advanced Photon Source (APS) is constructing a soft X-ray spectroscopy beamline (2ID-C) covering the photon energy range from 500 eV to 3 keV. It is based on a grazing incidence spherical grating monochromator [1]. The optical geometry is such that multilayer optical components (mirrors and gratings) will be necessary to reach energies above 2.6 keV. The optical element considered was the horizontal focusing mirror of 2ID-C in which the undulator beam has an incidence angle of 88.75°. With a conventional single layer Rh coating, the calculated reflectivity drops very rapidly above 2.6 keV. The multilayer parameters were selected by comparison of several geometries using scalar reflectivity calculations. These calculations indicated that a Ni-C multilayer with 7 layer pairs, a d-spacing of 135Å, and a gamma value of 0.33 would give us optimum performance. In the first of our measurements, we have tested the reflectivity of a multilayer sample produced with the triode sputtering system of the multilayer technology laboratory of Sincrotrone Trieste. The multilayer was deposited onto a float glass substrate with a measured 6Å rms surface roughness.

The reflectivity measurements were made with the UHV reflectometer at X8A [2]. With the grazing incidence angle of the sample set at 1.25°, the X8 double-crystal monochromator energy was scanned. The incident beam intensity and the reflected intensity were recorded, the ratio being shown in figure 1. The measured reflectivity agrees well with scalar calculation values including surface roughness. We plan to optimize parameters for this particular optical component by including both depth and lateral gradation of the d-spacing. Further, we plan to make measurements of test gratings with multilayer coatings.

The X8-A reflectometer is extremely valuable to us since we can perform trial measurements on inexpensive sample substrates. This is necessary because of the cost of the high quality ($\leq$1 μrad slope error) water-cooled substrates required at the APS. Stripping and recoating of such optics, due to incorrect choice of multilayer parameters, will not be possible.

[1] K.J. Randall, J.Z. Xu, and E. Gluskin. Rev Sci Instr 66 4081 (1995).
[2] D.E. Graessle, J.J. Fitch, R. Ingram, J. Zhang Juda and R.L. Blake. Rev Sci Instr 66 2095 (1995).

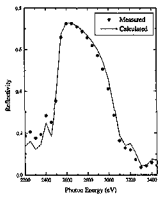


Figure 1. Comparison of measured and calculated multilayer reflectivity.

* Work supported in part by the U.S. Department of Energy, Basic Energy Sciences-Materials Sciences, under contract No. W-31-109-ENG-38.

Iridium Optical Constants from X-ray Transmission Measurements, 2-12 keV	X8A, X8C

R. L. Blake (LANL), J. J. Fitch, D. E. Graessle, B. Harris, J. Juda (SAO), E. M. Gullikson (LBL), and M. L. Shattenburg (MIT)

Precise transmission measurements of free standing Ir foils and of Ir coatings on thin polyimide films have been made from 2 to 12 keV. These measurements were conducted to provide Ir optical constants in support of NASA's Advanced Astrophysics Facility (AXAF). Transmission measurements were made at small energy increments, matching those used for reflectivity measurements, across the Ir M- and L-edge regions to study detailed edge structures. From these data the imaginary part (absorption coefficient) of the complex optical constant was derived at each energy increment. Real parts were computed from the imaginary parts via the Kramers-Kronig dispersion integrals. Most of the measurements had an accuracy within one percent for transmissions. Derived absorption coefficients are less accurate in the 6-12 keV range because the foil thicknesses were not optimum, and in the 2-7 keV range because of foil thickness uncertainty and possible nonuniformity. Absorption coefficients were compared to the semi-empirical compilations commonly called the Henke Tables, with agreement as good as the estimated accuracy of those tables. Transmission derived absorption coefficients were also compared with reflectivity derived values, with agreement to plus or minus ten percent over 2-12 keV and within a two percent range over the high absorption region of the M-edges. At 10 keV transmission, reflection, and Henke Table results agreed within a two percent range. No other measured Ir absorption coefficients have been found in the literature. Our work will continue on additional foils and mirrors until systematic errors have been reduced to the one percent level.

Crystal Structure of the Metallo-beta-lactamase from *B. fragilis*, and Preliminary Crystallographic Data for Enzyme-I and a Deletion Mutant of the Class A Beta-lactamase from *S. Aureus*	X8C

N. Concha, U. Pieper, S. Banerjee, and O. Herzberg (U. of Maryland)

We had previously determined the structure of the metallo- beta-lactamase from B. fragilis at 1.85 Angs. resolution by MAD methods using the intrinsic zinc ions as the anomalous scatterers. A new data set was obtained at 2.15 Angs. using the CCD area detector at the X8C beamline. Diffraction data was collected from crystals obtained in the presence of cadmium instead of zinc. The crystals are isomorphous with those of the Zn-containing form with unit cell dimensions: a=b=78.1 Angs., c=139.7 Angs., and belong to the tetragonal space group, P4(3)2(1)2. The crystals were soaked in a solution containing a poor substrate, Tazobactam, with the goal of producing a stable complex that could be observed crystallographically. The 2Fo-Fc map of the refined structure shows no indication of any species bound in the active site. However, the data enable comparison between the Zn- and the Cd-bound molecule.

In addition to the experiments on the metallo-beta-lactamase, we carried out a number of feasibility studies on crystals of a deletion mutant of a class A beta-lactamase from S. aureus. These crystals had a low rate of success upon freezing, and the few that froze well deteriorated a short time after starting data collection. Nevertheless, we were able to collect a partial data set. In addition, crystals of the bacterial Enzyme I, a member of the phosphotransfer system (PTS) involved in sugar transport across the bacterial membrane were checked. The enzyme I crystals diffracted to 7 Angs. resolution.

Fimbrin and the Cytoskeleton	X9B

S. Almo, S. Goldsmith, M. Sullivan (AECOM)

The strutucre of fimbrin, one of the members of a family of actin cross-linking proteins, is currently being examined by synchrotron crystallography. Fimbrin binds and cross-links filamentous actin, contributing to cytoskeletal structure and function. Fimbrin contains a calcium binding domain as well as two actin binding domains. Two actin binding domains of fimbrin have been crystallized and the strutucre will be solved using multiple isormorphous replacement. These crystals diffract to about 2.5 angstroms. To date, diffraction data has been obtained from the native crystal as well as from two heavy atom derivatives. Preliminary protein electron density maps, calculated from the diffraction data, show alpha helics to be a predominant secondary structural feature of fimbrin. Ultimately, to improve this protein map it will be necessary to collect data from the heavy atom derivatives to higher resolution.

Synchrotron Crystallography Structural Analysis of Profillin	X9B

S. Almo, M. Sullivan, J. Eads, N. Mahoney (AECOM)

Profilin is a ubiquitous 15kD protein required for the normal distribution of filamentous actin structures in vivo. Profilin binds PIP2, suggesting a possible link to signal transduction pathways. Profilins from different organisms have limited sequence homology, but highly homologous 3D structures, indicating an evolutionary pressure to maintain the protein fold. It has been the goal of our laboratory to combine crystallography and in vivo studies to examine the role of profilin in the cell. Two profilin data sets were collected at X9B.

Crystals of P2 profilin, (a profilin isoform of Acanthamoeba castellani), which diffracted only to 4.0A using a rotating anode and diffracted to 2.0A at X9B, has a space group of F432 and unit cell parameters of a=b=c=241.28, a=b=g=90o. The atomic structure of P2 profilin will aid in the creation of mutants with which to study the specific lipid binding activity of this protein. Crystals of Saccharomyces cerevisiae profilin which diffracted weakly using a rotating anode, diffracted to 3.0 A at X9B. The S. Cerevisiae crystals are of the P432 space group with unit cell parameters of a=b=c=127.66, a=b=g=90o and were successfully reduced and scaled with an Rmerge of 5.8 percent. Most importantly, the S. Cerevisiae structure will allow us to design rational mutants for future in vivo structure function and studies on profilin.

EXAFS Studies of the Zinc Derivative of Cytochrome-C: An Unusual Coordination State	X9B

H. Anni (Thom. Jeff. Med. Coll.), J. Vanderkooi (U. of Penn.), M.R.Chance, E. Scheuring (AECOM)

The structure of zinc (II)-substituted cytochrome c (Zn-Cytc), recently resolved by NMR, suggested that Zn is in an unusual coordination with six ligands (Anni et al., Biochemistry 1995, 34, 5744-5753). Furthermore, fluorescence line narrowing spectroscopy has shown that Zn becomes penta- coordinated upon protein unfolding. An hexa-coordinated state of Zn in Cytc is unique since there are no examples of any hexa-coordinated Zn-proteins, and there are no hexa-coordinated Zn-porphyrins in solution. Moreover, the particular coordination of Zn with five nitrogens and one sulfur ligand in Cytc is surprising, because even among the Zn organic compounds that are hexa-coordinated (27% of the 428 crystal structures) none is of the type (N) 5-Zn-(S) 1. Taken together these findings point to a tight protein modulation of the binding preference and strength of Zn to its ligands in Cytc. The Zn-edge extended X- Ray absorption fine structure (EXAFS) studies of Zn-Cytc were undertaken in order to define the central metal environment, specifically the distances of the Zn metal to its ligands and their nature. Both native and guanidine-denatured Zn-Cytc at neutral pH were measured, alongside with the corresponding Fe(III)-Cytc references.

The absorption spectra of the samples after EXAFS spectroscopy were measured to reconfirm protein integrity. Sets of experimental EXAFS data were fit to theoretical curves (FEFF 6.01) using a novel global mapping and refinement procedure (AUTOFIT 1.0) were obtained. This data analysis establishes the coordination of the Zn site in Cytc: an hexa- coordinated Zn in the native protein environment (Zn-Np=2.052A, Zn-Met80 (SD) =2.34A, Zn- His(NE)=2.371A) and a mixture of penta-coordinated Zn states in the denatured sample (Zn-Np=2.10A, Zn-His(NE) =2.10-2.20A).

Resonance X-ray Diffraction Studies of Membrane Protein Monolayers	X9B

J. K. Blasie, L. Prokop, E. Nordgren, J. Stzalka, L. Kneller, A. Edwards, R. Fischetti (Univ. of Penn.)

Both soluble proteins and detergent-solubilized integral membrane proteins can be tethered to the surface of inorganic substrates via bifunctional organic chain molecules possessing a headgroup specific for the substrate surface and an endgroup specific for one or more residues exposed on the protein's surface. Such tethering can provide a single, vectorially-oriented monolayer of the fully- functional protein on the surface of the substrate which is ideal for correlated structural and functional studies, especially if the solid substrate has been suitably tailored by Molecular Beam Epitaxy for x-ray (or neutron) diffraction studies.

We have most recently employed sulfhydryl-endgroups for covalently tethering yeast cytochrome c, in which the heme iron atom was isomorphously replaced by cobalt, to the surface of Ge/Si multilayer substrates; the so-tethered cytochrome c monolayer was then used as a template to electrostatically bind detergent-solubilized mitochondrial cytochome aa3 oxidase to thereby form a vectorially-oriented monolayer of the bimolecular cytochrome c-cytochrome oxidase complex on the substrate's surface.

Resonance x-ray diffraction effects on the meridional kinematical x-ray diffraction from the cytochrome c heme cobalt atom and from the cytochrome oxidase heme a and heme a3 iron atoms have been detected, utilizing a position-sensitive proportional counter, with good signal-to-noise over a sufficiently wide range of photon momentum transfer Qz. The on-going analysis of these resonance effects on the meridional diffraction will permit an unambiguous determination of the locations of the resonant atoms within the already determined nonresonant profile structure of the bimolecular complex within the tethered monolayer. Such structural studies are critical to our understanding of the actual structure of this bimolecular complex and the role of this structure in intermolecular electron transfer phenomena, including the possible electrogenic nature of the intermolecular electron transfer in the generation of transmonolayer electrochemical potentials.

Heterotropic Effects on the Active Site Structure of Hemocyanin	X9B

L. Bubacco, R. Magliozzo, M. Wirt, J. Peisach (AECOM), L. Powers, (Utah St.U.)

K-edge x-ray absorption and extended x-ray absorption fine structure (EXAFS) spectroscopies were used to investigate the effects of allosteric modifiers of oxygen affinity, on the coordination geometry of Cu(I) in Panulirus interruptus deoxy-Hc and subunit II of Limulus polyphemus deoxy-Hc. These modifiers included hydrogen ions, L-lactate, and chloride. The coordination geometry of the metal, which is evaluated based on the intensity of the 1s 4pz transition, changes from pseudotetrahedral to trigonal with increasing pH. This structural alteration is correlated with increased oxygen affinity of the proteins at alkaline pH (Bohr effect).

EXAFS analysis of both deoxy proteins at high and low pH demonstrate that coordination number and Cu-L bond lengths are not sensitive to pH. Thus, modulation of the coordination geometry of Cu(I) is a feature of the active site governed by the Bohr effect in Hc.

Kinetics and Mechanism of Lipid Phase Transitions	X9B

M. Caffrey (OhioSU)

All of our kinetic measurements rely upon access to the corresponding equilibrium behavior of the lipid/water systems under investigation. Thus, temperature-composition (T-C) phase diagram construction is an integral part of our time-resolved studies. A separate ongoing project, concerned with establishing the relationship between lipid molecular structure, overall sample composition and mesophase behavior, also requires T-C phase diagram construction. Much of the mesophase identification and structure characterization required for mapping out a phase diagram can be done using an in-house rotation anode. However, our phase diagrams extend up to 100° C and occasionally go as high as 140°C where time-dependent sample decomposition becomes becomes a major problem To obviate this limitation, all such measurements at and above 50°C are now done using synchrotron radiation where exposure times are down by an order of magnitude compared to the rotating anode. For this purpose, we have specially built a temperature-regulated sample holder accommodating up to 7 samples at a time that is used in conjunction with a multiple-frame image plate detector. Most recently, the temperature-composition phase diagram of monovaccenin (a C18:1c11 monoacylglycerol) in water was constructed using small- and wide-angle x-ray scattering in the range of ca 0 C to 111°C and ca 0% to 60% (w/w) water in the hearting direction. The phase identified in the system include the lamellar crystalline (Lc) phase, the lamellar liquid crystalline (L) phase, the fluid isotropic (Fl) phase, two inverted cubic phases (Q230,la3d; Q224, Pn3m), and the inverted hexagonal (HII) phase. The monovaccenin/water phase diagram is remarkably similar to that of the monoolein (aC18:1c9 monoacylglycerol)/water system. A portion of the current T-C phase diagram for the monovaccenin system shows evidence of non-equilibrium behavior in the region below 60°C and above 20% (w/w) water that will require more detailed investigation.

Protein Footprinting: Structures of Molten Globule States and Mass Spectrometic Analysis	X9A

M.R.Chance, M.D. Brenowitz (AECOM)

Protein cleavage by x-ray generated hydroxyl radicals is much more difficult, than nucleic acid cleavage, occurring on timescales 10 x longer. Thus, it is not immediately apparent that these methods will be a boon to time resolved folding studies. However, they can identify solvent accessible regions in unusual pH states or where other (generally enzymatic) cleavage methods fail. Of longer term significance is our preliminary observations that substantial modification, revealed by mass spectrometry, occurs to the native protein after 50-150 milliseconds of exposure to the x-ray beam.

For apomyoglobin, these modifications are revealed as a widening of the peak of the native protein in Matrix-Assisted Laser Desorption Time-of-Flight mass spectrometry methods. Electrospray-quadoupole MS, has identified variants with single modifications after only 150 ms exposure to the x-ray beam. These are currently being analyzed by enzymatic digest to pinpoint the regions of modification, which will then become reliable markers of folding processes or protein-protein interactions, and possible open up and entirely new avenue for footprinting research.

Time-Resolved Synchrotron X-ray Footprinting	X9A

M.R.Chance, M.D. Brenowitz, B. Sclavi, M. Sullivan (AECOM)

Hydroxyl radicals (OH) can cleave the phosphodiester backbone of nucleic acids and are valuable reagents in the study of nucleic acid structure and protein-nucleic acid interactions. Irradiation of solutions by high flux "white light" x-ray beams based on bending magnet beamlines at the National Synchrotron Light Source (NSLS) yields sufficient concentrations of OH so that quantitative nuclease protection ("footprinting") studies of DNA and RNA can be conducted with a duration of exposure in the range of 50 - 100 msec. The sensitivity of DNA and RNA to x-ray mediated OH cleavage is equivalent. Both nucleic acids are completely protected from synchrotron x-ray induced cleavage by the presence of thiourea in the sample solution, demonstrating that cleavage is mediated exclusively by free radicals. The utility of this time-dependent approach to "footprinting" is demonstrated by obtaining a synchrotron x-ray "footprint" of a protein-DNA complex and by a time-resolved "footprinting" analyses of the Mg2+-dependent folding of the Tetrahymena thermophilia L-21 Sca I ribozyme RNA.

Equilibrium titrations reveal differences among the ribozyme domains in the cooperativity of Mg2+-dependent folding. RNA folding progress curves over timescales of 30 sec. to several minutes were obtained for several regions of the ribozyme. The rate constants obtained for the P3-P7, P4-P6 and P5 domains are comparable with those obtained by Zarrinkar Williamson [Science 265: 918-924, 1994] using a hybridization-competition assay and confirm the hierarchy of the folding of the ribozyme domains established by these investigators. The folding rates obtained for individual regions within domains suggest additional steps in the folding pathway. Synchrotron x-ray "footprinting" is a new approach of general applicability for the study of time-resolved structural changes of nucleic acid conformation and protein-nucleic acid complexes (J. Mol. Bio., in press).

Beamline X-9A : A Resource Devoted to Time-Resolved X-ray Footprinting	X9A

M.R. Chance, M.D. Brenowitz, M. Sullivan (AECOM)

The demonstration of footprinting technology and the purchase and construction of a stopped flow instrument dedicated to the project created a dilemma for the Resource that has been resolved by the completion of construction of a new beamline dedicated to footprinting. Prior to this summer, all footprinting experiments had been conducted as a guest user on beamline X-19A of the NSLS. When the technology was under proof-of-principle development, this was not a hindrance.

Generally, one beamline experimental day every 10 was available and the progress of experimentation was adequate. As the method has become more reliable not enough beamtime was available.

The Resource had previously abandoned the construction of beamline X-9A, as a copy of beamline X-9B, since there was not a demonstrated need for a full second line devoted to XAS and diffraction. Yet, the beamline was substantially complete and the Resource, along with funds provided from the grants of Dr. Brenowitz and Dr. Chance, had the capability and expertise (in the person of Mr. Sullivan) to complete the line as a white beamline station, substantially closer to the source than X-19C, thus with an estimated 3-4 fold increased. As of 9/30/96, this station is in regular use. Thus, in the coming year, a substantial increase in footprinting results is expected.

1-We currently have available to users a stopped flow device for rapid mixing and exposure to the x-ray beam.

2-We also have a fast shutter for precisely defining the exposure time for "static" experiments.

AUTOFIT 1.0 : A New Software for XAS Global Mapping	X9B

M.R.Chance, W. Huang, E.Scheuring (AECOM)

We have developed a global mapping procedure, where crystal strutucre coordinates are refined to XAS data using the ab initio XAS code FEFF 6.01. A grid of hundreds of simulations are directly compared to the experimental data without the use of non-linear least squares fitting procedures to find the interatomic distances. Instead, each simulation is performed with different interatomic distances. The emphasis is on mapping the local and global minima and providing a detailed visual picture and error analysis in the comparison of alternative structures.

The three dimensional structural coordinates utilized in the simulations are based on crystal structure models derived from structural databases. Thus, a particular geometry for the metal site is incorporated in this choice. Alternative structures with different geometries can also be selected, processed, and compared. This makes the structural assumptions about the site explicit and they must be justified based on ancillary structural information. Our suite of programs (called AUTOFIT 1.0) vary selected bond distances, compare the resulting ab initio simulations to the experimental data, and compute and plot a figure that displays 400-500 alternative solutions simultaneously. These programs are available to outside users free of charge and have been readied for release along with a manual for using the code.

Global Mapping of EXAFS Data : Structure of the Photoproduct of Mb*CO	X9B

M.R. Chance, E. Scheuring, W. Huang (AECOM)

X-Ray methods based on synchrotron technology have the promise of providing time- resolved structural data based on the high flux and brightness of the X-Ray beams. One of the most closely examined problems in this area of time-resolved structure determination has been the examination of intermediates in ligand binding to myoglobin. Recent crystallographic experiments using synchrotron radiation have identified the protein tertiary and heme structural changes that occur upon photolysis of the myoglobin-carbon monoxide complex at cryogenic temperatures (Schlichting, I., Berendzen, J., Phillips, G, Sweet, R. Nature, 371, p.808-812 (1994)). However, the precision of protein crystallographic data (0.2 Å) is insufficient to provide precise metrical details of the iron-ligand bond lengths. Since bond length changes on this scale can trigger reactivity changes of several orders of magnitude, such detail is critical to a full understanding of metalloprotein structure-function relationships.

Extended X-Ray Absorption Fine Structure (EXAFS) spectroscopy has the potential for analyzing bond distances to a precision of 0.02 A, but is hampered by its relative insensitivity to the geometry of the backscattering atoms. Thus, it is often unable to provide a unique solution to the structure without ancillary structural information. We have developed a suite of computer programs that incorporate this ancillary structural information and compute the expected experimental spectra for a wide ranging series of Cartesian Coordinate sets. The programs systematically increment the distance of the metal to various coordinating ligands (along with their associated higher shells). Then, utilizing the ab initio EXAFS code FEFF 6.01, simulated spectra are generated, compared to the actual experimental spectra, and the differences computed. Thus, the details of the local minimum as well as the global problem are revealed in a single plot. This allows direct evaluation of the adequacy of competing solutions.

The power of these programs are demonstrated in the examination of high signal to noise EXAFS data from a photolyzed solution sample of the myoglobin-carbon monoxide complex at 10 K. Evaluation of this data using our global mapping procedures placed the iron to pyrrole nitrogen average distances close to the value for deoxy myoglobin (2.05 +/-0.01 A), while the distance from iron to the proximal histidine nitrogen is seen to be 2.20 +/- 0.04 A. It is also shown that one cannot uniquely position the CO ligand based on the EXAFS data alone, as a number of reasonable minima (from the perspective of the EXAFS) are observed. This provides a reasonable explanation for the multiplicity of solutions that have been previously reported. The results presented here are seen to be in complete agreement with the crystallographic results within the respective errors of the two techniques however, the Extended X-Ray Absorption Fine Structure data allows the iron-ligand bond lengths to be precisely defined.

Time-Resolved X-ray Spectroscopy on Microsecond Timescales | X9B

M.R.Chance, E. Scheuring, A. Xie (AECOM)

Time-resolved structure determinations are at the forefront of attempts to understand the mechanisms of protein reactions. We have demonstrated a system for collecting high quality x-ray absorption spectroscopy data on microsecond timescales. The method can be used for both full spectra accumulation and kinetic spectrophotometry. These experiments have vast potential, not only for examining metalloproteins, but also for observing the dynamic behavior of a wide range of chemical elements in conjunction with photochemical, rapid mixing, and temperature jump techniques. The following accomplishments have been made in the preceeding 12-month period:

1) We have successfully increased the effective X-ray flux more than 10 fold by implementing the sagittal dynamic focusing monochromator.

2) We have increased the signal-to-noise ratio by nearly 3 times, with the design, construction and reliable operation of time-resolved 14 channel window discriminator copuled to a computer controlled data acquisition system.

3) We have permanently installed a 20 Hz Nd-YAG laser system with 532 and 355 nm pump beams on beamline X-9B for initiating time-resolved photo-reactions.

4) We have published two papers detailing these improvements, along with several published abstracts and meeting presentations and have another manuscript in preparation.

5) We have examined the dynamics of the myoglobin-CO photoproduct after a laser flash and observe the transit of water into the heme pocket consistent with the last step of the photo-dissociation reaction.

X-ray Reflectivity of Mechanically and Optically Rubbed Polyimides * | X9B

S. S. Ghosh, P. A. Heiney, M. R. Stetzer, O. Y. Mindyuk (UPenn) and S. T. Sun (Alliant Techsystems)

We have measured the X-ray reflectivity of rubbed polyimide films used for liquid crystal alignment. Both mechanically rubbed polyimides and polyimides 'rubbed' by linearly polarized UV light were examined. The mechanical rubbing process creates microgrooves on the surface of the polyimide film. These microgrooves have a particular average spacing perpendicular to the rubbing direction, but in general run parallel to the rubbing direction. The off-specular reflectivity from a mechanically rubbed film featured additional intensity when the film was oriented with its rubbing direction parallel to the incident X-ray beam. This off-specular scattering arises from the height-height correlations of the microgrooves to the film-glass interface.

The analysis of the specular reflectivities obtained from these films will produce a comparison of the roughness associated with both mechanically and optically rubbed films, parallel and perpendicular to the rubbing direction. We are able to use specular reflectivity to deduce an anisotropy in the roughness along the film surface because our resolution function is asymmetric. Since the resolution function extends much farther out of the scattering plane than in the scattering plane, the specular reflectivity can provide more information than just the electron density perpendicular to the surface. Some information about the film along its surface can also be deduced from the reflectivity.



Figure 1. The reflectivity of a mechanically rubbed polyimide film with the rubbing direction a) parallel and b) perpendicular to the incident X-ray beam. The Kiessig fringes, total external reflection and the off-specular scattering are all evident in the image.

* This work was supported by NSF Grant No DMR MRL 92-20668 and DMR 93-15341

XAS Studies of the Structure and Function of Ni in Chromatium Vinosum Hydrogenase	X9B

Z. Gu, C.B. Allan, S.B. Choudhury, M.J. Maroney (U. of Massachusetts)

The Ni, Fe hydrogenases (H_2ases) usually exhibit five forms with distinct epr spectral characteristics and spanning four oxidation states. One question central to understanding te mechanism of the enzyme is the degree of participation of Ni center in the redox chemistry. Of the five forms, A and B have the same oxidation state (both are oxidized), but differ greatly in their rates of reductive activation, and have distinct epr spectra. Forms A and B are reduced to an epr silent intermediate (SI) and then to form C, which is an active redox state of the enzyme and exhibits a distinct epr signal from an S = 1/2 center containing Ni. The enzyme can be further reduced to form R, which is fully reduced and epr silent.

This report summarizes an XAS structural study of the Ni site in Chromatium vinosum H_2ase as a function of redox poise. Data are presented for forms A, B, C, and R. Figure 1 shows the comparison of the Ni K-edge XANES spectra for these four forms. They reveal a maximum shift in the edge energy of 1.4(2) eV from B to R. A peak assigned to a 1s→3d transition is discernible in all four spectra, but is ca. 3 - 6x larger in the oxidized forms (A and B) relative to the reduced forms (C and R). None of the spectra reveal a 1s→4p_z (plus shakedown) transition near the edge that is diagnostic for four-coordinate planar geometry. Figure 2 compares the EXAFS spectra obtained from the four forms. The best fits to the data are Form A: 3 S 2.19(2)Å + 2 N(O) 1.91(2) Å + 1 Fe 2.69(5) Å; Form B: 3 S 2.10(2) Å+ 3 S 2.56(2)Å; Form C: 4 S @ 2.20(2)Å + 1 Fe 2.54(5) Å; Form R: 2 S 2.16(2)Å + 2 S 2.22(2) Å + 1 S 2.66(5) Å. These fits indicate the difficulty of discerning a Ni-Fe vector expected at 2.6 Å in the presence of a long S scattering atom at a similar distance, as predicted from the crystal structure of the H_2ase form D. gigas . They predict that the coordination sphere of the Ni contains only S in all but form A.

This work is supported by NIH grant GM-38829 (MJM). Samples of C,v, H $_2$ase were provided by Simon P.J. Albracht (U. of Amsterdam). We are grateful for technical support from Hai Yang and Michael Sullivan.

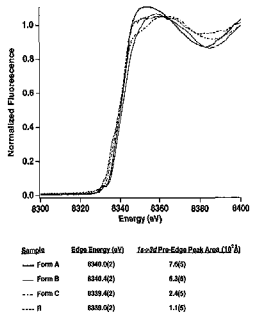


Figure 1. Ni K-edge XANES of Spectra taken on redox poised samples of Chromatium vinosum hydrogenase.

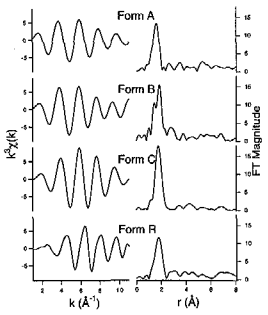


Figure 2. Ni K-edge EXAFS Spectra taken on redox poised samples of Chromatium vinosum hydrogenase.

Structure and Kinetics: A Molecular Basis for Ligand Affinity In Hemeproteins	X9B

C. Lee, E. Scheuring, M.R. Chance, J. Peisach (AECOM)

This investigation aims at understanding the relationship between metal-ligand electron- nuclear coupling and bond lengths in oxyCo(II) porphyrin complexes, active site models of Co(II)- substituted globins. Co(II)-substituted globins are functional and paramagnetic analogues of O2-carrying hemoproteins. Coupling of the unpaired electron on the oxyCo unit of these proteins and models to an axial cobalt-bound 14N nucleus can be studied by electron spin echo envelope modulation (ESEEM) spectroscopy. The magnitude of the ESEEM-derived 14N electron-nuclear hyperfine coupling and nuclear quadrupole coupling constants have been correlated with the electronic configuration of the trans cobalt- dioxygen bond. Both ligand hyperfine and nuclear quadrupole coupling decrease with an increase in the ionicity of the cobalt-dioxygen bond, i.e., its electronic structure shifts from a Co2+-O2 towards a Co3+- O2- configuration. An increase in the ionicity of the cobalt-oxygen bond would also suggests a shorter bond. Furthermore, a decrease in the axial 14N nuclear quadrupole coupling is indicative of an increase in the overlap between the 14N sp2 hybrid and the Co dz2 orbital and thus implies a decrease in the axial cobalt-nitrogen bond length. The present study therefore aims at testing the hypothesis that a decrease in cobalt-axial nitrogen electron-nuclear coupling is accompanied by a shortening of both the axial cobalt- nitrogen bond and the trans cobalt-oxygen bond using EXAFS spectroscopy.

Axial cobalt-ligand bond length measurements have been carried out on several sets of samples. The first set is oxyCo[tetraphenylporphyrin(TPP)][1-methylimidazole (1-MeIm)] in 100 percent toluene, 9:1 (v/v) toluene:CH2Cl2 and 1:1 toluene: CH2Cl2. ESEEM studies has found decreases 14N(1-MeIm) electron-nuclear couplings with increasing polarity of the solvent (Aiso from 3.14 to 2.75 MHz, e2qQ from 2.32 to 2.25 MHz). The second set of samples is oxyCo[(o-R)1TPP][1-MeIm] in 2.26 toluene, where R=H, NHCOC(CH3)3, NHCOCH3 and NHCONHC6H5. The amide proton on R, the para substituent of one of the meso phenyls of TPP, is believed to interact electrostatically with the cobalt-bound axial O2. ESEEM studies has found decreases in 14N(1-MeIm) electron-nuclear couplings with increasing electron- withdrawing strength of R (or increasing acidity of the amide proton) (Aiso from 3.14 to 2.57 MHz, e2qQ from 2.32 to 2.13 MHz). EXAFS spectroscopy is used to test whether shorter cobalt-oxygen and shorter cobalt-nitrogen bonds are found for those complexes with smaller electron-nuclear coupling constants. Using our global mapping technique, we have seen that for the cobalt model compound in toluene, the iron oxygen bond length is 1.90 A, the iron-imidazole bond length is 2.00 A, and the average distance of iron to the equatorial nitrogen bond lengths is 1.96 A (Co-Np). EXAFS studies of the methylene chloride induced structure show a contraction of the Co-Np distance by 0.02 A and a contraction of the Co-N axial imidazole distance by 0.05 A, while the cobalt-oxygen distance is unchanged within the error. This provides a definitive structural correlation for the changes seen in ESEEM data and illustrates a strutctural mechanism for controling oxygen binding rates.

Biological Metal Clusters	X9B

M. Maroney, S. Choudhury, C. Allan, Z. Ge (U Mass)

Enzyme and protein active sites containing two or more interacting metal centers now figure prominently in metallobiochemistry. Systems containing metal clusters composed of Fe atoms (e.g. ferredoxins, sulfite reductase, hemerythrin, ribonucleotide reductase, methane monooxygenase), Cu atoms (e.g. hemocyanin, tyrosinase, ceruloplasmin), Mn atoms (photosystem II, catalase) and more than one element, or heteropolynuclear clusters (e.g. nitrogenase-Mo,Fe; cytochrome oxidase-Fe,Cu; hydrogenase and carbon monoxide dehydrogenase-Ni,Fe), have been identified. The ultimate goals of this project are to elucidate the structures of metal clusters in metalloproteins, to determine the roles these clusters serve in the function of the protein, and to understand how nature designs a cluster for a specific purpose. This knowledge will provide a detailed understanding of biological processes and will aid in the design of pharmaceutical enzyme inhibitors and catalysts for various reactions. During the current report period, we have completed studies of the structural changes that occur in the Ni site in Thiocapsa roseopersicina hydrogenase during the binding of CO, a competitive inhibitor of the enzyme that has been shown to bind in a terminal fashion to the enzyme. The XAS studies do not show any evidence that the CO molecule binds directly to the Ni site. The CO complex is light sensitive and exhibits reversible photodissociation of the CO ligand. During photochemical cycling, the edge energy shifts by 0.5 eV in a cyclic fashion, suggesting that the CO binds near the Ni site and influences its electronic structure. A likely binding site is the Fe atom 2.7 A distant from the Ni in the recently published crystal structure of the D. gigas enzyme. These results support earlier studies indicating that Ni is not the substrate/inhibitor binding site in the enzyme.

A Low Angle Diffraction Study of the Effects of Nucleotide Binding on the Structure of the Actomyosin Complex	X9B

K. Poole, P. Ellison, M. Lorenz, K. Holmes, (Max Planck Inst.), G. Evans, G. Rosenbaum, (ANL), P. Boesecke (ESRF), C. Cremo (Wash. St. U)

With an atomic model for the actin filament (Holmes et.al. 1990, Nature, 347: 44-49; Lorenz et. al. 1995, J. Mol. Biol. 246: 108-119) and the atomic coordinates for at least one form of the myosin motor protein (Rayment et.al. 1993, Science 262: 50-58) we are in a position to make use of high angle fibre diffraction data from myosin decorated actin filaments to refine a model structure of the complex. Nucleotide-free myosin subfragment-1 (S1) isolated from both chicken skeletal and smooth muscles was introduced into overstretched rabbit psoas muscle fibres. In both cases the protein binds tightly to actin and this results in the intensification of the actin based layer lines in the X-ray pattern. Refining an actomyosin atomic model against the nucleotide-free skeletal S1 data produced a best fit which was similar to the model suggested by Rayment et. al. (1993) based on electron microscope evidence. ADP binding had very little effect on this diffraction pattern. The nucleotide-free (unphosphorylated or thiophosphorylated) smooth muscle S1 decorated filaments produced a very different diffraction pattern and the binding of ADP was shown to induce a structural change in the head resulting in a pattern similar to that from skeletal S1 decorated fibres. The Kd for ADP binding was shown to be ca. 2 micromolar.

It is most interesting that the two rigor complexes are structurally different. If the rigor structure represents the end of the power stroke then the data imply that at least some part of the power stroke in these two motors is produced by different configurational changes of the actomyosin complex. Alternatively, we must question our interpretation of the rigor structures themselves. We are in the process of refining the model against the smooth muscle S1 data but it is clear that the ADP induced structural change in the myosin head is very large and certainly involves the distal part of the head. This may reflect the tail wagging motion described by Whittaker et. al. 1995, Nature 378: 748-751, from their electron microscopic evidence.

Data were collected on Fuji imaging plates at beamlines X9B at the NSLS, Brookhaven and BL4, ID2 at the ESRF, and scanned using a Fuji BAS2000 system.

The *E. Coli* Primase Zinc Structure is Sensitive to the Binding of ATP and High Magnesium	X9B

L. Powers, M. Griep (Utah State U.)

Enzyme and protein active sites containing two or more interacting metal centers now figure prominently in metallobiochemistry. Systems containing metal clusters composed of Fe atoms (e.g. ferredoxins, sulfite reductase, hemerythrin, ribonucleotide reductase, methane monooxygenase), Cu atoms (e.g. hemocyanin, tyrosinase, ceruloplasmin), Mn atoms (photosystem II, catalase) and more than one element, or heteropolynuclear clusters (e.g. nitrogenase-Mo,Fe; cytochrome oxidase-Fe,Cu; hydrogenase and carbon monoxide dehydrogenase-Ni,Fe), have been identified. The ultimate goals of this project are to elucidate the structures of metal clusters in metalloproteins, to determine the roles these clusters serve in the function of the protein, and to understand how nature designs a cluster for a specific purpose. This knowledge will provide a detailed understanding of biological processes and will aid in the design of pharmaceutical enzyme inhibitors and catalysts for various reactions. During the current report period, we have completed studies of the structural changes that occur in the Ni site in Thiocapsa roseopersicina hydrogenase during the binding of CO, a competitive inhibitor of the enzyme that has been shown to bind in a terminal fashion to the enzyme. The XAS studies do not show any evidence that the CO molecule binds directly to the Ni site. The CO complex is light sensitive and exhibits reversible photodissociation of the CO ligand. During photochemical cycling, the edge energy shifts by 0.5 eV in a cyclic fashion, suggesting that the CO binds near the Ni site and influences its electronic structure. A likely binding site is the Fe atom 2.7 A distant from the Ni in the recently published crystal structure of the D. gigas enzyme. These results support earlier studies indicating that Ni is not the substrate/inhibitor binding site in the enzyme.

Active Site Targeting of Protein Tyrosine Phosphatase 1B by Synchrotron Crystallography	X9B

Y. A. Puius, Y. Zhao, M. Sullivan, D. Lawrence, Z.-Y. Zhang, S. C. Almo (Albert Einstein College of Medicine)

A collaborative project between Dr. Steven Almo (crystallographer), Dr. Zhong-Yin Zhang (enzymologist) and Dr. David Lawrence (synthetic chemist) has been established in order to design potential therpeutic agents based on the structures of protein tyrosine phosphatases. Since data collected on a rotating anode source have not been of sufficient resolution to adequately define the binding mode of ligands to the proteins in question, this effort has been undertaken using single-crystal diffraction data collected at beamline X9B.

Using synchrotron methods, the structure of human protein tyrosine phosphatase 1B (PTP1B) has been solved in complex with several synthetic non-peptide substrates to high resolution. The most promising of these complexes has been the structure (1.9Å resolution, $R_{merge} = 5.2\%, R_{cryst} = 18.2\%$) of an inactive mutant of PTP1B bound to a compound with a micromolar K_m. It was expected that this ligand, a phosphotyrosine mimic, would bind in the active site; however, it actually possessed two mutually exclusive binding modes, one in the canonical pTyr-binding site, and the second in a previously unobserved phosphophenyl binding site. Since pTyr had not been seen to bind outside the active site before, this prompted a crystallographic investigation of PTP1B crystallized in the presence of high ($> 10K_m$) concentrations of pTyr. In this high pTyr-complex (1.85Å resolution, $R_{merge} = 4.2\%, R_{cryst} = 18.1\%$), the second phosphotyrosine was in fact observed at the same location where the second non-peptide ligand bound.

The elucidation of this second phosphotyrosine-binding site has provided information crucial to the design of a new class of tight-binding inhibitors of high specificity for PTP1B, which is becoming more important as the role of PTP1B in oncogenesis and non-insulin dependent diabetes mellitus becomes clear.

Additional experiments include the solution of complexes between PTP1B and peptides to understand the determinants for binding extended substrates. One of these complexes (1.9Å resolution, $R_{merge} = 3.5\%, P2_12_12_1, a = 66.35$ Å, $b = 72.54$ Å, $c = 88.47$ Å) is currently undergoing refinement.

EXAFS Studies of Nonheme Iron Enzymes | X9B

L. Que, L. Shu, X. Wang, S. Mandal, K. Chen (U. of Minnesota)

Several metalloproteins containing nonheme-iron centers have been investigated in the past year. This class includes methane monooxygenase, purple acid phosphatase, and stearoyl-ACPΔ-9 desaturase. Data was collected on methane monooxygenase hydroxylase (MMOH), one of the most extensively studied diiron enzymes. XAS analysis of MMOH suggests the presence of two Fe-Fe distances of about 3 $\AA$ and 3.4 $\AA$, which are proposed to reflect two populations of MMOH molecules with either a bis(μ-hydroxo) (μ-carboxylato)- or a (μ-hydroxo)(μ-carboxylato) diiron (III) core structure, respectively. This paper has been published (1). We have also collected and analyzed data on an Fe(III) Zn(II) derivative of the purple acid phosphatase from porcine uterus which allows us to look at the Fe(III) and the Zn(II) sites separately. In the phosphate complex of this derivative, the observation of Fe-Zn and M-P (M = Fe, Zn) distances of 3.3 and 3.2 $\AA$, respectively, indicates an FeZn(OR)2 core structure and phosphate is proposed to bind to the metal center in a bridging mode. This paper is in press (2). EXAFS data are being processed on stearoyl-ACPΔ-9 desaturase, which is a new member of the class of nonheme diiron enzymes. With the crystallographic data available for hemerythrin, ribonucleotide reductase and the hydroxylase component of methane monooxygenase, kidney bean phosphatase, and EXAFS data for the other proteins, we will be able to identify the common structural features that make up these dimetallic sites within this class and to discern the variations in structure that control mechanism and function.

EXAFS analysis has also been crucial for the structure determination of unstable model complexes related to intermediate of nonheme proteins. Data was taken and analyzed on copper model complexes modeling copper dioxygen chemistry in metalloproteins, and this paper is in press (3). EXAFS data on iron model complexes have also been taken and are being processed.

1-Shu, L., Liu, Y., Lipscomb, J.D., Que, L. Jr. "X-Ray Absorption Spectroscopic Studies of the Methane Monooxygenase Hydroxylase Component from Methylosinus trichosporium OB3b." JBIC 1, 209-217 (1996). 2-Wang, X., Randall, C.R., Que, L. Jr. "X-Ray Absorption Spectroscopic Studies of an FeZn Derivative of Uteroferrin." Biochemistry (1996), in press. 3-Mahapatra, S., Halfen, J.A., Wilkinson, E.C., Pan, G., Wang, X., Young, V.G., Jr., Cramer, C.J., Que, L., Jr., Tolman, W.B. "Structural , Spectroscopic, and Theoretical Characterization of Bis(m-oxo)dicopper Complexes, Novel Intermediates in Copper-Mediated Dioxygen Activation." J. Am. Chem. Soc. (1996) in press.

XAFS Analysis of a Transition State Inhibitor of Chloroplast CF-1 ATPase | X9B

I. Sagi, C. Carmelli (Weizmann Inst.)

The membranes of chloroplast mitochondria and bacteria contain a proton ATPase which utilizes the electrochemical potential of protons for the synthesis of ATP from ADP and Pi. Similar to enzymes of other energy-transducting membranes, the chloroplast H+ ATPase consists of an intrinsic membrane sector CFO which mediates proton translocation and an extrinsic catalytic section CF1. From the known chemistry of GTP and ATP hydrolysis in other systems, it might be expected that catalysis in F- type ATPase proceeds through a pentacovalent phosphate intermediate. A penta-covalent phosphorous is also assumed to be a transition state intermediate since it is readily inhibited by the Pi analog vanadate. X- ray Absorption Fine Structure (XAFS) data on vanadium edge were collected on vanadate-CF1 complex. Direct XAFS analysis of the pre-edge transitions and the EXAFS region clearly show a pentacovalent structure at the active site. These results suggests that a pentacovalent phosphorous exists as a transition state during ATP hydrolysis in CF1-ATPase from chloroplast.

Fe-S Centers in Energy Transducing Enzymes	X9B

I. Sagi, Z. Mingtao, C. Carmelli (Weizmann Inst.)

Light absorbed by the photosynthetic pigments induces charge separation in photosystems I (PSI) driving electron transport from water to NADP+. One of the early electron acceptors in photosystem I (PSI) is a very low potential iron-sulfur cluster, Fx. Understanding the mechanism of action of PSI requires a knowledge of the structure of Fx and the structural changes induced by the electron transfer process through Fx. Although many of the components of PSI and their function are known, there is a little information about their special arrangement and their interaction with the amino acid residues of the polypeptide chains. Site directed mutations were performed on the psaB gene from the cyanobacterium on the two conserved cysteines 556 and 565. Each cysteine was substituted once with serine and once with histidine resulting in overall of four mutants of the B subunit, these cysteines are proposed to serve as two of the four ligands that binds the iron in Fx. We present the X-ray absorption fine structure (XAFS) spectra of the mutated Fx in comparison to the native Fx spectra. The XAFS analysis of the mutated metal site provides a direct assignment of the different ligands.

Solution Iron-Edge XAS of Native Soybean Lipoxygenase-1	X9B

R. Scarrow, N. Taufen, R. Ghiladi (Haverford Coll.)

Lipoxygenases catalyze reactions of polyunsaturated fatty acids with dioxygen to form lipid hydroperoxides; in humans this is the first step in production of leukotrienes from arachidonic acid, a process involved in inflammatory response. All lipoxygenases have conserved amino acid sequence regions, a single non-heme iron, and share many spectroscopic and kinetic properties.

Two independent crystal structures of the inactive native form of soybean lipoxygenase establish three histidine residues and the C-terminal carboxylate as ligands to the iron(II) (Boyington, J. C.; Gaffney, B. J.; Amzel, L. M. Science 1993, 260, 1482-1486; Minor, W.; Steczko, J.; Bolin, J. T.; Otwinowski, Z.; Axelrod, B. Biochemistry 1993, 32, 6320-6323.) An asparagine side-chain carbonyl is suggested to bind iron in one structure, and both structures show a "vacant" coordination site which could be occupied by a water ligand. Our previous EXAFS analyses of frozen solutions of native lipoxygenase indicate a predominantly five-coordinate environment for the iron (II), but that this can be shifted to a six-coordinate environment by addition of 20 mM methanol, or higher concentration of glycerol, prior to freezing. As the coordination number increases, the average bond length increases by 4 pm, from 213 pm to 217 pm (Scarrow, R. C.; Trimitsis, M. G.; Buck, C. P.; Grove, G. N.; Cowling, R. A.; Nelson, M. J. Biochemistry 1994, 33, 15023-15035). We recently re-investigated the effects of methanol on the X-ray absorption spectrum of native lipoxygenase, this time in solution at 4 C. The experiments were carried out at beam line X9B using a solution cell and constant temperature bath provided by the beam line. The spectra change very little for 0 to 10 percent (2 M) methanol, and are all similar to the spectrum of native lipoxygenase frozen without methanol. The refined bond lengths from EXAFS are 212 pm. Thus the iron(II) in native soybean lipoxygenase-1 remains five-coordinate upon addition of methanol unless the sample is subsequently frozen.

Global Mapping of XAS Data from Cobalamin Enzymes | X9B

E. Scheuring, M. Chance (AECOM), R. Banerjee (U. of Nebraska.), R. Matthews (U. of Michigan)

Cobalamin ezymes are unique in biology as the only active organometallic species known (cobalt-carbon bonds). The octahedral cobalt centered cofactors carry out critical methylation reactions and unusual carbon-carbon bond rearrangements in amino acid biosynthesis and fatty acid metabolism. Substantial progress in understanding the structure-function relationships of these enzymes was recently provided. Crystallographic data on the 27 kDa fragment of the methyl-cobalamin (Mecbl) dependent enzyme methionine synthase (MS) from E. Coli [C. L. Drennan et al. Science, 266, 1669 (1994)] and on the 5-deoxyadenosyl-cobalamin (Adocbl) dependent enzyme methylmalonyl-coenzyme A mutase (MMCoA) from Propionibacterium shermanii [F. Mancia et al. Structure, 1996, 4, 339.] show that in both enzymes the cofactor undergoes dramatic structural changes upon enzyme binding. The most significant change involves the dimethylbenzimidazole (DMB) group of the cofactor, which in both cases is detached from cobalt and replaced by a His group of the enzymes.

Both X-ray crystallographic structures have their limitations; the MS structure at 3 A resolution is not able to show distance variations in the cofactor structure in the order of 0.2 A or less with respect to the free cofactor state and the MMCoA structure was collected on a dominantly Co(II) form of the cofactor lacking the adenosyl moiety.

In order to examine the cobalt-ligand bond distances of free cofactor compared to enzyme bound species, we have collected XAS and compared it to FEFF calculations. Our results show that the structure of the cofactor stays the same in the Mecbl dependent enzyme MS both in the wild type Co(III)-methyl and in the Co(II) forms with respect to the free states but changes in the Adocl dependent MMCoA. The Co-N axial bond to the DMB of Adocbl in MMCoA is very long (2.45 A) similar to the crystallographic data which shows a 2.5 A Co-N axial distance for the Co(II) state. Our EXAFS data for the Co-C bond shows two minima, one at around 1.99 A and one at 2.25 A. Based on recent RR data [R. Banerjee at al., unpublished results], the longer distance can be ruled out.

We have also examined mutant forms of MS to examine the role of the His759, Asp757, and Ser810 residues in the hydrogen bonding network that controls the electronic structure of the ligand trans to the cobalt-carbon bond. X-ray edge results (in agreement with EPR data) on the Co(II) form of the MS mutant H759G shows that replacing His759 with a Gly residue causes the formation of a four-coordinate species (identified by the 1s-4pz transition with no Gly ligation to the Co. This mutant shows five magnitude decrease in the catalytic activity with respect to the wild-type Co(II) (Matthews et al., Biochemistry, submitted). This is supported by our earlier result that a four-coordinate Co(II) corrinoid species is very unstable (Wirt et al., J. Am. Chem. Soc., 1993, 115, 5299 and Scheuring et al, J. Phys. Chem., 1996, 100, 3344). The EXAFS results also support a four-coordinate species with an average Co- Neq distance of 1.89±0.01 A similar to other cobalamin species. The Co(II) form of mutant D757N, in which Asp757 is replaced by a Glu, indicates similar geometry to that of the wild-type Co(II). EPR data shows that this mutant is 70% bas-off and its activity is impaired by 50-fold. These results show that His759 in MS is essential to the catalytic activity and any change in the hydrogen bonding network decreases the activity substantially.

The Relationship Between Structure and Conductivity in Polymer Electrolytes | X9B

L. Sharpe, L. Lyons (Grinnell Coll.)

This project involves the investigation of the coordination environments around transition metal ions incorporated in oxymethylene-linked poly(ethylene oxide), OPEO, and poly[bis((methoxyethoxy)ethoxy)phosphazene], MEEP, using EXAFS spectroscopy. Both polymers exhibit ionic conductivity when mixed with various inorganic salts. They have the advantage of being completely amorphous at room temperature, an important property for high ionic conductivities. Little is known about the coordination environment around the metal or counter ions in the polymer salt complexes. We have systematically studied the ionic conductivity, composition, and ion coordination environment in the polymer electrolyte composed of CuCl2 dissolved in OPEO. The objective of this work is to determine the extent ion pairing occurs and how it effects the ion conductivity. The experimental strategy involved the preparation of a series of polymer electrolytes of varying CuCl2 concentration in OPEO and then correlating the resulting conductivities to the copper coordination environment. We have found that both chloride ion and oxygen are present in the copper coordination sphere and that the degree of chloride ion coordination does affect the conductivity by reducing the number of free ions. In addition, the fact that Tg (glass transition temperature) varies in a similar manner as the Cl/O coordination ratio suggests that the chloride ions are in effect cross-linking the polymer chains which increases Tg. The increase in Tg indicates a reduction in polymer motion which also contributes to the decrease in the ion conductivity. This work has been published in RChemistry of MaterialsS(Vol. 6, 1994, 1912). Presently, we are finishing work on the OPEO-CuBr2 system in which we have collected both Cu and Br EXAFS data. In the latest experimental run, we collected data on the MEEP-CuBr2 polymer electrolyte system. It will be interesting to compare the CuBr2 coordination environments in the comb branched MEEP polymer system to the linear OPEO polymer system.

Active Site Structure in Cytochrome c Peroxidase and Myoglobin Mutants	X9B

R. Sinclair, S. Hallam, M. Chen, L. Powers (Utah St. U.), B. Chance (U. of Penn.)

The globins and peroxidases, while performing completely different chemistry, share features of the iron heme active site: a protoporphyrin IX prosthetic group is linked to the protein by the proximal histidine residue. X-Ray absorption spectroscopy (XAS) provides a method to determine the local structure of iron heme active sites in proteins. Our previous studies using X-Ray absorption spectroscopy have revealed a significant difference in the Fe-N (e) bond length between the peroxidases and the globins (for a review, see Powers, L. in Molecular Electronics and Molecular Electronic Devices 3, 211: 1994, CRC Press Inc., Boca Raton, Florida). Globins typically have a Fe-N (e) distance close to 2.1A while the Fe-N (e) distance in the peroxidases is closer to 1.9A. We have proposed (Sinclair, R., Powers, L., Bumpus, J., Albo, A., Brock, B. Biochem. 31: 4892, 1994) that strong hydrogen bonding to the proximal histidine is responsible for the shorter bond length in the peroxidases. Here we use site-specific mutagenesis to eliminate the strong proximal hydrogen bonding in cytochrome c peroxidase and to introduce strong proximal hydrogen bonding in myoglobin. Consistent with our hypothesis, elimination of the Asp-235-His hydrogen bond in CcP results in elongation of Fe-N (e) from 1.9 to 2.1Å. Conversely, introduction of a strong proximal hydrogen bond in myoglobin shortens Fe-N (e) from 2.1 to 1.9Å. These results correlate well with other biochemical data.

Time-Resolved RNA Footprinting: Structure-Function of Splicing Intermediates of the Tetrahymena Ribozyme	X9A

S. Woodson (Univ. of Md.), M. Brenowitz, B. Sclavi, M. Sullivan, M. Chance (AECOM)

The Mg2+ bound and Mg2+ free forms of the RNA ribozyme exhibit distinctly different patterns of hydroxyl radical reactivity. This illustrates the structural changes as solvent accesible regions become protected from hydroxyl radical (OH) attack upon folding.

Thermodynamic analysis of ribozyme folding. The Tetrahymena ribozyme adopts a compact tertiary structure upon the addition of divalent cations. Protection from OH cleavage is believed to predominantly result from the decreased solvent accessibility of the phosphodiester backbone within the interior of the folded ribozyme. Thus, the isotherms and progress curves determined from the OH protection data are interpreted to reflect the folding of the ribozyme. It is assumed in this analysis that the rate of OH cleavage of RNA is linearly related to the solvent accessibility of the phosphodiester backbone. Quantification of individual sites of protection as a function of [Mg2+] reveals that the domains of the ribozyme bind Mg2+ with unique values for cooperativity and/or stoichiometry.

The three sites analyzed within the P3-P7 domain are all characterized by Hill coefficients (nH) of 3-4, consistent with the high Mg2+ cooperativity observed in other studies.The equivalence of nH values for the three sites within the P3-P7 domain is indicative of the highly concerted nature of Mg2+ binding by the ribozyme. The high cooperativity of the Mg2+-dependent folding of the P3-P7 domain contrasts with the more moderate values (nH values clustering around 2) determined for the other domains of the ribozyme; these values are comparable with the "average" value of nH = 3 determined previously. The conclusion that can be drawn from these results is that the effects of Mg2+ ion binding are not uniformly distributed throughout the ribozyme. It is tempting to speculate that the binding of an additional Mg2+ ion is linked to the folding of the P3-P7 domain since nH cannot exceed the stoichiometry of the binding reaction. (However, identical Mg2+ stoichiometries with the cooperativity of Mg2+-dependent folding being more highly concerted in the P3-P7 domain is an interpretation not excluded by the data.) The suggestion that an additional Mg2+ ion is linked to the folding of the P3-P7 domain is consistent with the conclusion that Mg2+ binding follows the rate-limiting folding of P3 to form the active ribozyme. In the three-dimensional model of the Tetrahymena ribozyme core) this highly conserved region is buried deep in the core of the domain and forms the interface between the P4-P6, P3-P7 and P1 domains.

Kinetic analysis of ribozyme folding. The results developed in the last year demonstrate that time-resolved synchrotron x-ray "footprinting" is sensitive to time-dependent changes in local regions of OH protection of RNA. The rate of formation of tertiary interactions is followed in this assay by measuring changes in the accessibility of local regions of the RNA to the OH probe. The internal consistency of the OH kinetics data, and the consistency of the OH kinetics and hybridization-competition studies provides compelling evidence that these approaches accurately monitor the RNA folding reaction. We are continuing these studies at sub second timescales to better understand the folding process (J. Mol. Bio., in press)

X-Ray Absorption and Resonance Raman Spectroscopy of Human Myeloperoxidase — X9B

K. Yue, K. Taylor, J. Kinkade, R. Sinclair, L. Powers (Utah SU)

Myeloperoxidase (MPO), an important enzyme in the oxygen-dependent host defense system of human polymorphonuclear leukocytes, utilizes hydrogen peroxide to catalyze the production of hypochlorous acid, an oxidizing bactericidal agent. While MPO shows significant sequence homology with other peroxidases and this homology is particularly striking among the active site residues, MPO exhibits unusual spectral features and the unique ability to catalyze the oxidation of chloride ions. We have investigated the MPO active site with x-ray absorption and resonance Raman spectroscopies at neutral pH and also at the physiological acidic pH and have compared these results with those of horseradish peroxidase. The MPO heme environment was found to be inhomogeneous. At pH 7.5, the iron heme active site is 6-coordinate where the distal ligand is likely oxygen or nitrogen, but not sulfur. The heme is distorted compared to HRP, other peroxidases, and heme compounds, but at pH3, the distal ligand is lost and the heme is less distorted. HRP also loses its loosely associated distal water at this pH, but little change in heme distortion is observed. This change suggests that loss of the distal ligand in MPO releases stress on the heme which may facilitate binding of chloride ion.

X-Ray Characterization of Magnetic Epitaxial Multilayer Thin Films — X10A

C-H. Lee (National Tsing Hua Univ), M.Y.Chern, C.Y.Huang (National Taiwan Univ), M.T.Tang (SRRC,Taiwan) and K.S.Liang (Exxon)

Recently, we have successfully made epitaxial magnetic multilayers of yttrium iron garnet/gadolinium gallium garnet (YIG(111)/GGG(111)) on the GGG single crystal substrates using the laser ablation deposition method. In this work, x-ray measurement which includes x-ray reflectivity, in-plane and plane normal x-ray diffractions and truncation rod measurement, were carried out to characterize in detail the epitaxial relation of the multilayer, noting that both YIG and GGG have the same cubic structure with a nearly identical lattice constant (0.03% difference). The prefection of epitaxy can be best revealed in the observation of the in-plane "forbidden" (1-10) peak (not shown) and truncation rod measurment which is shown in the following figure.

The figure shows the truncation rod intensity of a sample measured from the in-plane GGG(2-42) peak along the plane normal direction. The sample consists of 12 alternative layers of YIG/GGG with each layer a thickness of one unit cell. The peak positions found in the truncation rod profile correspond to the period of superlattice of one YIG/GGG layer. This result indicates that the multilayer was grown epitaxially in a well-ordered solid on solid fashion.

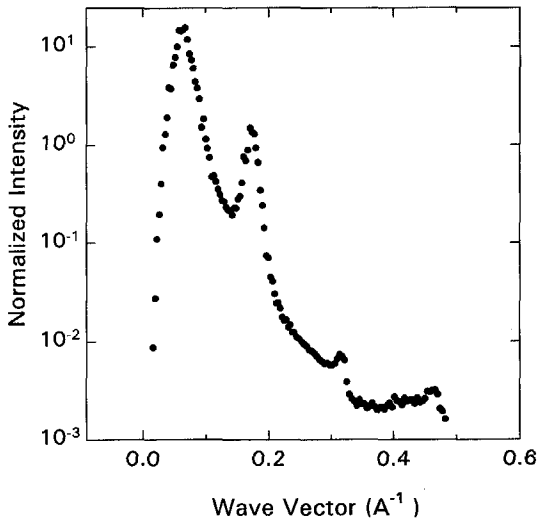


Figure 1.

Small-angle X-ray Scattering Studies of the Growth of Particles in Cethyltrimethylammoniumbromide Micellar Solution Added with Tetraethoxysilane *	X10A

T.-L. Lin, W.-J. Liu (Nat. Tsinghua U.), H. H. Shao, K. S. Liang (Exxon)

0.1 ml of tetraethoxysilane (TEOS) was added to 10 ml of 1% cetyltrimethylammoniumbromide (CTAB) micellar solution. The sample was kept at room temperature. Small-Angle X-ray scattering measurements were started at 12.5 hours from the addition of TEOS. The scattering angle was scanned from low to high angles. Each scattering curve took about three hours to finish. Figure 1 shows the measured scattering curves at different periods of the growing process. The scattering intensities were found to increase with time. This indicates that the particles grow larger with time. Simple Gunier plots give the radius of gyration of the particles of 11.2, 13.2, 15.1, and 15.4 nm at 12.5, 15.5, 19, 24.5, and 28 hours, respectively. It is also noticeable that a small paek developes at Q near 1.2 1/nm. This may indicate there is some ordered structure. More detailed analysis is needed to determine the structure of the particles growed with the CTAB micelles as the template.

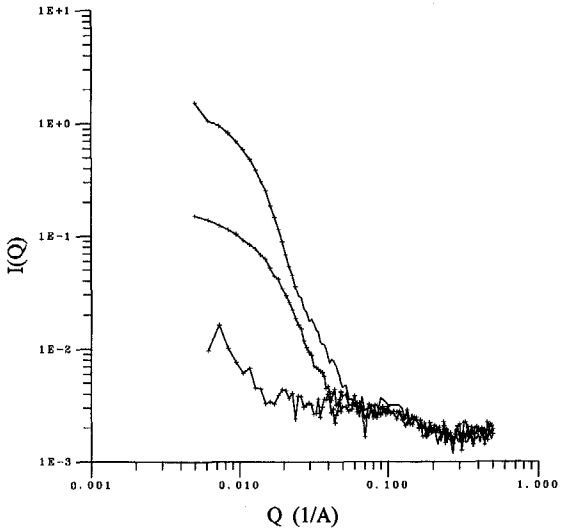


Figure 1. The scattering intensity in relative units as a function of the scattering vector measured at the time as indicated after the addition of TEOS to the 1% CATB micellar solution.

* This work was supported by NSC, ROC.

Chirality, Structure and Free Energy of DNA Liquid Crystals	X10A

H.H. Strey, R. Podgornik, D.C. Rau and V.A. Parsegian (NIH/DCRT/LSB), J. Wang (XFD/ANL), and E. Sirota (Exxon)

Liquid crystals of DNA are the simplest model systems for DNA packing in cell nuclei (e.g. dinoflagellates) or in phage heads. In these systems typically just one extremely long (from 10m up to 1m) DNA molecule forms a macroscopic liquid crystal. We present a structural study on highly oriented DNA liquid crystals measuring the three dimensional structure factor S(q) using small angle x-ray scattering at X10A (BNL). The density of the DNA mesophases was controlled by the osmotic stress method. This method allows us to measure the equation of state and consequently changes in free energy in these systems.

At high densities DNA orders in a columnar liquid crystal with short range and long range orientational bond order (line hexatic or N+6). The line hexatic phase is the three dimensional analog to the hexatic phase in two dimensions. At lower DNA densities we found an intermediate region with two distinct peaks in the x-ray structure factor, a sharper one with six-fold symmetry and a broader isotropic one. Since we hold all intensive variables (p,T,μs) fixed the measured S(q) should result from a single phase. At that point it is not yet clear whether this structure corresponds to a new phase located in between a columnar (non chiral) and cholesteric (chiral) arrangement of the DNA molecules. At even lower pressures we then found a phase transition to a cholesteric phase with a single broad first order maximum in S(q). The figure below shows a series of images showing the in-plane x-ray structure factor while passing through the line hexatic to cholesteric transition In these experiments the highly oriented samples were positioned in such a way that the average director points in the direction of the x-ray beam. The density of the samples was lowered by incresing the temperature of the bathing PEG 20,000MW solution.

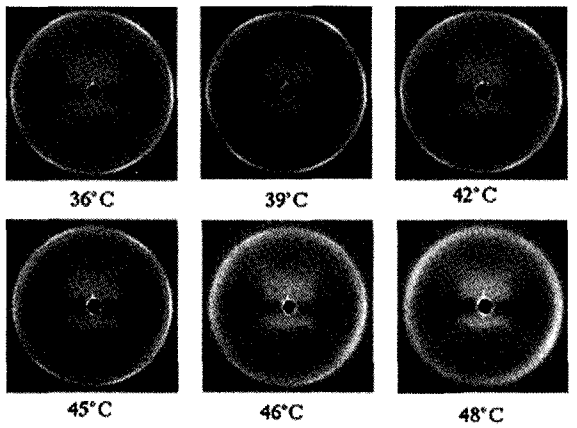


Figure 1.

Unexpected Structure and Properties of ω-unsaturated Thiols Self-assembled Monolayers on Au(111) *	X10B

T.Y.B. Leung, P. Fenter, F. Schreiber, P. Eisenberger and G. Scoles (Princeton U.)

A systematic surface x-ray diffraction study of the structures of monolayers of 1-alkenethiols (CH_2=$CH(CH_2)_{n-2}SH$) self-assembled on the gold (111) surface has been performed. Although the perturbation caused by the double bond insertion at the end of hydrocarbon chain was not expected to be significant, the structure of the undecenethiol (n=11) monolayer has been found to be very different from the methyl-terminated alkanethiol monolayer ($CH_3(CH_2)_{n-1}SH$). The unit mesh of the monolayers can be described as $(\sqrt{3}\times 4\sqrt{3})R30°$, in contrast to a $c(4\sqrt{3}\times 2\sqrt{3})R30°$ unit mesh found for undecanethiol (n=11) monolayers. In addition to the structural differences, the undecenethiol monolayers have been found to be thermally more stable than the methyl-terminated counterparts. We find that although the methyl-terminated monolayers melt at ~100°C, the undecenethiol monolayers only begin to thermally anneal at ~130°C.

We have also investigated if the same phenomenon exists for other chain lengths. We find that the even-chain thiols (n=10 and 18) adopt the same 2-dimensional symmetry and show similar thermal behavior as the methyl-terminated alkanethiols of the same chain-length. Therefore, these preliminary results indicate that the unusual structure and stability of the undecenethiol monolayers may occur only for ω-unsaturated thiols with an odd number of carbons. Therefore we are actively preparing to measure the structures of other alkenethiols where n is odd. The above observations show that the self-assembly process is governed by a delicate balance of many interactions and that the introduction of a small perturbation can have an unexpectedly large impact. It is also possible that the behavior of the undecenethiol monolayers is caused by radiation induced phenomena such as a dimerization of the hydrocarbon groups that contain the double bonds. If confirmed by further work the results could open up a new avenue of research since most previous work on radiation-induced structural effects involved the production of defects (beam damage) instead of a new type of order.

* This work is supported by DOE under grant DE-FG02-93ER45503.

Structure of Rigid Biphenyl Monolayers by Vapor and Solution Phase Growth *	X10B

F. Schreiber, T. Y. B. Leung, P. Fenter, and G. Scoles (Princeton U.)

We have used grazing incidence x-ray diffraction to study the growth and the structural phases of self-assembled monolayers (SAMs) of biphenyl thiols (CH_3-C_6H_4-C_6H_4-SH) on Au(111).

For growth from solution we find diffraction peaks consistent with a $\sqrt{3}\times\sqrt{3}$ - structure (hexagonal phase). The average domain size, however, was only about 65 Å.

In an attempt to improve the structural quality and to explore possible other phases, we employed growth from vapor under UHV conditions, which also enabled us to follow the growth in-situ. For growth at low temperatures (10 °C), we found in-plane Bragg peaks corresponding to a real-space distance of 3.4 Å, which suggests that the phenyl rings of neighboring molecules are arranged in a pancake-like fashion. However, these peaks are not observed for higher sample temperatures.

For growth at higher temperatures, where we think the layer is closer to its equilibrium structure, we find a completely different structure characterized by unit cell dimensions of 10 Å× 11.56 Å. A possible structural model which would be consistent with the observed peaks features two molecules per unit cell with their long axes lying down on the surface and the sulfurs at opposite ends for the two molecules. While we have established the 2-D map of the diffraction peaks, the out-of-plane structure (rodscans) has not yet been fully determined.

The structural quality of these SAMs is very high with domain sizes well above 1000 Å. Another remarkable feature is the high thermal stabilty of the above-described structure. In several annealing and melting experiments we found the layers to be stable up to about 160 °C. A high-quality layer could be regained upon cooling back to room temperature. Even for exposures of several hours (at relatively low flux based on the vapor pressure) the structure did not change significantly, and a transition to the hexagonal phase has not yet been observed.

In future experiments, we will explore further the vapor phase growth and try to find conditions, under which the hexagonal phase can be achieved. Moreover, we will study the growth kinetics and compare these to decane thiol SAMs which are more flexible with their hydrocarbon chain compared to the rigid phenyl rings.

* This work supported by DOE (DE-FG02-93ER45503) and DFG (Schr537/2-1).

Study of the Structure and Growth of Co-assembled Surfactant/Silica Films	X10B

L. Zhou, P. Fenter, I. Aksay and P. Eisenberger (Princeton U.)

In-situ and *ex-situ* X-ray studies have been performed on the self- assembled surfactant/silica thin films which are synthesized with CTAC and TEOS in a diluted acidic solution on freshly cleaved mica substrate. Although the growth of the bulk materials has been well studied, much less is known about the mechanism of growth of well-defined films.

Under these solution conditions a film spontaneously adsorbs to the mica substrate [1]. *Ex-situ* X-ray measurements coupled with AFM measurements show that the film consists of a lattice of hexagonally packed tubes which are oriented parallel to the substrate surface. These films are highly ordered, well aligned along the substrate surface normal and strained with respect to the bulk hexagonal structure [1]. A striking feature of our data is that despite the quasi-hexagonal structure of the mica surface the tubes are only aligned along two of the equivalent next-nearest-neighbor directions of the mica substrate surface. The absence of the alignment in the third direction (which is distinctive due to the distorted atomic arrangement of mica), provides direct evidence that the alignment of the tubes is due to an epitaxial arrangement in spite of the large lattice mismatch betwwen the film and the substrate spacings.

Our *in-situ* X-ray measurement shows that there is a 7 hour induction time in the film nucleation. In Fig. 1, we show the specular reflectivity measurement at different times. We found no evidence of film growth or any ordered structure for 7 hours after the substrate is exposed to the growth solution. After 7 hours, the film begins to grow rapidly with an increasing growg growth rate, such that the film thickness exceeds 1 micron after 2 hours following nucleation (Fig. 2). The 7 hour induction time and nonlinear growth rate of the film are both very surprising and interesting. We have also found similar growth behavior for silica substrate, which suggests that this growth behavior is independent of the nature of the substrate. These data suggest that the film growth proceeds in a very unusual fashion, and raise questions concerning the fundamental nature of the initial nucleation process and the microscopic mechanism of the growth.

[1] I.A.Aksay et al. Science, 273, 892-897 (1996)

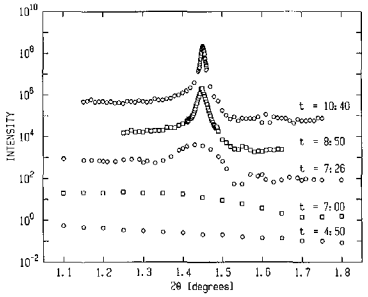


Figure 1.

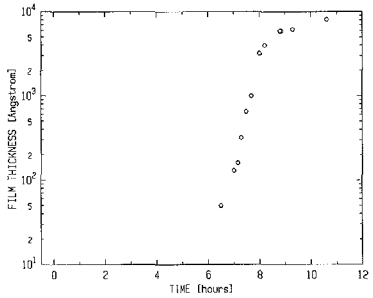


Figure 2.

Local Structure of V_2O_3 During the Metal-Insulator Transition	X11A

A.Frenkel. E.A.Stern (U. of Washington) and F.A.Chudnovsky (Phys.-Tech. Inst., St. Petersburg, Russia)

V_2O_3 undergoes a phase transition from an antiferromagnetic insulator to paramagnetic metal with the crystal structure changing from monoclinic to trigonal with a 1.4% decrease in volume and 0.11 Å decrease in some of the V-V distances as the temperature is increased above 155 K. Measurements of the *local* structure by XAFS may help to determine the mechanism of the transition.

We performed single crystal XAFS measurements, orienting the *c*- axis parallel and perpendicular to the polarization of the synchrotron radiation. XAFS measurements were performed at the NSLS on beamline X11A at two temperatures below the phase transition for each orientation and two temperatures above. XAFS signals were analyzed by the UWXAFS software [1]. Theoretical scattering amplitudes and phases were generated using the FEFF6 code [2] for the monoclinic crystal structure.

The results of the fits (Fig. 1) showed that the local structure of the samples remained monoclinic at all temperatures. The V_0 - V_2 distance (between the pair of atoms lying nearly in the basal plane) decreased above the transition by 0.070 ± 0.025 Å, but its absolute value remained 0.040 ± 0.025 Å longer than given by the trigonal structure of the diffraction measurement [3]. Another characteristic distance (along the *c*-axis) between V_0 - V_1 remained about 0.025 ± 0.02 Å longer than in the trigonal structure, consistent with the static displacement of V_0 and V_2 atoms in opposite directions in monoclinic structure.

More distant group of collinearly arranged V atoms was analyzed separately. This group would produce two sets of paths with half path lengths of 7.255 Å and 7.47 Å for the monoclinic structure and one group (7.38 Å) for the trigonal structure. Figure 2 shows that the two distances remain split above the phase transition. Monoclinic distortions, therefore, persist locally in both phases.

[1] E. A. Stern *et al.*, Physica B **208 & 209**, 117 (1995).
[2] S. I. Zabinsky *et al.*, Phys. Rev. B **52**, 2995 (1995).
[3] P. D. Dernier and M. Marezio, Phys. Rev. B **2**, 3771 (1970).

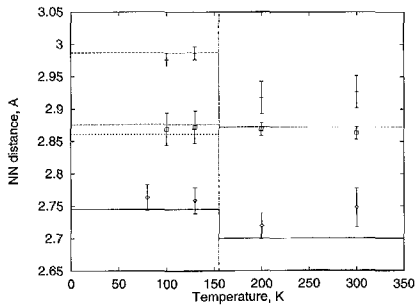


Figure 1. V-V distances as determined by XRD (lines) and XAFS (symbols) for the nearest neighbors.

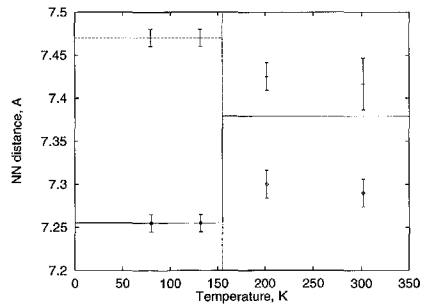


Figure 2. V-V distances as determined by XRD (lines) and XAFS (symbols) for the more distant neighbors.

XAFS Study of Cation Valence State and Site Distribution in Natural Schorlomite and Melanite Garnet * — X11A

A.F. Gualtieri, S. Quartieri (U. of Modena, Italy), K. Pandya (NCSU) and G.M. Lamble (BNL - NSLS)

Natural garnets are widespread rock-forming minerals in the Earth crust and upper mantle; they play a paramount role in the high temperature and high pressure petrogenetic processes and they are as well important markers of contact and regional metamorphic grade. The general chemical formula is $X_3Y_2Z_3O_{12}$ where X is an eight-coordinated site commonly occupied by Ca, Mg, Fe and Mn; Y is an octahedral site occupied by Al, Fe, Ti and Cr; Z is a tetrahedral site mainly occupied by Si and in minor amount by Fe, Al and Ti. Schorlomite is a species of garnet containing more than one atom of Ti per formula unit. Melanite is the complementary varietal name for Ti-andradite which contains less than 1 Ti atom per formula unit [1]. In shorlomite, the tetrahedral site is not fully occupied by Si. This deficiency coupled with a large concentration of Ti and both Fe_{3+} and Fe_{2+} makes the interpretation of the cation site distribution to be rather doubtful. Although several studies have been attempted on the role of Ti and Fe in shorlomite and Ti-andradite, no general agreement has been reached on this issue. Regarding Zr, at present a systematic study is still lacking. The present study attempts to clarify the crystal chemical role of Ti, Fe and Zr in schorlomite samples from Kola-Karelia ijolite-carbonatic complex (Russia) and melanite samples from Monte Vulture (Italy). The samples show a slight Si deficiency and thus are good candidates for Si replacement by Fe and/or Ti in the tetrahedral Z site. The presence of Ti_{3+} has recently been claimed in melanite samples from Monte Vulture (Malitesta et al., 1995). Preliminary Fe and Ti-K-edges XANES and EXAFS spectra collected at the Frascati synchrotron facility (Italy) indicate that at least two different crystallographic sites are involved for both Ti and Fe (Quartieri et al., 1993a; 1993b). Experiments were carried out at X11A beamline which is equipped with a sagitally focusing double Si(111) crystal monochromator. Samples were dispersed in boron nitride and the powder was loaded on an Al sample holder which was fixed on a liquid N_2 cold finger, allowing the data collection to be performed at low temperature. XANES and EXAFS spectra were collected both in transmission and fluorescence (Lytle detector) mode depending on the amount of the investigated element in the sample. Energy calibration was continuously checked by simultaneously monitoring reference spectra using an additional ion chamber detector placed behind the transmission set-up. Higher harmonic reflections from the monochromator were rejected by detuning the parallelism of the Si(111) crystals until the harmonic content was negligible. The K absorption edges which were investigated are: Ti at 4.9637 KeV, Fe at 7.111 KeV, Zr at 18.2271 KeV. The data analysis of the XANES and EXAFS spectra is still in progress.

[1] Deer W.A., Howie R.A., Zussman J. (1982) Andradite. In Rock forming minerals. Vol. 1A: Orthosilicates (2nd ed.), 617-641, Longman, London. [2] Malitesta C., Losito I., Scordari F., Schingaro E. (1995) Eur.J.Mineral. 7(847-858). [3] Quartieri S., Antonioli G., Lottici P.P., Artioli G. (1993a) Mineral. Mag. 57(249-256). [4] Quartieri S., Antonioli G., Artioli G., Lottici P.P. (1993b) Eur.J. Mineral. 5(1101-1109).

* This work was carried out under DOE Contract Numbers DE-AC02-76CH00016 and DE-FG05-89ER45384.

Sr-induced Local Distortions in $La_{2-x}Sr_xCuO_4$ — X11A

D.Haskel and E.A.Stern (U. of Washington)

Sr^{+2} substitution for La^{+3} in $La_{2-x}Sr_xCuO_4$ leads to high T_c superconductivity for $0.075 \leq x \leq 0.25$ by inducing hole carriers in the Cu-O planes. The mechanism of charge transfer, however, is not yet understood partly because of the lack of knowledge of the structure around the Sr atoms. Diffraction techniques yield Sr-O bond lengths which are necessarily the same as La-O ones since Sr substitutes at the La site [1].

Recent experiments showed that the ratio of out of plane, O $2p_z$, to in plane, O $2p_{x,y}$ orbital character of the doped holes increases with Sr doping [2] suggesting a key role of the O(2) apical oxygens in the hole doping mechanism. An accurate picture of the Sr environment is needed to address these findings.

We measured Sr K-edge polarized XAFS on oriented powder with $x = 0.075, 0.1$ at T=20K. We discovered that Sr resides at the La lattice site (Sr-Cu and Sr-La distances are, within 0.01 Å, the same as La-Cu and La-La found in our La K-edge XAFS analysis [3]) but induces major structural distortions in neighboring oxygen atoms. In particular, its O(2) apical oxygen is split into two sites separated by 0.30(4) Å along the c-axis (see fig. 1). This anomaly was not found for the La-O(2) apical distance [3] and could result from a fluctuating number of holes at the Cu site nearby Sr atoms (fig. 1) creating two equilibrium positions for the O(2) atoms. This hole-lattice interaction could be involved in the pairing mechanism leading to high T_c [4]. In addition, the O(2) site closer to the Cu-O planes couples more effectively to them and could explain the increase in O $2p_z$ character of holes with doping [2]. Fig 2 summarizes the distortions induced by Sr substitution. Further details will be reported elsewhere [5].

We acknowledge the valuable help of F. Perez, M. Suenaga and S. Heald in orienting the samples. This research has been supported by D.O.E. grant #DE-FG06-90ER45425.

[1] P. G. Radaelli *et. al.*, Phys. Rev. B **49**, 4163 (1994).
[2] C. T. Chen *et. al.*, Phys. Rev. Lett. **68**, 2543 (1992).
[3] D. Haskel *et. al.*, Phys. Rev. Lett., **76**, 439 (1996).
[4] P. W. Anderson *et. al.*, Phys. Rev. Lett. **60**, 132 (1988).
[5] D. Haskel *et. al.*, to be published.

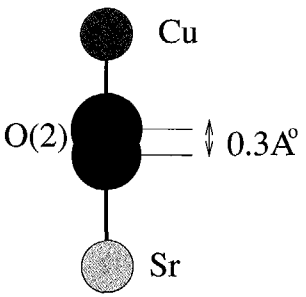


Figure 1. Two site configuration of the O(2) apical to Sr.

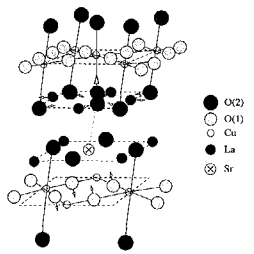


Figure 2. Schematic representation of the pattern of atomic displacements induced by Sr substitution.

X-Ray Absorption Spectroscopy Analysis of Lead and Zinc Speciation in a Contaminated Groundwater Aquifer | X11A

D. Hesterberg, D. E. Sayers, W. Zhou, G. M. Plummer, and W. P. Robarge (NCSU)

The mobility and bioavailability of heavy metals in the environment is influenced by the solubility of the solid-phase chemical species present and aqueous phase speciation. The design of successful remediation technologies for contaminated sites also depends on chemical speciation. The formation of metal sulfides in the environment can potentially reduce the solubility and bioavailability of heavy metals, and have bearing on the optimal approach for remediation design. This project was initiated to assist in assessing remediation strategies for the By-pass 601 Superfund Site in Concord, North Carolina. The site was formerly used for a lead battery recycling operation. The objective of this study was to determine whether PbS and ZnS were dominant solid-phase species in samples taken from different parts of the aquifer at the study site. The occurrence of metal sulfide minerals would depend on the redox conditions in the aquifer. Groundwater aquifer samples were analyzed using EXAFS and XANES spectroscopies at Beamline X-11 to determine whether lead and zinc sulfide were dominant mineral phases. Aquifer solids collected from turbid groundwater samples by filtration contained between 150 and 1,800 mg Pb/kg and between 100 and 250 mg Zn/kg. Results showed that none of the samples analyzed contained PbS as a dominant solid phase. XANES and EXAFS data both showed that one sample contained 70% of zinc bonded to sulfur, indicating that this portion of the aquifer had been under a sufficiently low redox potential to generate sulfides. In all other samples, first-shell bonding of Pb and Zn was primarily to oxygen. Comparison with standards indicated that PbO, $PbCO_3$, $PbSO_4$, and ZnO were not dominant species in the samples. Figure 1 shows that Zn-S bonding was dominant only in sample Zn23, and therefore, remediation should target metal-oxygen bonded species.

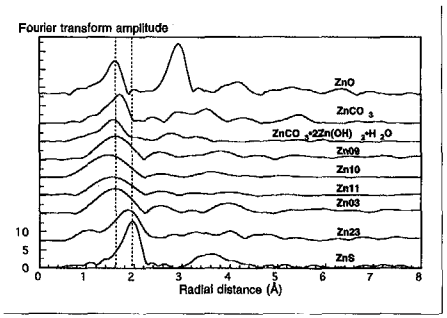


Figure 1. Stacked radial structure functions for Zn K-EXAFS data (k^3-weighted) from solid-phase aquifer samples (Zn03, Zn09, Zn10, Zn11, and Zn23) and selected standards. Data are not corrected for phase shift.

XAFS Characterization of Copper in Model Aqueous Systems of Humic Acid and Illite | X11A

D. Hesterberg, D. E. Sayers, W. Zhou, W. P. Robarge, and G. M. Plummer (NCSU)

Adsorption of heavy metals at mineral surfaces and complexation with reactive organic-matter functional groups are important processes regulating the solubility and fate of soil contaminants. The objective of this study was to determine spectroscopic features that distinguish Cu(II) bonding to soil humic acid (HA) from bonding on an aluminosilicate mineral surface, and to characterize bonding in a mixed clay-organic system. EXAFS analyses were conducted on aqueous suspensions containing Cu(II) in various forms: (i) complexed with soil humic acid (HA) at various HA:Cu ratios, (ii) bound to illite, or (iii) bound in a mixture of illite and HA. Samples of pH 5.6 or 7.2 contained between 2.5 and 9 mmol Cu(II)/kg. XAFS analyses were done at Beamline X-11. Samples were analyzed in fluorescence mode at the Cu K-edge (8,979 eV) using a multielement detector. EXAFS fitting results in Table 1 show that at both pH 5.6 and 7.2, the average first-shell Cu-O bond lengths in the HA suspensions were consistently shorter than those of Cu-O in the illite suspensions (1.92 to 1.93Åversus 1.95Å, respectively). The average Cu-O bond length in the mixed illite-HA suspensions (1.94Å) was intermediate between those of the single adsorbent systems at pH 5.6, and equal to that of Cu(II) in HA at pH 7.2 (1.93Å) (Table 1). Average coordination numbers (N) and Debye-Waller factors (DW) tended to be higher in the illite suspensions compared with the HA suspensions. Although N also tended to be higher in the mixed suspensions compared with HA alone, no consistent trend in DW was observed. For the HA suspensions at pH 5.6, there appeared to be little effect of HA:Cu ratio on EXAFS results. Our results indicated that the addition of relatively low levels of HA to illite suspensions had a significant effect on average local bonding structure.

Sample	N (± 0.5)	R (Å) (± 0.01)	DW (Å²) (± 0.0004)
Cu-acetate standard	6.0	1.95	0.0000
HA = 300 mg OC/kg, pH 5.6	5.4	1.93	0.0005
HA = 600 mg OC/kg, pH 5.6	5.8	1.93	0.0008
HA = 1200 mg OC/kg, pH 5.6	5.8	1.93	0.0009
HA = 1800 mg OC/kg, pH 5.6	5.4	1.93	0.0005
HA = 2400 mg OC/kg, pH 5.6	5.7	1.92	0.0005
illite + HA - 12.5 mg OC/kg, pH 5.6	5.9	1.94	-0.0004
illite + HA - 25 mg OC/kg, pH 5.6	6.4	1.94	0.0010
illite, pH 5.6	6.6	1.95	0.0010
HA = 300 mg OC/kg, pH 7.3	6.5	1.93	0.0011
illite + HA - 12.5 mg OC/kg, pH 7.3	6.5	1.93	0.0003
illite, pH 7.3	6.9	1.95	0.0016

Figure 1. First-shell EXAFS fitting results for Cu in humic acid (HA), illite, and mixed illite-HA suspensions using a 5 mM Cu-acetate solution as a standard (N = coordination number, R = 1st-shell bond length, and DW = Debye-Waller factor). Numbers in parentheses are parameter standard deviations given as output from the University of Washington FEFF fitting program.

Application of X-ray Absorption Spectroscopy for Studying Pyromorphite Formation in Lead Contaminated Soil	X11A

D. Hesterberg, W. Zhou, P. Zhang, D. E. Sayers, J. A. Ryan, and W. P. Robarge (NCSU and US-EPA)

In-situ remediation techniques for soil contaminants are being developed to reduce the cost of managing hazardous-waste sites. One technique being explored for lead-contaminated sites is treatment of contaminated soil with hydroxyapatite [$Ca_5(PO_4)_3OH$] to fix lead as the very insoluble mineral chloropyromorphite [$Pb_5(PO_4)_3Cl$]. The objective of this study was to determine using extended x-ray absorption fine structure (EXAFS) spectroscopy whether pyromorphite was formed following experimental soil treatments with hydroxyapatite. The contaminated soil samples came from the site of a lead smelter in the western U.S. and contained 8,106 mg Pb/kg (39 mmol/kg). Laboratory experiments conducted at the US-EPA Central Hill Facility involved incubating hydroxyapatite-treated soil (P:Pb molar ratio = 5:1) for 240 d. Lead L_{III}-EXAFS analyses completed at Beamline X-11A were used to characterize untreated soil, hydroxyapatite-treated soil, and residual soil Pb that was not removed from the treated soil by a sequential chemical extraction. Air-dried soil samples were analyzed at room temperature in fluorescence mode using a multielement detector, and a synthesized chloropyromorphite standard was analyzed in transmission mode. High-quality, low-temperature (10 K) EXAFS spectra were also obtained for the extracted soil and pyromorphite standard. EXAFS data showed a shift to a longer average first-shell Pb-O bond length in the treated soil, indicating that the treatment had changed the bonding structure of Pb. Low-temperature EXAFS spectra for the extracted soil lead and pyromorphite were remarkably similar in terms of the frequencies of the oscillations and the beat pattern (Fig. 1), which provided strong evidence that the extraction residue was dominated by pyromorphite. A multiple-scattering peak at 4.4 $Å^{-1}$ in the pyromorphite spectrum only suggested that the soil pyromorphite was poorly crystalline.

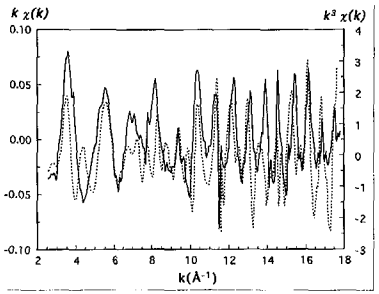


Figure 1. Comparison of Pb L_{III} EXAFS spectra for the soil extraction residue (solid line, left axis) and chloropyromorphite (dotted line, right axis).

Characterization of Heavy Metal Incorporation in Calcite by XAFS Spectroscopy	X11A

R.J. Reeder, P. Northrup (SUNY Stony Brook) and G.M. Lamble (BNL- NSLS)

Coprecipitation is one of the environmentally important processes governing the distribution and fate of dissolved heavy metals in near-surface waters. Recently reported experimental work on the coprecipitation of divalent Co, Zn, Mn, Fe, Cd, Sr, Pb, and Ba with calcite (a common authigenic phase in soils and aquifer materials) has shown strongly selective uptake in structurally distinct surface sites on the calcite 1014 face, resulting in element-specific, differential incorporation during crystal growth. XAFS spectra of individual divalent heavy metals (Co, Zn, Pb, and Ba) coprecipitated with calcite were collected (X11A) and analyzed to determine local coordination in the bulk following surface-controlled differential uptake. Results of multi-shell fitting using FEFF6 and FEFFIT show that, despite their large difference in size, all four metals attain a coordination with six oxygens at distances that are consistent with octahedral coordination. Substitution of the metal ions therefore occurs in the Ca site, which is confirmed by second-shell distances. One conclusion is that despite distinct surface-site preferences and uptake patterns varying in magnitude by more than a factor of ten, bulk coordination differs only minimally. Therefore, differential surface uptake need not result in different coordination in the bulk calcite as heavy metal ions are buried during growth. A further conclusion is that relaxation around an impurity ion is very localized, and the corner-sharing structural topology of calcite facilitates the observed wide spectrum of impurity substitution.

XAFS Characterization of Heavy-Metal Contamination in the Unsaturated and Saturated Zones of a Soil Profile — X11A

D. E. Sayers, D. Hesterberg, W. Zhou, W. P. Robarge, and G. M. Plummer (NCSU)

The fate of heavy-metal contaminants in the environment, and the design and success of remediation strategies at hazardous waste sites depend on the chemical speciation of the contaminants. XAFS spectroscopy has the potential for providing molecular-scale speciation of metals occurring at low concentrations in complex media such as soils. The objective of this study was to determine the chemical forms (species) of heavy metals occurring at different depths in a contaminated soil at a superfund site in the lower eastern coastal plain of North Carolina. Because the saturated zone of this soil is at ~1 m depth, redox potential was expected to play a significant role in metal speciation, particularly with regard to metal-sulfide formation. Copper, zinc, lead, and chromium in field samples were characterized using XANES and EXAFS spectroscopies at Beamline X-11. The samples contained 1,780 to 2,160 mg Cu/kg, 4,970 to 5,500 mg Zn/kg, 3,730 to 4,550 mg Pb/kg, and 60 to 94 mg Cr/kg; and were analyzed in fluorescence mode using a multielement detector. Copper K-EXAFS data showed that the amount of first-shell Cu-S bonding increased relative to Cu-O bonding with depth in the soil profile (see radial structure functions in Fig. 1). Based on relative coordination numbers of Cu-O and Cu-S bonding derived from EXAFS data fitting, the following percentages of Cu-S bonding were calculated for the soil samples: 36% (28-56 cm depth), 77% (56-71 cm), and 81% (71-86 cm). K-XANES spectra suggested that CuS was the dominant mineral species in the subsurface sample, consistent with expectations of a low oxidation-reduction potential in the water-saturated subsoil. Both Zn(II) and Pb(II) were predominantly bonded with oxygen throughout the soil profile, indicating that available sulfide was preferentially bound with Cu(II). CuS is thermodynamically more stable than ZnS and PbS. Cr K-XANES spectra showed that the less mobile and less toxic Cr(III) species was dominant throughout the soil profile. The results suggest that the surface and subsurface horizons at the study site will respond differently to remediation treatments.

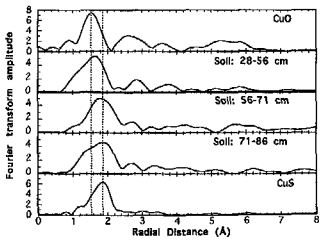


Figure 1. Radial structure functions for Cu(II) in soil samples from different depths and selected standards. Data are not corrected for phase shift.

The Kinetics of Nickel Sorption on Pyrophyllite as Monitored by X-ray Absorption Fine Structure (XAFS) Spectroscopy — X11A

A. M. Scheidegger, D. L. Sparks (U. of Delaware), and G. M. Lamble (NSLS)

The study examines the effect of reaction time (minutes to months) on the surface coordination environment of Ni sorbed onto pyrophyllite (2:1 clay with little deviation from the ideal chemical formula ($Al_2Si_4O_{10}(OH)_2$) using XAFS. Ni sorption on pyrophyllite at pH = 7.5 ($[Ni]_{initial}$ = 3 mM, ionic strength I = 0.1 M ($NaNO_3$)) resulted in the presence of multinuclear Ni complexes within minutes. This can be clearly demonstrated in Figure 1. There is a small peak at R = 2.8 Å in the radial structure function (RSF) of pyrophyllite treated with Ni for 15 minutes (Fig. 1f). The presence of multinuclear Ni complexes after a sorption time of only 15 minutes (28% of the initial Ni sorbed; Table I.) is a rather surprising finding. Traditionally, adsorption (strictly a two-dimensional process) is considered to be the predominant sorption mode responsible for metal uptake on mineral surfaces within the first few hours. As reaction time progressed (15 min. to 24 h) and relative Ni removal in solution increased from 28% to 97% (Table I.) the number of Ni second-neighbor (N) atoms at a distance of 2.99-3.03 Å increased from N = 1.4-4.5. This finding suggests the formation of multinuclear Ni complexes increasing in size with progressing reaction time. We propose that the formation of mixed Ni-Al hydroxides may explain the observed bond distances and coordination numbers. Ni-Ni bond distances (3.0-3.03 Å; Table I.) correspond well with those found in mixed Ni-Al hydroxides (3.03-3.05 Å), but are distinctively shorter than those in Ni(OH)2(s) (3.09 Å) [1]. Aluminum could have been released into solution and incorporated into mixed (Al, Ni) hydroxides. Indeed, macroscopic data suggest that the dissolution of pyrophyllite is enhanced during reaction with Ni relative to the dissolution in the bulk solution [1].

[1]. Scheidegger, A. M., Lamble, G. M. and Sparks, D. L. 1996. J. Colloid Interface Sci. in press.

Structural information derived from XAFS analysis using EXCURV90: Interatomic distances (R, Å), Coordination numbers (N), and Debye-Waller factors ($2\sigma^2$, Å^2). The reported values are accurate to within R ±0.02 Å, $N_{(Ni-O)}$ ±20%, $N_{(Ni-Ni)}$ ±20%, $N_{(Ni-Si/Al)}$ ±40%.

		Ni-O			Ni-Ni			Ni-Si/Al		
	relative Ni removal (%)	R (Å)	N	$2\sigma^2$	R (Å)	N	$2\sigma^2$	R (Å)	N	$2\sigma^2$
15 minutes	28	2.03	6.0	0.009	2.99	1.4	0.007	2.96	1.5	0.004
75 minutes	44	2.03	6.4	0.01	3.01	2.1	0.009	3.04	1.6	0.01
3 hours	67	2.02	6.2	0.009	3.03	3.4	0.01	3.07	1.6	0.011
12hours	95	2.03	6.4	0.01	3.02	4.1	0.009	3.07	2.1	0.009
24 hours	97	2.03	6.5	0.01	3.02	4.2	0.01	3.07	1.8	0.013
3 months		2.03	6.5	0.01	3.02	4.5	0.011	3.07	2.4	0.016

Figure 1. Radial structure functions (RSFs) of pyrophyllite samples reacted with Ni for a.) 3 months, b.) 24h, c.) 12h, d.) 3h, e.) 75min, and f.) 15 min. The spectra are uncorrected for phase shift. Note the appearance of a peak at a R of about 2.8 Å with increasing reaction time.

In Situ XAS Studies Of Metal-Semiconductor Interactions * | X11A

Z. Wang, P.T. Goeller, B.I. Boyanov, D.E. Sayers, and R.J. Nemanich (NCSU)

A UHV system for *in-situ* studies of metal-semiconductor interactions has been designed and assembled at NCSU and recently installed and tested at beamline X-11A at the NSLS. The UHV system consists of interconnected deposition and analysis chambers, each of which is capable of maintaining a base pressure of approximately 1×10^{-10} Torr. Up to three materials can be co-deposited on 25 mm wafers by electron-beam evaporation. Substrate temperature can be controlled in the range 30–1200°C during deposition, and the growth process may be monitored with RHEED. The deposited materials and their reaction products can be studied in-situ with a variety of techniques: XAFS, AES, XPS, UPS, and ARXPS/UPS. A schematic overview of the experimental apparatus appears in Figure 1.

We intend to use this equipment to study the stabilization of metal silicides co-deposited on epitaxial $Si_{1-x}Ge_x$ films. Initial EXAFS experiments on Co and Si co-deposited in a 1:2 ratio on $Si_{0.8}Ge_{0.2}$ films indicate a stable silicide-SiGe contact. The silicide overlayer exhibits a $CoSi_2$ structure at all annealing temperatures used in this study (500–700°C). Weak CoSi signature (attributed to slight Co excess is the overlayer) is detected below 600°C, and $CoSi_2$ formation is complete at 700°C. *In-situ* RHEED measurements indicate that $CoSi_2$ islands at the very early stages of growth when co-deposited on epitaxial SiGe/Si(100) films, even when $CoSi_2$ "template" layers are employed. We are currently investigating the implications of this result on the structure, resistivity, and stability of the $CoSi_2$-SiGe contact.

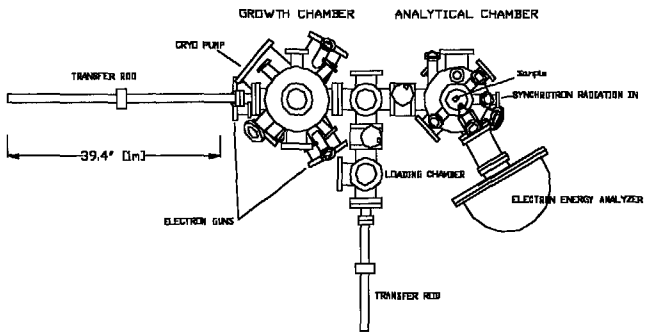


Figure 1.

* This work was supported by DOE grants DE-FG05-93ER79236 and DE-FG05-89ER45384

Evidence for Pb-phospate Cluster Formation at the Oxide-water Interface | X11A

F.J. Weesner and W.F. Bleam (U. of Wisconsin-Madison)

Surfaces of hydrous oxide soil minerals strongly influence the mobility of solutes in the soil/water system. The common oxides of iron and aluminum can adsorb ions of either charge to varying degrees depending on relative concentrations and solution pH. The extent to which the adsorption from solution of one solute is affected by the presence of second solute is not generally predictable by current theory. Multiple adsorbates will always be present in environmental systems, therefore it is important to examine the interactions of co-adsorbates at the oxide/water interface.

This abstract reports on progress in the understanding of Pb2+ binding to modified iron and aluminum oxide colloid surfaces in aqueous suspensions. Oxide surface modification is accomplished by populating the surface with excesses of common oxyanions such as HPO42- and SO42-. We believe ternary surface structures form at the interface under certain conditions. We collected X-ray absorption spectra (XAS) at the Pb LIII, S K and P K edges over the last year to test test this hypothesis.

In the case of phosphate modification, we observe dramatic changes to both the near edge and fine structure regions of XAS spectra. While not identical, the spectra of Pb adsorbed to the phospahte treated samples are similar to the phospahte mineral hydorxypyromorphite. The experimental spectra suffer from a relative high degree of static disorder owing to multiple unique adsorption sites on our oxide adsorbents. This prevented detailed analysis of the structural paramenter of the sites, yet simulations of using a 3 site model, guided by structure refinements of Pb phosphate minerals leads us to the conclusion that a direct reaciton of Pb and phospate takes place at the surface. P K-edge spectra supported this conclusion, however only the Al oxide system was studied due to high scattering background from the Fe oxide matirx.

Adsorption of phosphate and sulfate to aluminum hydrous oxides is thought to follow inner-sphere (ligand exchange) and outer-sphere (electrostatic) mechanisms, respectively. Our results support this hypothesis judging from the presence (phosphate case) or absence (sulfate case) of scattering intensity that could be reasonably assigned to Al in the second coordination shell.

Studies of the Nature of Binding Sites of First Row Transition Elements Bound to Aquatic and Soil Humic Substances Using X-ray Absorption Spectroscopy	X11A

K.Xia, W. Bleam, and P.A. Helmke (U. of Wisconsin-Madison)

The coordination environments of first row transition elements (Co, Ni, Cu, and Zn) complexed by aquatic and soil humic substances were studied using x-ray absorption spectroscopy (XAS). With the assistance of bond network analyses, analysis of x-ray absorption near edge structure (XANES) spectra and radial structure functions (RSF) derived from extended x-ray absorption fine structure (EXAFS) spectra of Co, Ni, Cu, and Zn in humic substances indicate octahedral binding environment for Co and Ni, a tetragonally-distorted octahedral binding environment for Cu, and 6-coordinate binding environment for Zn. Analysis of EXAFS spectra of each element provides detailed information on the internuclear distances, bond angles, and Debye-Waller factors within the first two atomic shells surrounding Co, Ni, Cu, and Zn bound to humic substances. We interpret the presence of carbon atoms in the second atomic shell of the metal binding site as further evidence that Co, Ni, Cu, and Zn form inner-sphere complexes with humic substances. The number and type of ligands involved in the binding are different for different elements.

Submitted to Geochim. Cosmochim. Acta., 1996.

Studies of the Nature of Cu^{2+} and Pb^{2+} Binding Sites in Soil Humic Substances Using X-ray Absorption Spectroscopy	X11A

K. Xia, W. Bleam, and P. A. Helmke (U. of Wisconsin-Madison)

We have investigated the binding environments of Cu^{2+} and Pb^{2+} complexed by soil humic substances using synchrotron-based x-ray absorption spectroscopy. With the assistance of bond network analysis, analysis of x-ray absorption near edge structure (XANES) and radial structure functions derived from extended x-ray absorption fine structure (EXAFS) spectra of Cu-humate at pH 4, 5, and 6 yielded a tetragonally-distorted octahedral binding environment with 4 O atoms at an average distance of 1.94Å, 2 O atoms at an average distance of 2.02Å, and 4 C atoms at an average distance of 3.13Å. Analysis of Pb-humate samples at pH 4, 5, and 6 yielded 4 O atoms at average distances between 2.46Åto 2.32Åand 2 C atoms at an average distance of 3.26Å. We interpret the presence of carbon atoms in the second atomic shell of the metal binding site as evidence that both Cu^{2+} and Pb^{2+} form inner-sphere complexes with soil humic substances. Within the pH range 4 to 6, there is no significant change in the structure of the binding site for either Cu or Pb.

Submitted to Geochim. Cosmochim. Acta,1996

X-Ray Absorption and Electron Paramagnetic Resonance Studies of Cu^{2+} Sorbed to Silica: Surface-Induced Precipitation at Low Surface Coverages	X11A

K. Xia, W.F. Bleam (U. of Wisconsin-Madison), A.Mehadi, and R.W. Taylor (Alabama A&M U.)

Both EPR and XAFS spectroscopy were used to characterize the sorption of Cu^{2+} on silica surfaces at extremely low surface coverage (0.8 percent and 9.9 percent monolayer). The binding structure of Cu^{2+} on silica surfaces revealed by XAFS experiment was compared to that predicted by EPR spectra. Our XAFS results show that Cu^{2+} hydroxide clusters form on silica surfaces even at surface coverage as low as 0.8 percent of a monolayer. However, we observed low EPR intensity and line-broadening which has been assigned to dipole-dipole interactions between isolated Cu^{2+} ions. The results of our XAFS studies indicate that the loss of EPR intensity and line-broadening can be traced to $Cu(OH)_2$ clusters on silica surfaces.

J. of Colloid Interface Sci. in print, 1996.

Structure of Zn-fingers 1-6 of Transcription Factor IIIA (TFIIIA) Bound to a 31 bp DNA Site	X12B

R.S. Brown, R.T. Nolte, S.C. Harrison, (HHMI and Children's Hospital Lab. of Molecular Medicine)

Crystals of fingers 1-6 of TFIIIA bound to a 31 bp DNA contain a longer protein fragment and a longer DNA site than other Zn-finger complexes studied to date. They are in space group P1 (a=61.3, b=64.8, c=78.1, α=90.12, β=92.87, γ=102.84). Diffraction extends to 3.1Å. Data from flash-frozen crystals were collected at X12B using a MAR detector. A total of 629 degrees of native data and 247 degrees of iodine derivative data were recorded. A difference Patterson has now been solved; there are two protein:DNA complexes per unit cell related by twofold non-crystallographic symmetry. Phase refinement and model building are in progress.

Large Strain Deformation Studies of Oriented Triblock Copolymers with a Cylindrical Morphology	X12B

C. Honeker, E. L. Thomas (MIT), M.C. Capel (BNL - Biology)

Single-crystal triblock copolymers with a cylindrical morphology are deformed to large strains with simultaneous measurement of load, sample extension and 2-D small-angle diffrac- tion. The sample is oriented such that the incident beam is directed perpendicular to the cylinder axis while stretching in the transverse direction. After the initial deformation during which the cylinders move apart, the symmetry of the diffraction pattern is broken whereby each Bragg peak splits into a pair of peaks which move off the force axis and towards lower q. This X pattern forms at a well-defined strain (100%). TEM of the deformed samples indicates that the cylinders have bent into a chevron texture. Upon further deformation, the angle between the arms of the X continues to open reaching an asymptote (*sim*120) at the highest deformations. In order to probe the influence of molecular structure on deformation we investigated sev- eral multi-block copolymers: a poly(styrene-isoprene-styrene) SIS triblock, a poly(styrene-buta- diene-styrene) SBS triblock and a 12-armed SI star-block copolymer (isoprene core). The block molecular weights are: 15-69-15 for the SIS triblock, 10-50-10 for the SBS triblock and 12-44 for each SI diblock arm of the star (giving a span molecular weight of 12-88-12). The compositions are: 30 wt%, 32 wt%, and 27 wt% PS for the SIS, SBS, and star respectively. Figure 1 shows the X-angle as a function of deformation on loading. The SIS and star samples parallel each other quite closely. The SBS curve indicates the formation of the X-angle at the lowest deformations. At higher deformations the SBS curve crosses over and reaches a smaller asymptotic limit. Examination of the Figure 2 shows that the SBS sample has a much higher load bearing capacity.

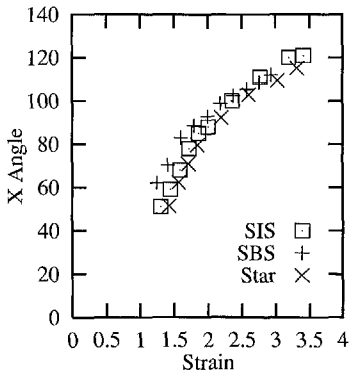


Figure 1. Angle between the arms of the 'X' observed in the 2-D diffraction patterns as a function of deformation. The SBS sample behaves qualitatively different than either the Star or the SIS samples.

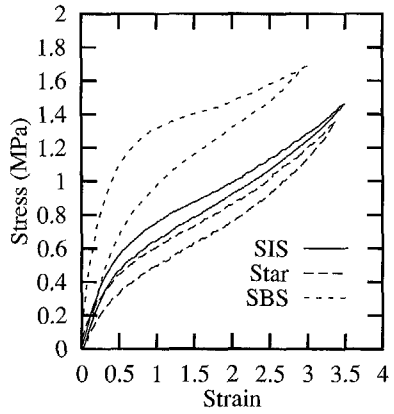


Figure 2. Stress vs. strain measured in-situ for the samples shown in Figure 1. Note that the SBS sample has a much higher load-bearing capacity than either the Star or SIS samples.

The Crystal Structure Determination of the SecA Translocation ATPase	X12B, X4A

J.F. Hunt and J. Deisenhofer (HHMI, UT Southwestern)

SecA is the engine which drives the ATP-powered translocation of secretory proteins through the bacterial periplasmic membrane. Although SecA exists in a fully water-soluble form, it undergoes cycles of membrane insertion and retraction in the course of its ATPase cycle. SecA is believed to function as a molecular ratchet in the protein translocation reaction, pulling segments of the secretory protein through the membrane concomitant with the ATP-driven membrane insertion cycles. SecA also auto-regulates its own translation by binding to a specific RNA sequence overlapping the initiator codon in its messenger RNA. The SecA protein possesses two tandem ATP-binding domains with approximately 30 percent identity to the ATP-binding cassettes of the ABC transporter superfamily of transmembrane transport proteins. Based on its domain organization, its sequence homology, and its activity, it has been proposed that SecA may have structural and mechanistic similarities to the ABC transporters.

The crystal structure determination of the soluble, membrane-retracted state of SecA is now almost completed. Data collected on beamlines X12B and X4A at NSLS were instrumental in this process. Because our crystals only diffract to 3.5 angstroms using a rotating anode source, our high resolution data (currently to 2.9 angstroms) was collected on beamline X12B. This beamline was also used for rapid derivative screening. Candidate crystals soaked in either Pt, Au, or Hg compounds were mounted and measured with the energy of the beam tuned to optimize anomalous data from the element in question. 2 X 4 degrees of data were collected very quickly in inverse beam geometry, and the anomalous chi-square at low resolution was used used as the criterion to determine whether collection of a complete data set was merited. The breakthrough derivative for the project was identified in this manner. Data collected on beamline X4A from a selenomethionyl derivative of SecA allowed the position of 33 methionines in the protein to be observed in an anomalous difference fourier using MIR phases (the 3.8 angstrom diffraction from this crystal was too weak to be useful for MAD phasing).

The refinement of the structure is currently in progress. A working model for the domain rearrangements in the course of the SecA ATPase / transport cycle has been formulated, and, on this basis, further experiments are being designed to try to elucidate the structural mechanism by which the hydrolysis of ATP is coupled to transmembrane transport of nascent polypeptide chains.

Structural Studies of the Yeast Bleomycin Hydrolase, Gal6 * — X12B

L. Joshua-Tor, J. Rosenbaum (Cold Spring Harbor Lab), W. Zheng, H. Whelan and S. A. Johnston (UT-Southwestern)

Resistance to antineoplastic drugs, whether intrinsic or acquired, is a central problem in treatment of human cancers. Bleomycin hydrolase is a cysteine protease discovered by its ability to hydrolyze the anticancer drug bleomycin and thus to limit its use in cancer therapy. The recent discovery of homologs of this intracellular, hexameric, 300 kD protein in yeast and bacteria implies a conserved cellular function for this protein, yet the only known natural substrate, bleomycin, is almost never seen by any of these cells. The yeast protein, Gal6 was found to bind nucleic acids. It binds preferentially to single-stranded DNA or RNA with a K*d* of 10 nM, and to nicks in double-stranded DNA Moreover, its expression is regulated by galactose and the iGAL regulon and Gal6 itself acts as a repressor for galactose regulated genes. Bleomycin hydrolase turns out to be, therefore, a rather surprising enzyme. It is a cysteine protease that binds nucleic acids, has been conserved from bacteria to humans, yet its cellular function is still unknown. In recent years, there has been considerable interest in intracellular proteases, since they seem to be involved in important regulatory processes. We are investigating the properties of the bleomycin hydrolases, both in terms of understanding how the various activities of the protein are linked and in understanding the mechanism for drug resistance. These will facilitate the elucidation of the conserved cellular function that is implied from its conservation from bacterial to humans.

Having solved the structure of the mature yeast enzyme, we have begun to study various mutants and complexes. The first mutant is one where we replaced the active site cysteine with an alanine. Since the protein undergoes an autocleavage reaction, by clipping off its own C-terminal amino acid, this would enable us to have a look at one natural substrate, the C-terminus, sitting in the active site of the protein. This mutant was crystallized and similar to the case with the native crystals, these crystals are rather thin and diffract to about 3.5 Åon our home source. Therefore, it was essential to collect data using a synchrotron source. Due to radiation sensitivity, the crystal was cryocooled using an Oxford Cryosystem device and data were collected from a single crystal on beamline X12B to a maximum resolution of 2.05 Å. The data are 97.3% complete with a final scaling R-factor is 0.077 to that resolution. The structure was determined using the native structure of Gal6 and is currently being refined. The C-terminus including the last amino acid, which is cleaved in the mature enzyme, is clearly seen in the electron density maps.

* This work is supported by NIH grant R01-CA71746 to L.J.; NIH grant R01-CA67982 and a Tobacco Research grant to Stephen A. Johnston.

Structure and Relaxation of Polyimides Using Small Angle X-ray Scattering — X12B

S. X. Lu , P. Cebe (Tufts U.), and Malcolm Capel (BNL - Biology)

The thermoplastic polyimide, NEW-TPI, has been investigated using small angle X-ray scattering and thermally stimulated depolarization current measurements. SAXS was used to study the development of lamellar structure during isothermal or non-isothermal crystallization. The one-dimensional electron density correlation function was used to determine the structural parameters, such as long period, lamellar thickness, and linear crystallinity. The long period, lamellar thickness, and amorphous layer thickness all increase as the crystallization temperature increases from 300C to 360C. By combining melting point data with SAXS results we determine the side and fold surface free energy for the crystals, which are 29+/-3 and 41+/-3 ergs/cm-cm, respectively. Real-time SAXS was carried out during non-isothermal heating at 5C/min. The long period decreases while the lamellar thickness, linear crystallinity, and inter-phase thickness increase with increasing temperature. Results are interpreted using a lamellar insertion model.

Sharon X. Lu, Peggy Cebe, and Malcolm Capel, "NEW-TPI Thermoplastic Polyimide: Structure and Relaxation Using SAXS and TSDC" J. Applied Polymer Science, vol. 57, 1359-1372 (1995).

Structure of Horse Liver Alcohol Dehydrogenase at 1.25 A Resolution	X12B

S. Ramaswamy, H. Eklund (Swedish U. of Agricultural Sciences) and B.V. Plapp (U. of Iowa)

The structure of horse liver alcohol dehydrogenase (LADH), has been worked on for more than two decades. The structure of the protein has been refined to 1.8 Ang resolution. Bryce Plapp has been studying the mechanism of enzyme catalysis of this enzyme, also for more than two decades. LADH shows evidence of tunneling and low barrier H-bonds from isotope effects (1), but the x-ray resolution is not high enough to confirm this structurally. The nicotinamide rings of the coenzyme rings in complexes with substrate analogs (NAD+ with pentafluorobenzyl alcohol or NADH with formylpiperdine) may be distorted, as suggested by molecular dynamics. The protein is a dimer of 374 residues per monomer, and the subunits may not be equivalent, as determined at 2.1 Ang. (2). The frozen crystals of the monoclinic form diffract to better than 1.2 A resolution. We have collected and processed a data set to 1.25 A and also computed initial maps. The maps were computed using the coordinates of the structure refined at 1.7 A resolution for a different complex. The intial difference map (figure 1) clearly indicates the position of the Penta fluoro benzyl alcohol. Initial look at the density around the Nicotinamide ring of the NAD (figure 2)suggests that the C4 atom probably has the additional Hydrogen and NAD has been reduced to NADH.

Refinment using maximum likelyhood methods followed by SHELX96 is in progress. There are 1500 residues in the asymmetric unit and more than a million reflections were measured to get over 350,000 unique reflections. This is probably the structure at this resolution with this many residues in the asymmetric unit.

Acknowledgement: The project was supported by the Swedish NFR for HE and by NIH for BVP.

REFERENCES: (1) B. Bahnson, D.-H. Park, K.-H. Kim, B. V. Plapp, and J. P. Klinman (1993) Unmasking of Hydrogen Tunneling in the Horse Liver Alcohol Dehydrogenase Reaction by Site-Directed Mutagenesis, Biochemistry 32: 5503-5507. (2) S. Ramaswamy, H. Eklund, and B. V. Plapp (1994) Structures of Horse Liver Alcohol Dehydrogenase Complexed with NAD and Substituted Benzyl Alcohols, Biochemistry 33:5230-5237.

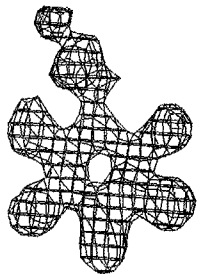


Figure 1.

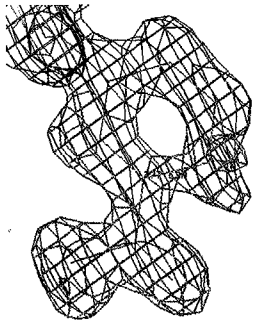


Figure 2.

Crystalization and Preliminary X-ray Analysis of Aα Subunit of Protein Phosphatase 2A *	X12B

M. Skidmore, M. Sawaya (UCSD), S. Parkin, B. Rupp (LLNL), H. Hope (UCD), and G. Walter (UCSD)

Protein phosphatase 2A (PP2A) is the most abundant serine/threonine phosphatase in mammalian cells and is important in a number of cellular processes such as cell division, development, and signal transduction. The dimeric core enzyme is composed of a catalytic C and regulatory A subunit which at times is bound by one of a family of regulatory B subunits. PP2A also forms complexes with the small DNA tumor viruses SV40 and polyoma and is involved in tumorigenesis. The A subunit has 15 nonidentical repeats of 38 - 43 amino acids. A model has been proposed whereby each repeat forms two amphipathic alpha helices that pack against the next repeat to make a long rod shape consistent with biophysical and site directed mutagenesis data[1].

The Aα subunit of human protein phosphatase 2A forms crystals in space group P21 with cell dimensions a = 104.0, b = 174.9, c = 168.2 $\AA$, and β angle = 90.2°. At cryogenic temperatures the crystals diffracted to a resolution of about 3.0 $\AA$. Based on the unit cell dimensions and a calculated molecular mass of 65,277 / Da, the Matthews coefficient of 3.17 $\AA^3$ / Da suggests eight molecules in the asymmetric unit. Data were collected on a single native crystal at NSLS Beamline X12B with a MAR Research imaging plate and Oxford Cryostream at 93 K. The final reduced data set has a maximum resolution of 3.0 $\AA$ in the shell with $> I < / \sigma = 1.8$. A total of 188,109 observations were collected with 93,490 unique reflections in a data set that is 81 % complete with $R_{sym} = 0.076$. Additional time was used for screening possible heavy atom derivatives and collecting another data set on one putative derivative[2].

[1] Ruediger R, Hentz M, Fait J, Mumby M, and Walter G. 1994. Molecular Model of the A subunit of protein phosphatase 2A: Interaction with other subunits and tumor antigens. J. Virol. 68:123-129

[2] Skidmore M, Sawaya M, Parkin R, Rupp B, Hope H, Everse S, and Walter G. 1996. Crystallization of the Aα subunit of protein phosphatase 2A. Protein Science 5:1198-1200.

* This work was supported by PHS grant CA-36111 and UC-TRDRP to GW, DOE contract No. W-7405-ENG-48 to BR and NIH grant 5 T32 DK07233-20 to MRS.

A Bent-Laue Crystal Monochromator for Monochromatic Radiography with an Area Beam — X12A

Z. Zhong(NSLS), D. Chapman(CSRRI), W. Thomlinson, F. Arfelli, N. Gmür and R. Menk (NSLS)

A bent Laue crystal monochromator which can diffract a large area of monochromatic x-rays from a polyenergetic x-ray rotating anode source has been developed and tested at the X12A beam line using K fluorescence x-rays of Ba, La, Mo and Ag targets. The monochromatic beam, with a solid angle of more than 5 degrees × 5 degrees and energy range tunable from 15 keV to 100 keV, is completely separated from the white beam at a distance of less than 1 meter from the source. The absolute reflectivity of the monochromator ranges from 10 to 40% (depending on the energy of the x-rays being diffracted and the source size). The energy bandwidth of around 2% is controllable by varying the diffraction planes used, the crystal thickness, asymmetry angle and the bending radius. A single emission line from an x-ray tube source can be selectively diffracted into the entire exit-beam solid angle. Potential applications of the device include monochromatic beam diagnostic radiography and dual-energy subtraction imaging when the beam energy is tuned to bracket the K-edge of the radiographic contrast elements such as iodine.

Fluorescence radiation from the target excited by the synchrotron white beam was used as the point x-ray source. The size of the source spot can be changed by changing the size of the incident synchrotron beam on the target (Fig.1). [111] reflections of 0.46 mm thick silicon crystals with different asymmetry angles were tested with bending radii between 0.3 and 1 meters. Differential bending was found essential to match the angle of the crystal planes with the divergence of the source at any point on the crystal to reflect the area beam uniformly. Fig.2 shows the image of the reflected beam after the crystal is aligned to reflect both the $K_{\alpha 1}$ and $K_{\alpha 2}$ lines of a molybdenum target. The bending radius was 0.378 m which gave a source to crystal distance of 0.331 m. The image plate was placed at 300 mm from the crystal. It can be seen that the crystal is capable of staying within the FWHM of the reflection in the 25 mm high by 50 mm wide crystal except at the corners. The corresponding image size is 50 mm high by 100 mm wide. The vertical lines (glitches) in the diffracted beam were explained and indexed by simultaneous diffraction effects.

This work was supported by US DOE contract DE-AC02-76CH00016 and ARPA contract AOB227.

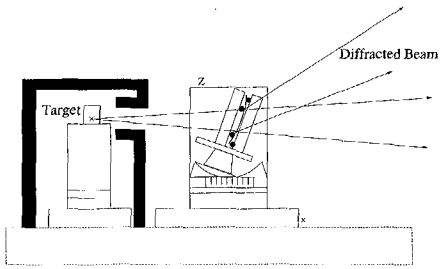


Figure 1. Experimental setup

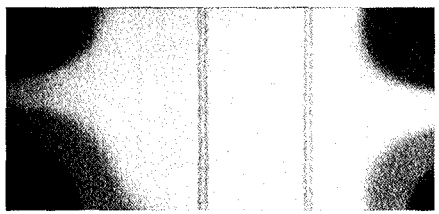


Figure 2. Image of the diffracted beam

The Structure of Calicivirus — X12, X25

L. Zhou and M. Luo (U. of Alabama at Birmingham)

Introduction: The recent rapid spread of a rabbit calicivirus through Australia to Europe demonstrated a potentially dangerous situation if a human calicivirus emerges. It is estimated that at least 42% of outbreaks of nonbacterial gastroenteritis in the U.S. are caused by this group of viruses [1]. The main difficulty in dealing with infections of small round-structured viruses (SRSV's) is the large diversity of the viral capsid protein [2].

Experimental: We have purified and crystallized FCV strain F9 and a large amount (50% complete) of X-ray diffraction data to 3.0Å resolution have been collected at synchrotron stations [3]. The space group of the crystal is C222, a=889Å, b=996Å, c=436Å. A total of 226 images afforded 1,396,078 reflections, which is about 40% complete to 3.5Å resolution. There are two independent particles in the unit cell, one sits on the *a* axis, the other on the *b* axis. Each of the particles is rotated by less than 2° from the ideal orientation. Model coordinates have been constructed based on the cryo-EM structure. The high resolution structure determination is well under way by using the molecular replacement density averaging-phase extension method. Although there were no improvement this time on the quality of the diffraction data collected at NSLS, we expect to collect better data in the future by use of the cryo-freezing technique.

Discussion: Caliciviruses resemble the picornaviruses with which they were originally classified. Like the picornaviruses, the genomes of calicivirus bear a covalently attached protein (VPg) at the 5′ end, and there is no cap structure at the 5′ end of the subgenomic mRNA. However, caliciviruses differ from members of the picornavirus group in that RNA species smaller than the genomic RNA are synthesized intracellularly. A striking difference between caliciviruses and picornaviruses was found in their genome organization. The genomic RNA of picornaviruses encodes a single polyprotein which is co- and post-translationally processed to yield the mature viral proteins. No single large polyprotein precursor to all the viral proteins is known for calicivirus. The genes encoding for the structural polypetides are located near the 3′ end of the genomic RNA.

In our studies a feline calicivirus strain F9 was used for the X-ray structure determination. The comparative sequence analysis of capsid precursor proteins from FCV strains F9 and CFI/68 FIV demonstrated that variation was concentrated in two areas.

Reference: Kaplan, J.E., R. Feldman, D.S. Campbell, C. Lookabaugh and G.W. Gary (1982), The frequency of a Norwalk-like pattern of illness in outbreaks of acute gastroenteritis. Am. J. Public Health 72:1329-1332.

Wang, J., X. Jiang, H.P. Madore, J. Bray, U. Desselberger, T. Ando, Y. Seto, I. Oishi, J.F. Lew, K.Y. Green and M.K. Estes, 1994. Sequence diversity of small, round-structured viruses in the Norwalk virus group. J. Virol. 68:5982-5990.

Zhou, L. and Luo, M. "Preliminary Analysis of Feline Calicivirus Crystals", Acta Crystallogr. D51:850-852, (1995).

X-ray Crystal Structures of the S229A Mutant and Wild Type MurB in the Presence of the Substrate Enolpyruvyl-UDP-N-Acetylglucosamine at 1.8 Resolution	X12C

T. Benson, C. Walsh and J. Hogle (Harvard Medical School)

Data were collected on two variants of the enzyme, UDP-Nacetylenolpyvurylglucosamine reductase (MurB), wild type and a Ser 229 Ala mutant, in complex with the enolpyruvylglucosamine substrate. MurB catalyzes the second step of peptidoglycan biosynthesis in bacteria by reducing the enolpyruvyl moiety to a lactyl ether which serves to link the glycan and peptide strands of this biopolymer. Previously, synchrotron data had been collected on the wild type crystal to 2.7 both at X4A (NSLS) and A1 (CHESS). The beamline geometry at X12C with the 30cm Mar detector and 2theta arm for the detector made possible for the first time the collection of the high resolution data. The data collection and computational support during our run at X12C enabled us to complete indexing and integration of the data before leaving the synchrotron. Data were collection to the diffraction limit of the crystals, 1.8 resolution. The data collection statistics gave Rsym values of 4.1% for wild type and 4.2% for the Ser229Ala mutant with an average I/s of 31.8 and 24.8 respectively. Both structures have been refined to 1.8 with a crystallographic R-factor of 20.3% (wild type) and 20.2% (mutant) and with a free R-factor of 25.6% (wild type) and 24.6% (mutant).

Biochemical comparison of the wild type and mutant enzymes revealed a dramatic kinetic defect observed for the Ser 229 Ala mutant in the second half reaction (an approximately 107 fold decrease in the reoxidation of FADH2). Comparison of the two high resolution structures revealed that the mutation eliminated a hydroxyl group which has previously been proposed to play a critical role as a proton donor during the second half reaction of MurB, namely reoxidation of FADH2 and reduction of the enolpyruvyl substrate. This single point mutation of residue 229 from serine to alanine also removed the water molecule which is hydrogen bonded to the serine hydroxyl in the wild type structure, thereby changing the hydrogen bonding network with in the active site. Structural analysis confirmed that the kinetic defect observed in the mutant is a direct result of the loss of the serine hydroxyl moiety rather than other nonspecific active site changes or general structural defects.

Crystal Structure of the FASCICULIN2-MOUSE *Acetylcholinesterase* Complex	X12C

Y. Bourne (TSRI), R.B.G. Ravelli (Lab. Crystall.& Structual Chem.), M. L. Raves, J. L. Sussman (Weizmann Inst.), P. Taylor and P. Marchot (UCSD)

Acetylcholinesterase (AChE) terminates the action of the neurotransmitter, acetylcholine, at central and peripheral cholinergic synapses. Fasciculins, that belong to the family of three-fingered snake toxins are the only known peptidic inhibitors of AChE. We have determined the crystal structure of fasciculin2 (Fas2) in complex with a recombinant, monomeric AChE from mouse (mAChE) at 3.2 Å resolution [1]. The complex generated two indistinguishable hexagonal crystal forms, A and B, that belonged to space group $P6_522$ with cell dimensions, a=b=75.5 Å, c=556.2 Å for form A, and a=b=128.4 Å, c=556.6 Å for form B [2]. Separation of the diffraction spots along the c axis was achieved at beam line X12C, owing to its MarResearch 300 mm imaging plate mounted on a CAD-4 diffractometer (Enraf-Nonius). A 3.2 Å resolution data set,(85% complete, R_{sym}=8.9%), was collected from four form A crystals with a crystal-to-detector distance of 862 mm (λ=1) or 538 mm (λ=1.5) and a 10.6 ° and 12.4° tilt, respectively. A second data set, at 3.5 Å resolution (87% complete, R_{sym}=9.4%), was collected from four form B crystals with a distance of 757 mm (λ=1.15) and a 10° tilt. The structure of form A was solved by a combination of molecular replacement and model building techniques, and refined to a crystallographic R-factor of 18.4% (R-free=29.4% for 5% of the reflections) using all 13,823 data in the 10 Å to 3.2 Å resolution range. The structure of form B was solved by molecular replacement using the refined model A, and refined to an R-factor of 20.8% (R-free=32.2%) using all 29,167 data in the 10 Å to 3.5 Å resolution range. Model B was found essentially identical with model A. [1] Y. Bourne, P. Taylor and Pascale Marchot. (1995) Cell 83, 503-512. [2] P. Marachot, R.B.G. Ravelli, M.I. Raves, Y. Bourne, D.C. Vellom, J. Kanter, S. Camp. J.L. Sussman, P. Taylor, (1996) Protein Sci. 5, 672-679

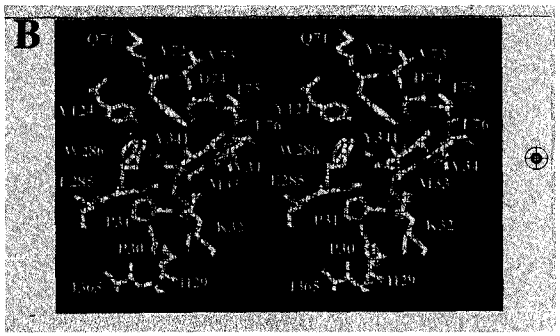


Figure 1. Stereo pair view of the 3.2Å resolution omit Fo-Fc electron density map (contoured at 2.5 σ) showing the stacking interaction between Fas2 Met33 and mAChE Trp286 (middle)

Structure of the Hydroxylase Component of Methane Monooxygenase from Methylosinus trichosporium OB3b at 2 A Resolution	X12C

N. Elango, R. Radhakrishnan, W.A. Froland, C.A. Earhart, J.D. Lipscomb and D.H. Ohlendorf (U of Minnesota)

Methane monooxygenase (MMO) catalyzes the insertion of an oxygen atom from molecular oxygen into the C-H bond of methane. MMO can be found in two forms–a membrane-bound copper-containing protein and a soluble iron-containing protein. Unlike cytochromes P-450 which use a heme prosthetic group to generate a high valent iron-oxo moeity (Fe^{V}=O) capable of performing this chemistry, soluble MMO uses a μ-oxo bridged diiron center. In both cases these iron metalloenzymes are rather promiscuous recognizing a variety of alkanes, alkenes, ethers, and alicyclic, heterocyclic and aromatic compounds as substrates. A structural study of soluble MMO was undertaken to provide a structural foundation for understanding the basis of the catalytic process.

Soluble MMO is composed of 3 protein components: a 245 kDa catalytically-competent $\alpha_2\beta_2\gamma_2$ hydroxylase (MMOH), a 38 kDa NAD(P)H-dependent reductase, and a 16 kDa regulatory protein known as component B. The structure of diferric form of MMOH from the type II methanotroph *Methylosinus trichosporium* OB3b has been determined to a resolution of 2 Å using data collected at 20°C on beamline X12C of the NSLS. The final structural model has 510 of 526 residues of the α chain, 385 of 394 residues of the β chain, 167 of 168 residues of the γ chain, and 729 solvent molecules and produces a crystallographic R value of 0.162 using 75570 reflections between 5 and 2 Å resolution with F>2σ. The exceptionally clear electron density map revealed 15 isolated errors in the reported amino acid sequence including Glu209α, a ligand to Fe1 in the active site, which had been reported to be an aspartate and 28 consecutive errors in the γ chain apparently arising from a shift in the reading frame. The two irons at the active site are octahedrally coordinated with a histidine and two glutamates plus a bridging glutamate and 2 bridging hydroxyls. The irons differ in the sixth ligand–a solvent molecule for Fe1 and a glutamate for Fe2.

The structure of MMOH from the type I methanotroph *Methylococcus capsulatus* Bath has been determined by others using data collected at 4°C and at -160°C. As expected from the 66% homology in the amino acid sequence, the structures of these proteins are very similar (RMS difference in Cα's = 0.8 Å. The active site structure of MMOH from *M. trichosporium* OB3b we determined at 20°C is more similar to that of *M. capsulatus* Bath determined at -160°C than that determined at 4°C. In the frozen *M. capsulatus* Bath MMOH, the irons are separated by 3.1 Å and they are bridged by two hydroxyls. In the *M. trichosporium* OB3b MMOH the Fe-Fe distance is 3 Å with the same bridging hydroxyls. In the *M. capsulatus* Bath MMOH determined at 4°C the Fe-Fe distance is 3.4 Å and one of the bridging hydroxyls has been replaced by an acetate. As this Fe-Fe distance is more similar to that of the reduced MMOH, we suggest that the reported structure of *M. capsulatus* Bath MMOH determined at 4°C is that of the partially reduced protein.

Structural Studies of Nucleosomes. *	X12C

J. M. Harp, D. E. Timm (UTK), and G. J. Bunick (ORNL)

We have been involved in a project directed toward the solution of the high resolution structure of the nucleosome core particle. Diffraction quality of the nucleosome core particle crystals had been improved by reconstituting the particle using a 146 bp DNA palindrome based on a nucleosome phasing sequence on alpha satellite DNA from the human X chromosome. Crystallization of the nucleosome particles was done in the microgravity environment provided on the United States Microgravity Laboratory (USML-2). Because of prolonged lauch delays we were only able to obtain a few small crystals. Data was collected on one of these crystals at 100K using the MAR image plate detector on beamline X12C at the NSLS. The crystal provided excellent data to 2.5 Å with an overall linear R-factor of 0.053. Recent experiments aboard the Mir space station have provided much larger crystals.

As an adjuct to the nucleosome core particle studies, data were also collected on crystals of the histone octamer core of the nucleosome. Complete data sets were collected on a native chicken histone octamer crystal and on two heavy atom derivatives. The data were collected at 100K on beamline X12C using the MAR image plate detector. The native crystal provided useful data to 2.5 Å . Anomalous diffraction data were collected from a mercury thiocyanate derivative crystal and data were also collected from a mercury acetate derivative. These data sets are being used to solve the structure of the histone octamer at low temperature.

* Research sponsored by the Office of Health and Environmental Research, USDOE, under contract No. DE-AC05-960R22464 with Lockheed Martin Energy Systems, Inc., and NIH Grant No. GM29818.

The Structure of the Complex of Concanavalin A with Methyl Alpha-D-Arabinofuranoside	X12C

A.J. Kalb (Gilboa), F. Frolow, A.G. Evdokimov and R. Ventura (Weizmann Institute)

Concanavalin A, a saccharide-binding protein (lectin) from the Jack bean, binds simple and complex saccharides having non-reducing gluco- or manno-pyranoside end groups as well as those having the five-membered-ring arabinofuranoside structure. High resolution crystal structures for saccharide-free concanavalin A and for its complexes with gluco- and manno-pyranosides have been reported. Recently, we have crystallized a complex of concanavalin A with methyl alpha-D-arabinofuranoside. At the resolution of the earlier study (2.7A), it was not possible to determine the conformation of the bound saccharide because the intrinsic flexibility of the five-membered ring precluded the use of an explicit model for the bound sugar. The present experiment has resolved this problem by extending the resolution limit to 1.7A, where the detailed structure of the bound saccharide can be clearly observed. This was accomplished by flash freezing of the crystal and the use of the high intensity, highly monochromatic X-ray beam,the excellent cryostatic device (Oxford Cryostream) and the high quality imaging plate area detector (MAR30) available at beamline X12C. Data collection was greatly facilitated by the excellent, user-friendly software and by the goniostatic crystal mount in use at this beamline. Data processing was easily accomplished simultaneously with data collection by means of an interface between the data collection and data processing programs. We collected 53,746 unique reflections with R(sym) of 6% on intensity, average redundancy of 3 and 95% completeness. Currently, the structure of the complex has a conventional R-factor of 26% (R-free 30%) with excellent geometry. The bound methyl alpha-D-arabinofuranoside, although smaller than the gluco- and mannopyranosides, interacts with the saccharide-binding site of the protein in much the same way - via a network of seven hydrogen bonds and a multitude of van der Waals contacts. This mode of interaction corresponds closely to that which we predicted earlier on the basis of molecular mechanical considerations.

Crystal Structures of Two Thermostable Bacterial Alcohol Dehydrogenases	X12C

Y. Korkhin, F. Frolow, A.J. Kalb (Gilboa) (Weizmann Institute of Science)

Crystal structures of secondary alcohol dehydrogenases from *Thermoanaerobium brockii* (TBADH) and *Clostridium beijerinckii* (CBADH) have been determined. These NADP-dependent enzymes have 75% sequence identity but differ by 26°C in thermal stability as measured by the temperature of half inactivation in 60 min. Both enzymes were crystallized in holo- and coenzyme-free forms [1]. Four data sets were collected at beamline X12C. A 2.05 Å data set was collected from holo-CBADH crystals at 100K with an overall completeness of 88.2%. Two data sets were collected from apo-CBADH crystals at 100K: the first data set to a resolution of 2.15 Å with an overall completeness of 79% and the second to a resolution of 2.4 Å with an overall completeness of 98%. A 2.5 Å data set was collected at ambient temperature from holo-TBADH crystals with an overall completeness of 88.4%. The structures were solved by molecular replacement using previously determined 2.8 Å MIR apo-CBADH structure as a model. Holo-CBADH structure was refined with X-PLOR to an R-factor of 21.6% (R-free=26.8%) and holo-CBADH was also refined with X-PLOR to an R-factor of 21.7% (R-free=27%). Apo-CBADH structure refinement at 2.15 Å resolution is currently underway.

Comparison of CBADH and TBADH crystal structures has revealed the structural determinants of enhanced thermal stability of TBADH, which, apparently, comes from strengthening the interface between its subunits.

Having compared apo- and holo-CBADH structures we identified the structural determinats for coenzyme specificity. Additionaly, a new zinc atom coordination and possible modulation of this coordination by the presence of the cofactor in the active site of the enzyme were revealed.

1. Korkhin, Y., Frolow, F., Bogin, O., Peretz, M., Kalb(Gilboa), A.J., and Burstein Y."Crystalline alcohol dehydrogenases from the mesophilic bacterium *Clostridium beijerinckii* and the thermophilic bacterium *Thermoanaerobium brockii*: preparation, characterization and molecular symmetry". *Acta Cryst.*, **D52**, 882-886 (1996).

Structure of Lyme Disease Antigen OspA Complexed with a Fab * | X12C

H. Li and C.L. Lawson (BNL - Biology)

OspA is an abundant lipoprotein and a major antigen of the Lyme disease spirochete, Borrelia burgdorferi. The crystal structure of a soluble recombinant form of OspA was solved in a complex with the Fab fragment of a mouse monoclonal antibody and refined to a resolution of 1.9 Å, based on data collected at NSLS beamlines X12C and X25 (Fig. 1). Each data set was collected from a single crystal flash-cooled to 100 degrees K. Data set Cys84-II was employed as the final native. Diffraction images were collected using MAR mage plate/scanner systems and were processed with DENZO.

OspA has a novel repetitive antiparallel topology with a region of freestanding sheet. Conserved residues and a hydrophobic cavity buried in a positively charged cleft suggest a binding site for an unknown ligand. An exposed hypervariable region is predicted to be an important factor in the worldwide effectiveness of vaccines based on OspA.

Diffraction Data and Phasing Statistics for the OspA-Fab184.1 Complex

Dataset	Cys84-I X12C	Cys84-II X25	K_2PtCl_4 X12C	Iodo-Y X12C	$Pb(CH_3)_3$ X12C
observed	155965	254719	87304	70488	89601
unique	36731	58870	20837	17419	23461
Resol	2.30	1.95	2.80	2.85	2.70
Compl.%	97.9	97.1	98.2	88.5	99.3
R_{merge},%	5.2 (22.4)	4.8 (21.6)	8.0 (21.7)	8.6 (19.5)	6.9 (23.2)
R_{iso},%			6.8	10.5	6.6
Phasing			1.61(1.69)	1.24	1.09(1.37)

Figure 1. Numbers in parentheses indicate values for highest resolution shell (R-merge) or for anomalous component (phasing power).

* supported by BNL-LDRD, NIH-NIAID, and DOE-OHER

Crystal Structure of Δ^9 Stearoyl-acyl Carrier Protein Desaturase from Castor Seed and its Relationship to other Diiron Proteins. | X12C

Y. Lindqvist, W Huang, G. Schneider (Karolinska Institute) and J. Shanklin (BNL-Biology)

The three-dimensional structure of recombinant homodimeric D9 stearoyl-acyl carrier protein desaturase, the key enzyme in the conversion of saturated to unsaturated fatty acids, has been determined by protein crystallographic methods to a resolution of 2.4 . The structure was solved by a combination of single isomorphous replacement, anomalous contribution from the iron atoms to the native diffraction data and six-fold noncrystallographic symmetry averaging. The enzyme subunit of 363 amino acids consists of a single domain built up from eleven α-helices. Nine of these form an antiparallel helix bundle. The fold of the enzyme subunit resembles that of the iron-containing subunit of ribonucleotide reductase and the hydroxylase component of the methane monooxygenase. The subunits in the dimer are tightly packed while the dimers pack loosely along a noncrystallographic threefold screw-axis. The enzyme subunit contains a diiron center, with ligands from four of the α-helices in the helix bundle. The iron ions are bound in a highly symmetric environment, with one of the irons forming interactions with the side chains of E196 and H232 and the second iron with the side chains of E105 and H146. Two additional glutamic acid side chains, E143 and E229 are within coordination distance to both iron ions. A water molecule is found within the second coordination sphere from the iron atoms, but there is no indication for a μ-oxo bridge in the electron density maps. The lack of the μ-oxo bridge and the rather long Fe-Fe distance (4.3) suggest that the crystals are the diferous form of the enzyme.

Structure of Photolyzed Myoglobin	X12C

G.N. Phillips, Jr. (Rice U.), J. Berendzen, (LANL), I. Schlichting, (Max Planck-Hedelberg), and R.M. Sweet (BNL - Biology)

Myoglobin is a globular heme protein that reversibly binds ligands, such as O2, CO, and others. Single photons of visible light can break the covalent bond between CO and the haem iron in carbonmonoxy-myoglobin and thus form an unstable 'geminate' state with the CO inside the protein. Using beamline X12C and a specially constructed helium cryo- stat, this geminate stated was trapped at about 20K while a complete data set was taken to 1.5 Angstroms resolution. This work would not have been accomplished without the high quality beamline at X12C.

The work has been published in Nature:

Schlichting, I., Berendzen, J., Phillips, G.N., Jr., and Sweet, R.M., Crystal Structures of Photolysed Carboxy Myoglobin, Nature, 371, 808-812 (1994).

Structure of a Plant Profilin at 1.6 by MAD at X12C	X12C

R. Shigeta, K. Thorn (Princeton U.), H. Christensen (Nat U. Singapore), U. Lindberg (Stockholm U.), N.-H. Chua (Rockefeller U.), C. Schutt, (Princeton U.)

Profilins are small eukaryotic proteins involved in modulating the assembly of actin microfilaments in the cytoplasm. Plant profilins are of interest because immunological cross-reactivity between pollen and human profilin may be the cause of hay fever and broad allergies to pollens.

Collecting data on NSLS Beamline X12C, the determination of the Arabidopsis thaliana profilin isoform 1 structure using multiwavelength anomalous diffraction (MAD) proceeded in approximately 10 days from data collection to structure refinement to 1.6Å.

The fold of Arabidopsis profiin is quite similar to other classes of profilins solved previously (Figure 1), but comparison of the structures of profilins from lower eukaryotes, mammals with a plant profilin allowed us to understand several important aspects of profilin function.

For instance, although the actin-binding residues on profilin are not conserved, a comparison of these three structures allowed identification of conserved features of the contact surface at the level of atom type (Figure 2). These two surface features are conserved amongst nearly all profilins and may be responsible for the immune cross-reactivity of antibodies between human and plant profilins.

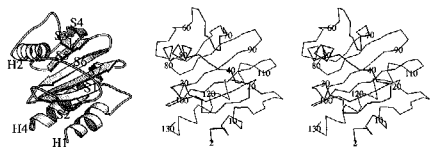


Figure 1. Overall structure of Arabidopsis profilin.(left) Ribbon diagram of the fold of Arabidopsis profilin 1. profilin 1; every tenth residue is numbered. Figure 2. (right) The actin binding face of profilins. Residues correponding to the actin binding surface of (a) Arabidopsis profilin I, (b) Acanthameoba profilin I and (c) bovine profilin. Residues which are thought to contact actin are displayed on a ribbon representation (left column) and on a dark grey CPK van der Waals surface (right column).

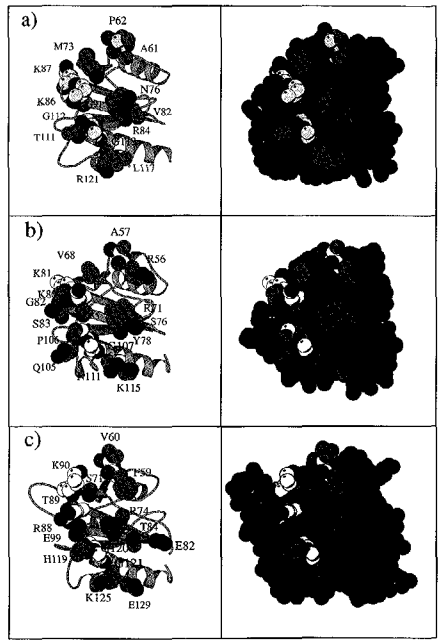


Figure 2. (continued) Only six structural features appear to be conserved binding determinants with actin across the kingdoms despite a near identity of the profiin binding site of actin.

Crystallographic Studies of hnRNP A1 | X12C

R-M. Xu (Cold Spring Harbor Lab.)

Heterogeneous nuclear ribonucleoprotein (hnRNP) A1 is one of the most abundant hnRNP proteins in the hnRNP complex. hnRNP A1 has been shown to be involved in regulating alternative 5' splice site selection. It facilitates the efficient annealing of complementary RNA or DNA molecules. hnRNP A1 also contains a nuclear export signal, which is responsible for the hnRNP A1 shuttling between the nucleus and the cytoplasm.

We have crystallized the RNA-binding domain of the hnRNP A1, termed UP1, which contains two RNA-recognition motifs. UP1 crystallizes in spacegroup P21 with cell parameters a=37.98 Å, b=43.92 Å, c=55.75 Å, beta=94.2 degree. A complete native data set to 1.9 Å resolution has been collected. One mercuril derivative data set to 2.5 Å resolution and one platinum derivative data set to 2.4 Å have also been collected. The mercurial derivative shows good isomorphism to 2.5 Å with the native crystal and it has produced interpretable electron density map.

Structural Basis for Dimerization of Hepatitis Delta Antigen | X12C

H. Zuccola and J. Hogle (Harvard Medical School)

Data was collected on a peptide that corresponds to the oligomerization domain of hepatitis delta antigen. The hepatitis delta antigen is the only protein encoded by the Hepatitis D virus. This region of the protein (amino acids 12-60, which represent 25% of the full length protein) is important in replication of the virus. If dimerization does not take place the virus cannot replicate. The high intensity beam at X12C allowed us to collect a data set to 1.73E, which had a Rsym of 4.4% with an I/s of 45.1. This is a vast improvement over the quality of the data we have been able to collect in our own laboratory, a 2.2E dataset with Rsym of 5.9% with an I/s of 14.3.

We are still in the process of refining the structure to high resolution. With the aid of the high resolution data we have been able to model a number of sidechains with multiple conformers. We believe we can use the high resolution structure of the peptide to aid in the design of new antivirals for hepatitis D. The structure will also represent the first high resolution structure of a antiparallel coiled coil and may lend itself in the aid of designing new coiled coil structures.

The help from the staff at Brookhaven was indispensable. Not only were they sincerely interested in our input, but suggestions to programs were incorporated while we were there collecting our data. The X12C environment is extremely user friendly, from wet lab preparations to data collection to processing. Finally, I would like to emphasize that the data collection software at X12C is far superior to any other software I have used. I believe it made this the first actual pleasurable synchrotron trip I have ever been a part of.

Characterization of the Elliptical Polarized Wiggler at the Iron K-edge *	X13

W. A. Caliebe, C.-C. Kao, P. Stefan, E. Johnson, D. P. Siddons, and J. B. Hastings (NSLS)

The straight section of the NSLS X-ray ring is used to test newly developped insertion devices. The newst device is an elliptically polarized wiggler, which has already been used intensively in the soft X-ray region between 500 eV and 1000 eV.

Using a flat Si(111) monochromator the flux between 5 keV and 12 keV and the degree of polarization at the Fe K edge have been measured. Both measurements have been done with the EPW operating in DC-mode, which results in one helicity. The flux for both helicities is shown in fig.1. The difference in intensity results from different positions of the beam relative to the slit in front of the monochromator. The change in intensity at 7.1 keV results from Iron in the Be-windows. The flux is approximately $2{\cdot}10^{10}$ ph/s in a bandwidth of 0.2% and a solid angle of 0.1 mrad×1 mrad.

The degree of polarization has been determined using the difference of absorption of left and right circular polarized X-rays by a magnetized iron foil. The experiment has been done by inverting the direction of the magnetic field for one helicity, which gives the same information. The results for both helicities and opposite magnetic fields are shown in fig.2. The effect in these measurements is of the order of 0.05%. Comparing this value with published date and taking the polarization factor of the monochromator into account one obtains a degree of polarization of 50% for the EPW.

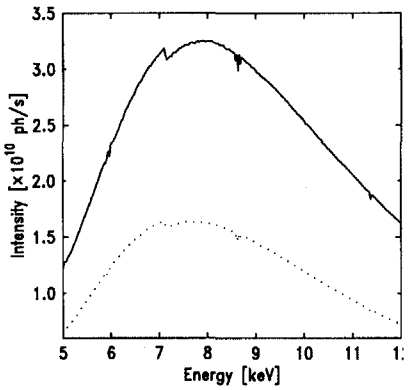


Figure 1. Flux of the EPW

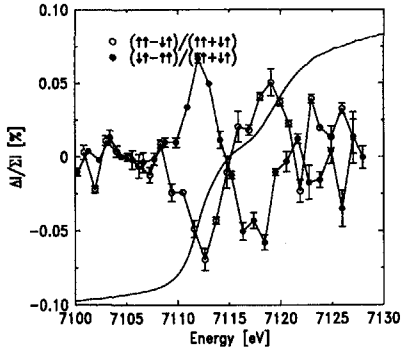


Figure 2. MCD of Iron at the Fe K-edge

* This work was supported by US DOE grant DE-AC02-76CH00016.

Generation of Coherent Soft X-rays with the Prototype Small Gap Undulator. *	X13

E. Dufresne, S.B. Dierker (U. Michigan) L.E. Berman and Z. Yin (NSLS)

We investigated the suitability of the Prototype Small Gap Undulator (PSGU) at X13 to generate coherent X-rays for X-ray Photon Correlation Spectroscopy (XPCS) experiments [1]. Since the coherent flux is proportional to the brightness times the wavelength squared, this new set up, compared to previous ones at X25[1], increases the coherent flux by using a longer wavelength and by using the large increase in brightness provided by the PSGU at 3 keV. The only optical element in the beamline was a Be window, so we were able to isolate its effect on the beam spatial profile. One meter downstream of it, we measured large spatial variations appearing as long horizontal stripes, with a vertical spacing of $\approx$ 20 μm. The variation amplitude was larger at 3 keV than at 9 keV, and diminished when the beam was profiled 4 cm behind the window. The energy and distance dependence seems qualitatively consistent with a focussing effect caused by the refraction of X-rays by the rough Be [2]. To limit the incident beam size to its smallest transverse coherence length ($\approx$ 10μm)[1], we developed new slits for XPCS experiments controlled by DC motors. The slit opening could be controlled to a fraction of a μm reproducibly. They were designed to use inclined soft transmitting edges in order to reduce the parasitic diffraction from the slits at wavevectors near 10^{-3} $\AA^{-1}$. We observed a "phase peak" in the Fraunhofer diffraction patterns of these slits, caused by a periodic phase variation of the X-rays transmitted through the soft edges. The results are in good agreement with a simple model. In an attempt to increase the usable coherent flux, we focussed the beam by a factor of 20 in the vertical direction with a simple float glass mirror [3]. However, due to a systematic figure error and a large demagnification ratio, the transverse coherence was greatly reduced. To preserve the transverse coherence, we replaced the focussing mirror with a double multilayer monochromator. With the fundamental set at 4.1 $\AA$, we measured 2×10^8 ph/s at 300mA in a 10 μm pinhole, and observed a diffraction pattern from this pinhole. In order to further optimize the flux, we used a double flat glass mirror assembly, which transmitted the full bandwidth of the fundamental. We obtained a substantial increase of coherent flux of $3{\times}10^9$ ph/s at 300mA in a 10 μm pinhole. Unfortunately, we found that the coherent flux decreased continuously with X-ray exposure by a factor of 300. We measured a 4 $\AA$ rms roughness for the unexposed mirrors. After approximately 13 days of X-ray exposure, the rms roughness of both mirrors increased to values ranging from 84 to 284 $\AA$ on the center of the beam footprint, indicating that the loss of coherent flux was caused by permanent X-ray damage. Although, the coherent flux increases for soft X-rays, an XPCS experiment is more difficult to perform at 3keV than at 8keV because the experiment must be done in He to reduce air absorption. The stronger absorption also limits the scattered intensity from the sample, which reduces the gain made in coherent flux.

[1] See S. Dierker, NSLS Newsletter, July 1995 and references within. [2] A. Snigirev et al. NIM A 370 (1996) 634 [3] Z. Yin, L. Berman, S. Dierker, E. Dufresne, D.P. Siddons, SPIE Proceedings 2856, Dec. 1996.

* E.D. acknowledges the support of NSERC. This work was supported by NSF Grant No. DMR-92-17956 and by DOE contract No DE-AC02-76CH00016.

A Simple X-Ray Focusing Mirror Using Float Glass * | X13

Z. Yin, L. Berman (NSLS), S. Dierker, E. Dufresne (U. Michigan) and D.P.Siddons (NSLS)

In our recent x-ray photon correlation spectroscopy (speckle) experiments at NSLS, one of the challenges is to increase the coherent photon flux through a pinhole, whose size is chosen to match the beam's horizontal transverse coherence length l_h. We adopted an approach to vertically focus the x-ray beam so as to match its vertical transverse coherence length l_v (at NSLS X13, $l_v \sim 50 l_h$, $l_h \sim 12$ μm at 3 KeV) with l_h. By demagnifying the vertical size by a factor of l_v/l_h, we expect to increase the intensity of the x-rays through the pinhole by the same factor while keeping the beam coherent.

A piece of commercial 3/8" thick float glass, by virtue of its low surface roughness ($\sim 3\AA$ rms), good reflectivity in the low photon energy range of interest and low cost, was chosen as the mirror material. A computer controlled motorized bender with a four point bending mechanism was designed and built to bend the float glass to a continuously variable radius of curvature from -700m (intrinsic curvature of the glass surface) to < 300m, as measured with the Long Trace Profiler at the BNL Metrology Lab. This mirror bender assembly allows us to continuously change the focal length of the x-ray mirror down to 0.5 m under our experimental conditions.

At the NSLS X13 Prototype Small Gap Undulator (PSGU) beamline, we were able to focus the x-ray beam from a vertical size of 0.5 mm to ~ 25 μm at the focal point 54 cm from the mirror center, thus increasing the photon flux density by a factor of 20. Results also show that, as expected, at an incident angle of 9 mrad, the mirror cuts off the harmonics of the undulator spectrum, leaving a clean 3 KeV fundamental for our experiments.

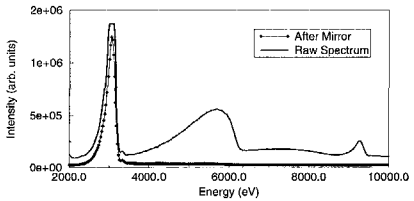


Figure 1. X13 PSGU spectrum before and after the mirror. The mirror (tilted at 9 mrad glancing incident angle) "cuts off" the higher harmonics, leaving a clean 3.1 KeV fundamental for the XPCS experiment.

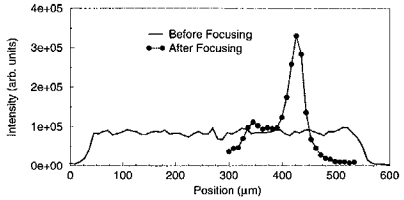


Figure 2. Vertical focusing by the float glass mirror. An incident beam of 0.5mm vertical height is focused to 25 μm (FWHM).

* Work supported by DOE under contract No. DE-AC02-76CH00016 and NSF Grant No. DMR 92-17956. ED acknowledges the support from NSERC.

Ordered Phases of a Langmuir Monolayer of an Azobenzene-containing Molecule. * | X14A

M.K. Durbin, A. Malik, A.G. Richter, C.J. Yu, V. Bhashyam(Northwestern Univ.), R. Eisenhower(ORNL), and P. Dutta(Northwestern Univ.)

We have used grazing incidence X-ray diffraction to study Langmuir monolayers of the molecule 4-octyl-4'-(carboxytrimethyleneoxy) azobenzene. We found only two phases over a broad range of temperatures and pressures, and the transition between them is strongly first order (compared to the weakly first order transition between two similar phases in straight-chain fatty acids). The diffraction patterns from these phases are shown in Figure 1, as intensity contour plots in the K_{xy}-K_z plane. Both phases have in-plane order, with a distorted hexagonal (DH) lattice. The low pressure phase has molecular tilt towards a nearest neighbor (NN tilt). At 12.5dyn/cm, there is a first order transition to a phase with tilt towards a next-nearest neighbor (NNN). These data are unexpected because studies of these monolayers using Brewster Angle Microscopy[1] and UV absorption[2] have suggested that the low pressure phase is fluid-like, while the high-pressure phase is solid-like. Our X-ray data clearly show that both phases have some degree of order and the two sets of peaks have similar full widths at half maximum, implying correlation lengths from 100$\AA$ to 300$\AA$.

1. Y. Tabe and H. Yokoyama, J. Phys. Soc. Jpn. 63, 2472 (1994).
2. T. Kawai, J. Umemura, T. Takenaka, Langmuir 5, 1378 (1989).

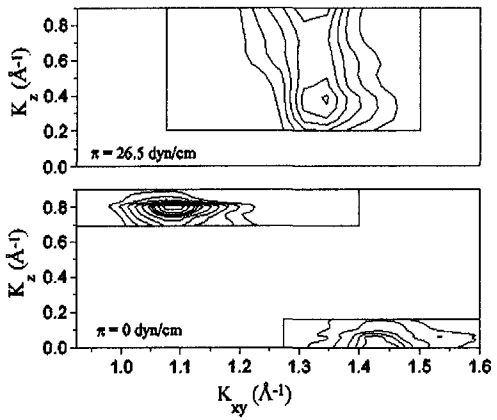


Figure 1. Contour plots of intensity (arbitrary units) as a function of wavevector components K_xy and K_z, (top) at 26.5 dyn/cm,indicating an NNN tilted phase, and (bottom) 0 dyn/cm,typical of an NN tilted phase.

* This work was supported under DOE grant no. DE-FG02-84ER45125

Inelastic X-Ray Scattering Measurement of the Many-Body Local-Field Factor in Aluminum	X14A

B. C. Larson, J. Z. Tischler (ORNL), E. D. Isaacs (Lucent Technologies), P. Zschack (U. of IL,), A. Fleszar (U. Würzburg), and A. G. Eguiluz (U. of TN & ORNL)

Electron-electron interactions play an important role in the physical properties of metals, and, indeed, a large theoretical effort has been exerted toward understanding many-body exchange-correlation effects in electronic systems at metallic densities. Until now, however, quantitative analyses of large wave-vector ($\sim 2k_F$) measurements of the dynamical structure factor, $S(q,\omega)$, in terms of the many-body local-field factor (LFF) have not been available. In this study[1], we have made inelastic x-ray scattering measurements on aluminum in the $2k_F$ region using the X-14A beam line, and we have used first principles dynamical electronic response calculations, that include the actual band structure, to analyze these measurements in terms of the LFF, $G(q,\omega)$. This work represents the first quantitative test of the LFF for simple metals in the critical large wave-vector range.

The real and imaginary parts of the LFF were determined within a Hubbard model for q's ranging from 0.7-$2.5 7k_F$ (ω from 10-70 eV) by adjusting the LFF (assumed to be constant in ω) to match the $S(q,\omega)$ measurements; excellent agreement was obtained. As shown in the figure, for $q < 1.5k_F$, the real part of the LFF is in rather good agreement with (static, i.e. real) theoretical calculations, resolving a long standing difference between theory and electron scattering measurements of $G(q,\omega)$ for that region. However, for $q \sim 2k_F$ and larger, the experimentally determined LFF values are nearly twice as large as all calculations, suggesting that dynamical electron correlations are quite strong even in simple metals, and posing a challenge for theory. The combination of inelastic x-ray scattering measurements (at both 2nd and 3rd generation synchrotrons) and first principles electronic response calculations now provides the potential for detailed investigations of electronic excitations on a wide range of materials.

1. B. C. Larson et al. Phys. Rev. Lett. **77**, 1346 (1996)

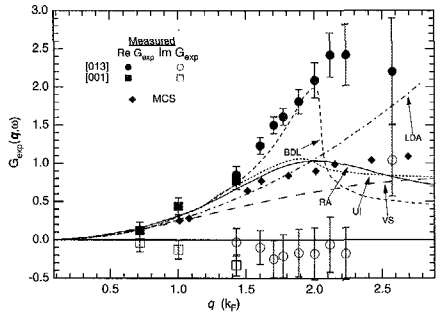


Figure 1. Real and imaginary parts of the measured LFF, $G(q,\omega)$, for Al (full and empty symbols, respectively). Selected LFF's calculated for jellium with $r_s = 2.07$ are shown; see ref. 1 for details.

Resonant Raman Scattering Excited by GeK$_\alpha$ Radiation Internal and External to the Ge Atom	X14A

C.J. Sparks, T. Gog, G.E. Ice (ORNL), R.A. Eisenhower (U. of Illinois)

A low-energy satellite to K_α fluorescence has long been observed, which has been shown to result from the emission of **two** electrons and one photon.[1] This radiative Auger effect challenges our understanding of x-ray excitation and decay processes. Despite the identification of the radiative Auger effect for almost 30 years, no previous measurements have been made of the energy dependent behavior of the radiative Auger effect. All previous experiments were performed with incident photon and electron energies far above an absorption edge.[1]

Our experiment compares the inelastic scattering from a Ge sample excited by synchrotron radiation tuned to the Ge K_α energy (9876 eV) to the inelastic scattering from the same Ge sample excited by synchrotron radiation tuned near and above the K edge (11103 eV). Above threshold, the atom interacts with both the primary radiation field (11103 eV) and the self emitted Ge K_α fluorescence (9876 eV). As shown in Fig. 1, there is a marked energy shift between the inelastic spectra excited above and below threshold in the vicinity of the radiative Auger satellite. The measurements with the sample excited by 9876 eV x-rays contain a resonant Raman scattering peak in the vicinity of the radiative Auger satellite energy. This asymmetric peak results from a resonant excitation of the K hole and subsequent filling of the hole by an L electron.[2] Hence the resonant Raman line is designated the Ge K-L resonant Raman peak. The measurements at and above threshold include both resonant Raman scattering and the radiative Auger satellite. As illustrated in Fig. 1, there is ~80 eV difference in energy at the leading edges marked by arrows.

[1] T. Aberg, J. Utriainen, Phys. Rev. Lett. **22**, 1346 (1969); O. Keski-Rahkonen, J. Utriainen, J. Phy. **B7**, 55 (1974) [2] C.J. Sparks, Phys. Rev. Lett. **33**, 262 (1974)

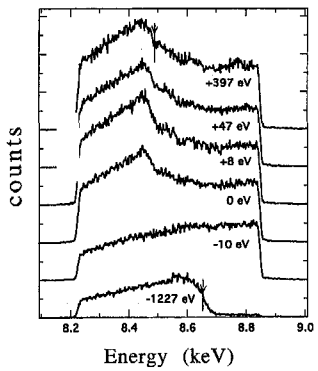


Figure 1. Inelastic resonant scattering from a Ge crystal excited with x-rays of energies which differ from the Ge K edge of 11103 eV by the energies shown. The incident energy for the resonant Raman curve labeled -1227 eV is Ge K at 11103 eV - 1227 eV = 9876 eV which is the Ge K_α energy.

Adsorption and structure of selenite on the calcite ($10\bar{1}4$) surface * | X15A

L. Cheng, P.F. Lyman (Northwestern U.), N.C. Sturchio (ANL) and M.J. Bedzyk (Northwestern U. and ANL)

The adsorption of Se at the water-mineral interface is a phenomenon of major significance in environmental science. Se is potentially harmful to human and animal health. It is known that, in water, Se exists predominantly in the forms of two divalent inorganic oxyanions—selenite (SeO_3^{2-}) and selenate (SeO_4^{2-}).

The adsorption of selenite ions from a dilute aqueous solution onto a freshly-cleaved calcite ($10\bar{1}4$) surface was studied with the X-ray standing wave (XSW) technique. SeO_3^{2-} was found to selectively adsorb at the CO_3^{2-} site at the calcite surface, forming a two-dimensional solid-solution of the form $Ca(SeO_3)_x(CO_3)_{1-x}$ at the interface. The local structure at the SeO_3^{2-} adsorbate site was determined by the XSW triangulation of the site of the Se atom using the ($10\bar{1}4$), the (0006) and the ($11\bar{2}0$) reflection planes of calcite. These results are consistent with the geometry where the SeO_3^{2-} trigonal pyramid lies on the extrapolated CO_3 plane upon adsorption, with its apex Se atom pointing outward from the calcite crystal. The SeO_3^{2-} adsorption saturated at a coverage of 0.02 monolayer. In addition, it was found that selenate (SeO_4^{2-}) adsorption on calcite under identical conditions resulted in a much lower level of coverage.

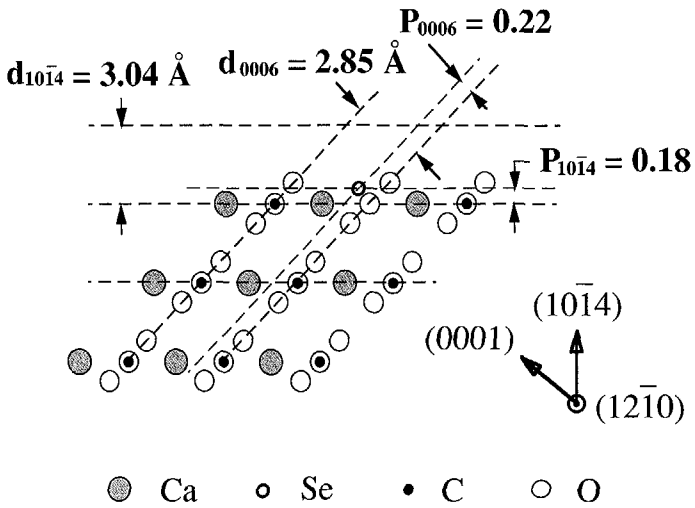


Figure 1.

* Research supported by DOE BES contract No. W-31-109-ENG-38 to ANL.

Spatial Resolution of the Variable-Period X-Ray Standing Wave Method * | X15A

R. Itri, R. Zhang and M. Caffrey (Ohio State U.)

The variable period x-ray standing wave (XSW) technique has been applied in studies of Langmuir Blodgett (LB) films deposited on a gold mirror surface rendered hydrophobic with a self assembled octadecylthiol (ODT) monolayer. Films composed of the zinc salt of unbranched, saturated alkanoates with hydrocarbon chains varying in length from 16 to 24 carbons (C16 to C24) were investigated with a view to establishing the spatial resolution of the technique. X-ray reflectivity data indicates a mean value for the gold mirror surface roughness of 1.29 nm. Values of the first ($\ll z \gg$, mean position) and second (σ^2, variance) moments of the zinc label atom distribution within the films were obtained from x-ray fluorescence yield profile data. The results show that it is possible to observe differences in zinc position on the order of 0.1-0.2 nm which corresponds to the spatial resolution of the XSW method in the current application. Further, by assuming that the hydrocarbon chains of the zinc alkanoates are fully extended in an all-trans conformation, the results suggest that the long axis of the chains are tilted at an angle of $\approx 36°$ from the normal to the mirror surface for C18, $\approx 28°$ for C20 and C21 and $\approx 20°$ for C22 and C23. For zinc lignocerate (C24) the hydrocarbon chain is oriented perpendicular to the mirror surface. In all cases, an apparent distribution half-width, σ, of the zinc around the mean position in the adsorbed lipid layers was 1.63 nm. This corresponds to an intrinsic distribution half-width, σ_{in}, of 1.0 nm, independent of hydrocarbon chain length, when mirror surface roughness has been deconvoluted. The $\ll z \gg$ value found for samples composed of zinc arachidate (C20) covered with an inverted bilayer of ω-tricosenoic acid (ωTA) indicates that the chains of zinc arachidate are also tilted in relation to the gold surface, with an angle of 18° from the surface normal. For such films, a value of $\sigma_{in} = 0.7$ nm was found which indicates that the zinc ions in the lipid bilayer have a sharper distribution width in comparison with the uncoated zinc arachidate. Samples composed by zinc alkanoates (C21 and C24) with 2 inverted bilayers of ωTA sandwiched between the hydrophobic gold mirror and the zinc-containing bilayer were found to have their hydrocarbon chains tilted at an angle of $\approx 23°$ for C21 and perpendicular to the mirror surface for C24. Such films have the same zinc label distribution width as those without the intermediate ωTA bilayers.

To M. Caffrey and R. Itri thanks FAPESP/SP and CNPq of Brazil for financial support. R. Zhang was supported by a University Posdoctoral fellowship from the graduate school of The Ohio State University.

* Research supported by NIH (DK 36849 and DK46925) and the Petroleum Research Foundation of the American Chemical Society (3057-AC7). To M. Caffrey and R. Itri thanks FAPESP/SP and CNPq of Brazil for financial support. R. Zhang was supported by a University Postdoctoral fellowship from the gradue school of Ohio State U.

Structural Study of 0.2 ML In/GaAs(001) 4x2 Surface *	X15A

T.-L. Lee (Northwestern U.), J. Zegenhagen (Max-Planck-Institut, Germany), P.F. Lyman (Northwestern U.) and M.J. Bedzyk (ANL & Northwestern U.)

From a previous a scanning tunneling microscopy (STM) investigation [1], the indium-terminated GaAs(001) surface exhibited a (4x2)/c(8x2) reconstruction with bright straight rows running along the [110] direction. Based on this study, a dimer model, which is similar to the one proposed by Biegelsen et al. [2] for a (4x2) Ga-rich GaAs(001) clean surface, was proposed for the In structure in the monolayer regime. However, the detailed local structure for the In ad-atoms was not resolvable from the STM image. In this work, we applied the higher-resolution x-ray standing wave (XSW) technique to investigate the adsorbate - surface structure of low coverage In on GaAs(001).

A (2x4) GaAs(001) clean surface was prepared in UHV by thermal desorption of an arsenic-capped GaAs(001) substrate. The (4x2)/c(8x2) In-terminated surface (Θ_{In} = 0.2 ML) was obtained by In deposition at room temperature and a subsequent annealing at 450° C using our UHV-MBE system. The (004) XSW measurement (Fig. 1) shows that the In ad-atoms are located 1.61 Å above the (004) diffraction planes. At higher In coverages (up to ~ 0.6 ML) we measured lower (004) coherent fractions. This is consistent with the ladder- type pattern observed by STM for $\Theta_{In} \geq 0.5$ ML [1], which suggests that more than one In structure coexists on the surface. For $\Theta_{In} \sim 0.2$ ML, we found that our off-normal XSW measurements do not agree with the dimer model proposed in Ref. [1]. We are consequently developing a new model for this surface structure.

[1] U. Resch-Esser, N. Esser, C. Springer, J. Zegenhagen, W. Richter, M. Cardona, and B.O. Fimland, J. Vac. Sci. Technol. B 13(4), 1672 (1995).

[2] D.K. Biegelsen, R.D. Bringans, J.E. Northrup, and L.-E. Swartz, Phys. Rev. B 41, 5701 (1990).

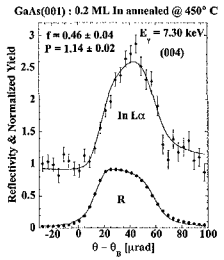


Figure 1.

* Research supported by DOE BES contract No. W-31-109-ENG-38 to ANL and by NSF under contract No. DMR-9120521 to the MRC at NU.

Atomic Resolution X-Ray Standing Wave Characterization of Self-Assembled Chromophoric Superlattices *	X15A

W. Lin, T. -L. Lee, P. F. Lyman, J. Lee, T. J. Marks (Northwestern U.), M. J. Bedzyk (ANL & Northwestern U.)

There is much current interest in molecule-based second-order nonlinear optical materials because of their potential applications in second harmonic generation, electrooptic, and photorefreactive devices. The synthesis of these materials, however, present a significant challenge for synthetic chemists because of the requirement of non-centrosymmetric arrangement of molecular chromophores. We have recently developed a self-assembly approach to constructing intrinsically acentric, structurally regular chromophoric superlattices which exhibit very large second-order nonlinear optical (NLO) responses.

In this work, we have undertaken the first X-ray standing wave characterization of self-assembled multilayers (SAMs). These siloxane-based self-assembled stilbazolium multilayers possess intrinsic acentricity and exhibit very large second-order nonlinear optical responses. The locations of bromide anions within the SAMs were precisely determined using X-ray standing waves generated by total external reflection from mirror surfaces as well as by Bragg diffraction from layered synthetic microstructures. The large coherent fraction (i.e., small Gaussian distribution width) of the Br atoms provides a direct evidence for the high structural regularity of these self-assembled multilayers. Moreover, the anion surface coverage measured (2.5(5) x 10^{14} Br^-/cm^2) is in excellent agreement with the cation surface coverage measured by second harmonic generation (2(1) x 10^{14} molecules/cm^2). These results clearly demonstrate the utility of X-ray standing wave analyses as a quantitative structural probe for self-assembled mono- and multi-layers, especially for SAMs with incommensurate structures.

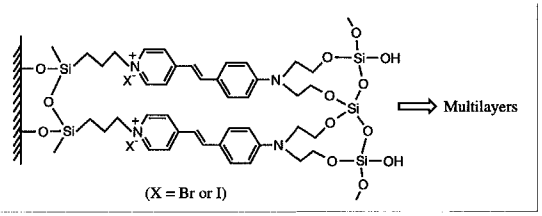


Figure 1. blank

* Research supported by DOE BES contract W-31-109-ENG-38 to ANL and by NSF contract DMR-9120521 to the MRC at NU.

Dynamical Diffraction of Trapped X-rays on a Curved Crystal Surface *	X15A

C. Liu (Harvard U.) and J. A. Golovchenko (Harvard U. & Rowland Inst. for Science)

We report the first observation of the dynamical diffraction of surface trapped x-ray waves at the beam line X15A. A number of experiments have been performed at X15A during the past few years to explore the propagation of hard x-rays (wavelength ~1 angstrom) on the surface of a curved silicon mirror. The x-ray wave is confined on the concave surface via total external reflection, forming a true x-ray surface bound state. The evanescent tail of each surface state penetrates into the bulk and interacts with the underlying crystal lattice, giving rise to diffraction effects. In particular, under the Bragg condition the surface eigenmode becomes the superposition of a forward and a diffracted waves, analogous to the x-ray eigenmode inside the bulk of a crystal under the Laue diffraction geometry. This year at X15A we have successfully excited and detected such diffracting surface eigenmodes on a curved thin silicon mirror. The discovery may have important applications in developing x-ray optical elements like lenses and wave guides, x-ray surface studies, and x-ray lithography applications in the future.

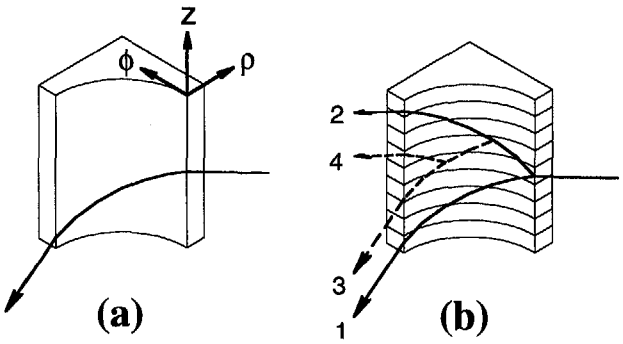


Figure 1. A schematic representation of the diffraction of surface trapped x-rays. (a) An incident x-ray beam at a glancing angle with respect to the mirror surface propagates along a helical trajectory in the ϕ and $z$direction. (b) Under Bragg condition the surface trapped x-ray is diffracted by the underlying crystal lattice, whose reciprocal lattice vector is parallel to the z direction. The actual propagation is described by the cynamical diffraction theory.

* We acknowledge the assistance from Dr. Paul F. Lyman and Prof. Michael J. Bedzyk at Northwestern U. and ANL and the support from JSEP (N00014-89-J-1023).

Local Adsorption Geometry of Te/Si(001) Studied by XSW *	X15A

Paul F. Lyman (Northwestern U.), Michael J. Bedzyk (Northwestern U. and ANL), and Pedro A. Montano (U. of Illinois - Chicago & ANL)

Adsorption of Te on Si is the critical first step in the growth of the direct, wide-bandgap semiconductor CdTe on Si. Apart from the potential commercial importance of that process, the adsorption of a group VI element (Te) on the (001) face of a group IV semiconductor (Si) might result in near-perfect passivation of the Si surface; the two dangling bonds per surface Si atom could be satisfied by a (1x1) arrangement of the hexavalent Te atoms.

A recent LEED and STM study of the Te/Si(001) surface [1] revealed that although the local arrangement of Te atoms does appear to be (1x1), the larger size of the strongly adsorbed Te atoms results in occasional missing rows of Te; these relieve strain in the overlayer by allowing lateral expansion of the Te layer. We undertook an x-ray standing wave investigation to quantify the adsorption site, spatial distribution, and structural perfection of the Te adsorbate layer. Although good agreement was found with the lateral expansion of the Te atoms adumbrated by the STM work, a surprisingly large spatial distribution was found in the direction normal to the plane, not evident in the STM work. Also, it was quantitatively established that this vertical distribution is independent of coverage, indicating that the adatom-adatom interactions on the surface are likely to be attractive.

[1] S.A. Yoshikawa et al., Surf. Sci. 321, L183 (1994).

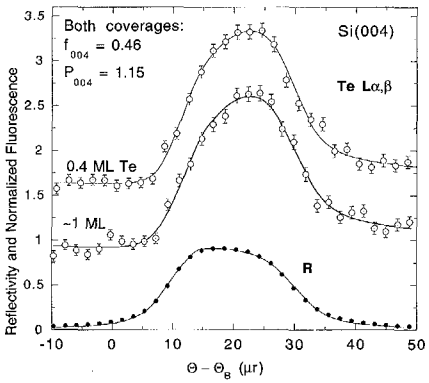


Figure 1. Te fluorescence and x-ray reflectivity from (004) XSW scan of Te/Si(001) surfaces with ≈ 1 ML and 0.4 ML Te coverage.

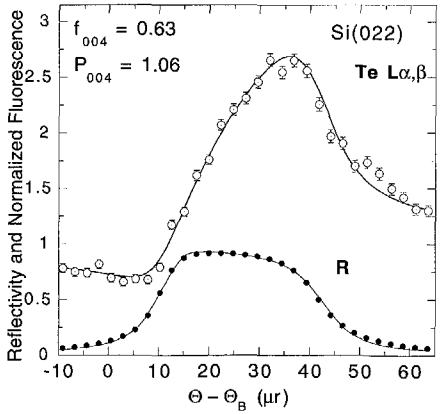


Figure 2. Te fluorescence and x-ray reflectivity from (022) XSW scan of Te/Si(001) surface with ≈ 1 ML Te coverage.

* This work sponsored by the U. S. DOE, Office of Basic Energy Sciences, Div. of Materials Sciences, contract W-31-109-ENG-38, and by the NSF under contract to the MRC at Northwestern U.

Surface Relaxation by X-ray Standing Wave and Surface-extendedXx-ray Absorption Fine Structure * — X15A

J. Woicik (NIST)

We have determined the atomic coordinates of the well characterized 1/3 ML Si(111) 3x3-Ga interface through a combination of x-ray standing wave and surface-extended x-ray absorption fine structure. By independently measuring the perpendicular distance of the Ga atoms to the Si bulk diffracting planes from XSW and the bong length of the Ga atoms to the top layer Si substrate atoms from SEXAFS, our structural determination includes the degree of substrate relaxation, a critical yet experimentally overlooked interfacial parameter. The Ga-first-Si layer bond length is determined to be 2.48 0.02 Å, in complete agreement with the calculations of Northrup; however, the perpendicular distance of the Ga atoms to the Si bulk diffraction planes is found to deviate by nearly 0.2Å. Future polarization-dependent SEXAFS which will measure the Ga-second-layer Si atom bond length should resolve this dilemna.

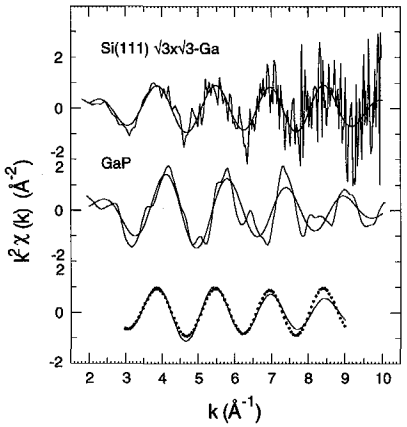


Figure 1. Surface EXAFS performed at the Ga K edge for 1/3 monolayer of Ga on Si(111). Note that the Ga-first-Si layer bond length is significantly larger than the Ga-P bond length in cryatalline GaP (2.36 Å).

* This work was sponsored by the U.S. DOE, Office of Basic Energy Sciences, Div. of Materials Sciences, contract W-31-109-ENG-38, & by the NSF under contracts to the MRC at Northwestern U.

Extremely Dilute Impurities in Silica Optical Waveguides — X15B

L. Niu, R. M. Atkins, M. A. Marcus, D. C. Jacobson, P. F. Glodis, and P. H. Citrin (Bell Labs)

Optical transmission loss is one of the most important factors in defining the utility of a waveguide material. A long suspected source of small but significant losses in manufacturing silica fiber has been trace metal impurities such as Fe. Supporting evidence has only been suggestive because earlier measurements were either too insensitive, ill-defined, or far removed from early stages of fabrication where identification is least reliable (and most costly). NEXAFS measurements on a single silica preform, taken as a function of position within core vs cladding regions from two preform slices of different loss, established that between 3-5 times more Fe was indeed present within the core, and that a similar factor existed between the cores of the different slices. The concentration of Fe in the more lossy core was < 10 ppb. Future work with a more efficient detector will allow greater accessibility to more dilute impurities (Cr and Ni), better overall quantification, and identification of different metal oxidation states.

Optically Active Er Centers in Si — X15B

L. Niu, D. C. Jacobson, D. J. Eaglesham, and P. H. Citrin (Bell Labs)

Because of its potential utility in optoelectronics, the 1.54-μm luminescence observed from excited Er in Si has generated a great deal of interest. Our previous EXAFS measurements of Er implanted in Czochralski and float-zone Si had identified two very different local structures around the Er: a sixfold cage of O atoms and a twelvefold cage of Si atoms, respectively. Only the former was argued to be optically active. Recent theoretical and experimental studies have since reported apparently conflicting evidence about the symmetry, composition, and relative concentrations of these structures depending upon the implantation dose and energy of Er and the oxygen content and temperature of the Si host. More extensive EXAFS measurements, along with TEM micrographs, were obtained from Er implanted in Si under varying conditions. The new data clarify, reconcile, or correct all the conclusions of these recent works. Key to this study were the measured Er nearest-neighbor bond lengths, the coordination numbers, and the presence of silicide precipitates that had gone undetected.

Pb-induced Instability in ZBLAN Glass — X15B

L. Niu, A. R. Kortan, N. Kopylov, and P. H. Citrin (Bell Labs)

The predicted ultra-low optical losses at near-infrared wavelengths of ZBLAN (Zr/Ba/La/Al/Na) fluoride glasses holds promise for their application in optical waveguides and photonic devices. Their complex structure, however, has severely limited understanding how to optimize their composition for practical use. In particular, Ba is substituted with Pb to change its refractive index, but at some critical Pb concentration the glass devitrifies (recrystallizes). To gain insight into this phenomenon and see if it can be avoided, NEXAFS and EXAFS data from varying amounts of Pb-doped ZBLAN material in both glassy and intentionally crystallized phases were obtained, showing that the observed glass instability for Pb concentrations $> 10\%$ is directly related to changes in the local electronic and geometric structure around the Ba cations. The instability was also seen to be strongly correlated with the similarity between the local Ba^{2+} environments in the glassy and crystallized phases. These results show that the Pb-induced glass instability is driven by the reduced effectiveness of the smaller Pb^{2+} to modify the network of ZrF_n polyhedra, an unavoidable problem in these forms of fluoride glasses.

Ti Silicides in Submicron Dimensions | X15B

L. Niu, R. Tung, M. A. Marcus, and P. H. Citrin (Bell Labs)

The C54 phase of $TiSi_2$ has the lowest resistivity of all refractory-metal silicides and is thus the material of choice for sub-0.25-μm ultra-large-scale-integrated technology. However, in narrow wires or thin films this thermodynamically stable phase is preceded by formation of a kinetically-favored, higher-resistivity C49-$TiSi_2$ phase. It is therefore important to determine growth procedures which facilitate the C49 $\rightarrow$ C54 transformation in confined silicide dimensions, and to develop methods for establishing the success of that process in as-prepared material. An EXAFS study was initiated of $TiSi_2$ samples grown in 0.05-μm-thick films and 0.35-μm-wide wires on crystalline- and on heated, pre-amorphized-Si substrates. The relative concentrations of the C49 and C54 polymorphs were determined and found to be in excellent agreement with the trend of sheet resistivities measured from these same four samples. These preliminary results demonstrate that EXAFS data can provide direct, non-destructive characterization of silicides grown in small dimensions and under conditions where resistivity measurements might be impractical. They also suggest the possibility of structurally characterizing systems considerably smaller than those studied here, e.g., 0.1 μm.

Distorted, Inequivalently Charged C_{60} Anions in $Yb_{2.75}C_{60}$ | X15B

S. Schuppler (Bell Labs), E. Ozdas (Hacettepe U.), K. B. Lyons, A. R. Kortan, and P. H. Citrin (Bell Labs)

NEXAFS measurements from the highly reactive, superconducting, single-phase rare-earth fulleride, $Yb_{2.75}C_{60}$, establish that the Yb cations are exclusively divalent, indicating that the average negative formal charge of the C_{60} anions is 5.5. EXAFS (and Raman) measurements also show that the C_{60} anions are distorted in shape, despite their well ordered local structure around the Yb cations. Along with the fact that $Yb_{2.75}C_{60}$ contains three very different crystallographically inequivalent types of C_{60} anions surrounded by 8, 10, or 12 Yb cations, these findings are used to argue that the charge transferred from Yb to C_{60} is both anisotropically distributed on the anions and inequivalently partitioned among them within the unit cell. Specifically, the interactions between Yb and C_{60} are partly covalent, similar to (albeit weaker than) those between Pt and C_{60} in $[(C_6H_5)_3P]_2Pt\text{-}C_{60}$, and the charge states of the three types of C_{60} anions are different, similar to (and more pronounced than) those of O in $YBa_2Cu_3O_7$. Our results are shown to provide insight into the novel structure of $Yb_{2.75}C_{60}$ and to explain the origin of its unique value and distribution of anion charge.

Structure of the Incommensurate Au/Si(100)-5x1 Surface * | X16a

P. Bennett (ASU), D. Walko and I. K. Robinson (U.of Illinois)

We have studied the Au/Si(100) surface with nominally 1 Ml Au annealed to 800C using surface X-ray diffraction. In previous LEED studies this structure was indexed as rt26x3. STM observations (Lin et al PRB47, 1993 p 3671) suggested instead a 5x3 unit cell with a prominent row structure in the 5 direction and a disordered pattern in the 3 direction with a regular rt26 phase slip between rows. We find that it is in fact a 5x1 structure with a very strong incommensurate modulation vector Q_{IC}=(0.44, 0.68). Preliminary analysis of the diffraction data suggest a missing-row model with 4 occupied and 2 missing Au rows in the 5x1 unit cell, giving a chisquare of 3 and a match with the data as shown in the figure below for a single domain. The incommensurate reflections are also shown but are not included in the structural analysis. They comprise a lattice of Q_{IC} convoluted with the 5x1 unit cell, with however most intensities nearly zero. In the figure we also show a simulated image produced by modulating the 5x1 missing rows model with the Q_{IC} vector. This bears a striking resemblance to the STM image of Lin et al. In particular, an approximate 5x3 ordering is apparent. Further refinement of the model to include displacements, structure factors for the incommensurate reflections and out of plane data (truncation rod profiles) is in progress.

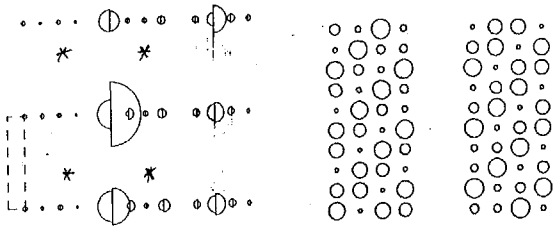


Figure 1.

* Work supported in part by NSF grants DMR9528503 (PAB) and DMR93-15691 (IKR).

Oxygen-Induced Facetting of Cu(115) | X16A

I. K. Robinson and D. A. Walko (U. of Illinois), H. L. Meyerheim and M. Albrecht (Inst. f. Kristallographie, U. Muenchen)

We monitored the distribution of facets on a Cu(115) surface as a function of oxygen dose at 300C. We measured diffraction in a plane intersecting the (115) crystal truncation rods (CTRs), at a distance of 0.9Å^{-1} below the (111) bulk Bragg peak. Most of the facet peaks were found to lie in the vertical plane perpendicular to the expected step-edges of the (115) surface, which is scanned in Fig 1. Additional facet CTRs were observed to form along {104} directions. "Peak I" in figure 1 corresponds to the (115) facet direction, which is present on the clean surface.

"Peak I" evolves into "Peak II" after a latency period of 10L dose. No changes are visible in the diffraction pattern throughout this latency period. Presumably, oxygen is decorating the ordered (115) facets without strong stuctural changes, until they become saturated with oxygen. "Peak II" then appears very suddenly with an abrupt transition. Unlike "Peak I", "Peak II" is not a well-defined facet direction, and slides continuously as a function of dose, until it arrives at a position of roughly (114). In figure 2, it can be seen that the heights of the two peaks interchange over a narrow range of dose, and that the width passes through a minimum. The position of "Peak II" then varies roughly linearly after "Peak I" has gone.

Finally, the intensity of "Peak II" then starts to drop and "Peak III" appears, which corresponds to a (113) facet. Simultaneous with the debut of "Peak II", the two 104 facet CTRs begin to appear and rise linearly with dose after that; it is expected that the relative areas of the three facets will conserve a net (115) surface. The dose dependence of the various peak heights, positions and widths is shown in figure 2.

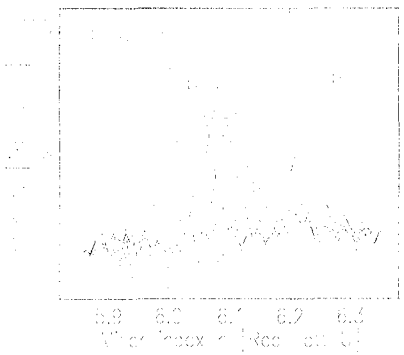


Figure 1. Oxygen dose-dependence of the CTR diffraction near the (111) bulk Bragg peak. Different peaks correspond to differrent facet directions. As the dose increases, the peak moves from left to right.

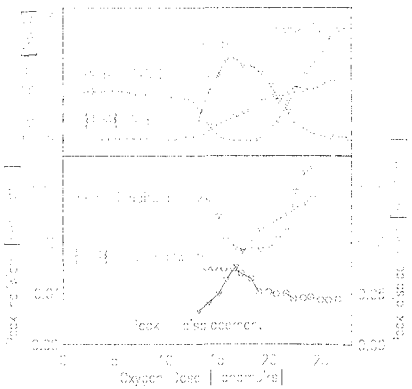


Figure 2. Dose dependence of the peak heights and widths corresponding to the data of fig.1.

Surface Structure of α-Ga(001) — X16A

D. A. Walko, I. K. Robinson (U. of Illinois), Ch. Grütter, and J. H. Bilgram (ETH Zürich)

Orthorhombic α-Ga is unique among elemental metals in that its atoms form partially covalent bonds, resulting in dimers which are angled $\pm 16.9°$ from the [001] direction. Thus it is possible to form inequivalent (001) surfaces: by separating pairs of dimers (surface "A" in Fig. 1) or by cutting through the dimers (surface "B" in Fig. 1). Adding considerable challenge to any structural study of α-Ga is the material's low melting point, 29.76°C.

Ab initio, total energy calculations have been performed [M. Bernesconi *et al.*, Phys. Rev. Lett. **70**, 3295 (1993)] which investigate the stability of the various α-Ga (001) surface structures. These calculations determined that bulk truncations "A" and "B" are both unstable with respect to a new structure, which is a rearrangement of surface "A," and was termed a self-wetting of α-Ga by two layers of Ga-III.

We have performed x-ray diffraction experiments in the X16A UHV chamber. Because of α-Ga's low melting point, the chamber was equipped with a load lock to install the samples without breaking vacuum in the chamber. After cleaning the surface with several Ar sputtering cycles, we measured structure factors along several rods (one of which is shown with fit in Fig. 2). Preliminary fits to the data indicate the surface is a rearrangement of surface "B," rather than the two-layer Ga-III model. A refinement of fitting parameters and determination of atomic positions is ongoing.

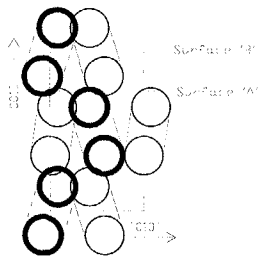


Figure 1. Atomic structure of bulk Ga, showing two possible places to form an (001) surface. Thick and thin circles represent atoms at x = 0 and x = 0.5 respectively. Covalent dimerization of atoms is also schematically indicated.

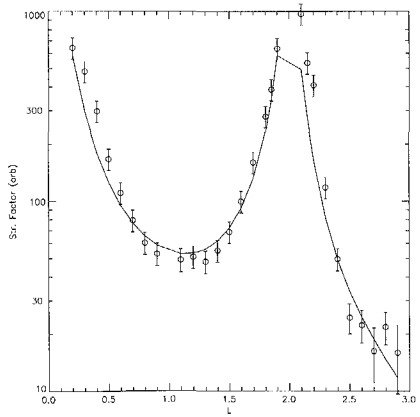


Figure 2. The (20L) rod (circles) and the best fit to date (line).

Oxide Growth on Cu(111) in Acidic Solution — X16C

Y. S. Chu and I. K. Robinson (U. of Illinois)

The formation of aqueous oxide on a Cu(111) single crystal surface in perchloric acid at pH 4 was studied in-situ using X-ray diffraction. Formation and removal of copper oxide was controlled by imposing external electrostatic potential at the interface. Fig. 1 (Top) shows a typical cyclic voltammetry of Cu(111), in which the positive peak around -0.3 V corresponds to formation of oxide, and the negative peak around -0.55 V corresponds to removal of oxide. Two distinct epitaxial oxides were observed. Both were identified as cubic cuprite (Cu2O) with the (111) axis perpendicular to the surface but different in-plane orientations: 180 deg rotation between them at the interface (see Fig.2). In a native oxide on Cu(111), both aligned and reversed oxides grow with about an equal ratio. However, in the solution at pH 4, an entirely different growth mechanism was observed. Fig. 1 (Bottom) shows the growth of both oxides as the potential was cycled. As the ptetnial was swept from A to B, both oxides grew at a comparable ratio, but, beyond B, only the reverse oxide continued to grow while the aligned oxide remained constant and eventually diminished. The amount of diffracted intensity and the L-diffraction profile indicate that the alined oxide never grows more than a few monolayers thick. This preferential oxide growth mechanism suggests that the aligned cuprite may be acting as a barrier to inhibit further oxidation.

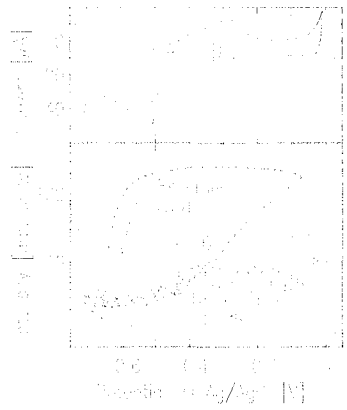


Figure 1. Growth of epitaxial copper oxide. Top: cyclic voltammetry of Cu(111) in perchlorate solution at pH 4 and 10 mV/sec. Positive and negative peaks correspond to formation and removal of Cu2O, respectively. Bottom: Bragg peak during cycling of the potential.

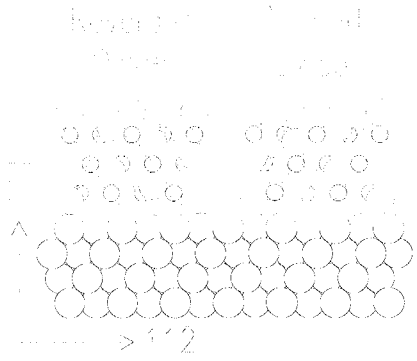


Figure 2. Side view of aligned and reversed oxides. In the oxide, the copper atoms are shaded.

Chemical Ordering in Lead Magnesium Niobate | X16C

D. M. Fanning and I. K. Robinson (U. of Illinois, UC)

Superstructure reflections of a single crystal (2mm per side) of lead magnesium niobate ($Pb[Mg_{1/3}Nb_{2/3}]O_3$) were studied at beamline X16C. PMN is a ferroelectric relaxor with a Curie temperature of -7 C. It has a broad, frequency dependent transition to the ferroelectric state. PMN's structure is perovskite with the mixed B-site containing a Mg^{2+} or Nb^{5+}*ion.*

Integrated intensities were measured for about 80 reflections by scanning in the ¡100¿directions. The width of each superstructure reflection was roughly constant and indicative of an ordered domain size of 20 A from the Scherrer equation:

$L=2\pi \cdot 0.94/\Delta q_{FWHM}$

The crystal was carefully mounted so that the beam entered and exited through the same face. In this way, the absorption correction was simply $1/(\sin\theta \sin\chi)$. However, this correction is important as it critically affects the form of the data.

The corrected structure factors as a function of momentum transfer are plotted in Figure 1. The shape of the data suggests that chemical ordering is the cause of PMN's superstructure reflections. In a chemically ordered sample, the structure factors are simply proportional to the difference in the ordered chemicals' form factors. Without the absorption correction, the data increase at first with q and then decrease. This would suggest a displacement ordering model.

The fit to the data in Figure 1 represents our proposed model. We assumed one-to-one Mg:Nb chemical ordering within PMN's ordered regions and allowed the oxygen ions to displace towards or away from the B-sites (Figure 2). The best fit was found with an oxygen displacement of 0.1 A towards the smaller Nb^{5+} ion and away from the Mg^{2+} ions. The Pb ions are believed to be randomly displaced about their ideal position, and we were unable to improve our fit by displacing those ions.

PMN is unique in that its ratio of different B-site ions (Mg:Nb) is 1:2, yet it chemically orders in a 1:1 ratio. Of course, the charge imbalance greatly restricts the size of these ordered domains. In future experiments, we plan to look at La-doped PMN crystals in which the La^{3+} ions provide an extra positive charge compared to the Pb^{2+} ions. This reduces the charge imbalance in the ordered domains, allowing them to grow larger.

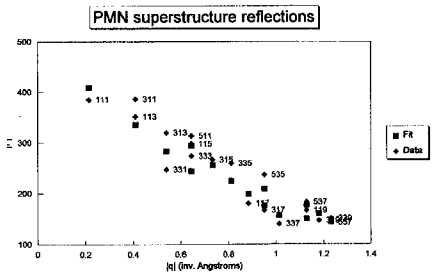


Figure 1. Structure factors of the type (h+1/2,k+1/2,l+1/2) v. momentum transfer.

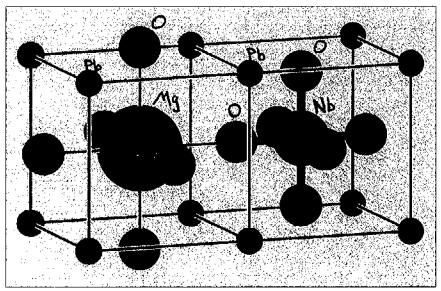


Figure 2. Ordered Mg and Nb ions in adjacent unit cells.

Strain of GaN Thin Films on Sapphire (0001) | X16C

C. Kim, I. K. Robinson, J. Myoung, K.-H. Shim, and K. Kim (U. of Illinois, Urbana-Champaign)

Recent interest in a short wavelength optical devices attracted much attention to III-nitrides as wide band gap materials. With this increasing interest, much work has been done previously on optical and electronic properties of III-nitrides. However, the strain of thin III-nitride has not been extensively studied. Since the electronic and optical properties couple with the strain in thin films, a clear understanding of it is very important.

We grew a series of GaN thin films on AlN buffer layer with sapphire (0001) substrate and measured both in-plane and out-of-plane lattice constants using x-ray diffraction as a function of film thickness. With Van der Merwe's equilibrium theory, we could explain our in-plane lattice constant results (Fig.1). The fit was derived from the assumption that the total energy of the system is at minimum. It was in excellent agreement with the experimental results even though we assumed that the effective range of the dislocation field is constant. More detailed consideration of energy terms for dislocation field did not affect the fit very much.

The out-of-plane lattice constant is then fitted from the in-plane value using a Poisson ratio $\nu = 0.38$ (Fig.2). The best fit was obtained with ν=0.44 which could be considered to be Poisson ratio for a thin GaN film. The critical thickness of this GaN film was obtained using the fit, and gave a value of 29 $\pm$ 4 Å. This compares favorably with the theoretical value obatined by Fischer of 31.5 Å.

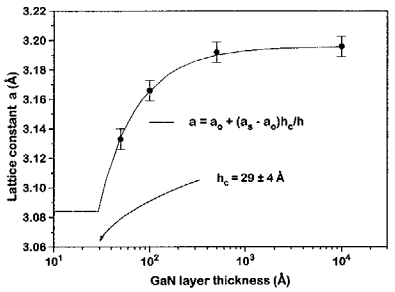


Figure 1. A fit of in-plane lattice constant of GaN.

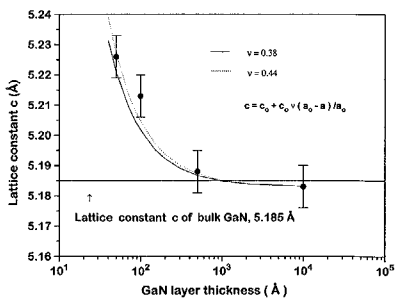


Figure 2. A fit of out-of-plane lattice constant of GaN.

Measurement of the Fission Branch for the 103 keV State in ^{235}U	X17B1

N. N. Ajitanand (SUNY, Stony Brook), D. P. Siddons, and J. B. Hastings (NSLS)

From experimental studies of proton and alpha induced fission of ^{235}U at deep sub-barrier energies an argument has been made for the existence of a fission branch of about 10^{-4} in a low lying level around 103 keV. However, from all known theoretical considerations the fission probability of such a state is vanishingly small because of the formidable fission barrier. To investigate the experimental situation further it was decided to do a complementary experiment where the fission branch is measured for the level populated by resonance absorption of photons of appropriate energy.

A single bunch white beam (3mm x 8mm) was incident on a silicon monochromator. The diffracted beam (peak 103 keV, fwhm 1.2 keV) was incident on a 200 mg/cm^2 metallic ^{235}U target (A). The fission detector (lexan plastic) covered the target on its upstream side. Another ^{235}U foil (B) covered by plastic was kept just outside the incident beam to record background fissions due to neutrons and high energy photons (fig. 1). The incident photon spectrum was monitored by an InGe detector (fig. 2). Two irradiation runs, each lasting about 40 hours, were taken. In one run a neutron source was kept in the proximity of the uranium foils. The plastics were etched in 6.25N NaOH for 20 minutes at 70°C to reveal fission tracks. In the case of the run with the neutron source, similar numbers of well defined fission tracks were seen in both the plastics indicating that the transiting beam did not alter the properties of the plastic. In the run without any neutron source, no fission tracks were seen in either plastic. The total number of photons incident on the target in this run as measured by an Argon filled gas ion chamber was 5 x 10^{14}. The width of the 103.02 keV state was calculated to be 1.2 x 10^{-3} eV from its known life time (3.5 psec). This meant that the population of the state through resonant absorption was 5 x 10^8. This translated to an upper limit of 2 x 10^{-9} for the fission branch ruling out the state as a possible contributor to the observed sub-barrier fission enhancement in the particle experiments.

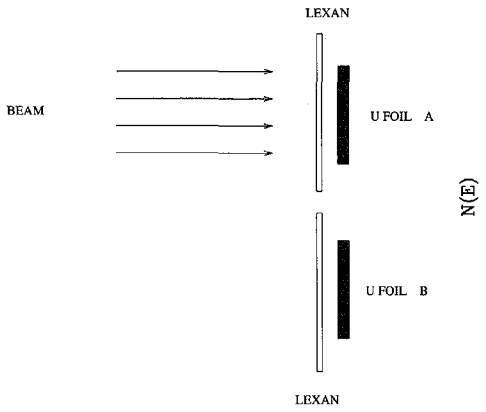


Figure 1. Arrangement of targets.

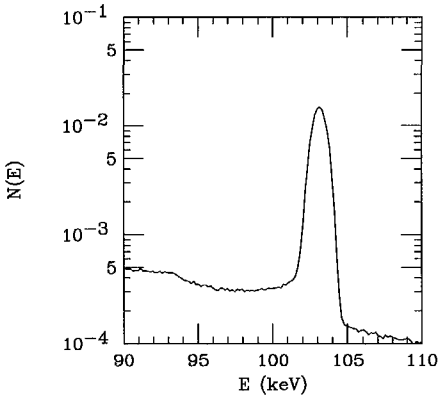


Figure 2. Incident spectrum.

In-situ Measurement of the Rheology of Silicate Garnets at High Pressure	X17B1

J.Ando, J.Chen, D.J.Weidner Y.Wu (CHiPR, SUNY, Stony Brook), and Y.Wang (CARS, APS)

We have examined the rheological properties of silicate garnets using the DIA type cubic anvil apparatus (SAM-85) at the X17B1 beam line. The mechanical data of deformation are collected from the shape change of diffraction peaks. This method was devised by Weidner *et al.*[1,2] at this beam line. We then observe the microstructures of recovered samples by TEM to understand the mechanisms of deformation processes. Using this experimental method, it is possible to observe the rheological behavior of mantle minerals under mantle conditions. Here we report the results for four garnets. They are Py_{100}, $Py_{50}Mj_{50}$, $Py_{23}Al_{48}Gr_{28}Sp_1$ and $Py_{68}Al_{18}Gr_{14}Sp_1$. The first two samples are synthetic garnets, and last two samples are garnets from natural rocks. Experimental conditions are 9 GPa confining pressure and temperatures up to 860°C. Significant compositional effects of strength at all temperature range were observed for these samples. $Py_{50}Mj_{50}$ and $Py_{68}Al_{18}Gr_{14}Sp_1$ were considerably stronger at higher temperature than the other samples. Natural samples suggest that yield strength of garnet increases with increasing pyrope content. But synthetic pure pyrope is weaker than $Py_{23}Al_{48}Gr_{28}Sp_1$. This weakness may be caused by new phase occurred between pyrope grains during experiment or minor glass phase in starting synthesized pyrope. TEM observation supports the first effect. Our result shows that the rheological behavior of silicate garnet depend greatly on it's composition.

References:

[1] D.J.Weidner, Y.Wang, NSLS Activity Report, p310 (1992);
[2] D.J.Weidner, Y.Wang, M.T. Vaughan, Science, 266, p419-422, (1994)

In-situ Equation of State Measurements of Antigorite	X17B1

K. Bose, A. Navrotsky (CHiPR, Princeton U.), P. J. Schields, J. Chen and D. J. Weidner (CHiPR, SUNY,Stony Brook)

The extent to which dense hydrous magnesium silicates can transport water to the mantle via mature, relatively cold subducting slabs depends on the thermodynamic properties of "lower" pressure and temperature minerals such as talc and antigorite. In addition to thermoelastic data on talc, phase equilibria experiments of key reactions and calorimetric studies of phases in the MgO-H_2O-SiO_2 system that we have reported previously, we present here the results of *in-situ* equation of state measurements of natural antigorite, $(Mg_{.96}Fe_{.04})_{48}Si_{34}O_{85}(OH)_{62}$).

The molar volume of antigorite, as a function of pressure (to 6 GPa) and temperature (to 823 K) was measured *in-situ* in a DIA-type multi-anvil high-pressure apparatus (SAM-85) at the National Synchrotron Light Source. NaCl was used as pressure calibrant and also to reduce the deviatoric stress, which ranged from $\sim$ 1 % (for samples that were pressurized prior to heating) to less than 0.2 % of total pressure for samples that were cycled to high temperature after pressurization. Macroscopic deviatoric stress in the NaCl was determined from the relative strains of the diffraction peaks. The relative changes in V/V_0 as functions of pressure and temperature were determined by indexing the diffraction lines to a single layer monoclinic cell.

The 298K unit cell volume data (V_0= 365.5 Å^3) can be fitted to a second-order Birch-Murnaghan equation of state ($K'_{298} = 4$) with $K = 58.7(3)$ GPa or to a third-order Birch-Murnaghan equation with $K = 60.4$ (2.9) GPa, and $K'_{298} = 3.2$ (0.1). We are currently indexing the hight temperature data (at P) to obtain thermal expansivity as the next step in the construction of a comprehensive, self-consistent data set.

Elasticity of Single Crystal MgO from Simultaneous X-ray and Ultrasonic Measurements to 9 GPa and 1500 K in a Multi-Anvil Apparatus	X17B1

G. Chen, Y. Sinelnikov, J. Cooke, D. J. Weidner and R. C. Liebermann (CHiPR SUNY, Stony Brook)

The equation-of-state of MgO is of importance in understanding the seismic profiles of the lower mantle and in applications to in situ pressure standards in high temperature-pressure experiments. In our laboratory, we have developed techniques to enable precise ultrasonic interferometeric measurements of wave velocities in minerals to be performed to pressures of 9 GPa and temperatures of 1500 K using a DIA-type, cubic-anvil apparatus (SAM 85) installed on the superconducting wiggler beamline (X17B) at the National Synchrotron Light Source of the Brookhaven National Laboratory. X-ray spectra of both the polycrystalline specimen and the NaCl medium which surrounds it are monitored continuously; the former provides PVT data to compliment the velocity measurements and the latter the pressure standard. We have obtained new data on single-crystal MgO to simultaneous pressures of 7 GPa and temperatures of 1500 K, and compare these new data to the acoustic measurements of Spetzler (1970) to 0.8 GPa and 800 K using a specially-designed pressure-temperature path (see figure).

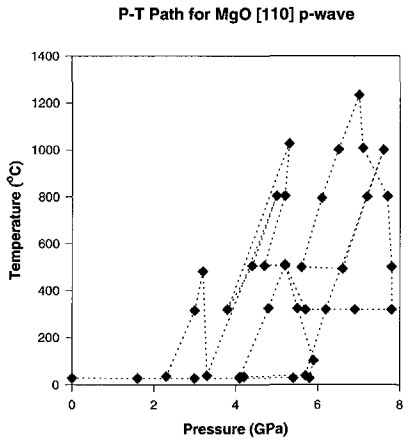


Figure 1. P-T Path of Ultrasonic Experiment

Rheology of Dry and Hydrous Phases of the α and β Forms of $(Mg,Fe)_2SiO_4$	X17B1

J. Chen, T. Inoue, Y. Wu, D. J. Weidner and M. T. Vaughan (CHiPR, SUNY, Stony Brook)

Rheological properties of the different phases of olivine, both dry and hydrous, are important properties that constrain mantle convection and have implications regarding the origin of deep focus earthquakes. It is widely recognized that water considerably weakens olivine at confining pressures less than one GPa. However, in the β-phase, hydrogen is structurally bound, with uncertain implications on its ability to mechanically weaken this material.

We carried out rheology measurements on these phases by monitoring the diffraction peak broadening as a function of pressure, temperature and time. The cubic-type multi-anvil press SAM85 at the X17B1 beamline was employed in the experiments. The technique to derive strains of crystal grains produced by deviatoric stress in the high pressure cell has been described elsewhere.

The dry α-phase sample is San Carlos olivine, and the β-phase and hydrous β-phases were synthesized using the USSA2000 press at Stony Brook. Recovered samples were ground and repressurized at room temperature up to 9 GPa in SAM85, then temperature was increased to 600°C. FWHM analysis of the energy dispersive diffraction patterns showed that β-phase is generally stronger than the olivine (α) phase, and the hydrous olivine is much weaker than dry olivine by 400°C. Strength of the hydrous β-phase is similar to dry beta at this temperature and becomes slightly lower than dry beta by 600°C. Thus, structurally bound water in the β-phase may not significantly weaken this material.

Pressure Induced Amorphization in Zirconium Tungstate ZrW_2O_8	X17B1

J. Chen, J. B. Parise, R. Li (CHiPR, SUNY, Stony Brook) and A. W. Sleight (OSU)

ZrW_2O_8 has been reported to show a highly unusual property of isotropic negative thermal expansion over its entire stability temperature range of 0.3 to 1050 K at room pressure[1]. Evans *et al.*[2] recently observed a phase transformation from cubic to orthorhombic structure at 2 kbar and room temperature. The high pressure phase also shows a negative thermal expansion from 0 to 300 K. This suggests that this material may have very unusual behavior under high pressure.

We have carried out *in situ* x-ray diffraction measurements at very high pressure up to 200 kbar at X17B1. A newly developed T-cup multi-anvil high pressure cell[3] was used for the pressure generation. The x-ray diffraction shows that under compression, ZrW_2O_8 undergoes amorphization at 10 kbar, and the amorphous phase remains stable until 200 kbar at room temperature (Figure 1). Upon heating, the amorphous phase decomposes at 1000 K and 18 kbar. The behavior of ZrW_2O_8 under pressure is interesting. The mechanism of the amorphization is under investigation.

References:
[1]T. A. Mary, J. S. O. Evans, T. Vogt, and A. W. Sleight, Science 272, 90 (1996).
[2]J. S. O. Evans, J. D. Jorgensen, D. N. Argriou, Z. Hu, S. Short, R. Osborn, and A. W. Sleight (in preparation).

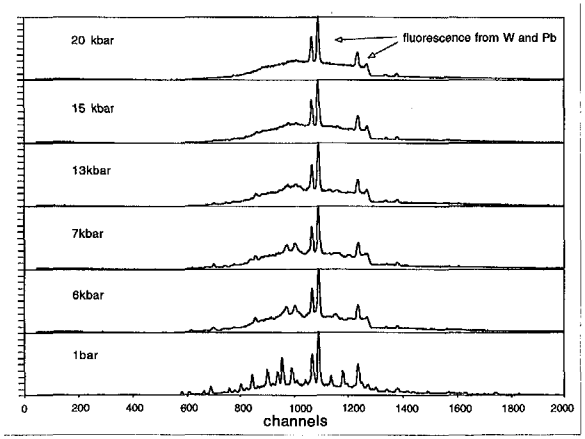


Figure 1. Diffraction patterns of ZrW_2O_8 at different pressures

Structural Studies of Ag_2SO_4 and TlX (X = Cl, Br, I) by *In-Situ* ED-XRD to 6GPa and 550°C

X17B1

Q. Chen and R. A. Secco, (U. West. Ont.), E.A. Secco, (St. Francis Xavier U.), J. Chen, M.T. Vaughan, G. Chen, J.Z. Zhang, and D.J. Weidner (CHiPR, SUNY, Stony Brook)

High pressure (P) electrical conductivity measurements on TlX (X = Cl, Br, I) and Ag_2SO_4 show distinct conductivity jumps with increasing temperature (T). For Ag_2SO_4, this is associated with a transformation from low T orthorhombic (β-phase) to high T hexagonal (α-phase) structure. The α-β phase boundary reaches a maximum at 1.6 GPa (observed only by differential thermal analysis (Pistorius, 1965, J. Chem. Phys. 46, 2167)) and is accompanied by anomalous decreasing activation energy of conduction with P in this region. *In-situ* XRD experiments were therefore carried out to check for possible structural cause(s) of this anomalous behaviour. In the TlX system, structural studies were also carried out to investigate the nature of the conductivity increases. Energy dispersive XRD experiments were carried out at X17B1 using SAM85 with NaCl as the internal pressure calibrant.

Ag_2SO_4: The ortho-hex structural transformation is confirmed in the XRD patterns at low P but there are marked differences at T > 450°C between P < 1.6 GPa and P > 1.6 GPa as shown in the figure below suggesting a possible new phase in the high P, T region. The similarity of patterns at 22°C and 1 atm. before and after high P,T exposure indicate lack of reaction between sample and boron nitride container.

TlX (X = Cl, Br, I): Both TlCl and TlBr do not show any evidence of P- or T-induced modification of their 22°C and 1 atm cubic (CsCl) structure at P up to 6GPa and T up to 550°C. In comparison, changes observed in TlI patterns are more complex as shown in the figure below.

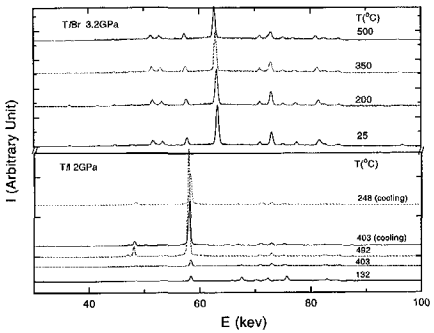


Figure 1.

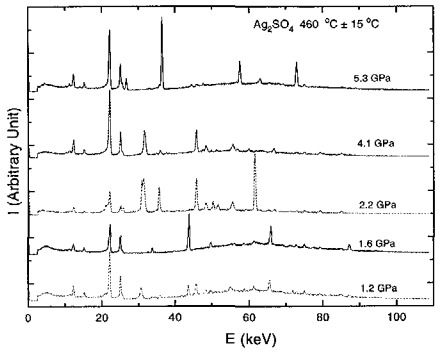


Figure 2.

Microbeam Irradiation of Duck Embryo Brains: Relevance to Microbeam Radiation Therapy [MRT] of Brain Tumors in Infants

X17B1

F.A. Dilmanian, X.Y. Wu, X. Huang, M. Kershaw, B. Ren, D.N. Slatkin, K. Trandem (Medical, BNL), R. Menk, W.C. Thomlinson, and Z. Zhong (NSLS)

X-ray microbeam radiations have been studied at the NSLS [1] for their significant tissue-sparing effect when used unidirectionally. This effect allows microbeam radiation therapy [MRT] by crossfiring at the target volume (and thus diminishing the tissue sparing effect inside that volume). Because of the relatively small damage that MRT of a brain tumor would cause to normal tissues outside the target volume, and because of the extraordinary radiosensitivity of the maturing brain, our goal is to treat intractable brain tumors in infants. We studied the radiosensitivity of the duck embryo brain, a surrogate for the human infant brain, to parallel microbeams delivered 3-4 days before hatching (i.e., 24-25 days into incubation).

The beam bundle comprised 52 or 104 parallel microplanar beams, each 25 μm wide and 11 mm high, 200 or 100 μm apart on center, respectively. The beam's critical energy was $\approx$ 69 keV and the skin-entrance absorbed doses in the microbeams were 78, 156, or 312 Gy. Neither the polar nor the azimuthal angle of beam incidence on the head axis was known. An interim tabulation of survival quality is as follows. The ducks' age at the time of evaluation was $\approx$ 4 months for Exp. I and $\approx$ 3 months for Exp. II.

Exp. #	Beam spac. on center (μm)	Entrance absorbed dose (Gy)	# of eggs	Number hatched	COMPLICATIONS		
					neuro-logic	non-neuro.	none
I	200	78	8	7	1	2	4
	200	156	8	8	0	0	8
	unirradiated		16	16	0	1	15
II	200	156	5	4	1	0	3
	100	78	5	5	1	0	4
	100	156	5	4	1	0	3
	100	312	5	3	1	0	2
	unirradiated		8	4	0	0	4

Duck embryos move spontaneously in their shell. This could have blurred the dose distribution and thereby elicited neurologic complications. Most of the irradiated ducks exhibited an $\approx$ 10% lag in weight gain as compared with the unirradiated ducks; this lag disappeared by $\approx$ 3 months. The survival results may be relevant clinically, as entrance doses in the 70-300 Gy range are likely to be used for MRT of infants' brain tumors. Gross examination and appropriate histological studies of the formalin-fixed brains have yet to be performed.

[1]. D.N. Slatkin, P. Spanne, F.A. Dilmanian, J.-O. Gebbers, and J.A. Laissue, Proc. Natl. Acad. Sci. USA 92, 8783-8787, 1995.

We would thank K. A. Bonti, A.B. Chituk, D.H. Corwin, W. F. Dean, J.F. Gatz, A. N. Gifford, N. F. Gmür, J.C. Heinrichs, D.D. Joel, O. Rahmanan, P. Ramcharan, K.E. Rising, C.L. Rissland, T. S. Sandhu, R.B. Setlow, P. Som, K.A. Vodopia, and A.D. Woodhead for assistance. This research was supported by the Office of Health and Environmental Research, and U.S. DOE.

Elasticity of Polycrystalline $MgSiO_3$-Majorite from Simultaneous X-ray and Ultrasonic Measurements to 9 GPa and 1000 K in a Multi-Anvil Apparatus	X17B1

G. D. Gwanmesia (DSU), G. Chen, Y. Sinelnikov, J. Cooke, L. Flesch, M. T. Vaughan and R. C. Liebermann (CHiPR, SUNY, Stony Brook)

Polycrystalline specimens of $MgSiO_3$-majorite have been hot-pressed in a 2000-ton uniaxial split-sphere apparatus (USSA-2000) using a 10 mm MgO octahedral cell assembly and the techniques developed previously by Gwanmesia and Liebermann (1992; see also Gwanmesia *et al.*, 1993). These specimens have bulk densities identical to the X-ray density and exhibit compressional and shear wave velocities within 0.2% of the Hashin-Shtrikman bounds calculated from the single-crystal elastic moduli of Pacalo and Weidner (1996). In our laboratory, we have developed techniques to enable precise ultrasonic interferometeric measurements of wave velocities in minerals to be performed to pressures of 9 GPa and temperatures of 1500 K using a DIA-type, cubic-anvil apparatus (SAM 85) installed on the superconducting wiggler beamline (X17B) at the National Synchrotron Light Source of the Brookhaven National Laboratory. X-ray spectra of both the polycrystalline specimen and the NaCl medium which surrounds it are monitored continuously; the former provides PVT data to compliment the velocity measurements and the latter the pressure standard. We have obtained new data on P and S velocities in the polycrystalline $MgSiO_3$-majorite to 7 GPa at 1000 K. An example of the high quality of the acoustic interference patterns is given in the figure below.

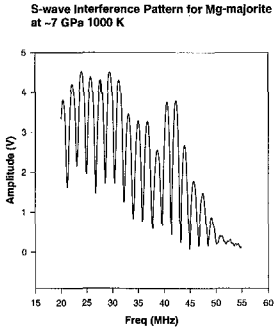


Figure 1.

Rheological Study of Hydrous γ-Phase Using *in situ* X-ray Diffraction	X17B1

T. Inoue, J. H. Chen, Y. Wu, D. J. Weidner and M. T. Vaughan (CHiPR, SUNY, Stony Brook)

Water influences rheological properties of minerals. Especially, γ-Mg_2SiO_4, which is a high pressure polymorph of olivine, can accommodate a few wt% H_2O in the crystal structure. It is important to examine the rheological property of hydrous γ-phase because γ-phase is the most abundant mineral in the mantle transition zone.

Hydrous γ-phase was synthesized at a pressure of 19 GPa and a temperature of 1300°C using the MA-8 type apparatus (USSA-2000) at SUNY, Stony Brook. The composition of the recovered sample was measured by EPMA and the H_2O content was measured by SIMS. The present hydrous γ-phase includes about 2 wt% H_2O.

Using a T-Cup[1], which is a new high-pressure apparatus for *in-situ* X-ray studies, embedded in SAM-85 at the X17B1 beam line, we studied the temperature-time dependence of microscopic deviatoric stress using the method developed by Weidner[2]. Pressure was increased to approximately 19 GPa at room temperature, and then heated to 400°C, 600°C, 800°C and finally 1000°C. At each temperature, the data was collected every 60 s for 40 to 80 min. We analyzed the microscopic strains from peak broadening for the (311) diffraction line.

At 400°C, the microscopic strain was approximately 0.017, and slightly decreased with time. At 600°C and 800°C, those are approximately 0.01 and 0.005, respectively, and the strain was completely relaxed at 1000°C. The above results shows that the microscopic strain remains at even 800°C. Comparing with our previous studies of olivine, hydrous γ-phase is much stronger than olivine. We will continue to do this type of experiments of various minerals to clarify the rheology of the mantle transition zone.

References:

[1] D.J. Weidner, Y.B. Wang, M.T. Vaughan, C.C. Koleda and I.C. Getting: T-Cup: A New High-Pressure Apparatus for X-ray Studies, NSLS Activity Report, 140 (1995).

[2] D.J. Weidner, Y.B. Wang and M.T. Vaughan: Strength of Diamond, Science, 266, 419-422 (1994)

Elasticity of Polycrystalline Beta-Mg_2SiO_4 From Simultaneous X-ray and Ultrasonic Measurements to 7 GPa and 900 K in a Multi-Anvil Apparatus	X17B1

B. Li, J. Liu, L. Flesch (CHiPR, SUNY, Stony Brook), G. D. Gwanmesia (DSU), J. Chen and R. C. Liebermann (CHiPR, SUNY, Stony Brook)

Polycrystalline specimens of the beta phase of Mg_2SiO_4 have been hot-pressed in a multi-anvil high pressure apparatus using the techniques described previously by Gwanmesia and Liebermann (1992). These specimens have bulk densities which are 99.8% of the theoretical density and, compressional and shear wave velocities which are within 0.5% of the of Hashin-Shtrikman bounds calculated from the single-crystal elastic moduli of Sawamoto *et al.* (1984). In our laboratory, we have developed techniques to enable precise ultrasonic interferometeric measurements of wave velocities in minerals to be performed to pressures of 9 GPa and temperatures of 1500 K using a DIA-type, cubic-anvil apparatus (SAM 85) installed on the superconducting wiggler beamline (X17B) at the National Synchrotron Light Source of the Brookhaven National Laboratory. X- ray spectra of both the polycrystalline specimen and the NaCl medium which surrounds it are monitored continuously; the former provides PVT data to compliment the velocity measurements and the latter the pressure standard. We have obtained new data on P and S velocities for a polycrystalline beta phase specimen to 7 GPa and 900 K. In the figure below, we plot the travel time of shear waves *vs.* pressure at room temperature for the beta phase.

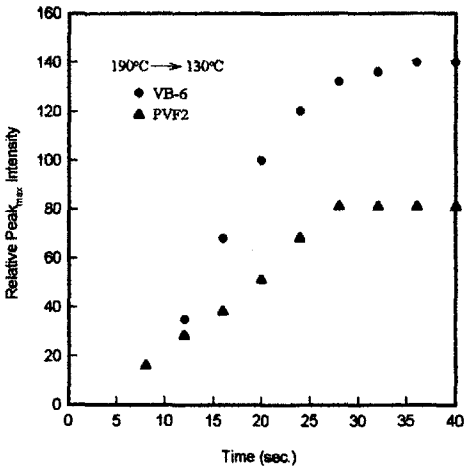


Figure 1. S-wave Travel Time vs. Pressure at Ambient T for beta phase.

Simultaneous X-Ray and Acoustic Measurements of Equations of State of Solids at High Pressures and Temperatures in Multi-Anvil Apparatus	X17B1

R. C. Liebermann, G. Chen, B. Li, G. D. Gwanmesia, J. Cooke, L. Flesch, J. Liu, Y. Sinelnikov, M. T. Vaughan, J. Chen, J. Zhang, Y. Wang and D. J. Weidner (SUNY, Stony Brook)

We have developed "specimen friendly" cell assemblies for multi- anvil, high-pressure apparatus which enable precise ultrasonic interferometeric measurements of wave velocities in minerals to be performed to P > 12 GPa and T > 1300 K. These experiments initially utilized a 1000-ton Kennedy-Getting type press and a split cylinder module of Walker's design (USCA-1000) combined with an ANUTECH ultrasonic interferometer to study both polycrystalline and single crystal specimens (Li *et al.*, GRL, 23,2259, 1996; Chen *et al.*, Science, 272, 979, 1996). We have recently adapted these techniques for use in a DIA-type, cubic-anvil apparatus (SAM 85) installed on the superconducting wiggler beamline (X17B) at the National Synchrotron Light Source of the Brookhaven National Laboratory (see figure below). In this case, pressure is monitored continuously by observing with X-rays the change of volume of the NaCl standard which surrounds the sample. P wave measurements to 9.7 GPa on Lucalox alumina showed behavior very consistent with the data from the experiments in the USCA-1000 apparatus, in which pressure was estimated from observing the phase transitions in Bi and ZnTe. Subsequent experiments achieved simultaneous conditions of 7 GPa and approximately 1500 K and included direct determinations of the cell volume of the sample. Studies on polycrystalline specimens of $MgSiO_3$-majorite and the beta phase of Mg_2SiO_4 and single crystals of MgO are reported elsewhere in this report by G. Gwanmesia, B. Li and G. Chen.

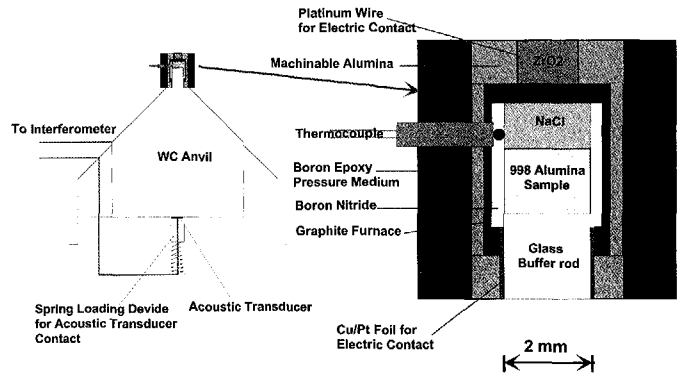


Figure 1. Diagram of Anvil Insert and Cell Assembly for Ultrasonic Experiments in SAM 85

Thermal Equation of State of Stishovite	X17B1

J. Liu, J. Zhang, D. J. Weidner, L. Flesch, G. Chen, B. Li and R. C. Liebermann (SUNY, Stony Brook)

The pressure-volume-temperature (P-V-T) behavior in SiO_2-stishovite has been studied using a DIA-type, cubic-anvil apparatus (SAM 85) and *in situ* synchrotron X-ray diffraction.

A polycrystalline specimen previously hot-pressed in a uniaxial split-sphere apparatus was used. The P-V-T data to $P > 10$GPa and $T > 1000°$C were analysized using several approaches, including a temperature-dependent Birch-Murnaghan equation-of-state, isothermal compression and isobaric thermal expansion. The bulk modulus (K_0) and axial compressibilities of stishovite are compared with values obtained from Brillouin scattering and diamond-anvil cell X-ray studies on single crystal stishovite and ultrasonic studies on polycrystalline specimens.

The results obtained from different approaches show the whole data set is internally consistant. The temperature derivative of bulk modulus at zero pressure $(\frac{\partial K_0}{\partial T})_{P_0}$ is measured for the first time to be -0.0355(106) GPa/K.

Bronchial Imaging Using Xenon K-Edge Dichromography	X17B2

R. H. O'Neil, J. Giacomini, E. Rubenstein, A. Van Kessel, H. Gordon (Stanford), W. Thomlinson, N. Gmur, Z. Zhong (NSLS) and D. Chapman (IIT)

Using medical imaging techniques pioneered at NSLS on X17B2 for coronary angiography, we have developed the use of xenon gas as a contrast agent for studies of the bronchial airways. Xenon gas has a K-edge absorption at 34.561 keV, slightly higher than the iodinated contrast agent used in previous coronary angiography studies. This similarity led to the use of xenon to perform the same task in the bronchial airways as iodine performed in the coronary arteries; the highlighting of the airways against other tissues. In this technique a mixture of 80% xenon and 20% oxygen is slowly inhaled by the subject to fill the anatomical dead space but not the alveolar space of the lungs. Unlike earlier contrast agents used in bronchography, xenon is a non-toxic inert gas requiring only a single 500 ml inhalation to acquire an image. After inhalation the subject is scanned through two coplanar beams of X-rays bracketing the K-edge of xenon. Two 600 element line detectors capture the data which is processed to produce a difference image that yields clear images of only the xenon filled structures. The images in figures 1 and 2 clearly show the trachea, mainstem bronchus and the bronchi down to the tertiary branch. Early detection of pulmonary disease processes may be possible using this technique. Work funded under DOE contracts DE-AC02-76CH00016 and DE-FG03-87ER60527.

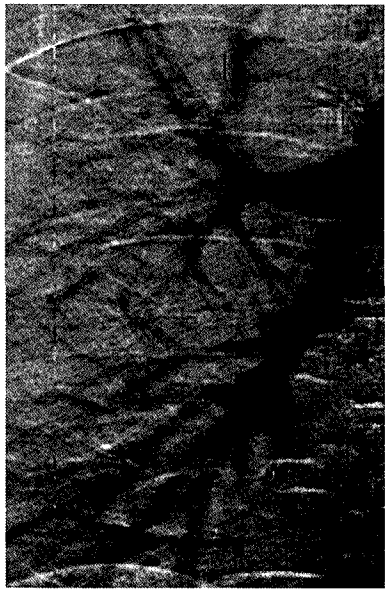


Figure 1. Right Bronchi.



Figure 2. Left Bronchi.

Elasticity of Ca(Ti,Si)O_3 Perovskite.	X17B1

Y. D. Sinelnikov, J. Zhang, and R. C. Liebermann (CHiPR, SUNY, Stony Brook)

Elastic properties in the $CaTiO_3$ - $CaSiO_3$ system have been in the focus of this work. Polycrystalline specimens of end-member $CaTiO_3$ perovskite and intermediate $Ca(Ti_{.75}Si_{.25})O_3$, $Ca(Ti_{.5}Si_{.5})O_3$ perovskites were hot-pressed in a 2000-ton uniaxial split-sphere apparatus (USSA-2000). Intermediate compounds were synthesized at pressures of 15GPa and temperatures above 1500°C. Compressional and Shear wave velocities were measured using ultrasonic interferometry technique at room pressure and temperature. Densities of the synthesized specimens has been found by Archimedes immersion to be within 1% of the X ray density. Estimated from the acoustic measurements value of bulk moduli for intermediate $Ca(Ti_{.5}Si_{.5})O_3$ perovskite and end-member $CaTiO_3$ perovskite are 188(1) GPa and 175(1) GPa, and the shear moduli are G=109(1) GPa and 106(1) GPa, respectively. *In-situ* P-T synchrotron X ray diffraction study yielded isothermal bulk moduli of $Ca(Ti_{.5}Si_{.5})O_3$ and $CaTiO_3$, 182(5) GPa and 171(5) GPa, respectively. For unquenchable $CaSiO_3$ perovskite elasticity systematics leads the bulk modulus, K = 212(7) GPa and shear modulus, G = 112(5) GPa. Thus, predicted shear modulus of $CaSiO_3$ perovskite is 60% lower than that of $MgSiO_3$ perovskite. This implies the substantial importance of $CaSiO_3$ perovskite elastic properties in constraining the composition of the lower mantle.

Rheology of Cubic Boron Nitride at High Temperatures and Pressures	X17B1

J. S. Sweeney, J. Chen, D. J. Weidner, M. T. Vaughan (CHiPR, SUNY, Stony Brook)

The rheological properties of powdered and sintered polycrystalline cubic boron nitride (cBN) were investigated at 9.3 GPa and up to 1820 K. The cBN was strained by hydrostatic pressure in a DIA-type multi-anvil apparatus and by local deviatoric stresses induced by grain-to-grain contacts within the samples. Strain rates were investigated by heating the cBN and then collecting time-resolved energy dispersive x-ray diffraction spectra at intervals between 30 and 120 s. Strain due to deviatoric stress broadens the x-ray diffraction peaks. Strain-broadening is deconvolved by Fourier analysis from instrumental effects that are estimated from spectra at room temperature and pressure. For this analysis, diffraction peaks are fit to a split Pearson VII function since a split function accommodates asymmetry in the peaks and the Pearson VII function approximates the data better than Cauchy and Gaussian functions. Due to the quantity of data, automated proceedures are implemented for peak identification, background subtraction, peak fitting, and deconvolution.

Phase Relations and Equations of State for High-Pressure Phases of Ferrosilite and Enstatite	X17B1

M. T. Vaughan, D. H. Lindsley, and Y. Silnelnikov (CHiPR, SUNY, Stony Brook)

In two separate experiments, we have begun studying the high pressure phase of $FeSiO_3$ known as ferrosilite III, and the ilmenite phase of $(Mg_{.9}Fe_{.1})SiO_3$.

As can be seen in the figure below, the Ilmenite phase of $(Mg_{.9}Fe_{.1})SiO_3$ occurs at high pressure, just below that of the perovskite phase. We lost the thermocouple during the experiment, so we were unable to get a good EOS. The EOS measurements were done outside the ilmenite stability field (using power to estimate temperature), and we were concerned that the ilmenite sample would convert to a lower pressure phase when heated. This, in fact, did not occur, so in future experiments we should be able to go to higher temperature.

Ferrosilite III is known only as a phase quenched from high temperature (~1200C) and modestly high pressure (2-3 GPa). The quench phase is a 9-repeat pyroxenoid polymorph of ferrosilite, with the formula $FeSiO_3$. The purpose of the experiment is to determine if the quench phase is also the stable phase under the conditions at which it was formed. Due to experimental difficulties, the answer is still not known.

In the first run, we started with the quench phase and increased pressure at room temperature to about 3 GPa, then heated. We had to heat fast, because we didn't want the sample to transform to orthoferrosilite, which is the stable phase at this pressure and lower temperatures. Unfortunately, we overshot the Fs-III field, and melted the sample. In a second attempt, the thermocouple failed and temperature had to be estimated based on heater power. The sample at the final data point had transformed to orthoferrosilite, so we must have been slightly low in temperature.

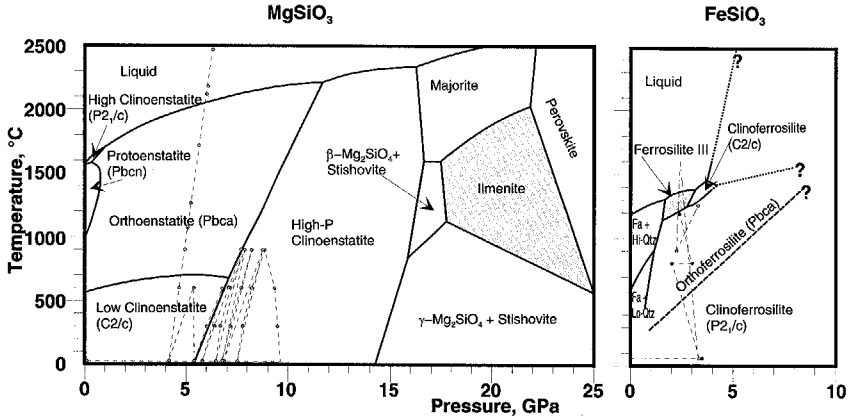


Figure 1. Phase relations in $MgSiO_3$ and $FeSiO_3$.

T-CUP: A New High-Pressure Apparatus for X-Ray Studies - Continued	X17B1

M. T. Vaughan, D. J. Weidner, and J. Chen (SUNY, Stony Brook)

Last year we reported on the development of the TCUP apparatus[1], a two-stage device using eight-cubic anvils to generate high pressure, with x-ray access. This year we have made the following advances in this apparatus:

a) Extended the pressure range to 21 GPa, through the use of reverse-tapered 10 mm Toshiba grade F WC anvils. Figure 1 shows cell pressure *vs* oil pressure data taken on the study of ZrW_3O_8.[2]

b) Developed cell assemblies for making Equation of State measurements, including using lanthanum chromite heaters.

c) Extended the method for making strain measurements to higher pressure[2,3]. Figure 2 shows the P-T path used for the β-$(Mg,Fe)_2SiO_4$[3]

[1]NSLS Activity Report, page B-140, 1995

[2]J. Chen, *Pressure Induced Amprphization in Zirconium Tungstate*, this Report.

[3]T. Inoue, *Rheological study of hydrous γ-phase using in situ x-ray diffraction* and J. Chen, *Rheology of dry and hydrous phases of the α and β forms of $(Mg,Fe)_2SiO_4$*, both in this Report.

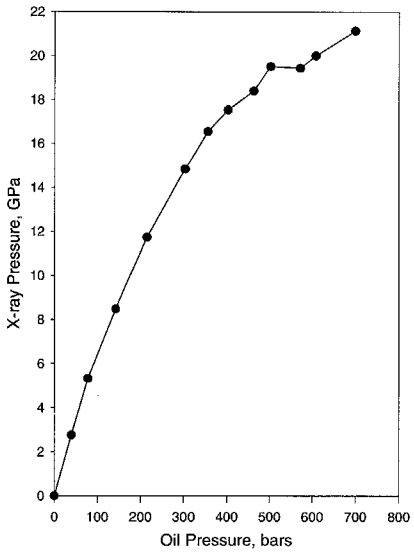


Figure 1. Pressure performance of TCUP apparatus.

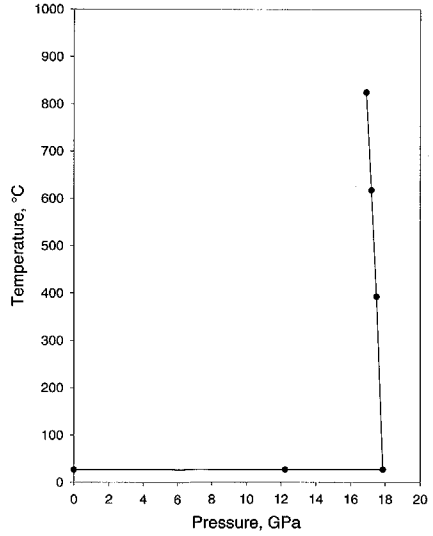


Figure 2. P-T path for one of the strain measurements.

A New Anvil Geometry for SAM-85 for High P, T X-ray Studies * | X17B1

Y. B. Wang, D. J. Weidner, M. T. Vaughan (CHiPR, SUNY, Stony Brook), and I. C. Getting (CHiPR, U. Colorado)

We have modified the conventional DIA anvils in order to improve their performance in terms of pressure capability and reliability. Figure 1 shows geometry of our new tapered WC anvils and Figure 2 the attainable pressure with the tapered anvils as compared to that of the conventional straight-flank anvils. Several points about this new geometry are worth noticing.

1. As is evident from Figure 2, we have gained 30% in maximum attainable pressure compared to the conventional anvil geometry. Thus the tapered WC anvils give the pressure range comparable to that of straight sintered diamond anvils.
2. The wedged anvil gaps act as pressure seals, thereby significantly reduced the number of blowouts, which used to cause failures in the experiments.
3. The tapered anvil geometry greatly reduced hysteresis in the pressure -load relation, enabling us to obtain multiple heating cycles at various pressures, and allowed complete P-V-T measurements within the entire P- T space with a single experiment.
4. The tapered anvil geometry significantly increased survival rate of the thermocouples to close to 100%. Counting all the factors together, we have increased our efficiency in the P-V-T experiments by a factor of 4 with the tapered anvils.

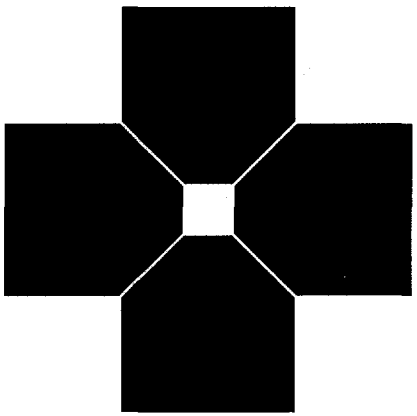


Figure 1. Geometry of tapered anvils (four shown). The light gray portions are removed, leaving the dark gray anvil

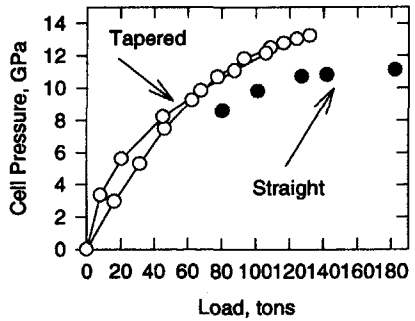


Figure 2. Pressure *vs.* load for the 4/3.5 mm tapered anvils (open circles) and the 4 mm straight anvils. Note that the curve for the straight anvils levels off at about 120 tons, where the tapered anvils generate a pressure that is about 30% higher.

* This work was supported by the National Science Foundation under a grant to the Center for High Pressure Research.

Contrast Imaging and Image Quantification With the Monochromatic CT - MECT * | X17B2

X.Y. Wu, F.A. Dilmanian, X. Huang, E.C. Parsons, B. Ren (BNL, Medical), W.C Thomlinson, Z. Zhong (NSLS), L.D. Chapman (I.I.T.), T.M. Button, and M.J. Petersen (SUNY, Stony Brook)

One of the advantages of monochromatic x-ray beams for computed tomography (CT) is in imaging with contrast agents, where the monochromatic beam energy can be tuned just above the K-edge of the contrast element. Comparative iodine phantom studies between Multiple Energy Computed Tomography [MECT] at X17B2 and a conventional CT [CCT] showed that 33.3-keV MECT has a 3-fold advantage in iodine image contrast over 120-kVp CCT. However, iodine's K-edge is too low an energy for the CT of human body, except for the neck and the limbs. The present studies show that such an advantage exists also for Gd as a contrast agent.

An 18-cm diameter acrylic phantom with thirty 11-mm diameter channels filled with Gd solutions from 0 to 1600μg Gd/ml was imaged with MECT at 50.34 keV and with CCT at 120 kVp. For the 1600 μg Gd/ml channels, MECT yields 138 HU while CCT only gives 64 HU. The noise ratio of MECT (50.34keV) to CCT(120kVp) is 1.4HU:1.9HU, as obtained from computer simulations. These simulations used the experimental MECT system parameters for both MECT and CCT (i.e., 3 rad surface absorbed dose, 3 mm beam height, 0.922 mm detector pitch, and 0.25 mm detector-element dead space). Defining "constrast-to-noise ratio" (CNR) as the figure of merit for judging CT image quality, we find from the above-mentioned results a ~3-fold CNR advantage for MECT compared to CCT.

The Gd image contrast for the above measurements was accurate within the limits of the solution's concentration accuracy. For CCT, however, such a quantification requires the knowledge of the effective beam energy throughout the image. Our computer simulations with an 18-cm water phantom that included small bone inserts as image-contrast indicators exhibited an average of 2.5 keV beam hardening for a 120-kVp CCT, despite the 1st-order beam hardening corrections (i.e., Cupping corrections). The simulations also show that the difference between the bone image contrast at the phantom's center and at its edge is 20 HU (typical noise was 2-3 HU). This corresponds to a 0.5 keV differential beam hardening. These results indicate the potential value of MECT in contrast imaging and in image quantification.

* We thank J.A. Coderre, J.M. Dobbs, F. Giron, N. F. Gmür, D. Greenberg, J.B. Hastings, S. Marcovici, R. Menk, C.T. Roque, D.P. Siddons, and D.N. Slatkin for their assistance. Research supported by the Office of Health and Environmental Research, and U.S. DOE.

Rheology Study of $Py_{60}Mj_{40}$ Garnet at High Pressure and High Temperature	X17B1

Y. Wu, D.J. Weidner, J. Chen, G. Gwanmesia, and M. Vaughan (CHiPR, SUNY, Stony Brook)

In situ X-ray diffraction measurements of the rheological properties of $Py_{60}Mj_{40}$ garnet was completed up to 16GPa and 1000°C at the X-17B1 beam line using the newly designed high pressure apparatus T-cup[1]. The powder $Py_{60}Mj_{40}$ garnet was first compressed to 16GPa and heated up gradually to 1000°C. By analysing the peak broadening for the (400) diffraction, we get the microscopic strains of the sample.

Our result shows that the garnet sample reached yield point less than 6GPa at room temperature. This is quite consistent with our earlier results[2]. Then the strength increased slowly with the increasing pressure. Under 16GPa confining pressure, we increased the temperature gradually, first to 400°C, 620°C, then 800°C, and finally to 1000°C. The microscopic strain decreased noticeably with the increasing temperatures. Around 1000°C, the strain decreased almost to zero. At the specific temperature, we can see the microstrain decreased monotonically with time. And there is a linear relationship between $\log(\varepsilon)$ and $\log(t)$. And the slope of the $\log(\varepsilon)$ *vs* $\log(t)$ indicates that the exponent n of the power-law relationship decreases from 50 at 400°C to about 10 around 810°C. This suggests the $Py_{60}Mj_{40}$ garnet may still be in the plastic regime at 800°C. Also, the strain rate in the order of 10^{-6} s^{-1} was measured for these temperature ranges.

References:
[1]Weidner, NSLS Activity Report, B-140 (1995);
[2]Wu, NSLS Activity Report, B-141 (1995).

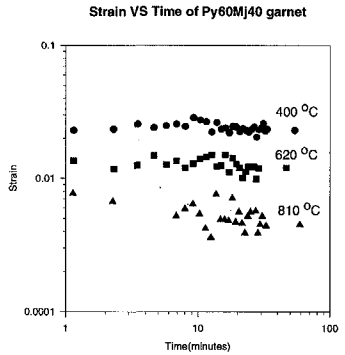


Figure 1. Strain in $Py_{60}Mj_{40}$ garnet as a function of time.

Equation of State of Calcite-Structure Carbonates	X17B1

Jianzhong Zhang and Richard J. Reeder (CHiPR, SUNY, Stony Brook)

Pressure-volume-temperature measurements have been carried out on $NiCO_3$ and $MnCO_3$ carbonates using a DIA-type, cubic-anvil, high-pressure apparatus interfaced with synchrotron X-ray diffraction. These data, along with those obtained previously for magnesite ($MgCO_3$) and siderite ($FeCO_3$) using the same technique[1,2], allow us to systematically study equation of state of the calcite-structure carbonates.

A linear correlation between M-O bond length and the room-temperature bulk modulus is, as expected, found in $NiCO_3$, $FeCO_3$ and $MnCO_3$ carbonates. The product of the room-temperature bulk modulus and unit-cell volume at ambient condition is observed to be constant in these three compounds, similar to literature observations in other systems of isostructural series. Magnesite, however, deviates significantly from the linear trends in both correlations. It is speculated that carbonates with alkaline elements as cations behavior differently at high pressures from those with transition metals as cations.

References:
[1]Zhang, J., I. Martinez, F. Guyot, and S. K. Saxena: *In situ* X-ray diffraction study on magnesite at high pressure and temperature, Phys. Chem. Mineral, in press.
[2]Zhang, J., I. Martinez, and F. Guyot: *In situ* X-ray diffraction studies on mgnesite and siderites at high pressure and temperature, Terra Nova Suppl., V. 8, p70, 1996.

Effect of Silicon Incorporation in Iron: Equation of State and Phase Transition	X17B1

J. Zhang (CHiPR, SUNY, Stony Brook) and F. Guyot (U. of Paris)

Experiments have been carried out on iron and two iron-silicon alloys, $Fe_{0.91}Si_{0.09}$ and $Fe_{0.83}Si_{0.17}$, at high pressure and temperature up to 9 GPa and 1473 K, using a DIA-type, cubic-anvil, high-pressure apparatus interfaced with synchrotron X-ray diffraction. Pressure-volume-temperature data were obtained for iron and $Fe_{0.91}Si_{0.09}$ and are analyzed using Birch-Murnaghan equation of state. With fixed K_0 at 4, we obtain for iron:

$$K_0 = 154(2)GPa$$

$$(\delta K/\delta T)_P = -0.041(5)GPaK^{-1}$$

and

$$\alpha_{300-773} = 4.46(12)K^{-1};$$

for $Fe_{0.91}Si_{0.09}$, we have

$$K_0 = 156(2)GPa$$

$$(\delta K/\delta T)_P = -0.044(6)GPaK^{-1}$$

and

$$\alpha_{300-773} = 4.71(14)K^{-1}.$$

These results indicate that substitution of small amount of Si in iron would not have a significant effect on the equation of state parameters. Phase transition were studied in two experiments, one with iron and $Fe_{0.91}Si_{0.09}$ loaded in the boron nitride container and the other $Fe_{0.91}Si_{0.09}$ and $Fe_{0.83}Si_{0.17}$. The bcc-fcc phase transition in $Fe_{0.91}Si_{0.09}$ was observed at 7.5 and 9 GPa, but the temperatures of transition are more than 300 K higher than those in iron. Phase transition was not observed at 5 GPa and lower pressures in $Fe_{0.91}Si_{0.09}$ and in the entire experimental pressure and temperature range for $Fe_{0.83}Si_{0.17}$. These observations indicate that incorporation of Si in iron strongly stabilizes the bcc structure in the system Fe-Si. In comparison with literature data at 1 atm., the present results also provide constraints on the compositional maxima of the γ-loop for the system Fe-Si as a function of pressure.

Rheology, Strength, and Elasticity Anisotropy of Iron at High Pressures	X17C

H. Mao, J. Shu, R. J. Hemley (Carnegie Institute), and A. K. Singh (Nat. Aeronautical Lab., India)

The seismic anisotropy of the inner core may reflect the rheology of its solid constituents. We have conducted a 3-dimensional x-ray diffraction study of iron under uniaxial compression in a diamond cell at X17C of National Synchrotron Light Source. Rheological properties of */epsilon*-Fe, including orientational texture, shear strength, and elastic anisotropy, are studied at megabar pressures.

With the 3-d x-ray diamond cell, energy dispersive x-ray diffraction (EDXD) can be obtained at any */phi*, the angle between the diamond-cell axis and the diffraction vector. Relative intensities of EDXD peaks as a function of */phi* reveals the preferred orientation of the polycrystalline sample. Under uniaxial stress, the */phi*-Fe sample flows in the radial direction perpendicular to the stress. The intensity of 002 reflection of the hexagonal close-packed iron reaches a maximum at */phi* = 00 and a minimum at */phi* = 900, indicating the c-axis of */epsilon*-Fe preferentially aligns with the maximum stress direction and the a-axis aligns with the maximum shear (flow) direction.

The elastic moduli tensor ($C_{(}ij$)), maximum stress (axial direction), minimum stress (radial direction), and average pressure can be calculated from the energy (or d-spacing) of EDXD peaks as a function of */phi*. The difference between the maximum and minimum stresses provides an estimation of strength. At 52 GPa and 300K, we obtained $C_{(}11) = 689$, $C_{(}12) = 298$, $C_{(}33) = 702$, $C_{(}13) = 270$, $C_{(}44) = 419$, and C66 = (C11 - C12)/2 = 195; all units in GPa. Calculated longitudinal velocities have a minimum in the a- (8.3 km/sec) and c- (8.3 km/sec) direction but a maximum in between a and c (9.5 km/sec). The 10% anisotropy in velocity is significantly larger than the 3% of the inner core. The present results, however, are consistent with the a-axis of e-Fe partially aligning with the shear direction perpendicular to the spin axis as a result of drag at the IOC interface.

Compression of Seven ScS Compositions with Sc Lattice Vacancies | X17C

S. Peiris and D. Heinz (U. of Chicago)

The early transition metal chalcogenides display a wide range of compositions formed via metal or chalcogen deficiency from a parent stoichiometry. The Sc_xS compositions ($0.8<x<1.0$) are such a system formed by vacancies in the metal sublattice of the rocksalt structure of Sc_1S.

Samples (synthesized by Tuenge [1]) from each composition were compressed to 50 GPa, at room temperature in a Mao-Bell [2] diamond anvil cell. Energy dispersive x-ray diffraction was done on beamline X17C with the detector at a 2θ angle of 15°. Pressures were determined by including a few specks of gold with the sample and using a standard equation of state for gold [3]. The pressure(P)-volume(V) data obtained were fit with fourth order Birch-Murnghan equations of state [4], to calculate thermodynamic parameters. Some of the equations of state thus obtained are shown in Fig. 1, and the thermodynamic parameters are shown in Fig. 2.

We usually expect phases with lattice vacancies to be more compressible than space-filled lattices, which are more dense. However, our experiments reveal the isothermal bulk moduli (Ko) increasing with increasing vacancy content. These observations were explained by the Extended Huckel calculations performed. The compositions with higher vacancy content have stronger, stiffer Sc-S bonds, because the higher oxidation state of Sc (>2) in the compositions with more vacancies, allow higher interaction of Sc 3d orbitals with S 3p orbitals [5,6].

The data obtained, and the P-V/Vo equations of state for each composition, start converging by about 40 GPa. In addition the unit cell volumes obtained after decompression from 50 GPa to below 20 GPa are higher than the pre- compression volumes for the compositions with more vacancies. We suggest that these effects are due to the formation of dumbells-shaped S pairs at very high pressure in the compositions with more Sc vacancies. If these pairs were retained upon decompression the Sc in the lattice would be reduced to an oxidation state closer to +2, giving less compact Sc-S bonds and resulting larger unit cell volumes.

1. R. T. Tuenge et al., J. Chem. Phys., 65, 2400 (1976).
2. H. K. Mao et al., Rev. Sci. Instrum., 50, 1002 (1979).
3. D. L. Heinz and R. Jeanloz, J. Appl. Phys., 55, 885 (1984).
4. F. Birch, J. Geophys. Res., 83, 3543 (1978).
5. J. K. Burdett and J. F. Mitchell, Chem. Mater., 5, 1465 (1993).
6. S. M. Peiris et al., Inorg. Chem., submitted. (1996).

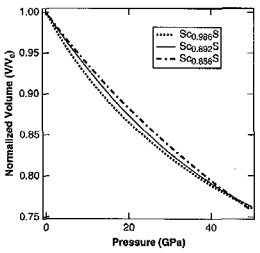


Figure 1. Pressure-Volume equations of state for three ScS compositions.

x in Sc_xS	Bulk Modulus K_0 (GPa)	$(\partial K_0/\partial P)$ K_0'	$(\partial K_0'/\partial P)$ K_0''
1.013±0.005	108±25	4±5	-5±1
0.986±0.005	104±14	4±3	3.7±0.5
0.892±0.003	135±18	0.8±0.4	17±3
0.875±0.006	130±29	1±5	24±5
0.864±0.006	148±22	-0.4±3	23±3
0.856±0.007	145±28	2±4	3.5±0.7
0.838±0.004	149±23	-2±3	44±7

Figure 2. Thermodynamic parameters obtained from P-V data.

Pressure Induced Structural Transitions in Nanometer Size Particles of PbS | X17C

S. B. Qadri, E. F. Skelton, Y. Yang, B. R. Ratna (NRL), and J. Z. Hu (CIW)

Semiconductors with reduced dimensions recently have been shown to exhibit electronic and optical properties which vary with the size of the particles. PbS and other Pb chalcogenides have attracted much attention due to their tunability over a wide spectrum. Relative to bulk crystals, the bandgap of the PbS nanoparticles was significantly blue shifted from the near-IR into the visible and near UV region with decreasing particle size. At elevated pressure (2.5 GPa), PbS undergoes a first order phase transition from the NaCl or B1 structure to an orthorhombic structure. The effects of particle sizes in the nanometer range on this transition have been investigated using energy-dispersive x-ray diffraction and diamond anvil cell. Relative to the bulk crystals, the onset of transition pressure showed a significant increase with decreasing particle size. The results also show that compressibility increases with decreasing particle size: this increase is continuous through the phase transition.

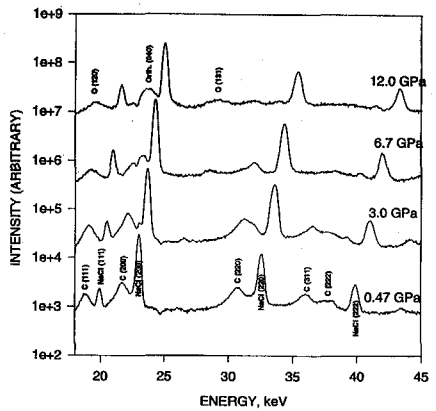


Figure 1. Diffraction spectra for the 54 particles recorded at various pressures from the B1 (C) to the orthorhomica (O) phase.

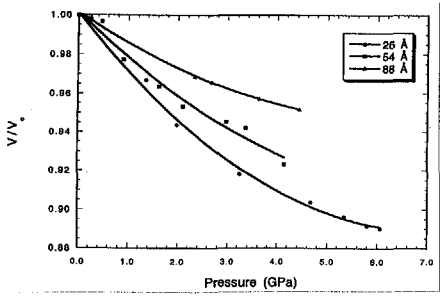


Figure 2. V/Vo vs. pressure for three different particle sizes.

High P-T Phase Diagram and Equation of State of Iron *	X17C

G. Shen, J. Hu, R. J. Hemley, H. Mao (Carnegie Institute), and T. S. Duffy (GSECARS)

An accurate determination of phase diagrams and P-V-T equations of state of iron provides critical constraints for models of the core. Laser-heated diamond-anvil cell, capable of generating ultrahigh pressures and temperatures has been improved with advancement and integration of in-situ x-ray microprobe and double hot-plate heating techniques. Significant progress in shaping and defining the temperature distribution in a laser-heated diamond cell has been made by coordinating the optimal laser characteristics, sample configuration, and optical arrangement. With double-focusing K-B x-ray mirrors, the spatial resolution and sensitivity of the x-ray diffraction microprobe have also been greatly improved, which enables precise measurements of a sample under uniform, well-defined high P-T conditions.

For each pressure, temperature was varied, and x-ray diffraction patterns were taken for phase identification and density determination. For example, at 23 GPa at ambient temperature iron crystallizes in hexagonal-close-packed (hcp) e-Fe structure. As the temperature was raised to 1860 K, the hcp diffraction lines disappeared completely, and new lines corresponding to the face-centered- cubic (fcc) g phase appeared. The diffraction peaks of g iron disappeared above 2380 K and reappeared when the temperature was lowered to 2220 K, bracketing the melting temperature. The completeness of the transition is a clear indication that the sampled region for x-ray diffraction has uniform P-T, a major improvement from previous experiments. The liquidus phase changes from g -Fe at 45 GPa to e-Fe at 68 GPa, indicating a g-e-liquid triple point near 50 GPa. At high pressures, the present data indicate a melting curve close to but slightly higher than that of Boehler.1

R. Boehler, Nature 363, 534 (1993).

* This work is supported by NSF.

In Situ Measurement of the Structural Transition Rate in Pd Associated with the Electrochemical Absorption of Deuterium	X17C

E. F. Skelton, P. L. Hagans, S. B. Qadri, D. D. Dominguez (NRL), and J. Z. Hu (CIW)

Structural changes induced by the absorption of deuterium (D) into a Pd lattice were studied with very high energy (> 60 keV) photons. The α-to-β phase transition induced by the absorption of Pd into a 1 mm diameter Pd wire was monitored in a microspot 18 x 10^{-12} m^3 in volume as D was electrochemically loaded into the wire. Because of the long absorption length of 60+ keV photons, structural changes could be measured from the high energy diffraction peaks of Pd. The (422)-peak was monitored as a function of position and time from the edge to the core of the wire. From these data, it was determined that, under an electrochemical loading current of about 100 ma, the α-to-β phase transition moved from the edge to the core at a speed of 48 nm/sec. It also was determined that the α phase persists about 30% longer in the core that on the surface. These data represent the first time that the Pd lattice expansion and α-to-β transition rate have been measured in an electrochemical cell with a cylindrical cathode as a function of distance across the cathode.

Structure and Phase Transitions of Krypton in Porous Vycor | X18A

D. W. Brown, P. E. Sokol (Penn. State U.), and S. N. Ehrlich (Purdue U.)

The equilibrium properties and kinetics of a fluid confined in mesoporous media are dramatically different from those in the bulk. The phase equilibria are substantially altered by the combined effects of finite pore size and substrate forces. Studies of the macroscopic behavior of the liquid-solid transition under such confinement have been published recently. Measurements of bulk thermodynamic variables, such as heat capacity, pressure, and the velocity of sound have been used to study the freezing of a variety of liquids in porous materials. In general, a large suppression of the liquid-solid transition temperature, up to 20% from the bulk, has been observed accompanied by a hysteresis between freezing and melting. The nature of the depression in the freezing point, whether due to finite size effects and related shifting of the phase diagram or inhibited nucleation of the solid, remains open.

We have undertaken a study of the structure of krypton confined in the pores of thirsty Vycor glass. Vycor glass is approximately 70% SiO_2 and 29% B_2O_3. The B_2O_3 is chemically leached out to leave small pores making up 29% of the volume of the glass. The pores are considered to be approximatly cylindrical with and aspect ratio of 7:1. In our case the pores have a radius of approximately 70 A.

Our sample was cooled to 120 K, in the liquid phase of bulk Kr. The Vycor was then loaded to various filling fractions with Kr gas. Diffraction measurements were done on cooling and warming. Typical x-ray diffraction patterns, with the pores filled to half of their capacity, can be seen in Fig. 1 as a function of temperature. The two broad peaks are due to the Vycor and the two sharp peaks on the right are due to the Be windows on the sample cell. The disappearance of the Kr diffraction peaks signifies the melting point of the liquid. The bulk freezing point of Kr is 115.8 K. We have observed the freezing point to be at 101 K and the melting point to be at 106 K with the pores full to capacity. The freezing point drops to below 80 K and the melting point to 89 K when the pores are filled to 25% of capacity (Fig. 2). More complete analysis will yield information about such things as the mechanism of solidification, the strain the crystal is under, and the size of the crystallites. Work supported by a Petroleum Research Fund Grant ACS-PRF31907-AC5 & DOE Grant DE-FG02-85ER45183.

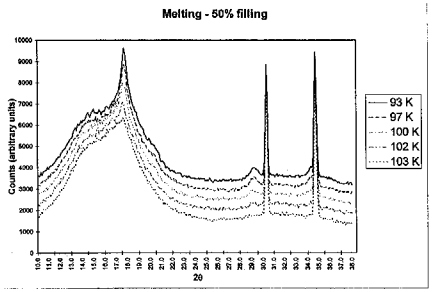


Figure 1.

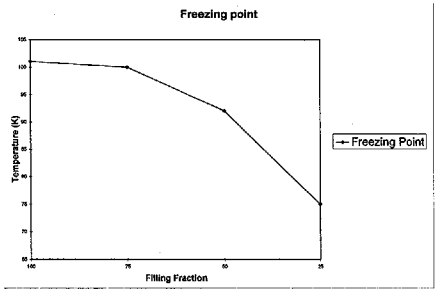


Figure 2.

Multiple X-ray Diffraction Studies of Decagonal Quasicrystals. | X18A

R. Eisenhower, R. Colella (Purdue U.), B. Grushko (Jülich)

The problem under investigation is the structure of decagonal quasicrystals, the issue of centrosymmetry, and the effect of stoichiometry and composition. Phase information on structure factors is an important ingredient for structural investigations and the method used in this work is based on Multiple Bragg Scattering [Also called: "Umweganregung" = detour radiation. See: Q. Shen and R. Colella, Nature **329** 232 (1987)], a situation in which two or more Bragg reflections are simultaneously excited in the crystal. Preliminary results were presented in the 1995 NSLS Annual Report, for $Al_{68}Cu_{11}Co_{21}$ and $Al_{71}Ni_{24}Fe_5$.

In this abstract we report data for a different material: $Al_{72.5}Ni_{16.5}Co_{11}$. The lattice constants of all three quasicrystals are surprisingly identical. There are, however, differences in their structures. These differences are manifested in the phases of the Bragg reflections involved. What is measured, in a three-beam experiment, is the **triplet invariant**: $= \delta = \phi_{\mathbf{H}} + \phi_{\mathbf{P-H}} - \phi_{\mathbf{P}}$, a linear combination of the phases. The main reflection for which azimuthal scans are presented below is called **P**, the simultaneous reflection is **H** and **P - H** is the coupling reflection. An example of the structural differences between two seemingly isomorphous quasicrystals is shown below. While the main and simultaneous reflections are the same for both plots, there are noticeable differences in the two "umweg" plots. While the plot for $Al_{71}Ni_{24}Fe_5$ (Fig. 1) shows a strong asymmetry, the plot for $Al_{72.5}Ni_{16.5}Co_{11}$ (Fig. 2) is very symmetric, indicating a δ value close to 90°, for which there would be no asymmetry at all. In both cases, the δ values (50° and 83°) are far from 0° and 180°, the only values compatible with a centrosymmetric structure. It is concluded that $Al_{72.5}Ni_{16.5}Co_{11}$ is also non-centrosymmetric.

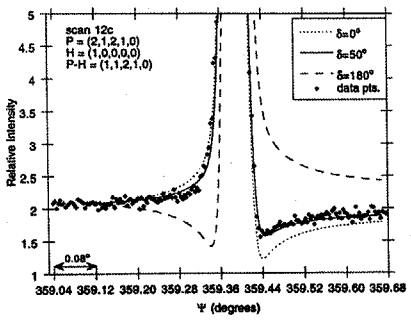


Figure 1.

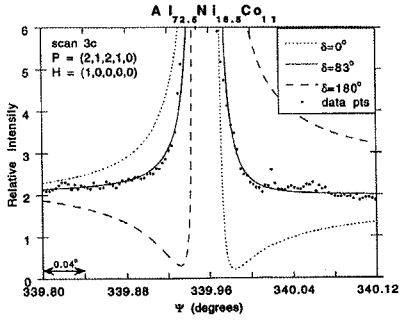


Figure 2.

Spot Shapes of Bragg Reflections in Decagonal Quasicrystals	X-18A

R. Eisenhower (U. of Illinois), Steve Ehrlich (Purdue U.), Benjamin Grushko (Forschungszentrum Juelich, Germany)

Decagonal quasicrystals consist of periodically stacked quasicrystalline layers. Each layer exhibits a classically forbidden 10-fold rotational symmetry axis. Existing in the transformation region between 3-D quasicrystalline and periodic structures, their structure is highly dependent upon stoichiometry and growth conditions. Complicating the study of the decagonal quasicrystal structure is the existence of the microcrystal structure, which consists of rotated rhombohedral domains and closely mimicks the decagonal structure. High-resolution reciprocal space scans on microcrystals reveal distinctive peak splitting. Similar experiments were performed on $Al_{68}Cu_{11}Co_{21}$ and $Al_{71}Ni_{24}Fe_5$ decagonal quasicrystals. In contrast to the microcrystalline phase, the precession photographs of the Al-Cu-Co and Al-Ni-Fe quasicrystals revealed normal spot shapes, and synchrotron rocking curve widths were narrow (.015 degrees FWHM). However, high-resolution reciprocal space scans reveal a complicated structure for the decagonal phase as well. Non-uniform smearing of intensity in the azimuthal direction was seen for the (10000) and equivalent reflections, whereas typical (i.e. bullseye pattern) was seen for the (12110) and equivalent reflections.

Anomalous X-ray Scattering Studies of a Lead Magnoniobate Single Crystal *	X18A

V. Gosula, H. Chen (U. of Illinois), S. Teslic and T. Egami (U. of Pennsylvannia)

Half integer superlattice reflections characteristic of ordered structure in $Pb(Mg_{1/3}Nb_{2/3})O_3$ (PMN) single crystal have been measured using resonantv x-ray scattering near the Pb L_{III} absorption edge. These superlattice peaks have been previously measured through electron diffraction and explained by the two-phase Nb/Mg ordering model. The microscopic origin of these peaks remained controversial, specially since the effective scattering factor for these peaks is significantly smaller than in the case of complete ordering. By a similar approach, Nb was shown to contribute heavily to the scattering factor of the superlattice peaks, indicating its presence in the superstructure. In this experiment, the partial structure factor of the peaks with respect to lead was determined for three different half-integer peaks and showed a strong correlation. This constitutes strong evidence that Pb is involved in the superstructure, either through atomic exchange or large displacements.

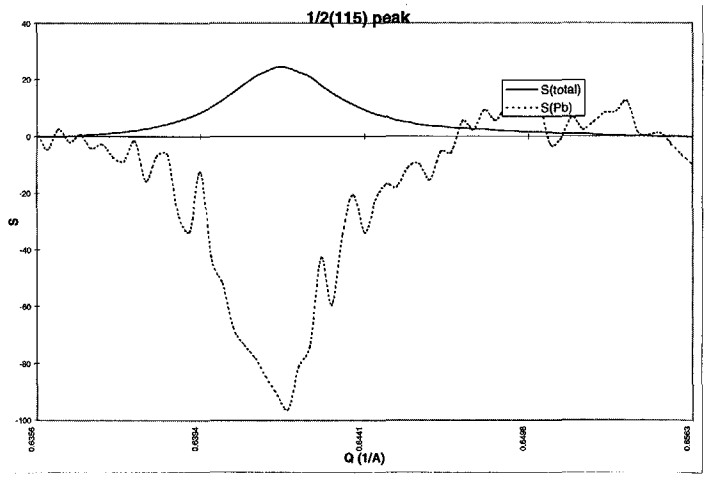


Figure 1. Plot showing both the total structure factor [S(T)] and its partial with respect to Pb [S(Pb)] for the 1/2(115) superlattice peak.

* Work supported by DOE under grants DE-FG02-ER45183, DE-FG02-91ER45439 and IBHE-HECA.

High Temperature Studies of X-ray Scattering in a Lead Magnoniobate Single Crystal *	X18A

V. Gosula, H. Chen (U. of Illinois), S. Teslic and T. Egami(U. of Pennsylvannia)

A $Pb(Mg_{1/3}\ Nb_{2/3})O_3$ (PMN) single crystal was used for the study of ordering evolution as a function of temperature. The half-integer superlattice peaks were measured and the partial of the structure factor with respect to lead was determined using resonant x-ray scattering near the Pb L_{III} edge (two different energies). The intensities of several bragg peaks were also measured in order to determine the debye-waller factors of all the atoms involved in the structure. The intensities were shown to increase with the increase in temperature and aging was also noticed, as the intensities increased with aging time. The aging and temperature effects must be separated before the debye-waller factors and the ordering evolution of the superstructure can be appropriately determined. Thus, further work is needed in these high temperature scattering experiments.

* Work supported by DOE under grants DE-FG02-ER45183, DE-FG02-91ER45439 and IBHE-HECA.

Time and Depth Dependence Study of the Azimuthal Orientation in Confined Hybrid Smectic C* Films *	X18A, X22B

L. J. Martínez-Miranda, Y. F. Hu, T. K. Misra and M. W. Haung (U. of Maryland)

Confined hybrid liquid crystal films experience a competition between the aligning forces of the bounding surfaces. We have performed a depth profile dependence study of the in-plane ordering of a smectic C* liquid crystal mixture, mx5112, confined between a grated glass substrate and the air surface. This compound mixture has the following phase transitions: sm3 - smC* at 22.65°C; smC* - smA at 49.5°C; and smA - I at 57°C. The corresponding smectic layer spacings are 33.303Åfor the smA phase; 29.97Åfor the smC* phase; and 31.639Åfor the sm3 phase.

The in-plane layer spacing oscillates between the bulk values of the smA and smC* phases as a function of time. This value varies also as a function of depth within the films and is close to the average of the two bulk spacings close to the liquid crystal glass interface. The azimuthal orientation of the layers varies both as a function of depth and of time within the films. In-plane layers close to the liquid crystal glass interface align close to the direction of the gratings' axis. The orientation of the layers close to the liquid crystal air interface rotate as a function of time to a direction perpendicular to the axis of the gratings, for samples thicker than 10μm, as illustrated on Table I. The mechanism for this rotation, which was previously observed both in samples thicker than 10μm and thinner than 3μm, is not clear at present. We are in the process of studying the depth dependence of the azimuthal orientation in greater detail.

Layer Spacing (Å)	ϕ(°) - 15 µm	ϕ(°) - 13 µm
30.710	159	
30.770		20
30.830	38	
30.360	24	
30.050		20
30.640		20
30.120	23	
31.160		90
31.020		78
30.630		102

Figure 1. Table of Values of the azimuthal peak ϕ corresponding to the layer spacing of the maximum peak for the 15-μm and 13-μm films. Data were obtained over a 16 hour period for the 15μm sample and over a 90 hour period for the 13 μm sample.

* This research was supported by a NSF-VPW Grant No. GER-94-50118, and a NSF Grant No. ECS-96-96069.

Time Dependence Study of In-Plane Layers in Confined Hybrid Smectic C* Films *	X18A, X22B

L. J. Martínez-Miranda, Y. F. Hu, T. K. Misra and M. W. Huang (U. of Maryland)

Liquid crytalline materials in constrained geometries exhibit properties that can vary significantly from the bulk properties of the material. Confined hybrid liquid crystal films experience a competition between the aligning forces of the bounding surfaces. We have studied the in-plane ordering of a smectic C* liquid crystal mixture, mx5112, confined between a grated glass substrate and the air surface. This compound mixture has a the following phase transitions: sm3 - smC* at 20.65°C, smC* - smA at 49.5°C and smA - I at 57°C. The corresponding bulk layer spacings are: 31.303Åfor the smA phase; 29.97Åfor the smC* phase; and 31.639Å for the low temperature Sm3 phase.

We have observed that the in-plane layer spacing oscillates between values close to the smA bulk layer spacing and the smC* bulk layer spacing for samples with thicknesses in the range 10 - 20 μm. This oscillation is aperiodic in time, as shown in the Figure below. By contrast, thinner films show a slower variation of the value of the layer spacing with time, with a 0.6 percent oscillation over a 10 hour period.

A depth profile study of the films shows that those layers located furthest from the glass grating interface show the largest variation in layer spacing over a 48 hour period. The layer spacing at the end of this period is approximately 0.3 percent larger than the bulk smC* spacing. In contrast, those layers closest to the glass grating interface remain close to the intermediate spacing value of 30.6Å.

The time oscillation may be the result of the competition between the two aligning surfaces in the smC* film. The in-plane layer at the grating interface favors a smA-like ordering, which relaxes through the thickness of the film. This relaxation is enhanced the farther the layers are from the glass interfaces or the thicker the films. The time oscillation and depth dependence of the layer spacings affect both the temperature and field dependence of these films. We are in the process of studying this behavior.

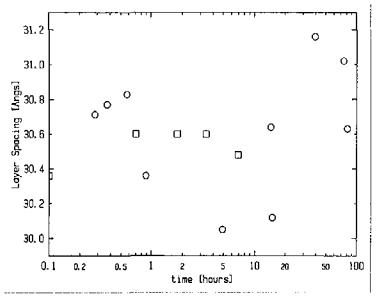


Figure 1. Open circles: Time dependence of a 15μm and a 13μm film (combined). Open squares: time dependence of a 5μm film.

* This work was supported by a NSF-VPW Grant No. GER-94-50118, and a NSF Grant No. ECS-96-96069.

Anisotropic X-ray Diffuse Scattering Features in $La_{0.6}Pb_{0.4}MnO_3$	X18A

R. McQueeney (U. of Pennsylvania)

We have observed strong anisotropies in x-ray diffuse scattering from a single crystal of $La_{0.6}Pb_{0.4}MnO_3$ studied at room temperature with the X18A beamline using an incident energy of 12 keV.Two features distinguish themselves in the diffuse scattering. The first feature is the presence of square constant intensity contours for cuts in the hk-plane at constant l near the (4,0,0) Bragg reflection, as shown in the figure. Since the crystal is approximately a cubic perovskite, the diffuse scattering due to phonons should be isotropic. In addition to this feature, there also exists a large anisotropy of the diffuse scattering for the (h,+k,0)and (h,-k,0) regions near the (4,0,0) Bragg point. This, too, cannot be explained by the thermal diffuse scattering.

The presence of these features indicates that there are significant atomic displacements above that due to phonons, and that special symmetry requirements are needed to explain the shape of the diffuse scattering. There is also a strong similarity to the diffuse scattering observed in the $La_{2-x}Sr_xCuO_4$ and $La_{2-x}Sr_xNiO_4$ which show square intensities. In the case of the cuprate, the square is rotated by 45 degrees. This diffuse scattering has been attributed to atomic strains caused by the inhomogeneous hole distributions within the transition metal-oxygen plane which arise from the substitutional doping. Thus, the manganese oxide compound may contain inhomogeneous charge distributions in the Mn-O plane similar to the nickelate and cuprate compounds, which could shed some light on their interesting magnetic properties. These diffuse scattering features will be studied in much more detail in the future.

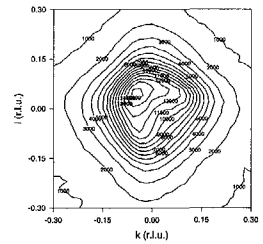


Figure 1. Square diffuse scattering observed in within the (3.9,k,l) plane at room temperature for $La_{0.6}Pb_{0.4}MnO_3$.

Anomalous Diffraction Studies of CMR Materials *	X18A

S. M. Mini (Northern Illinois U. & ANL), J. Mitchell, D. Hinks (ANL) and S. N. Ehrlich (Purdue U.)

We report the x-ray diffraction of a series of pseudo-perovskite, $La_{1-x}Sr_xMnO_3$, prepared at different pressures. The system is interesting because it is prototypical of colossal magneto resistive (CMR) materials. This perovskite system exhibits unusual coupling among magnetism, electronic transport, and structure. It is also thought to be mixed valent Mn^{+3}/Mn^{+4}. The Mn K-edge XANES on these materials show a small shift of increased energy indicating increasing Mn valence as Sr content is increased. The MXCD of the Mn K-edge [1] shows a negatve first peak, which is indicative of negative p-like spin density at the Fermi level, and an imbalance in the spin-dependent electronic density of states above the Fermi energy. Diffraction measurements were made at X18A, above and below the Mn K-edge (6539 eV), in in effort to clarify the electronic properties and structure of the Mn in these systems.

[1] S.M. Mini, et al, Mat. Res. Soc. Symp. Proc. Spring '96.

* This work was supported by the State of Illinois under the IBHE/HECA Grant and the U.S. Department of Energy, Basic Energy, Science, Materials Sciences under Contract No. W-31-109-ENG-38 and DE-FG02-85ER45183 of the MATRIX PRT at the NSLS.

The Defect Structure Studies of $La_{2-x}Ca_xCuO_{4-y}$ Superconductors *	X18A

X. Shi, J. B. Cohen, and T. O. Mason (Northwestern U.)

The local structure about Ca atoms in $La_{2-x}Ca_xCuO_{4-y}$ samples is being studied by x-ray absorption fine structure (XAFS). The point defect modeling study of the Ca-doped system suggest that the majority defect species associate with the oxygen deficit ($y>0$) results primarily from dopant-vacancy associates rather than isolated oxygen vacancies. (L. Shen, P. A. Salvador, and T. O. Mason,J. Am. Ceram. Soc, bf 77[1], 81-88, (1994)). The association of oxygen vacancies with dopant will change the surrounding of the dopant. We have carried out studies on samples prepared with different oxygen partial pressures. Our XRD data shown there is no *average* structural change for the two samples. The fluorescence EXAFS was measured from below the Ca-K absorption edge to k=12 $Å^{-1}$ above the edge. A "different" EXAFS technique is being used in the data analysis. The analysis of the results of defect structure is still underway.

* This work was supported by DOE Grant No. DE-FG02-84ER45097/A015.

Atomic Structure of PMN Studied by Resonant X-ray Diffraction * | X18A

S. Teslic, T. Egami (U. of Penn.), V. Gosula and H. Chen (U. of Ill)

We have studied the atomic structure of a PMN ($Pb(Mg_{1/3}Nb_{2/3}O_3$ single crystal using resonant x-ray scattering near the Pb L absorption edge. Superlattice peaks 1/2<1,1,1> have been observed in PMN by electron diffraction and were used in support of a two-phase Nb/Mg ordering model to explain the relaxor ferroelectric behavior of PMN. In that model the peak arises because of 1:1 Mg/Nb ordering, and the system phase separates into the micro-domains of Mg/Nb ordered phase and the Nb rich phase. However, such a phase segragation would produce huge charge imbalance and electrostatic energy cost. On the other hand, ordering of alternating layers of Nb and $Mg_{2/3}Nb_{1/3}$ in the <111> direction is more likely. In this case the mixed layer would be chemically disordered with the sites randomly occupied by Mg and Nb.

In the previous experiment Teslic, Egami and Vakhrushev observed that Nb heavily contributed to the 1/2 <1,1,1> peak, which is consistent with the idea of Nb/Mg, or $Nb/(Mg_{1/3}Nb_{2/3}$, chemical ordering. The intensity of superlattice diffraction intensity can be explained by oxygen participation, since O tends to move toward Nb^{5+} which is smaller and higher in valence. At the same time, Pb atoms are displaced toward Mg atoms, since Pb-Mg repulsion is weaker than the Pb-Nb repulsion. These Pb and O displacements alternates from one (1,1,1) layer to another in the zone-center ferroelectric displacements.

In this experiment small Pb contribution to the superlattice peaks was observed. Even without the detailed quantitative analysis we found this observation to be in agreement with the above analysis. Therefore, we propose that frustration between the local antiferroelectric tendency and the global ferroelectric tendency for Pb drives the system to the relaxor ferroelectric state, just as the mixture of ferromagnetic and antiferromagnetic interactions results in a spin-glass behavior.

* Work at the University of Pennsylvania was supported by the Office of Naval Research through N00014-91-J-1036.

Structural Study of Giant Magnetoresistance Effect in La-Ca-Mn-O Epitaxial Films | X18A

T. S. Tsai (NCHU, Taiwan), M.Y. Chen(NTU, Taiwan), M.C. Shih (NCHU, Taiwan)

Recently a considerable attention was attracted to the perovskite Mn oxides due to a giant magnetoresistance response in these materials. Since the reported magnetoresistance ratio in epitaxial grown La-Ca-Mn-O films are much larger than metallic materials or bulk peroviskite structured oxides, therefore we intend to study the possible relation between the MR effect and the epitaxial grown films. The object of this experiment is to investigate whether the structures of deposited films will depend on the films' thickness as its magnetroresistance properties do. Samples examined were prepared with same nominal composition but in various thickness. Experiments were carried to exam structures both parallel to the surface and normal to the surface. Since the substrate ($LaAlO_3$) has smaller lattice constant (≈3.79Å) than the bulk La-Ca-Mn-O (≈3.89Å) polycrystalline structure, therefore, deposited films were expected to have larger lattice constant in the z direction if the substrates do imposed strains on the film. However, no significant shift in the films' peak positions were observed. Oscillatory diffraction intensities can be clearly observed alone the (00l) direction in every samples prepared and these information insure the quality and the uniformity of deposited films. In-plane diffraction data roughly support this observation that films' peaks are quite different from the substrate's in plane peak. Nonetheless, the deposited films all show the same four fold symmetry as the substrate's structure. Although there is no obvious difference in the films' structure as their thickness increase, any possible subtle feather is still under analysis.

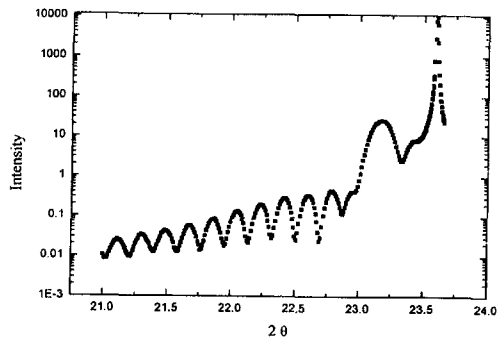


Figure 1. (001) diffraction data of a 600Å thick La-Ca-Mn-O film on $LaAlO_3$ substrate.

Epitaxial Structures of Butane and Hexane Monolayers Adsorbed on a Ag(111) Surface *	X18A

Z. Wu (U. of Missouri-Columbia), S. N. Ehrlich (Purdue U.), B. Matthies, K. W. Herwig, and H. Taub (U. of Missouri-Columbia)

Synchrotron x-ry diffraction has been used to study the structure of butane (n-C_4H_{10}) and hexane (n-C_6H_{14}) monolayers adsorbed on a single-crystal Ag(111) surface. For both monolayers, two Bragg peaks are observed in plane at fixed azimuths with respect to the Ag(10) direction, suggesting a higher-order commensurate phase. Assuming a herringbone structure as found for these monolayers on a graphite basal plane surface[1,2] allows indexing the peaks as the (20) and (11) of the hexane monolayer. Once indexed and assuming three monolayer domains separated by 120°, we can use the azimuthal angle between the two peaks and their radial position in reciprocal space to conclude that the unit cells of both monolayers are slightly oblique. In the case of butane, the peak positions are found to shift azimuthally by ~0.5° and the film to compress slightly as the coverage is increased from one to three layers; but the unit cell remains oblique with an included angle in the range 84-85°.

We have measured the temperature dependence of the butane monolayer (20) and hexane monolayer (21) peak positions both in the radial (Q_{par}) and transverse (theta) directions. In the left-hand figure, we see that the butane monolayer expands by ~0.3% upon heating from 85 K to the melting point. Concomitant with this expansion, the monolayer rotates 0.25° toward the Ag(10) azimuth. A similar rotation was also observed for the hexane monolayer as shown in the figure on the right. We suggest that this phenomenon may be an example of the Novaco-McTague effect in an elastically anisotropic molecular monolayer.[3]

[1]K. W. Herwig, J. C. Newton, and H. Taub, Phys. Rev. B **50**, 15287 (1994).

[2]H. Taub, in *The Time Domain in Surface and Structural Dynamics*, NATO ASI, Vol. 228, Ser. C (Kluwer, Dordrecht, 1988), p.467.

[3]A. D. Novaco and J. P. McTague, Phys. Rev. Lett. **38**, 1286 (1977); J. P. McTague and A. D. Novaco, Phys. Rev. B **19**, 5299 (1979).

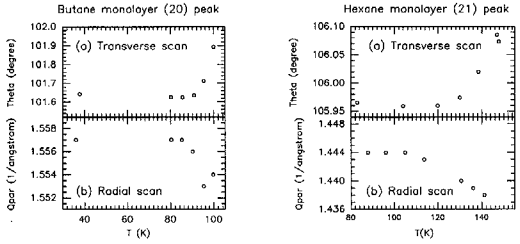


Figure 1.

* Supported by NSF Grant Nos. DMR-9011069 and DMR-9314235, the PRF Fund of the ACS, and DOE Grant No. DE-FG02-85ER45183 of the MATRIX PRT at the NSLS.

Structure and Growth of n-Alkane Films Adsorbed on the Ag(111) Surface *	X18A

Z. Wu, J. Wang (U. of Missouri-Columbia), S. N. Ehrlich (Purdue U.), B. Matthies, K. W. Herwig, and H. Taub (U. of Missouri-Columbia)

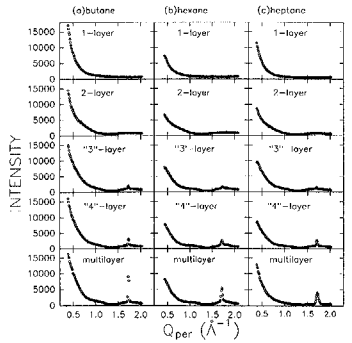
We have continued our study of the structure of butane (n-C_4H_{10}), hexane (n-C_6H_{14}), and heptane (n-C_7H_{16}) films adsorbed on a single-crystal Ag(111) surface. From the two Bragg peaks observed for both the butane and hexane monolayers, we infer a herringbone (HB) arrangement of these molecules which have an even number of carbon atoms. The unit cell appears to be slightly oblique rather than the rectangular cell originally assumed as is found for the HB phase of these monolayers on graphite.[1,2] However, for the odd-numbered heptane molecule, the single monolayer Bragg peak is consistent with a rectangular-centered structure as found on graphite.[3] For all three monolayers, the Bragg peaks have a fixed in-plane angle with respect to the Ag(10) azimuth, indicating a higher-order commensurate phase on the Ag(111) surface.

The growth mode of the odd-carbon-numbered heptane film on the Ag(111) substrate has been compared with that of even-numbered butane and hexane films. All three films show the same coverage dependence of the specular reflectivity (see figure). Above two layers, a two-component lineshape emerges: a smoothly varying component attributed to the film and a sharp Bragg peak from the bulk particles having a specific crystal plane parallel to the surface. Apparently, a bulk plane is selected in which the molecular orientations are most compatible with those of the film. Thus we infer the same quasiepitaxial growth mode for the heptane film as for butane and hexane on Ag(111) and for butane on graphite.[2] Our results suggest that it may be a general feature of alkane adsorption on solid surfaces.

[1]H. Taub, in *The Time Domain in Surface and Structural Dynamics*, NATO ASI, Vol. 228, Ser. C (Kluwer, Dordrecht, 1988), p.467.

[2]K. W. Herwig, J. C. Newton, and H. Taub, Phys. Rev. B 50, 15287 (1994).

[3]B. Matthies, K. W. Herwig, and H. Taub, unpublished.



* Supported by NSF Grant Nos. DMR-9011069 and DMR-9314235, and DOE Grant No. DE-FG02-85ER45183.

Structural Studies of Self-Assembled Alkynyl Thin Film Materials * | X18A

C.-M. Yam, A. K. Kakkar (McGill U.), A. Richter and P. Dutta (Northwestern U.)

An evaluation of the structure of molecularly self-organized thin films containing long chain rigid-rod alkynyl and dialkynyl chromophores via exclusive pi-pi interactions, is an essential and crucial step for any device applications based on such systems in the field of optoelectronics, conductivity, photoresists etc. We have recently developed efficient synthetic methodologies to such supramolecular structures molecularly self-assembled on inorganic oxide surfaces. Monolayers of a variety of alkynyl and dialkynyl chromophores with varied chain lengths and acetylenic microstructures were prepared on single crystal silicon wafers (1"x3" single side polished, 95-105 mils thick). These thin films were first analyzed by in-house ellipsometry, followed by X-ray reflectivity studies on the X-18A beamline at the NSLS synchrotron facility. We are still analyzing the data from our last trip to NSLS (Sept. 3-10). A preliminary scanning of the data suggests that, in general, there is a good agreement in the thicknesses from X-ray reflectivity and ellipsometry measurements. Our ultimate goal is to study surface topochemical polymerization in these oriented alkynyl mono- and multilayered structures. Two of the major requirements for the latter process are orientation of alkynyl chromophores at an angle to the surface, and uniformity. X-ray reflectivity studies in combination with ellipsometry and FTIR-ATR are invaluable techniques to address these issues. We have also been interested in determining the effect of X-rays on the alkynyl thin films, since alkynyl chromophores are subject to radiation damage. In our future trips to BNL, we shall concentrate on the study of the structure of dialkynyl thin film assemblies before and after topochemical polymerization, to understand the mechanistic details of this phenomenon, and to develop a rational approach to materials based on alkynyl thin films.

* Supported by Natural Sciences and Engineering Council of Canada.

The Structure of Diffuse Scattering in the Reciprocal Space of Al-Pd-Mn Quasicrystal. | X18A

Y. Zhang, R. Colella (Purdue U.), S. Ehrlich (NSLS), S. Kycia, A. Goldman, (Iowa StateU.)

Diffuse scattering has been measured along several planar sections of reciprocal space, perpendicular to a two-fold axis, in the neighborhood of the (0 4 6 0 4 6; M = 336, N = 208) Bragg reflection. The contour plots display the expected 2-fold symmetry, and are elongated along the H direction (Fig. 1). Very similar patterns are obtained at low temperature (20 K). Since icosahedral quasicrystals are supposed to be isotropic [P.S. Spoor, J. D. Mainard, and A. R. Kortan. Phys. Rev. Letters **75**, 3462 (1995)] the observed anisotropy can be used to obtain the polarization directions of the atomic displacements responsible for the observed diffuse intensity. At large distances from the Bragg reflection, the contours split into "lobes" (Fig. 2). Peaks of diffuse intensity, as sharp as Bragg reflections, are found at even further distance from the Bragg reflection. (for example, at $\Delta Q = 0.0817$ Å^{-1}). These are probably Bragg reflections corresponding to large values of the Miller indices. The temperature dependence of one particular such reflection, called peak B, is similar to that of a Bragg reflection, indicating the non-thermal origin of the peak. While the intensity near a Bragg reflection decreases like $1/q^2$ with a good approximation, a somewhat different dependence ($1/q^{2.2}$) is observed near peak B.

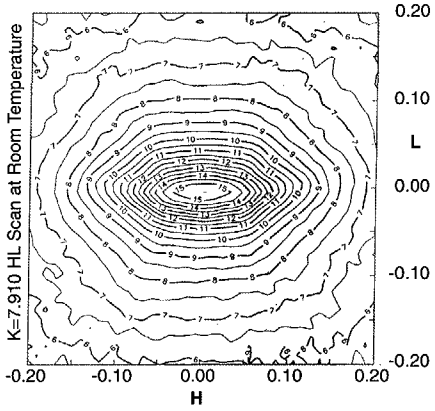


Figure 1.

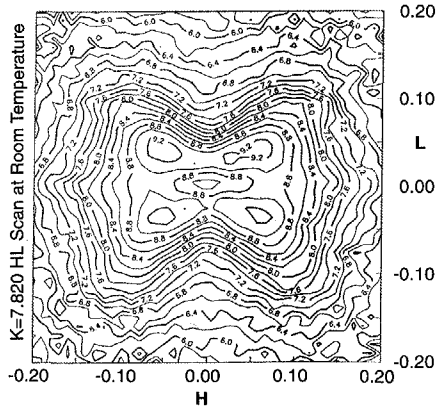


Figure 2.

Photocatalytic Reduction of Heavy Metal Ions on Derivatized Titanium Dioxide Nano-Particle Surface Studied by EXAFS	X18B

L. X. Chen, T. Rajh, D. M. Tiede, P. A. Montano and M. C. Thurnauer (ANL)

Photoirradiation on semiconductor particles, such as TiO2, creates charge separation on the particle surfaces. Consequently, the TiO2 particles with such a photoinduced charge separation act as either electron donors or acceptors to reduce or oxidize materials in the surrounding media. TiO2 colloid nanoparticles, especially surface-derivatized TiO2 particles, present different electronic properties than those of the bulk material. In some cases, the photoinduced redox reactions occur more effectively. This redox function has very important applications in environmental remediation and cleanup. However, the reaction mechanisms for the enhanced reactivity on the surfaces of the nanoparticles of TiO2 are not well understood. We have conducted in- situ EXAFS studies at the K-edge of titanium as well as the absorption edges of the heavy metals to extract structural information of TiO2 surface and metal ion surroundings in the photoreduction processes. As the first step towards characterization of the surface structure, we characterized the structures for the interior and surface TiO2 respectively by comparing the EXAFS spectra of TiO2 particles of different sizes. We have identified systematic changes on the pre-edge structures and the Fourier transformed EXAFS features according to the sizes of the TiO2 particles. These changes are the indications of increasing surface lattice disorder as the particle size gets smaller. In addition, we monitored the metal ion photoreduction of Cu+2 and Hg+2 on TiO2 colloid surface with and without surface-derivatization. The oxidation state of the metal ions in these processes can be identified directly by XANES at respective metal absorption edges. Derivatization of TiO2 surface by alanine enhances the efficiency of Cu+2 photoreduction compared to neat TiO2. We have identified the complex of alanine and Cu+2 by EXAFS and measured time dependence of Cu0 production with photoillumination of TiO2. Part of the results are shown in Fig. 1 and 2, which not only positively verified the formation of Cu0, but also indicated multisteps of forming the metal clusters. Similar study was also conducted on Hg+2 solution. The structure and function relationship of the species involved in photoreduction will be discussed.

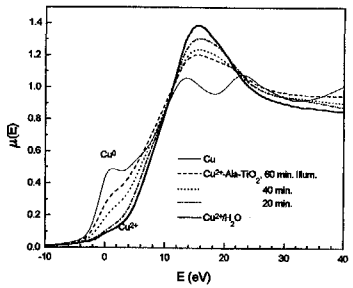


Figure 1. XANES of Cu+2 as a functyion of illumination time in the TiO2 catalyzed photoreduction with alanine derivatization.n

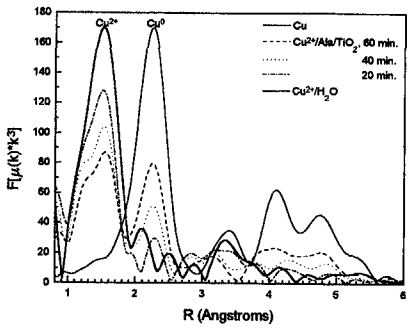


Figure 2. FT-EXAFS of Cu+2 on during the photoreduction on alanine derivatized TiO2 colloid surfaces.

Structure of Supported Alkali and Alkaline Earth Modified Catalysts by X-ray Absorption Spectroscopy	X18B

E.J. Doskocil, S. V. Bordawekar, and R. J. Davis (U. of Virginia)

Alkali and alkaline earth oxides, both alone and on supports, are known to be solid base materials. However, very little is known about these materials despite their potential for many industrially important reactions. In an attempt to explore solid base structure-property relationships, we have been using *in situ* x-ray absorption spectroscopy (EXAFS and XANES) to determine the atomic structure near rubidium and strontium supported on a variety of carriers.

X-ray absorption studies were performed at the Rb K edge on 5 wt% rubidium supported materials of various acidity. The XANES for these materials, as seen in Figure 1, varied on supports like carbon, silica, alumina, magnesia, and titania after heating to 773 K in flowing helium and cooling to 77 K. Analysis of the radial structure functions revealed that the Rb-O distance correlates with support electronegativity, with the Rb-O distance being 2.94 Å for Rb on basic MgO and 2.80 Å for Rb on acidic SiO_2. These results suggest that surface compounds have been formed by the incorporation of the alkali. Additional *in situ* XAS investigations involving the local structure near the rubidium atoms were conducted in the presence of 2-propanol in helium at a reaction temperature of 573 K for rubidium supported on carbon and alumina. The gaseous 2-propanol environment significantly affected the XANES for Rb on carbon by causing a narrowing of the white line, contrasting the negligible effect of adsorption observed for Rb on alumina.

Results from XAS associated with the Sr K edge for 5 wt% strontium indicate that the structure near strontium is largely unaffected by the support environment. The radial structure functions shown in Figure 2 contain two peaks for Sr on MgO. The peak at 2 Å is associated with Sr-O and the one at 4 Å corresponds to either Sr-Sr or Sr-Mg distances. The second feature at 4 Å is less prominent in the case of the carbon sample and is absent in the SiO_2 sample. The Sr-O interatomic distances obtained through curve fitting are similar to that of the bulk oxide. Apparently the support plays a more crucial role in the structural rearrangement of the supported alkali than for the alkaline earth.

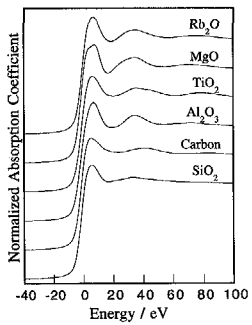


Figure 1. Rb K edge of various Rb modified supports.

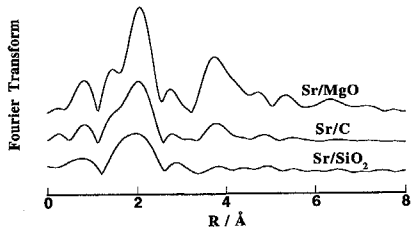


Figure 2. Radial structure function of various Sr modified supports.

Stabilization of Pd^{2+} Ions on H-ZSM-5 and Other Acidic Supports During the Selective Reduction of NO by CH_4 *	X18B

D. E. Resasco, S. Stagg, W. Alvarez, and A. Ali (U. of Oklahoma)

The selective reduction of NO by methane has been studied on a series of Pd Catalysts. When supported on non-acidic materials, palladium is totally unselective for the conversion of NO and very active for the combustion of methane. By contrast, low-loading Pd catalysts supported on acidic (protonic) materials (H-ZSM-5, H-Mordenite, sulfated zirconia) exhibit much higher selectivity.

X-ray absorption studies (XANES and EXAFS) were conducted on several Pd catalysts before and after the reduction of NO in the presence of oxygen. These studies have demonstrated that, upon exposure to the reaction mixture (CH_4 + NO + O_2), Pd gets oxidized. The morphology of the oxidized Pd species strongly depends on the metal loading and the acidity of the support. On low Pd loading catalysts over acidic supports, the metallic Pd particles, initially present, are rapidly transformed in Pd^{2+} ions by the reaction mixture. By contrast, on the non-acidic materials, the Pd particles are transformed into PdO clusters. These clusters have high catalytic activity for the methane combustion, resulting in low SCR selectivities.

* This work was supported in part by the Donors of the Petroleum Research Fund administered by ACS

Observation of Local Structural and Electronic Changes Accompanying Photodoping of $YBa_2Cu_3O_{6+x}$	X18B

T. A. Tyson, J. F. Federici, D. Chew, W. Savin (NJIT), L. Furenlid (NSLS), and W. Wilber (ARL)

It was discovered by Kudinov *et al.* [1] that changes occur in the normal state conductivity of oxygen deficient $YBa_2Cu_3O_{6+x}$ (YBCO) on exposure to optical radiation (photodoping). The resistance was found to decrease by as much as 50 % with a maximum near x=0.38. This enhanced photoconductivity has been explained by two primary mechanisms, oxygen ordering and F-center formation, based on indirect measurements and qualitative arguments. Analysis of our c-polarized x-ray absorption measurements on thin films has revealed that photodoping of YBCO produces a local distortion of the CuO_x chains. The axial Cu(1)-O(4) bond distribution splits into two components (see also Fig. 1) and the corresponding Cu-O correlations are found to be enhanced. In addition, changes in the XANES features indicate that a transfer of hole density into the CuO_2 planes accompanies photodoping. These results constitute the first direct structural evidence of photoinduced oxygen ordering and charge transfer in this system.

[1] V. I Kudinov*et al.*, Phys. Rev. B 47, 9017 (1993).

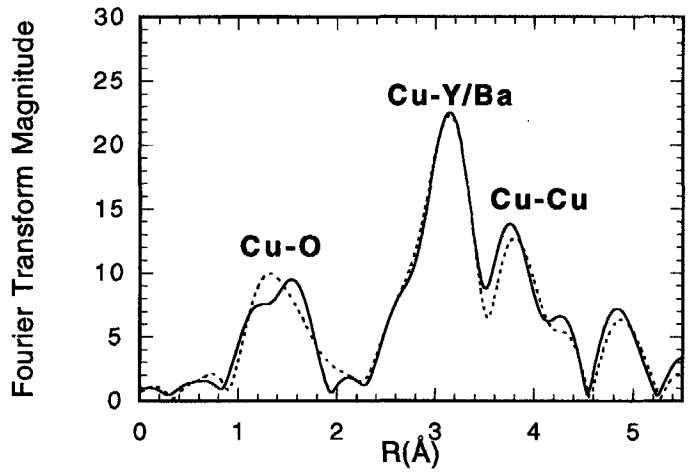


Figure 1. Magnitude of the Fourier transform of k^3 * XAFS for k = 2.8 - 11.7$Å^{-1}$ for normal (solid line) and photodoped (dotted line) $YBa_2Cu_3O_{6.4}$ system. The first peak (1-2 Å) corresponds to the c-axis Cu-O bond distribution.

Characterization of Phenyl Cuprate Solutions Using XANES | X19A

H. Huang, J. Penner-Hahn (U. Michigan)

Phenyl-copper reagents permit facile transfer of aryl groups in organic synthesis[1]. Of particular utility are solutions with a 1:1 ratio of PhLi:CuI. Although the crystal structures of several phenyl-copper(I) compounds are now available, the solution structures of phenyl lithium/CuI mixtures remain poorly defined. We have previously measured EXAFS data for solutions of PhLi+CuI. These data were consistent with the presence of the crystallographically characterized[2] $[Cu_5Ph_6]^-$ ion in solution. In order to characterize the stoichiometry of this species and to explore the possibility that other phenylcuprates might exist in solution, we have completed an EXAFS titration of the PhLi+CuI system. The XANES data for PhLi:CuI ratios of 0.6 to 1.2 are shown in Fig. 1. There are three isosbestic points, demonstrating that only two spectroscopically distinguishable species contribute to the XANES over this concentration range, one with Ph/Cu $\geq$ 1.2, the other with Ph/Cu $\leq$ 0.6. The titration data for PhLi:CuI ratios of 1.2 to 2.0 are shown in Fig. 2. Once again, these are consistent with only two distinguishable absorbing species, one with Ph/Cu $\geq$ 2.0, the other with Ph/Cu $\leq$ 1.2. Since the spectra are different over the two concentration ranges, the overall solution system must have at least three distinct species, one with a Ph/Cu ratio $\leq$ 0.6, one with a Ph/Cu ratio 2.0 and one with a Ph/Cu of 1.2. These results provide a substantially improved description of the solution structure: At intermediate PhLi:CuI ratios, the dominant ion is solution is $[Cu_5Ph_6]^-$; EXAFS data (not shown) suggest that the species with Ph/Cu $\geq$ 2.0 is most consistent with the $[CuPh_2]^-$; The identity of the species with Ph/Cu $\leq$ 0.6 remains uncertain. These data provide direct evidence that there is no significant concentration of a species with a Ph/Cu ratio 1.0 in these solutions, in contrast with the standard picture of phenylcuprate chemistry.

1. Posner, G. H. *An introduction to Synthesis Using Organocopper Reagents*; Wiley: New York, N. Y., 1980. 2. Edwards, P. G.; Gellert, R. W.; Marks, M. W.; Bau, R. *J. Am. Chem. Soc.* **1982**, *104*, 2072.

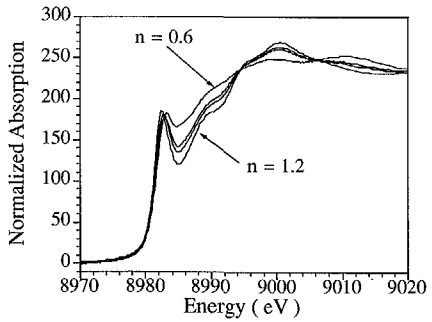


Figure 1. XANES spectra for titration of CuI with PhLi for PhLi:CuI < 1.2

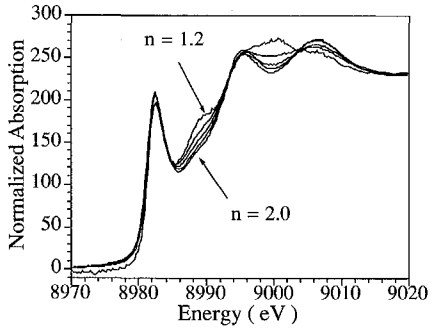


Figure 2. XANES spectra for titration of CuI with PhLi for PhLi:CuI > 1.2

Zn Speciation in Developing *Xenopus* Embryos as Detected by XANES * | X19A

K. Peariso, C. van Huis, R. Denver, and J. Penner-Hahn (U. Michigan)

Zinc plays a crucial role both in development and in numerous other biochemical processes. Consequently, eggs that are fertilized and develop in the absence of additional maternal nutrition must contain, at the time of fertilization, sufficient Zn (and other trace metals) for complete development. Thus, zebrafish and *Xenopus* (the African clawed toad) eggs both contain ca. 1 mM Zn. We have shown previously [1] that the XANES spectra for fertilized zebrafish eggs show characteristic changes as a function of time after fertilization. We have now extended this work to *Xenopus*. The relatively large diameter (ca. 1 mm) of *Xenopus* eggs has permitted us to make measurements on single eggs with greater temporal resolution than was possible in the past. We find (Figure 1) that there are substantial changes in the average Zn environment in *Xenopus* as a function of time after fertilization. It is notable that these changes are complex and appear to reflect the formation of multiple Zn sites. This illustrates that we are observing a more complex process than simple consumption of a Zn binding protein. Detailed analysis of these data is in progress.

[1] Walrath, L.; Tierney, D.; Penner-Hahn, J.; Berg, J., manuscript in preparation.

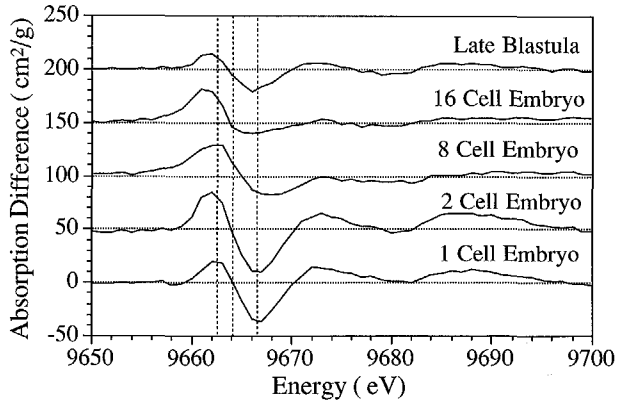


Figure 1. Time-dependent Zn XANES spectra of *Xenopus* eggs following fertilization. Spectra shown are difference spectra relative to an unfertilized control sample. Vertical dashed lines at 9662.5 eV, 9664.1 eV, and 9666.6 eV mark the critical points for the 1 cell difference spectrum, illustrating the change in spectra with time.

* Supported in part by the NIH, Grant GM-38047

Structural Characterization of Ga-Substituted Ferredoxins * — X19A

J. Penner-Hahn, K. Peariso (U. Michigan) E. Vo, H. Liu and J. Germanas (U. Houston)

Ferredoxins are Fe/S electron transport proteins. In many cases, the Fe can be removed and replaced by a variety of other metals. Gallium replacement is attractive from the perspective of giving a protein that is amenable to characterization by NMR. The difficulty, however, with Ga substiution is that it is difficult to confirm that Ga has been subsituted into the correct location within the protein.

Previous work [1] has shown that substitution of Ga into the Fe_2S_2 site in *Pseudomonas putida* ferredoxin gives rise to a mononuclear Ga ferredoxin, with $Ga(SR)_4$ ligation. More recent work has shown that the Fe_2S_2 ferredoxins from *Anabaena* and *Trichomonas vaginalis* can be substituted under conditions that place two Ga ions into each protein [2]. We have now used gallium K-edge EXAFS to determine the structure of the Ga substituted ferredoxins from *Anabaena* and *T. vaginalis*.

The Fourier transform of the resulting EXAFS data is shown in Fig. 1. These data are dominated by a large Ga-S peak at ca. 2.3 Å. In addition, there is a characteristic second shell peak at ca. 3 Å, which is attributable to a Ga-Ga interaction. Detailed analysis of these data is in progress.

[1] S. Kazanis, T.C. Pochapsky, T.M. Barnhart, J.E. Penner-Hahn, U.A. Mirza, B.T. Chait, *J. Am. Chem. Soc.*, **117** (1995) 6625-6626.[2] Germanis, J. et al., *J. Am. Chem. Soc.* **118** (1996) in press.

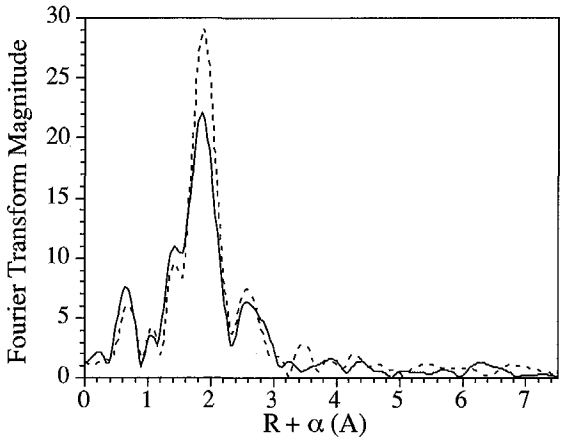


Figure 1. FT of EXAFS data for Ga-substituted ferredoxins. Solid line, *T. vaginalis*; Dashed line, *Anabena.*

* This work was supported by NIH Grant R01-GM-38047 and by the Texas Advanced Research Program.

XANES Studies of Oxidation States of S in Humic Substances From Different Environmental Settings — X19A

K. Xia, F. Weesner, and W. F. Bleam (U. of Wisconsin-Madison), P. R. Bloom, and U. L. Skyllberg (U. of Minnesota)

Sulfur K-edge X-ray absorption near-edge structure spectroscopy (XANES) was used to illustrate the existence of multiple sulfur oxidation states in humic substances. Each oxidation state of sulfur in humic substances from aquatic and terrestrial environment was identified and the relative content of sulfur at each oxidation state was estimated. Our experiment results provide direct evidence for the existence of six major sulfur functional groups in humic substances studied: sulfhydryl or sulfides/polysulfides, thiophenes, sulfoxides, sulfites/sulfones, sulfonates, and sulfates. The results appear to reflect the environmental settings where the humic substances originally formed. The percentage of the most reduced organic sulfur (sulfhydryl or sulfide/polysulfide) in humic substances follow the sequence: aquatic sample higher than organic soil and higher than mineral soil. The percentage of most oxidized sulfur (sulfate ester) is the highest in humic substances from mineral soil, and the lowest in aquatic humic substances. Our study showed that there is great potential of using XANES to study the geo-transformation of sulfur in the environment. (Submitted to *J. of Soil Sci. Soc. of Am.*, 1996)

Structure of Ti in TiO_2-SiO_2 Catalysts *	X19A

J. Zhao, J. Rockwell, F. E. Huggins, F. Lu, and G. P. Huffman (U. of Kentucky)

Mixed metal oxide catalysts are generally regarded as a solid solution of two oxides in which a small amount of minor oxide is incorporated into the major oxide by cation substitution. The generation of acidic sites is caused by an excess of positive or negative charge in binary oxide structure.[1]

XAFS measurements were conducted for a series TiO_2-SiO_2 catalysts prepared by coprecipitation over a range of Ti/Si ratio and the results were compared with several different forms of TiO_2. The XANES for an initial precipitate of TiO_2 (no SiO_2) exhibits an enhanced pre-edge peak, in similar fashion to that for ferrihydrite.[2,3] For ferrihydrite, the phenomenon is attributed to tetrahedral Fe^{3+} sites at the nanoparticle surface. After calcination, the intensity of the peak is reduced due to the formation of crystalline TiO_2 (anatase). Although the main spectral features of the TiO_2-SiO_2 resemble those for rutile TiO_2, the XANES shows a stronger pre-edge peak while the Fourier transform shows reduced peak heights at d¿2A, indicating the presence of small rutile TiO_2 particles. Therefore instead of a solid solution, the TiO_2-SiO_2 catalyst may be described as a composite in which small TiO_2 particles are embedded in a SiO_2 medium.

[1] K. Tanabe, Solid Acids and Bases, Academic Press, New York (1970). [2] J. Zhao, F. E. Huggins, Z. Feng, F. Lu, N. Shah, and G. P. Huffman, J. Catal, 143, 499 (1993) [3] J. Zhao, F. E. Huggins, Z. Feng, and G. P. Huffman, Clays & Clay Minerals, 42, 737 (1994)

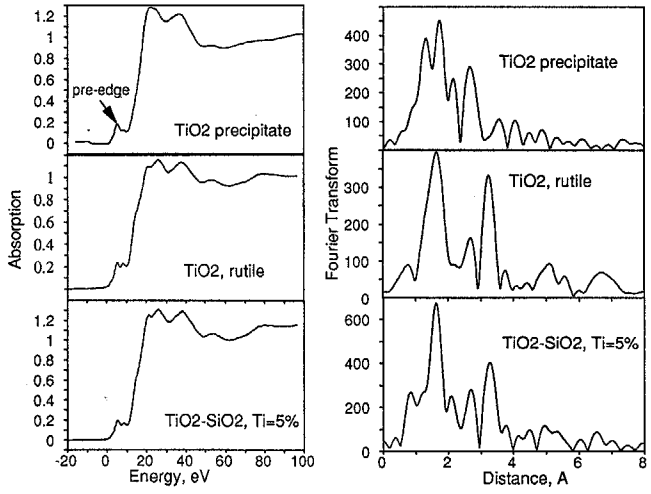


Figure 1.

* This work was supported by DOE contract No.DE-FC22-93PC3035.

Sychrotron White Beam X-ray Topography Investigation of Influence of Annealing on CdZnTe Substrate *	X19C

Y. Chen, M. Dudley (SUNY Stony Brook), D. R. Rhiger (Hughes Santa Barbara Research Center)

CdZnTe, a technologically important II-VI compound semiconductor, is the leading candidate material for use as substrates for the growth of HgCdTe layers. Since structural defects can propagate into a newly grown layer during epitaxial growth, it is important to improve the structural perfection of CdZnTe substrates. Due to the retrograde solubility of Te in solid CdZnTe resulting in the supersaturation of Te during cooling, Te precipitates are often observed in CdZnTe crystals. Post-growth annealing under Cd vapor is often performed to reduce the density of these precipitates. Synchrotron White Beam X-ray Topography has been used to study the influence of annealing on CdZnTe substrate under Cd vapor overpressure. Figure 1 and 2 show corresponding x-ray topographs recorded in reflection geometry of two samples which are cut from the same original CdZnTe wafer. These samples are unannealed, and annealed at high temperature, respectively. Te precipitates are clearly observed as two kinematic lobes of dark contrast positioned in $\pm$g directions seperated by a large lattice distortion region showing no contrast in these figures. X-ray topographs revealed that the size and density of Te precipates is strongly influenced by the annealing. A low density and small sizes of Te precipitates are observed in the annealed samples. For the unannealed sample, high density and larger sizes of Te precipitates are observed. Other defects such as twins, subgrain boundaries are also revealed in these figures.

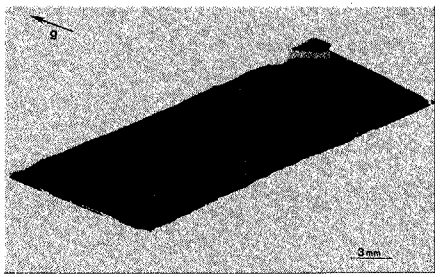


Figure 1.

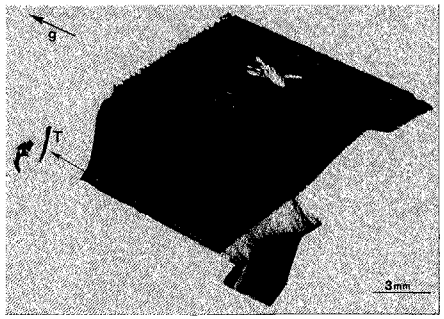


Figure 2.

* Work performed on the Synchrotron Topography Project, Beam Line X-19C, and supported by Hughes Santa Barbara Research Center.

Characterization of Processing Induced Defects in Silicon Device Using Synchrotron White Beam X-ray Topography	X19C

Y. Chen, W. Huang, W. Chen, M. Dudley (SUNY Stony Brook)

Processing induced defects play an important role in silicon device yield. Synchrotron White Beam X-ray Topography has been applied to nondestructively investigate such defects in devices fabricated on (111) Si single crystals. By using a specially designed scanning system, defect distributions with respect to device positions in 3 inch wafers can be clearly revealed. Precipitates, individual dislocations and slip bands generated by thermal and mechanical stress induced during thermal oxidation are observed and characterized. In Figure 1 and 2, transmission topographs recording by using $(\bar{1}3\bar{1})$ and $(3\bar{1}\bar{1})$ refections show two sets of slip bands S_1, S_2 running parallel to the [211], [112] direction, respectively. It is also observed that S_1 is out of contrast on the $(3\bar{1}\bar{1})$ reflection and S_2 is out of contrast on the $(\bar{1}3\bar{1})$ reflection. By using the g·b=0 criterion, the Burgers vectors of dislocations in two slip bands are determined to be parallel to the $[0\bar{1}1]$ and $[1\bar{1}0]$ directions, respectively. In these figures, we also can see some white areas which are actually regions of zero intensity caused by orientation contrast.The areas are associated with processing induced strain, which can lead to dislocation generation. The influence of these defect structures on device performance is being investigated.

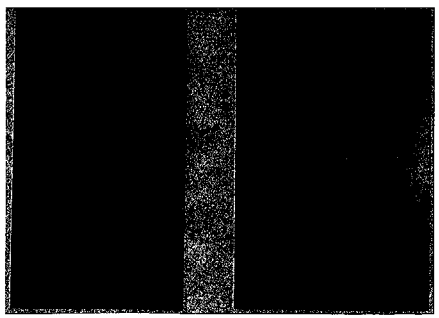


Figure 1.

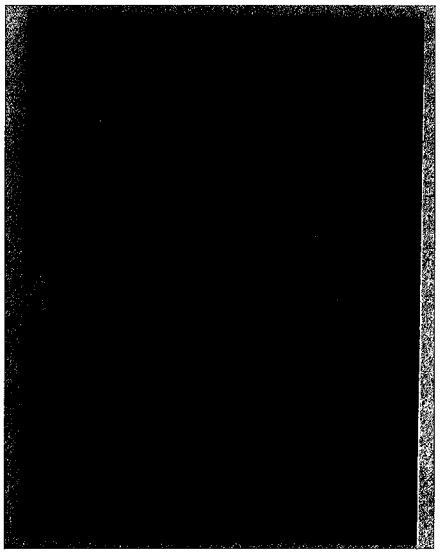


Figure 2.

Characterization of Structural Defects in Microgravity Grown CdZnTe Single Crystals Using Synchrotron White Beam X-ray Topography II *	X19C

H. Chung, B. Raghothamachar, M. Dudley, and D. J. Larson, Jr. (SUNY Stony Brook)

A systematic study of defect structures in the ten wafers sliced from GCRC 2/USML-1 revealed a very high structural perfection in the region free from wall contact, while a pronounced twin structure was evident in wall contact regions. Figure 1 is a reflection topograph recorded from wafer 7. In the wall contact region, a twin (T_1) running across the wafer was observed. Systematic investigation of the position of this twin in all the ten wafers sliced from GCRC 2 enabled one to reconstruct the twin configuration in this boule. The result is shown in Figure 2. It is worth noting that this twin was nucleated from the shoulder region and propagated through the boule during crystal growth. The twinned region occupies approximately 35 percent of the crystal volume. In addition, other two twins (T_2 and T_3) nucleated from wall contact peripheral regions were also revealed on Figure 1. In addition, an individual grain (G), nucleated from the partial wall contact region, is also observed. This indicates that the magnitude of stresses associated with wall contact can be very large, giving rise to the formation of a single grain separated from the twin oriented region (T_1) by a curved, high angle grain boundary. In the matrix, which is solidified without wall contact, no formation of twins is observed. The distribution of these twins strongly indicated that they were nucleated during crystal growth to relieve stresses associated with wall contact.

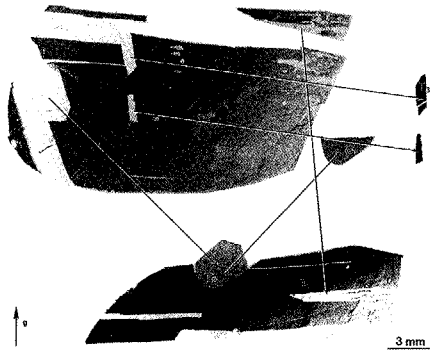


Figure 1.

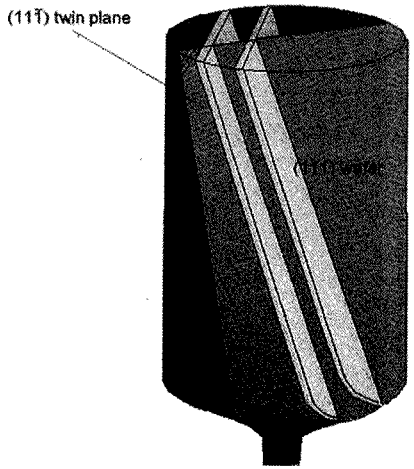


Figure 2.

* Work performed on the Stony Brook Synchrotron Topography Facility, Beamline X-19C, and supported in part by NASA under contract No. NAS8-38147.

Investigations of Dislocation Distributions in Microgravity Grown CdZnTe Single Crystals Using Synchrotron White Beam X-ray Topography *	X19C

H. Chung, B. Raghothamachar, M. Dudley, and D. J. Larson, Jr. (SUNY Stony Brook)

X-ray topographic observations revealed an uneven distribution of dislocations between the matrix and twin oriented regions. Figure 1 is a highly magnified reflection X-ray topograph recorded from the wafer 7/GCRC 2 showing the detailed defect structures. In the twin oriented region (T_1), a well defined mosaic structure was revealed, while individual dislocations were clearly discerned in the matrix. Dislocation mosaic structures in CdZnTe crystals can be generated by dislocation gliding and climbing during post solidification cooling processes because supersaturated vacancies and thermal stresses induced during crystal cooling can facilitate dislocation movements to form an energetically preferred configuration (Mcdevitt et al, Mater. Lett. 4, p.451 (1986)). On the other hand, the twins are produced during growth so that they are created before the generation of the dislocation mosaic structures. The twin boundaries may act as barriers to the propagation of dislocations so that no formation of mosaic structure was observed in the matrix.



Figure 1.

* Work performed on the Stony Brook Synchrotron Topography Facility, Beamline X-19C, and supported in part by NASA under contract No. NAS8-38147.

Studies of Defect Structures in Microgravity Grown CdZnTe Single Crystals Using Synchrotron White Beam X-ray Topography I *	X19C

H. Chung, B. Raghothamachar, M. Dudley and D. J. Larson, Jr. (SUNY Stony Brook)

Two flight samples (GCRC 1 and GCRC 2) were grown during the first United States Microgravity Laboratory mission (USML-1) using the seeded Bridgman-Stockbarger method of crystal growth. Figure 1 and 2 are Laue diffraction patterns recorded from wafers 1 and 2 sliced from GCRC 1. These wafers were cut from the region encompassing the seed transition region. It is worth noting that there are two sets of diffraction patterns superimposed. Since no twin relationship between the two grains could be determined, this observation indicated that two grains were nucleated in the initial stages of growth. The first grain (G_1), which nucleated from the seed, is highly strained. On the other hand, the nucleation of a second grain (G_2) near to the ampoule wall was observed (figure 1). The newly nucleated grain showed high crystalline quality and became dominant in the subsequent stages of growth (figure 2), while the growth of the highly strained grain (G_1) was terminated. This was perhaps due to unfavorable growth conditions for the initial grain. Study of all thirteen wafers from this boule enabled a reconstruction of the grain structure in this sample to be performed. The result is shown in Figure 3.

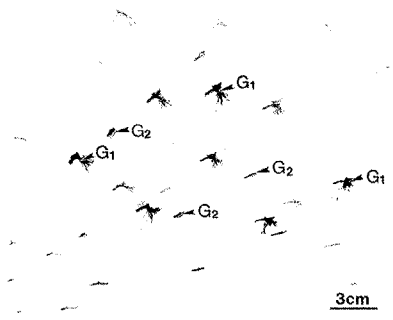


Figure 1.

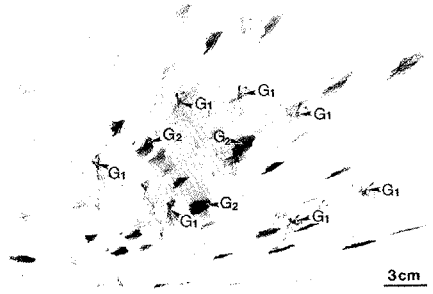


Figure 2.

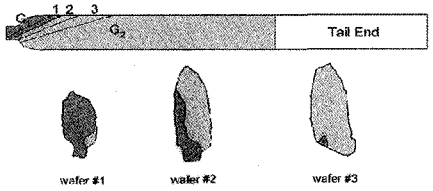


Figure 3.

* Work performed on the Stony Brook Synchrotron Topography Facility, Beamline X-19C, and supported in part by NASA under contract No. NAS8-38147.

Studies of the Influence of Cooling Rate to Defect Microstructure Development in Microgravity Grown CdZnTe Single Crystals *	X19C

H. Chung, B. Raghothamachar, M. Dudley and D. J. Larson, Jr. (SUNY Stony Brook)

Figures 1 (a) and (b) are reflection topographs recorded from a wafer sliced from GCRC 1 showing the defect structures in both the steady-state and gradient-freeze growth regions. The solidification rate of the latter is ten times larger than that of steady state growth. This change is strongly reflected by the different defect structures observed in the two regions. An X-ray topograph recorded from the gradient-freeze region [figure 1 (b)] shows a highly distorted image, indicating that this region is heavily strained. It is believed that very large axial thermal stresses can be generated by the large axial temperature gradient imposed by the rapid cooling process leading to severe deformation processes. In contrast, the crystalline quality of the steady-state growth regions (i.e., the lower part of figure 1 (a)) is significantly higher than that of the gradient-freeze growth regions. Two sets of long, straight asymmetrically distributed small angle tilt boundaries (SB_1 and SB_2), nucleated near the ampoule wall, and propagating into the interior of the wafer along the crystallographic $[10\bar{1}]$ and $[0\bar{1}1]$ directions were evident. The separation and overlapping of these images arises from different senses of tilt between the neighboring subgrains. The tilt angles, which can be estimated from the variations of image width as a function of specimen-film distance, were determined to be of the order of 30~40 arc seconds. The configuration of these small angle tilt boundaries strongly suggests the onset of both slip and dislocation polygonization processes on the $[10\bar{1}]/(\bar{1}11)$ and $[0\bar{1}1]/(\bar{1}11)$ slip systems [Durose and Russell, J. Cryst. Growth, 86, p.471 (1986)].

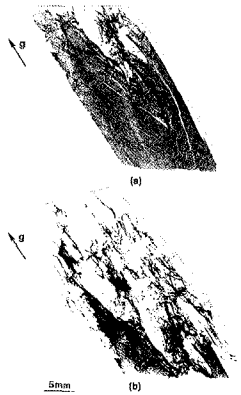


Figure 1.

* Work performed on the Stony Brook Synchrotron Topography Facility, Beamline X-19C, and supported in part by NASA under contract No. NAS8-38147.

Investigation of the Distribution and Configuration of Dislocations in Sulphur Doped InP Single crystals I *	X19C

H. Chung, W. Si, and M. Dudley (SUNY, Stony Brook), D. F. Bliss (Rome, AFB), A. Maniatty (RPI)

During crystal growth, dislocations can be generated if growth accidents such as large temperature fluctuations and compositional inhomogeneity occur. In addition, dislocation multiplication and propagation can occur if thermal stresses are introduced during the cooling process. Investigations of the distribution and configuration of dislocations are important to determine the relationship between dislocation generation and the growth conditions used. Figure 1 is a highly magnified X-ray topograph enlarged near the outer surface of the crystal where the concave interface was observed. A region of very high dislocations density is revealed by the X-ray topograph. In contrast, regions of very low dislocation density were observed in the interior of the crystal (as shown in figure 2) where the growth interface remained convex to the melt. In the MLEK growth method, the axial temperature gradient in the melt is low (20-40°C/cm) so that a small temperature fluctuation can influence the stability of crystal growth [D. F. Bliss et. al. J. Cryst. Growth, 128, p. 451]. An abrupt change in the morphology of the growth interface indicates the occurrence of a significant temperature fluctuation when the pulling process started. This can potentially upset the stability of crystal growth and lead to the high density of dislocations generated in this region to relieve large thermal stresses induced by the temperature fluctuations.

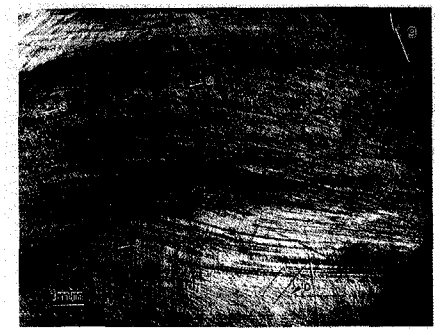


Figure 1.

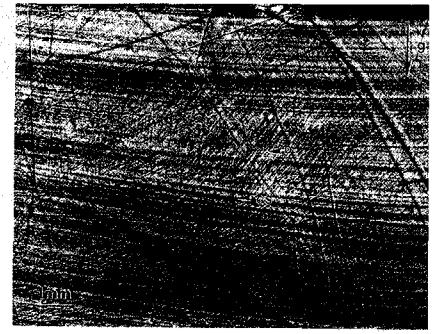


Figure 2.

* Work performed on the Stony Brook Synchrotron Topography Facility, Beamline X-19C, and supported by ARPA/AFOSR Consortium of Crystal Growth Research under Contract No. F496209510407

Investigation of the Distribution and Configuration of Dislocations in Sulphur Doped InP Single Crystals II *	X19C

H. Chung, W. Si, and M. Dudley (SUNY Stony Brook), D. F. Bliss (Rome Laboratory, AFB), and A. Maniatty (RPI)

X-ray topographic observations (figure 1 (a)) revealed numerous slip bands (**S**) nucleated from the cylindrical outer surface of the boule and propagating into the interior of the crystal. In the growth of indium phosphide, boric oxide is used as an encapsulant to prevent the decomposition of the melt. The encapsulant also reduces the radiative heat loss from the outer surface of the crystal since B_2O_3 acts as a heat shield. The maximum heat loss, therefore, occurs at the point where the hot solid material emerges from the encapsulant, which gives rise to maximum temperature gradients in this region. X-ray topographs revealed that slip bands are most likely to be nucleated at this stage to relieve the large thermal stresses. The distribution of excess resolved shear stresses in the crystal at various stages in the growth process has been calculated using an anisotropic thermo-elastic finite element model for InP single crystals. The result is shown in figure 1 (b). It is worth noting that the maximum excess resolved shear stresses are generated on the outer surface of the crystal at the point where the crystal emerges from the encapsulant. The calculated result is in good accord with the slip band distributions revealed by X-ray topography.



Figure 1.

* Work performed on the Stony Brook Synchrotron Topography Facility, Beamline X-19C, and supported by ARPA/AFOSR Consortium of Crystal Growth Research under Contract No. F496209510407.

Investigation of the Distribution and Configuration of Dislocations in Sulphur Doped InP Single Crystals III *	X19C

H. Chung, W. Si, and M. Dudley (SUNY Stony Brook), D. F. Bliss (Rome Laboratory, AFB), and A. Maniatty (RPI)

Numerous slip bands nucleated from the periphery of the crystal were observed. The diffuse contrast in the slip bands and in their surrounding crystal volume revealed in most of reflections is due to the long-range strains associated with a high density of dislocations piling up on their slip planes. A judicious choice of proper projection and diffraction conditions enabled individual dislocations within a slip band to be clearly resolved. Figure 1 comprises transmission X-ray topographs recorded from a slip band showing the contrast variations of slip dislocations in different reflections. It is worth noting that individual dislocations are clearly visible in both (111) and (040) reflections, while only faint contrast associated with the intersection of the slip band on the X-ray exit surface can be discerned in both $(11\bar{1})$ and (400) reflections. The dislocation Burgers vector b can, therefore, be determined by using the g· b =0 criterion, where g is the diffraction vector. The slip plane can also be determined by analyzing the projected direction and length of slip dislocations in different reflections. This slip band is, therefore, characterized to belong to the $[011]/(1\bar{1}1)$ slip system. Systematic characterization of all of the slip dislocations in this sample reveals that nine of the twelve possible <110>/{111} slip systems are activated at different stages of the growth process. Since slip processes were initiated from regions of stress concentration, studies of the spatial configuration of slip bands and the activation of slip systems in the as-grown crystal enable one to understand the relationship between the thermal conditions used and the crystalline perfection of the as grown crystals and provides useful information on thermal stress modeling.

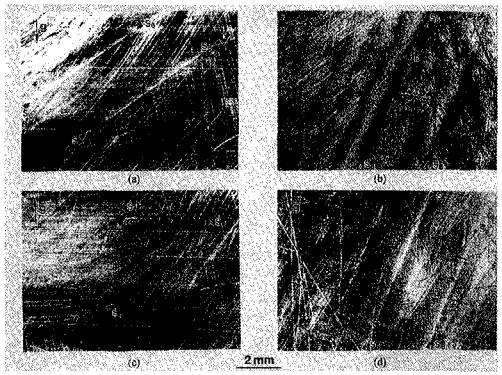


Figure 1.

* Work performed on the Stony Brook Synchrotron Topography Facility, Beamline X-19C, and supported by ARPA/AFOSR Consortium of Crystal Growth Research under Contract No. F496209510407.

Modeling the Distribution of Dislocations Observed in MLEK Grown Fe Doped InP Single Crystals *	X19C

H. Chung, W. Si, and M. Dudley (SUNY Stony Brook), D. F. Bliss (Rome Laboratory, AFB), and A. Maniatty (RPI)

X-ray topographic studies of dislocation distributions revealed that the density of dislocations changed along different crystallographic directions. In most of the wafers studied, a high density of dislocations can be observed near the peripheral regions along <100> directions, while it reached a minimum along <110> directions. Figure 2 shows a well defined four-fold symmetric distribution of dislocations observed in wafers sliced from the intermediate growth stages. In order to investigate the origin of such dislocation distributions, a thermal stress model composed of uniformly distributed, compressive radial stress was introduced.

Slip in crystals with the zinc blende structure such as InP can be activated on twelve {111}/<110> slip systems. The resolved shear stress for each of these slip systems for crystals grown along the [001] direction can be calculated using Schmid's law. Figure 1 shows the calculated shear stress distribution on the (001) plane. The shear stress reached its maximum along the crystallographic <100> directions, while it reached a minimum along the <110> directions. Since the overall dislocation density is proportional to the total excess resolved shear stress, which in turn is related to the local shear stress value, the calculated result is in good accord with the observed dislocation distributions. It is, therefore, expected that the compressive radial shear stresses likely to be experienced by the crystal during growth can give rise to dislocation generation which leads to the observed distribution.

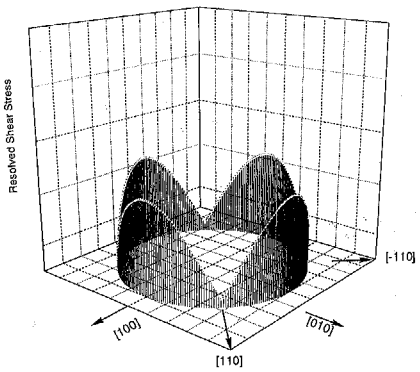


Figure 1.

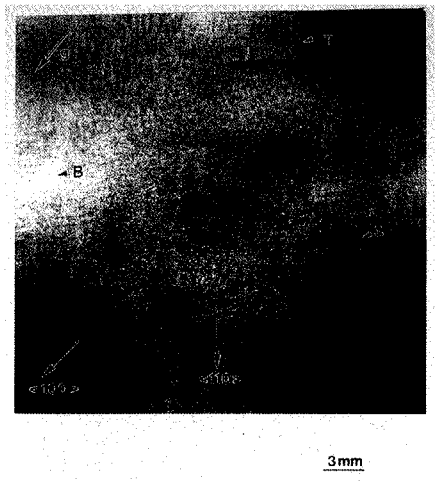


Figure 2.

* Work performed on the Stony Brook Synchrotron Topography Facility, Beamline X-19C, and supported by ARPA/AFOSR Consortium of Crystal Growth Research under Contract No. F496209510407.

Observation of Growth Striations in MLEK Grown InP Single Crystals Using Synchrotron White Beam X-ray Topography *	X19C

H. Chung, W. Si, and M. Dudley (SUNY, Stony Brook), D. F. Bliss (Rome, AFB), and A. Maniatty (RPI)

In crystal growth, the morphology of the solid-liquid growth interface is strongly influenced by the growth conditions. Important information regarding the temperature profile of the melt, microscopic growth rate variations and the relationship between growth conditions and crystal perfection can be directly deduced through the observation of the shape of the growth interface at the various stages of growth. In Liquid Encapsulated Czochralski (LEC) growth methods, growth rate fluctuations caused by effects such as unstable thermal convection and crystal rotation can give rise to inhomogeneous dopant segregation along the instantaneous solid-liquid interface. Due to the effect of dopant incorporation, a lattice distortion (mainly a lattice parameter variation) across the solid-liquid interface can be introduced. If the lattice distortion creates a local misorientation which is greater than the perfect crystal rocking curve width, growth striations can be revealed on X-ray topographs as contours of equal effective misorientation. The high degree of strain sensitivity ($\triangle d/d \sim 10^{-5}$-$10^{-8}$) of X-ray topography is particularly well suited for detecting the small strains associated with the small changes in dopant concentration. Thus the shape of the solid-liquid interface at various stages of growth can be determined through the observation of these striations. Figure 1 is a transmission X-ray topograph (g=004, λ=0.45Å) recorded from a (110) wafer sliced longitudinally from a heavily sulphur doped ($1 \sim 2 \times 10^{18}$ atoms/cm^3) InP crystal showing the morphology of growth interfaces at different stages of crystal growth.

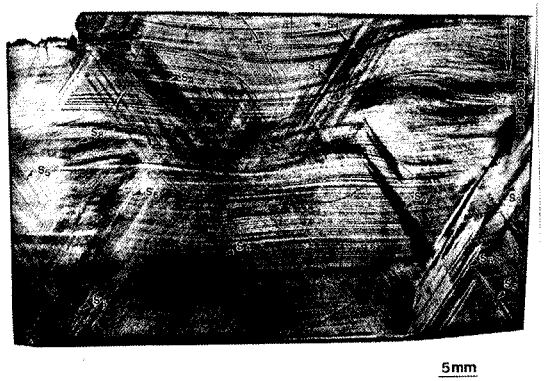


Figure 1.

* Work performed on the Stony Brook Synchrotron Topography Facility, Beamline X-19C, and supported by ARPA/AFOSR Consortium of Crystal Growth Research under Contract No.F496209510407.

Observation of Growth Striations in MLEK grown InP Single Crystals Using Synchrotron White Beam X-ray Topography II *	X19C

H. Chung, W. Si, and M. Dudley (SUNY Stony Brook), D. F. Bliss (Rome Laboratory, AFB), A. Maniatty (RPI)

The morphology of the growth interface at the different stages of crystal growth is clearly revealed by X-ray topography. In the initial growth period, when the flat shoulder of the crystal was formed, no pulling was employed. A growth interface convex to the melt is observed. However, a significant change in growth interface morphology occurred when the pulling process was initiated. A bimodal shape of growth interface, comprising a convex region in the center and two concave regions near the outer surface of the crystal was developed. The likely reasons for this lie in the fact that the convection flow driven by buoyancy and surface tension changes when the pulling process begins. At this point, as the shoulder of the crystal emerges from the melt into the encapsulant, the thickness of the encapsulant above the crystal decreases as encapsulant moves into the region between the outer boule circumference and the crucible wall. Figure 1 is a schematic diagram showing the modification of the geometric configuration of the encapsulant at the various stages of the growth process and the corresponding growth interface morphology revealed by X-ray topographs. This change in the geometric configuration of the encapsulant leads to a dramatic modification of the convection and radiation heat transfer from both the top and cylindrical outer surfaces of the boule. These effects modify the global heat transfer environment of the growth process and potentially cause a change in the flow pattern of the melt, which gives rise to a modification of the growth interface morphology.

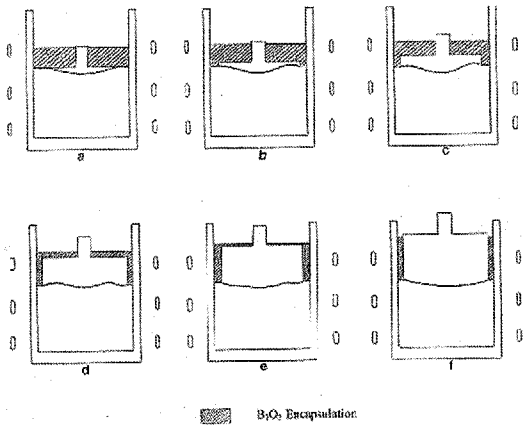


Figure 1.

* Work performed on the Stony Brook Synchrotron Topography Beamline X-19C, and supported by ARPA/AFOSR under Contract No. F496209510407.

Studies of Dislocation Distributions in MLEK Grown Fe Doped InP Single Crystals Using Synchrotron White Beam X-ray Topography *	X19C

H. Chung, W. Si, and M. Dudley (SUNY Stony Brook), D. F. Bliss (Rome Laboratory, AFB), and A. Maniatty (RPI)

A series of wafers sliced perpendicular to the [001] growth direction from a Fe doped InP boule were studied. The recorded X-ray topographs revealed that the density and distribution of dislocations changed at the different stages of crystal growth. A uniform distribution of dislocations of very high density were observed in both the initial and final stages of crystal growth, while in the intermediate growth stages, a four-fold symmetric distribution of dislocations was revealed separated by regions of low dislocation density. Figure 1 (a) is a transmission X-ray topograph recorded from a wafer sliced near to the seed. A twin lamella (T) nucleated from the flat shoulder of the crystal was observed. The X-ray topograph also revealed that a high density of dislocations was generated in this region. The density of dislocations reaches a maximum in the peripheral regions of the wafer along the crystallographic <100> directions. Figure 1 (b) and (c) are transmission topographs recorded from wafers sliced from the intermediate growth stages. A well defined four-fold symmetric distribution of dislocations is evident. The regions of high dislocation density are again observed to lie near the periphery of the wafer along <100> directions, while the density of dislocations reaches a minimum along <110> directions. Figure 1 (d) is a transmission X-ray topograph recorded from a wafer sliced near to the tail end of the boule. This topograph revealed a uniformly distributed, high density of dislocations.

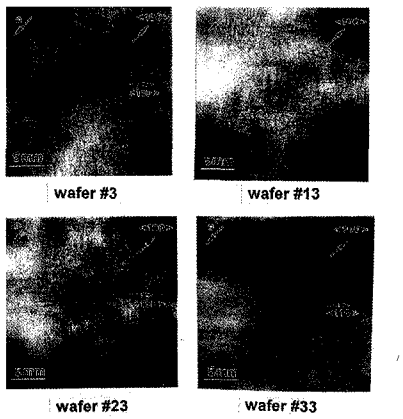


Figure 1.

* Work performed on the Stony Brook Synchrotron Topography Beamline X-19C, and supported by ARPA/AFOSR under Contract No. F496209510407.

Characterization of Defect Structures in 3C-SiC Single Crystals using Synchrotron White Beam X-ray Topography *	X19C

W. Huang, M. Dudley (SUNY Stony Brook), and C. Fazi (Army Research Lab.)

3C-SiC is one of the most promising of the SiC polytypes for application to active devices. However, large and high quality 3C-SiC crystal are very difficult obtaine. Recently, the Baikov method has been used to grow relatively large size (111) 3C-SiC crystals. In order to examine the crystal quality, Synchrotron White Beam X-ray Topography (SWBXT) is employed to provide detailed characterization of defect content in these crystals. Due to its unique capabilities, SWBXT can reveal the overall uniformity of crystal structure as well as local defect configurations. Figure 1 shows an X-ray transmission topograph

recorded from a 3C-SiC crystal. The presence of Pendellosung fringes, labeled PF, at the top left edge of the crystal indicates the high quality of this crystal. Stacking faults are found in the middle of the crystal, as indicated by SF. Dislocations, indicated by D, are also observed. Partial dislocations bounding the stacking faults are indicated by PD and inclusions by I. Some evidence for the existence of growth sector boundaries, G, is also visible. The presence of growth sector boundaries is likely to be indicative of differences in impurity segregation rates between adjacent sectors. Such differences may have a detrimental influence on device performance. Lines indicated by L are related to the surface step morphology. Since the bottom of the crystal is attached to a carbon rod during the growth process, this region is covered by carbon and does not show a clear facet feature. Layer structures of double positioning twins, 3C(I) and 3C(II), are also found in most of the crystals examined. A thin layer of 3C(II) is located at the bottom of the crystal and its quality is relatively poor compared with that of the 3C(I) region.

Apparently this kind of structural preference eliminates the influence of double positioning boundaries, which benefits device fabrication.

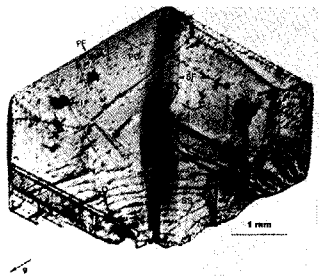


Figure 1. Synchrotron white beam x-ray transmission topograph showing defect structures in 3C-SiC crystal.

* Research supported by U.S. Army Research Laboratory, Adelphi, MD, and U.S. Army Research Office (Grant numbers DAAH04-94-G-0091 and DAAH04-94-G-0121, contract monitor Dr. John T. Prater). Topography carried out at the Stony Brook Synchrotron Topography Station, Beamline X19C, at the National Synchrotron Light Source in Brookhaven National Laboratory, which is supported by DOE.

Characterization of Slip Dislocations in 6H-SiC Single Crystals Using Synchrotron White Beam Topography *	X19C

W. Huang, M. Dudley (SUNY, Stony Brook), C. Fazi (ARL), and D. Willkinson (Novecon Technologies)

Major types of defects in commercial PVT 6H-SiC wafers are super-screw dislocations approximately perpendicular to the basal plane and dislocation networks lying in the basal plane. However, in the Lely SiC platelet examined recently, super-screw dislocations are not observed. As shown in figure 1, in addition to stacking faults, indicated by S and basal plane dislocations, indicated by D, slip bands, indicated by SB, are visible. Similar slip bands are also observed in a 6H-SiC wafer cut from a boule, as shown in figure 2. These slip dislocations appear to be edge or mixed in character. They are slightly inclined to the surface normal of the wafer. Slip bands appear to emanate from the inclusions, indicated by I, in both crystals. The regions with highest dislocation density also have the highest inclusion density, underlying the connection between the two.

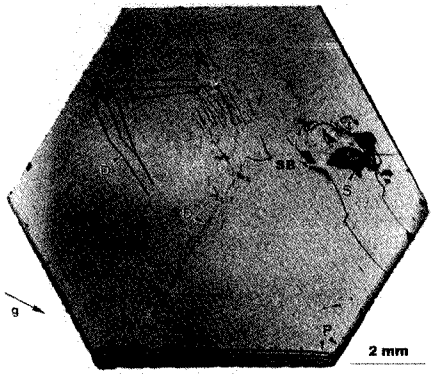


Figure 1. Synchrotron white beam x-ray transmission topograph showing defect distribution in Lely 6H-SiC platelet.



Figure 2. Synchrotron white beam x-ray reflection topograph showing defect distribution in 6H-SiC wafer.

* Research supported by U.S. Army Research Laboratory, Adelphi, MD, and U.S. Army Research Office (Grant numbers DAAH04-94-G-0091 and DAAH04-94-G-0121, contract monitor Dr. John T. Prater). Topography carried out at the Stony Brook Synchrotron Topography Station, Beamline X19C, at the NSLS in BNL, which is supported by DOE.

Experimental Proof of the Energy Dispersion in Contrast Theory on Micropipe Image Formation*	X19C

W. Huang, M. Dudley (SUNY Stony Brrok), S. Wang (ATMI), and C. Fazi (Army Research Lab.)

Double images of super-screw dislocations and micropipes in SiC single crystals can be observed in synchrotron white beam x-ray transmission topograph, as shown in figure 1(a). Analysis of these images enables the magnitudes of the tilt of the lattice planes relative to the core to be determined. Super-screw dislocations of opposite sign can also be distinguished. Crystal lattice on either side of a micropipe tilt on opposite directions, which corresponds to the strain field of a screw dislocation [2].

It is believed that energy dispersion ($\Delta\lambda/\lambda$) of synchrotron white beam contributes to direct image formation in SXBXT. This has been proved experimentally. A Mo filter, with an absorption edge at 0.6198 Å, was used so as to impose an abrupt change in spectrum intensity near the peak of the spectrum. The specimen was properly oriented so that the range of diffraction wavelengths around micropipe spans the absorption edge of the filter. Therefore the intensity of one side of the micropipe is lower than that of the other side, as shown in figure 2(b).

* Research supported by U.S. Army Research Laboratory, Adelphi, MD, and U.S. Army Research Office (Grant numbers DAAH04-94-G-0091 and DAAH04-94-G-0121, contract monitor Dr. John T. Prater). Topography carried out at the Stony Brook Synchrotron Topography Station, Beamline X19C, at the NSLS in BNL, which is supported by DOE.

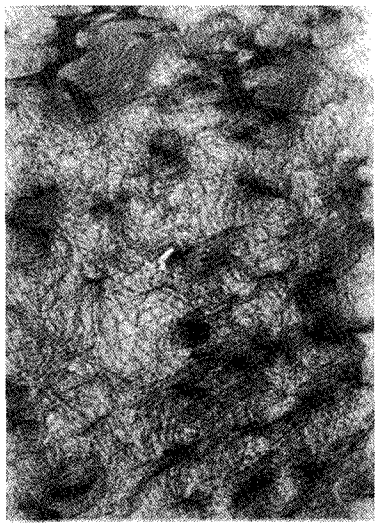


Figure 1. (a). Transmission topograph showing micropipes in SiC wafer.

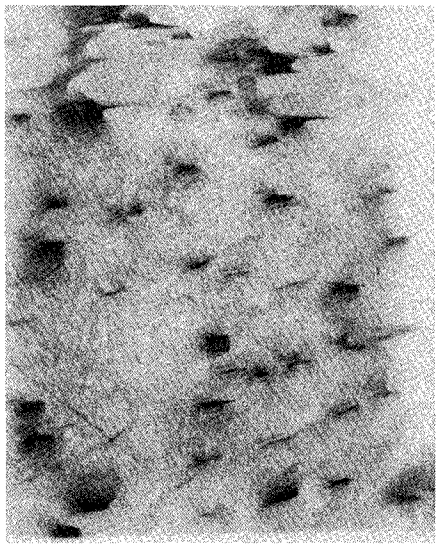


Figure 2. (b). Same topograph recorded using Mo filter.

Synchrotron White Beam Topography Studies of Residual Stress in SiC Single Crystal Wafers with Epitaxial Thin Films *	X19C

W. Huang, Q. Wang, M. Dudley, F. P. Chiang (SUNY, Stony Brook), J. Parsons (Oregon Graduate Institute), and C. Fazi (ARL)

The deposition of epitaxial layers and metallization layers often induces stresses in both the epitaxial layers and underlying substrates, which greatly affect the microelectronic performance of subsequently manufactured devices, potentially even causing device failure. Therefore the characterization of stress and strain fields in the thin films and substrates is essential in device fabrication. Synchrotron white beam x-ray topography (SWBXT), which is commonly used to image individual defects and defect distributions in single crystals, is employed to determine the deformation in 6H-SiC single crystals with 3C-SiC thin films grown on them. Due to the mismatch of mechanical and thermal properties between the substrate and epitaxial layer, residual stress exists in both. When the film is deposited, it strains the substrate, which bends until equilibrium is reached. The curvature of the substrate can be determined by absorption-edge-contour (AEC) mapping. Figure 3 (a) through (d) (g)=$10\bar{1}$, λ =0.618Å) show a series of AEC recorded from one of the samples analyzed. Figure 1(e) shows an AEC map obtained by rotating the specimen through increments of 0.1°C. To calculate the in-plane film stress, Stoney's equation was modified. Figure 2 show the stress distribution in two mutually perpendicular directions in part of a wafer. The coordinate system was selected such that the wafer lies in xy plane and the origin is at a point on wafer edge. The film free area is indicated by "substrate" while the film covered area is indicated by "film". Because of the high contour resolution and high efficiency of data collection, this technique is considered to be superior to monochromatic x-ray contour mapping.

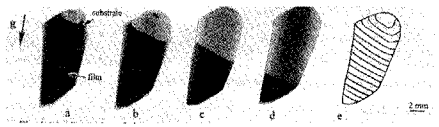


Figure 1. (a)-(d) a series of absorption edge contours and (e) absorption edge contour map.

* Research supported by U.S. Army Research Laboratory, Adelphi, MD, and U.S. Army Research Office (Grant numbers DAAH04-94-G-0091 and DAAH04-94-G-0121, contract monitor Dr. John T. Prater). Topography carried out at the Stony Brook Synchrotron Topography Station, Beamline X19C, at the National Synchrotron Light Source in Brookhaven National Laboratory, which is supported by DOE.

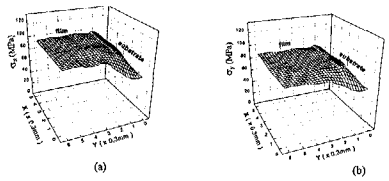


Figure 2. Distribution of stress (a) in x direction and (b)in y direction in part of a wafer.

In-plane Structure of the Liquid-Vapor Interfaces of Dilute Bismuth: Gallium Alloys	X19C

N. Lei, Z. Huang, and S. A. Rice (U. of Chicago)

The in-plane structure functions in the liquid-vapor interfaces of two bismuth:gallium alloys (0.18 atomic % Bi and 0.07 atomic % Bi) have been studied by grazing incidence x-ray diffraction. The higher concentration alloy exhibits, at 25°C, 43°C and 77°C, segregation of Bi into nearly complete monolayer atop the bulk alloy; at each temperature the Bi monolayer has the structure of a two-dimensional supercooled liquid. The intensity distribution of the diffuse x-ray scattering at $q_z = 1.0\ \AA^{-1}$ and $1.5\ \AA^{-1}$ is used to calculate the surface tension of the alloy at 77°C; the value obtained is 570 ± 30 dynes/cm. This value is related to the structure of the liquid-vapor interface. The in-plane diffraction data for the lower Bi concentration sample can be explained by assuming that the segregated Bi atoms form dimers and trimers.

Structure of the Liquid-Vapor Interface of Tin: Gallium Alloy	X19C

N. Lei, Z. Huang, and S. A. Rice (U. of Chicago)

The liquid-vapor interface structure of a tin (wt 9%):ga alloy has been studied by in-plane grazing incidence x-ray diffraction, and by diffuse and specular x-ray reflectivity measurements. The in-plane data, suggest that there is tin segregation at the interface, in excess of its concentration in the bulk liquid. The specular reflectivity data suggest a layered structure for the interface. The data (specular) taken at 41 °C and 57 °C suggest that the distance between the segregated tin and the top layer of ga is about 2.5Å, which is smaller than the sum of the radii of ga and tin in their pure liqquid phases. At 26 °C, this distance is about 2.8 Å, still smaller than the sum of the pure liquid atomic radii, possibly indictive of a phase transformation between 26 °C and 41 °C. Sample shape measurements yield a surface tension which increases with increasing temperature, consistent with the fact, according to the Gibbs adsorption iosterm for an ideal mixture, at higher temperatures there are fewer tin atoms at the interface.

Studies On the Formation Mechanism of Small Angle Tilt Boundaries in Ga Doped Ge Single Crystals by X-ray Topography *	X19C

B. Raghothamachar, H. Chung, M. Dudley (SUNY, Stony Brook), and D C. Gillies (NASA)

Dislocation structures in Ga doped Ge single crystals were characterised by synchrotron white beam x-ray topography in the reflection geometry. Figure 1 shows a triangular shaped region of high dislocation density originating from the seed. The dislocations are aligned to form dislocation cell structures and small angle tilt boundaries. During growth from the seed, dislocations present in the seed crystal are replicated into the newly grown regions of the crystal formed during the subsequent stages of solidification. Dislocations can also be generated from high stress concentration sites such as the shoulder regions of the crystal and the initial transient growth stage when growth conditions are not stable. These dislocations lying on the (111) planes can propagate into the newly formed crystal in the directions normal or nearly normal to the growth front. The growth interfaces are highly concave to the melt initially and hence, the replicated dislocations will be directed towards the center of the crystal since line directions normal to the growth front are energetically preferred. Thus the dislocations converge towards the central region and as the growth conditions stabilize, the curvature of the growth interface is reduced and very few dislocations are generated. The replicated dislocations which have converged at the central region form pileups and are pinned by the doped atoms. Further propagation is therefore eliminated and the dislocations realign during post solidification cooling to form cellular structure and small angle tilt boundaries.

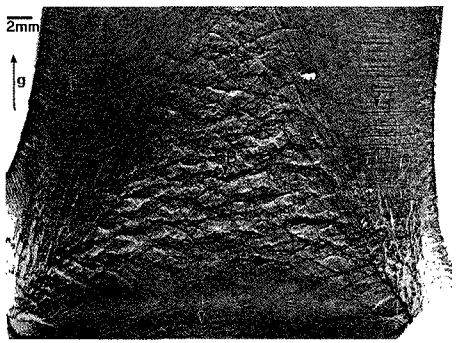


Figure 1. Reflection topograph ($\mathbf{g} = 333$, $\lambda = 0.87\mathring{A}$) from a Ga doped Ge crystal showing the dislocation cell structures (**C**) and small angle tilt boundaries (**SB**)

* Work performed on the Synchrotron Topography Project, Beamline X-19C, NSLS, BNL and supported by NASA Marshall Space Flight Center

Visibility of Growth Interfaces and Striations As a Function of Diffraction Geometry in Ga Doped Ge Single Crystals *	X19C

B. Raghothamachar, H. Chung, M. Dudley (SUNY, Stony Brook), and D C. Gillies (NASA)

Figures 1(a) and (b) are two reflection topographs recorded from a Ga doped Ge single crystal subjected to Peltier pulsing during growth in two different sample geometries. In fig 1(a), the diffraction vector **g** is along the growth direction and therefore perpendicular to the growth interface. The melt back interface and the growth striations generated by Peltier pulsing are clearly visible. In figure 1(b), the diffraction vector used was perpendicular to the growth direction and therefore parallel to the growth interface. In this image, the melt back interface and most of the striations are invisible; only very faint striation contrast from the highly curved interfaces can be discerned. Rocking curve width calculations reveal that the latter reflection is more strain sensitive than the former and hence, any displacement components parallel to the interface should be visible. Since, no contrast is observed from the interface, it indicates that the lattice is distorted normal to the growth front and hence the displacement vector associated with the growth interface is normal to the interface plane. Hence, the growth striations are invisible when the g vector is parallel to the interface ($\bar{g}.\bar{u}$=0 criterion). Thus the visibility of growth interfaces is a sensitive function of diffraction geometry and choice of proper diffraction vector with respect to the interface is important.

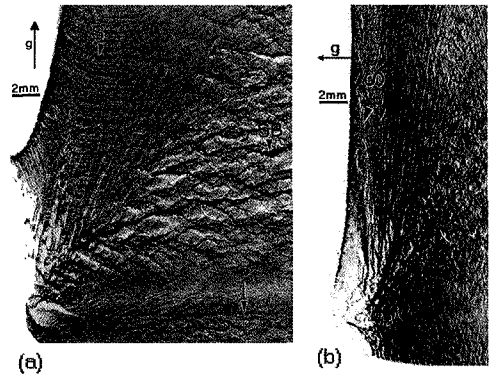


Figure 1. Reflection topographs recorded using different diffraction geometries (a) $\mathbf{g} = 333$, $\lambda = 0.87$ $\mathring{A}$ and (b) $\mathbf{g} = 246$, $\lambda = 0.65$ $\mathring{A}$, showing contrast variations in the images of the melt back interface (**I**) and growth striations (**S**) generated by Peltier pulsing

* Work performed on the Synchrotron Topography Project, Beamline X-19C, NSLS, BNL and supported by NASA Marshall Space Flight Center

Characterization of Structural Defects in Vapor Grown CdTe Single Crystals by Synchrotron White Beam X-ray Topography *	X19C

B. Raghothamachar, H. Chung, M. Dudley (SUNY, Stony Brook), D.C. Gillies, and W. Palosz (NASA)

Defect structures in vapor grown CdTe single crystals were characterized by synchrotron white beam x-ray topography in the reflection geometry. Figure 1 shows a reflection topograph recorded from a CdTe single crystal. A twin $\mathbf{T_1}$ is revealed by orientation contrast. Another twin $\mathbf{T_2}$ is also present as shown but there is no orientation contrast from this region because for this particular reflection, the reflecting planes in the matrix and twinned region are coincident. However, diffraction contrast clearly demarcates the twin and matrix regions. By detailed analysis of back reflection Laue patterns recorded from each twin related region, it was determined that the twins $\mathbf{T_1}$ and $\mathbf{T_2}$ are 180° rotation twins about the $(1\bar{1}1)$ and $(11\bar{1})$ plane normals respectively. It has also been observed that the twinned regions themselves undergo twinning. Second order ($\mathbf{TB^2}$) and third order ($\mathbf{TB^3}$) twin boundaries are observed. The central regions of the crystal appear to have much lower dislocation density than the peripheral regions. In some regions on the periphery, cellular arrangement of dislocations can be discerned. Higher dislocation density at the periphery indicates dislocation generation due to stresses from wall contact. Several spots of white contrast are probably precipitates or inclusions. These are concentrated in the matrix regions. Subgrain boundaries which are usually formed by polygonization of dislocations are also present in some regions.

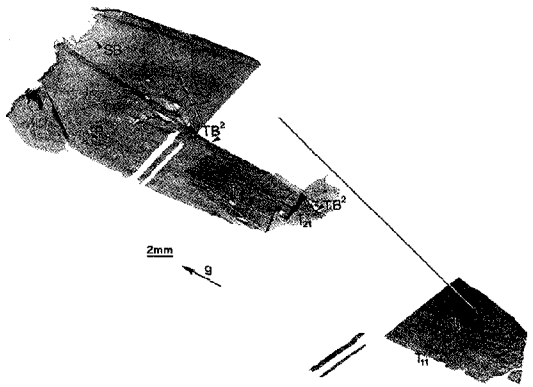


Figure 1. Reflection topograph taken from a CdTe single crystal showing the two twinned regions ($\mathbf{T_1}$ and $\mathbf{T_2}$), twin boundaries (**TB**), subgrain boundaries (**SB**) and inclusions (**P**)

* Work performed on the Synchrotron Topography Project, Beamline X-19C, NSLS, BNL and supported by NASA Marshall Space Flight Center

Comparison of Defect Structures in Microgravity (μg) and Terrestrially (1g) Grown CdZnTe Single Crystals by Synchrotron White Beam X-ray Topography *	X19C

B.Raghothamachar, H. Chung, M. Dudley, and D. Larson Jr. (SUNY, Stony Brook)

In a microgravity environment, gravity-dependent effects such as buoyancy, convection and hydrostatic pressure are minimized and diffusion controlled non-wetting growth can be achieved resulting in reduced stress generation which in turn minimizes the occurrence of twinning and deformation. CdZnTe wafers sliced from boules grown in microgravity and in normal gravity conditions were characterized by synchrotron white beam x-ray topography. Figure 1 shows a transmission topograph ($\mathbf{g} = \bar{1}\bar{1}3$, $\lambda = 0.42$ Å) recorded from wafer no.4 sliced from the steady state growth region of microgravity grown boule GCRC-2. The image shows a very low dislocation density ($5X10^2$-$1.2X10^3/cm^2$) with individual dislocations (**D**) being clearly resolved. Other defects observed are Te precipitates revealed by singular dark spots(**P**) and lamellar 180° rotation twins(**T**) about the $(11\bar{1})$ plane normal. Figure 2 shows a transmission topograph ($\mathbf{g} = \bar{1}\bar{1}3$, $\lambda = 0.42$ Å) taken from a sample sliced from NDVDT-3 which was grown under identical growth conditions except for gravity. Slip bands generated from the peripheral regions are clearly visible. The sample shows a very high dislocation density of the order of 10^5-$10^6/cm^2$. Clearly, the microgravity samples show much higher structural perfection than ground-based samples due to minimization of growth stresses.

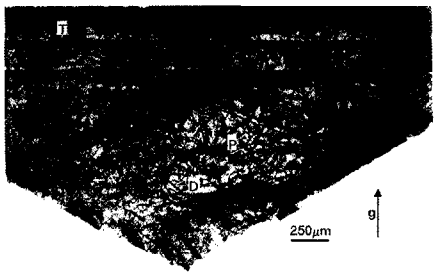


Figure 1.

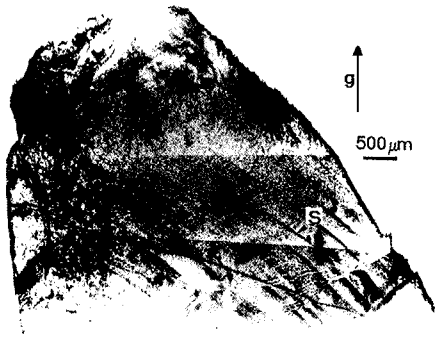


Figure 2.

* Work performed on the Synchrotron Topography Project, Beamline X-19C, NSLS, BNL and supported by NASA Marshall Space Flight Center

Investigations On the Effects of the Asymmetrical Gravity Vector on the Defect Distributions in Microgravity Grown CdZnTe Single Crystals *	X19C

B. Raghothamachar, H. Chung, M. Dudley, and D. J. Larson Jr. (SUNY, Stony Brook)

Defect distributions in CdZnTe single crystals grown by the Bridgman-Stockbarger method in a microgravity environment were compared to similar crystals grown terrestrially under the same conditions. Synchrotron white beam x-ray topography in the reflection geometry was used to characterize the defect distributions. Figures 1(a) and (b) respectively show reflection topographs imaged from wafers sliced from the steady state growth regions in microgravity grown sample GCRC-1 and terrestrially grown boule NDVDT-1. An asymmetrical distribution of slip bands along the $[10\bar{1}]$ and the $[0\bar{1}1]$ directions on either side of the sample is observed in figure 1(a). In contrast, figure 1(b) shows a more symmetrical distribution of dense slip bands. These slip bands are nucleated in the peripheral regions by stresses generated from wall contact. The microgravity grown boule was subjected to an asymmetrical residual gravitational field which induced non-uniform wall contact resulting in different levels of stress around the circumference of the boule which caused the asymmetrical slip band distribution. In ground based samples the hoop stresses generated by uniform wall contact are symmetic resulting in a symmetric slip pattern. Note that the magnitude of stress in microgravity conditions is much lesser than that under gravity and therefore the slip bands in ground based samples are much denser than the microgravity samples.

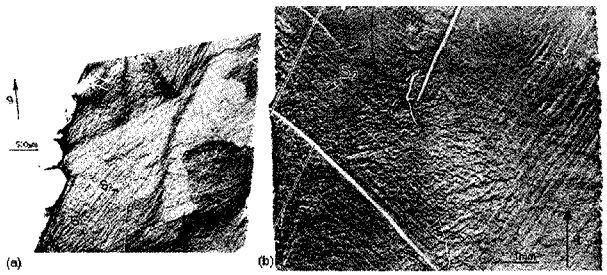


Figure 1. (a)Reflection topograph($\mathbf{g} = 133$, $\lambda = 0.98$Å) from wafer #4 of μg grown boule GCRC-1 showing two sets of asymmetrically distributed slip bands ($\mathbf{S}_1$ and $\mathbf{S}_2$); (b)Reflection topograph($\mathbf{g} = 335$, $\lambda = 0.7$Å) from a wafer of ground based boule NDVDT-1 showing two sets of symmetrically distributed slip bands ($\mathbf{S}_1$ and $\mathbf{S}_2$).

* Work performed on the Synchrotron Topography Project, Beamline X-19C, NSLS, BNL and supported by NASA Marshall Space Flight Center

Studies On the Surface of a Microgravity Grown CdZnTe Boule by Synchrotron White Beam X-ray Topography *	X19C

B. Raghothamachar, H. Chung, M. Dudley, and D. J. Larson Jr. (SUNY, Stony Brook)

Results obtained from previous microgravity experiments strongly indicate that single crystals grown under non-uniform wall contact conditions show an asymmetrical defect density distribution with lower defect densities observed in regions with no wall contact because of lower stresses. Therefore, a special tapered boule geometry as shown in fig 1(a) was developed so that crystal growth free from wall contact can be achieved. A boule with this geometry (GCRC-2) was grown aboard space shuttle flight USML-2. Figure 1(a) shows an optical photograph of the as grown boule . A region approximately 2cm in length free from wall contact was grown. Synchrotron white beam x-ray topography was used to study the surface of the as grown boule in order to characterize the true microstructure developed during the growth process. Figure 1(b) shows a reflection topograph taken from the surface of the boule. The seed transition region reveals the presence of 180° rotation twin lamellae about the (111) plane normal. Because of the rough surface morphology of the region grown without wall contact, resolution of defects is not possible but the topograph indicates that no twins are nucleated and no significant lattice distortion is apparent. However, as soon as this region reestablishes wall contact, a twin is nucleated indicating that stresses associated with wall contact may have an effect on twin generation.

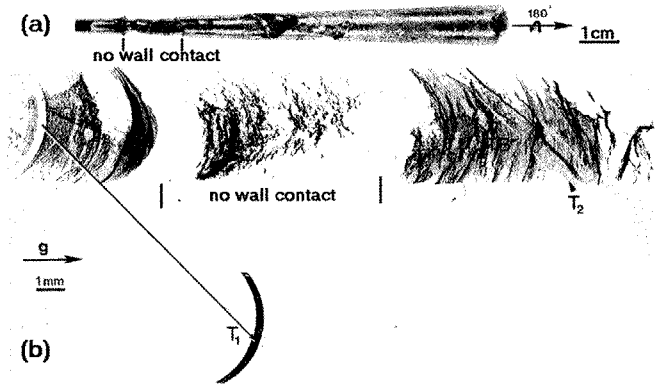


Figure 1. (a)Optical photograph and (b) X-ray reflection topograph recorded from the tapered microgravity grown sample GCRC-2 (USML-2) showing the morphology and defect structures (twins $\mathbf{T}_1$ and $\mathbf{T}_2$).

* Work performed on the Synchrotron Topography Project, Beamline X-19C, NSLS, BNL and supported by NASA Marshall Space Flight Center

Synchrotron White Beam X-ray Topographic Characterization of Growth Defects in Bridgman-Stockbarger Grown CdZnTe Single Crystals *	X19C

B. Raghothamachar, H. Chung, M. Dudley, and D. J. Larson Jr. (SUNY, Stony Brook)

Vertical Bridgman -Stockbarger method of crystal growth was used to grow a single crystal boule of CdZnTe. (111) wafers sliced from this boule were examined by synchrotron white beam x-ray topography in the reflection geometry. Figure 1 shows a reflection topograph imaged from wafer 3 which was cut from the initial part of the steady state growth region of the boule. Several slip bands running across the middle of the boule are observed. These slip bands overlap a previously existing dislocation cellular structure indicating that slip could possibly have occured during post solidification cooling. By analysing projected directions in different reflections, the slip system was determined to be $[10\bar{1}]/(1\bar{1}1)$. A twin **T** is revealed by orientation contrast. By detailed analysis of back reflection Laue patterns recorded from the twin related region, it was determined that the twin is 180 rotation twin about the $(11\bar{1})$ plane normal. The twinned region has two sets of slip bands $[10\bar{1}]/(1\bar{1}1)$ and $[\bar{1}10]/(11\bar{1})$ respectively). Absence of a second slip system in the matrix indicates that the slip was initiated in the twinned region and did not propagate into the matrix since the twin boundaries act as barriers to slip dislocations. Since the twin was formed before deformation occurred it is probably a growth twin.

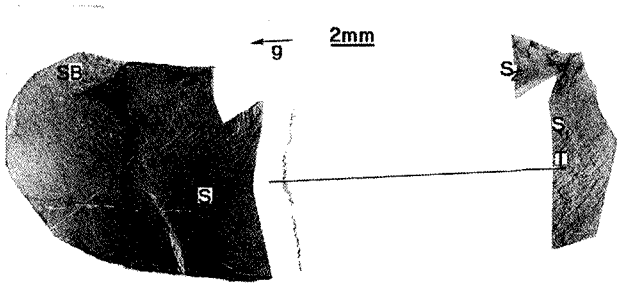


Figure 1. Reflection topograph ($\mathbf{g} = 335$) from wafer 3 of CdZnTe boule N2FST-1 showing defects such as slip bands ($\mathbf{S_1}$ and $\mathbf{S_2}$), subgrain boundaries (**SB**) and a 180° rotation twin (**T**)

* Work performed on the Synchrotron Topography Project, Beamline X-19C, NSLS, BNL and supported by NASA Marshall Space Flight Center

Morphology of Basal Plane Dislocations in 4H-SiC Single Crystal Wafers *	X19C

W. Si and M. Dudley (SUNY Stony Brook), R. Glass, V. Tsvetkov, and C. Carter, Jr. (Cree Research, Inc)

In PVT grown 4H-SiC single crystals, there are mainly two types of dislocation structures: superscrew dislocations with their Burgers vectors running along the [0001] axis, and basal plane dislocations whose both line directions and Burgers vectors are confined on the {0001} planes. In X-ray topography of low absorbing crystals such as SiC, the dislocation lines become visible by the kinematic contrast due to effective misorientation of the reflecting lattice planes in the elastically strained region surrounding the dislocation core. In a high quality (0001) 4H-SiC wafer we studied, the bimodal, double line contrast was observed from these basal plane dislocations, as shown in a synchrotron transmission topograph. The dislocation **A** seems to be pinned at points **P1** and **P2** by other dislocations and bows out to form the beginnings of a Frank-Read source. Detailed analyses of these dislocations including determination of their Burgers vectors and calculation of dislocation image width are being investigated.

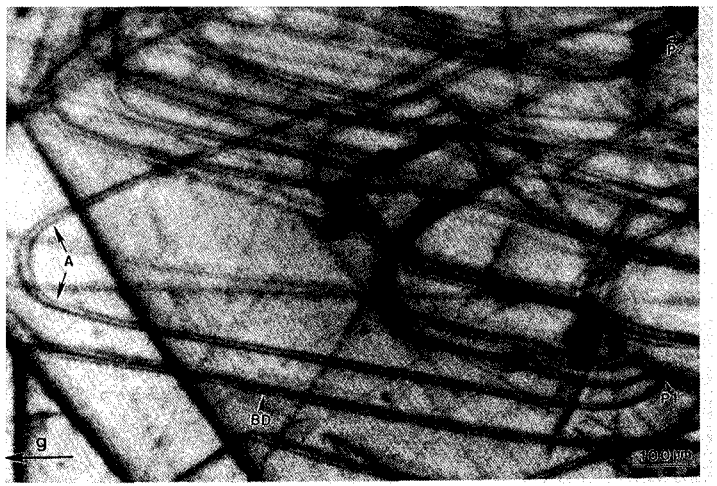


Figure 1. A synchrotron transmission X-ray topograph from a (0001) 4H-SiC wafer, $\mathbf{g} = 1\bar{2}10$, $\lambda = 0.75$ Å, **BD** indicates basal plane dislocations.

* Work performed on the Synchrotron Topography Project, Beamline X-19C, and supported by ARPA/AFWL under Grant No. FY1457-95-03108.

Study of 6H-SiC Polytype Inclusions in 4H-SiC Single Crystals * | X19C

W. Si and M. Dudley (SUNY Stony Brook), R. Glass, V. Tsvetkov, and C. Carter, Jr. (Cree Research, Inc)

SiC is well known for its exhibition of many polytype structures. Currently more than 200 polytypes of SiC have been reported. The common polytypes with technical importance are 4H, 6H, and 3C-SiC. Since these polytypes coexist over a wide range of temperatures, inclusions of secondary polytypes can occur when crystals are grown inproperly. In a $(11\bar{2}0)$ oriented 4H-SiC single crystal wafer we studied, small regions (inclusions) with different color from the substrate have been occasionally observed using optical microscopy. In order to identify the character of these inclusions, synchrotron transmission Laue diffraction patterns were recorded from these regions as shown in Figure 1. By analyzing and indexing this pattern, it is found that the inclusion belongs to a 6H-SiC polytype. Similar result has been reported that 15R-SiC inclusions exist in 6H-SiC single crystals[1]. 1. Shaoping Wang, Ph.D. Thesis, State University of New York at Stony Brook, 1996, p. 85.

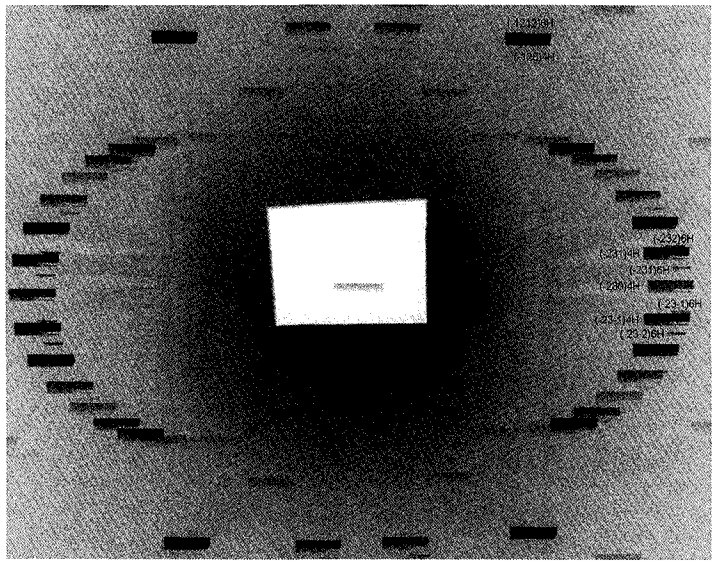


Figure 1. Synchrotron transmission Laue patterns recorded from a $(11\bar{2}0)$ 4H-SiC wafer containing a 6H-SiC region close to the edge of the wafer. $[\bar{1}\bar{1}20]$ direction is parallel to the incident X-ray beam direction.

* Work performed on the Synchrotron Topography Project, Beamline X-19C, and supported by ARPA/AFWL under Grant No. FY1457-95-03108.

Investigations of 4H-SiC Epilayers on $(11\bar{2}0)$ 4H-SiC Single Crystal Substrates * | X19C

W. Si and M. Dudley (SUNY Stony Brook), H. S. Kong, J. Sumakeris, and C. Carter, Jr. (Cree Research, Inc.)

In order to investigate the effects of 4H-SiC substrates on the crystalline quality of 4H-SiC epilayers, $(11\bar{2}0)$ oriented substrates, other than commonly used (0001) oriented substrates, were used to grow 4H-SiC epilayers. Figure (a) shows the surface morphology of a 4H-SiC epilayer grown on a $(11\bar{2}0)$ 4H-SiC substrate. The epilayer surface is smooth, specular, and featureless, which implies very good crystalline quality of the epilayer. The faint line on the picture indicates a micropipe in the substrate. Figure (b) is the reflection topograph recorded from the same region. The major defects revealed are superscrew dislocations in the substrate, probably due to the fact that the strain fields of the superscrew dislocations in the substrate penetrate into the newly grown epilayer and therefore are picked up by reflection topography. There is no polytype other than 4H-SiC in the epilayer revealed in the reflection topograph. The reflection topograph recorded from the epilayer is very similar to that from the substrate before epitaxy growth, and the quality of epilayers grown on the $(11\bar{2}0)$ substrates is very good.

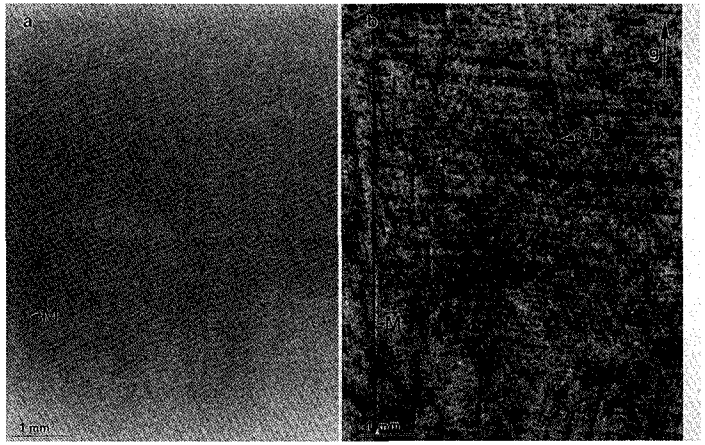


Figure 1. 4H-SiC epilayers on $(11\bar{2}0)$ 4H-SiC substrates, (a). a NOM micrograph and (b) the reflection topograph ($g = 2\bar{2}02$, $\lambda = 0.71$ Å) recorded from the same region, M indicates a micropipe, **SD** indicates superscrew dislocations.

* Work performed on the Synchrotron Topography Project, Beamline X-19C, and supported by ARPA/AFWL under Grant No. FY1457-95-03108.

Investigations of Triangular Inclusions in 4H-SiC Epilayers on 4H-SiC Single Crystal Substrates: (I) Identification of Phases *	X19C

W. Si and M. Dudley (SUNY Stony Brook), H. S. Kong, J. Sumakeris, and C. Carter, Jr. (Cree Research, Inc.)

In the case of 4H-SiC epitaxial growth on (0001) substrates, one of the big obstacles is the occurrence of triangular inclusions in the epilayer. In this study, Synchrotron White Beam X-ray Topography (SWBXT) and Nomarski Optical microscopy (NOM) have been used to study the character of these triangular inclusions. The 4H-SiC substrates used are misoriented by 3.5° from (0001) toward <11$\bar{2}$0>. It has been revealed by analysis of X-ray diffraction patterns that there are two additional phases, 3C(I)-SiC and 3C(II)-SiC, present in the 4H-SiC epilayer[1]. The detailed correlation between the NOM micrograph and reflection topographs is shown in Figures (a) to (d). Evidently, all triangular inclusions belong to one or the other of the two 3C-SiC structural configurations. Most of the triangular inclusions are single crystal 3C-SiC, although they appear to be severely strained. There is only one triangular inclusion consisting of both 3C(I) and 3C(II)-SiC, which implies the existence of a double position boundary (DPB) within the inclusion[2]. Therefore it is unambiguous that those triangular defects in 4H-SiC epilayers studied are 3C-SiC inclusions.

1. W. Si *et al*, 1995 NSLS Annual Activity Report, p. B-173.
2. H. S. Kong *et al*, J. Mater. Res., Vol. 4, No. 1, (1989), p. 204.

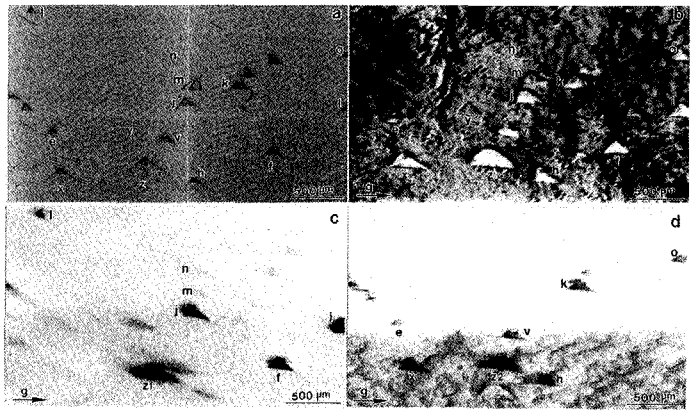


Figure 1. 4H-SiC epilayers on 4H-SiC substrates misoriented by 3.5° from (0001), (a). a NOM micrograph, (b). the reflection topograph from the same region, 4H-SiC, g = 1$\bar{1}$06, λ = 0.78 Å , (c). the reflection topograph of 3C(I)-SiC, g = 202, λ = 0.91 Å , and (d). the reflection topograph of 3C(II)-SiC, g = 131, λ = 0.67 Å.

* Work performed on the Synchrotron Topography Project, Beamline X-19C, and supported by ARPA/AFWL under Grant No. FY1457-95-03108.

Investigations of Triangular Inclusions in 4H-SiC Epilayers on 4H-SiC Single Crystal Substrates: (II) Effects of Superscrew Dislocations in substrates *	X19C

W. Si and M. Dudley (SUNY Stony Brook), H. S. Kong, J. Sumakeris, and C. Carter, Jr. (Cree Research, Inc.)

It is well known that in 4H-SiC single crystal substrates, there exist superscrew dislocations along the [0001] axis with their magnitudes of Burgers vectors equal to a multiple of the lattice constant c (c = 10.05 Å). Figure 1 shows (a) a NOM micrograph of the epilayer and (b) a back-reflection topograph. Triangular inclusions (TI), growth pits (P), and scratch (S) marks are observed on the micrograph. The triangular inclusions consist of the shallow and hillock-like varieties with roughly the same size. The directions from the apex of the triangle to the base are [12$\bar{1}$0] directions, which correspond to the down-step directions (direction of lateral step growth). The length of altitude from base of the triangle to the peak is around 97 to 120 μm. The density of growth pits is approximately $3.5x10^4 cm^{-2}$, and the diameter is around 1 μm. Superscrew dislocations including micropipes (M) and elementary screw dislocations (ED) show circular white features on the topograph. By comparison, it is evident that there is no obvious correlation between superscrew dislocations and 3C-SiC triangular inclusions. Also there is no evidence showing that the growth pits are related to the superscrew dislocations since the density of growth hillocks is one order of magnitude higher than that of superscrew dislocations (about $10^3 cm^{-2}$).

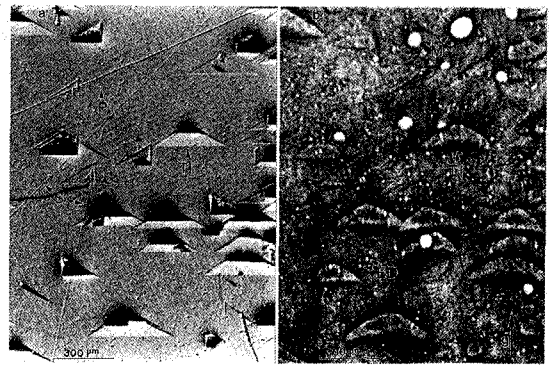


Figure 1. 4H-SiC epilayers on the 4H-SiC substrates misoriented by 3.5° from (0001), (a). a NOM micrograph, and (b) the back-reflection topograph recorded from the same region, g = 00024, λ = 0.83 Å.

* Work performed on the Synchrotron Topography Project, Beamline X-19C, and supported by ARPA/AFWL under Grant No. FY1457-95-03108.

Investigations of Triangular Inclusions in 4H-SiC Epilayers on 4H-SiC Single Crystal Substrates: (III) Effects of Off-axis Angles of Substrates *	X19C

W. Si and M. Dudley (SUNY Stony Brook), H. S. Kong, J. Sumakeris, and C. Carter, Jr. (Cree Research, Inc.)

One method of preventing the formation of triangular inclusions during SiC epitaxial growth is to use substrates misoriented from (0001). The vicinal surfaces of such off-axis substrates provide high densities of surface steps, which promotes a step-flow mechanism and facilitates the SiC homoepitaxy. However, in 4H-SiC epitaxy, the occurrence of triangular inclusions still existed when substrates misoriented by 3.5° from (0001) were used. One possible way to reduce or eliminate the occurrence of inclusions in 4H-SiC epilayers is to further increase the off-axis angle of the approximately (0001) oriented substrates, i.e., from the commonly used 3.5° misorientation to 6.5° and 8.0°. Figure (a) shows a reflection topograph recorded from the epilayer grown on a 6.5° off-axis 4H-SiC substrate. It was found that both density and dimension of triangular inclusions is greatly reduced. In the case of substrates misoriented by 8.0° from (0001), the triangular inclusions were virtually eliminated, as shown in Figure (b). The crystalline quality of 4H-SiC epilayers grown on the substrates misoriented by 8.0° from (0001) was very good.

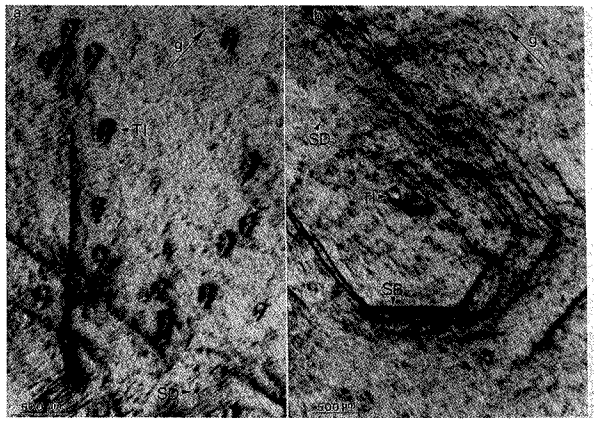


Figure 1. Reflection topographs (g = $11\bar{2}4$, $\lambda = 0.78$ Å) recorded from epilayers grown on 4H-SiC substrates misoriented by (a) 6.5° from (0001) and (b) 8.0° from (0001), showing superscrew dislocations (SD), small angle boundaries (SB), and triangular inclusions (TI).

* Work performed on the Synchrotron Topography Project, Beamline X-19C, and supported by ARPA/AFWL under Grant No. FY1457-95-03108.

Studies of Growth Striations and Impurity Distribution of LEC Grown GaInSb Single Crystal	X19C

J. Su, M. Dudley (SUNY Stony Brook), D. Fletcher, and W. Bonner (Johnson Matthey Electronics)

The LEC grown $Ga_{0.97}In_{0.03}Sb$ single crystal have been studied using synchrotron white beam X-ray topography (SWBXT).The transmission topopographs recorded from the sample reveal high contrast growth striations which are perpendicular to the growth direction.These striations offer a convenient way to study the crystal growth because they clearly delineate the crystal growth profile.In present studies, efforts have been made to investigate the relationship between impurity distributions and growth striations by using SWBXT and a CAMEBAX electron microprobe with a resolution of 10^{-6}wt% and a penetration depth of 0.5 μm. Figures 1 and 2 below show the measurement results of two lines performed along the growth direction. The results reveal that indium concentrations have periodic distributions when crossing the growth striations. The indium concentrations measured just on the striations show relatively higher values, such as positions #3, #15, #18 in Figure 1, and #9, #14, #22 in Figure 2. The indium concentrations on the regions immediately after the striations show lower values, such as #7, #8 in Figure 1, and #4, #8, #12 in Figure 2. The present studies show that the impurity concentrations change with the formation of growth striations, and the striations have highest indium content. The reason can be explained as that the indium accumulates at the solid-liquid interface during growth, and its content influences the latent heat of the solidification which will influence the microscopic growth rate. This fluctuation in the instantaneous microscopic growth rate during the LEC growth will give rise to the periodic accumulation of indium concentration. This difference in impurity content will cause the local lattice strain which produces the growth striation images in X-ray topography.

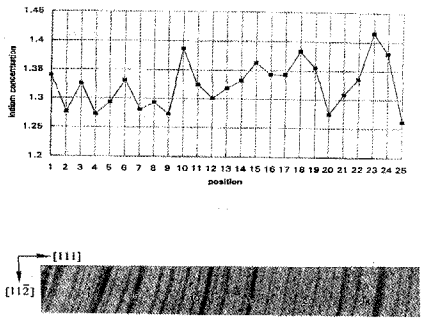


Figure 1. Indium concentration as a function of positions along line #4, (a) indium concentration distribution (b) measurement position map.

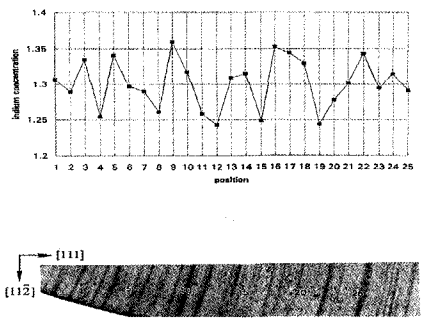


Figure 2. Indium concentration as a function of positions along line #5, (a) indium concentration distribution (b) measurement position map.

Synchrotron White Beam X-ray Topographic Studies of LEC GaInSb Seed Transition Region	X19C

J. Su, M. Dudley (SUNY, Stony Brook), D. Fletcher, and W. Bonner (Johnson Matthey Electronics)

Ternary III-V semiconductor materials become more attractive due to their selectable lattice parameters and bandgaps. However, obtaining defect-free ternary semiconductor substrates is still an object that people make efforts. In this study, Synchrotron White Beam X-ray Topography (SWBXT) was applied to analysize the defect mechanisms in the [111] LEC grown $Ga_{0.97}In_{0.03}$ seed transition region which is the critical region of LEC growth. A longitudinally cut slice has been studied using SWBXT. Figure 1 is an X-ray topograph with (g=111λ=0.54Å) showing that growth striations (**GS**) and the (111) facets (**F**). The high contrast growth striations are observed through the whole wafer, the (111) facets (**F**)are clearly revealed perpendicular to the growth direction at the central region. The dislocations (**D**) are also revealed. The feature marked **SS** are surface scratches. Another transimission X-ray topograph with (g=$\bar{1}$11λ=0.56Å)is shown in Figure 2. The dislocations which appeared in Figure 1 show no contrast or weak contrast in Figure 2. Therefore, the Burgers vector of these dislocations can be determined as 1/2[110]. The studies indicate that 1/2[110] dislocations can be generated at the shoulder region during LEC growth, and some dislocation are observed to propagate inside the bulk from the seed transition region.

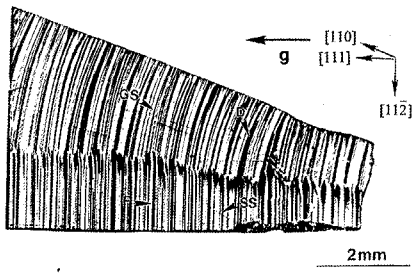


Figure 1. Transmission X-ray topograph (g=111 λ=0.54Å) recorded from $Ga_{0.97}In_{0.03}Sb$ seed transition region showing dislocations (**D**), growth striations (**GS**), and (111) facets (**F**).

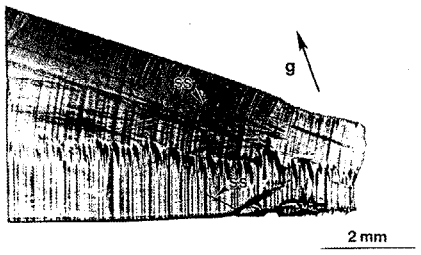


Figure 2. Transmission X-ray topograph (g=$\bar{1}$11 λ=0.56Å)recorded from $Ga_{0.97}In_{0.03}Sb$ seed transition region showing that the dislocations appeared in (a)have no or weak contrast.

A Comparison of Synchrotron White Beam and Lang X-Ray Topography of 6H-SiC Single Crystal Wafers *	X19C

W. M. Vetter and M. Dudley (SUNY, Stony Brook)

Back-reflection Synchrotron White Beam (SWB) images of basal-cut SiC wafers (as in figure 1) are characterized by black rings with white centers of various diameters that are associated with the surface intersections of superscrew dislocations of various sized Burgers vectors. Such SWB images are a composite of a harmonic series of reflections (006n), where n=3,4,5... in the the case of the X19C beamline white beam spectrum. Nevertheless, their contrast is sharp. The Lang image shown in figure 2 (g=(0018), λ=CuK$_{\alpha 1}$=1.54Å, θ_B=66.5°, FWHM=15.6μrad) taken using copper characteristic radiation has a Full Width Half Maximum (FWHM) and a Bragg angle comparable to those of the g=(0024) SWB reflection (λ=1.24Å, θ_B=80°, FWHM=19.9μrad) which is the fourth harmonic in the series. The similarities between these values and those between the features in these two topographs suggest that g=(0024) is the most important component of the back-reflection image. The Lang image shows ring-like images for the largest Burgers vector superscrew dislocations similar to those seen in the SWB image, however the black rings are larger and their centers are smaller. In the cases of the smaller Burgers vector superscrew dislocations, the white centers are absent.

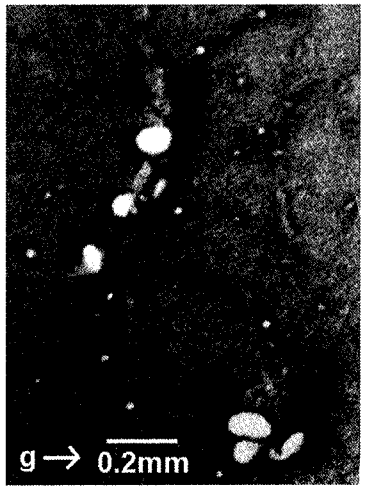


Figure 1. Back-reflection SWB topograph.

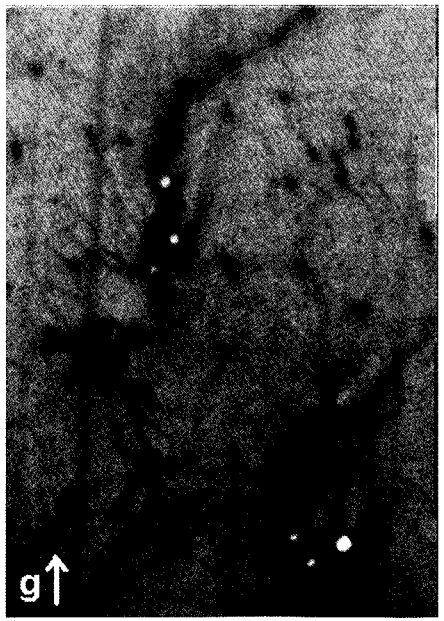


Figure 2. Lang topograph using Cu radiation.

* Work performed at Beamline X-19C, supported by U.S Army Research Office under grants, DAAL09-94-G-0091 & DAAL04-94-G-0121.

Synchrotron White Beam X-Ray Topography of a Single Superscrew Dislocation in 6H-SiC Through All{100} Faces *	X19C

W. M. Vetter and M. Dudley (SUNY Stony Brook)

Micropipes, the hollow cores of superscrew dislocations that lie along the c-direction in SiC single crystals, are quite deleterious to the performance of semiconductor devices. In the x-ray topography of longitudinal-cut samples of these crystals, topographs in the reflection (006) show dislocation image contrast associated with strain along the c-axis of the crystal, which is also the direction of the dislocations' Burger's vectors. In a (110) reflection, whose g-vector is perpendicular to the c-axis and the dislocations' Burger's vector, there is also an image of the superscrew dislocation formed, albeit weaker than the corresponding image in the (006) reflection. This dislocation image is thought to represent the strain components of the superscrew dislocation in directions perpendicular to the c-axis, resulting from stresses arising at the surface of the micropipe.

To determine whether these strains are anisotropic in all possible reflections where $\mathbf{g} = \{110\}$, we have excised a hexagonal prism-shaped section from a 6H-SiC wafer, 100μm wide, polished along the six {100} crystallographic faces, such that a single micropipe ran along the axis of the sample. The x-ray topographs in figure 1, taken through three of these {100} faces using three different {110} g-vectors, show that the dislocation images in each are essentially similar–two dark lines with a constant separation. However, the contrast may change somewhat between different g-vectors at the same point along the dislocation line, perhaps reflecting varying stresses and the emission of dislocations along an irregularly surfaced micropipe.

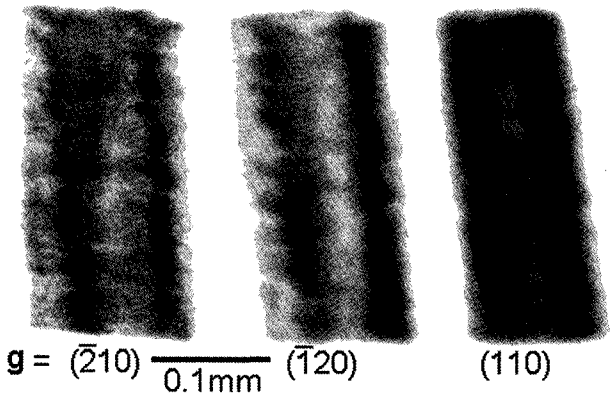


Figure 1. X-ray topographs using three different g={110} reflections.

* Work performed at the Synchrotron Topography Project Station, Beamline X-19C, supported by U.S. Army Research Office under grant numbers: DAAL09-94-G-0091 and DAAL04-94-G-0121.

Surface Scattering from Ternary Mixtures of Oil, Water, and Surfactant	X19C

S.M. Williams, Z. Zhang, D.M. Mitrinovic, M.L. Schlossman (U. of IL- Chicago), and Z. Huang (BNL)

We have made x-ray scattering measurements from the oil-microemulsion interface of several ternary mixtures that include one of the surfactants, C_4E_1, C_6E_2, or $C_{10}E_4$ (n-alkyl polyglycol ether $CH_3(CH_2)_{i-1}(OCH_2CH_2)_jOH$).

The mixtures using C_4E_1 or C_6E_2 yield qualitatively similar results. The mixtures with $C_{10}E_4$ have much rougher interfaces ($\sigma > 200$ Å) and data interpretation for this system is at a primitive stage. Here we discuss studies of a C_4E_1-water-decane (1:1:3) mixture at 35.00°C prepared in a vapor-tight sample cell. Under these conditions the solution is in a three-phase state with a middle-phase microemulsion. The primary experimental challenge is that the x-ray beam fully traverses the diameter of one of the bulk phases. The concurrent absorption and bulk scattering requires a small sample that, in turn, demands a very small x-ray beam (10 μm vertically) with a small divergence (20 μrads). In our sample cell design, the x-rays pass through 75 mm of the upper phase, necessitating the use of high energy x-rays. The absorption length of the upper decane-rich phase (at 35°C) at 15 keV is 15 mm, resulting in an absorption loss of 99%. By using a multilayer monochromator crystal at the X19C surface spectrometer we have adequate intensity to perform these experiments (10^{11} photons/sec at 15 keV in a 0.5 mm x 1 mm spot).

The reflectivity data (from the oil-microemulsion interface) is fit very well by the distorted wave Born approximation yielding a roughness $\sigma = 57 \pm 3$ Å. This value is much larger than the largest molecular size (~10 Å) and is indicative of a strongly fluctuating interface. Surface diffuse scattering was measured as a function of varying reflection angle for fixed incident angle. Using the distorted wave Born approximation and the roughness determined from the reflectivity only, it is not possible to make an adequate fit to the data. An excellent fit is obtained if the roughness parameter along with the interfacial tension and a constant background are fit. This fit has a roughness, σ=75 $\pm$ 5 Å, that is much larger than that determined from the reflectivity. For both fits the interfacial tension is similar (for $\sigma = 75 \pm 5$ Å,$\gamma = 0.08$ dynes/cm; for $\sigma = 57 \pm 3$ Å, $\gamma = 0.12$ dynes/cm).

Although the reason for the failure of the distorted wave Born approximation to describe this data is unclear at this stage, it may be due to the assumption of a step-function interface in describing the diffuse scattering. If true, this would be the first experiment to show the effect of a more complicated interface on the surface diffuse scattering, thereby providing an experimental probe of complex and strongly fluctuating interfaces.

Studies of Influence of Defects on the Performance of 4H-SiC Devices Using Synchrotron White Beam X-ray Topography: I. Defect Configuration	X19C

C. Yang and M. Dudley (SUNY Stony Brook), H. M. Hogood and S. Seshadri (Northrop Grumman Science and Tech. Center)

Currently SiC development is shifting from 6H to 4H polytype because of the larger electron mobility (800 vs 370 cm^2/V-s) and lower donor activation energy (45 vs 90 meV) of 4H-SiC compared to 6H-SiC. Two 4H-SiC wafers (both with diodes on one surface) were characterized using synchrotron white beam X-ray topography. The influence of defects on performance of these 4H-SiC devices has been investigated. Figure 1 shows Back-reflection topograph of wafer A (g=00024, λ=0.829Å) and figure 2 shows Back-reflection topograph of wafer B (g=00024, λ=0.831Å). In both figure 1 and figure 2, the small white circles are associated with elementary screw dislocations (b=1c, where c is the lattice parameter along <0001> axis) (marked as **S**) are visible. Also some trapezium shaped defects are visible. They are associated with 3C-SiC polytype inclusions (marked as **P**). The size of the inclusions is about 150 μm. It is noteworthy that one inclusion (marked as **P1**) could not be observed through optical microscopy was clearly revealed by back-reflection topography. This is because this inclusion is below the surface of the epilayer. Work performed on the synchrotron topography project, beamline X19C and supported by Northrop Grumman Science Tech. Center under U.S. Goverment Prime Contract N00014-95-C-0132.

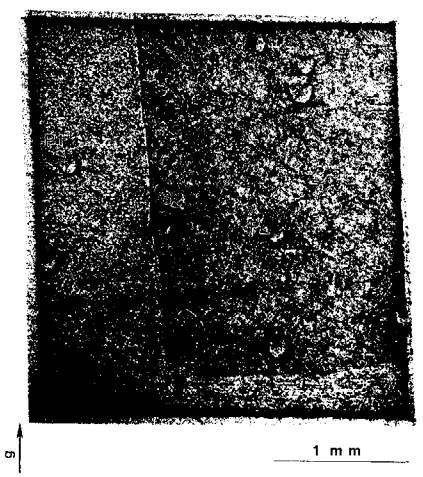


Figure 1.

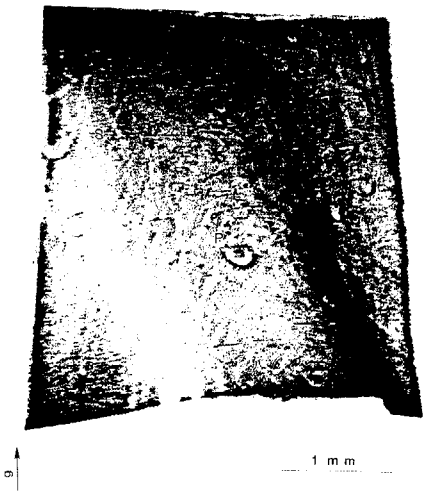


Figure 2.

Studies of Influence of Defects on the Performance of 4H-SiC Devices Using Synchrotron White Beam X-ray Topography: II - Influence of Defects *	X19C

C. Yang and M. Dudley (SUNY, Stony Brook), H. M. Hobgood and S. Seshadri (Northrop Grumman Science Tech. Center)

The influence of polytypes as well as elementary screw dislocations on the performance of the 4H-SiC devices has been investigated. First, by comparing the topographs and optical micrographs of the two wafers with the map of diodes (See Table 1), it is found that all diodes with 3C-SiC inclusions in them show poor performance. In other words, all diodes with good performance are free of 3C inclusions. It is concluded that the polytypes have detrimental effects on the performance of the devices. Second, we can also make a comparison of the superscrew dislocation density between the diodes with good performance and those with poor performance (See Table 2). From the table we can see clearly that the superscrew dislocation density in poor performance devices is much higher than that in good performance. This suggests that the superscrew dislocations may have adverse effect on the performance of the devices. Further study of the effect of superscrew dislocations on the performance of devices are planned subject.

Diode	Performance	Number of Polytypes Observed	Diode	Performance	Number of Polytypes observed
a1	P	1	w1	G	0
a2	P	1	w2	G	0
a3	P	1	w3	G	0
b1	P	1	x1	P	1
b2	P	0	x2	G	0
b3	P	0	x3	P	3
c1	G	0	y1	G	0
c2	P	1	y2	G	0
c3	G	0	y3	P	1
c4	G	0	y4	G	0
c5	G	0	y5	P	1
c6	P	1	y6	P	1
c7	G	0	y7	G	0
d1	G	0	z1	G	0
d2	P	1	z2	G	0
d3	P	1	z3	P	1
d4	G	0	z4	P	1
d5	G	0	z5	G	0
d6	G	0	z6	G	0
d7	G	0	z7	G	0

Note: 'G' stands for 'good'; 'P' stands for 'poor'

Figure 1.

* Work performed on the Synchrotron Topography Project Beamline X-19C and supported by Northrop Grumman Science Tech. Center under U.S. Government Prime Contact No. N00014-95-C-0132

Superscrew dislocation density ($x10^{-3}/\mu m^2$)	Diodes with good performance	Diodes with poor performance
Diodes of type "a1"	7.080	12.98
Diodes of type "b1"	6.731	8.162
Diodes of type "c1"	9.997	16.94
All diodes	8.625	10.62

Figure 2.

Characterization of Defects in 4H-SiC Single Crystals by Synchrotron White Beam X-ray Topography *	X19C

C. Yang, W. Si and M. Dudley(SUNY, Stony Brook), H. M. Hobgood and S. Seshadri (Northrop Grumman)

It has been established [1] that synchrotron x-ray back-reflection geometry is particularly useful for imaging superscrew dislocations in 6H-SiC single crystals. Here we report the application of this technique to 4H-SiC single crystals. Figure 1 shows a high magnification back-reflection topograph of a 4H-SiC wafer. In this figure the black rings with white centers of various diameters correspond to superscrew dislocations. The larger of these circular features on this topograph are associated with 'micropipes'(marked as **M**). The smallest of these circular features are associated with elementary screw dislocations (marked as **S**). Besides there are some black and white lines connecting the circular features ,which correspond to the basal plane dislocations (marked as **BD**). The total numbers of micropipes in this figure is 7 and their density is 78/cm^2. The density of elementary screw dislocations in region A (See figure 1) is 2800 /cm^2. The observation of individual basal plane dislocations and elementary screw dislocations is an indication of the good crystalline quality of this region.

[1] M. Dudley, S. Wang, W. Huang, C. Carter, V. Tsvetkov and C. Fazi, J. Phys. D: Appl. Phys. 28(1995) A63-A68.

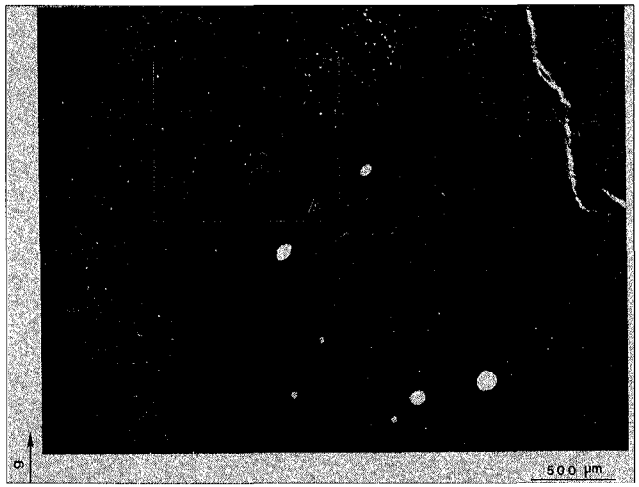


Figure 1.

* Work performed on the Synchrotron Topography Project Beamline X-19C and supported by Northrop Grumman Science Tech. Center under U.S. Government Prime Contact No. N00014-95-C-0132

X-ray Scattering Studies of the Passive Film on Fe(001) and Fe(110)	X20A

A. J. Davenport (U. Manchester), L. J. Oblonsky, M. P. Ryan (BNL), M. F. Toney (IBM), and C. Vitus (BNL)

Despite decades of work, the passivating oxide films that protect (normally reactive) metals from corrosion are still poorly understood. This is because the films are very thin (typically a few nanometers) and are formed in aqueous environments so that ex-situ measurements are susceptible to changes in the film upon removal from the solution in which they grew. The structure of the passive film on iron has been the subject of particularly intense study (1,2 and References therein), but there is still no consensus on questions as basic as to whether the film is amorphous or crystalline. However, recent in-situ STM measurements of the passive film formed on Fe suggest that the surface is crystalline with a proposed γFe_2O_3-Fe_3O_4 structure (2) that is supported by in-situ XANES (1). To confirm and expand upon these results, we have conducted in-situ and ex-situ X-ray scattering experiments on the passive film formed at high potentials on Fe(110) and (001).

The Fe crystals were passivated by potentiostatic polarization for one hour at +0.4V vs. MSE in borate buffer (pH 8.4). Our methodology is to collect a complete data set ex-situ (where the background scattering is small), and then to collect selected in-situ data to compare with the ex-situ experiments. In such a comparison there is excellent agreement, which demonstrates that the passive film formed under these conditions is not altered by emersion.

The diffraction data show that the passive films are epitaxially aligned with the Fe crystals. For the film on Fe(110), we find oxide(111)||Fe(110) and oxide[$\bar{1}$10]||Fe[002], whilst for Fe(001), oxide(001)||Fe(001) and oxide[100]||Fe[110]. From the peak widths, we estimate in-plane domains sizes of 60$\AA$ and 45$\AA$ for films formed on Fe(001) and Fe(110), respectively. A quantitative crystal refinement of the integrated diffraction intensities has been conducted for the passive film on Fe(001). We conclude that the film structure is **not** one of the bulk forms of iron oxide (see figure). Rather the film sturcture is similar to the spinel Fe_3O_4, but with a large fraction of the tetrahedral sites vacant (≈80% occupancy), a smaller fraction of the octahedral sites vacant (≈95% occupancy), and some displacement of the (full occupied) oxygen anions from the positions occupied in Fe_3O_4. Further experiments will probe the dependence of the oxide structure on potential.

1. A.J. Davenport and M. Sansone, J. Electrochem. Soc. 142, 725 (1995).
2. M.P. Ryan et al., J. Electrochem. Soc. 142, L177 (1995).

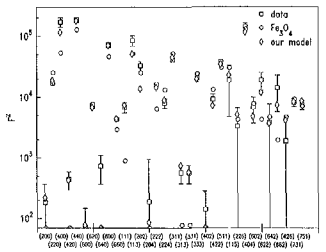


Figure 1. Experimental and model structure factors.

Time-Resolved Measurements of Overlayer Ordering in Electrodeposition *	X20A

A.C. Finnefrock, L.J. Buller, H.D. Abruña, and J.D. Brock (Cornell U.)

In many electrochemical systems, one or more monolayers of an adsorbate may be deposited at a potential less negative than the Nernst potential. The growth mechanisms involved in this so-called underpotential deposition (UPD) have been the subject of intense controversy for over a decade. Recent static x-ray scattering measurements on the underpotential deposition of Cu^{2+} on Pt(111) in the presence of Cl^- in an $HClO_4$ solution have noted the existence of a structure ascribed to an adsorbed CuCl bilayer.

We have performed *in situ* time-resolved surface x-ray scattering measurements on this UPD system. Our data show that copper is electrodeposited onto the surface less than 0.02 seconds after the potential is stepped. In contrast, our time-resolved x-ray scattering data indicate that the overlayer structure requires from 2 to 5 seconds to develop long-range order. Because the surface ordering and charge transfer rates are so distinct, we effectively have a deposition process followed by a two-dimensional ordering process.

We are presently extending these measurements to include absolute reflectivity measurements of the specular and off-specular crystal truncation rods. Through these, we hope to study mass-transfer of ions near the electrode surface and other aspects of the deposition process.

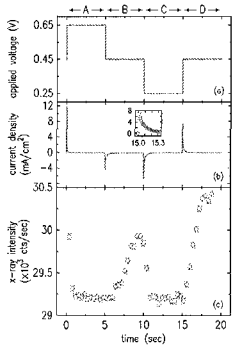


Figure 1. (a) Applied potential steps. (b) Transient current response. (c) Peak intensity of overlayer super-lattice peak. The development of long-range periodic order in the overlayer (panel c) requires significantly more time than that required for the electrodepositionof material onto the electrode surface (panel b).

* This work was supported by Cornell University's Materials Science Center, NSF Grant No. DMR-88-1858-A02.

Using X-ray Scattering to Examine Supra-molecular Organization and Surface-melting at Molecular Interfaces. *	X20A

S.E. Girdwood, A.R. Kennedy, J.N. Sherwood (U. Strathclyde) and K.J. Roberts (Heriot-Watt U.)

Our work involves a study of the structural nature of the solid/liquid interactions taking place at the growth interface of crystals. Of particular interest to us is the development of a more generally ecceptable model for the growth interface. To carry out this work we are using a powerful combination of X-ray reflectivity and surface diffraction techniques to probe the nature of molecular ordering on organic surfaces and how such ordering is changed during crystallisation. Information gained from these experiments is being used to refine our current model of the growth interface structure and hence, to improve the predictive capability of crystal growth morphology computation routines.

Whilst surface x-ray techniques have been applied to inorganic systems quite extensively, their application within the broader areas of organic interface and materials chemistry has been very limited and is ripefor exploitation. The success of this project depends on linking predictive computational chemistry techniques with experimental evidence of interface structures under realistic conditions. This experimental work is only possible using synchrotron radiation and results from it will have major ramifications, at both fundamental and appliad levels, to a range of fields in which control of crystal morphology is of great importance such as materials purification, colloid science, biotechnology and surface engineering.

* We wish to acknowledge the UK Engineering and Physical Sciences Research Council for the funding of this work

Structure and Kinetics of the Sliding Q_1 CDW in $NbSe_3$ *	X20A, X25

K.L. Ringland, S.G. Lemay, R.E. Thorne, and J.D. Brock (Cornell U.)

We have performed detailed measurements of both the structure of the sliding Q_1 charge-density wave (CDW) and the kinetics of its relaxation from the sliding to the pinned state. High q-resolution data obtained at X25 demonstrate unambiguously that the equal time phase-phase correlation function does not decay algebraically at large distances. That is,

$$\lim_{|\vec{r}-\vec{r}'|\to\infty} \langle e^{i\phi(\vec{r})} e^{-i\phi(\vec{r}')} \rangle \neq \frac{1}{|\vec{r}-\vec{r}'|^{\eta}} .$$

The detailed structure of the sliding state is still a major issue and recent models have predicted an assymptotic algebraic decay of the phase-phase correlation function[‡]. An algebraic decay produces a line-shape that traces out the resolution function near the center of the peak but has additional scattering in the wings. In contrast, we measure the full width at half maximum of the Q_1 satellite in the sliding state to be roughly 66% broader at 10× threshold than the same satellite in the pinned state. (The Q_1 satellite in the pinned state is also broader than our resolution.)

Similarly, our time resolved measurements of the relaxation of the Q_1 CDW from the sliding to the pinned state also contradict the predictions of the suggested equations of motion. Specifically, the peak intensity increases monotonically with time after the current is switched off. The solution to the proposed equation of motion has the form

$$\langle |\phi(\vec{q},t)|^2 \rangle = \langle |\phi(\vec{q},0)|^2 \rangle e^{-2q^2Dt} + \frac{\langle |F(\vec{q})|^2 \rangle}{D^2q^4} (1 - e^{-q^2Dt})^2$$

where $F(\vec{q})$ is the quenched random field and D is the diffusivity. This expression has a "dip" in the intensity. Our data does not exhibit such a dip. This discrepancy implies that either a non-linear term is missing from the equation of motion or that the random field, $F(\vec{q})$, is not quenched.

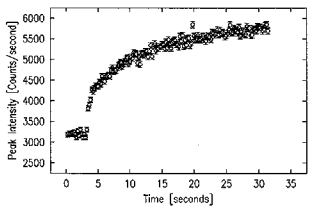


Figure 1. Peak intensity of (0 1+Q_1 0) satellite as a function of time. Current is turned off at t = 3 seconds.

* This work was supported by NSF Grant No. DMR-9501119

Nanosuspensions in Helium	X20B

V.Kiryukhin, B.Keimer (Princeton U.), E.Gordon, and V.Khmelenko (IEPCP, Russia)

The structure and thermal properties of a novel type of suspension of impurity atoms and molecules in helium were studied in a series of x-ray diffraction measurements. The suspensions were prepared by injecting a jet of helium containing diluted amounts of impurity atoms or molecules (especially Ne and N_2) into superfluid helium at T=1.5K. By this technique the formation of microcrystals of the impurity species is prevented. X-ray powder patterns taken after preparation of the suspensions indicated the presence of a bulk amount ($\sim$1cm^3) of nanocrystallites of the impurity species (typical diameter 30Å) in the liquid (see Fig 1, 2). There is also evidence for even smaller entities (e.g. single atoms) dissolved in the liquid. The suspensions were stable for many hours, remarkably even after the liquid helium was drained out of the sample cell. The nitrogen nanocrystallites persisted essentially unchanged up to temperatures of about 15K, far above 4.2K, the evaporation temperature of pure helium. At T=15K the diffraction profiles suddenly became instrumentally narrow, indicating a sudden coalescence into microcrystallites. The coalescence temperature of the neon nanocrystals was about 2.5K.

These results can only be understood by hypothesizing a shell of helium bound to the nanocrystals by van-der-Waals interactions, which prevents their coalescence at low temperatures. Helium is the only element whose large zero-point motion prevents it from forming a solid phase at ambient pressure. The observation of nongaseous helium in the van-der-Waals shells at temperatures up to 15K is therefore remarkable and must be explained in the framework of quantum many-body physics. In addition to fundamental concepts in quantum physics, our experiments are also expected to stimulate new developments in matrix isolation spectroscopy.

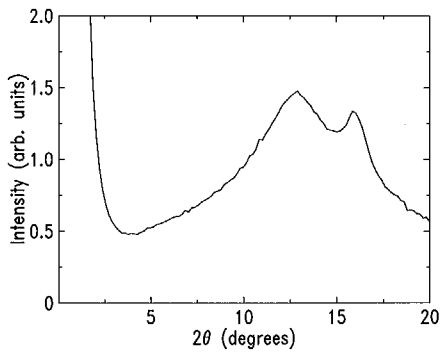


Figure 1. X-ray powder pattern for the nanosuspension of Ne in helium at T=1.5K. The signal is the superposition of liquid helium and neon nanoclusters signals.

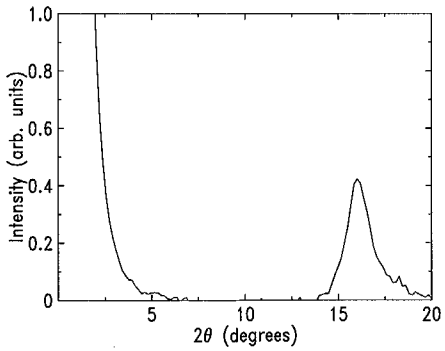


Figure 2. The data of Fig 1 with the liquid helium signal subtracted. This data shows that the sample is composed of Ne nanoclusters (typical size $\sim$30Åand smaller). Neon atoms in the clusters form close packed structure.

Morphological Investigation of Nylon 66 Fibers Using Radial Distribution Function Analysis — X20B

J. R. Sharrow, J. M. Schultz (U. of Delaware), B. S. Hsiao, and H. Chang (DuPont)

The morphology of nylon 66 fibers was probed by application of Radial Distribution Functions (RDFs) to diffraction patterns. A four circle diffractometer, operating at a wavelength of 0.7092Å, was used to obtain equatorial scans of various fibers previously exposed to different processing conditions. Each sample was held in a fixed position, as the 2θ arm was rotated from 148° to 4° in intervals of 0.075 degrees (1.24 nm^{-1} $\leq q \leq$ 9.39 nm^{-1}).

RDFs are real space operations giving the number density of atoms displaced a distance r from an atom selected to be at the center. Physically, the RDF is expressed as $4\pi r^2 \rho(r)$, and commonly presented as a reduced RDF, $G(r) = 4\ 4\pi r[\rho(r)-\rho_o]$, where ρ_o is the average number density. The RDF is computed as a Fourier transform of the measured intensity after correction for incoherent scattering. This type of transformational method offers the advantage that the calculation of the correlation length requires no prior assumption as to the presence or absence of a crystalline phase. The correlation length is the distance at which the amplitude of the fairly periodic oscillations on the order of several angstroms, becomes similar to that of the "noise". This noise is caused by the upper limit of integration. Fourier transformation involves integration in reciprocal space from 0 to infinity, but it is impossible to obtain such data experimentally. Therefore, the structurally dependent oscillations in the RDF curves are moderated by "noise" in the form of wavelets. These wavelets, with a period of $2\pi/K_{max}$, determine the resolution in real space.

Figure 1 displays the reduced radial distribution function, G, as a function of r. The spacing of the oscillations in these curves is on the order of the intracrystalline spacing, about 4Å. The control fibers, prepared in the absence of heatsetting, are characterized by a correlation length of approximately 65Å while fibers subject to wet heatsetting, have an increased correlation length of 75Å. Drops in magnitude, present at approximately 16Å and 38Å, are noticeable in both curves and persist over a spacing of a few Angstroms. These observations imply that crystalline fibril is roughly 65Å to 75Å in the dimension transverse to the fiber axis, but contain small defects at consistent spacings. This work supported BY NSF-GOALI grant (DMR-9629825).

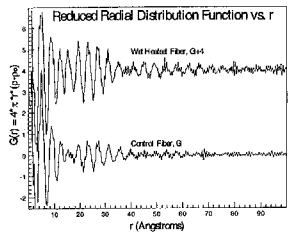


Figure 1. Reduced radial distribution func. for control fiber, wet-heatset fiber.

Effects of Rubbing Polyimide Films — X20C

J.M. Sands, S.K. Kumar (Penn State U.), T.P. Russell, and M.F. Toney (IBM)

In the process of characterizing the effects of rubbing polymer surfaces under finite loads, we have performed a series of experiments in which various parameters involved with rubbing polymer surfaces have been varied, and grazing incidence x-ray scattering (GIXS) has been applied in order to characterize the effects which occur as a result of rubbing and curing polymer films. Synchrotron based GIXS experiments using a well defined incident beam allow one to probe the range of polymer films structure in a depth dependence geometry ranging from 5 nm to bulk film scattering.

Following recent experiments, a model describing the orientation of polymer chains in the surface under rubbing is being developed which shows how the effects of rubbing are consistent with the usual pheomena of yielding in polymer materials; the concept is expected, though perhaps not obvious as the polymer material investigated has a high modulus (10.5 GPa), high strength (300 MPa), and high glass transition temperature (≈400°C).

Polymer films of BPDA-PDA (bisphenylenedianhydride-p-diamine) were prepared on silicon substrates by spin casting from a precursor solution of poly(amic acid). The precursor films are subsequently heated to temperatures from 200 to 400°C in order to create the polyimides. Films prepared in this way show that the structual order present is dependent upon the imidization conditions (figure 1.)

Rubbing parameters which have been investigated include rubbing distance, applied load, and film thickness. In each of these classes, a critical value exists above which changes in the structural characteristics of teh scattering profiles are observable. The existenc of these threshhold values support the high probability of yielding as the primary mechanism of deformation. Since the applied force is not the "observed force" at the polymer surface, it is necessary to show how the results observed by GIXS are consistent with the yielding model in a free standing polymer film. This task remains to be completed at this time.

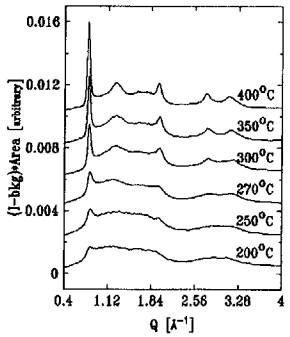


Figure 1. Effects of imidization temperature on the scattering profiles observed for BPDA-PDA films on Si(100) substrates. The samples were heated for 3 hours at the temperatures indicated in the inset.

Resonant Raman Scattering at the Fe K-edge in Fe_2O_3 * | X21

W. A. Caliebe, C.-C. Kao, and J. B. Hastings (NSLS)

Resonant Raman scattering (RRS) is a two-photon scattering process where the energy of the incident photon is tuned through the absorption edge and the fluorescence is analyzed. This method allows to seperate different electronic excitations in the absorption edge because the energy resolution is not dominated by the core hole life time of the deep lying core hole.

The experiment has been done at the Fe K-edge in Hematite (Fe_2O_3). The absorption edge is shown in fig.1. Observing the fluorescence for these three different incident energies (see fig.2) reveals three different transitions which are clearly seperated. The first two transitions are excitations into empty 3d-orbitals. The 3d-orbitals split in an octahedral field into the e_g and t_{2g} orbitals which are seperated by approximately 1.5 eV. Excitations into these orbitals result into relatively sharp peaks at $\hbar\omega_1 - \hbar\omega_2$=705.5 eV for $\hbar\omega_1$=7113.4 eV and $\hbar\omega_1 - \hbar\omega_2$=707.2 eV for $\hbar\omega_1$=7114.8 eV. These narrow peaks are also observed as small steps in the scan for $\hbar\omega_1$=7118.8 eV. This last scan measures excitations into states with s- and p-character. Calculations to explain these data are planned for the future.

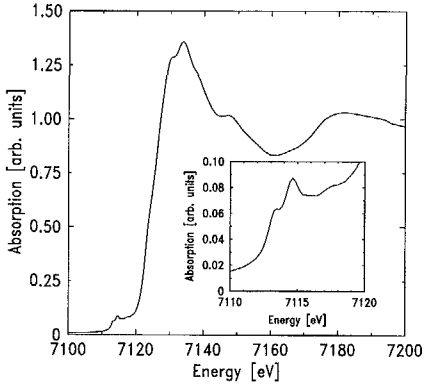


Figure 1. Fe K absorption edge in Hematite. The absorption spectrum starts with some weak fine structure at E=7110 eV (see the inset), which corresponds to excitations into empty 3d-levels. This absorption has quadrupol character and is thus very weak. This structure is followed by the dominating "white line" at E=7130 eV, which is the absorption into empty 4p-levels.

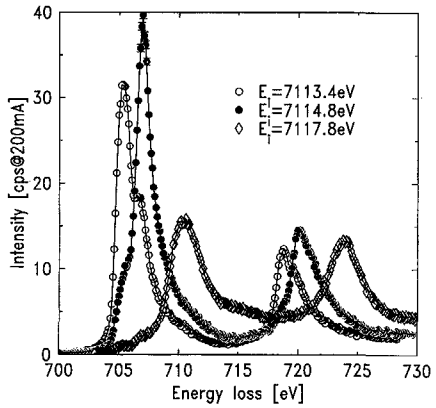


Figure 2. Resonant Raman scattering of Hematite at $\hbar\omega_1$=7113.4 eV (open circles), $\hbar\omega_1$=7114.8 eV (full circles) and $\hbar\omega_1$=7117.8 eV (rhombs). The error bars are given by small vertical lines or are smaller than the symbol size.

* This work was supported by US DOE grant DE-AC02-76CH00016

High Energy Resolution Beamline * | X21

W. A. Caliebe, C,-C. Kao, D. P. Siddons, and J. B. Hastings (NSLS)

The wiggler beamline X21 is dedicated for inelastic X-ray scattering with high energy resolution. In order to obtain an energy resolution of better than 0.3 eV a new monochromator and a toroidal mirror have been installed.

A high energy resolution is usually obtained using a dispersive set-up of two crystals. The problem of this set-up is that the beam moves for energy changes. This problem has been solved using two double crystal monochromators which have one asymmetric and one symmetric reflection. The sequence of the reflections is asymmetric-symmetric-symmetric-asymmetric. The two symmmetric reflections in the middle have no influence on the resolution. Their only purpose is to keep the exit of the beam fixed.

The asymmetric reflections have miscuts of 16° and -16° respectively. These two reflections are aligned dispersively resulting in a resolution of ΔE=220 meV. The monochromators are directly behind the source because a focussed beam coming from a mirror would worsen the resolution.

The mirror is a Zerodur glass with bending radius R=1 km and r=42 mm. The mirror is coated with Platinum in order to reject higher harmonics. The mirror is located in 16 m from the source and 8 m from the sample. The focus at the sample is 500×300 μm^2. The flux at the sample is $22'\cdot10^{10}$ photons/s.

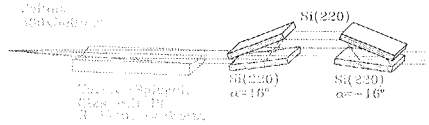


Figure 1. New optics of the inelastic X-ray scattering beamline X21: the four-bounce monochromator and the toroidal mirror.

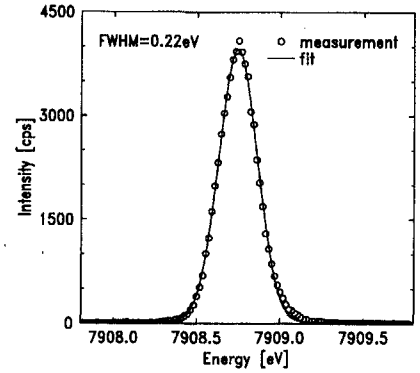


Figure 2. Energy resolution of the spectrometer: The resolution is determined by measuring the quasielastic scattering of a peace of PMMA. The full width half maximum is ΔE=270 eV which is the convolution of the monochromator and analyzer widths.

* This work was supported by US DOE grant DE-AC92-76CH00016.

Inelastic Xray Scattering from Single Crystal Sodium | X21

P.C.Chow and S.C. Moss (U. Houston), C.C. Kao and J.P. Hill (BNL)

In condensed matter physics, unlike high energy physics, we know the identity of the particles of interest (electrons) and their interactions (Coulomb). What is of difficulty is handling the consequences of the many-body interactions in order to explain the physical properties of a system. Inelastic xray scattering data, $S(q,\omega)$, contain information on the time and space correlations of the electrons of the system. Because of the weak intereaction of xrays with electrons, inelastic xray scattering is an ideal method for measuring many-body effects in solids. In our initial experiments on X21, our approach is to study the simple metal free-electron metal sodium. We have prepared a single crystal of Na, 11 mm in diameter, and sliced the crystal to produce a 2 mm thick slab with mosaic spread of 0.2°. The spectrometer analyzer was a Si(555) spherically bent cyrstal, set to accept 9839 eV xrays. Our monochromator consisted of 2 pairs of Si (220) crystals. The inelastic spectra were taken by changing the incident energy, yielding energy loss data. The overall energy resolution was about 1 eV and data was taken in transmission geometry. For $K=K_F$, a peak in the spectrum 7 eV away from the elastic line was clearly seen, which corresponds to the plasmon collective excitation of the conduction electrons in Na. For $K=2K_F$, see Fig.1, the broadening of the spectrum is attributed to single particle excitations. The feature at 30eV corresponds to the Na L edge. In other systems, corresponding spectra shows a double peak structure, whose cause is still to be determined. Our data show that this feature is absent in Na. Future studies will concentrate on collecting data in high symmetry directions of the single crystal.

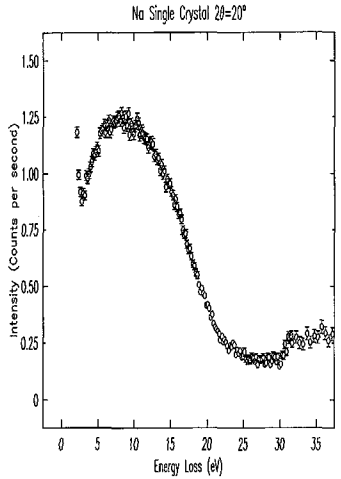


Figure 1. Inelastic scattering of single crystal Na in the [211] direction at $K=2K_F$

High Resolution Kα Emission Studies of Iron(III) Porphyrins | X21

K. A. Daly (U. of Michigan), W. Caliebe, C.-C. Kao (NSLS) and James E. Penner-Hahn (U. of Michigan)

High resolution x-ray emission has been used to investigate hyperfine electronic structure of transition metal complexes. Electronic interactions that were previously detectable only with polarized measurements on oriented crystals have been resolved using isotropic samples. X-ray emission intensity was collected as a function of excitation and emission energy producing a three-dimensional surface plot. Data were collected in the excitation regions of $1s \rightarrow 3d$, $1s \rightarrow 4p$ and other transitions in the edge area. The emission region data were collected in the area of Kα emission ($2p \rightarrow 1s$) for $[Fe(III)(octaethylporphyrin)(THF)_2]ClO_4$. Each iron exists in a Jahn-Teller distorted octahedral environment and is in a high-spin state. The data display information on d-orbital degeneracy, atomic orbital occupancy, coordination environment and electronic interactions. Figure 1 shows representative Kα emission spectra collected at various points before and on the K-absorption edge. The Kα lines of the three excitation energies show different peak maxima energies, a slight change in $K\alpha_1$:$K\alpha_2$ peak height ratio, and a significant peak width fluctuation. These changes are all indicative of changes in the overall spin and angular momentum of the system. Calculations performed with Frank de Groot of the University of Groningen show the effects are not predicted through simple continuum state multiplet calculations in conjunction with resonant Raman theory. Interpretation of a complete data set, to be collected at a later date, should give more detailed information on the electronic structure and orbital occupancy of the molecule.

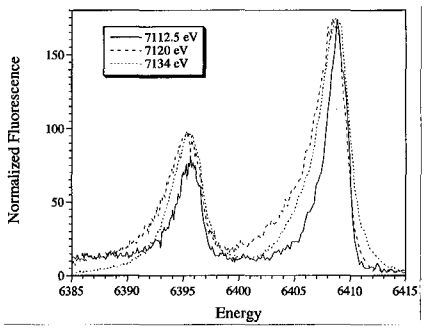


Figure 1. Kα emission spectra of $[Fe(III)(OEP)(THF)_2]ClO_4$. The $K\alpha_1$ and $K\alpha_2$ emission lines were collected at excitation energies of 7112.5 eV, which is in the pre-edge region, 7120 eV, which is low on the absorption edge, and 7134 eV, which is at the maximum of the absorption edge. The spectra are normalized to the same peak height.

Near-Threshold Behaviour of the Cu $K\alpha_{1,2}$ Emission Spectrum | X21

M. Deutsch, O. Gang, M. Fritsch (Bar-Ilan U., Israel) and C.C. Kao (BNL)

The Cu $K\alpha_{1,2}$ emission spectrum was studied by photoexcitation near the K edge, using the new four-bounce monochromator/focussing mirror combination, and a spherically bent Si(444) analyzer.The measured FWHM resolution of the system was ~0.45 eV at an incident energy of $E_{incident} \approx 9$ keV.

Three regimes were observed with increasing $E_{incident}$. The first, $E_{incident} <$ 8981 eV, is just below the edge at 8981 eV. The linear peak shift, the fast intensity decrease and the line shape distortions, due to the Resonant Raman Effect, are all clearly observed as shown in Fig. 1.

The second regime, 8981eV$\leq E_{incident} \leq$8995 eV is above the K edge, but still below the threshold for 3*d*-spectator transitions which require an aditional 10-15 eV photon energy to create the initial $\underline{1s3d}$ hole state. Unlike for higher energies, the lineshape here is a pure lorentzian, as shown by the solid line in Fig. 2.

In the third regime, $E_{incident} \geq$ 9000eV, 3*d*-spectator transitions are energetically allowed, and contribute with increasing intensity to the lineshape. As shown in Fig. 2, these contributions are most pronounced on the low-energy side of the $K\alpha_1$ line. This study then demonstrates clearly that the well-known asymmetric lineshapes of the emission lines of the iron-group elements originate in the 3*d*-spectator transitions. While the analysis is still in progress, the results so far indicate that the intensity of the 3*d*-spectator transitions increase smoothly from threshold and saturates at ~100 eV above it, indicating a shake-off origin for these transitions, as we also found recently for the $K\alpha_{3,4}$ satellites of copper[1].

1. M. Deutsch, O. Gang, K. Hämäläinen and C. C. Kao, *Phys. Rev. Lett.* **76**, 2424 (1996).

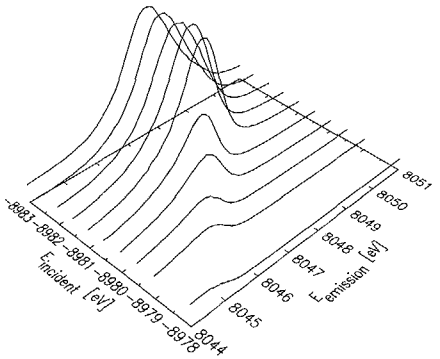


Figure 1. The Cu $K\alpha_1$ emission spectra *vs.* excitation energy in the Resonant Raman regime near the K edge.

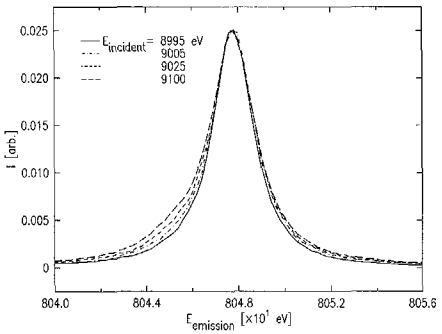


Figure 2. The $K\alpha_1$ line-shape variation above the threshold for the 3*d*-spectator transitions.

Resonant and Non-resonant Inelastic X-ray Scattering Studies of Electronic Excitations | X21

J.P. Hill, C.-C. Kao and W.A.C. Caliebe (BNL)

Inelastic x-ray scattering offers unique capabilities in the study of electronic excitations, allowing regimes of momentum and energy transfer to be probed that are inaccessible with any other technique. In simple metals, this opens up the important regime of wave-vectors around $2k_F$, where dramatic departures are seen from the simplest many-body theory, the RPA. The origin of these discrepancies has been the source of some considerable debate. One explanation is that it is higher order corrections to the RPA that are relevant. The second view holds that band structure effects are significant. By studying the excitation spectrum in both liquid and solid phases, the influence of the LRO may be determined experimentally. Following on from our earlier work, on liquid Li and Na, we have studied Al, which is of particular interest as a nearly-free-electron metal, yet displays significant orientation-independent fine structure in the response. As shown in Fig. 1, the response in the liquid phase is very similar to that of the solid, suggesting that the overall shape of the response is not determined by the LRO. However, the fine structure evident in the solid phase is much reduced in the liquid phase, demonstrating unambiguously that it results from the LRO and is not a many-body effect. These results support our earlier conclusions from the Li and Na data.

In a separate body of work, we have carried out resonant inelastic scattering studies on Nd_2CuO_4, the parent compound of a high-T_C family. In these experiments, the incident photon energy is tuned through the Cu K-edge, and the energy loss spectrum is studied. In the vicinity of the K-edge, a resonant feature is seen with a constant energy loss of ~ 6 eV. It is speculated that this is a charge transfer process, involving the Cu site and the Oxygen ligand.

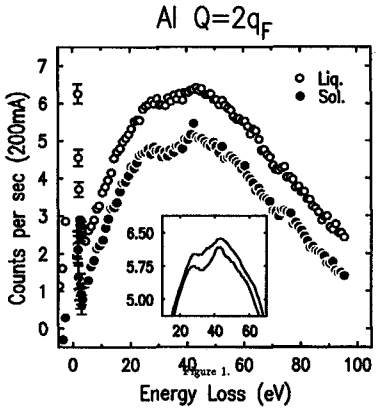


Figure 1.

Inelastic X-ray Scattering Spectroscopy in $Sr_2CuO_2Cl_2$ | X21

E.D. Isaacs, P. Platzman (Bell Labs), C. Burns (Western Michigan U.), P. Abbamonte, M. Klein (U. of Illinois), and L. Miller (Ames Lab)

The electronic structure of the cuprate superconductors continues to be the focus of intensive study because of the possibility of gaining insight into the mechanism of high-T_C superconductivity. Since superconductivity evolves continuously from the insulator by doping, the electronic structure of the parent insulators is of particular interest. Optical studies (q=0 $\AA^{-1}$) show that the lowest lying excitation in all of the parent high-T_C insulators is at about 2 eV. These studies have also shown a transfer of spectral weight upon doping from the feature at 2 eV to a mid-gap excitation at lower energies. The exact nature of of these excitations are not well understood. Characterization of the excitations at intermediate energies is important for theories on high-T_C in order to test the various model Hamiltonians.

We have studied the electronic excitation spectrum at in the parent high-T_C coumpound $Sr_2CuO_2Cl_2$ with 0.5 eV energy resolution. Our spectra reveal a feature at 2 eV, near the insulating gap observed optically, and an optically forbidden transition at about 5.5 eV (see figure 1). We assign the 2 eV excitation to a charge transfer from an occupied oxygen p-band to an unoccupied copper d-level. The 5.5 eV excitation we ascribe to an intra-d-band transition which may be directly related to the Hubbard U. We have also measured the momentum transfer dependence along two directions in the Cu-O plane. Along the (210) direction the charge-transfer gap disperses weakly giving a band width of about 0.5 eV. In contrast, along the (110) direction there is a feature that disperses by as much as 1.5 eV. These results are consistent with very recent electron energy loss spectra taken in the same material. They ascribe the anisotropic dispersion to the anisotropy of the antiferromagnetic background and the fact that an electron-hole pair can move through the lattice more easily than a single hole.

These studies have been made possible by recent advances at beamline X21 and our development of spherically bent analyzers. The main advance at X21 is the new monochromator with 0.2 eV energy resolution. With further improvements expected at X21, in particular larger horizontal accpetance, we expect to be able to reduce our collection times by a factor of two to four. The scan shown in figure 1 took about 15 hours to obtain.

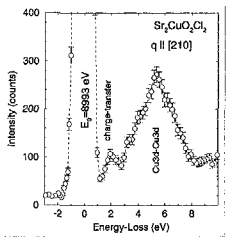


Figure 1. Inelastic x-ray scattering in the parent high-T_C insulating compound $Sr_2CuO_2Cl_2$ at a momentum transfer, q=0.8 $\AA^{-1}$. This scan was taken at beamline X21 with an energy resolution of 0.5 eV with q along the [210].

X-Ray Resonant Raman Scattering in NiO: Resonant Enhancement of the Charge Transfer Excitations * | X21

C.-C. Kao, W. A. Caliebe, J. B. Hastings (NSLS), and J.-M. Gillet (U. Marne, France)

We report the results of a hard x-ray high resolution XRRS study of NiO, one of the prototypical Mott-Hubbard systems. Inelastic x-ray scattering spectra near the NiO valence band emission energy were measured as the incident photon energy scanned through the Ni K absorption edge.

A new spectral feature, which is not observed for incident energies far away from the absorption edge, appears in the inelastic scattering spectra in addition to the valence band emission spectrum. While the average energy of the valence band emission spectrum remains constant, the average energy of this new feature disperses linearly with the incident photon energy. The average energy transfer of this new feature is about 6.5 eV, close to the recently reported anion-to-cation charge transfer energy of NiO.

The new loss featureand its resonant behavior are interpreted in terms of a cluster model or the Anderson impurity model.

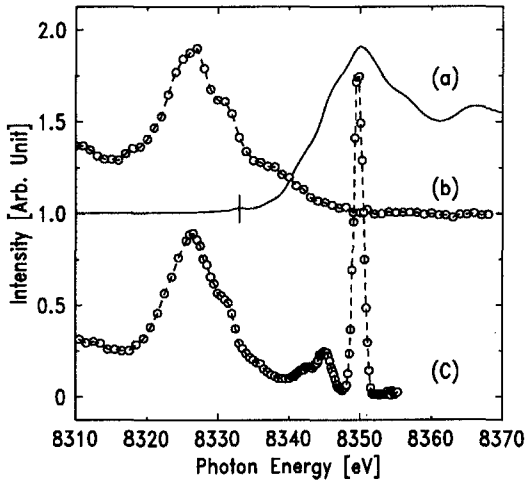


Figure 1. a) Ni Kabsorption spectrum of NiO; b) normal valence band x-ray emission spectrum of NiO; c) Resonant inelastic x-ray scattering spectrum of NiO obtained with the incident photon energy tuned to the main peak of the absorption spectrum (a)

* This work was supported by US DOE grant DE-AC02-76CH00016.

Spin-Polarized Mn K-Edge Measurements of Doped $LaMnO_3$	X21

T. A. Tyson (NJIT), C.-C. Kao, W. Caliebe (NSLS), and J. J. Neumeier (FAU)

Recent work by von Helmolt *et al.* [1], revealed that $La_{1-x}A_xMnO_3$ (A=Ca, Sr, ...), exhibits large magnetoresistance values at low temperature and high fields (60 kOe and 77 K). The large change in conductivity is concomitant with a insulator to metal transition. No detailed studies of the changes in the Mn 3d spin density with temperature or doping have been performed.

The Mn K_β spectrum provides a direct method to probe the total Mn 3d unpaired spin (S) and effective charge density on the Mn sites. Temperature dependent K_β emission spectra are shown below (Fig. 1) for the 30% Ca system measured above and below T_c= 250 K. There is a reduction in intensity of the main line above the Curie temperature. Hence S may be changing with temperature. The effective charge on the average Mn site is not changing, however. It is possible that the degree of hybridization i.e. the mixing of the Mn 3d and O 2p changes with temperature in concert with local structural changes [2] previously found. Models of the CMR materials must incorporate these effects. Detailed analysis of Mn K_β spectra will assist in determining the essential physics and correct Hamiltonian (see [3]) for this system.

[1] R. von Helmolt *et al.*, Phys. Rev. Lett. **71**, 2331 (1993).
[2] T. A. Tyson *et al.*, Phys. Rev. B, **53**, 13985 (1996) and references therein.
[3] A. J. Millis, P. B. Littlewood and B. I. Shraiman, Phys. Rev. Lett. **74**, 5144 (1995).

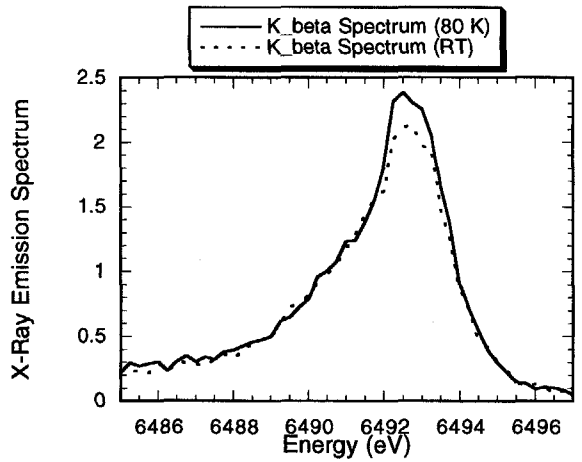


Figure 1. The Mn K_β spectrum of 30% Ca doped $LaMnO_3$ measured at 80 K (solid line) and room temperature (RT = 300 K, dotted line).

Real-Time X-ray Scattering Study of Sputter-deposited $LaNiO_3$ Thin Films on Si Substrates	X22A

H. Y. Lee (SRRC, Taiwan), C. H. Lee (National Tsing Hua U., Taiwan) and K. S. Liang (Exxon)

$LaNiO_3$ (LNO) is a perovskite-type metallic oxide having the same type of structure as that of ferroelectric films, which provides a good crystallographic compatibility with the ferroelectric layers and can be used as the bottom electrode in fabricating the integrated ferroelectric capacitors on Si. Recently, highly (100)-oriented LNO films on different substrates by radio frequency magnetron sputtering method was prepared successfully[1]. In a previously study[2], an intermediate layer of about 10 nm was found at the interface between substrate and overlayer. This particular layer of unidentifiable structure is of great interest in the understanding of the growth mechanism of LNO thin films and the subsequent development of highly textured ferroelectric thin films. In this work, real-time x-ray reflectivity and diffraction measurements under in-situ sputtering conditions were applied to study the growth mechanism of LNO on Si substrate. The experiment was performed at the nearly commissioned beamline X22A using 10.4 KeV phptons. Samples were prepared via a 6 kW/cm2 rf magnetron sputtering system under 10 mTorr of O_2 and Ar mixture gases. Different structures of thin films were found under different growth conditions. However, we were able to tune sputtering conditions to simulate the growth of the special structure of our interest. In a particular growth condition, our results clearly identify an intermediate layer which grows in the first 10 min of deposition, as observed from the reflectivity curves shownat left. The in-situ x-ray diffraction patterns (at right) show that this intermediate layer is an amorphous layer. Sequential growth measurements show the development of the film texture in details. As shown, a significant increase of (100) diffraction intensity relative to that of (110) as the deposition time increase, indicating that the preferred (100) textural structure is developed on the top of this intermediate layer.Detailed data analysis is in progress. The authors would like to thank the hospitality and help from Dr. B. Ocko, Ms. J. Wang and Mr. S. Coburn at X22A beamline. 1. C.C.Yang, et.al., Appl. Phys. Lett., 66, 2643 (1995). 2. H.Y.Lee and T.B.Wu, J.Mater. Res.

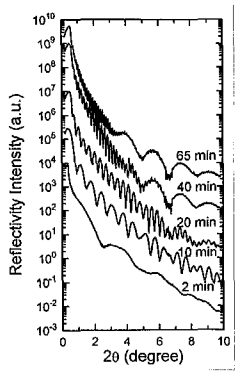


Figure 1.

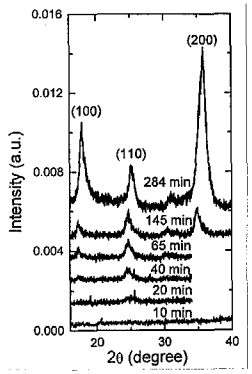


Figure 2.

Structure Analysis of the Cu Metallization of AlN Using the Polyol Method *	X22A

L. J. Martínez-Miranda (U. of Maryland), G. M. Chow, L. K. Kurihara, D. Ma and P. E. Schoen (NRL)

The polyol method was used to produce the electrodeless Cu metallization of AlN substrates. This method results in the formation of a nanostructured Cu powder. The substrates were placed in the polyol solution and brought to reflux for times ranging from 15 to 60 minutes. For each time, the substrates were placed horizontally near the bottom of the solution, or vertically dipped in the solution. We used a combination of small angle xray sacttering and grazing incidence asymmetric Bragg scattering (GIAB) to characterize the structure evolution of the deposited films.

Films deposited at short reflux times (15 minutes) did not show evidence of Cu metallization. In addition, we observed a difference in the small angle signal between horizontally depososited films and vertically deposited films, which became more apparent the longer the reflux time. The figure below shows a comparison between the small angle signal for the vertically and horizontally depostied films, refluxed for 45 minutes. There is a signal in the 4nm range for the vertically deposited film at glancing incidence. The abscence of such a signal for the horizontally deposited film can be attributed to the presence of copper oxide in this film. Although the oxide is present in both vertical and horizontal films, our GIAB measurements show that the latter have a large concentration of oxide near the surface of the film. This layer is polycrystalline in nature, but does not consist of nanometer size building blocks. A more detailed analysis of these films is in progress.

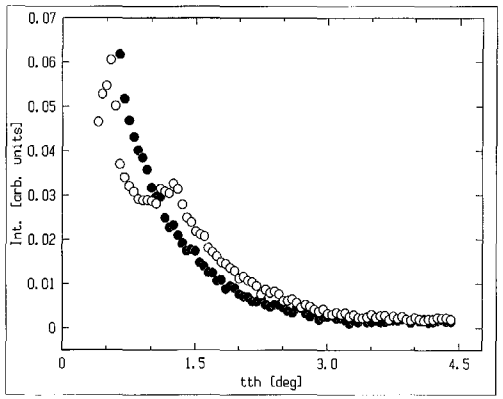


Figure 1. Comparison of the small angle signal at glancing incidence for the V-45 (open circles) and H-45 samples (closed circles).

* This work was supported by an internal UMD Grant and by the NRL 6.2 and NRL-TEW programs on Nanostructured Materials.

In situ Structural Characterization of Lithium-ion Battery Electrode Materials	X27A, X22A

T.R. Thurston, N.M. Jisrawi, S. Mukerjee, X.Q. Yang, J. McBreen (BNL - DAS), M.L. Daroux, and X.K. Xing (Gould Electronics)

The low cost, high operating voltage, and low toxicity of $Li_xMn_2O_4$ make it a good candidate for use as a cathode in lithium-ion battery cells. However, this material can not be reproducibly manufactured yet, a problem which arises in large part because the structural properties of $Li_xMn_2O_4$ vary considerably with synthesis conditions. The structure also changes during the lithium intercalation process, so studies of operating battery cells may help resolve some of these issues by allowing one to separate structural properties dependent on the lithium content from those dependent on the underlying manganese-oxygen skeleton. We report here some of our initial results from combined electrochemical and synchrotron x-ray scattering measurements performed on operating cells.

X-ray diffraction experiments were performed at X27A with 24.5 keV photons and at X22A with 10 keV photons. Cells of approximate dimensions 2cm x 3cm x 0.5mm were manufactured by Gould Electronics, sealed at the factory, and mounted in a transmission geometry on the spectrometer with *no modifications*. Even though the x-ray beam must penetrate through the external case, electrolyte, and binding materials in this geometry, the high flux of a synchrotron allows data with reasonable counting rates to be taken [1].

An example of the structural information that can easily be obtained with this technique is illustrated in the right figure. Here 2θ scans taken through the $Li_xMn_2O_4$ (333), (511), (440), and (531) peaks are presented (the (440) peak is partially obscured by an aluminum peak at 20.3°). The data have been offset from each other for clarity, and they show the evolution of these peaks as the cell was discharged from 3.90 volts to 2.94 volts. The data indicate that expanded and nonexpanded phases coexist over a certain range of voltages. Other structural properties such as this two phase coexistence and their relationships to electrochemical properties are discussed in reference [2].

[1] T.R. Thurston *et al.* Appl. Phys. Lett. **69**, 194 (1996).
[2] N.M. Jisrawi *et al.* J. Electrochem. Soc., submitted.

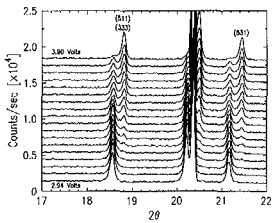


Figure 1. 2θ scans (λ=0.501Å) showing the evolution of two-phase coexistence as a battery cell is discharged.

In Situ Measurements of Texture and Phase Development in Bi-2223 Silver Cladded Superconducting Wires	X27A, X22A

T.R. Thurston, U. Wildgruber, N.M. Jisrawi, M. Suenaga, Y.L. Wang (BNL), and P. Haldar (IGC Corporation)

During the past two years, techniques for characterizing silver-cladded Bi-2223 superconducting wires with hard x-rays have been developed at X27A [1]. In order to penetrate through the silver cladding, the incident x-ray energy is tuned just below the silver edge at 25.5 keV. The samples are also examined in a transmission geometry, so bulk structural properties are probed. Using these techniques, we have previously shown in *ex situ* experiments that both the c-axis alignment (texture) and Bi-2223 phase development have large effects on the current carrying capacity of fully processed wires.

More recently, we have begun experiments where the phase and texture development of Bi-2223 are monitored as it grows from precursor materials (typically Bi-2212 plus CuO *etc.*) within its silver sheath. This *in situ* work has been done in an x-ray compatible furnace with temperature stability of 0.2°C at 830°C. The figure below shows the phase and texture development of a typical sample during the first 50 hours of processing. The solid line represents the temperature program followed. The furnace was ramped from room temperature up to 600°C, held at 600°C for 6 hours, ramped again from 600°C to 840°C over a period of 12 hours, and then held at 840°C. Bi-2223 phase content (represented by the open triangles) began to develop only after reaching 840°C. On the other hand, the weighted average of the Bi-2212 and Bi-2223 texture, represented by the (200) FWHM (closed circles), improved significantly while the sample was being ramped from 600°C to 840°C. Thus, the texturing and phase development mechanisms are largely decoupled. The implications of this and many other *in situ* experimental results are discussed in reference [2].

[1] T.R. Thurston *et al.* J. Appl. Phys. **79**, 3122 (1996).
[2] T.R. Thurston *et al.* J. Mat. Res., submitted.

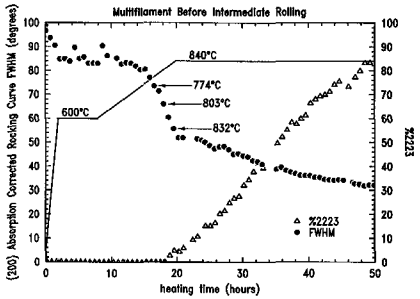


Figure 1. Time Dependence of the Phase and Texture Development in a Multifilament Wire.

Anomalous Lattice Expansion of an Underpotentially Deposited Ag Bilayer on Pt(111)	X22A

J.X. Wang, R.R. Adzic, and B.M. Ocko (BNL, Physics)

Incommensurate metal monolayers and bilayers are usually compressed compared to the bulk solids because of the reduced coordination at the surface. Here, we show an unusual example of lattice expansion in both, lateral and vertical directions in a hexagonally close-packed bilayer. The bulk lattice constant of Ag is larger by 4 percent than that of Pt. At high underpotentials, Ag forms a commensurate (1x1) monolayer on Pt(111). Near the bulk deposition potential, a second Ag layer is deposited which causes restructuring of the first adlayer. The two mutually commensurate Ag adlayers form a hexagonal Ag bilayer which is rotationally aligned but incommensurate in lattice spacing with the Pt substrate. As shown in Fig. 1a, the diffraction peak (dashed line) is centered at 0.94 along the (0,K) axis. At potential 20 mV negative of the bulk deposition potential, an additional peak appears at 0.96 (solid line) which corresponds to the bulk Ag lattice spacing. These data demonstrate that the in-plane lattice spacing of the Ag bilayer is expanded by 2.1 percent compared to the bulk Ag. From analysis of the specular reflectivity (Fig. 1b), and the surface rods at (0.94,0.94) and (0,0.94) (Fig. 2), we find that the Ag-Ag layer spacing is 2.56 Å which indicates an expansion of 8.4 percent from the layer spacing of bulk Ag(111). These unusual lattice expansions are likely due to the charge transfer from the Ag bilayer to the Pt substrate which has been reported from surface stress and x-ray photoelectron spectroscopic measurements. Other aspects of this system, such as, surface alloy formation and fcc/hcp stacking of the second layer, will be discussed at a later date.

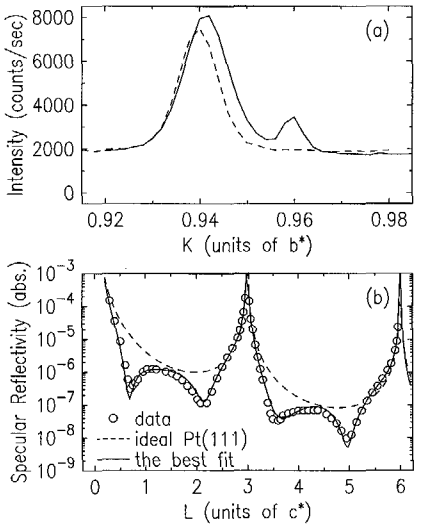


Figure 1.

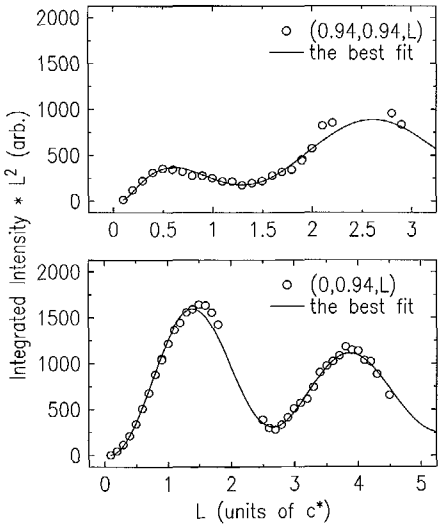


Figure 2.

Effect of Metallic Caplayers on the Magnetic Structure of Thin Cr(001) Films * — X22B

P. Bödeker and H. Zabel (Inst. für Experimentalphysik/Festkörperphysik, Ruhr-U. at Bochum, Germany)

We have investigated the effect of 20 Å thick metal cap layers on the spin structure in 2000 Å thick epitaxial Cr(001) films. In bulk Cr there exist three equally populated domains with SDWs propagating along the three {001}-directions in the bcc lattice. Our previous measurements on plain Cr(001) films as well as on Cr films capped with a thin Fe layer have shown a strong redistribution of the occupation of these three domains. In the case of the Fe capped Cr film the SDW becomes completely re-oriented with a single **Q**-vector now laying in the film plane. We have now continued our investigation of possible proximity effects between magnetic cap layers and Cr SDWs, as well as effects due to hybridization and epitaxial strain induced by the cap layer. To this end we have chosen ferromagnetic Co and paramagnetic Pd cap layers. In the left panels of Fig. 1 we show the incommensurate satellite peaks at the Cr(011) position and around the Cr(002) reflection. Between the left and right panels the scattering geometry and scan directions are sketched. For Co on Cr only SDWs occur in the K-direction similar to the situation already observed for Fe on Cr. Pd, although not ferromagnetic, exhibits a large Stoner enhancement factor. Our results for the SDWs in the Pd/Cr sample are shown in the right panel of Fig. 1. Here satellites in both scan directions can be recognized, indicating that the respective SDWs propagate in the film as well as perpendicular to it. Thus here only a partial re-orientation of the CDW/SW occurs. The re-orientation of the SDWs by ferromagnetic cap layers may be understood in terms of frustration effects induced by steps and kinks at the interface of monatomic height which disturb the interlayer exchange coupling between the FM layer and Cr. This frustration is also expressed in a short coherence length of the SDWs and in distorted line shapes. In contrast, the behavior of the SDWs in the Pd/Cr sample is completely different. The satellite peaks are narrow and sharp indicating well defined SDWs with much longer coherence. In fact, in Pd/Cr the satellite peaks are much better defined than in pure Cr layers of comparable thickness. We suggest that the Pd cap layer becomes exchange polarized by Cr, which in turn, acts as an amplification of the SDW in the Cr layer.

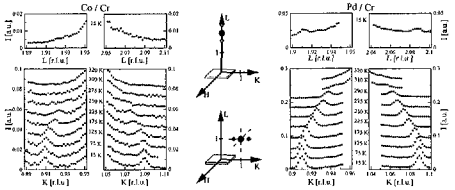


Figure 1. Scans around the Cr(011) and Cr(002) Bragg-reflection through possible positions of satellite reflections in a 2000 Å Cr(001) film capped with 20 Å details see text.

* Supported by the DFG through SFB 166

X ray Reflectivity Study of Gold Colloid Monolayers — X22B

C.J. Clarke, R.B. Lennox (McGill U), B.M. Ocko, D. Nguyen (BNL, Physics), M.H. Rafailovich, J. Sokolov and Z. Li (SUNY, Stony Brook)

The structure of Langmuir films of gold colloids, consisting of 2nm diameter gold particles coated with C_{14} thiol chains, was studied by X ray reflectometry and grazing incidence diffraction, over a range of compression and surface pressure. Figure 1 shows the isotherm, and figure 2 shows the specular reflectivities measured at the points marked. At large values of the area per particle (i.e. low surface pressure) the reflectivity indicates a single layer, approximately 1.5nm thick, corresponding to a monolayer of the gold colloid. The roughness of this layer is about 1nm, which probably arises from polydispersity in the size of the gold colloid, and incomplete monolayer coverage at large areas (islands of the colloid film can be seen on the water surface until a certain compression is reached). At an area of approximately 6.5nm^2 per particle, a transition occurs. This is seen as a steep rise in the isotherm. Fringes appear in the reflectivity, indicating a change in thickness. The data can be interpreted by a model, consisting of water, a 2.5nm gold layer, a 1.5nm hydrocarbon layer, and a second 2.5nm gold layer. Thus a monolayer to bilayer transition has taken place. In the bilayer, the centre to centre spacing of the gold layers is 4nm. As the layer is compressed further, the amplitude of the fringes increases, indicating that more of the film is being converted from monolayer to bilayer.

The in-plane structure of the layers was studied with grazing incidence diffraction, at the same points on the isotherm as the specular reflectivity. In each case, a diffraction peak was observed at an angle of 2.9°. This corresponds to an in plane spacing of 3.8nm, between the centres of the gold particles (in good agreement with the 4nm from specular reflectivity of the bilayer). No higher order peaks are observed, and the peak is fairly broad. This indicates that while there is a constant nearest neighbour spacing in the layer, there is no long range order. The intensity of the peak drops sharply at the point where the monolayer-bilayer transition occurs, and the peak width correspondingly increases. This suggests that there is no correlation in the position of the particles between the two layers.

Further experiments have also investigated the effects of temperature and alkyl chain length in this system.

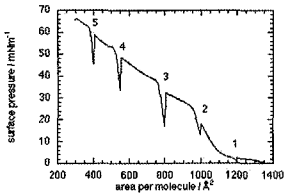


Figure 1. Surface pressure - area isotherm for the gold colloid. The points indicate the ions where the reflectivity was measured. Features in the isotherm, can be indentified with changes in the structure of the layer with the aid of techniques such as reflectivity.

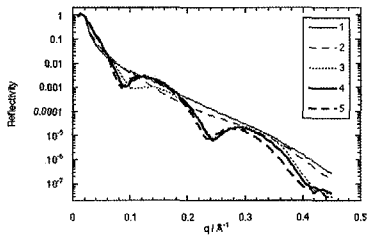


Figure 2. The specular reflectivites corresponding to the points marked on the isotherm in figure 1. The fringes arise when the film goes from a monolayer to a bilayer.

Temperature Dependent Surface Structure of Liquid Mercury | X22B

E. DiMasi, O. M. Magnussen, B. M. Ocko (BNL, Physics), M. Deutsch (Bar-Ilan U., Israel), H. Tostmann, O. G. Shpyrko, M. J. Regan, and P. S. Pershan (Harvard)

The free surface of a liquid metal presents a special challenge to theory. Both the rapid change in density at the interface and the presence of the free electron gas are expected to contribute to the atomic structure at the surface. One prediction is that atomic layering should occur at the liquid–vapor interface, and this has recently been observed in surface x-ray scattering studies of liquid gallium and liquid mercury. One unresolved issue is to what extent such intrinsic layering may be independent of thermal fluctuations.

We have extended x-ray reflectivity measurements of the Hg surface from room temperature to just above the melting point of −38.9 °C. The sample is contained in a glass cell in which the Hg sample can be poured under a passivating hydrogen atmosphere. A small liquid nitrogen cryostat and cold finger are suspended underneath the sample cell. The apparatus is supported on an active vibration isolation unit mounted directly on the Harvard/BNL liquid surface spectrometer.

Fig. 1 shows the reflectivity $R(q_z)$ for q_z up to 2.5 Å^{-1}, for several different temperatures. At room temperature (dashed line), the reflectivity is attenuated faster than that predicted by Fresnel theory for a flat Hg interface (R_F, solid line), indicating a surface roughness of order 1 Å. The broad peak in the reflectivity at $q \approx 2.2$ Å^{-1}, emphasized in the plot of R/R_F (Fig. 2), indicates atomic layering close to the surface. As the temperature is reduced (symbols), the amplitude of the peak increases substantially, demonstrating the reduced effect of thermally induced disorder on the surface layering.

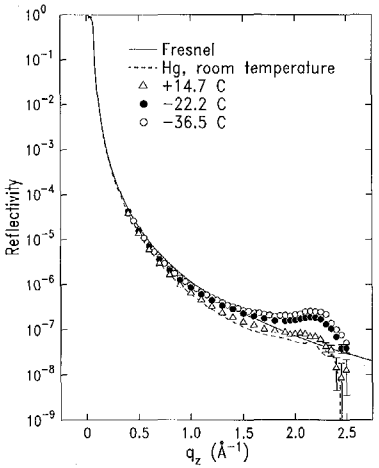


Figure 1. Temperature dependence of the X-ray reflectivity $R(q_z)$ of liquid mercury.

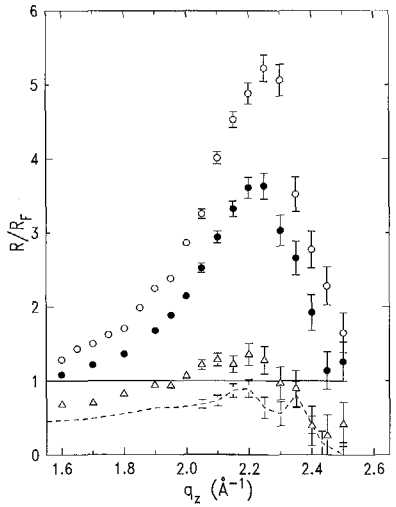


Figure 2. Measured reflectivity normalized to the Fresnel reflectivity R_F.

X-ray Reflectivity of Silane Multilayers | X22B

E. DiMasi, B.M. Ocko (BNL, Physics), W. Ke, R. Maoz, and J. Sagiv (Weizmann Institute of Science, Israel)

The assembly of molecules into ordered films on solid substrates is of considerable technological interest. Up to now, such multilayers have been produced in a stepwise linear fashion, where the topmost layer serves as a template for the next in each cycle of the assembly process.

Recently a novel stepwise exponential growth method has been reported for long-chain silane multilayers on Si substrates [1]. Here, additional layers are produced by an intercalation process in which each layer within the film acts as a template for assembly, so that the entire film is replicated at each iteration. So far these "self replicating" films have been studied by infrared spectroscopy and scanning force microscopy, which yield information about the bulk material deposited, molecular orientation, and surface morphology. However, these studies do not probe the structure of individual layers in the film.

We have performed x-ray reflectivity measurements of silane multilayers prepared by both self replication and conventional layer-by-layer growth. Our study provides direct evidence for the multilayer structure of films obtained by the self replicating process.

The reflectivity $R(q_z)$ for 8-layer films produced by both methods is shown in Fig. 1. The reflectivity decreases faster at large q_z than that of a perfectly flat Si interface, indicating a substantial surface roughness of order 5 Å. The existence of multiple oscillations demonstrates the presence of well ordered layers. The broad, weaker peak at ≈ 0.34 Å in the self replicated film is due to a bilayer length scale which is not produced in the layer by layer process. Measurements on 4-layer films show less pronounced oscillations, demonstrating that the thinner multilayers are more susceptible to the effects of substrate roughness.

We are grateful to Dr. K. Ogawa of Matsushita Electric Ind. Co. Ltd. (Kyoto) for providing NTS material. [1] R. Maoz, S. Matlis, E. DiMasi, B. M. Ocko, and J. Sagiv, accepted to Nature (Oct. 1996).

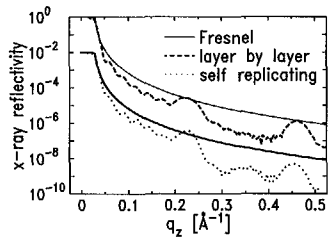


Figure 1. X-ray reflectivity $R(q_z)$ for 8-layer films grown layer by layer (– – –) and by self replication (···, offset $\times 10^{-2}$ for clarity). Solid line: Fresnel reflectivity of a sharp Si interface.

X-Ray Scattering Study of C_{60}-propylamine Adduct Monolayers at the Gas-Water Interface | X22B

M. Fukuto, K. Penanen, R.K. Heilmann, P.S. Pershan (Harvard U.), and D. Vaknin (Ames Lab & Iowa State)

We have performed reflectivity and grazing-incidence diffraction(GID) on C_{60}-propylamine adduct(C60PA) Langmuir monolayers(LM) on water (22°C), contained in a sealed teflon trough filled with He. Brewster angle microscopy confirmed the suggestions from previous isotherm (Fig. 1b) and reflectivity measurements[1] that the LM is homogeneous at A$\sim$150Å^2/molec. For A$>$150$\sim$160Å^2/mol. , the LM coexists with empty regions that vanish on compression. GID scans (background scattering subtracted) are shown in Fig. 1a. The peak position at $\sim$0.42Å^{-1} for A= 180 and 140Å^2/mol. roughly corresponds to the average nearest neighbor distance of $2\pi/Q_{xy}^{peak} \sim 15$Å, which is comparable to the diameter of a C60PA molecule. The widths indicate that at these areas the LM is a 2-D amorphous phase which BAM images indicate is solid-like. We believe that this is the first observation of the x-ray structure factor for an *amorphous 2-D LM*. The slight shift in the GID peak position for 100Å^2/mol. is much smaller than would be expected if the LM was homogeneously compressed. Fig. 2a shows reflectivity data normalized to the Fresnel reflectivity for water. The data for A= 180 and 140Å^2/mol. can both be fit by a single layer model (Fig. 2b, c). The excess electron density in the model for 180Å^2 is lower than for 140Å^2, consistent with the observed lower reflectivity for the inhomogeneous LM. In contrast, the data for 80Å^2/mol. requires a 2-box model(Fig. 2d), suggestive of the onset of a second layer. Harvard contribution to this work was supported by NSF-DMR-95-23440 and NSF-DMR-94-00396. Ames Lab is operated by ISU for the DOE under Contract No. W-7405-Eng-82. Reference: [1] D. Vaknin et al., Langmuir 11, 1437 (1995); M. Fukuto et al., NSLS Act. Rept.(1995)

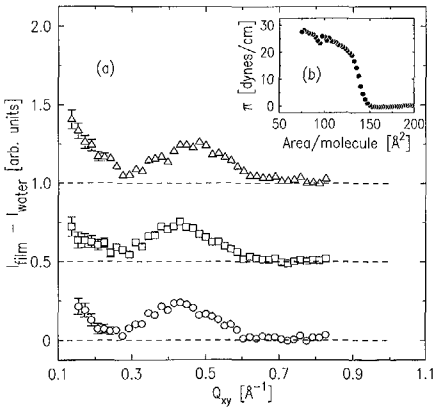


Figure 1. (a)GID scans for 180(o), 140(sqr), and 100Å^2(△). (b) Isotherm.

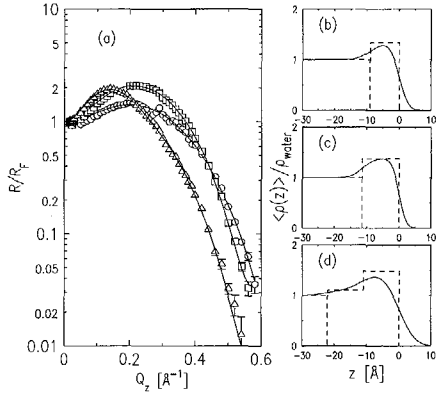


Figure 2. R/R$_F$(a) and elec. density for 180(o,b), 140(sqr,c), and 80Å^2(△,d).

Structure Control of Surface Freezing in Alcohol Melts by Additives | X22B

O. Gang(Bar-Ilan U., Israel), X.Z. Wu(ANL), B. Ocko(BNL), E. Sirota(EXXON), M. Deutsch(Bar-Ilan U.)

Following the discovery of surface freezing (SF) in alkane and alcohol melts[1], we explored the possibility of controlling SF by specific additives. Due to the bilayer structure of their surface phase, and ability to form H-bonds by their OH groups, alkanols ($C_nH_{2n+1}OH$, denoted C_n) were studied first with water and 1,3-propanediol (PD) as additives. In water vapour environment, the shorter period of the observed modulations of hydrated C_n (Fig. 1) indicates a swelling of the bilayer by a fixed 2.2-2.8 Å for all lengths studied, $n = 16 - 28$. This is attributed to water molecules intercalating in between, and H-binding to, the top and bottom layers of the bilayer, as found also for bulk hydrated alkanols. A model based on this structure (Fig. 1 inset) fits the data very well, as shown in Fig. 1. PD doping also swells the bilayer equally. Strikingly, it allows tuning of the surface layer between a bilayer and a monolayer by varying the temperature and PD concentration. Fig. 2 show a period doubling of curve (a) relative to (b), indicating a bilayer-to-monolayer structural transition. The sharp intensity jumps in the inset indicate first-order transitions between these phases. These studies demonstrate that structural control of surface-frozen layers by judiciously chosen additives may indeed be possible.

1. X. Z. Wu *et al.*, *Phys. Rev. Lett.* **70**, 958(1993);*Eur. Lett.* **30**, 283(1995).

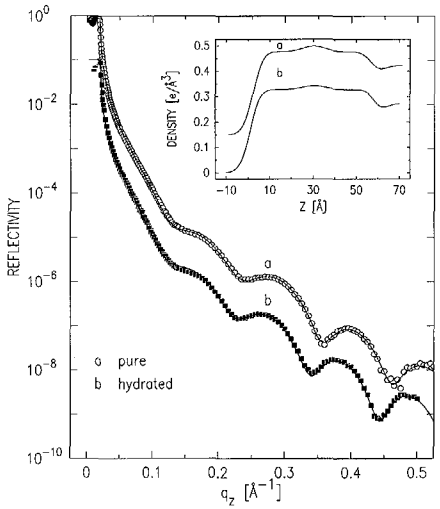


Figure 1. Reflectivities of surface-frozen crystalline bilayers on pure and hydrated C_{22} alkanol melts. Inset: The model densities of the fits shown in solid lines.

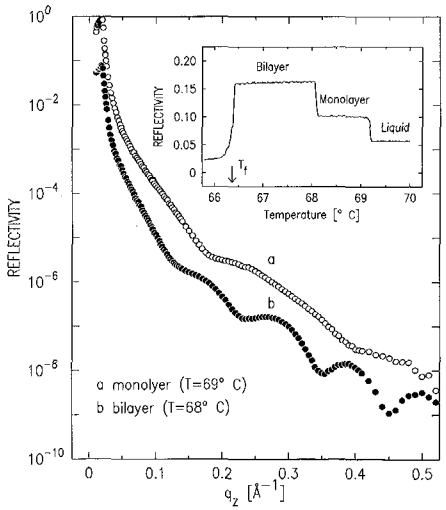


Figure 2. Reflectivities of a surface-frozen monolayer (a) and bilayer (b) of a 5% PD-doped C_{22} alkanol. Inset: Reflectivity at a constant $q_z = 0.2$Å^{-1}. T_f is the bulk freezing temperature.

X-ray Scattering From Discotic Liquid Crystalline Compounds at the Air-water Interface. *	X22B

D. Gidalevitz, O. Mindyuk, J. Strzalka (U.Penn.), B. Ocko (BNL, Physics) and P. A. Heiney (U.Penn.)

We present the first grazing incidence X-ray diffraction study of Langmuir films of discotic compounds at the air-water interface. Such films are the precursors to heavily studied Langmuir-Blodgett films; the disc-shaped molecules are expected to adopt a face-on (triangular) or edge-on (columnar) structure. The subjects of our study were two model discotic liquid crystalline compounds: the hexa-(p-n-dodecyloxybenzoyl) derivative of hexasubstituted azacrown-N_6 (compound **1**) and hexapentyloxytriphenylene (compound **2**). The X-ray specular reflectivity (XR) and grazing incidence X-ray diffraction (GIXD) measurements were performed at X22B beamline at NSLS of Brookhaven National Laboratory at 18°C. Compounds **1** and **2** were spread from chloroform on the pure water surface displaying areas per molecule of $220\text{Å}^2/mol$ (compound **1**) and $70\text{Å}^2/mol$ (compound **2**). GIXD measurements of azacrown compound did not yield any peaks while triphenylene compound yield the single peak at q_{xy}=0.45Å^{-1}, which corresponds to lateral spacing of 13.90Å. The specular reflectivity data were analyzed using the two-box model (Fig. 1). The model reflectivity curve for compound **1** yielded the face on arrangement of the molecules on the water surface, the calculated reflectivity curve for compound **2** shows the edge on composition.

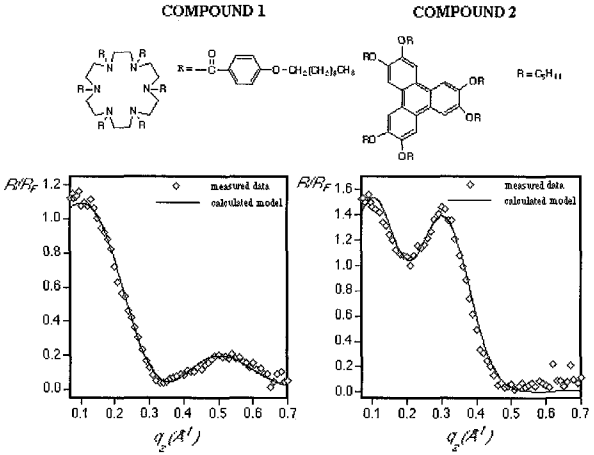


Figure 1. Measured and calculated x-ray specular reflectivities (normalized to Fresnel reflectivity R/R_F of the pure water) of compounds **1** (left) and **2** (right) on the pure water surface.

* We are grateful to D. Vaknin for the use of his trough. This work was supported by NSF-DMR-92-20668 and NSF-DMR-93-15341.

An X-ray Photoinduced Insulator-to-Metal Transition in a Colossal-Magnetoresistance Manganite	X22B

V. Kiryukhin, D. Casa, B. Keimer (Princeton U.), J.P. Hill, A. Vigliante (BNL), Y. Tomioka, and Y. Tokura (JRCAT, Japan)

Recently manganese oxides of general formula $A_{1-x}B_xMnO_3$ have captured the attention of many physicists and engineers. For some compositions these materials undergo magnetic field driven insulator-to-metal transitions ("colossal magnetoresistance"), the physics of which is still poorly understood. Here we report that in one such compound, $Pr_{0.7}Ca_{0.3}MnO_3$, a transition from an insulating, antiferromagnetic, to a metallic, ferromagnetic state can also be driven by illumination with x-rays at low temperatures (lt40K).

At high temperatures $Pr_{0.7}Ca_{0.3}MnO_3$ is metallic. At T~200K it undergoes metal-to-insulator transition which is associated with charge and magnetic ordering of the charge carriers. The charge ordering is accompanied by the lattice distortion. The low temperature magnetic structure is antiferromagnetic with small spin canting. The material can be driven back to the metallic state by applying magnetic field of about 4 Tesla at low temperatures. This metallic state is ferromagnetic and does not show charge ordering. This field induced transition is associated with large hysteresis; the material remains metallic after the field is ramped back to zero, but reverts to the charge ordered state upon subsequent heating above 60K.

We report that the insulator-to-metal transition at low temperatures can also be induced by the x-ray irradiation. Fig 1 shows that the intensity of the charge ordering reflection decreases continuously with x-ray illumination; no change is observed when the beam is switched off. The diminution of the charge ordering is accompanied by the dramatic increase in conductance (more than 6 orders of magnitude, see Fig 1). With the x-ray beam off, the system remains in the metallic state for many hours without degradation. The x-ray induced conductivity can be annealed out on heating above 60K, as shown in Fig 2. This temperature is equal to the annealing temperature of the magnetic field induced phase. Also, both phases have the same value of conductivity at low temperatures. This close analogy between the photoinduced and field induced phases strongly suggests that they are identical. In this case the*magnetic*properties of the sample change dramatically with illumination from canted antiferromagnetic to ferromagnetic. To our knowledge, a photoinduced antiferromagnetic-to-ferromagnetic transition has thus far not been observed. This effect may have applications in x-ray detection and x-ray lithographic patterning of ferromagnetic nanostructures.

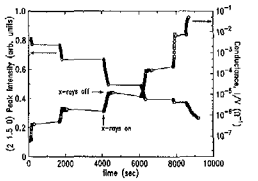


Figure 1. X-ray exposure dependence of the intensity of (2 1.5 0) Bragg reflection characteristic of charge ordering, and of the electrical conductance, at T=5K.

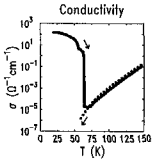


Figure 2. Conductivity measured on cooling before x-ray illumination (dotted curve) and on heating after illumination with x-rays for a moderate amount of time (solid curve).

Time Dependence Study of In-Plane Layers in Confined Hybrid Smectic C* Films *	X18A, X22B

L. J. Martínez-Miranda, Y. F. Hu, T. K. Misra and M. W. Huang (U. of Maryland)

Liquid crytalline materials in constrained geometries exhibit properties that can vary significantly from the bulk properties of the material. Confined hybrid liquid crystal films experience a competition between the aligning forces of the bounding surfaces. We have studied the in-plane ordering of a smectic C* liquid crystal mixture, mx5112, confined between a grated glass substrate and the air surface. This compound mixture has a the following phase transitions: sm3 - smC* at 20.65°C, smC* - smA at 49.5°C and smA - I at 57°C. The corresponding bulk layer spacings are: 31.303Åfor the smA phase; 29.97Åfor the smC* phase; and 31.639Å for the low temperature Sm3 phase.

We have observed that the in-plane layer spacing oscillates between values close to the smA bulk layer spacing and the smC* bulk layer spacing for samples with thicknesses in the range 10 - 20 μm. This oscillation is aperiodic in time, as shown in the Figure below. By contrast, thinner films show a slower variation of the value of the layer spacing with time, with a 0.6 percent oscillation over a 10 hour period.

A depth profile study of the films shows that those layers located furthest from the glass grating interface show the largest variation in layer spacing over a 48 hour period. The layer spacing at the end of this period is approximately 0.3 percent larger than the bulk smC* spacing. In contrast, those layers closest to the glass grating interface remain close to the intermediate spacing value of 30.6Å.

The time oscillation may be the result of the competition between the two aligning surfaces in the smC* film. The in-plane layer at the grating interface favors a smA-like ordering, which relaxes through the thickness of the film. This relaxation is enhanced the farther the layers are from the glass interfaces or the thicker the films. The time oscillation and depth dependence of the layer spacings affect both the temperature and field dependence of these films. We are in the process of studying this behavior.

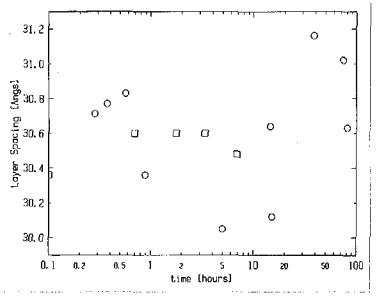


Figure 1. Open circles: Time dependence of a 15μm and a 13μm film (combined). Open squares: time dependence of a 5μm film.

* This work was supported by a NSF-VPW Grant No. GER-94-50118, and a NSF Grant No. ECS-96-96069.

Time and Depth Dependence Study of the Azimuthal Orientation in Confined Hybrid Smectic C* Films *	X18A, X22B

L. J. Martínez-Miranda, Y. F. Hu, T. K. Misra and M. W. Haung (U. of Maryland)

Confined hybrid liquid crystal films experience a competition between the aligning forces of the bounding surfaces. We have performed a depth profile dependence study of the in-plane ordering of a smectic C* liquid crystal mixture, mx5112, confined between a grated glass substrate and the air surface. This compound mixture has the following phase transitions: sm3 - smC* at 22.65°C; smC* - smA at 49.5°C; and smA - I at 57°C. The corresponding smectic layer spacings are 33.303Åfor the smA phase; 29.97Åfor the smC* phase; and 31.639Åfor the sm3 phase.

The in-plane layer spacing oscillates between the bulk values of the smA and smC* phases as a function of time. This value varies also as a function of depth within the films and is close to the average of the two bulk spacings close to the liquid crystal glass interface. The azimuthal orientation of the layers varies both as a function of depth and of time within the films. In-plane layers close to the liquid crystal glass interface align close to the direction of the gratings' axis. The orientation of the layers close to the liquid crystal air interface rotate as a function of time to a direction perpendicular to the axis of the gratings, for samples thicker than 10μm, as illustrated on Table I. The mechanism for this rotation, which was previously observed both in samples thicker than 10μm and thinner than 3μm, is not clear at present. We are in the process of studying the depth dependence of the azimuthal orientation in greater detail.

Layer Spacing (Å)	ϕ(°) - 15 µm	ϕ(°) - 13 µm
30.710	159	
30.770		20
30.830	38	
30.360	24	
30.050		20
30.640		20
30.120	23	
31.160		90
31.020		78
30.630		102

Figure 1. Table of Values of the azimuthal peak ϕ corresponding to the layer spacing of the maximum peak for the 15-μm and 13-μm films. Data were obtained over a 16 hour period for the 15μm sample and over a 90 hour period for the 13 μm sample.

* This research was supported by a NSF-VPW Grant No. GER-94-50118, and a NSF Grant No. ECS-96-96069.

The 2D Ising Model: Br Electrodeposited on Ag(100) | X22B

B.M. Ocko and J.X. Wang (BNL, Physics), T. Wandlowski (Ulm)

One of the basic tenets in the theory of second order phase transitions is the notion of universality; the critical behavior is determined by the symmetry and dimensionality. The present grazing incident angle x-ray scattering study shows that the electrodeposition of halides (chloride, bromide, and iodide) on the Ag(100) electrode represents an example of the 2D Ising phase transition. As displayed in Fig. 1, the disordered state is characterized by the random (lattice gas) adsorption in four-fold hollow sites and the ordered state is characterized by a c(2x2) structure. At a critical potential there is a second order transition between these two states.

In Fig. 2 we show the correspondence between the cyclic voltammetry and the x-ray scattering results for Br on Ag(100). The change in intensity at (1,0,0.12) below the critical potential occurs because the bromide preferentially adsorbs in the four-fold hollow sites. By modeling the intensity as an interference between the scattering from the silver and bromide, we are able to obtain a measure of the bromide coverage over the entire potential range. The maximum coverage thus obtained, 0.47, is in good agreement with the coverage of 1/2 determined from the in-plane diffraction pattern. In addition, the intensity at (1/2,1/2,0.12) should scale as a power-law with an exponent twice that of the order parameter. The fitted exponent of 0.15 (solid line) is slightly greater than the Ising prediction of 1/8 (dashed line).

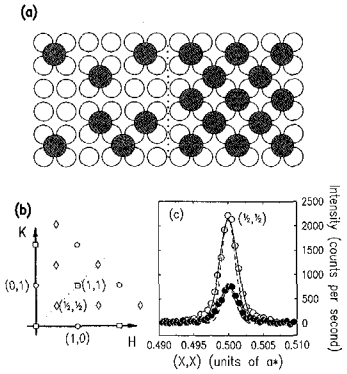


Figure 1. (a) Real Space model of adsorbed bromide (filled circles) on the Ag(100) surface (open circles). Left side shows random (lattice gas) adsorption in four-fold sites and right side shows the ordered c(2x2) adlayer. (b) Reciprocal space pattern where the diamonds correspond to diffraction features from the c(2x2) structure. (c) X-ray scattering intensity at the lowest order in-plane position from the c(2x2) structure.

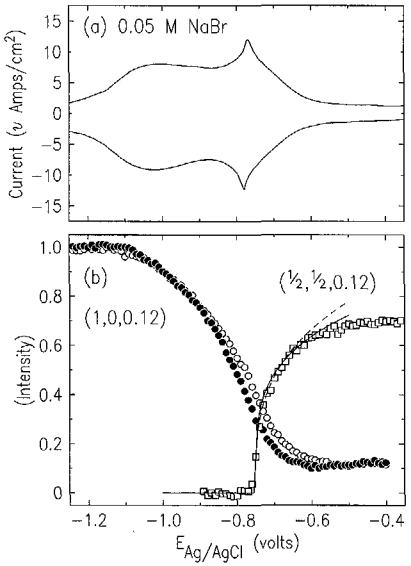


Figure 2. (a) Cyclic voltammetry. (b) X-ray scattering intensity at (1/2,1/2,0.12) shows the formation of the c(2x2) phase.

Two-Dimensional Monomolecular Pigment Assemblies at The Air-Water Interface | X22B

D. Vaknin, B.W. Gregory, J. D. Gray, T.M. Cotton, W. S. Sturve (Ames Lab) and B.M. Ocko (BNL, Physics)

Synchrotron X-ray diffraction at grazing angles of incidence (GID) and reflectivity techniques have been employed to determine the structure of charged water soluble pigments that are absorbed to oppositely charged lipid monolayers at the air-water interface. Surface pressure versus molecular area isotherms and X-ray scattering studies of the lipid dihexadecyl phosphate (DHDP) show substantial differences when spread on pure water or when spread on micro-molar solution of phthalocyanines (PC) or porphyrins (PY). Figure 1 shows the normalized reflectivity from a monolayer of DHDP on PC solution along with the corresponding refelctivity from the same monolayer on pure water (dotted line). The analyses of the reflectivity in terms of three strata (3-box model, i.e., lipid tail, lipid head group, and pigment) suggest that the pigment forms a homogeneous densely-packed monomolecular layer incorporating iodine and water molecules. Furthermore, GID scans from the same monolayer reveal that a highly ordered pigment-lipid monolayer is formed at the air-water interface as indicated by Bragg reflections and their corresponding rod scans (see Fig. 2). On the other hand, GID scans from the lipid on pure water show a single 2D Bragg reflection corresponding to the hexagonal ordering of individual untilted alkyl chains (dashed line Fig. 2), consistent with the reflectivity measurements (see Fig. 1.) . This reflection is significantly affected by the presence of the pigment showing that the pigment modifies the ordering of the lipid. Our detailed structural studies on the molecular length scale help in the design of light harvesting devices that mimic photosynthesis.

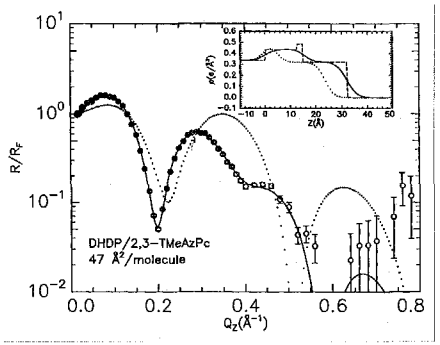


Figure 1. Normalized reflectivity from a DHDP monolayer spread on micro-molar solution of PC. Solid curve is the calculated reflectivity based on the electron density model structure shown in inset. The dotted line shows the measured reflectivity from DHDP when spread on pure water.

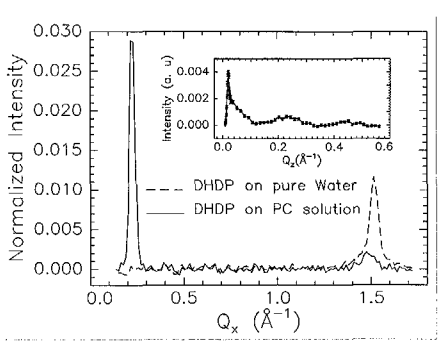


Figure 2. In-plane diffration patterns at grazing angles of incidence from monolayers of DHDP spread on PC solution (solid line) and on pure water (dashed line). Inset shows the rod scan of the 2D Bragg reflection associated with the ordering of the complex pigment-lipid monolayer at 0.22 (InvAngs).

Surface Reconstruction at Metal-solid Polymer Electrolyte Interfaces | X22B

J.X. Wang and R.R. Adzic (BNL, Physics)

The structure of the Au(111) surface in contact with a recast Nafion film has been studied as a function of potential by using grazing incident angle x-ray diffraction. The high penetration depth of x-ray makes possible to probe the electrode surface covered by 1-3 μm Nafion film. Unlike usual aqueous electrolyte solutions, where both cations and anions are free to move, the negatively charged sulfonated groups in Nafion are fixed on the polymer chain and the balance of the interface charge is achieved mainly through a change of the cation concentration within the double layer as shown in Fig. 1a. At sufficiently negative potentials, four diffraction peaks (Fig. 1b) appear around (0,1), which are characteristic of the Au(111) $(23 \times \sqrt{3})$reconstruction. The diffraction intensity at a reconstruction peak position was monitored while cycling the potential in the double layer potential region. As shown in Fig. 2a, the background subtracted diffraction intensity vanishes completely at the most positive potential. This provides a convincing example of a charge-induced lifting of the Au(111) reconstruction in the absence of anion adsorption. In comparison with the Au(111) electrode in $NaClO_4$ solution, the lifting of reconstruction is shifted positively by about 0.2 V. This is likely due to the increase of the separation between the planes carrying charge at the Nafion/electrode interface compared to at a solution/electrode interface where the negative charges are carried by the mobile anions and are located close to the electrode surface. This, in turn, causes a slower positive charge increases at the metal surface with increasing potential which is necessary for the reconstruction lifting. These results demonstrate that the Nafion coating is stable over a large potential range and is suitable for studying surface properties and the ion distribution effects on surface electrochemical processes at single crystal surfaces.

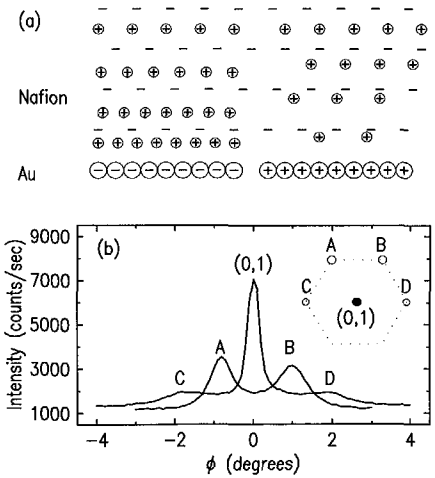


Figure 1.

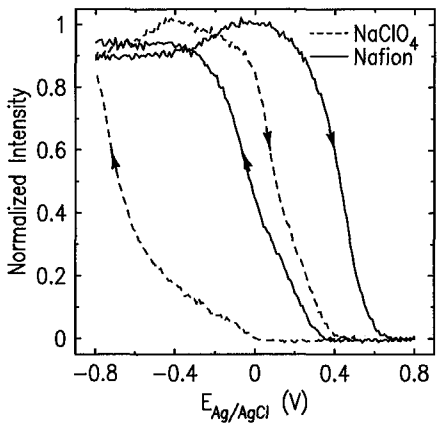


Figure 2.

Resonant Magnetic X-ray Scattering in Er Films with Monolayer Y Superlattice Doping | X22C

M. J. Conover, C. P. Flynn (U. of Illinois), A. Vigliante, and D. Gibbs (BNL, Physics)

Below its 85K Néel temperature, Er has a c-axis modulated (CAM) phase, in which individual atomic moments lie along the hcp c-axis but are subject to a longitudinal sinusoidal modulation. From about 52K to the 20K Curie temperature, a basal-plane spiral with the same periodicity, τ_m, is added to the CAM structure. Past synchrotron experiments have shown that, for several small ranges of temperature below 54K, τ_m locks to values commensurate with the lattice via a series of periodic phase advances known as spin slips. In the present experiment, we study the lock-in states of τ_m for Er films which have been altered by periodically introducing monolayers of Y into the Er structure. Three such samples were studied, with superlattice periods Λ = 19.4, 28.9, and 32.6 atomic layers. Measurement of τ_m vs temperature was accomplished by tuning the photon energy to the L_{III} absorption edge (E = 8.362 keV) of Er and measuring the position of the primary magnetic satellite to the (004) reflection. The temperature dependence of τ_m for the three samples is shown in Fig. 1. The Λ=19.4 sample has strong lock-ins at 5/19 and at 2/7, while the Λ=28.9 has no 2/7 lock-in and has a more gradual approach to the 5/19 state. Lock-in behavior to a single wave vector is suppressed in the Λ=32.6 sample. Epitaxial strain is thought to couple the Er magnetic states to the Y layers, both as an overall homogeneous strain and as a periodic strain modulation. One possible explanation of the 5/19 lock-in state in the Λ=19.4 sample is that the strain modulation couples to the spin-slip period of 19 layers, although the evidence from the other samples indicates the influence of the homogeneous strain term.

The University of Illinois portion of this project is supported by grant ONR N0014-94-I-0068. Work performed at Brookhaven is supported by the US DOE under contract no. DE-AC02-76CH00016.

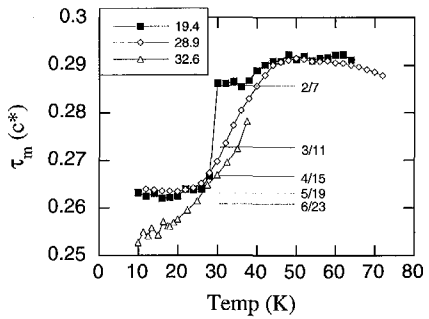


Figure 1. Magnetic wave vector τ_m (in units of c*) in Er/Y for superlattice 28.9, and 32.6 atomic layers.

Resonant Magnetic X-ray Scattering in Ho Films with Monolayer Dy Superlattice Doping	X22C

M. J. Conover, C. P. Flynn (U. of Illinois), A. Vigliante, and D. Gibbs (BNL, Physics)

Below its 132K Néel temperature, hcp Ho has a spiral magnetic phase, in which atomic moments lie in the basal plane and rotate by a temperature-dependent turn angle ϕ with each layer along the c axis. Basal plane anisotropy distorts the spiral by pulling the spins toward the six easy b-axis directions, and it favors magnetic wave vectors τ_m which are commensurate with the lattice. Past synchrotron experiments have shown that, over small temperature ranges, the magnetic wave vector τ_m locks to the lattice via a series of periodic phase advances known as spin slips. In the present experiment, we study the lock-in states of τ_m for two Ho films which have been altered by periodically introducing monolayers of Dy into the Ho structure and compare them to a pure Ho film of the same total thickness and grown by the same method. Measurement of τ_m vs temperature was accomplished by tuning the photon energy to the L_{III} absorption edge (E = 8.075 keV) of Ho and measuring the position of the primary magnetic satellite of the (004) reflection. Figure 1 summarizes the τ_m data. The low-temperature lock-in state of τ_m reaches progressively lower values with increasing concentration of Dy, although the bulk 1/6 phase which accompanies the ferromagnetic transition in bulk Ho is not reached in any of these samples. Past studies of Ho films indicate that epitaxial strain and clamping tend to increase the lock-in value of τ_m relative to that of bulk Ho, but the present study suggests that the Dy layers partially overcome this epitaxial influence, either via lattice mismatch strains or by changing the in-plane anisotropy barrier. The University of Illinois portion of this project is supported by grant ONR N0014-94-I-0068. Work performed at Brookhaven is supported by the US DOE under contract no. DE-AC02-76CH00016.

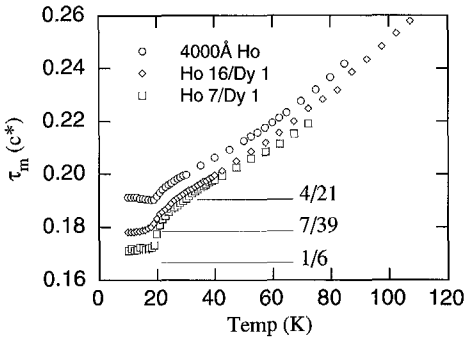


Figure 1. Magnetic wave vector τ_m (in units of c*) in Ho/Dy for two superlattices (Ho 16 layers / Dy 1 layer, and Ho 8 / Dy 1) and a film of Ho with no Dy.

Determination of Magnetic Moment Directions Using X-ray Resonant Exchange Scattering *	X22C

C. Detlefs, A. H. M. Z. Islam, A. I. Goldman, C. Stassis, P. C. Canfield (Ames Lab & ISU), J. P. Hill, and D. Gibbs (BNL, Physics)

We present magnetic structure determinations for $SmNi_2B_2C$ and $NdNi_2B_2C$ by means of x-ray resonant exchange scattering (XRES). Both compounds order in a commensurate antiferromagnetic structure with modulation wave vector $(\frac{1}{2}, 0, \frac{1}{2})$. Using an asymmetric geometry that is particularly convenient for small crystals, we measured the variation of the integrated intensity of the magnetic reflections as a function of the Bragg angle to determine the magnetic moment directions. The measured data are in good agreement with model calculations assuming magnetic moment directions parallel to (1,0,0) for the Nd compound and (0, 0, 1) for $SmNi_2B_2C$ (Fig. 1). A resonant feature observed below the Sm L_3-absorption edge (Fig. 2), similar to unexplained effects found in other light rare earth compounds, is identified as quadrupolar XRES and is further used to obtain additional information about the direction of the magnetic moment.

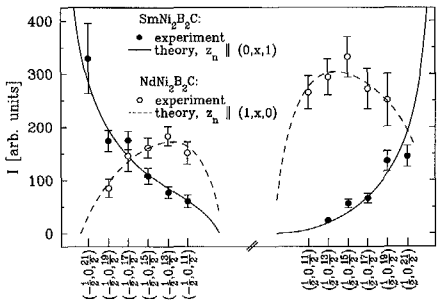


Figure 1. The integrated intensity of magnetic reflections of $SmNi_2B_2C$ (filled circles) and $NdNi_2B_2C$ (open circles) along with model calculations for a magnetic moment parallel to the (0, 0, 1) (solid line) and (1, 0, 0) (dashed line) axes of the samples.

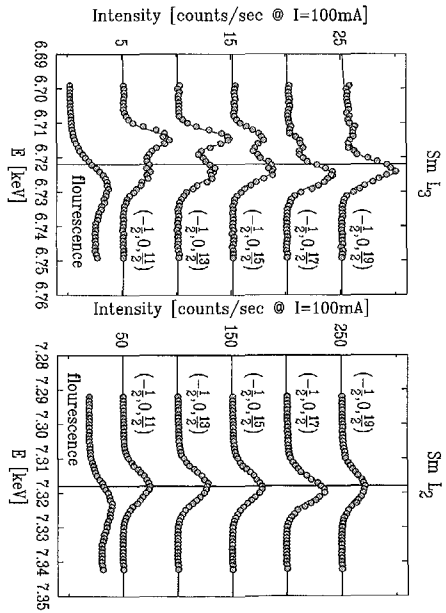


Figure 2. Energy scans of the $(-\frac{1}{2}, 0, l)$ magnetic reflection across the Sm $L_{2,3}$ absorption edges. The fluorescence yield is plotted as an energy reference.

* Work supported by U.S. DOE W-7405-Eng-82 and DE-AC02-76CH00016

Magnetic and Structural Properties of Erbium Films | X22C

G. Helgesen (IFE, Norway), Y. Tanaka (RIKEN, Japan), J.P. Hill, P. Wochner, D. Gibbs (BNL), C.P. Flynn and M.B. Salamon (U. of Illinois)

The magnetic and structural properties of two erbium thin films (thickness $\geq 1\mu$m) grown epitaxially on Lu and Y substrates have been studied using resonant magnetic x-ray scattering. These substrates, respectively, compress or expand the erbium a-axis lattice constants relative to the bulk and clamp them at the film/substrate interfaces, thereby introducing epitaxial strain. The temperature dependence of the c- and a-axis lattice constants, magnetic wave vector τ, and magnetic order parameters of the films were measured. The qualitative features of the magnetic phase behavior mirror those of the bulk, including scaling of the critical exponent β of the observed harmonics and the existence of lock-in transisitions to commensurate wave vectors found in the bulk. The magnetic phase transitions, however, exhibit marked hysteresis and the magnetic structures are characterized by multiphase coexistence and limited correlation lengths. The low temperature $\tau = 5/21$ phase of bulk erbium is supressed in both films, and is replaced in Er/Lu by two new phases with wave vectors $\tau = 6/25$ and 12/49. Qualitative c-axis strain profiles were deduced from specular reflectivity measurements and reveal that the Er/Y film is more distorted than the Er/Lu film.

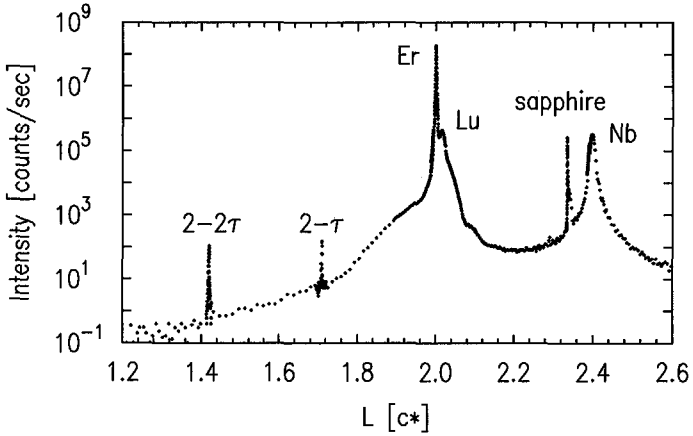


Figure 1. Scan along the (0,0,L) direction in reciprocal space for the 9500 Å Er film on a Lu substrate at temperature T = 60 K. The photon energy was tuned to the Er L_{III} absorption edge at E = 8.36 keV.

Resonant X-ray Scattering From a Thin Film of UPd_2Al_3 | X22C

A. Hiess (EITU, CEA-Grenoble), S. Langridge (EITU, ESRF), M. Huth (U. Mainz, Germany), D. Gibbs (BNL, Physics), and G. H. Lander (EITU)

UPd_2Al_3 is a so called magnetic heavy-fermion superconductor. An antiferromagnetic order ($T_N = 14$K) of ferromagnetic (0 0 1) layers of moments coupled + - + - along the hexagonal c direction with a relatively large ordered moment of $m = 0.85\mu_B$ coexists at low temperatures with superconductivity ($T_c = 2$K). To understand the interplay of superconductivity and magnetism in the compound, an important question relates to the dimensionality of the magnetic interactions. Thin films of UPd_2Al_3 were prepared (in Mainz) by electron beam co-evaporation of the elements on a $LaAlO_3$ substrate resulting in a film that was ordered in the hexagonal c direction. The mosaicity of the film used (thickness = 1500Å) was about 0.3deg. for the specular reflections (0 0 L).

We have observed magnetic scattering from the (0 0 1/2) specular reflection (Fig. 1) for temperatures $T < 9$K using photons tuned to the M_{iv} absorption edge ($E = 3.728$keV) of uranium. The intensity was about 1000cts/sec at $T = 3.8$K, the lowest temperature available. The principal results are as follows: (1) The magnetic correlations are the same as found in the bulk material ($T_N = 14$K), but exist only at significant lower temperatures. (2) Although the transport properties indicate an antiferromagnetic ordering at about $T = 9$K, the x-ray results on the thin film show no sign of saturation down to $T = 3.8$K. (3) The widths of the magnetic reflection in both the transverse and longitudinal directions seem to saturate at about $T = 6$K and are at low temperatures not significantly different from those of the charge peaks. (4) Surprisingly, the (0 0 3/2) magnetic reflection was not observed.

In conclusion our x-ray results establish that the magnetic correlations in the film are of the same form as in the bulk, but static disorder in the arrangement or the quasi-twodimensional geometry seems to prevent the formation of true long-range order in the film.

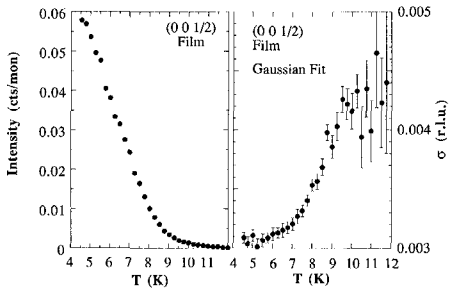


Figure 1. Temperature dependence of the intensity and the width of the magnetic reflection at the (0 0 1/2) position.

K-Edge Resonant Magnetic Scattering from a Transition Metal Oxide: NiO	X22C, X25

J.P. Hill (BNL, Physics), C.-C. Kao (NSLS) and D.F. McMorrow (Riso)

Resonant x-ray magnetic scattering exploits enhancements in the cross-section occurring when the incident photon energy is tuned through an atomic absorption edge. Large enhancements were first observed at the $L_{II,III}$ edges in Ho and explained in terms of electric multipole transitions. In addition to the L edges much larger enhancements are expected, and observed, at the $M_{IV,V}$ edges of the actinides for which the dipole excitation is to the localized, highly polarized 5f levels. Conversely, resonant scattering at a K-edge is expected to be considerably weaker because the strong (dipole) transitions involve *s* and *p* levels for which there is no spin-orbit correlation of either the core level or the intermediate state. Nevertheless, K-edge studies would be of some interest because of the window they would provide on transition metal compounds, which make up arguably the most interesting of magnetic systems.

We report the observation of K-edge resonant magnetic scattering in the antiferromagnet NiO, for which an approximately two-fold increase in the scattering is observed at an energy corresponding to a quadrupolar feature in the absorption spectrum (Fig.1). Quadrupole excitations couple to d-like states at a K-edge and for transition metals these are the magnetic states. Thus, the high degree of polarization of the localized $3d^8$ states compensates for the small size of the quadrupolar matrix elements and an observable enhancement results. From the ratio of the non-resonant to resonant magnetic scattering, we estimate that the first order quadrupolar resonant scattering amplitude is $0.016r_0$, which is of the same order of magnitude as similar terms in the rare earths. These studies provide for the possibility of element specific magnetic diffraction in such notable transition metal oxides as the high T_C cuprates and colossal magnetoresistance manganites.

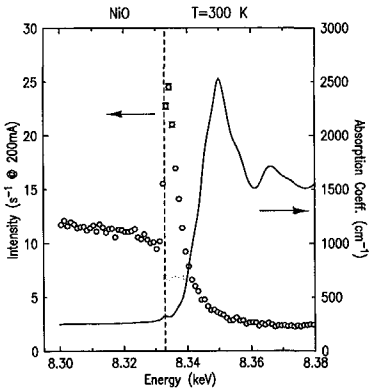


Figure 1.

Charge Ordering in the Layered Perovskite $La_{0.5}Sr_{1.5}MnO_4$	X22C

J.P. Hill and B.J. Sternlieb (BNL, Physics)

There has been intense recent interest in the phenomena of charge ordering in various perovskite systems. Motivation for this is twofold. First, high-T_C cuprates for which, in some materials, a real space separation of holes and spins into an ordered phase consisting of antiferromagnetic "stripes" has been observed. This ordering competes with, and coexists, with the superconductivity and sheds new light on the background electronic and magnetic state from which the superconductivity arises. Secondly, the colossal magnetoresistance maganites, which are 3D perovskites of the form $A_{1-x}B_xMnO_3$, where A=lanthanide, B=Ca, Sr or Ba, also exhibit charge ordering. In these systems, the charge ordering is associated with dramatic changes in the conductivity. For some compositions this is reversed be an applied magnetic field, resulting in an insulator-metal transition; the colossal magnetoresistance.

We have carried out x-ray studies of the charge ordering in a layered perovskite $La_{0.5}Sr_{1.5}MnO_4$, which is isostructural with the nikelates $La_{2-x}Sr_xNiO_4$ and $La_2NiO_{4+\delta}$ for which the striped order was first observed. The x-ray experiments, together with complimentary neutron scattering studies, revealed that the formal valence of $Mn^{+3.5}$ orders at $T_{co} \sim 217$ K, in an alternating Mn^{+3}/Mn^{+4} pattern, with a unit cell of $\sqrt{2}a \times \sqrt{2}a \times c$. Experiments with as-prepared, and freshly cleaved samples revealed that this ordering is extremely sensitive to changes in the stoichiometry and domains of $2\sqrt{2}a \times 2\sqrt{2}a \times c$ were also seen in coexistence with the preferred ordering in the samples that had been exposed to the air for some time. This explains previous disrepancies in the literature between various electron diffraction studies. The neutron scattering work revealed that at $T_N \sim$ 110 K, the moments on the Mn ions order antiferromagnetically, with a unit cell of $2\sqrt{2}a \times 2\sqrt{2}a \times 2c$.

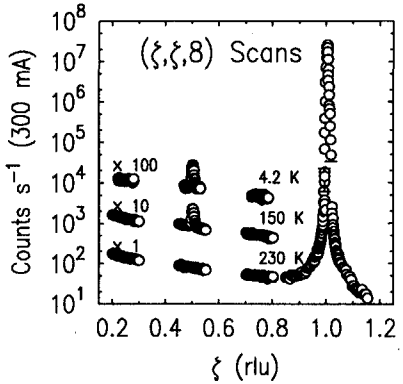


Figure 1.

Studies of Zero Field Magnetic Structures of $TbNi_2Ge_2$	X22C

A. H. M. Z. Islam, C. Detlefs, A. I. Goldman, P. C. Canfield (Ames Lab), J. P. Hill, and D. Gibbs (BNL, Physics)

The magnetic properties of $TbNi_2Ge_2$ are intriguing. This material crystallizes in $ThCr_2Si_2$ structure (I4/mmm). Susceptibility measurements have shown that this compound is anisotropic with two magnetic transitions at $\approx$9.25K and $\approx$16.5K in small applied field. As a first step to understanding the microscopic magnetic behavior, the zero field magnetic structures were studied using the technique of x-ray resonant exchange scattering on beam line X22C. The magnetic wave vector of the low temperature structure is (0 0 3/4), while the higher temperature phase orders with a wave vector of (0 0 0.76). All the data were collected at the Tb L_{III}-edge where the resonant enhancement was the largest. The **Q**-dependence of magnetic satellites in both the phases were carefully measured using symmetric [0 0 L$\pm\tau$] and asymmetric [$\pm$1 0 7$\pm\tau$] scattering geometries where τ = 3/4 and 0.76. Detailed modelling of the magnetic structures to best fit the observed **Q**-dependence is in progress. Preliminary analysis shows a large c-axis moment at the Tb sites. It is assumed that Ni is not moment bearing in this material as known from measurements on similar compounds.

Verifying Magnetic Structures Using X-Rays - Neodymium A Test Case.	X22C

D. Watson, W.J. Nuttall, E.M. Forgan, D.Fort (U. Birmingham, UK), and S.C. Perry (Keele U., UK)

We report here further progress on our investigations of the antiferromagnetic ordering of elemental neodymium. These measurements build upon our previous determination of the energy dependencies of the resonantly enhanced magnetic scattering at the Nd L-edges and also a detailed study of the incommensurate magnetic modulation wavevector [1]. Those measurements allowed us to address the question as to whether the modulation wavevectors in neodymium exhibit lock-ins to a subtle series of commensurate values [2]. The natural high resolution of the x-ray technique allowed us to confirm that the wavevector modulation is indeed smoothly incommensurate.

Recently we have made measurements, on resonance at the L_{II} edge, of a large number of magnetic satellites from the double-q structure of Nd at 10 K, and have shown that these intensities can be used in a refinement of the magnetic structure. There is remarkably good agreement with all the major components of moment on the hexagonal sites, but the cubic site moments given by x-rays are a factor of 2 smaller than the neutron ones. This is probably not due to the different temperatures (10K vs. 6K), since a less complete neutron experiment at 10K [3] also gives moments on the cubic sites that are larger than the X-ray ones. These results are currently being prepared for publication [4].

Following the formalism outlined by Hill and McMorrow [5] we have recently extended our measurements to include a quantitative assessment of the polarization properties of the magnetic scattering, and have measured the incommensurate lattice distortion satellites associated with the magnetic ordering. These measurements complement our related neutron diffraction studies of this material under hydrostatic pressure [6].

We intend to continue our x-ray measurements at X22-C to include a fuller consideration of the ordering of the 'cubic sites' within the double-hexagonal close packed structure. This will require the use of the Joule-Thompson liquifier available at X22-C in order to assess those phases (triple-q and quadruple-q) in which the cubic sites are also spontaneously ordered. Such ordering of the cubic sites occurs for temperatures below 8K.

References

[1] B.Lebech, J.Wolny and R.M.Moon, J.Phys., Cond.Mat., 6, 5201 (1994)
[2] D.Watson, E.M.Forgan, W.J.Nuttall, W.G.Stirling and D.Fort, Phys.Rev.B 53, 726 (1996)
[3] B.Lebech, J.Appl.Phys., 52, 2019 (1981)
[4] D. Watson, W.J. Nuttall, E.M. Forgan, D. Fort and S.C. Perry, (to be published).
[5] J.P.Hill and D.F.McMorrow, Acta Cryst. A52, 236 (1996)
[6] D. Watson, E.M. Forgan, W.J. Nuttall, P.E. Sokol, S.J. Shaikh, S.W. Zochowski and D. Fort, J. Phys.: Condens. Matter 8, 5049 (1996).

Ir(100) Surface Structure Determination by X-ray Scattering *	X22C

G.Watson (UMBC), D.Gibbs (BNL, Physics), V.Jahns and D.Zehner (ORNL)

The (001) surfaces of Au and Pt reconstruct in vacuum to form quasihexagonal overlayers. These overlayers exhibit temperature-dependent incommensurabilities and rotational transformations. At the highest temperatures, the Au(001) surface disorders while Pt roughens. Previous LEED work has shown that the Ir(001) surface reconstructs to form a commensurate (1x5) overlayer at 300K. We were motivated by these results to use x-ray scattering to determine if the Ir(001) surface reconstruction becomes incommensurate on heating to higher temperatures and whether at the highest temperatures the surface disorders or roughens.

We find that the Ir(001) surface is commensurate from 300 to 2000 K, and that above 2000K the surfaces appears rough.

We have performed specular and non-specular reflectivity measurements of the Ir(001) surface for temperatures between 300 and 2200 K. The temperature dependence of the specular reflectivity is illustrated in Fig. 1 where, at high temperatures, the scattering at the (001) anti-Bragg position is shown to be diffuse and to exhibit a power-law dependence on transverse wavevector as expected for a rough surface. This identification is supported by the temperature dependence of the superstructure and off-specular truncation rod intensities at grazing incidence.

On the other hand, we have also investigated the metastable (1x1) phase which exists on Ir(001) at room temperature. This phase has considerable intensity in the off-specular truncation rod reflections as compared to the high temperature (1x1) phase.

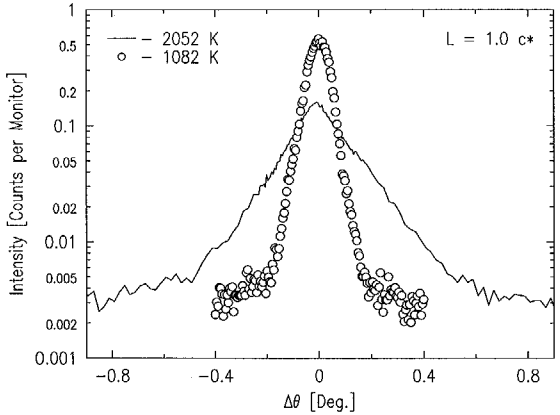


Figure 1. Specular reflectivity profiles obtained at 1082 and 2052 K.

* Research at ORNL is sponsored by the US Division of Materials Sciences, US DOE, contract No. DE-AC05-96OR22464 with Lockheed Martin Energy Research Corp. Work performed at BNL is supported by the US DOE contract DE-AC02-76CH00016.

Characterization of the Magnetic Disorder at the (001) Surface of UO_2	X22C, X25

G.M. Watson, D. Gibbs (BNL, Physics), L.E. Berman (NSLS), G.H. Lander, H. Matzke (EITU), W. Ellis (LANL), and B.D. Gaulin (McMaster U.)

In our earlier work, we showed that the temperature-dependence of the scattering along a (110)-type magnetic truncation rod of a UO_2(001) surface appeared to vanish continuously as the temperature is raised to the bulk Néel temperature, T_N = 30.2 K.[1] This is suprising since the bulk transition, as observed by neutron and x-ray scattering, is discontinuous.[2] This behavior may be understood as an example of surface induced disorder wherein magnetic disorder propagates from the near surface volume into the bulk as the temperature approaches T_N. In order to further characterize this behavior, we have performed measurements of the four equilavent (110)-type magnetic truncation rods and of the specular magnetic reflectivity. Rod intensities were obtained both as a function of temperature at fixed wavevector and as a function of momentum transfer at a number of temperatures. The magnetic specular reflectivity shown in Fig. 1 is especially sensitive to the decay of the magnetic order parameter profile along the surface normal direction. At the higher temperatures, the reflectivity away from the bulk Bragg reflection falls off faster than it does at lower temperartures. This indicates that the width of the magnetic profile increases with temperature. In fact, our data seem to suggest that this width diverges as T approaches T_N.

[1] G.M. Watson, *et al.*, Physica B **221**, 405 (1996); *ibid.* Phys. Rev. Lett. **77**, 751 (1996).

[2] B.C. Frazer *et al.*, Phys. Rev **140**, A1448 (1965); B.M.T. Willis and R.I. Taylor, Phys. Rev. Lett **17**, 188 (1965); G.M. Watson *et al.*, Phys. Rev. B **53**, 686 (1996).

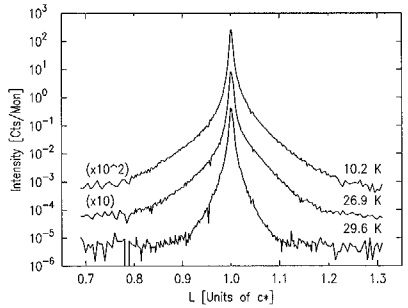


Figure 1. Specular magnetic reflectivity profiles near the (001) bulk magnetic Bragg reflection obtained at 10.2, 26.9, 29.6 K utlizing a Au(111) reflection for a polarization analyzer. Peak count rates at beam line X25 were approximately $5x10^5$ cps at a beam current of 200 mAmp.

Cr-K-edge X-ray-Absorption Study of Cr Dopants in Mg_2SiO_4 and Ca_2GeO_4 Sol-gel Glasses	X23A2

K. E. Miyano (Brooklyn College), J. C. Woicik (NIST), Ding Huang (Brooklyn College), P. Sujatha Devi, and H. D. Gafney (Queens College)

Cr doping has been central to the development of tunable solid-state lasers. PetriΣo(,c)eviΣo(,c) et al. have developed promising lasers from Mg2SiO4. In this host Cr3+ and Cr4+ coexist: Cr3+ substitutes for Mg2+ in octahedrally-coordinated sites, while Cr4+ substitutes for Si4+ in tetrahedrally-coordinated sites. Cr4+ emission is involved in the laser action: it occurs in the important near-IR band centered around 1.25 mm. Using x-ray absorption we studied the site and oxidation state of Cr dopants in sol-gel-grown Mg2SiO4 as well as the closely-related Ca2GeO4. Sol-gel processing is particularly suited to Ca2GeO4, which can't be prepared at high-temperature due to preferential evaporation of GeO2 and polymorphism. Absorption spectra were recorded using a pair of Si (311) crystals. Fluorescence yield spectra were measured with a Lytle-type detector equipped with a vanadium filter. Lineshape features and the energy position of the x-ray absorption near edge structure (XANES) characterizes the oxidation state of the absorbing atom. In the present study we followed the position of the main absorption edge and used this trend to identify the oxidation of the Cr dopants. Cr metal, CrCl2, Cr2O3, CrO2, and CrO3, cover formal Cr oxidation states of 0, 2+, 3+, 4+, and 6+, respectively and were used as standards. The figure below plots for the standards the position of the main absorption edge, taken as the peak in the first-derivative spectrum, versus formal oxidation state. There is a direct correlation between these quantities. The absorption profile of Ca2GeO4 is plotted below: the main absorption edge lies at 6006.5 eV, indicative of Cr4+ oxidation. The absorption profile of Mg2SiO4 is more complicated, due to contributions from both Cr3+ and Cr4+, and will be described in detail elsewhere. Finally, the extended x-ray absorption fine structure (EXAFS) was used to extract information on the site of the Cr atoms. In particular, EXAFS gives the bond lengths and coordination numbers of near neighbors of the Cr atoms, in this case oxygen atoms. Qualitatively, the Cr dopants in Ca2GeO4 are observed to lie at only one site, whereas the Cr dopants in Mg2SiO4 lie at two distinct sites: the signal from Cr in Ca2GeO4 exhibits one strong oscillation, whereas the others exhibit a complicated interference between multiple first shell bond lengths. The localization of the Cr ion to a single site in Ca2GeO4 is in fact expected from ionic radius considerations.

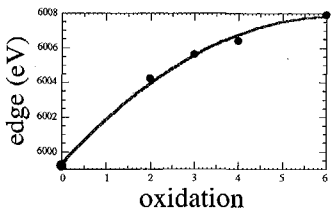


Figure 1. The peak in the first derivative is plotted versus oxidation state for the various standards.

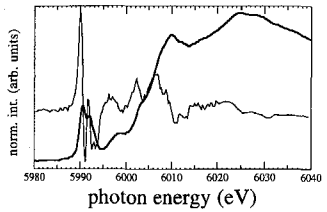


Figure 2. The Cr K near edge absorption spectrum for Ca_2GeO_4 and its first derivatives are plotted.

X-ray Absorption Studies of Battery Materials	X23A2, X23B

P. E. Stallworth (USNA); M. L. denBoer, S. Kostov, S. Greenbaum (CUNY, Hunter), and C. Lampe-Onnerud (Quantum Energy Technologies)

In the past year we have investigated the structure and electronic properties of a number of lithium battery cathodes, including the alloyed spinels, $LiMn_{2-y}Fe_yO_4$ and $LiMn_{2-y}Cr_yO_4$, a nickel-based spinel series, a hydrogen manganese sulfate-based cathode series and the system $Li_xV_6O_{13}$, using solid state nuclear magnetic resonance (NMR) to examine the environment of the Li and x-ray absorption to study the environment of the transition metal host. We report here results on the system $Li_xV_6O_{13}$ which demonstrate that the material goes through several distinct regimes as a function of Li intercalation x. [1]

$Li_xV_6O_{13}$ samples with x = 0, 0.5, 1, 1.5, 2, 3, 4, 5, and 6 were measured. Representative V K edge x-ray absorption spectra are shown in Fig. 1(a). The "white line" peak after the edge is proportional to the number of $s \rightarrow p$ transitions, in effect probing unoccupied p final states. The white line peak, Fig. 1(c), grows dramatically with x. The "pre-edge" region is due to $s \rightarrow d$ transitions which, while dipole-forbidden, become allowed in non-octahedral symmetry as the V $3d$ states mix with the Op states. Therefore the strength of this transition is proportional to the deviation from local octahedral symmetry of the vanadium site. Fig. 1(b) shows this transition first increases slightly with increasing x for $x < 1$ and then decreases rapidly for $x > 1.5$. These changes are summarized in Fig. 2(a), which also shows the result of EXAFS analysis of the V K edge. Both the near-edge and EXAFS show a slight increase in the distortion from octahedral symmetry with increasing x for $x < 1$, followed by a dramatic increase in such distortion from x = 1 to 3, with little change thereafter. The increase in the ratio of the first to second EXAFS peak, shown in Fig. 2(b), indicates disorder beyond the first V-O distance increases rapidly beyond $x = 1$. NMR shows at low x, Li ions occupy a single site, increasingly favoring locations near V^{+5} ions as x increases. At higher x, Li ions occupy a variety of sites, and strong relaxation mechanisms become important as the lithium content increases, due to paramagnetic interactions with both V^{+4} and V^{+3}.

[1] P. E. Stallworth, S. Kostov, M. L. denBoer, S. G. Greenbaum and C. Lampe-Onnerud, submitted to J. App. Phys.

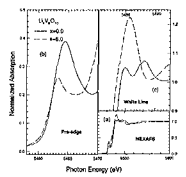


Figure 1.

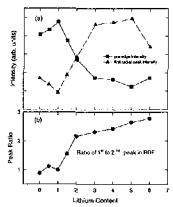


Figure 2.

XANES and EXAFS Characterization of Copper Halides in Nylon 6,6	X23A2, X23B

J. N. Weber, H. D. Rosenfeld (DuPont) and M. A. Walters (NYU)

Copper halides have been added to nylon polymer for over 40 years and are widely recognized as one of the most effective anti-oxidants for polyamides. Despite their long commercial use little is known about the structural and chemical details of the copper halides in the polymer, in part due to their low concentrations, on the order of 100 ppm Cu. XANES and EXAFS coupled with polymer and model compound synthesis and other analytical techniques offer a very promising approach to study this important chemical system in situ.

Our XANES results indcate that, independent of the oxidation state of the metal, Cu(I) or Cu(II), when the copper halide anti-oxidant is added to the polymer during processing, the initial state of the copper upon extrusion is the Cu(I) ion. As the nylon polymer is permitted to equilibrate with the atmosphere, absorbing oxygen and moisture, the cuprous ion is oxidized to cupric ion which we have observed in almost all equilibrated samples. Thus in the final commercial polymer the copper appears predominantly as the cupric ion. In addition, we have confirmed earlier work by others that the lavender/pink color occasionally seen in copper-containing polyamides is due to colloidal copper metal. We have also observed orientation effects for Cu(II) phthalocyanine pigment in nylon fiber using polarized XANES. The pigment forms needle-like crystals in the polymer which are oriented along the fiber axis during spinning and drawing. We believe that this is the first observation of orientation of an additive in fibers using XANES.

Our preliminary EXAFS results indicate that the cupric ion in nylon is coordinated by the amine and carboxylate end groups of the polymer and that the amide function does not play a significant role in coordination. We have prepared a series of model cupric amine nitrate compounds and one model cupric amine acetate compound which reproduce very closely the EXAFS spectra of the cupric ion in nylon. These spectra are distinctly different from those of Cu(II) carboxylate model compounds. In these amine-containing model systems the copper ion is coordinated by four planar amine groups and two axial nitrate or acetate groups which form a distorted octahedral environment around the cupric ion. Thus we believe that the cupric ion in nylon is coordinated in a similar manner. Solubility studies of cupric ion in low molecular wt. liquid amides provides additional evidence that the amide function is not significantly coordinated to the cupric ion in amides. Current work in progress includes the study of the environment surrounding the halide ions in nylon and the chemical reactions occurring in the anti-oxidant during oxidation of the polymer.

A Look Inside the Unit Cell of Strained GeSi	x23A2

J.C. Woicik, C.E. Bouldin (NIST), K.E. Miyano, (Brooklyn College), and C.A. King (Lucent Technologies)

The local structure within the unit cell of strained GeSi layers grown on Si(001) has been examined by polarization-dependent extended x-ray absorption fine structure (pd-EXAFS). First-neighbor bond lengths are found to deviate only slightly from their natural values; however, strain-induced distortions of the cubic-unit cell lead to measurable polarization-dependent changes in first-shell coordination and second-shell distances. A unifying picture of bond lengths and elasticity in strained-layer semiconductors is presented.

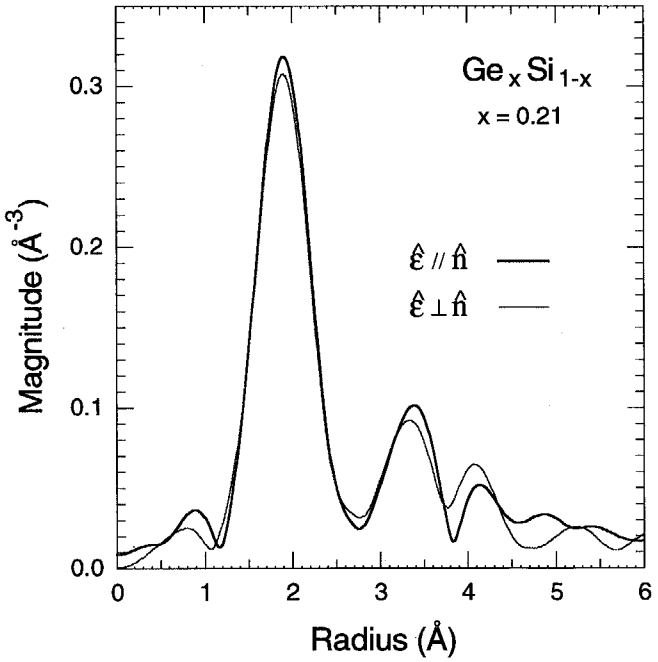


Figure 1. Fourier transforms of the Ge K-edge EXAFS from a 21 % Ge GeSi alloy grown on Si(001). The data were taken with the polarization vector aligned normal and parallel to the sample normal.

Surface Defects and Fracture of Sapphire Single Crystals	X23A3

David Black, Harold Burdette (NIST) and Dan Harris (NAWC)

Modulus Of Rupture (MOR) bars are used to measure the fracture strength of sapphire in four point bending. It is expected that surface defects will control the fracture strength. In order to produce sapphire of the highest strength at the lowest cost we must understand which flaws control fracture and how they are introduced into the surface. In a preliminary experiment we have used x-ray topography to record surface reflection images of 15 MOR bars prior to fracture. After fracture testing 5 bars survived in only two pieces and were examined again. We observed a variety of features in the images such as, subgrain boundaries, scratches, sleaks, gouges and dislocations. We then tried to correlate the features observed in these images with the measured fracture strength. Based on our preliminary observations we have arrived at several general conclusions: 1) Strength is not correlated to the presence of a subgrain boundary, misoriented by 7 arcseconds, in the gauge region; 2) Longitudinal gouges (parallel to the tensile direction) do not degrade the strength; 3) The strongest samples showed no wide transverse scratches and/or sleaks; 4) Wide transverse scratches and/or sleaks can weaken the sample. It was also observed that the residual scratches/sleaks observed by topography are not observed by optical microscopy in reflection, transmission or Nomarski. Based on these preliminary observations a statistically significant sample set is being tested.

Polishing Effects in Single-crystal Sapphire	X23A3

David Black, Harold Burdette (NIST) and Frederick Schmid (Crystal Systems)

Because of its combination of optical and thermal properties, large single-crystal sapphire is being used as uncooled windows and domes for anti-ballistic missiles. In these applications the crystals will experience thermal shocking and large thermally induced stresses. These stresses may lead to failure. One factor affecting the fracture strength of these brittle materials is surface flaws. To produce the strongest windows and domes, processing induced surface and subsurface damage must be controlled. Therefore, diagnostic tools are required which are sensitive to this damage. To this end we have used grazing incidence x-ray topography to examine sapphire surfaces. In this technique the sample is oriented for a selected asymmetric surface diffraction. The incidence energy is then tuned so that the incident angle is near the critical angle for total external reflection. This provides high sensitivity to defects at or very near the surface. The sensitivity of this method was demonstrated by observing a (1129) diffraction at a nominal energy of 9.4 keV. When the energy was increased 100 electron volts the polishing related features in the image became much more distinct.

X-ray Diffraction Imaging of Electrically Fixed Holograms in Strontium Barium Niobate (SBN)	X23A3

G. Fogarty, B. Steiner (NIST), T. Chang, and J. Hong (Rockwell International)

High resolution x-ray diffraction imaging has been used to obtain the first images of fixed photorefractive holograms in strontium barium niobate (SBN). The results of these experiments should help in the optimization of the fixing process in SBN, and in the development of high density holographic optical data storage systems.

In electrical fixing, an electric field pulse slightly lower in amplitude than the ferroelectric coercive field is applied to a photorefractive crystal in which a hologram has been written. It has been believed that the superposition of this applied field and the photorefractive space-charge field causes the formation of a ferroelectric domain pattern that mirrors the original hologram. Since the domains are stable, the fixed hologram has a much longer lifetime than the as-written hologram, which tends to decay quickly. The original hologram is also easily reconstructed by apllication of an electric field pulse of the opposite polarity to the fixing pulse. However, the fixed ferroelectric domain pattern had never been observed directly until recently, and this has made optimization of the fixing process a difficult task.

Diffraction imaging was performed on a 1mm thick sample of SBN in which a simple plane wave photorefractive hologram of 11 micrometers period had been recorded and fixed electrically. Laue geometry (002) images (Figure 1) clearly show the fixed hologram. The fixed hologram is not seen in Laue geometry images with diffraction vector perpendicular to [001], confirming that the fixing is indeed achieved via the formation of anti-parallel ferroelectric domains. No individual domains can be distinguished in any of the images, indicating that any micro-domains present are below the 1 micrometer resolution limit of the nuclear emulsion plates used to record the images. This is encouraging, as the size of micro domains will be a limiting factor in the ultimate storage capacity of any system using electrically fixed holograms.

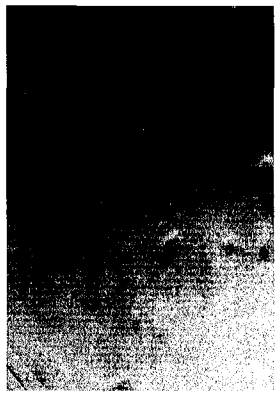


Figure 1. Enlargement of (002) diffraction image at 10keV in Laue geometry of SBN sample with 11 micrometer period fixed photorefractive hologram.

In situ X-ray Diffraction Imaging of Electrically Fixed Photorefractive Holograms in Barium Titanate	X23A3

G. Fogarty, B. Steiner (NIST), M. H. Garrett, J. Martin, and R. Uhrin (Deltronic Crystal Ind.)

High resolution x-ray diffraction imaging has recently been used to investigate one of the principle problems hindering the development of commercial holographic optical data storage systems.

Photorefractive materials, such as barium titanate, have long been considered potential media for very high density volume holographic optical data storage systems. While the potential data density is high (10^9 bits/cm^3), several problems have hindered the development of commercial holographic data storage systems. The principle difficulty has been the short lifetime of as-recorded holograms in the most efficient materials (barium titanate and SBN). Over time, the optically induced photorefractive space-charge distribution that encodes the hologram will dissipate, lowering the signal-to-noise-ratio of the hologram, and eventually erasing it. One solution to this problem is to "fix" the space charge distribution by applying to the photorefractive material a uniform electric field with amplitude slighty lower than the coercive field necessary to produce ferroelectric domain reversal. The superposition of this uniform field with the spatially varying space-charge field is believed to produce a spatially varying ferroelctric domain pattern that mimics the original space-charge field. However, this ferroelectric domain pattern had never been directly observed.

This model of the electrical fixing process has been tested by in situ diffraction imaging of photorefractive holograms written and fixed in real time on beamline X23A3. One such diffraction image can be seen in Figure 1. It proved possible to watch the growth of the ferroelectric domain pattern of the fixed hologram in real time via a medium resolution (10 micrometer) resolution x-ray video camera. High resolution (1 micrometer) nuclear emulsion plate images (Figure 1) show even greater detail, including individual domains within the fixed hologram. Preliminary analysis of the images has shown that the quality of the fixed hologram is strongly degraded by pre-existing ferrolectric domains, and is also influenced byt the presence of other crystal defects.. High quality, completely poled samples are thus required for successful fixing.

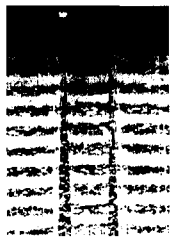


Figure 1. Enlargement of (002) diffraction image at 10 keV in Laue geometry of an electrically fixed hologram in barium titanate. The period of the hologram is 50 micrometers.

In situ Measurements of Dislocation Structure Evolution in Al Single Crystals Deformed in Tension	X23A3

L. E. Levine (WSU), G. G. Long, D. R. Black and Robb Thomson (NIST)

When a metal is plastically deformed, its material properties change dramatically in a process usually referred to as work hardening. The underlying reason for these changes is the evolution of complicated dislocation structures that take the form of cells at large strains. This dislocation pattern formation is very sensitive to such parameters as the crystallographic orientation of the strain axis, sample temperature, strain rate and the starting microstructure of the sample. We are conducting experiments on single-crystal Al to examine this dislocation structure evolution *in situ* while simultaneously measuring the stress and strain of the sample.

Since the formation of dislocation cells is a bulk process and since these cells usually extend over several micrometers in size, a minimum sample thickness of approximately 50 micrometers is required for *in situ* experiments. This eliminates the use of electrons as a possible probe leaving X-rays and neutrons as the most viable candidates. The high brightness and small source size of X-ray synchrotron radiation, along with the high spatial resolution and sensitivity of X-ray detectors, makes X-rays the preferred probe for these *in situ* measurements. The most suitable X-ray techniques include high-resolution diffraction imaging and small angle X-ray scattering (SAXS); these *in situ* experiments are being conducted on X23A3.

To conduct these X-ray experiments, we first designed and built a computer-controlled low-profile tensile stage that is both small and light enough to be mounted on an X-ray goniometer. It can deform a specimen *in situ* while simultaneously measuring the average longitudinal stress and the average linear strain.

These experiments require dog-bone shaped single-crystal specimens with a low defect density. To produce the required samples, we designed and built our own crystal growing facility that uses a modified soft-mold growth process. Since any mechanical processing of the single-crystal Al samples would introduce unacceptable numbers of defects, all processing is done chemically.

Stereographic diffraction images were obtained from a single 1 mm thick Al crystal deformed *in situ*; these images were taken at strain values of 0%, 0.45%, 1.06%, 1.94%, 2.74%, and 3.65%. Individual images were then taken at strains of 4.52%, 5.40%, 7.20% and 9.00%. In these images we observed small-angle tilt boundaries, dislocation braids, slip bands, cell structure evolution, local accumulation of single-signed edge dislocations, and a pronounced inhomogeneity of the local dislocation structure evolution. The stress-strain curve for this sample was obtained simultaneously with the X-ray measurements.

Using an identically oriented crystal, SAXS scans were obtained *in situ* at strains of 0%, 0.47%, 1.28%, 2.50%, 5.0%, 8.33%, and 16.67%. The power law behavior of these scans shows large systematic changes, thus demonstrating that these SAXS measurements are very sensitive to changes in the dislocation structure of the deforming sample.

To interpret these and future scattering results, we have developed our own theoretical approach to the problem of X-ray scattering from dislocated materials and have finished a thorough and rigorous analysis of scattering from screw dislocations. Comparison between our resulting analytical model and computer simulations shows near-perfect agreement. We are currently working to extend this analysis to edge dislocations which should allow quantitative parameters to be extracted from our X-ray scattering data.

Crack Correlation in Tensilely Strained Multifilamentary High-Tc Superconductor Composite Tapes	X23A3

R. D. Spal (NIST), G. N. Riley and C. J. Christopherson (American Superconductor Corp.)

To study fracture in high-Tc superconductor composite tapes, a Bi-2223/Ag tape consisting of 19 Bi-2223 filaments sheathed in a Ag matrix was microradiographed at zero strain (as received), then tensilely strained along its axis to 0.80% and microradiographed again. The microradiography was done at 24.75 keV with an asymmetric Bragg diffraction microscope operating at 38X magnification, equipped with an x-ray sensitive two-dimensional CCD array with 19 μm pixels, producing images with 0.5 μm pixels. The face of the 150 μm thick tape was oriented perpendicular to the beam.

Figure 1 is a microradiograph of a 1100 X 330 μm^2 region of the tape at 0.80% strain, in which the tape axis is vertical. The dark regions on the left and right sides, in which the average transmission is about 12%, are 5 (left side) and 4 (right side) filaments stacked along the beam, while the bright region in the middle, in which the average transmission is about 16%, is the matrix. The bright lines, running roughly horizontally across the full width of each dark region, are cracks in the filaments, which are strain-induced since they are absent from the zero strain image. In both stacks of filaments, the cracks are concentrated in two distinct bands, about 90 to 150 μm apart in the left stack and 55 μm apart in the right one. The upper band in the left stack connects by extrapolation smoothly to the lower one in the right stack, and likewise to a band in the adjacent stack on the left side (not shown), suggesting a tendency for crack correlation between adjacent stacks. The axial strain across the two bands in the left stack, determined by comparing the zero and non-zero strain images, is about 5%. Since this value is more than 20 times the fracture strain of bare Bi-2223 filaments, it is expected that all 5 filaments in the stack are fractured in this region. Examination of a larger region containing 13 crack bands reveals an average band spacing of 320 μm, and a tendency for bands to occur in closely spaced pairs, as in Fig. 1. These observations provide parameters for electrical and mechanical models of the tape.



Figure 1. Microradiograph of 1100 X 330 μm^2 region of tape at 0.80% strain. Black areas are outside field of view.

Residual Disorder in Low Pressure, Low Thermal Gradient LEC Gallium Arsenide Observed in High Resolution Diffraction Imaging	X23A3

B. Steiner, L.E. Levine (NIST), M. Brown, and D. Larson (Grumman)

High resolution diffraction images of low thermal gradient, low pressure, LEC silicon-doped gallium arsenide reveal a degree of crystalline order far higher than that found in earlier in undoped conventional LEC crystals.

In one of these modified LEC crystals, no distinct volume irregularity was observed where it is unstrained by its mount.

In a second modified LEC crystal, only a set of surface-treatment-related dislocations was prominent.

The third crystal exhibits two distinct sets of quasi periodic dislocations. One of these, shown in Figure 1, consists of a set of 60° dislocations. The second, Figure 2, consists of a set of 30° dislocations, which are composed of alternating screw and 60° dislocations, which have the same Burgers vector. All result from slip along {111} planes, but different ones.

In all three crystals, the streaking features characteristic of conventional LEC material are greatly reduced. Moreover, the cellular defect arrangement and the very low angle <110> subgrain boundaries also characteristic of conventional LEC material are completely absent. Silicon thus seems to have inhibited, but not prevented completely, the strain associated with {110} antiphase boundaries in this material.

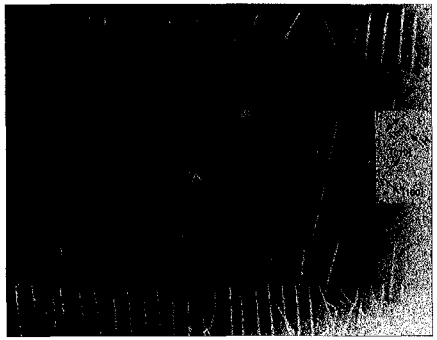


Figure 1. Asymmetric (202) diffraction image of set of 60° dislocations oriented in the [011] direction. They display 1/2 [110] Burgers vectors, whicih are associated with glide along the (111) system. These images were recorded at 10 keV.

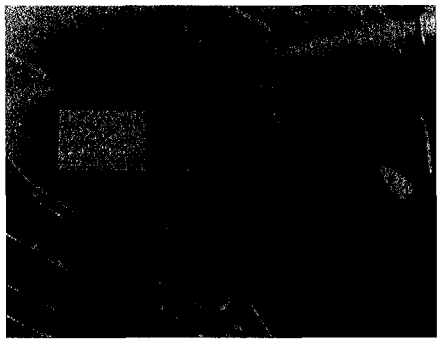


Figure 2. Asymmetric (202) diffraction image of set of 30° dislocations oriented in the [112] direction. These are compound dislocations, consisting of alternating [101] screw and [011] 60° dislocations, both with 1/2 [101] Burgers vectors, associated with glide along the (111) system. These images were recorded at 10 keV.

X-ray Absorption Studies of Battery Materials	X23A2, X23B

P. E. Stallworth (USNA); M. L. denBoer, S. Kostov, S. Greenbaum (CUNY, Hunter), and C. Lampe-Onnerud (Quantum Energy Technologies)

In the past year we have investigated the structure and electronic properties of a number of lithium battery cathodes, including the alloyed spinels, $LiMn_{2-y}Fe_yO_4$ and $LiMn_{2-y}Cr_yO_4$, a nickel-based spinel series, a hydrogen manganese sulfate-based cathode series and the system $Li_xV_6O_{13}$, using solid state nuclear magnetic resonance (NMR) to examine the environment of the Li and x-ray absorption to study the environment of the transition metal host. We report here results on the system $Li_xV_6O_{13}$ which demonstrate that the material goes through several distinct regimes as a function of Li intercalation x. [1]

$Li_xV_6O_{13}$ samples with x = 0, 0.5, 1, 1.5, 2, 3, 4, 5, and 6 were measured. Representative V K edge x-ray absorption spectra are shown in Fig. 1(a). The "white line" peak after the edge is proportional to the number of $s \rightarrow p$ transitions, in effect probing unoccupied p final states. The white line peak, Fig. 1(c), grows dramatically with x. The "pre-edge" region is due to $s \rightarrow d$ transitions which, while dipole-forbidden, become allowed in non-octahedral symmetry as the V $3d$ states mix with the Op states. Therefore the strength of this transition is proportional to the deviation from local octahedral symmetry of the vanadium site. Fig. 1(b) shows this transition first increases slightly with increasing x for $x < 1$ and then decreases rapidly for $x > 1.5$. These changes are summarized in Fig. 2(a), which also shows the result of EXAFS analysis of the V K edge. Both the near-edge and EXAFS show a slight increase in the distortion from octahedral symmetry with increasing x for $x < 1$, followed by a dramatic increase in such distortion from x = 1 to 3, with little change thereafter. The increase in the ratio of the first to second EXAFS peak, shown in Fig. 2(b), indicates disorder beyond the first V-O distance increases rapidly beyond $x = 1$. NMR shows at low x, Li ions occupy a single site, increasingly favoring locations near V^{+5} ions as x increases. At higher x, Li ions occupy a variety of sites, and strong relaxation mechanisms become important as the lithium content increases, due to paramagnetic interactions with both V^{+4} and V^{+3}.

[1] P. E. Stallworth, S. Kostov, M. L. denBoer, S. G. Greenbaum and C. Lampe-Onnerud, submitted to J. App. Phys.

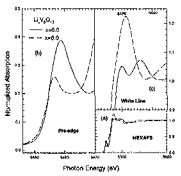


Figure 1.

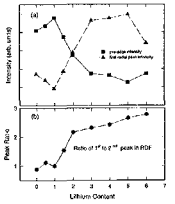


Figure 2.

Measure of Hexavalent Chromium in Contaminates Soils * | X23B

M. Szulczewski, W.F. Bleam, and P. A. Helmke (U. Wisconsin-Madison)

Because chromium is a common industrial contaminant, accurate characterization of chromium speciation in the environment is important. An independent method, such as XANES, is needed to verify current methods of extraction or exchange.

The pre-edge regions of the XANES spectra for Cr(VI) and Cr(III) are dramatically different. A strong pre-edge peak appears due to a 3d-4p mixing orbital whenever Cr(VI) present. It is well-known that the area of this peak is proportional to the amount of Cr(VI) present in a sample. Figure 1 shows an overlay of this pre-edge region of the XANES spectra of 6 physical mixtures with varying fraction of Cr(VI):Cr(III) ratios in the standards. The deconvolution of the pre-edge region into a linear combination of four gaussian peaks and an arctangent step function gives a value for the normalized area of the 3d-4p mixing peak. The correlation curve derived from these areas displays the linear relationship between the relative area of the pre-peak and the fraction of Cr(VI) present (Figure 3). We then deconvoluted the pre-edge region of the XANES spectrum for each of our contaminated soils, and obtained a value for the fraction of Cr(VI) present based on the correlation curve. Even in the extremely contaminated soils, the Cr(VI):Cr(III) ratio was never over 0.5.

The advantage of XANES spectroscopy is that the total quantity of Cr(VI) is seen, regardless of its chemical state (dissolved, adsorbed, or precipitated). When we compare the amount of Cr(VI) detected by XANES spectroscopy analysis, we see that current analytical methods (performed elsewhere) greatly underestimate the concentration of Cr(VI) present in contaminated soils.

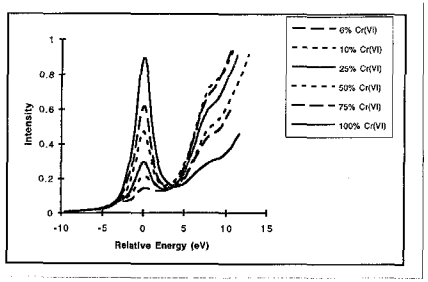


Figure 1. Cr K-edge spectra of the pre-edge region of standard physical mixtures with varying fractions of Cr(VI):Cr(III).

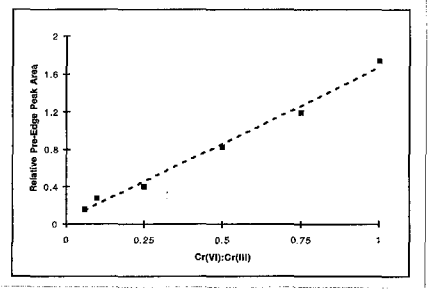


Figure 2. Calibration curve from physical mixtures of varying fractions of Cr(VI):Cr(III).

* Research supported by U.S. Department of Agriculture Hatch Program No. WI-3681. We would like to acknowledge the assistance of Drs. Geraldine Lamble, Lars Furenlid, John Kirkland, and Timothy Elam.

XANES and EXAFS Characterization of Copper Halides in Nylon 6,6 | X23A2, X23B

J. N. Weber, H. D. Rosenfeld (DuPont) and M. A. Walters (NYU)

Copper halides have been added to nylon polymer for over 40 years and are widely recognized as one of the most effective anti-oxidants for polyamides. Despite their long commercial use little is known about the structural and chemical details of the copper halides in the polymer, in part due to their low concentrations, on the order of 100 ppm Cu. XANES and EXAFS coupled with polymer and model compound synthesis and other analytical techniques offer a very promising approach to study this important chemical system in situ.

Our XANES results indcate that, independent of the oxidation state of the metal, Cu(I) or Cu(II), when the copper halide anti-oxidant is added to the polymer during processing, the initial state of the copper upon extrusion is the Cu(I) ion. As the nylon polymer is permitted to equilibrate with the atmosphere, absorbing oxygen and moisture, the cuprous ion is oxidized to cupric ion which we have observed in almost all equilibrated samples. Thus in the final commercial polymer the copper appears predominantly as the cupric ion. In addition, we have confirmed earlier work by others that the lavender/pink color occasionally seen in copper-containing polyamides is due to colloidal copper metal. We have also observed orientation effects for Cu(II) phthalocyanine pigment in nylon fiber using polarized XANES. The pigment forms needle-like crystals in the polymer which are oriented along the fiber axis during spinning and drawing. We believe that this is the first observation of orientation of an additive in fibers using XANES.

Our preliminary EXAFS results indicate that the cupric ion in nylon is coordinated by the amine and carboxylate end groups of the polymer and that the amide function does not play a significant role in coordination. We have prepared a series of model cupric amine nitrate compounds and one model cupric amine acetate compound which reproduce very closely the EXAFS spectra of the cupric ion in nylon. These spectra are distinctly different from those of Cu(II) carboxylate model compounds. In these amine-containing model systems the copper ion is coordinated by four planar amine groups and two axial nitrate or acetate groups which form a distorted octahedral environment around the cupric ion. Thus we believe that the cupric ion in nylon is coordinated in a similar manner. Solubility studies of cupric ion in low molecular wt. liquid amides provides additional evidence that the amide function is not significantly coordinated to the cupric ion in amides. Current work in progress includes the study of the environment surrounding the halide ions in nylon and the chemical reactions occurring in the anti-oxidant during oxidation of the polymer.

X-ray Standing Wave Investigation of S/Ni(100) | X24A

D. Heskett, J. Warner, and G. Sabatino (U. Rhode Island), D. Mullins (ORNL) and L.E. Berman (NSLS)

We have used the technique of Back-Reflection X-ray Standing Waves (BRXSW) to investigate the structure and geometry of sulfur on the Ni(100) surface (Ref. 1). We prepared this system by dosing H_2S in 100L increments onto the Ni(100) surface at room temperature. The dosing was then followed by an anneal to ~500K. The purpose of the anneal was to drive off residual H atoms that were left on the surface after the H_2S dissociated. Based on the intensity of the S 1s core level, we found that 200L was sufficient to saturate the surface with sulfur (see Figure 1). Based on our own and other previous investigations of the S/Ni(100) system, the saturated S/Ni(100) surface corresponds to a well-ordered (2x2) structure.

We next performed x-ray standing wave measurements of this overlayer in both the (200) and (111) Bragg reflection geometries. Based on the high coherent fractions measured in both geometries, we can conclude that the sulfur atoms were very well-ordered both parallel and perpendicular to the Ni(100) surface. Based on triangulation of the coherent positions from both sets of measurements, we determined that the S atoms were bonded in four-fold hollow sites at a distance of 1.32±.02 Å above the ideal (100) Ni plane (see Figure 2), in good agreement with other structural measurements of this system (Ref. 2).

We are in the process of carrying out a similar XSW study of methanethiol/Ni(100). The strong cross-section to excite the S 1s core level as shown in our spectra indicates that this technique can be employed to investigate sub-monolayer coverages of sulfur and sulfur-containing molecules on surfaces.

1. D. Heskett, J. Warner, G. Sabatino, D. Mullins, and L. Berman, in preparation.
2. T. Yokohama, H. Hamamatsu, Y. Kitajima, Y. Takata, S. Yagi, and T. Ohta, Surf. Sci. 313, 197 (1994).

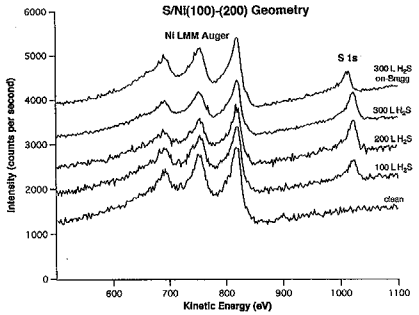


Figure 1. S 1s core level spectra of the system S/Ni(100) as a function of H_2S exposure.

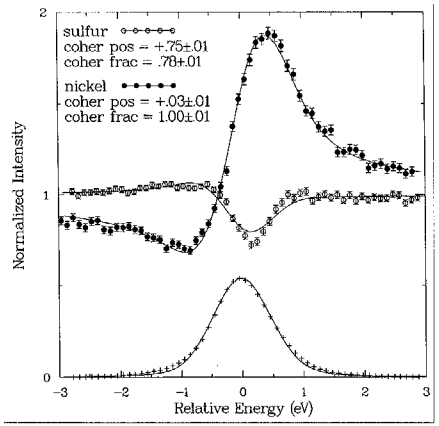


Figure 2. Measured XSW yields of the Ni LMM Auger and S 1s core emissions as the bulk Ni(200) Bragg reflection (at bottom) was scanned, compared with theoretical fits, for (2x2) S/Ni(100).

X-Ray Standing Wave Studies of Self-Assembled Monolayer Growth | X24A

F. Schreiber, P. Fenter, G. Scoles, P. Eisenberger (Princeton U.), L. Berman (NSLS) M. Bedzyk (Northwestern U. & ANL)

We have followed the vapor phase growth of the self-assembled monolayer of decane thiol (C10) on Au(111) surfaces using both x-ray standing waves (XSW) and x-ray photoelectron spectroscopy (XPS). In contrast to a number of studies which find that solution phase growth of this system proceeds via simple Langmuir growth with a single time constant, we have found that there are two time scales in the vapor phase adsorption process: a fast process which saturates with rather small exposures (~20L), and a slow process which does not reach completion until exposures of~10000L. From the sulfur signal at the saturation at each "plateau" of the uptake curve (and correcting for electron attenuation through the completed monolayer), we derive a sulfur coverage of ~0.35±0.1ML for the initial adsorption process (1 ML=4.6×10^{14} molecules/cm^2, which is the coverage of the saturation c(4x2) phase). This coverage is consistent with the coverage of the known "striped" phase, in which the molecules lie down on the surface and has a coverage of 0.27ML. These data provide unambiguous evidence that the vapor phase growth of C10/Au(111) proceeds in a two-step process, with the first rapid step covering the surface, and the second slower step bringing the monolayer to completion.

How does the sulfur-Au 'bond' vary through the growth process, as the monolayer goes from the low density "striped" phase to the saturation c(4x2) phase? To determined this directly, we have used x-ray standing waves, using the back reflection geometry to probe the sulfur position with respect to the underlying Au lattice. While a full characterization of the S/Au bonding structure is not yet completed, we have performed measurements in the (111) Bragg reflection geometry, which probes the height of sulfur above the gold surface, d. From these measurements, we have found that d=2.56±.02Åfor a coverage of ~0.27ML (corresponding to the "striped" phase), while d=2.59±.02Åfor a coverage of 1.0ML (corresponding to the saturated c(4x2) phase; see Figure 1), with similar results at intermediate coverages. This implies that there is no significant change in the vertical S-Au spacing in the growth process, so the drastic changes of the monolayer structure are due to changes in the density of adsorbed molecules and the related orientation of the hydrocarbon chain, as opposed to changes in the S/Au bond.

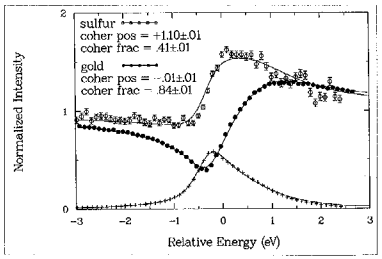


Figure 1. Measured XSW yields of the Au M_5 and S 1s core emissions as the bulk Au(111) Bragg reflection (at bottom) was scanned, compared with theoretical fits, for c(4x2) C10/Au(111).

Angular Correlation Between Subsequently Emitted Auger Electrons | X24A

R. Wehlitz, L. Pibida, J. C. Levin, and I. A. Sellin (U. of Tenn.)

Using the single-bunch mode of the X-ray ring, we have measured the angular correlation between Auger electrons which are emitted in a cascade-like decay process after resonant photoexcitation. The set-up used for this experiment consists of a time-of-flight (TOF) spectrometer whose axis is aligned with the electric vector of the monochromatized synchrotron radiation and a cylindrical mirror analyzer (CMA) whose axis is aligned perpendicular to the TOF spectrometer and the photon beam direction. The monochromator was tuned to the Ar $1s \rightarrow 4p$ resonance (3203.5 eV) and the photon beam was intersecting an effusive beam of argon atoms. The CMA, equipped with a position sensitive detector (PSD) mounted downstream of its energy selection aperture, permits registering not only the energy, but also the azimuthal and polar angles of emission in the source region, which is imaged 1 to 1 in the CMA image space, for all azimuthal angles and a band of polar angles simultaneously. Thus energy-selected Ar $KL_{2,3}L_{2,3}$ Auger electrons were collected at a variety of angles relative to the axis of the TOF spectrometer which was used to detect in coincidence the entire group of LMM Auger electrons from about 120 eV to 230 eV kinetic energy simultaneously. In other words, the TOF was detecting the LMM Auger electrons at one angle while the CMA was detecting the precursor $KL_{2,3}L_{2,3}$ Auger electrons from 48° to 132° with respect to the TOF axis. We accumulated enough intensity to see a remarkable angular correlation between a distinct slice (b) of the LMM Auger group and the KLL Auger electrons while other slices (a and c) of the LMM group exhibit isotropy. The large non-isotropic angular correlation observed for the distinct slice accompanies the detection of the first-step KLL Auger electron in a particular direction, thereby breaking the symmetry so as to reveal the correlation. Because the KLL and LMM energies are so different, we believe the large non-isotropic angular correlation observed represents an alignment effect rather than a dynamical post-collision interaction effect.

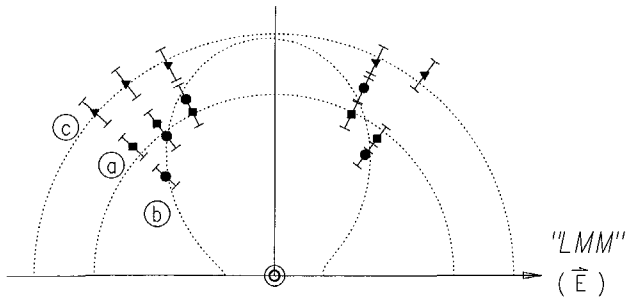


Figure 1. Polar plot showing the angular correlation between three slices (a, b, and c) of the LMM Auger group and the $KL_{2,3}L_{2,3}$ Auger electrons.

Band Structure of Nonlinear Crystal LiB_3O_5 in VUV Region Obtained From Reflection Spectra * | X24C

Tian-Jie Chen (Southern Illinois U.), W.R.Hunter (Sachs Freeman Assoc.), J. C. Rife (Naval Research Center), and R. Tao (Southern Illinois U)

The production of coherent VUV and soft x-ray radiation by nonlinear optical techniques is a highly desirable goal. Lithium triborate (LBO) is a popular nonlinear optical crystal, favored for its high nonlinear susceptibility, high damage threshold, and broad transparency spectrum. French[1] has calculated the band structure, has not been verified experimentally. LBO's strong interband absorption begins at about 165 nm (≈7.5 eV), and transmission is poor at higher photon energies; therefore, it was thought that it was impossible to generate second harmonic beyond this energy. To sidestep this obstacle, it has been proposed[2] that in the case of strong absorption a reflection configuration can be used for second harmonic generation as far as a double resonance condition is met.

To find the suitable energy band sets which meet the double-resonance condition, we have measured the reflection spectra in the 6-11 ev region. The experiments were carried out at the X-24C beamline of the National Synchrotron Light Source at Brookhaven National Laboratory. The samples were LBO crystals $6 \times 6 \times 2$ mm^3 and laser grade polished. A oscillator model[3] was used to derive the refractive indices and extinction indices from the spectra. Six absorption peaks were found from the extinction index curves.

The results show:

(1) By the comparison with the data calculated by group theory and French's numbers, the six observed peaks are identified as the nB_1-mA_2 transitions.

(2) The strong absorption edge originates from the second highest valance band, instead the highest valence band.

(3) There are two band sets which meet the double-resonance condition with accuracy $\hbar\omega_{21} - \hbar\omega_{32} < \pm 0.10ev$ where 1, 2, and 3 is the initial, intermediate and final state respectively; $\hbar\omega_{21}$, $\hbar\omega_{23}$, $\hbar\omega_{31}$ is the energy difference among them. ω_L is the fundamental laser frequency. The double resonance condition requires: $\omega_L = \omega_{12}$, $2\omega_L = \omega_{32}$; and all three dipole transitions $1 \rightarrow 2$, $2 \rightarrow 3$, and $1 \rightarrow 3$ are allowed.

[1]R.French,J.Ling,F.Ohuchi,C.Chen,*Phys.Rev.B***44**,8496(1991).[2]T.Chen, R.Zitter,R.Tao,*Phys.Rev.A***51**,706 (1995).[3]T.Chen, R.Zitter,R.Tao,W.Hunter, and J.Rife,*Phys.Rev.B***52**,13703(1995).

* *This research is supported by the IllinoisConsortium for Advanced Radiation Sources(CARS); and the U.S. Department of Energy under contract DE AC 02-76CH00016 through NSLS at Brookhaven National Lab.

Characterization of Multilayer Coated Gratings and Mirrors	X24C

J. F. Seely, M. P. Kowalski, J. C. Rife, W. R. Hunter, and R. G. Cruddace (NRL)

Diffraction gratings and mirrors with multilayer coatings are characterized in the soft x-ray and extreme ultraviolet regions. The multilayer coatings are designed to have high reflectance at wavelengths and angles of incidence that are important for the study of laboratory, solar, and astrophysical plasmas. The efficiencies of the multilayer coated gratngs, and the reflectances of the mirrors with similar coatings, are measured as functions of the angle of incidence and the wavelength of the incidence light. The measured reflectance is compared to model calculations that account for the layer thicknesses, the interfacial roughness parameters, and the optical constants of the materials. The gratings have blazed or laminar groove profiles and are fabricated by the holographic ion-beam etched process. The multilayer coating is matched to the groove profile so that the coated grating has optimal efficiency at the angle and waveband of interest.

Structure of the Quaternary NF-ATp/Fos/Jun/DNA Complex	X25

L. Chen, S.C. Harrison, * (*HHMI) A. Rao †, P. Hogan †, (†Harvard Medical School)

Activation of NF-AT (nuclear factor of activated T-cells) is a key step in signaling from the antigen-stimulated T-cell receptor. NF-AT consists of a specific component (NF-ATp) and the Fos/Jun heterodimer of AP-1. Crystals of the DNA-binding domain (approx. 300 residues) of NF-ATp, the bZIP elements of Fos and Jun, and a 20 bp segment of DNA bearing a site from the IL-2 enhancer, are in space group $P2_1$ (a=64.9, b=85.7, c=83.6, β=112.4°). Diffraction from flash-frozen crystals extends to 2.6 Å. Data have been collected at X25 from crystals containing SeMet-substituted NF-ATp (3 wavelengths) and from crystals derivatized with $CH_3\ Hg^+$ (1 wavelength - Hg L-edge). The Hg locations have been determined from an anomalous difference Patterson; the Se sites have been determined; a MAD/MIR phase determination is in progress (August 28, 1996).

The Near-Threshold Evolution of the CuK$\alpha_{3,4}$ Satellites | X25

M. Fritsch (Bar-Ilan U., Israel), K. Hämäläinen (Helsinki U., Finland), C. C. Kao (NSLS), O. Gang, M. Deutsch (Bar-Ilan U.)

Our previous measurements[1] of the near-edge-photoexcited Cu K$\alpha_{3,4}$ satellites showed that (a) the onsets of the $\alpha_3+\alpha_3'$ and the $\alpha_4+\alpha'$ lines are separated by 10-15 eV, and (b) the spectral *shape* saturates ~50 eV above threshold, above which only the *intensity* increases but no shape changes occur. Those studies did not resolve accurately the threshold energies, nor the spectral shape changes in the immediate vicinity of the threshold, issues that were addressed this period. Fig. 1 shows an accurate determination of the different onset energies for the four satellite lines. The shape evolution is shown in Fig. 2. The spectra were corrected for various energy dependent effects, and subtracted by the Kα contribution. The shape is observed to change considerably with increasing excitation energy due to the different thresholds and cross-section energy dependences of the individual lines underlying this highly overlapping spectrum. Quantitative analysis, now in progress, will determine these dependences and providing the first such data for the virtually unexplored adiabatic regime of the x-ray satellite emission process.

1. M. Deutsch *et al*,*Phys. Rev. Lett.* **76**, 2424(1996).

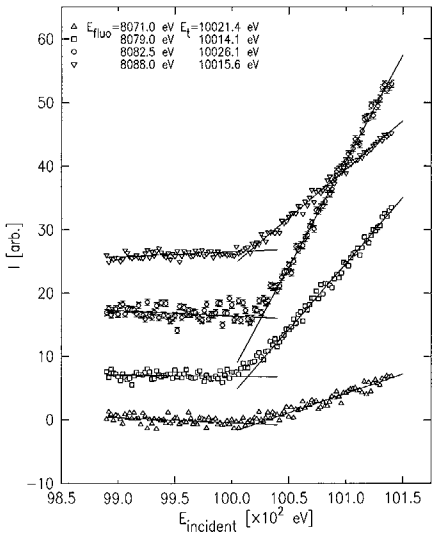


Figure 1. Onset energies of the satellite spectrum components.

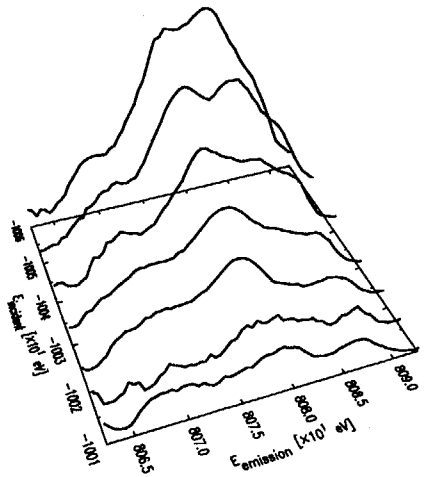


Figure 2. The spectral shape evolution near threshold.

Structural Investigation of GaP Clusters in a Si Matrix, using Multiple Energy X-ray Holography (MEXH) | X25

T. Gog (ORNL), R.-H. Menk (NSLS), R. Eisenhower,(U of Illinois) G. Le Duc, L. Berman, Z. Yin (NSLS)

Measurements using Multiple Energy X-ray Holography (MEXH) have been conducted to study the structure of small (50 Å) GaP clusters in a single crystal silicon matrix. These measurements were of particular interest, both in terms of extending the novel MEXH technique into the realm of "diluted" samples, i.e. samples with concentrations of fluorescing atoms equivalent to only a few monolayers, and for the sake of this novel nano-crystal material, where implanted clusters are closely lattice matched with the host matrix thus making a seperation of substrate and cluster contributions in regular diffraction experiments extremely difficult.

A flat-plate sample was mounted on a six-circle diffractometer and oriented with respect to a substrate reflection perpendicular to its surface. Tuning the energy of the incident x-ray beam to values above the Ga K absorption edge and rotating the sample around the surface normal at varying incident angles, Ga fluorescence was recorded, which, after a removal of background and application of absorption and detector dead time corrections yielded a preliminary hologram. Inversion of this hologram by Fouriertransformation shows an as of yet ill-resolved direct image of the GaP clusters, however, the four-fold symmetry of the Ga sublattice with atoms at an approximately correct distance can easily be discerned, providing proof that x-ray holographic methods with atomic resolution in connection with current synchrotron radiation sources are capable of addressing structural questions in diluted samples. However, collection of data covering reciprocal space in finer increments and more complete volumes are neccessary to generate acceptable direct images of GaP clusters embedded in their host Si matrix.

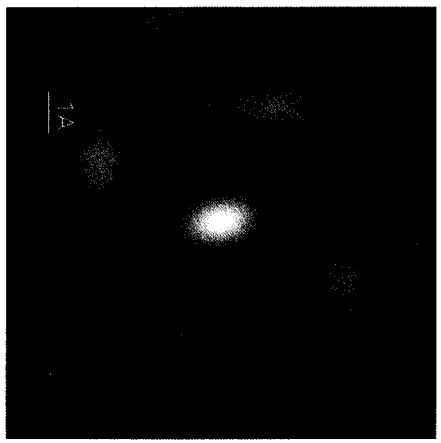


Figure 1. Reconstruction of the GaP(001) plane at z=0

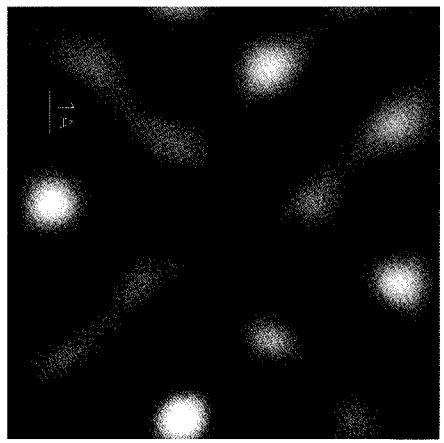


Figure 2. Reconstruction of the GaP(001) plane at z=0.5 a

K-Edge Resonant Magnetic Scattering from a Transition Metal Oxide: NiO	X22C, X25

J.P. Hill (BNL, Physics), C.-C. Kao (NSLS) and D.F. McMorrow (Riso)

Resonant x-ray magnetic scattering exploits enhancements in the cross-section occurring when the incident photon energy is tuned through an atomic absorption edge. Large enhancements were first observed at the $L_{II,III}$ edges in Ho and explained in terms of electric multipole transitions. In addition to the L edges much larger enhancements are expected, and observed, at the $M_{IV,V}$ edges of the actinides for which the dipole excitation is to the localized, highly polarized 5f levels. Conversely, resonant scattering at a K-edge is expected to be considerably weaker because the strong (dipole) transitions involve *s* and *p* levels for which there is no spin-orbit correlation of either the core level or the intermediate state. Nevertheless, K-edge studies would be of some interest because of the window they would provide on transition metal compounds, which make up arguably the most interesting of magnetic systems.

We report the observation of K-edge resonant magnetic scattering in the antiferromagnet NiO, for which an approximately two-fold increase in the scattering is observed at an energy corresponding to a quadrupolar feature in the absorption spectrum (Fig.1). Quadrupole excitations couple to d-like states at a K-edge and for transition metals these are the magnetic states. Thus, the high degree of polarization of the localized $3d^8$ states compensates for the small size of the quadrupolar matrix elements and an observable enhancement results. From the ratio of the non-resonant to resonant magnetic scattering, we estimate that the first order quadrupolar resonant scattering amplitude is $0.016r_0$, which is of the same order of magnitude as similar terms in the rare earths. These studies provide for the possibility of element specific magnetic diffraction in such notable transition metal oxides as the high T_C cuprates and colossal magnetoresistance manganites.

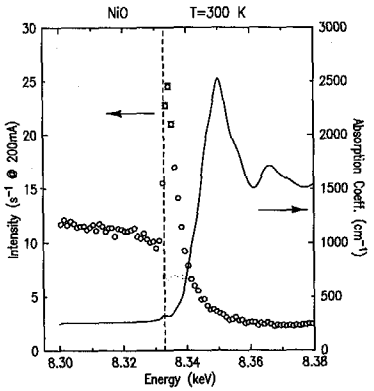


Figure 1.

High-Resolution XAS Investigations of MnO_2 Spinel-Based Li^+ Intercalation Battery Systems	X25

C.R. Horne, E.J. Cairns (LBNL/UC, Berkeley), M.M. Grush and S.P. Cramer (LBNL/UC, Davis)

The purpose of this research is to develop a thorough atomic and electronic understanding of the intersertion process for Li^+ in $Li_xMn_2O_4$ and derivative manganese oxides in order to improve the Li storage capability and/or insertion rate of high-performance, rechargeable Li cells. $Li_xMn_2O_4$-based compounds are desirable positive electrodes for Li cells as they possesses high potential vs, Li/Li^+, low toxicity, and are relatively low cost. To achieve the goals, we are applying synchrotron radiation X-ray techniques. The Li^+ intsertion reaction for $Li_xMn_2O_4$ occurs over two voltage regions depending on x, the level of Lil. $Li_{0.0}Mn_2O_4$ + x Li^+ + xe-↔ $Li_xMn_2O_4$.

For $0 \leq x < 1$, the cell discharges at 4V while for 1 x 1.8, the discharge occurs on a 3V plateau. As Li^+ inserts, the Mn(IV) species are reduced to Mn(III). X-ray diffraction experiments have shown that for $x > 1$, the cubic spinel lattice distorts into a tetragonal structure with c/a = 1.16 through a cooperative Jahn-Teller distortion due to the Mn reduction[1,2]. Initial experiments at NSLS Beamline X-25 involved measuring the XANES for a series of $Li_xMn_2O_4$ battery electrodes discharged to values of x = 0.0 to 2.2 at intervals of 0.2. The cells were discharged slowly and allowed to equilibrate before the $Li_xMn_2O_4$-containing positive electrode was removed. The transmission spectra for each electrode are shown below. Upon examination of the spectra, several features stand out. Within the 4V plateau a slight difference in the edge is noticed for $x > 0.6$ which coincides with a small drop in cell voltage within the 4V plateau. For the 3V plateau an inflection in the edge becomes prominent which is indicative of distorted Mn-O octahedra,in agreement with XRD results in the literature[2].

Between x = 1.4 and x = 1.6 the tetragonal distortion increases to the degree that the XANES resembles that of a square planar structure as the axial oxygen ligands move away from the MnO_4 plane lowering the $1s \rightarrow 4p_z$ transition energy versus transitions to the co-planar Mn $4p_x$ and $4p_y$ orbitals. Additionally, there is a higher frequency component appearing at approximately 7 eV above the main peak and the pre-edge region changes in the spectra of $x \geq 1.6$ samples. References: 1. M.M. Thackeray, W.I.F. David, P.G. Bruce, and J.B.Goodenough, Mat. Res. Bull., 18, 461-472 (1983). 2. T. Ohzuku, M. Kitawaga, and T. Hirai, J. Electrochem. Soc., 137, 769-775 (1990).

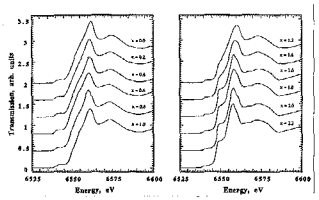


Figure 1. XANES of $Li_xMn_2O_4$ for: LH - $x \leq 1.0$, RH- $x > 1.0$.

Crystallographic Studies of Cell Signaling and DNA Replication | X25

J. Kuriyan (Rockefeller U. & HHMI)

Structure of the C-terminal region of p21WAF1/CIP1 complexed with human PCNA:

The arrest of DNA replication in response to the detection of DNA damage is a fundamental mechanism by which the cell minimizes the potential transmission of lethal mutations. One mediator of this response is the protein p21WAF1/CIP1 (hereafter referred to as p21), an inhibitor of the cyclin dependent protein kinases (cdks) that control the initiation of the S phase of the cell cycle and concomitant DNA replication. An elevation of nuclear levels of the tumor suppresser protein p53 occurs upon detection of DNA damage. This stimulates transcription of p21 as part of a p53 signaling pathway in which the cessation of DNA replication is coupled to stalling of cellular mitosis.

p21 is a member of a family of cdk inhibitory proteins, including p27Kip1 , p57Kip2 and p27XIC1 that share sequence similarity in their N- terminal regions. These highly conserved regions are by themselves sufficient to inhibit cyclin-cdks that function at major transition points in the cell cycle. p21 is also able to directly inhibit DNA replication by binding tightly to and blocking the action of the DNA polymerase processivity factor PCNA (proliferating cell nuclear antigen). PCNA is a DNA tracking protein that is required for the rapid and processive replication of DNA by the polymerases d and e because it forms a sliding clamp that tethers the polymerase to DNA during strand synthesis. The C-terminal region of p21WAF1/CIP1 is distinct from that in p27Kip1 and p57Kip2, and contains a PCNA-binding sequence. The overexpression in mammalian cells of C-terminal fragments containing this region is sufficient to arrest DNA replication. The PCNA-binding functionality of p21 appears to reside entirely in the C-terminal 22 residues of the protein, which also suffice to block PCNA-mediated DNA replication directly. A peptide corresponding to these 22 residues binds to human PCNA with high affinity, comparable to that of the intact p21 protein (Kd 2.5 nM, as measured by biosensor analysis), and efficiently inhibits DNA synthesis in vitro.

Using data measured at beamline X25, we have determined the crystal structure of human PCNA complexed with a peptide corresponding to the 22 C-terminal residues of p21, determined at a resolution of 2.6 Angstroms.. p21 binds to PCNA in a 1:1 stoichiometry, with an extensive array of interactions that include the formation of a b sheet with the inter-domain connector loop of PCNA. An intact trimeric ring is maintained in the structure of the p21- PCNA complex, with a central hole available for DNA interaction. The ability of p21 to inhibit the action of PCNA is therefore likely to be due its masking of elements on PCNA that are required for the binding of other components of the polymerase assembly.

The p21-PCNA interface has the hallmarks of a tight and specific molecular interaction, and by its ability to block DNA replication it maps regions of the PCNA surface that are likely to be important for polymerase attachment. These regions on PCNA are also potential targets for the design of small molecule analogs that might mimic the action of the p21 peptide.

Multiple Energy Speckle in Reflectivity From Si(111) Wafers | X25

J. L. Libbert, J. A. Pitney and I. K. Robinson (U. of Illinois, Urbana-Champaign)

When a coherent x-ray beam is reflected from a rough surface the intensity distribution on a screen far away from the surface exhibits a granular structure commonly referred to as "speckle." This speckle pattern arises from random phase shifts across the coherent wave front due to reflection from differing heights on the rough surface. The speckle pattern can be thought of as Fraunhofer diffraction from an aperture illuminated by a wave with unit amplitude but with a randomly varying phase. The phases are proportional to q_z and the height of the suraface relative to some arbitrary zero height. Thus, if one could recover the phases from the speckle pattern, the morphology of the illuminated region of sample would be known. It may be possible to recover the phases up to additions of multiples of 2π. Removing this ambiguity from the phases could be accomplished by taking a second speckle pattern of the same region but with slightly different phase contrast. In an attempt to recreate the surface morphology of a Si (111) wafer over a length scale of several hundred microns we have measured the speckle patterns of the same region of the sample at several different energies. The multiple energies gives us a phase contrast mechanism that should allow the unambiguous determination of the phases. Figure 1 shows a series of scans across the reflected beam from a Si (111) wafer illuminated at grazing incidence by a 5μm diameter coherent x-ray beam. The same region of the sample is being illuminated in each scan while the x-ray energy is changed. The differences arise from the enhanced sensitivity to surface roughness at higher q_z. The scans were taken by scanning a 24μm pinhole across the reflected beam in the 2θ direction at a distance of 1.25m from the sample.

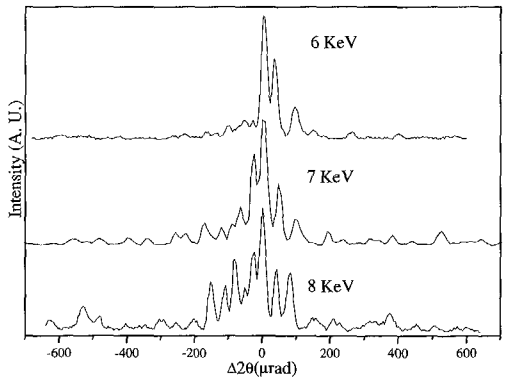


Figure 1. Speckle patterns in the reflected beam from a Si (111) wafer. The same region of the sample is illuminated in all three scans but the x-ray energy is varied.

X-ray Studies of Liquid Metal Surfaces: Oxidation and Alloy Surfaces | X25

M.J. Regan, H. Tostmann, P.S. Pershan (Harvard U.), O.M. Magnussen, E. DiMasi, B.M. Ocko (BNL), M. Deutsch (Bar-Ilan U., Israel)

We have studied the oxidation of liquid Ga surfaces and the effect of alloying on the surface structure by x-ray reflectivity (XR). By exposing liquid Ga at room temperature to O_2 doses as small as 180 Langmuirs (L), well-defined oscillations in the XR are observed (Fig. 1), indicating the formation of a 5 Å thick oxide film. The oxide thickness and roughness do not change with dosage up to 1600 L nor with temperature up to 300 °C [1]. This is in contrast to bare liquid Ga, which is already roughened significantly at 170 °C [2]. This is a good indication that the oxide layer provides rigidity to the liquid surface and is likely a solid; grazing-incidence diffraction measurements indicate that the film is amorphous or poorly crystallized. Results on a liquid Ga-In alloy at the eutectic composition show a clear enrichment of In at the topmost surface layer, expected from the Gibbs adsorption rule due to the smaller surface tension of In. The 25% increase of the XR over the Fresnel, observed in Fig. 2b for $0.7Å^{-1} < q_z < 1.8Å^{-1}$, is a clear sign of surface enrichment by a layer of electron density higher (i.e. In) than the bulk (Ga-In). Model fits assign the enrichment to a single In layer, with subsequent layers at the bulk eutectic composition (Fig. 2b). This work has been supported by grants from the DOE, DE-FG02-88-ER45379 and DE-AC02-76-CH00016, and the NSF, DMR-94-00396 and DMR-91-13782. [1] M.J. Regan *et al.*, submitted to *Phys. Rev. B* (1996). [2] M.J. Regan *et al.*, *Phys. Rev. B* **54**, 9730 (1996).

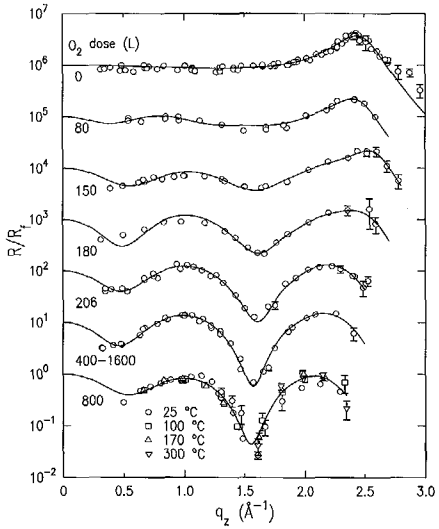


Figure 1. Fresnel-normalized reflectivities of liquid Ga surfaces *vs.* O_2 dosage.

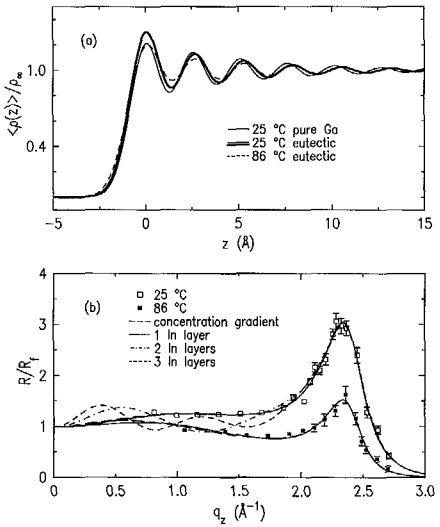


Figure 2. Fitted density profiles (a) and Fresnel-normalized reflectivity curves (b) for the liquid Ga-In eutectic alloy.

Structure and Kinetics of the Sliding Q_1 CDW in $NbSe_3$ * | X20A, X25

K.L. Ringland, S.G. Lemay, R.E. Thorne, and J.D. Brock (Cornell U.)

We have performed detailed measurements of both the structure of the sliding Q_1 charge-density wave (CDW) and the kinetics of its relaxation from the sliding to the pinned state. High q-resolution data obtained at X25 demonstrate unambiguously that the equal time phase-phase correlation function does not decay algebraically at large distances. That is,

$$\lim_{|\vec{r}-\vec{r}'|\to\infty} \langle e^{i\phi(\vec{r})} e^{-i\phi(\vec{r}')} \rangle \neq \frac{1}{|\vec{r}-\vec{r}'|^{\eta}} .$$

The detailed structure of the sliding state is still a major issue and recent models have predicted an assymptotic algebraic decay of the phase-phase correlation function[‡]. An algebraic decay produces a line-shape that traces out the resolution function near the center of the peak but has additional scattering in the wings. In contrast, we measure the full width at half maximum of the Q_1 satellite in the sliding state to be roughly 66% broader at 10× threshold than the same satellite in the pinned state. (The Q_1 satellite in the pinned state is also broader than our resolution.)

Similarly, our time resolved measurements of the relaxation of the Q_1 CDW from the sliding to the pinned state also contradict the predictions of the suggested equations of motion. Specifically, the peak intensity increases monotonically with time after the current is switched off. The solution to the proposed equation of motion has the form

$$\langle |\phi(\vec{q},t)|^2 \rangle = \langle |\phi(\vec{q},0)|^2 \rangle e^{-2q^2Dt} + \frac{\langle |F(\vec{q})|^2 \rangle}{D^2q^4} (1 - e^{-q^2Dt})^2$$

where $F(\vec{q})$ is the quenched random field and D is the diffusivity. This expression has a "dip" in the intensity. Our data does not exhibit such a dip. This discrepancy implies that either a non-linear term is missing from the equation of motion or that the random field, $F(\vec{q})$, is not quenched.

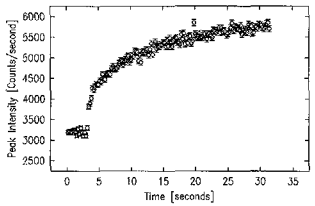


Figure 1. Peak intensity of (0 1+Q_1 0) satellite as a function of time. Current is turned off at t = 3 seconds.

* This work was supported by NSF Grant No. DMR-9501119

Characterization of the Magnetic Disorder at the (001) Surface of UO_2	X22C, X25

G.M. Watson, D. Gibbs (BNL, Physics), L.E. Berman (NSLS), G.H. Lander, H. Matzke (EITU), W. Ellis (LANL), and B.D. Gaulin (McMaster U.)

In our earlier work, we showed that the temperature-dependence of the scattering along a (110)-type magnetic truncation rod of a UO_2(001) surface appeared to vanish continuously as the temperature is raised to the bulk Néel temperature, T_N = 30.2 K.[1] This is suprising since the bulk transition, as observed by neutron and x-ray scattering, is discontinuous.[2] This behavior may be understood as an example of surface induced disorder wherein magnetic disorder propagates from the near surface volume into the bulk as the temperature approaches T_N. In order to further characterize this behavior, we have performed measurements of the four equilavent (110)-type magnetic truncation rods and of the specular magnetic reflectivity. Rod intensities were obtained both as a function of temperature at fixed wavevector and as a function of momentum transfer at a number of temperatures. The magnetic specular reflectivity shown in Fig. 1 is especially sensitive to the decay of the magnetic order parameter profile along the surface normal direction. At the higher temperatures, the reflectivity away from the bulk Bragg reflection falls off faster than it does at lower temperartures. This indicates that the width of the magnetic profile increases with temperature. In fact, our data seem to suggest that this width diverges as T approaches T_N.

[1] G.M. Watson, *et al.*, Physica B **221**, 405 (1996); *ibid.* Phys. Rev. Lett. **77**, 751 (1996).

[2] B.C. Frazer *et al.*, Phys. Rev **140**, A1448 (1965); B.M.T. Willis and R.I. Taylor, Phys. Rev. Lett **17**, 188 (1965); G.M. Watson *et al.*, Phys. Rev. B **53**, 686 (1996).

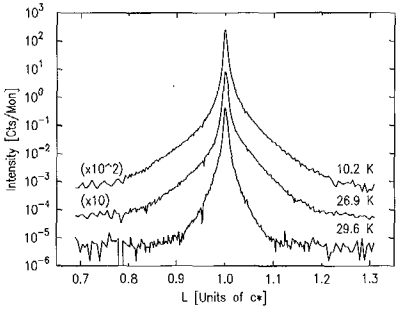


Figure 1. Specular magnetic reflectivity profiles near the (001) bulk magnetic Bragg reflection obtained at 10.2, 26.9, 29.6 K utlizing a Au(111) reflection for a polarization analyzer. Peak count rates at beam line X25 were approximately 5x10^5 cps at a beam current of 200 mAmp.

Structure Determination of the Entire Extracellular Portion of Human CD4	X25, X4A

H. Wu, P.D. Kwong and W.A. Hendrickson (Columbia U.)

Diffraction data from two different selenomethionyl CD4 crystals were collected at the selenium K-shell edge at beamlines X4A and X25 of NSLS. CD4 crystals were extremely weak which mandate high flux synchrotron radiation. Both data sets were recorded with Fuji imaging plates at 100K. These two data sets belong to space groups P41(2)22 and P2, respectively and were used to obtain molecular replacement solutions. Selenium anomalous difference Fouriers were used to confirm the correctness of the structures.

Two Beam Diffraction Interference Method for 2D Crystallography | X25

Y. Yacoby (Hebrew U.), H. Baltes, R. Pindak, L. Pfeiffer (Lucent Technologies), R. Clarke (U. of Michigan), and L. Berman (NSLS)

The two beam diffraction interference method [1] provides the amplitude and phase of the Fourier transform of the X-ray dielectric function of 2D crystals allowing a direct determination of their structure. This method was tested using an aperiodic GaAs/AlAs multilayer epitaxially grown on [110] cleaved GaAs. After exposure to air, a 1000Å gold film was evaporated on several samples. The X-ray beam entered the samples as shown in Fig.1 and the diffracted beams (d) were observed from the top. In the samples with the gold, the incident beam was reflected and the reflected beam was also diffracted. The main objective of the experiments was to establish if these two diffracted beams interfere and to obtain the phase information.

We measured the intensity of the diffracted beams as a function of position along 4 distinct Bragg rods for samples with and without the gold film and for different angles of incidence, α. In samples without the gold film, and hence no reflected beam, it was confirmed that the intensity of the diffracted beams is independent of α. One spectrum along the [h,h,1] Bragg rod is shown in Fig.2. The calculated spectrum, assuming the nominal epitaxial growth structure but with 5 amorphous, oxided, capping layers and with a roughness of ± 2 layers, is also shown (solid line). When the gold film is present the intensities depend on α (solid circles in Fig.2). The intensities were calculated both assuming that the diffracted beams coherently interfere (solid line in Fig.2) and without interference (dotted line). It is evident that interference must be included. Using the measured intensity spectra of samples with and without the gold layer the differential phase, $\cos(\theta_1 - \theta_2 - \phi)$, was calculated along each Bragg rod. An example for [h,h,1] is shown as solid circles in Fig.1. Here, ϕ is the phase difference between the incident and reflected beams and θ_1 and θ_2 are the phases of the X-ray dielectric Fourier transform function at pairs of points separated by $\Delta q_z = 2ksin(\alpha)$. We calculated the same function using the structural parameters described above. The result (solid line in Fig.1) is in fair agreement with the experimental determination proving that the pairs of diffracted beams are coherent and interfere with each other providing phase information.

[1] Y. Yacoby, Solid State Communications, **91**, 529 (1994).

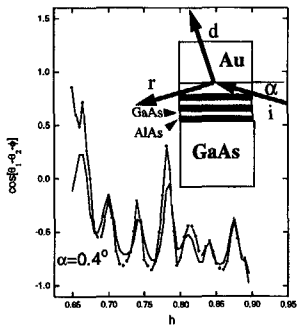


Figure 1.

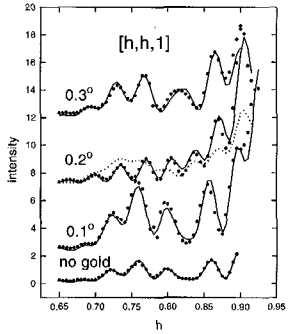


Figure 2.

The Structure of Calicivirus | X12, X25

L. Zhou and M. Luo (U. of Alabama at Birmingham)

Introduction: The recent rapid spread of a rabbit calicivirus through Australia to Europe demonstrated a potentially dangerous situation if a human calicivirus emerges. It is estimated that at least 42% of outbreaks of nonbacterial gastroenteritis in the U.S. are caused by this group of viruses [1]. The main difficulty in dealing with infections of small round-structured viruses (SRSV's) is the large diversity of the viral capsid protein [2].

Experimental: We have purified and crystallized FCV strain F9 and a large amount (50% complete) of X-ray diffraction data to 3.0Å resolution have been collected at synchrotron stations [3]. The space group of the crystal is C222, a=889Å, b=996Å, c=436Å. A total of 226 images afforded 1,396,078 reflections, which is about 40% complete to 3.5Å resolution. There are two independent particles in the unit cell, one sits on the *a* axis, the other on the *b* axis. Each of the particles is rotated by less than 2° from the ideal orientation. Model coordinates have been constructed based on the cryo-EM structure. The high resolution structure determination is well under way by using the molecular replacement density averaging-phase extension method. Although there were no improvement this time on the quality of the diffraction data collected at NSLS, we expect to collect better data in the future by use of the cryo-freezing technique.

Discussion: Caliciviruses resemble the picornaviruses with which they were originally classified. Like the picornaviruses, the genomes of calicivirus bear a covalently attached protein (VPg) at the 5′ end, and there is no cap structure at the 5′ end of the subgenomic mRNA. However, caliciviruses differ from members of the picornavirus group in that RNA species smaller than the genomic RNA are synthesized intracellularly. A striking difference between caliciviruses and picornaviruses was found in their genome organization. The genomic RNA of picornaviruses encodes a single polyprotein which is co- and post-translationally processed to yield the mature viral proteins. No single large polyprotein precursor to all the viral proteins is known for calicivirus. The genes encoding for the structural polypetides are located near the 3′ end of the genomic RNA.

In our studies a feline calicivirus strain F9 was used for the X-ray structure determination. The comparative sequence analysis of capsid precursor proteins from FCV strains F9 and CFI/68 FIV demonstrated that variation was concentrated in two areas.

Reference: Kaplan, J.E., R. Feldman, D.S. Campbell, C. Lookabaugh and G.W. Gary (1982), The frequency of a Norwalk-like pattern of illness in outbreaks of acute gastroenteritis. Am. J. Public Health 72:1329-1332.

Wang, J., X. Jiang, H.P. Madore, J. Bray, U. Desselberger, T. Ando, Y. Seto, I. Oishi, J.F. Lew, K.Y. Green and M.K. Estes, 1994. Sequence diversity of small, round-structured viruses in the Norwalk virus group. J. Virol. 68:5982-5990.

Zhou, L. and Luo, M. "Preliminary Analysis of Feline Calicivirus Crystals", Acta Crystallogr. D51:850-852, (1995).

Tissue Localization of Metals Bioaccumulated in Marine Organisms Living in Sediments * — X26A

W. J. Berry, D. J. Borsay (US Env. Prot. Agency), and K. W. Jones (BNL - DAS)

The sediments of many of the rivers, lakes, and estuaries of the United States are contaminated with toxic metals and other compounds from municipal and industrial sources. Physiological effects on test organisms caused by metals in sediments cannot be understood from dry weight metals concentrations alone. This understanding requires the knowledge of which phases in the sediment are controlling bioavailability. Much work has already been done on the factors controlling the bioavailability of cadmium, copper, lead, nickel, and zinc, and mixtures of these metals. The results of this work indicate that the ratio of acid volatile sulfide (AVS) and simultaneously extracted metal (SEM: the metal measured in the extract from the AVS procedure) can be used to predict the acute and chronic toxicity of metals in sediments. Sediments in which the ratio of SEM/AVS is < 1.0 are not toxic, while sediments with SEM/AVS ratios greater than 1.0 may be toxic. This phenomenon is related to the capacity of sulfide to bind divalent metal when SEM/AVS is $<$ 1.0, such that the metal will not be bioavailable. Several bioaccumulation studies have been done in which test organisms have accumulated metals from sediments with SEM/AVS ratios of $<$ one. This is not what would be predicted by the theory, and as a result, we are interested in finding out where in the organism the metals are bioaccumulated. If the metal accumulated in these sediments with SEM/AVS ratios < 1.0 is primarily adsorbed on the surface epithelium of the organism or a component of sediment incompletely purged from the gut, and not incorporated into the tissues, this would help to confirm our theories about bioavailability in these sediments. If the metal is accumulated in the tissues themselves, this may force us to reconsider some of our hypotheses. It is difficult to get adequate samples for chemical analysis of individual tissues from these test organisms, because they are typically quite small. Synchrotron-radiation induced x-ray emission (SRIXE) is a tool that can localize sites of metals accumulation with both good spatial resolution and sensitivity, a task which is difficult using other methods. As a first step we exposed a typical marine bioaccumulation test organism, the clam worm, Nereis virens, to a mixture of cadmium and nickel in a water-only test to evaluate the usefulness of SRIXE in localizing metal accumulation in this species. Clam worms were exposed to a mixture of 1,250 g/L nickel and 500 g/L cadmium in filtered seawater for 7 days in individual glass beakers. Exposures were conducted in the dark at 15 C. Tissues were embedded in paraffin and sectioned at 10 m and mounted on 7.6 m thick polyimide film. Data were accumulated for Ca, Fe, Ni, and Zn. Cd could be observed, but the intensity was too low for measurements to be made in scan mode. Ca, Fe, Ni, and Zn were found in the epithelium, as well as in muscle, nerve, and gut tissues, as might be expected from a water-only exposure. The results obtained show that SRIXE is suitable for these investigations and that further testing using metals-spiked sediments can be performed. In this next phase, worms exposed to a series of sediments spiked with various levels of SEM/AVS will be examined to pinpoint the location of bioaccumulated metal, especially in those worms exposed to sediments with SEM/AVS < 1.0.

* Research suppported in part by US DOE Contract No. DE-AC02-76CH00016.

Lead in Tadpole Brain * — X26A

H. T. Cline (Cold Spring Harbor Laboratory), S. Witte (U. of Iowa), and Keith Jones (BNL - DAS)

Many studies both in humans and animals have established the deleterious effects of lead on the developing brain. There have also been a number of animal studies. For example, Lindh et al. [1] measured the microscopic distribution of lead in the cerebellum of suckling rats using micro-proton-induced x-ray emission (PIXE). They measured lead concentrations in white matter and the granular, Purkinje, and molecular layers and found values of about 20 5g/g dry weight. The concentrations were high enough to permit a detailed mapping of the lead distribution with the microprobe. Cline et al. [2] have investigated the effects of much lower lead concentrations on the neuronal growth in the retinotectal system of frog tadpoles. In this experiment, the concentrations of lead are so low that making maps of the lead distribution was not easily practicable. However, their work showed changes in the histology of the retinal ganglion cell axon arborizations that was a function of the magnitude of the lead dose. Further, they found that treatment with the chelating agent, 2,3 dimercaptosuccinic acid (DMSA) helped to reverse the damage caused by lead. A direct measurement of the lead concentration in the optic tectum was desired to directly verify the presence of lead in the region of study. The amount of material available for analysis precluded determinations using techniques such as atomic absorption spectroscopy (AAS). It was anticipated from the nanomolar doses administered to the test animals that it would be feasible to make the determination with SRIXE albeit with some difficulty. Samples were prepared by making 1 5m microtomed sections from 10 different animals that had been exposed to lead and 10 that had not been. The sections were mounted on 7.6 5m polyimide film for SRIXE analysis. The measurements were carried out blind. Each section was measured for varying times of about 5500 s with an 8 5m 8 5m size beam. The estimated concentrations found were about 200 and 100 parts per billion (ppb) dry weight. Estimates of the ratios between the two sets of specimens were made by considering the Pb/Zn ratio so that dependence on specimen thickness was removed. The results confirmed the presence of lead in the optic tectum. In retrospect, the precision of the measurement could have been improved by the use of thicker sections and a larger beam size. Making a detailed map of the lead distribution probably awaits, however, the use of an undulator at a third generation synchrotron source such as the Argonne Advanced Photon Source (APS) or the European Synchrotron Radiation Facility (ESRF). The results of the work demonstrate, in any case, the way in which SRIXE can be applied to the determination of a very small number of atoms in a small sample volume. [1] U. Lindh, N. G. Conradi, and P. Sourander. Acta Neuropathol. 79, 149 (1989). [2] Cline, H. T., Witte, S., and Jones, K. W. Proc. Nat. Acad. Sci. USA 93, 9915-20 (1996).

* Research supported in part by US DOE Contract No. DE-AC02-76CH00016.

Distribution of Catalysts in Polyolefin Polymerization Particles * | X26A

W. C. Conner, Jr. (U. of Massachusetts) and K. W. Jones (BNL - DAS)

Supported catalysts of various types play a major role in petroleum refining and in the manufacture of various type of polymers. Measurements on several types of catalysts have been made at the NSLS X26 beam lines using SRIXE and computed microtomography (CMT) as complementary techniques. The methods have been applied to the study of polyolefin polymerization particles, fluid catalytic cracking (FCC) catalysts, and hydrotreating catalysts with most of the effort devoted to examination of the polymerization particles. Two types of supported catalysts used in production of polyolefin polymerization particles were studied: silica-supported Cr and Ti-supported MgCl2. They are ideal for study using CMT. X-ray CMT is normally based on the contrast provided by differences in the linear x-ray absorption coefficients of materials in the path of the beam. Both catalysts and supports are much more highly absorbing than the polymer material. Fragments of the initial catalyst particle are thus readily detected and their positions within the growing polymer particles are determined. CMT has proved to be a unique, powerful technique to study the catalyst/polymer agglomerate in situ (3- m pixel size). This information provided the first detailed picture of the changes in this complex industrial process as a function of the amount of polymer produced. Initial studies showed that, for certain commercial catalysts, the catalyst fragments were convected toward the periphery of the catalyst/polymer particle during the initial stages. This has many ramifications as to the heat and mass transfer during the beginning of the polymerization process. This knowledge has already been employed in the design of new catalysts and the control of current polyolefin processes. As the polymerization proceeds, the catalyst fragments become too small to be readily detected by CMT. We used SRIXE (10 m beam size) to analyze the distribution of catalyst fragments for higher yields. Thin sections of the polymer were cut using a microtome. Two-dimensional maps of the concentrations of the catalysts and supports could then be made. The map was obtained using 17- m and 33- m steps in the two-dimensions in a 40 12 matrix. Interestingly, this clearly shows the location of large catalyst fragments, as seen in the tomographic sections, but, in addition, a uniform distribution of the catalyst was found over the entire area of the polymerization particle giving evidence of smaller catalyst fragments. The results suggest the possibility of following the overall process of fragmentation in much more detail than has been possible in the past. These analyses are crucial to understand not only the progress of polymerization at higher yields, but, more significantly, the recently developed (and developing) commercial processes involving sequential polymerizations. In these processes the product polymer/catalyst from a first reactor ise sent to a second reactor where a second polymerization is run producing a polymer of different composition. In this manner, a micro-mixed composite polymer is produced. The same catalyst catalyzes both processes; although, different monomer compositions, activators and modifiers are present in the second reactor. It is crucial to understand the catalyst fragment distribution coming from the first reactor in order to understand the polymerization process in the second reactor, including the mass and energy transport throughout the growing catalyst/polymer particle. Many co-polymerization processes are being developed based on this sequential polymerization approach.

* Research supported in part by US DOE Contract No. DE-AC02-76CH00016.

Chemical Compositions of "Cluster" Interplanetary Dust Particles | X26A

G. J. Flynn (SUNY Plattsburgh), S.R. Sutton (The U. of Chicago), and S. Bajt (LLNL)

Interplanetary dust particles (IDPs) are collected from the Earth's stratosphere by impact onto a rigid collection surface, covered with a thin layer of silicone oil, carried by a high-speed aircraft. IDPs are separated into two types, based crudely on structural strength: 1) those which remain intact, and, 2) those which fragment on collection (called "cluster particles") which are recognized by a high concentration of fragments in a small region on the collector surface.

Messenger et al. [1] reported that deuterium enrichments in cluster particles are "larger, more common, and have higher variability than previously measured IDPs." We undertook a chemical comparison between cluster particles and IDPs collected intact. Fragments from 8 different clusters were analyzed using the X-ray Fluorescence Microprobe at X26A. One fragment showed significant depletions in Zn ($<$0.01xCI), Ge, and S, compared to the abundances in primitive CI-type meteorites. This pattern was previously observed in IDPs which experienced severe atmospheric entry heating [2]. Two fragments showed smaller Zn depletions (0.2 to 0.4xCI), suggesting less severe heating. The other 5 fragments have Zn contents $\geq$CI, suggesting they experienced comparatively little entry heating, and little thermal alteration of their chemistry.

The five cluster fragments which show no evidence of severe atmospheric entry heating each have contents of the volatile elements Cl, Cu, Zn, Ga, Ge, Se, and Br which exceed CI-type meteorite concentrations, and S which is near or exceeds CI. The average pre-atmospheric content of elements having nebular condensation temperatures lower than Mn is enriched relative to CI by factors of 2 to 6 for Cu, Zn, Ga, Ge, and Se, and by a much larger factor for Br in these cluster fragments. This equals or exceeds the average concentrations of these elements previously measured in small ($\sim$10 microns) IDPs collected from the Earth's stratosphere [3]. Sulfur, usually present at $\sim$CI level in smaller IDPs [3], averages 1.4xCI in these 5 fragments. These cluster fragments have substantially higher concentrations of the elements having low nebular condensation temperatures than we measured in large ($>$35 micron) IDPs collected intact [4], suggesting a correlation between structural strength and chemical composition, with the weakest particles being the most volatile rich.

1) Messenger, S. et al. (1996) Lunar Planet. Sci. XXVII, 867-868.
2) Flynn, G. J. et al. (1993) Lunar Planet. Sci. XXIV, 497-498.
3) Flynn, G.J. et al. (1996) "The Abundance Pattern of Elements...", ASP Conference Series, Vol. 140, ASP Press, 291-294.
4) Flynn, G.J. et al. (1995) Meteoritics, 30, 505.

Spatial Distribution of Lead in Chick Tibia * | X26A

C. S. Fullmer (Cornell U.) and K. W. Jones (BNL - DAS)

Lead in bone is of interest for several reasons. From the practical standpoint, the in-vivo measurement of lead in bone has been widely used for epidemiological studies and to a lesser extent for clinical diagnostic applications. Nevertheless, the kinetics for the accumulation and desorption of lead in bone are not well understood. On a more fundamental level, lead in bone is of interest for two reasons. First, bone is the largest repository of the body burden of lead which may be mobilized during a number of physiological and pathological conditions such as endocrine status, osteoporosis, renal disease, certain nutritional challenges, and, in particular, during pregnancy and lactation. Second, it is now known that lead may influence bone development, growth, and function in a variety of ways. Clinical and experimental studies have shown that Pb ingestion may both increase and decrease serum levels of the vitamin D hormone 1,25-dihydroxyvitamin D, thereby altering intestinal Ca absorption and, presumably, parathyroid hormone (PTH) levels. Each of these is critical to normal bone cell function and mineralization. Thus, there is an enormous potential for both direct and indirect Pb-Ca interactions at the cellular and extracellular level, with lead, exerting multiple influences on several biological processes. The purpose of this experiment was twofold. First, to evaluate, histologically, the changes in bone development due to Pb intoxication in normal Ca and Ca-deficient animals. Second, to assess the feasibility of synchrotron-radiation induced x-ray emission (SRIXE) analysis of the microdistribution of lead in bone, as well as the changes in Ca distribution which accompany lead intoxication. For these studies, two-week old normal growing chickens were changed to diets either normal or deficient in Ca, each containing either 0 or 0.3% lead, for an additional two weeks. The histological sections showed that Pb ingestion resulted in somewhat diminished metaphyseal cartilage cores, but had no apparent effect on the epiphyseal growth plate or secondary spongiosa. Low Ca chicks, as compared to normal, exhibited a substantially thinner growth plate, as well as thinner and shorter metaphyseal cartilage cores. In chicks ingesting the low Ca diet containing Pb, the growth plate was markedly thicker than normal and the cartilage cores were greatly reduced in width and distal projection. In addition, the primary spongiosa was relatively wide and the secondary spongiosa was poorly defined with few and thin trabeculae. These results indicate that the effects of Pb on bone growth and development are very much dependent on dietary Ca level. However, whether the observed effects are due to direct actions of Pb on bone, indirect effects on calciotropic hormones, or both, remain to be determined. SRIXE was used to produce two-dimensional maps of significant areas of the bones that included both cartilage, trabecular, and compact bone. The maps demonstrate the potential of SRIXE in detailing the tissue distribution of Pb as well as its relationship to Ca distribution. In each case, normal Ca and low Ca, Pb and Ca are similarly distributed in the columns of calcifying cartilage of the primary spongiosa. Especially evident in the low Ca situation is the Pb-associated disruption of new trabecular bone formation (secondary spongiosa) with substantially diminished deposition of both Ca and Pb. These results indicate that Pb and Ca deposition in bone are similar and that disruption of bone growth and mineralization by Pb influences the distribution of both cations.

* Research supported in part by US Department of Energy Contract No. DE-AC02-76CH00016.

Migration and Reduction of Cr(VI) in the Presence of Fe(II) * | X26A

D.B. Hunter, E.J. Gall, P.R. Nuessle and P.M. Bertsch (U. of Georgia)

Contamination of soils and groundwater by Cr(VI) is of increasing concern because of its high mobility in the environment and its toxicity to plants, animals, and humans. Chemical reduction of Cr(VI) by Fe(II) salts can immobilize Cr(III) as insoluble (Fe,Cr) oxyhydroxide phases, thus limiting the possibility of reoxidation and leaching. The conditions under which Cr(III) could be remobilized are dependent upon the solid phase speciation and coassociation of Cr with other soil constituents following implementation of *in situ* reduction technologies. These conditions are influenced by the geochemistry of the system, including mineralogy, solution pH and chemistry, and the presence or absence of natural organic materials. Thus, success of reduction/immobilization of Cr(VI) as an *in situ* remediation technology is dependent on controlling the reduction process to favor the formation of specific mixed (Fe,Cr) oxyhydroxide phases. We have developed a column transport assembly in which Cr(VI) containing ion exchange phases are introduced above various model soil constituents (sand, mixed cationic/anionic exchange resins, etc.) and placed in the x-ray microprobe at X26A to examine the efficacy of various *in situ* remediation technologies based on reduction/immobilization. Solutions containing Fe(II) salts can be injected into these columns at varying flow rates and the resultant transport and reduction of Cr(VI) can be monitored by XRF and XANES under a wide range of solution and substrate chemistries. Figure 1A illustrates the relative spatial distribution of Cr in a typical column after reaction with Fe(II) (data points represent the average of a section 0.3 mm wide by 0.01 mm tall). Cr is localized at the original region of packing approximately 1 mm from top of column, as well as two more localized regions at 4 and 8 mm. XANES measurements at these locations indicate complete reduction of Cr(VI) to Cr(III) inferred by the loss of the sharp pre-edge feature indicative of Cr(VI). Figure 1B shows a typical XANES spectra for oxidized Cr at 1 mm before Fe(II) injection and Figure 1C illustrates reduced Cr at all locations after injection. These results indicate significant migration of Cr down the column despite reduction of Cr(VI) to the relatively insoluble Cr(III) species. These initial experiments are being expanded to investigate additional aspects migration and oxidation state behaviors of Cr(VI) under environmentally relevant and well defined model situations.

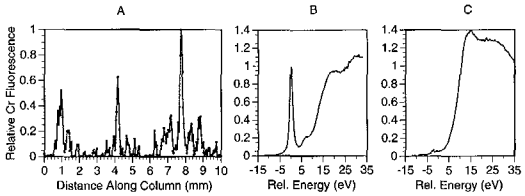


Figure 1.

* This reserch was supported by Financial Assistance Award Number DE-FC09-96SR18546 from the U.S. DOE to the University of Georgia Research Foundation and by ERDA/WSRC subcontract AA46420T

Composition of Dredged Material From The NY/NJ Harbor * | X26A

K. W. Jones (BNL - DAS) and S.-R. Song (BNL and Yale U.)

Shipping activities in the NY-NJ Harbor are threatened by restrictions on dredging of navigational channels and private berthing areas because of concerns about the fate and effects of contaminated sediments caused by ocean disposal of dredged materials. Current proposals for solutions to the problem include the use of confined disposal facilities, borrow pits, land disposal, and various decontamination technologies. While many investigations of the nature of organic and metallic sediment contaminants have been performed, further measurements are needed to understand the transport of contaminants in the sediments at the particle-size scale, to give insight into the efficacy of various decontamination technologies, and to verify the stability of post-treatment end products. The present investigation is based on the use of x-ray beams from the NSLS to investigate samples using synchrotron-induced x-ray emission (SRIXE), x-ray absorption near-edge structure (XANES), and computed microtomography (CMT). The micrometer-scale spatial resolution made possible by the high-intensity synchrotron beams are essential for study of the sediments since a major fraction of dredged sediment particles are less than a few hundred micrometers in diameter. Initial experiments were performed with sediments from Newtown Creek, an estuary that forms a natural boundary between the Boroughs of Brooklyn and Queens in New York City. These sediments are typical of those found across the Harbor and contain elevated levels of toxic organic and metallic compounds. Native sediments were size-fractioned by water washing and sieving and subjected to SRIXE measurement. Metal concentrations were relatively constant for particle sizes up to 1 mm. Hence, simple physical separation of the sediments by size is unlikely to be a useful technique for segregating high- from low-contaminant-bearing particles. Further measurements will be made to determine the variability of the metal concentrations in the bulk samples and for individual grains within each size distribution as well as by different particle types, i.e., clay or quartz. Investigations of the spatial distributions of contaminants were begun by measuring the radial concentrations in spherical concentrations. Preliminary results verify the common assumption that the metals are contained in a surface layer rather than distributed through the entire volume of the particle. Some measurements were also made on particles that had been treated by different decontamination technologies to ascertain their differences. XANES measurements were carried out to determine the quantity of the carcinogenic Cr6+ present relative to the less toxic Cr3+. We plan to explore the feasibility of making combined absorption and fluorescent CMT measurements to determine the structure and composition of individual grains of the sediments before and after processing as well as the particle/pore space relationship.

* Research support in part by US DOE Contract No. DE-AC02-76CH00016 and Section 405 of the Water Resources Devlopment Act of 1992 Agreement No DW89941692 with the US Environmental Protection Agency.

Behavior of Dissolved Molybdenum during Localized Corrosion of Austenitic Stainless Steel | X26A

H.S. Isaacs and S.-M. Huang (BNL-DAS)

An *in situ* study of chemistry of molybdenum during localized corrosion of stainless steel in chloride solutions has been carried using energy dispersive x-ray techniques. An artificial pit was used to maintain a one dimensional diffusion geometry by dissolving back the cross section of strip of Type 316 stainless steel foil mounted in an epoxy resin. A high intensity 8 mm diameter polychromatic x-ray beam at Beamline X26A was scanned across the steel, a salt layer on the steel, and the concentrated dissolution products within the artificial pit. The resulting x-ray fluorescence was analyzed to determine changes in concentration of the constituent alloying elements. It has been found that the salt layer on the steel was formed mainly by iron chloride and all other alloying elements present at relatively lower concentrations than in the steel. Virtually no chromium remained in the salt layer. Also, little molybdenum was present negating proposed corrosion inhibition by a definitive molybdenum forming salt layer. Within the concentrated artificial pit solution it was found that alloying elements dissolved and migrated down a concentration gradient, but closer to the mouth of deep (approx. 2mm) pits, precipitation of molybdenum occurred to a minor extent that did not affect the localized corrosion processes.

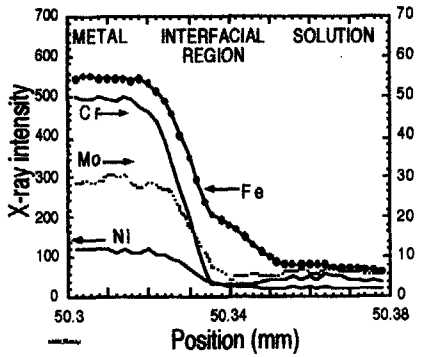


Figure 1. Variations of X-ray Intensity for Fe Cr, Ni and Mo across the steel/solution interface at a potential of 3 Vsce.

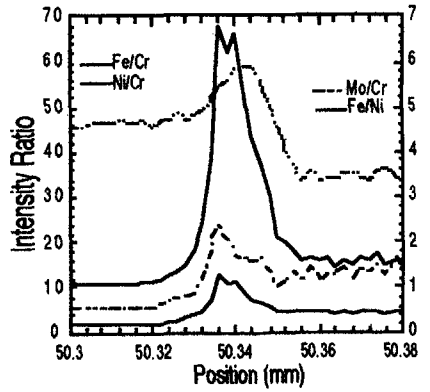


Figure 2. Ratios of the X-ray intensities of elements shown in (a) across the interface.

Synchrotron Radiation in the Study of the Annual Growth Ring of Trees *	X26A

R. R. Martin, T. K. Sham (U. of Western Ontario), and K. W. Jones (BNL - DAS)

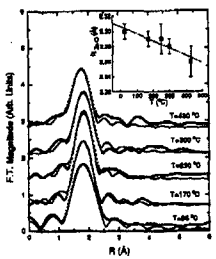
We have carried out a preliminary study of the content and spatial (seasonal) distribution of metals in a tree-ring specimen at the X26C microprobe beamline using the Synchrotron X-ray Fluorescence Analysis (SXRFA) technique. This study was carried out in connection with some other studies (SEM, SIMS) which show that some elements seem to be confined to regions on the order of micrometers in the tree rings. In this study, the x-ray fluorescence results show that the distribution of Ca and K across the tree ring exhibit a close correspondence consistent with conventional wisdom. The perhaps more interesting observation was the distribution of Cr, Co, Fe and Mn. The appearance and disappearance of these elements are incredibly abrupt across a site within approximately 10 microns. This is the first time such an aggregate has been observed in situ by any technique. Based on these results, we are convinced that SXRFA has the desired sensitivity and spatial resolution for the study of metals in tree rings. It will be an exciting new area of research in dendrochemistry.

* Research supported in part by US DOE Contract No. DE-AC02-CH00016.

Structure Studies of Transition Metal Complexes in Fluid Inclusions at Elevated Temperatures	X26A

R. A. Mayanovic (Southwest Missouri State U.), A. J. Anderson (St. Francis Xavier U.-Canada), and S. Bajt (LLNL)

There is a significant lack of understanding concerning the molecular structure of metal complexes in hydrothermal environments leading up to and above supercritical conditions. Fluid inclusions, which are microscopic pockets of fluid (containing ppm concentrations of Zn, Fe, Pb, etc.) trapped in host crystals, are ideally suited for temperature-dependent studies on coordination and structure of metal ions in hydrothermal fluids using XAFS. Temperature dependent Zn and Fe K-edge XAFS spectra were collected in the fluorescence mode from individual fluid inclusions (dia. $\sim$60 μm) in quartz from a pegmatite dyke in the Saxonian Granulite Massif, Germany. Fitting of the Zn K-edge Fourier transform data using FEFF6 (see figure) indicates that the dominant zinc complex in the inclusions at all temperatures ranging from 25°C to 430°C was $ZnCl_4^{2-}$. The Zn-Cl mean-square relative displacement σ^2 increased uniformly with temperature, from a value of 0.0043Å^2 at 25°C to 0.0089Å^2 at 430°C. The clear dominance of $ZnCl_4^{2-}$ in the inclusions at all meaurement temperatures can partly be attributed to the high chloride concentration of the inclusions (est. up to 9 mol/kg). The Zn-Cl bonds of the $ZnCl_4{}^{2-}$ complex were found to exhibit a reduction in length (by nearly 2% at 430°C compared to the value at 25°C) with temperature (see inset figure). We speculate that the contraction of the Zn-Cl bond length is due to either a progressive reduction of the dielectric constant of the liquid phase or due to the $ZnCl_4^{2-}$ complex becoming increasingly more dehydrated with temperature, resulting in stronger Zn-Cl bonding. Preliminary results from fitting of the Fe K-edge data indicate that the iron ion was predominantly hydrated from 25°C to 100 °C and probably somewhat above this temperature. The Fe-O distance was close to 2.10Å with roughly six water molecules in the first hydration shell at both temperatures. At 200°C and above (to 500°C), the iron ion was predominantly coordinated by the chlorine ligands, coinciding with the dissolution of the halite (NaCl), which typically occurs at about $\sim$260°C. The FE K-edge XANES changed progressively with temperature, indicating that the overall nature of the iron chloro complex(es) might have been changing. The average number of chlorine ligands increased uniformly from roughly three at 200°C to four at 500°C. Conversely, the Fe-Cl bond length decreased uniformly from 2.29Å at 200°C to 2.25Å at 500°C.



Stroke and Calcium Concentrations in the Brain *	X26A

G. Newman, S. Trowbridge (SUNY Stony Brook), and K. W. Jones (BNL -DAS)

There are wide reaching disturbances of Ca+2 metabolism under conditions of ischemia. At ischemia onset, there is depolarization of the tissue with release and accumulation of glutamate and K^+ in the extracellular space (ECS). Early depolarization results in a rise of free cytoplasmic Ca+2 due to release of Ca+2 from intracellular stores and influx from ECS. As hypoxia limits ATP generation and acidosis results from the anaerobic glycolysis which accelerates in an effort to compensate, Ca+2 cannot be properly sequestered and concentration gradients in the cell gradually disintegrate. As Ca+2 rises toward 5 5M in the cytoplasm the mitochondria develop membrane pores which permit free movement of all molecules less than 1000 MW. Eventually, ischemic brain undergoes anoxic depolarization with massive release of K^+ into the ECS and entry of Ca+2 into the cell.

The present experiment was designed to test the hypothesis that tissue Ca+2 is regulated independent of extracellular Ca+2 concentration. Brain slices isolated from rat hippocampus were incubated in buffers with a range of Ca+2 concentrations from 4.5 mM to 0.001 mM. Buffer Ca+2 was labeled with 45Ca. A volume of distribution for 45Ca was calculated at each buffer Ca+2 and total tissue Ca+2 can be calculated from that volume. Contrary to expectations, based on the experiments with 45Ca, it appears that the volume of distribution remains nearly constant from 4.5 mM to below 0.5 mM so that tissue Ca+2 is directly related to extracellular Ca+2. Even below 0.5 mM external Ca+2, the rise in the volume of distribution is not very great so that the relationship between tissue and buffer Ca+2 remains very nearly linear. In this experiment, it is assumed that 1) all tissue Ca+2 pools are labeled by 45Ca during the one hour incubation with isotope or at least that 2) the fraction of labeled tissue Ca+2 remains constant at all buffer Ca+2. Either or both of these assumptions may be incorrect. There is need, therefore, to measure tissue Ca+2 independently of radiolabeling by exchange equilibrium and thus determine the fraction of tissue Ca+2 which equilibrates as a function of buffer Ca+2.

The approach we chose was to repeat the slice incubations to create the concentration response curve, but without 45Ca in the buffer and to measure tissue Ca+2synchrotron-radiation induced x-ray emission (SRIXE) which has high-spatial resolution combined with excellent minimum detection levels. Measurements were made on 450 5m thick sections of rat hippocampus for buffer concentrations from 0 to 4.5 mM. The Ca concentrations were normalized to the tissue K concentrations to remove uncertainties arising from variations in tissue thickness.

These experiments suggest that the assumption that 45Ca labels either all or a constant fraction of Ca+2 is not valid. Certainly the results suggest that when buffer Ca+2 is below 1 mM a significant portion of the tissue Ca+2 is not labeled by 45Ca. A rough estimate of the size of the unlabeled Ca+2 pool is about 0.1 mM. Questions surrounding the 45Ca measurements take on greater significance in light of our recent finding that, in brain slices, ischemic injury is accompanied by irreversible uptake of 45Ca in a tissue compartment. The nature of the compartment may hold an important clue for how Ca+2 contributes to irreversible tissue injury in ischemia.

* Research supported in part by US DOE Contract No. DE-AC02-76CH00016 (KWJ); NINDS S28429-01A1 and VA Merit Review (GCN, ST).

Study of Chemical State of Toxic Metals During the Life Cycle of Fly Ash Using X-Ray Absorption Near-Edge Structure *	X26A

J. Osán, B. Török, S. Török (KFKI Atomic Energy Research Institute, Hungary), and K. W. Jones (BNL - DAS)

The non-destructive X-Ray Absorption Near-Edge Structure (XANES) method was applied for the quantitative determination of chromium and arsenic species in coal fly ash. In order to study the chemical state changes caused by deposition and sedimentation of the particles, land fill and river sediment samples obtained in the neighbourhood of power plants were also investigated. The XANES measurements were carried out in fluorescent mode. For achieving quantitative results on the ration of the close lying oxidation state forms, a nonlinear fitting model was developed to process the obtained XANES spectra. The features of the spectra such as the white line, the multiple scattering resonance peak and the absorption edge are modelled with analytical functions. The obtained results show that chromium is present mostly ($> 95\%$) as Cr(III) in fly ash and the chemical state remains the same after deposition and sedimentation. Arsenic is present in pentavalent form in fly ash and land fill samples, while the possible As(III) content of sediment samples is around 40%. To be published in *X-Ray Spectroscopy*

* Research supported in part by US Dept. of Energy Contract No. DE-AC02-76CH00016.

X-ray Fluoresence Imaging of Zinc in *Xenopus* Embryos * | X26A

K. Peariso, D.L. Tierney, C. VanHuis, R. J. Denver, and J. E. Penner-Hahn (U. of Michigan)

Xenopus embryos have been shown to have relatively large amounts of zinc, on the order of 1 mM [1]. Since the embryo develops without the influx of maternal nutrients, the metals it contains at the time of fertilization must supply its needs throughout development. Our initial work has focused on the characterization of spatial changes in zinc that take place during development. Preliminary x-ray fluoresence images (Figures 1 and 2) have been obtained for different stages of development using the NSLS x-ray microprobe at X26A. The 10um x 10um spot size offers the resolution necessary to observe localization trends of the zinc in the embryos at various stages during their early development. By determining the location of Zn during embryonic development, coupled with information provided by XANES and EXAFS, we may gain insight into the role of zinc in the development of the Xenopus embryo. [1] Montorzi, M., Falchuck,K.H., and Vallee, B.L. (1994)*Biochem. Biophys. Res. Commun.* **200**, 1407-1413.

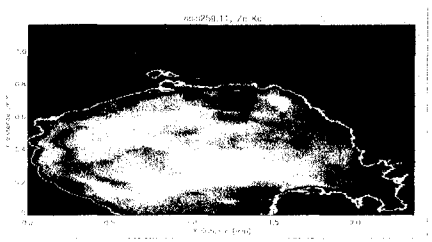


Figure 1. White beam, two-dimensional x-ray fluoresence image of an unfertilized Xenopus oocyte.

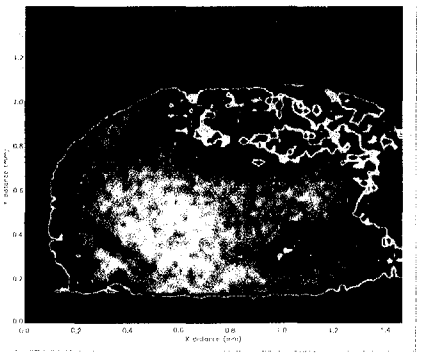


Figure 2. White beam, two-dimensional x-ray fluoresence image of an 8-cell Xenopus embryo.

* Supported in part by the NIH Grant GM-38047

XANES Mapping of Zinc in *Xenopus* Embryos * | X26A

K. Peariso, D. L. Tierney, C. VanHuis, R. J. Denver and J. E. Penner-Hahn (U. of Michigan)

Differences have been observed in the zinc XANES of unfertilized Xenopus oocytes compared to their embryos at various stages of development. Preliminary x-ray fluoresence images have been made using a monochromatic beam on the NSLS microprobe at X-26. The energy selective, two-dimensional images obtained at wavelengths corresponding to the largest deviations in the XANES spectra show distinct differences in their regions of peak fluoresence intensity (Figures 1 and 2). Determining differencesin the fluoresence intensity at specific wavelengths will offer the opportunity to map the location of different types of zinc during various stages of Xenopus embryo development. Characterizing the spatial and temporal changes for different types of zinc will aid our ability to determine the role that different zinc environments play in embryogenesis.

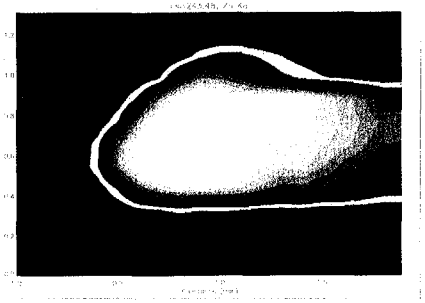


Figure 1. Two-dimensional x-ray fluoresence image of a 16-cell Xenopus embryo at 9665 eV.

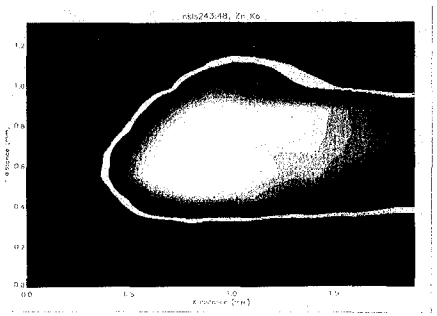


Figure 2. Two-dimensional x-ray fluoresence image of a 16-cell Xenopus embryo at 9693 eV.

* Supported in part by the NIH Grant GM-38047

Spatially Resolved Trace Element Heterogeneities in Apatite Measured via Synchrotron X-ray Fluorescence Microanalysis	X26A

John Rakovan and Richard J. Reeder, (SUNY, Stony Brook)

Apatite, $Ca_5(PO_4)_3(F,OH,Cl)$, is the most abundant naturally occurring phosphate mineral on earth, and the behavior of trace elements in apatite is of considerable significance in geology, materials science, and biology. For example, the presence of Mn and REEs in apatite gives it luminescence properties that are of great utility in both the phosphor and laser industries, and heavy metal sequestering by apatite is important in our understanding of the fate and transport of toxic species in the body. We have conducted extensive studies of trace element distributions in apatite using synchrotron X-ray fluorescence microanalysis (SXRFMA) at the X26A beamline of the National Synchrotron Light Source. These analyses are part of a larger study on the influence of the surface structure of apatite on trace element incorporation during growth. SXRFMA and cathodoluminescence show step specific incorporation of REEs, Y, Sr, and Mn in apatite. Growth steps with orientations [001] and <011> on the face show different affinities for the trace elements studied. In the trivalent REE series La, Ce, and Pr are enriched in regions under the [001] steps (vicinal subsectors), relative to <011> steps. REEs heavier than Pr are depleted in the [001] vicinal subsector, relative to <011> vicinal subsectors. Figure 1 shows the concentration of La and Y for line scans between the [001] and <011> subsectors. This reversal in the distribution trend of the $REEs^{3+}$ suggests that ionic size plays an important role in the differential incorporation. It is proposed that differences in the atomic structure, specifically the characteristics of protosites, between [001] and <011> steps lead to differential incorporation and the observed differential distribution of trace elements (intrasectoral zoning). Atomic scale models of protosites on these steps show coordination differences that are consistent with this proposal (Rakovan and Reeder, 1996). Genetically similar trace element heterogeneities, known as sectoral zoning, have also been found. The observed sectoral zoning of Sm and Nd has been used in a novel manner to determine the age of crystallization for apatites from Llallagua, Bolivia (Rakovan and Reeder, submitted). *Ref*. Rakovan, J., & Reeder, R.J. (1996) Geochimica et Cosmochimica Acta (in press). Rakovan, J., McDaniel, D.K., & Reeder R.J. (submitted) Earth and Planetary Science Letters.

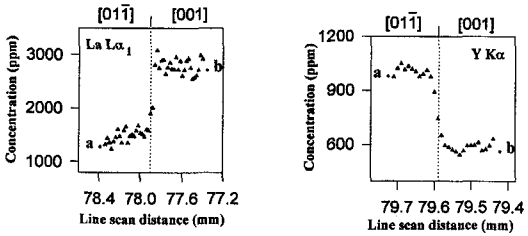


Figure 1.

Selective Uptake of Co and Zn in Surface Sites on Calcite During Growth	X26A

R.J. Reeder (SUNY Stony Brook)

Coprecipitation experiments from aqueous solution at room temperature reveal that Co(II) and Zn(II) exhibit opposite preferences for incorporation among multiple surface sites present on the calcite 1014 face during spiral growth. Polygonized regions that compose the flanks of growth hillocks (so-called vicinal faces) consist of predominantly straight fundamental growth steps whose orientations differ from one vicinal to the next. Metal incorporation sites within the growth steps have been shown to differ in local coordination between nonequivalent steps, resulting in differential incorporation of trace metals during crystal growth.

Synchrotron X-ray fluorescence microanalysis using an EDS detector was used to document the patterns and magnitude of the incorporation differences for divalent Co and Zn. Despite their similar ionic size, Co(II) and Zn(II) exhibit exactly opposite preferences of step-selective incorporation, as shown by SXRFMA traverses across boundaries separating nonequivalent vicinals (Figs. 1 and 2). This observation demonstrates that factors other than size (and charge) govern the uptake and final incorporation of metal ions into nonequivalent surface sites on calcite. Consequently, future attention should be focused on the structural characteristics of surface sites, as well as on the nature of the species and reactions at the growth surface.

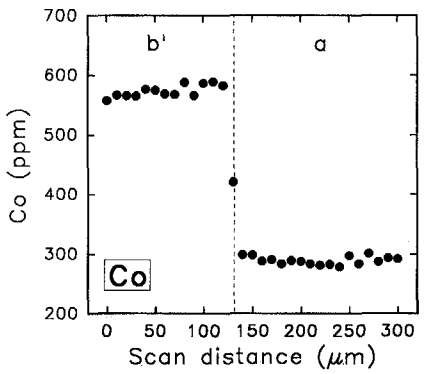


Figure 1. Traverse across a near-surface section of a calcite (1014) face showing the in Co(II) concentration between nonequivalent vicinal faces b' and a, having growth steps with different orientations.

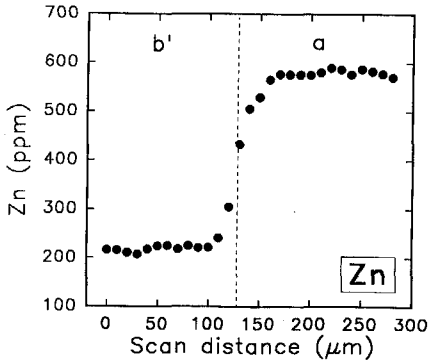


Figure 2. Traverse across a near-surface section of a calcite (1014) face showing the in Zn(II) concentration between nonequivalent vicinal faces b' and a. trend is opposite that for Co(II).

Elemental Microanalysis and Elemental Mapping on Biological Tissues	X26A

R. Rizzo (U. of Trieste, Italy)

Alginate gel beads are used to immobilise cells for a number of fermentation processes. The suitability of the immobilisation technique depends on the microscopical gel strength. For alginate the above property depends on the calcium distribution. In fact, calcium is the gelling-inducing agent in alginate systems. We investigated gel beads as large as 0.7 mm with a resolution of 20 microns. The data obtained showed that calcium is not homogeneously distributed across bead sections exhibiting the highest concentration at the bead surface. This result led to conclude that the gel strength is higher at the bead surface than in the core of the system. Beads obtained in different experimental conditions, such as calcium concentration and ionic strength, are presently under investigation.

A current problem of the radiologists is a precocious diagnosis of arthritis by Magnetic resonance imaging (MRI). This non-invasive technique shows that articular cartilage present a discontinuous laminar appearance due to the presence in the tissue of bound and free water in different proportion. A certain identification and knowledge of the distribution of the cartilage components responsible of the water immobilisation become necessary to establish if a perturbation of their normal distribution can be linked to a variation in the NMR images and to the beginning of the pathological status.

On this line we have compared the distribution of both collagen type II (the principal protein of cartilage), and proteoglycans (a complex of glycosaminoglycans and proteins) with the NMR images of the tissue. Collagen was characterised by histological procedures and by the biochemical determination of the amount of hydroxyproline (a characteristic amino acidic component). Glycosaminoglycans have been characterised by histological examinations, by the content of uronate (a characteristic sugar component) and by SRIXE for their sulphur contents. Evidences have been obtained that while collagen distribution parallels the laminar appearance of MR images, the distribution of proteoglycans is more uniform. The sulphur distribution show that glycosaminoglycans are differently distributed in the habitually loaded and unloaded regions of articular cartilage. It was therefore concluded that the MR images reflect more the water bound to collagen than that bound the proteoglycans.

Elemental analysis of hairs from Egyptian Mummies has been performed using a microbeam in order to investigate only the core of the hairs. The elemental abundance has been compared with modern hairs. Preliminary experiments on the Fe, Zn, and Sr distribution determination have been performed in order to check the suitability of the microscopic x-ray emission analysis for these fossil materials.

Manganese Oxidation: A Characteristic of Susceptibility in the *Pyricularia* - Rice Disease (Rice Blast) System	X26A

D. G. Schulze, D.M. Huber, A.K.M. Shahjahan, M. Levy(Purdue U.), S. Bajt (U. of Chicago), and B. Illman (USDA Forest Products Lab.)

Micro x-ray absorption near edge structure (XANES) spectroscopy documented that manganese was oxidized from the physiologically active Mn^{2+} form to the non-available Mn^{4+} form in necrotic lesions on rice leaves infected by *Pyricularia grisea*, the causal agent of rice blast. Detailed analysis of six isogenic rice cultivars differing in resistance/susceptibility to twelve races of the fungal pathogen demonstrated that manganese oxidation occurred only in compatible (susceptible) combinations of the pathogen and plant. Although manganese was oxidized in the few necrotic cells invaded by the pathogen in hypersensitive type resistant reactions, pathogenesis was restricted to the few cells invaded by the pathogen and there was no chlorosis of tissues surrounding the necrotic cells. Manganese oxidation was not detected in fully resistant reactions, although this may be due to the small size of these lesions relative to the x-ray beam. The concentration of Mn^{2+} in chlorotic tissues surrounding susceptible reactions was lower than observed in adjacent healthy tissue. Similar manganese-oxidation reactions were not observed in mechanically wounded rice tissue, and indicate that the oxidation of manganese in necrotic tissue is pathogen induced and not a result of mechanical disruption of the plant cell by fungal invasion. The fungus is a strong oxidizer of manganese in culture, and the ability to oxidize manganese may be a significant factor determining the virulence of *P. grisea* and susceptibility of the rice plant to disease.

Analysis of Trace Elements: Au in Sulfides and Ni, Zn, Ga, Y and Zr in Garnet	X26A

I.M. Steele (U. of Chicago)

Synchrotron based x-ray fluorescence has the potential for trace element analysis from small samples. In particular we have used this technique for two geologically significant studies. The first involves the concentration and distribution of low levels of gold in sulfides from potential ore bodies. This information is important to determine both the economic viability and benefaction procedures necessary for mining. The second study involves the analysis of indicator minerals whose chemistry may indicate the presence of diamonds either in exploration or at particular mining sites.

Using samples of sulfides bearing rocks from a working mine in Brasil, polished section were made of representative samples. Sulfides were first characterized by electron microprobe and were found to include arsenopyrite, pyhrrotite, and pyrite. Energy dispersive analysis is not possible because all sulfides have significant arsenic which has a intense interference near the gold L-alpha lines. Wavelength scans using the wavelength dispersive spectrometer clearly showed resolution of the Au line albeit on a steep background from As. Using sulfide standards peak and background positions were determined and a detection level based on counting statistics of about 2 ppm was determined. For most applications this level is below the economic level of gold for profitable mining; it does not compare with levels based on SIMS techniques.

Using the test samples, analysis were made for the 3 main sulfides. Gold was detectable in nearly all arsenopyrites, some pyrrhotites, and in no pyrites for all samples. The overall levels of Au correlated with bulk Au analyses but the specific new information was in which phases the Au was concentrated. The Au distribution was not homogeneous; analyses of arsenopyrite from any one sample could show a range of 5 in concentration. Parallel analyses for these same samples for the same grains are being also made at the Geological Survey of Canada. Initial results show a fair correlation between the two techniques. The fair agreement is most likely a function of inhomogeneity and the different spatial volume for analysis. A joint publication is being prepared comparing the techniques and describing the application to the specific geologic problem.

Trial analyses for trace elements in garnet showed that Ni (a geothermometer) can be easily analyzed at the several ppm level with an error of less than 5% based on counting statistics. Ga and Zn are at very low levels but can be detected. Y and Zr present problems as neither can be analyses with the WDS system. The EDS analyses are time consuming and qualitative at best. Major efforts will be made to perfect WDS analyses of all 5 elements. Samples obtained from new kimberlite fields in western Canada are being supplied as the diamond bearing quality has been determined; this will be the major activity in the coming year.

Selenium XANES of Contaminated Soils, Plant Residue, and Algae	X26A

T.K. Tokunaga (LBNL), S.R. Sutton (U. of Chicago), S. Bajt (LLNL), P. Nuessle (U. of Georgia), and G. Shea-McCarthy (U. of Chicago)

Mechanistic understanding of selenium cycling between surface waters, sediments, and organisms requires information on its oxidation state in the various environmental compartments of the cycle. This study, conducted at NSLS beamline X26A, utilizes XANES for determination of Se oxidation states of sediments, decomposing plant residue, and algae. All of these samples were in previously exposed to Se in its most oxidized, water-soluble form, Se(VI). Sediment samples came from Kesterson Reservoir (CA), and from Goose Lake (WY). The Kesterson Reservoir sediment samples were analyzed as (1) a depth profile spanning 10 mm of an intact surface soil crust (i.e., micro-XANES), (2) a homogenized sample, and (3) the separated plant tissue residue fraction (primarily roots of annual grasses). The Goose Lake sediment was analyzed in homogenized form. Algae samples were collected from a seasonal pool at Kesterson Reservoir, and from the San Luis Drain which previously (1981-1986) served as the conveyance structure for delivering seleniferous agricultural drain waters to Kesterson Reservoir. XANES of these environmental samples were compared with those of model compounds Se(0), Se(IV), Se(VI), Se-cystine, and Se-methionine, mixed as dry powders into soil matrices.

All samples contained Se in reduced forms. Absorption edge spectra of these samples indicate that Se occurs as a mixture of Se(0) and organo-Se forms. Contributions due to Se(VI) and Se(IV) were less than 10% of the total Se in each sample. These results are very similar to those obtained at the later stages of an Se reduction, micro-XANES experiment conducted at X26A during the previous year. The outstanding problem of distinguishing Se(0) and various organo-Se forms in these environmental samples will be pursued in upcoming studies. This will include collection of higher-quality spectra on environmental samples, and inclusion of additional Se model compounds. The clear identification of Se(0) versus various organo-Se forms is environmentally important because the elemental form is of relatively much lower toxicity than many of the simple organic forms.

Real-Time Electromigration Strain Measurement on Individual Al Interconnect Lines by White Beam Microdiffraction | X26C

G. S. Cargill III and P.-C. Wang, Columbia University, and I. C. Noyan, E. G. Liniger, C.-K. Hu and K. Y. Lee, IBM Research

A synchrotron-based x-ray microdiffraction system has been developed and used on beamline X26C for the first real-time electromigration related strain measurements with micron scale spatial resolution and strain sensitivity on the order of 2E-4. A tapered glass capillary was used to form a concentrated 10μm diameter white x-ray beam. The samples studied were 10μm-wide, 0.5μm-thick and 200μm-long Al interconnect lines covered with a 1.5μm-thick SiO_2 passivation layer. The electromigration test was performed at 267oC by passing 0.6E6 A/cm^2 current through the Al line for about 69 hours. With an energy-dispersive detector the reflections from Al(111) planes at nine positions along the conductor line were collected repeatedly during electromigration in a symmetric reflection geometry, and thus the Al(111) plane spacings perpendicular to the sample surface were determined. Figure 1 shows the values of the "effective lattice parameter" a_{eff} obtained from the measured Al(111) plane spacings at the chosen positions along the conductor line at T = 267oC before electromigration and after 15 hours and 69 hours of electromigration. Before electromigration the Al line was in a biaxial compressive thermal stress state, and due to Poisson expansion the perpendicular values of a_{eff} were larger than the strain-free value a_0. After 15 hours of electromigration, the perpendicular values of a_{eff} at the first three positions (no. 7, 8 and 9) decreased due to the relief of the in-plane compressive stress, while the values at the rest of the positions near the anode end (no. 1-6) increased because of the enhancement of the in-plane compressive stress. This result can be explained qualitatively by the removal of atoms from the grain boundaries near the cathode end of the conductor line, and the deposition of atoms into grain boundaries near the anode end. After 69 hours of electromigration, further stress relaxation at positions 6-8 had brought the perpendicular values of a_{eff} closer to the strain-free value. The values of a_{eff} indicating stress-buildup at positions 2-6 after 15 hours had been replaced by a less uniform, more relaxed set of values, attributed to plastic deformation of the aluminum and deformation or fracture of the passivation.

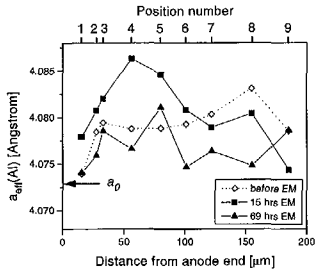


Figure 1. Measured perpendicular values of a_{eff} along the interconnect line before electromigration, and after 15 hours and 69 hours of electromigration. The arrow indicates the strain-free value of aeff.

X-ray Diffraction Data Collection for Microcrystals | X26C

J. Pluth, L. Clark , S. Sutton (U. of Chicago), M. Helliwell (U. of Manchester), G. Harlow (Am. Museum of Nat. Hist.), and G. Shea-McCarthy (U. of Chicago).

The purpose of the study was to determine whether beamline NSLS X26C could be used to collect data for very small single crystals. The data were collected using the oscillation method, monochromatic radiation and recorded on Fuji image plates. A diffraction pattern was collected for each crystal to determine if it was single. Full data sets were then recorded for high quality crystals. The final goal of this study was to solve the unknown crystal structures of the microcrystals. The smallest crystal for which a data set was collected was raite (5x5x100μ^3). The data sets are currently being processed, data quaility is being evaluated and attempts to solve the unknown crystal structures are being made. A summary of the crystals studied and their current status is given below:

raite: $Na_4Mn_3Si_8(O,OH)_{24}.9H_2O$, C222, a=30.6 b=5.31 c=18.20, 5x5x100μ^3, data collected at 5 deg. steps in one minute, 19 frames, wavelength=1.127.

choloalite: $CuPb(TeO_3)_2.H_2O$, cubic, a=12.519, 20x20x20μ^3, 5 deg. steps in one min., 0-95 deg., 19 frames, wavelength=0.966.

epistolite: $Na_5TiNb_2(Si_2O_7)_2O_3F.5H_2O$, monoclinic, 10x50x50$\mu^3$, crystals bad.

quetzalcoatlite: $Cu_4Zn_8(TeO_3)_3(OH)_{18}$,C6322, a=10.097 c=4.944, 60x60x60μ^3, crystals gave no diffraction pattern.

karnasurtite: $(Ce,La,Th)(Ti,Nb)(Al,Fe^{+3})(Si,P)_2O_7(OH)_4 .3H_2O$, Trigonal, 20x100x100$\mu^3$,crystals bad.

tokkoite: $K_4Ca_4Si_7O_{17}(O,OH,F)_4$,triclinic, a=10.37 b= 25.39 c=7.27 α=91.67 β=100.66 γ=92.09, 20x100x100μ^3, good crystal found but lost.

diopside: $MgCaSi_2O_6$, C2/c, a=9.752 b=8.927 c=5.252 β=105.82, 30μ^3, diffraction pattern recorded, 10 deg. 30 sec.

zorite: Cmmm, a=23.24 b=7.24 c=6.96(x2?) from powder, 10x10x2μ^3, a few spots that could be from crystal were recorded.

Fabrication of a mm-Wave Accelerating Cavity, Using Deep X-ray Lithography * | X26C

J.J. Song, Y.W. Kang, R.L. Kustom, B. Lai, D.C. Mancini, A. Nassiri (ANL), and V. White (U. Wisconsin)

The possibility of fabricating mm-wave radio frequency cavities using deep x-ray lithography (DXRL) is being investigated. The frequency of operation can be from 30 GHz to 300 GHz, operating mode in either TM or TE-mode, depending on the application. For most applications, a complete structure consists of two mirror-image planar half structures assembled face-to-face. The fabrication process includes manufacture of precision x-ray masks, exposure of positive resist by x-rays through the mask, resist development, and electroforming of the final microstructure. The precision Hard x-ray mask was made by means of an surface mask, using soft x-ray lithography for pattern transfer into poly-methylmethacrylate (PMMA) on a 200-μm thick Si wafer, followed by electroplating of 35-μm Au at CXrL (Center of X-ray Lithography) in Wisconsin.

For the DXRL process, PMMA was used as the positive resist, either as an 1-mm sheet glued or 200-μm film cast onto a Cu substrate. The NSLS (National Synchrotron Light Source) X26C beamline in Brookhaven was used to expose the resist. Fig.1 shows transmitted x-ray intensity through various filters during PMMA exposures for DXRL at NSLS. 99.9% OFC(oxygen free copper) was electroplated onto the developed PMMA structure, and then polished by the diamond-lapping. Fig.2 shows SEM picture of the rectangular cells of the constant-impedance 30-cell 108-GHz cavity structure.The cavity will be aligned with the optical fibers on the grooves and then initial test will be performed with HP 8510 network analyzer.

[1] J.J.Song, et. al., will be presented and submitted to SPIE'96 Symposium on Micromachining and Microfabrication, Austin, TX, Oct 14-15, 1996.

[2] J.J.Song, et. al., submitted to 1996 Proc. on Workshop under the Joint Auspices of Division of Particles and Fields and Division of Physics of Beams, Snowmass, Colorado, July 8, 1996.

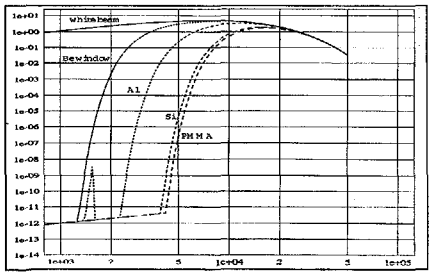


Figure 1. Transmitted x-ray intensity during PMMA exposures for DXRL at NSLS, (watt/cm^3)

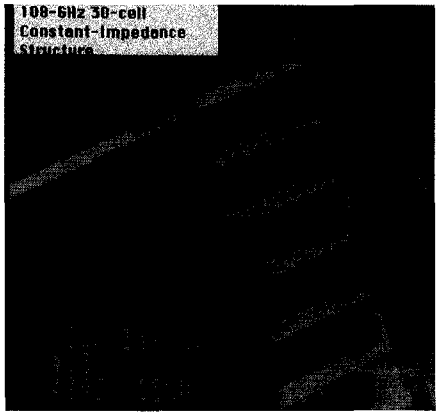


Figure 2. SEM picture of the rectangular cells of the constant-impedance cavity.

* This work was supported by DOE Contract W-31-109-ENG-38.

Characterization of Defects in Protein Crystals by Diffractometry and Topography | X26C

V. Stojanoff (ESRF), D. P. Siddons (NSLS), E. Snell (NASA), T. Boggon and J. R. Helliwell (U. Manchester, UK.).

We have studied the crystalline perfection of several samples of proteins grown both in space (i.e. zero-gravity conditions) and in ground-based control experiments. We were able to perform triple-axis diffractometry on selected diffraction spots using an imaging-plate system to index the crystal orientation, followed by conventional diffractometry. A superficial view of the data provides no definite pattern to the qualities of the earth- grown *vs* the space-grown samples. Figure 1 shows a contour map of the diffracted intensity in theta-2theta space, clearly showing two strong, well- seperated peaks. Figure 2 shows a diffraction topograph taken at the low-angle peak. Note that the outline of the diffracting region is not sharp, i.e. the sample 'domains' are not physically distinct. The optical configuration for these measurements included a silicon (1,1,1) monochromator and analyser, with no focussing elements.

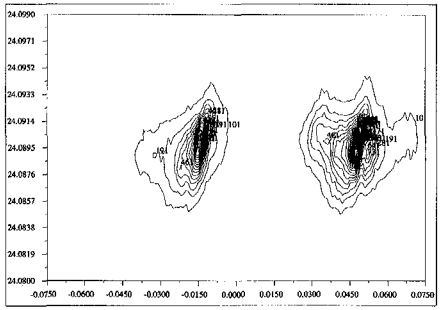


Figure 1. Θ-2Θ map of the (3,-11,-8) Bragg peak, showing 2 well-seperated peaks.

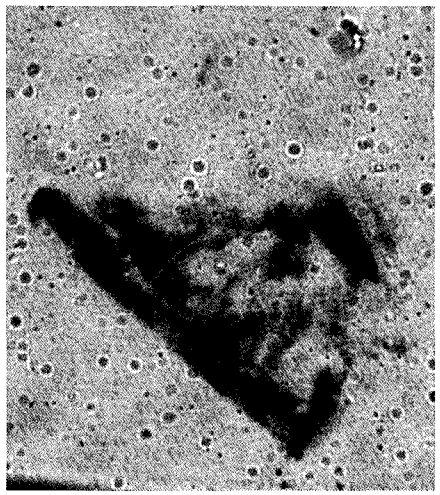


Figure 2. X-ray diffraction topograph of the same Bragg spot, with Θset to coincide with the low-angle peak in figure 1.

In situ Structural Characterization of Lithium-ion Battery Electrode Materials	X27A, X22A

T.R. Thurston, N.M. Jisrawi, S. Mukerjee, X.Q. Yang, J. McBreen (BNL - DAS), M.L. Daroux, and X.K. Xing (Gould Electronics)

The low cost, high operating voltage, and low toxicity of $Li_xMn_2O_4$ make it a good candidate for use as a cathode in lithium-ion battery cells. However, this material can not be reproducibly manufactured yet, a problem which arises in large part because the structural properties of $Li_xMn_2O_4$ vary considerably with synthesis conditions. The structure also changes during the lithium intercalation process, so studies of operating battery cells may help resolve some of these issues by allowing one to separate structural properties dependent on the lithium content from those dependent on the underlying manganese-oxygen skeleton. We report here some of our initial results from combined electrochemical and synchrotron x-ray scattering measurements performed on operating cells.

X-ray diffraction experiments were performed at X27A with 24.5 keV photons and at X22A with 10 keV photons. Cells of approximate dimensions 2cm x 3cm x 0.5mm were manufactured by Gould Electronics, sealed at the factory, and mounted in a transmission geometry on the spectrometer with *no modifications*. Even though the x-ray beam must penetrate through the external case, electrolyte, and binding materials in this geometry, the high flux of a synchrotron allows data with reasonable counting rates to be taken [1].

An example of the structural information that can easily be obtained with this technique is illustrated in the right figure. Here 2θ scans taken through the $Li_xMn_2O_4$ (333), (511), (440), and (531) peaks are presented (the (440) peak is partially obscured by an aluminum peak at 20.3°). The data have been offset from each other for clarity, and they show the evolution of these peaks as the cell was discharged from 3.90 volts to 2.94 volts. The data indicate that expanded and nonexpanded phases coexist over a certain range of voltages. Other structural properties such as this two phase coexistence and their relationships to electrochemical properties are discussed in reference [2].

[1] T.R. Thurston *et al.* Appl. Phys. Lett. **69**, 194 (1996).
[2] N.M. Jisrawi *et al.* J. Electrochem. Soc., submitted.

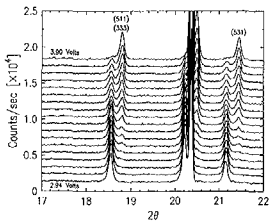


Figure 1. 2θ scans (λ=0.501Å) showing the evolution of two-phase coexistence as a battery cell is discharged.

An Investigation into the Spatial Texture Distribution in Thermomechanically Deformed $Nd_2Fe_{14}B$-based Permanent Magnets	X27A

T.R. Thurston, L.H. Lewis, U. Wildgruber, D.O. Welch (BNL- DAS), and V. Panchanathan (Magnequench International)

Quantifying the relationship between crystallographic texture and magnetic properties is highly desirable for engineering high energy-product magnets. However, determining the texture of melt-quenched magnets from $Nd_2Fe_{14}B$-based alloys is challenging because they possess a nano-scaled microstructure that is complicated by the presence of multiple phases, both ferromagnetic and paramagnetic. This microstructure leads to exchange-spring type magnetic behavior which nullifies standard magnetic remanence procedures for texture determination.

To overcome these experimental difficulties, new techniques for measuring the texture of bulk permanent magnets have been explored recently. Hard x-ray transmission geometry diffraction experiments were performed on a series of $Nd_2Fe_{14}B$-based magnets with varying die-upsets. The spatial homogeneity of the c-axis alignment was examined perpendicular and parallel to the pressing axis. The figure shows the FWHM of the rocking curve of the (006) peak along the direction perpendicular to the pressing axis for a 60% die-upset sample. It can be seen that the c-axis alignment is best in the center region of the magnet and becomes progressively worse as the perimeter of the magnet is approached. Samples with lower deformation levels possess more uneven texture distributions than do those with high deformation levels, and the degree of orientation seems to develop discontinuously around a deformation level of 50%.

Bulk magnetization measurements were also performed on each sample and correlated with the texture properties determined from x-ray diffraction. It was found that the coercivity is much more sensitive to the degree of c-axis alignment than is the remanence. The coercivity decreases significantly with increasing deformation level, while the remanence is largely unaffected for deformation levels exceeding 30%. More details of this work, as well as recommendations for improving production procedures which follow from these experiments, are given in reference [1].

[1] L.H. Lewis *et al.*, submitted to J. Mag. & Mag. Mat.

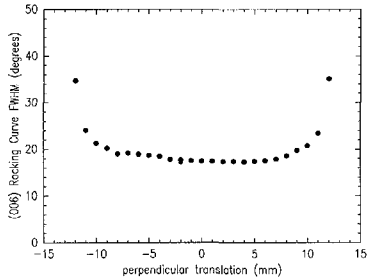


Figure 1. Spatial Homogeneity of the Texture in a 60% Die Upset Sample.

In Situ Measurements of Texture and Phase Development in Bi-2223 Silver Cladded Superconducting Wires	X27A, X22A

T.R. Thurston, U. Wildgruber, N.M. Jisrawi, M. Suenaga, Y.L. Wang (BNL), and P. Haldar (IGC Corporation)

During the past two years, techniques for characterizing silver-cladded Bi-2223 superconducting wires with hard x-rays have been developed at X27A [1]. In order to penetrate through the silver cladding, the incident x-ray energy is tuned just below the silver edge at 25.5 keV. The samples are also examined in a transmission geometry, so bulk structural properties are probed. Using these techniques, we have previously shown in *ex situ* experiments that both the c-axis alignment (texture) and Bi-2223 phase development have large effects on the current carrying capacity of fully processed wires.

More recently, we have begun experiments where the phase and texture development of Bi-2223 are monitored as it grows from precursor materials (typically Bi-2212 plus CuO *etc.*) within its silver sheath. This *in situ* work has been done in an x-ray compatible furnace with temperature stability of 0.2°C at 830°C. The figure below shows the phase and texture development of a typical sample during the first 50 hours of processing. The solid line represents the temperature program followed. The furnace was ramped from room temperature up to 600°C, held at 600°C for 6 hours, ramped again from 600°C to 840°C over a period of 12 hours, and then held at 840°C. Bi-2223 phase content (represented by the open triangles) began to develop only after reaching 840°C. On the other hand, the weighted average of the Bi-2212 and Bi-2223 texture, represented by the (200) FWHM (closed circles), improved significantly while the sample was being ramped from 600°C to 840°C. Thus, the texturing and phase development mechanisms are largely decoupled. The implications of this and many other *in situ* experimental results are discussed in reference [2].

[1] T.R. Thurston *et al.* J. Appl. Phys. **79**, 3122 (1996).
[2] T.R. Thurston *et al.* J. Mat. Res., submitted.

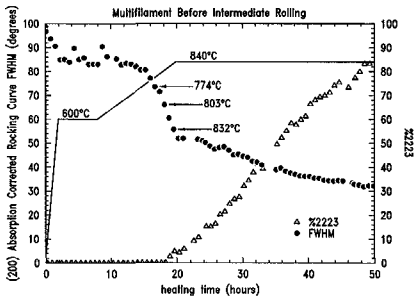


Figure 1. Time Dependence of the Phase and Texture Development in a Multifilament Wire.

Determination of Topology and Transport in Porous Media Using Synchrotron Computed Microtomography *	X27C

P.M. Adler, J.-F. Thovert (IPGP, France), K.W. Jones, A.M. Peskin, D.P. Siddons, B. Andrews, and B. Dowd (BNL)

We have previously examined1 the geometrical structure of the pore space in a sample of Fontainebleau sandstone using synchrotron computed microtomography (CMT). The tomographic data made it possible to obtain the topology of the void space of the sample and its macroscopic permeability and conductivity using the method of reconstructed porous media.2 The present work is aimed at extending the investigation to a number of samples which cover a range of porosity values. The work was carried out using the computed microtomography apparatus at the NSLS X27 beam line. Our initial survey work was done with a voxel size of 15 5m on samples of Vosges sandstone, Massangi's limestone, and Laroux limestone. A comparison of the results of the present investigation of these materials with the initial results obtained for the Fontainebleau sandstone will

be made. The intent is to develop an approach which can be used to model large scale petroleum reservoir structures

1. P. Spanne, J. F. Thovert, C. J. Jacquin, W. B. Lindquist, K. W. Jones, and P. M. Adler. Phys. Rev. Lett. 73, 2001 (1994). 2. J. Yao, P. Frykman, F. Kalaydjian, J. F. Thovert, and P. M. Adler. J. Colloid. Interface Sci. 156,

478 (1993) and references therein.

*Research supported in part by US Department of Energy Contract No. DE-AC02-76CH00016.

* Research supported in part by USDOE Contract DE-AC02-76CH00016.

Region of Interest Tomography Correction for Subvolumes of Large Core Samples	X27C

B. Andrews, B.A. Dowd, D.P. Siddons, and J. Yung (NSLS)

Typically, data generated by X-Ray computed microtomography on geological samples require full volume imaging of the sample. In other words, the linear dimension of the detector array must extend beyond the projected width of the material under study. This is typically called global tomography; a map of the linear attenuation coefficients over the entire exposed volume is generated. In local tomography, only a region of interest within the full volume is reconstructed. We have been using conventional global tomography algorithms to process full volume microtomography data. With our present configuration, however, only 1 to 2 mm diameter cores can be fully imaged with high resolution (3 to 5 microns).

In our first efforts to construct high resolution tomograms over a 1 mm region of interest within cylindrical volumes of 2 to 20 mm, we have applied a straightforward geometrical correction to the global algorithms already in place. Only the transmission data through the region of interest was needed to implement this correction and perform the reconstruction. The effect of the correction can be seen in the figures below. Without the correction, a significant cupping artifact is evident. The correction has been applied with good result, to oil reservoir sandstone, basalt, fontainebleu, and berea. Further work is being carried on to allow us to extend the algorithm to any geometry, and to improve contrast and resolution for region of interest X-Ray microtomography.

*Thanks to B. Illman, USDA Forest Products Lab.

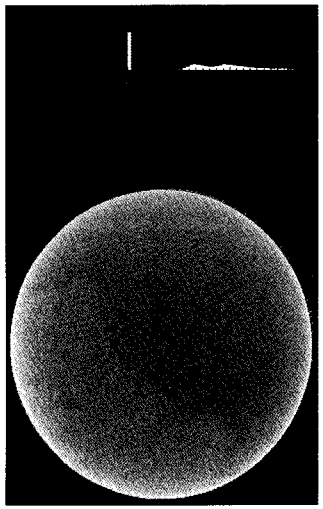


Figure 1. Global reconstruction applied to 1mm of 6mm D basalt,with no correction.

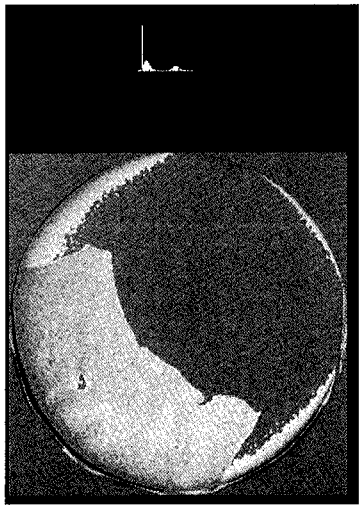


Figure 2. Same 1mm diameter of basalt, with subvolume correction, histograms included.

X-Ray Microtomography Applications to the Characterization of Oil Reservoir Seal and Source Lithologies	X27C

W. Bell , R.D. Hazlett (Mobil Corp.), B. Andrews, B.A. Dowd, K.W. Jones, A. Peskin, and D.P. Siddons (BNL)

Synchrotron X-Ray microtomography has been used, for the first time, to look at the 3-D structure of source and seal rocks. Source rocks contain the material from which useful hydrocarbons (oil and gas) are generated by prolonged application of heat and pressure associated with burial of sediments. Expelled from their site of origin, these hydrocarbons can migrate, primarily under buoyant forces, through porous rocks. The barriers to further (upward) migration of reaction products are called seals. The physical properties of the seal and source rocks determine the holdup, flow rate, leak rate, and accumulation of migrating oil as well as its quality (gas to oil ratio.) Characterization of these materials is important in the development of models that predict oil and gas accumulations in potential petroleum basins.

The material examined, seals a deep (~10000-ft) producing reservoir in the Gulf of Mexico. Traditional physical methods of analysis have elucidated some physical characteristics. Mercury porosimetry studies, N2 absorption analysis, as well as novel gas and brine permeability experiments have established the following properties:

Table 1 Physical Characterization of GOM Seal Material

He Expan. BET Surf. Area Perm. @ 1500psi Conf. Sample Grain Water Porosity N2 Horiz. Vert. Vert. Depth Density loss. vol% gas gas brine ft g/cc vol% m2/g m2/cc ~10000 2.72 25. 24. 43. 94. 20 mmD 2 mmD 2 nD

Mercury porosimetry shows significant pore sizes (necks and bodies) distributed around 400 and 2000 Angstrom diameters; the data is shown in Figures 1 and 2.

Microtomography experiments will continue to investigate these novel materials. Macroscopic features such as fractures and unexpected disconnected voids have been identified; pore structure is below the current resolution limit of this technique. This work has demonstrated our potential ability to capture the intricate geometry of either natural or induced microfractures. The spatial distribution of minerals has also been of significant interest.

This work was funded in part by ACTI grant from USDOE DE-AC0276CH00016.

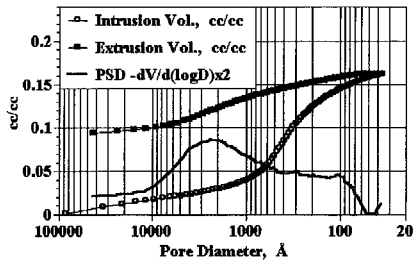


Figure 1. Mercury Porosimeter Data on Seal Rock: GOM 10,000 ft

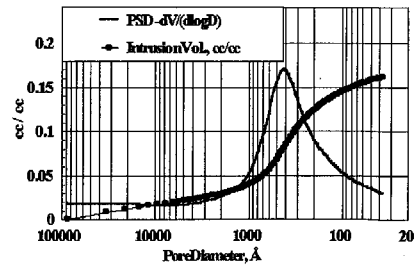


Figure 2. Hg Intrusion Poresize Distribution

X-ray Refraction Imaging (XRI) Applied to Mammography	X27C

D. Chapman (Illinois Inst. of Tech.), W.Thomlinson, N. Gmür, A. Zhong, R. Menk (NSLS), R.E. Johnson, D. Washburn,E. Pisano (U. of North Carolina), F. Arfelli (Sincrotrone Trieste), and D.Sayers (NCSU)

We discuss here an imaging technique, X-ray Refraction Imaging (XRI) which can be used to independently visualize the refraction and absorption of an object. This technique can be applied to thick and therefore highly absorbing materials. It is not limited to materially thin samples and/or high x-rays experience in traversing the object. The images are almost completely scatter-free. The combination of these properties has resulted in images of mammography phantoms which have dramatically improved contrast and spatial resolution over standard imaging techniques. It is potentially applicable to mammography and other fields of medical x-ray imaging and to radiology in general, such as non-destructive testing and x-ray computed tomography.

Screening mammography has proven to be an effective procedure in identifying early breast cancer. Two large randomized trials have demonstrated that breast cancer mortality among screened women over 50 years old can be reduced at least 30% when compared with unscreened controls. The cancers found by mammography tend to be smaller and of less advanced stages than those found by breast physical examination or breast self-examination. Smaller and lower stage breast cancers have better survival rates. Unfortunately, approximately 10% of clinically obvious breast cancers are not visible with mammography. This occurs most frequently in patients with large amounts of breast glandular tissue. The density of this tissue tends to obscure underlying pathology. Premenopausal women and women undergoing estrogen replacement therapy are more likely to have dense glandular breasts. The National Cancer Institute, The American College of Radiology (ACR) and the American Cancer Society (ACS), among other organizations currently advocate annual screening mammograms for women over the age of 50. Screening under age 50 is more controversial. It is desirable to increase the sensitivity of mammography applied to younger women so that their cancers are apparent at a much earlier stage of development. This earlier detection may result in significantly reduced mortality in this population.

Applications of Synchrotron Microtomography in Experimental Petrology: Absorption Tomography of Pore Features in Synthetic Rock Samples *	X27C

T. Cohen, E. B. Watson (Rensselaer Polytech Inst.), B. Dowd, D. P. Siddons, B. Andrews and K. W. Jones (BNL)

The nature of fluid-filled porosity in rocks of the Earth's lower crust and upper mantle is of basic interest. In these regions, the elevated P-T conditions result in significant solubilities of the rock-forming minerals in any contacting pore fluids that might be present. Under these circumstances, the fluid/rock assemblage will tend toward geometric configuration that minimizes the total interfacial energy of the system. Generally speaking, if the energy of the mineral/fluid interface is low relative to the grain boundaries (mineral/mineral interfaces), the fluid will tend to penetrate grain edges to form a continuously interconnected network of grain edge channels. If, on the other hand, the energy of the mineral/fluid interface is relatively high, the fluid will segregate to grain corners to form isolated pores. These contrasting fluid distributions have profoundly different implications for the bulk properties of the rock: in simple terms, a rock containing an interconnected fluid phase is likely to exhibit markedly enhanced transport properties such as electrical conductivity, dissolved component diffusivities, and permeability. The "wetting" behavior of C-O-H fluids in a variety of monomineralic rocks can be investigated by subjecting synthetic samples to high P-T conditions in the presence of small amounts of fluid. By use of quenching experiments, it is possible to show that some fluids in some rocks are indeed interconnected (e.g., water in quartzite at 800 C and 10 kbar), while others exist as isolated pores (e.g., CO2 in dunite). However, it is necessary to rely almost exclusively on indirect methods of geometric characteristics including assessment based on a single 2D section, or on the observed enhancement of bulk-rock diffusion by the presence of a fluid. Synchrotron computed microtomography has been used for direct and thorough characterization of pore features produced in high P-T experiments. Porous, cylindrical rock specimens with grain sizes of 50-100 m were synthesized in a piston-cylinder apparatus. An experimental measurement was made of the microgeometry of the inclusions. Pore spaces were clearly delineated. Work is currently in progress to determine the porosity and connectivity of the specimen using the medial axis formalism developed previously with W. B. Lindquist and coworkers. The results will be compared to values inferred from bulk porosimetry measurements.

* Research supported in part by USDOE Contract DE-AC02-76CH00016.

X-Ray Microtomography of Reservoir Sandstone for the Characterization of Porosity and Permeability *	X27C

M.E. Coles, R.D. Hazlett, E.L. Muegge (Mobil Corp.), B. Andrews, B.A. Dowd, K.W. Jones, A. Peskin, D.P. Siddons (BNL), M. Schlackman (GTE), W.E. Soll (LANL), and P. Spanne (ESRF)

Synchrotron X-ray microtomography at the X27C beamline has been used to provide large, high resolution 3-D renderings of pore networks in reservoir rocks supplied by Mobil Corporation. The data gathered over the past year has been used to model single and multiphase flow properties in actual digital representations of the porous rocks from which hydrocarbons are produced. With this kind of information, we have been able to examine the tortuous pathways available for fluids to flow within the rock. We have been able to simulate experiments related to hydrocarbon extraction efficiency through the use of network modeling. Furthermore, the thresholded CMT images have served as the boundary condition framework for more rigorous computational fluid dynamics simulations of oil being displaced by injected fluids.

A sample of a North Sea Brent sandstone acquired at 2.7 micron resolution is shown in the accompanying figure. We show a 3-D representation of the cylindrical volume with a wedge removed to reveal the interior. Given also are interior orthogonal slices which reveal the extent of detail captured in this 470 md sample. These images demonstrate the ability of CMT to simultaneously capture intergranular porosity and elements of microporosity in a 3-D pore network. The sharpness of grain boundaries at this magnification attests to the quality of image data. We can certainly see variations in mineralogy and can begin to digest surface compositional information important for rock-fluid interactions, i.e. wettability. Such high resolution CMT images of the actual pore interconnections in rocks will provide necessary data for the development and testing of improved multiphase flow relations and physically correct upscaling methods.

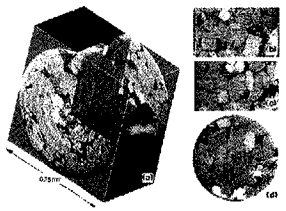


Figure 1. High resolution CMT subvolume of a North Sea Brent sandstone, k=470md: with cutaway, b) X-directional slice, c) Y-directional slice, d)Cross section

* Work sponsored by ACTI grant for collaborative work between BNL, Mobil, and GTE, through DOE contract DEAC02-76CH00016

X-Ray Microtomography of Fungal Deterioration of Wood *	X27C

B.L. Illman (U. Wisconsin and Forest Products Lab.), B.A. Dowd and D.P. Siddons (NSLS)

A new class of synchrotron x-ray computed tomography was used to make nondestructive tomographic images of solid Southern yellow pine (SYP) wood and SYP during degradation by wood decay fungi. Computed microtomographic (CMT) images were obtained with spatial resolution of 3 microns using the recently assembled station at X27 (Dowd, 1996). This third generation CMT station employs Charge Coupled Device (CCD) area detectors for higher resolutions and faster acquisition times, optimized reconstruction algorithms and fiber optic link to a 3-dimensional stereo viewing theater. Wood samples (3mm cubes) were scanned at high resolution using CCD detector array with 329 x 259 small pixels where 1 row of pixels constitutes a single 2-dimensional slice of the specimen. The 500 horizontal slices comprising each data set were stacked to reconstruct the 3-dimensional volume of the specimen. Color images were computer-generated in 2-dimension to portray single slices of select cross sectional areas (Figure 1) and 3-dimensional volumes of the wood. Reconstructed volumes were viewed on 3-dimensional video at the stereo viewing theater. The CMT images of SYP and decay fungi provide information about spatial relationship between xylem vessels, inter- and intracellular areas of tracheids and clear structural alterations by degrading fungi. The models developed in this work will provide needed information about the chronology and location of structural damage to wood and aid in determining the chemical mechanisms of lignocellulose degradation.

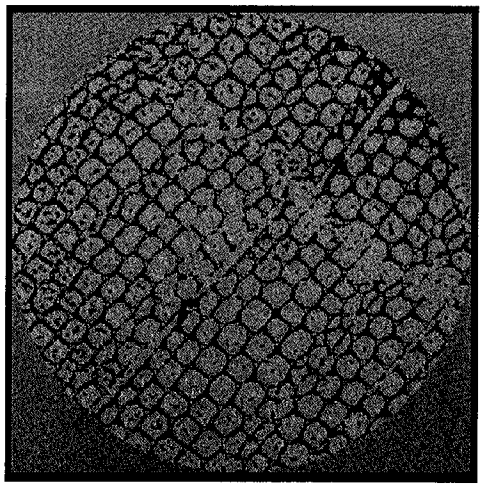


Figure 1.

* This research was supported by USDA grant 94371031016 and USDA Forest Service.

MECT's Bent Laue-Laue Monochromator: Design and Test Results | X27C

B. Ren, F.A. Dilmanian, X.Y. Wu, (BNL- Medical), L.D. Chapman, I. Ivanov (CSRRI, IIT) and Z. Zhong (NSLS)

A bent Laue-Laue monochromator has been constructed in a collaboration between the Center for Synchrotron Radiation Research and Instrumentation (CSRRI), Illinois Institute of Technology (IIT) and the Multiple Energy Computed Tomography (MECT) group. The design, which was inspired by the earlier bent Laue-Laue work by D. Chapman and C. Schulze, was chosen because of: a) the rocking curve is wide and has a flat top, thus minimizing the sensitivity of the two-crystal system to individual crystals' vibrations and distortions; b) the system has a high throughput; c) the sytem has low harmonics; and d) the energy bandwidth is low in the Cauchois geometry. The design includes the following features (see table below): a) the crystals are Si$<$ 331 $>$ with 22^o asymmetric angle; b) both crystals are bent to about 20-m radius; c) both crystals employ Laue diffraction "upper case" to eliminate Laue spot contamination; d) the crystals are 1.1 mm thick (1st) and 1.5 mm thick (2nd); e) the benders are four-rod mechanisms, with two fixed and two adjustable rods. The force on each adjustable rod is cotrolled by two independent springs on the ends, allowing removal of crystal twisting and facilitating symmetric bending.

Radius	Thickness	Darwin Width	Integ. Reflect.	Max. Reflectivity
Flat	1.1 mm	1.6 μrad	0.9 μrad	
20 m	1.1 mm	47.5 μrad	30.3 μrad	64%
20 m	1.5 mm	64.6 μrad	39.3 μrad	61%

The tests used an 1/4" Al beam filter, the full 8-cm horizontal width of the X27C beam, and a 0.5-mm vertical beam height. First, the tilt angle χ was adjusted using both crystals unbent. Next, for each crystal at different bending radii the rocking curve was measured using the other crystal unbent as an analyzer; the bending radii were deduced from these widths. The Darwin widths were set to 43 and 63 μradian for the 1st and 2nd crystal, the corresponding bending radii were 22 m and 21 m respectively. Figure 1 shows the corresponding single bent crystal rocking curves obtained with a 3 mm x 0.5 mm beam.

We thank E. Black, B. Dowd, D. Feske, G. Haigis, J.B. Hastings, A. King, W. Lavender, A. Lenhard, C. Schulze, M. Shelton, D.P. Siddons, S. Simpose, W.C. Thomlinson, G. Vanderleski, S. Wang for assistance. Research supported by the Office of Health and Environmental Research, U.S. Department Of Energy.

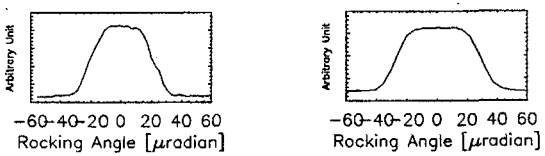


Figure 1. Shows the corresponding single bent crystal rocking curves obtained with a 3 mm x 0.5 mm beam.

X-Ray Microtomography of Basalts * | X27C

D. Sahagian (U.N.H.), B.A. Dowd, K.W. Jones, D.P. Siddons, S. Song (BNL)

Models of volcanic eruption dynamics are related to the understanding of the kinetics of bubbles. There is a strong dependence on the expansion or migration of bubbles during the magma rise for both explosive and effusive volcanos. The shape and size distribution of bubbles in basaltic magma are the important parameters needed to estimate lava viscosity and flow rate and nucleation, growth, coalescence rates of bubbles in erupting magmas and active lava flows. Meanwhile, the distribution of bubbles may be used to infer paleoelevation and/or paleoatmospheric pressure. The connectivity and tortuosity of the bubbles will tell us about water transport through the rock, of interest to hazardous waste disposal sites. But, current measurements of bubble size morphology and distribution in basaltic lava flows are limited because of the lack of techniques for obtaining three-dimensional images. To overcome this limitation, we have explored the use of synchrotron x-ray computed microtomography (CMT) at the X27C beamline to quantitatively measure the properties of bubbles in basaltic lava flows. These basaltic samples, collected from Africa, are rich in different size fractions of vesicles. The preliminary results show very good 3D images of bubble morphology, size distributions and connectivity in vesiculated basaltic samples. A typical volume image is shown in the Figure. Further plans include the use of 3D medial-axial method to quantitatively determine the properties of bubbles, such as porosity, permeability, and size distributions.

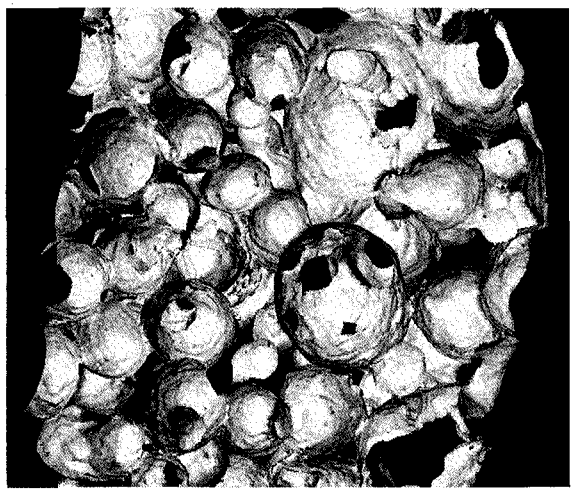


Figure 1. 3-D Rendering of an African basalt. Pore sizes are on the order of 0.5 mm.

* Work supported by USDOE Contract DE-AC02-76CH00016.

Microstructures of Antarctic Meteorites in the Millimeter Size Range *	X27C

S.R. Sutton (The U. of Chicago), B.A. Dowd, K.W. Jones, D.P. Siddons, B. Andrews, A. Peskin (BNL)

High energy synchrotron radiation can be used to image the internal microstructures of extraterrestrial objects, such as rare Antarctic meteorites using computed microtomography (CMT). The microtomography technique allows a number of physical properties of the specimen to be determined non-destructively such as locations and size distributions of clasts, fusion crust thickness, modal abundance of phases, porosity, density, and possibly the distributions of terrestrial weathering products. The location of clasts is of interest, for example, in developing sampling strategies and allocation plans for rare objects such as those from the Moon and Mars. Fusion crust thickness is important in understanding the velocity and trajectory distribution of the millimeter -sized objects that make up the bulk of the extraterrestrial matter accreted by the Earth. For example, the surprisingly small degree of heating experienced by some large (30 micrometer) micrometeorites is not predicted by atmospheric heating models. Twenty-one ordinary chondrite (L5) specimens in the 4-9 mm diameter range have been obtained to test the value of this approach. Initial CMT images show the well-defined spatial distribution, size distribution and morphologies of clasts in the "pebbles". The resolution used in this initial survey was not high enough to resolve the fusion crust on the objects. Future work using higher resolution will allow a detailed study of fusion crusts to be conducted.

* This work supported under NASA grant NAGW-3651.

PUBLICATIONS

NSLS USERS

Beamline U1A

B.E. Bent, "Mimicking Aspects of Heterogeneous Catalysis: Generation, Isolation and Reacting Proposed Surface Intermediates on Single Crystals in Vacuum", *Chemical Reviews*, **96**, 1361, (1996).

J.G. Chen, "Carbide and Nitride Overlayers on Early Transition Metal Surfaces: Preparation, Characterization and Reactivities", *Chemical Reviews*, **96**, 1477, (1996).

J.G. Chen, B. Frühberger, J. Baumgartner, and B.D. DeVries, "Characterization of the Electronic, Structural and Catalytic Properties of Vanadium Carbide: A Comparison of VC/V(110) Model System with Powder VC Catalysts", The Chemistry of Transition Metal Carbides and Nitrides, edited by S.T. Oyama, Blackie Academic and Professional, New York, p. 439, (1996).

J.G. Chen, B. Frühberger, and M.L. Colaianni, "NEXAFS Characterization of the Surface and Bulk Properties of Transition Metal Oxides", *J. of Vac. Sci. and Tech.*, **A14**, 1668, (1996).

B. Frühberger, J.G. Chen, J. Eng, Jr., and B.E. Bent, "Reactivities of Carbon- and Nitrogen-Modified Mo(110): A Comparison of Modification Effects by Surface and Interstitial Adatoms", *J. Of Vac. Sci. and Tech.*, **A14**, 1475, (1996).

G. Haehner, A. Marti, W. R. Caseri, and N. D. Spencer, "Orientation and Electronic Structure of Methylene Blue on Mica: A Near Edge X-Ray Absorption Fine Structure Spectroscopy Study", *J. Chem. Phys.*, **104/19**, 7749, (1996).

M.X. Yang, M. Xi, Y. Yuan, and B.E. Bent, "NEXAFS Studies of Halobenzenes and Phenyl Groups on Cu(111)", *Surf. Sci.*, **341**, 9, (1995).

Beamline U2B

J.V. Badding, and D.C. Nesting, "Thermodynamic Analysis of the Formation of Carbon Nitrides Under Pressure", *Chem. Mat.*, **8**, 535, (1996).

G.L. Carr, D. DiMarzio, M.B. Lee, and D.J. Larson, Jr., "Infrared Microspectroscopy of Semiconductors at the Diffraction Limit" Semiconductor Characterization: Present Status and Future Needs, edited by Bullis, Seiler, and Diebold, AIP Press, p. 418, (1996).

A.F. Goncharov, V.V. Struzhkin, M.S. Somayazulu, R.J. Hemley, and H. Mao, "Compression of Ice to 210 GPa: Infrared Evidence for a Symmetric Hydrogen Bonded Phase", *Science*, **273**, 218, (1996).

R.J. Hemley, H.K. Mao, A.F. Goncharov, M. Hanfland, and V.V. Struzhkin, "Synchrotron Infrared Spectroscopy to 0.15 eV of H_2 and D_2 at Megabar Pressures", *Phys. Rev. Lett.*, **76**, 1667, (1996).

Beamline U3C

H. Tao, U. Diebold, V. Chakarian, D.K. Shuh, J.A. Yarmoff, N.D. Shinn, and T.E. Madey, "RadiationInduced Decomposition of PF_3 on Ru(0001)", *J. Vac. Sci. Technol.*, **A13**, 2553-2557, (1995).

Beamline U4A

K. Breuer, C. Stagarescu, K.E. Smith, M. Greenblatt, and K. Ramanujachary, "Observation of Hidden Fermi Surface Nesting in a Two Dimensional Conductor", *Phys. Rev. Lett.*, **76**, 3172, (1996).

J.E. Rowe, D.M. Riffe, G.K. Wertheim, and J.C. Bean, "Photoemission Measurement of Equilibrium Segregation at GeSi Surfaces", *J. Appl. Phys.*, **76**, 4915, (1994).

K.E. Smith, K. Breuer, D.M. Goldberg, M. Greenblatt, W. McCarroll, and S.L. Hulbert, "Defects in Quasi-One Dimensional Oxide Conductors: $K_{0.3}MoO_3$", *Mat. Res. Soc. Proc.*, **375**, 133, (1995).

H.-S. Tao, C.-H. Nien, T.E. Madey, J.E. Rowe and G.K. Wertheim, "Faceting of W(111) Induced by Pd and Pt Adlayers - A Photoemission Study", *Surf. Sci.*, **357**, 55, (1996).

G.K. Wertheim, J.E. Rowe, D.N.E. Buchanan, and P.H. Citrin, "Surface-Ion Core-Level Shifts in Alkali Halides", *Surf. Sci. Lett.*, **319**, L41, (1994).

G.K. Wertheim, J.E. Rowe, D.N.E. Buchanan, and P.H. Citrin, "Experimental Interatomic Auger Rates in Sodium Halides", *Phys. Rev.* **B51**, 13669, (1995).

G.K. Wertheim, J.E. Rowe, D.N.E. Buchanan, and P.H. Citrin, "Valence-Band Structure of Alkali Halides Determined From Photoemission Data", *Phys. Rev.* **B51**, 13675, (1995).

Beamline U4B

V. Chakarian, Y.U. Idzerda, H.-J. Lin, C.J. Gutierrez, G.A. Prinz, G. Meigs, and C.T. Chen, "Canted Coupling of Buried Magnetic Multilayers", *Phys. Rev.*, **B53**, 11313, (1996).

V. Chakarian, H.-J. Lin, Y. U. Idzerda, E. E. Chaban, G. Meigs, J.-H. Park, C. J. Gutierrez, G. A. Prinz, and C. T. Chen, "Element-Specific Vector Magnetometry (ESVM) Via Soft X-ray Magnetic Circular Dichroism", Mat. Res. Soc. Symp. Proc., p. 375, (1995).

C.T. Chen, Y.U. Idzerda, C.-C. Kao, L.H. Tjeng, H.-J. Lin, and G. Meigs, "Magnetic Properties of Multilayers from Soft X-ray Magnetic Circular Dichroism", *J. Mat. Sci and Eng.*, **B31**, 49, (1995).

C.T. Chen, Y.U. Idzerda, C.-C. Kao, H. Tjeng, H.-J. Lin, and G. Meigs, "Magnetic Structure of Multilayers from Soft X-ray Magnetic Circular Dichroism," *Mat. Res. Soc.*, **375**, 59, (1995).

Y. Fukumoto, A.R. Moodenbaugh, M. Suenaga, D.A. Fischer, K. Shibutani, T. Hase, and S. Hayashi, "Effect of Oxygen Partial Pressure During Postheat Treatment on $Bi_2Sr_2CaCu_2O_y$/Ag Tapes", *J. Appl.. Phys.*, **80**, 1, (1996).

A.R. Moodenbaugh, D.A. Fischer, Y.L. Wang, and Y. Fukumoto, "Superconductivity, Oxygen Content, and Hole State Density in $Bi_2Sr_{1.75}Ca_{1.25}Cu_2O_{8.18+y}$($-0.09<y\leq$) and $Bi_{1.6}Pb_{0.4}Sr_{1.9}Ca_2Cu_3O_z$", *Physica*, **C268**, 107-114, (1996).

J.-H. Park, C.T. Chen, S.-W. Cheong, W. Bao, G. Meigs, V. Chakarian, and Y.U. Idzerda, "Electronic Aspects of the Ferromagnetic Transition in Manganese Perovskites", *Phys. Rev. Lett.*, **76**, 4215, (1996).

Beamline U4IR

M.R. Chance, A. Xie, Q. He, and R.M. Hochstrasser, "Ultrafast Studies of Electronics States and Protein Bound Water Molecules in Bacteriorhodopsin", *J. Biophysical*, **70**, A241, (1996).

C.J. Hirschmugl, and G.P. Williams, "Chemical Shifts and Coupling Interactions for the Bonding Vibrational Modes for Co/Cu(111) and (100) Surfaces", *Phys. Rev.*, **B52**, 14177, (1995).

A.E. Russell, L. Rubasingham, P.L. Hagans, and T.H. Ballinger, "Cell and Optics Design for *in situ* Farinfrared Spectroscopy of Electrode Surfaces", *Electrochimica Acta*, **41**, 637, (1996).

G.P. Williams, "Infrared Synchrotron Radiation: Introduction and History", *Synch. Rad. News*, **8./5**, 8, (1995).

A. Xie, Q. He, K. Hellingwerf, W.D. Hoff, E.M. Scheuring, B. Sclavi, M.R. Chance, K. Wynne, and G. Haran, "Far-infrared Synbchrotron Spectroscopy of Functionally Important Low Frequency Modes in Proteins", *J. Biophysical*, **70**, A338, (1996).

Beamline U8B

T.D. Durbin, D.A. Lapiano-Smith, F.R. McFeely, F.J. Himpsel, and J.A. Yarmoff, "The Chemisorption and Reaction of Dichlorosilane on Ge(100) and Ge(111) Surfaces", *Surf. Sci.*, **330**, 147-155, (1995).

S. Lee, M. M. Banaszak Holl, W. H. Hung, and F. R. McFeely, "Photoemission Assignments of H_xSiO_{4-x} Fragments in the Si/SO_x Interface Region", *Appl. Phys. Lett.*, **68**, 1081, (1996).

F.R. McFeely, K.Z. Zhang, M. M. Banaszak Holl, S. Lee, and J.E. Bender IV., "An Inquiry Concerning the Principles of Si 2p Core Level Shift Assignments at the Si/SiO_2 Interface", *J. Vac. Sci. Technol.*, **B14**, 2824, (1996).

W.C. Simpson, T.D. Durbin, P.R. Varekamp, and J.A. Yarmoff, "The Growth of GaF_3 Films on GaAs(110) at Elevated Temperatures Studied with Soft X-ray Photoelectron Spectroscopy", *J. Appl. Phys.*, 77, 2751-2758, (1995).

W.C. Simpson, W.M. Tong, C.B. Weare, D.K. Shuh, and J.A. Yarmoff, "The Temperature Dependence of the Cl_2/GaAs(110) Surface Product Distribution", *J. Chem. Phys.*, **104**, 320-325, (1996).

W.C. Simpson, P.R. Varekamp, D.K. Shuh, and J.A. Yarmoff, "Soft X-ray Photoelectron Spectroscopy Study of the Reaction of XeF_2 with GaAs", *J. Vac. Sci. Technol.*, **A13**, 1709-1713, (1995).

J.A. Yarmoff, V. Chakarian, T.D. Durbin, C.W. Lo, D.K. Shuh, W.C. Simpson, and P.R. Varekamp, "Photon Stimulated Desorption of Halogens", *Nucl. Instrum. Meths.*, **101**, 60-63, (1995).

Beamline U9B

E.R. Arndt, and E.S. Stevens, "A Conformational Study of Agarose by Vacuum UV CD", *Biopolymers*, **34**, 1527-1534, (1994).

E.R. Arndt, and E.S. Stevens, "Vacuum Ultraviolet Circular Dichroism of Gellan-Family Polymer Films from Water and Dimethy Sulfoxide", *Carbohydrate Research*, **280**, 15-26, (1996).

A. Buku, U. Mirza, and K. Polewski, "Circular Dichroism (CD) Studies on Biological Activity of Mast Cell Degranulation (MCD) Peptide Analogs", *Int. J. Peptide Protein Res*, **44**, 410-413, (1994).

J.M. Flanagan, J.S. Wall, M.S. Capel, D.K. Schneider, and J. Shanklin, "Scanning Transmission Electron Microscopy and Small-Angle Scattering Provide Evidence that Native *Escherichia coli* ClpP is a Tetradecamer with an Axial Pore", *Biochemistry*, **34**, 10910-10917, (1995).

L.L. France, P.G. Paitti, J.F.E. Newman, and F. Brown, "Modeling Biologically Relevant Peps using Circular Dichroism with Synchrotron Radiation and High Temperature Molecular Dynamics", Molecular Modeling, edited by T.F. Kumosinsky and M.N. Liebman, American Chemical Society, pp. 45-60, (1994).

L.L. France, P.G. Piatti, J.F.E. Newman, I. Toth, W.A. Gibbons, and F. Brown, "Circular Dichroism, Molecular Modeling and Serology Indicate that the Structural Basis on Antigenic Variation in Foot-andmouth Disease Virus is α-helix formation", *Proc. Natl. Acad. Sci.,* **91**, 8442-8446, (1994).

R.B. Hill, J.M. Flanagan, and J.H. Prestegard, "^{1}H and ^{15}N Magnetic Resonance Assignments, Secondary Structure and Tertiary Fold of *Eshcerichia coli* DnaJ(1-78)", *Biochemistry*, **34**, 5587-5596, (1995).

E. Johnson, and J.C. Sutherland, "Ultraviolet Free-Electron Laser Facility at Brookhaven National Laboratory", Synchrotron Radiation in the Biosciences, edited by B. Chance, D. Deisenhofer, S. Ebashi, D.T. Goodhead, J.R. Helliwell, H.E. Huxley, T. Iizuka, J. Kirz, T. Mitsui, E. Rubenstein, N. Sakabe, T. Sasaki, G. Schmahl, H. Sturhmann, K. Wuthrich, and G. Zaccai, Clarendon Press, Oxford, pp. 739-747, (1994).

L.A. Kelly, J.G. Trunk, K. Polewski, and J.C. Sutherland, "Simultaneous Resolution of Spectral and Temporal Properties of UV and Visible Fluorescence using Single-Photon Counting with a PositionSensitive Photomultiplier", *Rev. Sci. Instrum.*, **66**, 1496-1498, (1995).

S. Krinsky, and C.-C. Kao, "Time Varying Elliptically Polarized Wiggler at the NSLS", *Synch. Rad. News*, **8/5**, 38-39, (1995).

J.H. Kycia, V. Biou, F. Shu, S.E. Gerchman, V. Graziano and V. Ramakrishnan, "Prokaryotic Translation Initiation Factor IF3 is an Elongated Protein Consisting of Two Crystallizable Domains", *Biochemistry,* **34**, 6183-6187, (1995).

A. Lempicki, M.H. Randles, D. Wisniewski, M. Balcerzyk, C. Breacher, and A.J. Wojtowicz, "$LuAlO_3$: Ce and other Aluminate Scintillators", *IEEE Trans. in Nucl. Sci.*, **42**, 280, (1995).

A. Lempicki, A.J. Wojtowicz, and C. Brecher, "Inorganic Scintillators", Wide-Gap Luminescent Materials: Theory and Applications, edited by S.R. Rotman, pp. 1-65, (1996).

O.C. Mullins, and X. Wang, "Fluorescence Lifetime Studies of Crude Oils", *Applied Spectroscopy*, **48**, 977-984, (1994).

K. Polewski, D. Zinger, J. Trunk, D. Monteleone, and J.C. Sutherland, "Fluorescence of Matrix Isolated Guanine and 7-Methylguanine", *J. Of Photochemistry and Photobiology*", **B24**, 169-177, (1994).

C.Y. Ralston, S. Mitra-Kirtley, and O.C. Mullins, "Small Population of One to Three Fused-Aromatic Ring Moities in Asphaltenes", *Energy & Fuels*, **10**, 623-630, (1996).

J.C. Sutherland, "Circular Dichroism Using Synchrotron Radiation: From Ultraviolet to X-rays", Circular Dichroism: Conformational Analysis of Biomolecules, edited by G.D. Fasman, pp. 599-633, (1996).

X. Wang, and O. Mullins, "Fluorescence Lifetime Studies of Crude Oils", *Applied Spectroscopy*, **48**, 977984, (1994).

A.J. Wojtowicz, M. Balcerzyk, E. Berman, and A. Lempicki, "$Ce_xLa_{1-x}F_3$: Optical Spectroscopy and Scintillation Mechansisms", *Phys. Rev.,* **B49**, 14880, (1994).

Beamline U10

C.L. Foerster, "Ultra-High Vacuum System of the Brookhaven National Synchrotron Light Source", Proceedings International Conference on Vacuum Science & Technology and SRS Vacuum SystemsINCOVAST 95, *Accelerators and SRS Systems*, **1**, pp. 36-57, (1995). BNL 62537.

C.L. Foerster, C. Lanni, J.R. Noonan, and R.A. Rosenberg, "Photon Stimulated Desorption Measurement of an Extruded Aluminum Beam Chamber for the Advanced Photon Source", *J. Vac. Sci. Technol.*, **A14/3**, 1273, (1996). BNL 62542.

C.L. Foerster, C. Lanni, C. Perkins, M. Calderon, and W. Barletta, "Photon Stimulated Desorption (PSD) Measurements of Extruded Copper and of Welded Copper Beam Chambers for the PEP II Asymmetric B-factory", *J. Vac. Sci. Technol.*, **A13/3**, 581, (1995). BNL 61082

Beamline U11

P.S. Monks, L.J. Stief, D.C. Tardy, J.F. Liebman, Z. Zhang, S.C. Kuo, and R.B. Klemm, "A Discharge Flow-Photoionization Mass Spectrometric Study of HOI: Photoionization Efficiency Spectrum and Ionization Energy", *J. Phys. Chem.*, **99**, 16566, (1995).

D.C. Tardy, S.C. Kuo, Z. Zhang, and R.B. Klemm, "Ionization Energy of *tert*-Butyl-d_9 Alcohol and the Appearance Energy of Protonated Acetone: A Nonequilibrium Dissociation", *J. Phys. Chem.*, **100**, 8144, (1996).

R.P. Thorn, Jr., P.S. Monks, L.J. Stief, S.C. Kuo, Z. Zhang, and R.B. Klemm, "The Photoionization Efficiency Spectrum, Ionization Energy and Heat of Formation of Br_2O", *J. Phys. Chem.*, **100**, 12199, (1996).

Z. Zhang, P.S. Monks, L.J. Stief, J.F. Liebman, R.E. Huie, S.C. Kuo, and R.B. Klemm, "Experimental Determination of the Ionization Energy of IO($X^2\Pi_{3/2}$) and Estimations of the Heat of Formation of IO^+ and the Proton Affinity of IO", *J. Phys. Chem.*, **100**, 63, (1996).

Beamline U13UA

J.C. Levin, G.B. Armand, and I.A. Sellin, "Photoionization and Compton Double Ionization of Helium from Threshold to 20 keV", *Phys. Rev. Lett.*, **76**, 1220, (1996).

B. Sinkovic, E. Shekel, and S. L. Hulbert, "Spin-Resolved Fe $L_3M_{45}M_{45}$ Auger Transition *on*- and *off*Resonance: The Effect of Exchange Correlation", *Phys. Rev.*, **B52**, 15703, (1995). BNL 62536

Beamline U13UB

J.E.Bjorkholm, A.A.MacDowell, O.R.Wood II, Z.Tan, B.LaFontaine, and D.M.Tennant, "Phase Measuring Interferometry" *J.Vac.Sci. Technol.*, **B13/6**, 2919, (1995).

Beamline U14A

Z.M. Stadnik, G.W. Zhang, M. Akbari-Moghanjoughi, A.-P. Tsai, and A. Inoue, "Physical Properties of Al-Cu-Fe-Mn Icosahedral Alloys" Proceedings of the 5th International Conference on Quasicrystals, Avignon, 1995, edited Ch. Janot and R. Mosseri, World Scientific, Singapore, p. 530, (1995).

G.W. Zhang, and Z.M. Stadnik, "Partial and Total Densities of States in Icosahedral $Al_{70}Pd_{20}Mn_{10}$", Proceedings of the 5th International Conference on Quasicrystals, Avignon, 1995, edited by C.H. Janot and R. Mosseri, World Scientific, Singapore, p. 552, (1995).

Beamline U15

S. Huang, Z.H. Ming, Y.L. Soo, Y.H. Kao, M. Tanaka, and H. Munekata, "X-ray Scattering and Absorption Studies of MnAs/GaAs Heterostructures", *J. Appl. Phys.*, **79**, 1435, (1996).

C.I. Ma, D.M. Hanson, K. Lee, and R.G. Hayes, "Dynamical Behavior of Electronic States of NH_3^{2+} Prepared From N 1s Ionization of Ammonia", *J. Electron Spectrosc. Relat. Phenom.*, 75, 83, (1995).

Z.H. Ming, S. Huang, Y.L. Soo, K.H. Kao, T. Carns, and K.L. Wang, "Interfacial Roughness Scaling and Strain in Lattice Mismatched $Si_{0.4}Ge_{0.6}$ Thin Films on Si", *Appl. Phys. Lett.*, **67**, 629, (1995).

Y.L. Soo, S.W. Huang, Z.H. Ming, Y.H. Kao, H. Munekata, and L.L. Chang, "III-V Diluted Magnetic Semiconductor: Substitutional Doping of Mn in InAs", *Phys. Rev.*, **B53**, 4905, (1996).

Beamline X1A

H. Ade, B. Hsiao, G. Mitchell, E. Rightor, A. P. Smith, and R. Cieslinski, "X-ray Microscopy of Polymeric Materials", *Mat. Res. Soc. Proc.* **375** , 293-302, (1995).

H.N. Chapman, J. Fu, C. Jacobsen, and S. Williams, "Dark-Field X-ray Microscopy of Immunogold-labeled Cells", *J. Micro. Soc. Am.*, **2**, 53-62, (1996).

H.N. Chapman, C. Jacobsen, and S. Williams, "A Characterization of Darkfield Imaging of Colloidal Gold Labels in a Scanning Transmission X-ray Microscope", *Ultramicroscopy*, **62**, 191-213, (1995).

G. D. Cody, R. E. Botto, H. Ade, and S. Wirick, "Soft X-ray Microscopy and Microanalysis: Applications in Organic Geochemistry", *SPIE*, **2516**, 185-196, (1996).

T. Crowder and H. Ade, "A Low Pressure Parallel Plate Proportional Counter Optimized for Detection of Nitrogen Fluorescence", *Rev. Sci. Instrum.*, **66**, 2303-2305, (1995).

K. K. Goncz and S. S. Rothman, "A Trans-Membrane Pore can Account for Protein Movement Across Zymogen Granule Membranes", *Biochim., Biophys. Acta,* **1238**, 91-93, (1995).

W.S. Haddad, I. McNulty, J.E. Trebes, and E.H. Anderson, "Ultrahigh Resolution X-ray Tomography", *SPIE*, **2516**, 102-107, (1995).

C.-H. Ko, J. Kirz, K. Maier, B. Winn, H. Ade, S. Hulbert, E. Johnson, and E. Anderson, "Chemical State Mapping on Material Surfaces with the X1A Second Generation Scanning Photoemission Microscope (X1A SPEM-II)", *SPIE*, **2516**, 150-159, (1995).

J. Maser, H. Chapman, C. Jacobsen, A. Kalinovski, J. Kirz, A. Osanna, S. Spector, S. Wang, B. Winn, S. Wirick, and X. Zhang, "The Scanning Transmission X-ray Microscope at the NSLS: From XANES to Cryo", *SPIE*, **2516**, 78-89, (1995).

X. Zhang, R. Balhorn, J. Mazrimas, and J. Kirz, "Mapping and Measuring DNA to Protein Ratios in Mammalian Sperm Head by XANES Imaging", *J. Struct. Bio.*, **116**, 335-344, (1996).

Beamline X1B

S. Eisebitt, J. Lüning, J.E. Rubensson, T. van Buuren, S.N. Patitsas, T. Tiedje, M. Berger, S. Arens-Fischer, S. Frohnhoff, and W. Eberhardt, "Soft X-Ray Emission of Porous Silicon Nanostructures", *J. Electr. Spectr.*, **79**, 135, (1996).

P.D. Johnson, Y. Liu, Z. Xu, and D.-J. Huang, "Spin-Polarized Photoemission Studies of the 3s Core Levels in Fe and Co", *J. Electr. Spectr.*, **75**, 245, (1995).

B. Kempgens, B. Itchkawitz, K.J. Randall, J. Feldhaus, A.M. Bradshaw, H.M. Köeppe, F.X. Gadea, D. Nordfors, J. Schirmer, and L.S. Cederbaum, "Dynamic Effects in the C 1s Excitation Spectra of Ethene Isotopomers", *Chem. Phys. Lett.*, **246**, 347, (1995).

A. Kivimäcki, M. Neeb, B. Kempgens, H.M. Köeppe, and A.M. Bradshaw, "The C 1s Auger Decay Spectrum of the CH4 Molecule: The Effects of Vibrational Fine Structure, Double Excitations and Shake-Up Transitions", *J. Phys.*, **B29**, 27091, (1996).

H.M. Köeppe, B. Kempgens, A.L.D. Kilcoyne, J. Feldhaus, and A.M. Bradshaw, "Autoionisation of Doubly Excited States in the C 1s Photoexcitation of CO", *Chem. Phys. Lett.*, **53**, 4120, (1996).

H. M. Köeppe, B.S. Itchawitz, A.L.D. Kilcoyne, J. Feldhaus, B. Kempgens, A. Kivimäeki, M. Neeb, and A.M. Bradshaw, "High-Resolution C 1s Photoelectron Spectra of Methane", *Phys. Rev.*, **A53**, 4120, (1996).

H.M. Köeppe, A.L.D. Kilcoyne, J. Feldhaus, and A.M. Bradshaw, "Relaxation Effects in C 1s Photoionisation of CO: A High Resolution Photoelectron Study in the Near-Threshold Region", *J. Electr. Spectrosc. Rel. Phen.*, **75**, 97, (1995).

M. Neeb, A. Kivimäeki, B. Kempgens, H.M. Köeppe, J. Feldhaus, and A.M. Bradshaw, "Core Hole Double-Excitation and Atomic-Like Auger Decay in N_2", *Phys. Rev. Lett.*, **76**, 2250, (1995).

M. Neeb, A. Kivimäeki, B. Kempgens, H.M. Köeppe, and A.M. Bradshaw, "Excitation Energy Dynamics Observed in N_2 Auger Spectra Near the K-Shell Threshold", *J. Electr. Spectrosc. Rel. Phen.*, **79**, 445, (1995).

J-E. Rubensson, J. Lüning, M. Neeb, M. Biermann, B. Kuepper, and W. Eberhardt, "Core-Level Photoionization-Decay Coincidence Spectroscopy of Free Molecules", *J. Elect. Spect. Rel. Phen.* , **75**, 47, (1996).

J-E. Rubensson, J. Lüning, M. Neeb, B. Kuepper, S. Eisebitt, and W. Eberhardt , "Photoelectron-Soft-X-ray-Fluorescence Coincidence Spectroscopy on Free Molecules", *Phys. Rev. Lett*, **76**, 3919, (1996).

M. Schmidbauer, A.L.D. Kilcoyne, H.M. Köeppe, J. Feldhaus, and A.M. Bradshaw", Shape Resonances and Multi-Electron Effects in the Core-Level Photoionization of CO_2", *Phys. Rev.*, **A52**, 2095, (1995).

Z. Xu, Y. Liu, P.D. Johnson, and B.S. Itchkawitz, "Magnetic Structure of Monolayer-Range Cr Films Deposited on Fe(001)", *Phys. Rev.*, **B52**, 15393, (1995).

Beamline X2A

A.P. Baddorf, A.K. Swan, and J.F. Wendelken, "Comment on In-Plane Lattice Reconstruction of Cu(001)", *Phys. Rev. Lett.*, **76**, 3658, (1996).

K. Kimura, J.B. Cohen, S. Chandavarkar, and K.S. Liang, "Surface Atomic Ordering of $Cu_3Au(001)$ Above T_c", *Physica*, **B221**, 101, (1995).

R. Paniago, S. Schmid, T.H. Metzger, P.C. Chow, H. Reichert, S.C. Moss, J. Peisl, and K.S. Liang, "Surface Induced Changes in the Critical Behavior of the β_1-β_2 Phase Transition in V_2H", *Physica,* **B221**, 210, (1995).

Beamline X2B

F.M. Auzerais, J.H. Dunsmuir, B. Ferreol, N. Martys, J. Olsen, T.S. Ramakrishnan, D.H. Rothman, and L.M. Schwartz, "Transport in Sandstone: A Study Based on Three Dimensional Microtomography", *Geophys. Res. Letts.*, **23**/7, 705-708, (1996).

B.B. Ferreol and D.H. Rothman, "Lattice Boltzmann Simulations of Flow Through Fontainebleau Sandstone", *Transport in Porous Media*, **20**, 3-20, (1995).

E.N. Landis, E.N. Nagy, D.T. Keane, and N. Huynh, "Observations of Internal Fracture in Mortar using X-ray Microtomography", Proceedings of the 1996 ASCE Engineering Mechanics Specialty Conference, pp. 637-640, (1996).

E.N. Landis, E.N. Nagy, D.T. Keane, and S.P. Shah, "Observations of Internal Crack Growth in Mortar using X-ray Microtomography", Proceedings of the 2nd International Conference on Nondestructive Testing of Concrete in the Infrastructure, pp. 54-59, (1996).

A.M. Lanzillotto, T.S. Leu, M. Amabile, R. Wildes, and J.H. Dunsmuir, "Applications of X-ray Micro-Imaging, Visualization, and Motion Analysis Techniques to Fluidic Microsystems", Solid State Sensor and Actuator Workshop, pp. 123-126, (1996).

Beamline X3A1

T. Gasparik, J.B. Parise, B. Eiben ,and J.A. Hriljac, "Stability and Structure of a new High Pressure Silicate $Na_{1.8}Ca_{1.1}Si_6O_{14}$", *Am. Mineral*, **80**, 1269, (1995).

Y. Ko, K. Tan, J.B. Parise, and A. Darovsky, "The Synthesis of a Novel 2-Dimensional Antimony Sulfide, $[C_4H_{10}N]_2[Sb_8S_{13}]0.15H_2O$ and its Structure Solution using Synchrotron Imaging Plate Data", *Chem. Mat.*, **8**, 493-496, (1996).

J.B. Parise, L. Abrams, J.C. Calabrese, D.R. Corbin, J.M. Newsam, S. Levine, and C. Freeman, "Molecular Dynamic and Structural Studies of the Interactions of HFC-134 and CFC-13 with the Faujasite Framework", Zeolite Science 1994: Recent Progress and Discussions, edited by H.G. Karge, and J. Weitkamp, Elsevier, Amsterdam, pp. 248-249, (1995). Also in Studies in *Surf Sci and Catal.*, **98**, 248-249, (1995).

M.R. Pressprich, B.-J. Fransen, A. Darovsky, and P. Coppens, "A Simple Device for Increasing the Accessibility of Reciprocal Space in Low-Temperature Area-Detector Experiments", *J. Appl. Cryst.*, **28**, 650, (1995).

K. Tan, Y. Ko, J.B. Parise, and A. Darovsky, "Hydrothermal Growth of Single Crystals of TMA-CuGS-2, $(Cu_{0.44}Ge_{0.56}S_{2.23})4(Ge_4S_8)_3.6(CH_3)_4N$ and Their Characterization using Synchrotron Imaging Plate Data", *Chem. Mat.*, **8**, 448, (1996).

Beamline X3A2

B. Chu, and G. Wu, "Structure and Dynamics of Copoly(oxyethylene-oxypropylene-oxyethylene) in Xylene/ Water Mixtures", *Macromol. Symp.*, **90**, 251, (1995).

B. Chu, F.-J. Yeh, E.L. Sokolov, S.G. Starodoubtsev, and A.R. Khokhlov, "Interaction of Slightly Cross-Linked Gels of Poly(Diallyl-dimethylammonium Chloride) with Surfactants", *Macromolecules*, **28**, 8447, (1995).

T. Dobashi, F.-J. Yeh, Q. Ying, K. Ichikawa, and B. Chu, "An Experimental Investigation of the Structure of Microcapsules", *Langmuir*, **11**, 4278, (1995).

B.S. Hsiao, S.Z.D. Cheng, and R.M. Ho, "Time-Resolved X-ray Study of Crystalline Phase Transition in Poly(Aryl Ether Ketone Ketone) Containing Alternated Terephthalic/Isophthalic Moieties", *J. Polym. Sci. Polym. Phys.*, **33/17**, 2439-2447, (1995).

M.R. Pressprich, B.-J. Fransen, A. Darovsky, and P. Coppens, "A Simple Device for Increasing the Accessibility of Reciprocal Space in Low-Temperature Area-Detector Experiments", *J. Appl. Cryst.*, **28**, 650, (1995).

R. Verma, B.S. Hsiao, and A. Biswas, "Analysis of SAXS Data from Semicrystalline Ionomeric Systems", *ACS Polym. Prep.*, **37/1**, 415-417, (1996).

Beamline X3B1

R.N. Bhargava, D. Gallagher, T. Sosnowski, P.B. Klein, T.B. Norris, Y.L. Soo, Y.H. Kao, T.A. Kennedy, and E.R. Glaser, "Ultrafast and Efficient Recombination in Doped Nanocrystals of Semiconductors", Proc. 22nd International Conference on Physics of Semiconductor, Vancouver, Canada, World Scientific, Singapore, p. 2007, (1995).

R.E. Dinnebier, P.W. Stephens, S. Wies, and W. Eysel, "Structures and Phase Transition of $Bi_2CdO_2[GeO_4]$", *J. Solid State Chem.*, **123**, 371, (1996).

W.C. Elliott, P.F. Miceli, T. Tse, and P.W. Stephens, "Orientation Dependence of Homoepitaxy: an *in situ* x-ray scattering study of Ag", *Physica*, **B221**, 65, (1996).

G. Faigel, G. Bortel, M. Tegze, L. Gránásy, S. Pekker, G. Oszlányi, O. Chauvet, G. Baumgartner, L. Forró, P.W. Stephens, G. Mihály, and A. Jánossy, "Distribution of K Ions in Intermediate K_1C_{60}", *Phys. Rev.*, **B52**, 3199, (1995).

J.E. Fischer, G. Bendele, R. Dinnebier, P.W. Stephens, C.L. Lin, N. Bykovetz, and Q. Zhu, "Structrual Analyisis of Fullernene and Fulleride Solids From Synchrotron X-ray Powder Diffraction", *J. Phys. Chem. Solids*, **56**, 1445, (1995).

S. Huang, Z.H. Ming, Y.L. Soo, Y.H. Kao, M. Tanaka, and H. Munekata, "X-ray Scattering and Absorption Studies of MnAs/GaAs Heterostructures", *J. Appl. Phys.* **79**, 1435, (1996).

D.C. Johnston, T. Ami, F. Borsa, M.K. Crawford, J.A. Fernandez-Baca, K.H. Kim, R.L. Harlow, A.V. Mahjan, L.L. Miller, M.A. Subramanian, D.R. Torgeson, and Z.R. Wang, "Superconductivity, Magnetism, and Metal-Insulator Transitions in Some Ternary and Pseudoternary 3d-, 4d- and 5d-Metal Oxides", Proceedings of the 17th International Taniguchi Symposium on Theoretical Physics", *Springer Series in Solid-State Sciences*, **119**, 241-254, (1995).

J.A. Kaduk, and J. Faber, "Crystal Structure of Zeolite Y as a Function of Ion Exchange", *The Rigaku Journal*, **12/2**, 14-34, (1995).

J.A. Kaduk, and S. Pei, "The Crystal Structure of Hydrated Sodium Aluminate $NaAlO_2$-5/4 H_2O and its Dehydration Product", *J. Solid State Chem.*, **115**, 126-139, (1995).

C.E. Kerr, B.E. Eaton, and J.A. Kaduk, "Synthesis of Stable (4-Vinyallene)Iron Tricarbonyl Complexes: Preparation, Fluxionality, and X-ray Crystal Structure Analysis", *Organometallics*, **14**, 269-273, (1995).

M. Kunz, R. Dinnebier, L.K. Cheng, E.M. McCarron, D.E. Cox, J.B. Parise, M. Gehrke, J. Calabrese, P.W. Stephens, T. Vogt, and R. Papoular, "$Cs(Ti,As)O_5$ and $Cs(Ti,P)O_5$: A Disordered Parent Structure of $ABOCO_4$ Compounds", *J. Solid State Chem.*, **120**, 299-310, (1995).

Z.H. Ming, Y.L. Soo, S. Huang, Y.H. Kao, K. Stair, G. Devane, and C. Choi-Feng, "Thickness Modulation of InGaAs/GaAs Superlattices Studied by Large Angle X-ray Scattering", *Appl. Phys. Lett.*, **66**, 165, (1995).

Y.L. Soo, S.W. Huang, Z.H. Ming, Y.H. Kao, H. Munekata, and L.L. Chang, "III-V Diluted Magnetic Semiconductor: Substitutional Doping of Mn in InAs" *Phys. Rev.*, **B53**, 4905, (1996).

R.L. Whetten, J.T. Khoury, M.M. Alvarez, S. Murthy, I. Vezmar, Z.L. Wang, P.W. Stephens, C.L. Cleveland, W.D. Luedtke, and U. Landman, "Nanocrystal Gold Molecules", *Adv. Mater.*, **8**, 428-433, (1996).

Beamline X4

F.K. Athapilly, and W.A. Hendrickson, "Structure of the Biotinyl Domain of Acetyl-Coenzyme A Carboxylase Determined by MAD Phasing", *Structure*, **3**, 1407-1419, (1995).

F.T. Burling, W.I. Weis, K.M. Flaherty, and A. Brunger, "Direct Observation of Protein Solvation and Discrete Disorder with Experimental Crystallographic Phases", *Science*, **271**, 72-77, (1996).

D.H. Fremont, W.A. Hendrickson, P. Marrack, and J. Kappler, "Structures of an MHC Class II Molecule with Covalently Bound Single Peptides", *Science*, **272**, 1001-1004, (1996).

J.H. Geiger, S. Hahn, S. Lee, and P.B. Sigler, "Crystal Structure of the Yeast TFIIA/TBP/DNA Complex", *Science*, **272**, 830-836, (1996).

T. Glumoff, S. Helin, P. Mazur, J.W. Kozarich, and A. Goldman, "Crystallization and Preliminary Crystallographic Analysis of 3-carboxy-cis,cis-muconate Lactonizing Enzyme from *Neurospora crassa*", *Acta Cryst.* **D52**, 221-223, (1996).

J.A. Hirsch and A.K. Aggarwal, "Structure of Even Skipped Homeodomain Bound to an AT Rich DNA: New Perspectives on Homeodomain Specificity", *EMBO J.*, **14**, 6280-6291, (1995).

J. Labahn, O.D. Scharer, A. Long, K. Ezaz-Nikpay, G.L. Verdine, and T.E. Ellenberger, "Structural Basis for the Excision Repair of Alkylation-Damaged DNA", *Cell*, **86**, 321-329, (1996).

D.J. Leahy, I. Aukhil, and H.P. Erickson, "2.0Å Crystal Structure of a Four-Domain Segment of Human Fibronectin Encompassing the RGD Loop and Synergy Region", *Cell*, **84**, 155-164, (1996).

C.-H. Lee, K. Saksela, U.A. Mirza, B.T. Chait, and J. Kuriyan, "Crystal Structure of the Conserved Core of HIV-1 Nef Complexed with a Src Family SH3 Domain", *Cell*, **85**, 931-942, (1996).

Y.-H. Lee, C. Ogata, J.W. Pflugrath, D.G. Levitt, R. Sarma, L.J. Banaszak, and S. J. Pilkis, "Crystal Structure of the Rat Liver Fructose-2,6-bisphosphatase Based on Selenomethionine Multiwavelength Anomalous Dispersion Phases", *Biochemistry*, **35**, 6010-6019, (1996).

C.D. Lima, M.G. Klein, I. B. Weinstein, and W.A. Hendrickson, "Three-Dimensional Structure of Human Protein Kinase C interacting Protein 1, a Member of the HIT family of Proteins", *Proc. Natl. Acad. Sci. USA*, **93**, 5357-5362, (1996).

M. Mohammadi, J. Schlessinger and S. R. Hubbard, "Structure of the FGF Receptor Tyrosine Kinase Domain Reveals a Novel Autoinibitory Mechanism", *Cell*, **86**, 577-587 (1996).

A.V. Nickitenko, S. Trakhanov and F.A. Quiocho, "2 Å Resolution Structure of DppA, a Periplasmic Dipeptide Transport/Chemosensory Receptor", *Biochemistry*, **34**, 16585-16595, (1995).

T.S. Peat, E.G. Frank, J.P. McDonald, A.S. Levine, R. Woodgate, and W.A. Hendrickson, "Structure of the UmuD' Protein and its Regulation in Response to DNA Damage", *Nature*, **380**, 727-730, (1996).

T.S. Peat, E.G. Frank, R. Woodgate, and W.A. Hendrickson, "Production and Crystallization of a Selenomehionyl Variant of UmuD', an *escherichia coli* SOS Response Protein", *Proteins: Structure, Function, and Genetics*, **25**, 506-509, (1996).

A. Qu and D. Leahy, "The Role of the Divalent Cation in the Structure of the I Domain form the CD11a/CD18 Integrin", *Structure*, 4, 931-942, (1996).

J. Sondek, A. Bohm, D. G. Lambright, H. E. Hamm, and P. B. Sigler, "Crystal Structure of a G_A protein ßγ Dimer at 2.1Å Resolution", *Nature*, **379**, 369-374, (1996).

U.K. Urs, D.J. Sharkey, T.S. Peat, W.A. Hendrickson, and K. Murthy, "Characterization of Crystals of the Thermostable DNA Polymerase I From *Thermus aquaticus*", *Proteins: Structure, Function, and Genetics*, **23**, 111-114, (1995).

X. Xie, T. Kokubo, S.L. Cohen, U.A. Mirza, A. Hoffmann, B.T. Chait, R.G. Roeder, Y. Nakatani, and S.K. Burley, "Structural Similarity Between TAFs and the Heterotetrameric Core of the Histone Octamer", *Nature*, **380**, 316-322, (1996).

X. Zhu, X. Zhao, W.F. Burkholer, A. Gragerov, C.M. Ogata, M.E. Gottesman, and W.A. Hendrickson, "Structural Analysis of Substrate Binding by the Molecular Chaperone Dnak", *Science*, 272, 1606-1614, (1996).

Beamline X5

A.M. Sandorfi, and W. Leidemann, "The Signature of Diprotons in ^{3}He(γ,pp)n", *Phys. Rev.*, **C53**, 1506, (1996).

Beamline X6A

L. Lee, and C.M. Ogata, "Simultaneous Multiwavelength Anomalous Diffraction (SMAD): an Energy-Dispersive Synchrotron Diffraction Method for Macromolecules", *J. Appl. Cryst.*, **28**, 661, (1995).

Beamline X6B

J. Bai, E.E. Fullerton, and P.A. Montano, "Resonant X-ray Reflectivity Study of Fe/Cr Superlattices", *Physica* , **B221**, 411, (1996).

L.X. Chen, Z. Wang, J.K. Burdett, P.A. Montano, and J.R. Norris, "X-ray Absorption Studies on Electronic Spin State Transitions of Fe(II) Complexes in Different Media", *J. Phys. Chem.*, **99**, 7958-7964, (1995).

A. Malik, M.K. Durbin, A.G. Richter, K.G. Huang, and P. Dutta, "Structures of Head-group and Tail-group Monolayers in a Langmuir-Blodgett Film", *Phys. Rev.*, **B52/16**, 654-657, (1995).

H. You, K.G. Huang, and R.T. Kampwirth, "Off-Specular Reflectivity Study of Sputter-Deposition of During Growth", *Physica*, **B221**, 77, (1996).

H. You, Z. Nagy, K.G. Huang, and S.S. Yoo, "*In Situ* Synchrotron X-ray Scattering Study of Incipient Formation Porous Silicon", Electrochemical Soc. Proc., **92/25**, 230, (1995).

Beamline X7A

W. Dmowski, T. Egami, R.J. Gorte, and J.M. Vohs, "Structure of Oxide Overlayer Studied by Energy Dispersive X-ray Diffraction", *Physica,* **B221**, 420, (1996).

W. Dmowski, S. Fu, T. Egami, R. Gorte, and J. Vohs, "Structure of Ceria Overlayer on Zirconia Crystal Studied by Surface Diffraction", *Mat. Res. Soc. Conf. Proc.*, **401**, 115, (1996).

T. Egami, W. Dmowski, P. Kosmetatos, M. Boord, T. Tomida, E. Oikawa and A. Inoue, "Deformation Induced Bond Orientational Order in Metallic Glasses", *J. Non-Cryst. Solids.*, **192/193**, 591, (1995).

C. Eylem, Y.-C. Hung, H.L. Ju, J.Y. Kim, D.C. Green, T. Vogt, J.A. Hriljac, B.W. Eichorn, R.L. Greene, and L. Salamanca-Riba, "Unusual Metal-Insulator Transitions in the $LaTi_{1-x}V_xO_3$ Perovskite Phases", *Chem. Mat.*, **8**, 418, (1996).

C. Eylem, J.A. Hirljac, V. Ramamurthy, D.R. Corbin, and J.B. Parise, "Structure of a Zeolite ZSM-5-Bithiophene Complex as Determined by High Resolution Synchrotron X-ray Powder Diffraction", *Chem. Mat.*, **8**, 844, (1996).

J.E. Fischer, "Fulleride Superconductors: What we Know and What we Don't Know", NATO ARW Series, edited by W. Andreoni, *Kluwer, Dordrecht*, **E316**, p. 359, (1996).

C. C. Freyhardt, M. Tsapatsis, R. F. Lobo, K. J. Balkus, Jr., and M. E. Davis, "A High-Silica Zeolite with a 14 Tetrahedral-Atom Pore Opening", *Nature*, **381**, 295, (1996).

J.B. Higgins, and K.D. Schmitt, "ZSM-10: Synthesis and Tetrahedral Framework Structure", *Zeolites*, **16**, 236, (1996).

D. C. Johnston, T. Ami, F. Borsa, M. K. Crawford, J. A. Fernandez-Baca, K. H. Kim, R. L. Harlow, A. V. Mahjan, L. L. Miller, M. A. Subramanian, D. R. Torgeson, and Z. R. Wang, "Superconductivity, Magnetism, and Metal-Insulator Transitions in Some Ternary and Pseudoternary 3d-, 4d- and 5d-Metal Oxides", Proc. 17th International Taniguchi Symp. on Theoretical Physics, *Springer Series in Solid-State Sciences*, **119**, 241, (1995).

K. Kniaz, J. E. Fischer, L. A. Girifalco, A. R. McGhie, R. M. Strongin, and A. B. Smith III, "Fullerene Alloys", *Solid State Commun.*, **96**, 739, (1995).

M. Kunz, R. Dinnebier, L.K. Cheng, E.M. McCarron, D.E. Cox, J.B. Parise, M. Gehrke, J. Calabrese, P.W. Stephens, T. Vogt, and R. Papoular, "$Cs(Ti,As)O_5$ and $Cs(Ti,P)O_5$: A Disordered Parent Structure of $ABOCO_4$ Compounds", *J. Solid State Chem.*, **120**, 299, (1995).

K. I. Pandya, S. M. Heald, J. A. Hriljac, L. Petrakis,, and J. Fraissard, "Characterization by EXAFS, NMR and Other Techniques of Pt/Na-Y Zeolite at Industrially Relevant Low Concentration of Platinum", *J. Phys. Chem.*, **100**, 5070, (1996).

R. J. Papoular, and D. E. Cox, "Model-free Search for Extra-Framework Cations in Zeolites Using Powder Diffraction", *Europhysics Letters*, **32**, 337, (1995).

J.B. Parise, "Structural Case Studies of Inclusion Phenomena in Zeolites: Xe in RHO and Stilbene in ZSM-5", *J. Incl. Phenom. Molec. Recog. Chem.*, **21**, 79, (1995).

P.G. Radaelli, D.E. Cox, M. Marezio, S.-W. Cheong, P.E. Schiffer, and A.P. Ramirez, "Simultaneous Structural, Magnetic, and Electronic Transitions in $La_{1-x}Ca_xMnO_3$ with x=0.25 and 0.5", *Phys. Rev. Lett.*, **75**, 4488, (1995).

D. Ramprasad, G.P. Pez, B.H. Toby, T.J. Markley and R.M. Pearlstein, "Solid State Lithium Cyanocobaltates with High Capacity for Reversible Dioxygen Binding: Synthesis, Reactivity and Structures", *J. Am. Chem. Soc.*, 117, 10694, (1995).

M. A. Subramanian, W. J. Marshall, and R. L. Harlow, "NH_4CoAlF_6: a Pyrochlore-Related Phase Existing in Both Ordered and Disordered Forms", *Mat. Res. Bull*, **31**, 585, (1996).

O. Terasaki, T. Ohsuna, H. Sakuma, D. Watanabe, Y. Nakagawa, and R. C. Medrud, "Direct Observation of "Pure MEL Type" Zeolite", *Chem. Materials*, **8**, 463, (1996).

G. Vitale, L.M. Bull, R.E. Morris, A.K. Cheetham, B.H. Toby, C.G. Coe, and J.E. MacDougall, "Combined Neutron and X-ray Powder Diffraction Study of Zeolite Ca LSX and a 2H NMR Study of its Complex with Benzene", *J. Phys. Chem.*, **99**, 16087, (1995).

J.K. Warner, A.K. Cheetham, and D.E. Cox, "Determination of the Cation Distribution in $NiFe_2(PO_4)_2$ by Resonant X-ray and Neutron Powder Diffraction", *J. Appl. Cryst.*, **28**, 495, (1995).

T. Yildirim, L. Barbedett, J.E. Fischer, C.L. Lin, J. Robert, and P.Petit, "Fulleride Superconductors: Dependence of T_c on Average Molecular Valence in $Na_2Cs_xC_{60}$, $0 < x < 1$", *Synthetic Metals*, 77, 195, (1995).

T. Yildirim, L. Barbedette, J. E. Fischer, C. L. Lin, J. Robert, P. Petit, and T.T.M. Palstra, "T_c vs Carrier Concentration in Cubic Fulleride Superconductors", *Phys. Rev. Lett.*, 77, 167 (1996).

Q. Zhu, "Polymer and Dimer Formation in Alkali-Metal Intercalated C60", Recent Advances in the Chemistry and Physics of Fullerenes and Related Materials, edited by K.M. Kadish and R.S. Ruoff, **2**, 798, (1995).

Q. Zhu, A. Botchkarev, W. Kim, O. Atkas, A. Salvador, B. Sverdlov, H. Morkoç, S-C. Y. Tsen, and D. J. Smith, "Structural Properties of GaN Films Grown on Sapphire by Molecular Beam Epitaxy", *Appl. Phys. Lett.*, **68**, 1141, (1996).

Beamline X7B

J. Aizenberg, J. Hanson, T.F. Koetzle, L. Leiserowitz, S. Weiner, and L. Addadi, "Biologically-Induced Reduction in Symmetry: A Study of Crystal Texture of Calcitic Sponge Spicules", *Chem: A European Journal*, **1**, 414-422, (1995).

A.N. Christensen, P. Norby, and J.C. Hanson, "A Synchrotron X-Ray Powder Diffraction Study of $CoAl_2O_4$ and $CoGa_2O_4$ by PSD Diffractometer Technique", *Powder Diffraction*, **10**, 185-188, (1995).

A. N. Christensen, P. Norby and J. C. Hanson, "Time-Resolved Synchrotron X-Ray Powder Diffraction Study on Samples from the Samples from the System MgO-$MgCl_2$-H_2O", *Acta Chem Scand.*, **49**, 331-334, (1995).

M. Helliwell, J.R. Helliwell, J.C. Hanson, T. Ericsson, Å. Kvick, V. Kaucic, C. Frampton, and A. Cassetta, "Determination of the Nickel Atom Site in an Aluminophosphate Crystal by Anomalous Dispersion Techniques Using Synchrotron Radiation", *Acta Cryst.*, **B52**, 479-486, (1996).

P. Norby, I.G. Krogh Andersen, E. Krogh Andersen, and N.H. Andersen, "The Crystal Structure of Lanthanum Manganate (III), $LaMnO_3$, at Room Temperature and at 1273 K under N_2", *Solid State Chem.*, **119**, 191-196, (1995).

Q.M. Zhang, and J.Z. Larese, "Freezing Transitions and Order-Disorder Processes in Multilayer Xenon Films on Graphite", *Phys. Rev.*, **B52**, 11335-11338, (1995).

Beamline X8A

G. Chartas, G. Garmive, J. Nousek, L. Townsley, F. Powell, R. Blake, and L Graessle, "ACIS UV/Optional Blocking Filter Calibration at the National Synchrotron Light Source", *SPIE*, **B2805**, 44-54, (1996).

J.J. Fitch, D.E. Graessle, B. Harris, J.P. Hughes, D.T. Nguyen, D.A. Schwartz, and R.L. Blake, "Analysis of Ioidium Reflectance Measurements for AXAF Witness Mirrors from 2-12 keV", *SPIE*, **B2805**, 311-322, (1996).

D.E. Graessle, A.M. Clark, J.J. Fitch, B. Harris, D.A. Schwartz, and R.L. Blake, "Reflectance Calibrations of AXAF Witness Mirrors using Synchrotron Radiation, 2-12 keV", *SPIE*, **B2805**, 18-31, (1996).

B. Harris, D.E. Graessle, J.J. Fitch, J. Juda, R.L. Blake, M.L. Schattenburg, and E.M. Gullikson, "Ioidium Optical Constants from X-ray Transmission Measurements over 2-12 keV", *SPIE*, **B2805**, 323-334, (1996).

T.H. Markert, D. Dewey, J.E. Davis, K.A. Flanagan, D.E. Graessle, J.M. Bauer, and C.S. Nelson, "Modeling the Diffraction Efficiencies of the AXAF High Energy Transmission Gratings", *SPIE*, **2518**, (1995).

Beamline X9B

E. Anni, J.M. Vanderkooi, and M.R. Chance, "Extended X-Ray Absorption Fine Structure Studies of Zinc Derivative of Cytochrome c", *Biophysical J.*, **70**, A153, (1996).

D.S. Auld, K.H. Falchuck, K. Zhang, M. Motorzi, and B.L. Vallee, "X-ray Absorption Fine Structure as a Monitor of Zinc Coordination Sites During Oogenesis of Xenopus Laevis", *Proc. Natl. Acad. Sci.*, **93**, 3227-3231, (1996).

B. A. Brennan, G. Alms, M. J. Nelson, L. T. Durney, and R. C. Scarrow, "Nitrile Hydratase from Rhodococcus rhodochrous J1 Contains a Non-Corrin Cobalt Ion with Two Sulfur Ligands", *J. Am. Chem. Soc.*, **115**, 9194-9195, (1996).

J. Briggs, H. Chung, and M. Caffrey, "The Temperature-Composition Phase Diagram and Mesophase Structure Characterization of the Monoolein/Water System" *J. Physique II France,* **6**, 723-751, (1996).

M.R. Chance, R. Fischetti, L.M. Miller, E.M. Scheuring,. B. Sclavi, Y. Hai, and M. Sullivan, "Global Mapping of Structural Solutions Provided by the Extended X-ray Absorption Fine Structure *ab initio* Code FEFF 6.01: Structure of the Cryogenic Photoproduct of the Myoglobin-Carbon Monoxide Complex", *Biochemistry,* **35**, 9014-9023, (1996).

D. Chen, and L. Powers, "Synthesis and Structures of $Zn(C_6H_{12}OS_2)_2(C10_4)_2$ and $Zn(C_3H_6NS_2)_2(C_3H_4N_2)$ - Model Compounds for the Zinc Sites in RNA Polymerase", *J. Inorg. Biochem.*, **58**, 245, (1995).

A. Cheng, and M. Caffrey, "Chain Melting Transition Mechanism in Model Membranes", *J. Phys. Chem.*, **100**, 5608-5610, (1996).

A. Cheng, and M. Caffrey, "Free Radical Mediated X-Ray Damage of Model Membranes", *Biophys. J.*, **70**, 2212-2222, (1996).

A. Cheng, A. Mencke, and M. Caffrey, "Manipulating Mesophase Behavior of Hydrated DHPE: An X-Ray Diffraction Study of Temperature and Pressure Effects", *J. Phys. Chem.*, **100**, 299-306, (1996).

B. He, R. Sinclair, R. Makino, G. Schonbaum, L. Powers, and I. Yamazaki, "The Structure ↔ Function Relationship and Reduction Potentials of High Oxidation States of Myoglobin and Peroxidase", *Biochemistry*, **35**, 2413, (1996).

K.C. Holmes, "Solving the Structure of Macromolecular Complexes with the Help of X-ray Fiber Diffraction Diagrams", *J. of Struct. Bio.*, **115**, 151-158, (1995).

M.J. Maroney, M.A. Pressler, S.A. Mirza, J.P. Whitehead, R.J. Gurbiel, and B.M. Hoffman, "Insights into the Role of Nickel in Hydrogenase", in Mechanistic Bioinorganic Chemistry, edited by H. Thorp, and V. Pecoraro, *Advances in Chemistry*, **246**, 21-60, (1995).

L.M. Miller, M. Patel, and M.R. Chance, "Identification of Conformational Substates in Oxy Myoglobin Through the pH-Dependence of the Low Temperature Photoproduct Yield", *J. Amer. Chem. Soc.*, **118**, 4511-4517, (1996).

L.M. Miller, E.M. Scheuring, H. Wang, G. Peng, S.P. Cramer, and M.R. Chance, "L-Edge X-Ray Absorption Spectroscopy of Ligand-Bound and Photoproduct States of Myoglobin", *Biophysical J.*, **70**, A219, (1996).

M.A. Murphy, E. Nordgren, R.F. Fischetti, J.K. Blasie, L.J. Peticolas, and J.C. Bean, "A Structural Study of the Annealing of Akylsiloxane Self-Assembled Monolayers on Silicon by High-Resolution X-Ray Diffraction", *J. Phys. Chem.*, **99/38**, 14039-14051, (1995).

M.J. Nelson, B.A. Brennan, D.B. Chase, R.A. Cowling, G.N. Grove, and R.C. Scarrow, "Structure and Kinetics of Formation of Catechol Complexes of Ferric Soybean Lipoxygenase-1", *Biochemistry*, **34**, 15219-15229, (1995).

L.A. Prokop, R.M. Strongin, A.B. Smith, III, J.K. Blasie, L.J. Peticolas, and J.C. Bean, "Profile Structures of Vectorially Oriented Monolayers of Detergent-Solubilized Ca^{+2}ATPase from Sarcoplasmic Reticulum", *Biophys. J.*, **70**, 2131-2143, (1996).

P.J. Riggs-Gelasco, T.L. Stemmler, and J.E. Penner-Hahn, "XAFS of Dinuclear Metal Sites in Proteins and Model Compounds", *Coord. Chem. Rev.* , **144**, 245-286, (1995).

M.J. Ryle, W.N. Lanzilotta, L.C. Seefeldt, R.C. Scarrow, and G.M. Jensen, "Circular Dichroism and X-ray Spectroscopies of Azotobacter Vinelandii Nitrogenase Iron Protein", *J. Biol. Chem.*, **271**, 1551-1557, (1996).

R.C. Scarrow, B.A. Brennan, J.G. Cummings, H. Jin, D.J. Duong, J.T. Kindt,and M.J. Nelson, "X-Ray Spectroscopy of Nitrile Hydratase at pH 7 and 9", *Biochemistry*, **35**, 10078, (1996).

E.M. Scheuring, W. Clavin, M.D. Wirt, L.M. Miller, Y. Lu, N. Mahoney, A. Xie, J.J. Wu, and M.R. Chance, "Time-Resolved X-ray Absorption Spectroscopy of an Enzymatically Important Coenzyme B_{12} Derivative", *J. Phys. Chem.*, **100**, 3344-3348, (1996).

E.M. Scheuring, S.Huang, R.G. Matthews, and M.R. Chance, "Structure-Function of Cobalamin Dependent Enzymes: X-Ray Absorption Studies on Methionine Synthase from *E. Coli*", *Biophysical J.*, **70**, A437, (1996).

L.C. Seefeldt, M.J. Ryle, W.N. Lanzilotta, R.C. Scarrow, and G.M. Jensen, "Circular Dichroism and X-Ray Spectroscopies of Azotobacter Vinelandii Nitrogenase Iron Protein: MgATP and MgADP Induced Protein Conformational Changes Affecting the [4Fe-4S] Cluster and Characterization of a [2Fe-2S]=46orm", *J. Biol. Chem.* **271**, 1551-1557, (1996).

R. Sinclair, B. Copeland, I. Yamazaki, and L. Powers, "X-Ray Absorption Spectroscopy Comparison of the Active Site Structures of *Phanerochaete Chrysosporium* Lignin Peroxidase Isoenzymes H2, H3, H4, H5, H8, and H10", *Biochemistry*, **34**, 13176, (1995).

T.L. Stemmler, Kinetic and Spectroscopic Characterization of the Native and Inhibitor Bound Forms of the *Lactobacillus Plantarum* Mn Catalase and Related Proteins. PhD. Thesis., University of Michigan, May 1996.

T.L. Stemmler, T.M. Barnhart, J.E. Penner-Hahn, C.E. Tucker, P. Knochel, M. Bohme, and G. Frenking, "Structural Characterization of Organocuprate Reagents. EXAFS Spectroscopy of *Ab Initio* Calculations", *J. Am. Chem. Soc.*, **117**, 12489-12497, (1995).

H.T. Tsang, C.J. Batie, D.P. Ballou, and J.E. Penner-Hahn, "Structural Characterization of the Mononuclear Iron Site in *Pseudominas Cepacia* Phthalate DB01 Dioxygenase Using X-Ray Absorption Spectroscopy", *J. Biol. Inorg. Chem.*, **1**, 24-33, (1996).

K. Zhang, and D.S. Auld, "Structures of Binary and Ternary Inhibitor Complexes of Zinc and Cobalt Carboxypeptidase A as Determined by XAFS", *Biochemistry*, **34**, 16306-16312, (1995).

T. Zhu, The Effect of Anti-Viral Peptides on the Physical Properties of Membranes, PhD. Thesis, Ohio State University, June 1996.

Beamline X10A

W.H. De Jeu, J.D. Shindler, S. Chandavarkar, R.M. Geertman, and K. Liang, "On the (Absence of) Surface Melting in Biphenyl", *Surf. Sci.*, **342**, 341, (1995).

J.H. Je, D.Y. Noh, H.K. Kim, and K.S. Liang, "A Real-Time X-ray Scattering Study of Sputtering Growth of TiN Films", in Application of Synchrotron Radiation Techniques to Materials Science, edited by D.L. Perry, et al., *MRS Symp. Proc.*, **375**, 1, (1995).

J. Li, K.S. Liang, N. Camillone III, T.Y.B. Leung, and G. Scoles, "The Structure of n-Octadecane Thiol Monolayers Self-Assembled on Au(001) Studied by Synchrotron X-ray and Hellium Atom Diffraction", *J. Chem. Phys.*, **102**, 5012, (1995).

J. Li, K.S. Liang, G. Scoles, and A. Ulman, "Counterion Overlayers at the Interface Between an Electrolyte and an w-Functionalized Monolayer Self-Assembled on Au. An X-ray Specular Reflectivity Study", *Langmuir*, **11**, 4418, (1995).

D.Y. Noh, M. Hong, Y. Hwu, J.H. Je, and J.P. Mannaerts, "Strain Relaxation in Fe3(Al,Si)/GaAs: An X-ray Scattering Study", *Appl. Phys. Lett.*, **68**, 1528, (1996).

D.Y. Noh, Y. Hwu, and M. Hong, "X-ray Scattering Studies of the Interfacial Structure of Au/GaAs", *Phys. Rev.*, **B51**, 4441, (1995).

S.B. Rivers, W.N. Unertl, H.H. Hung, and K.S. Liang, "Order-Disorder Transition at the (001) Surface of a 3 at.% Au-rich Cu_3Au Crystal", *Phys. Rev.*, **B52**, 12601, (1995).

E.B. Sirota, H.E. King, Jr., H.H. Shao, and D.M. Singer, "Rotator Phases in Mixtures of n-Alkanes", *J. Phys. Chem.*, **99**, 798, (1995).

X.Z. Wu, H.H. Shao, B.M. Ocko, M. Deutsch, S.K. Sinha, M.W. Kim, H.E.J. King, and E.B. Sirota, "Surface Crystallization and Thin Film Melting in Normal Alkanes", Dynamics in Small Confining Systems II, edited by J.M. Drake, J. Klafter, R. Kopelman, and S.M. Troian, *Mat. Res. Soc. Symp. Proc.*, **366**, 15, (1995).

Beamline X11A

D.B. Aldrich, Y.L. Chen, D.E. Sayers, and R.J. Nemanich, "Titanium Germanosilicide Phase Formation During the Ti-$Si_{1-x}Ge_x$ Solid Phase Reactions", *Mat. Res. Soc. Symp. Proc.*, **402**, 405, (1996).

D.B. Aldrich, Y.L. Chen, D.E. Sayers, R.J. Nemanich, S.P. Ashburn, and M.C. Ozturk, "Effect of Composition on Phase Formnation and Morphology in Ti-$Si_{1-x}Ge_x$ Solid Phase Reactions", *J. Mater. Res.*, **10**, 2849, (1995).

D.B. Aldrich, Y.L. Chen, D.E. Sayers, R.J. Nemanich, S.P. Ashburn, and M.C. Ozturk, "Stability of C54 Titanium Germanosilicide on a Silicon-Germanium Alloy Substrate", *J. Appl. Phys.*, 77, 5107, (1995).

D.B. Aldrich, H.L. Heck, Y.L. Chen, D.E. Sayers, and R.J. Nemanich, "Film Thickness Effects in the Ti-$Si_{1-x}Ge_x$ Solid Phase Reaction", *J. Appl. Phys.*, **78**, 4958, (1995).

D.B. Aldrich, F.M. D'Heurle, D.E. Sayers, and R.J. Nemanich, "Interface Stability of $Ti(Si_{1-y}Ge_y)_2$ and $Si_{1-x}Ge_x$ Alloys", *Mat. Res. Soc. Symp. Proc.*, **402**, 21, (1996).

D.B. Aldrich, R.J. Nemanich, and D.E. Sayers, "Bond-Length Relaxation in $Si_{1-x}Ge_x$ Alloys", *Phys. Rev.*, **B50**, 15026, (1994).

E.M. Coe, L.H. Bowen, J.A. Speer, Z. Wang, D.E. Sayers, and R.D. Bereman, "The Characterization of a Polysaccharide Iron Complex (Niferex)", *J. Inorgan. BioChem.*, **58**, 269, (1995).

Y. Dao, A.M. Edwards, R.J. Nemanich, and D.E. Sayers, "Local Structural Studies of $(Ti_{1-x}Zr_x)Si_2$ Thin Films on Si(111)", *Physica*, **B208-209**, 513, (1995).

Y. Dao, A.M. Edwards, H. Ying, Y.L. Chen, D.E. Sayers, and R.J. Nemanich, "Structural and Electrical Properties of $(Ti_{0.9}Zr_{0.1})Si_2$ Thin Films on Si(111)", *Appl. Phys. Lett.*, **65**, 2413, (1994).

Y. Dao, D.E. Sayers, and R.J. Nemanich, "Morphology and Stability of $(Ti_{0.9}Zr_{0.1})Si_2$ Thin Films on Si(111) and Si(100) Formed in UHV" *Thin Solid Films*, **270**, 544, (1995).

Y. Dao, D.E. Sayers, and R.J. Nemanich, "Phase Stabilities and Surface Morphologies of $(Ti_{1-x}Zr_x)Si_2$ Thin Films on Si(111)", *J. Appl. Phys.*, **78**, 6584, (1995).

P.T. Goeller, Z. Wang, D.E. Sayers, J.T. Glass, and R.J. Nemanich, "Epitaxial Films of Cobalt Disilicide (100) Evaporated onto Si(100) From a Mixed Source", *Mat. Res. Soc. Symp. Proc.*, **402**, 511, (1996).

Q. Lu, "XAFS Investigations of Structural Properties at Internal Interfaces", Ph.D. Dissertation, Notre Dame University, May 1996.

A.N. Mansour, C.A. Melendres, S.J. Poon, Y. He, and G.J. Shiflet, "An X-ray Absorption Near-edge Study of the Structure of Passive Films on Amorphous Al-Fe-Ce Alloys", *J. Electrochem. Soc.*, **143**, 614, (1996).

M. Marcus, D. Jacobson, A. Vredenberg, and G.M. Lamble, "Concentrations and Annealing Effects on Photoluminescence and Local Structure of Erbium Implanted Silica", *J. Of Non-Crystl. Solids*, **95**, 232, (1996).

R.A. Mayanovic, and B.A. Bunker, "Observation of Anisotropic Vibrational Amplitudes due to Thermal Motion at a Cu/Al_2O_3 Interface", *Phys. Lett.*, **A202**, 225, (1995).

J. McBreen, X.Q. Yang, and H.S. Lee, "X-ray Absorption Studies of $NiBr_2(PEO)_8$ and $ErBr_3(PEO)_{12}$ Complexes", *Macromol. Symp.*, **105**, 185, (1996).

W.E. O'Grady, K.I. Pandya, K.E. Swider, and D.A. Corrigan, "*In Situ* X-ray Absorption Near Edge Structure Evidence for Quadrivalent Nickel in Nickel Battery Electrodes", *J. Electrochem. Soc.*, **143**, (1996).

K.I. Pandya, S.W. Heald, and J.A. Hriljac, "Characterizations by EXAFS, NMR and Other Techniques of Pt/NaY Zeolites at Industrially Relevant Low Concentrations of Platinum", *J. Phys. Chem.*, **100**, 5070, (1996).

G. Pfeiffer, J.J. Rehr, and D.E. Sayers, "The Near-Edge Structure of a-As_2S_3 and Pressure Induced Changes", *Physica*, **B208/209**, 385, (1995).

G. Pfeiffer, J.J. Rehr, and D.E. Sayers, "XAFS Near-Edge Structure of As_2S_3: A Comparison of Experiment and Theory", *Phys. Rev.* , **B51**, 804, (1995).

A.M. Scheidegger, G.M. Lamble, and D.L. Sparks, "Ni Absorption on Pyrophyllite: An XAS Study", *Environ. Sci. Tech.*, **30**, 548, (1996).

N.D. Triantafillou, S.E. Deutsch, O. Alexeev, J.T. Miller, and B.C. Gates, "Ir/KLTL Zeolites: Structural Characterization and Catalysis of η-Hexane Reforming", *J. Of Catalysis*, **159**, 14, (1996).

Z. Wang, D.B. Aldrich, Y.L. Chen, D.E. Sayers, and R.J. Nemanich, "Silicide Formation and Stability of Ti/SiGe and Co/SiGe", *Thin Solid Films*, **270**, 555, (1995).

Z. Wang, D.B. Aldrich, P. Goeller, R.J. Nemanich, and D.E. Sayers, "Characterization of Zirconium Germanosilicide Formed by Solid State Reaction of Zr with $Si_{1-x}Ge_x$ Alloys", *Mat. Res. Soc. Symp. Proc.*, **402**, 387, (1996).

Z. Wang, R.J. Nemanich, and D.E. Sayers, "EXAFS and XRD Studies of Phase Formations of Co in Reactions with Si-Ge Alloys", *Physica*, **B208/209**, 567, (1995).

A. Zhao, and B.C. Gates, "Hexairidium Clusters Supported on Y-Al_2O_3: Synthesis, Structure, and Catalytic Activity for Toluene Hydrogenation", *J. Am. Chem. Soc.*, **118**, 2458, (1996).

Beamline X12B

M.V. Brillhart, P. Cebe, and M.S. Capel, "Real-Time X-ray Scattering of Binary Polymer Blends: Poly(Butylene Terephthalate)/Polycarbonate", Advances in X-ray Analysis, edited by Predecki, *et al*, *Plenum*, **38**, p. 489, (1995).

M.S. Capel, G.C. Smith and B. Yu, "One- and Two-Dimensonal X-ray Detector Systems at NSLS Beamline X12B, for Time-Resolved and Static X-ray Diffraction Studies", *Rev. Sci. Instr*um., **66/2**, 2295, (1995).

Y.Y. Cheng, P. Cebe, M.S. Capel, H. Schreuder-Gibson, A. Bluhm, and W. Yeomans, "Small-Angle X-ray Scattering Study of Liquid-Crystalline Polycarbonates based on Alpha-Methyl Stilbene Mesogen and Methylene-Containing Flexible Spacer", *J. Polymer Sci, Part B-Polymer Phy.*, **33/17**, 2331, (1995).

J.M. Flanagan, J.S. Wall, M.S. Capel, D.K. Schneider and J. Shanklin, "Scanning Transmission Electron Microscopy and Small-Angle Scattering Provide Evidence that Native *Eschericia coli* ClpP is a Tetradecamer with an Axial Pore", *Biochem.*, **34**, 10910, (1995).

J.L. Fulton, D.M. Pfund, J.B. McClain, T.J. Romack. E.E. Maury, J.R. Combes, E.T. Samulski, J.M. Desimone and M.S. Capel, "Aggregation of Amphiphilic Molecules in Supercritical Carbon-Dioxide-a Small-Angle X-ray Scattering Study", *Langmuir*, **11**, 4241, (1995).

R.B. Knott, M.S. Capel, S. Hansen, and R.E. Schumacher, "A Small-Angle Scattering Study of the Binding of Cyclosporin-a to Cyclophillin", *J. Appl. Cryst.*, **28**, 546, (1995).

S.X. Lu, P. Cebe, and M.S. Capel, "Structure and Relaxation using SAXS and TSDC", *J. Appl. Polymer Sci.*, **57**, *1359, (1995).*

S.X. Lu, P. Cebe, and M.S. Capel, "Thermal Stability and Thermal Expansion Studies of PEEK and Related Polyimides", *Polymer*, **37/14**, 2999, (1996).

A.J. Quantock, N.J. Fullwood, E.J-M.A. Thonar, S.R. Waltman, M.S. Capel, M.C. Kincaid, M. Ito, S.M. Verity and D.J. Schanzlin, "Stromal Descements and Endothelial Changes in Macular Dystrophy Type II", *Invest. Opthamol. & Vis. Sci.*, **37**, 1019, (1996).

A.J. Quantock, G.K. Klintworth, D.J. Schanzlin, M.S. Capel, M.E. Lenz, and E.J-M.A. Thonar, "Proteoglycans contain a 4.6 Å Repeat in Macular Dystrophy Corneas: X-ray Diffraction Evidence", *Biophys. J.*, **70**, 1966, (1996).

G.J. Salomons, M.A. Singh, J.A. Gupta, W.A. Foran, M.S. Capel, and J.R. Clarke, "Apparatus for SAXS Measurements of Polymer Deformation", *Rev. Sci. Instrum.*, **67/4**, 1748, (1996).

G.J. Salomons, M.A. Singh, L.G. Hiltz, L.H. Pan & W.R. Newson, "SAXS Study of Deformation Mechanisms in Liquid Rubber-Toughened Polystyrene", *NIM,* **B97**, 282-286, (1996).

H.S. Subramanya, A.J. Doherty, S.R. Ashford, and D.B. Wigley, "Crystal-Structure of an ATP-Dependent DNA-Liagse from Bacteriophage T-7", *Cell,* **85/4**, 607-616, (1996).

Y. Tselikas, N. Hadjichristidis, R.L. Lescanec, C.C. Honeker, M. Wohlgemuth, and E.L. Thomas, "Architecturally-Induced Tricontinous Cubic Morphology in Compositionally Symmetric Miktoarm Starblock Copolymers", *Macromolecules*, **29**, 3390-3396, (1996).

D. Xia, C.A. Yu, J. Deisenhoffer, J.Z. Xia, and L. Yu, "3-Dimensional Structure of Beef Heart Mitochondrial Cytochrome BC(1) Complex", *Biophysical J.*, **7/2**, TMU5, (1996).

X. Xie, T. Kokubo, S.L. Cohen, U.A. Mirza, A. Hoffmann, B.T. Chait, R.G. Roeder, Y. Nakatani, and S.K. Burley, "Structural Similarity Between TAFS and the Heterotetrameric Core of the Histone Octamer", *Nature*, **380**, 316-322, (1996).

C.A. Yu, J.Z. Xia, A.M. Kachurian, L. Yu, D. Xia, H. Kim, and J. Deisenhofer, "Crystallization and Preliminary Structure of Beef Heart Mitochondrial Cytochrome BC(1) Complex", *Biochim. et Biophys. Acta-Bioenerg.*, **1275/12**, 47-53, (1996).

Beamline X12C

N.O. Concha, B.A. Rasmussen, K. Bush, and O. Herzberg, "Crystal Structure of the Wide-Spectrum Binuclear Zinc β-Lactamase from *Bacteroides Fragilis*", *Structure*, **4**, 823-836, (1996).

J.Z. Ding, W.J. McGrath, R.M. Sweet, and W.F. Mangel, "Crystal Structure of the Human Adenovirus Proteinase with its 11-Amino-Acid Cofactor", *EMBO*, **15**, 1778-1783, (1996).

J. Fajer, K.M. Barkigia, D. Melamed, R.M. Sweet, H. Kurreck, J. von Gersdorff, M. Plato, H.C. Rohland, G. Elger, and K. Mobius, "Molecular Structures of Porphyrin-Quinone Models for Electron Transfer", *J. Phys. Chem.*, **100**, 14236-14239, (1996).

C.H. Kang, R. Chan, I. Berger, C. Lokshin. L. Green, L. Gold, and A. Rich, "Crystal Structure of the T4 regA Translational Regulator Protein at 1.9 Å Resolution", *Science*, **268**, 1170-1173, (1995).

Y. Kim, S. Eom, J. Wang, D. Lee, W. Suh, and T. Steitz, "Crystal Structure of Thermus Aquaticus DNA Polymerase", *Nature*, **376**, 612-616, (1995).

T. Klabunde, N. Straeter, R. Froehlich, H. Witzel, and B. Krebs, "Mechansim of Fe(III)-Zn(II) Purple Acid Phosphatase Based on Crystal Structures", *J. Mol. Biol.*, **259**, 737-748, (1996).

A. Matte, H. Goldie, R. Sweet, and L. Delbaere, "Crystal Structure of *Escherichia coli* Phosphoenolpyruvate Carboxykinase- A new Structural Family with the P-loop Nucleotide Triphosphate Hydrolase Fold", *J. Mol.. Biol.*, **256**, 126-143, (1996).

Beamline X13

Z. Xu, I. McNulty, K.J. Randall, L. Yang, E. Gluskin, E.D. Johnson, and T. Oversluizen, "X13A: A Versatile Soft X-ray Undulator Beamline", *Rev. Sci. Instrum.*, **66**, 1827, (1995).

Beamline X14A

T. Gog, P.M. Len, G. Materlik, D. Bahr, C.S. Fadley, and C. Sanchez-Hanke, "Multiple-Energy X-ray Holography: Atomic Images of Hematite (Fe_2O_3)", *Phys. Rev. Lett.*, **76/17**, 3132-3135, (1996).

T. Gog, R.H. Menk. F. Arfelli, P.M. Len, C.S. Fadley, and G. Materlik, "X-ray Holography with Atomic Resolution: Trying to Make it Work", *Synch. Rad. News*, **9/3**, 30-35, (1996).

A. Goyal, E.D. Specht, D.M. Kroeger, and T.A. Mason, "Effect of Texture on Grain Boundary Misorientation Distributions in Polycrystalline High Temperature Superconductors", *Appl. Phys. Letts.*, **68**, 711, (1996).

A. Goyal, E.D. Specht, D.M. Kroeger, J.E. Tkaczyk, C.L. Briant, and J.A. DeLuca, "Crystallization of Colonies of Locally Aligned Grains During Thallination of Spray-Pyrolyzed $TlBa_2Ca_2Cu_3O_x$ Thick Films", *Appl. Phys. Letts.*, **67**, 2563, (1995).

G.E. Ice, G.S. Painter, L. Shaffer, C.J. Sparks, F.W. Averill and X. Jiang, "Nanoscale Structure in Crystalline Solid Solution Alloys", *Nanostructured Materials.*, 7, 147, (1996).

B.C. Larson, J.Z. Tischler, E.D. Isaacs, P. Zschack, A. Fleszar, and A.G. Eguiluz, "Inelastic X-ray Scattering as a Probe of the Many-Body Local-Field Factor in Metals, *Phys. Rev. Lett.*, 77/7, 1346, (1996).

H. Roelofs, B. Schonfeld, G. Kostorz, W. Buhrer, J.L. Robertson, and P. Zschack, "Atomic and Magnetic Short-Range Order in Cu-17at. % Mn", *Scripta Mater.*, **34**, 1393, (1996).

E.D. Specht, and A. Goyal, "Microdiffraction Measurements of the Effects of Grain Alignment on Critical Current in High Temperature Superconductors", X-Ray Microbeam Technology and Applications, Edited by W. Yun, *SPIE*, p. 170, (1995).

J.Z. Tischler, B.C. Larson, L.A. Boatner, E.E. Alp, and T. Mooney, "Time-Sliced Mossbauer Absorption Spectroscopy using Synchrotron Radiation and a Resonant Bragg Monochromator", *J. Appl. Phys.*, **79**, 3686, (1996).

Beamline X15A

K.G. Huang, J. Zegenhagen, J.M. Phillips, and J.R. Patel, "Interface and Overlayer Structure of Epitaxial CaF_2 Thin Films on Si(111): An X-ray Scattering Study", *Physica*, **B221**, 19, (1996).

T.-L. Lee, Y. Qian, P.F. Lyman, J.C. Woicik, J.G. Pellegrino and M.J. Bedzyk, "The Use of X-ray Standing Waves and Evanescent-Wave Emission to Study Buried Strained-Layer Heterostructures", *Physica,* **B221**, 437, (1996).

P.F. Lyman, Y. Qian, and M.J. Bedzyk, "Analysis of the Dimerized Sb/Si(001)-(2x1) Surface by X-Ray Standing Waves", *Mat. Res. Soc. Symp. Proc.*, **375**, 121, (1995).

P.F. Lyman, Y. Qian,T.-L. Lee, and M.J. Bedzyk, "Adsorbate Structure and Vibrations on the Bi/Si(001)-(1x2) Surface", *Physica*, **B221**, 426, (1996).

Y. Qian, P.F. Lyman, and M.J. Bedzyk, "X-Ray Standing Wave Studies of Metal Ad-Dimers on Si(001)", *Scanning Microscopy,* **9**, 969, (1995).

Y. Qian, P.F. Lyman, T. Lee, and M.J. Bedzyk, "Thermal Vibration Amplitudes and Structure of Sb on Si(001)", *Physica*, **B221**, 436, (1996).

Beamline X15B

L. Niu, A.R. Karlicek, M. Geva, and P.H. Citrin, "Dopant Quantification by X-ray Absorption Spectroscopy: Zn in InP", *Mat. Res. Soc., Proc.*, **406**, 509, (1996).

Beamline X16A

C.A.M. Carvalho, H. Hashizume, A.W. Stevenson, and I.K. Robinson, "Electron Density Maps for the Si(111) 7-7 Surface Calculated with the Maximum-Entropy Technique using X-ray and Electron-Diffraction Data", Proceedings of the 4th International Conference on Surface X-ray and Neutron Scattering, *Physica*, **B221**, 469-486, (1996).

H.L. Meyerheim, S. Pflanz, R. Schuster, and I.K. Robinson, "Surface X-ray Diffraction on the Potassium Induced Reconstruction of the Ag(001) Surface", Proceedings of the 4th International Conference on Surface X-ray and Neutron Scattering, *Physica*, **B221**, 140-143, (1996).

H.L. Meyerheim, S. Pflanz, R. Schuster, and I.K. Robinson, "X-ray Structure Analysis on the K-Induced Reconstruction of Ag(001)", Proceedings of the 4th International Conference on Surface X-ray and Neutron Scattering, *Physica*, **B221**, 134-140, (1996).

I.K. Robinson and P. J. Eng, "Comparison of Surface and Bulk Short-Range Order in Cu_3Au", *Phys. Rev.* **B52**, 9955-63, (1995).
I.K. Robinson, W. Moritz, F. Jona, and M.A. van Hove, "In-Plane Lattice Reconstruction of Cu(100)", *Phys. Rev. Letts.*, **76**, 3659, (1996).

I.K. Robinson, K.L. Whiteaker, and D.A. Walko, "Cu Island Growth on Cu(110)", Proceedings of the 4th International Conference on Surface X-ray and Neutron Scattering, *Physica*, **B221**, 70-76, (1996).

R. Schuster, and I.K. Robinson, "Reconstruction-Induced Compression of the Cu(110) Surface", *Phys. Rev. Lett.*, **76**, 1671, (1996).

K.L. Whiteaker, I.K. Robinson, C. Benson, D.M. Smilgies, N. Onda, and H. von Kaenel, "Disordered Structure of Cubic Iron Silicide Films on Si(111)", *Phys. Rev.*, **B51**, 9715-21, (1995).

Beamline X16C

L.H. Greene, A.C. Abeyta, I.V. Roshchin, I.K. Robinson, J.F. Dorsten, T.A. Tanzer, and P.W. Bohn, "Optical Detection of the Superconducting Proximity Effect", *SPIE*, **2696**, 215-222, (1996).

Beamline X17B1

M. Kunz, K. Leinenweber, J.B. Parise, T.C. Wu, W.A. Bassett, K. Brister, D.J. Weidner, M.T. Vaughan, and Y. Wang, "The Baddeleyite-Type High Pressure Phase of Ca(OH)2", *High Press. Res.*, **14**, 311-319, (1996).

I. Martinez, J. Zhang, and R.J. Reeder, "*In Situ* X-ray Diffraction at High Pressure and High Temperature of Aragonite and Dolomite. Evidence for Dolomite Breakdown to Aragonite and Magnesite", *Amer. Min.*, **81**, 611-624, (1996).

Y. Wang, and D.J. Weidner, "(dm/dT)P of the Lower Mantle", *Pageoph Special Issue*, **146**, 533-549, (1996).

Y. Wang, D.J. Weidner, and F. Guyot, "Thermal Equation of State of $CaSi_{03}$ Perovskite", *J. Geophys. Res.*, **101**, 661-672, (1996).

J. Zhang, B. Li, W. Utsumi, and R.C. Liebermann, "*In Situ* X-ray Observations of the Coesite-Stishovite Phase Transition: Reversed Phase Boundary and Kinetics", *Phys. Chem. Miner.*, **23**, 1-10, (1996).

Beamline X17B2

R.E. Johnston, D. Washburn, E. Pisano, W.C. Thomlinson, D. Chapman, N.F. Gmür, Z. Zhong, and D. Sayers, "Preliminary Experience with Monoenergetic Photon Mammography" *SPIE*, **2432**, 434-441, (1996), BNL 62393.

J.A. Laissuc, P. Spanne, F.A. Dilmanian, M.M. Nawrocky, J.-O. Gebbers, D.N. Slatkin, and D.D. Joel, "Mikrobestrahlung von Gliosarkomen der Ratte: Zell-und Gewebeläsionen", *Schweiz. Med. Wochenschr.*, **125**, 1887, (1995).

E. Rubenstein, J.C. Giaocomini, H.J. Gordon, J.A.L. Rubenstein and G. Brown, "Xenon K-Edge Dichromographic Bronchography: Synchrotron Radiation Based Medical Imaging" *Nucl. Instrum. and Meth. in Phys. Res.*, **A364**, 360, (1995).

W. Thomlinson, "Synchrotron Radiation Applications in Medical Research", Proceedings of the International Conference on Industrial Applications of Synchrotron Radiation, pp. 98-126, (1996), BNL 62631.

W. Thomlinson, "Transvenous Coronary Angiography in Humans with Synchrotron Radiation", Proceedings of the International School of Physics "Enrico Fermi", Course CXXVIII-Biomedical Applications of Synchrotron Radiation, edited by E. Burattini, and A. Balera, IOS Press, pp. 127-153, (1996), BNL 60834.

Beamline X17C

J. Akella , "The Diamond Anvil Cell: Probing the Behavior of Metals under Ultrahigh Pressures", Science and Technology Review of Lawrence Livermore National Laboratory, pp. 17-27, (1996).

T. S. Duffy, J. Shu, H. K. Mao, and R. J. Hemley, "Single-Crystal X-ray Diffraction of Brucite to 14 GPa", *Phys. Chem. Minerals,* **22**, 277-281, (1995).

T. S. Duffy, C.-S. Zha, R. T. Downs, H. K. Mao, and R. J. Hemley, "Elastic Constants of Forsterite Mg_2SiO_4 to 16 GPa", *Nature*, **378**, 170-173, (1995).

H. Hua, J. Liu and Y. K. Vohra, "Pressure-Induced Amorphization in Gadolinium Scandium Gallium Garnet by X-ray Diffraction and Spectroscopic Studies", *J. Phys., Condense. Mat.*, **8** , 139-145, (1996).

K. J. Kingma, H. K. Mao, and R. J. Hemley, "Synchrotron X-ray Diffraction of SiO_2 to Multi-Megabar Pressures", *High Pressure Res.*, **14**, 363-374, (1996).

J. Liu and Y. K. Vohra , "Photoluminescence and X-ray Diffraction Studies on -Sm Doped Yttrium Aluminum Garnet to Ultrahigh Pressures of 338 GPa", *J. Appl. Phys.*, **79**, 7978-7982, (1996).

J. Liu and Y. K. Vohra , "Fluorescence Emission from High Purity Synthetic Diamond Anvil to 370 GPa", *Appl. Phys. Lett.*, **68**,. 2049-2051, (1996).

H. K. Mao and R. J. Hemley, "Energy Dispersive X-ray Diffraction of Micro-Crystals at Ultrahigh Pressures", *High Pressure Res.*, **14**, 257-267, (1996).

H. K. Mao and R. J. Hemley, "Experimental Studies of Earth Deep Interior: Accuracy and Versatility of Diamond Cells", *Phil. Trans. R. Soc. Lond.*, **A354**, 1-18, (1996).

L. J. Parker, T. Atou, and J. B. Badding, "Transition Element-like Chemistry for Potassium under Pressure", *Science*, **273**, 95-97, (1996).

S. M. Peiris, J. S. Sweeney, A. J. Campbell, and D. L. Heinz, "Pressure-Induced Amorphizations of Covellite, CuS", *J. Chem. Phys.*, **104**, 11-16, (1996).

S. K. Saxena, "Earth's Core", *Current Science*, **69**, 914-917, (1995).

S. K. Saxena, L. S. Dubrovinsky, P. Haggkvist, Y. Cerenius, G. Shen, and H. K. Mao, "Synchrotron X-ray Study of Iron at High Pressure and Temperature", *Science*, **269**, 1703-1704, (1995).

M. S. Somayazulu, L. W. Finger, R. J. Hemley, and H. K. Mao, "New High-Pressure Compounds in Methane-Hydrogen Mixtures", *Science*, 271, 1400-1402, (1996).

C. S. Yoo, J. Akella, A. J. Campbell, H. K. Mao, and R. J. Hemley, "Phase Diagram of Iron by *in situ* X-ray Diffracton: Implications for the Earth's Core", *Science*, **270**, 1473-1475, (1995).

Beamline X18A

F.Y. Hansen, L. W. Bruch, and H. Taub, "The Mechanism of Melting in Submonolayer Films of Nitrogen Molecules Adsorbed on the Basal Planes of Graphite", *Phys. Rev.*, **B52**, 8515-8527, (1995).

K. W. Herwig, B. Matthies, and H. Taub, "Solvent Effects on the Monolayer Structure of Long n-Alkane Molecules Adsorbed on Graphite", *Phys. Rev. Lett.*, 75, 3154-3157, (1995).

K. Hongladarom, V. Ugaz, D. Cinader, W. R. Burghardt, J. P. Quintana, B. S. Hsiao, M. D. Dadmun, W. A. Hamilton and P. D. Butler, "Birefringence, X-ray Scattering and Neutron Scattering Measurements of Molecular Orientation in Sheared Liquid Crystalline Polymer Solutions", *Macromolecules*, **29**, 5346-5355, (1996).

S. Mansour, G. Liedl and R. Vest, "Microstructural Developments and Dielectric Properties of Rapid Thermally Processed PZT Thin Films Derived by Metallo-organic Decomposition", *J. Am. Ceram. Soc*, **78/6**, 1617-23, (1995).

S.M. Williams, S. Maglic, C. Thomas, C.T. Lin, M.J. Wagoner, R.P.H. Chang, and J.B. Ketterson, "Growth and *in situ* Characterization of $YBa_2Cu_3Ox/LaAlO_3$ Superlattices", *Appl. Phys. Lett.*, **68**, 1485, (1996).

Yao, S. N. Ehrlich, G. Liedl and J. M. Honig, "Properties of NiS_{2-x} Se x (x = 0.51, 0.55, 0.63)", Metal-insulator Transitions Revisited, Edited by P. P. Edwards and C. N. R. Rao, Taylor & Francis Ltd., pp. 129-142, (1995).

Beamline X18B

K.C.C. Kharas, D.-J. Liu, and H.J. Robota, "Structure-Function Properties in Cu-ZSM-5 NO Decomposition and NO SCR Catalysts", *Catalysis Today*, **26/2**, 129, (1995).

D.-J. Liu, and H.J. Robota, "X-ray Absorption Spectroscopic Study of Cu in Cu-ZSM-5 During No Catalytic Decomposition", Reduction of Nitrogen Oxide Emissions, edited by U.S. Ozkan, S.K. Agarwal, and G. Marcelin, *ACS Symposium Book Series, No. 587*, **12**, 147, (1995).

Beamline X19A

K. Chae, S. Jung, Y. Lee, C. Whang, Y. Jeon, M. Croft, D. Sills, P. Ansari, and K. Mack, "Local Density of Unoccupied States in Ion-Beam-Mixed Pd-Ag Alloys", *Phys. Rev.*, **B53**, 10328, (1996).

K. Chae, Y. Lee, S. Jung, Y. Jeon, M. Croft, and C.Whang, "Valence Band Electronic Redistribution in Ion-Beam-Mixed Pd-Ag Alloys", *Nucl. Instrum. and Meths. In Phys. Rev.*, **B106**, 60, (1995).

E. Devlin, A. Kostikas, A. Simopoulos, A. Jankowski, M. Croft, and T. Tsakalakos, "Hyperfine Interactions and Magnetic Properties of Fe/Pt Multilayers", *J. Nano., Mat.*, **6**, (1995).

G.P. Huffman, Z. Feng, D. Bailey, J. Rockwell, J. Zhao, and F.E. Huggins, "Liquefaction of Commingled Waste Plastics Containing PVC", *ACS Div. Fuel Chem.*, **41/3**, 1043, (1996).

F.E. Huggins, F. Goodarzi, and C.J. Lafferty, "Mode of Occurrence of Arsenic in Subbituminous Coals", *Energy & Fuels*, **10/4**, 1001, (1996).

F.E. Huggins, S. Srikantapura, B.K. Parekh, L. Blanchard, and J.D. Robertson, "XANES Spectroscopic Characterization of Selected Elements in Deep-Cleaned Fractions of Kentucky #9 Coal", *ACS Div. Fuel Chem.*, **41/3**, 764, (1996).

F.E. Huggins, J. Zhao, G.P. Huffman, C.-H. Kao, and A.R. Tarrer, "Investigation of Zinc Additives in Coliquefaction of Waste Lubricating Oil and Bituminous Coal", *J. Environ. Sci. Health*, **A31**, 1755, (1996).

S. Morante, L. Furenlid, G. Schiavo, R. Zwilling, and C. Montecucco, "Zinc Coordination in Tetanus Neurotoxin, Astacin, Thermolysink and Alkaline Protease Studied by X-ray Absorption Spectroscopy", *Eur. J. Biochem.*, **235**, 606, (1996).

M.J. Nelson, B.A. Brennan, D.B. Chase, R.A. Cowling, G.N. Grove, and R.C. Scarrow, "Structure and Kinetics of Formation of Catechol Complexes of Ferric Soybean Lipoxygenase-1", *Biochemistry*, **34**, 15219, (1995).

R.C. Scarrow, B.A. Brennan, J.G. Cummings, H. Jin, D.J. Duong, J.T. Kindt, and M.J. Nelson, "X-ray Spectroscopy of Nitrile Hydratase at pH 7 and 9", *Biochemistry*, **35**, 10078, (1996).

C.L. Senior, L.E. Bool, G.P. Huffman, and F.E. Huggins, "A Fundamental Investigation of Toxic Substances from Coal Combustion", *ACS Div. Fuel Chem.*, **41/3**, 786, (1996).

A. Sahiner, M. Croft, Z. Zhang, M. Greenblatt, I.Perez, P. A. Metcalf, H. Jahns, G. Liang, and Y. Jeon "Electronic Structure Anisotropy and d-Configuration in Ni-Based Materials", *Phys. Rev.*, **B53**, 9745, (1996).

A.D. Shah, G.P. Huffman, F.E. Huggins, N. Shah, and J.J. Helble, "Behavior of Carboxyl-Bound Potassium during Combus ion of an ion-exchanged Lignite", *Fuel Proc. Technol.*, **44**, 105, (1995).

N. Shah, J. Zhao, F.E. Huggins, and G.P. Huffman, "*In Situ* XAFS Spectroscopic Studies of Direct Coal Liquefaction Catalysts", *Energy & Fuels*, **10/2**, 417, (1996).

T. Yamamoto, M. Croft, R. Shull, and H. Hahn, "Phase Identification of a Superparamagnetic Iron-Oxide/Silver Nanocomposite", *J. Nano. Mat.*, **6**, 965, 1995).

J. Yan, M. Greenblatt, A. Sahiner, D. Sills, and M. Croft, "Ruddlesden-Popper Zirconium Sulfides— a Novel Preparation Method and Characterization of Electronic Structure", *J. of Alloys and Compounds*, **229**, 126, (1995).

J. Zhao, F.E. Huggins, Z. Feng, and G.P. Huffman, "Characterization of Impregnated Iron Catalysts on Coal", *Energy & Fuels*, **10/1**, 250, (1996).

Beamline X19C

H. Chung, M. Dudley, M.E. Brown, and M.D. Hollingsworth, "Synchrotron White Beam X-ray Topography Characterization of Defect Structures in 2,10 Undecanedione/Urea Inclusion Compounds", *Mol. Cryst Liq. Cryst.*, **276**, 203, (1996).

H. Chung, B. Raghothamachar, M. Dudley, and D.J. Larson, Jr., "Synchrotron White Beam X-Ray Topography Characterization of Structural Defects in Microgravity and Ground Based CdZnTe Crystals", Space Processing of Materials, *SPIE*, **2809**, 45, (1996).

H. Chung, B. Raghothamachar, W. Zhou, M. Dudley, and D.C. Gillies "Studies of Interface Demarcation and Structural Defects in Ga doped Ge Single Crystals by Synchrotron White Beam X-Ray Topography", Applications of Synchrotron Radiation to Materials Science, edited by L. Terminello, S. Mini, D. L. Perry, and

H. Ade, *Mat. Res. Soc. Symp. Proc.,* **437**, (1996).

M. Dudley, "Growth Defect Studies in SiC Single Crystals", *Mol. Cryst Liq. Cryst.*, **278**, 37 , (1996).

Z. Huang, A. A. Acero, N. Lei, S. A. Rice, Z. Zhang, and M. L. Schlossman, "Structural Studies of Semi-Fluorinated Hydrocarbon Monolayers at the Air/Water Interface", *J. Chem. Soc., Faraday Trans.,* **92**, 545 (1996).

W. Huang, M. Dudley, and C. Fazi, "Characterization of Defect Structures in 3C-SiC Single Crystals", III-Nitride, SiC and Diamond Materials for Electronic Devices, edited by D.K. Gaskill, C. Brabdt and R. J. Nemanich, *Mat. Res. Soc. Symp. Proc.,* **423**, (1996).

W. Huang, Q. Wang, M. Dudley, F.P. Chiang, J. Parsons, and C. Fazi, "Synchrotron White Beam Topography Studies of Residual Stress in SiC Single Crystals Wafers with Epitaxial Thin Films", Evolution of Epitaxial Structure and Morphology , edited by A. Zangwill, D. Jesson, R. Clarke, and D. Chambliss, *Mat. Res. Soc. Symp. Proc.,* **399**, 425, (1996).

W. Huang, S. Wang, M. Dudley, P. Neudeck, J.A. Powell, and C. Fazi, "Characterization of Defect Structures in Lely 6H-SiC Single Crystals Using Synchrotron White Beam X-ray Topography", Applications of Synchrotron Radiation Techniques to Materials Science, edited by L. Terminello, N. Shinn, G. Ice, K. D'Amico, and D. Perry, *Mat. Res. Soc. Symp. Proc.*, **375**, 313, (1995).

X. Hu, I. Baker, and M. Dudley, "Dynamic *In Situ* Synchrotron X-ray Topographic Observations of Dislocations in Notched Ice Crystals", Applications of Synchrotron Radiation to Materials Science, edited by L. Terminello, S. Mini, D. L. Perry, and H. Ade, *Mat. Res. Soc. Symp. Proc.,* **437**, (1996).

X. Hu, I. Baker, and M. Dudley, "*In Situ* X-ray Topographic Observations of Notches in Ice", *Scripta Met.,* **34**, 491, (1996).

K. Jia, I. Baker, F. Liu, and M. Dudley, "Observation of Slip Transmission Through a Grain Boundary in Ice", *J. Mater. Sci.,* **31**, 2373, (1996).

N. Lei, Z. Huang and S.A. Rice, "Surface Segregation and Layering in the Liquid-Vapor Interface of a Dilute Bismuth:Gallium Alloy", *J. Chem. Phys.,* **104**, 4802, (1996).

F. Liu, I. Baker, and M. Dudley, "Dislocation/Grain Boundary Interactions in Ice Crystals'", *Phil. Mag.,* **A71**, 15, (1995).

F. Liu, I. Baker, and M. Dudley, "Thermally Induced Dislocation Loops and Stacking Faults in Polycrystalline Ice", *Phil. Mag.,* **A71**, 1, (1995).

W. Si, H. Chung, M. Dudley, V. Prasad, A. Anselmo, and D.F. Bliss, "Study of Defect Structures in MLEK Grown InP Single Crystals by Synchrotron White Beam X-ray Topography", Proceedings of the Eighth International Conference on Indium Phosphide and Related Materials, *Institute of Electrical and Electronics Engineers,* p. 610, 1996).

W. Si, M. Dudley, C. H. Carter, Jr., R. Glass, and V. F. Tsvetkov, "Determination of Burgers Vectors of Screw Dislocations in 6H-SiC Single Crystals by Synchrotron White Beam X-ray Topography", Applications of Synchrotron Radiation to Materials Science, edited by L. Terminello, S. Mini, D. L. Perry, and H. Ade, *Mat. Res. Soc. Symp. Proc.,* **437**, (1996).

W. Si, M. Dudley, P. Li and R. Wu, "Microstructure and Interfaces in TiB2/Ti-46Al-3Cr Alloy Composites", Covalent Ceramics III-Science and Technology of Non-Oxides, edited by A.F. Hepp, G.S. Fischmann, P.N. Kumpta, A.E. Kaloyeros, and J.J. Sullivan, *Mat. Res. Soc. Symp. Proc.,* **410**, 405, (1996).

W. Si, M. Dudley, P. Li and R. Wu, "Solid State Interfacial Reactions Between TiC Thin Films and Ti_3Al Substrates" Thermodynamics and Kinetics of Phase Transformations, *Mat. Res. Soc. Symp. Proc.,* **398**, 275, (1996).

W.M. Vetter and M. Dudley, "Characterization of Micropipes and other Defect Structures in 6H-SiC Through Fluorescence Microscopy", Diagnostic Techniques for Semiconductor Materials Processing, edited by O. Glembocki, S.W. Pang, F.H. Pollack, and F. Celii, *Mat. Res. Soc. Symp. Proc.,* **406**, 561, (1996).

G.M. Watson, B.D. Gaulin, D. Gibbs, G.H. Lander, T.R. Thurston, P.J. Simpson, H.J. Matzke, S. Wang, M. Dudley, and S. Shapiro, "On the Origin of the Second Length Scale Found Above TN in UO2", *Phys. Rev.,* **B53**, 686, (1996).

J.M. Winter, Jr., and R.E. Green, Jr., "Real-Time Synchrotron Topography Using a CID Array Camera with Digital Image Acquisition and Processing", *Adv. in X-ray Analysis,* **38**, 215, (1995).

Beamline X20

J.R.A. Carlsson, "Properties and Crystallization of Amorphous Si-Based Binary Alloy Thin Films", Ph.D., Linkoping University, (1995).

Q. Feng, "Study of the Three Dimensional Random Field Ising Model: Magnetic X-ray and Neutron Scattering, Magnetization and Heat Capacity", Ph.D., MIT, (1996).

Q.J. Harris, "Synchrotron X-ray Scattering Studies of Novel Phase Transitions in Systems with Coupled Order Parameters", Ph.D., MIT, (1996).

Q.J. Harris, Q. Feng, R.J. Birgeneau, K. Hirota, G. Shirane, M. Hase, and K. Uchinokura, "Large Length-Scale Fluctuations at the Spin-Peierls Transition in $CuGeO_3$", *Phys. Rev.*, **B52/21**, 15420, (1995).

J.L. Jordan-Sweet, P.M. Mooney, M.A. Lutz, R.M. Fennstra, J.O. Chu, and F.K. LeGoues, "Unique X-ray Diffraction Pattern at Grazing Incidence from Misfit Dislocations in SiGe Thin Films", *J. Appl. Phys.*, **80/1**, 89, (1996).

P.M. Mooney, J.L. Jordan-Sweet, G.B. Stephenson, F.K. LeGoues, and J.O. Chu, "High Resolution X-Ray Diffraction Measurements of Strain Relaxed SiGe/Si Structures", *Advances in X-ray Analysis*, **38**, 181, (1995).

P.M. Mooney, J.L. Jordan-Sweet, K. Ismail, J.O. Chu, R.M. Feenstra, and F.K. LeGoues, "Relaxed $Si_{0.7}Ge_{0.3}$ Buffer Layers for High Mobility Devices", *Appl. Phys. Lett.*, **67/16**, 2373, (1995).

M. J. Ramstad, "Instabilities of Vicinal Silicon (111) Surfaces", Ph.D., MIT, (1996).

R.F. Saraf, C. Dimitrakopoulos, M.F. Toney, and S.P. Kowalczyk, "Near Surface Structure of Solvent-Free Processed Polyimide Thin film", *Langmuir*, **12**, 2802, (1996).

S. Song, "Faceting and Tricriticality in the Orientational Phase Diagram of Stepped Si(113) Surfaces: Synchrotron X-ray Scattering Results", Ph.D., MIT, (1996).

V. Svilan, "Texture Analysis in Submicron Structures of Titanium Silicide", M.S., MIT, (1996).

G. M. Watson, D. Gibbs, S. Song, A. R. Sandy, S. G. J. Mochrie, and D. M. Zehner, "Faceting and Reconstructions of Stepped Au(111)", *Phys. Rev.*, **B52**, 12329, (1995).

D. Weller, A. Carl, R.J. Savoy, T.C. Huang, M.F. Toney, and C. Chappert, "Structural Transitions and Magnetic Anisotropy in Ultrathin Co Wedges on Pt(111) Investigated with the Magneto-Optical Kerr Effect", *J. Phys. Chem. Solids*, **56**, 1563, (1995).

Y. Xie, K.F. Ludwig, Jr., R. Bansil, P. Gallagher, X. Cao, and G. Morales, "Small-Angle X-ray Scattering Studies of Semidilute Polystyrene-Cyclohexane Solutions", *Physica*, **A232**, 94, (1996).

M.J. Young, "Equilibrium and Non-Equilibrium Phenomena in Two- and Three-Dimensional Correlated Systems", Ph.D., MIT, (1996).

Beamline X21

W.A. Caliebe, C.-C. Kao, L.E. Berman, J.B. Hastings, M.H. Krisch, F. Sette, and K. Hämäläinen, "Spin-Resolved Resonant Raman Scattering", *J. Appl. Phys.*, **79**, 6509, (1996).

M. Deutsch, O. Gang, K. Hämäläinen, and C.-C. Kao, "The Onset and Near Threshold Evolution of the Cu K-α X-ray Satellites", *Phys. Rev. Lett.*, **76**, 2424, (1996).

E.D. Isaacs, "Inelastic X-ray Scattering and the Metal-Insulator Transition", *Ferroelectrics*, **176**, 249, (1996).

E.D. Isaacs, and P.M. Platzman, "Inelastic X-ray Scattering", *Physics Today*, **49/2**, 40, (1996).

E.D. Isaacs, P.M. Platzman, P. Metcalf, and J.M. Honig, "Inelastic X-ray Scattering Study of the Metal-Antiferromagnetic Insulator Transition in V_2O_3", *Phys. Rev., Lett.*, **76**, 4211, (1996).

A.T. Macrander, R.C. Blasdell, P.A. Montano, and C.-C. Kao, "Inelastic X-ray Scattering from 6H-SiC", Wide Bandgap Semiconductors and Devices, edited by F. Ren, et al, *Electrochemical Society*, **95/21**, 98-102, (1995).

Beamline X22A

B.M. Ocko, O.M. Magnussen, J.X. Wang, R.R. Adzic, and T. Wandlowski, "The Structure and Phase Behavior of Electrodeposited Halides on Single-Crystal Metal Surfaces", *Physica*, **B221**, 238-244, (1996).

B.M. Ocko, O.M. Magnussen, J.X. Wang, and T. Wandlowski, "One-Dimensional Commensurate-Incommensurate Transition: Bromide on The Au(100) Electrode", *Phys. Rev.*, **B53**, R7654, (1996).

M. Suenaga, V. Fukumoto, P. Haldar, T.R. Thurston, and U. Wildgruber, "Effects of Axial Tensile and Bending Strains on Critical Currents of Mono- and Multicored $(Bi,Pb)_2Sr_2Ca_2Cu_2)_{10}$-Ag Tapes", *Appl. Phys. Lett.*, **67**, 3025, (1995).

T.R. Thurston, U. Wildgruber, N. Jisrawi, P. Haldar, M. Suenaga, and Y.L. Wang, "Synchrotron X-ray Scattering Measurements of Bulk Structural Properties in Superconducting $(Bi,Pb)_2Sr_2Ca_2Cu_3O_{10}$-Ag Tapes", *J. Appl. Phys.*, **79**, 3122, (1996).

T.R. Thurston, N.M. Jisrawi, S. Mukerjee, X.Q. Yang, J. McBreen, M.L. Daroux, and X.K. Xing, "Synchrotron X-ray Diffraction Studies of the Structural Properties of Electrode Materials in Operating Battery Cells", *Appl. Phys. Lett.*, **69**, 194, (1996).

T.H. Wandlowski, J.X. Wang, O.M. Magnussen, and B.M. Ocko, "Structural and Kinetic Aspects of Bromide Adsorption on Au(100)", *J. Phys. Chem.* ,**100**, 10277, (1996).

Beamline X22B

R.R. Adzic, and J.X. Wang, "Atomic Structure of Active Sites in O_2 Reduction on Au(111)/Tlad Electrodes in Acid and Alkaline Solutions", Proceedings of the Symposium on Oxygen Electrochemistry, Edited by R.R. Adzic, F.C. Anson and K. Kinoshita, *Electrochemical Society*, **95/26**, 61, (1995).

V. Kiryukhin, B. Keimer, J.P.Hill, and A. Vigliante, "Soliton Lattice in Pure and Diluted $CuGeO_3$", *Phys. Rev. Lett.*, **76**, 4608, (1996).

O.M. Magnussen, M.J. Regan, E.H. Kawamoto, B.M. Ocko, P.S. Pershan, N. Maskil, M. Deustch, S. Lee, K. Penanen, and L.E. Berman, "X-ray Reflectivity Studies of The Surface Structure of Liquid Metals", *Physica,* **B221**, 257, (1996).

X.Z. Wu, B.M. Ocko, M. Deutsch, E.B. Sirota, and S.K. Sinha, "Surface Freezing and Surface-Phase Behaviors in Binary Mixtures of Alkanes", *Physica*, **B221**, 261, (1996).

Beamline X22C

C. Detlefs, A.I. Goldman, J.P. Hill, D. Gibbs, C. Stassis, P.C. Canfield, and B.K. Cho, "The Magnetic Structure of Gd_2NiB_2C by Resonant and Non-resonant X-ray Scattering", *Phys. Rev.*, **B53**, 6335, (1996).

P.M. Gehring, A. Vigliante, D.F. McMorrow, D. Gibbs, C.F. Majkrzak, G. Helgesen, R.A. Cowley, R.C.C. Ward, and M.R. Wells, "Observation of Two Length Scales Above T_n in a Holmium Thin Film", *Physica,* **B221**, 398, (1996).

J.P. Hill, C. Detlefs, B.J. Sternlieb, A.I. Goldman, D. Gibbs, C. Stassis, P.C. Canfield, and B.K. Cho, "Incommensurate Antiferromagnetism in the Intermetallic Superconductor $HoNi_2B_2C$", *Phys. Rev.*, **B53**, 3487, (1996).

J.P. Hill, and D.F. McMorrow, "X-ray Resonant Exchange Scattering: Polarization Dependence and Correlation Functions", *Acta Cryst.*, **A52**, 236, (1996).

W.J. Nuttall, S. Langridge, W. G. Stirling, G. H. Lander, B. Lebech and O. Vogt, "X-ray Scattering Study of the Two Magnetic Correlation Lengths in Uranium Antimonide", *Phys. Rev.*, **B52**, 4409, (1996).

B.J. Sternlieb, J.P. Hill, U.C. Wildgruber, G.M. Luke, B. Nachumi, Y. Moritomo, and Y. Tokura, "Charge and Magnetic Order in $La_{0.5}Sr_{1.5}MnO_4$", *Phys. Rev. Lett.*, **76**, 2169, (1996).

D. Watson, E.M. Forgan, W.J. Nuttall, W.G. Stirling and D. Fort, "High Resolution Magnetic X-ray Diffraction From Neodymium", *Phys. Rev.*, **B53**, 726, (1996).

G.M. Watson, B.D. Gaulin, D. Gibbs, G.H. Lander, T.R. Thurston, P.J. Simpson, H.J. Matzke, S. Wang, M. Dudley, and S.M. Shapiro, "On the Origin of the Second Length Scale Found Above T_n In UO_2", *Phys. Rev.*, **B53**, 686, (1996).

G.M. Watson, D. Gibbs, G.H. Lander, H.J. Matzke, B.D. Gaulin, L.E. Berman, and W. Ellis, "Grazing-Incidence X-ray Magnetic Scattering Studies of UO_2(001) Surfaces", *Physica,* **B221**, 405, (1996).

G.M. Watson, D. Gibbs, G.H. Lander, B.D. Gaulin, F.E. Berman, H.J. Matzke, and W. Ellis, "An X-ray Scattering Study of the Magnetic Structure Near the (001) Surface of UO_2", *Phys. Rev. Lett.*, 77, 751, (1996).

Beamline X23A2

K.A. Carrado, and S.R. Wasserman, "Stability of Cu(II)- and Fe(III)-Porphyrins on Montmorillonite Clay: An X-ray Absorption Study", *Chem. Mater.*, **8**, 219, (1996).

V. Chakarian, Y.U. Idzerda, K.M. Kemner, J.-H. Parks, G. Meigs, and C.T. Chen, "Giant Magnetic Effects in the L-edge EXAFS of 3d Transition Metals", *J. Appl. Phys.*, **79**, 6493, (1996).

G.M. Chow, L.K. Kurihara, K.M. Kemner, P. Schoen, A.M. Ervin, S. Keller, Y.D. Zhang, N. Shen, J. Budnick, and T. Ambrose, "Structural, Morphological, and Magnetic Study of Nanocrystalline Co-Cu Powders Synthesized by the Polyol Process", *J. Mat. Res.*, **10**, 1546, (1995).

D. Fauteux, A. Massucco, M. vanBuren, B. Ouyang, S.G. Greenbaum, S. Kostov, and M.L. denBoer, "A Comparitive Study of $LiMn_2O_4$ from Various Sources", *Mat. Res. Soc. Symp. Proc.*, **369**, 29, (1995).

C.L. Foiles, M.R. Franklin, and R. Loloee, "Structure and Magetism in Mo/Co Multilayers", Magnetic Ultrathin Film, Multilayers and Surfaces", edited by A. Fert, G. Guntherodt, B. Heinrich, W.F. Eglehoff, JR., E.E. Marinero, and R.L. White, *Mat. Res. Soc. Symp.Proc.*, **384**, 97, (1995).

K.M. Kemner, W.T. Elam, V.G. Harris, Y.U. Idzerda, and J.A. Wolf, "Distinguishing the hcp and fcc Phases of the Metalizastion of Diamond by Polarization-Dependent EXAFS", *J. Vac. Sci. Technol.*, **B14**, 3207, (1996).

K.M. Kemner, W.T. Elam, D.B. Hunter, and P.M. Bertsch, "EXAFS Studies of the Local Environment of Cs in CsBr-dibenzo-18-crown-6 Ether Solutions and Powders", *J. Phys. Chem.*, **100**, 11698, (1996).

K.M. Kemner, W.T. Elam, Y.U. Idzerda, J.A. Wolf, and G.A. Prinz, "Polarization-Dependent Extended X-ray Absorption Fine Structure Measurements of Metastable Fcc Co on (100) Diamond", *Appl. Phys. Letts.*, **68**, 3389-3391, (1996).

K.M. Kemner, V.G. Harris, V. Chakarian, Y.U. Idzerda, W.T. Elam, C.-C. Kao, Y.C. Feng, J.C. Lodder, and J.C. Woicik, "The Role of Ta and Pt in Segregation within Co-Cr-Ta and Co-Cr-Pt Thin Film Magnetic Recording Media", *J. Appl. Phys.*, **79**, 5345, (1996).

K.M. Kemner, V.G. Harris, W.T. Elam, Y.C. Feng, D.E. Laughlin, and J.C. Woicik, "Polarization-Dependent XAFS Studies on the Role of Ta in the Compositional Segregation of Co-Cr-Ta Magnetic Recording Media", *IEEE Trans. on Mag.*, **31**, 2806, (1995).

K.M. Kemner, V.G. Harris, W.T. Elam, and J.C. Lodder, "EXAFS Studies and Simulations of Local Anisotropy in $Co_{78}Cr_{22}$ Films", *Mat. Res. Soc. Symp. Proc.*, **375**, 21, (1995).

J.P. Kirkland, and W.T. Elam, "An UHV-Compatible Fixed-Exit Two-Crystal Monochromator", *Rev. Sci. Instrum.*, **66/2**, 2135-2137, (1995).

J.P. Kirkland, and W.T. Elam, "The Naval Research Laboratory's new Hard X-ray Beamline at the National Synchrotron Light Source", *Rev. Sci. Instrum.*, **66/2**, 1709-1711, (1995).

J.P. Kirkland, V.E. Kovantsev, C.M. Dozier, J.V. Gilfrich, W.M. Gibson, Q.-F. Xiao, and K Umezawa, "Wavelength-Dispersive X-ray Fluorescence Detector", *Rev. Sci. Instrum.*, **66/2**, 1410-1412, (1995).

J. McBreen, X.Q. Yang, H.S. Lee, and Y. Okamoto, "EXAFS Studies of Mixed Salt $CoBr_2$/LiBr-PEO Complexes", *Electrochimica Acta*, **40**, 2115, (1995).

S. Mukerjee, and J. McBreen, "Hydrogen Electrocatalysis by Carbon Supported Pt and Pt Alloys", *J. Electrochem. Soc.*, **143**, 2285, (1996).

B. Ouyang, X. Cao, H.W. Lin, S. Slane, S. Kostov, M.L. denBoer, and S.G. Greenbaum, "Lithium-7 NMR Studies of $Li_{1-x}CoO_2$ Battery Cathodes", *Mat. Res. Soc. Symp. Proc.*, **369**, 59, (1996).

L. Soderholm, U. Staub, S. Skanthakumar, and M.R. Antonio, "The Oxidation State and Magnetic Behaviour of Tb in High-T_c Related Materials", *Mat. Res. Soc.Proc.*, **376**, 529, (1995).

U. Staub, L. Soderholm, S. Skanthakumar, and M.R. Antonio, "Oxidation State and Magnetic Properties of $Pb_2Sr_2Tb_{1-x}Y_xCu_3O_8$", *Phys. Rev.*, **B52**, 9736, (1995).

S.R. Wasserman, R.E. Winans, and R. McBeth, "Iron Species in Argonne Premium Coal Samples: An Investigation using X-ray Absorption Spectroscopy", *Energy Fuels*, **10**, 392, (1996).

Beamline X23A3

A.J. Allen, S. Krueger, G.G. Long, H.M. Kerch, H. Hahn, and G. Skandan, "Small-Angle Neutron Scattering Studies of Ceramic Nanophase Materials", *Nanostructured Materials*, 7, 113-126, (1996).

A.J. Allen, S. Krueger, G. Skandan, G.G. Long, H. Hahn, H.M. Kerch, J.C. Parker, and M.N. Ali, "Microstructural Evolution During the Sintering of Nanostructured Ceramic Oxides", *J. Am. Ceram. Soc.*, **79**, 1201-1212, (1996).

A.J. Allen, G.G. Long, H.M. Kerch, S. Krueger, G. Skandon, H. Hahn, and J.C. Parker, "Sintering Studies of Nanophase Ceramic Oxides", *Ceramic International*, **22**, 275-280, (1996).

G. Fogarty and M. Cronin-Golomb, "The Strain Problem in Photorefractive Crystals", *Optics Letters*, **20**, 2276-2278, (1995).

G. Fogarty and M. Cronin-Golomb, "Surface Strain Effects on Photorefractive Gratings", CLEO 95, OSA 1995 Technical Digest Series, p. 261, (1995).

G. Fogarty, B. Steiner, M. Cronin-Golomb, R. Uhrin, and J. Martin, "High-Resolution X-ray Diffraction Imaging of Anti-Parallel Ferroelectric Domains in Barium Titanate and Strontium Barium Niobate", Technical Digest of Photorefractive Materials, Effects, and Devices, pp. 9-12, (1995).

S. Krueger, A.J. Allen, G. Skandon, G.G. Long, H. Hahn, and H.M. Kerch, "Small-Angle Scattering Methods for Studying the Sintering of Nanophase Ceramic Compacts", Neutron Scattering in Materials Science, edited by D.A. Neumann, T.P. Russell, and B. Wuensch, *MRS Symp. Proc.*, **376**, 359-364, (1995).

Beamline X23B

G.M. Chow, L.K. Kurihara, K.M. Kemner, P. Schoen, A.M. Ervin, S. Keller, Y.D. Zhang, N. Shen, J. Budnick, and T. Ambrose, "Structural, Morphological, and Magnetic Study of Nanocrystalline Co-Cu Powders Synthesized by the Polyol Process", *J. Mater. Res.*, **10**, 1546, (1995).

K.M. Kemner, W.T. Elam, D.B. Hunter, and P.M. Bertsch, "EXAFS Studies of the Local Environment of Cs in CsBr-dibenzo-18-crown-6 Ether Solutions and Powders", *J. Phys. Chem.*, **100**, 11698, (1996).

K.M. Kemner, W.T. Elam, Y.U. Idzerda, J.A. Wolf, and G.A. Prinz, "Polarization-Dependent Extended X-ray Absorption Fine Structure Measurements of Metastable fcc Co on (100) Diamond", *Appl. Phys. Letts.*, **68**, 3389, (1996).

K. M. Kemner, V. G. Harris, V. Chakarian, Y. U. Idzerda, W. T. Elam, C. -C. Kao, Y. C. Feng, J.C. Lodder, and J. C. Woicik, "The Role of Ta and Pt in Segregation Within Co-Cr-Ta and Co-Cr-Pt Thin Film Magnetic Recording Media", *J. Appl. Phys.*, **79**, 5345, (1996).

K. M. Kemner, V. G. Harris, W. T. Elam, Y. C. Feng, D. E. Laughlin, and J. C. Woicik, "Polarization-Dependent XAFS Studies on the Role of Ta in the Compositional Segregation Within Co-Cr-Ta Magnetic Recording Media", *IEEE Trans. Magn.* **31**, 2806, (1995).

K.M. Kemner, V.G. Harris, W.T. Elam, and J.C. Lodder, "EXAFS Studies and Simulations of Local Anisotropy in $Co_{78}Cr_{22}$ Films", *Mat. Res. Soc. Symp. Proc.*, **375**, 21, (1995).

J.P. Kirkland, and W.T. Elam, "An UHV-Compatible Fixed-Exit Two-Crystal Monochromator", *Rev. Sci. Instrum.*, **66/2**, 2135, (1995).

J.P. Kirkland, and W.T. Elam, "The Naval Research Laboratory's new Hard X-ray Beamline at the National Synchrotron Light Source", *Rev. Sci. Instrum.*, **66/2**, 1709, (1995).

J.P. Kirkland, V.E. Kovantsev, C.M. Dozier, J.V. Gilfrich, W.M. Gibson, Q.-F. Xiao, and K. Umezawa, "Wavelength-Dispersive X-ray Fluorescence Detector", *Rev. Sci Instrum.*, **66/2**, 1410, (1995).

Beamline X24A

S.M. Butorin, D.C. Mancini, J.-H. Guo, N. Wassdahl, J. Nordgren, M. Nakazawa, S. Tanaka, T. Uozumi, A. Kotani, Y. Ma, K.E. Miyano, B.A. Karlin, and D.K. Shuh, "Resonant X-ray Fluorescence Spectroscopy of Correlated Systems: A Probe of Charge-Transfer Excitations", *Phys. Rev. Lett.*, 77, 574, (1996).

B. Krassig, M. Jung, D.S. Gemmell, E.P. Kanter, T. LeBrun, S.H. Southworth, and L. Young, "Nondipolar Asymmetries of Photoelectron Angular Distributions", *Phys. Rev. Lett.*, **75**, 4736, (1995).

T. LeBrun, S.H. Southworth, M.A. MacDonald, and Y. Azuma, "A Comparison of Radiative and Non-Radiative Resonant Raman Studies of the Inner Shell Electronic Structure of Atoms", Atomic and Molecular Photoionization, *Universal Academy Press*, p. 303, (1996).

P.S. Shaw, U. Arp, and S.H. Southworth, "Measuring Nondipolar Asymmetries of Photoelectron Angular Distributions", *Phys. Rev.*, **A54**, 1463, (1996).

J.C. Woicik, T. Kendelewicz, S.A. Yoshikawa, K.E. Miyano, G.S. Herman, P.L. Cowan, P. Pianetta, and W.E. Spicer, "Surface Sensitive X-ray Standing Wave Study of Si(111) $\sqrt{3}x\sqrt{3}$ -Ag" *Phys. Rev.*, **B53**, 15425, (1996).

J.C. Woicik, K.E. Miyano, J.G. Pellegrino, P.S. Shaw, S.H. Southworth, and B.A. Karlin, "Strain and Relaxation in InAs and InGaAs Films Grown on GaAs(001)", *Appl. Phys. Lett.*, **68**, 3010, (1996).

Beamline X24C

T.-J. Chen, R.N. Zitter, R. Tao, W.R. Hunter, and J.C. Rife, "Optical Constants of Lithium Triborate Crystals in the 55-71 eV Region," *Phys. Rev.*, **B52**, 13703 (1995).

M.P. Kowalski, T.W. Barbee, R.G. Cruddace, Jr., J.F. Seely, J.C. Rife, and W.R. Hunter, "Efficiency and Long-Term Stability of a Multilayer-Coated, Ion-Etched Blazed Holographic Grating in the 125-133 A Wavelength Region", *Appl. Opt.*, **34**, 7338, (1995).

M.P. Kowalski, R.G. Cruddace, Jr., J.F. Seely, J.C. Rife, W.R. Hunter, and T.W. Barbee, Jr., "The EUV Performance of an Ion-Etched Blazed Diffraction Grating", *J. Electron. Spectro. Related Phenom.*, **80**, 473, (1996).

J.P. Long, B.S. Itchkawitz, and M.N. Kabler, "Photoelectron Spectroscopy of Laser-Excited Surfaces by Synchrotron Radiation", *J. Opt. Soc. Am.*, **B13**, 201, (1996).

J.P. Long, V.M. Bermudez, and D.E. Ramaker, "Structural Determination of β SiC(100)-c(2x2) from C 1s Surface Core Exciton and Si 2p Absorption", *Phys. Rev. Lett.*, **76**, 991, (1996).

P.E. Pehrsson, J.P. Long, J.E. Butler, and M. Marchywka, "Electrochemically-Induced Surface Chemistry and Negative Electron Affinity on Diamond (100)", *Appl. Phys. Lett.*, **67**, 3414, (1995).

J.F. Seely, R.G. Cruddace, M.P. Kowalski, W.R. Hunter, T.W. Barbee, J.C. Rife, R. Eby, and K.G. Stolt, "Polarization and Efficiency of a Concave Multilayer Grating in the 135-250 Å Region and in Normal-Incidence and Seya-Namioka Mounts", *Appl. Optics* **34**, 7347 (1995).

J.F. Seely, W.R. Hunter, and M.P. Kowalski, "Transmittance of a Thin Saran Film in the 45-584 Å Wavelength Region", *Appl. Opt.*, **34**, 7945, (1995).

J.F. Seely, M.P. Kowalski, R.G. Cruddace, J.C. Rife, T.W. Barbee, Jr., and W.R. Hunter, "High Resolution Spectroscopy Using Normal-Incidence Multilayer Gratings", UV and X-ray Spectroscopy of Astrophysical and Laboratory Plasmas, edited by K. Yamashita and T. Watanabe, *Universal Academy Press*, p. 225, (1996).

J.F. Seely, M.P. Kowalski, R.G. Cruddace, J.C. Rife, T.W. Barbee, Jr., W.R. Hunter, and G.E. Holland, "High-Efficiency Holographic Ion-Etched Gratings with Multilayer Coatings and Operating On-Blaze at Normal Incidence in the 130-300 Å Range", Multilayer and Grazing Incidence X-Ray-EUV Optics III, *SPIE*, 2805, (1996).

J.F. Seely, M.P. Kowalski, W.R. Hunter, T.W. Barbee, Jr., R.G. Cruddace, and J.C. Rife, "Normal-Incidence Efficiencies in the 115-340 Å Wavelength Region of Replicas of the Skylab 3600 1/mm Grating With Multilayer and Gold Coatings", *Appl. Opt.*, **34**, 6453, (1995).

Beamline X25

W.A. Caliebe, C.C. Kao, L.E. Berman, J.B. Hastings, M.H. Krisch, F. Sette, and K. Hämäläinen, "Spin Resolved Resonant Raman Scattering", *J. Appl. Phys.*, **79**, 6509-6511, (1996).

M. Deutsch, O. Gang, K. Hämäläinen, and C.-C. Kao, "Onset and Near Threshold Evolution of the Cu Kα X-Ray Satellites", *Phys. Rev. Lett.*, **76**, 2424-2427, (1996). (key publication).

E. Dufresne, R. Brüning, M. Sutton, B. Rodricks, and G.B. Stephenson, "A Statistical Technique for Characterizing X-Ray Position-Sensitive Detectors", *Nucl. Instrum. Methods Phys. Res.*, **A364**, 380-393, (1995).

B.A. Everitt, M.B. Salamon, B.J. Park, C.P. Flynn, T. Thurston, and D. Gibbs, "X-Ray Magnetic Scattering from Nonmagnetic Lu in a Dy/Lu Alloy", *Phys. Rev. Lett.*, **75**, 3182-3185, (1995).

J. Goldberg, A. Nairn, and J. Kuriyan, "Structural Basis for the Regulation of Calmodulin-Dependent Protein Kinase I", *Cell*, **84**, 875-887, (1996).

G. Helgesen, J.P. Hill, T.R. Thurston, and D. Gibbs, "An X-Ray Scattering Study of Higher Harmonic Satellites Near the Antiferromagnetic Phase Transitions in Rare Earth Metals", *Phys. Rev.*, **B52**, 9446-9454, (1995).

D. Heskett, P. Xu, L. Berman, C.C. Kao, and M.J. Bedzyk, "The Geometric Structure of Rb/Cu(111) Investigated with X-Ray Standing Waves: Rb Coverage Dependence", *Surf. Sci.*, **344**, 267-275, (1995).

D.G. Lambright, J. Sondek, A. Bohm, N.P. Skiba, H.E. Hamm, and P.B. Sigler, "The 2.0 Å Crystal Structure of a Heterotrimeric G Protein", *Nature*, **379**, 311-319, (1996).

J.C. Levin, G.B. Armen, and I.A. Sellin, "Photoionization and Compton Double Ionization of Helium from Threshold to 20 keV", *Phys. Rev. Lett.*, 76, 1220-1223 (1996). (key publication)

O.M. Magnussen, M.J. Regan, E.H. Kawamoto, B.M. Ocko, P.S. Pershan, N. Maskil, M. Deutsch, S. Lee, K. Penanen, and L.E. Berman, "X-Ray Reflectivity Studies of the Surface Structure of Liquid Metals", *Physica*, **B221**, 257-260, (1996).

J. Sondek, A. Bohm, D.G. Lambright, H.E. Hamm, and P.B. Sigler, "Crystal Structure of a G-Protein β–γ Dimer at 2.1 Å Resolution", *Nature*, **379**, 369-374, (1996).

L. Tong, C. Qian, M.-J. Massariol, P.R. Bonneau, M.G. Cordingley, and L. Lagace, "A New Serine-Protease Fold Revealed by the Crystal Structure of Human Cytomegalovirus Protease", *Nature*, **383**, 272-275, (1996). (Key publication)

M.A. Wall, D.E. Coleman, E. Lee, J.A. Iniguezlluhi, B.A. Posner, A.G. Gilman, and S.R. Sprang, "The Structure of the G Protein Heterotrimer G(I-α-1)β(1)γ(2)", *Cell*, **83**, 1047-1058, (1995).

G.M. Watson, D. Gibbs, G.H. Lander, B.D. Gaulin, L.E. Berman, H.J. Matzke, and W. Ellis, "X-Ray Scattering Study of the Magnetic Structure Near the (001) Surface of UO_2", *Phys. Rev. Lett.*, 77, 751-754, (1996). (Key publication)

G.M. Watson, D. Gibbs, G.H. Lander, H.J. Matzke, B.D. Gaulin, L.E. Berman, and W. Ellis, "Grazing-Incidence X-ray Magnetic Scattering Studies of UO_2(001) Surfaces", *Physica*, **B221**, 405-407, (1996).

Beamline X26A

J.S. Delaney, S. Bajt, M.D. Dyar, S.R. Sutton, G. McKay, and P. Roeder, "Comparsion of Quantitative Synchrotron Micro XANES FeIII/(FeII+FeIII) Results for Amphibole and Silicate Glass with Independent Measurements", *Lunar Planet Sci.*, XXVII, 299, (1996).

J.S. Delaney, S. Bajt, S.R. Sutton, and M.D. Dyar, "*In Situ* Microanalysis of $Fe^{3+}/\Sigma Fe$ Ratios in Amphibole by X-ray Absorption Near Edge Structure (XANES) Spectroscopy", *Mineral Spectroscopy*, **5**, 165, (1996).

J. Flynn, S. Bajt, and S.R. Sutton, "Evidence of Weakly Bound Bromine in Large Interplanetary Dust Particles from the Stratosphere", *Lunar Planet. Sci.*, XXVII, 367, (1996).

J. Flynn, F. Hörz, S. Bajt, and S.R. Sutton, "*In Situ* Chemical Analysis of Extraterrestrial Material Captured in Aerogel", *Lunar Planet. Sci.*, XXVII, 369, (1996).

D.I. Kaplan, M.E. Sumner, P.M. Bertsch, and D.C. Adriano, "Chemical Conditions Conducive to the Release of Mobile Colloids from Ultisol Profiles", *Soil Sci. Soc. Am. J.*, **60**, 269, (1996).

R.J. Reeder, "Interaction of Divalent Cobalt, Zinc, Cadmium, and Barium with the Calcite Surface During Layer Growth", *Geochimica et Cosmochimica Acta,* **60**, 1543, (1996).

R. Rizzo, M. Grandolfo, C. Godeas, K.W. Jones, F. Vittur, "Calcium, Sulphur, and Zinc Distribution in Normal and Arthritic Articular Equine Cartilage: a Synchrtoron Radiation Induced X-ray Emission (SRIXE) Study", *J. Exptl. Zoology*, **273**, 82, (1995).

D. Schulze, T. McCay-Buis, S.R. Sutton, and D.M. Huber, "Manganese Oxidation States in *Gauemannomyces* Infested Wheat Rizospheres Probed by Micro XANES Spectroscopy", *Phytopathology*, **85**, 990, (1995).

D. Schulze, S.R. Sutton, and S. Bajt, "Determination of Manganese Oxidation State in Soils Using X-ray Absorption Near-Edge Structure (XANES) Spectroscopy", *Soil Sci. Soc. of Amer. J.*, **59**, 1540, (1995).

R. Sutton, S. Bajt, and R. Jones, "*In Situ* Determination of Chromium Oxidation State in Olivine from Chondrules", *Lunar Planet, Sci.*, XXVII, 1291, (1996).

Beamline X26C

J.M. Bolduc, D.H. Dyer, W.G. Scott, R.M. Sweet, D.E. Koshland, and B.L. Stoddard, "Mutagenesis and Laue Structures of Enzyme Intermediates - Isocitrate Dehydrogenase", *Science*, **268**, 1312, (1995).

P.J. Eng, M.L. Rivers, B.X. Yang, and W. Schildkamp, "Microfocusing 4-keV to 65-keV X-rays with Bent Kirkpatrick-Baez Mirrors", *SPIE*, **2516**, 41, (1995).

K. Moffat, "Macromolecular Crystallography on the Millisecond to Nanosecond Time Domain", Time Resolved Electron and X-ray Diffraction, edited by P.M. Rentzepis, *SPIE*, **2521**, 182, (1995).

K. Moffat, and R. Henderson, "Freeze Trapping of Reaction Intermediates", *Curr. Opin. Struct. Biol.*, **5**, 656, (1995).

K. E. Ng, G. Getzoff, and K. Moffat, "Optical Studies of a Bacterial Photoreceptor Protein, Photoactive Yellow Protein, in Single Crystals", *Biochemistry*, **34**, 879, (1995).

Z. Ren and K. Moffat, "Deconvolution of Energy Overlaps in Laue Diffraction", *J. Appl. Cryst.*, **28**, 482, (1995).

Z. Ren and K. Moffat, "Quantitative Analysis of Synchrotron Laue Diffraction Patterns in Macromolecular Crystallography", *J. Appl. Cryst.*, **28**, 461, (1995).

Z. Ren, K. Ng, G.E.O. Borgstahl, E.D. Getzoff, and K. Moffat, "Quantitative Analysis of Time-Resolved Laue Diffraction Patterns", *J. Appl. Cryst.*, **29**, 246, (1996).

B.L. Stoddard, A. Dean, and P.A. Bash, "Combining Laue Diffraction and Molecular Dynamics to Study Enzyme Intermediates", *Nature Struct. Biology*, **3**, 590, (1996).

X. Yang, and K. Moffat, "Insights into Specificity of Cleavage and Mechanism of Cell Entry from the Crystal Structure of the Highly Specific Asfergillus Ribotoxin, Restrictocin", *Structure*, **4**, 837, (1996).

Beamline X27A

M. Suenaga, Y. Fukumoto, P. Haldar, T.R. Thurston, and U. Wildgruber, "Effects of Axial Tensile and Bending Strains on Critical Currents Mono-and Multicored $(Bi,Pb)_2Sr_2Ca_2Cu_3O_{10}$-Ag Tapes", *Appl. Phys. Letts.*, 67, 3025, (1995).

T.R. Thurston, N.M. Jisrawi, S. Mukerjee, X.Q. Yang, J. McBreen, M.L. Daroux, and X.K. Xing, "Synchrotron X-ray Diffraction Studies of the Structural Properties of Electrode Materials in Operating Battery Cells", *Appl. Phys. Letts.*, **69**, 194, (1996).

T.R. Thurston, U. Wildgruber, N. Jisrawi, P. Haldar, M. Suenaga, and Y.L. Wang, "Synchrotron X-ray Scattering Measurements of Bulk Structural Properties in Superconducting $(Bi,Pb)_2Sr_2Ca_2Cu_3O_{10}$-Ag Tapes", *J. Of Appl. Phys.*, 79, 3122, (1996).

Beamline X27C

R.E. Johnston, D. Washburn, E. Pisano, W. Thomlinson, D. Chapman, N.F. Gmür, Z. Zhong, and D. Sayers, "Preliminary Experience with Monoenergetic Photon Mammography", Medical Imaging 1995, Physics of Medical Imaging, *SPIE*, **2432**, 434, (1995).

W.B. Lindquist, S.-M. Lee, D.A. Coker, K. Jones, and P. Spanne, "Medial Axis Analysis of Void Structure in Three Dimensional Tomographic Images of Porous Media", *J. Of Geophys. Res. Sol. Earth*, **B101**, 8297, (1996), BNL 61573.

PUBLICATIONS

NSLS STAFF

M. Babzien, I. Ben-Zvi, J. Fischer, A.S. Fisher, K. Kusche, I.V. Pogorelsky, and T. Srinivasan-Rao, "A High Power Picosecond Nd:YAG/CO_2 Laser System for Electron Guns Laser Acceleration and FEL", Proceedings of Lasers '94 Conference, Quebec, Canada, STS Press, p. 253, (1995), BNL 61399.

I. Ben-Zvi, E. Blum, E.D. Johnson, S. Krinsky, J.B. Murphy and L.H. Yu, "NSLS Source Development Laboratory", SPIE Conference Proceedings Electron Beam Sources Sources and Charged-Particle Optics, edited by Eric Munro and Henry P. Freund, *SPIE*, **2522**, 483, (1995). BNL 62173.

E.B. Blum, "A Proposed NSLS X-Ray Ring Upgrade Using B Factory Technology", Proceedings of the 1995 Particle Accelerator Conference and International Conference on High Energy Accelerators, p. 263, (1995), BNL 61744, May 1995.

E. Bozoki, A. Friedman, and S. Ramamoorthy, "First Results with a Nonlinear Digital Orbit Feedback System at the NSLS", Particle Accelerator Conference and International Conference on High-Energy Accelerator, 4, pp. 2696-2698, (1995), BNL 61745.

K. Breuer, K.E. Smith, M. Greenblatt, W. McCarroll, and S.L. Hulbert, "Dominant Role of the Surface in Photoemission from Quasi-one Dimensional Conductors: $K_{0.3}MoO_3u$", *J. Phys. Chem. Solids*, **57**, 1803, (1996), BNL 63984.

W. Broome, R. Biscardi, J. Keane, P. Mortazavi, M. Thomas, and J.M. Wang, "RF System for the NSLS Coherent Infrared Radiation Source", Proceedings of the 1995 Particle Accelerator Conference, **3**, 1626, (1995), BNL 61759.

C.J. Buckley, S.J. Bellamy, X. Zhang, G. Dermody, and S. Hulbert, "The NEXAFS of Biological Calcium Phosphates", *Rev. Sci. Instrum.*, **66**, 1322, (1995), BNL 63149.

S.V. Bulanov, T.J. Esirkepov, N.M. Naumova, F. Pegoraro, and I.V. Pogorelsky, and A.M. Pukhov, "Controlled Wake Field Acceleration via Laser Pulse Shaping", *IEEE Trans. on Plasma Sci.*, **24**, 393, (1996), BNL 62847.

D. Chapman, W. Thomlinson, F. Arfelli, N. Gmur, Z. Zhong, and R. Menk, et al. "Mammography Imaging Studies Using a Laue Crystal Analyzer", *Rev. Sci. Instrum.*, **67**, 9, (1996), BNL 62394.

T.T. Chou, C.N. Yang, and L.H. Yu, "Bose-Einstein Condensation of Atoms in a Trap", *Phys. Rev. Lett.*, **A53/6**, 4257, (1996), BNL 63638.

S.B. Dierker, R. Pindak, R.M. Fleming, I.K. Robinson, and L. Berman, "X-Ray Photon Correlation Spectroscopy Study of Brownian Motion of Gold Colloids in Glycerol", *Phys. Rev. Lett.*, **75/3**, 449-452, (1996), BNL 62551.

M. Deutsch, O. Gang, K. Hamalainen, and C.-C. Kao, "Onset and Near Threshold Evolution of the Cu *K*% X-ray Satellites", *Phys. Rev. Letts.*, **76/14**, 2424, (1996), BNL 63776.

Y.P. Feng, S.K. Sinha, E.E. Fullerton, G. Grubel, D. Abernathy, D.P. Siddons, and J.B. Hastings, "X-Ray Fraunhofer Diffraction Patterns from a Thin-film Waveguide", *Appl. Phys. Lett.*, **67/24**, 3647-3649, (1996), BNL 62734.

C.L. Foerster, C. Lanni, J.R. Noonan, and R.A. Rosenberg, "Photon Stimulated Desorption Measurement of an Extruded Aluminum Beam Chamber for the Advanced Photon Source", *J. Vac. Sci. Technol.*, **A14/3**, 1273, (1996), BNL 62542.

F. Gao, G.L. Carr, C.D. Porter, D.B. Tanner, G.P. Williams, C.J. Hirschmugl, B. Dutta, X.D. Wu, and S. Etemad, "Quasiparticle Damping and the Coherence Peak in $Yba_2Cu_3O_{7-d}$", *Phys. Rev.*, **B54/1**, 700, (1996), BNL 63692.

E. Gluskin, D. Franchon, P.M Ivanov, J. Maines, E.A. Medvodko, E. Trakhtenberg, L.R. Turner, I. Vasserman, G.I. Erg, Y.A. Evtushenko, N.G. Gavrilov, G.N. Kulipanov, A.S. Medvedko, S.P. Petrov, V.M. Popik, N.A. Vinokurov, A. Friedman, S. Krinsky, G. Rakowsky, and O. Singh, "The Elliptical Multipole Wiggler Project", Proceedings of the 1995 Particle Accelerator Conference, pp. 1426-1428, (1996), BNL 61858.

K. Hämäläinen, S. Manninen, C.-C. Kao, W. Caliebe, J.B. Hastings, A. Bansil, S. Kaprzyk, and P.M. Platzman, "High Resolution Compton Scattering Study of Be", *Phys. Rev.*, **B54/8**, 5453, (1996).

C.J. Hirschmugl, and G.P. Williams, "Chemical Shifts and Coupling Interactions for the Bonding Vibrational Modes for Co/Cu(111) and (100) Surfaces", *Phys. Rev.*, **B52**, 14177, (1995), BNL 62539.

G. Ingold, I. Ben-Zvi, L. Solomon, and M. Woodle, "Fabrication of a High-Field, Short-Period Superconducting Undulator", *Nucl. Instrum. and Meth. in Phys. Res.*, **A375**, 451, (1996), BNL

R.E. Johnston, D. Washburn, E. Pisano, W.C. Thomlinson, L.D. Chapman, F. Arfelli, G. Gmür, Z. Zhong, and D. Sayers, "Mammographic Phantom Studies with Synchrotron Radiation", *Radiology*, **200**, 659-663, (1996), BNL 62733.

R.E. Johnston, D. Washburn, E. Pisano, W.C. Thomlinson, D. Chapman, N.F. Gmür, Z. Zhong and D. Sayers, "Preliminary Experience with Monoenergetic Photon Mammography", *SPIE*, **2432**, 434, (1996), BNL 62393.

M.H. Kirsch, F. Sette, U. Bergmann, C. Masciovecchio, R. Berbeni, J. Goulon, W. Caliebe, and C.-C. Kao, "Observation of Magnetic Circular Dichroism in Resonant Inelastic X-ray Scattering at the L_3 Edge of Gandolinium Metal", *Phys. Rev.*, **B54/18**, 12673, (1996), BNL 63772.

C.-H. Ko, J. Kirz, H. Ade, E. Johnson, S. Hulbert, and E. Anderson, "Development of a Second Generation Scanning Photoemission Microscope with a Zone Plate Generated Microprobe at the National Synchrotron Light Source", *Rev. Sci. Instrum.*, **66**, 1416, (1995), BNL 63148.

B. LaFontaine, D.L. White, O.R. Wood, II, A.A. MacDowell, Z.Q. Tan, G.N. Taylor, D.M. Tennant, and S.L. Hulbert, "Real-Time Observations of Extreme Ultraviolet Aerial Images by Fluorescence Imaging", *J. Vac. Sci. Technol.*, **B12**, 3576, (1994), BNL 63153.

A.T. Macrander, P.A. Montano, D.L. Price, V.I. Kushnir, C.R. Blasdell, C.-C. Kao, and E.R. Cooper, "Inelastic X-ray Scattering from TiC Single Crystals", *Phys. Rev.*, **B54/1**, 305, (1996), BNL 63774.

S. Morante, L. Furenlid, G. Schizvo, F. Tonello, R. Zwilling, and C. Montecucco, "Zinc Coordination in Tetanus Neurotoxin, Astacin, Thermolysin, and Alkaline Protease Studied by XRay Absorption Spectroscopy", *Eur. Journ. of Biochem.*, **235**, 606, (1996), BNL 62541.

J.B. Murphy, "Issues and State of Art for Short Bunches in e+/e- Storage Rings", AIP Conference Proceedings, **367**, p. 109, (1996), BNL 63851.

R.J. Nawrocky, and S.L. Kramer, "Single-Turn Beam Position Monitor for the NSLS VUV Electron Storage Ring", Proceedings of the 1995 PAC and International Conference on HighEnergy Accelerators, p. 2509, (1995), BNL 61758.

D.T. Palmer, R.H. Miller, H. Winick, X.J. Wang, K. Batchelor, M. Woodle, and I. Ben-Zvi, "Microwave Measurements of the BNL/SLAC/UCLA 1.6 Cell Photocathode RF Gun", 1995 Particle Accelerator Conference, (1995), BNL 61851.

D.T. Palmer, R.H. Miller, H. Winick, X.J. Wang, K. Batchelor, M. Woodle, and I. Ben-Zvi, "Simulations of the BNL/SLAC/UCLA 1.6 Cell Emittance Compensated Photocathoce RF Gun Low Energy Beam Line", 1995 Particle Accelerator Conference, p. 2432, (1995), BNL 61852.

I.V. Pogorelsky, "Relativistically Strong CO_2 Laser Driver for Plasma-Channeled Particle Acceleration", STS Press, pp. 104-111, (1996), BNL 62845.

I.V. Pogorelsky, I. Ben-Zvi, W.D. Kimura, N.A. Kurnit, and F. Kannari, "Picosecond CO_2 Laser for Relativistic Particle Acceleration", *Infrared Phys. and Tech.*, **36/1**, 341-354, (1995), BNL 60452.

I.V. Pogorelsky, A. vanSteenbergen, M. Babzien, I. Ben-Zvi, R. Fernow, J. Gallardo, K.P. Kusche, T. Srinivasan-Rao, X.J. Wang, W.D. Kimura, G.H. Kim, R.D. Romea, Y. Liu, D. Cline, J.R. Fontana, A. Fisher, J. Sandweiss, X.J. Qui, and J.-M. Fang, "Inverse Cherenkov and Inverse FEL Accelerator Experiments at the Brookhaven Accelerator Test Facility", STS Press, pp. 96-103, (1996), BNL 62846.

A. Pullia, L. Furenlid, H.W. Kraner, G. Bertuccio, P.J. Pietraski, and D.P. Siddons, "High Resolution Multi-Element Solid-State Detectors", *Rev. Sci. Instrum.*, **67/9**, 1, (1996), BNL 62735.

X. Qui, K. Batchelor, I. Ben-Zvi, and X.J. Wang, "Demonstration of Emittance Compensation Through the Measurement of the Slice Emittance of a 10 Picosecond Electron Bunch", *Phys. Rev. Lett.*, **76/20**, 3723, (1996), BNL 62386.

X.Z. Qiu, X.J. Wang, K. Batchelor, and I. Ben-Zvi, "Conceptual Design of a Charged Particle Beam Energy Spectrometer Utilizing Transition Radiation Grating", Proceedings 1995 Particle Accelerator Conference, p. 2411, (1995), BNL 61743.

X.Z. Qui, X.J. Wang, K. Batchelor, and I. Ben-Zvi, "Transition Radiation Electron Beam Diagnostic Study at the ATF", 1995 Particle Accelerator Conference, p. 2530, (1995), BNL 61850.

S. Ramamoorthy, P Pearson, and J. Smith, "Error Handling in the NSLS Control System", 1995 Particle Accelerator Conference and International Conference on High-Energy Accelerator, 4, 2250-2253, (1995), BNL 61761.

J.L. Rothman, and E.B. Blum, "Charge Balancing Fill Rate Monitor", Proceedings 1995 Particle Accelerator Conference and International Conference on High Energy Accelerators, 4, p. 2450, (1995), BNL 61760, May 1995.

J. Safranek, "A Low Emittance Lattice for the NSLS X-ray Ring", Proceedings of the 1995 IEEE Particle Accelerator Conference, pp. 266-268, (1995), BNL 61847.

J. Safranek, O. Singh, and L. Solomon, "Orbit Stability Improvement at the NSLS X-ray Ring", Proceedings of the 1995 IEEE Particle Accelerator Conference, pp. 2711-2713, BNL 61848.

J. Safranek, "Experimental Determination of Linear Optics including Quadrupole Rotations", Proceedings of the 1995 IEEE Particle Accelerator Conference, pp. 2817-2819, BNL 61853.

M.L. Shek, "Soft X-ray Studies of a c(4x2)* B-SiC(100) Surface", *Surf. Sci.*, **349**, 317-332, (1996), BNL 62177.

D. Siddons, Y. Feng, S. Sinha, E. Fullerton, G. Grubel, D. Abernathy, and J. Hastings, "X-ray Fraunhofer Diffraction Patterns from a Thin-Film Waveguide", *Appl. Phys. Lett.*, **67/24**, 3647, (1996), BNL 63146.

O. Singh, S. Krinsky, P.M. Ivanov, and E.A. Medvedko, "Orbit Compensation for the Time Varying Elliptically Polarized Wiggler", *Rev. Sci. Instrum.*, **67/9**, 1-6, (1996), BNL 63952.

O. Singh, S. Ramamoorthy, J. Sheehan, and J. Smith, "Upgrade of NSLS Timing System", 1995 Particle Accelerator Conference and International Conference on High-Energy Accelerator, 4, pp. 2223-2225, (1995), BNL 61756.

B. Sinkovic, E. Shekel, and S. Hulbert, "Spin-resolved $FeL_3M_{45}M_{45}$ Auger transition On and Off Resonance: The Effect of Exchange Correlation", *Phys. Rev.*, **B52**, 15703, (1995), BNL 62536.

J. D. Smith, S. Ramamoorthy, and Y.N. Tang, "NSLS Control System Upgrade", *Nucl. Instrum. And Meths. In Phys. Rev.*, **A352**, 114, (1994), BNL 61019.

P. Stefan and S. Krinsky, "Experience With Small-Gap Undulators", *Rev. Sci. Instrum.*, **67/9**, 3346, (1996), BNL 63150.

P.M. Stefan, S. Krinsky, G. Rakowsky, and L. Solomon, "Small Gap Undulator Experiment on the NSLS X-Ray Ring", Proceeding 1995 IEEE Particle Accelerator Conference, p. 2435, (1995), BNL 61878. May 1995.

Y.N. Tang, and J.D. Smith,. "History Data Collection, Retrieving and Display in the NSLS Control System", 1995 Particle Accelerator Conference and International Conference of High Energy Accelerators, 4, pp. 2253-2255, (1995), BNL 61757.

W. Thomlinson, "Synchrotron Radiation Applications in Medical Research", Proceedings of the Internationl Conference on Industrial Applications of Synchrotron Radiation, Hyogo Prefecture, Japan, pp. 98-126, (1996), BNL 62631.

W. Thomlinson, "Transvenous Coronary Angiography in Humans with Synchrotron Radiation", Proceedings of the International School of Physics "Enrico Fermi", Course CXXVIII-Biomedical Applications of Synchrotron Radiation, edited by E. Burattini and A. Balera, IOS Press, Washington, DC, pp. 127-153, (1996), BNL 60834.

X.J. Wang, M. Babzien, K. Batchelor, I. Ben-Zvi, R. Malone, I.V. Pogorelsky, X. Qui, J. Sheehan, J. Skaritka, and T. Srinivasan-Rao, "Experimental Chararacterization of High Brightness Electron Photoinjector", *Nucl. Instrum. & Meths.*, **A375**, 82, (1996), BNL 62623.

X.J. Wang, T. Srinivasan-Rao, K. Batchelor, M. Babzien, I. Ben-Zvi, R. Malone, I. Pogorelsky, X. Qui, J. Sheehan, and J. Skaritka, "Experimental Results of the ATF In-Line Injection System", 1995 Particle Accelerator Conference, p. 890, (1995), BNL 61743.

L. H. Yu, "An Exact Solution for Quantum Tunneling in a Dissipative System", *Phys. Rev.*, **A54**, 3779, (1996), BNL 63106.

BNL Formal and Informal Reports

F. Arfelli, C. Burns, D. Chapman, N. Gmür, R.E. Johnson, R. Menk, E. Pisano, D. Sayers, W. Thomlinson, D. Washburn, and Z. Zhong, "Data Acquisition and Analysis of Mammography Images at the NSLS", BNL 62935, (1996).

I. Ben-Zvi, and S. Krinsky, (Editors), "Program and Abstracts - 17th Intl. Free Electron Laser Conference and 2nd International FEL Users Workshop", BNL 61982, October 1995.

E.B. Blum, "Short Bunch Research at Brookhaven National Laboratory, Micro Bunches Workshop", BNL 62388, November 1995.

E.B. Blum, "Observation of Coherent Transition Radiation at the Accelerator Test Facility", BNL 62738, February 1996.

W. Broome, and J. Wang, "Reactive Robinson Instability in the NSLS X-Ray Ring", BNL 62789, January 1996.

D. Corridon, "Design of a Diagnostic Area-Type Beam Position Monitor for X-Ray Beamlines at the National Synchrotron Light Source", BNL 63383, August 1996.

N. Gmur, "Structural Biology Research at the National Synchrotron Light Source", BNL 62916.

J. Hastings, "Workshop: Research and Development Plans for High Power Spallation Neutron Testing at BNL", BNL 63614, August 1996.

NSLS Staff and Collaborators, "Lighting the Way to the Future: An Anthology of Improvements, Developments, and Research by NSLS Staff and Collaborators", BNL 63477, September 1996.

I.V. Pogorelsky, "CO_2 Laser Technology for Advanced Particle Accelerators", Presented at Meeting of the American Physics Society, BNL 63249, May 1996.

I.V. Pogorelsky, "High Intensity Laser Synchrotron X-ray Source", BNL 62447, November 1995.

X. Qiu, J. Sheehan, and J. Skaritka, "High-Brightness Electron Beam Generation Using Emittance Compensation in a High-Gradient Photocathode RF Gun", BNL 62336, October 1995.

A.G. Ruggiero, "Negative Ion Injection by Charge Exchange at 2.4 GeV", BNL 62310, October 1995.

A.G. Ruggiero, "Design Considerations on a Proton Superconducting Linac", BNL 62312, October 1995.

X.J. Wang, T. Srinivasan-Rao, K. Batchelor, M. Babzien, I. Ben-Zvi, J. Fischer, R. Malone, I. Pogorelsky, X. Qiu, J. Sheehan, and J. Skaritka, "High-Brightness Electron Beam Generation using Emittance Compensation in a High-Gradient Photocathode RF Gun", BNL 62336, May 1996.